

# **ORBITAL INTERACTIONS IN CHEMISTRY**

# **ORBITAL INTERACTIONS IN CHEMISTRY**

**Second Edition**

By

***Thomas A. Albright  
Jeremy K. Burdett  
Myung-Hwan Whangbo***

**WILEY**

Copyright © 2013 by John Wiley & Sons, Inc. All rights reserved

Published by John Wiley & Sons, Inc., Hoboken, New Jersey  
Published simultaneously in Canada

No part of this publication may be reproduced, stored in a retrieval system, or transmitted in any form or by any means, electronic, mechanical, photocopying, recording, scanning, or otherwise, except as permitted under Section 107 or 108 of the 1976 United States Copyright Act, without either the prior written permission of the Publisher, or authorization through payment of the appropriate per-copy fee to the Copyright Clearance Center, Inc., 222 Rosewood Drive, Danvers, MA 01923, (978) 750-8400, fax (978) 750-4470, or on the web at [www.copyright.com](http://www.copyright.com). Requests to the Publisher for permission should be addressed to the Permissions Department, John Wiley & Sons, Inc., 111 River Street, Hoboken, NJ 07030, (201) 748-6011, fax (201) 748-6008, or online at <http://www.wiley.com/go/permission>.

**Limit of Liability/Disclaimer of Warranty:** While the publisher and author have used their best efforts in preparing this book, they make no representations or warranties with respect to the accuracy or completeness of the contents of this book and specifically disclaim any implied warranties of merchantability or fitness for a particular purpose. No warranty may be created or extended by sales representatives or written sales materials. The advice and strategies contained herein may not be suitable for your situation. You should consult with a professional where appropriate. Neither the publisher nor author shall be liable for any loss of profit or any other commercial damages, including but not limited to special, incidental, consequential, or other damages.

For general information on our other products and services or for technical support, please contact our Customer Care Department within the United States at (800) 762-2974, outside the United States at (317) 572-3993 or fax (317) 572-4002.

Wiley also publishes its books in a variety of electronic formats. Some content that appears in print may not be available in electronic formats.  
For more information about Wiley products, visit our web site at [www.wiley.com](http://www.wiley.com).

*Library of Congress Cataloging-in-Publication Data:*

Albright, Thomas A.

Orbital interactions in chemistry / Thomas A. Albright, Jeremy K. Burdett,  
Myung-Hwan Whangbo. – 2nd edition.

pages cm

Includes index.

ISBN 978-0-471-08039-8 (hardback)

I. Molecular orbitals. I. Burdett, Jeremy K., 1947- II. Whangbo,  
Myung-Hwan. III. Title.

QD461.A384 2013

541'.28–dc23

2012040257

Printed in the United States of America

ISBN: 9780471080398

10 9 8 7 6 5 4 3 2 1

# Contents

Preface xi

About the Authors xiii

<b>Chapter 1</b>	<b>Atomic and Molecular Orbitals</b>	1
1.1	Introduction 1	
1.2	Atomic Orbitals 1	
1.3	Molecular Orbitals 7	
Problems	13	
References	14	
<b>Chapter 2</b>	<b>Concepts of Bonding and Orbital Interaction</b>	15
2.1	Orbital Interaction Energy 15	
2.1.1	Degenerate Interaction 16	
2.1.2	Nondegenerate Interaction 18	
2.2	Molecular Orbital Coefficients 20	
2.2.1	Degenerate Interaction 21	
2.2.2	Nondegenerate Interaction 22	
2.3	The Two-Orbital Problem—Summary 24	
2.4	Electron Density Distribution 26	
Problems	31	
References	31	
<b>Chapter 3</b>	<b>Perturbational Molecular Orbital Theory</b>	32
3.1	Introduction 32	
3.2	Intermolecular Perturbation 35	
3.3	Linear H <sub>3</sub> , HF, and the Three-Orbital Problem 38	
3.4	Degenerate Perturbation 43	
Problems	45	
References	46	
<b>Chapter 4</b>	<b>Symmetry</b>	47
4.1	Introduction 47	
4.2	Symmetry of Molecules 47	
4.3	Representations of Groups 53	
4.4	Symmetry Properties of Orbitals 59	
4.5	Symmetry-Adapted Wavefunctions 62	
4.6	Direct Products 65	
4.7	Symmetry Properties, Integrals, and the Noncrossing Rule 67	
4.8	Principles of Orbital Construction Using Symmetry Principles 69	
4.9	Symmetry Properties of Molecular Vibrations 73	
Problems	75	
References	77	

<b>Chapter 5   Molecular Orbital Construction from Fragment Orbitals</b>	<b>78</b>
5.1 Introduction 78	
5.2 Triangular H <sub>3</sub> 78	
5.3 Rectangular and Square Planar H <sub>4</sub> 82	
5.4 Tetrahedral H <sub>4</sub> 84	
5.5 Linear H <sub>4</sub> 86	
5.6 Pentagonal H <sub>5</sub> and Hexagonal H <sub>6</sub> 88	
5.7 Orbitals of Cyclic Systems 91	
Problems 94	
References 96	
<b>Chapter 6   Molecular Orbitals of Diatomic Molecules and Electronegativity Perturbation</b>	<b>97</b>
6.1 Introduction 97	
6.2 Orbital Hybridization 98	
6.3 Molecular Orbitals of Diatomic Molecules 99	
6.4 Electronegativity Perturbation 105	
6.5 Photoelectron Spectroscopy and Through-Bond Conjugation 112	
Problems 118	
References 122	
<b>Chapter 7   Molecular Orbitals and Geometrical Perturbation</b>	<b>123</b>
7.1 Molecular Orbitals of AH <sub>2</sub> 123	
7.2 Geometrical Perturbation 128	
7.3 Walsh Diagrams 131	
7.4 Jahn-Teller Distortions 134	
7.4.1 First-Order Jahn-Teller Distortion 135	
7.4.2 Second-Order Jahn-Teller Distortion 136	
7.4.3 Three-Center Bonding 139	
7.5 Bond Orbitals and Photoelectron Spectra Of AH <sub>2</sub> Molecules 141	
Problems 147	
References 150	
<b>Chapter 8   State Wavefunctions and State Energies</b>	<b>151</b>
8.1 Introduction 151	
8.2 The Molecular Hamiltonian and State Wavefunctions 152	
8.3 Fock Operator 154	
8.4 State Energy 156	
8.5 Excitation Energy 157	
8.6 Ionization Potential and Electron Affinity 160	
8.7 Electron Density Distribution and Magnitudes of Coulomb and Exchange Repulsions 160	
8.8 Low versus High Spin States 162	
8.9 Electron-Electron Repulsion and Charged Species 164	
8.10 Configuration Interaction 165	
8.11 Toward More Quantitative Treatments 170	
8.12 The Density Functional Method 174	
Problems 176	
References 177	

<b>Chapter 9   Molecular Orbitals of Small Building Blocks</b>	<b>179</b>
9.1 Introduction 179	
9.2 The AH System 179	
9.3 Shapes of AH <sub>3</sub> Systems 182	
9.4 π-Bonding Effects of Ligands 190	
9.5 The AH <sub>4</sub> System 193	
9.6 The AH <sub>n</sub> Series—Some Generalizations 198	
Problems 201	
References 202	
<b>Chapter 10   Molecules with Two Heavy Atoms</b>	<b>204</b>
10.1 Introduction 204	
10.2 A <sub>2</sub> H <sub>6</sub> Systems 204	
10.3 12-Electron A <sub>2</sub> H <sub>4</sub> Systems 208	
10.3.1 Sudden Polarization 211	
10.3.2 Substituent Effects 214	
10.3.3 Dimerization and Pyramidalization of AH <sub>2</sub> 218	
10.4 14-Electron AH <sub>2</sub> BH <sub>2</sub> Systems 220	
10.5 AH <sub>3</sub> BH <sub>2</sub> Systems 223	
10.6 AH <sub>3</sub> BH Systems 232	
Problems 234	
References 238	
<b>Chapter 11   Orbital Interactions through Space and through Bonds</b>	<b>241</b>
11.1 Introduction 241	
11.2 In-Plane σ orbitals of Small Rings 241	
11.2.1 Cyclopropane 241	
11.2.2 Cyclobutane 246	
11.3 Through-Bond Interaction 253	
11.3.1 The Nature of Through-Bond Coupling 253	
11.3.2 Other Through-Bond Coupling Units 256	
11.4 Breaking a C—C Bond 258	
Problems 265	
References 269	
<b>Chapter 12   Polyenes and Conjugated Systems</b>	<b>272</b>
12.1 Acyclic Polyenes 272	
12.2 Hückel Theory 274	
12.3 Cyclic Systems 277	
12.4 Spin Polarization 285	
12.5 Low- versus High-Spin States in Polyenes 289	
12.6 Cross-Conjugated Polyenes 291	
12.7 Perturbations of Cyclic Systems 294	
12.8 Conjugation in Three Dimensions 303	
Problems 306	
References 310	
<b>Chapter 13   Solids</b>	<b>313</b>
13.1 Energy Bands 313	
13.2 Distortions in One-Dimensional Systems 328	
13.3 Other One-Dimensional Systems 334	
13.4 Two- and Three-Dimensional Systems 339	

13.5 Electron Counting and Structure 350	
13.6 High-Spin and Low-Spin Considerations 353	
Problems 353	
References 357	
<b>Chapter 14   Hypervalent Molecules</b>	<b>359</b>
14.1 Orbitals of Octahedrally Based Molecules 359	
14.2 Solid-State Hypervalent Compounds 373	
14.3 Geometries of Hypervalent Molecules 383	
Problems 392	
References 399	
<b>Chapter 15   Transition Metal Complexes: A Starting Point at the Octahedron</b>	<b>401</b>
15.1 Introduction 401	
15.2 Octahedral $ML_6$ 402	
15.3 $\pi$ -Effects in an Octahedron 406	
15.4 Distortions from an Octahedral Geometry 416	
15.5 The Octahedron in the Solid State 423	
Problems 431	
References 434	
<b>Chapter 16   Square Planar, Tetrahedral <math>ML_4</math> Complexes, and Electron Counting</b>	<b>436</b>
16.1 Introduction 436	
16.2 The Square Planar $ML_4$ Molecule 436	
16.3 Electron Counting 438	
16.4 The Square Planar-Tetrahedral $ML_4$ Interconversion 448	
16.5 The Solid State 453	
Problems 460	
References 463	
<b>Chapter 17   Five Coordination</b>	<b>465</b>
17.1 Introduction 465	
17.2 The $C_{4v}$ $ML_5$ Fragment 466	
17.3 Five Coordination 468	
17.4 Molecules Built Up from $ML_5$ Fragments 480	
17.5 Pentacoordinate Nitrosyls 489	
17.6 Square Pyramids in The Solid State 492	
Problems 498	
References 500	
<b>Chapter 18   The <math>C_{2v}</math> <math>ML_3</math> Fragment</b>	<b>503</b>
18.1 Introduction 503	
18.2 The Orbitals of A $C_{2v}$ $ML_3$ Fragment 503	
18.3 $ML_3$ -Containing Metallacycles 511	
18.4 Comparison of $C_{2v}$ $ML_3$ and $C_{4v}$ $ML_5$ Fragments 518	
Problems 523	
References 525	
<b>Chapter 19   The <math>ML_2</math> and <math>ML_4</math> Fragments</b>	<b>527</b>
19.1 Development of the $C_{2v}$ $ML_4$ Fragment Orbitals 527	
19.2 The $Fe(CO)_4$ Story 529	
19.3 Olefin- $ML_4$ Complexes and $M_2L_8$ Dimers 533	
19.4 The $C_{2v}$ $ML_2$ Fragment 537	

19.5 Polyene-ML <sub>2</sub> Complexes	539
19.6 Reductive Elimination and Oxidative Addition	552
Problems	561
References	566
<b>Chapter 20   Complexes of ML<sub>3</sub>, MCp and Cp<sub>2</sub>M</b>	<b>570</b>
20.1 Derivation of Orbitals for a C <sub>3v</sub> ML <sub>3</sub> Fragment	570
20.2 The CpM Fragment Orbitals	582
20.3 Cp <sub>2</sub> M and Metallocenes	592
20.4 Cp <sub>2</sub> ML <sub>n</sub> Complexes	595
Problems	607
References	613
<b>Chapter 21   The Isolobal Analogy</b>	<b>616</b>
21.1 Introduction	616
21.2 Generation of Isolobal Fragments	617
21.3 Caveats	621
21.4 Illustrations of the Isolobal Analogy	623
21.5 Reactions	634
21.6 Extensions	639
Problems	646
References	649
<b>Chapter 22   Cluster Compounds</b>	<b>653</b>
22.1 Types of Cluster Compounds	653
22.2 Cluster Orbitals	657
22.3 Wade's Rules	660
22.4 Violations	671
22.5 Extensions	677
Problems	681
References	687
<b>Chapter 23   Chemistry on the Surface</b>	<b>691</b>
23.1 Introduction	691
23.2 General Structural Considerations	693
23.3 General Considerations of Adsorption on Surfaces	696
23.4 Diatomics on a Surface	699
23.5 The Surface of Semiconductors	721
Problems	728
References	731
<b>Chapter 24   Magnetic Properties</b>	<b>735</b>
24.1 Introduction	735
24.2 The Magnetic Insulating State	736
24.2.1 Electronic Structures	736
24.2.2 Factors Affecting the Effective On-Site Repulsion	738
24.2.3 Effect of Spin Arrangement on the Band Gap	740
24.3 Properties Associated with the Magnetic Moment	741
24.3.1 The Magnetic Moment	741
24.3.2 Magnetization	743
24.3.3 Magnetic Susceptibility	743
24.3.4 Experimental Investigation of Magnetic Energy Levels	745

<b>24.4 Symmetric Spin Exchange</b>	<b>745</b>
24.4.1 Mapping Analysis for a Spin Dimer	745
24.4.2 Through-Space and Through-Bond Orbital Interactions Leading to Spin Exchange	748
24.4.3 Mapping Analysis Based on Broken-Symmetry States	751
<b>24.5 Magnetic Structure</b>	<b>754</b>
24.5.1 Spin Frustration and Noncollinear Spin Arrangement	754
24.5.2 Long-Range Antiferromagnetic Order	755
24.5.3 Ferromagnetic and Ferromagnetic-Like Transitions	759
24.5.4 Typical Cases Leading to Ferromagnetic Interaction	760
24.5.5 Short-Range Order	763
<b>24.6 The Energy Gap in the Magnetic Energy Spectrum</b>	<b>763</b>
24.6.1 Spin Gap and Field-Induced Magnetic Order	763
24.6.2 Magnetization Plateaus	765
<b>24.7 Spin–Orbit Coupling</b>	<b>766</b>
24.7.1 Spin Orientation	766
24.7.2 Single-Ion Anisotropy	770
24.7.3 Uniaxial Magnetism versus Jahn–Teller Instability	771
24.7.4 The Dzyaloshinskii–Moriya Interaction	774
24.7.5 Singlet–Triplet Mixing Under Spin–Orbit Coupling	777
<b>24.8 What Appears versus What Is</b>	<b>778</b>
24.8.1 Idle Spin in Cu <sub>3</sub> (OH) <sub>4</sub> SO <sub>4</sub>	778
24.8.2 The FM–AFM versus AFM–AFM Chain	779
24.8.3 Diamond Chains	780
24.8.4 Spin Gap Behavior of a Two-Dimensional Square Net	782
<b>24.9 Model Hamiltonians Beyond the Level of Spin Exchange</b>	<b>785</b>
<b>24.10 Summary Remarks</b>	<b>785</b>
<b>Problems</b>	<b>786</b>
<b>References</b>	<b>789</b>

**Appendix I Perturbational Molecular Orbital Theory** 793

**Appendix II Some Common Group Tables** 803

**Appendix III Normal Modes for Some Common Structural Types** 808

**Index** 813

# Preface

Use of molecular orbital theory facilitates an understanding of physical properties associated with molecules and the pathways taken by chemical reactions. The gigantic strides in computational resources as well as a plethora of standardized quantum chemistry packages have created a working environment for theoreticians and experimentalists to explore the structures and energy relationships associated with virtually any molecule or solid. There are many books that cover the fundamentals of quantum mechanics and offer summaries of how to tackle computational problems. It is normally a straightforward procedure to “validate” a computational procedure for a specific problem and then compute geometries and associated energies. There are also prescriptions for handling solvation. So, does it mean that all a chemist needs to do is to plug the problem into the “black-box” and he or she will receive understanding in terms of a pile of numbers? We certainly think not.

This book takes the problem one step further. We shall study in some detail the mechanics behind the molecular orbital level structures of molecules. We shall ask why these orbitals have a particular form and are energetically ordered in the way that they are, and whether they are generated by a Hartree–Fock (HF), density functional, or semiempirical technique. Furthermore, we want to understand in a qualitative or semiquantitative sense what happens to the shape and energy of orbitals when the molecule distorts or undergoes a chemical reaction. These models are useful to the chemical community. They collect data to generate patterns and ideally offer predictions about the directions of future research. An experimentalist must have an understanding of why molecules of concern react the way they do, as well as what determines their molecular structure and how this influences reactivity. So too, it is the duty and obligation of a theorist (or an experimentalist doing calculations on the side) to understand why the numbers from a calculation come out the way they do. Models in this vein must be simple. The ones we use here are based on concepts such as symmetry, overlap, and electronegativity. The numerical and computational aspects of the subject in this book are deliberately de-emphasized. In fact there were only a couple of computational numbers cited in the first edition. People sometimes expressed the opinion that the book was based on extended Hückel theory. It, in fact, was and is not. An even more parochial attitude (and unfortunately common one) was expressed recently “I imagine that there are still people that do HF calculations too. But these days they cannot be taken too seriously.” In this edition, computational results from a wide variety of levels have been cited. This is certainly not to say that computations at a specific level of theory will accurately reproduce experimental data. It is reassuring to chemists that, say, a geometry optimization replicates the experimental structure for a molecule. But that does not mean that the calculation tells the user why the molecule does have the geometry that it does or what other molecules have a similar bonding scheme. The goal of our approach is the generation of global ideas that will lead to a qualitative understanding of electronic structure no matter what computational levels have been used.

An important aim of this book is then to show how common orbital situations arise throughout the whole chemical spectrum. For example, there are isomorphisms between the electronic structure of  $\text{CH}_2$ ,  $\text{Fe}(\text{CO})_4$ , and  $\text{Ni}(\text{PR}_3)_2$  and between the Jahn–Teller instability in cyclobutadiene and the Peierls distortion in solids. These relationships will be highlighted, and to a certain extent, we have

chosen problems that allow us to make such theoretical connections across the traditional boundaries between the subdisciplines of chemistry.

Qualitative methods of understanding molecular electronic structures are based on either valence bond theory promoted largely by Linus Pauling or delocalized molecular orbital theory following the philosophy suggested by Robert Mulliken. The orbital interaction model that we use in our book, which is based on delocalized molecular orbital theory, was largely pioneered by Roald Hoffmann and Kenichi Fukui. This is one of several models that can be employed to analyze the results of computations. This model is simple and yet very powerful. Although chemists are more familiar with valence bond and resonance concepts, the delocalized orbital interaction model has many advantages. In our book, we often point out links between the two viewpoints.

There are roughly three sections in this book. The first develops the models we use in a formal way and serves as a review of molecular orbital theory. The second covers the organic main group areas with a diversion into solids. Typical concerns in the inorganic–organometallic fields are covered in the third section along with cluster chemistry, chemistry on the surface, and magnetism in solids. Each section is essentially self-contained, but we hope that the organic chemist will read on further into the inorganic–organometallic chapters and vice versa. For space considerations, many interesting problems were not included. We have attempted to treat those areas of chemistry that can be appreciated by a general audience. Nevertheless, the strategies and arguments employed should cover many of the structure and reactivity problems that one is likely to encounter. We hope that readers will come away from this work with the idea that there is an underlying structure to all of chemistry and that the conventional divisions into organic, inorganic, organometallic, and solid state are largely artificial. Introductory material in quantum mechanics along with undergraduate organic and inorganic chemistry constitutes the necessary background information for this book.

The coverage in the second edition of this book has been considerably expanded. The number of papers that contain quantum calculations has exploded since the first edition 28 years ago and, therefore, more examples have been given especially in the inorganic–organometallic areas. We have emphasized trends more than before across the Periodic Table or varying substituents. A much fuller treatment of group theory is given and the results from photoelectron spectroscopy have been highlighted. Each self-contained chapter comes with problems at the end, the solutions to which are located at [ftp://ftp.wiley.com/public/sci\\_tech\\_med/orbital\\_interactions\\_2e](ftp://ftp.wiley.com/public/sci_tech_med/orbital_interactions_2e). Finally, two new chapters, one on surface science and the other on magnetism, have been added.

It is impossible to list all the people whose ideas we have borrowed or adapted in this book. We do, however, owe a great debt to a diverse collection of chemists who have gone before us and have left their mark on particular chemical problems. Dennis Lichtenberger graciously provided us with many of the photoelectron spectra displayed here. The genesis of this book came about when the three of us worked at Cornell University with Roald Hoffmann. This book is dedicated to the memory of our old friend and colleague, Jeremy Burdett, who passed away on June 23, 1997. We would like to thank our wives, Janice and Jin-Ok, as well as our children Alex, Holly, Robby, Jonathan, Rufus, Harry, Jennifer and Albert, for their patience and moral support.

THOMAS A. ALBRIGHT  
JEREMY K. BURDETT\*  
MYUNG-HWAN WHANGBO

April 2012

\* Deceased

## About the Authors

**Thomas Albright** is currently Professor Emeritus at the Department of Chemistry, University of Houston. He has been awarded the Camille and Henry Dreyfus Teacher Scholar and Alfred P. Sloan Research fellowships. He is the author and coauthor of 118 publications. He has been elected to serve on the Editorial Advisory Board of *Organometallics* and the US National Representative to IUPAC. His current research is directed toward reaction dynamics in organometallic chemistry. He received his PhD degree at the University of Delaware and did postdoctoral research with Roald Hoffmann at Cornell.

**Jeremy Burdett\*** was a Professor and Chair in the Chemistry Department, University of Chicago. He was awarded the Tilden Medal and Meldola Medal by the Royal Chemical Society. He was a fellow of the Camille and Henry Dreyfus Teacher Scholar, the John Guggenheim Memorial, and the Alfred P. Sloan Research foundations. He has published over 220 publications. He received his PhD degree at the University of Cambridge and did postdoctoral research with Roald Hoffmann at Cornell.

**Myung-Hwan Whangbo** is a Distinguished Professor in the Chemistry Department at North Carolina State University. He has been awarded the Camille and Henry Dreyfus Fellowship, the Alexander von Humboldt Research Award to Senior US Scientists, and the Ho-Am Prize for Basic Science. He is the author and coauthor of over 600 journal articles and monographs. His current research interests lie in the areas of solid-state theory and magnetism. He has been elected to the editorial advisory board of *Inorganic Chemistry*, *Solid State Sciences*, *Materials Research Bulletin*, and *Theoretical Chemistry Accounts*. He received his PhD degree at Queen's University and did postdoctoral research with Roald Hoffmann at Cornell.

\* Deceased June 23, 1997.

# Atomic and Molecular Orbitals

---

## 1.1 INTRODUCTION

---

The goal of this book is to show the reader how to work with and understand the electronic structures of molecules and solids. It is not our intention to present a formal discussion on the tenets of quantum mechanics or to discuss the methods and approximations used to solve the molecular Schrödinger equation. There are several excellent books [1–6], which do this, and many “canned” computer programs that are readily available to carry out the numerical calculations at different levels of sophistication with associated user manuals [7–9]. The real challenge, and the motivation behind this volume, is to be able to understand where the numbers generated by such computations actually come from. The first part of the book contains some mathematical material using which we have built a largely qualitative discussion of molecular orbital (MO) structure. Let us see how the molecular orbitals of complex molecules or solids may be constructed from smaller portions using concepts from perturbation theory and symmetry. Furthermore, we show how these orbitals change as a function of a geometrical perturbation, the substitution of one atom for another, or as a result of the presence of a second molecule as in a chemical reaction. Many concepts and results together form a common thread, which enables different fields of chemistry to be linked in a satisfying way. The emphasis of this book is on qualitative features and not on quantitative details. Our feeling is that just this perspective leads to predictive capabilities and insight.

---

## 1.2 ATOMIC ORBITALS

---

The molecular orbitals of a molecule are usually expressed as a linear combination of the atomic orbitals (LCAOs) centered on its constituent atoms, which is discussed in

*Orbital Interactions in Chemistry*, Second Edition.

Thomas A. Albright, Jeremy K. Burdett, and Myung-Hwan Whangbo.

© 2013 John Wiley & Sons, Inc. Published 2013 by John Wiley & Sons, Inc.

**TABLE 1.1** Angular Components of Some Common Wavefunctions

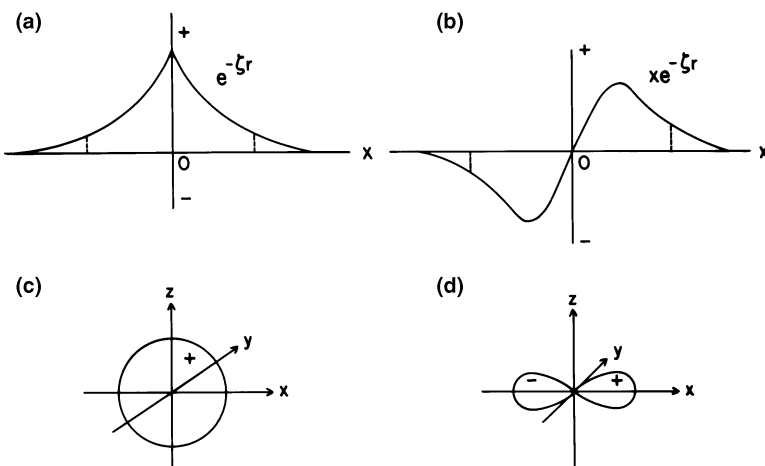
Orbital Type		Expression for $Y$
s		
$p_x$	$x/r$	$\sin \theta \cos \phi$
$p_y$	$y/r$	$\sin \theta \sin \phi$
$p_z$	$z/r$	$\cos \theta$
$d_{x^2-y^2}$	$(x^2 - y^2)/r^2$	$\sin^2 \theta \cos 2\phi$
$d_{z^2}$	$(3z^2 - r^2)/r^2$	$3\cos^2 \theta - 1$
$d_{xy}$	$xy/r^2$	$\sin^2 \theta \sin 2\phi$
$d_{xz}$	$xz/r^2$	$\sin \theta \cos \theta \cos \phi$
$d_{yz}$	$yz/r^2$	$\sin \theta \cos \theta \sin \phi$

Section 1.3. These atomic orbitals (AOs) using polar coordinates have the form shown in equation 1.1. This is a simple product of a function,  $R(r)$ ,

$$\chi(r, \theta, \phi) = R(r)Y(\theta, \phi) \quad (1.1)$$

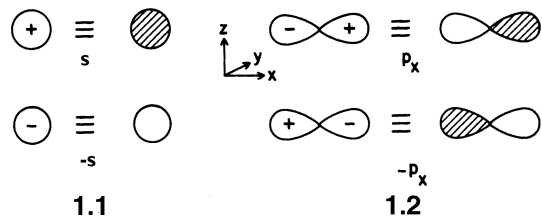
which only depends on the distance,  $r$ , of the electron from the nucleus, and a function  $Y(\theta, \phi)$ , which contains all the angular information needed to describe the wavefunction. The Schrödinger wave equation may only be solved exactly for one-electron (hydrogenic) atoms (e.g., H, Li<sup>2+</sup>) where analytical expressions for  $R$  and  $Y$  are found. For many-electron atoms, the angular form of the atomic orbitals is the same as for the one-electron atom (Table 1.1), but now, the radial function  $R(r)$  is approximated in some way as shown later. The center column in Table 1.1 gives the form of  $Y$  in Cartesian coordinate space while that in the far right-hand side uses polar coordinates.

Figure 1.1a shows a plot of the amplitude of the wavefunction  $\chi$  for an electron in a 1s orbital as a function of distance from the nucleus. This has been chosen to be the  $x$ -axis of an arbitrary coordinate system. With increasing  $x$ , the amplitude of  $\chi$  sharply decreases in an exponential fashion and becomes negligible outside a certain region indicated by the dashed lines. The boundary surface of the s orbital, outside of which the wavefunction has some critical (small) value, is shown in Figure 1.1c. The corresponding diagrams for a 2p<sub>x</sub> orbital are shown in Figure 1.1b, d. Note that the

**FIGURE 1.1**

Radial part of the wavefunction for a 1s (a) and 2p (b) orbitals showing an arbitrary cutoff beyond which  $R(r)$  is less than some small value. The surface in three dimensions defined by this radial cutoff is shown in (c) for the 1s orbital and in (d) for the 2p orbital.

wavefunction for this  $p$  orbital changes sign when  $x \rightarrow -x$ . It is often more convenient to represent the sign of the wavefunction by the presence or absence of shading of the orbital lobes as in 1.1 and 1.2. The characteristic features of  $s$ ,  $p$ , and  $d$  orbitals



using this convention are shown in Figure 1.2 where the positive lobes have been shaded. Each representation in Figure 1.2 then represents an atomic orbital with a positive coefficient. Squaring the wavefunction and integrating over a volume element gives the probability of finding an electron within that element. So, there is a correspondence between the pictorial representations in Figure 1.2 and the electron density distribution in that orbital. In particular, the probability function or electron density is exactly zero for the  $p_x$  orbital at the nucleus ( $x = 0$ ). In fact, the wavefunction is zero at all points on the  $yz$  plane at the nucleus. This is the definition of a nodal plane. In general, an  $s$  orbital has no such angular nodes, a  $p$  orbital one node, and a  $d$  orbital two. The exact form of  $R(r)$  for a  $1s$  hydrogenic atomic orbital is

$$R(r)_{1s} = \frac{1}{\sqrt{\pi}} \left( \frac{Z}{a_0} \right)^{3/2} \exp\left(-\frac{Zr}{a_0}\right)$$

while that for a  $2s$  atomic orbital is

$$R(r)_{2s} = \frac{1}{4\sqrt{2\pi}} \left( \frac{Z}{a_0} \right)^{3/2} \left( 2 - \frac{Zr}{a_0} \right) \exp\left(-\frac{Zr}{2a_0}\right)$$

where  $a_0$  is 1 bohr (i.e.,  $0.5292 \text{ \AA}$ ) and  $Z$  is the nuclear charge. When  $r = 2a_0/Z$ , the wavefunction is zero for the  $2s$  function. This defines a radial node. In general, an

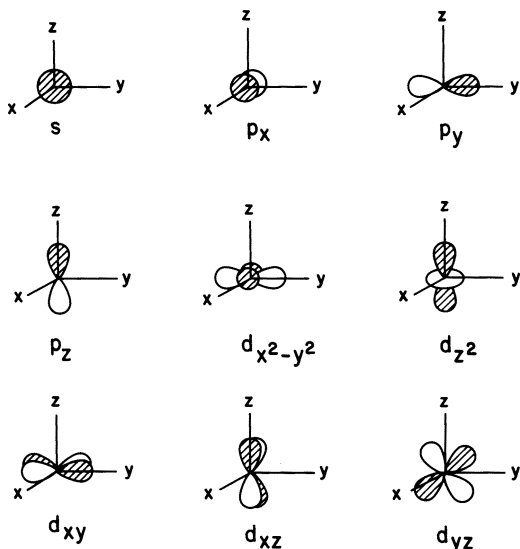


**FIGURE 1.2**

Atomic  $s$ ,  $p$ , and  $d$  orbitals drawn using the shading convention described in the text.

atomic wavefunction with quantum numbers  $n, l, m$  will have  $n - 1$  nodes altogether, of which the  $l = 0$  are angular nodes, and, therefore,  $n - l - 1$  are radial nodes. (Sometimes it is stated that there are  $n$  nodes altogether. In this case, the node that always occurs as  $r \rightarrow \infty$  is included in the count.) Contour plots of some common atomic orbitals are illustrated in Figure 1.3. The solid lines represent positive values of the wavefunction and the dashed lines negative ones. Dotted lines show the angular nodes. One important feature to notice is that the  $2s$  atomic orbital is more diffuse than the  $1s$  one. A probability density, defined as the probability of finding an electron within a finite volume element, is given for a hydrogenic atom by  $R_{n,l}^2(r)r^2$ . The maximum for the plot of this function when  $Z = 1$  occurs at  $1a_0$  for the  $1s$  orbital and  $5.2a_0$  for the  $2s$  orbital. The maximum for the  $2p$  function ( $Z = 1$ ) occurs at  $4a_0$ . These maxima correspond to the most probable distance of finding the electron from the nucleus, in a sense the radius associated with the electron. The value of the radius changes a little when the angular quantum number  $l$  varies. However, as one proceeds down a column in the periodic table (i.e., the principal quantum number  $n$  is larger), the valence orbitals become progressively more diffuse.

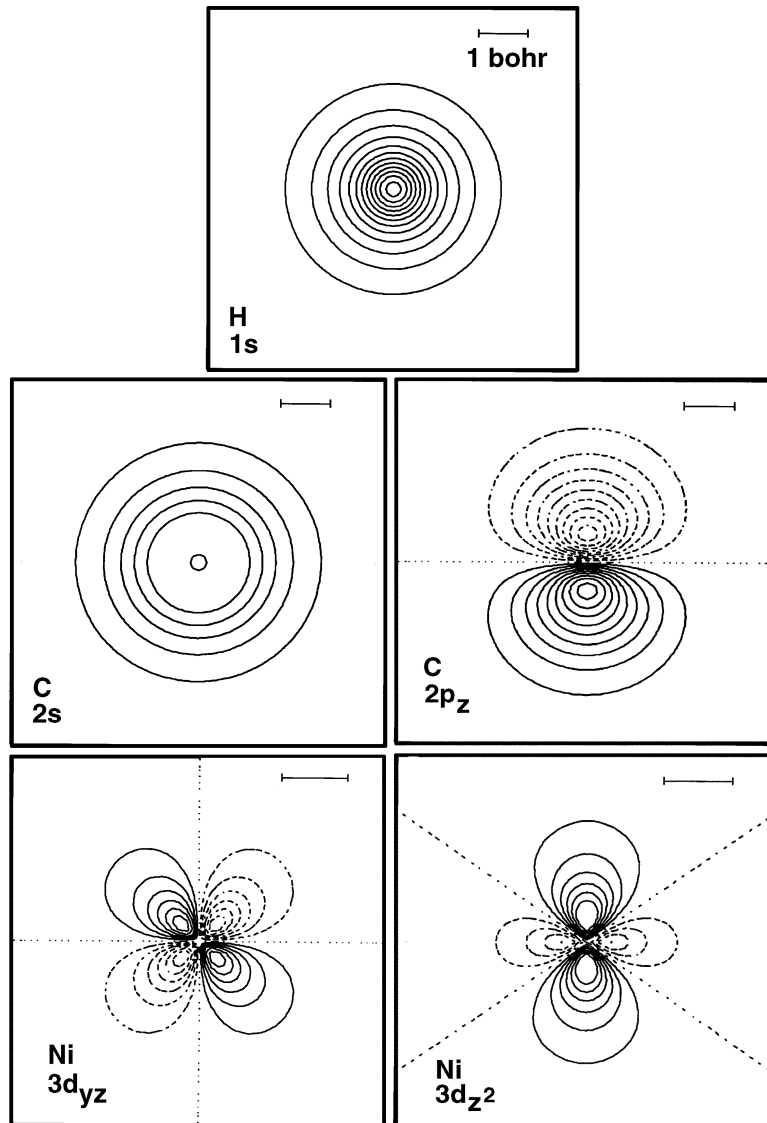


**FIGURE 1.3**

Contour plots for some common atomic orbitals. The solid lines are positive values of the wavefunction and dashed lines correspond to negative ones. The dotted lines plot angular nodes. The distance marker in each plot represents 1 bohr and the value of the smallest contour is  $1 \text{ bohr}^{3/2}$  for the  $s$  and  $p$  atomic orbitals and  $2 \text{ bohr}^{3/2}$  for the two  $d$  atomic orbitals. The value of each successive contour is  $1/2$  of the value of the inner one. These orbitals are STO-3G functions; therefore, there is no radial node associated with the C  $2s$  orbital.

The two nodal planes for the  $d_{yz}$  (as well as for  $d_{xy}$ ,  $d_{xz}$ , and  $d_{x^2-y^2}$ ) are at right angles to each other. There are two nodal cones associated with the  $d_{z^2}$  atomic orbital (see the representation in Figure 1.2). In the contour plot of Figure 1.3, the angle made between the node and the z-axis is  $54.73^\circ$ .

As mentioned earlier, the radial function  $R(r)$  for many-electron atoms needs to be approximated in some way. The atomic orbitals most frequently employed in molecular calculations are Slater type orbitals (STOs) and Gaussian type orbitals (GTOs). Their mathematical form makes them relatively easy, especially the latter, to handle in computer calculations. An STO with principal quantum number  $n$  is written as

$$\chi(r,\theta,\phi) \propto r^{n-1} \exp(-\zeta r) Y(\theta,\phi) \quad (1.2)$$

where  $\zeta$  is the orbital exponent. The value of  $\zeta$  can be obtained by applying the variational theorem to the atomic energy evaluated using the wavefunction of equation 1.2. This theorem tells us that an approximate wavefunction will always overestimate the energy of a given system. So, minimization of the energy with respect to the variational parameter  $\zeta$  will lead to determination of the best wavefunction of this type. A listing of the energy optimized  $\zeta$  values for the neutral main group atoms in the periodic table [10] is shown in 1.3. The value of

**This probably refers to the outmost orbital, because core orbitals should be more compact.**

<b>H</b> 1.30								<b>He</b> 1.69
<b>Li</b> 0.64	<b>Be</b> 0.96	<b>B</b> 1.29 1.21	<b>C</b> 1.61 1.57	<b>N</b> 1.92 1.92	<b>O</b> 2.24 2.23	<b>F</b> 2.56 2.55	<b>Ne</b> 2.88 2.88	
<b>Na</b> 0.84	<b>Mg</b> 1.10	<b>Al</b> 1.37 1.36	<b>Si</b> 1.63 1.43	<b>P</b> 1.88 1.63	<b>S</b> 2.12 1.83	<b>Cl</b> 2.36 2.04	<b>Ar</b> 2.59 2.25	
<b>K</b> 0.87	<b>Ca</b> 1.10	<b>Ga</b> 1.76 1.55	<b>Ge</b> 2.01 1.70	<b>As</b> 2.23 1.89	<b>Se</b> 2.44 2.07	<b>Br</b> 2.64 2.26	<b>Kr</b> 2.83 2.44	
<b>Rb</b> 1.01	<b>Sr</b> 1.21	<b>In</b> 1.90 1.68	<b>Sn</b> 2.13 1.82	<b>Sb</b> 2.32 2.00	<b>Te</b> 2.51 2.16	<b>I</b> 2.68 2.32	<b>Xe</b> 2.84 2.48	
<b>Cs</b> 1.06	<b>Ba</b> 1.21	<b>Tl</b> 2.37 1.97	<b>Pb</b> 2.57 2.17	<b>Bi</b> 2.76 2.29				

### 1.3

$\zeta$  for the valence s orbital is directly below the atomic symbol and that for the valence p below it. There are no entries for the valence p atomic orbitals in groups 1 and 2 since there are no p electrons for the neutral atoms in their ground state; however, one would certainly want to include these orbitals in a molecular calculation. Note from the functional form of equation 1.2 that when  $\zeta$  becomes larger, the atomic orbital is more contracted. Therefore, in 1.3,  $\zeta$  is larger going from left to right across a column in the periodic table; it scales similar to the electronegativity of the atom. The  $r^{n-1}$  factor in the radial portion of the STO ensures that the orbital will become more diffuse and have a maximal probability at

a farther distance from the nucleus as one goes down a column. In fact, that distance,  $r_{\max}$ , is given by

$$r_{\max} = \frac{n^2 a_0}{Z^*} \quad (1.3)$$

where the effective nuclear charge  $Z^*$  is given by the nuclear charge  $Z$  minus the screening constant  $S$ , which commonly is determined by a set of empirical rules [4,5] devised by Slater or more realistic ones from Clementi and Raimondi [11]. Notice also from 1.3 that the values of  $\zeta$  for the  $s$  and  $p$  atomic orbitals of an atom are increasingly more dissimilar as one goes down from the second row. This also occurs with  $Z^*$  using the Clementi and Raimondi values. In particular, the valence  $s$  orbital becomes more contracted than the  $p$ . We have used this result in Chapter 7. A simplified rationale for this behavior can be constructed [12] along the following lines. There is a Pauli repulsion experienced by valence electrons which prevents them from penetrating into the core, since atomic orbitals with the same angular quantum number must be orthogonal. There is, however, a special situation for the first row elements. The  $2p$  atomic orbitals have no corresponding core electrons, so they do not experience the Pauli repulsion that the  $2s$  electrons do from the  $1s$  core. The sizes for the  $2s$  and  $2p$  atomic orbitals in the first row are then similar, whereas in the remaining portion of the periodic table, both  $s$  and  $p$  core electrons exist and the valence  $p$  functions are more diffuse than the  $s$ . The STOs in equation 1.2 have no radial nodes, unlike their hydrogenic counterparts. This does not cause any particular problem in a calculation for an atom with, say,  $1s$  and  $2s$  atomic orbitals because of the orthogonality constraint, which is presented in Section 1.3. Sometimes, one may wish to be more exact and choose a double zeta basis set for our molecular calculation made up of wavefunctions of the type

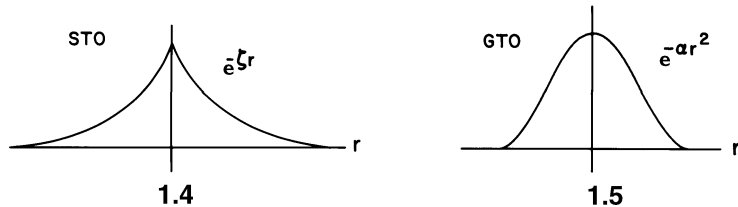
$$\chi \propto r^{n-1} [c_1 \exp(-\zeta_1 r) + c_2 \exp(-\zeta_2 r)] Y(\theta, \phi) \quad (1.4)$$

where now the atomic energy has been minimized with respect to  $\zeta_1$  and  $\zeta_2$ . This gives the wavefunction greater flexibility to expand or contract when more or less electron density, respectively, becomes concentrated on the atomic center in a molecule. For example, the valence atomic orbitals of carbon for  $\text{CH}_3^-$  should be more diffuse than those for  $\text{CH}_3^+$  because of the presence of two additional electrons. A double or triple zeta basis set allows for this. Furthermore, the STOs for the  $d$  orbitals in the transition metals yield radial distributions, which mimic full atomic calculations only when a double zeta formulation is used. Often it is found that observables such as molecular geometry or electron correlation calculations are best carried out by ab initio calculations if “polarization” functions are added to the basis set. For example, for carbon, nitrogen, and oxygen atoms ( $n=2$ ), we might add  $3d$  functions that have the angular function,  $Y$ , corresponding to a  $d$  orbital and the radial part of equation 1.2 for  $n=3$ . Commonly,  $p$  functions are added to the basis set for hydrogen atoms. These polarization functions will lower the total energy calculated for the molecule according to the variation principle, and their inclusion may lead to a better matching of observed and calculated geometries. However, these polarization functions do not generally mix strongly into the occupied molecular orbitals and are not chemically significant. The increased angular nodes of polarization functions tailor the electron density.

A general expression for a Gaussian type orbital is

$$\chi(x, y, z) \propto x^i y^j z^k \exp(-\alpha r^2) \quad (1.5)$$

where  $i, j, k$  are positive integers or zero and represent the angular portion using Cartesian coordinates. Here  $\alpha$  is the orbital exponent. Orbitals of  $s$ ,  $p$ , and  $d$  type result when  $i+j+k=0, 1, 2$ , respectively. For example, a  $p_x$  orbital results for  $i=1$  and  $j=k=0$ . The one major difference between STOs and GTOs is shown in 1.4 and 1.5. Unlike GTOs, STOs are not smooth functions at the origin like their



hydrogenic counterparts. The great convenience of GTOs, however, lies in the fact that evaluation of the molecular integrals needed in ab initio calculations is performed much more efficiently if GTOs are used. In practice, the functional behavior of an STO is simulated by a number of GTOs with different orbital exponents (equation 1.6)

$$\exp(-\zeta r) \approx c_1 \exp(-\alpha_1 r^2) + c_2 \exp(-\alpha_2 r^2) + \dots \quad (1.6)$$

where GTOs with large and small exponents are designed to fit the center and tail portions, respectively, of an STO. If  $n$  GTOs are used to fit each STO, then the atomic wavefunctions are of STO- $nG$  quality, using terminology in current usage. The contour plots in Figure 1.3 are in fact STO-3G orbitals. A very common basis set for the main group elements is designated as 3-21G. Here, all orbitals corresponding to the core electrons consist of three primitive Gaussian functions contracted as in equation 1.6 while the valence atomic orbitals are constructed by two primitive Gaussians contracted together and a single Gaussian function which is more diffuse. Thus, they are of the “double zeta quality” for the valence region. A much more accurate basis, normally restricted to atoms of the first and second rows in the periodic table, is 6-311G\*\*. Now there are six primitive Gaussians contracted to one for the core, a “triple zeta” formulation for the valence where three, one, and one Gaussians are used, and  $d$  polarization functions are added for all atoms except hydrogen, which uses  $p$  functions. There is considerable choice as to the basis set (equations 1.2–1.6) and indeed of the exponents,  $\zeta$ , themselves. In practice, the details of the basis set chosen for a given problem rely heavily on previous experience [6,7,13,14].

### 1.3 MOLECULAR ORBITALS

For a molecule with a total of  $m$  atomic basis functions  $\{\chi_1, \chi_2, \dots, \chi_m\}$ , there will be a total of  $m$  resultant molecular orbitals constructed from them. For most purposes, these atomic orbitals can be assumed to be real functions and normalized (equation 1.7) such that the probability of finding an electron in  $\chi_\mu$  when integrated over all space is unity. Here  $\chi_\mu^*$  is the complex conjugate of  $\chi_\mu$ . In equation 1.8, we show an alternative, useful way of writing such integrals.

$$\int \chi_\mu^* \chi_\mu d\tau = \int \chi_\mu^2 d\tau = \int \chi_\mu^2 dx dy dz = 1 \quad (1.7)$$

$$\int \chi_\mu^* \chi_\mu d\tau = \langle \chi_\mu | \chi_\mu \rangle \quad (1.8)$$

The molecular orbitals of a molecule are usually approximated by writing them as a linear combination of atomic orbitals such that

$$\psi_i = c_{1i}\chi_1 + c_{2i}\chi_2 + \cdots + c_{mi}\chi_m = \sum_{\mu} c_{\mu i} \chi_{\mu} \quad (1.9)$$

where  $i = 1, 2, \dots, m$ . These MOs are normalized and orthogonal (i.e., orthonormal), namely,

$$\langle \psi_i | \psi_j \rangle = \int \psi_i^* \psi_j d\tau = \delta_{ij} \quad (1.10)$$

where  $\delta_{ij} = 1$  if  $i = j$  and  $\delta_{ij} = 0$  if  $i \neq j$ . Note that the sum in equation 1.9 runs over all the atomic orbitals of the basis set. The  $c_{\mu i}$ s are called the molecular orbital coefficients. They may be either positive or negative, and the magnitude of the coefficient is related to the weight of that atomic orbital in the molecular orbital. An organizational note is in order here. We shall use Greek characters to represent atomic orbitals and the Roman alphabet in italics for molecular orbitals in generalized situations. For the mixing coefficients, the former will always be indexed before the latter. Thus,  $c_{\mu i}$  stands for the mixing coefficient of the  $\mu$ th atomic orbital in the molecular orbital  $i$  for a general situation and  $c_{12}$  represents that for atomic orbital 1 in molecular orbital 2 in a specific situation. Equation 1.9 is perhaps at first sight the most frightening aspect of delocalized molecular orbital theory. For a molecule of any reasonable size, this obviously represents quite a large sum. In fact, not all of the  $c_{\mu i}$ s will be significant in a given molecular orbital  $\psi_i$ . We shall learn how to gauge this using perturbation theory in Chapter 3. Some will be exactly zero, forced to be so by the symmetry of the molecule. In general, the more symmetric the molecule, the larger the number of  $c_{\mu i}$ s which are zero. Furthermore, symmetry requirements often dictate relationships (sign and magnitude) between orbitals on different atoms. This is covered in Chapter 4. We devote a considerable amount of effort to provide simple ways to understand how and why the orbital coefficients in the molecular orbitals of molecules and solids turn out the way they do.

The molecular orbital coefficients  $c_{\mu i}$  ( $\mu, i = 1, 2, \dots, m$ ) which specify the nature, and hence, energy of the orbital  $\psi_i$ , are determined by solving the eigenvalue equation of the effective one-electron Hamiltonian,  $H^{\text{eff}}$ , associated with the molecule (equation 1.11):

$$H^{\text{eff}} \psi_i = e_i \psi_i \quad (1.11)$$

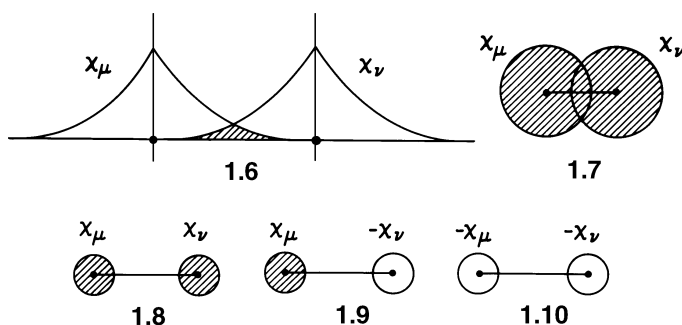
We shall leave for the moment what  $H^{\text{eff}}$  exactly is and discuss this more fully in Chapters 2 and 8. The resultant energy  $e_i$  measures the effective potential exerted on an electron located in  $\psi_i$ . This molecular orbital energy is the expectation value of  $H^{\text{eff}}$ , that is,

$$e_i = \frac{\int \psi_i H^{\text{eff}} \psi_i d\tau}{\int \psi_i^2 d\tau} = \frac{\langle \psi_i | H^{\text{eff}} | \psi_i \rangle}{\langle \psi_i | \psi_i \rangle} \quad (1.12)$$

$$= \langle \psi_i | H^{\text{eff}} | \psi_i \rangle \quad (1.13)$$

Given two atomic orbitals  $\chi_{\mu}$  and  $\chi_{\nu}$  centered on two different atoms, the overlap integral  $S_{\mu\nu}$  is defined as

$$S_{\mu\nu} = \langle \chi_{\mu} | \chi_{\nu} \rangle \quad (1.14)$$



Its origin is clear from the spatial overlap of the two wavefunctions in 1.6, where we have chosen two 1s orbitals from Figure 1.1 as examples. An alternative representation 1.7 shows this in terms of two orbital lobes. For the purposes of graphical clarity, this is better written as in 1.8. According to the sign convention of 1.1, the overlap integrals in 1.9 and 1.10 are given by equations 1.15 and 1.16, respectively. This simply shows

$$\langle \chi_\mu | -\chi_\nu \rangle = (-1) \langle \chi_\mu | \chi_\nu \rangle = -S_{\mu\nu} \quad (1.15)$$

$$\langle -\chi_\mu | -\chi_\nu \rangle = (-1)^2 \langle \chi_\mu | \chi_\nu \rangle = S_{\mu\nu} \quad (1.16)$$

that the overlap integral between two orbitals is positive when lobes have the same sign within the internuclear region of overlap and negative when the two lobes have opposite signs within this region.

The qualitative magnitude of the overlap integral is a principal topic of concern throughout this book. When two orbitals interact with each other, the extent of the interaction is determined by their overlap. There are several ways to gauge this without recourse to numerical calculation. As indicated earlier, symmetry often will dictate whether the overlap integral is precisely zero (or not). This is covered in Chapter 4. Second, the type of overlap will frequently determine its magnitude in a qualitative sense. Figure 1.4 shows pictorially some of the various types of overlap integrals that are encountered in practice. The  $\sigma$  type overlaps shown in Figure 1.4a–d contain no nodes along the internuclear axis, the  $\pi$  type overlaps (Figure 1.4e–g) are between orbitals with one nodal plane containing this axis, and those of  $\delta$  type (Figure 1.4h, i) contain two such nodal planes. Nodes along the internuclear axis decrease the mutual overlap between orbitals and, therefore, the important general result is that the overlap integral varies in the order  $\sigma > \pi > \delta$ . There are, of course, many exceptions to this rule of thumb that can be presented, that is, the overlap between two uranium 1s atomic orbitals will be smaller than the  $\pi$  overlap between two carbon 2p orbitals. However, when one considers valence orbitals from atoms

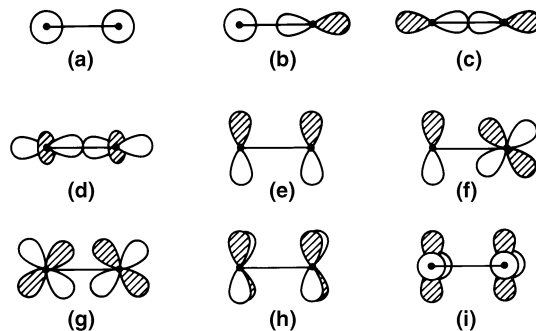
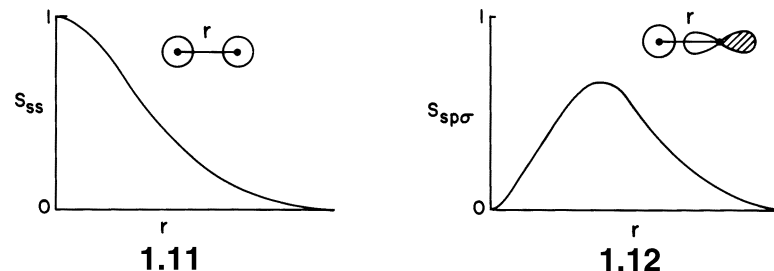


**FIGURE 1.4**

Types of overlap integrals between atomic orbitals, (a)–(d) correspond to  $\sigma$  overlap, (e)–(g) correspond to  $\pi$  overlap, and (h), (i) correspond to  $\delta$  overlap.

in the same row of the periodic table, then this order is universal. Third, overlap depends on the  $n$  quantum number of the atomic orbitals involved. From Section 1.2 recall that the atomic orbital becomes more diffuse as  $n$  increases; this in turn normally creates a smaller overlap. Thus, the overlap between two  $3p$  atomic orbitals will be less than that between two  $2p$  orbitals. A cautionary note needs to be added here. Overlap, as we shall see, is very sensitive to the internuclear distance between the two atoms. It does not immediately follow that, for example, the  $\pi$  overlap between two boron  $2p$  atomic orbitals is less than that between two fluorine atoms because boron is much less electronegative than fluorine and, consequently, its orbitals are more diffuse. The two distances are certainly going to be quite different and each will have a maximal overlap at a different distance. In transition metal complexes, one also has a situation that runs counter to the generalization just given. The metal  $3d$  orbitals are actually so contracted that at reasonable metal-ligand distances,  $4d$  and  $5d$  valence atomic orbitals actually overlap with the ligand orbitals to a greater extent than the  $3d$  valence orbitals do. The contracted  $3d$  atomic orbitals compared to  $4d$  and  $5d$  counterparts will also play an important role in determining spin states (Chapters 15, 16 and 24). Last, overlap is very sensitive to the geometry present in a molecule or solid. The variation of the overlap integral with the distance between the two atomic centers depends in detail on the form of  $R(r)$  chosen in equation 1.1, but clearly will approach zero at large internuclear distances. When the two interacting orbitals are identical, the overlap integral will be unity when the separation is zero as shown by equation 1.7 for this hypothetical example. A complete  $S$  versus  $r$  curve for the case of two  $1s$  orbitals is shown in 1.11. It may be readily seen from Figure 1.1 that the overlap between an  $s$  orbital and a  $p$  orbital at  $r = 0$  is identically zero, as shown in 1.12.



Maximal overlap will occur at some finite value of  $r$  which depends on the magnitude of the orbital exponents for the two atoms. The angular dependence of the overlap integral follows immediately from the analytic form of  $Y(\theta, \phi)$  in equation 1.1 and expressed in Table 1.1. We can often write the overlap integral as in equation 1.17:

$$S_{\mu\nu} = S_{\mu\nu}(\lambda, r) f(\text{angular geometry}) \quad (1.17)$$

$S_{\mu\nu} = S_{\mu\nu}(\lambda, r)$  depends on the distance between the two orbitals and the nature ( $\lambda = \sigma, \pi$ , or  $\delta$ ) of the overlap between them. It is also, of course, strongly dependent upon the identity of the atoms on which the orbitals  $\mu$  and  $\nu$  are located. The angular geometry dependent term is independent of the nature of the atoms themselves and only depends on the description ( $s$ ,  $p$ , or  $d$ ) of the two orbitals [15]. The angular variations of some of the more common types of overlap integral are shown in Figure 1.5. In the first three examples, the overlap is precisely zero when the probe  $s$  atomic orbital enters the nodal plane of the other orbital. Also notice that the overlap with a  $d_{z^2}$  (in terms of absolute magnitude) is considerably less at the torus than along the  $z$ -axis. The angular variations displayed in Figure 1.5 will be used many times in this book.

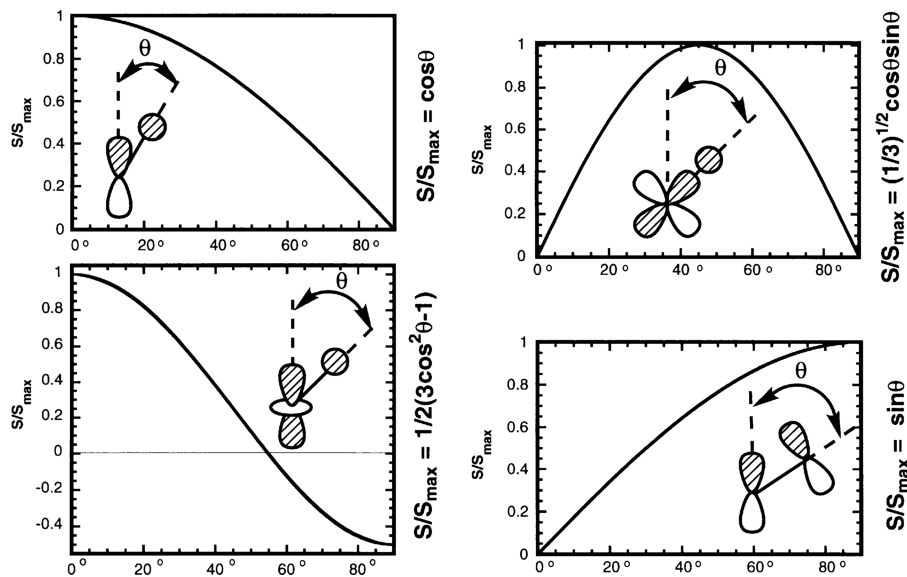


**FIGURE 1.5**  
Angular dependence of the overlap integral for some commonly encountered pairs of atomic orbitals.

The energy of interaction associated with two overlapping atomic orbitals  $\chi_\mu$  and  $\chi_\nu$  is given by

$$H_{\mu\nu} = \langle \chi_\mu | H^{\text{eff}} | \chi_\nu \rangle \quad (1.18)$$

The diagonal element  $H_{\mu\mu}$  (when  $\nu=\mu$  in equation 1.18) refers to the effective potential of an electron in the atomic orbital  $\chi_\mu$ . It then has some relationship to the ionization potential of an electron in  $\chi_\mu$ , which will be modified by the effective field of the other electrons and nuclei in the molecule. The off-diagonal element  $H_{\mu\nu}$  is often called the resonance or hopping integral. It measures the potential of an electron when it is associated with  $\chi_\mu$  and  $\chi_\nu$ . The magnitude of  $H_{\mu\nu}$  will then determine how much a bonding molecular orbital is stabilized and an antibonding one destabilized. It can be approximated by the equation

Should try to see how good this formula is.

$$H_{\mu\nu} = \frac{1}{2} K (H_{\mu\mu} + H_{\nu\nu}) S_{\mu\nu} \quad (1.19)$$

which is known as the **Wolfsberg–Helmholtz formula**. ( $K$  is a proportionality constant.) Since the  $H_{\mu\nu}$ s are negative quantities,  $H_{\mu\nu} \propto -S_{\mu\nu}$ , which implies that the interaction energy between two orbitals is negative (i.e., stabilizing) when their overlap integral is positive. There are a number of ways to compute  $H_{\mu\nu}$  depending upon the level of approximation. The important result, however, is that, whatever the exact functional form, there is a direct relationship between  $H_{\mu\nu}$  and  $S_{\mu\nu}$ . Furthermore, as indicated earlier, there are a number of ways to gauge the magnitude of  $S_{\mu\nu}$  (and, hence  $H_{\mu\nu}$ ) in a qualitative sense.

The overlap integral,  $S_{\mu\nu}$ , and the interaction integral  $H_{\mu\nu}$  are symmetric such that  $S_{\mu\nu} = S_{\nu\mu}$  and  $H_{\mu\nu} = H_{\nu\mu}$ . (This second equality arises because of the Hermitian properties of the Hamiltonian.) For an arbitrary function  $\psi_i$  (equation 1.9), the integrals needed in equation 1.12 may be written as

$$\begin{aligned} \langle \psi_i | \psi_i \rangle &= \left\langle \sum_{\mu} \chi_{\mu} c_{\mu i} \middle| \sum_{\nu} \chi_{\nu} c_{\nu i} \right\rangle \\ &= \sum_{\mu} \sum_{\nu} c_{\mu i} S_{\mu\nu} c_{\nu i} \equiv A \end{aligned} \quad (1.20)$$

and

$$\begin{aligned}\langle \psi_i | H^{\text{eff}} | \psi_i \rangle &= \left\langle \sum_{\mu} \chi_{\mu} c_{\mu i} | H^{\text{eff}} | \sum_{\nu} \chi_{\nu} c_{\nu i} \right\rangle \\ &= \sum_{\mu} \sum_{\nu} c_{\mu i} H_{\mu \nu} c_{\nu i} \equiv B\end{aligned}\quad (1.21)$$

If  $\psi_i$  is an eigenfunction of  $H^{\text{eff}}$ , then it will be normalized to unity and equation 1.12 will result. However, for an arbitrary  $\psi_i$ ,  $A$  will not be equal to unity. From equation 1.12, the energy  $e_i$  is given by

$$e_i = \frac{\langle \psi_i | H^{\text{eff}} | \psi_i \rangle}{\langle \psi_i | \psi_i \rangle} = \frac{B}{A} \quad (1.22)$$

According to the variational theorem, the coefficients  $c_{\mu i}$  (recall that  $\mu, i = 1, 2, \dots, m$  for  $m$  atomic orbitals) are chosen such that the energy is minimized, that is,

$$\frac{\partial e_i}{\partial c_{1i}} = \frac{\partial e_i}{\partial c_{2i}} = \dots = \frac{\partial e_i}{\partial c_{mi}} = 0 \quad (1.23)$$

For any arbitrary coefficient  $c_{\kappa i}$  ( $\kappa = 1, 2, \dots, m$ )

$$\begin{aligned}\frac{\partial e_i}{\partial c_{\kappa i}} &= \frac{\partial}{\partial c_{\kappa i}} \left( \frac{B}{A} \right) = \frac{1}{A} \left( \frac{\partial B}{\partial c_{\kappa i}} \right) - \frac{B}{A^2} \left( \frac{\partial A}{\partial c_{\kappa i}} \right) \\ &= \frac{1}{A} \left( \frac{\partial B}{\partial c_{\kappa i}} - e_i \frac{\partial A}{\partial c_{\kappa i}} \right) = 0\end{aligned}\quad (1.24)$$

Therefore,

$$\frac{\partial B}{\partial c_{\kappa i}} - e_i \frac{\partial A}{\partial c_{\kappa i}} = 0 \quad (1.25)$$

Since the indices  $\mu$  and  $\nu$  in equations 1.20 and 1.21 are only used for summation,

$$\begin{aligned}\frac{\partial A}{\partial c_{\kappa i}} &= \sum_{\nu} S_{\kappa \nu} c_{\nu i} + \sum_{\mu} S_{\mu \kappa} c_{\mu i} \\ &= 2 \sum_{\mu} S_{\mu \kappa} c_{\mu i}\end{aligned}\quad (1.26)$$

Similarly,

$$\frac{\partial B}{\partial c_{\kappa i}} = 2 \sum_{\mu} H_{\kappa \mu} c_{\mu i} \quad (1.27)$$

Combining equations 1.25–1.27,

$$\sum_{\mu} H_{\kappa \mu} c_{\mu i} - e_i \sum_{\mu} S_{\mu \kappa} c_{\mu i} = \sum_{\mu} (H_{\kappa \mu} - e_i S_{\mu \kappa}) c_{\mu i} = 0 \quad (1.28)$$

Here as a reminder,  $i$  indexes the molecular orbital level while  $\mu$ ,  $\nu$ , and  $\kappa$  index the  $\mu$ th,  $\nu$ th, and  $\kappa$ th atomic orbitals, respectively, in the LCAO expansion of equation 1.9. Equation 1.28 is satisfied for  $\kappa = 1, 2, \dots, m$ , and the explicit form of these  $m$  equations called the *secular equations*, is

$$\begin{aligned}(H_{11} - e_i S_{11}) c_{1i} + (H_{12} - e_i S_{12}) c_{2i} + \dots + (H_{1m} - e_i S_{1m}) c_{mi} &= 0 \\ (H_{21} - e_i S_{21}) c_{1i} + (H_{22} - e_i S_{22}) c_{2i} + \dots + (H_{2m} - e_i S_{2m}) c_{mi} &= 0 \\ \vdots &\quad \vdots \quad \vdots \\ (H_{m1} - e_i S_{m1}) c_{1i} + (H_{m2} - e_i S_{m2}) c_{2i} + \dots + (H_{mm} - e_i S_{mm}) c_{mi} &= 0\end{aligned}\quad (1.29)$$

A well-known mathematical result from the theory of such simultaneous equations requires the following determinant, called the secular determinant, to vanish.

$$\begin{vmatrix} H_{11} - e_i S_{11} & H_{12} - e_i S_{12} & \cdots H_{1m} - e_i S_{1m} \\ H_{21} - e_i S_{21} & H_{22} - e_i S_{22} & \cdots H_{2m} - e_i S_{2m} \\ \vdots & \vdots & \vdots \\ H_{m1} - e_i S_{m1} & H_{m2} - e_i S_{m2} & \cdots H_{mm} - e_i S_{mm} \end{vmatrix} = 0 \quad (1.30)$$

Solution of the polynomial equation that results from expansion of the secular determinant equation 1.30 provides  $m$  orbital energies  $e_i$  ( $i = 1, 2, \dots, m$ ) which, according to the variational theorem, are a set of upper bounds to the true orbital energies. Written in matrix notation, equation 1.30 becomes

$$|H_{\kappa\mu} - e_i S_{\kappa\mu}| = 0 \quad (1.31)$$

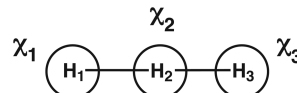
As seen in Chapter 2, the coefficients  $c_{\mu i}$  are determined from the secular equations (equation 1.29) and the normalization condition

$$\langle \psi_i | \psi_i \rangle = \sum_{\mu} \sum_{\nu} c_{\mu i} S_{\mu\nu} c_{\nu i} = 1 \quad (1.32)$$

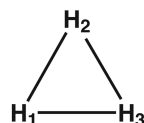
The reader should not despair at the complexity introduced by equations 1.29 and 1.30. Symmetry and perturbation theory will allow us to treat any problem as an example of two or three orbitals interacting with each other. The former will be explicitly treated in Chapter 2 using equations 1.29 and 1.30.

## PROBLEMS\*

- I.1.** Consider the  $\text{H}_3$  molecule composed of one atomic s AO on each atom with the linear geometry shown below:

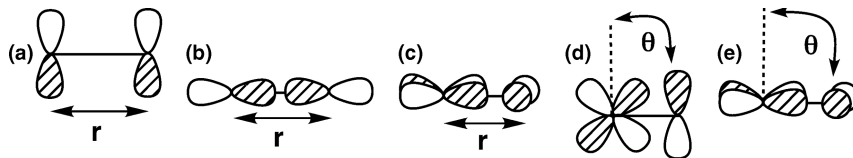


- a. Write down the secular determinant and equations for the general case (not specifying anything about  $r_{12}$  and  $r_{23}$ ).
- b. Let  $r_{12} = r_{23}$ ; write the new secular determinant.
- c. Now, suppose that the  $r_{13}$  distance is long enough so that  $S_{13} \approx 0$ . Simplify the secular determinant further.
- d. Using the results from (c) let  $H_{11} = -13.60 \text{ eV}$ ,  $H_{12} = -14.18 \text{ eV}$  and  $S_{12} = 0.596$ . Solve for  $e_1 - e_3$  and determine the orbital coefficients for  $\psi_1 - \psi_3$ .
- e. For  $\text{H}_3$  in a geometry given by an equilateral triangle write down the secular determinant and equations. Using the parameters in part (d) compute the eigenvalues and eigenvectors associated with each MO.



\* Solutions to chapter problems are located at [ftp://ftp.wiley.com/public/sci\\_tech\\_med/orbital\\_interactions\\_2e](ftp://ftp.wiley.com/public/sci_tech_med/orbital_interactions_2e).

**I.2.** Draw a qualitative sketch of  $S_{\mu\nu}$  for each of the situations shown below.



**I.3.** Given a set of AOs  $\{\chi_1, \chi_2\}$ , the LCAO-MOs  $\psi_i$  ( $i = 1, 2$ ) are obtained by solving the Schrödinger equation

$$H^{\text{eff}}\psi_i = e_i\psi_i (i = 1, 2)$$

This equation gives rise to the following matrices defined in terms of the AOs:

$$\mathbf{S} = \begin{pmatrix} S_{11} & S_{12} \\ S_{21} & S_{22} \end{pmatrix}, \quad \mathbf{H} = \begin{pmatrix} H_{11} & H_{12} \\ H_{21} & H_{22} \end{pmatrix}, \quad \mathbf{C} = \begin{pmatrix} C_{11} & C_{12} \\ C_{21} & C_{22} \end{pmatrix}, \quad \mathbf{e} = \begin{pmatrix} e_1 & 0 \\ 0 & e_2 \end{pmatrix}$$

- a. What is the relationship between the above four matrices?
- b. The elements of the matrix  $\tilde{\mathbf{H}}$  are defined in terms of the MOs as  $\tilde{H}_{ij} = \langle \psi_i | H^{\text{eff}} | \psi_j \rangle$  ( $i, j = 1, 2$ ). Likewise, the elements of the matrix  $\tilde{\mathbf{S}}$  are defined in terms of the MOs as  $\tilde{S}_{ij} = \langle \psi_i | \psi_j \rangle$  ( $i, j = 1, 2$ ). Show the elements of the matrices  $\tilde{\mathbf{H}}$  and  $\tilde{\mathbf{S}}$ .
- c. What is the terminology describing the transformation from  $\mathbf{H}$  to  $\tilde{\mathbf{H}}$ ?

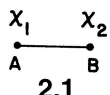
## REFERENCES

1. T. Helgaker, P. Jorgensen, and J. Olsen, *Molecular Electronic-Structure Theory*, John Wiley & Sons, Chichester (2000).
2. J. A. Pople and D. L. Beveridge, *Approximate Molecular Orbital Theory*, McGraw-Hill, New York (1970).
3. M. J. S. Dewar, *The Molecular Orbital Theory of Organic Chemistry*, McGraw-Hill, New York (1969).
4. L. Piela, *Ideas of Quantum Chemistry*, Elsevier, Amsterdam (2007).
5. W. Kutzelnigg, *Einführung in die Theoretische Chemie, Band 2*, Verlag Chemie, Weinheim (1978).
6. A. Szabo and N. S. Ostlund, *Modern Quantum Chemistry*, McGraw-Hill, New York (1989).
7. W. J. Hehre, L. Radom, P. v. R. Schleyer, and J. A. Pople, *Ab Initio Molecular Orbital Theory*, John Wiley & Sons, New York (1986).
8. J. B. Foresman and Å. Frisch, *Exploring Chemistry with Electronic Structure Methods*, 2nd edition, Gaussian Inc., Pittsburgh (1996).
9. F. Jensen, *Introduction to Computational Chemistry*, 2nd edition, John Wiley & Sons, Chichester (2007); C. J. Cramer, *Essentials of Computational Chemistry*, 2nd edition, John Wiley & Sons, Chichester (2004).
10. E. Clementi and C. Roetti, *At. Nucl. Data Tables*, **14**, 177 (1974).
11. E. Clementi and D. L. Raimondi, *J. Chem. Phys.*, **38**, 2868 (1963).
12. W. Kutzelnigg, *Angew. Chem. Int. Ed.*, **23**, 272 (1984).
13. R. Poirier, R. Kari, and I. G. Csizmadia, *Handbook of Gaussian Basis Sets*, Elsevier, Amsterdam (1985); S. Huzinaga, *Gaussian Basis Sets for Molecular Calculations*, Elsevier, Amsterdam (1984).
14. K. L. Schuchardt, B. T. Didier, T. Elsethagen, L. Sun, V. Gurumoorthi, J. Chase, J. Li, and T. L. Windus, *J. Chem. Inf. Model.*, **47**, 1045 (2007). A rather complete collection of basis sets may be found at <https://bse.pnl.gov/bse/portal>.
15. J. K. Burdett, *Molecular Shapes*, John Wiley & Sons, New York (1980).

# Concepts of Bonding and Orbital Interaction

## 2.1 ORBITAL INTERACTION ENERGY

The derivations of Chapter 1 were very general ones. Here we look in some detail at the illustrative case of a two-center two-orbital problem. Two atomic orbitals,  $\chi_1$  and  $\chi_2$ , are centered on the two atoms A and B (2.1). (In Chapter 3, we show how



the results can be generalized to the case of two orbitals located on molecular fragments A and B.) The molecular orbitals (MOs) resulting from the interaction between  $\chi_1$  and  $\chi_2$  can be written as:

$$\begin{aligned}\psi_1 &= c_{11}\chi_1 + c_{21}\chi_2 \\ \psi_2 &= c_{12}\chi_1 + c_{22}\chi_2\end{aligned}\quad (2.1)$$

For the mixing coefficients,  $c_{\mu\nu}$ , we use the convention that the first subscript refers to the atomic orbital and the second to the molecular orbital. The overlap and interaction integrals to consider are as follows:

$$\begin{aligned}\langle \chi_1 | \chi_1 \rangle &= \langle \chi_2 | \chi_2 \rangle = 1 \\ \langle \chi_1 | \chi_2 \rangle &= S_{12}\end{aligned}\quad (2.2)$$

and

$$\begin{aligned}\langle \chi_1 | H^{\text{eff}} | \chi_1 \rangle &= H_{11} = e_1^0 \\ \langle \chi_2 | H^{\text{eff}} | \chi_2 \rangle &= H_{22} = e_2^0 \\ \langle \chi_1 | H^{\text{eff}} | \chi_2 \rangle &= H_{12}\end{aligned}\quad (2.3)$$

Recall from Section 1.3 that  $S_{12} = S_{21}$  so that  $H_{12} = H_{21}$ . If the phases of  $\chi_1$  and  $\chi_2$  are arranged so that  $S_{12}$  is positive, then from equation 1.19,

$$H_{12} \propto -S_{12} < 0 \quad (2.4)$$

The molecular orbital energies in this two-orbital case,  $e_i$  ( $i = 1, 2$ ), are obtained by solving the secular determinant (equation 1.30) shown in equation 2.5 for this particular example

$$\begin{vmatrix} e_1^0 - e_i & H_{12} - e_i S_{12} \\ H_{12} - e_i S_{12} & e_2^0 - e_i \end{vmatrix} = 0 \quad (2.5)$$

Expansion of equation 2.5 leads to

$$(e_1^0 - e_i)(e_2^0 - e_i) - (H_{12} - e_i S_{12})^2 = 0 \quad (2.6)$$

The solutions for  $e_i$  in this equation will be examined for a degenerate case ( $e_1^0 = e_2^0$ ) and for the general nondegenerate case ( $e_1^0 \neq e_2^0$ ).

### 2.1.1 Degenerate Interaction

For  $e_1^0 = e_2^0$ , solution of equation 2.6 leads to two values for the  $e_i$  ( $i = 1, 2$ )

$$\begin{aligned}e_1 &= \frac{e_1^0 + H_{12}}{1 + S_{12}} \\ e_2 &= \frac{e_1^0 - H_{12}}{1 - S_{12}}\end{aligned}\quad (2.7)$$

When the interaction between  $\chi_1$  and  $\chi_2$  is not strong ( $S_{12}$  is small), some very useful mathematical approximations may be used to simplify equation 2.7. Using the first two expressions in Table 2.1, results in equations 2.8 and 2.9;

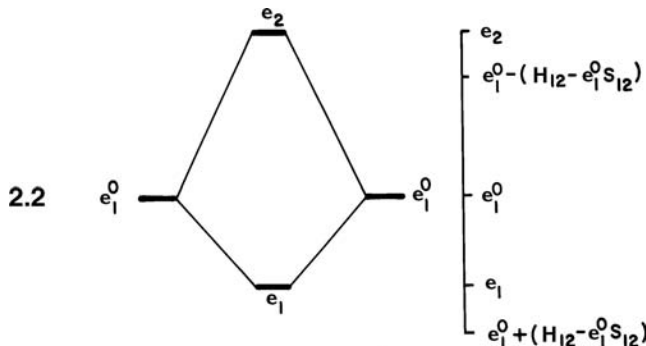
$$\begin{aligned}e_1 &= \frac{e_1^0 + H_{12}}{1 + S_{12}} = (e_1^0 + H_{12})(1 - S_{12} + S_{12}^2 - \dots) \\ &\approx e_1^0 + (H_{12} - e_1^0 S_{12}) - S_{12}(H_{12} - e_1^0 S_{12})\end{aligned}\quad (2.8)$$

$$\begin{aligned}e_2 &= \frac{e_1^0 - H_{12}}{1 - S_{12}} = (e_1^0 - H_{12})(1 + S_{12} - S_{12}^2 + \dots) \\ &\approx e_1^0 - (H_{12} - e_1^0 S_{12}) - S_{12}(H_{12} - e_1^0 S_{12})\end{aligned}\quad (2.9)$$

**TABLE 2.1 Some Mathematical Simplifications**

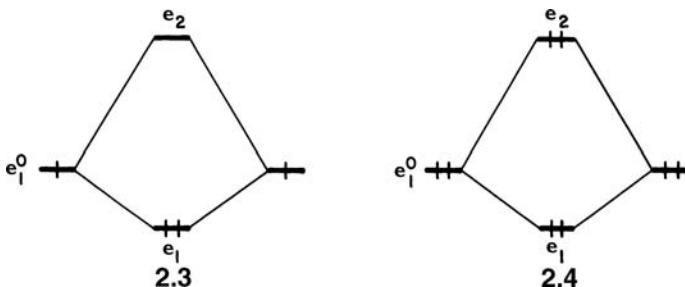
Function	Approximate Expression
$\frac{1}{1+x}$	$1 - x + x^2 - \dots$
$\frac{1}{1-x}$	$1 + x + x^2 + \dots$
$\sqrt{1+x}$	$1 + \frac{1}{2}x - \dots$
$\frac{1}{\sqrt{1+x}}$	$1 - \frac{1}{2}x + \dots$

For any realistic case,  $e_i^0$  is negative and normally ( $H_{12} - e_i^0 S_{12}$ ) is negative too (i.e.,  $|H_{12}| > |e_i^0 S_{12}|$ ). Hence,  $\psi_1$  is stabilized by the presence of the second term in equation 2.8, but  $\psi_2$  is destabilized by the second term in equation 2.9. Both levels are destabilized by the third term in equations 2.8 and 2.9. These results are shown pictorially in 2.2. The important result is that with respect to the atomic orbital at an



energy  $e_i^0$  the raising (destabilization) of the  $e_2$  level is greater than the lowering (stabilization) of the  $e_1$  level. The origin of this effect is easy to see. It arises because the orbitals  $\chi_1$  and  $\chi_2$  are not orthogonal (i.e.,  $S_{12} \neq 0$ ). Putting  $S_{12} = 0$  in equation 2.7 leads to  $e_i = e_i^0 \pm H_{12}$  and this asymmetry disappears.

Putting electrons into these resultant molecular orbitals allows calculation of the total interaction energy,  $\Delta E$ , on bringing together the two atomic orbitals  $\chi_1$  and  $\chi_2$ . Two important cases are shown in 2.3 and 2.4, the two-orbital two-electron case and the two-orbital four-electron case, respectively. These orbital interaction diagrams



indicate the relative energy of the starting and resultant orbitals by use of heavy bars drawn in the horizontal direction. Then, the vertical axis is a scale of the energy associated with each orbital and the “tie-lines” show which orbitals interact with

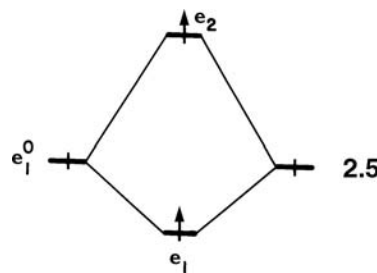
each other. The small vertical lines represent electrons. Using the results of equations 2.8 and 2.9, and weighting each orbital energy by the number of electrons in that orbital leads to

$$\begin{array}{ll} \text{2-e-in-2-orbital} & \Delta E^{(2)} = 2e_1 - 2e_1^0 \approx 2(H_{12} - e_1^0 S_{12})(1 - S_{12}) \\ \text{2-e-in-2-orbital} & \end{array} \quad (2.10)$$

$$\Delta E^{(4)} = 2(e_1 + e_2) - 4e_1^0 \approx -4S_{12}(H_{12} - e_1^0 S_{12}) \quad (2.11)$$

Since for  $S_{12} > 0$  the term  $(H_{12} - e_1^0 S_{12})$  is negative, the two-orbital–two-electron interaction is stabilizing (i.e.,  $\Delta E^{(2)} < 0$ ) but the two-orbital–four electron interaction is destabilizing (i.e.,  $\Delta E^{(4)} > 0$ ).

The arrangement shown in 2.3 is not the only way to put two electrons into these two molecular orbitals. An alternative pattern is shown in 2.5 with a total interaction energy of  $\Delta E^{(4)}/2$ . The pattern in 2.5 is called the high-spin case, to be contrasted with the low-spin arrangement of 2.3, where they are paired. We shall



consistently employ arrows throughout the book to indicate the electron spin when it is important, as in 2.5. The stability of the high-spin state compared to the low-spin state will be examined in detail in Chapter 8. As a general rule of thumb, when the interaction between the atomic orbitals is strong, the resultant molecular orbitals are split by a moderate to large amount, and the low-spin situation is favored. When the two molecular orbitals are degenerate or close together in energy then the high-spin arrangement is more stable. This is the molecular analog of Hund's rule.

### 2.1.2 Nondegenerate Interaction

When  $e_1^0 \neq e_2^0$  without loss of generality  $e_1^0$  may be assumed to be lower in energy than  $e_2^0$ , that is,  $e_2^0 - e_1^0 > 0$ . Rearrangement of equation 2.6 leads to

$$(1 + S_{12}^2)e_i^2 + (2H_{12}S_{12} - e_1^0 - e_2^0)e_i + (e_1^0 e_2^0 - H_{12}^2) = 0 \quad (2.12)$$

and the solutions of this quadratic equation are given by

$$\begin{aligned} e_1 &= \frac{-b - \sqrt{D}}{2a} \\ e_2 &= \frac{-b + \sqrt{D}}{2a} \end{aligned} \quad (2.13)$$

where

$$a = 1 - S_{12}^2$$

$$b = 2H_{12}S_{12} - e_1^0 - e_2^0 \quad (2.14)$$

$$D = b^2 - 4ac$$

with

$$c = e_1^0 e_2^0 - H_{12}^2$$

Approximate expressions for  $e_1$  and  $e_2$  are found as follows. First  $D$  can be expanded as

$$\begin{aligned} D &= (2H_{12}S_{12} - e_1^0 - e_2^0) - 4(1 - S_{12}^2)(e_1^0 e_2^0 - H_{12}^2) \\ &= (e_1^0 - e_2^0)^2 + 4(H_{12} - e_1^0 S_{12})(H_{12} - e_2^0 S_{12}) \end{aligned} \quad (2.15)$$

From Table 2.1,

$$\begin{aligned} \sqrt{D} &= -(e_1^0 - e_2^0) \left[ 1 + \frac{4(H_{12} - e_1^0 S_{12})(H_{12} - e_2^0 S_{12})}{(e_1^0 - e_2^0)^2} \right]^{1/2} \\ &\approx -(e_1^0 - e_2^0) \left[ 1 + \frac{2(H_{12} - e_1^0 S_{12})(H_{12} - e_2^0 S_{12})}{(e_1^0 - e_2^0)^2} \right] \end{aligned} \quad (2.16)$$

assuming a small interaction between  $\chi_1$  and  $\chi_2$  as before. We have a negative sign in front of  $e_1^0 - e_2^0$  ( $<0$ ) to ensure that  $\sqrt{D} > 0$ . By manipulation of equations 2.13, 2.14, and 2.16,

$$\begin{aligned} 2(1 - S_{12}^2)e_1 &= e_1^0 + e_2^0 - 2H_{12}S_{12} + (e_1^0 - e_2^0) \left[ 1 + \frac{2(H_{12} - e_1^0 S_{12})(H_{12} - e_2^0 S_{12})}{(e_1^0 - e_2^0)^2} \right] \\ &= 2 \left[ e_1^0 - 2H_{12}S_{12} + \frac{(H_{12} - e_1^0 S_{12})(H_{12} - e_2^0 S_{12})}{e_1^0 - e_2^0} \right] \quad (2.17) \\ &= 2 \left[ e_1^0(1 - S_{12}^2) + \frac{(H_{12} - e_1^0 S_{12})^2}{e_1^0 - e_2^0} \right] \end{aligned}$$

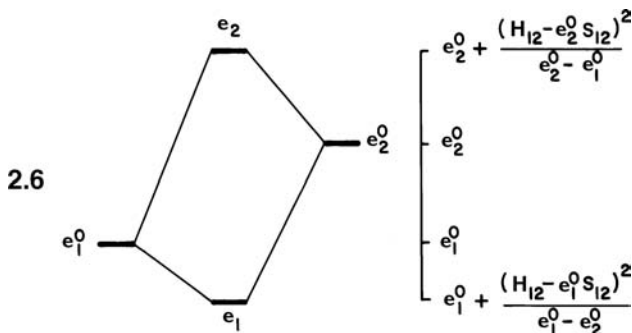
and so

$$e_1 \approx e_1^0 + \frac{(H_{12} - e_1^0 S_{12})^2}{e_1^0 - e_2^0} \quad (2.18)$$

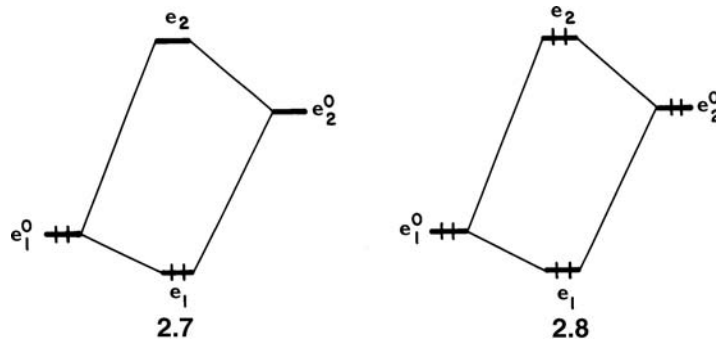
A similar expression is found analogously for  $e_2$ :

$$e_2 \approx e_2^0 + \frac{(H_{12} - e_2^0 S_{12})^2}{e_2^0 - e_1^0} \quad (2.19)$$

The orbital energies are shown pictorially in 2.6. As a result of the interaction, the lower level  $e_1^0$  is depressed in energy, and the higher level  $e_2^0$  is raised in energy.



Notice that since  $0 > e_2^0 > e_1^0$ ,  $(H_{12} - e_1^0 S_{12})^2 < (H_{12} - e_2^0 S_{12})^2$ . In other words, the higher energy orbital is destabilized more than the lower energy orbital is stabilized, just as found for the degenerate case above. The total interaction energies for the analogous two-orbital two-electron and the two-orbital four-electron cases of 2.7 and 2.8 are simply obtained. Since  $e_1^0 - e_2^0 < 0$ ,  $\Delta E^{(2)}$  is negative, that is, the



$$\Delta E^{(2)} = 2e_1 - 2e_1^0$$

$$\approx 2 \frac{(H_{12} - e_1^0 S_{12})^2}{e_1^0 - e_2^0} \quad (2.20)$$

$$\Delta E^{(4)} = 2(e_1 + e_2) - 2(e_1^0 + e_2^0)$$

$$\approx -4S_{12} \left( H_{12} - \frac{e_1^0 + e_2^0}{2} S_{12} \right) \quad (2.21)$$

two-orbital–two-electron interaction is stabilizing. We have already noted that  $(H_{12} - e_1^0 S_{12})$  and  $(H_{12} - e_2^0 S_{12})$  are negative if  $S_{12} > 0$  and thus  $\Delta E^{(4)}$  is positive, that is, the two-orbital–four-electron interaction is destabilizing.

## 2.2 MOLECULAR ORBITAL COEFFICIENTS

The MO coefficients  $c_{1i}$  and  $c_{2i}$  of equation 2.1 are determined from the simultaneous equation 1.29 (shown for the present case in equation 2.22) and the normalization condition, equation 2.23.

$$\begin{aligned} (e_1^0 - e_i)c_{1i} + (H_{12} - e_i S_{12})c_{2i} &= 0 \\ (H_{12} - e_i S_{12})c_{1i} + (e_2^0 - e_i)c_{2i} &= 0 \end{aligned} \quad (2.22)$$

$$\langle \psi_i | \psi_i \rangle = c_{1i}^2 + 2c_{1i}c_{2i}S_{12} + c_{2i}^2 = 1 \quad (2.23)$$

The coefficients  $c_{1i}$  and  $c_{2i}$  for  $i = 1, 2$  will be obtained for the degenerate and nondegenerate cases described earlier.

### 2.2.1 Degenerate Interaction

Since  $e_1^0 = e_2^0$  either of the equations 2.22 leads to

$$\frac{c_{21}}{c_{11}} = -\frac{e_1^0 - e_1}{H_{12} - e_1 S_{12}} = 1 \quad (2.24)$$

and so from equation 2.23,

$$c_{11} = c_{21} = \pm \frac{1}{\sqrt{2 + 2S_{12}}} \quad (2.25)$$

which leads to

$$\psi_1 = \pm \frac{1}{\sqrt{2 + 2S_{12}}} (\chi_1 + \chi_2) \quad (2.26)$$

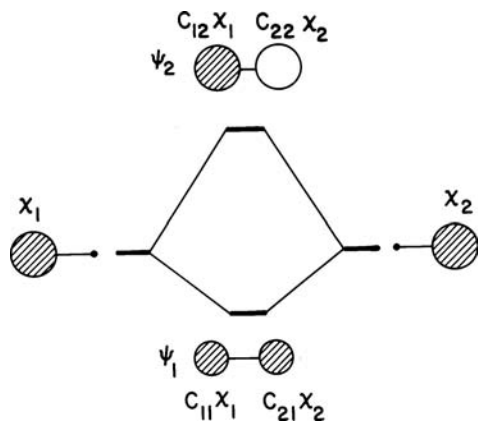
The coefficients of the  $\psi_2$  molecular orbital are obtained in a similar manner

$$\frac{c_{12}}{c_{22}} = -\frac{e_1^0 - e_2}{H_{12} - e_2 S_{12}} = -1 \quad (2.27)$$

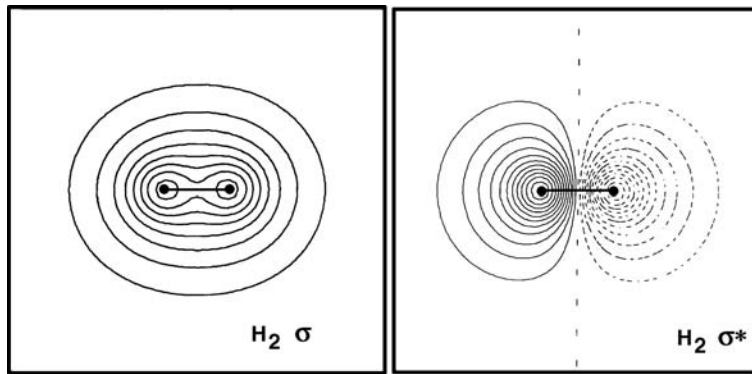
Use of the normalization condition leads to

$$\psi_2 = \pm \frac{1}{\sqrt{2 - 2S_{12}}} (\chi_1 - \chi_2) \quad (2.28)$$

The nodal properties of the MOs  $\psi_1$  and  $\psi_2$  are shown in the orbital interaction diagram, Figure 2.1, where the positive signs from equations 2.26 and 2.28 are arbitrarily chosen. Equation 1.11 shows that if  $\psi_i$  is an eigenfunction of  $H^{\text{eff}}$ , so is  $-\psi_i$ . What is important, therefore, is not the overall sign of the MO  $\psi_i$ , but the relative signs of its MO coefficients. Irrespective of the overall sign chosen for  $\psi_i$ , the important point is that  $\chi_1$  and  $\chi_2$  are combined in-phase for the lower lying orbital  $\psi_1$  and out-of-phase in the higher lying orbital  $\psi_2$ . Henceforth, we only show one sign for our MOs. Contour plots for  $\psi_1$  and  $\psi_2$  ( $\sigma$  and  $\sigma^*$  orbitals, respectively) in H<sub>2</sub> using an Slater type orbital (STO)-3G basis set are shown in Figure 2.2. The solid contours plot the positive values of the wavefunction and the dotted lines negative ones. The dashed line indicates the nodal plane in  $\sigma^*$ , which bisects the H–H internuclear axis.



**FIGURE 2.1**  
Molecular orbital diagram showing details of the degenerate interaction between the two atomic  $s$  orbitals,  $\chi_1$ , and  $\chi_2$ .

**FIGURE 2.2**

Contour plots of the  $\sigma$  and  $\sigma^*$  molecular orbitals of  $\text{H}_2$ . The positive and negative values of the wavefunction are represented by solid and dotted lines, respectively.

While  $c_{11} = c_{21}$  and  $c_{12} = |c_{22}|$ , it is clear from equations 2.26 and 2.28 that  $c_{11} \neq c_{12}$ . This is a consequence of the relationship  $1 > S_{12} > 0$ . The general result is that the atomic coefficients for the higher lying level in Figure 2.1 are larger than those for the lower lying level. This is also evident from the contour plots of the  $\sigma$  and  $\sigma^*$  molecular orbitals for  $\text{H}_2$  in Figure 2.2.

### 2.2.2 Nondegenerate Interaction

From equations 2.18 and 2.22,

$$\frac{c_{21}}{c_{11}} = -\frac{e_1^0 - e_1}{H_{12} - e_1 S_{12}} = \frac{t}{1 - t S_{12}} \quad (2.29)$$

where  $t = (H_{12} - e_1^0 S_{12}) / (e_1^0 - e_2^0)$ . From Table 2.1, this ratio may be rewritten as:

$$\frac{c_{21}}{c_{11}} = \frac{t}{1 - t S_{12}} = t(1 + t S_{12} + \dots) \approx t \quad (2.30)$$

by neglecting terms greater than second order in  $t$  and  $S_{12}$ . Using the normalization condition (equation 2.23) and this result

$$\left(\frac{1}{c_{11}}\right)^2 = 1 + 2\left(\frac{c_{21}}{c_{11}}\right)S_{12} + \left(\frac{c_{21}}{c_{11}}\right)^2 = 1 + 2tS_{12} + t^2 \quad (2.31)$$

From Table 2.1, this may be rearranged and approximated as

$$c_{11} = \frac{1}{\sqrt{1 + 2tS_{12} + t^2}} \approx 1 - tS_{12} - \frac{1}{2}t^2 \quad (2.32)$$

Combined with equation 2.30,

$$c_{21} = tc_{11} = t\left(1 - tS_{12} - \frac{1}{2}t^2\right) \approx t \quad (2.33)$$

where, as before, terms greater than second order in  $t$  and  $S_{12}$  have been neglected. The final form of the MO  $\psi_1$  is then

$$\psi_1 \approx \left(1 - tS_{12} - \frac{1}{2}t^2\right)\chi_1 + t\chi_2 \quad (2.34)$$

with a similar expression for  $\psi_2$

$$\psi_2 \approx t' \chi_1 + \left(1 - t' S_{12} - \frac{1}{2} t'^2\right) \chi_2 \quad (2.35)$$

where  $t' = (H_{12} - e_2^0 S_{12}) / (e_2^0 - e_1^0)$ . The two functions  $t$  and  $t'$  are often called the mixing coefficients because  $t$ , for example, describes how orbital  $\chi_2$  mixes into  $\chi_1$  to give an orbital still largely  $\chi_1$  in character.

Since invariably  $H_{12} - e_i^0 S_{12} < 0$ ,

$$t = \frac{(H_{12} - e_1^0 S_{12})}{(e_1^0 - e_2^0)} = \frac{(-)}{(+)} > 0 \quad (2.36)$$

and

$$t' = \frac{(H_{12} - e_2^0 S_{12})}{(e_2^0 - e_1^0)} = \frac{(-)}{(+)} < 0 \quad (2.37)$$

where the symbols (+) and (-) indicate that the mathematical quantities represented by the parentheses have the positive and negative signs, respectively. In a normal case of orbital interaction, therefore, the higher energy orbital  $\chi_2$  mixes in-phase into the lower level  $\chi_1$  to give the lower lying MO  $\psi_2$ , whereas the lower level  $\chi_1$  mixes out-of-phase into the higher level  $\chi_2$  to give the higher lying MO  $\psi_1$ . The magnitudes of the mixing coefficients  $t$  and  $|t'|$  are small when  $S_{12}$  and  $H_{12}$  are small. Hence, the major orbital character of the lower lying MO,  $\psi_1$ , is given by the lower atomic orbital  $\chi_1$ . Conversely, the major orbital character in  $\psi_2$  is contributed by  $\chi_2$ . As the two levels  $e_1^0$  and  $e_2^0$  become closer in energy, the weight of the higher atomic level  $\chi_2$  in the lower lying MO  $\psi_1$  increases, as does the weight of  $\chi_1$  in  $\psi_2$ . As examined in the degenerate case, when  $e_1^0 = e_2^0$ ,  $\chi_1$  and  $\chi_2$  have equal weights in  $\psi_1$  and  $\psi_2$ . The nodal properties of the MOs  $\psi_1$  and  $\psi_2$  are illustrated in Figure 2.3. One last graphical convention is needed here to represent the qualitative features of molecular orbitals. The relative magnitudes of the coefficients  $c_{1i}$  and  $c_{2i}$  ( $i = 1, 2$ ) are represented by the relative sizes of the orbital lobes  $\chi_1$  and  $\chi_2$ , respectively. Here again it may easily be shown that  $|t'| > t$ , or in other words, that the atomic coefficients for the high-lying level  $\psi_2$  in Figure 2.2 will be larger than those for the low-energy combination  $\psi_1$ .

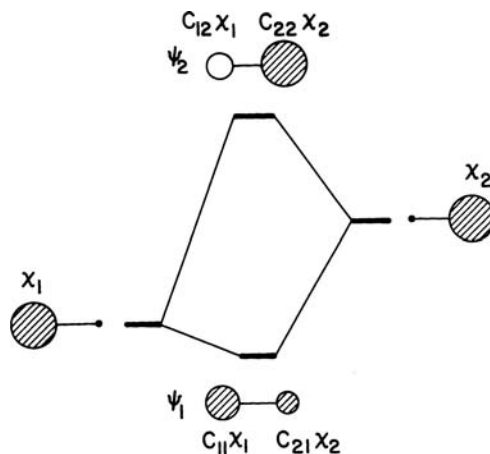


**FIGURE 2.3**

Molecular orbital diagram showing details of the nondegenerate interaction between two atomic s orbitals,  $\chi_1$  and  $\chi_2$ .

**TABLE 2.2** Summary of Orbital Interactions

Case	Orbital Interaction Energy
<b>2.3</b> degenerate	$\Delta E^{(2)} \propto -S_{12}$
<b>2.4</b> degenerate	$\Delta E^{(4)} \propto S_{12}^2$
<b>2.7</b> nondegenerate	$\Delta E^{(2)} \propto -\frac{S_{12}^2}{ e_1^0 - e_2^0 }$
<b>2.8</b> nondegenerate	$\Delta E^{(4)} \propto S_{12}^2$

### 2.3 THE TWO-ORBITAL PROBLEM—SUMMARY

The two-orbital problem is extremely important in that many of the bonding situations in chemistry can be distilled into just this form. We have waded through a laborious mathematical derivation. Let us review what we have uncovered thus far.

The qualitative aspects of the energy associated with orbital interactions are summarized in Table 2.2, which shows that:

1. In both degenerate and nondegenerate cases, the resultant upper molecular level is destabilized more than the lower molecular level is stabilized.
2. Regardless of whether the orbital picture contains two or four electrons, the magnitude of the total interaction energy increases with increasing overlap.
3. In a nondegenerate orbital interaction, the magnitude of the interaction energy is inversely proportional to the energy difference between the interacting orbitals.
4. In both degenerate and nondegenerate orbital interaction cases, a two-orbital–two-electron interaction is stabilizing, while a two-orbital–four-electron interaction is destabilizing.

It is worth mentioning that the destabilization associated with the two-orbital–four-electron situation is behind the nonexistence of a bound molecule for  $\text{He}_2$  or  $\text{Ne}_2$ , which have this orbital situation. The situation is complicated for three electrons. Using equations 2.8 and 2.9 for the degenerate case, along with equations 2.18 and 2.19 for the nondegenerate one, we find that there is a net stabilization still present as long as  $S_{12}$  remains small. However, when the overlap becomes large there is a critical point ( $S_{12} = 1/3$  for the degenerate situation) when the net interaction becomes repulsive.

In any two-orbital interaction, the resultant molecular orbitals display the following patterns:

1. The lower (more stable) molecular orbital is always mixed in-phase (bonding), and the upper molecular orbital is out-of-phase (antibonding) for the degenerate and nondegenerate cases. Thus, the lower molecular orbital contains no nodes perpendicular to and contained within the internuclear axis, and the upper level contains one such node.
2. In the degenerate and nondegenerate cases, the mixing coefficients for the antibonding orbitals are larger than their bonding counterparts.
3. For the nondegenerate situation, the molecular orbital most strongly resembles that starting atomic orbital closest to it in energy. The reader is referred to Figure 2.3.

The results here are very general and will be used throughout the course of this book. They will also apply to situations wherein one or both of the starting orbitals are not atomic orbitals but molecular orbitals from a fragment, which is covered in Chapter 3.

One point that frequently causes concern is the placement of starting and resultant orbitals in an orbital interaction diagram, for example, that shown in Figure 2.3 for a nondegenerate case. There are two qualitative aspects that must be considered. First, the amount that  $\chi_1$  is stabilized and  $\chi_2$  is destabilized (relative to the starting energies,  $e_1^0$  and  $e_2^0$ , respectively) after interaction is directly proportional to  $H_{12}^2$ . From equation I.19 recall that this is proportional to  $S_{12}^2$ ; a detailed discussion of the factors that influence  $S_{12}$  has been given in Section I.3. The stabilization and destabilization of the resultant molecular orbitals are also inversely dependent on the energy gap between  $\chi_1$  and  $\chi_2$ ,  $e_1^0 - e_2^0$ . Second, we must have some idea about where to position the energy of  $\chi_1$  relative to that of  $\chi_2$ . The experimental state averaged ionization potentials, in electron volts, for the main group atoms are shown in 2.9 [1]. However, those  $p$  atomic orbitals for groups 1 and 2 and for the  $s$  and  $p$

<b>H</b> -13.6								<b>He</b> -24.5
<b>Li</b> -5.4 -3.6*	<b>Be</b> -9.3 -6.1*	<b>B</b> -14.0 -8.3	<b>C</b> -19.4 -10.7	<b>N</b> -25.5 -13.2	<b>O</b> -32.4 -15.8	<b>F</b> -40.2 -18.6	<b>Ne</b> -48.5 -21.6	
<b>Na</b> -5.1 -3.2*	<b>Mg</b> -7.6 -4.6*	<b>Al</b> -11.3 -6.0	<b>Si</b> -14.9 -7.8	<b>P</b> -18.8 -9.6	<b>S</b> -22.7 -11.6	<b>Cl</b> -25.2 -13.7	<b>Ar</b> -29.2 -15.8	
<b>K</b> -4.3 -2.7*	<b>Ca</b> -6.1 -4.1*	<b>Ga</b> -12.6 -5.9	<b>Ge</b> -16.0 -7.5	<b>As</b> -18.9 -9.2	<b>Se</b> -21.4 -10.8	<b>Br</b> -24.4 -12.5	<b>Kr</b> -27.5 -14.2	
<b>Rb</b> -4.2 -2.8*	<b>Sr</b> -5.7 -3.8*	<b>In</b> -11.9 -5.6	<b>Sn</b> -14.6 -7.0	<b>Sb</b> -16.7 -8.4	<b>Te</b> -18.7 -9.8	<b>I</b> -20.9 -11.2	<b>Xe</b> -23.4 -12.6	
<b>Cs</b> -4.0* -2.6*	<b>Ba</b> -5.5* -3.6*	<b>Tl</b> -12.2* -5.3*	<b>Pb</b> -15.4* -6.7*	<b>Bi</b> -18.7* -8.2*				

## 2.9

orbitals of the sixth row are not experimentally known and hence, calculated values (indicated by an asterisk) have been used [2,3]. The latter include relativistic corrections. The general trends are easy to see. As we proceed from the left to the right in any row, the  $s$  and  $p$  orbitals go down in energy. This is a consequence of the fact that the valence electrons do not screen each other effectively. Thus, the addition of one proton to the nucleus and one electron does not cancel; instead, the valence electrons “feel” an increased nuclear charge. This is especially true for the  $s$  electrons because they penetrate closer to the nucleus than the  $p$  electrons do. Therefore, the  $s-p$  energy gap increases on going from left to right in the periodic table. The valence orbitals become more diffuse and the most probable distance of the electron to the nucleus increases as one descends a column in the periodic table. The energies of the valence electrons consequently increase. There are, however, two exceptions. The filled  $3d$  shell of electrons does not completely screen the  $4s$  and  $4p$  electrons. This effect is more important for the  $4s$  electrons so that the  $4s$  orbitals of Ga, Ge, and As are

actually lower in energy than the 3s orbitals of Al, Si, and P, respectively. Second, there is an important relativistic effect at work for the sixth row. The heavy mass of the nucleus for Tl through Bi causes a contraction of the inner s and p shells, which is transmitted out to the valence region. Again, this is more important for the 6s electrons than the 6p because of the greater penetration of the former. We might think that the s–p energy gap will decrease as one goes down a column in the periodic table since the valence orbitals become more diffuse. This does, indeed, happen in comparing the second and third rows. However, this is not a general phenomenon because the two factors, as just discussed, operate in the opposite direction. It is these considerations that yield screening constants and effective nuclear charges, discussed in Section 1.2. The values of the valence orbital energies in 2.9 should not be taken in a quantitative fashion when constructing an orbital interaction diagram. They merely are a guide. The values of  $e_1^0$  and  $e_2^0$  will also be sensitive to charging effects in the molecular environment. The most common way [4] to incorporate charging effects is to scale the orbital energies by

$$e^0 = Aq^2 + Bq + C$$

where  $q$  is the charge computed for the atom in the molecule,  $A$  and  $B$  are constants that depend on the atom type, and  $C$  is the orbital energy given in 2.9. A more useful guide to qualitative placement of orbital energies is the electronegativity of the atom. Electronegativity has been defined in many ways, perhaps the most common being the Pauling, Mulliken, and Allred–Rochow scales. The particular formulation, which we use, was developed by Allen [1]. Here, the electronegativity,  $\chi_{\text{spec}}$ , is defined as

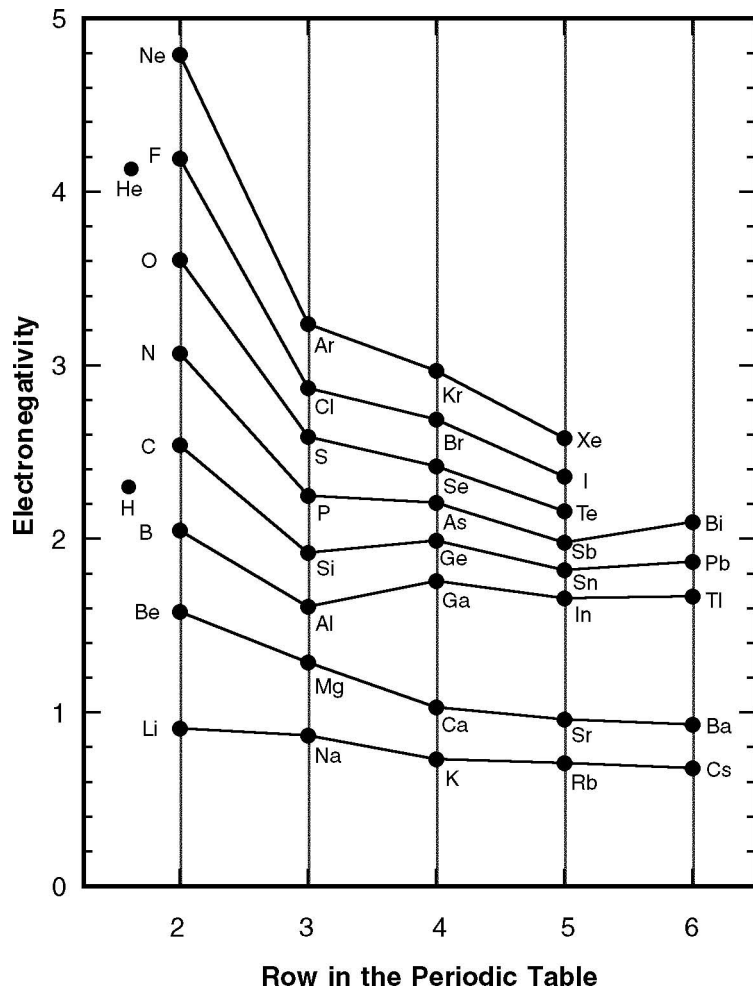
$$\chi_{\text{spec}} = K \frac{me_p^0 + ne_s^0}{m + n}$$

where  $e_p^0$  and  $e_s^0$  are the valence p and s energies, respectively, taken from 2.9,  $m$  and  $n$  are the number of valence p and s electrons, respectively, and  $K$  is a single scale factor, which sets the electronegativity values in the Allen scale on par to those from the Pauling and Allred–Rochow scales. A plot of  $\chi_{\text{spec}}$  is shown in Figure 2.4. This very conveniently encompasses all of the trends that we have just discussed. Namely, the electronegativity increases going from the left to the right along a row (the vertical direction in Figure 2.4). Along a column, it always decreases from the second to third rows and then is relatively constant with only minor decreases or in some cases even increases.

## 2.4 ELECTRON DENSITY DISTRIBUTION

One way that provides further insight into the energy changes that occur when  $\chi_1$  and  $\chi_2$  are allowed to interact is to use equation 1.13 along with the form of the  $\psi_i$  to calculate the new orbital energies

$$\begin{aligned} e_1 &= \langle \psi_1 | H^{\text{eff}} | \psi_1 \rangle \\ &= \left\langle \left( 1 - tS_{12} - \frac{1}{2}t^2 \right) \chi_1 + t\chi_2 | H^{\text{eff}} | \left( 1 - tS_{12} - \frac{1}{2}t^2 \right) \chi_1 + t\chi_2 \right\rangle \quad (2.38) \\ &\approx (1 - 2tS_{12} - t^2)e_1^0 + 2tH_{12} + t^2e_2^0 \end{aligned}$$

**FIGURE 2.4**

Plot of the **electronegativity** versus row for the main group atoms in the periodic table.

Here, terms greater than second order in  $t$  and  $S_{12}$  have been omitted. It is easy to show that equations 2.38 and 2.18 are identical. An analogous equation holds for  $e_2$ :

$$e_2 \approx (1 - 2t'S_{12} - t'^2)e_2^0 + 2t'H_{12} + t'^2e_1^0 \quad (2.39)$$

The origin of the various terms in these two equations is well known by looking at the electron density distribution associated with  $\psi_1$  and  $\psi_2$ . This is given in general by  $\psi_i^2$ . In a way analogous to the derivation of equations 2.38 and 2.39, this can be seen to be

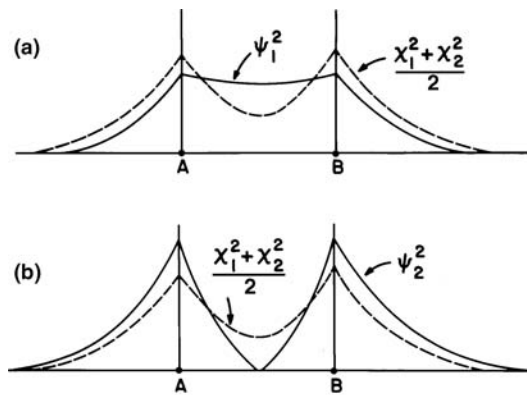
$$\psi_1^2 \approx (1 - 2tS_{12} - t^2)\langle\chi_1|\chi_1\rangle + 2t\langle\chi_1|\chi_2\rangle + t^2\langle\chi_2|\chi_2\rangle \quad (2.40)$$

and

$$\psi_2^2 \approx (1 - 2t'S_{12} - t'^2)\langle\chi_2|\chi_2\rangle + 2t'\langle\chi_1|\chi_2\rangle + t'^2\langle\chi_1|\chi_1\rangle \quad (2.41)$$

Upon integration over space and recalling that the atomic orbitals are normalized,

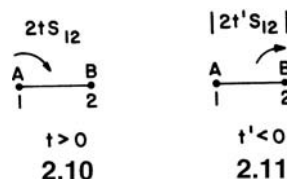
$$\text{For } \psi_1 : 1 = (1 - 2tS_{12} - t^2) + 2tS_{12} + t^2 \quad (2.42)$$

**FIGURE 2.5**

(a) Buildup of electron density between the nuclei in  $\psi_1$  compared to two superimposed atomic densities (dashed curve).  
 (b) Depletion of electron density between the nuclei in  $\psi_2$  compared to two superimposed atomic densities (dashed curve).

$$\text{For } \psi_2 : 1 = (1 - 2t'S_{12} - t'^2) + 2t'S_{12} + t'^2 \quad (2.43)$$

These equations show that the electron density associated with  $\psi_1$  may be decomposed into a density  $(1 - 2t'S_{12} - t'^2)$  in the region of atom A which holds orbital  $\chi_1$ , a density  $t^2$  in the region of atom B which holds orbital  $\chi_2$ , and a density  $2t'S_{12}$  in the region between A and B. A similar decomposition occurs for  $\psi_2$ . For positive  $t$  (the case for  $\psi_1$ ) then, as shown in 2.10, there occurs a shift of electron



density from the region of A to that between A and B. Energetically from equation 2.38 a stabilization results. The A and B atoms will experience an attractive contribution to their pair wise energy if  $\psi_1$  is occupied by electrons. Thus,  $\psi_1$  is a bonding molecular orbital. For the case of  $\psi_2$ ,  $t'$  is negative and this results (2.11) in removal of electron density from the region between A and B (equation 2.43). A corresponding destabilization (equation 2.39) results and  $\psi_2$  is thus an antibonding orbital. Figure 2.5 shows this for the degenerate interaction in terms of the electron density distribution along the internuclear axis.  $\psi_1^2$  is larger than  $(\chi_1^2 + \chi_2^2)/2$  and  $\psi_2^2$  is smaller than  $(\chi_1^2 + \chi_2^2)/2$  in the bonding region.

For a polyatomic molecule with molecular orbitals described in general by equation 2.44, this analysis may be extended to give

$$\psi_i = \sum_{\mu} c_{\mu i} \chi_{\mu} \quad (2.44)$$

the net electron population of an atomic orbital ( $P_{\mu\mu}$ ) and the overlap population ( $P_{\mu\nu}$ ) between two atomic orbitals  $\chi_{\mu}$  and  $\chi_{\nu}$  located on two atoms A, B in the molecule.  $P_{\mu\mu}$  corresponds to the amount of electron density left behind in orbital  $\chi_{\mu}$  after the interaction between the constituent atomic orbitals of the molecule, and  $P_{\mu\nu}$  to the amount transferred to the region between A and B, which will contribute

to A–B bonding. If each molecular orbital  $\psi_i$  contains  $n_i$  electrons ( $n_i = 0$ , 1, or 2), then

$$P_{\mu\mu} = \sum_i n_i c_{\mu i}^2 \quad (2.45)$$

$$P_{\mu\nu} = \sum_i 2n_i c_{\mu i} c_{\nu i} S_{\mu\nu} \quad (2.46)$$

a larger overlap population,  $P_{\mu\nu}$ , implies a stronger bond and a larger bond order between the two atoms, A and B. But the actual numbers must be used with care. A transition metal–transition metal single bond will invariably have a smaller overlap population than a carbon–carbon single bond. The overlap integral,  $S_{\mu\nu}$ , in equation 2.46 is expected to be smaller between two diffuse metal  $d$  orbitals than between 2s and 2p atomic orbitals on carbon. The gross population of  $\chi_\mu$ ,  $q_\mu$ , is defined as

$$q_\mu = P_{\mu\mu} + \frac{1}{2} \sum_{v(\neq\mu)} P_{\mu v} \quad (2.47)$$

Notice that the shared electron density,  $P_{\mu\nu}$  is divided equally between the two atoms in question. The gross atomic charge on each atom is simply the sum of all the  $q_\mu$ , belonging to that atom minus the nuclear charge of the atom on which orbital  $\chi_\mu$  is located. This is called the Mulliken population analysis. The computed charge on an atom of a molecule is influenced by a number of factors such as the basis set chosen, the exact details of  $H^{\text{eff}}$ , and whether electron correlation is taken into consideration or not. The Mulliken scheme is arbitrary in that it partitions the shared electron density equally between the two atoms. There are many other methods for population analysis, some perhaps preferable in that they do not appear to be as method and basis set dependent as the Mulliken scheme.

We will now apply these ideas specifically to the orbital situations depicted in **2.3**, **2.4**, **2.7**, and **2.8**. Initially for the degenerate interaction of **2.2** with the orbital occupation given in **2.3**

$$P_{11} = P_{22} = 2 \left( \frac{1}{\sqrt{2 + 2S_{12}}} \right)^2 = \frac{1}{1 + S_{12}} < 1 \quad (2.48)$$

and

$$P_{12} = 4 \left( \frac{1}{\sqrt{2 + 2S_{12}}} \right)^2 S_{12} = \frac{2S_{12}}{1 + S_{12}} > 0 \quad (2.49)$$

This shows a positive bond overlap population and a loss of electron density from orbitals  $\chi_1$  and  $\chi_2$  into the bonding region. This gives rise to a stabilizing situation. The converse is true for the four-electron case of **2.4**, however. Here

$$P_{11} = P_{22} = 2 \left( \frac{1}{\sqrt{2 + 2S_{12}}} \right)^2 + 2 \left( \frac{1}{\sqrt{2 - 2S_{12}}} \right)^2 = \frac{2}{1 - S_{12}^2} > 0 \quad (2.50)$$

and

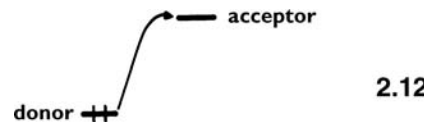
$$P_{12} = 4 \left( \frac{1}{\sqrt{2 + 2S_{12}}} \right)^2 S_{12} - 4 \left( \frac{1}{\sqrt{2 - 2S_{12}}} \right)^2 S_{12} = \frac{-4S_{12}^2}{1 - S_{12}^2} < 0 \quad (2.51)$$

Now there is a transfer of electron density out of the bonding region such that  $P_{ii} > 2$  and the bond overlap is negative. This stems from the result, shown in Figure 2.5, that

**TABLE 2.3** Summary of Population Analyses Cases

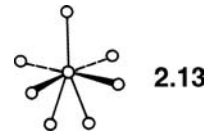
Quantity\Case	2.3	2.4	2.7	2.8
$P_{11}$	$\frac{1}{1 + S_{12}}$	$\frac{2}{1 - S_{12}^2}$	$2(1 - 2tS_{12} - t^2)$	$2(1 + S_{12}^2)$
$P_{22}$	$\frac{1}{1 + S_{12}}$	$\frac{2}{1 - S_{12}^2}$	$2t^2$	$2(1 + S_{12}^2)$
$P_{12}$	$\frac{2S_{12}}{1 + S_{12}}$	$\frac{-4S_{12}^2}{1 - S_{12}^2}$	$4tS_{12}$	$-4S_{12}^2$
$q_1$	1	2	$2(1 - tS_{12} - t^2)$	2
$q_2$	1	2	$2(tS_{12} + t^2)$	2

with respect to the superposed atomic orbital density ( $\chi_1^2 + \chi_2^2$ )/2, the electron gain resulting from occupation of  $\psi_1$  in the region between A and B is smaller than the electron loss from this region by occupation of  $\psi_2$ . These results and the corresponding ones for the nondegenerate case with the electron occupations of **2.7** and **2.8** are summarized in Table 2.3. These are broadly similar. The two-orbital two-electron case results in a positive bond overlap population; the two-orbital four-electron situation creates a negative bond overlap population. In the former, there occurs an electron density shift from  $\chi_1$  to  $\chi_2$  as a result of the orbital interaction (i.e.,  $P_{22} = 2t^2 > 0$ ). A two-orbital–two-electron interaction is therefore often called a charge transfer interaction. As shown in **2.12**, the initially doubly occupied and



empty orbitals  $\chi_1$  and  $\chi_2$  are called the donor and acceptor orbitals, respectively.

Having progressed this far with a simple two-orbital problem, how do the results change for a many orbital system? The details of this case are discussed in Chapter 3. However, it is not too surprising that for the particular example of **2.13**



(i.e., a single “central” atom surrounded by some ligands) then the single term of equation 2.18 is replaced by an energy sum

$$e_1 \approx e_1^0 + \sum_{j \neq 1} \frac{(H_{1j} - e_1^0 S_{1j})^2}{e_1^0 - e_j^0} \quad (2.52)$$

with a corresponding summation term to describe the new wavefunction. (In this simple expression we have, of course, neglected interactions between orbitals located on different ligands.)

---

## PROBLEMS

---

- 2.1.** Let us do a calculation on the Li–H molecule. For this calculation, we shall just consider a 1s AO on hydrogen,  $\chi_1$ , and the 2s AO on lithium,  $\chi_2$ . We will use  $H_{11} = -13.60$  and  $H_{22} = -5.40$  eV which have been taken from **2.9** in the text.  $S_{12}$  was computed to be 0.3609 using an STO with orbital exponents given in **1.3** at a Li–H bond distance of 3.015 bohr. For the resonance integral use the Wolfsberg–Helmholtz approximation:

$$H_{12} = K \frac{(H_{11} + H_{22})}{2} S_{12} \text{ with } K = 1.75$$

- a. Set up the secular determinant and secular equations. Solve them explicitly.
- b. Do a Mulliken population analysis on Li–H using your answer in (a). The dipole moment,  $\mu^*$ , for a neutral diatomic molecule can be calculated using the point charge approximation as  $\mu^* = 2.54Qr$ , where  $Q$  is the charge on one of the atoms and  $r$  is the distance between the two atoms. Calculate the dipole moment for Li–H using your charges.
- c. The table below lists some results from a HF SCF calculation on Li–H. Here, the 1s AO and the three 2p AOs on Li have been explicitly included in the calculation. For the minimal basis set, there is essentially one STO used for the 1s, 2s, and 2p AOs on Li and the 1s AO on H. In the extended basis set, there are three functions for Li 2s, 2p, and H 1s. In addition, polarization functions ( $d$  on Li and  $p$  on H) are added to the basis. Listed are the charges on the atoms,  $Q$ , the total Mulliken overlap population,  $P_{\text{LiH}}$ , the dipole moment computed using the point charge approximation,  $\mu^*$ , and the computed dipole with no approximations,  $\mu$ . Describe in general terms why your answers are very different for  $Q$ ,  $P_{\text{LiH}}$ , and  $\mu^*$  compared to those at the minimal basis set level and what happens to these quantities going from the minimal to extended basis level.
- d. Describe in physical terms why  $\mu^*$  is much less than  $\mu$  and why the two computed  $e_1$  values are very much different from the one that you calculated.

Property	Minimal Basis	Extended Basis
$Q_{\text{H}}$	-0.2194	-0.3569
$Q_{\text{Li}}$	0.2194	0.3569
$P_{\text{LiH}}$	0.7556	0.7428
$\mu^*$	1.68	2.73
$\mu$	5.89	6.00
$e_1$	-8.07	-8.14

- 2.2.** Throughout this chapter, it was emphasized that a two-electron-two-center interaction was stabilizing. Of course with one electron this is also true, albeit to a lesser extent. With four electrons, there is always a net destabilization. But what happens when a bond has three electrons? Using the two solutions for a degenerate interaction (equation 2.7) show under what condition the three-electron–two-center bond is stable.

---

## REFERENCES

---

1. L. C. Allen, *J. Am. Chem. Soc.*, **111**, 9003 (1989); L. C. Allen, *J. Am. Chem. Soc.*, **114**, 1510 (1992); L. C. Allen, *Acc. Chem. Res.*, **23**, 175 (1990).
2. A. Vela and J. L. Gazquez, *J. Phys. Chem.*, **92**, 5688 (1988).
3. J. P. Desclaux, *At. Nucl. Data Tables*, **12**, 311 (1973).
4. S. P. McGlynn, L.G. Vanquickenborne, M. Kinoshita, and D. G. Carroll, *Introduction to Applied Quantum Chemistry*, Holt, Rinehart, and Winston, New York (1972).

**C H A P T E R 3**

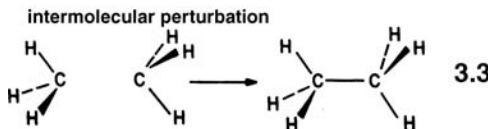
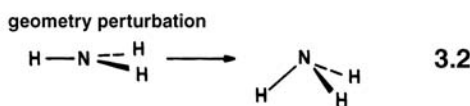
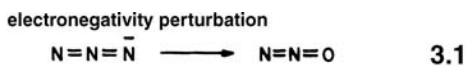
# **Perturbational Molecular Orbital Theory**

---

## **3.1 INTRODUCTION**

---

In principle, we can perform some sort of molecular orbital calculation on molecules of almost any complexity. It is, however, often extremely profitable to relate the properties of a complex system to those of a simpler one. Take, for example, the hydrogen atom in an electric field. It is much more instructive to see how the unperturbed levels of the atom are altered as a field is applied, than to solve the Schrödinger wave equation for the more complex case of the molecule with the field on. Analogously, to appreciate the orbital structure of complex systems it is much more insightful to start off with the levels of a simpler one and “switch on” a perturbation. **3.1–3.3** show three examples of different types of perturbations



which we frequently use. We are interested in seeing how the levels of the species at the left-hand side of these figures are altered electronically during a perturbation involving molecular assembly, geometrical change, or atomic substitution. The theoretical technique that will be used is perturbation theory. We do not derive the elements of the theory itself (this is done in Appendix I) but make use of its mathematical results [1–4], which will very quickly show a striking resemblance to the orbital interaction results of Chapter 2.

Consider a set of unperturbed (zeroth order in the language of perturbation theory) orbitals  $\psi_i^0$  with energy  $e_i^0$  corresponding to the left-hand side of 3.1–3.3. In general, these orbitals are given in terms of atomic orbitals as

$$\psi_i^0 = \sum_{\mu} c_{\mu i}^0 \chi_{\mu} \quad (3.1)$$

which we assume to be the eigenfunctions of  $H^{\text{eff}}$ . Thus,

$$H^{\text{eff}} \psi_i^0 = e_i^0 \psi_i^0 \quad (3.2)$$

Now, importantly, within the framework of perturbation theory, the new wavefunctions that result after the perturbation have been switched on may be written as a linear combination of the unperturbed orbitals, that is,  $\psi_i$  is given by

$$\psi_i = t_{ii} \psi_i^0 + \sum_{j \neq i} t_{ji} \psi_j^0 \quad (3.3)$$

The coefficients  $t_{ii}$  and  $t_{ji}$  ( $j \neq i$ ), known as mixing coefficients, are expanded as

$$t_{ii} = t_{ii}^0 + t_{ii}^{(1)} + t_{ii}^{(2)} + \dots \quad (3.4)$$

$$t_{ji} = t_{ji}^0 + t_{ji}^{(1)} + t_{ji}^{(2)} + \dots \quad (3.5)$$

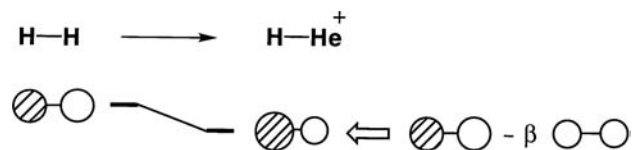
This series represents a set of “corrections” to the unperturbed wavefunction,  $\psi_i^0$ . Subscripts are problematic in this chapter. Recall the convention that Greek characters are reserved for atomic orbitals and the Roman alphabet in italics is used for molecular orbitals (i.e., some combination of atomic orbitals whether they are for a molecule or a fragment in a molecule). Thus,  $c_{\mu i}$  stands for the  $\mu$ th atomic orbital in molecular orbital  $i$ . The order of the subscripts in equations 3.3 and 3.5 are important;  $t_{ji}^{(q)}$  stands for how much molecular orbital  $j$  mixes into molecular orbital  $i$  to the “ $q$ th” order of perturbation. Before the perturbation is switched on,  $t_{ii} = 1$  and all  $t_{ji} = 0$ . Later, the weight of  $\psi_i^0$  (i.e., the mixing coefficient  $t_{ii}$ ) has to be smaller than one since  $\psi_i$  is normalized to unity just like  $\psi_i^0$  itself.

The energy changes of the orbitals as a result of the perturbation are expanded in the same way

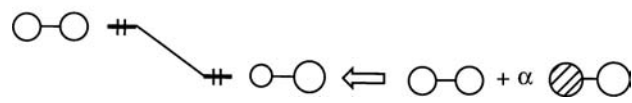
$$e_i = e_i^0 + e_i^{(1)} + e_i^{(2)} + \dots \quad (3.6)$$

Here,  $e_i^{(1)}$  and  $e_i^{(2)}$  are the first- and second-order energy corrections, respectively, to the unperturbed level  $e_i^0$ . Perturbation theory gives recipes for evaluating the terms of equations 3.4–3.6.

As a simple example which illustrates both changes in energy and the form of the wavefunction consider the “transmutation” reaction  $\text{H}_2 \rightarrow \text{H} - \text{He}^+$ . The orbitals

**FIGURE 3.1**

How the orbitals of the  $\text{H}-\text{He}^+$  molecule may be written in terms of linear combinations of those of  $\text{H}_2$ .



and energies of the two systems are shown in Figure 3.1. It is easy to see in principle how in qualitative terms the new wavefunctions may be written in the form of equation 3.3 in terms of the old using mixing coefficients of  $\alpha$  and  $\beta$ . The energies of both bonding and antibonding orbitals lie deeper in  $\text{H}-\text{He}^+$  than in  $\text{H}_2$  because of the large contribution from the more electronegative He 1s basis orbital (see Figure 2.4). The signs of  $\alpha$  and  $\beta$  are determined from the results of the nondegenerate, two-orbital problem (see Section 2.4 and Figure 2.3). The bonding orbital is more concentrated on the more electronegative He atom and the reverse is true for the antibonding orbital.

To discuss these changes in detail via the expressions of equations 3.4–3.6, we need to examine what happens to the molecular integrals  $\langle \psi_i^0 | \psi_j^0 \rangle$  and  $\langle \psi_i^0 | H^{\text{eff}} | \psi_j^0 \rangle$  as a consequence of electronegativity, geometry, or intermolecular perturbation. When there is no perturbation, the zeroth order orbitals are orthonormal and are eigenfunctions of  $H^{\text{eff}}$ . After the perturbation is switched on, some or all of the  $S_{\mu\nu}$  and  $H_{\mu\nu}$  elements change in size. For example, the perturbation of replacing a nitrogen with a more electronegative oxygen in 3.1 will result in a change in the  $H_{\mu\mu}$  elements on this end atom and a change in all the interaction elements involving orbitals located on that atom. Recall via the Wolfsberg–Helmholz relationship (equation 1.19):  $H_{\mu\nu} \propto S_{\mu\nu}(H_{\mu\mu} + H_{\nu\nu})$ . Since the oxygen atom orbitals have different exponents (they are more contracted, see 1.3) than those orbitals on the nitrogen atom they replace, the changes in  $H_{\mu\nu}$  elements will arise via changes in both  $S_{\mu\nu}$  and  $H_{\mu\mu}$ , where  $\mu$  represents an orbital on the substituted atom. The geometry perturbation 3.2 will involve changing  $H_{\mu\nu}$  values between some of the atomic orbitals of the basis as a result of a change in the corresponding overlap integrals  $S_{\mu\nu}$  demanded by the geometry change. Simple examples of this were given in Section 1.3. The intermolecular perturbation 3.3 switches on some initially zero  $S_{\mu\nu}$  and  $H_{\mu\nu}$  values between the atomic orbitals of one fragment and those of the other as the two fragments are brought to bonding distances from infinity. Perturbation theory is used in this book as an analytical device. We will not be interested in exact numerical details, rather we wish to understand how the relative energies of molecular orbitals and their shapes change after the perturbation is switched on. In 3.1 and 3.2, the orbital structure and energies are easy to construct for the unperturbed molecules on the left side of the drawings. They are given largely by symmetry. Perturbation theory is then used in these two examples to show (qualitatively) what occurs when the symmetry is lowered. Likewise, it is much easier to construct the molecular orbitals of a “complicated” molecule from two smaller pieces, as in 3.3.

Let us denote the changes in  $S_{\mu\nu}$  and  $H_{\mu\nu}$  induced by the perturbation as  $\delta S_{\mu\nu}$  and  $\delta H_{\mu\nu}$ , respectively. It is more convenient to represent modifications in the

overlap and resonance integrals using a molecular rather than atomic basis. This is done in equations 3.7 and 3.8, respectively.

$$\sum_{\mu} \sum_{\nu} c_{\mu i}^0 \delta S_{\mu\nu} c_{\nu j}^0 = \tilde{S}_{ij} \quad (3.7)$$

$$\sum_{\mu} \sum_{\nu} c_{\mu i}^0 \delta H_{\mu\nu} c_{\nu j}^0 = \tilde{H}_{ij} \quad (3.8)$$

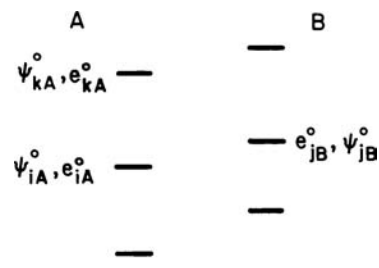
When  $i \neq j$ ,  $\tilde{S}_{ij}$  and  $\tilde{H}_{ij}$  represent the deviation of the overlap and resonance integrals from zero after the perturbation has been turned on between molecular orbitals  $i$  and  $j$  ( $i$  and  $j$  are normalized and orthogonal for the unperturbed case). Importantly, equations 3.7 and 3.8 show that the magnitudes of  $\tilde{S}_{ij}$  and  $\tilde{H}_{ij}$  are given by how much the overlap and resonance integrals change between pairs of atomic orbitals ( $\mu$  and  $\nu$ ) weighted by the size of the mixing coefficients associated with the atomic orbitals in molecular orbitals  $i$  and  $j$ . It is also very important to note that  $\tilde{H}_{ij}$  and  $\tilde{S}_{ij}$  are related by

$$\tilde{H}_{ij} \propto -\tilde{S}_{ij} (i = j \text{ or } i \neq j) \quad (3.9)$$

The relationship between  $\tilde{S}_{ij}$  and  $\tilde{H}_{ij}$  will be exploited so that a qualitative assessment of the magnitude (and sign) of  $\tilde{S}_{ij}$  can easily be made. For  $\tilde{S}_{ij}$  to be nonzero there must be a change of the overlap integral between pairs of atomic orbitals and their atomic coefficients in molecular orbitals  $i$  and  $j$  must be nonzero. Thus, the variation in the magnitude of  $\tilde{S}_{ij}$  exactly parallels that for the general trends for  $S_{\mu\nu}$  in Section 1.3. In what follows we shall use the techniques of perturbation theory to evaluate the  $e_i^{(q)}$ ,  $t_{ii}^{(q)}$  and  $t_{ji}^{(q)}$ . The reader who wishes to know more about perturbation theory itself is referred to the Reference section and Appendix I in this book. Our aim here is to show how the basic principles may be used in orbital construction for intermolecular perturbations. Electronegativity and geometrical changes are covered in Sections 6.4 and 7.2, respectively.

## 3.2 INTERMOLECULAR PERTURBATION

An intermolecular perturbation leads to modification of the orbitals of one molecule (or fragment) by those of another. A hypothetical example of intermolecular perturbation is shown in 3.4. The orbitals are ordered into two stacks, one



3.4

belonging to fragment  $A$  and the other to fragment  $B$ , which are brought together to form the molecule  $AB$ . Let us assume for simplicity that, when two fragments

interact with each other, no geometry change occurs within each fragment so that there is no geometry perturbation to consider within each fragment. To obtain the orbitals of the fragments A and B joined by a single bond, one might break the bond to generate A<sup>·</sup> and B<sup>·</sup> radicals, A<sup>+</sup> and B<sup>-</sup> ions, or A<sup>-</sup> and B<sup>+</sup> ions and then carry out molecular orbital calculations for these fragments. In self-consistent-field (SCF) molecular orbital calculations, the energy levels and their atomic orbital coefficients of a molecular species depend on the number of electrons it contains (see Chapter 8 for further discussion). For example, the orbitals of the A<sup>+</sup>, A<sup>·</sup>, and A<sup>-</sup> species are not identical. Since we are interested only in qualitative features of intermolecular perturbation, we shall neglect the dependence of the fragment orbitals on the number of electrons. Namely, it is assumed that the fragment orbitals are obtained by a non-SCF method, so the orbitals of say the A<sup>+</sup>, A<sup>·</sup>, and A<sup>-</sup> species are identical, that is,  $\tilde{H}_{ij}$  and  $\tilde{S}_{ij}$ , along with  $e_i^0$  and  $\psi_i^0$  will be treated as being invariant with respect to the partitioning scheme.

Therefore, for those atomic orbitals  $\chi_\mu$  and  $\chi_\nu$  located on the fragments A and B, respectively, the  $\delta H_{\mu\nu}$  and  $\delta S_{\mu\nu}$  values are simply the  $H_{\mu\nu}$  and  $S_{\mu\nu}$  values of the composite system AB, respectively. The following perturbation integrals are obtained between the fragment orbitals  $\psi_{nA}^0$  ( $n=i, k$ ) and  $\psi_{jB}^0$ :

$$\begin{aligned}\tilde{S}_{nj} &= \sum_{\mu \in A} \sum_{\nu \in B} c_{\mu n}^0 S_{\mu\nu} c_{\nu j}^0 = \langle \psi_{nA}^0 | \psi_{jB}^0 \rangle \\ \tilde{H}_{nj} &= \sum_{\mu \in A} \sum_{\nu \in B} c_{\mu n}^0 H_{\mu\nu} c_{\nu j}^0 = \langle \psi_{nA}^0 | H^{\text{eff}} | \psi_{jB}^0 \rangle\end{aligned}\quad (3.10)$$

The subscripts A and B have been added only to help the reader to keep track of which fragment a particular orbital has originated from. The symbol  $\lambda \in X$  ( $\lambda = \mu, \nu; X = A, B$ ) includes all orbitals  $\lambda$  that are located on atom X.  $\tilde{S}_{nj}$  is the overlap integral between  $\psi_{nA}^0$  and  $\psi_{jB}^0$ , and  $\tilde{H}_{nj}$  is the corresponding interaction energy. An orbital  $\psi_{iA}^0$  on the fragment A will be influenced both by orbitals  $\psi_{kA}^0$  on the same fragment and orbitals  $\psi_{jB}^0$  on the other fragment B. We rewrite equation 3.3 as

$$\psi_i = (1 + t_{ii}^{(2)})\psi_{iA}^0 + \sum_{j \in B} t_{ji}^{(1)}\psi_{jB}^0 + \sum_{k \in A, k \neq i} t_{ki}^{(2)}\psi_{kA}^0 \quad (3.11)$$

where, using equation 3.9,

$$t_{ii}^{(2)} = - \sum_{j \in B} \left[ \tilde{S}_{ij} t_{ji}^{(1)} + \frac{1}{2} \left( t_{ji}^{(1)} \right)^2 \right] \quad (3.12)$$

$$t_{ji}^{(1)} = \sum_{j \in B} \frac{\tilde{H}_{ij} - e_{iA}^0 \tilde{S}_{ij}}{e_{iA}^0 - e_{jB}^0} \quad (3.13)$$

**This line might be wrong**  $\propto \sum_{j \in B} \frac{-\tilde{S}_{ij}}{e_{iA}^0 - e_{jB}^0}$

$$t_{ki}^{(2)} = \sum_{j \in B} \frac{(\tilde{H}_{ij} - e_{iA}^0 \tilde{S}_{ij})(\tilde{H}_{jk} - e_{iA}^0 \tilde{S}_{jk})}{(e_{iA}^0 - e_{kA}^0)(e_{iA}^0 - e_{jB}^0)} \quad (3.14)$$

$$\propto \sum_{j \in B} \frac{\tilde{S}_{ij} \tilde{S}_{jk}}{(e_{iA}^0 - e_{kA}^0)(e_{iA}^0 - e_{jB}^0)}$$

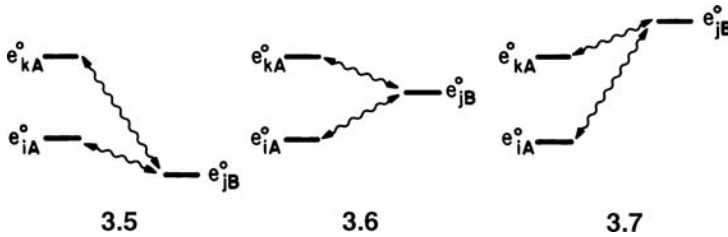
The apparently complex expression for the resultant wavefunction,  $\psi_i$ , is a function of three terms and may be broken down in the following way.

After the perturbation is turned on  $\psi_{jB}^0$  mixes into  $\psi_{iA}^0$  with a first-order mixing coefficient  $t_{ji}^{(1)}$  and  $\psi_{kA}^0$  mixes into  $\psi_{iA}^0$  with a second-order mixing coefficient  $t_{ki}^{(2)}$ . The term  $(1 + t_{ii}^{(2)})$  in equation 3.11 represents a correction to normalize  $\psi_i$ . From equation 3.12 one can see that  $t_{ii}^{(2)}$  will be small in magnitude. It is sufficient to remember that the weight of  $\psi_{iA}^0$  is less than (but close to) one in most cases of our applications. It is important to realize that  $|1 + t_{ii}^{(2)}| > |t_{ji}^{(1)}| > |t_{ki}^{(2)}|$ . Thus, the leading term in the construction of  $\psi_i$  is the zeroth order, unperturbed  $\psi_{iA}^0$  itself and

$$\psi_i \cong \psi_{iA}^0 + \sum_{j \in B} t_{ji}^{(1)} \psi_{jB}^0 + \sum_{k \in A, k \neq i} t_{ki}^{(2)} \psi_{kA}^0 \quad (3.15)$$

Suppose that the orbital phases of  $\psi_{iA}^0$  and  $\psi_{jB}^0$  are arranged so that  $\tilde{S}_{ij}$  is positive. Then, equation 3.13 shows that  $\psi_{jB}^0$  mixes into  $\psi_{iA}^0$  in a bonding way, with  $t_{ji}^{(1)} = (+)$ , if  $\psi_{jB}^0$  lies higher in energy than  $\psi_{iA}^0$  ( $e_{iA}^0 - e_{jB}^0 < 0$ ), but in an antibonding way, with  $t_{ji}^{(1)} = (-)$ , if  $\psi_{jB}^0$  lies lower ( $e_{iA}^0 - e_{jB}^0 > 0$ ). This is precisely the same equation as was determined from the two-orbital mixing problem in Section 2.2.B, see equations 2.36 and 2.37, now cast in terms of fragment orbitals  $i$  and  $j$ .

Equation 3.14 shows that a smaller second-order perturbation of the wavefunction can occur. Within the fragment A,  $\psi_{kA}^0$  mixes into  $\psi_{iA}^0$  with the second-order mixing coefficient  $t_{ki}^{(2)}$  when  $\psi_{iA}^0$  and  $\psi_{kA}^0$  both interact with  $\psi_{jB}^0$  of the fragment B, that is, when  $\tilde{S}_{ij}$  and  $\tilde{S}_{jk}$  are nonzero. Notice, however, that  $\tilde{S}_{ik} = 0$ . If the orbital phases of  $\psi_{iA}^0$ ,  $\psi_{kA}^0$ , and  $\psi_{jB}^0$  are arranged such that both  $\tilde{S}_{ij}$  and  $\tilde{S}_{jk}$  are positive, the sign of  $t_{ki}^{(2)}$  is simply determined by the relative ordering of the  $\psi_{iA}^0$ ,  $\psi_{kA}^0$ , and  $\psi_{jB}^0$  levels. Three situations that may be encountered in practice are shown in 3.5–3.7, which differ in



the ordering of these levels. For the case of 3.5,  $\psi_{kA}^0$  mixes into  $\psi_{iA}^0$  in second order with a sign given by

$$t_{ki}^{(2)} \propto \sum_{j \in B} \frac{\tilde{S}_{ij} \tilde{S}_{jk}}{(e_{iA}^0 - e_{kA}^0)(e_{iA}^0 - e_{jB}^0)} = \frac{(+)(+)}{(-)(+)} = (-) \quad (3.16)$$

and  $\psi_{iA}^0$  mixes into  $\psi_{kA}^0$  with a sign

$$t_{ik}^{(2)} \propto \sum_{j \in B} \frac{\tilde{S}_{kj} \tilde{S}_{ji}}{(e_{kA}^0 - e_{iA}^0)(e_{kA}^0 - e_{jB}^0)} = \frac{(+)(+)}{(+)(+)} = (+) \quad (3.17)$$

The signs of  $t_{ki}^{(2)}$  and  $t_{ik}^{(2)}$  for the other situations in 3.6 and 3.7 are shown in Table 3.1, which indicates that there are only two cases when the second-order mixing coefficient becomes negative: (1) when the mixing into lower lying orbital  $\psi_{iA}^0$

**TABLE 3.1** Signs of the Second-Order Mixing Coefficients

Coefficient	Case	3.5	3.6	3.7
$t_{ki}^{(2)}$	(−)	(+)	(+)	(−)
$t_{ik}^{(2)}$	(+) (−)	(+) (−)	(+) (−)	(+) (−)

occurs via a deeper, lower lying intermediate orbital  $\psi_{jB}^0$  and (2) when the mixing into the higher lying orbital  $\psi_{kA}^0$  occurs via an even higher lying orbital  $\psi_{jB}^0$ . These results are valid *only* when the phases of the orbitals  $\psi_{iA}^0$ ,  $\psi_{kA}^0$ , and  $\psi_{jB}^0$  are so arranged that both  $\psi_{iA}^0$  and  $\psi_{kA}^0$  make positive overlap with  $\psi_{jB}^0$ .

The energy  $e_i$  of the perturbed level  $\psi_i$  that originates from  $\psi_{iA}^0$  is given by

$$e_i = e_{iA}^0 + e_i^{(2)} \quad (3.18)$$

where the perturbation theory recipes lead to

$$\begin{aligned} e_i^{(2)} &= \sum_{j \in B} \frac{(\tilde{H}_{ij} - e_{iA}^0 \tilde{S}_{ij})^2}{e_{iA}^0 - e_{jB}^0} \\ &\propto \sum_{j \in B} \frac{\tilde{S}_{ij}^2}{e_{iA}^0 - e_{jB}^0} \end{aligned} \quad (3.19)$$

The second-order energy correction is stabilizing,  $e_i^{(2)} = (−)$ , when  $e_{iA}^0 - e_{jB}^0 < 0$  and it is destabilizing when  $e_{iA}^0 - e_{jB}^0 > 0$ . In other words, the level at higher energy always mixes in to stabilize the lower orbital and an orbital at lower energy will always destabilize an upper level provided that  $\tilde{S}_{ij} \neq 0$ . Note that the first-order orbital mixing between  $\psi_{iA}^0$  and  $\psi_{jB}^0$  (i.e.,  $t_{ji}^{(1)}$ ) leads to the second-order energy change  $e_i^{(2)}$ . The second-order orbital mixing between  $\psi_{iA}^0$  and  $\psi_{kA}^0$  leads to a third-order energy correction, which is not shown in equation 3.18.

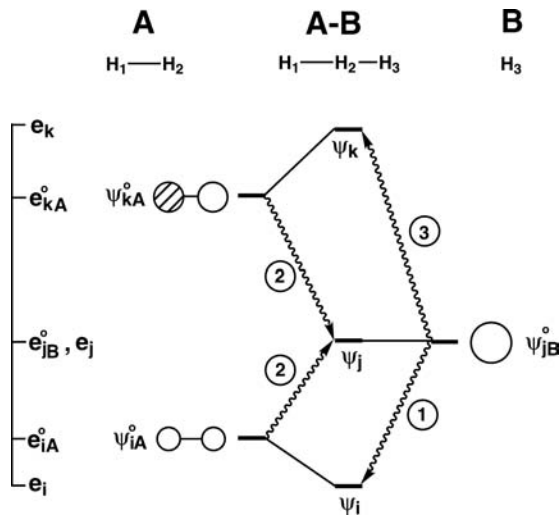
### 3.3 LINEAR H<sub>3</sub>, HF AND THE THREE-ORBITAL PROBLEM

An example shows the application of some of the ideas introduced above. Let us start with a simple three-orbital problem in which two orbitals on A interact with one on B as when the orbitals of linear H<sub>3</sub> are constructed from those of H<sub>2</sub> + H (3.8).



This is shown in Figure 3.2, where the “basis” of orbitals are  $\sigma$  and  $\sigma^*$  of H<sub>2</sub> on fragment A and an s atomic orbital on a hydrogen atom for fragment B. The shapes and energetic placement of these three orbitals follow the exhaustive treatment of the two-orbital problem in Chapter 2. The relative phases of the orbitals in Figure 3.2 have been chosen so that  $\tilde{S}_{ij}$  and  $\tilde{S}_{jk}$  are positive.

Let us first consider interaction ① in Figure 3.2. The orbital  $\psi_{iA}^0$  will be stabilized by interaction with  $\psi_{jB}^0$  since the energy denominator of the second-order energy

**FIGURE 3.2**

Derivation of the molecular orbital diagram for linear H<sub>3</sub> from that of H<sub>2</sub> plus H.

correction (equation 3.19) is negative ( $e_{iA}^0 - e_{jB}^0 < 0$ ), that is,

$$\begin{aligned} e_i &= e_{iA}^0 + e_i^{(2)} \\ e_i^{(2)} &\propto \frac{\tilde{S}_{ij}^2}{e_{iA}^0 - e_{jB}^0} = \frac{(+) }{(-)} = (-) \end{aligned} \quad (3.20)$$

From equations 3.13–3.15, the resulting orbital is given as

$$\psi_i \cong \psi_{iA}^0 + t_{ji}^{(1)} \psi_{jB}^0 + t_{ki}^{(2)} \psi_{kA}^0 \quad (3.21)$$

where

$$t_{ji}^{(1)} \propto \frac{-\tilde{S}_{ij}}{e_{iA}^0 - e_{jB}^0} = \frac{-(+)}{(-)} = (+)$$

and

$$t_{ki}^{(2)} \propto \frac{\tilde{S}_{ij} \tilde{S}_{jk}}{(e_{iA}^0 - e_{jB}^0)(e_{jB}^0 - e_{kA}^0)} = \frac{(+)(+)}{(-)(-)} = (+)$$

The coefficient  $t_{ji}^{(1)}$  is readily seen to be positive since  $\psi_{jB}^0$  lies higher in energy than  $\psi_{iA}^0$ , and from Table 3.1,  $t_{ki}^{(2)}$  is also positive. (The situation in Figure 3.2 corresponds to case 3.6.) Thus, both  $\psi_{jB}^0$  and  $\psi_{kA}^0$  mix into  $\psi_{iA}^0$  with the same phases as are given in Figure 3.2. At this stage we introduce a useful shorthand notation to indicate the first- and second-order contributions to a perturbed orbital. Since in most qualitative applications, the coefficients  $t_{ji}^{(1)}$  and  $t_{ki}^{(2)}$  are small compared to unity, what is most important is their sign. The first-order contribution  $t_{ji}^{(1)} \psi_{jB}^0$  will be written using parentheses as in equation 3.22,

$$\begin{aligned} t_{ji}^{(1)} \psi_{jB}^0 &= (\psi_{jB}^0) \quad \text{if} \quad t_{ji}^{(1)} > 0 \\ t_{ji}^{(1)} \psi_{jB}^0 &= -(\psi_{jB}^0) \quad \text{if} \quad t_{ji}^{(1)} < 0 \end{aligned} \quad (3.22)$$

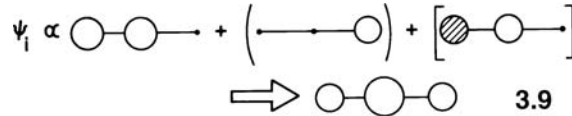
and the second-order contribution  $t_{ki}^{(2)}\psi_{kA}^0$  using brackets as in equation 3.23.

$$\begin{aligned} t_{ki}^{(2)}\psi_{kA}^0 &= [\psi_{kA}^0] \quad \text{if} \quad t_{ki}^{(2)} > 0 \\ t_{ki}^{(2)}\psi_{kA}^0 &= -[\psi_{kA}^0] \quad \text{if} \quad t_{ki}^{(2)} < 0 \end{aligned} \quad (3.23)$$

The new orbital  $\psi_i$  is then constructed as

$$\psi_i \cong \psi_{iA}^0 + (\psi_{jB}^0) + [\psi_{kA}^0]$$

It is diagrammatically shown by 3.9. It is important to recall that these mixing



coefficients are smaller than one, as discussed already. The consequence of the second-order term is to diminish the atomic orbital coefficient on the left H atom and reinforce the coefficient on the middle one. If the two close H—H distances are equal, then by symmetry the atomic orbital coefficients of the left and right H atom orbitals in the resultant  $\psi_i$  must be equal.

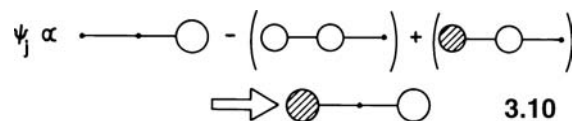
The new level  $e_j$  represents the sum of two interactions given by ② in Figure 3.2. The resulting energy can be expressed as

$$\begin{aligned} e_j &= e_{jB}^0 + \frac{(\tilde{H}_{jk} - e_{jB}^0 \tilde{S}_{jk})^2}{e_{jB}^0 - e_{kA}^0} + \frac{(\tilde{H}_{ji} - e_{jB}^0 \tilde{S}_{ji})^2}{e_{jB}^0 - e_{iA}^0} \\ &= e_{jB}^0 + \frac{(-)^2}{(-)} + \frac{(-)^2}{(+)} = e_{jB}^0 \end{aligned} \quad (3.24)$$

The interaction with  $\psi_{iA}^0$  is destabilizing ( $e_{jB}^0 - e_{iA}^0 > 0$ ), and that with  $\psi_{kA}^0$  is stabilizing ( $e_{jB}^0 - e_{kA}^0 < 0$ ). The net result is that  $\psi_j$  does not shift in energy. The new orbital  $\psi_j$  is given by equation 3.25,

$$\begin{aligned} \psi_j &= \psi_{jB}^0 + t_{kj}^{(1)}\psi_{kA}^0 + t_{ij}^{(1)}\psi_{iA}^0 \\ t_{kj}^{(1)} &\propto \frac{-\tilde{S}_{jk}}{e_{jB}^0 - e_{kA}^0} = \frac{-(+)}{(-)} = (+) \\ t_{ij}^{(1)} &\propto \frac{-\tilde{S}_{ij}}{e_{jB}^0 - e_{iA}^0} = \frac{-(+)}{(+)}) = (-) \\ \psi_j &= \psi_j^0 + (\psi_k^0) - (\psi_i^0) \end{aligned} \quad (3.25)$$

a diagrammatic representation of which is shown in 3.10. Notice that the first-order mixing coefficients serve to reinforce the atomic orbital coefficient on the left-hand H atom of  $\text{H}_3$  but diminishes at the central atom. If the two H—H distances are equal



then the second and third terms in **3.10** are equal in magnitude but opposite in sign. A precise cancellation occurs and a node develops at the central H atom. The astute reader will have noticed that the two energy denominators in equation 3.24 although opposite in sign, are not equal in magnitude, since we showed in Chapter 2 that the bonding combination of H<sub>2</sub> was stabilized less than the antibonding combination was destabilized. In particular, the denominator in the second term is larger than that for the third. However, recall the magnitudes of the coefficients in  $\psi_{kA}^0$  are larger than those in  $\psi_{iA}^0$ . This leads to a larger magnitude for  $(\tilde{H}_{jk} - e_{jB}^0 \tilde{S}_{jk})$  compared to  $(\tilde{H}_{ji} - e_{jB}^0 \tilde{S}_{ji})$ . Thus, the last two terms in equation 3.24 become of equal magnitude and do in fact exactly cancel.

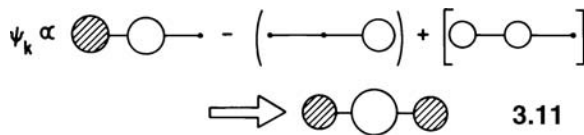
Finally, considering interaction ③ in Figure 3.2 the  $\psi_{kA}^0$  level is destabilized by  $\psi_{jB}^0$  since

$$\begin{aligned} e_k &= e_{kA}^0 + e_k^{(2)} \\ e_k^{(2)} &\propto \frac{\tilde{S}_{ij}^2}{e_{kA}^0 - e_{jB}^0} = \frac{(+) }{(+) } = (+) \end{aligned} \quad (3.26)$$

and the resultant molecular orbital  $\psi_k$  is given by equation 3.27.

$$\begin{aligned} \psi_k &\cong \psi_{kA}^0 + t_{jk}^{(1)} \psi_j^0 + t_{ik}^{(2)} \psi_i^0 \\ t_{jk}^{(1)} &\propto \frac{-\tilde{S}_{ij}}{e_{kA}^0 - e_{jB}^0} = \frac{-(+)}{(+) } = (-) \\ t_{ik}^{(2)} &\propto \frac{\tilde{S}_{ij} \tilde{S}_{jk}}{(e_{kA}^0 - e_{iA}^0)(e_{kA}^0 - e_{jB}^0)} = \frac{(+)(+)}{(+)(+) } = (+) \\ \psi_k &= \psi_{kA}^0 - (\psi_{jB}^0) + [\psi_{iA}^0] \end{aligned} \quad (3.27)$$

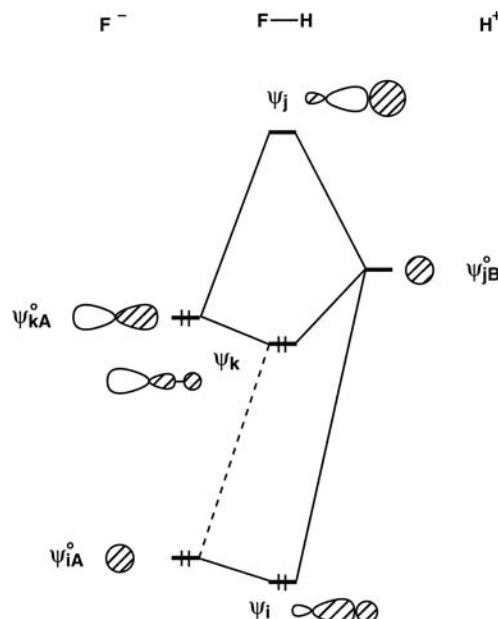
The term  $t_{ik}^{(2)}$  is positive from Table 3.1, and  $t_{jk}^{(1)}$  is negative since  $e_{jB}^0 - e_{kA}^0 < 0$ . A diagrammatic representation of  $\psi_k$  is shown in **3.11**. Notice again that the second-



order polarization serves to diminish the amplitudes of the wavefunction on the end hydrogen and reinforces at the middle.

As another simple example which illustrates the essence of the three-orbital problem, let us consider s and p orbitals (denoted as  $\psi_{iA}^0$  and  $\psi_{kA}^0$ , respectively) of a fluoride ion (i.e., A) interacting with an s orbital (denoted as  $\psi_{jB}^0$ ) of a proton (i.e., B) along the internuclear axis (i.e., A–B). In this case,  $\tilde{H}_{ij} = H_{ij}$ ,  $\tilde{H}_{jk} = H_{jk}$ ,  $\tilde{S}_{ij} = S_{ij}$ , and  $\tilde{S}_{jk} = S_{jk}$ . In Figure 3.3, the orbitals are arranged such that both  $S_{ij}$  and  $S_{jk}$  are positive and their energetic placement follows that in **2.9**. The second-order energy correction stabilizes  $\psi_{iA}^0$  by the higher lying  $\psi_{jB}^0$ . According to equation 3.15,  $\psi_i$  is written as

$$\psi_i \cong \psi_{iA}^0 + t_{ji}^{(1)} \psi_{jB}^0 + t_{ki}^{(2)} \psi_{kA}^0 \quad (3.28)$$

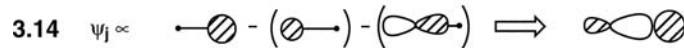
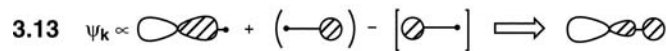
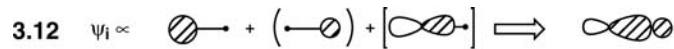
**FIGURE 3.3**

An orbital interaction diagram for the construction of the  $\sigma$  orbitals in HF.

Since  $\psi_{jB}^0$  lies higher in energy than  $\psi_{iA}^0$ ,  $t_{ji}^{(1)}$  is positive.  $\psi_{jB}^0$  lies higher than  $\psi_{iA}^0$  and  $\psi_{kA}^0$  as in 3.7 so that  $t_{ki}^{(2)}$  is also positive. Consequently, equation 3.28 can be rewritten as

$$\psi_i \cong \psi_{iA}^0 + (\psi_{jB}^0) + [\psi_{kA}^0] \quad (3.29)$$

A graphical representation of this equation is given in 3.12. This shows the formation of an  $sp$  hybrid-type orbital on the left-hand atom (e.g., fluorine) as a result of interaction with a single hydrogen 1s orbital. We have taken the liberty to introduce the result of mixing two atomic orbitals with different angular momentum quantum numbers on the same atom. The details are formally presented in Section 6.2. All that is necessary here is to note that orbitals add like vectors, therefore mixing an s and a  $p$  orbital on the same atom with the phases given in 3.12 cause a reinforcement of the



wavefunction on the right side of the fluorine atom and a diminution on the left side. For  $\psi_k, e_{kA}^0 - e_{jB}^0 < 0$ , and, therefore,  $e_k^{(2)} < 0$ . The resultant molecular orbital for  $\psi_k$  can be expressed as in equation 3.30

$$\begin{aligned} \psi_k &\cong \psi_{kA}^0 + t_{jk}^{(1)} \psi_{jB}^0 + t_{ik}^{(2)} \psi_{iA}^0 \\ &= \psi_{kA}^0 + (\psi_{jB}^0) - [\psi_{iA}^0] \end{aligned} \quad (3.30)$$

and a pictorial representation of the creation is illustrated in **3.13**. The hybridization now serves to polarize the molecular orbital to the left side, away from the hydrogen atom. The construction of **3.13** makes it clear that this molecular orbital is bonding between the fluorine *p* and hydrogen *s*, but it is antibonding between fluorine *s* and hydrogen *s*. Consequently  $\psi_k$  is perhaps best described as a nonbonding orbital. There is a bit of additional detail here. One might think that since the energy gap between  $\psi_{jB}^0$  and  $\psi_{kA}^0$  is less than that between  $\psi_{jB}^0$  and  $\psi_{iA}^0$ , there should be a greater stabilization afforded to  $\psi_{kA}^0$ . This will be certainly true considering only the second-order energy corrections. In this particular case there is also a third-order correction to the energy, given by the dashed tie-line in Figure 3.3. There is always a third-order correction to the energy whenever a second-order mixing occurs. But we are only interested in a qualitative placement of the relative energies. The consideration of  $e_k^{(3)}$  being positive needs only to be remembered for the middle orbital in case **3.7** (which is the situation here) or the middle level in **3.5** in which  $e_i^{(3)}$  is negative (stabilizing). Finally the highest molecular orbital,  $\psi_j$  in Figure 3.3, is destabilized to second order by  $\psi_{iA}^0$  and  $\psi_{kA}^0$ . The construction of the wavefunction is given by

$$\begin{aligned}\psi_j &\cong \psi_{jB}^0 + t_{ij}^{(1)}\psi_{iA}^0 + t_{kj}^{(1)}\psi_{kA}^0 \\ &= \psi_{jB}^0 - (\psi_{iA}^0) - (\psi_{kA}^0)\end{aligned}\quad (3.31)$$

and is illustrated by **3.14**. The reader should carefully work through the “master” equations 3.13–3.15, and 3.19 to derive those given for the second-order energy corrections and the mixing coefficients in this example. This is a tedious process at first, but it becomes trivial after a little practice.

We have illustrated here the two examples for a three-orbital pattern which are encountered in this book; the most common occurrence is in fact the hybridization example for HF. In both instances, the resultant molecular orbital at lowest energy is the most bonding combination of the fragment orbitals (**3.9** and **3.12**) and the highest molecular orbital is the most antibonding one (**3.11** and **3.14**). The molecular orbital caught in the middle (**3.10** and **3.13**) is nonbonding between the two fragments. For H<sub>3</sub> notice, the number of nodes perpendicular to the internuclear axis increases upon going from **3.9** (no nodes) to **3.10** (one node) to **3.11** (two nodes). For HF, the wavefunction in the lowest and highest molecular orbitals is hybridized toward the second fragment, whereas, in the middle level it is hybridized away from the *B* fragment. These are universal trends which occur regardless of the relative placement for the starting three fragment orbitals. So in principle, the orbitals of a complex molecule (albeit H<sub>3</sub> and HF) may be simply derived by using the ideas of perturbation theory. In particular, we have covered all of the elements of orbital interaction that we shall need for the whole book; namely the two-orbital and three-orbital patterns. We will construct the orbitals of much more complex molecules along similar lines by studying the first- and second-order interactions which occur as the result of a perturbation of a less complex system. Many examples of intermolecular perturbation are examined in Chapter 5.

### 3.4 DEGENERATE PERTURBATION

Let us consider an intermolecular perturbation where an orbital  $\psi_{iA}^0$  of the fragment A is degenerate with an orbital  $\psi_{jB}^0$  of the fragment B. Two very simple examples of this might be the assembly of the H<sub>2</sub> molecule from two H atoms or that of ethane

from two  $\text{CH}_3$  units. We arrange the orbital phases of  $\psi_{iA}^0$  and  $\psi_{jB}^0$  such that  $\tilde{S}_{ij} > 0$  and thus  $\tilde{H}_{ij} < 0$ . Then the orbitals defined in equation 3.31,

$$\frac{\psi_{iA}^0 + \psi_{jB}^0}{\sqrt{2 + 2\tilde{S}_{ij}}} \quad (3.31)$$

$$\frac{\psi_{iA}^0 - \psi_{jB}^0}{\sqrt{2 - 2\tilde{S}_{ij}}}$$

which are simply linear combinations of the two zeroth order orbitals  $\psi_{iA}^0$  and  $\psi_{jB}^0$ , lead to the first-order energy corrections given by equation 3.32

$$e_i^{(1)} = (\tilde{H}_{ij} - e_{iA}^0 \tilde{S}_{ij}) \propto -\tilde{S}_{ij} \quad (3.32)$$

$$e_j^{(1)} = -(\tilde{H}_{ij} - e_{iA}^0 \tilde{S}_{ij}) \propto \tilde{S}_{ij}$$

The second-order energy corrections resulting from these orbitals are given by equation 3.33.

$$e_i^{(2)} = e_j^{(2)} = -\tilde{S}_{ij}(\tilde{H}_{ij} - e_{iA}^0 \tilde{S}_{ij}) \propto -\tilde{S}_{ij}^2 \quad (3.33)$$

This is analogous to our discussion in Section 2.1. concerning a two-center-two-orbital problem (see equations 2.8 and 2.9). It is the second-order energy correction which makes the bonding combination less stabilized than the antibonding one is destabilized. Those two orbitals defined in equation 3.31 may further engage in nondegenerate interactions with other orbitals of the fragments A and B, thereby leading to second-order energy corrections. In a general case of intermolecular perturbation, both degenerate and nondegenerate interactions may occur between the fragments A and B. Then, it is convenient to derive the orbitals of the composite system AB in two steps: (1) first, we carry out only degenerate interactions, the resulting orbitals of which are nondegenerate. (2) Second, we include these orbitals among other nondegenerate orbitals and carry out nondegenerate interactions using the combined set of orbitals. Particularly, illustrative examples of this are the generation of the orbital diagrams for a diatomic molecule in Section 6.3 and linear  $\text{H}_4$  in Section 5.5.

In the intermolecular perturbation, the first-order term  $e_i^{(1)}$  is zero for non-degenerate interactions but nonzero for degenerate interactions (under the two assumptions stated in the beginning part of Section 3.2). As a consequence, degenerate and nondegenerate orbital interactions are often called first- and second-order orbital interactions, respectively. Here, it is important to stress the use of some terminology to avoid confusion later on in this book. We briefly mentioned this problem earlier. The nondegenerate interaction between  $\psi_{iA}^0$  and  $\psi_{jB}^0$  involves a first-order change in the character of the orbital but a second-order change in the energy. It will then always be important when using the expressions “first order” and “second order” to state whether we are referring to energy changes or orbital mixing.

Finally, we briefly comment on those cases in which neither the degenerate nor the nondegenerate perturbation treatment is quite satisfactory [5]. To simplify our discussion, let us consider only the lower lying orbital  $\psi_i$  and its energy  $e_i$  that result from two interacting orbitals  $\psi_{iA}^0$  and  $\psi_{jB}^0$ . For a nondegenerate interaction with

$e_{iA}^{(1)} < e_{jB}^{(1)}$ , the expressions for  $e_i$  and  $\psi_i$  are given by

$$e_i = e_{iA}^0 + \frac{(\tilde{H}_{ij} - e_{iA}^0 \tilde{S}_{ij})^2}{e_{iA}^0 - e_{jB}^0} \quad (3.34)$$

and

$$\psi_i \cong \psi_{iA}^0 + \left( \frac{\tilde{H}_{ij} - e_{iA}^0 \tilde{S}_{ij}}{e_{iA}^0 - e_{jB}^0} \right) \psi_{jB}^0 \quad (3.35)$$

These expressions are close to the exact ones if equation 3.36 is satisfied, that is,

$$(\tilde{H}_{ij} - e_{iA}^0 \tilde{S}_{ij})^2 \ll |e_{iA}^0 - e_{jB}^0| \quad (3.36)$$

Thus, they are appropriate when the extent of perturbation is small in magnitude compared with the energy difference between the unperturbed levels. For a degenerate interaction with  $e_{iA}^0 = e_{jB}^0$ , the expressions for  $e_i$  and  $\psi_i$  are given by

$$e_i = e_{iA}^0 + (\tilde{H}_{ij} - e_{iA}^0 \tilde{S}_{ij}) - S_{ij}(\tilde{H}_{ij} - e_{iA}^0 \tilde{S}_{ij}) \quad (3.37)$$

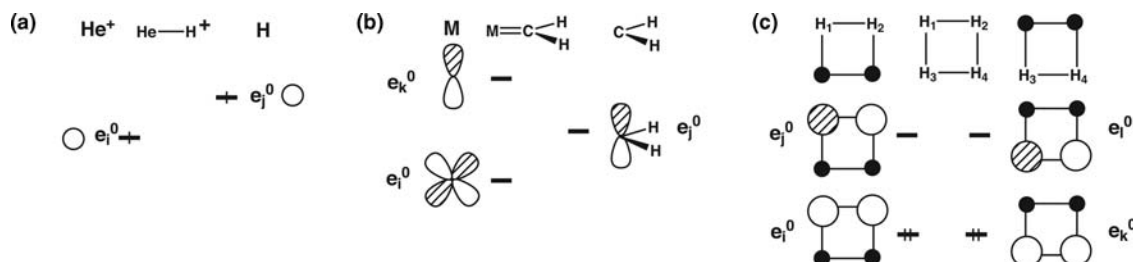
and

$$\psi_i = \frac{\psi_{iA}^0 + \psi_{jB}^0}{\sqrt{2 + 2\tilde{S}_{ij}}} \quad (3.38)$$

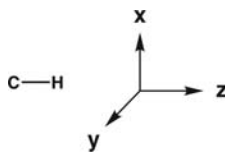
From the viewpoint of numerical accuracy, a problematic situation arises when the two levels  $e_{iA}^0$  and  $e_{jB}^0$  are different but close in energy so that equation 3.36 is not quite satisfied. In such a case, direct solution of the appropriate  $2 \times 2$  secular determinant (as described in Chapter 2) reveals the following trend: as the upper level  $e_{jB}^0$  is lowered and comes closer to the lower level  $e_{iA}^0$ , the weight of  $\psi_{iA}^0$  in  $\psi_i$  decreases gradually and that of  $\psi_{jB}^0$  in  $\psi_i$  increases gradually. Eventually, when  $e_{iA}^0 = e_{jB}^0$ , the weights of  $\psi_{iA}^0$  and  $\psi_{jB}^0$  become equal as given by equation 3.38. What is important in our qualitative applications of perturbation theory is to recognize which orbital has a greater weight. Thus, equation 3.35 may be used even for this problematic case since it shows that  $\psi_{iA}^0$  has a greater weight than does  $\psi_{jB}^0$ . Of course, when the two levels are very close (still  $e_{iA}^0 < e_{jB}^0$ ), equation 3.38 may be a more accurate description for  $\psi_i$  than equation 3.35. Nevertheless, the weight of  $\psi_{iA}^0$  would be greater, though slightly, than that of  $\psi_{jB}^0$ .

## PROBLEMS

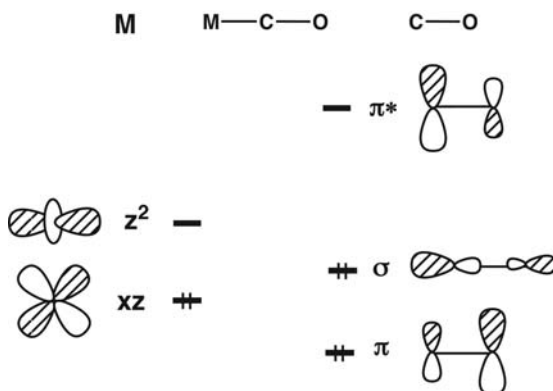
- 3.1.** Use perturbation theory to work out the signs associated with the energy corrections and mixing coefficients for the examples shown below. Draw out the resultant MOs.



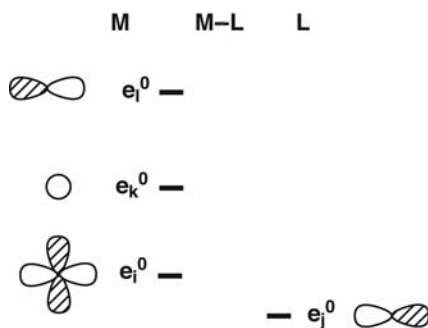
- 3.2.** Using the AOs for C and H determine the qualitative energy corrections and draw the corrected wavefunctions for C–H via perturbation theory. Find the starting orbital energies for C and H in **2.9** and use the coordinate system shown below.



- 3.3.** In this exercise, we shall work out the qualitative details for the interaction of CO with a transition metal, M. Using the starting orbitals listed below, determine the sign associated with the  $e^{(2)}$  values for each orbital and complete the orbital interaction diagram. Use perturbation theory to determine the shape of each resultant MO. Be careful here when determining the overlap between the fragment orbitals; many of them are zero!



- 3.4.** We have used examples where two and three orbitals interact with each other. As a final exercise, consider a case for a generic M–L  $\sigma$  bond where now there are four orbitals to be considered. Draw out the resultant interaction diagram and orbital shapes using perturbation theory.



## REFERENCES

1. A. Imamura, *Mol. Phys.*, **15**, 225 (1968).
2. L. Libit and R. Hoffmann, *J. Am. Chem. Soc.*, **96**, 1370 (1974).
3. M.-H. Whangbo, H. B. Schlegel, and S. Wolfe, *J. Am. Chem. Soc.*, **99**, 1296 (1977).
4. M.-H. Whangbo, *Computational Theoretical Organic Chemistry*, I. G. Csizmadia and R. Daudel, editors, Reidel, Boston (1981), p. 233.
5. D.-K. Seo, G. A. Papoian, and R. Hoffmann, *Int. J. Quantum Chem.*, **77**, 408 (2000).

# Symmetry

---

## 4.1 INTRODUCTION

---

Symmetry plays an important role in chemistry. There are many everyday facts we take for granted which have a strong underlying symmetry aspect to them. One  $ns$ , three  $n\pi$ , five  $nd$ , and so on, atomic orbitals come from the underlying symmetry of the atom; the paramagnetism of the oxygen molecule is a result of the presence of a doubly degenerate  $\pi$  orbital mandated by its linear structure. Geometrical instabilities in molecules occur as a result of the presence of degenerate electronic states that are a consequence of a highly symmetric geometry. In this chapter, we do not describe in detail the mathematics behind what chemists call group theory, but extract, as in our use of perturbation theory in Chapter 3, the elements we need in our task. It will be impossible in a short chapter to provide anything but a general outline. For the reader who wishes to know more, there are several excellent books available [1–5].

---

## 4.2 SYMMETRY OF MOLECULES

---

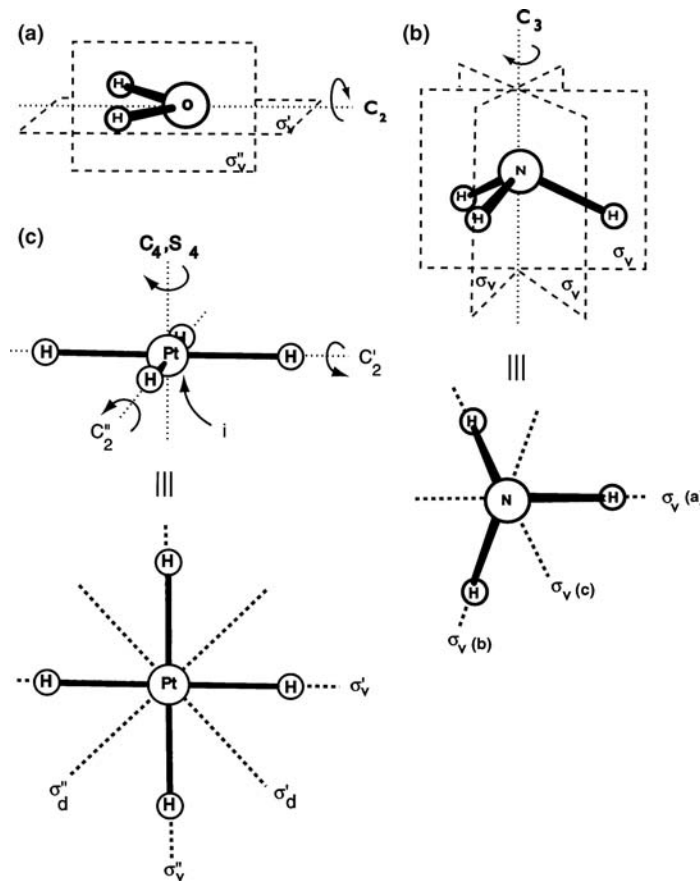
What is symmetry? In this book we are interested in two uses of this word. First, we are interested in the “symmetry” of a molecule. When looking at objects, we invariably have some feel as to whether they are highly symmetric or alternatively not very symmetric. This needs to be quantified in some way. Second, we need to classify, in terms of some symmetry description, the molecular orbitals of molecules and fragments. It is just this aspect that tremendously simplifies the construction of molecular orbitals rather than blindly, mechanically solving the secular determinant and equations of Chapter 1. Once this symmetry classification has been done, with the use of a few mathematical tools, we will be in a good position to understand how symmetry controls the orbital structure in molecules.

Geometrical objects (including molecules, if they are regarded as being made up of balls and spokes) possess an associated set of symmetry elements or operations  $\{R\}$ ,

**TABLE 4.1 Definitions of the Symmetry Operations**

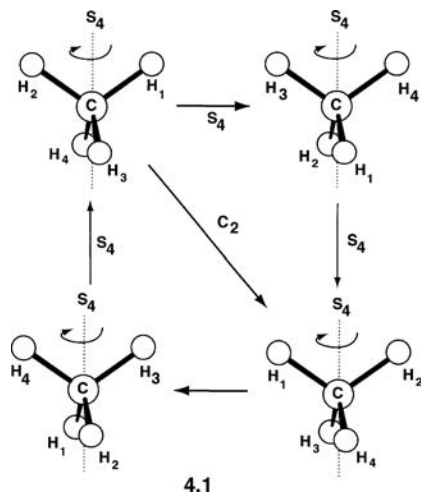
$E$	The null operation, the identity
$C_n$	A rotation around an axis by $360^\circ/n$
$C_n^x$	A rotation around an axis by $x(360^\circ/n)$ ; $x$ sequential $C_n$ operations
$\sigma_v$	A vertical mirror plane containing the principal rotation axis (the one of highest order)
$\sigma_h$	A horizontal mirror plane, one perpendicular to the principal rotation axis
$\sigma_d$	A dihedral mirror plane, one which bisects two $\sigma_v$ or $C_2$ operations
$S_n$	An improper rotation axis; rotation around an axis by $360^\circ/n$ followed by reflection in a plane perpendicular to this axis
$S_n^x$	$x$ sequential $S_n$ operations

rotation axes, mirror planes, and combinations of the two. To qualify such a symmetry element, the molecule must be geometrically indistinguishable as a result of the operation. Table 4.1 lists the various types of symmetry elements,  $\mathcal{R}$ , which are possible for molecules. Figure 4.1 shows the collection of symmetry elements for three simple species, nonlinear  $\text{H}_2\text{O}$ , pyramidal  $\text{NH}_3$ , and the square planar  $\text{PtH}_4^{2-}$  ion, which we use to illustrate many concepts described in the chapter. All molecules possess the identity operation,  $E$ ; this is simply the null operation where we do nothing. The  $n$ -fold rotation axis,  $C_n$ , is defined by a clockwise rotation of  $360^\circ/n$ . Molecules that possess a  $C_n$  also possess a  $C_n^x$  axis (where  $x < n$ ) where the rotation is by  $x(360^\circ/n)$ . Clearly there is some redundancy in notation. Thus,  $C_n^n = E$ ,  $C_4^2 = C_2$ , and  $C_3^2$  is equivalent to a counterclockwise rotation of  $120^\circ$  ( $-360^\circ/3$ ), that is,  $C_3^{-1}$ . Three types of mirror plane are distinguished,  $\sigma_v$ ,  $\sigma_h$ , and  $\sigma_d$ . The  $\sigma_v$  mirror plane ( $v = \text{vertical}$ ) is the

**FIGURE 4.1**

Symmetry operations for (a) the water molecule of point group  $C_{2v}$ , (b) the ammonia molecule of point group  $C_{3v}$ , and (c) the  $\text{PtH}_4^{2-}$  ion of point group  $D_{4h}$ .

one that contains the highest order rotation axis in the molecule, the principal axis of rotation (see all three molecules of Figure 4.1). The  $\sigma_h$  plane ( $h$  = horizontal) lies perpendicular to the principle axis of rotation, and  $\sigma_d$  ( $d$  = dihedral) bisects two  $\sigma_v$  planes or two  $C_2$  axis (see the  $\text{PtH}_4^{2-}$  molecule of Figure 4.1c). The inversion operation,  $i$ , sends a point located at  $\{x, y, z\}$  to another point at  $\{-x, -y, -z\}$ . This is one way where two trans H atoms are related to each other in the  $\text{PtH}_4^{2-}$  ion. Perhaps the most difficult symmetry operation to visualize is the improper rotation axis,  $S_n$ . This is a composite operation, combining a rotation of  $360^\circ/n$  around an axis followed by a reflection perpendicular to this axis. 4.1 shows this operation in the



methane molecule. Notice that  $S_4^2 = C_2$  and  $S_4^4 = E$ . For an  $S_n$  axis with  $n = \text{odd}$ ,  $S_n^n = \sigma_h$  and  $S_n^{2n} = E$ .

Although facets of all three molecules of Figure 4.1 are used as examples in this chapter, we have chosen the ammonia molecule to examine most of the details. Thus, Figure 4.2 shows the formal results of operating on the molecule with the set of operations of Figure 4.1b. Although the hydrogen atoms have been labeled for convenience, clearly, the two geometrical arrangements before and after each operation are indistinguishable.

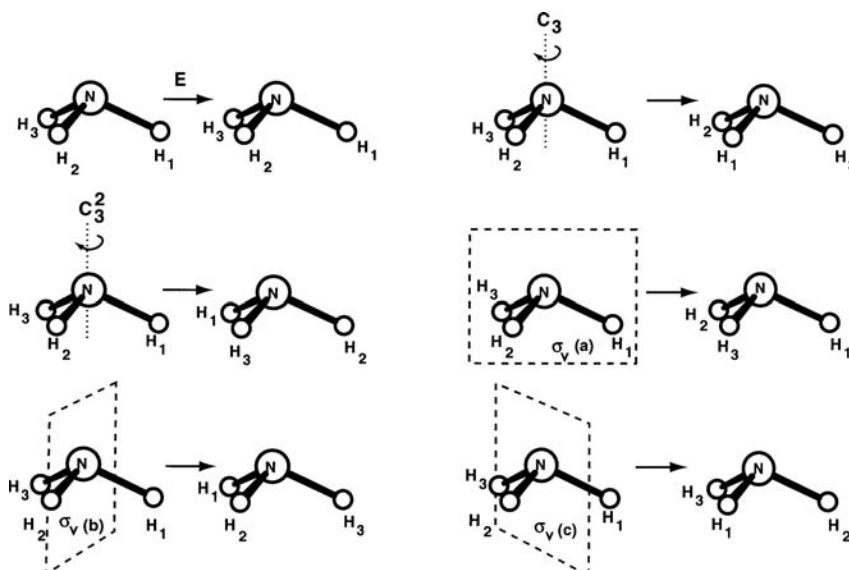
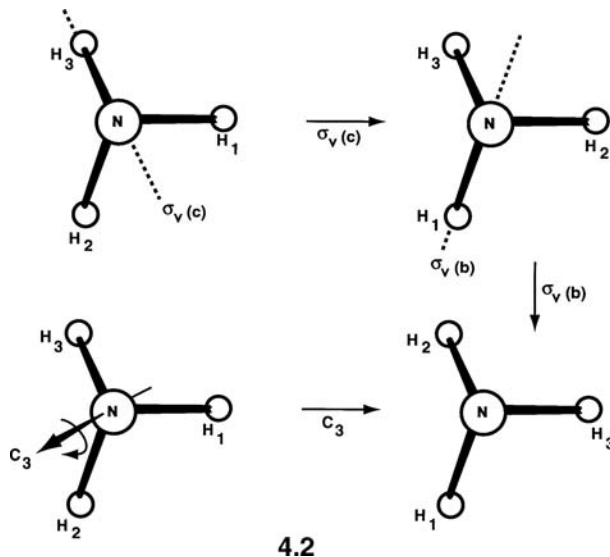


**FIGURE 4.2**

Operation with the symmetry operations for the ammonia molecule of point group  $C_{3v}$ .

The product of two symmetry operations,  $\mathcal{AB} = \mathcal{C}$ , means that each symmetry operation is executed consecutively in the order of right to left, for example,  $S_n = \sigma_h C_n$ . 4.2 shows how for ammonia  $\sigma_b \sigma_c = C_3$ . In most cases, the order of



execution is important, namely,  $\mathcal{AB} \neq \mathcal{BA}$ , that is,  $\mathcal{A}$  and  $\mathcal{B}$  do not commute. A complete collection of all such products for this molecule is

$$\begin{aligned}
 \sigma_a \sigma_b &= \sigma_b \sigma_a = \sigma_c \sigma_a = C_3 \\
 \sigma_b \sigma_a &= \sigma_c \sigma_b = \sigma_a \sigma_c = C_3^2 \\
 C_3 \sigma_b &= \sigma_b C_3^2 = C_3^2 \sigma_c = \sigma_c C_3 = \sigma_a \\
 C_3 \sigma_c &= \sigma_c C_3^2 = C_3^2 \sigma_a = \sigma_a C_3 = \sigma_b \\
 C_3 \sigma_a &= \sigma_a C_3^2 = C_3^2 \sigma_b = \sigma_b C_3 = \sigma_c \\
 C_3 C_3 &= C_3^2 C_3^2 C_3^2 = C_3 \\
 \sigma_a^2 &= \sigma_b^2 = \sigma_c^2 = C_3 C_3^2 = C_3^2 C_3 = E \\
 E\mathcal{R} &= \mathcal{R}E = \mathcal{R}, \text{ for all } \mathcal{R}
 \end{aligned} \tag{4.1}$$

Notice how the rotations and the reflections do not commute with each other (i.e.,  $\mathcal{AB} \neq \mathcal{BA}$ , where  $\mathcal{A}$  and  $\mathcal{B}$  refer to operations), but the sets of reflections or rotations taken separately do. The situation is quite different for the water molecule (see Figure 4.1a). Here, all of the operations commute,  $\mathcal{AB} = \mathcal{BA}$ . A complete set of all products is

$$\begin{aligned}
 \sigma_v' \sigma_v'' &= \sigma_v'' \sigma_v' = C_2 \\
 \sigma_v' C_2 &= C_2 \sigma_v' = \sigma_v' \\
 \sigma_v'' C_2 &= C_2 \sigma_v'' = \sigma_v' \\
 E\mathcal{R} &= \mathcal{R}E = \mathcal{R}, \text{ for all } \mathcal{R}
 \end{aligned} \tag{4.2}$$

We may also define the inverse operation ( $\mathcal{R}^{-1}$ ) as one that undoes the operation  $\mathcal{R}$ . Clearly the inverse of  $C_n$  is  $C_n^{-1} = C_n^{n-1}$ . Sometimes, an operation is its own

inverse, so  $E^{-1} = E$  and  $\sigma^{-1} = \sigma$ . Alternatively, we can define the inverse operation via  $\mathcal{R}^{-1}\mathcal{R} = E$ . Thus, the inverses of the symmetry elements for the ammonia molecule are

$$\begin{aligned} E^{-1} &= E \\ C_3^{-1} &= C_3^2 \\ (C_3^2)^{-1} &= C_3 \\ \sigma_i^{-1} &= \sigma_i (i = a, b, c) \end{aligned} \tag{4.3}$$

and for water are

$$\begin{aligned} E^{-1} &= E \\ C_2^{-1} &= C_2 \\ (\sigma_v^i)^{-1} &= \sigma_v^i (i = I, II) \end{aligned} \tag{4.4}$$

The complete set of symmetry operations for the molecule together form a mathematical entity known as a group. The properties of such groups are interesting and will form the basis of the application of symmetry to molecular orbital problems. There are four rules that must be satisfied:

- (i) The product  $\mathcal{AB}$  of two elements of the group is also an element of the group.
- (ii) The product is associative,  $\mathcal{A}(\mathcal{BC}) = (\mathcal{AB})\mathcal{C}$ .
- (iii) The group contains the identity element such that  $\mathcal{AE} = E\mathcal{A} = \mathcal{A}$ .
- (iv) Each element has an inverse such that  $\mathcal{R}^{-1}\mathcal{R} = \mathcal{RR}^{-1} = E$ , and the inverse is also a member of the group.

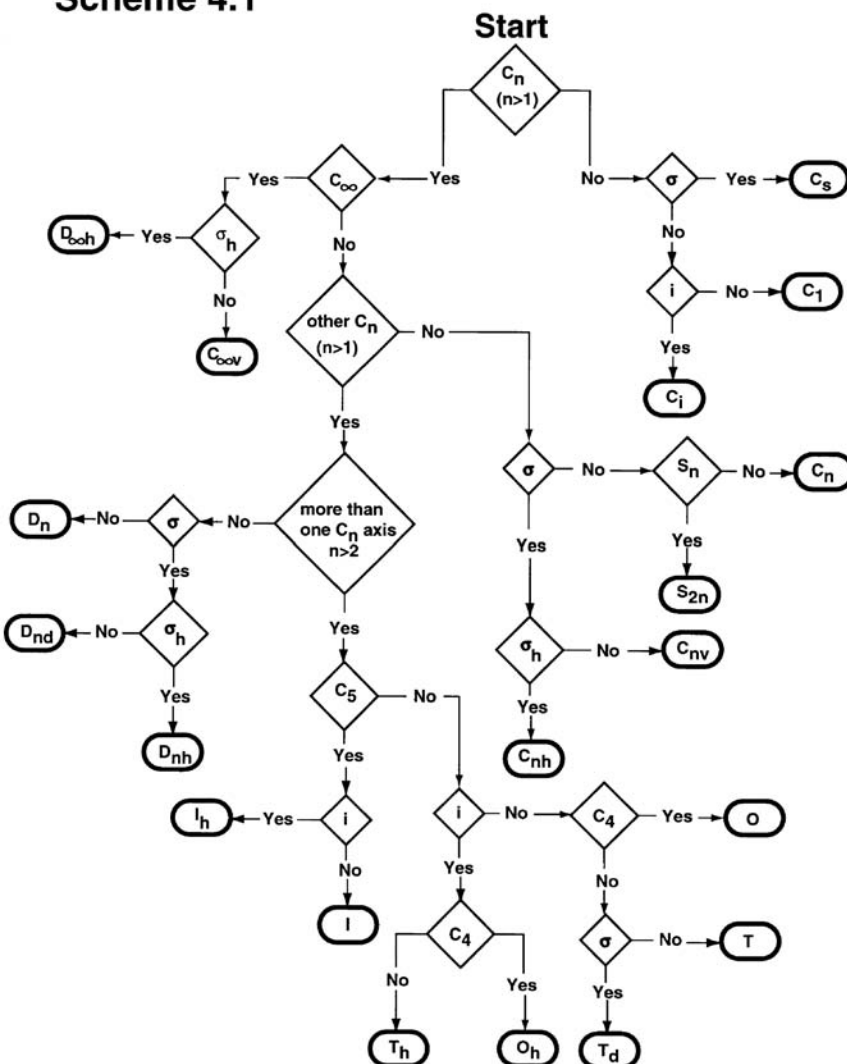
Rules (i) and (iv) have already been illustrated for ammonia. How the associative rule works is easy to show for this case too. Consider the product  $\sigma_a C_3 \sigma_c$  as an example. We have already worked out the products needed in equation 4.1. So,

$$\sigma_a(C_3 \sigma_c) = \sigma_a \sigma_b = C_3$$

$$\text{and } (\sigma_a C_3) \sigma_c = \sigma_b \sigma_c = C_3$$

Geometrically, these rules set some stringent restrictions on the collections of symmetry elements that are possible. Consider the  $\text{PtH}_4^{2-}$  molecule of Figure 4.1c. The presence of the fourfold axis demands the presence of two vertical mirror planes; a single plane is not possible. Similarly, there must be more than just one  $C_2$  axis perpendicular to this  $C_4$ . The reader can show that the complete set of symmetry elements which describe this molecule are indeed those shown in Figure 4.1c, namely,  $\{E, C_4, C_4^3, C_2, 2C_2', 2C_2'', i, S_4, S_4^3, \sigma_h, \sigma_v, \sigma_v', \sigma_d', \sigma_d''\}$ . The order of the group is just the total number of elements in it and is given the symbol  $g$ . The complete set of symmetry elements for a given molecule defines the point group. The point group symbols appropriate for the collection of symmetry elements in Figure 4.1 are  $C_{2v}$  and  $C_{3v}$  for water and ammonia, respectively, and  $D_{4h}$  for the  $\text{PtH}_4^{2-}$  molecule. An algorithm useful in identifying

Scheme 4.1



the correct point group is given in Scheme 4.1. The flowchart here asks a series of questions whether or not a particular symmetry operation exists in the molecule. It ultimately leads to the Schoenflies symbol for the point group, which is given in the ellipsoidal boxes. Here,  $n$  for some of the Schoenflies symbols stands for the principal rotation axis.

It is convenient to divide the elements (symmetry operations) of a group into conjugacy classes,  $\mathcal{R}$ . Two elements  $A$  and  $B$  are said to be conjugate to each other if there is an element  $R$  such that  $A = R^{-1}BR$ . In this relationship,  $A$  is called the similarity transform of  $B$  by  $R$ . So, for any particular element of the group,  $A$ , we can determine a subset of the elements which are all conjugate to  $A$  (and in fact to each other) by evaluating all products of the type  $R^{-1}AR$ . This subset is called a conjugacy class, and the elements of the group can be divided into a number of such mutually exclusive classes. The number of elements in the  $k^{\text{th}}$  class is given by  $g_k$ . This can be done for the  $C_{3v}$  elements appropriate for ammonia.

Starting with  $\mathcal{A} = \sigma_a$ ,

$$\begin{aligned}
 E^{-1}\sigma_a E &= \sigma_a \\
 C_3^{-1}\sigma_a C_3 &= C_3^2(\sigma_a C_3) = C_3^2\sigma_b = \sigma_c \\
 (C_3^2)^{-1}\sigma_a C_3^2 &= (C_3\sigma_a)C_3^2 = \sigma_c C_3^2 = \sigma_b \\
 \sigma_a^{-1}\sigma_a \sigma_a &= \sigma_a \\
 \sigma_b^{-1}\sigma_a \sigma_b &= \sigma_b(\sigma_a \sigma_b) = \sigma_b C_3 = \sigma_c \\
 \sigma_c^{-1}\sigma_a \sigma_c &= \sigma_c(\sigma_a \sigma_c) = \sigma_c C_3^2 = \sigma_b
 \end{aligned} \tag{4.5}$$

So,  $\sigma_a$ ,  $\sigma_b$ , and  $\sigma_c$  are three mutually conjugate elements. Analogously, one finds that  $C_3$  and  $C_3^2$  belong to the same class. The identity operation always falls in a class by itself. In short, we may write the elements of the group in terms of these classes as  $\{E, 2C_3, 3\sigma_v\}$ . An interesting result is found for the point group appropriate for the water molecule. Since the elements of this group all commute with each other, each element falls into its own class, that is,  $g_k = I$ , for all  $\mathcal{K}$ . Such groups are called Abelian groups, and they have some other distinctive properties, which are described later.

### 4.3 REPRESENTATIONS OF GROUPS

Suppose we take the hydrogen atoms in the ammonia molecule in Figure 4.2 and examine what will occur when the  $C_3$  operation is carried out. This can be expressed in terms of a set of linear equations

$$\begin{aligned}
 H'_1 &= (0)H_1 + (1)H_2 + (0)H_3 \\
 H'_2 &= (0)H_1 + (0)H_2 + (1)H_3 \\
 H'_3 &= (1)H_1 + (0)H_2 + (0)H_3
 \end{aligned}$$

where the primes refer to the new position of each hydrogen atom. Alternatively, the  $C_3$  operation can be written in matrix form as

$$\begin{bmatrix} H'_1 \\ H'_2 \\ H'_3 \end{bmatrix} = \begin{bmatrix} 0 & 1 & 0 \\ 0 & 0 & 1 \\ 1 & 0 & 0 \end{bmatrix} \begin{bmatrix} H_1 \\ H_2 \\ H_3 \end{bmatrix}$$

and for the  $\sigma_v(a)$  operation as

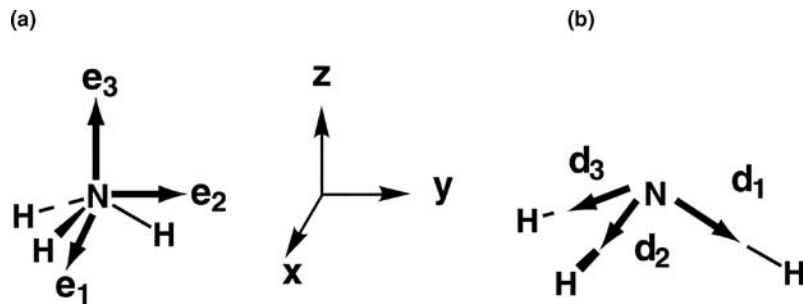
$$\begin{bmatrix} H'_1 \\ H'_2 \\ H'_3 \end{bmatrix} = \begin{bmatrix} 1 & 0 & 0 \\ 0 & 0 & 1 \\ 0 & 1 & 0 \end{bmatrix} \begin{bmatrix} H_1 \\ H_2 \\ H_3 \end{bmatrix} \tag{4.6}$$

One particularly useful way to describe the symmetry operations of a molecule is to write  $\mathcal{R}$  in terms of a transformation matrix  $\mathbf{D}(\mathcal{R})$ , the  $3 \times 3$  matrix in equation 4.6, which determines the manner in which a set of basis vectors  $\mathbf{x}$  are transformed into a new set  $\mathbf{x}'$  as a result of the symmetry operation.

$$\mathbf{x}' = \mathbf{D}(\mathcal{R})\mathbf{x} \tag{4.7}$$

**FIGURE 4.3**

Two different bases for representations: (a) the  $\mathbf{e}_i$  and (b) the  $\mathbf{d}_i$  bases.



Given the set of vectors  $\mathbf{e}_i$  ( $i = 1, 2, 3$ ) which lie along the Cartesian axes of Figure 4.3a the transformation matrices for the set of operations of the  $C_{3v}$  point group are given by the following:

$$\begin{aligned}
 E &= \begin{pmatrix} 1 & 0 & 0 \\ 0 & 1 & 0 \\ 0 & 0 & 1 \end{pmatrix} & C_3 &= \begin{pmatrix} -\frac{1}{2} & -\frac{\sqrt{3}}{2} & 0 \\ \frac{\sqrt{3}}{2} & -\frac{1}{2} & 0 \\ 0 & 0 & 1 \end{pmatrix} & C_3^2 &= \begin{pmatrix} -\frac{1}{2} & \frac{\sqrt{3}}{2} & 0 \\ -\frac{\sqrt{3}}{2} & -\frac{1}{2} & 0 \\ 0 & 0 & 1 \end{pmatrix} \\
 \sigma_a &= \begin{pmatrix} -1 & 0 & 0 \\ 0 & 1 & 0 \\ 0 & 0 & 1 \end{pmatrix} & \sigma_b &= \begin{pmatrix} \frac{1}{2} & -\frac{\sqrt{3}}{2} & 0 \\ -\frac{\sqrt{3}}{2} & -\frac{1}{2} & 0 \\ 0 & 0 & 1 \end{pmatrix} & \sigma_c &= \begin{pmatrix} \frac{1}{2} & \frac{\sqrt{3}}{2} & 0 \\ \frac{\sqrt{3}}{2} & -\frac{1}{2} & 0 \\ 0 & 0 & 1 \end{pmatrix}
 \end{aligned} \tag{4.8}$$

The products of these matrices will reflect the products of the type evaluated pictorially in Figure 4.2. As an example,

$$\begin{aligned}
 \sigma_c \sigma_b &= \begin{pmatrix} \frac{1}{2} & \frac{\sqrt{3}}{2} & 0 \\ \frac{\sqrt{3}}{2} & -\frac{1}{2} & 0 \\ 0 & 0 & 1 \end{pmatrix} \begin{pmatrix} \frac{1}{2} & -\frac{\sqrt{3}}{2} & 0 \\ -\frac{\sqrt{3}}{2} & -\frac{1}{2} & 0 \\ 0 & 0 & 1 \end{pmatrix} \\
 &= \begin{pmatrix} \frac{1}{4} - \frac{3}{4} + 0 & -\frac{\sqrt{3}}{4} - \frac{\sqrt{3}}{4} + 0 & 0 + 0 + 0 \\ \frac{\sqrt{3}}{4} + \frac{\sqrt{3}}{4} + 0 & -\frac{3}{4} + \frac{1}{4} + 0 & 0 + 0 + 0 \\ 0 + 0 + 0 & 0 + 0 + 0 & 0 + 0 + 1 \end{pmatrix} \\
 &= \begin{pmatrix} -\frac{1}{2} & -\frac{\sqrt{3}}{2} & 0 \\ \frac{\sqrt{3}}{2} & -\frac{1}{2} & 0 \\ 0 & 0 & 1 \end{pmatrix} = C_3
 \end{aligned} \tag{4.9}$$

which is the same result as shown graphically in 4.2. Notice that since the order of operation for group theory proceeds from right to left and the rules for matrix multiplication are left to right, the product in equation 4.9 is then evaluated in inverted order.

This set of matrices form a *representation* of the group, and the vectors  $\{\mathbf{e}_i\}$  form the *basis of the representation* ( $\Gamma_a$ ). An equally valid set ( $\Gamma_b$ ) of vectors  $\{\mathbf{d}_i\}$  ( $i = 1, 2, 3$ ) which may be used to describe the atomic coordinates  $i$  are shown in Figure 4.3b. The transformation matrices for this case are readily shown to be

$$\begin{aligned} E &= \begin{pmatrix} 1 & 0 & 0 \\ 0 & 1 & 0 \\ 0 & 0 & 1 \end{pmatrix} & C_3 &= \begin{pmatrix} 0 & 1 & 0 \\ 0 & 0 & 1 \\ 1 & 0 & 0 \end{pmatrix} & C_3^2 &= \begin{pmatrix} 0 & 0 & 1 \\ 1 & 0 & 0 \\ 0 & 1 & 0 \end{pmatrix} \\ \sigma_a &= \begin{pmatrix} 1 & 0 & 0 \\ 0 & 0 & 1 \\ 0 & 1 & 0 \end{pmatrix} & \sigma_b &= \begin{pmatrix} 0 & 0 & 1 \\ 0 & 1 & 0 \\ 1 & 0 & 0 \end{pmatrix} & \sigma_c &= \begin{pmatrix} 0 & 1 & 0 \\ 1 & 0 & 0 \\ 0 & 0 & 1 \end{pmatrix} \end{aligned} \quad (4.10)$$

It is clear that there is an infinite collection of sets of vectors (some of which are orthogonal, the  $\mathbf{e}_i$ , and some which are not, the  $\mathbf{d}_i$ ), which may be used to define the atomic coordinates. We need to find a measure that defines the properties of these representations and which is independent of the basis. This is the *character*,  $\gamma(\mathcal{R})$  of the group element  $\mathcal{R}$ . It is simply the sum of the diagonal elements (or the trace) of the transformation matrix. Table 4.2 shows how the characters of the two representations,  $\Gamma_a$ ,  $\Gamma_b$ , are in fact the same even though their transformation matrices  $\mathbf{D}(\mathcal{R})$  are very different. The set of characters, one for each element of the group is termed the *character of the representation*. Interestingly, the  $\gamma(\mathcal{R})$  are equal for all  $\mathcal{R}$  in the same class  $\gamma(\mathcal{K})$ . Recall that  $\mathcal{K}$  represents one symmetry operation in all classes, whereas  $\mathcal{R}$  corresponds to all symmetry operations. The reader should be aware that traditionally [1–5] representations are given by the symbol  $\Gamma$  and the characters of those representations by  $\chi$ . We need to reserve the latter symbol, however, for atomic orbitals (along with  $\phi$  for combinations of atomic orbitals and  $\psi$  for molecular orbitals), and thus the use of  $\gamma$  here.

The two representations  $\Gamma_a$  and  $\Gamma_b$  although *equivalent* (have the same character) are in fact different in the following sense. Notice that  $\Gamma_a$ , although a three-dimensional representation (there are three basis vectors), may be written in block diagonal form for all operations  $\mathcal{R}$  as

$$\mathbf{D}(\mathcal{R}) = \begin{bmatrix} \mathbf{D}'(\mathcal{R}) & 0 \\ 0 & \mathbf{D}''(\mathcal{R}) \end{bmatrix} \quad (4.11)$$

**TABLE 4.2** The Characters of the Two Representations  $\Gamma_a$  and  $\Gamma_b$

	$\Gamma_a$	$\Gamma_b$
$E$	$1 + 1 + 1 = 3$	$1 + 1 + 1 = 3$
$C_3$	$-1/2 - 1/2 + 1 = 0$	$0 + 0 + 0 = 0$
$C_3^2$	$-1/2 - 1/2 + 1 = 0$	$0 + 0 + 0 = 0$
$\sigma_a$	$-1 + 1 + 1 = 1$	$1 + 0 + 0 = 1$
$\sigma_b$	$1/2 - 1/2 + 1 = 1$	$0 + 1 + 0 = 1$
$\sigma_c$	$1/2 - 1/2 + 1 = 1$	$0 + 0 + 1 = 1$

where  $\mathbf{D}'(\mathcal{R})$  contains elements which involve only  $\mathbf{e}_1$  and  $\mathbf{e}_2$  ( $x, y$ ) and  $\mathbf{D}''(\mathcal{R})$  elements which contain  $\mathbf{e}_3$  ( $z$ ).  $\Gamma_b$  is thus called a *reducible representation* since it may be written as a *direct sum* of the matrices  $\mathbf{D}'(\mathcal{R})$  and  $\mathbf{D}''(\mathcal{R})$ . We can envisage that there is some similarity transformation which is able to block-diagonalize the set of transformation matrices. For the case described here, this leads to a one-dimensional and one two-dimensional representation. Ultimately, it will be impossible to block-diagonalize the set of transformation matrices further. In this case, one has reached an *irreducible representation* (IR).

At this point we need to ask what the possible irreducible representations for a given point group are. Just as there is a set of rules that define the formation of a point group, so there is a pair of rules that define the possible set of IRs of a group.

- (i) For a group which possesses  $k$  different classes, there are  $k$  different irreducible representations,  $\Gamma_1, \Gamma_2, \dots, \Gamma_k$  whose dimensions  $m_1, m_2, \dots, m_k$  satisfy the relationship

$$m_1^2 + m_2^2 + \dots + m_k^2 = g \quad (4.12)$$

where  $g$  is the order of the group.

- (ii) The characters  $\gamma_i(\mathcal{R})$  or  $\gamma_i(\mathcal{K})$  of the irreducible representations satisfy the relationship

$$\sum_{\mathcal{K}} g_k \gamma_i^*(\mathcal{K}) \gamma_j(\mathcal{K}) = g \delta_{ij} \quad (4.13)$$

or

$$\sum_{\mathcal{R}} \gamma_i^*(\mathcal{R}) \gamma_j(\mathcal{R}) = g \delta_{ij} \quad (4.14)$$

In short, where the sums are implied whenever there is product of the  $\Gamma$ s, equations 4.13 and 4.14 are simplified as in equations 4.15 and 4.16, respectively.

$$g_k \Gamma_i(\mathcal{K}) \Gamma_j(\mathcal{K}) = g \delta_{ij} \quad (4.15)$$

and

$$\Gamma_i(\mathcal{R}) \Gamma_j(\mathcal{R}) = g \delta_{ij} \quad (4.16)$$

If  $i=j$  then

$$\sum_{\mathcal{K}} g_k [\gamma_j(\mathcal{K})]^2 = g \quad (4.17)$$

or

$$\sum_{\mathcal{R}} [\gamma_j(\mathcal{R})]^2 = g \quad (4.18)$$

**TABLE 4.3** The Group Table for  $C_{2v}$ 

$C_{2v}$	$E$	$C_2$	$\sigma_v(xz)$	$\sigma_v(yz)$	
$A_1$					$z^a$
$A_2$			-	-	
$B_1$		-		-	$x$
$B_2$		-	-		$y$

<sup>a</sup>In the last column of the character table, it is customary to list some useful functions that have the transformation properties shown. From Table 1.1 it can be seen that the angular part of a  $p_z$  orbital, for example, is simply equal to  $z/r$ . As a result, from the character table, a  $p_z$  orbital located at a point, which contains all of the symmetry elements of the group, will transform as  $a_1$  symmetry.

and if  $i \neq j$  then

$$\sum_{\mathcal{R}} g_k \gamma_i^*(\mathcal{R}) \gamma_j(\mathcal{R}) = 0 \quad (4.19)$$

or

$$\sum_{\mathcal{R}} \gamma_i^*(\mathcal{R}) \gamma_j(\mathcal{R}) = 0 \quad (4.20)$$

(All of the groups we come across in this book contain real characters, and thus, the use of the  $\gamma^*$  notation will not be necessary.) For each point group, these rules lead to only one choice for the irreducible representations of the group. The results are depicted in a character table. Those for the  $C_{2v}$ ,  $C_{3v}$ , and  $D_{4h}$  groups are shown in Tables 4.3–4.5. The character tables for all of the common groups are collected together in Appendix II. The reader may use the structure of these tables to verify the rules described here. Notice the important result for the Abelian group  $C_{2v}$ . Since each element falls into its own class, there are same number of irreducible representations as elements, and each irreducible representation is one-dimensional. In all groups, the first entry consists of a set of figures  $\gamma_i(\mathcal{R}) = +1$  for all classes. This corresponds to the *totally symmetric representation* since a +1 is found for every  $\gamma_i(\mathcal{R})$ .

Each of the irreducible representations could be labeled in a simple way,  $\Gamma_1$ ,  $\Gamma_2$ , . . . ,  $\Gamma_n$ , but there is a notation due to Mulliken, which is very useful.  $A$  and  $B$  refer to one-dimensional representations where  $A$  refers to a representation for which the character corresponding to the highest order rotation axis is +1 and  $B$  when it is -1.  $E$  and  $T$  refer to doubly and triply degenerate representations, respectively. From the definition of these characters, the entry in the character table for the identity operation,  $\gamma_i(E)$  defines the order of the representation. (1 for  $A$ , 2 for  $E$ ; 3 for  $T$ , etc.) If there is more than one representation with the same label, then they are distinguished by subscripts 1, 2, . . . , and so on.

**TABLE 4.4** The Group Table for  $C_{3v}$ 

$C_{3v}$	$E$	$2C_3$	$3\sigma_v$	
$A_1$				$z$
$A_2$			-	
$E$	2	-	0	$(x, y)$

**TABLE 4.5** The Group Table for  $D_{4h}$ 

$D_{4h}$	$E$	$2C_4$	$C_2$	$2C_2'$	$2C_2''$	$i$	$2S_4$	$\sigma_h$	$2\sigma_v$	$2\sigma_d$	
$A_{1g}$		+	+			+	+	+	+	+	$x^2 + y^2, z^2$
$A_{2g}$		+	+	-	-	+	+	+	-	-	
$B_{1g}$		-	+	+	-	+	-	+	+	-	$x^2 - y^2$
$B_{2g}$		-	+	-	+	+	-	+	-	+	$xy$
$E_g$	2	0	-2	0	0	2	0	-2	0	0	$(xz, yz)$
$A_{1u}$		+	+	+	+	-	-	-	-	-	
$A_{2u}$		+	+	-	-	-	-	-	+	+	$z$
$B_{1u}$		-	+	+	-	-	+	-	-	+	
$B_{2u}$		-	+	-	+	-	+	-	+	-	
$E_u$	2	0	-2	0	0	-2	0	2	0	0	$(x, y)$

For some groups, the character table may be written in a particularly simple form as

$$\begin{array}{ccccc} & & \{1\} & \{2\} & \\ g \text{ or }' & X & Y & & \\ u \text{ or }'' & X & -Y & & \end{array} \quad (4.21)$$

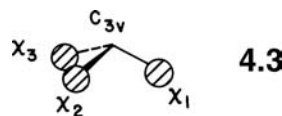
These groups are called *product groups* since they may readily be derived from a simpler group (whose character table is given by  $X$  alone) by the introduction of a  $\sigma_h$  or  $i$  operation. The  $D_{4h}$  group (Table 4.5) appropriate for the  $\text{PtH}_4^{2-}$  ion is one of these. Here, the  $D_{4h}$  group,  $\{1\} + \{2\} = \{E, C_4, C_4^3, C_2, 2C_2', 2C_2'', i, S_4, S_4^3, \sigma_h, 2\sigma_v, 2\sigma_d\}$  is generated by adding an  $i$  to the set of operations for the  $D_4$  group  $\{1\} = \{E, C_4, C_4^3, C_2, 2C_2', 2C_2''\}$ . Addition of the single operation  $i$  is not possible on its own. Inclusion of the larger set of operations  $\{2\} = \{i, S_4, S_4^3, \sigma_h, 2\sigma_v, 2\sigma_d\}$  is required to satisfy the rules determining the structure of the group. The two sets of operations are equal in number. Thus, we would write  $D_{4h} = D_4 \otimes i$ . In general, for  $n$  even,  $C_{nh} = C_n \otimes i$  and  $D_{nh} = D_n \otimes i$ ; for  $n$  odd,  $D_{nd} = D_n \otimes i$  and  $O_h = O \otimes i$ . Notice in each case the form of the character table in Appendix II. Representations for which  $\gamma_j(i) = +1$  are given a subscript *g* (German; gerade = even) and those for which  $\gamma_j(i) = -1$  are given a label *u* (ungerade = odd). A similar result applies to product groups involving  $\sigma_h$ . For example for  $n$  odd,  $D_{nh} = C_n \otimes \sigma_h$ . Thus, the form of the character table for  $D_{3h}$  is just as in equation 4.21. The representations with  $\gamma_j(\sigma_h) = +1$  are given by a superscript *'*, and those with  $\gamma_j(\sigma_h) = -1$  by a superscript *''*.

There are special labels for the linear point groups  $D_{\infty h}$  and  $C_{\infty v}$ .  $\Sigma$  refers to one-dimensional representations and  $\Pi, \Delta, \Phi, \dots$  refer to different two-dimensional ones. In spherical systems (atoms), the labels  $S, P, D, F, \dots$  refer to 1, 3, 5, 7, ... dimensional representations, respectively. These labels (in their lowercase form) are just those used to describe the orbitals of atoms.

Insight into the meaning of these character tables can be gained when we remind ourselves that the character is the trace of the relevant transformation matrix. For one-dimensional representations, whether a  $+1$  or  $-1$  appears under a given operation  $R$  specifies whether a basis function described by this character set is respectively symmetric (converted into itself) or antisymmetric (converted into minus itself) as a result of that symmetry operation. For irreducible representations, which are of higher dimension, such considerations are less obvious since by definition, it is the behavior of two functions (for an  $E$  representation) or three functions (for a  $T$  representation), which are being considered.

## 4.4 SYMMETRY PROPERTIES OF ORBITALS

Of particular importance in this book are the symmetry properties of a collection of orbitals and the electronic states that arise by populating them with electrons. For a given basis set of valence atomic orbitals for a molecule  $\{\chi_i\}$ , it is of interest to ask what set of irreducible representations they fall into (in the mathematical terms, in the foregoing discussion). There are two types of functions to consider: those associated with atoms, which lie at the point through which all of the symmetry elements pass, and those that do not. In the molecules of Figure 4.1, the orbitals of the central atom fall into the first class and those of the hydrogen atoms fall into the second. They may both be treated analogously. Consider as an example the set of hydrogen 1s orbitals in the NH<sub>3</sub> molecule (4.3), which we use as a representation. The first task is to generate the character of this representation



by examining the trace of the relevant transformation matrices,  $D(\mathcal{R})$  or  $D(\mathcal{K})$ . This is easier than it seems at first sight. If a particular basis function,  $\chi_j$ , is left unchanged during a symmetry operation, then a +1 will reside on the diagonal (the  $jj$  entry) of the matrix. If a basis function is transformed to another function then, a 0 will remain on the diagonal. If the function is converted into minus itself then a -1 will appear on the diagonal. With this set of rules, it is easy to generate the set of characters appropriate for the representation using the three hydrogen 1s orbitals of the ammonia molecule as a basis ( $\Gamma_{sH}$ ). It is given by

C <sub>3v</sub>	E	2C <sub>3</sub>	3σ <sub>v</sub>
Γ <sub>sH</sub>	3	0	1

(4.22)

Obviously, since the E operation is the null operation, the entry  $\gamma(E)$  is equal to the number of basis orbitals (3 in this case). The C<sub>3</sub> operation leads to all basis functions changing positions; the same is true for the C<sub>3</sub><sup>2</sup> operation. This is a general result:  $\gamma_i(\mathcal{K}) = \gamma_i(\mathcal{R})$ . In this instance,  $\gamma(2C_3) = 0$ . Using any one of the mirror planes changes positions of two members of the basis, and the third (which resides on the mirror plane) is left unshifted, so  $\gamma(3\sigma) = 1$ . Certainly, by inspection, this representation is reducible since its dimension (3) is greater than the largest dimension permissible in this point group (Table 4.4). The process of reducing a reducible representation of this type to a set of irreducible representations is an important step in the construction of molecular orbitals. The way we do this makes use of the properties of the irreducible representations noted earlier.

Let us assume that some reducible representation may be written as the sum of a set of irreducible representations as in equation 4.23.

$$\Gamma_{\text{red}} = m_1 \Gamma_1 + m_2 \Gamma_2 + \cdots + m_h \Gamma_h \quad (4.23)$$

that is,

$$\gamma^{\text{red}}(\mathcal{R}) = \sum_{i=1}^h m_i \gamma_i(\mathcal{R}) \quad (4.24)$$

or

$$\gamma^{\text{red}}(\mathcal{K}) = \sum_{i=1}^h m_i \gamma_i(\mathcal{K}) \quad (4.25)$$

Then,

$$\Gamma_i \Gamma_{\text{red}} = m_1 \Gamma_i \Gamma_1 + m_2 \Gamma_i \Gamma_2 + \cdots + m_i \Gamma_i \Gamma_i + \cdots + m_h \Gamma_i \Gamma_h \quad (4.26)$$

Using the shorthand notation introduced in equations 4.15 and 4.16, all such products will be zero except that for  $j=i$ .

$$\Gamma_i \Gamma_{\text{red}} = m_i \Gamma_i \Gamma_i \quad (4.27)$$

and so

$$m_i = \frac{\Gamma_i \cdot \Gamma_{\text{red}}}{\Gamma_i \cdot \Gamma_i} \quad (4.28)$$

which in terms of the characters is just

$$m_i = \frac{1}{g} \sum_{\mathcal{R}} g_{\mathcal{R}} \gamma^{\text{red}}(\mathcal{R}) \gamma_i(\mathcal{R}) \quad (4.29)$$

or

$$m_i = \frac{1}{g} \sum_{\mathcal{R}} \gamma^{\text{red}}(\mathcal{R}) \gamma_i(\mathcal{R}) \quad (4.30)$$

Using this result for the hydrogen 1s orbitals of  $\text{NH}_3$  (4.3) leads to a reduction of the reducible representation (see equations 4.22 and 4.29 along with Table 4.4) as

$$\begin{aligned} m_{a_1} &= \frac{1}{6} [(1)(3)(1) + (2)(0)(1) + (3)(1)(1)] = 1 \\ m_{a_2} &= \frac{1}{6} [(1)(3)(1) + (2)(0)(1) + (3)(1)(-1)] = 0 \\ m_e &= \frac{1}{6} [(1)(3)(2) + (2)(0)(-1) + (3)(1)(0)] = 1 \end{aligned} \quad (4.31)$$

or  $\Gamma_{\text{sH}} = a_1 + e$ . We say then that the 1s orbitals of hydrogen *span*, or *belong to the*  $a_1 + e$  *representations* or *transform as the*  $a_1 + e$  *symmetry species* of this point group or are just of  $a_1 + e$  *symmetry* in this point group. Notice we have used lowercase letters here for the Mulliken labels. Conventionally, uppercase characters are used for electronic states, whereas lowercase labels apply to atomic and molecular orbitals and also for describing molecular vibrations.

A similar process may be employed for the hydrogen 1s orbitals of water (4.4).



The reducible representation is simply generated as in equation 4.32

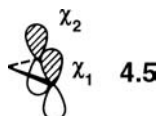
$C_{2v}$	$E$	$C_2$	$\sigma_v(xz)$	$\sigma_v(yz)$	(4.32)
$\Gamma_{\text{sH}}$	2	0	0	2	

and applying equation 4.30 leads to

$$\begin{aligned} m_{a_1} &= \frac{1}{4}[(2)(1) + (0)(1) + (0)(1) + (2)(1)] = 1 \\ m_{a_2} &= \frac{1}{4}[(2)(1) + (0)(1) + (0)(-1) + (2)(-1)] = 0 \\ m_{b_1} &= \frac{1}{4}[(2)(1) + (0)(-1) + (0)(1) + (2)(-1)] = 0 \\ m_{b_2} &= \frac{1}{4}[(2)(1) + (0)(-1) + (0)(-1) + (2)(1)] = 1 \end{aligned} \quad (4.33)$$

So the pair of hydrogen 1s orbitals in water transform as  $a_1 + b_2$ .

Another example is shown in 4.5. Suppose that instead of OH<sub>2</sub>, the molecule of



interest was OF<sub>2</sub> and we wished to know how the two  $p_x$  orbitals on the fluorine atoms transformed. Then the set of characters for the two orbitals is given by

$C_{2v}$	$E$	$C_2$	$\sigma_v(xz)$	$\sigma_v(yz)$
$\Gamma_{xF}$	2	0	0	-2

(4.34)

The entry under  $\sigma_v(yz)$  is of different sign from the corresponding one in equation 4.32 since this symmetry operation sends each F  $p_x$  orbital to  $-p_x$ . Reduction of equation 4.34 either by inspection or using equation 4.30 gives us the result that these two  $p_x$  orbitals transform as  $a_2 + b_1$ . Although equation 4.30 allows access to the results of interest, with a little practice, the reducible representation may be reduced by inspection of the character table.

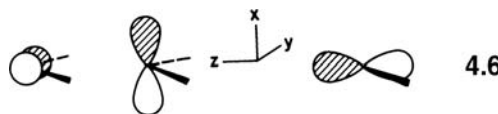
It is important at this point to comment on one consequence of these results. All of the molecular orbitals of the water molecule which contain hydrogen 1s character must be either of  $a_1$  or  $b_2$  symmetry. The wavefunction of  $a_1$  symmetry must be symmetric with respect to all symmetry operations of the molecule, while that of  $b_2$  symmetry is symmetric with respect to some and antisymmetric with respect to other symmetry operations. If of  $a_1$  symmetry, then  $\chi_1$  and  $\chi_2$  will have the same sign and magnitude; if of  $b_2$  symmetry, then  $\chi_1$  and  $\chi_2$  will have equal weight but their orbital coefficients will be of opposite sign.

Evaluation of the symmetry species of orbitals on the central atoms proceeds analogously. For the oxygen 2s orbital of the water molecule this is particularly simple. The characters of the representation given by the oxygen 2s orbital ( $\Gamma_{sO}$ ) are written as

$C_{2v}$	$E$	$C_2$	$\sigma_v(xz)$	$\sigma_v(yz)$
$\Gamma_{sO}$	1	1	1	1

(4.35)

By inspection,  $\Gamma_{sO} = a_1$ . This is a general result; s orbitals located on atoms, through which all the symmetry elements of the point group pass, always transform as the totally symmetric representation. The characters of the representation given by the oxygen 2p orbital ( $\Gamma_{pO}$ ) are generated in the same way (4.6). Here, of course, a contribution of -1 is found whenever a given  $\mathcal{R}$  sends one of these functions to minus itself.



4.6

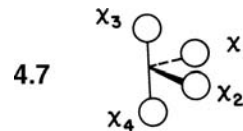
$C_{2v}$	$E$	$C_2$	$\sigma_v(xz)$	$\sigma_v(yz)$
$\Gamma_{pO}$	3	-1	1	1

(4.36)

Reduction of this representation leads to  $\Gamma_{pO} = a_1 + b_1 + b_2$ . These  $p$  orbitals change sign on going from  $+x$ ,  $+y$ , or  $+z$  to  $-x$ ,  $-y$ , or  $-z$ , respectively. In sets of character tables, the last columns often show the transformation properties of useful functions. In general, all that needs to be done to identify the symmetry species of such atomic  $p$  orbitals located at the point in space, which contains all of the point symmetry elements, is to identify those of  $x$ ,  $y$ , and  $z$ . Notice that in the  $C_{3v}$  point group  $x$ ,  $y$ , and  $z$  transform as  $\Gamma_{xyz} = e + a_1$ . Thus, the  $p_x$  and  $p_y$  orbitals on the central atom are degenerate ( $e$ ) in this point group. Similar considerations apply to  $d$  orbitals;  $d_{xy}$  and  $d_{xz}$  transform as the functions  $xy$  and  $xz$ , for example. Inspection of the character table for the  $D_{4h}$  point group then immediately tells us the symmetry species of the  $3d$  orbitals needed to construct a molecular orbital diagram for  $\text{PtH}_4^{2-}$ . They are  $\Gamma_{dPt} = a_{1g} + b_{1g} + b_{2g} + e_g$ .

## 4.5 SYMMETRY-ADAPTED WAVEFUNCTIONS

After having identified the symmetry properties of basis sets of atomic orbitals, we need to explore how to build wavefunctions with given symmetry properties from a particular basis. First we need to introduce the concept of symmetry-equivalent atoms or orbitals. Clearly, the two hydrogen 1s orbitals of water **4.4** are equivalent, specifically because any symmetry operation of the  $C_{2v}$  point group will either send  $\chi_1$  to itself or to  $\chi_2$  and likewise send  $\chi_2$  to itself or to  $\chi_1$ . Thus,  $\{\chi_1, \chi_2\}$  form a completely equivalent set. The  $\text{SF}_4$  molecule of **4.7** also belongs to the  $C_{2v}$  point group. Here, however, no symmetry operation sends  $\chi_1$  or  $\chi_2$  to  $\chi_3$  or  $\chi_4$ , or vice



versa. The orbitals  $\chi_1$  and  $\chi_2$  are permuted amongst themselves, as are the orbitals  $\chi_3$  and  $\chi_4$ , by the symmetry operations of the group. So  $\{\chi_1, \chi_2\}$  and  $\{\chi_3, \chi_4\}$  form two different sets of symmetry-equivalent orbitals.

We now generate the orbitals of  $a_1$  and  $b_2$  symmetry for the hydrogen 1s orbitals of water. Since the symmetry properties of the resulting function must satisfy each entry  $\gamma_i(\mathcal{R})$  of the relevant row of the character table, starting with the full complement of symmetry-equivalent orbitals ( $\chi_1$  and  $\chi_2$  in this case), we force the resulting wavefunction to have particular symmetry properties by construction using the character table itself. We write

$$\phi(i) \propto \sum_{\mathcal{R}} \gamma_i(\mathcal{R}) \mathcal{R} \xi_i \quad (4.37)$$

Here,  $\xi_1$  is any member of a complete symmetry-equivalent set. It does not matter whether we start off with  $\chi_1$  or  $\chi_2$  in this equation. Since they are symmetry equivalent, the same result will be found. For the  $C_{2v}$  point group, the results of the operations  $\mathcal{R}(\chi_1)$  and  $\mathcal{R}(\chi_2)$  are given by

$$\begin{aligned} E \cdot \chi_1 &= \chi_1; & E \cdot \chi_2 &= \chi_2 \\ C_2 \cdot \chi_1 &= \chi_2; & C_2 \cdot \chi_2 &= \chi_1 \\ \sigma_v(yz) \cdot \chi_1 &= \chi_1; & \sigma_v(yz) \cdot \chi_2 &= \chi_2 \\ \sigma_v(xz) \cdot \chi_1 &= \chi_2; & \sigma_v(xz) \cdot \chi_2 &= \chi_1 \end{aligned} \quad (4.38)$$

The characters  $\gamma_i(\mathcal{R})$  are given in Table 4.3. For  $i = a_1$ ,

$$\begin{aligned} \phi(a_1) &\propto \chi_1 + \chi_2 + \chi_2 + \chi_1 \\ &\propto \chi_1 + \chi_2 \end{aligned} \quad (4.39)$$

This is shown pictorially in 4.8 and may be normalized if desired. For  $i = b_2$  then,



4.8



4.9

$$\begin{aligned} \phi(b_2) &\propto \chi_1 - \chi_2 - \chi_2 + \chi_1 \\ &\propto \chi_1 - \chi_2 \end{aligned} \quad (4.40)$$

This is shown pictorially in 4.9. This technique using equation 4.37 is a very general and powerful way to construct functions of this type. The operator in this equation is called a *projection operator*.

Group theory from equation 4.33 describe that only functions of  $a_1$  and  $b_2$  symmetry were permitted. What happens if we try to construct a function of  $a_2$  symmetry?

$$\phi(a_2) \propto \chi_1 + \chi_2 - \chi_2 - \chi_1 = 0 \quad (4.41)$$

The result is meaningless.

The case of the water molecule involved a low symmetry point group where all of the possible representations are nondegenerate. In general, this appears in the character table (Table 4.3) with a +1 entry under the identity operation  $E$ . Higher symmetry point groups contain degenerate representations. Any point group that contains a threefold (or higher) rotation axis will contain at least one degenerate representation and as we have noted, the entry under  $E$  reveals the order of the degeneracy. Everything we have said so far holds for degenerate representations, except we need to be a little careful in using equation 4.37 for generating the wavefunctions. An example shows the problem encountered and the way it is overcome.

4.3 shows the three 1s orbitals on the hydrogen atoms in ammonia, which belongs to the  $C_{3v}$  point group. Using the approach described earlier, we showed that these three orbitals  $\chi_1 - \chi_3$  transform as  $a_1 + e$ , that is, one nondegenerate plus one doubly degenerate representation. Generation of the  $a_1$  wavefunction is easy. Using equation 4.30

$$\begin{aligned} \phi(a_1) &\propto \chi_1 + \chi_2 + \chi_3 + \chi_1 + \chi_2 + \chi_3 \\ &\propto \chi_1 + \chi_2 + \chi_3 \end{aligned} \quad (4.42)$$

The same answer is obtained from equation 4.30, irrespective of which of  $\chi_1$ ,  $\chi_2$ , or  $\chi_3$  is used as  $\xi_1$  in equation 4.30. For the doubly degenerate wavefunction, however, using equation 4.30 with  $\chi_1$  gives

$$\phi_a(e) \propto 2\chi_1 - \chi_2 - \chi_3 \quad (4.43)$$

Now if instead of using  $\chi_1$  in equation 4.8, we use  $\chi_2$ , the result is

$$\phi'(e) \propto 2\chi_2 - \chi_1 - \chi_3 \quad (4.44)$$

And finally, if  $\chi_3$  is used, we find

$$\phi''(e) \propto 2\chi_3 - \chi_1 - \chi_2 \quad (4.45)$$

The result is three (not two!) different wavefunctions, which apparently describe a doubly degenerate situation. The problem here is that  $\phi_a(e)$ ,  $\phi'(e)$  and  $\phi''(e)$  are not orthogonal. The solution is to use a technique known as the Schmidt orthogonalization process. First we accept equation 4.43 as one component of the doubly degenerate pair.

The atomic orbitals  $\chi_1$ ,  $\chi_2$ , and  $\chi_3$  are normalized, and in 4.3 the overlap between any two of them are the same. Thus,

$$\begin{aligned} \langle \chi_1 | \chi_1 \rangle &= \langle \chi_2 | \chi_2 \rangle = \langle \chi_3 | \chi_3 \rangle = 1 \\ \langle \chi_1 | \chi_2 \rangle &= \langle \chi_2 | \chi_3 \rangle = \langle \chi_3 | \chi_1 \rangle = S \end{aligned} \quad (4.46)$$

Consequently, we obtain

$$\langle 2\chi_1 - \chi_2 - \chi_3 | 2\chi_1 - \chi_2 - \chi_3 \rangle = 6(1 - S) \quad (4.47)$$

so that  $\phi_a(e)$  is normalized as

$$\phi_a(e) = \frac{1}{\sqrt{6(1-S)}} (2\chi_1 - \chi_2 - \chi_3) \quad (4.48)$$

Similarly,  $\phi'(e)$  and  $\phi''(e)$  are normalized as follows:

$$\begin{aligned} \phi'(e) &= \frac{1}{\sqrt{6(1-S)}} (2\chi_2 - \chi_3 - \chi_1) \\ \phi''(e) &= \frac{1}{\sqrt{6(1-S)}} (2\chi_3 - \chi_1 - \chi_2) \end{aligned} \quad (4.49)$$

The orbital  $\phi'(e)$  is not orthogonal to  $\phi_a(e)$  since

$$\begin{aligned} \langle \phi'(e) | \phi_a(e) \rangle &= \frac{1}{6(1-S)} \langle 2\chi_1 - \chi_2 - \chi_3 | 2\chi_2 - \chi_3 - \chi_1 \rangle \\ &= \frac{1}{6(1-S)} [3S - 3] = -\frac{1}{2} \end{aligned} \quad (4.50)$$

However, the orbital  $\phi_b(e)$  defined in the special way of equation 4.51 is orthogonal to  $\phi_a(e)$ ,

$$\begin{aligned} \phi_b(e) &\propto \phi'(e) - \langle \phi'(e) | \phi_a(e) \rangle \phi_a(e) \\ &\propto \chi_2 - \chi_3 \end{aligned} \quad (4.51)$$

Using equation 4.51 then “projects out” that portion of  $\phi'(e)$  which is not orthogonal to  $\phi_a(e)$ . Since

$$\langle \chi_2 - \chi_3 | \chi_2 - \chi_3 \rangle = 2(1 - S) \quad (4.52)$$

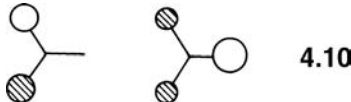
$\phi_b(e)$  is normalized as

$$\phi_b(e) = \frac{1}{\sqrt{2(1 - S)}} (\chi_2 - \chi_3) \quad (4.53)$$

We note that use of the orbital  $\phi''(e)$  in place of  $\phi'(e)$  in equation 4.51 does not produce a new orbital that is orthogonal to both  $\phi_a(e)$  and  $\phi_b(e)$  since

$$\phi''(e) - \langle \phi''(e) | \phi_a(e) \rangle \phi_a(e) - \langle \phi''(e) | \phi_b(e) \rangle \phi_b(e) = 0 \quad (4.54)$$

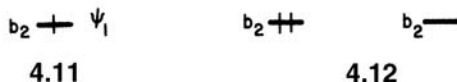
Therefore,  $\psi_a(e)$  and  $\psi_b(e)$  are a set of two orthonormal orbitals belonging to the  $e$  representation. In fact, there is considerable choice as to the form of the degenerate wavefunctions. Any linear combination of  $\psi_a(e)$  and  $\psi_b(e)$  are also valid wavefunctions. 4.10 shows the form of the functions of equations 4.43 and 4.51.



There is a repeated occurrence of orbitals that look similar to these in this book.

## 4.6 DIRECT PRODUCTS

Very often we need to be able to write down the symmetry species of a function which is a simple product of two functions whose symmetry we know. For example, we may wish to know the symmetry species of the electronic state which arises from the orbital occupancy shown in 4.11. The symmetry labels that describe the



4.11

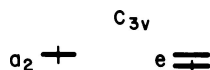
4.12

wavefunctions  $\psi_1$  and  $\psi_2$  are written alongside the molecular orbital levels, using lowercase letters. The simplest function that might be expected to describe the behavior of this electronic state is just  $\psi_1 \cdot \psi_2$ . (Chapter 8 describes how to tackle this problem properly.) The symmetry species of such a product function is obtained by multiplying the respective characters  $\gamma_{b_1}(\mathcal{K}) \times \gamma_{b_2}(\mathcal{K})$  as in equation 4.55. The result is clearly the set of characters corresponding to the  $a_2$  irreducible

$C_{2v}$	$E$	$C_2$	$\sigma_v(xz)$	$\sigma_v(yz)$	(4.55)
$B_1$	1	-1	1	-1	
$B_2$	1	-1	-1	1	
$B_1 \otimes B_2$	1	1	-1	-1	

representation, that is,  $b_1 \otimes b_2 = a_1$ . The electronic state corresponding to **4.11** is thus an  $A_2$  state, where uppercase letters are used to distinguish state symmetry from orbital symmetry. Depending upon whether the electron spins are oriented parallel or antiparallel, respectively, a triplet ( ${}^3A_2$ ) or a singlet ( ${}^1A_2$ ) state results. Using the same approach, it may readily be shown that the orbital occupation situations of **4.12** give rise to  $A_1$  electronic states, that is,  $b_2 \otimes b_2 = a_1$  and  $b_1 \otimes b_1 = a_1$ . This result is found in all point groups. Any product of the two functions  $\psi_a$  and  $\psi_b$  which have the same symmetry species will always belong to the totally symmetric representation of the point group. This observation leads to the simplifying result that all closed shells of electrons give rise to electronic states that are totally symmetric. In determining the symmetry species corresponding to a given orbital occupation, all we need to do, as a result, is to look at those electrons outside of completely filled orbitals (i.e., closed shells). Thus **4.11** may just represent the valence orbitals of a system, which are partially filled. The symmetry species of the electronic state is not influenced by the core of completely filled levels.

Two examples involving degenerate levels are shown in **4.13** and **4.14**. For **4.13**,



**4.13**      **4.14**

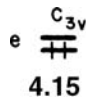
it is readily seen from Table 4.4 that  $a_2 \otimes e = e$ , which leads to  $E$  and  ${}^3E$  electronic states, depending upon the orientation of the electron spins. In **4.14**, the product of the characters leads to a reducible representation

$C_{3v}$	$E$	$2C_3$	$3\sigma_v$
$E$	2	-1	0
$E$	2	-1	0
$E \otimes E$	4	1	0

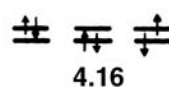
(4.56)

and we need to use equation 4.30 to break it down into a sum of irreducible representations. In this way, or by inspection, we find  $e \otimes e = a_1 + a_2 + e$ . Depending, then, upon the electron spin orientation, the electronic states that result are  ${}^1A_1$ ,  ${}^1A_2$ ,  ${}^1E$  and  ${}^3A_1$ ,  ${}^3A_2$ ,  ${}^3E$ . Note that in each of these products, the total number of singlets or total number of triplets corresponded to the simple product of the dimensions of the representations involved. So  $b_1 \otimes b_2$  gave a ( $1 \times 1 = 1$ ) one-dimensional product ( $a_1$ ),  $e \otimes a_2$  gave a ( $2 \times 1 = 2$ ) two-dimensional product ( $e$ ), and  $e \otimes e$  gave a ( $2 \times 2 = 4$ ) four-dimensional product ( $a_1 + a_2 + e$ ).

Problems involving degenerate levels are not always as simple. **4.15** shows double



**4.15**



**4.16**



**4.17**

occupancy of an  $e$  orbital. **4.16** and **4.17** show that because of the restrictions of the Pauli principle, there can only be three singlets and one triplet and not (as in **4.14**) four of each. In this case, we need to define a different sort of direct product. The usual simple product leads to the characters defined in equation 4.57. But the symmetric

$$\gamma_{i \otimes j} = \gamma_i(\mathcal{K})\gamma_j(\mathcal{K}) \quad (4.57)$$

direct product which we use to generate the singlet levels of **4.15**, is defined by

$$\chi_{e^2}^+(\mathcal{R}) = 1/2 [\gamma_i(\mathcal{R})\gamma_i(\mathcal{R}) + \gamma_i(\mathcal{R}^2)] \quad (4.58)$$

The antisymmetric direct product, which we use to generate the triplet levels of **4.15**, is defined by

$$\chi_{e^2}^-(\mathcal{R}) = 1/2 [\gamma_i(\mathcal{R})\gamma_i(\mathcal{R}) - \gamma_i(\mathcal{R}^2)] \quad (4.59)$$

First, we need to identify the operations corresponding to  $\mathcal{R}^2$  in equations 4.58 and 4.59. For the  $C_{3v}$  point group,

$$\begin{aligned} E \times E &= E; & C_3^2 \times C_3^2 &= C_3 \\ C_3 \times C_3 &= C_3^2; & \sigma_v \times \sigma_v &= E \end{aligned} \quad (4.60)$$

and we may readily evaluate the relevant characters as

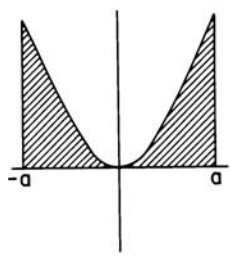
$C_{3v}$	$E$	$C_3$	$C_3^2$	$\sigma_a$	$\sigma_b$	$\sigma_c$
$\gamma_e(\mathcal{R})$	2	-1	-1	0	0	0
$\gamma_e(\mathcal{R}^2)$	2	-1	-1	2	2	2
$\gamma_e(\mathcal{R})^2$	4	1	1	0	0	0
$\chi_{e^2}^+(\mathcal{R})$	3	0	0	1	1	1
$\chi_{e^2}^-(\mathcal{R})$	1	1	1	-1	-1	-1

(4.61)

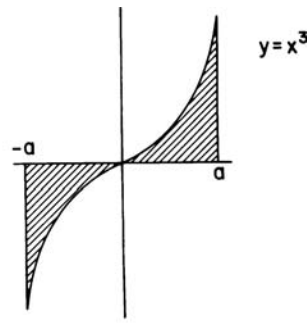
The set of characters for  $\chi_{e^2}^+(\mathcal{R})$  are seen to give rise to an  $a_1 + e$  representation with the aid of Table 4.4. The set for  $\chi_{e^2}^-(\mathcal{R})$  corresponds to  $a_2$ . So in the  $C_{3v}$  point group, a configuration with two electrons in an  $e$  symmetry orbital gives rise to electronic states with symmetry  ${}^1A_1$ ,  ${}^1E$ , and  ${}^3A_2$ .

## 4.7 SYMMETRY PROPERTIES, INTEGRALS AND THE NONCROSSING RULE [6–8]

The use of symmetry is extremely powerful in being able to simplify many orbital problems by quickly identifying those interactions that are exactly zero. In particular, the rule, which we investigate in this section, requires that all integrals of the overlap  $\langle \psi_a | \psi_b \rangle$  or interaction  $\langle \psi_a | H^{\text{eff}} | \psi_b \rangle$  type are zero unless  $\psi_a$  and  $\psi_b$  transform as the same irreducible representation of the molecular point group. To see why this is so consider the integrals shown in **4.18** and **4.19**. Clearly, the integral in equation 4.62 is nonzero



4.18

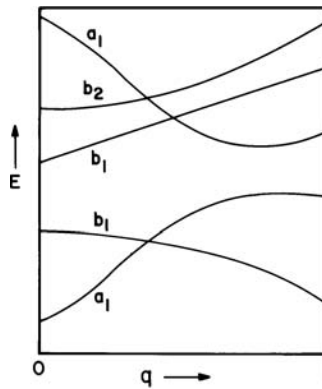


4.19

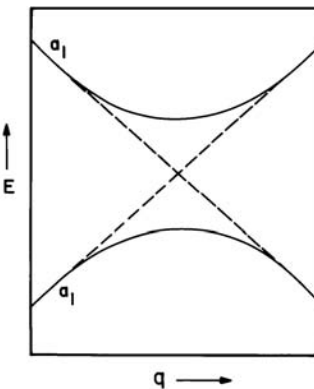
$$\int_{-a}^a y \, dx \quad (4.62)$$

for the symmetric function  $y = x^2$  but is identically zero for the antisymmetric function  $y = x^3$ . In other words, the presence of an operation which sends  $y$  to  $-y$  (in the case of **4.19** this is simply replacing  $x$  by  $-x$ ) immediately causes the integral to become zero. Applied to our overlap and interaction integrals this means that the integrand must be totally symmetric with respect to all symmetry operations of the point group, that is, all the characters must be equal to +1 for the integral to be nonzero. In the case of the overlap integral  $\langle \psi_a | \psi_b \rangle$ , this means that the function  $\psi_a \psi_b$  must contain the totally symmetric (a) representation. As we have seen earlier, the only way this can be true is if  $\psi_a$  and  $\psi_b$  belong to the same irreducible representation of the point group. We will not, however, prove it here but the Hamiltonian operator is also totally symmetric. This implies that in the interaction integral  $\langle \psi_a | H^{\text{eff}} | \psi_b \rangle$ , both  $\psi_a$  and  $\psi_b$  must transform as the same symmetry species of the point group for it to be nonzero. It immediately follows that *only orbitals of the same symmetry may interact with each other*.

This result is of immediate importance. Assume that a system with a set of energy levels  $e_i$  is transformed in some way along a reaction coordinate to a product. This coordinate may be a reaction in the traditional sense or perhaps a geometrical distortion. During the process, some of the levels (which may correspond to molecular orbital energy levels, or those of electronic states) will go up in energy and others will drop. In general, we will be able to correlate the levels before the distortion ( $q = 0$ ) with those afterwards ( $q = 1$ ) as in **4.20**. By making use of the point



4.20



4.21

symmetry along the reaction coordinate, these levels may be given symmetry labels. The noncrossing rule forbids levels with the same symmetry to cross each other. It is easy to see why. **4.21** shows two levels of the same symmetry crossing each other in energy in the  $E$  versus  $q$  (energy vs reaction coordinate) diagram (dashed lines). At the crossing point they will be degenerate. If the two levels have the same symmetry, then the overlap and interaction integrals  $\langle \psi_a | \psi_b \rangle$  and  $\langle \psi_a | H^{\text{eff}} | \psi_b \rangle$  will be nonzero, and the levels given by the dashed lines will interact via a degenerate interaction as described in Chapter 3. Away from the crossing point, the levels will interact by a nondegenerate process. In both cases the dashed lines will appear to “repel” each other and the solid curves will result. Although we distinguish between degenerate and nondegenerate cases here for convenience, the strength of the interaction between  $\psi_a$  and  $\psi_b$  varies continuously as they approach each other in energy. This is called an avoided crossing. How much the two levels repel each other depends on the actual magnitude of

$\langle \psi_a | H^{\text{eff}} | \psi_b \rangle$  and, hence, is related to  $\langle \psi_a | \psi_b \rangle$ . A strongly avoided crossing is a case where the integrals are sizable. There is then a little curvature for the two levels along  $q$ . A weakly avoided crossing occurs when the two molecular orbitals have the same symmetry, but their mutual overlap along  $q$  for some reason is small. The two levels will then nearly touch each other before turning around.

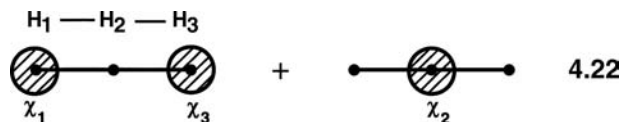
It is important to remember that orbitals of different symmetry can and will cross each other along a reaction coordinate. The most important case where this occurs is when the highest occupied molecular orbital (HOMO) crosses the lowest unoccupied molecular orbital (LUMO). Such HOMO-LUMO crossings are said to be symmetry forbidden and engender a high activation barrier. We describe many examples of this behavior in later chapters and the way molecules conspire to get around the high barrier.

Since electronic states also possess symmetry, one can examine the energetic variation of several states along a reaction coordinate. The same noncrossing rule applies. This vantage point is sometimes more appropriate for cases when there is a manifold of states at close energies. This is frequently encountered in photochemically excited reactions and rearrangements.

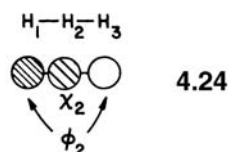
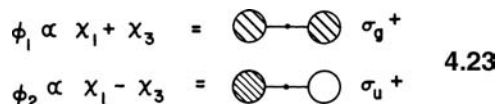
## 4.8 PRINCIPLES OF ORBITAL CONSTRUCTION USING SYMMETRY PRINCIPLES [1–9]

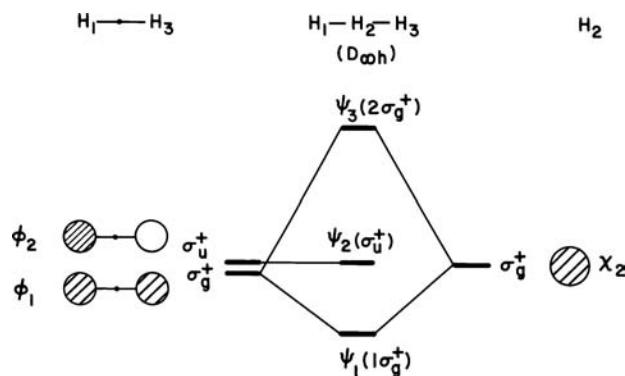
The requirement, set out in Section 4.7, that two orbitals will not interact unless they are of the same symmetry species is an extremely useful one when the energy levels of molecules are constructed. We start off by looking at a simple system, that is, linear  $H_3$ .

Section 3.4 showed one way of generating the orbitals which used first- and second-order perturbation ideas. There is, as in many problems, another way that this can be done which also helps in our understanding of the level structure. 4.22



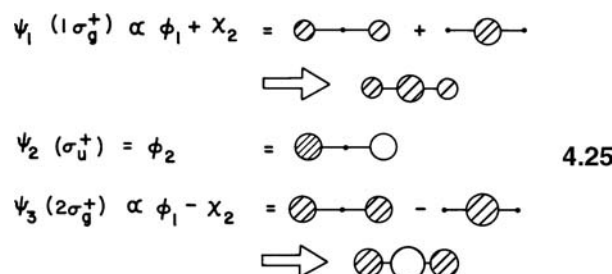
shows the assembly of  $H_3$  from the pair of orbitals  $\chi_1$  and  $\chi_3$  and the single central orbital  $\chi_2$ . Generation of the orbitals of molecules by combining the atomic orbitals of the central atom plus surrounding “ligands” is a very useful way of tackling this problem, and is the one we use extensively in this book. First we need the symmetry properties of the pair of symmetry-equivalent H 1s orbitals  $\chi_1$  and  $\chi_3$ . The point group of linear  $H_3$  is  $D_{\infty h}$ , and by using the techniques discussed earlier (and the characters of  $D_{\infty h}$  in Appendix II) it is very easy to show that these orbitals simply transform as  $\sigma_u^+ + \sigma_g^+$ . (Note the special Mulliken symbols for linear molecules.) Use of equation 4.37 allows generation of the proper symmetry adapted functions shown in 4.23. The central atom orbital  $\chi_2$  is seen to be of  $\sigma_g^+$  symmetry.



**FIGURE 4.4**

Derivation of the molecular orbital diagram for linear  $H_3$  from a central H atom orbital plus those of two “ligands.”

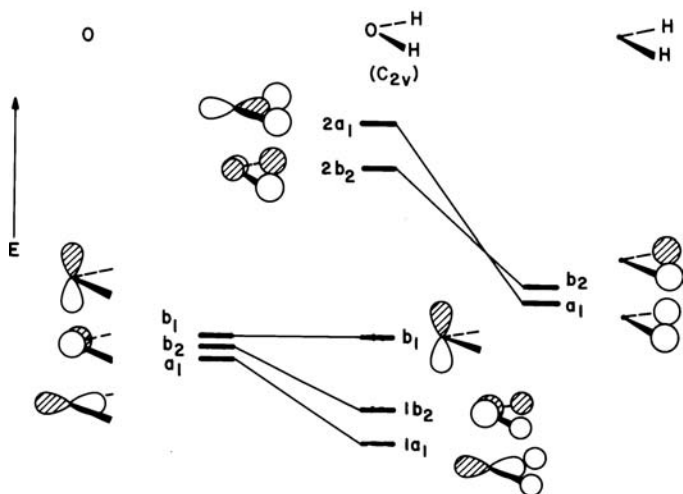
When the interactions between  $\chi_1$  and  $\chi_2$  are switched on, then  $\chi_2$  will only overlap and interact with the  $\sigma_g^+$  combination shown in 4.23. The  $\sigma_u^+$  function will be left nonbonding since it is of the wrong symmetry to interact with  $\chi_2$ . Their overlap integral is precisely zero (4.24). Since  $\chi_1$  and  $\chi_3$  are not nearest neighbors, their overlap integral is small and so the two combinations  $\phi_1$  and  $\phi_2$  will be close in energy. Figure 4.4 shows the orbital interaction diagram. The phases of the various orbitals have been drawn so that the overlap between  $\psi_1$  and  $\chi_2$  is positive. Note that  $\psi_3$  is destabilized more than  $\psi_1$  is stabilized, a result exactly analogous to the situation in Chapter 2, where we treated the simple two-center-two-orbital problem. The details of the generation of the molecular orbitals are shown in 4.25.



As another example let us take the  $H_2O$  molecule. It may be visualized as being assembled from a central oxygen atom plus two symmetry-equivalent hydrogen atoms. The hydrogen 1s orbitals we have already seen transform as  $a_1 + b_2$ . (The forms of the wavefunctions are given in 4.8 and 4.9.) The oxygen  $p_x$ ,  $p_y$ ,  $p_z$  orbitals (4.6) transform as  $b_1$ ,  $b_2$ , and  $a_1$ . Thus, the hydrogen  $a_1$  combination may only interact with the oxygen  $p_z$  orbital, and the hydrogen  $b_2$  combination may only interact with the oxygen  $p_y$  orbital. In each case, a bonding and antibonding pair of orbitals result (Figure 4.5). The oxygen  $b_1$  orbital finds no ligand counterpart with the same symmetry and remains nonbonding. How the oxygen s orbital enters into this picture is described in Chapter 7.

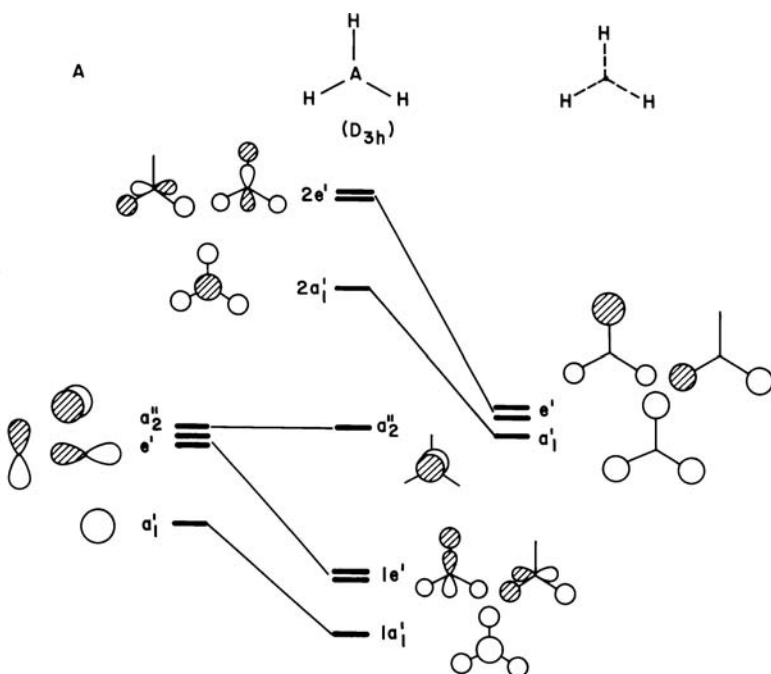
This technique is a very general one for the construction of a diagram for a central atom plus ligands. As noted earlier, instead of working out the symmetry species of the central atom orbitals, we may often use information listed at the right-hand side of the character tables. Recall that the central atom s orbital always transforms as the totally symmetric representation.

Figure 4.6 shows the assembly of the molecular orbital diagram of a planar  $AH_3$  molecule, point group  $D_{3h}$ . The H 1s orbitals transform as  $a_1' + e'$ , using analogous techniques to those used earlier for water and ammonia. Using equation 4.37, the

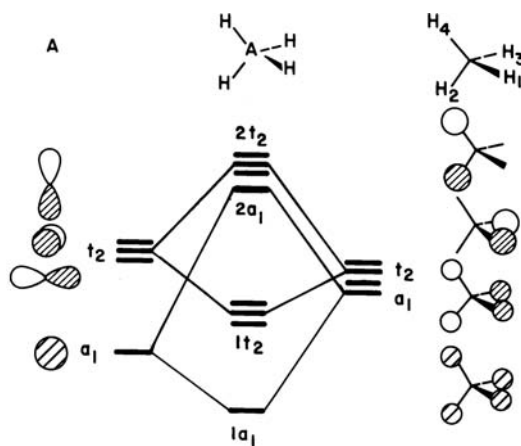
**FIGURE 4.5**

Assembly of the molecular orbital diagram for water ( $C_{2v}$  point group) using symmetry-adapted orbitals on the ligands and the central atom  $p$  orbitals.

symmetry adapted linear combinations of these basis orbitals are shown at the right-hand side Figure 4.6. Note that the form of the degenerate pair of orbitals is just as we derived in **4.10**. Also, since the hydrogen orbitals themselves are symmetric with respect to reflection in the molecular plane, their representations carry a single prime. It is interesting to see at this stage that each of the  $e'$  orbitals is nicely set up to interact with a  $p_x$  and  $p_y$  orbital on the central atom. Indeed,  $p_x$  and  $p_y$  on the A atom transform as  $e'$ ;  $p_z$  and s transform as  $a_2''$  and  $a_1'$ , respectively. The  $a_1'$  ligand combination has just the right symmetry to interact with the central atom s orbital. The level structure for planar AH<sub>3</sub> is simply produced by constructing in-phase (bonding) and out-of-phase (antibonding) molecular orbitals from orbitals at the left and right sides with the same symmetry. Of all the orbitals, the  $p_z$  orbital on the central atom finds no suitable ligand combination and so remains nonbonding.

**FIGURE 4.6**

Assembly of the molecular orbital diagram for the planar AH<sub>3</sub> molecule ( $D_{3h}$  point group) using symmetry-adapted orbitals on the ligands and the central s and  $p$  orbitals.

**FIGURE 4.7**

Assembly of the molecular orbital diagram for the tetrahedral  $\text{AH}_4$  molecule ( $T_d$  point group) using symmetry-adapted orbitals on the ligands and the central atom  $s$  and  $p$  orbitals.

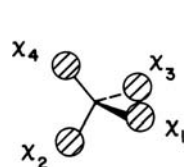
Figure 4.7 shows a diagram for tetrahedral  $\text{AH}_4$  which belongs to the  $T_d$  point group. Here we find that the four hydrogen 1s orbitals transform as  $a_1 + t_2$ , that is, a nondegenerate and a triply degenerate representation. The central atom  $p$  orbitals transform as  $t_2$  and the central atom  $s$  orbital as  $a_1$ . Generation of the orbital diagram is therefore quite a simple process by creating bonding and antibonding orbital pairs from central atom and ligand orbital combinations of the right symmetry. These symmetry ideas do not give any detail about the magnitude of the energy shifts involved. Specifically in this case, whether the upper  $t_2$  orbital lies below or above the upper  $a_1$  orbital is a matter that has to be resolved by perturbation theory considerations or numerical calculation. Shown in this diagram are the forms of the triply degenerate hydrogen 1s orbital combinations, which can be determined using the Schmidt process described earlier. Algebraically, with reference to 4.26 one choice for these degenerate functions is

$$\begin{aligned}\phi_a(t_2) &= \frac{1}{2}(\chi_1 - \chi_2 + \chi_3 - \chi_4) \\ \phi_b(t_2) &= \frac{1}{\sqrt{2}}(\chi_1 - \chi_3) \\ \phi_c(t_2) &= \frac{1}{\sqrt{2}}(\chi_2 - \chi_4)\end{aligned}\quad (4.63)$$

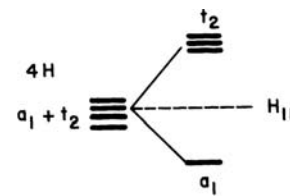
and that for the  $a_1$  orbital is of course

$$\phi(a_1) = \frac{1}{2}(\chi_1 + \chi_2 + \chi_3 + \chi_4) \quad (4.64)$$

where the factors before the parentheses are normalization constants, assuming that the overlap integrals between these orbitals are tiny enough to be ignored (i.e.,  $\langle \chi_i | \chi_j \rangle = \delta_{ij}$ ).



4.26



4.27

How does the picture change however if, instead of being interested in the  $\text{AH}_4$  molecule, we wanted the orbital diagram for a tetrahedral  $\text{H}_4$  molecule? Now, putting the overlap integrals  $\langle \chi_i | \chi_j \rangle = S_{ij}$  ( $i \neq j$ ), the normalization constants of equations 4.63 and 4.64 change, but importantly, the coefficients before the  $\chi_i$  within the parentheses do not change. The new wavefunctions are simply

$$\phi_b(t_2) = \frac{1}{\sqrt{2(1-S)}}(\chi_1 - \chi_3) \quad (4.65)$$

$$\phi(a_1) = \frac{1}{2\sqrt{(1+3S)}}(\chi_1 + \chi_2 + \chi_3 + \chi_4) \quad (4.66)$$

where we have shown one  $t_2$  component. If the  $\text{H}_4$  problem is characterized by interaction integrals  $\langle \chi_i | H^{\text{eff}} | \chi_j \rangle = H_{12}$  ( $i \neq j$ ), then substitution of equations 4.65 and 4.66 into equation 1.13 leads to the values of the energies,

$$e(t_2) = \frac{H_{11} - H_{12}}{1 - S} \quad (4.67)$$

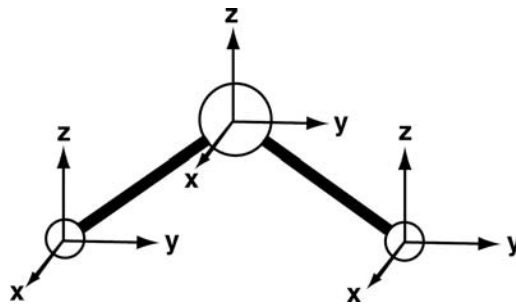
$$e(a_1) = \frac{H_{11} + 3H_{12}}{1 + 3S} \quad (4.68)$$

and therefore the ready synthesis of the orbital diagram of 4.27. For simple molecules of this type, the level structure down to the relative energy of the levels involved is dominated by the symmetry of the system and may be qualitatively understood in a few lines as we have shown here.

## 4.9 SYMMETRY PROPERTIES OF MOLECULAR VIBRATIONS

Although this book is concerned with orbitals, and this chapter has so far described their symmetry properties, in several places we are concerned with the symmetry properties of the vibrations of molecules [9–11]. For a collection of  $N$  unconnected atoms, the total kinetic energy is simply the sum of the contributions from each ( $x, y, z$ ) degree of freedom of each atom, namely,  $3N$  of them. Now when the atoms are linked together, a nonlinear molecule with  $N$  atoms has three translational and three rotational degrees of freedom so that there are  $3N - 6$  vibrational degrees of freedom ( $3N - 5$  for linear molecules) which describe the internal energy of the molecule. The vibrations may be largely involved in bond stretching, bond bending, or torsional motion. The prescription for determining the symmetry properties of the vibrational degrees of freedom is really quite straightforward. As shown in Figure 4.8 for the water molecule (point group  $C_{2v}$ ) vectors pointing in the  $x, y$ , and  $z$  directions attached to each atom may be used as a basis for a representation. The representation that is generated in exactly the same way as for an orbital basis (it is always reducible) is  $3N$  dimensional. After reduction in the usual way, the translational degrees of freedom (which transform as  $x, y$ , and  $z$ ) and the rotational degrees of freedom (which transform as  $R_x, R_y$ , and  $R_z$ ) may be subtracted and the remaining representations give the symmetry properties of the vibrations. For the case of Figure 4.8 this process proceeds as follows:

$C_{2v}$	$E$	$C_2$	$\sigma_v(xz)$	$\sigma_v(yz)$	(4.69)
$\Gamma_{xyz}$	9	-1	1	3	

**FIGURE 4.8**

Vectors pointing in the  $x$ ,  $y$ , and  $z$  directions used as a basis to determine the symmetry species of molecular vibrations.

Reduction of this reducible representation gives

$$\Gamma_{xyz} = 3a_1 + a_2 + 2b_1 + 3b_2 \quad (4.70)$$

By inspection of the  $C_{2v}$  character table in Appendix II,

$$\Gamma_{\text{trans}} = a_1 + b_1 + b_2 \quad (4.71)$$

and

$$\Gamma_{\text{rot}} = a_2 + b_1 + b_2 \quad (4.72)$$

and thus by subtraction

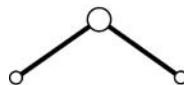
$$\Gamma_{\text{vib}} = \Gamma_{xyz} - \Gamma_{\text{trans}} - \Gamma_{\text{rot}} = 2a_1 + b_2 \quad (4.73)$$

Notice that lowercase letters are used to describe the symmetry species of the vibrations.

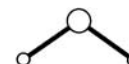
What do these particular vibrations look like? In this case it is quite simple. First, instead of using the  $x$ ,  $y$ , and  $z$  vectors as a basis in Figure 4.8, use those shown in 4.28



4.28



4.29



4.30

which represent stretching of the O—H bonds. The result will give the symmetry of the stretching vibrations. Now, from equation 4.74,

$C_{2v}$	$E$	$C_2$	$\sigma_v(xz)$	$\sigma_v(yz)$
$\Gamma_{xyz}$	2	0	0	2

$$(4.74)$$

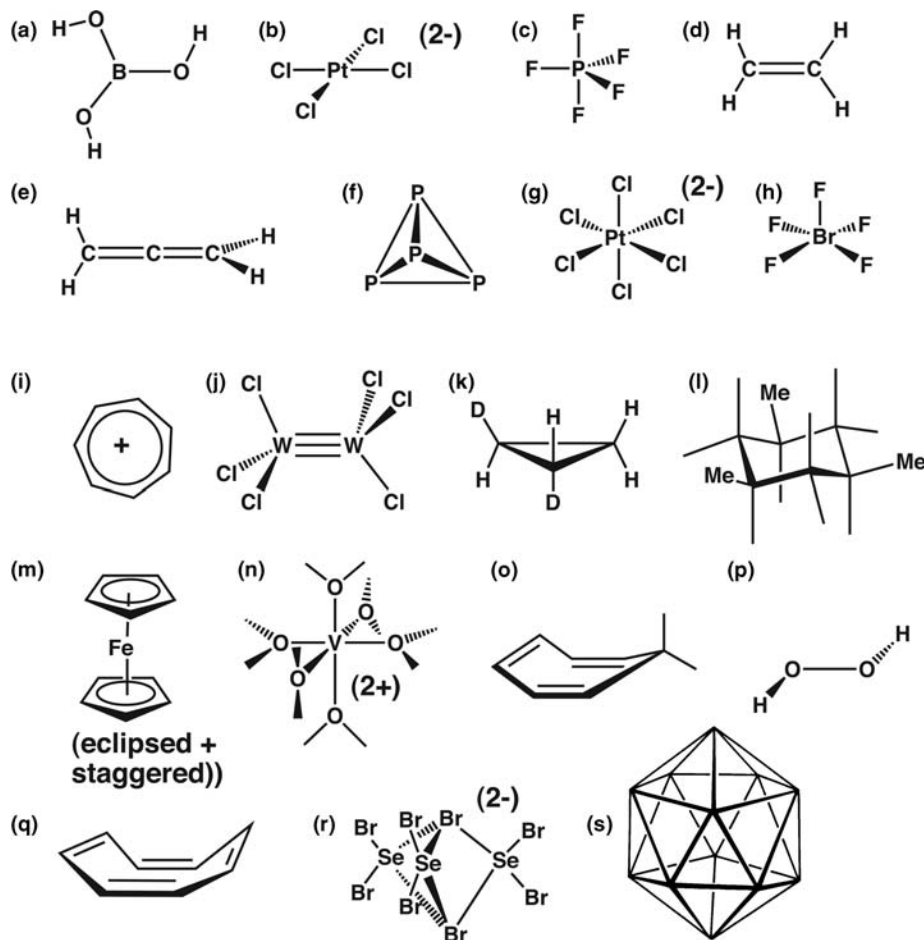
Reduction of this reducible representation gives

$$\Gamma_{\text{stretch}} = a_1 + b_2 \quad (4.75)$$

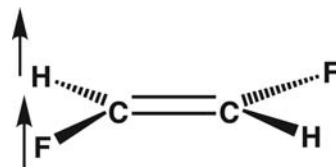
By use of the projection operator, in exactly the same fashion as for the construction of molecular orbitals, one readily finds the result of **4.29**, the symmetric and antisymmetric stretching vibrations. One can simply guess at the identity of the other  $a_1$  vibration. It is just the bending motion shown in **4.30**. These motions are called the symmetry modes of the molecule. Just as in molecules where orbitals of the same symmetry may mix together, vibrational modes of the same symmetry may mix together to give the normal modes of the molecule. Thus, of the two  $a_1$  vibrations one will be largely a O—H stretching vibration but with some admixture of H—O—H bending, whereas the other will be largely an H—O—H bending vibration with a small admixture of O—H stretching. It is important to realize that the vectors used for stretching and bending vibrations are equally valid where their direction is reversed. Therefore, the  $a_1$  mode in **4.30** also takes a  $C_{2v}$  molecule toward a linear  $D_{\infty h}$  one. The general principles outlined here are applicable [!!] to more complex systems. Some other vibrations of interest are shown in Appendix III of this book.

## PROBLEMS

**4.1.** Classify the following molecules according to the Schonflies point group to which they belong. Note: Wedges signify bonds coming out toward you and dashes indicate bonds going away from you.



- 4.2.** Set up a group multiplication table for *trans*-difluoroethylene as an example of the  $C_{2h}$  group. The arrows by the hydrogen and fluorine atoms will help. Are any of the operations in the same class?



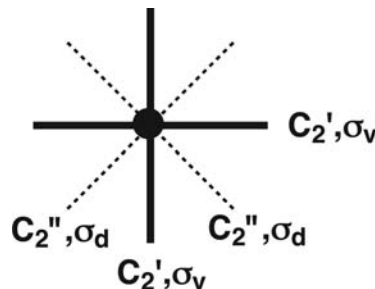
- 4.3.** Reduce the following representations and check your answers by adding the irreducible representations:

$C_{3v}$	$E$	$2C_3$	$3\sigma_v$
$\Gamma_1$	12	0	0
$\Gamma_2$	5	2	1

$C_4$	$E$	$C_4$	$C_2$	$C_4^3$
$\Gamma_3$	3	1	-1	1
$\Gamma_4$	11	1	3	1

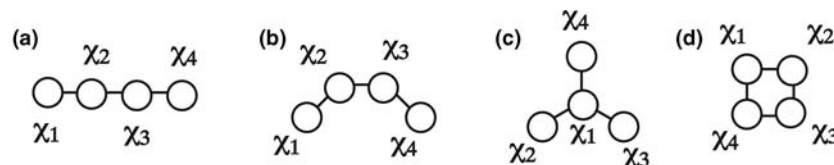
$D_{3h}$	$E$	$2C_3$	$3C_2$	$\sigma_h$	$2S_3$	$3\sigma_v$
$\Gamma_5$	13	-2	-1	-5	-2	1
$\Gamma_6$	5	2	1	3	0	1

- 4.4.** Consider an object, shown below, which has  $D_{4h}$  symmetry. The mirror planes and  $C_2$  axis are those labeled.

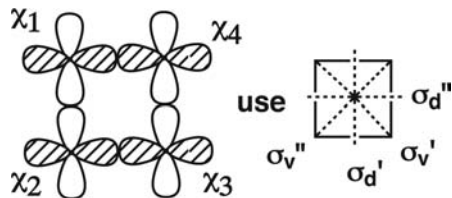


- Write out the transformation matrix for the  $C_4^3$  symmetry operation for a point  $P_1$  with arbitrary coordinates  $x_1, y_1, z_1$  moving to position  $P_2$  with coordinates  $x_2, y_2, z_2$ .
- Do the same thing for the  $i$  symmetry operation.
- Show that  $C_4$  and  $C_4^3$  are in the same class.

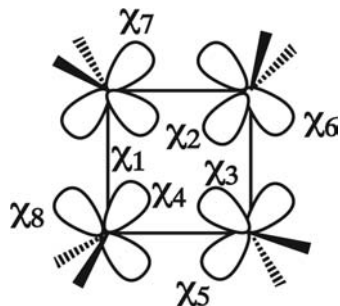
- 4.5.** Consider four H 1s atomic orbitals in the geometries shown below. Work out the irreducible representations generated by these functions and determine the form of the symmetry adapted functions using a formula and a drawing. If there are two basis that have the same irreducible representation, then take linear combinations of them.



- 4.6.** Consider a square  $M_4$  cluster. Write the symmetry adapted combinations of  $\chi_1-\chi_4$ ; (there is no need to determine the normalization constants) and draw them.



- 4.7.** In this problem, we are going to develop the  $\sigma$  orbitals of a flat cyclobutane molecule using  $C_{4v}$  symmetry. The basis are labeled  $\chi_1-\chi_8$  in the drawing below. Use the definitions of  $\sigma_d$  and  $\sigma_v$  as shown in Problem 4.6.



- 4.8.** Determine the symmetry for all possible electronic states associated with triangular  $H_3^+$  in  $C_{2v}$  symmetry. The orbitals are constructed in Figure 5.2.

## REFERENCES

1. F. A. Cotton, *Group Theory and Its Applications*, 2nd edition, Wiley-Interscience, New York (1971).
2. E. Heilbronner and H. Bock, *The HMO Model and Its Application*, John Wiley & Sons, New York (1976).
3. M. Orchin and H. H. Jaffe, *Symmetry, Orbitals and Spectra*, Wiley-Interscience, New York (1971).
4. D. M. Bishop, *Group Theory*, Oxford University Press, New York (1973).
5. D. S. Schonland, *Molecular Symmetry*, Van Nostrand, New York (1965).
6. R. McWeeney, *Coulson's Valence*, Oxford University Press, New York (1979).
7. L. Salem, *Electrons in Chemical Reactions*, John Wiley & Sons, New York (1982).
8. R. B. Woodward and R. Hoffmann, *The Conservation of Orbital Symmetry*, Academic Press, New York (1969).
9. S. F. A. Kettle, *Symmetry and Structure*, John Wiley & Sons, New York (1977).
10. E. B. Wilson, J. C. Decius, and P. C. Cross, *Molecular Vibrations*, McGraw-Hill, New York (1955).
11. G. Herzberg, *Infrared and Raman Spectra*, Van-Nostrand, New York (1945).

## CHAPTER 5

# Molecular Orbital Construction from Fragment Orbitals

---

## 5.1 INTRODUCTION

---

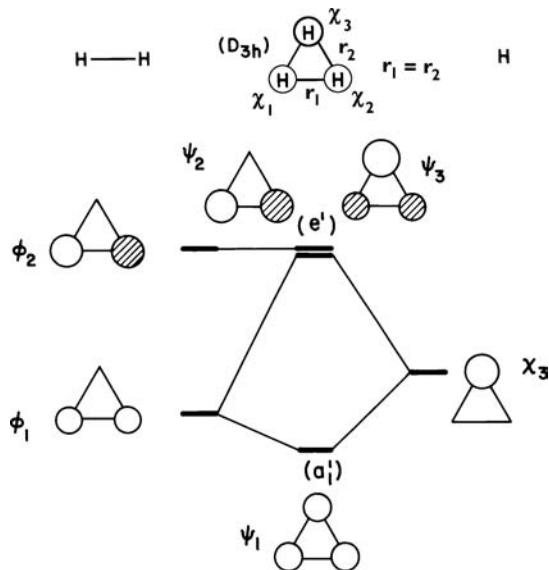
The practical aspects of perturbation molecular orbital theory discussed in Chapter 3 will now be illustrated further by constructing the orbitals of simple molecular systems. While being illustrative in their own right, the level patterns are the representatives of several of the orbital patterns we will come across later and illustrate the typical ways that molecular orbitals can be constructed from the orbitals of smaller fragments. The molecules examined in this chapter have the common feature that all the atoms of the molecule are identical, and each contributes one atomic orbital. At its simplest, then, these are  $H_n$  molecules (hypothetical for the most part) but all of the arguments for these planar systems carry directly over to the  $\pi$  level structures of polyenes where one  $p_{\pi}$  orbital per carbon atom only is considered. In our discussion, the first- and second-order mixing coefficients  $t_{ji}^{(1)}$  and  $t_{ki}^{(2)}$  are assumed to be small. Their signs are determined simply by the signs of the relevant overlap integrals  $\tilde{S}_{ij}$  and  $\tilde{S}_{kj}$  in equations 3.13 and 3.14 and by the relative energetic ordering of the orbitals involved. The reader should carefully work through the perturbation formulae for these rather transparent examples.

---

## 5.2 TRIANGULAR $H_3$

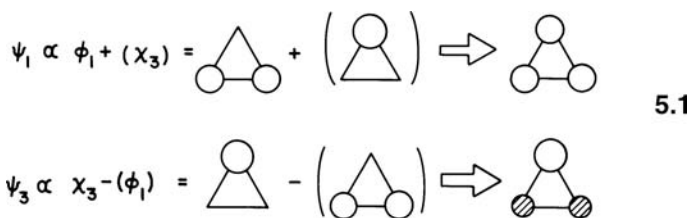
---

The form of the orbitals for a  $D_{3h}$   $H_3$  species was discussed in the previous chapter using group theory alone. Here, we shall use intermolecular perturbation theory to establish the relative energies and resultant molecular orbitals first for the example,  $D_{3h}$ . This case may be constructed as in Figure 5.1 from the orbitals of a diatomic

**FIGURE 5.1**

Assembly of the orbital interaction diagram for equilateral triangular H<sub>3</sub> ( $D_{3h}$ ) from those of H<sub>2</sub> + H.

H<sub>2</sub> unit comprised of  $\chi_1$  and  $\chi_2$  which yield fragment orbitals  $\phi_1$  and  $\phi_2$ , the bonding and antibonding combinations, and the orbital of a single H atom,  $\chi_3$ . The relative energies of the starting, zeroth-order orbitals shown on the far right and left of Figure 5.1 are simply a reflection of the two-orbital problem discussed in Chapter 2. Thus,  $\chi_3$  lies between  $\phi_1$  and  $\phi_2$ ; it is energetically closer to  $\phi_1$  since  $\phi_1$  is stabilized less than that  $\phi_2$  is destabilized when forming the two fragment orbitals from  $\chi_1$  and  $\chi_2$  (which are at the same energy as  $\chi_3$ ). It is easy to see by inspection that  $\langle \phi_2 | \chi_3 \rangle = 0$ , a result that follows too from symmetry arguments;  $\phi_2$  and  $\chi_3$  are of different symmetry species. We do not need to investigate this in any great detail rather than to note that one is symmetric (a character of +) and the other antisymmetric (a character of -) with respect to the reflection in the plane containing  $\chi_3$  and the bisector of  $\chi_1-\chi_2$ . With the relative phases for the fragment orbitals in Figure 5.1,  $\langle \phi_1 | \chi_3 \rangle = (+)$ . The molecular orbitals,  $\psi_1-\psi_3$ , are produced with resultant energies shown in the middle of the orbital interaction diagram in Figure 5.1. The final wavefunctions are constructed as in 5.1. Namely,  $\phi_1$  is stabilized



by mixing the higher lying  $\chi_3$  into it in a bonding fashion to give  $\psi_1$  and, likewise,  $\chi_3$  is destabilized by  $\phi_1$  to give  $\psi_3$ . The fragment orbital  $\phi_2$  is rigorously nonbonding; the zeroth-order solution is the final, one yielding the molecular orbital  $\psi_2$ . The classic two-orbital pattern is again found. What is not clear in this approach is that in the orbital  $\psi_1$ , all the atomic orbitals are of equal weight, but in its antibonding equivalent  $\psi_3$ ,  $\chi_3$  carries twice the weight of  $\chi_1$  or  $\chi_2$ . Intuitively, one might expect this since the first-order mixing coefficients (associated with  $\chi_3$  in  $\psi_1$  and  $\phi_1$  in  $\psi_3$ ) are smaller than the zeroth order, leading term of the perturbation expansion for the wavefunction. Neither is it clear that  $\psi_3$  is destabilized to exactly the same energy as the nonbonding orbital  $\psi_2$ . These results drop straight out of the group theoretical

treatment of Chapter 4. Since the three H 1s orbitals are related by the threefold axis of the triangle by symmetry, they are constrained to form three molecular orbitals, one of which is nondegenerate,  $a'_1$ , and a pair which is degenerate,  $e'$ , just as we showed in a step preparatory to the construction of the diagram for planar  $\text{AH}_3$  in Section 4.8. The form of these orbitals is shown in 4.10; they are of course identical to the resultant molecular orbitals drawn in the center of Figure 5.1. Using these wavefunctions and the expression for the energy in equation 1.13, then, since  $H_{11} = H_{22} = H_{33}$  and  $H_{12} = H_{13} = H_{23}$ ,

$$e_{a'_1} \propto \langle \chi_1 + \chi_2 + \chi_3 | H^{\text{eff}} | \chi_1 + \chi_2 + \chi_3 \rangle \propto H_{11} + 2H_{12} \quad (5.1)$$

and

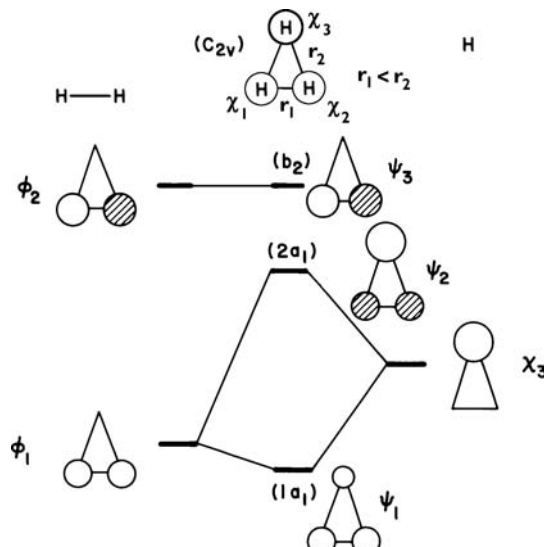
$$e_{e'} \propto \langle \chi_1 - \chi_2 | H^{\text{eff}} | \chi_1 - \chi_2 \rangle \propto H_{11} - H_{12} \quad (5.2)$$

or

$$e_{e'} \propto \langle 2\chi_1 - \chi_2 - \chi_3 | H^{\text{eff}} | 2\chi_1 - \chi_2 - \chi_3 \rangle \propto H_{11} - H_{12} \quad (5.3)$$

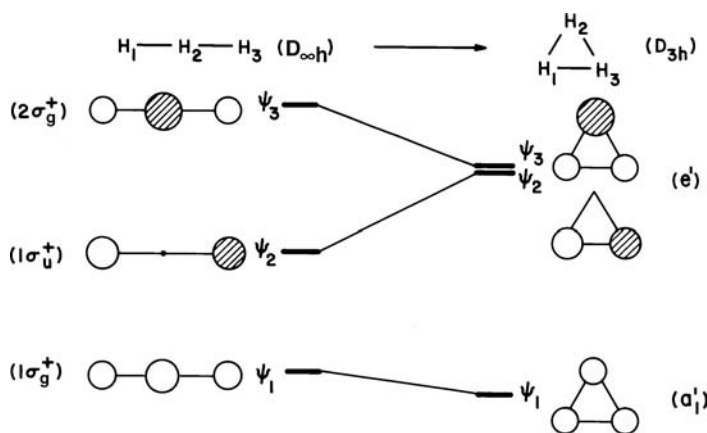
So, from the three isolated s orbitals, the splitting pattern appears as in Figure 5.1.

Suppose that one H—H distance in  $\text{H}_3$  is shorter than the other two. The orbitals for such an isosceles triangle are constructed in an exactly analogous way to the equilateral triangle problem of Figure 5.1. Now, since the threefold axis of the latter is absent, the two orbitals,  $\psi_2$  and  $\psi_3$ , are not degenerate. The level pattern is generated in Figure 5.2 where we assume that  $r_1$  (see the top of Figure 5.2) is shorter than that for the equilateral triangle but that  $r_2$  remains the same. Shortening  $r_1$  causes the magnitude of  $\langle \chi_1 | \chi_2 \rangle$  to increase; recall the exponential dependence on this overlap integral with respect to distance in 1.11. This stabilizes  $\psi_1$  since there is a bonding interaction between hydrogen atoms 1 and 2 in this orbital. For the same reason,  $\psi_2$  does not rise as high in energy as it did in Figure 5.1. On the other hand, when  $r_1$  becomes smaller, there is greater antibonding in  $\psi_3$ , and so, it is destabilized. Quantitatively, the energy levels of the isosceles triangular structure may be derived from those of equilateral triangular structure by making  $H_{13} = H_{23} \neq H_{12}$  in equations 5.1 and 5.3. Now, equations 5.2 and 5.3 do not lead to the same energy. This is reflected too in



**FIGURE 5.2**

Assembly of the orbital interaction diagram for an isosceles triangular  $\text{H}_3$  ( $C_{2v}$ ) molecule from those of  $\text{H}_2 + \text{H}$ .

**FIGURE 5.3**

An orbital correlation diagram linking the level structures of linear ( $D_{\infty h}$ ) and equilateral triangular ( $D_{3h}$ )  $H_3$ .

the symmetry species of the levels. In the new point group ( $C_{2v}$ ), there are no degenerate representations and the pair of functions that used to be of  $e'$  symmetry in  $D_{3h}$  have now split into molecular orbitals of  $a_1 + b_2$  symmetry.

Figure 5.3 shows how the molecular orbital levels of  $H_3$  change as the molecular geometry changes from the linear to equilateral triangular structure. This is called an orbital correlation diagram. The initial and final orbital energies are simply connected via straight lines. The orbitals of linear  $H_3$  have been covered before in Section 3.4. As the  $H—H—H$  angle decreases from  $180^\circ$  to  $60^\circ$ , the overlap integrals  $\langle \chi_1 | \chi_2 \rangle$  and  $\langle \chi_2 | \chi_3 \rangle$  do not change, provided the  $H_1—H_2$  and  $H_2—H_3$  distances remain fixed. What happens, of course, is that overlap between  $\chi_1$  and  $\chi_3$  is switched on. This stabilizes  $\psi_1$  and  $\psi_3$ , since  $\chi_1$  and  $\chi_3$  enter with the same relative phase in both of these orbitals. During the bending process, these orbitals mix together such that the atomic orbital coefficients in  $\psi_1$  become equal at the equilateral triangular geometry. This perturbation will be covered in some depth in Chapter 7. In  $\psi_2$  of the linear system,  $\chi_1$  and  $\chi_3$  are of opposite phase. Therefore, as the  $H—H—H$  angle decreases,  $\psi_2$  rises in energy and eventually becomes degenerate with  $\psi_3$ . The reader should check the resultant molecular orbitals shown in the right-hand side of Figure 5.3 and compare them with those derived in Figure 5.1. The results are, of course, the same. We shall use both techniques, namely, distortion of one geometry to another and assembly from smaller fragments, to view the level structure of more complex systems.

Our discussion of the  $H_3$  system has neglected the impact of the electron count on the relative energies for each geometry that has been investigated in this section. We shall amplify the details in Section 7.4. For  $H_3^+$  with two electrons,  $\psi_1$  is filled. Therefore, by the inspection of Figure 5.3, one can see that the equilateral triangle will be more stable than the linear geometry. The  $a'_1$  molecular orbital is more stable than  $1\sigma_g^+$ . On the other hand, with the electronic configuration of  $(\psi_1)^2(\psi_2)^2$  for  $H_3^-$ , the linear geometry will be more stable than the equilateral triangle. The component of  $e'$  is stabilized more on going to the  $D_{\infty h}$  structure than the  $a'_1$  molecular orbital is destabilized. In other words, the loss of antibonding in  $\psi_2$  between  $H_1$  and  $H_3$  is greater than the loss of bonding between those in this pair in  $\psi_1$ . Both predictions are correct. The geometry for  $H_3^+$  is  $D_{3h}$  with a  $H—H$  distance of  $0.872 \text{ \AA}$  [1]; this is elongated from that in  $H_2$  ( $0.741 \text{ \AA}$ ). Returning to Figure 5.1, one could formally treat  $H_3^+$  as having  $\phi_1$  doubly occupied and  $\chi_3$  empty. Upon interaction of  $H_2$  with  $H^+$ , electron density is transferred from  $\phi_1$ , which is bonding between  $\chi_1$  and  $\chi_2$  to  $\chi_3$ . Therefore, the  $H_1—H_2$  bond length increases on going from  $H_2$  to  $H_3^+$ . Another way to describe this is to consider that  $H_3^+$  possesses “electron deficient” bonding, which is a term arising from the historical preoccupation with the

idea of a two-center–two-electron bond. There are only two electrons spread out over three bonds, and this will create long bond distances (the bond distance in  $\text{H}_2^+$  increases by 0.303 Å from that in  $\text{H}_2$ ).  $\psi_1$  is stabilized appreciably; the reaction of  $\text{H}_2$  with  $\text{H}^+$  to give  $\text{H}_3^+$  is exothermic by 106 kcal/mol<sup>1</sup>. For  $\text{H}_3^-$ , the  $D_{\infty h}$  structure is the transition state for the  $\text{H}^- + \text{H}_2$  reaction with an H—H bond distance of 1.084 Å and an energy of 11.6 kcal/mol higher than the reactants [2,3]. The arguments presented here presume that the relative energy of a molecule is directly related to the energetic variation of its molecular orbitals upon changing the geometry. This topic will be addressed further in Section 8.4, and it will be used frequently throughout the book. A cautionary note, however, must be added. The energetic consequences of internuclear repulsion, interelectron repulsion, and charging effects have been neglected. The energies associated with  $\psi_1$ – $\psi_3$  will all be shifted upward on going from  $\text{H}_3^+$  to  $\text{H}_3^-$ . The increased interelectron repulsion on going from  $\text{H}_3^+$  to  $\text{H}_3^-$  is also certainly behind why the H—H bond distance increases. This effect should not create difficulty since we are only interested in a qualitative judgment of the relative energies. The neglect of internuclear repulsion, when carried to the extreme, can lead to unphysical situations. Since the overlap between two hydrogen s atomic orbitals increases exponentially when the distance decreases, therefore, on the basis of orbital energies alone, the bond distance in  $\text{H}_2$  should be zero! Likewise, fixing the  $r_2$  distance for the isosceles triangle in Figure 5.2 and allowing  $r_1$  to vary for an  $\text{H}_3^+$  molecule would generate the unphysical result that  $r_1 = 0$  for the optimal structure. As in any qualitative theory, one must be careful to remember the approximations that have been implemented.

### 5.3 RECTANGULAR AND SQUARE PLANAR $\text{H}_4$

The orbitals of rectangular  $\text{H}_4$  are constructed in an analogous manner to those of  $\text{H}_3$  in Figure 5.4. The molecular orbitals  $\phi_1$ ,  $\phi_1'$  are degenerate as are  $\phi_2$  and  $\phi_2'$ .  $\psi_1$  and  $\psi_2$  are the bonding and antibonding combinations of  $\phi_1$  and  $\phi_1'$  while  $\psi_3$  and  $\psi_4$  are the analogs from  $\phi_2$  and  $\phi_2'$ . The wavefunctions  $\psi_1$ – $\psi_4$  are correct to first order in the energy.  $\psi_1$ ,  $\psi_2$  are orthogonal to  $\psi_3$ ,  $\psi_4$  because  $\langle \phi_1 | \phi_2' \rangle = \langle \phi_2 | \phi_1' \rangle = 0$ , so no second-order interaction between them occurs. Since the atomic coefficients

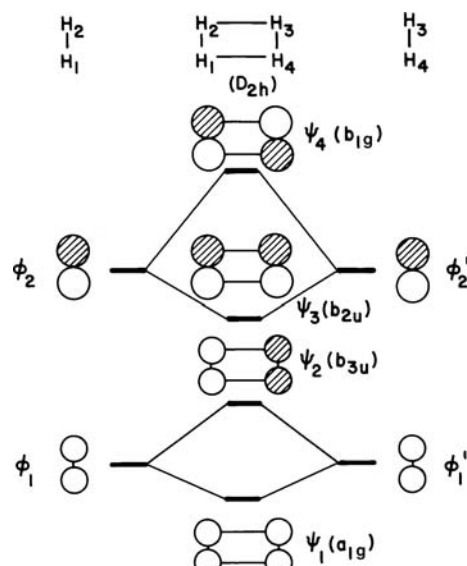
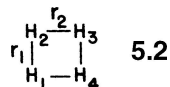


**FIGURE 5.4**

Assembly of the orbital interaction diagram for rectangular  $\text{H}_4$  ( $D_{2h}$ ) from those of two  $\text{H}_2$  units.

in the antibonding  $\phi_2$  are larger than those in bonding  $\phi_1$ , the overlap between  $\phi_2$  and  $\phi'_2$  will be larger than that for  $\phi_1$  and  $\phi'_1$ . Therefore, the splitting associated with  $\psi_3$  and  $\psi_4$  is expected to be larger than that between  $\psi_1$  and  $\psi_2$ .

Consider what happens when the rectangular H<sub>4</sub> molecule distorts to a square, that is,  $r_1$  becomes longer and  $r_2$  shorter (5.2). The overlap between H<sub>1</sub> and H<sub>4</sub> and



between H<sub>2</sub> and H<sub>3</sub> will increase, and the overlap between H<sub>1</sub> and H<sub>2</sub> and between H<sub>3</sub> and H<sub>4</sub> will decrease. Increasing overlap leads to an increasing stabilization if the two atomic orbitals have the same phase in a molecular orbital and a destabilization if they have opposite phases. The results are displayed in Figure 5.5. Thus,  $\psi_1$  and  $\psi_4$  remain at approximately the same energy. For example, in  $\psi_1$ , the increase in bonding between H<sub>1</sub> and H<sub>4</sub> (and H<sub>2</sub>–H<sub>3</sub>) when  $r_1$  decreases is counterbalanced by the loss of bonding between H<sub>1</sub> and H<sub>2</sub> (and H<sub>3</sub>–H<sub>4</sub>) when  $r_2$  increases. But, this is not the case for  $\psi_2$  and  $\psi_3$ ;  $\psi_2$  rises and  $\psi_3$  drops in energy. The energetic consequences associated with changing  $r_1$  and  $r_2$  work in the same manner for each molecular orbital. Thus, for  $\psi_2$ , the decreased bonding by lengthening  $r_1$  and the increased antibonding by shortening  $r_2$  both cause  $\psi_2$  to be destabilized. A similar explanation can easily be constructed for the stabilization of  $\psi_3$ . At the square planar geometry,  $\psi_2$  and  $\psi_3$  have the same energy, that is, they are degenerate and have e<sub>u</sub> symmetry (combination of four hydrogen s orbitals at a square ( $D_{4h}$ ) geometry yields irreducible representations of  $a_{1g} + e_u + b_{2g}$ ). It would have been just as easy to construct the orbitals of square H<sub>4</sub> by interacting two H<sub>2</sub> units along the lines for the rectangular ( $D_{2h}$ ) geometry in Figure 5.4. The interactions are identical, but now  $\langle\phi_1|\phi'_1\rangle$  and  $\langle\phi_2|\phi'_2\rangle$  are greater and yield larger first-order energy corrections than that shown in Figure 5.4 since  $r_2$  has become shorter. The energy difference between  $\phi_1$  and  $\phi_2$  has also become smaller, because  $r_1$  is longer. The net result is that  $\psi_2$  and  $\psi_3$  are destabilized and stabilized, respectively, compared with that in Figure 5.4 while  $\psi_1$  and  $\psi_4$  stay at the same energies.

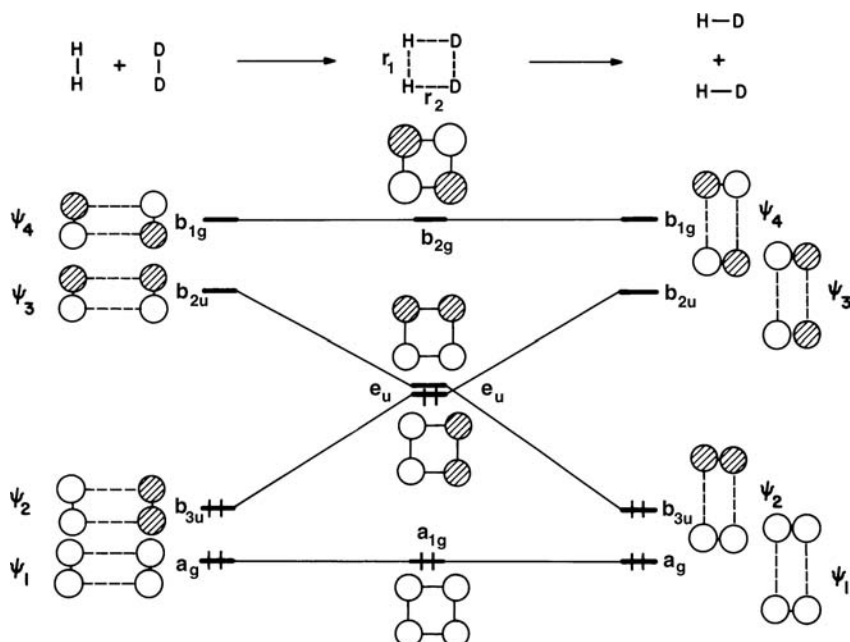
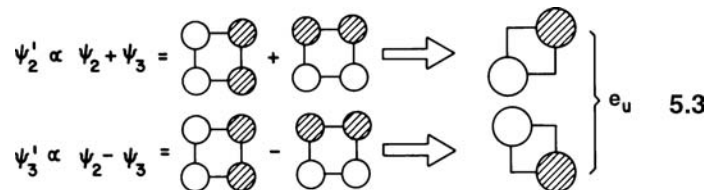


FIGURE 5.5

An orbital correlation diagram associated with the H/D exchange for H<sub>2</sub> + D<sub>2</sub> proceeding via a square ( $D_{4h}$ ) geometry.

As shown in Chapter 4, there is always a choice to be made in writing degenerate wavefunctions. Recall that two new functions may be generated by taking a linear combination of the old. An alternative pair of wavefunctions is shown

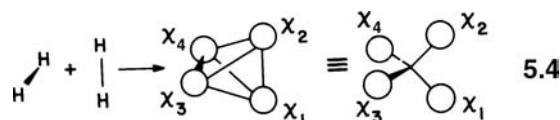


in 5.3 for the case of the  $e_u$  set in  $D_{4h}$   $H_4$ . Note that each pair of functions is orthogonal to each other and that the nodal planes have been rotated by  $45^\circ$  relative to their original positions.

The orbital correlation diagram in Figure 5.5 is intimately related [1,4,5] to the question of the  $H_2 + D_2$  exchange reaction. This is clearly a symmetry forbidden reaction (Section 4.7) since  $\psi_2$  and  $\psi_3$  cross at the square geometry and are orthogonal throughout the entire reaction coordinate. A high activation energy is predicted for the process if it occurs by this pathway. Notice also that at the square geometry, there are two electrons in a degenerate combination. Forming the direct product and using the lowering and raising operations in Section 4.5 then yields electronic states of  ${}^3A_{2g}$ ,  ${}^1B_{1g}$ ,  ${}^1A_{1g}$ , and  ${}^1B_{2g}$  symmetry for this species. Very accurate calculations [1] order the states as given in increasing energy and the two lowest,  ${}^3A_{2g}$  and  ${}^1B_{1g}$ , have energies of 145.4 and 152.4 kcal/mol, respectively, higher than the ground state of two  $H_2$  molecules. Considering that the H—H bond energy in  $H_2$  is 109.5 kcal/mol, these are very high energies indeed! The conversion of one H—H bonding orbital ( $\psi_2$  in Figure 5.5) to a nonbonding one at the square geometry is reflected in a large increase in the H—H distance. The computed values of  $r_1 = r_2$  for the  ${}^3A_{2g}$  and  ${}^1B_{1g}$  states were 1.157 and 1.224 Å, respectively. This should be compared with the 0.741 Å in  $H_2$  itself. Figures 5.4 and 5.5 also highlight the fact that the  $H_2 + D_2$  reaction is essentially a two-orbital four-electron problem. The net destabilization along the reaction pathway is proportional to  $\langle \phi_1 | \phi_1' \rangle^2$  (see Table 2.2), which increases exponentially when  $r_2$  decreases.

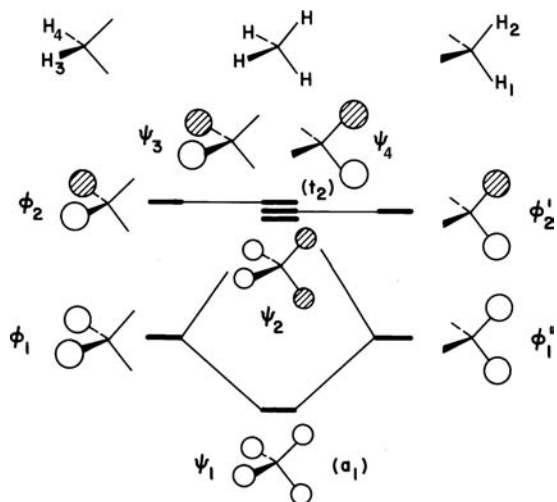
## 5.4 TETRAHEDRAL $H_4$

In the previous section, two  $H_2$  units were linked together in a planar geometry. If they are joined together in a perpendicular manner (as in 5.4) then a tetrahedral ( $T_d$ )



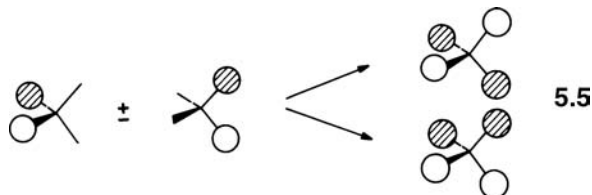
$H_4$  system results. Using the atomic orbital basis functions shown in 5.4, an orbital interaction diagram can be constructed as in Figure 5.6. All of the overlap integrals between the two units are zero except for  $\langle \phi_1 | \phi_1' \rangle$  which with the phases given is positive. So, the molecular orbitals of tetrahedral  $H_4$  are simply

$$\begin{aligned}\psi_1 &\propto \phi_1 + \phi'_1 \\ \psi_2 &\propto \phi_1 - \phi'_1 \\ \psi_3 &\propto \phi_2 \\ \psi_4 &\propto \phi'_2.\end{aligned}$$

**FIGURE 5.6**

Assembly of the orbital diagram for tetrahedral H<sub>4</sub> ( $T_d$ ) from those of two H<sub>2</sub> units. (The solid lines in this diagram that are associated with the geometrical figures are used to help the reader visualize the molecular geometry. The “bonds” between connected atoms, usually depicted by lines, have been left off for clarity.)

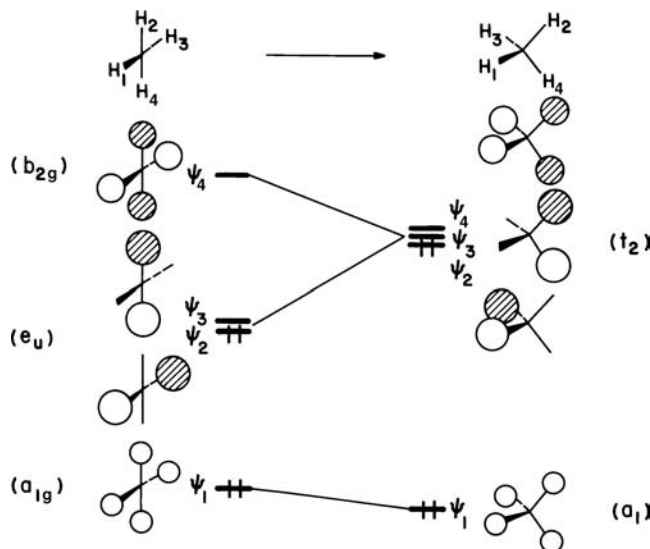
Although it is not at all obvious from this treatment,  $\psi_2$ ,  $\psi_3$ , and  $\psi_4$  are degenerate. This was shown quite clearly, however, in Section 4.7 where we used symmetry arguments to assemble the H<sub>4</sub> orbital diagram from four isolated H orbitals. A single bonding ( $a_1$ ) and triply degenerate antibonding ( $t_2$ ) set resulted. We can simply show how in Figure 5.6  $\psi_2$  and  $\psi_3$  have the same energy as  $\psi_4$  by taking linear combinations of  $\psi_3$  and  $\psi_4$  as in 5.5. Returning to the H<sub>2</sub> + D<sub>2</sub> exchange



reaction, a tetrahedral species is not expected to serve as the transition state or intermediate either. Two electrons are placed in  $\psi_1$ , and the remaining two enter the triply degenerate  $t_2$  level ( $\psi_2-\psi_4$ ). This will be an unstable situation for the same reasons the square H<sub>4</sub> assembly is unfavorable. Another way to look at the problem is to realize that since  $\psi_1$  is not stabilized as much as  $\psi_2$  is destabilized, then the electronic situation that results is again a simple two-orbital four-electron destabilization.

The orbital correlation diagram for the square planar to tetrahedral transformation is shown in Figure 5.7. The hydrogen atoms at the top of the figure have been labeled for reference. Let us allow the H<sub>1</sub>-H<sub>3</sub> and H<sub>2</sub>-H<sub>4</sub> distances to become shorter while those for H<sub>1</sub>-H<sub>2</sub> and H<sub>3</sub>-H<sub>4</sub> to stay roughly constant along the distortion pathway. It is easy to see by inspection that  $\psi_1$  and  $\psi_4$  are stabilized since bonding is turned on between H<sub>1</sub> and H<sub>3</sub> along with that between H<sub>2</sub> and H<sub>4</sub>.  $\psi_2$  and  $\psi_3$  are destabilized; antibonding between H<sub>1</sub>-H<sub>3</sub> and H<sub>2</sub>-H<sub>4</sub> is increased. Notice that using the alternative descriptions for the degenerate orbitals  $\psi_2$  and  $\psi_3$  in 5.3 for the square planar geometry leads directly to the appropriate combinations for the triply degenerate tetrahedral levels that we chose in Figure 5.6.

We are now in a position, with the aid of the orbital correlation diagrams in Figures 5.5 and 5.7, to evaluate the relative energies of the H<sub>4</sub> system (although

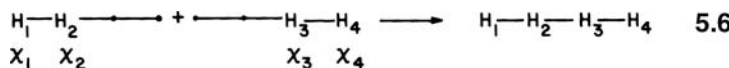
**FIGURE 5.7**

An orbital correlation diagram linking the level structures of square planar and tetrahedral  $\text{H}_4$  molecules.

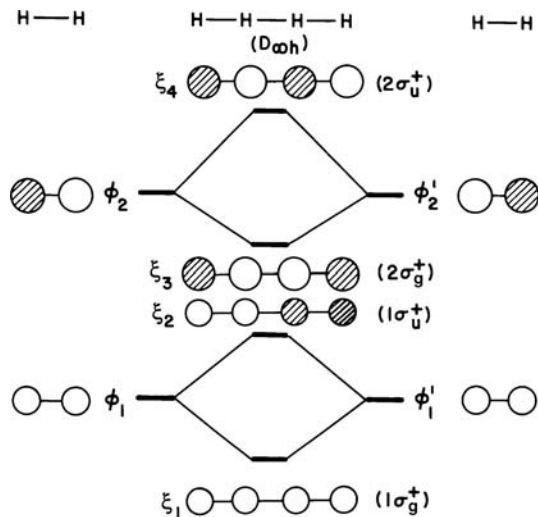
certainly other geometries could be chosen and included) as a function of the electron count. For  $\text{H}_4$  itself with four electrons, clearly a loose van der Waals complex in a rectangular geometry is preferred over the square that, in turn, is more stable than the tetrahedral arrangement since the  $e_u$  set in Figure 5.7 lies lower in energy than  $t_2$ . With two electrons,  $\text{H}_4^{2+}$ , the tetrahedral geometry is favored over square and certainly rectangular ones. High-level calculations [5] have shown, however, that the coulombic repulsion in this compound makes it unstable with respect to dissociation to  $\text{H}_3^+$  and  $\text{H}^+$ . It will be shown in Chapter 22 that a  $\text{Au-PR}_3$  unit electronically resembles a hydrogen atom. Experimentally [6], the structure of  $(\text{Au-PR}_3)_4^{2+}$ , where  $R = t\text{-Bu}$ , is in fact tetrahedral. This is a common pattern; electron deficient species (i.e., those with less than a formal pair of electrons per linkage) will prefer clustered geometries over more open ones (recall the difference in geometries on going from  $\text{H}_3^+$  to  $\text{H}_3^-$ ). With six electrons (neglecting coulombic and interelectron repulsion),  $\text{H}_4^{2-}$  will favor the square geometry over rectangular or tetrahedral ones. Both  $b_{2u}$  at  $D_{2h}$  and  $t_2$  at  $T_d$  are destabilized relative to  $e_u$ . Notice that the prediction of the optimal geometry changes as a function of the electron count. This is again a common theme that is followed throughout this book.

## 5.5 LINEAR $\text{H}_4$

The molecular orbitals of linear  $\text{H}_4$  (5.6) may be constructed by interacting the orbitals of two  $\text{H}_2$  fragments as shown in Figure 5.8 where the orbitals  $\phi_i$  and  $\phi'_i$  ( $i = 1, 2$ )

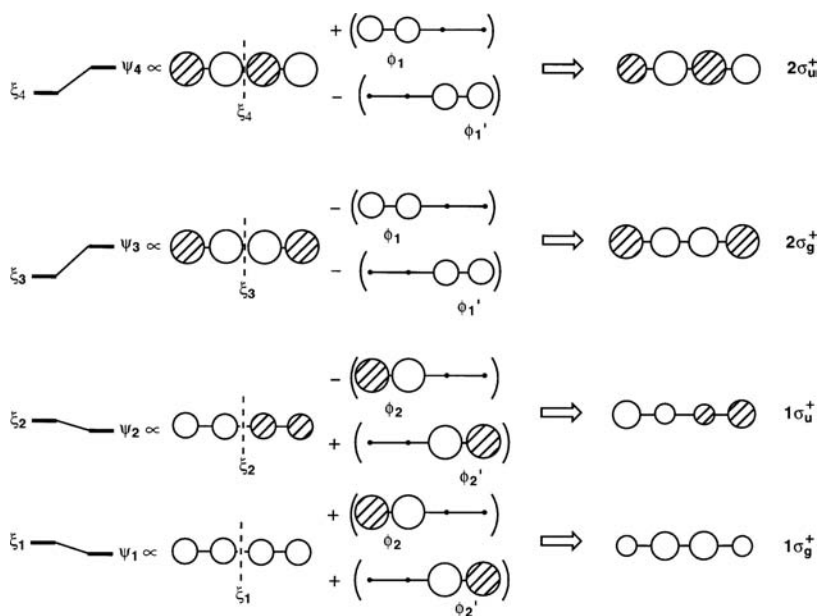


are arranged such that  $\langle \phi_i | \phi'_i \rangle = (+)$  and all adjacent H—H distances are assumed to be the same. The orbitals  $\phi_i$  and  $\phi'_i$  enter into degenerate interactions as shown in this figure. Thus,  $\xi_1$  and  $\xi_2$  are simply the bonding and antibonding combinations of  $\phi_1$  and  $\phi_1'$  while  $\xi_3$  and  $\xi_4$  are the bonding and antibonding combinations of  $\phi_2$  and  $\phi_2'$ . In  $\xi_1-\xi_4$ , each of the atomic orbital coefficients are equal for each atomic orbital.

**FIGURE 5.8**

Generation of the molecular orbital levels of linear H<sub>4</sub> from those of two collinear H<sub>2</sub> units. The construction of this diagram shows only the degenerate interaction.

However,  $\xi_1$  and  $\xi_3$  have the same symmetry (they are both symmetric with respect to the mirror plane between H<sub>2</sub> and H<sub>3</sub>; both are  $\sigma_u^+$ ). Likewise,  $\xi_2$  and  $\xi_4$  have  $\sigma_g^+$  symmetry (they are antisymmetric with respect to this mirror plane). Therefore, nondegenerate interactions must also be considered as shown in Figure 5.9. The second-order energy corrections are easy to see. Both of the  $\xi_1$  and  $\xi_2$  combinations will be stabilized by mixing in the higher lying  $\phi_2$  and  $\phi_2'$  fragments, whereas  $\xi_3$  and  $\xi_4$  are destabilized by  $\phi_1$  and  $\phi_1'$ . Care must be taken with the first-order mixing coefficients because the signs of the overlap integrals are not so easy to evaluate at first glance. The relative phases of  $\phi_i$  and  $\phi_i'$  in Figure 5.9 have been taken from Figure 5.8. The dashed lines for  $\xi_i$  in Figure 5.9 are to help the reader in determining the sign of  $\langle \phi_i | \xi_i \rangle$  by inspection. Recall that the different orbitals of each fragment are orthogonal (i.e., have zero overlap), i.e.,  $\langle \phi_1 | \phi_2 \rangle = \langle \phi_1' | \phi_2' \rangle = 0$ . Expanding

**FIGURE 5.9**

Nondegenerate interactions for H<sub>4</sub> using the results from Figure 5.8.

each  $\xi_i$  in terms of its fragment counterparts also will yield the appropriate sign of the overlap integrals, that is,

$$\langle \xi_1 | \phi_2 \rangle \propto \langle \phi_1 + \phi'_1 | \phi_2 \rangle = \langle \phi_1 | \phi_2 \rangle + \langle \phi'_1 | \phi_2 \rangle = (+) \quad (5.4)$$

$$\langle \xi_1 | \phi'_2 \rangle \propto \langle \phi_1 + \phi'_1 | \phi'_2 \rangle = \langle \phi_1 | \phi'_2 \rangle + \langle \phi'_1 | \phi'_2 \rangle = (+) \quad (5.5)$$

$$\langle \xi_2 | \phi_2 \rangle \propto \langle \phi_1 - \phi'_1 | \phi_2 \rangle = \langle \phi_1 | \phi_2 \rangle - \langle \phi'_1 | \phi_2 \rangle = (-) \quad (5.6)$$

$$\langle \xi_2 | \phi'_2 \rangle \propto \langle \phi_1 - \phi'_1 | \phi'_2 \rangle = \langle \phi_1 | \phi'_2 \rangle - \langle \phi'_1 | \phi'_2 \rangle = (+) \quad (5.7)$$

$$\langle \xi_3 | \phi_1 \rangle \propto \langle \phi_2 + \phi'_2 | \phi_1 \rangle = \langle \phi_2 | \phi_1 \rangle + \langle \phi'_2 | \phi_1 \rangle = (+) \quad (5.8)$$

$$\langle \xi_3 | \phi'_1 \rangle \propto \langle \phi_2 + \phi'_2 | \phi'_1 \rangle = \langle \phi_2 | \phi'_1 \rangle + \langle \phi'_2 | \phi'_1 \rangle = (+) \quad (5.9)$$

$$\langle \xi_4 | \phi_1 \rangle \propto \langle \phi_2 - \phi'_2 | \phi_1 \rangle = \langle \phi_2 | \phi_1 \rangle - \langle \phi'_2 | \phi_1 \rangle = (-) \quad (5.10)$$

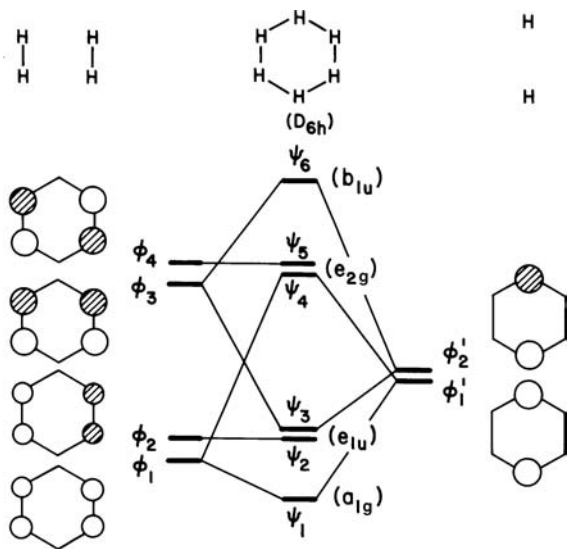
$$\langle \xi_4 | \phi'_1 \rangle \propto \langle \phi_2 - \phi'_2 | \phi'_1 \rangle = \langle \phi_2 | \phi'_1 \rangle - \langle \phi'_2 | \phi'_1 \rangle = (+) \quad (5.11)$$

Thus, the overlap integrals are all positive except those given by equations 5.6 and 5.10. Using equation 3.16, then for  $\psi_1$ , both  $\phi_2$  and  $\phi'_2$  mix in first order with positive coefficients; the numerator and denominator of equation 3.16 is negative. For  $\psi_2$ , one has the same situation for the  $\phi'_2$  component but that for  $\phi_2$  will have a positive numerator for the overlap term and a negative denominator for the energy gap. Therefore, the mixing coefficient will have the opposite phase to that in Figure 5.8. In both  $\psi_1$  and  $\psi_2$ , the fragment orbitals mix in a bonding fashion. The opposite is true for  $\psi_3$  and  $\psi_4$  where the lower lying  $\phi_1$  and  $\phi'_1$  mix into the degenerate combinations. Note that as a result of this nondegenerate perturbation, the pairs of degenerate combinations have mixed into each other so that they end up being orthogonal. The molecular orbitals are now polarized so that the amplitudes are not identical on each atomic orbital.

The reader should compare the orbitals of linear  $H_3$  on the left side of Figure 5.3 with those of linear  $H_4$  on the right side of Figure 5.9. In both cases, the number of nodes increases by one on going from a molecular orbital to the next one of higher energy. The absolute magnitude of the AO coefficients alternates in going from one MO to the next. The lowest molecular orbital is concentrated more in the middle; the next higher one is more heavily weighted on the two ends, and so on. There are other features in common, which we shall return to in Section 12.1.

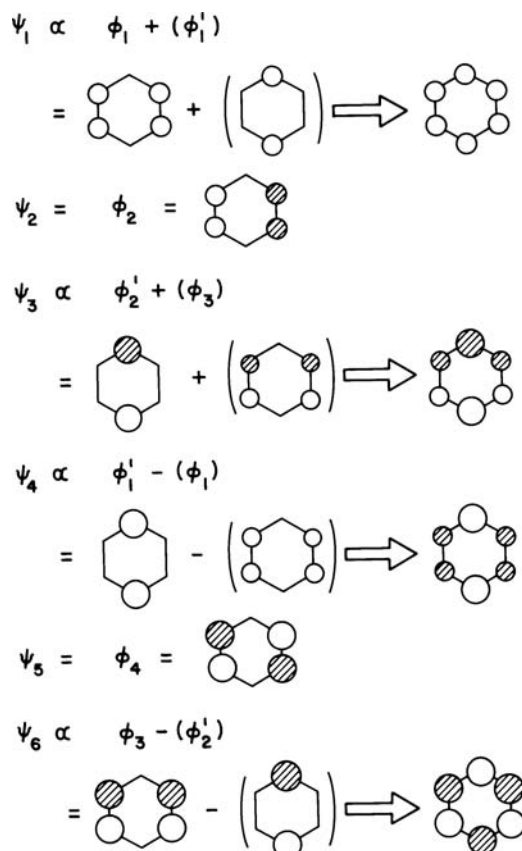
## 5.6 PENTAGONAL $H_5$ AND HEXAGONAL $H_6$

The level structure of hexagonal ( $D_{6h}$ )  $H_6$  may be derived as in Figure 5.10 from the orbitals of a pair of  $H_2$  units arranged in a rectangle and an  $H_2$  unit with a large H—H distance. The fragment orbitals for the pair of  $H_2$  units are simply those from the left side of Figure 5.5. There is only a weak interaction here since the H—H distance between each  $H_2$  unit is long. Thus,  $\phi_1$  and  $\phi_2$  are close in energy to  $H_2\sigma$ , and  $\phi_3$  and  $\phi_4$  to  $H_2\sigma^*$ . The energies of the two orbitals for the other fragment are positioned at that of the hydrogen s atomic orbital, again because of the very long H—H distance. The reason that this partitioning scheme has been chosen is not at all intuitive at first glance. Its virtue lies in the simple way that the fragment orbitals overlap and consequently interact with each other. From the inspection of the phases in Figure 5.10,  $\langle \phi_1 | \phi_1' \rangle$  and  $\langle \phi_3 | \phi_2' \rangle$  are positive and all other overlap integrals are zero. Another way to see this is by assigning the fragment orbitals irreducible

**FIGURE 5.10**

Assembly of the orbital diagram for hexagonal H<sub>6</sub> ( $D_{6h}$ ) from those of two H<sub>2</sub> units and a pair of H atoms.

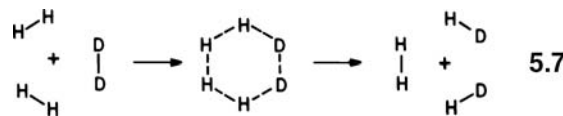
representations within  $D_{2h}$  symmetry that is common with respect to both fragments. Then, there is a two-orbital mixing pattern yielding  $\psi_1$  and  $\psi_4$ , and another yielding  $\psi_3$  and  $\psi_6$ . The other two fragment orbitals are rigorously nonbonding. Notice that the resultant molecular orbitals are positioned in energy by group theoretical considerations with the exception of  $\psi_1$  and  $\psi_6$ .  $\psi_2$  and  $\psi_3$  are a degenerate  $e_{1u}$  set that must be at the same energy as  $\phi_2$ , while  $\psi_4$  and  $\psi_5$  are an  $e_{2g}$  set at the same energy as  $\phi_4$ . The resulting first-order mixing of the orbitals is shown in Figure 5.11. The shape of

**FIGURE 5.11**

Generation of the orbital description of the levels of hexagonal H<sub>6</sub> from those of two H<sub>2</sub> units and a pair of H atoms.

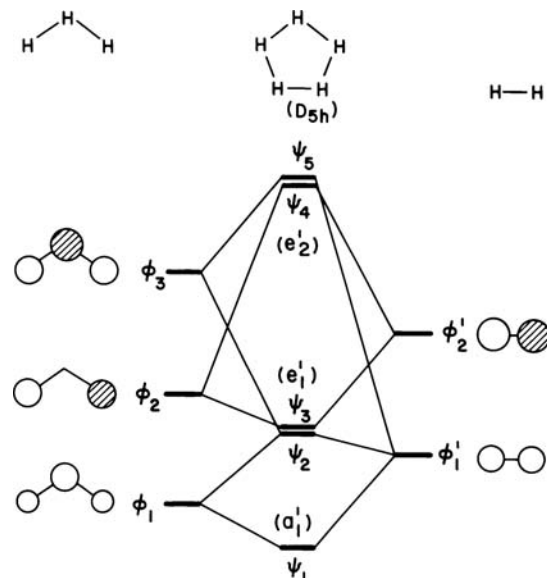
each resultant molecular orbital is easy to derive, although the fact that all atomic coefficients in  $\psi_1$  and  $\psi_6$  are equal is best appreciated by using group theory.

This is not the only way this diagram can be constructed. Other obvious routes are from six s orbitals using group theoretical techniques, from two bent H<sub>3</sub> fragments or from three H<sub>2</sub> fragments. This interesting last approach brings us back to the H<sub>2</sub>/D<sub>2</sub> exchange. 5.7 shows how two HD units may be produced from



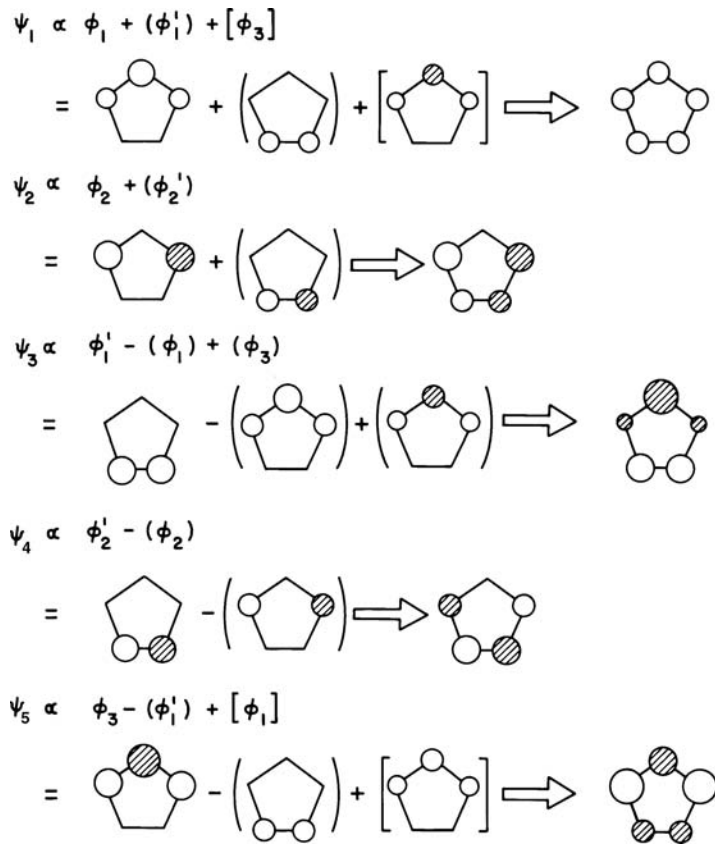
2H<sub>2</sub> + D<sub>2</sub> in a termolecular process. The transition state in the middle of the diagram will be described by the molecular orbitals of Figure 5.10. With a total of six electrons,  $\psi_{1-3}$  are doubly occupied. The degenerate pair  $\psi_{2,3}$  should lie only slightly above the bonding level in H<sub>2</sub> itself, since one would expect that the H—H distances in D<sub>6h</sub> H<sub>6</sub>, where there are six electrons delocalized over six bonds, will be somewhat longer than in H<sub>2</sub> where there is two-center–two-electron bonding. Consequently, a termolecular collision with this geometry is expected to be much more feasible than a bimolecular pathway (see Section 5.3) as indeed suggested by essentially exact calculations. D<sub>6h</sub> H<sub>6</sub> is a transition state that lies 67 kcal/mol above the energy of three H<sub>2</sub> molecules [7]. The H—H bond distances in it are 0.24 Å longer than those in H<sub>2</sub> [1].

The molecular orbitals of pentagonal ( $D_{5h}$ ) H<sub>5</sub> may be constructed in terms of the orbitals of a bent H<sub>3</sub> fragment and those of H<sub>2</sub> as shown in Figure 5.12. Both fragments share a common mirror plane that passes throughout the middle H atom in the H<sub>3</sub> fragment and bisects the H—H bond in H<sub>2</sub>. Therefore,  $\phi_1$ ,  $\phi_3$ , and  $\phi_1'$  are all symmetric with respect to this mirror plane, whereas  $\phi_2$  and  $\phi_2'$  are antisymmetric. With the phases assigned to each fragment orbital in Figure 5.12,  $\langle\phi_1'|\phi_1\rangle$ ,  $\langle\phi_1'|\phi_3\rangle$ , and  $\langle\phi_2'|\phi_2\rangle$  are positive and all other overlap integrals are zero. The relative energy placement of the fragment orbitals follows what has been covered before for building up the orbitals of H<sub>3</sub> itself (see Section 3.4, for example).  $\phi_1$  should lie between  $\phi_1$  and  $\phi_2$  while  $\phi_2'$  should be placed between  $\phi_2$  and  $\phi_3$  in terms



**FIGURE 5.12**

Assembly of the orbital diagram for pentagonal H<sub>5</sub> ( $D_{5h}$ ) from those of bent H<sub>3</sub> and H<sub>2</sub>.

**FIGURE 5.13**

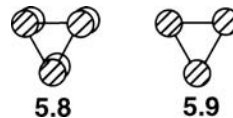
Generation of the orbital description of the levels of pentagonal H<sub>5</sub> from those of bent H<sub>3</sub> and H<sub>2</sub> using perturbation theory.

of energy. The resultant molecular orbitals follow a simple two orbital and a three-orbital pattern.  $\phi_2$  is stabilized by the higher lying  $\phi'_2$  to produce  $\psi_3$  and  $\phi'_2$  is destabilized by  $\phi_2$  to give  $\psi_4$ . For the three-orbital pattern,  $\phi_1$  is stabilized by  $\phi'_1$  and  $\phi_3$  is destabilized by  $\phi'_1$  to give the molecular orbitals  $\psi_1$  and  $\psi_5$ , respectively.  $\phi'_1$  is caught in the middle; it is destabilized by  $\phi_1$  and stabilized by  $\phi_3$  to produce  $\psi_2$ . We have shown that  $\psi_2$  is actually destabilized slightly. This is a reflection of the fact that the energy gap between  $\phi'_1$  and  $\phi_1$  is smaller than that between  $\phi'_1$  and  $\phi_3$ . Group theory also plays a role in setting the resultant energies. D<sub>5h</sub> H<sub>5</sub> must have molecular orbitals of  $a'_1 + e'_1 + e'_2$  symmetry. Therefore,  $\psi_2$  and  $\psi_3$  must be degenerate, as must  $\psi_4$  and  $\psi_5$ . Using the results of Table 3.1 for the second-order mixing of  $\phi_1$  and  $\phi_3$ , the orbital derivations of Figure 5.13 naturally follow. Recall the convention here that first-order mixings are placed in parenthesis while those for second order are in brackets and the weights of the perturbation expansion follow the order: zeroth > first > second order. In  $\psi_1$ , the fragment orbitals mix in a bonding fashion, and those in  $\psi_4$  and  $\psi_5$  in an antibonding fashion. The middle component of the three-orbital pair,  $\psi_3$ , is nonbonding. One might think from the expression for  $\psi_2$  in Figure 5.13 that it is a bonding orbital. This is not quite correct, in that  $\phi_2$  itself is nonbonding and, while  $\phi'_2$  mixes with it in a bonding fashion,  $\phi'_2$  is an antibonding orbital. Therefore,  $\psi_2$  along with its degenerate partner,  $\psi_3$ , is perhaps better described as being nonbonding.

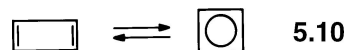
## 5.7 ORBITALS OF CYCLIC SYSTEMS

All of the examples used so far in this chapter have employed orbitals constructed from a single s orbital on each center. However, our arguments can be carried over

without change directly to the case of  $\pi$  orbitals in cyclic, planar systems. For example, the three  $p\pi$  orbitals of cyclopropenyl (**5.8**) may be represented as in **5.9**

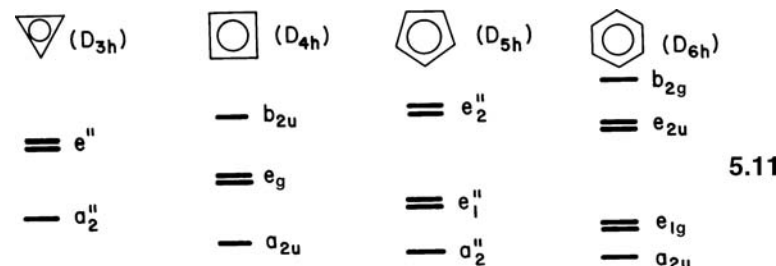


that shows the view of the upper lobes of the  $p$  orbitals projected onto the molecular plane. Thus, the level structure shown in Figure 5.1 for triangular  $H_3$  is identical to that for the  $\pi$  orbitals of cyclopropenyl, where the orbitals are shown in perspective in **5.8**. Correspondingly, the conversion of rectangular cyclobutadiene to the square (**5.10**) follows exactly the same analysis as detailed for the



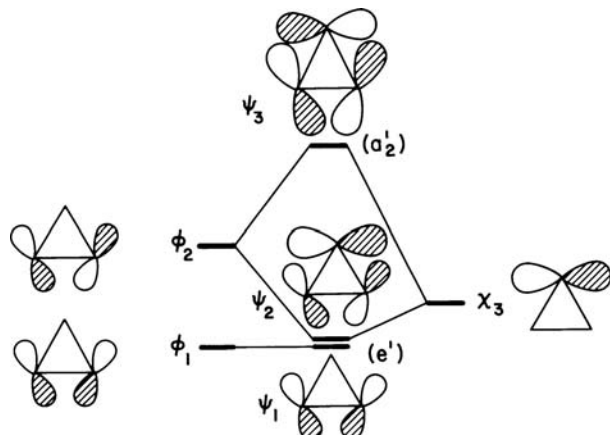
$H_4$  problem in Section 5.3 of this chapter. With a total of four  $\pi$  electrons in  $C_4H_4$ , the reader can readily see from Figure 5.5 that if they are arranged in the low spin configuration (all spins paired), then the square geometry is less stable than the rectangular one.

The orbital structure of cyclic  $H_n$  systems or their polyene counterparts form a very interesting series. We will investigate their level structure in more detail in Chapter 12, but note the emergence of a pattern in **5.11** (for polyene  $\pi$  orbitals)



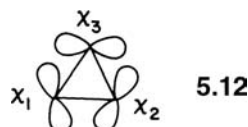
concerning the energy levels as the cycle becomes larger. The lowest energy orbital is always nondegenerate and combines the atomic orbitals in phase with equal coefficients. Then, the orbitals appear in degenerate pairs. In an odd-membered ring, therefore the highest energy orbital belongs to a degenerate set. In an even-membered ring, the highest energy orbital is nondegenerate and the atomic orbitals are equal in size but alternate in sign. Finally, the number of nodal planes increases by one on going to the next higher orbital set, that is, the lowest orbital contains no nodes, the next highest degenerate set contains one nodal plane, etc.

One striking difference between the  $p\pi$  orbitals of the cyclic polyene and those of the  $H_n$  molecules is that the symmetry labels are different. For example, the  $\pi$  levels of cyclopropenyl transform as  $a_2'' + e''$  (double primes since they are antisymmetric with respect to the reflection in the plane perpendicular to the threefold rotation axis), but the s orbitals of  $H_3$  transform as  $a'_1 + e'$  (single primes since these orbitals are symmetric with respect to this symmetry operation). The breakdown into nondegenerate and degenerate orbitals (one of each) as well as the bonding patterns is the same in both cases.

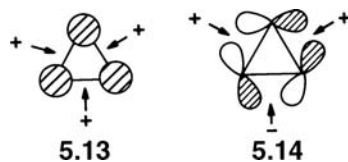
**FIGURE 5.14**

Assembly of the orbital diagram for the tangential in-plane  $p$  orbitals of cyclopropenium ( $D_{3h}$ ) from those of a diatomic unit and a single atom.

The in-plane  $p$  orbitals of cyclic organic systems may be derived in a similar way to their out-of-plane counterparts. For an equilateral triangle, the three in-plane tangential  $p$  orbitals **5.12** transform as  $a'_2 + e'$ . Figure 5.14 shows how the in-plane



orbital picture may be assembled along very similar lines to the  $H_3$  problem of Figure 5.1. Note that for the in-plane  $p$  orbital case, the level picture is a two-below-one pattern, but for the out-of-plane  $p$  (or  $H_3$ ) orbital case, a one-below-two situation occurs. This arises simply because of the nodal properties of  $\chi_3$ . It interacts with the higher energy orbital,  $\phi_2$  in Figure 5.14, but with the lower energy orbital in Figure 5.1. Another way of describing the same result is to classify these cyclic orbital problems as either of the Hückel or Möbius type [8]. Hückel systems either have a zero or even number of antibonding interactions between adjacent orbitals as in **5.13**. Möbius systems have an odd number of such interactions as in **5.14**. The general result is that the energy level pattern resulting

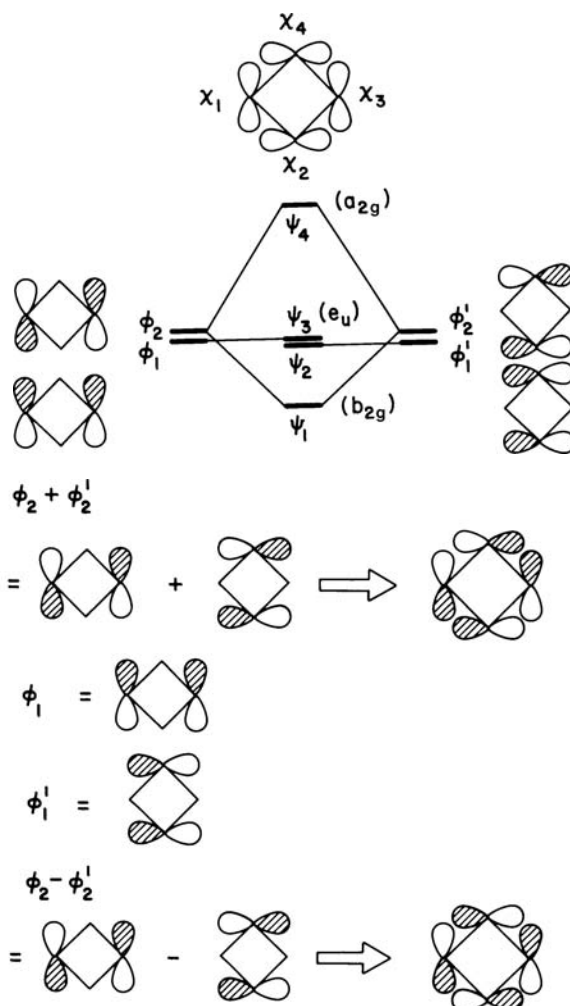


from the in-plane tangential orbitals of odd-membered rings is the reverse of the pattern for the out-of-plane  $p_\pi$  orbitals shown in **5.11**. (For even-membered rings, the level patterns for in- and out-of-plane orbitals are the same.)

Finally, consider the four in-plane orbitals of a square plane. The orbital picture is readily assembled as in Figure 5.15 where all overlap integrals between the  $\phi_i$  and  $\phi'_i$  are zero except  $\langle \phi_2 | \phi'_2 \rangle$  which is positive. The molecular orbitals are simply constructed using a degenerate interaction as in **5.15**. One maximally bonding orbital ( $\psi_1$ ) and one maximally antibonding ( $\psi_4$ ) orbital are produced.  $\psi_2$  and  $\psi_3$  are

**FIGURE 5.15**

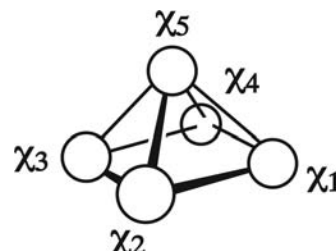
Assembly of the orbital diagram for the tangential in-plane orbitals of cyclobutadiene ( $D_{4h}$ ) from those of two diatomic units.



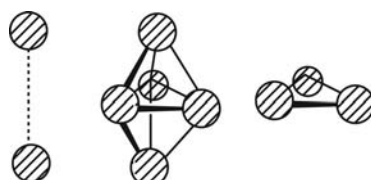
nonbonding. The phase relationships are identical to those of square  $H_4$  on the left side of Figure 5.7. Notice, however, how the phases on the orbitals  $\chi_1-\chi_4$  at the top of Figure 5.15 are chosen; there is either zero or an even number of changes in sign of the overlap integrals on moving round the ring. These in-plane orbitals thus form a Hückel rather than Möbius pattern, and the qualitative picture is the same as for the  $p_\pi$  levels of 5.11.

## PROBLEMS

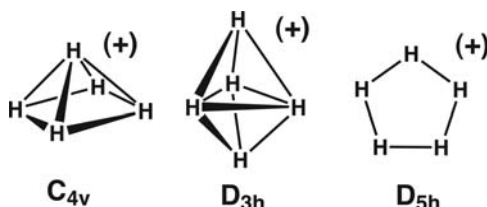
- 5.1. a.** Consider a molecule made up of five hydrogen atoms, as shown below. Consider that the H—H bond lengths are all the same. Form symmetry-adapted linear combinations of these and combine any two members of the basis if this is necessary. No need to normalize the resultant wavefunctions.



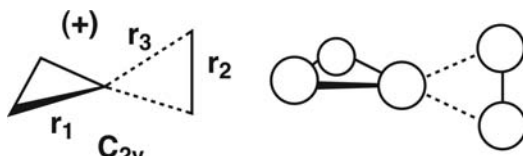
- b. Draw out the MOs and order them in energy according to the number of bonding/antibonding interactions present in them. What electron counts could possibly lead to a stable structure?
- 5.2.** Draw an orbital interaction diagram for another  $H_5$  geometry by interacting a  $D_{3h}$   $H_3$  fragment with an H—H unit. Again what electron counts are expected to be stable?



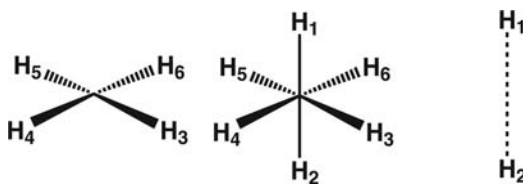
- 5.3.** Another simple geometrical alternative for  $H_5$  is the pentagonal  $D_{5h}$  structure. The orbitals for this geometry are constructed in Figures 5.12 and 5.13 in the text. Given the three structures below, determine which will be the most stable for  $H_5^{3+}$ ,  $H_5^+$ , and  $H_5^-$ .



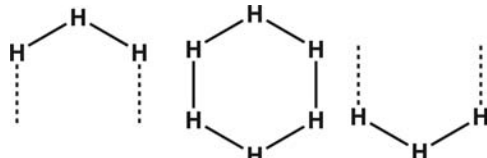
- 5.4.**  $H_5^+$  exists but not with any of the structures shown above. It is, in fact, a complex between  $H_3^+$  (recall that this is a very well-known molecule in its own right) and  $H_2$ . The basic structure is shown below where  $r_1 \approx r_2 < r_3$ . Interact the orbitals of cyclic  $H_3$  with those in  $H_2$ .



- 5.5.** Build up the MOs of octahedral  $H_6$  by interacting  $H_4$  with H—H. Interact these MOs with the s and p AOs of a main group atom, A, which is positioned at the center of the octahedron. Which electron counts are expected to be stable?

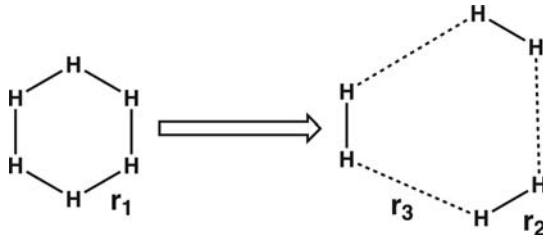


- 5.6.** Develop the orbitals of  $D_{6h}$   $H_6$  using two  $H_3$  fragments. Draw out the resulting MOs.

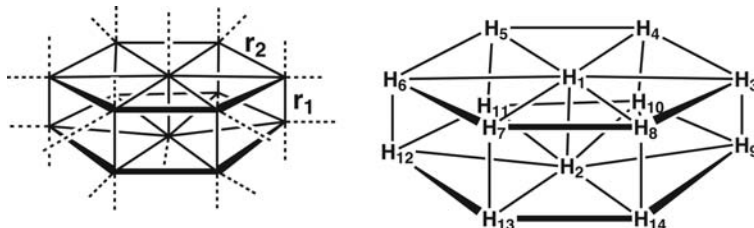


- 5.7.** In this question, we are going to study the breakup of  $H_6$  from the  $D_{6h}$  geometry to three separate  $H_2$  units in  $D_{3h}$  symmetry. Draw the orbitals from question 5.6 on the left side of the paper. Take symmetry-adapted combinations of  $H_2 \sigma$  and  $\sigma^*$  and carefully position the orbitals for the structure on the right side taking into account that the distance between the  $H_2$  molecules is large and draw an orbital correlation diagram for this

situation. Let  $r_2 < r_1 \ll r_3$ . Which structure is more stable? Offer an explanation for this behavior.



- 5.8.** For over 60 years, people have thought that molecular  $\text{H}_2$  at very high pressure might become metallic. Over 30 years ago, it was suggested that  $\text{H}_2$  at higher pressures might become a superconductor. Experiments in more recent times have shown that  $\text{H}_2$  does indeed become a conductor at  $\sim 250$  GPa. Also very sophisticated calculations have shown that at  $\sim 400$  GPa, it becomes a superconductor at  $230^\circ\text{K}$ . Astrophysicists have speculated that the cores of Jupiter and Saturn are primarily solid  $\text{H}_2$  and pressures of 400 GPa are possible. Thus, these two planets may have superconducting cores! This might offer an explanation of why the magnetic fields for the two planets are anomalous. A small unit of the proposed structure for this material is shown below. On the left side, the dotted lines show how the hydrogen atoms are translated. The numbering system for this  $\text{H}_{14}$  unit is shown on the right side. Here  $\text{H}_1-\text{H}_2 = \text{H}_3-\text{H}_9 = \text{H}_4-\text{H}_{10}$ , etc. =  $0.83\text{ \AA}$ . The  $\text{H}_3-\text{H}_4 = \text{H}_4-\text{H}_5 = \text{H}_5-\text{H}_6$ , etc. =  $1.38\text{ \AA}$ . For reference, the  $\text{H}-\text{H}$  distance in gaseous  $\text{H}_2$  is  $0.74\text{ \AA}$ .



- Determine the shapes of the MOs for an  $\text{H}_{12}$  fragment, that is,  $\text{H}_3-\text{H}_{14}$ . Specify the irreducible representation for each MO and order the energies with respect to an isolated  $\text{H}_2$  molecule where  $\sigma$  is at  $-17.4\text{ eV}$ ,  $\sigma^*$  is at  $4.2\text{ eV}$ , and the energy of the H atom =  $-13.6\text{ eV}$ .
- Carefully, draw an interaction diagram for interacting the orbitals of the  $\text{H}_{12}$  unit with the  $\text{H}_1-\text{H}_2$  fragment.
- In the “real” structure, the local environment for  $\text{H}_1-\text{H}_2$  becomes equivalent to  $\text{H}_3-\text{H}_9$ ,  $\text{H}_4-\text{H}_{10}$ , etc. Show what happens to the HOMO and LUMO in your answer for (b) when additional  $\text{H}_2$  pieces are added to the structure.

## REFERENCES

- J. S. Wright and G. A. DiLabio, *J. Phys. Chem.* **96**, 10793 (1992).
- A. Macias, *J. Chem. Phys.* **48**, 3464 (1968) A. Macias, *J. Chem. Phys.* **49**, 2198 (1969) F. Kiel and R. Ahlrichs, *J. Am. Chem. Soc.*, **98**, 4787 (1976).
- J. S. Wright, *Can. J. Chem.*, **53**, 549 (1975).
- W. Gerhartz, R. D. Poshusta, and J. Michl, *J. Am. Chem. Soc.*, **98**, 6427 (1976) W. Gerhartz, R. D. Poshusta, and J. Michl, *J. Am. Chem. Soc.*, **99**, 4263 (1977).
- M. N. Glukhovtsev, P. v. R. Schleyer, and K. Lammertsma, *Chem. Phys. Lett.*, **209**, 207 (1993).
- E. Zeller, H. Beruda, and H. Schmidbaur, *Inorg. Chem.*, **32**, 3203 (1993) For a theoretical analysis see J. K. Burdett, O. Eisenstein, and W. B. Schweizer, *Inorg. Chem.*, **33**, 3261 (1994).
- P. R. Taylor, A. Komornicki, and D. A. Dixon, *J. Am. Chem. Soc.*, **111**, 1259 (1989).
- K. Yates, *Hückel Molecular Orbital Theory*, Academic Press, New York (1978).

# Molecular Orbitals of Diatom Molecules and Electronegativity Perturbation

## 6.1 INTRODUCTION

In the previous chapter, we showed how the energy levels of a molecule could be derived by assembling a molecular orbital diagram from those of smaller fragments using perturbation theory. It was seen how the orbitals of a molecule, initially orthogonal, can mix together in the presence of another molecule via a second-order mixing process. There are other ways these orbitals may mix together without the presence of another fragment. One way is through an intramolecular perturbation that involves a change in the effective potential of an atomic orbital, which will be called an electronegativity perturbation (3.1). Another is via a geometry change, as typified by the example in 3.2, which is described in more detail in Chapter 7.

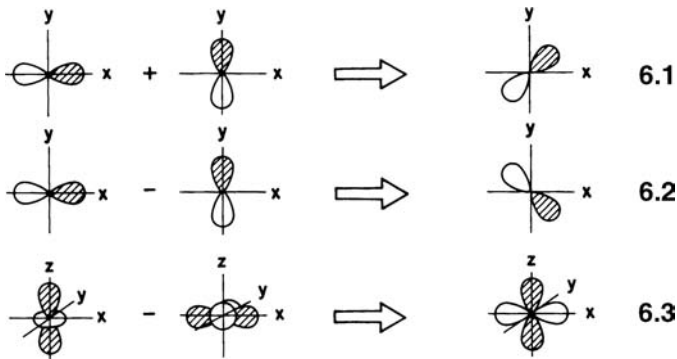
To examine the workings of electronegativity perturbation, we need to examine the orbitals of a molecule where the atoms are not all identical and where each atom carries more than one atomic orbital. An important feature which results is that of orbital hybridization, namely, the mixing of different atomic orbitals on the same center. In this chapter, we examine the nature of such hybridization, construct the molecular orbitals of diatomic molecules from different viewpoints, and describe the essence of electronegativity perturbations.

## 6.2 ORBITAL HYBRIDIZATION

When combined at a given atomic center, any two atomic orbitals add in a vectorial manner. For example, consider the orbital  $\phi$  defined by  $p_x$  and  $p_y$  atomic orbitals as

$$\phi \propto c_1 p_x + c_2 p_y \quad (6.1)$$

The orbital addition is shown in **6.1** and **6.2** for the two cases  $c_1 = c_2 > 0$  and  $c_1 = -c_2 > 0$ , respectively. The ratio  $c_1/c_2$  controls how much the orbital  $\phi$  is tilted



away from the  $x$  (or  $y$ ) axis. The linear combination between  $z^2$  and  $x^2 - y^2$  orbitals of **6.3** leads to a  $z^2 - x^2$  orbital, as readily appreciated from Table I.1, since

$$d_{z^2} - d_{x^2-y^2} \propto \left( \frac{3z^2 - r^2}{r^2} - \frac{x^2 - y^2}{r^2} \right) \exp(-\zeta r) \quad (6.2)$$

Because  $r^2 = x^2 + y^2 + z^2$ , this is proportional to

$$\left( \frac{z^2 - x^2}{r^2} \right) \exp(-\zeta r) \propto d_{z^2-x^2} \quad (6.3)$$

The mixing of atomic orbitals with different angular momentum quantum number is also controlled by a vectorial addition and leads to various types of hybrid orbitals shown in Figure 6.1. The variation of the overlap or interaction integrals of these functions with other orbitals as a function of geometry are given simply by a weighted sum of the contributions from each component. So if

$$\phi_{\text{hybrid}} = c_1 \chi_1 + c_2 \chi_2 \quad (6.4)$$

then

$$\langle \phi_{\text{hybrid}} | \chi_3 \rangle = c_1 \langle \chi_1 | \chi_3 \rangle + c_2 \langle \chi_2 | \chi_3 \rangle \quad (6.5)$$

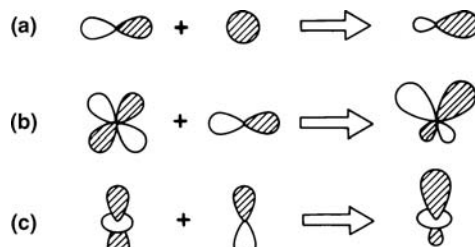
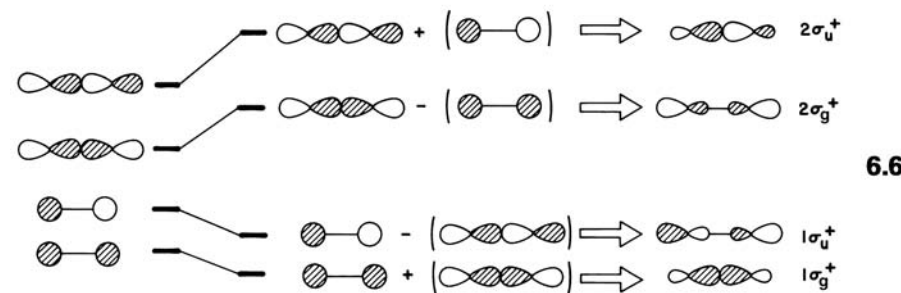


**FIGURE 6.1**

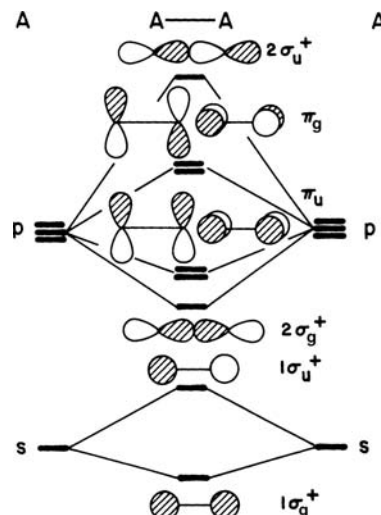
Hybridization of atom orbitals (a)  $s$  and  $p$ , (b)  $d_{xz}$  and  $p_z$ , (c)  $d_{z^2}$  and  $p_z$ .

### 6.3 MOLECULAR ORBITALS OF DIATOMIC MOLECULES

Let us examine the valence molecular orbitals of a homonuclear diatomic,  $A_2$  unit. The discussion here should be worked with care, for many of the elements presented will be found in other, more complex molecules. Each atom contributes four valence atomic orbitals ( $s, p_x, p_y, p_z$ ), and we identify the internuclear axis with the  $z$  direction. The basis orbitals naturally separate into those of  $\sigma$  ( $s, p_z$ ) and  $\pi$  ( $p_x, p_y$ ) type. The  $\pi$ -type orbitals enter into a degenerate interaction and lead to  $\pi$  bonding and antibonding orbitals shown in Figure 6.2. Alternatively, the  $p_x$  and  $p_y$  orbitals on the two centers transform as  $\pi_u + \pi_g$ . Use of equation 4.37 leads to an in-phase combination of  $p_x$  and  $p_y$  on the two atoms for  $\pi_u$  and hence a bonding pair of molecular orbitals and an out-of-phase combination for  $\pi_g$  leading to an antibonding pair. Similarly, the two  $s$  orbitals transform as  $\sigma_g^+ + \sigma_u^+$  and the orbitals, correct to first order in the energy, are shown in Figure 6.2. The two  $p_z$  orbitals also transform as  $\sigma_g^+ + 1\sigma_u^+$  and the result of their degenerate interaction is also shown. The result is three separate first-order energetic interactions. However, the  $\sigma$  orbitals generated by overlap of  $s+s$  and  $p_z+p_z$  functions are of the same symmetry, and just as in the case of the linear  $H_4$  molecule of Section 5.5, they can interact with each other via a second-order energy process. Using equation 3.19 (this is now a nondegenerate interaction),  $1\sigma_g^+$  and  $1\sigma_u^+$  are stabilized by the higher lying  $2\sigma_g^+$  and  $2\sigma_u^+$  molecular orbitals, respectively. Likewise,  $2\sigma_g^+$  and  $2\sigma_u^+$  become destabilized. To evaluate the non-degenerate first-order mixing using equation 3.13, care should be exercised in determining the sign of  $\tilde{S}_{ij}$ . Specifically, we need to determine  $\langle 1\sigma_g^+ | 2\sigma_g^+ \rangle$  and  $\langle 1\sigma_u^+ | 2\sigma_u^+ \rangle$ . This is shown schematically in 6.4 and 6.5 using the phases from Figure 6.2.



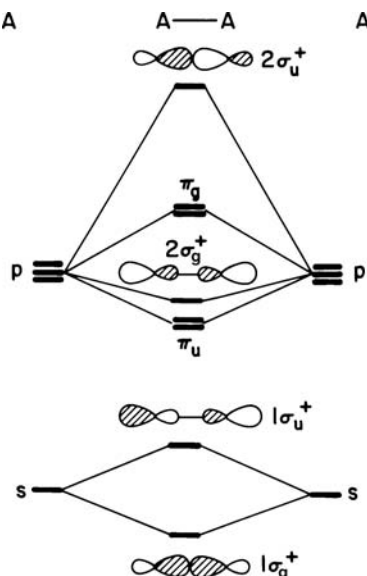
The overlap between atomic orbitals on the same center is zero; our atomic orbitals are orthonormal. It is the  $s-p$  overlap on nonadjacent centers that leads to nonzero values of  $\tilde{S}_{ij}$ . Notice that  $\langle 1\sigma_g^+ | 2\sigma_g^+ \rangle = (+)$ , but  $\langle 1\sigma_u^+ | 2\sigma_u^+ \rangle = (-)$ . Therefore, in equation 3.13, the numerator is negative for the first-order mixing between  $1\sigma_g^+$  and  $2\sigma_g^+$ , and positive for that between  $1\sigma_u^+$  and  $2\sigma_u^+$ . The  $t_{ji}^{(1)}$  mixing coefficients are then readily determined by the energy differences and are given in 6.6 along with the ultimate form of the wavefunctions. The nondegenerate  $e^{(2)}$  corrections for both  $1\sigma_g^+$  and  $1\sigma_u^+$  are negative (stabilizing) as indicated previously. However,  $t_{2\sigma_g^+, 1\sigma_g^+}^{(1)}$  is positive, whereas that for  $t_{2\sigma_u^+, 1\sigma_u^+}^{(1)}$  is negative because of the change in sign for the overlap term in the numerator of equation 3.13. The ultimate result of these nondegenerate intermixings between the  $s$  and the  $p_z$  atomic orbitals is shown in the orbital interaction diagram of Figure 6.3.

**FIGURE 6.2**

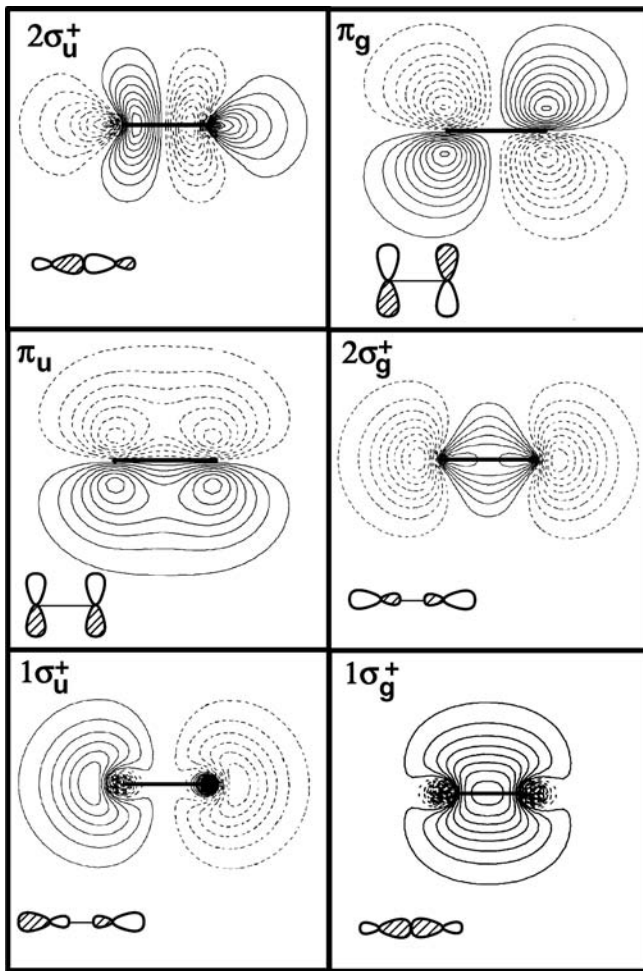
Orbitals of an  $A_2$  diatomic correct to the first order in energy.

Contour plots for the molecular orbitals of  $N_2$  are shown in Figure 6.4. Only one component in each of the  $\pi_u$  and  $\pi_g$  sets is shown. The solid and dashed contours represent positive and negative amplitudes, respectively, of the wavefunction where each contour is one half of the value of the next one proceeding from the nuclei. These results are obtained from Hartree–Fock ab initio calculations using an Slater type orbital (STO)-3G basis set (see Section 1.2). This is certainly not a particularly accurate level of calculation, but the general form of the wavefunctions will not be substantially altered upon going to a more sophisticated technique with a larger basis set. Below each wavefunction is the stylized graphical representation for it that is used throughout the text. The hybridization inherent in the  $1\sigma_g^+$  through  $2\sigma_u^+$  set of  $\sigma$ -type orbitals is quite apparent. There is a kind of three-orbital pattern that evolves in the  $\sigma$  set.  $1\sigma_g^+$  and  $2\sigma_u^+$  are the maximal bonding and antibonding orbitals, respectively. The  $1\sigma_u^+$  and  $2\sigma_g^+$  molecular orbitals tend to be nonbonding.

Just how much antibonding character there is in  $1\sigma_g^+$  or bonding in  $2\sigma_g^+$  depends on the amount of  $s-p$  mixing. Likewise, whether the  $2\sigma_g^+$  level lies below or above the

**FIGURE 6.3**

Orbitals of an  $A_2$  diatomic after the second-order energetic changes (6.6) have been included. Whether  $2\sigma_g^+$  or  $1\sigma_u$  lies lower in energy is system dependent.

**FIGURE 6.4**

Contour plots of the molecular orbitals of  $\text{N}_2$  along with their stylized representations. The positive values of the wavefunction are given by the solid lines and negative values by dashed lines. Each contour is one half of the value of the next one proceeding from the nuclei, outwards. Only one component of  $\pi_u$  and  $\pi_g$  are illustrated

$1\pi_u$  level (compare Figures 6.2 and 6.3) depends on the magnitude of this mixing and this is not a simple matter to predict. Table 6.1 lists the electronic configurations for the first- and second-row homonuclear diatomics along with the electronic state and bond length [1,2]. It turns out that  $2\sigma_g^+$  lies higher for the first-row diatomics up to and including  $\text{N}_2$ . From  $\text{O}_2$  onward,  $2\sigma_g^+$  lies lower. The situation for the second-row diatomics puts the  $2\sigma_g^+$  level always below the  $\pi_u$  set. The exact position, using an admittedly simplistic perturbation theory argument, will depend on the  $e^{(2)}$  correction associated with  $2\sigma_g^+$ , namely,

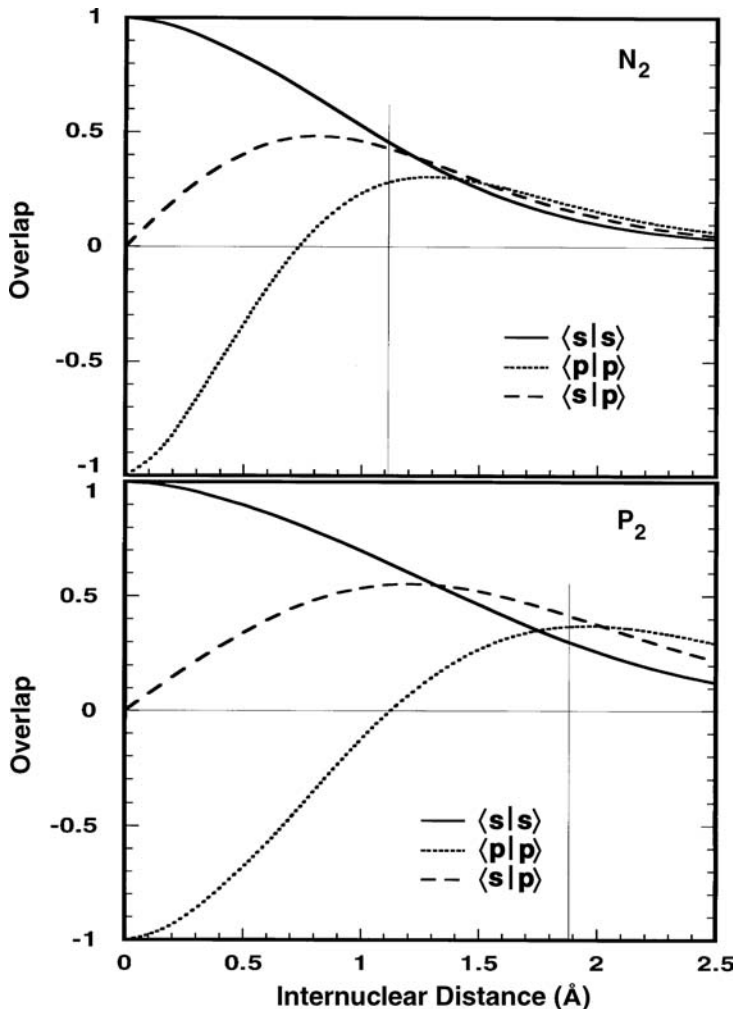
$$e_{2\sigma_g^+}^{(2)} \propto \frac{\tilde{S}_{1\sigma_g^+, 2\sigma_g^+}^2}{e_{2\sigma_g^+}^0 - e_{1\sigma_g^+}^0} \quad (6.6)$$

It was discussed in Section 2.3 that the atomic  $s-p$  energy gap increases on going from left to right in the periodic table. Consequently, equation 6.6 becomes smaller along this series for the first-row diatomics. Therefore, the amount of  $s-p$  mixing decreases from left to right along the periodic table and  $2\sigma_g^+$  falls below  $\pi_u$  for  $\text{O}_2$  and  $\text{F}_2$ . But the situation for the second (and third, etc.) row relies on a detailed inspection of the numerator of equation 6.6 since, as discussed in Section 2.3, the general trend is that the  $s-p$  energy gap becomes smaller upon descending a column

**TABLE 6.1** Summary of the First- and Second-Row Homonuclear Diatomics

Molecule	Electronic Configuration	State	$r_e$ (Å)	BO
$\text{Li}_2$	$(1\sigma_g^+)^2$	${}^1\Sigma_g^+$	2.67	1
$\text{Be}_2$	$(1\sigma_g^+)^2(1\sigma_u^+)^2$	${}^1\Sigma_g^+$	2.45	0
$\text{B}_2$	$(1\sigma_g^+)^2(1\sigma_u^+)^2(\pi_u)^2$	${}^3\Sigma_g^-$	1.59	1
$\text{C}_2$	$(1\sigma_g^+)^2(1\sigma_u^+)^2(\pi_u)^4$	${}^1\Sigma_g^+$	1.24	2
$\text{N}_2$	$(1\sigma_g^+)^2(1\sigma_u^+)^2(\pi_u)^4(2\sigma_g^+)^2$	${}^1\Sigma_g^+$	1.11	3
$\text{O}_2$	$\cdots(2\sigma_g^+)^2(\pi_u)^4(\pi_g)^2$	${}^3\Sigma_g^-$	1.21	2
$\text{F}_2$	$\cdots(2\sigma_g^+)^2(\pi_u)^4(\pi_g)^4$	${}^1\Sigma_g^+$	1.42	1
$\text{Ne}_2$	$\cdots(2\sigma_g^+)^2(\pi_u)^4(\pi_g)^4(2\sigma_u^+)^2$	${}^1\Sigma_g^+$	3.1	0
$\text{Na}_2$	$(1\sigma_g^+)^2$	${}^1\Sigma_g^+$	3.08	1
$\text{Mg}_2$	$(1\sigma_g^+)^2(1\sigma_u^+)^2$	${}^1\Sigma_g^+$	3.89	0
$\text{Al}_2$	$(1\sigma_g^+)^2(1\sigma_u^+)^2(2\sigma_g^+)^1(\pi_u)^1$	${}^3\Pi_u$	2.72	1
$\text{Si}_2$	$(1\sigma_g^+)^2(1\sigma_u^+)^2(2\sigma_g^+)^2(\pi_u)^2$	${}^3\Sigma_g^-$	2.25	2
$\text{P}_2$	$(1\sigma_g^+)^2(1\sigma_u^+)^2(2\sigma_g^+)^2(\pi_u)^4$	${}^1\Sigma_g^+$	1.89	3
$\text{S}_2$	$\cdots(2\sigma_g^+)^2(\pi_u)^4(\pi_g)^2$	${}^3\Sigma_g^-$	1.89	2
$\text{Cl}_2$	$\cdots(2\sigma_g^+)^2(\pi_u)^4(\pi_g)^4$	${}^1\Sigma_g^+$	1.99	1
$\text{Ar}_2$	$\cdots(2\sigma_g^+)^2(\pi_u)^4(\pi_g)^4(2\sigma_u^+)^2$	${}^1\Sigma_g^+$	3.76	0

in the periodic table. Figure 6.5 shows the results of computing the  $\sigma$ -type overlap integrals as a function of the internuclear distance in  $\text{N}_2$  and  $\text{P}_2$ . These are STO type orbitals with the orbital coefficients given in 1.3. The functional form of  $\langle s|s \rangle$  and  $\langle s|p \rangle$  are those given in 1.11 and 1.12, respectively. The  $\langle p|p \rangle$  curve, shown by the dotted line in Figure 6.5, initially has a value of  $-1$  when the internuclear distance is zero; the phases on each center have been arranged to be opposite hence at a normal internuclear distance, the overlap integral is positive. The thin vertical lines in Figure 6.5 mark the equilibrium distances associated with  $\text{N}_2$  and  $\text{P}_2$ . Notice from Table 6.1 that these distances are the shortest ones for the first and second-row diatomics. The more diffuse  $3s/3p$  atomic orbitals for  $\text{P}_2$  lead to maxima for  $\langle s|p \rangle$  and  $\langle p|p \rangle$  which are at considerably longer distances than those for  $\text{N}_2$ . For the first-row molecules, the values of  $\langle s|s \rangle$  and  $\langle p|p \rangle$  are not too different at reasonable internuclear distances (see Table 6.1). However,  $\langle p|p \rangle$  is larger than  $\langle s|s \rangle$  in the second-row molecules. This is a result of the fact that, as discussed in Section 1.2, the  $s$  and  $p$  orbitals of the first row are close in size. This is not true for the second row where the  $s$  atomic orbital is more contracted and this trend continues to the third, fourth, and fifth rows. Within the context of  $s-p$  mixing, the important, detail associated with Figure 6.5, is that  $\langle s|p \rangle$  is smaller for the second row compared to the first (e.g.,  $\langle s|p \rangle = 0.415$  and  $0.440$  for  $\text{P}_2$  and  $\text{N}_2$ , respectively) because of the contracted  $s$  functions for the second-row elements. Therefore, the numerator, and  $e_{2\sigma_g^+}^{(2)}$ , is smaller for the second-row diatomics. A second factor is that  $\pi$ -type overlap is much smaller than that for the first row, which is discussed shortly. Consequently,  $\pi_u$  is stabilized less for a second-row diatomic.  $2\sigma_g^+$  must energetically lie close to  $\pi_u$  for  $\text{Al}_2$  and  $\text{Si}_2$ . For  $\text{Al}_2$ , very high quality ab initio calculations have shown that the  ${}^3\Sigma_g^-$  state with an electronic configuration  $\cdots(\pi_u)^2$  lies  $130\text{ cm}^{-1}$  ( $0.37\text{ kcal/mol}$ ) higher than the ground  ${}^3\Pi_u$  state with the  $\cdots(2\sigma_g^+)^1(\pi_u)^1$  configuration [2]. Likewise in  $\text{Si}_2$ , the  ${}^3\Sigma_g^-$  state ( $\cdots(2\sigma_g^+)^2(\pi_u)^2$ ) is  $330\text{ cm}^{-1}$  ( $0.94\text{ kcal/mol}$ )

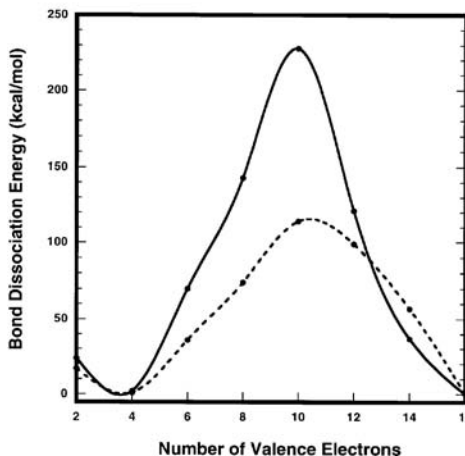
**FIGURE 6.5**

Plots of the  $s-s$ ,  $p-p$ , and  $s-p$  atomic overlap integrals in  $N_2$  and  $P_2$  as a function of the internuclear distance. The thin vertical line in each plot marks the equilibrium distance.

lower in energy than  $^3\Pi_u$  ( $\cdots(2\sigma_g^+)^1(\pi_u)^3$ ). The one electron perturbation theory arguments here can certainly not be used to predict the electronic ground state for cases similar to these; of great importance is electron correlation, which is discussed in Chapter 8. However, this qualitative approach does allow one to see and appreciate more global trends.

The bond order (BO) between two atoms is defined as the number of bonding minus the number of antibonding electrons divided by two. Table 6.1 lists the bond order for the first- and second-row homonuclear diatomics. We might think that the internuclear distance should scale with the bond order; that is, as the bond order increases the internuclear distance should decrease. Inspection of Table 6.1 shows that this is roughly the case. There are a couple of exceptions. The bond lengths for  $P_2$  and  $S_2$  are identical. Part of this is surely due to the very weak  $\pi$  overlap for second-row atoms. The bond distance for  $Be_2$  is shorter than that for  $Li_2$ . Li is very electropositive (see Figure 2.4). Therefore, its  $s$  and  $p$  orbitals are very diffuse and this will lead to a long bond distance. But there is more here with  $Be_2$  and its second-row congener,  $Mg_2$ . The  $(1\sigma_g^+)^2(1\sigma_u^+)^2$  configuration does not lead to a net repulsive situation as would naively be expected from forming the bonding and antibonding combinations of two  $s$  atomic orbitals. The  $s-p$  mixing, discussed earlier, leads to a more net nonbonding composition for  $1\sigma_u^+$ . Therefore, there does exist some

$\text{Li}_2$	$\text{B}_2$	$\text{C}_2$	$\text{N}_2$	$\text{O}_2$	$\text{F}_2$
24	70	143	228	121	37
$\text{Na}_2$	$\text{Al}_2$	$\text{Si}_2$	$\text{P}_2$	$\text{S}_2$	$\text{Cl}_2$
17	36	74	114	101	57
$\text{K}_2$	$\text{Ga}_2$	$\text{Ge}_2$	$\text{As}_2$	$\text{Se}_2$	$\text{Br}_2$
12	32	65	91	77	45
$\text{Rb}_2$	$\text{In}_2$	$\text{Sn}_2$	$\text{Sb}_2$	$\text{Te}_2$	$\text{I}_2$
11	24	48	71	62	36

**FIGURE 6.6**

Bond dissociation energies (kcal/mol) for the homonuclear diatomics from the first through fourth rows of the periodic table (a) and a plot of these for the first and second rows given by the solid and dashed lines, respectively (b).

residual net bonding in  $\text{Be}_2$  and  $\text{Mg}_2$  (with bond dissociation energies of 2 and 1 kcal/mol, respectively). Notice that the bond strength of  $\text{Be}_2$  is larger than that of  $\text{Mg}_2$  and its bond distance (see Table 6.1) appears to be much shorter than would be expected. This is consistent with larger  $s-p$  mixing for the first compared to the second-row elements. The same  $s-p$  hybridization situation applies to the diatomics made up from  $d^{10}s^2$  atoms:  $\text{Zn}_2$ ,  $\text{Cd}_2$ , and  $\text{Hg}_2$ . This underscores the weakness inherent in the concept of a bond order; the molecular orbitals are not all of equal strength in terms of their bonding or antibonding character. An equivalent way to view  $\text{Be}_2$  and  $\text{Mg}_2$  is to say that there is a strongly avoided crossing between the electronic state built up from the double occupation of two  $s$  atomic orbitals and the electronic state constructed from the bonding combination of the two  $s$  orbitals and the two  $p$  orbitals (both have  ${}^1\Sigma_g^+$  symmetry). This is not the situation for  $\text{Ne}_2$  and  $\text{Ar}_2$  where indeed we have only closed shell repulsions. These dimers are held together by van der Waals forces, which are brought about by the instantaneous correlation of electrons on each atom. The bond energies are very tiny (calories/mol) and the equilibrium distances, as indicated in Table 6.1, are very long.

A plot of the bond dissociation energy for the first- and second-row homonuclear diatomics is given at the bottom of Figure 6.6. The box at the top lists the actual numbers for the first through fourth rows of the periodic table. The idea that the bond strength should vary as a function of the bond order holds up very well indeed. For each row, the maximal bond dissociation energy occurs for 10 valence electrons ( $\text{N}_2$ ,  $\text{P}_2$ ,  $\text{As}_2$ , and  $\text{Sb}_2$ ). The increments in the bond dissociation energy are also reasonably constant. The curves in Figure 6.6 for the first- and second-row series are roughly parabolic from 4 to 16 valence electrons. It is also clear from this data that progressing down a column in the periodic table the bond strengths decrease significantly from the first to second row and then more slowly from the second to fourth rows. This is a reflection of orbital overlap which was discussed in Section 1.2 and is a common trend which appears in many contexts throughout the book. As shown in Figure 6.5, the  $\pi$  overlap between two  $p$  atomic orbitals follows the  $\langle s|s \rangle$  curve except that it dampens more rapidly. For the first row,  $\pi$  overlap is quite strong along with  $\langle s|s \rangle$  and  $\langle s|p \rangle$ . The  $\langle p|p \rangle$  curve in the

region of 1.1–1.5 Å, appropriate for the most first-row compounds with multiple bonds, is somewhat smaller. As a consequence, both  $\sigma$  and  $\pi$  bonding are strong for compounds with the first-row elements. The situation for the second row is different. Here the  $\langle p|p \rangle$  overlap is strong from 1.9 to 2.7 Å. The  $\langle s|s \rangle$  and even more so the  $\pi$  type overlap between two  $p$  orbitals is considerably weakened. Therefore, the important point is that while  $\sigma$  bond strengths do decrease slightly on going from the first to the second row, and so on, the  $\pi$  bond strengths decrease significantly [3,4]. Compounds which have  $\pi$  bonds with a second or greater row element then are quite reactive for the most part [4]. There is one anomaly associated with these trends. Notice from Figure 6.6 that the F<sub>2</sub> bond strength is considerably smaller than that for Cl<sub>2</sub> and it furthermore is peculiarly small. In fact the bond dissociation energy for F—Cl is 61 kcal/mol and F<sub>2</sub> is not bound at the ab initio level calculations even with good basis sets unless electron correlation is included. The reason for this is apparently tied to electron–electron repulsion. At an internuclear distance of 1.42 Å,  $\langle s|s \rangle$  and  $\langle p|p \rangle$  are still quite sizable (see Figure 6.5). With the longer bond length in Cl<sub>2</sub> and the more diffuse atomic orbitals, electron–electron repulsion is diminished.

## 6.4 ELECTRONEGATIVITY PERTURBATION

A useful strategy to get a qualitative idea about the molecular orbitals and associated energies in a molecule is first to do this for the most symmetrical example possible. One can then exploit symmetry to its fullest making the orbital interactions easier to construct. The orbitals of a less symmetrical molecule can subsequently be determined by intramolecular perturbation theory [5]. This can take one of two forms: a change in the geometry, which is covered in Chapter 7, or a change in one (or more) of the atoms which will take the form of an electronegativity perturbation. For simplicity, we will make an approximation in the perturbation which will lead to a simple form for the relevant corrections to the energy and wavefunction. We have just treated homonuclear diatomics, A<sub>2</sub>. Suppose we wanted to examine a heteronuclear variant, AB. An increase in the electronegativity of one of the atoms of the molecule shall be simulated by increasing the magnitude of the Coulomb integral for an orbital (on atom B) by a small amount  $\delta\alpha$ , that is,  $\langle \chi_\alpha | H^{\text{eff}} | \chi_\alpha \rangle = H_{\alpha\alpha} + \delta\alpha$ . Therefore,  $\delta\alpha < 0$  when B is more electronegative than A, and  $\delta\alpha > 0$  when B is more electropositive than A. In practice, such a change in  $\langle \chi_\alpha | H^{\text{eff}} | \chi_\alpha \rangle$  should lead to corresponding changes in those interaction integrals  $\langle \chi_\alpha | H^{\text{eff}} | \chi_\mu \rangle$  which are nonzero by symmetry and via the Wolfsberg–Helmholz relationship (equation 1.19). Also, associated with a change of  $H_{\mu\mu}$  values is a change in orbital exponent. As an orbital becomes more tightly bound it also becomes more contracted, see 1.3. These two effects shall be explicitly neglected in our discussion here, as well as, changes in geometry or charging effects.

Given that the perturbation is simply a change in  $\langle \chi_\alpha | H^{\text{eff}} | \chi_\alpha \rangle$  (in our case we identify  $\alpha$  with a specific atomic orbital on atom B), then using the approximations, as just discussed, lead to  $\delta H_{\mu\nu} = 0$  (for  $\mu \neq \nu$ ),  $\delta S_{\mu\nu} = 0$  and  $\delta H_{\mu\mu} = 0$  except for the case where  $\mu = \alpha$ . Here  $\delta H_{\alpha\alpha} = \delta\alpha$ . So in equation 3.7,  $\tilde{S}_{ij} = 0$  for all the molecular orbitals,  $i$  and  $j$ . In equation 3.8, the only term in the summation which is nonzero is that for  $\mu = \nu (= \alpha)$  and so  $\tilde{H}_{ij} = c_{\alpha i}^0 \delta\alpha c_{\alpha j}^0$ . As a result,  $\tilde{H}_{ij} - e_i^0 \tilde{S}_{ij} = c_{\alpha i}^0 c_{\alpha j}^0 \delta\alpha$ , which leads to

$$e_i = e_i^0 + e_i^{(1)} + e_i^{(2)}$$

where

$$e_i^{(1)} = (c_{\alpha i}^0)^2 \delta\alpha \quad \text{and} \quad e_i^{(2)} = \sum_{j \neq i} \frac{(c_{\alpha i}^0 c_{\alpha j}^0 \delta\alpha)^2}{e_i^0 - e_j^0} \quad (6.7)$$

and

$$\psi_i = \psi_i^0 + \sum_{j \neq i} t_{ji}^{(1)} \psi_j^0$$

where

$$t_{ji}^{(1)} = \frac{c_{\alpha i}^0 c_{\alpha j}^0 \delta\alpha}{e_i^0 - e_j^0}$$
(6.8)

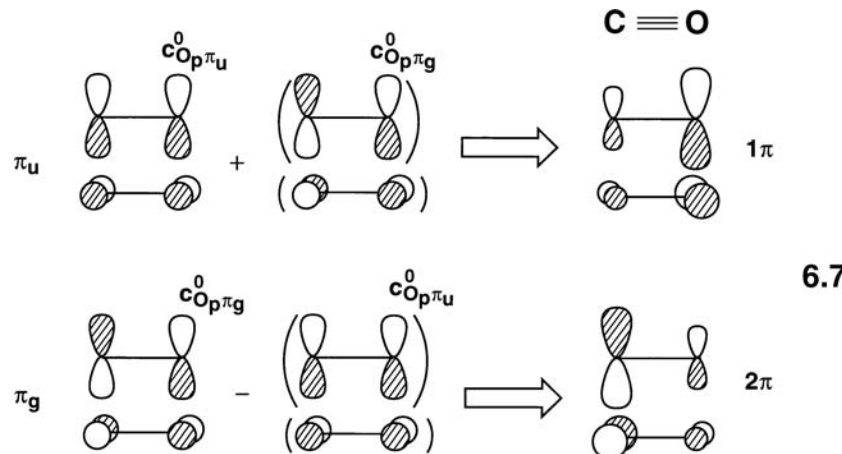
Remember that for the subscripts,  $\alpha$  refers to a specific atomic orbital on the atom(s) that is undergoing a change in electronegativity and that  $i$  and  $j$  refer to molecular orbitals. Therefore,  $c_{\alpha i}^0$  refers to the coefficient of the  $\alpha$  atomic orbital in the molecular orbital  $i$  for the unperturbed molecule.

These results may be immediately applied to the case of the  $p_\pi$  orbitals of  $A_2$  and AB. Let us take a specific example, going from  $C_2^{2-}$  to CO. The symmetry for CO is  $C_{\infty v}$  so the  $\pi_u$  and  $\pi_g$  orbitals of  $C_2^{2-}$  become  $1\pi$  and  $2\pi$ , respectively, in CO. For convenience, we arrange the  $\pi_u$  and  $\pi_g$  orbitals of  $C_2^{2-}$  such that the coefficients of the orbital  $\chi_{O_p}$  (a  $p$  orbital on oxygen) have an identical sign. Then identifying the  $\pi_u$  orbital with  $\psi_i$  and the  $\pi_g$  orbital with  $\psi_j$  of equation 6.8, along with  $e_i^0 = e_{\pi_u}^0$ ,  $c_{\alpha i}^0 = c_{O_p \pi_u}^0$ , and so on, and  $\delta\alpha = (-)$  (oxygen is more electronegative than carbon), we obtain

$$\begin{aligned}\psi_{1\pi} &= \psi_{\pi_u}^0 + t_{\pi_g \pi_u}^{(1)} \psi_{\pi_g}^0 \\ \psi_{2\pi} &= \psi_{\pi_g}^0 + t_{\pi_u \pi_g}^{(1)} \psi_{\pi_u}^0\end{aligned}\quad (6.9)$$

$$\begin{aligned}t_{\pi_g \pi_u}^{(1)} &= \frac{c_{O_p \pi_u}^0 c_{O_p \pi_g}^0 \delta\alpha}{e_{\pi_u}^0 - e_{\pi_g}^0} = \frac{(+)(+)(-)}{(-)} = (+) \\ t_{\pi_u \pi_g}^{(1)} &= \frac{c_{O_p \pi_g}^0 c_{O_p \pi_u}^0 \delta\alpha}{e_{\pi_g}^0 - e_{\pi_u}^0} = \frac{(+)(+)(-)}{(+)} = (-)\end{aligned}\quad (6.10)$$

This leads to the mixing shown in 6.7. The wavefunction in  $1\pi$  becomes concentrated on the more electronegative oxygen atom, whereas the opposite occurs in  $2\pi$ . This result could just as easily be obtained by an intermolecular perturbation



analysis where the  $p$  atomic orbitals of oxygen are set at a lower energy than those for carbon.

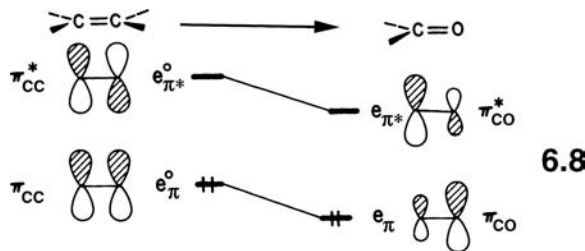
The new energies from equation 6.7 are given by

$$\begin{aligned} e_{1\pi} &= e_{\pi_u}^0 + \left( c_{O_p\pi_u}^0 \right)^2 \delta\alpha + \frac{\left( c_{O_p\pi_u}^0 c_{O_p\pi_g}^0 \delta\alpha \right)^2}{e_{\pi_u}^0 - e_{\pi_g}^0} \\ e_{2\pi} &= e_{\pi_g}^0 + \left( c_{O_p\pi_g}^0 \right)^2 \delta\alpha + \frac{\left( c_{O_p\pi_u}^0 c_{O_p\pi_g}^0 \delta\alpha \right)^2}{e_{\pi_g}^0 - e_{\pi_u}^0} \end{aligned} \quad (6.11)$$

where

$$\begin{aligned} \left( c_{O_p\pi_u}^0 \right)^2 \delta\alpha &< 0; & \left( c_{O_p\pi_g}^0 \right)^2 \delta\alpha &< 0 \\ \frac{\left( c_{O_p\pi_u}^0 c_{O_p\pi_g}^0 \delta\alpha \right)^2}{e_{\pi_u}^0 - e_{\pi_g}^0} &< 0; & \frac{\left( c_{O_p\pi_u}^0 c_{O_p\pi_g}^0 \delta\alpha \right)^2}{e_{\pi_g}^0 - e_{\pi_u}^0} &> 0 \end{aligned} \quad (6.12)$$

Both the first-order energy and the second-order energy corrections lower the energy of  $1\pi_{CO}$  relative to  $\pi_u$  in  $C_2^{2-}$ . The first- and second-order corrections work in the opposite directions for the  $2\pi$  orbital. Therefore,  $2\pi$  is stabilized to a lesser degree than is  $1\pi$ . In most cases, the first-order term dominates. For example, the  $\pi_{CO}$  and  $\pi^*_{CO}$  levels of a carbonyl double bond are invariably lower than the  $\pi_{CC}$  and  $\pi^*_{CC}$  levels of the comparable carbon–carbon double bond, as shown in 6.8. Because of its lower energy and larger carbon  $p$  coefficients, nucleophiles attack



the  $\pi^*_{CO}$  orbital of a carbonyl compound with greater facility than the  $\pi^*_{CC}$  orbital in an alkene. We focus our attention here on the highest occupied molecular orbital (HOMO)–lowest unoccupied molecular orbital (LUMO) interactions of the two reactants. This is where the smallest energy gap, in terms of a perturbation expression, will be found, and, therefore, the largest two-electron–two-orbital stabilizing interaction. A nucleophile will have a high-lying HOMO and, therefore, its interaction with the LUMO of an electrophile (the carbonyl group or C–C double bond) will dominate reactivity trends in these types of problems.

Let us now return to the  $C_2^{2-} \Rightarrow CO$  problem and examine what perturbations occur in the  $\sigma$  system. The four  $\sigma$  molecular orbitals appropriate for  $C_2^{2-}$  are taken from Figure 6.3 and displayed again on the left side of Figure 6.7 along with what we have found for the  $1\pi$  and  $2\pi$  molecular orbitals of CO. In principle, all the  $\sigma$ -type

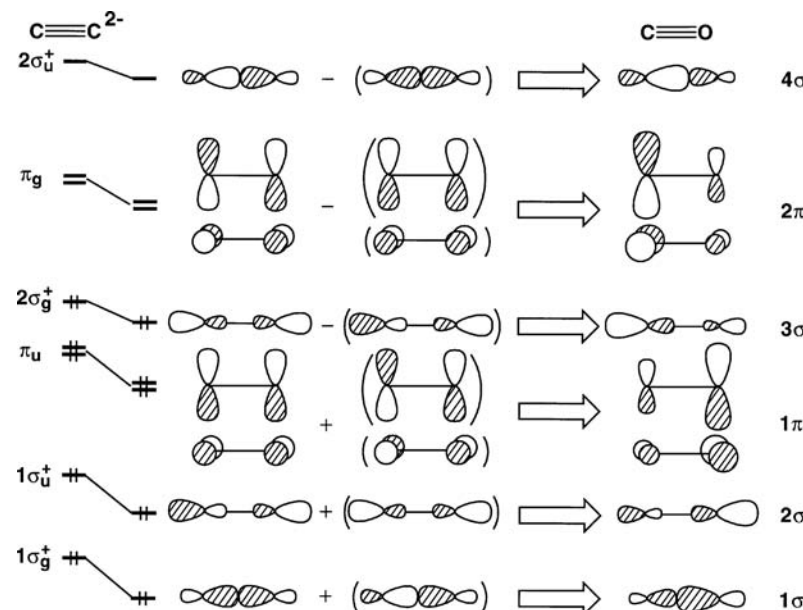


FIGURE 6.7

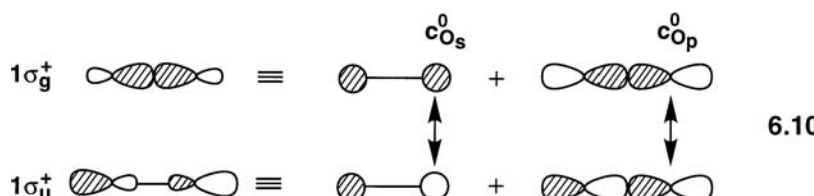
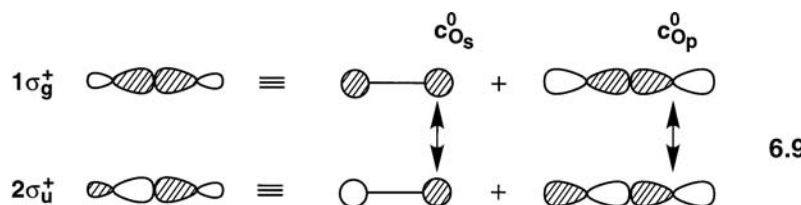
The electronegativity perturbation on going from C<sub>2</sub><sup>2-</sup> to CO.

orbitals can mix into 1σ<sub>g</sub><sup>+</sup>, for example. But the situation can be considerably simplified without loss of qualitative features. First consider the first-order mixing coefficients from equation 6.7. They are now given by

$$t_{2\sigma_u^+, 1\sigma_g^+}^{(1)} = \frac{(c_{\alpha 1\sigma_g^+}^0)(c_{\alpha 2\sigma_u^+}^0)\delta\alpha}{e_{1\sigma_g^+}^0 - e_{2\sigma_u^+}^0} = \frac{(c_{O_s 1\sigma_g^+}^0 c_{O_s 2\sigma_u^+}^0 + c_{O_p 1\sigma_g^+}^0 c_{O_p 2\sigma_u^+}^0)\delta\alpha}{e_{1\sigma_g^+}^0 - e_{2\sigma_u^+}^0} \quad (6.13)$$

$$t_{1\sigma_u^+, 1\sigma_g^+}^{(1)} = \frac{(c_{\alpha 1\sigma_g^+}^0)(c_{\alpha 1\sigma_u^+}^0)\delta\alpha}{e_{1\sigma_g^+}^0 - e_{1\sigma_u^+}^0} = \frac{(c_{O_s 1\sigma_g^+}^0 c_{O_s 1\sigma_u^+}^0 + c_{O_p 1\sigma_g^+}^0 c_{O_p 1\sigma_u^+}^0)\delta\alpha}{e_{1\sigma_g^+}^0 - e_{1\sigma_u^+}^0} \quad (6.14)$$

for the mixing of 2σ<sub>u</sub><sup>+</sup> and 1σ<sub>u</sub><sup>+</sup> into 1σ<sub>g</sub><sup>+</sup>, respectively. Because of the s–p hybridization, equations 6.13 and 6.14 each have two terms representing the coefficients of the O<sub>s</sub> and O<sub>p</sub> atomic orbitals in 1σ<sub>g</sub><sup>+</sup>, 1σ<sub>u</sub><sup>+</sup>, and 2σ<sub>u</sub><sup>+</sup>. The relationship between the relative phases for equation 6.13 is given in 6.9. Here, the O<sub>s</sub> and O<sub>p</sub> coefficients in



$1\sigma_g^+$  and  $2\sigma_u^+$  are the same, so

$$t_{2\sigma_u^+, 1\sigma_g^+}^{(1)} = \frac{[(+)(+) + (-)(-)](-)}{(-)} = (+) \quad (6.15)$$

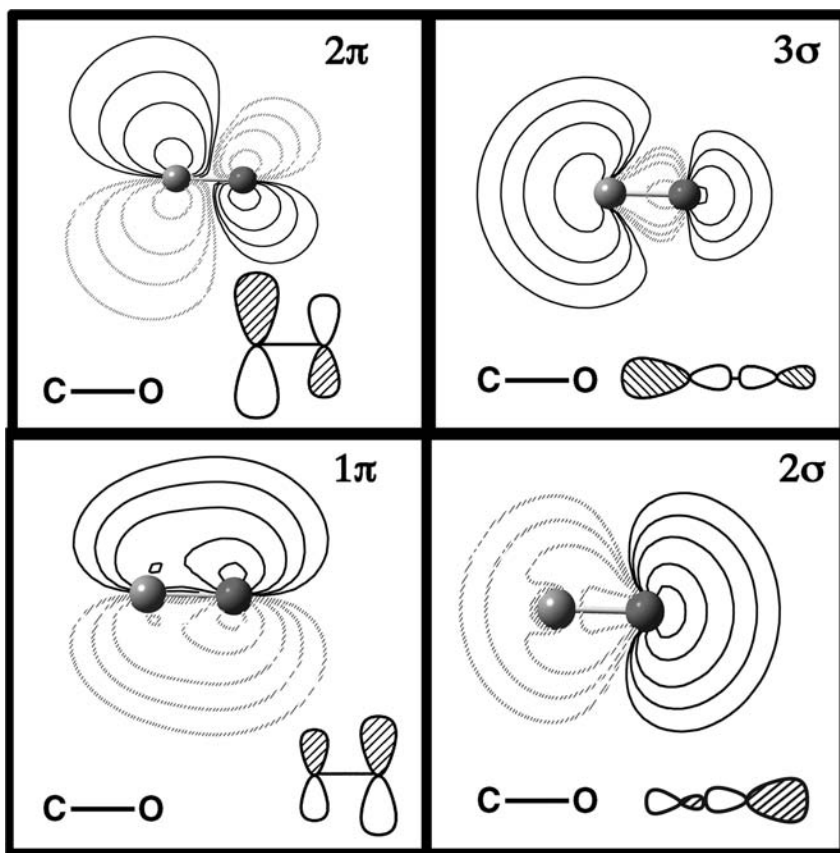
Both terms within the square brackets are positive; thus,  $t_{2\sigma_u^+, 1\sigma_g^+}^{(1)}$  is expected to be sizable. Now consider what occurs in equation 6.14 for the mixing of  $1\sigma_u^+$  into  $1\sigma_g^+$ . The relevant atomic orbital mixing coefficients are illustrated in 6.10. In this case, the coefficients of  $O_s$  have the opposite signs in  $1\sigma_g^+$  and  $1\sigma_u^+$ , but coefficients of  $O_p$  have the same sign. Therefore, equation 6.14 becomes

$$t_{1\sigma_u^+, 1\sigma_g^+}^{(1)} = \frac{[(+)(-) + (-)(-)](-)}{(-)} \cong 0 \quad (6.16)$$

so the numerator will be small. It should not be assumed that the two terms of the numerator are of equal magnitude. From Figure 6.4 and the discussion concerning the construction of the molecular orbitals of a homonuclear diatomic in the previous section, we note that in both  $1\sigma_g^+$  and  $1\sigma_u^+$  the coefficients of  $O_s$  are large, but coefficients of  $O_p$  are smaller. Therefore, the first term within the brackets of equation 6.16 is expected to be larger than the second. Since we are only interested in qualitative aspects,  $t_{1\sigma_u^+, 1\sigma_g^+}^{(1)}$  may be neglected. Likewise,  $1\sigma_u^+$  will only mix strongly with  $2\sigma_g^+$ . Simply speaking, only molecular orbitals with the same sense of hybridization mix strongly with each other. As shown in Figure 6.7, on going to CO, it is easy to see that  $1\sigma_g^+$  to  $\pi_u$  gain electron density at the more electronegative oxygen atom while the polarization is on the less electronegative carbon end for  $2\sigma_g^+$  to  $2\sigma_u^+$ . All the molecular orbitals will go down in energy because of the first-order energy correction. However,  $e^{(2)}$  is stabilizing (negative) for  $1\sigma_g^+$  and  $1\sigma_u^+$  and destabilizing (positive) for  $2\sigma_g^+$  and  $2\sigma_u^+$  for the same reasons as just discussed for the first-order mixing coefficients (the numerators have the same functional forms, see equations 6.7 and 6.8). Contour plots of  $1\pi$ ,  $3\sigma$  and  $2\pi$  for CO are shown in Figure 6.8. These are hybrid density functional (B3LYP) calculations with a 6-31+G\* basis that have been produced in a manner analogous to the  $N_2$  molecular orbitals in Figure 6.4. The reader should compare these two Figures 6.4 and 6.8. The polarization in the three molecular orbitals of CO are obvious and are what is predicted from the electronegativity perturbation results of Figure 6.7. This polarization in the highest occupied molecular orbital,  $3\sigma$  and lowest unoccupied molecular orbital  $2\pi$  set will play a very important role in the bonding of CO to transition metals, a topic that is extensively discussed in later chapters.

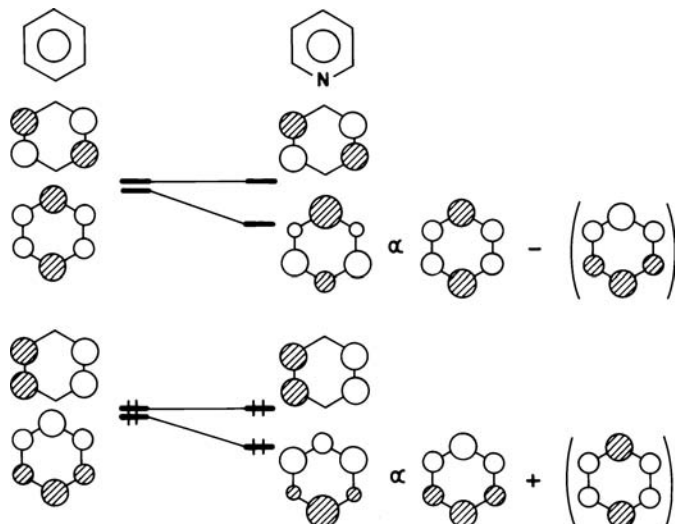
Another example of an electronegativity perturbation, shown in Figure 6.9, illustrates how the HOMOs and LUMOs of benzene may be used to construct the HOMO and LUMO of the pyridine molecule. In this treatment, we have considered only the highest occupied and lowest unoccupied orbitals of this system. The intermixing of the benzene  $\pi$  and  $\pi^*$  levels redistribute the electron density in pyridine. In the perturbed  $\pi$  level, the orbital density (via the atomic orbital coefficients) is increased on the nitrogen and two meta-carbon atoms. Correspondingly, the coefficients at the *para* and two *ortho* positions have increased in the perturbed  $\pi^*$  level. Electron density in the two  $\pi$  molecular orbitals is redistributed so that the *ortho* and two *para* carbons become electron deficient compared to the meta carbons. For these two reasons, nucleophiles are expected to attack *ortho* and/or *para* to this nitrogen atom and indeed they do.

As a final example, we return to the linear  $H_3$  problem and ask where a more electronegative atom ( $H'$ ) would lie in  $H_2H'$ ; at the end or in the middle of the

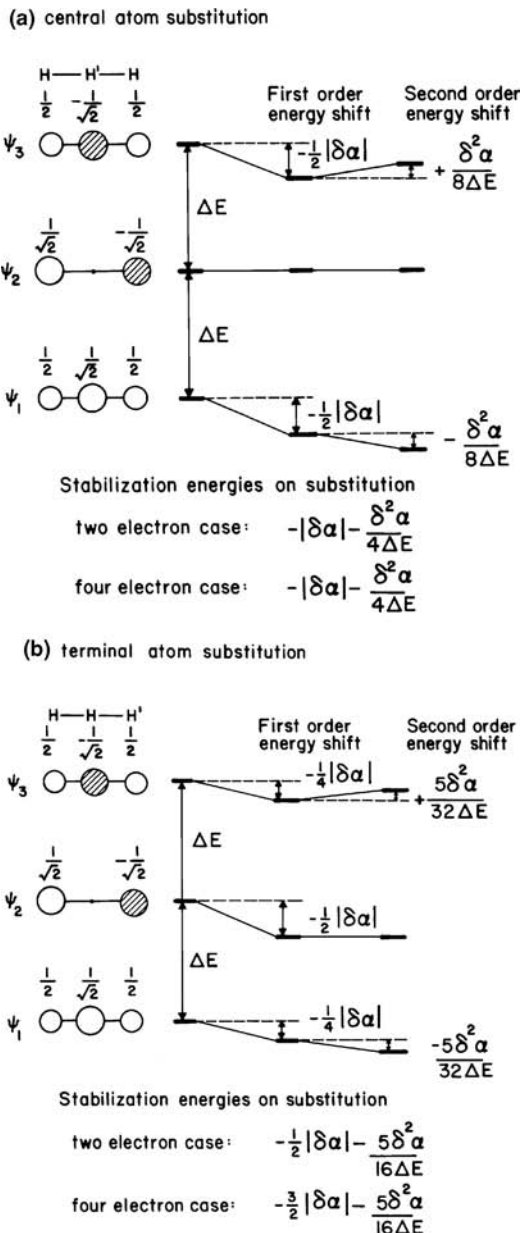
**FIGURE 6.8**

Contour plots of the important valence orbitals in CO. Details of the plots are the same as those in Figure 6.4. Only one component of  $1\pi$  and  $2\pi$  is shown.

molecule. This is worked out in Figure 6.10 where we have adopted a particularly simplified form of the energy level diagram for  $H_3$  itself. If overlap is neglected (except, of course, nonzero  $\langle \chi_1 | H^{\text{eff}} | \chi_3 \rangle$  type integrals remain), the bonding and antibonding  $\sigma_g^+$  orbitals,  $\psi_1$ , and  $\psi_3$ , are split in energy an equal distance ( $\Delta E$ )

**FIGURE 6.9**

Mixing of the HOMO and LUMO orbitals of benzene during an electronegativity perturbation to give the pyridine molecule.

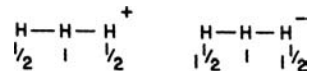
**FIGURE 6.10**

Energy level shifts, obtained via perturbation theory, which result on substitution of an atom of  $H_3$  by one of higher electronegativity. The two cases of central (a) and terminal (b) atom substitution are shown. (Within the Hückel model, described in Chapter 12,  $\Delta E = \sqrt{2}\beta$ .) The perturbation used is an increase in  $|H_{\alpha\alpha}|$  of the relevant orbital by  $|\delta\alpha|$  ( $\delta\alpha, H_{\alpha\alpha} < 0$ .)

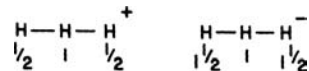
away from the exactly nonbonding  $\sigma_u^+$  orbital. The orbital coefficients in this zero overlap approximation (actually no different from simple Hückel theory as we will see in Section 12.2) are also easily evaluated and are shown in Figure 6.10. For a change in Coulomb integral of  $\delta\alpha$  for a hydrogen s orbital, the energy terms of equation 6.7 are readily evaluated as shown for the three levels. Replacement of the central atom by one with larger electronegativity (in Figure 6.10a) leads to no change in the energy of the  $\sigma_u^+$  orbital. This is understandable because it contains no central atom character at all. The energy change for the two-electron ( $H_3^+$ ) and four-electron ( $H_3^-$ ) cases are therefore identical and are given at the bottom of Figure 6.10a. Substitution of an end atom leads to the first-order energy changes for both orbitals (Figure 6.10b), but the second-order energy correction for  $\sigma_u$ ,  $\psi_2$ , is zero since it is pushed up by  $\psi_1$  an equal amount that it is pushed down by  $\psi_3$ . Now the energy changes are different for the two- and four-electron

cases and again are listed in terms of  $\delta\alpha$  and  $\Delta E$  at the bottom of Figure 6.10b. The prediction is that the more electronegative atom prefers to lie at a terminal position in electron-rich (four electron) three-center systems, and in the central position for electron deficient (two electron) three-center systems. The central atom substitution is more favorable for the two-electron case because the larger central atomic orbital coefficient leads to a greater first-order correction in  $\psi_1$ . For the electron-rich (four electron) three-center system, the nonvanishing first-order contribution for  $\psi_2$  gives preference to end substitution. The second-order energy terms are nearly equal and consequently are not expected to lead to a bias of one structural type over another. In N<sub>2</sub>O (3.1), there are a total of eight  $\pi$  electrons occupying two out of the three pairs of  $\pi$  orbitals in this molecule, a situation isomorphous with that of the H<sub>3</sub> problem with a four-electron count. Correspondingly, N<sub>2</sub>O is found as NNO and not as NON. Theory first predicted and then matrix isolation experiments confirmed that B<sub>2</sub>N and B<sub>2</sub>O exist as BX<sub>2</sub> (X = N, O) rather than the BBX isomers [6]. In these molecules, the electron filling is for four  $\pi$  electrons so that with respect to the situation in Figure 6.10 this is a case analogous to having just  $\psi_1$  filled with two electrons for both cases. Hence, the central atom now should be, and is, the more electronegative one.

It is interesting to correlate the electronic charge distribution for the two- and four-electron H<sub>3</sub> systems with the treatment given above. Using the wavefunctions shown in Figure 6.10, it is easy to generate the electron densities of 6.11 and 6.12. The details of the electronegativity perturbation results, therefore, in a preference



6.11



6.12

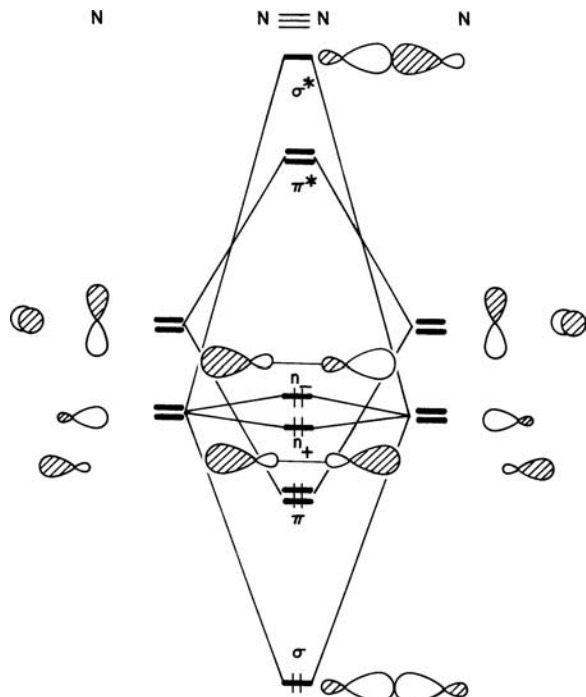
for the most electronegative atom of a substituted molecule to lie at the site of highest charge density in the unsubstituted parent. This is a very important result we shall use later.

---

## 6.5 PHOTOELECTRON SPECTROSCOPY AND THROUGH-BOND CONJUGATION

---

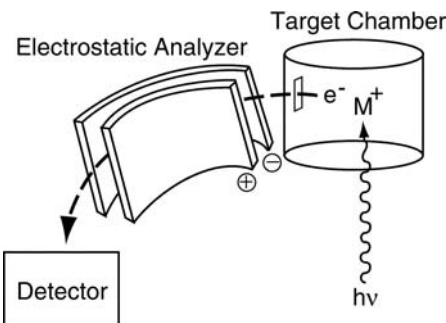
Notice from Figure 6.3 that as a result of the second-order interaction,  $2\sigma_g^+$  has been pushed up in energy and is now less bonding between the two A atoms than before. In fact, it has a resemblance to an orbital constructed via the in-phase addition of two lone pair orbitals (Figure 6.4).  $1\sigma_u^+$  has been pushed down in this process and resembles an out-of-phase mixture of lone pair orbitals.  $1\sigma_g^+$  remains the only  $\sigma$  orbital which is strongly bonding. We wish to explore the correspondence between the traditional Lewis structure for the 10 electron N<sub>2</sub> molecule and the orbital model developed in Section 6.3. Taking a classic valence bond (VB) approach, allow the formation of two  $sp$  hybrids which leaves two pure  $p$  atomic orbitals on each nitrogen atom. As Figure 6.11 shows, one of the  $sp$  hybrids on each nitrogen atom is used to form the  $\sigma$  and  $\sigma^*$  orbitals. The outward pointing  $sp$  hybrids are used to form the in-phase and out-of-phase lone pair combinations,  $n_+$  and  $n_-$ , respectively. Finally, the two  $p$  atomic orbitals on each center create the  $\pi$  and  $\pi^*$  orbitals. The splitting of the  $\sigma$  and  $n$  combinations follows the reasonable idea that the outward pointing hybrids will have much less overlap with each other than the inward pointing ones. The N<sub>2</sub> molecule then has the sequence of orbitals defined at the center of Figure 6.11.

**FIGURE 6.11**

Construction of the orbitals of  $\text{N}_2$  using two  $sp$  hybrids and two  $p$  atomic orbitals on each atom.

This is certainly a “standard” valence bond (VB) way to view the electronic structure in  $\text{N}_2$ , with the possible exception that we have taken a linear combination of lone pair orbitals. The three bonds between the nitrogen atoms would be identified with the double occupation of  $1\sigma_g^+$  and the two components of  $1\pi_u$  from Figure 6.3. As we have described, the lone pair orbitals are best identified with  $1\sigma_u^+$  and  $2\sigma_g^+$ . The perhaps surprising result from our LCAO technique in Figure 6.3 is that the in-phase combination lies at higher energy than the out-of-phase combination. Furthermore, the latter is at an energy well below  $\pi$  in the valence bond picture. Which model more accurately resembles reality? Photoelectron spectroscopy provides a direct experimental link to the orbital sequence.

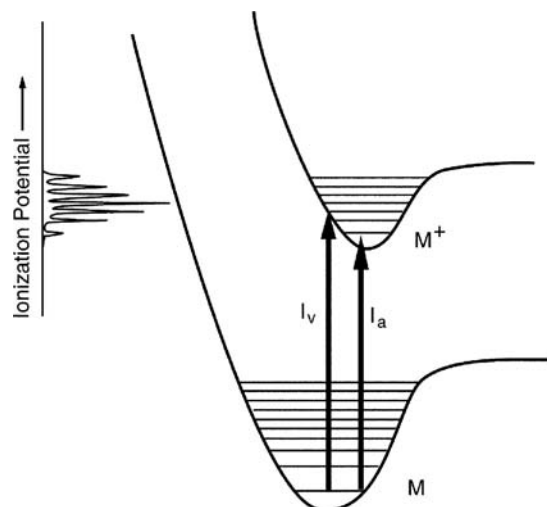
An electron in a molecular orbital  $\psi_i$  is under an effective potential  $e_i$ . As we will discuss in Chapter 8, Koopmans’ theorem shows that the ionization potential required to remove an electron from  $\psi_i$  is given by  $-e_i$  [7,8]. As schematically depicted in 6.13, a photoelectron spectrometer measures the kinetic energy of

**6.13**

electrons that are ejected from gas-phase molecules in the target chamber by an incident photon beam of energy,  $h\nu$ . Normally, He(I) and He(II) sources are used with energies of 21.1 and 40.8 eV, respectively, and with a synchrotron source a broad, tunable region is available [9]. The ejected electrons with kinetic energies, KE, are then sorted with respect to kinetic energy by an electrostatic analyzer and then detected. These photoelectrons originate from various molecular orbitals with different  $e_i$ 's and, therefore their kinetic energies are related by

$$e_i = h\nu - KE \quad (6.17)$$

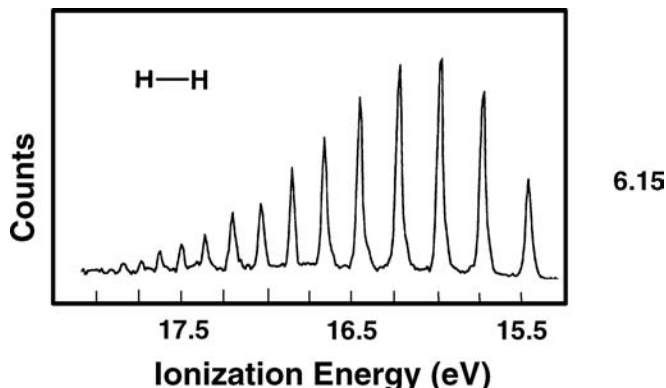
Photoelectron spectroscopy relates molecular orbital energies,  $e_i$ , obtained from molecular orbital calculations to experimentally observed ionization potentials via Koopmans' theorem which is usually found to be reasonably accurate for main group compounds using dependable theoretical techniques (transition metal complexes sometimes are problematic). Furthermore, there is not just one peak for a single molecular orbital. As shown in **6.14** each molecule, M, contains a set of



**6.14**

vibrational levels. So too the molecular ion,  $M^+$ , contains other vibrational levels, not necessarily at the same spacing as M and the geometry may well be different for  $M^+$ . Let us say that M in **6.14** is a diatomic. The horizontal direction in **6.14** for a diatomic molecule is the internuclear distance which in this case is slightly elongated for  $M^+$  at equilibrium in comparison to M. The kinetic energies of the photoelectrons have a range of discrete values corresponding to the different vibrational levels of  $M^+$  and the photoelectron spectrum shown vertically on the upper left side of **6.14** contains a series of closely spaced peaks. In more complicated molecules, this (as well as many other effects [7]) may smear the spectrum out into a broad peak. Two different ionizations are unique. The adiabatic ionization potential,  $I_a$ , is an ionization to the ground vibrational level of  $M^+$ . If the geometry of  $M^+$  is indeed very different, the ionization probability becomes small so that this peak may be experimentally difficult to observe. The vertical ionization potential,  $I_v$ , as may be appreciated from **6.14**, corresponds to the most probable ionization, and hence the tallest peak (or the top of a broad peak). It is for this reason that vertical ionizations are normally reported.

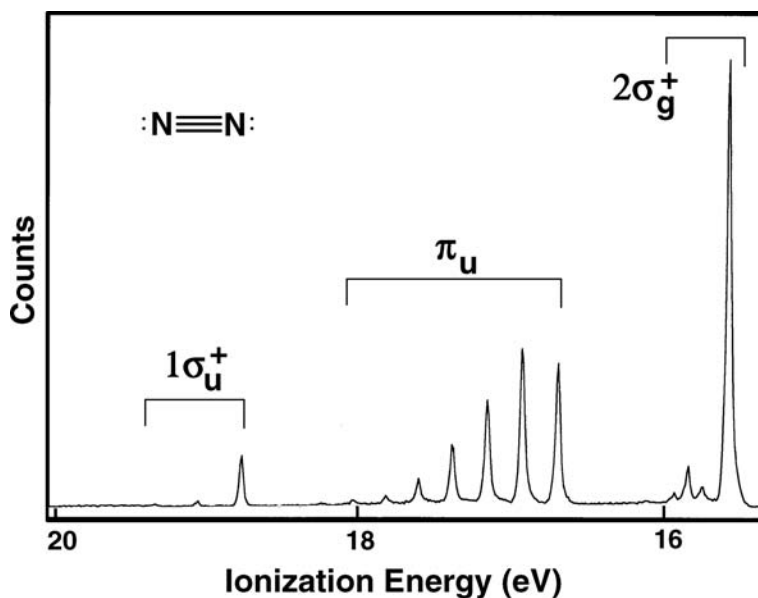
The photoelectron spectrum for H<sub>2</sub> in 6.15 nicely illustrates these features. From the vibrational splitting, an internuclear distance of 1.060 Å can be deduced for H<sub>2</sub><sup>+</sup>



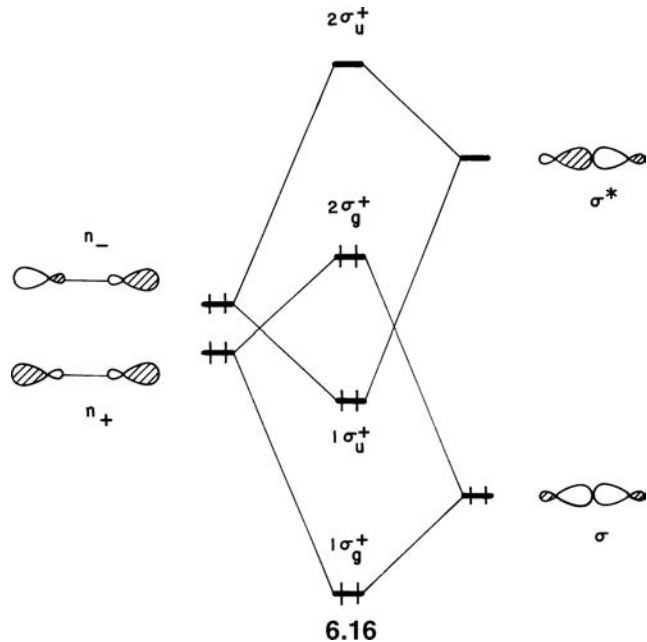
compared to 0.742 Å in H<sub>2</sub> itself [7]. This is, of course, consistent with 1σ<sub>g</sub><sup>+</sup> in H<sub>2</sub> being a bonding molecular orbital. Thus, in some cases photoelectron spectroscopy can be used to measure the extent of bonding present in a molecular orbital. The intensities of the bands are most conveniently described in terms of cross-sections that are a measure of the probability of photoionization from a specific molecular orbital. They are also sensitive to the energy of the ionizing radiation; the details may be found in two excellent, readable sources [7,9]. For our purposes, it is useful to note that they do not vary too much for most main group molecules. Therefore, compared to a nondegenerate orbital, a doubly-degenerate e set of orbitals will have twice the cross-section, and a triply-degenerate t set of orbitals three times the cross-section.

Given this exceedingly brief description of photoelectron spectroscopy, let us return to the problem at hand. Namely, does photoelectron spectroscopy support the VB picture with two ionizations corresponding to the lone pairs of N<sub>2</sub> just lower than the ionization potential associated with the π orbital set (Figure 6.11), or does the LCAO pattern in Figure 6.3 apply? The photoelectron spectrum of N<sub>2</sub> is shown in Figure 6.12. This spectrum was obtained with He(I) radiation and so the lowest molecular orbital corresponding to 1σ<sub>g</sub><sup>+</sup> is not observed. Its ionization potential (37.3 eV) is too large for the photon source used in Figure 6.12. As may be anticipated by the captions in Figure 6.12, the two ionizations at the lowest and highest ionization potential have much smaller cross-sections than the middle band. Therefore, they must be associated with the 1σ<sub>u</sub><sup>+</sup> and 2σ<sub>g</sub><sup>+</sup> molecular orbitals and the middle band with π<sub>u</sub>. Furthermore, the intensities affiliated with each vibrational progression uniquely identifies the 1σ<sub>u</sub><sup>+</sup> molecular orbital with I<sub>v</sub> = 18.8 eV and 2σ<sub>g</sub><sup>+</sup> with the ionization at 15.5 eV. This is in total agreement with the LCAO picture in Figure 6.3. The 3.3 eV splitting of the lone pairs is large indeed and perhaps even more perplexing is the fact that the out-of phase combination lies lower in energy than the in-phase one! Where has the VB approach of Figure 6.11 gone wrong?

The explanation for this lies in the details of the orbital mixing process of Figure 6.11. There is a nonvanishing overlap between each hybrid on the one center to the two on the other. In other words, the n<sub>+</sub> combination can and will mix with σ.

**FIGURE 6.12**Photoelectron spectrum for  $\text{N}_2$ .

Likewise,  $n_-$  interacts with  $\sigma^*$ . The appropriate scheme is given in **6.16**. Now  $n_+$  can be pushed up above  $n_-$  because it is destabilized by the lower lying  $\sigma$ . On the other



hand,  $n_-$  is stabilized by  $\sigma^*$ . This is a typical pattern of what is called through-bond interaction between lone pairs. The topic is discussed further in Section 11.3.

The vibrational frequency of  $\text{N}_2$  is  $2358 \text{ cm}^{-1}$  and the bond distance is  $1.098 \text{ \AA}$ . The vibrational data from the photoelectron spectra can be used to find out the nature of the bonding present within each molecular orbital [7]. Not surprisingly, the  $\pi_u$  molecular orbital is strongly bonding between the two centers, so the vibrational frequency for  $\text{N}_2^+$  in the  ${}^2\Pi_u$  electronic state (one electron has been removed from

$\pi_u$ ) decreases to  $1903\text{ cm}^{-1}$  and the bond distance increases to  $1.177\text{ \AA}$ . One would also expect that  $1\sigma_u^+$  is net antibonding. But the  $s-p$  mixing renders it less so. It turns out that the vibrational frequency for the  $^2\Sigma_u^+$  state of  $\text{N}_2^+$  does increase to  $2420\text{ cm}^{-1}$  and the bond distance does decrease, albeit slightly, to  $1.075\text{ \AA}$ . Now for the  $2\sigma_g^+$  molecular orbital. Of critical concern again is the extent of  $s-p$  mixing. In other words, do the overlap integrals  $\langle s|s\rangle$  and  $\langle p|p\rangle$  equal to more than twice  $\langle s|p\rangle$ ? This is the case. For the  $^2\Sigma_g^+$  state of  $\text{N}_2^+$  the vibrational frequency drops to  $2207\text{ cm}^{-1}$  and the bond distance increases to  $1.118\text{ \AA}$ . For the isoelectronic CO molecule the reverse is true. In CO the vibrational frequency increases from  $2170$  to  $2214\text{ cm}^{-1}$  upon the ionization of one electron from  $3\sigma$ . The photoelectron spectrum of CO is given in Figure 23.5b.

It is also interesting to compare  $\text{N}_2$  with its heavier congeners. Figure 6.13 plots the experimental ionization potentials for  $1\sigma_u^+$ ,  $\pi_u$ , and  $2\sigma_g^+$  in the  $\text{N}_2$ ,  $\text{P}_2$ , and  $\text{As}_2$  molecules [10]. Also plotted are the state-averaged ionization potentials of the  $s$  and  $p$  atomic orbitals in the bare atoms, which are correlated by the dotted lines in the figure. In each case the  $2\sigma_g^+$  and  $\pi_u$  molecular orbitals lie lower in energy than the  $p$  atomic orbital, as expected from Figures 6.2 or 6.3. Likewise, the  $1\sigma_u^+$  level lies higher in energy than the  $s$  atomic orbital. The three ionization potentials for  $\text{P}_2$  and  $\text{As}_2$  decrease compared to  $\text{N}_2$  and this roughly follows the ionization potentials for the atoms; the atom is becoming less electronegative on going from N to P to As, see Figure 2.4. The  $2\sigma_g^+$  molecular levels for  $\text{P}_2$  and  $\text{As}_2$  do fall just below  $\pi_u$ , a clear result of the decreased  $s-p$  mixing for the second- and third-row elements discussed in Section 6.3. But there is another interesting aspect associated with Figure 6.13. Notice that the energy difference between the atomic  $s$  and  $1\sigma_u^+$  levels decrease greatly upon going from  $\text{N}_2$  to  $\text{P}_2$  and  $\text{As}_2$ . This follows the decrease in  $\langle s|s\rangle$  for this series. In other words, when  $\langle s|s\rangle$  becomes smaller the  $1\sigma_u^+$  is destabilized less relative to the starting  $s$  atomic orbital. Likewise, the  $\pi$  type overlap decreases dramatically on going from the first- to the second- and third-row elements. The  $\pi_u-p$  energy difference is sizable for  $\text{N}_2$ , but much smaller for  $\text{P}_2$  and  $\text{As}_2$  and this is a reflection of the smaller overlap. The  $\pi_u-p$  energy difference is not identical to the amount of stabilization in  $\pi_u$ . There is a further complication, which is discussed in Chapters 8 and 9, but as a rough guide one can nicely see the

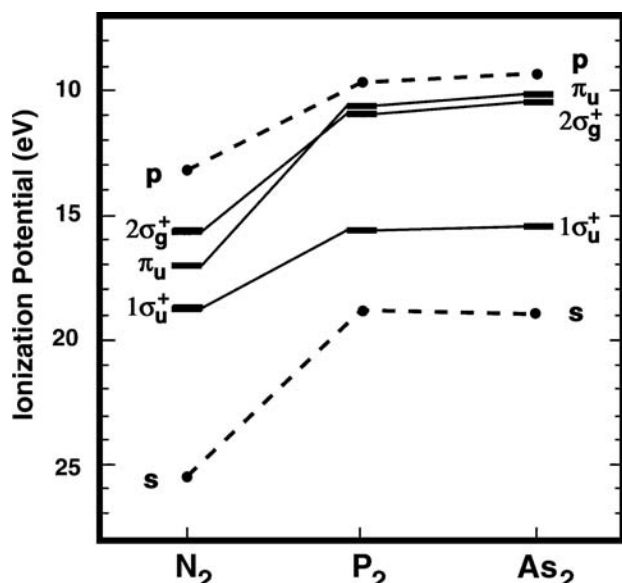


FIGURE 6.13

A comparison of the experimental ionization potentials for  $\text{N}_2$ ,  $\text{P}_2$ , and  $\text{As}_2$ . The dashed lines correlate the experimental state averaged ionization potentials from the atoms (from 2.9).

perturbation ideas built up in the prior chapters at work here from experiment and not solely from a calculation.

## PROBLEMS

**6.1.** In some of the exercises you will be given the results of an MO calculation obtained from a computer program. The first part of the computer output will list the coordinates of the atoms in the molecule. Always first draw a (right-handed!) Cartesian axis system and then figure out where the atoms will be in reference to your axis system. The MOs will also be listed in the output; each MO in the row will have the atomic orbital mixing coefficients listed. Above each MO will be the MO number and the orbital energy (eigenvalue) in electron volts (eV). Draw the atomic framework and then draw out the orbital shapes using the conventions that we established in Section 1.2 in terms of the sign of the phase and the size of the amplitude. There are two points to remember when you do this: first, the AO mixing coefficients are not related to the amount of mixing. It is the square of the coefficients. Therefore, coefficients with an amplitude of less than  $\sim 0.100$  do not contribute much to the MO. Second, when there is a degenerate set of MOs there are an infinite number of ways to express the combinations. Unfortunately, this sometimes means that the members of an e set, for example, will be an arbitrary combination of  $p_x$  and  $p_y$  coefficients instead of one being purely  $p_x$  and the other  $p_y$ . It is OK for you to change them back to the “pure,” more simple combinations!

Below is a MO calculation of  $C_2$ . Draw out the MOs and figure out what the C—C bond order is.

Cartesian coordinates					
	Name	No.	x	y	z
POS	C-1-0	1	0.000000	0.000000	0.000000
POS	C-2-0	2	0.000000	0.000000	1.240000

Molecular orbitals									
	Eigenvalues (eV)	1	2	3	4	5	6	7	8
$C-1-0$	s	1	0.5622	0.5037	0.0000	0.0000	0.2471	0.0000	0.0000
	$p_x$	2	0.0000	0.0000	-0.4954	-0.3663	0.0000	-0.5245	0.6761
	$p_y$	3	0.0000	0.0000	0.3663	-0.4954	0.0000	0.6761	0.5245
	$p_z$	4	0.0499	-0.4681	0.0000	0.0000	-0.6546	0.0000	1.2559
$C-2-0$	s	5	0.5622	-0.5037	0.0000	0.0000	0.2471	0.0000	0.0000
	$p_x$	6	0.0000	0.0000	-0.4954	-0.3663	0.0000	0.5245	-0.6761
	$p_y$	7	0.0000	0.0000	0.3663	-0.4954	0.0000	-0.6761	-0.5245
	$p_z$	8	-0.0499	-0.4681	0.0000	0.0000	0.6546	0.0000	1.2559

**6.2.** An MO calculation of CO is given below. Again draw out the MOs.

Cartesian coordinates					
	Name	No.	x	y	z
POS	C-1-0	1	0.000000	0.000000	0.000000
POS	O-1-0	2	0.000000	0.000000	1.130000

## Molecular orbitals

	Eigenvalues (eV)	1	2	3	4	5	6	7	8
C-1-0 s	1	-35.097	-19.332	-15.660	-15.660	-13.294	-9.133	-9.133	47.960
$p_x$	2	0.0000	0.0000	-0.3066	-0.2168	0.0000	0.9296	0.2548	0.0000
$p_y$	3	0.0000	0.0000	-0.2168	0.3066	0.0000	-0.2548	0.9296	0.0000
$p_z$	4	-0.1240	0.3595	0.0000	0.0000	-0.5271	0.0000	0.0000	1.2142
O-1-0 s	5	-0.7725	0.3001	0.0000	0.0000	0.0776	0.0000	0.0000	-1.2021
$p_x$	6	0.0000	0.0000	-0.6824	-0.4824	0.0000	-0.5879	-0.1612	0.0000
$p_y$	7	0.0000	0.0000	-0.4824	0.6824	0.0000	0.1612	-0.5879	0.0000
$p_z$	8	-0.0361	0.5335	0.0000	0.0000	0.7258	0.0000	0.0000	0.8425

**6.3.** The  $\text{Nb}_2$  molecule is a known molecule. Draw out the interaction diagram for this diatomic using first only the degenerate perturbation theory. Then add in the non-degenerate second-order mixing. For this it is important to realize that the  $4d$  AOs lie lower in energy than the  $5s$  and  $5p$  AOs. Also the  $4d-5s$  energy difference is less than the  $5s-5p$  one. What is Mullikan symbol for the ground state that you get? What is the  $\text{Nb}-\text{Nb}$  bond order?

**6.4.** The actual MO calculation  $\text{Nb}_2$  is listed below. Look at the MO coefficients and compare them to what you obtained in Problem 6.3. There is one “goofy” thing about the result: The  $1\pi_u$  set lies energetically below the  $1\sigma_g^+$  MO. We said before that in terms of overlap  $\sigma > \pi > \delta$ . This is apparently not the case here. Listed below is a table of overlap integrals for  $\text{Nb}_2$  at an internuclear distance of  $2.86\text{\AA}$  which is where the calculation shown below was taken from. Notice that while  $\langle s|s \rangle$  and  $\langle z|z \rangle$  ( $\sigma$ ) are greater than  $\langle x|x \rangle$  ( $\pi$ ), the value for  $\langle z^2|z^2 \rangle$  is very small, in fact it is less than that for  $\langle xz|xz \rangle$  ( $\pi$ ). The situation is even worse, the experimentally determined distance for  $\text{Nb}_2$  is actually very short  $2.08\text{\AA}$ , the overlap integrals for which are also included. Now the  $\langle xy|xy \rangle$  ( $\delta$ ) overlap is even greater than that between the two  $z^2$  orbitals! What is going on here?

Overlap	Type	$r = 2.86\text{\AA}$	$r = 2.08\text{\AA}$
$\langle s s \rangle$	$\sigma$	0.5198	0.6834
$\langle z z \rangle$	$\sigma$	0.3378	0.4555
$\langle x x \rangle$	$\pi$	0.1539	0.6059
$\langle xz xz \rangle$	$\pi$	0.1282	0.2437
$\langle xy xy \rangle$	$\delta$	0.0316	0.1144
$\langle z^2 z^2 \rangle$	$\sigma$	0.1157	0.0689

## Cartesian coordinates

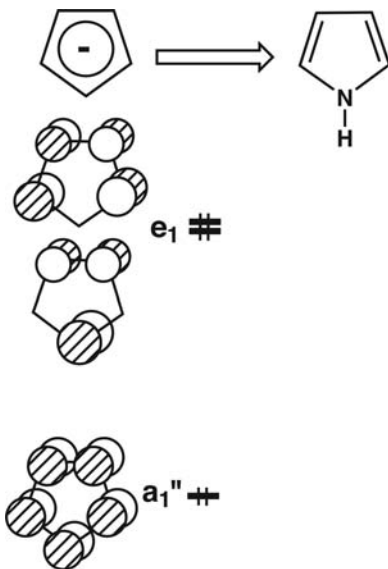
	Name	No.	x	y	z
POS	NB-1-0	1	0.000000	0.000000	0.000000
POS	NB-2-0	2	0.000000	0.000000	2.860000

Molecular orbitals													
	1	2	3	4	5	6	7	8	9	10	11	12	
Eigenvalues (eV)	-11.969	-11.969	-11.951	-11.253	-11.253	-11.021	-10.730	-10.730	-9.995	-9.965	-9.965	-7.370	
NB-1-0 s	1	0.0000	0.0000	-0.1712	0.0000	0.0000	0.5198	0.0000	0.0000	0.0726	0.0000	0.0000	0.4791
$p_x$	2	0.0393	-0.0234	0.0000	0.0000	0.0000	0.0000	0.0000	0.0000	0.1256	0.0554	0.0000	
$p_y$	3	0.0234	0.0393	0.0000	0.0000	0.0000	0.0000	0.0000	0.0000	0.0554	-0.1256	0.0000	
$p_z$	4	0.0000	0.0000	-0.0314	0.0000	0.0000	0.0670	0.0000	0.0000	0.0403	0.0000	0.0000	-0.4925
$dx2-y2$	5	0.0000	0.0000	0.0000	-0.6907	-0.0870	0.0000	0.6843	-0.2193	0.0000	0.0000	0.0000	0.0000
$dz2$	6	0.0000	0.0000	-0.6228	0.0000	0.0000	-0.2469	0.0000	0.0000	-0.7430	0.0000	0.0000	0.0120
$dxy$	7	0.0000	0.0000	0.0000	0.0870	-0.6907	0.0000	0.2193	0.6843	0.0000	0.0000	0.0000	0.0000
$dxz$	8	0.5648	-0.3368	0.0000	0.0000	0.0000	0.0000	0.0000	0.0000	0.0000	-0.6632	-0.2923	0.0000
$dyz$	9	0.3368	0.5648	0.0000	0.0000	0.0000	0.0000	0.0000	0.0000	0.0000	-0.2923	0.6632	0.0000
NB-2-0 s	10	0.0000	0.0000	-0.1712	0.0000	0.0000	0.5198	0.0000	0.0000	-0.0726	0.0000	0.0000	-0.4791
$p_x$	11	0.0393	-0.0234	0.0000	0.0000	0.0000	0.0000	0.0000	0.0000	-0.1256	-0.0554	0.0000	
$p_y$	12	0.0234	0.0393	0.0000	0.0000	0.0000	0.0000	0.0000	0.0000	-0.0554	0.1256	0.0000	
$p_z$	13	0.0000	0.0000	0.0314	0.0000	0.0000	-0.0670	0.0000	0.0000	0.0403	0.0000	0.0000	-0.4925
$dx2-y2$	14	0.0000	0.0000	0.0000	-0.6907	-0.0870	0.0000	-0.6843	0.2193	0.0000	0.0000	0.0000	0.0000
$dz2$	15	0.0000	0.0000	-0.6228	0.0000	0.0000	-0.2469	0.0000	0.0000	0.7430	0.0000	0.0000	-0.0120
$dxy$	16	0.0000	0.0000	0.0000	0.0870	-0.6907	0.0000	-0.2193	-0.6843	0.0000	0.0000	0.0000	0.0000
$dxz$	17	-0.5648	0.3368	0.0000	0.0000	0.0000	0.0000	0.0000	0.0000	0.0000	-0.6632	-0.2923	0.0000
$dyz$	18	-0.3368	-0.5648	0.0000	0.0000	0.0000	0.0000	0.0000	0.0000	0.0000	-0.2923	0.6632	0.0000

Molecular orbitals														
	13	14	15	16	17	18		Eigenvalues (eV)	-6.466	-6.466	-5.402	-1.865	-1.865	73.641
NB-1-0 s	1	0.0000	0.0000	0.2700	0.0000	0.0000	0.0000		0.0000	0.0000	0.0000	0.0000	0.0000	2.0768
$p_x$	2	-0.6025	0.0162	0.0000	-0.9145	0.0472	0.0000		-0.6025	0.0162	0.0000	-0.9145	-0.0472	0.0000
$p_y$	3	0.0162	0.6025	0.0000	-0.0472	-0.9145	0.0000		0.0162	0.6025	0.0000	-0.0472	-0.9145	0.0000
$p_z$	4	0.0000	0.0000	-0.6465	0.0000	0.0000	0.0000		0.0000	0.0000	-0.6465	0.0000	0.0000	1.7469
$dx2-y2$	5	0.0000	0.0000	0.0000	0.0000	0.0000	0.0000		0.0000	0.0000	0.0000	0.0000	0.0000	0.0000
$dz2$	6	0.0000	0.0000	0.0344	0.0000	0.0000	0.0000		0.0000	0.0000	0.0344	0.0000	0.0000	0.3091
$dxy$	7	0.0000	0.0000	0.0000	0.0000	0.0000	0.0000		0.0000	0.0000	0.0000	0.0000	0.0000	0.0000
$dxz$	8	0.1325	-0.0036	0.0000	-0.2735	0.0141	0.0000		0.1325	-0.0036	0.0000	-0.2735	0.0141	0.0000
$dyz$	9	-0.0036	-0.1325	0.0000	-0.0141	-0.2735	0.0000		-0.0036	-0.1325	0.0000	-0.0141	-0.2735	0.0000
NB-2-0 s	10	0.0000	0.0000	0.2700	0.0000	0.0000	0.0000		0.0000	0.0000	0.0000	0.0000	0.0000	-2.0768
$p_x$	11	-0.6025	0.0162	0.0000	0.9145	-0.0472	0.0000		-0.6025	0.0162	0.0000	0.9145	0.0472	0.0000
$p_y$	12	0.0162	0.6025	0.0000	0.0472	0.9145	0.0000		0.0162	0.6025	0.0000	0.0472	0.9145	0.0000
$p_z$	13	0.0000	0.0000	0.6465	0.0000	0.0000	0.0000		0.0000	0.0000	0.6465	0.0000	0.0000	1.7469
$dx2-y2$	14	0.0000	0.0000	0.0000	0.0000	0.0000	0.0000		0.0000	0.0000	0.0000	0.0000	0.0000	0.0000
$dz2$	15	0.0000	0.0000	0.0344	0.0000	0.0000	0.0000		0.0000	0.0000	0.0344	0.0000	0.0000	-0.3091
$dxy$	16	0.0000	0.0000	0.0000	0.0000	0.0000	0.0000		0.0000	0.0000	0.0000	0.0000	0.0000	0.0000
$dxz$	17	-0.1325	0.0036	0.0000	-0.2735	0.0141	0.0000		-0.1325	0.0036	0.0000	-0.2735	0.0141	0.0000
$dyz$	18	0.0036	0.1325	0.0000	-0.0141	-0.2735	0.0000		0.0036	0.1325	0.0000	-0.0141	-0.2735	0.0000

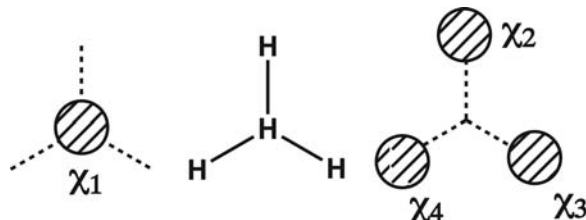
**6.5.** The ground state of  $B_2$  is  ${}^1\Sigma_g^-$  with an electronic configuration of  $(\sigma_g^+)^2(\sigma_u^+)^2(\pi_u)^2$ . On the other hand, the ground state for  $Al_2$  is  ${}^3\Pi_u$  with an electronic configuration of  $(\sigma_g^+)^2(\sigma_u^+)^2(2\sigma_g^+)^1(\pi_u)^1$ . Explain why the two molecules are different.

**6.6.** Using electronegativity perturbation theory, show what happens to the orbital energies in terms of  $e^{(1)}$  and  $e^{(2)}$  corrections along with the  $t^{(1)}$  corrections to the wavefunctions on going from the cyclopentadienyl anion to pyrrole for the three MOs shown below.

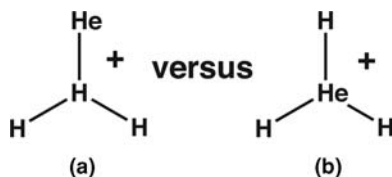


- 6.7.** Consider a hypothetical  $\text{H}_4$  molecule having  $D_{3h}$  symmetry and the geometry shown below.

- a. Construct an orbital interaction diagram for this molecule from an  $\text{H}_3$  fragment and a central hydrogen atom. Draw out the resultant MOs and indicate the orbital occupancy.

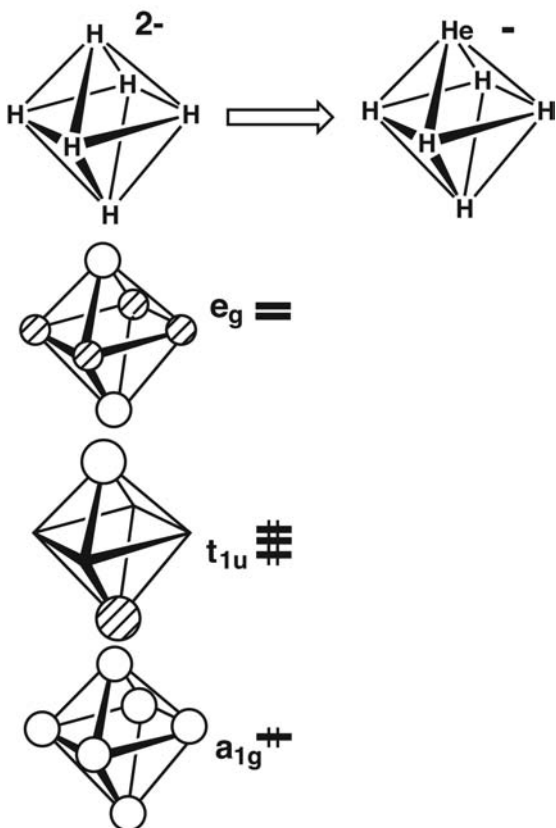


- b. Two structures are possible when a  $\text{He}^+$  atom replaces a hydrogen, structure **A** and **B** shown below. Using electronegativity perturbation theory, determine which is the more stable. You will need to use the MOs from (a) and normalize them with the approximation that  $\langle \chi_2 | \chi_3 \rangle \approx 0$  and  $\langle \chi_1 | \chi_2 \rangle = S$ .



- 6.8.** In this problem, we are going to investigate another hypothetical molecule,  $\text{H}_6^{2-}$  which has  $\text{O}_h$  symmetry. The MOs for this molecule were constructed in Problem 5.5. Here, we will only use the three MOs shown below.

- a. Show what happens using electronegativity perturbation theory when one of the hydrogen atoms is replaced by  $\text{He}^+$ .  
 b. In  $\text{H}_6^{2-}$ , all of the hydrogen atoms have the same charge. However, this is not the case for  $\text{H}_5\text{He}^-$ . Does electron density build up on the trans hydrogen or the cis-hydrogen? We shall see this applied to a realistic molecular example in Chapter 22.




---

## REFERENCES

---

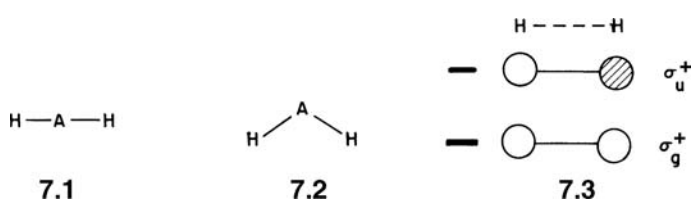
1. G. Herzberg, *Spectra of Diatomic Molecules*, Van Nostrand-Rheinhold, New York (1950); A. A. Radzig, and B. M. Smirnov, *Reference Data on Atoms, Molecules, and Ions*, Springer-Verlag, Berlin (1985); A. I. Boldyrev, N. Gonzales, and J. Simons, *J. Phys. Chem.*, **98**, 9931 (1994).
2. D. E. Woon and T. H. Dunning, Jr., *J. Chem. Phys.*, **101**, 8877 (1994) and references therein.
3. W. Kutzelnigg, *Angew. Chem. Int. Ed. Engl.*, **23**, 272 (1984).
4. N. C. Norman, *Polyhedron*, **12**, 2431 (1993).
5. E. Heilbronner and H. Bock, *The HMO Model and Its Application*, John Wiley & Sons, New York (1976).
6. J. M. L. Martin, J. P. Francois, and R. Gijbels, *Chem. Phys. Lett.*, **193**, 243 (1992) and references therein.
7. J. W. Rabalais, *Principles of Ultraviolet Photoelectron Spectroscopy*, John Wiley and Sons, New York (1977).
8. D. W. Turner, A. P. Baker, and C. R. Brundle, *Molecular Photoelectron Spectroscopy*, John Wiley & Sons, New York (1970).
9. J. C. Green, *Accts. Chem. Res.*, **27**, 131 (1994).
10. D. K. Bulgin, J. M. Dyke, and A. Morris, *J. Chem. Soc. Faraday Trans. 2*, **72**, 2225 (1976); S. Ebel, H. tom Dieck, and H. Walther, *Inorg. Chim. Acta*, **53**, L101 (1981).

# Molecular Orbitals and Geometrical Perturbation

## 7.1 MOLECULAR ORBITALS OF AH<sub>2</sub>

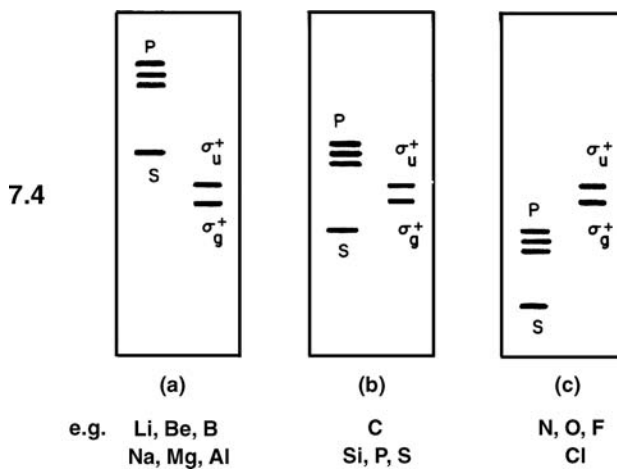
In this chapter, we will do basically two things—examine in some detail the form of the molecular orbitals for an AH<sub>2</sub> molecule and secondly find out how to predict the form and energetic consequences of molecular orbitals when a molecule is distorted via geometric perturbation theory. Furthermore, we see the physical underpinnings of why some molecules distort away from the most symmetrical structures and a technique of how to predict the sense of distortion.

Let us construct the MOs of a linear ( $D_{\infty h}$ ) and bent ( $C_{2v}$ ) AH<sub>2</sub> molecule shown in **7.1** and **7.2**, respectively, where the central atom A contributes four valence atomic orbitals s, x, y, and z. We will construct the MOs based upon the perturbation method of Chapter 3, and so it is convenient to construct AH<sub>2</sub> from A and H···H units. The orbitals of H···H are the in-phase,  $\sigma_g^+$ , and out-of-phase,  $\sigma_u^+$ , combinations of hydrogen s orbitals shown in **7.3**, where the energy gap between  $\sigma_g^+$  and  $\sigma_u^+$  is small since the H···H distance in **7.1** and **7.2** is large in most cases of interest.

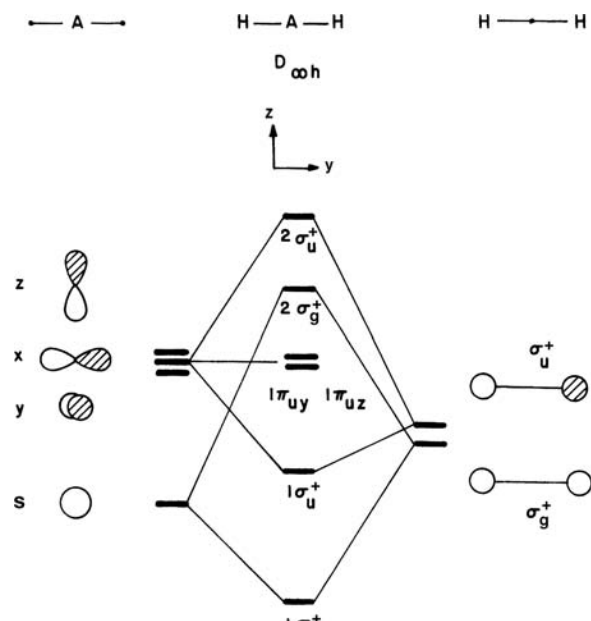


A number of relative ordering patterns conceivable for the orbitals of A and H···H are shown in **7.4**. For example, the orbitals of H···H lie in between the s and p orbitals of A in **7.4b**, which turns out to be relevant when A is carbon, phosphorus,

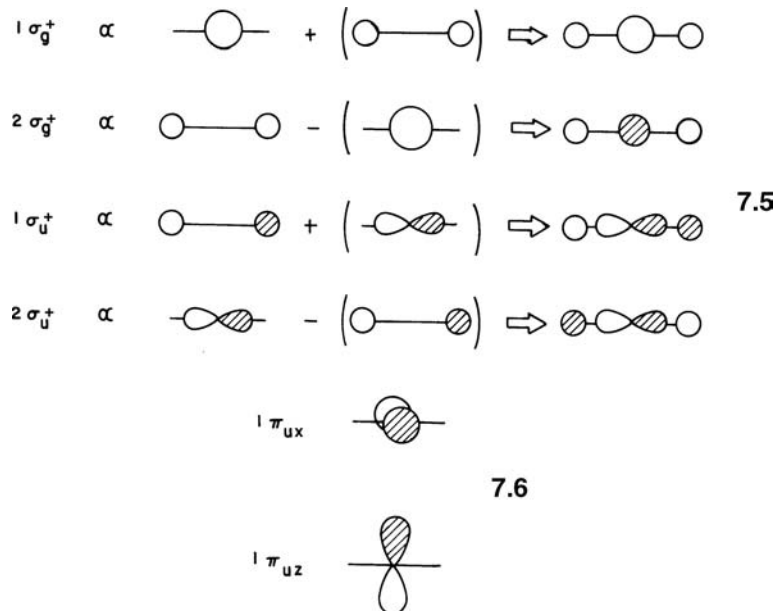
silicon, and so on. The orbitals of A shift upward or downward in energy with respect to those of carbon as A becomes more electropositive (**7.4a**) or electronegative (**7.4c**) than carbon, respectively. A numerical check of where the hydrogen s combinations should be found relative to the central atom may be found by inspection in **2.9** or more quantitatively from Figure 2.4. For simplicity, we will construct the MOs of  $\text{AH}_2$  for the case of **7.4b**.



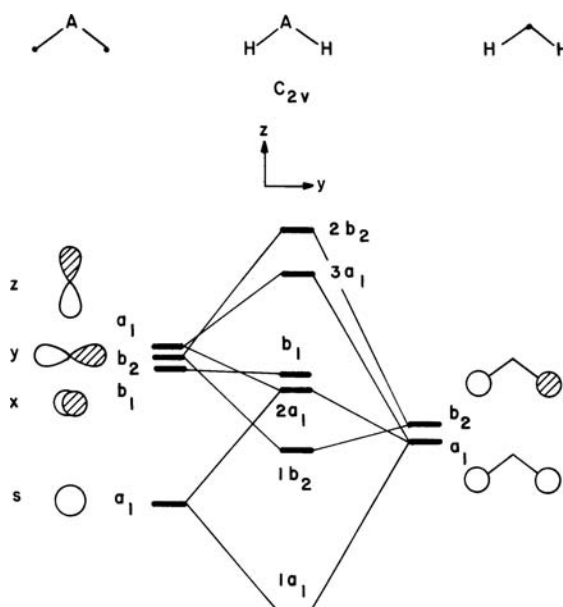
The orbital interaction diagram for linear  $\text{AH}_2$  is shown in Figure 7.1, where the MOs of  $\text{AH}_2$  are easily written down as shown in **7.5**. The s atomic orbital of A forms a bonding and antibonding combination with the  $\sigma_g^+$  orbital of  $\text{H} \cdots \text{H}$ . The y atomic orbital on A interacts with the  $\sigma_u^+$  combination to form bonding and antibonding molecular orbitals. The x and z orbitals of A do not overlap with any of the two orbitals of  $\text{H} \cdots \text{H}$ , so they become the nonbonding orbitals of  $\text{AH}_2$  (**7.6**). The number of nodal planes in the MOs increases upon going to orbitals of higher energy:  $1\sigma_g^+$  has zero;  $1\sigma_u^+$  and  $1\pi_u$  each have one;  $2\sigma_u^+$  has two; and finally there are three nodal planes in  $2\sigma_u^+$ .

**FIGURE 7.1**

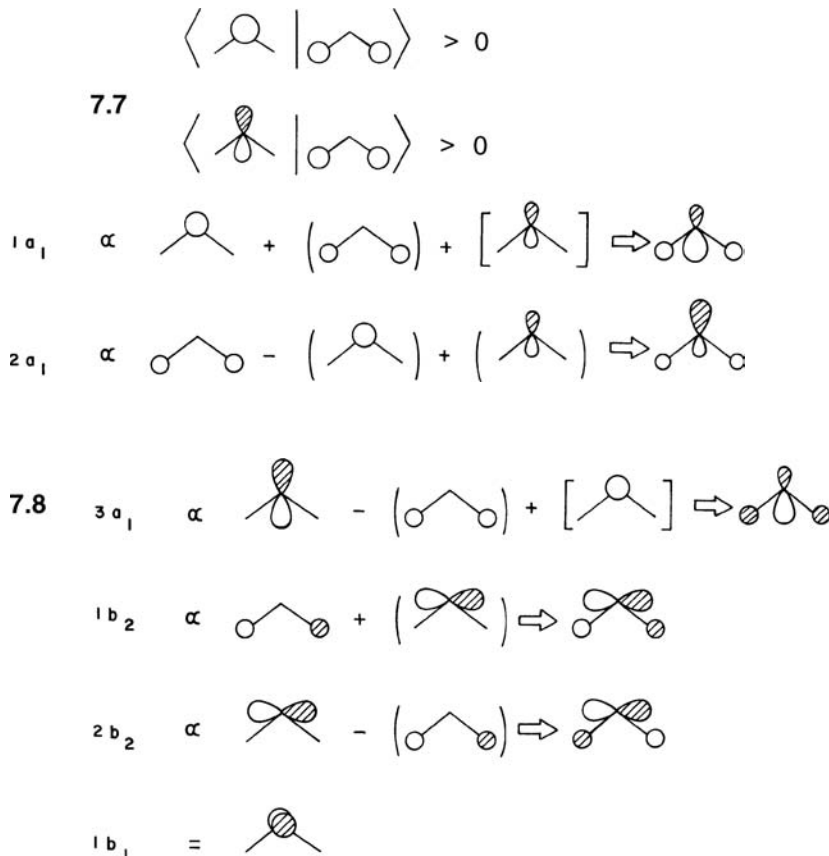
Orbital interaction diagram for linear  $\text{AH}_2$ .



The orbital interaction diagram for bent AH<sub>2</sub> is shown in Figure 7.2. We have already examined in Chapter 4 how to construct the MOs of a bent, C<sub>2v</sub>, AH<sub>2</sub> molecule based upon symmetry arguments alone. The two hydrogen s combinations, now of a<sub>1</sub> and b<sub>2</sub> symmetry, are again not split much in energy since for most cases of interest; the H··H distance is in the nonbonding region. In a bent structure, the overlap of the s and z orbitals of A with the a<sub>1</sub> fragment orbital of H··H is nonzero (7.7) so that this becomes a three-orbital problem; second-order orbital mixings occur between A atom s and z atomic orbitals via overlap with the a<sub>1</sub> orbital of H··H. The MOs of bent AH<sub>2</sub> may be constructed as in 7.8. The basic orbital shapes are the

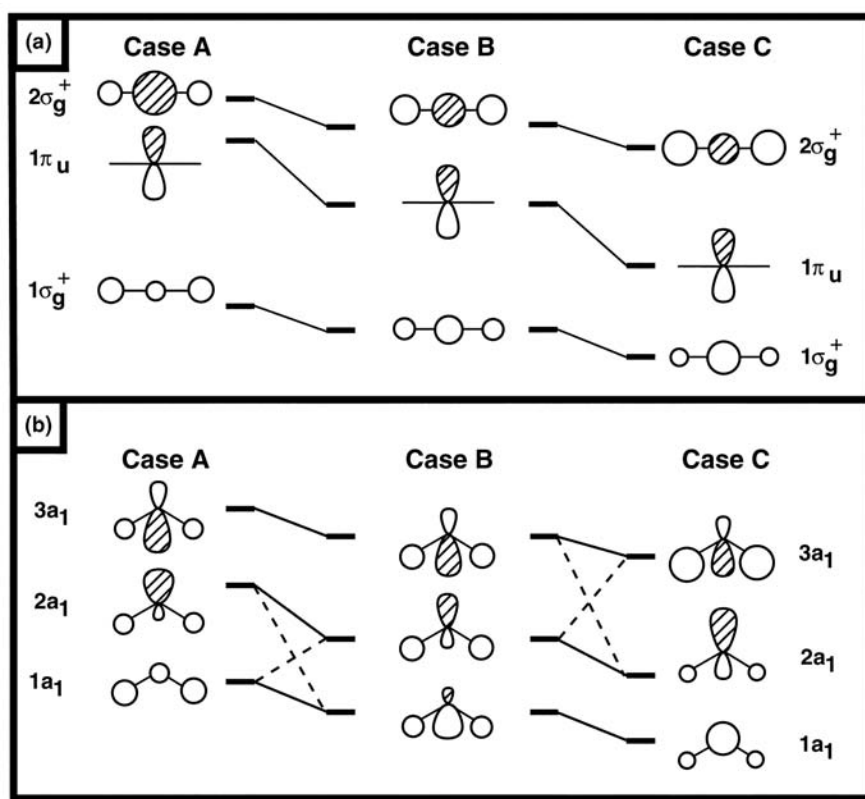
**FIGURE 7.2**

Orbital interaction diagram for bent AH<sub>2</sub>.



same as those for linear  $\text{AH}_2$  (7.5) except for the three of  $a_1$  symmetry. The s and z atomic orbitals of the central atom A mix with  $a_1$  of the  $\text{H} \cdots \text{H}$  fragment to produce a fully bonding ( $1a_1$ ) and a fully antibonding ( $3a_1$ ) molecular orbital. Notice that the z component in each mixes so as to maximize the magnitude of overlap between the central atom and the two hydrogens. The  $2a_1$  molecular orbital is hybridized away from the hydrogens. It remains, like  $1b_1$ , essentially nonbonding. The reader should carefully work through these interactions using the principles from Chapter 3.

Now, let us explore how much the form of the molecular orbitals change in  $D_{\infty h}$  and  $C_{2v}$   $\text{AH}_2$  when the electronegativity of A changes to that in 7.4a or 7.4c. Figure 7.3a highlights the situation for three molecular orbitals,  $1\sigma_g^+$ ,  $2\sigma_g^+$  and one component of  $1\pi_u$ , for the linear  $\text{AH}_2$  system which will figure predominantly in Section 7.3. Here, cases A, B, and C refer to 7.4a–c, respectively. It is a trivial matter to work through these situations using intermolecular perturbation theory; however, it is instructive to use the electronegativity perturbation technique from Chapter 6 starting from case B, in the figure. When the central atom A becomes more electropositive,  $\delta\alpha = (+)$ , so all the three molecular orbitals will rise in energy because  $e^{(1)}$  is always positive. As mentioned in equation 6.8,  $c_{\alpha i}^0$  for  $1\pi_u$  is larger than that for  $1\sigma_g^+$  or  $2\sigma_g^+$  simply because the  $1\pi_u$  molecular orbital is contained exclusively on A. Therefore,  $1\pi_u$  will rise more in energy than the other two molecular orbitals. The  $e^{(2)}$  correction (see equation 6.8) for  $1\sigma_g^+$  is negative, whereas, it is positive for  $2\sigma_g^+$ . Consequently,  $2\sigma_g^+$  will have a larger energy correction than  $1\sigma_g^+$ . Using the phases shown for  $1\sigma_g^+$  and  $2\sigma_g^+$  in Figure 7.3a for case B,  $t_{ji}^{(1)}$  (see equation 6.8) will be positive for  $t_{2\sigma_g^+, 1\sigma_g^+}^{(1)}$ . The coefficients on the hydrogen increase while the s character

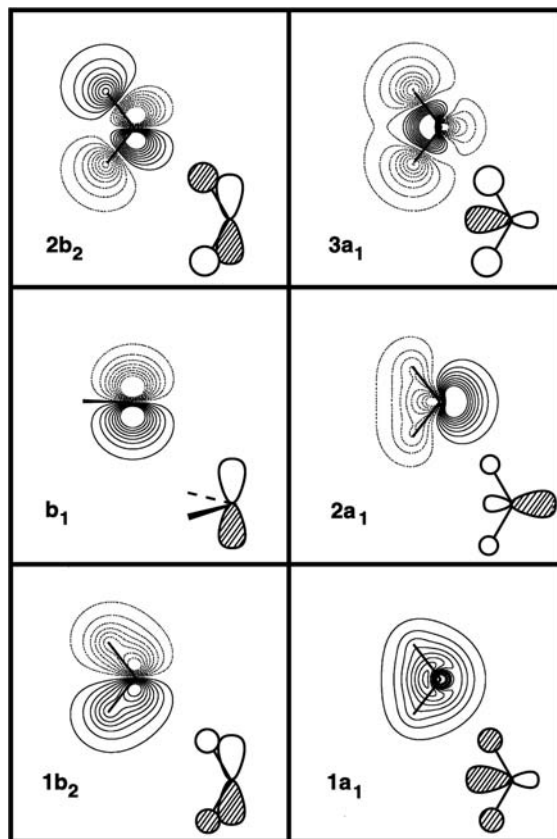
**FIGURE 7.3**

Correlation of some of the AH<sub>2</sub> molecular orbitals in a linear (a), and bent (b) geometry.

on A decreases. Exactly, the opposite occurs in 2σ<sub>g</sub><sup>+</sup>. The reader should work through the analogous situation on going from case B to case C. Now since A is more electronegative than H, 1σ<sub>g</sub><sup>+</sup> is more concentrated on A while 2σ<sub>g</sub><sup>+</sup> is more localized on H. Similar arguments can be advanced for the C<sub>2v</sub> molecule with 1a<sub>1</sub>, 2a<sub>1</sub>, and 3a<sub>1</sub>. The mixing coefficients are a little more difficult to deduce since each molecular orbital has s and p character. Figure 7.3b shows the results. It is worthwhile to list the form of the wavefunctions which evolve from an intermolecular perturbation theory perspective as

$$\begin{array}{ll}
 \text{Case A} & 3a_1 \propto z - (\sigma_g^+) + [s] \\
 & 2a_1 \propto s - (\sigma_g^+) - [z] \\
 & 1a_1 \propto \sigma_g^+ + (s) + (z) \\
 \text{Case B} & 3a_1 \propto z - (\sigma_g^+) + [s] \\
 & 2a_1 \propto \sigma_g^+ - (s) + (z) \\
 & 1a_1 \propto s + (\sigma_g^+) + (z) \\
 \text{Case C} & 3a_1 \propto \sigma_g^+ - (s) - (z) \\
 & 2a_1 \propto z + (\sigma_g^+) - (s) \\
 & 1a_1 \propto s + (\sigma_g^+) + (z).
 \end{array}$$

There is a kind of avoided crossing between the 1a<sub>1</sub> and 2a<sub>1</sub> molecular orbitals in terms of their composition on going from case A to case B. Likewise, an analogous crossing occurs between 3a<sub>1</sub> and 2a<sub>1</sub> for going from case B to case C. These are indicated by the dashed lines in Figure 7.3b. As a specific example, the valence molecular orbitals of H<sub>2</sub>O are plotted in Figure 7.4. These are again the results of an

**FIGURE 7.4**

Contour plots of the valence orbitals in  $\text{H}_2\text{O}$ . Solid and dashed lines refer to positive and negative values of the wavefunction, respectively.

ab initio calculation with a STO-3G basis set. Notice the similarity to the resultant MOs that were derived in **7.8** and reproduced to the lower right of each contour drawing. The important result here is that while the relative energies of the molecular orbitals change with different A atoms, and the relative weight of each atomic coefficient may change, the basic shape of the molecular orbitals is not altered. It is this “universal” nature that makes LCAO molecular orbital theory a powerful tool. The changes in localization or energy can readily be established by perturbation theory.

With the molecular orbitals of linear and bent  $\text{AH}_2$  derived separately, it is important to ask how the orbitals of one geometry are related to those of the other. In order to find this relationship, we need to understand how the MOs of a molecule are modified as a result of geometrical distortion.

## 7.2 GEOMETRICAL PERTURBATION

Suppose that a molecule undergoes a geometrical distortion. We can examine how the molecular orbitals of one geometry are related to those of another by considering the structural distortion as a perturbation. The molecular geometries before and after distortion are described as the unperturbed and perturbed structures, respectively. Given any two geometries of a molecule, either one may in principle be considered as the perturbed one. In practice, however, it leads to a substantially simpler analysis if the molecular geometry of the lower symmetry is chosen as the perturbed one. Group theory tells us in a simple, straightforward way

how to construct the molecular orbitals of molecules in a highly symmetric geometry. Geometrical perturbation theory can be used to see how the shapes and energies of the molecular orbitals change upon going to a less symmetric (perhaps the experimental) geometry.

As shown in Section 3.2, the first-order mixing coefficient and the first- and second-order energy terms are given by

$$\psi_i = \psi_i^0 + \sum_{j \neq i} t_{ji}^{(1)} \psi_j^{(0)} \quad (7.1)$$

where

$$t_{ji}^{(1)} = \frac{\tilde{H}_{ij} - e_i^0 \tilde{S}_{ij}}{e_i^0 - e_j^0} \propto \frac{-\tilde{S}_{ij}}{e_i^0 - e_j^0}$$

$$e_i = e_i^0 + e_i^{(1)} + e_i^{(2)} \quad (7.2)$$

where

$$e_i^{(1)} = \tilde{H}_{ii} - e_i^0 \tilde{S}_{ii} \propto -\tilde{S}_{ii}$$

and

$$e_i^{(2)} = \sum_{j \neq i} \frac{(\tilde{H}_{ij} - e_i^0 \tilde{S}_{ij})^2}{e_i^0 - e_j^0} \propto \sum_{j \neq i} \frac{-\tilde{S}_{ij}^2}{e_i^0 - e_j^0} \quad (7.3)$$

The matrix elements  $\tilde{H}_{ij}$  and  $\tilde{S}_{ij}$  are defined as

$$\begin{aligned} \tilde{H}_{ii} &= \sum_{\mu} \sum_{\nu} c_{\mu i}^0 \delta H_{\mu \nu} c_{\nu i}^0 \\ \tilde{H}_{ij} &= \sum_{\mu} \sum_{\nu} c_{\mu i}^0 \delta H_{\mu \nu} c_{\nu j}^0 \end{aligned} \quad (7.4)$$

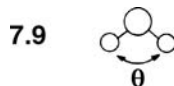
$$\begin{aligned} \tilde{S}_{ii} &= \sum_{\mu} \sum_{\nu} c_{\mu i}^0 \delta S_{\mu \nu} c_{\nu i}^0 \\ \tilde{S}_{ij} &= \sum_{\mu} \sum_{\nu} c_{\mu i}^0 \delta S_{\mu \nu} c_{\nu j}^0 \end{aligned} \quad (7.5)$$

where  $\delta H_{\mu \nu}$  and  $\delta S_{\mu \nu}$  are the changes in the resonance and overlap integrals, respectively, between atomic orbitals  $\mu$  and  $\nu$ .

Note that it is the MO coefficients of the unperturbed geometry (i.e.,  $c_{\mu i}^0$  and  $c_{\nu j}^0$ ) and the change in the matrix elements (i.e.,  $\delta H_{\mu \nu}$  and  $\delta S_{\mu \nu}$ ) which define the  $\tilde{H}_{ij}$  and  $\tilde{S}_{ij}$  terms. If the two geometries under consideration are identical,  $\delta H_{\mu \nu} = \delta S_{\mu \nu} = 0$  for all  $\mu$  and  $\nu$ . Consequently,  $\tilde{H}_{ij} = \tilde{S}_{ij} = (\tilde{H}_{ij} - e_i^0 \tilde{S}_{ij}) = 0$  for all  $\mu$  and  $\nu$ . A geometrical perturbation makes most  $\delta H_{\mu \nu}$  and  $\delta S_{\mu \nu}$  elements different from zero, so that the values of  $\tilde{H}_{ij}$  and  $\tilde{S}_{ij}$  are nonzero. Thus, the value of  $(\tilde{H}_{ij} - e_i^0 \tilde{S}_{ij})$  will often be nonzero for a geometrical perturbation. As in the previous two cases of perturbation theory, we have specifically neglected any two-electron factors, for example, the effect of Coulomb repulsion and charging terms that may change as a function of the geometry or environment.

The first-order energy correction,  $e_i^{(1)}$  is related to changes between atomic orbital overlap integrals when the geometry is modified. In general,  $e_i^{(1)}$  is stabilizing (i.e.,  $e_i^{(1)} < 0$ ) if the value of  $\tilde{S}_{ii}$  is positive, but destabilizing (i.e.,  $e_i^{(1)} > 0$ ) if the value of  $\tilde{S}_{ii}$  is negative. The value of  $\tilde{S}_{ii}$  is positive by enhancing a positive overlap, which strengthens bonding on perturbation or by diminishing a negative overlap, which weakens antibonding effects. Similarly, the value of  $\tilde{S}_{ii}$  is negative by diminishing a

positive overlap, which weakens bonding, or by enhancing a negative overlap, which enhances antibonding effects. For example, the  $1\sigma_g^+$  and  $1\pi_{uz}$  orbitals in linear  $\text{AH}_2$  are normalized to unity. Upon the linear to bent (i.e.,  $D_{\infty h} \rightarrow C_{2v}$ ) distortion, the  $1\sigma_g^+$  orbital does not remain normalized to unity since the overlap between the two s orbitals increases as indicated in 7.9. However, the  $1\pi_{uz}$  orbital remains normalized to unity because it has no orbital contribution from hydrogen. Thus, we obtain the results shown in 7.10 and 7.11 for  $\tilde{S}_{ii}$  in these two cases. According to 7.10, the first-order energy  $e_i^{(1)}$  is stabilizing (i.e., negative) for  $1\sigma_g^+$  since the value of  $\tilde{S}_{ii}$  becomes positive on the  $D_{\infty h} \rightarrow C_{2v}$  distortion. 7.11 shows that the first-order energy  $e_i^{(1)}$  is zero for  $1\pi_{uz}$  since the value of  $\tilde{S}_{ii}$  is zero during the  $D_{\infty h} \rightarrow C_{2v}$  distortion.



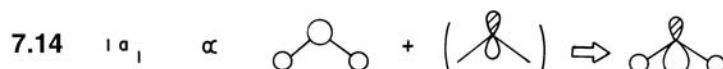
7.10  $\langle \text{---} | \text{---} \rangle > 1$

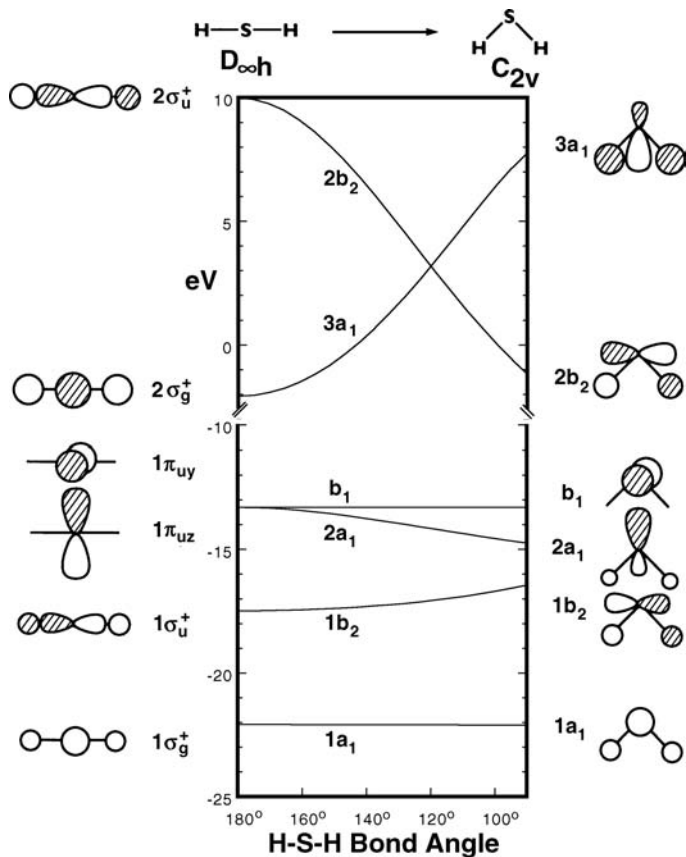
7.11  $\langle \text{---} | \text{---} \rangle = 1$

The first-order mixing coefficient,  $t_{ji}^{(1)}$ , and the second-order energy correction,  $e_i^{(2)}$ , reflect that molecular orbitals, formerly orthogonal, now may not remain so as a result of a change in the geometry and consequently can mix with each other. The magnitudes of  $t_{ji}^{(1)}$  and  $e_i^{(2)}$  are determined by the term  $(\tilde{H}_{ij} - e_i^0 \tilde{S}_{ij})$ . This is in general negative if the value of  $\tilde{S}_{ij}$  increases from zero, but positive if the value of  $\tilde{S}_{ij}$  decreases from zero. This stems from the fact that  $\tilde{H}_{ij} \propto -\tilde{S}_{ij}$ , and the absolute magnitude of  $\tilde{H}_{ij}$  is generally larger than that of  $e_i^0 \tilde{S}_{ij}$ . Therefore, equation 7.1 shows that, if  $\tilde{S}_{ij} > 0$ , the coefficient  $t_{ji}^{(1)}$  is positive for the mixing of an upper level  $\psi_j^0$  into the lower level  $\psi_i^0$  ( $e_i^0 - e_j^0 < 0$ ) while the coefficient  $t_{ji}^{(1)}$  is negative for the mixing of a lower level  $\psi_j^0$  into an upper level  $\psi_i^0$  ( $e_i^0 - e_j^0 > 0$ ). In addition, equation 7.3 shows that a given level  $\psi_i^0$  is lowered in energy by interaction with an upper level  $\psi_j^0$  but raised in energy by interaction with a lower level  $\psi_j^0$ . For example, the  $1\sigma_g^+$  and  $1\pi_{uz}$  orbitals of  $\text{AH}_2$  are orthogonal in a linear structure (7.12), but do not remain orthogonal in a bent structure (7.13) since the overlap between hydrogen s and z on A is nonzero (the overlap between s and z on A is still zero of course since the atomic orbitals are orthonormal). Thus, the  $1a_1$  orbital of bent  $\text{AH}_2$  can be approximately described in terms of  $1\sigma_g^+$  and  $1\pi_{uz}$  as 7.14, where use is made of the fact that, in a linear structure,  $1\sigma_g^+$  lies lower in energy than  $1\pi_{uz}$  (see Figure 7.3a). With respect to the  $1\sigma_g^+$  level of linear  $\text{AH}_2$ , the  $1a_1$  orbital of bent  $\text{AH}_2$  is lowered in energy since the first- and second-order energy terms are both stabilizing.

7.12  $\langle \text{---} | \text{---} \rangle = 0$

7.13  $\langle \text{---} | \text{---} \rangle = \langle \text{---} | \text{---} \rangle > 0$



**FIGURE 7.5**

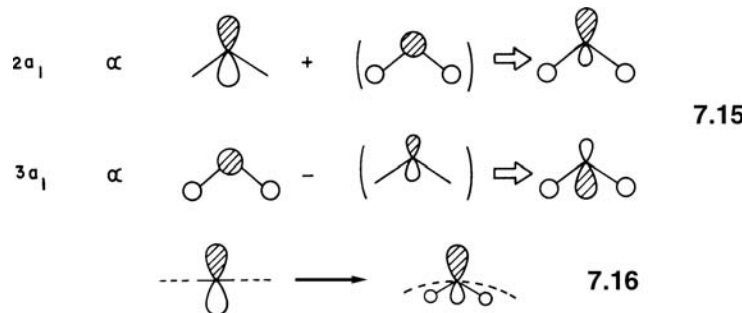
Walsh diagram for bending in  $\text{H}_2\text{S}$ .

### 7.3 WALSH DIAGRAMS

Figure 7.5 shows the energetic variation of the molecular orbitals for  $\text{H}_2\text{S}$  as a function of the H—S—H bond angle. Here, the MOs of linear and bent  $\text{H}_2\text{S}$  are labeled according to their point group symmetry. Diagrams such as those of Figure 7.5 which show how the MO levels of a molecule vary as a function of geometrical change are known as Walsh diagrams [1–5]. The specific computational method used here and for the rest of the Walsh diagrams in this book is the extended Hückel method. This is a one-electron theory where the  $H_{\mu\nu}$  terms in the Hamiltonian are given by the Wolfsberg–Helmholz formula (equation I.19). Thus, it is an analytical technique which nicely matches the perturbation formulation used here. Other levels of theory certainly can be used [4,5]. Note the break in the energy scale above  $-10 \text{ eV}$  in Figure 7.5. The two antibonding MOs are energetically well separated from the nonbonding and bonding valence orbitals.  $1\sigma_u^+$  is raised in energy upon distortion; overlap between the  $y$  atomic orbital on S and the hydrogen  $s$  atomic orbitals is lowered (see Figure I.5). This is a bonding orbital, so  $e_i^{(1)}$  is positive, and  $1b_2$  lies higher in energy than  $1\sigma_u^+$ . The situation for  $2\sigma_u^+$  is analogous; the decrease in the atomic orbital overlap in this antibonding molecular orbital when  $\text{H}_2\text{S}$  bends causes  $2\sigma_u^+$  to be stabilized ( $e_i^{(1)}$  is negative).  $D_{\infty h} \rightarrow C_{2v}$  distortion leads to a decrease in antibonding between the  $s$  and  $y$  orbitals but also to an increase in the antibonding between the two  $s$  orbitals on hydrogen. The former predominates over the latter in magnitude because of the large  $\text{H}\cdots\text{H}$  distance, so the net effect is that the  $2\sigma_u^+$  level is lowered by the  $D_{\infty h} \rightarrow C_{2v}$  distortion. The slope associated with  $2b_2$

is in fact much larger than that for  $1b_2$ . Equations 7.4 and 7.5 show that the absolute magnitude of  $\tilde{H}_{ij}$  and  $\tilde{S}_{ij}$  depend upon the magnitudes of the atomic orbital mixing coefficients which are larger in antibonding MOs ( $2b_2$ ) than in bonding counterparts ( $1b_2$ ) because of the normalization condition. The  $1\pi_{uy}$  level is not affected by the  $D_{\infty h} \rightarrow C_{2v}$  distortion since its overlap with other orbitals is zero at all points along the distortion coordinate (it is the single MO with  $b_1$  symmetry).

In Section 7.2, we showed why the  $1a_1$  orbital is lower in energy than the  $1\sigma_g^+$  orbital. As one can see from Figure 7.5, this effect is small indeed. For the  $1\pi_{uz}$  level, the first-order energy term  $e_i^{(1)}$  is zero according to 7.11. However, the overlap between  $1\pi_{uz}$  and  $2\sigma_g^+$  is nonzero in a bent structure (7.13), thereby leading to an orbital mixing between them and to nonzero second-order energy terms  $e_i^{(2)}$ . Thus, the  $2a_1$  and  $3a_1$  orbitals are lowered and raised with respect to  $1\pi_{uz}$  and  $2\sigma_g^+$ , respectively. The nodal properties of the  $2a_1$  and  $3a_1$  orbitals may be constructed as shown in 7.15, where the mixing of  $1\sigma_g^+$  into  $1\pi_{uz}$  or  $2\sigma_g^+$  was neglected. The reader can readily verify that  $1\sigma_g^+$  will mix into  $1\pi_{uz}$  with a phase opposite to that shown for  $1\sigma_g^+$  in 7.5. Therefore, the atomic s character on A is reinforced in  $2a_1$  by the first-order mixings while the atomic coefficients for the hydrogens become quite small. The nodal surfaces of  $1\pi_{uz}$  and  $2a_1$  are shown by the dashed lines in 7.16. Thus, the hydrogens basically follow the nodal surface in  $2a_1$  on bending. This reemphasizes our previous comment that  $2a_1$  is considered to be nonbonding.



But is it always true that  $2a_1$  will be stabilized upon bending? In other words, is the mixing of  $2\sigma_g^+$  into  $1\pi_u$  (which leads to stabilization of  $2a_1$ ) always larger than the absolute magnitude of  $1\sigma_g^+$  mixing into  $1\pi_u$  (which leads to destabilization of  $2a_1$ )? There are two effects to consider in equation 7.3, namely, the overlap and energy gap terms. One should refer back to Figure 7.3. For case A,  $2\sigma_g^+$  lies much closer to  $1\pi_u$  than  $1\sigma_g^+$  does. Because of the electronegativity difference between H and A,  $1\sigma_g^+$  is more localized on H, and this will lead to a larger value for  $\tilde{S}_{1\sigma_g^+, 1\pi_u}$ . However, recall that the coefficients associated with antibonding  $2\sigma_g^+$  will be intrinsically larger than those for  $1\sigma_g^+$ , which leads to a larger value for  $\tilde{S}_{2\sigma_g^+, 1\pi_u}$ . The two effects act in opposite directions and so  $\tilde{S}_{1\sigma_g^+, 1\pi_u} \approx \tilde{S}_{2\sigma_g^+, 1\pi_u}$ . For case C, the energy gaps are comparable, but the electronegativity and the antibonding factors work to make  $\tilde{S}_{1\sigma_g^+, 1\pi_u} \ll \tilde{S}_{2\sigma_g^+, 1\pi_u}$ . Case B simply represents an intermediate situation where energy gap and overlap arguments favor the mixing of  $2\sigma_g^+$  over  $1\sigma_g^+$  into  $1\pi_{uz}$ . Thus, the important result is that no matter where one is in the Periodic Table,  $2a_1$  is always stabilized when the H—A—H bond angle decreases. The rest of the molecular orbitals for other molecules also behaves in a way that matches the results of Figure 7.5. There is a universality associated with Walsh diagrams, not in terms of quantitative, but in terms of qualitative details that can be exploited.

As we will show extensively throughout this book, a major function of a Walsh diagram is to account for the structural regularity observed for a series of related molecules with the same number of valence electrons, and to see how molecules change structure with the number of electrons or spin state. Walsh's original rule for predicting molecular shapes may simply be stated as follows: A molecule adopts the structure that best stabilizes the HOMO. If the HOMO is unperturbed by the structural change under consideration, the occupied MO lying closest to it governs the geometrical preference.

Let us illustrate Walsh's rule by examining the shapes of  $\text{AH}_2$  molecules based on Figure 7.5. The HOMO of a four-electron  $\text{AH}_2$  molecule is  $1\sigma_u^+$ , and this orbital is destabilized on bending so that  $\text{BeH}_2$  is linear. The  $2a_1$  orbital of  $\text{AH}_2$  lies lower in a bent structure than  $1\pi_u$  while  $b_1$  of  $\text{AH}_2$  is energetically unaffected by the  $D_{\infty h} \rightarrow C_{2v}$  distortion. Consequently, the shape of  $\text{AH}_2$  molecules with 5–8 electrons is governed by the energetics of  $2a_1$ . Thus,  $\text{BH}_2$ ,  $\text{CH}_2$ ,  $\text{NH}_2$ , and  $\text{H}_2\text{O}$  all adopt a  $C_{2v}$  structure (see Table 7.1) [1,6]. Walsh's rule is predicated upon the supposition that the relative energy of a molecule is given by the sum of the occupied orbital energies (weighted by their occupancy). This is precisely what occurs in extended Hückel theory. As we shall see in Chapter 8, this is not the whole story. It is also dependent on a more delicate factor, namely, that the slope associated with the molecular orbitals will increase as one progresses from the lower to higher-lying MOs (discounting those situations where  $e_i^{(1)}$  and  $e_i^{(2)}$  terms are zero due to symmetry reasons). There is no theoretical justification for this behavior except to note that higher lying orbitals will have larger atomic orbital coefficients because of the orthogonality constraint and this will lead to larger values of  $\tilde{S}_{ii}$  (and  $|e_i^{(1)}|$ ). One can easily see from Figure 7.5 that the slopes associated with the  $3a_1$ ,  $2a_1$ , and  $1a_1$  levels decrease in the order  $3a_1 > 2a_1 > 1a_1$ . Returning to Table 7.1, in a more quantitative sense, the H—A—H bond angle should then be sensitive to the number of electrons occupying  $2a_1$ .  $\text{BH}_2$  and the  ${}^3\text{B}_1$  electronic state of  $\text{CH}_2$  have one electron in  $2a_1$ . Their bond angles (Table 7.1) are similar and much larger than the  ${}^1\text{A}_1$  state of  $\text{CH}_2$ ,  $\text{NH}_2$ , and  $\text{H}_2\text{O}$  which have two electrons in  $2a_1$  and, in turn, have essentially identical angles. The same situation applies for the second row molecules in the bottom half of the table. What is clearly different is that with 6–8 valence electrons the second row molecules all have more acute bond angles than their isoelectronic counterparts. We shall tackle this issue in Section 7.4. Walsh diagrams are also useful for an understanding of the shape of molecules in electronically excited states. For example, the ground electronic state of  $\text{NH}_2$  is of  ${}^2\text{B}_1$  symmetry

**TABLE 7.1** Typical Bond Angles in  $\text{AH}_2$  Molecules [6]

Molecule	Electronic Configuration	H—A—H Bond Angle
$\text{BeH}_2$	$(1\sigma_g^+)^2 (1\sigma_u^+)^2$	$180^\circ$
$\text{BH}_2$	$(1a_1)^2 (1b_2)^2 (2a_1)^1$	$127^\circ$
$\text{CH}_2^a$	$(1a_1)^2 (1b_2)^2 (2a_1)^1 (b_1)^1$	$134^\circ$
$\text{CH}_2^b$	$(1a_1)^2 (1b_2)^2 (2a_1)^2$	$102^\circ$
$\text{NH}_2$	$(1a_1)^2 (1b_2)^2 (2a_1)^2 (b_1)^1$	$103^\circ$
$\text{OH}_2$	$(1a_1)^2 (1b_2)^2 (2a_1)^2 (b_1)^2$	$104^\circ$
$\text{MgH}_2$	$(1\sigma_g^+)^2 (1\sigma_u^+)^2$	$180^\circ$
$\text{AlH}_2$	$(1a_1)^2 (1b_2)^2 (2a_1)^1$	$119^\circ$
$\text{SiH}_2^a$	$(1a_1)^2 (1b_2)^2 (2a_1)^1 (b_1)^1$	$118^\circ$
$\text{SiH}_2^b$	$(1a_1)^2 (1b_2)^2 (2a_1)^2$	$93^\circ$
$\text{PH}_2$	$(1a_1)^2 (1b_2)^2 (2a_1)^2 (b_1)^1$	$92^\circ$
$\text{SH}_2$	$(1a_1)^2 (1b_2)^2 (2a_1)^2 (b_1)^2$	$92^\circ$

<sup>a</sup>For the  ${}^3\text{B}_1$  state.

<sup>b</sup>For the  ${}^1\text{A}_1$  state.

with the electronic configuration of  $\cdots(2a_1)^2(b_1)^1$  and a bond angle of  $103^\circ$ . The first excited state,  ${}^2A_1$ , with  $a \cdots(2a_1)^1(b_1)^2$  configuration should have a larger bond angle since on excitation the electron is removed from the  $2a_1$  orbital and placed in  $b_1$ . In fact this is the case [6]; the bond angle for the  ${}^2A_1$  state is  $144^\circ$ . The same situation applies for the isoelectronic  $\text{PH}_2$  molecule [6]. It has a  $92^\circ$  bond angle in the  ${}^2B_1$  state and this enlarges to  $123^\circ$  for the  ${}^2A_1$  state.

## 7.4 JAHN–TELLER DISTORTIONS

In Section 7.3, we showed an important use of a Walsh diagram in predicting molecular shapes by simply focusing on the behavior of the HOMO (or an occupied MO lying close to it). Another important facet of a Walsh diagram lies in the ability to predict geometrical distortions by knowing how the HOMO (or an occupied MO lying close to it) is affected by the LUMO (or an unoccupied MO lying close to it) when the molecule undergoes some geometrical perturbation.

The ideas of Jahn and Teller [7–9], published in 1937, have had a strong influence on the way both molecular and solid state structures are viewed in electronic terms. Their initial ideas were centered around the geometric stability of molecules and ions in solids described by degenerate electronic states, but the approach has been taken further by others [8]. The Jahn–Teller theorem (we shall see later that strictly this should be called the first order Jahn–Teller theorem) is often stated in the following way. An orbitally degenerate electronic state of a nonlinear molecule is unstable with respect to a distortion which removes the degeneracy. The theory Jahn and Teller derived in fact specified the symmetry species of the “Jahn–Teller active” vibration and thus the possible structures of the distorted molecule or ion. They also noted that if the degeneracy arises through occupation of energy levels which have little effect on the bonding of the molecule (i.e., weakly bonding or antibonding, or nonbonding) then the instability is only a slight one.

The energy of the electronic ground state ( $|\Psi_i\rangle$ ) can be expanded as a function of some distortion coordinate  $q$ ,

$$E_i(q) = E_i^0 + E_i^{(1)}(q) + \frac{1}{2}E_i^{(2)}(q^2) + \dots \quad (7.6)$$

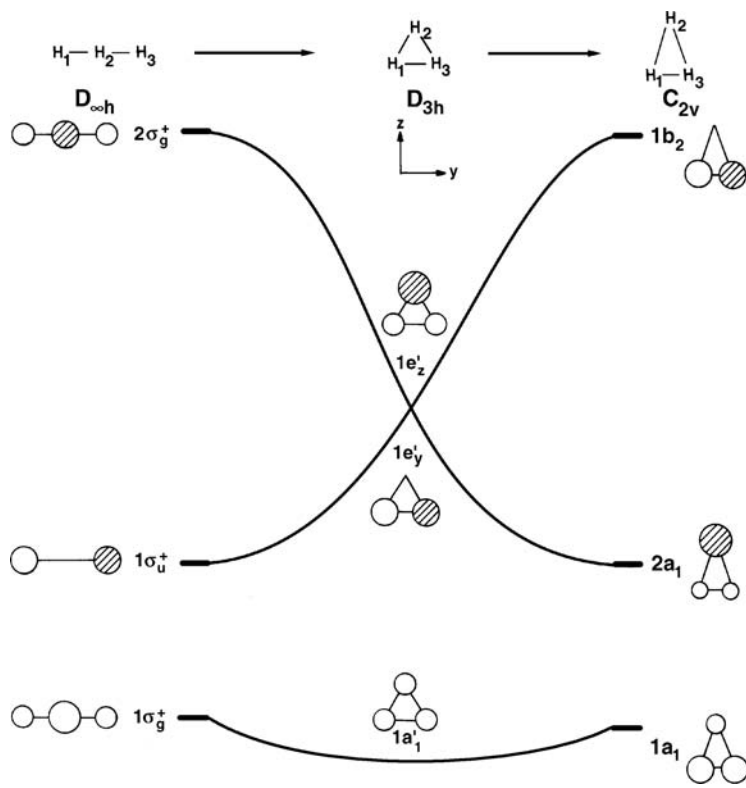
and evaluation of the relevant energy terms obtained by using perturbation theory. The result is simple to evaluate if the Hamiltonian,  $H$ , itself is expanded in a similar way,

$$H = H_i^0 + \left(\frac{\partial H}{\partial q}\right)_i q + \frac{1}{2}\left(\frac{\partial^2 H}{\partial q^2}\right)_i q^2 + \dots \quad (7.7)$$

Using the second and third terms of this equation as a perturbation then

$$\begin{aligned} E_i(q) &= E_i^0 + q\langle\Psi_i|\partial H/\partial q|\Psi_i\rangle + \frac{q^2}{2}\langle\Psi_i|\partial^2 H/\partial q^2|\Psi_i\rangle \\ &\quad + q^2 \sum_{j \neq i} \frac{\langle\Psi_i|\partial H/\partial q|\Psi_j\rangle^2}{E_i^0 - E_j^0} + \dots \end{aligned} \quad (7.8)$$

The first term represents the zero-order energy, but there then follow three terms, one in first order ( $q$ ) and two in second order ( $q^2$ ). Symmetry arguments allow rapid access to results of interest.

**FIGURE 7.6**

Walsh diagram for the MO levels of linear, equilateral, and isosceles triangular  $\text{H}_3$ .

#### 7.4.1 First-Order Jahn–Teller Distortion

Consider initially the first order term,  $q\langle\Psi_i|\partial H/\partial q|\Psi_i\rangle$ , for nondegenerate electronic states  $|\Psi_i\rangle$ . Since the Hamiltonian operator must be totally symmetric, for this term to be nonzero the symmetry representation of  $q$ ,  $\Gamma_q$ , must be contained in the symmetric direct product  $\Gamma_{\psi_i} \otimes \Gamma_{\psi_i}$  ( $= \Gamma_i \otimes \Gamma_i$ ). In all point groups direct products of nondegenerate representations lead to the totally symmetric representation. A totally symmetric vibration does not change the point group of the molecule. It may lead to a change in some of the bond lengths which may be readily absorbed into  $E_i^0$  by changing the reference geometry. Thus, a non-degenerate state is stable with respect to a distortion which lowers the symmetry. More interesting is the case for degenerate  $|\Psi_i\rangle$ , because an energy lowering by distortion is possible.

Shown in Figure 7.6 is the Walsh diagram for the equilateral triangle to linear or isosceles triangle (i.e.,  $C_{2v} \leftarrow D_{3h} \rightarrow D_{\infty h}$ ) distortion in a simple three-center system. It predicts that the two-electron molecule  $\text{H}_3^+$  should be an equilateral triangle while a four-electron one,  $\text{H}_3^-$ , should be linear or an isosceles triangle. In a  $D_{3h}$  structure, the HOMO of  $\text{H}_3^-$  is doubly degenerate and half-filled. The degeneracy is lifted by the  $D_{3h} \rightarrow D_{\infty h}$  or  $D_{3h} \rightarrow C_{2v}$  distortions since it stabilizes one component of the  $e'$  set in each of the two directions. Throughout the  $D_{3h} \rightarrow D_{\infty h}$  distortion the overlap of  $1e'_y$  with  $1e'_z$  or  $1a'_1$  vanishes, so that the stabilization of the  $1e'_y$  level is caused by a first-order energy change which results from decreasing the extent of antibonding interactions in the  $1e'_y$  orbital. The same is true for the distortion to the  $C_{2v}$  structure. This instability of  $D_{3h} \text{H}_3^-$  is an example of a first-order Jahn–Teller distortion.

A similar viewpoint arises from a state picture. There are two electrons in the  $1e'$  set for the  $D_{3h} \text{H}_3^-$  molecule so the possible electronic states are  ${}^3A'_2$ ,  ${}^1A'_1$ , and  ${}^1E'$ . Consider first the two  $A$  states. The symmetric direct product of  $a'_1$  or  $a'_2$  leads

to  $a_1'$ , so that both  $^3A'_2$  and  $^1A'_1$  states are stable with respect to a symmetry-lowering distortion. The symmetric direct product of  $e'$  leads to  $a_1' + e'$ , so a vibration of  $e'$  symmetry may lower the energy of the molecule. Appendix III shows two  $e'$  modes for the  $D_{3h}$   $A_3$  class of molecules. The  $e'$  vibrations lead to the  $C_{2v}$  and linear structures in Figure 7.6. Thus, for this case there is a nonzero value of the first-order term,  $\langle \Psi_i | \partial H / \partial q | \Psi_i \rangle$ .

Jahn and Teller worked through most of the important molecular point groups and showed that this result applies to all of them. Only for linear point groups is this first-order term always zero. This symmetry result leads to the first order Jahn–Teller theorem, namely, that orbitally (as distinct from spin) degenerate electronic states of nonlinear molecules will distort so as to remove the degeneracy. The presence of an orbitally degenerate electronic state is usually signaled by asymmetric occupation of degenerate energy levels as in the  $D_{3h}$ ,  $H_3^-$  example. This, however, is not always the case as we will see below. There are two important comments to make at this point. (i) The arguments are symmetry-based ones. This means that no prediction can be made concerning the magnitude of the effect. (ii) There are infinite ways of writing the normal modes of a degenerate vibration, just as for a degenerate wavefunction. What the distortion actually looks like is not predicted by the theorem, only its symmetry.

#### 7.4.2 Second-Order Jahn–Teller Distortion

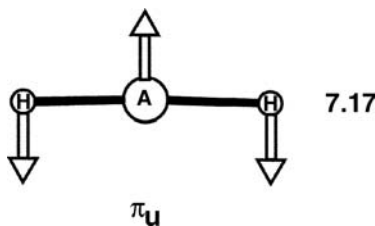
There are two parts to the expression for the second-order term in the energy of equation 7.8,  $E_i^{(2)}(q^2)$ .  $\langle \Psi_i | \partial^2 H / \partial q^2 | \Psi_i \rangle$  is the classical force constant which describes motion of the nuclei in the electronic state  $|\Psi_i\rangle$ , namely, the frozen electronic charge distribution of the undistorted,  $q = 0$ , structure. The second term,  $\sum_{j \neq i} \langle \Psi_i | \partial H / \partial q | \Psi_j \rangle^2 / (E_i^0 - E_j^0)$  is always negative (i.e., stabilizing) since  $E_i^0$  represents the ground electronic state. One can see that the stabilization occurs as a result of mixing an excited state ( $|\Psi_j\rangle$ ) into the electronic ground state. The sign of  $E_i^{(2)}(q^2)$  is thus set by the relative magnitudes of these two terms. The energy gap expression  $E_i^0 - E_j^0$  appears in the denominator, so that states  $|\Psi_j\rangle$  lying close to the ground state will be the most important for the energy stabilization. If the lowest lying one of these is of the correct symmetry for  $\langle \Psi_i | \partial^2 H / \partial q^2 | \Psi_i \rangle$  to be nonzero ( $\Gamma_q = \Gamma_i \otimes \Gamma_j$ ), then the lead term in this expansion can become important and  $E_i^{(2)}(q^2)$  may become negative. As a result the system will now distort away from the symmetrical structure along the coordinate ( $\Gamma_q$ ) whose symmetry is set by this symmetry prescription. There are two uses of the second-order term: one termed the pseudo Jahn–Teller effect and the other the second-order Jahn–Teller effect [3].

The pseudo Jahn–Teller effect examines the stability of nondegenerate electronic states which arise from a single electronic configuration. Square  $H_4$  with four electrons has the same type of orbital occupation pattern for the HOMO as  $H_3^-$  but its electron configuration does not lead to a degenerate electronic ground state (see Chapter 5.3). Instead the electronic states are  $^3A_{2g} + ^1A_{1g} + ^1B_{1g} + ^1B_{2g}$ . (This is a result restricted to a small number of point groups including both  $D_{4h}$  and  $D_{8h}$ .) In the singlet manifold, the lowest state is probably  $^1B_{1g}$ , followed by two low-lying excited states,  $^1A_{1g} + ^1B_{2g}$ . Thus,  $\Gamma_q = b_{1g} \otimes a_{1g}$  and  $\Gamma_q = b_{1g} \otimes b_{2g}$ , and the molecule is susceptible to a pseudo Jahn–Teller distortion along a  $b_{1g}$  or  $a_{2g}$  coordinate. As shown for the  $D_{4h}$   $A_4$  system in Appendix III, there are no normal modes of  $a_{2g}$  symmetry but the  $b_{1g}$  motion takes the square  $H_4$  to a rectangle, a result anticipated by the orbital correlation diagram in Figure 5.5. This very same state of affairs occurs in the  $\pi$  system of square cyclobutadiene.

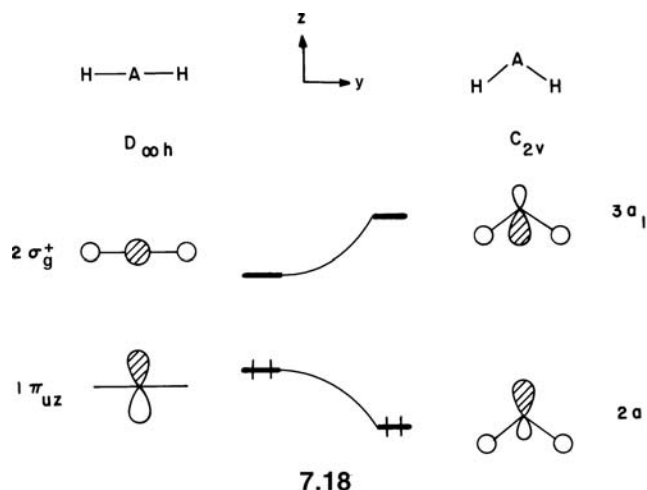
The second order Jahn–Teller effect couples electronic states which arise from different electron configurations. Because the symmetry species of the states  $|\Psi_i\rangle$  and  $|\Psi_j\rangle$  are determined by the symmetry of the orbitals which are occupied, the

problem often reduces to an orbital rather than state picture. Thus if the HOMO and LUMO are nondegenerate, then the symmetry species of  $q$  is given by  $\Gamma_q = \Gamma_{\text{HOMO}} \otimes \Gamma_{\text{LUMO}}$ . This makes the method easy to apply.

Let us take an eight-electron  $\text{AH}_2$  molecule as an example at the linear,  $D_{\infty h}$  geometry (see Figure 7.1). There are four electrons in the HOMO,  $1\pi_u$ , and the LUMO is  $2\sigma_g^+$ . There is a distortion coordinate then of symmetry  $\Gamma_q = \Gamma_{\pi_u} \otimes \Gamma_{\sigma_g^+} = \Gamma_{\pi_u}$ . The  $\pi_u$  mode is given in 7.17, this is simply bending the  $\text{H}_2\text{A}$  molecule. More precisely, in terms of the second-order Jahn–Teller theorem, the  ${}^1\Sigma_g^+$  ground electronic state has an  $\cdots(1\pi_u)^4$  electronic configuration. The first excited state will be a  $\cdots(1\pi_u)^3(2\sigma_g^+)^1$  configuration with  ${}^1\Pi_u$  symmetry. Bending the  $\text{H}_2\text{A}$  molecule leads to stabilization by mixing these two electronic states. There is a close relationship between the second-order Jahn–Teller theorem and the second-order energy expression from geometric perturbation theory (equation 7.3). The utility of the Jahn–Teller expression lies in the fact that it tells us which geometries to probe for potential distortions. The perturbation expression is most useful in making qualitative comparisons between molecules.



The HAH valence angles of eight-electron molecules  $\text{H}_2\text{O}$ ,  $\text{H}_2\text{S}$ ,  $\text{H}_2\text{Se}$ , and  $\text{H}_2\text{Te}$  are given in Table 7.2. They range from  $104.5^\circ$  to  $90.3^\circ$ . There is a steady decrease in the valence angle upon lowering the electronegativity of A with the biggest drop from  $\text{H}_2\text{O}$  to  $\text{H}_2\text{S}$ . Since it is the energetic behavior of  $1\pi_{uz}$  which determines the preference for a bent structure in eight-electron  $\text{AH}_2$  systems, we will examine the behavior of this orbital in terms of the simplified Walsh diagram of 7.18. As



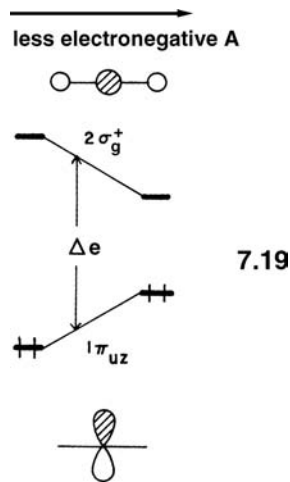
described by equation 7.3, the stabilization of  $2a_1$  is caused solely by the second-order term  $e_i^{(2)}$ , which is inversely proportional to the energy gap,  $\Delta e$ , between  $1\pi_{uz}$  and  $2\sigma_g^+$  of the linear geometry.

$$e_i^{(2)} = e(2a_1) - e^0(1\pi_{uz}) \propto -\frac{1}{\Delta e} \quad (7.9)$$

**TABLE 7.2** Bond Angles for Some Eight Valence Electron Species [1]

AH <sub>2</sub>	Angle	AH <sub>2</sub>	Angle
OH <sub>2</sub>	104.5°	NH <sub>2</sub> <sup>-</sup>	104°
SH <sub>2</sub>	92.1°	OH <sub>2</sub>	104.5°
SeH <sub>2</sub>	90.6°	FH <sub>2</sub> <sup>+</sup>	118.1°
TeH <sub>2</sub>	90.3°		

As shown in 7.19, the  $1\pi_{uz}$  level is raised in energy upon decreasing the electronegativity of A.  $2\sigma_g^+$ , although it contains A character, behaves differently. The A—H bond length increases with decreasing the electronegativity of A (e.g.,  $r_{A-H} = 0.956, 1.328, 1.460$ , and  $1.653 \text{ \AA}$  for H<sub>2</sub>O, H<sub>2</sub>S, H<sub>2</sub>Se, and H<sub>2</sub>Te, respectively) [6]. This is also a reflection of the fact that, with increasing the principal quantum number  $n$ , the  $np$  atomic orbital of A has maxima at larger distances from the nucleus. The overlap of O 2p, S 3p, and so on with H 1s is fairly constant at their optimal distances. Notice from 1.3, however, that the ns orbital becomes increasingly more

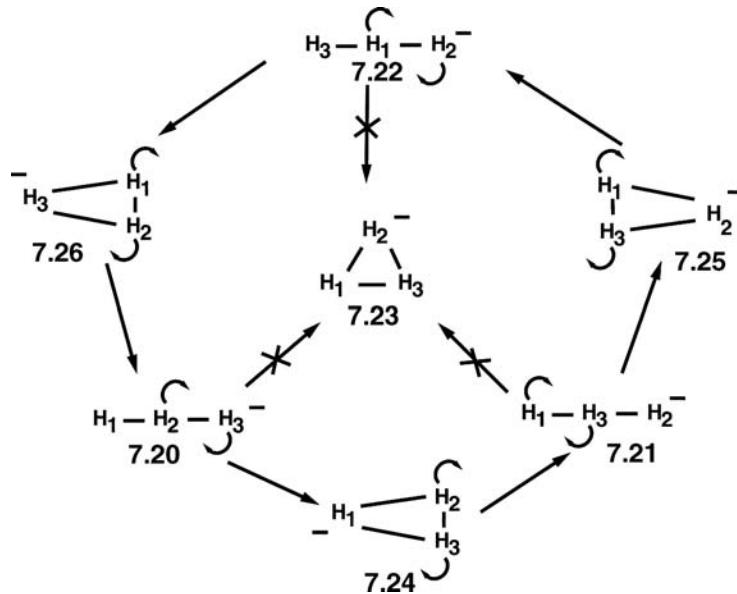


contracted than  $np$  as one proceeds down the sixth column. This leads to a smaller overlap between the ns AO and the  $\sigma_g^+$  H 1s combination. Thus, the antibonding in  $2\sigma_g^+$  is diminished as one goes down the column in the periodic table. The energy gap  $\Delta e$  between  $1\pi_{uz}$  and  $2\sigma_g^+$  becomes smaller and so the energy lowering of equation 7.9 increases upon decreasing the electronegativity of A. This provides a global explanation for the decrease in the HAH valence angles of nonlinear AH<sub>2</sub> molecules for the second row as compared to the third (see Table 7.1). It is also understandable that the inversion barrier (the amount of energy required to distort the molecule from a bent to linear geometry) increases in the order H<sub>2</sub>O < H<sub>2</sub>S < H<sub>2</sub>Se < H<sub>2</sub>Te. In other words, the downward slope of  $2a_1$  in 7.18 increases in this order because of the larger mixing of  $2\sigma_g^+$  into  $1\pi_{uz}$  as A becomes less electronegative. Another interesting comparison comes from the two electronic states of CH<sub>2</sub>, SiH<sub>2</sub>, and GeH<sub>2</sub>. We have discussed why in both cases the  ${}^1A_1$  states have smaller bond angles than the  ${}^3B_1$  states. It is also clear from the arguments we have just presented why the bond angles for SiH<sub>2</sub> and GeH<sub>2</sub> (in both states) are smaller than that in CH<sub>2</sub> (see Table 7.1; for GeH<sub>2</sub> the bond angles are 91.2° and 119.8° for the  ${}^1A_1$  and  ${}^3B_1$  states, respectively) [6]. It turns out that the  ${}^3B_1$  state for CH<sub>2</sub> lies 9.0 kcal/mol lower in energy than  ${}^1A_1$  [6]. In SiH<sub>2</sub> and GeH<sub>2</sub>, this ordering is reversed with  ${}^1A_1$  lying 22.8 and 23.2 kcal/mol, respectively, lower than  ${}^3B_1$  [6]. This is primarily a reflection of the difference in exchange integrals for second versus third and fourth row atoms which is discussed in Chapter 8, but one can also view this in terms of the fact that the much steeper slope of  $2a_1$  for SiH<sub>2</sub> and GeH<sub>2</sub> leads to a larger  $2a_1 - b_1$  gap (see Figure 7.5) thereby making the  ${}^1A_1$  state more favored.

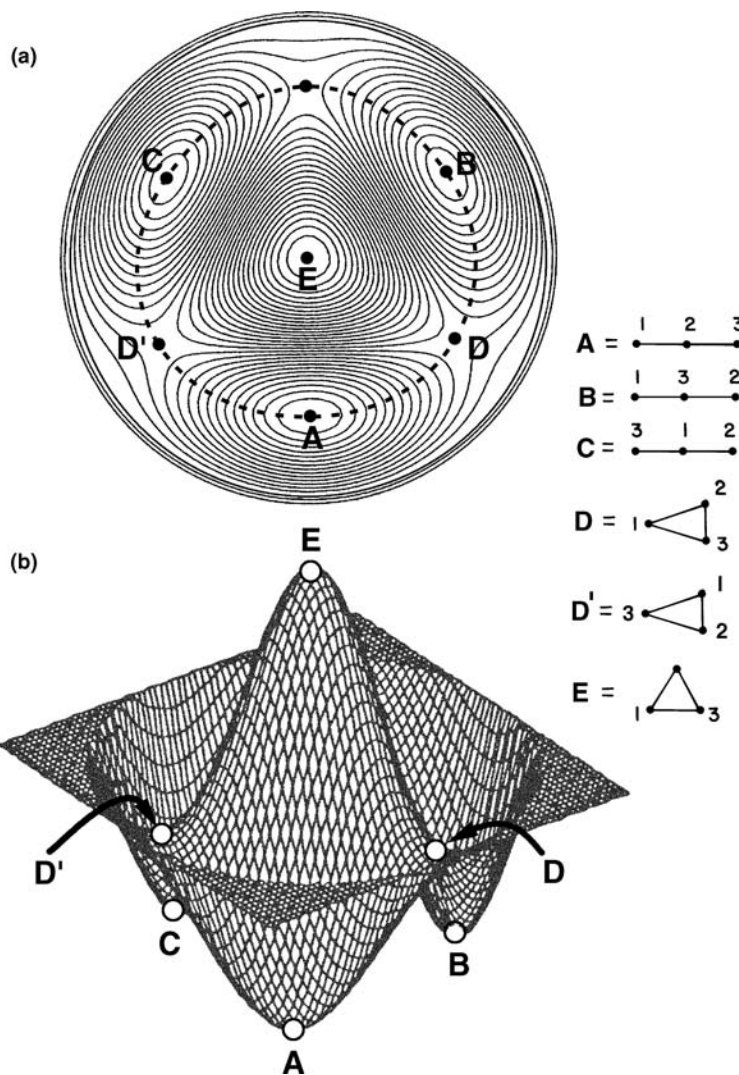
Another trend, although not quite so evident, comes from a comparison of molecules which are isoelectronic and lie in the same row of the periodic table. In the right half of Table 7.2 are three representative examples. The H—A—H bond angle tends to increase on going from  $\text{H}_2\text{N}^-$  to  $\text{H}_2\text{O}$  to  $\text{H}_2\text{F}^+$ , that is, from left to right in the periodic table. Referring back to Figure 7.3a we discussed at great length in Section 7.3 that  $2\sigma_g^+$  mixes more strongly into  $1\pi_{uz}$  than  $1\sigma_g^+$  does for all three situations. However, it does become clear that on going from case A to case B to case C (i.e., going from left to right in the periodic table) that the  $2\sigma_g^+$  orbital becomes progressively further away in energy from  $1\pi_u$ . As a result,  $e_i^{(2)}$  becomes smaller in absolute magnitude.

### 7.4.3 Three-Center Bonding

Recall that the degeneracy of  $\text{H}_3^-$  in a  $D_{3h}$  structure is lifted by the  $D_{3h} \Rightarrow D_{\infty h}$  distortion. Suppose now that we constrain the structure of  $\text{H}_3^-$  to be triangular. With this restriction the degeneracy of  $\text{H}_3^-$  in the  $D_{3h}$  structure can be lifted by the equilateral triangle to isosceles triangle (i.e.,  $D_{3h} \rightarrow C_{2v}$ ) distortion as shown in Figure 7.6. In terms of this diagram, let us examine the energetics of the reaction path appropriate for the exchange reaction given by the conversion of **7.20** to **7.21** or **7.22**. One conceivable reaction path for this exchange is via an the equilateral triangle,



**7.23.** However, an alternative path which goes through the isosceles triangle structures **7.24–7.26** is more favorable because of the Jahn–Teller instability (and therefore local energy maximum) at the  $D_{3h}$  geometry. This is a complicated geometrical motion given by the arrows in structures **7.20–7.22** and **7.24–7.26**. Figure 7.7a shows a somewhat idealized contour diagram of the potential energy surface for this interconversion and the corresponding three-dimensional surface is given in Figure 7.7b. The energy minima A, B, and C of Figure 7.7 represent the three equivalent, linear  $\text{H}_3^-$  structures. The energy maximum E lies at the equilateral triangle geometry, which is not a transition state for the interconversion since it is not a saddle point on the potential energy surface [10]. The saddle point D, located at an isosceles triangle geometry, is the transition state in the interconversion along the reaction coordinate A → B. We will see that the potential energy surface of Figure 7.7, often referred to as a Mexican hat surface, is characteristic of many chemical

**FIGURE 7.7**

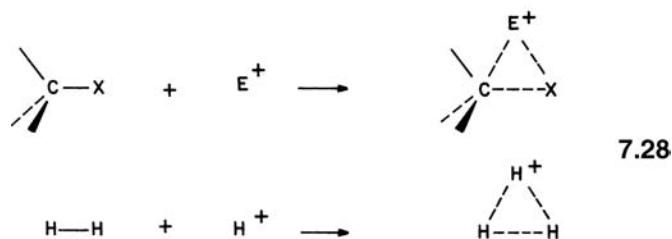
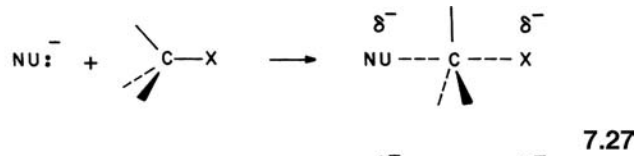
Potential energy surface for the interconversion 7.20–7.21.

(a) Shows the two-dimensional energy contours while (b) illustrates this surface in three dimensions where the height represents potential energy. The points A, B, and C are energy minima, but the point E is an energy maximum. D and D' are two of three equivalent transition states on this surface.

reactions where a least motion path passes through a point of first-order Jahn–Teller instability.

The linear or open arrangement of a three-center-four-electron system  $H_3^-$  bears a close resemblance to the transition state geometry associated with a nucleophilic attack on a tetrahedral carbon center shown in 7.27. Correspondingly, the triangular or closed arrangement of a three-center-two-electron system  $H_3^+$  is related to a front-side electrophilic attack as shown in 7.28. The relevant orbitals at the tetrahedral carbon consist of the C—X bonding and antibonding orbitals  $\sigma_{CX}$  and  $\sigma_{CX}^*$ , respectively. The electrophile or the nucleophile will possess an appropriate acceptor or a donor orbital, respectively [11]. Three MOs for the composite “supermolecule” can be readily derived which have the same local symmetry properties as the  $H_3$  system. Of the three MOs, only the lowest is filled in electrophilic attack so that, just like  $H_3^+$ , a closed rather than open geometry is preferred in 7.28. In a nucleophilic attack 7.27, the donor orbital of the nucleophile is filled, and thus there are now a total of four electrons to be placed into the three MOs. Consequently, a linear geometry is the more stable one. This is a general

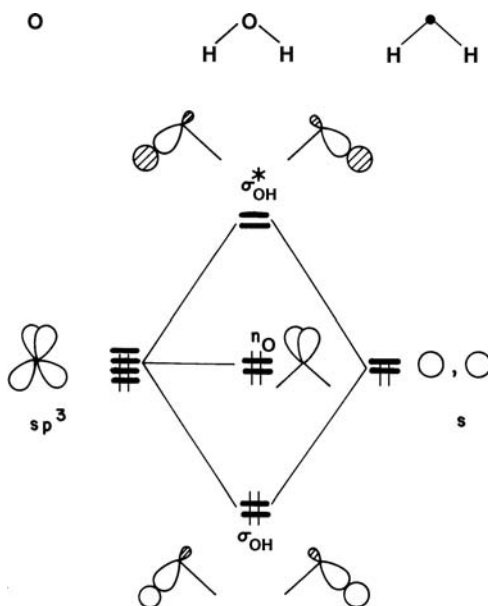
feature which will be highlighted in several problems throughout the book; namely, electron-deficient two electron-three-center bonding prefers a closed arrangement while electron-rich four electron-three-center bonding adopts an open geometry.



## 7.5 BOND ORBITALS AND PHOTOELECTRON SPECTRA OF AH<sub>2</sub> MOLECULES

The MOs of linear and bent H<sub>2</sub>S in Figure 7.5 correspond to the symmetry of the molecule, and hence are called symmetry adapted orbitals. Traditionally, molecular electronic structures are often described in terms of bond orbitals because of the one-to-one correspondence between a bond and a doubly occupied bonding orbital. When combined together with the valence-shell-electron-pair-repulsion (VSEPR) model which we shall cover in more detail in Chapter 14 [12], the bond orbital description provides a set of simple rules for predicting molecular shapes although its applicability is limited to the consideration of ligand arrangements around a single atom. Two important rules of the VSEPR model, which are sufficient to predict the shapes of simple molecules, are as follows: (a) the best arrangement of a given number of electron pairs in the valence shell of an atom is that which maximizes the distances between them. (b) A nonbonding pair of electrons occupies more space on the surface of an atom than a bonding pair. Since bond orbital and MO descriptions of molecular electronic structures are considerably different, it is important to examine how the two approaches are related to each other.

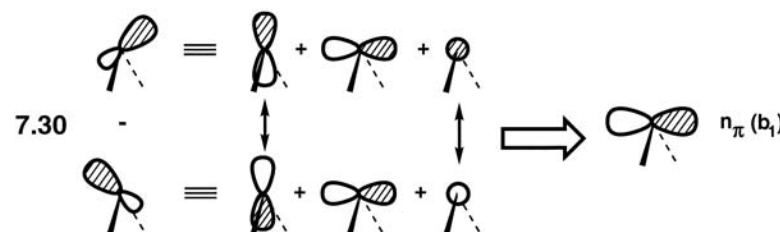
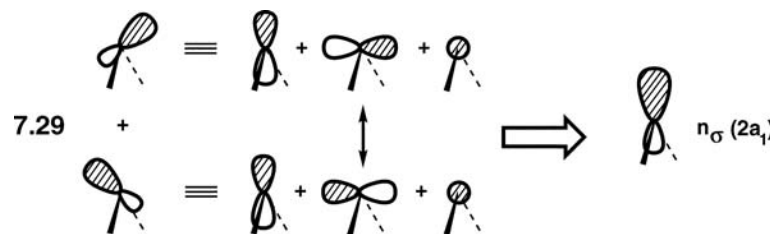
Suppose that the HOH valence angle of H<sub>2</sub>O is equal to the tetrahedral angle (i.e., 109.5°). Let us construct from the valence s and p orbitals the sp<sup>3</sup> hybrid orbitals on O as indicated in Figure 7.8. Two of these hybrid orbitals may be used to form bonding and antibonding orbitals with the hydrogen s atomic orbital along each O—H bond, and the other two hybrid orbitals remain nonbonding orbitals on O. Two σ bonding orbitals, σ<sub>OH</sub>, and two lone pairs on O, n<sub>O</sub>, are filled with two electrons each. This is the classic localized valence bond picture presented in introductory organic chemistry textbooks, for example. These bond orbitals (e.g., σ<sub>OH</sub>, n<sub>O</sub>, and σ<sup>\*</sup><sub>OH</sub> in Figure 7.8) do not, however, have the transformation properties with respect to the molecular geometry demanded by the character

**FIGURE 7.8**

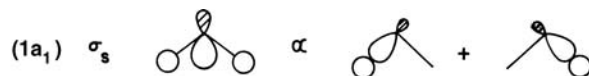
Orbital interaction diagram for  $\text{H}_2\text{O}$  using the bond orbital approach.

table of the  $C_{2v}$  point group (Table 4.3) to which this molecule belongs. In particular, each bond orbital is neither symmetric nor antisymmetric with respect to the  $C_2$  axis and one of the two mirror planes in the molecule. Unlike MOs, bond orbitals are therefore not eigenfunctions of the effective Hamiltonian  $H^{\text{eff}}$ . Consequently, the expectation value for the energy associated with them is undetermined.

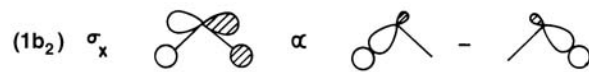
From the vector properties of orbitals, the bond orbitals  $\sigma_{\text{OH}}$ ,  $n_{\text{O}}$ , and  $\sigma^*_{\text{OH}}$  of Figure 7.8 may be decomposed into atomic orbital contributions as shown on the left-hand side of 7.29 for the two  $n$  bond orbitals. One can force the bond orbitals to have the full symmetry properties associated with the molecule by taking linear combinations of each degenerate set. Consider for instance the linear combinations of the two nonbonding orbitals  $n_{\text{O}}$ . The “positive” combination of the two, 7.29, leads to a molecular orbital we shall call  $n_{\sigma}$ . By decomposing each bond



orbital into their AO components, it is then easy to see that the s and the  $p_z$  AO from each has the same relative phase. However, the  $p_x$  AO component has opposite phases in the two bond orbitals (as shown by the double-headed arrow) and so this will result in a cancellation.  $n_{\sigma}$  is then comprised of s and  $p_z$  character and strongly resembles  $2a_1$  in the delocalized picture. The “negative” combination of  $n_{\pi}$  is shown in 7.30. Here, the s and  $p_z$  AO components cancel leaving only the  $p_x$  AO,  $n_{\pi}$ , which is identical to the  $b_1$  molecular orbital.  $n_{\sigma}$  and  $n_{\pi}$  do possess all of the symmetry properties appropriate for the  $C_{2v}$  point group. But notice that while the two  $n_{\sigma}$  bond orbitals are degenerate in energy (both are solely  $sp^3$  hybrids),  $n_{\sigma}$  and  $n_{\pi}$  clearly cannot lie at the same energy.  $n_{\sigma}$  has s and p character on O and consequently is expected to lie at a lower energy than  $n_{\pi}$  which has only p character on O. Similarly, linear combinations of the two  $\sigma_{OH}$  orbitals or the two  $\sigma_{OH}^*$  orbitals lift the degeneracy of the bond orbitals involved as shown in 7.31 and 7.32, respectively. Since these bond orbitals are not eigenfunctions of  $H^{eff}$ , the lifting of the bond orbital degeneracy is not surprising when linear combinations of them are taken. Bond orbitals are often used as a convenient starting point in the generation of symmetry adapted MOs; the symmetry correct representations of them in 7.29–7.32 display all of the necessary qualitative features that the fully delocalized ones constructed in 7.8 have.



7.31



7.32

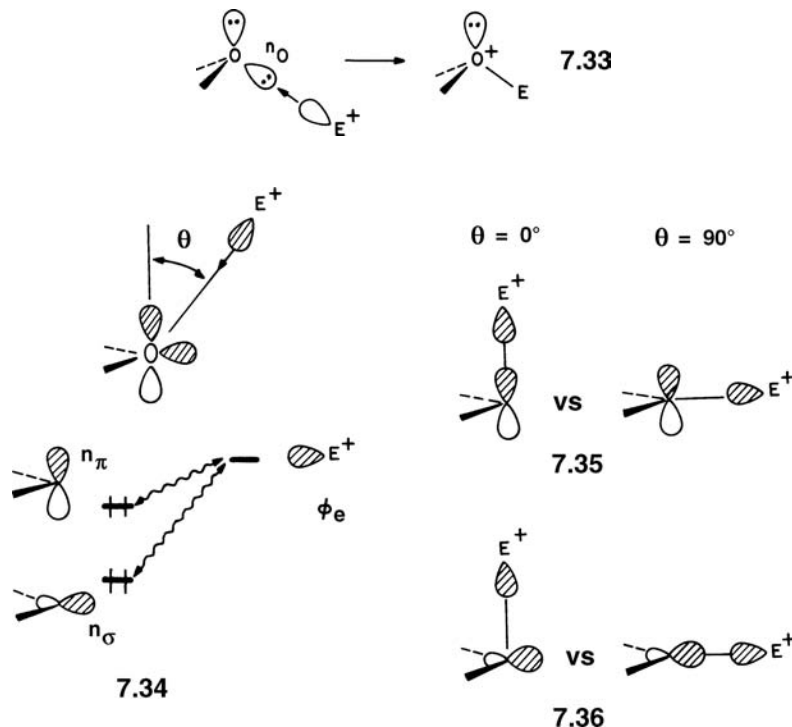


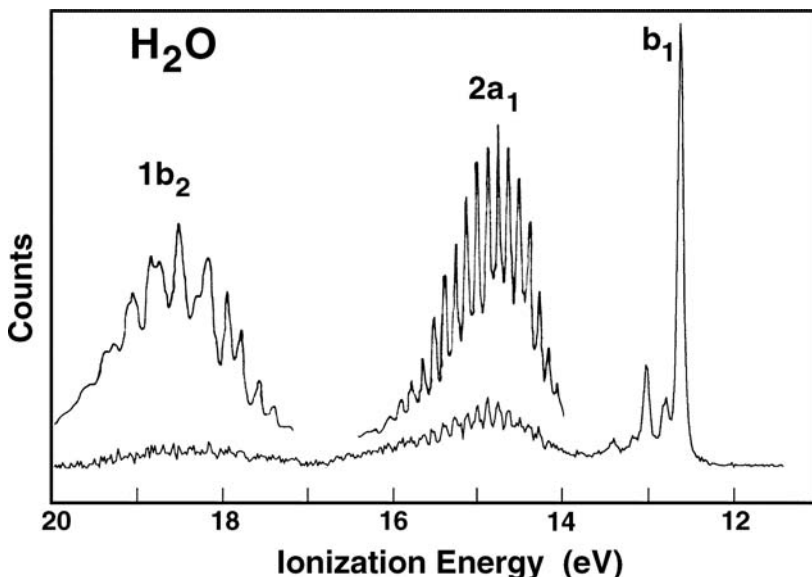
According to the bond orbital-MO correlation diagram in Figure 7.8, eight valence electrons of H<sub>2</sub>O are accommodated by 2 equiv  $\sigma_{OH}$  bond orbitals and 2 equiv  $n_{\sigma}$  lone pairs. A fully delocalized approach (Figure 7.2) yields four nondegenerate molecular orbitals. Apparently, the bond orbital and the MO descriptions of H<sub>2</sub>O are quite different, although the decomposition described above provides links between the two. Are the two lone pairs in H<sub>2</sub>O really different? That depends upon one’s perspective and needs for the problem at hand. It is worthwhile to comment upon the merits and limitations of the two different approaches.

The bond orbital approach very simply predicts that H<sub>2</sub>O is bent since the lowest energy arrangement for four electron pairs around an atom is a tetrahedral one in the VSEPR model. In addition, this approach rationalizes why the HOH angle is smaller than the tetrahedral angle since, on the surface of an atom, a nonbonding electron pair is supposed to occupy more space or provide more Coulomb repulsion than does a bonding electron pair. The MO approach based upon the Walsh diagram in Figure 7.5 predicts that H<sub>2</sub>O is bent, but it does not predict how small the HOH angle would be. Nevertheless, the MO approach provides an elegant explanation for

the decrease in the valence angles of eight-electron  $\text{AH}_2$  systems in the order  $\text{H}_2\text{O} > \text{H}_2\text{S} > \text{H}_2\text{Se} > \text{H}_2\text{Te}$ . It also rationalizes why the  $^3\text{B}_1$  electronic state of  $\text{CH}_2$  has a wider bond angle than the  $^1\text{A}_1$  state, and so on. Occasionally somewhat peculiar hybridization arguments have been constructed for molecules like  $\text{H}_2\text{S}$  and  $\text{H}_2\text{Se}$  which have rather acute bond angles. Since they are close to  $90^\circ$ ,  $p$  atomic orbitals are used to form the A—H bonds leaving the lone pair in an unhybridized  $s$  orbital on A. It is clear from the shape of  $1a_1$  and  $2a_1$  that this is far removed from reality.

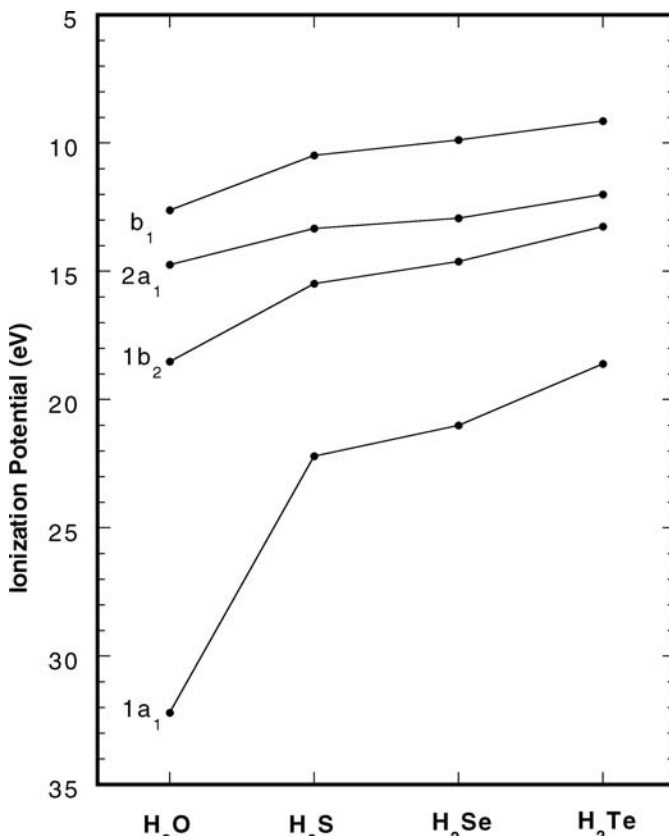
Let us consider how an electrophile  $\text{E}^+$  might attack  $\text{H}_2\text{O}$  to form  $\text{H}_2\text{O}^+-\text{E}$ . According to the bond orbital description 7.33, an electrophile would approach  $\text{H}_2\text{O}$  along the axis of one nonbonding orbital of oxygen since this allows for maximum overlap between the nonbonding orbital  $n_O$  and the acceptor orbital  $\phi_e$  of  $\text{E}^+$ . In the MO description, the interaction between  $\text{H}_2\text{O}$  and  $\text{E}^+$  can be discussed in terms of the simplified interaction diagram 7.34, where the  $(n_\pi - \phi_e)$  and  $(n_\sigma - \phi_e)$  interactions are both stabilizing. Let us define the approach angle  $\theta$  of  $\text{E}^+$  by reference to the  $p$  orbital axis of  $n_\pi$  as shown in 7.34. In terms of overlap, the magnitude of the  $(n_\pi - \phi_e)$  interaction is a maximum at  $\theta = 0^\circ$  and a minimum at  $\theta = 90^\circ$  as depicted in 7.35. The opposite situation is found for the case with the  $(n_\sigma - \phi_e)$  interaction as indicated in 7.36. Thus at  $\theta \sim 45^\circ$ , an electrophile can take advantage of both the  $(n_\pi - \phi_e)$  and  $(n_\sigma - \phi_e)$  interactions. However,  $n_\pi$  is closer in energy to  $\phi_e$  than is  $n_\sigma$  so that, in terms of orbital energy gap, the  $(n_\pi - \phi_e)$  interaction is more stabilizing than the  $(n_\sigma - \phi_e)$  interaction. Thus, the approach angle  $\theta$  becomes smaller if the energy gap between  $n_\pi$  and  $n_\sigma$  is made greater. From our discussion using 7.18 and 7.19, it is evident that the lowering of  $n_\sigma$  with respect to  $1\pi_{uz}$  is greater, and hence the energy gap between  $n_\pi$  and  $n_\sigma$  becomes greater, if the central atom of  $\text{AH}_2$  is made less electronegative. As a consequence, the approach angle  $\theta$  is predicted to be smaller for  $\text{H}_2\text{S}$  than for  $\text{H}_2\text{O}$  [13].



**FIGURE 7.9**

Photoelectron spectrum of water. The inserts for the 2a<sub>1</sub> and 1b<sub>2</sub> levels have been magnified several times. The ionization potential for the 1a<sub>1</sub> molecular orbital is at 32.2 eV.

The elements of photoelectron spectroscopy were presented in Chapter 6.5. The MO energies,  $e_i$ , are directly related to experimental ionization potentials via Koopmans' theorem. Since bond orbitals are not eigenfunctions of the effective Hamiltonian,  $H^{\text{eff}}$ , their energies do not refer to the effective potentials that can be directly related to experimental ionization potentials. For example, the photoelectron spectrum of H<sub>2</sub>O does not show ionization from two sets of degenerate levels as implied by the bond orbital picture in Figure 7.8 but four levels as expected from the MO picture derived from Figure 7.2. The photoelectron spectrum of H<sub>2</sub>O is presented in Figure 7.9. Three ionizations are observed with adiabatic ionization potentials of 12.6, 13.8, and 17.0 eV. These correspond to the b<sub>1</sub>, 2a<sub>1</sub>, and 1b<sub>2</sub> molecular orbitals, respectively. The ionization required for the 1a<sub>1</sub> MO is at 32.2 eV. With He(I) radiation one can obtain a photoelectron spectrum with ionization potentials less than 21 eV. Note that the 2a<sub>1</sub> and b<sub>1</sub> ( $n_{\sigma}$  and  $n_{\pi}$ ) nonbonding levels are separated by 1.2 eV or about 28 kcal/mol; they are in no way close to being degenerate. Analysis of the vibrational progression for the b<sub>1</sub> ionization has lead to a determination that in the <sup>2</sup>B<sub>1</sub> state the O—H bond lengths increase by 0.08 Å and the H—O—H bond angle increases by 4.4° [14]. These small changes are fully consistent with the identification of b<sub>1</sub> being a purely nonbonding molecular orbital. The 2a<sub>1</sub> MO is also nonbonding, but referring back to the Walsh diagram in Figure 7.5, removal of an electron from this orbital should cause the H—O—H bond angle to increase. The intricate fine structure associated with this ionization has been used to propose a linear geometry for the ion with a very small potential required to bend it [14]. The bond angles in BH<sub>2</sub>, <sup>3</sup>B<sub>1</sub> CH<sub>2</sub>, and <sup>2</sup>A<sub>1</sub> NH<sub>2</sub> are 127°, 134°, and 144°, respectively. These compounds have the electronic configuration  $\cdots(1a_1)^1(b_1)^x$ , where  $x = 0, 1$ , and 2 (in the latter case this is isoelectronic to the <sup>2</sup>A<sub>1</sub> ion of H<sub>2</sub>O<sup>+</sup>). The occupation of the b<sub>1</sub> MO should play a small role in setting the geometry. Given the discussion previously about the effect of the electronegativity on the geometry and slope of 2a<sub>1</sub>, it is clear that the bond angle in the <sup>2</sup>A<sub>1</sub> state of H<sub>2</sub>O<sup>+</sup> should be greater than 144°. The 1b<sub>2</sub> MO (see Figure 7.4) is O—H bonding via a p AO at O. Removal of an electron from this MO should cause the O—H bond distance to increase and the H—O—H bond angle

**FIGURE 7.10**

Comparison of the valence ionization potentials for the group 16  $H_2A$  molecules.

to decrease (see Figure 7.5, the  $1b_2$  orbital rises in energy on bending). This appears to be the case from the analysis of the vibrational fine structure. The O—H distance is thought to increase by  $\sim 0.2 \text{ \AA}$  and the H—O—H bond angle to decrease by  $\sim 18^\circ$  [14]. It is clear that the gross, as well as, fine details associated with the photoelectron spectrum of  $H_2O$  are fully consistent with the delocalized picture of bonding.

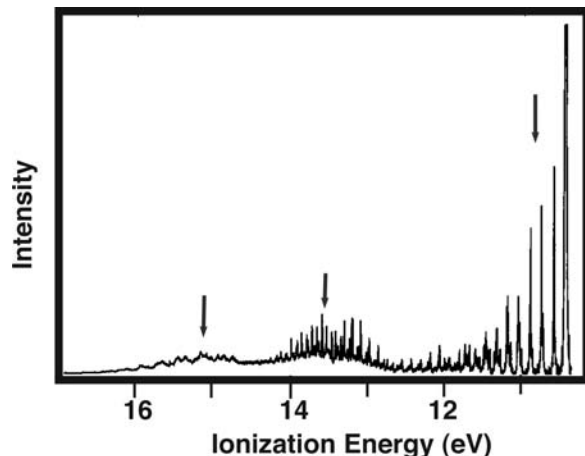
The vertical (not adiabatic, see 6.14) ionization potentials from photoelectron spectra [15] for all of the group 16  $AH_2$  molecules are presented in Figure 7.10. The variation of the ionization potentials follows very closely the changes in electronegativity measured, for example, by differences in the valence orbital energies of the  $A$  atoms in 2.9 for the majority of cases. The ionization potential decreases as one goes down a column in the periodic table with the largest jump from the second to third rows; a situation also found for the H—A—H bond angles. The one exception occurs for the  $2a_1$  and  $1b_2$  orbitals on going from  $H_2O$  to  $H_2S$  [16]. The  $b_1$  molecular orbitals are not sensitive to the geometry of the molecule. This is not the case for  $2a_1$  and  $1b_2$ . From Figure 7.5,  $2a_1$  is stabilized relative to  $b_1$  when the H—A—H angle decreases which is the case on going from  $H_2O$  to  $H_2S$  (the bond angles are  $104^\circ$  and  $92^\circ$ , respectively). Consequently, the decrease in the ionization potential for  $2a_1$  is not as large as it is for  $b_1$  on going from  $H_2O$  to  $H_2S$ . On the other hand,  $1b_2$  rises in energy when the H—A—H bond angle decreases so the  $b_1 - 1b_2$  difference rises. This provides an experimental validation of Walsh diagrams.

---

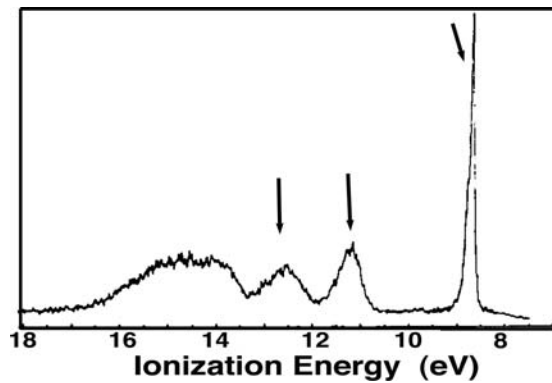
**PROBLEMS**


---

- 7.1.** a. The photoelectron spectrum of  $\text{H}_2\text{S}$  is shown below. Assign the three ionizations indicated by the arrows. For a full assignment with special emphasis on the vibrational structure, see Reference [17].



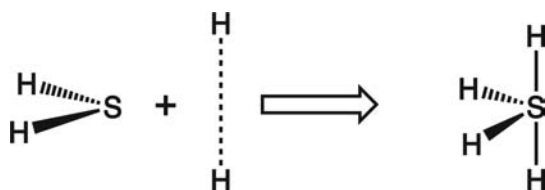
- b. The important MO's of dimethylsulfide,  $\text{S}(\text{CH}_3)_2$ , can easily be derived by taking  $sp^3$ -type fragment orbitals on the two methyl groups that point toward the S atom. Do this and assign the first three bands in the PE spectrum shown below. A full discussion of the substituents effects is given in Reference [18].



- c. Notice that the ionization potentials of the first two ionizations rise by the same extent, 1.7 eV compared to  $\text{H}_2\text{S}$ . What does this imply about the electronic effects of the methyl group compared to hydrogen.  
d. A listing of the first two ionizations for  $\text{R}_2\text{S}$  ( $\text{R}=\text{H, Me, t-Bu}$ ) is given below. The difference between  $\text{R} = \text{Me}$  versus  $t\text{-Bu}$  for the second ionization is more than twice that for the first ionization. Suggest a reason for this.

R	IE <sub>1</sub>	IE <sub>2</sub> (eV)
H	10.4	12.8
$\text{CH}_3$	8.7	11.2
$\text{C}(\text{CH}_3)_3$	8.1	9.9

- 7.2.** Determine the molecular orbitals for  $\text{SH}_4$  in a  $C_{2v}$  geometry, shown below, by interacting the orbitals of  $\text{H}_2\text{S}$  (at a bond angle of  $\sim 120^\circ$ ) with H—H. The MOs from a calculation are given below. Draw out the MOs and compare them with your answer.



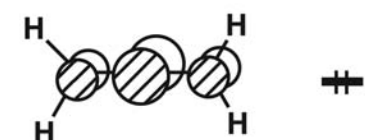
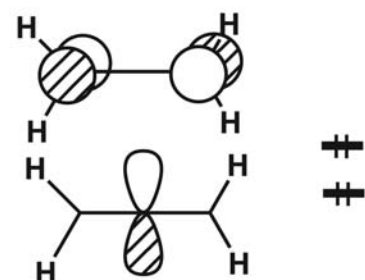
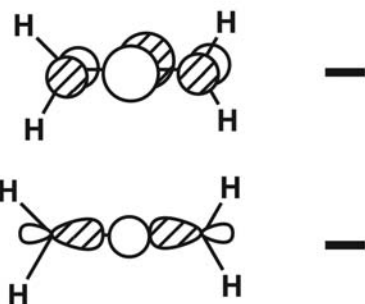
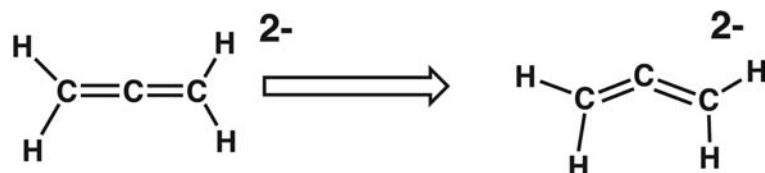
Cartesian coordinates					
Name	No.	x	y	z	
S	1	0.000000	0.000000	0.000000	
H-1	2	0.000000	0.000000	1.420000	
H-2	3	0.000000	0.000000	-1.420000	
H-3	4	1.230000	-0.710000	0.000000	
H-4	5	-1.230000	-0.710000	0.000000	

Molecular orbitals								
	1	2	3	4	5	6	7	8
S s 1	-21.982	-18.276	-17.871	-15.695	-8.222	9.321	17.888	23.380
P <sub>x</sub> 2	0.6229	0.0000	0.0000	0.1731	0.2560	0.0000	1.2909	0.0000
P <sub>y</sub> 3	0.0000	0.0000	0.5730	0.0000	0.0000	1.2440	0.0000	0.0000
P <sub>z</sub> 4	-0.0304	0.0000	0.0000	0.7436	0.6388	0.0000	-0.5457	0.0000
H-1 s 5	0.0000	-0.5484	0.0000	0.0000	0.0000	0.0000	0.0000	1.4999
H-2 s 6	0.2022	-0.3659	0.0000	0.2236	-0.5911	0.0000	-0.5297	-1.0820
H-3 s 7	0.2022	0.3659	0.0000	0.2236	-0.5911	0.0000	-0.5297	1.0820
H-4 s 8	0.2052	0.0000	0.3741	-0.2734	0.4252	-0.9181	-0.7596	0.0000

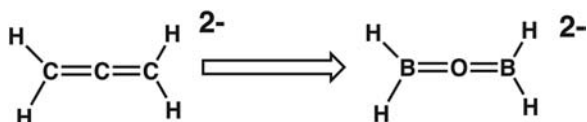
- 7.3.** Consider the two geometries for an  $\text{H}_4\text{A}_3$  molecule shown below. Interact the  $b_1$  orbitals on each  $\text{H}_2\text{A}$  fragment with the two  $p$  AO's on the central A atom to form the  $\pi$  bonds. Determine which structure is more stable when there are 2, 4, 6, and 8 electrons in the four resultant MOs.



- 7.4. a.** The dianion of allene is present in some solid-state compounds. Some of the MOs are shown below. The structure on the left-hand side and the corresponding MOs use a  $D_{2h}$  geometry. It turns out that the C—C—C bond angle in the real structure is  $127^\circ$ . Figure out the  $e^{(1)}$  and  $e^{(2)}$  corrections for this perturbation and draw a Walsh diagram.



- b. What is interesting is that the isoelectronic  $\text{H}_2\text{B}=\text{O}=\text{BH}_2$  unit also exists in the solid state. The  $\text{B}-\text{O}-\text{B}$  angle here is  $180^\circ$ . With the MOs from part (a) use electronegativity perturbation theory to show what happens to the orbital energies in the  $D_{2h}$  structure and describe why the bond angle remains at  $180^\circ$ .



- 7.5. Both  $\text{CH}_4^{2+}$  and the isoelectronic  $\text{BH}_4^+$  molecule have an unusual  $C_{2v}$  structure which might be thought of as having an  $\text{H}_2$  molecule coordinated to a four electron  $\text{AH}_2$  unit. There are two possible geometries that could be considered. They are illustrated below. Develop an interaction diagram for both geometries and discuss which is to be favored.



---

## REFERENCES

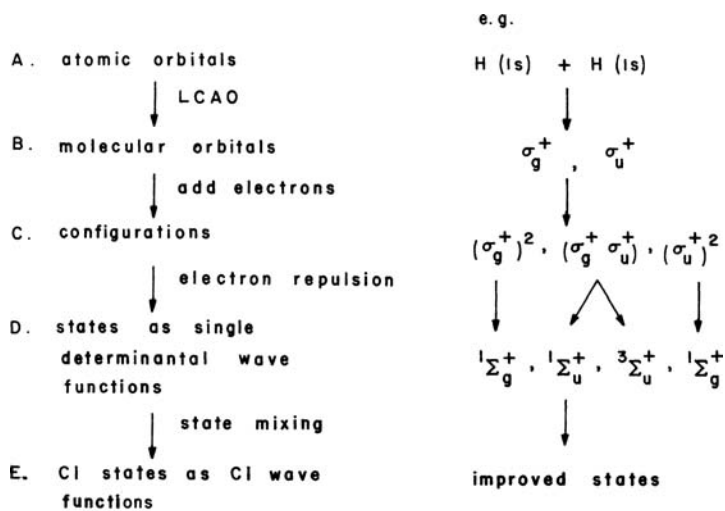
---

1. B. M. Gimarc, *Molecular Structure and Bonding*, Academic, New York (1980).
2. A. D. Walsh, *J. Chem. Soc.*, 2260, 2266, 2288, 2296, 2301, 2306, 2318, 2321, 2325, 2330 (1953).
3. J. K. Burdett, *Molecular Shapes*, Wiley, New York (1980).
4. R. J. Buenker, and S. D. Peyerimhoff, *Chem. Rev.*, **74**, 127 (1974).
5. L. C. Allen, *Theor. Chim. Acta*, **24**, 117 (1972).
6. A. I. Boldyrev, and J. Simons, *J. Chem. Phys.*, **99**, 4628 (1993). H. H. Michels, and R. H. Hobbs, *Chem. Phys. Lett.*, **207**, 389 (1993). G. Treboux, and J. C. Barthelat, *J. Am. Chem. Soc.*, **115**, 4870 (1993). H. F. Schaefer, III, *Science*, **231**, 1100 (1986). G. Herzberg, *Spectra of Diatomic Molecules*, Van Nostrand-Rheinhold, New York (1950). A. A. Radzig and B. M. Smirnov, *Reference Data on Atoms, Molecules, and Ions*, Springer-Verlag, Berlin (1985). J. Karolczak, W. W. Harper, R. S. Grev, and D. J. Clouthier, *J. Chem. Phys.*, **103**, 2839 (1995).
7. L. Salem, *The Molecular Orbital Theory of Conjugated Systems*, Benjamin, New York (1966).
8. L. S. Bartell, *J. Chem. Ed.*, **45**, 754 (1968). B. E. Applegate, T. A. Barckholtz, and T. A. Miller, *Chem. Soc. Rev.*, **32**, 38 (2003). I. Bersuker, *The Jahn-Teller Effect*, Cambridge University Press (2006).
9. H. A. Jahn, and E. Teller, *Proc. Roy. Soc.*, **A161**, 220 (1937).
10. J. W. McIver, and R. E. Stanton, *J. Am. Chem. Soc.*, **94**, 8618 (1972). See also, J. H. Ammeter, *Nouv. J. de Chim.*, **4**, 631 (1980).
11. N. T. Anh, and C. Minot, *J. Am. Chem. Soc.*, **102**, 103 (1980). A. Veillard and A. Dedieu, *J. Am. Chem. Soc.*, **94**, 6730 (1972). C. Minot, *Nouv. J. Chim.*, **5**, 319 (1981). L. Deng, V. Branchadell, and T. Ziegler, *J. Am. Chem. Soc.*, **116**, 10645 (1994). N. T. Anh, F. Maurel, B. T. Thanh, H. H. Thao, and Y. T. N'Guinessan, *New J. Chem.*, **18**, 473 (1994). N. T. Anh, F. Maurel, H. H. Thao, and Y. T. N'Guinessan, *New J. Chem.*, **18**, 483 (1994). N. T. Anh, B. T. Thanh, H. H. Thao, and Y. T. N'Guinessan, *New J. Chem.*, **18**, 489 (1994).
12. R. J. Gillespie, *Molecular Geometry*, Van Nostrand-Reinhold, London (1972).
13. P. A. Kollman, *J. Am. Chem. Soc.*, **94**, 1838 (1972).
14. J. W. Rabalais, *Principles of Ultraviolet Photoelectron Spectroscopy*, John Wiley & Sons, New York pp. 264–280. (1977).
15. A. W. Potts, and W. C. Price, *Proc. Roy. Soc. Lond. A.*, **326**, 181 (1972).
16. H. Bock, *Angew. Chem. Int. Ed. Engl.*, **16**, 613 (1977).
17. M. Hochlaf, K.-M. Weitzel, and C. Y. Ng, *J. Chem. Phys.*, **120**, 6944 (2004).
18. G. Wagner and H. Bock, *Chem. Ber.*, **107**, 68 (1974).

# State Wavefunctions and State Energies

## 8.1 INTRODUCTION

So far we have avoided discussion of the nature of the effective Hamiltonian,  $H^{\text{eff}}$ , that has figured prominently in the expressions for the interaction integrals. We have also postponed consideration of a related problem, shown in 2.3 and 2.5, until this chapter. Given two orbitals of different energies, and two electrons, what factors influence the relative stabilities of the possible singlet and triplet states? In the case of atoms where electrons enter degenerate  $p$  or  $d$  orbitals, one of Hund's rules tells us that the state of highest spin multiplicity will be most stable. To put this in perspective, 8.1 shows the strategy which we use in understanding molecular orbital



(MO) calculations. Much of what we have to say elsewhere is accessible by considering the steps A through C and describing problems in terms of one-electron energies. But as mentioned above, there are several situations that do not make sense until we take the next step and switch on electron–electron interactions. Finally, we also find some material that requires a higher level of treatment still and forces us to include the last step in 8.1. Discussion of these problems requires the study of the molecular Hamiltonian  $\hat{H}$  and the state wavefunction  $\Phi$  of a molecule. Since  $\hat{H}$  and  $\Phi$  should describe all the electrons, 1, 2, 3, . . . ,  $N$  present in a molecule, they are functions of the electron coordinates,

$$\hat{H} = \hat{H}(1, 2, 3, \dots, N) \quad (8.1)$$

$$\Phi = \Phi(1, 2, 3, \dots, N) \quad (8.2)$$

where each electron number  $\mu$  ( $= 1, 2, 3, \dots, N$ ) refers to the spatial coordinates  $x_\mu, y_\mu$ , and  $z_\mu$  as well as the spin coordinate  $s_\mu$  of the electron  $\mu$ . The importance of  $H$  and  $\Phi$  originates from the fact that the total energy of a molecule in the state is given by the expectation value

$$E = \langle \Phi | \hat{H} | \Phi \rangle \quad (8.3)$$

if  $\Phi$  is normalized to unity

$$\langle \Phi | \Phi \rangle = 1 \quad (8.4)$$

## 8.2 THE MOLECULAR HAMILTONIAN AND STATE WAVEFUNCTIONS [1]

In terms of atomic units, in which the electron mass  $m$ , charge  $e$ , and the constant  $h/2\pi$  are taken to be unity, the molecular Hamiltonian  $\hat{H}$  may be written as

$$\hat{H} = \sum_{\mu=1}^N \left\{ \hat{h}(\mu) + \sum_{\nu < \mu} \hat{g}(\mu, \nu) \right\} + \sum_{A>B} \sum \frac{Z_A Z_B}{r_{AB}} \quad (8.5)$$

where

$$\hat{h}(\mu) = -\frac{1}{2} \nabla_\mu^2 - \sum_A \frac{Z_A}{r_{\mu A}} \quad (8.6)$$

$$\hat{g}(\mu, \nu) = \frac{1}{r_{\mu\nu}} \quad (8.7)$$

The first term of the core-Hamiltonian,  $\hat{h}(\mu)$ , in equation 8.6 is the kinetic energy of the electron  $\mu$  which is expressed as in equation 8.8. The second term of  $\hat{h}(\mu)$  is the

$$-\frac{1}{2} \nabla_\mu^2 = -\frac{1}{2} \left( \frac{\partial^2}{\partial x_\mu^2} + \frac{\partial^2}{\partial y_\mu^2} + \frac{\partial^2}{\partial z_\mu^2} \right) \quad (8.8)$$

energy of attraction between the electron  $\mu$  and all the nuclei of the molecule, and  $r_{\mu A}$  is the distance between the electron  $\mu$  and the nucleus of atom A with charge  $Z_A$ . The electron–electron repulsion between electrons  $\mu$  and  $\nu$  is given by equation 8.7, where  $r_{\mu\nu}$  is the distance between electrons  $\mu$  and  $\nu$ . The total nuclear–nuclear repulsion  $V_{nn}$  is represented by the last term of equation 8.5

$$V_{nn} = \sum_{A > B} \sum \frac{Z_A Z_B}{r_{AB}} \quad (8.9)$$

where  $r_{AB}$  is the distance between the nuclei of atoms A and B.

The Pauli exclusion principle is equivalent to the requirement that the electronic state wavefunction  $\Phi$  be antisymmetric with respect to the interchange of any two-electron coordinates, that is,

$$\Phi(2, 1, 3, \dots, N) = -\Phi(1, 2, 3, \dots, N) \quad (8.10)$$

Within the framework of MO theory, the simplest wavefunction satisfying this antisymmetric property is the determinant constructed from all occupied MOs, which is known as the Slater determinant. As a general example, consider a  $2n$  electron closed-shell molecule that has doubly occupied levels  $\psi_1, \psi_2, \psi_3, \dots, \psi_n$  as in 8.2. The functions describing the up-spin and down-spin states of an electron  $\mu$

$$\begin{array}{c}
 \text{---} \quad \psi_{n+2} \\
 \text{---} \quad \psi_{n+1} \\
 \\ 
 \textbf{8.2} \quad \begin{array}{cc}
 \text{++} & \psi_n \\
 \text{++} & \psi_{n-1} \\
 \vdots & \\
 \text{++} & \psi_2 \\
 \text{++} & \psi_1
 \end{array}
 \end{array}$$

are written as  $\alpha(\mu)$  and  $\beta(\mu)$ , respectively. They satisfy the orthonormality relationship

$$\begin{aligned}
 \int \alpha(\mu) \alpha(\mu) ds_\mu &\equiv \langle \alpha(\mu) | \alpha(\mu) \rangle = 1 \\
 \int \beta(\mu) \beta(\mu) ds_\mu &\equiv \langle \beta(\mu) | \beta(\mu) \rangle = 1 \\
 \int \alpha(\mu) \beta(\mu) ds_\mu &\equiv \langle \alpha(\mu) | \beta(\mu) \rangle = 0
 \end{aligned} \quad (8.11)$$

The up-spin and down-spin wavefunctions for electron  $\mu$  in an MO  $\psi_i$  are given by the products  $\psi_i(\mu)\alpha(\mu)$  and  $\psi_i(\mu)\beta(\mu)$ , respectively. For the purpose of simplicity, we write these as

$$\begin{aligned}
 \psi_i(\mu)\alpha(\mu) &\equiv \psi_i(\mu) \\
 \psi_i(\mu)\beta(\mu) &\equiv \bar{\psi}_i(\mu)
 \end{aligned} \quad (8.12)$$

The Slater determinant  $\Phi$  for the electron configuration **8.2** is then given by

$$\Phi(1, 2, 3, \dots, N) = \frac{1}{\sqrt{(2n)!}} \begin{vmatrix} \psi_1(1) & \psi_1(2) & \psi_1(3) & \cdots & \psi_1(2n) \\ \bar{\psi}_1(1) & \bar{\psi}_1(2) & \bar{\psi}_1(3) & \cdots & \bar{\psi}_1(2n) \\ \psi_2(1) & \psi_2(2) & \psi_2(3) & \cdots & \psi_2(2n) \\ \bar{\psi}_2(1) & \bar{\psi}_2(2) & \bar{\psi}_2(3) & \cdots & \bar{\psi}_2(2n) \\ \vdots & \vdots & \vdots & \ddots & \vdots \\ \psi_n(1) & \psi_n(2) & \psi_n(3) & \cdots & \psi_n(2n) \\ \bar{\psi}_n(1) & \bar{\psi}_n(2) & \bar{\psi}_n(3) & \cdots & \bar{\psi}_n(2n) \end{vmatrix} \quad (8.13)$$

$$= \hat{A} \psi_1(1) \bar{\psi}_1(2) \psi_2(3) \bar{\psi}_2(4) \cdots \psi_n(2n-1) \bar{\psi}_n(2n) \quad (8.14)$$

The antisymmetrizing operator  $\hat{A}$ , when acting on the product function as in equation 8.14, leads to the Slater determinant.

### 8.3 FOCK OPERATOR [1]

We quote the following result without proof or further discussion. When applied to the state wavefunction  $\Phi$ , the variation principle leads to the Fock equation

$$\hat{F}\psi_i = e_i\psi_i \quad (8.15)$$

where  $\hat{F}$ , the Fock operator, controls the form of the MOs  $\psi_i$  and their “orbital energies”  $e_i$  and is the effective one-electron Hamiltonian  $H^{\text{eff}}$  for the configuration in **8.2**. Since  $\hat{F}$  and  $\psi_i$  depend only on the coordinate of a single electron, equation 8.15 may be written as

$$\hat{F}(\mu)\psi_i(\mu) = e_i\psi_i(\mu) \quad (8.16)$$

where  $\mu = 1, 2, 3, \dots, 2n$ .

The Fock operator is made up of three terms. The first is a one-electron term describing the core potential and the other two are two-electron terms that contain the electron–electron repulsion energies. For an electron  $\mu$  located in the MO  $\psi_i$ , the core potential, namely, the kinetic plus nuclear–electron attraction energies, is given by the expectation value of the core-Hamiltonian  $\hat{h}(\mu)$

$$\begin{aligned} h_i &= \int \psi_i(\mu) \hat{h}(\mu) \psi_i(\mu) d\tau_\mu \\ &\equiv \langle \psi_i(\mu) | \hat{h}(\mu) | \psi_i(\mu) \rangle \equiv \langle \psi_i | \hat{h} | \psi_i \rangle \end{aligned} \quad (8.17)$$

For two electrons  $\mu$  and  $\nu$  ( $\mu \neq \nu$ ) accommodated in the MOs  $\psi_i$  and  $\psi_j$ , respectively, the two-electron terms are the Coulomb repulsion  $J_{ij}$  and the exchange repulsion  $K_{ij}$  energies.

$$\begin{aligned} J_{ij} &= \iint \frac{\psi_i(\mu)\psi_i(\mu)\psi_j(\nu)\psi_j(\nu)}{r_{\mu\nu}} d\tau_\mu d\tau_\nu \\ &= \int \psi_i(\mu) \left( \int \frac{\psi_j(\nu)\psi_j(\nu)}{r_{\mu\nu}} d\tau_\nu \right) \psi_i(\mu) d\tau_\mu \\ &\equiv [\psi_i(\mu)\psi_i(\mu)|\psi_j(\nu)\psi_j(\nu)] \equiv (\psi_i|\psi_i|\psi_j|\psi_j) \end{aligned} \quad (8.18)$$

$$\begin{aligned}
K_{ij} &= \iint \frac{\psi_i(\mu)\psi_j(\mu)\psi_i(\nu)\psi_j(\nu)}{r_{\mu\nu}} d\tau_\mu d\tau_\nu \\
&= \int \psi_i(\mu) \left( \int \frac{\psi_j(\nu)\psi_j(\nu)}{r_{\mu\nu}} d\tau_\nu \right) \psi_j(\mu) d\tau_\mu \\
&\equiv [\psi_i(\mu)\psi_j(\mu)|\psi_i(\nu)\psi_j(\nu)] \equiv (\psi_i\psi_j|\psi_i\psi_j)
\end{aligned} \tag{8.19}$$

From these definitions, it follows that  $K_{ii} = J_{ii}$ . Also note that the Coulomb repulsion between two electrons is independent of their spins while the exchange repulsion vanishes unless their spins are the same.  $J_{jj}$  is repulsive (i.e., positive) and represents the electrostatic repulsion between electron  $\mu$  in orbital  $\psi_i$  and electron  $\nu$  in orbital  $\psi_j$ . It increases with increasing the overlap between the electron densities  $\psi_i\psi_i$  and  $\psi_j\psi_j$ . In other words, as the electrons become closer, their mutual repulsion becomes larger. The exchange integral arises purely as a result of the expansion of equation 8.13, that is, the requirement that the state wavefunction be antisymmetric with respect to electron exchange. Notice that the integrand of equation 8.19 involves the exchange of two electrons compared to equation 8.18; hence its name.  $K_{ij}$  represents, in a sense, a correction to the Coulomb repulsion term  $J_{ij}$  for the case of two electrons with parallel spins. When the electron spins are parallel, in another phrasing of the Pauli principle, they cannot occupy the same region of space. The exchange repulsion, therefore, has no classical analog. Although intrinsically positive, the exchange repulsion is subtracted from the Coulomb repulsion to give the total electron-electron repulsion energy (see below).

In order to specify the Fock operator  $\hat{F}$ , we introduce the Coulomb operator  $\hat{J}_j$  and the exchange operator  $\hat{K}_j$  for an electron in the MO  $\psi_j$ .

$$\hat{J}_j(\mu)\psi_i(\mu) = \left( \int \frac{\psi_j(\nu)\psi_j(\nu)}{r_{\mu\nu}} d\tau_\nu \right) \psi_i(\mu) \tag{8.20}$$

$$\hat{K}_j(\mu)\psi_i(\mu) = \left( \int \frac{\psi_j(\nu)\psi_i(\nu)}{r_{\mu\nu}} d\tau_\nu \right) \psi_j(\mu) \tag{8.21}$$

Then, the integrals  $J_{ij}$  and  $K_{ij}$  are simply the expectation values of the operators  $\hat{J}_j$  and  $\hat{K}_j$  (see equations 8.18 and 8.19),

$$\begin{aligned}
J_{ij} &= \int \psi_i(\mu)\hat{J}_j(\mu)\psi_i(\mu) d\tau_\mu \\
&\equiv \langle \psi_i(\mu)|\hat{J}_j(\mu)|\psi_i(\mu) \rangle \equiv \langle \psi_i|\hat{J}_j|\psi_i \rangle
\end{aligned} \tag{8.22}$$

$$\begin{aligned}
K_{ij} &= \int \psi_i(\mu)\hat{K}_j(\mu)\psi_i(\mu) d\tau_\mu \\
&\equiv \langle \psi_i(\mu)|\hat{K}_j(\mu)|\psi_i(\mu) \rangle \equiv \langle \psi_i|\hat{K}_j|\psi_i \rangle
\end{aligned} \tag{8.23}$$

In terms of  $\hat{h}(\mu)$ ,  $\hat{J}_j(\mu)$ , and  $\hat{K}_j(\mu)$ , the Fock operator  $\hat{F}(\mu)$  for 8.2 is written as

$$\hat{F}(\mu) = \hat{h}(\mu) + \sum_{j=1}^n [2\hat{J}_j(\mu) - \hat{K}_j(\mu)] \tag{8.24}$$

or, simply,

$$\hat{F} = \hat{h} + \sum_{j=1}^n [2\hat{J}_j - \hat{K}_j] \quad (8.25)$$

## 8.4 STATE ENERGY

The orbital energy  $e_i$  for the  $i$ th level of the electron configuration **8.2** is the expectation value of the Fock operator

$$e_i = \langle \psi_i | \hat{F} | \psi_i \rangle \quad (8.26)$$

Using equation 8.25,

$$\begin{aligned} e_i &= \langle \psi_i | \hat{h} | \psi_i \rangle + \left\langle \psi_i | \sum_{j=1}^n 2\hat{J}_j - \hat{K}_j | \psi_i \right\rangle \\ &= h_i + \sum_{j=1}^n (2J_{ij} - K_{ij}) \end{aligned} \quad (8.27)$$

Thus, an electron in one of the occupied MOs  $\psi_i$  ( $i = 1, 2, 3, \dots, n$ ) feels the core potential  $h_i$  as well as the electron-electron repulsion arising from the presence of other electrons. The Fock operator  $\hat{F}$ , although determined only in terms of the occupied MOs, determines the energy of both the occupied and the unoccupied levels. As Section 8.5, the orbital energy  $e_i$  of an unoccupied MO  $\psi_i$  ( $i = n+1, n+2, \dots$ ) refers to the potential that an extra electron feels if it were placed in that orbital.

The total electron-electron repulsion  $V_{ee}$  in **8.2** is given by

$$V_{ee} = \sum_{i=1}^n \sum_{j=1}^n (2J_{ij} - K_{ij}) \quad (8.28)$$

Thus, the total energy  $E$  of the configuration in **8.2** is simply

$$E = \left( \sum_{i=1}^n 2h_i \right) + V_{ee} + V_{nn} \quad (8.29)$$

Combining equations 8.27 and 8.29,

$$E = \left( \sum_{i=1}^n 2e_i \right) - V_{ee} + V_{nn} \quad (8.30)$$

The sum of the first two terms in equation 8.30 is the electronic energy. Note that the total energy is not equal to the sum of all the occupied orbital energies. However, it may be shown that [2]

$$-V_{ee} + V_{nn} \cong \frac{1}{3}E \quad (8.31)$$

and so

$$E \cong \frac{3}{2} \sum_{i=1}^n 2e_i \quad (8.32)$$

This relationship, though approximate, justifies in part the use of orbital energy changes alone in discussing molecular structure and reactivity problems.

## 8.5 EXCITATION ENERGY

Electron configuration **8.2** is a typical closed shell in which all the occupied MOs are doubly filled. Let us examine the stability of such a state with respect to those states in which some of the high lying occupied MOs are singly filled. To simplify our discussion, consider the various electronic configurations shown in **8.3**, which result

$\epsilon_2, \psi_2$	—	+	+	+	+	+
$\epsilon_1, \psi_1$	+	+	+	+	+	—
$\Phi_G$	$\Phi_T$	$\Phi'_T$	$\Phi_1$	$\Phi_2$	$\Phi_E$	

**8.3**

from a simple two-orbital-two-electron case. In the following treatment, the MOs  $\psi_1$  and  $\psi_2$  are to be determined from the eigenvalue equation associated with the singlet ground state configuration  $\Phi_G$

$$\hat{H}\Phi_G = E_G\Phi_G \quad (8.33)$$

where

$$\Phi_G = \frac{1}{\sqrt{2}} \begin{vmatrix} \psi_1(1) & \psi_1(2) \\ \bar{\psi}_1(1) & \bar{\psi}_1(2) \end{vmatrix} = \frac{1}{\sqrt{2}} [\psi_1(1)\bar{\psi}_1(2) - \bar{\psi}_1(1)\psi_1(2)] \quad (8.34)$$

and the energy  $E_G$  is given by

$$E_G = \langle \Phi_G | \hat{H} | \Phi_G \rangle \quad (8.35)$$

Application of the variation principle to equation 8.35 leads to the Fock equation

$$\hat{F}\psi_i = e_i\psi_i \quad (8.36)$$

where

$$\hat{F} = \hat{h} + 2\hat{J}_1 - \hat{K}_1 \quad (8.37)$$

Note that the MOs  $\psi_i$  ( $i = 1, 2$ ) are determined if  $\hat{F}$  is known, but  $\hat{F}$  is defined in terms of the occupied MO  $\psi_1$  (via  $\hat{J}_1$  and  $\hat{K}_1$ ) that is yet to be determined. This problem is solved by the method of self-consistent field (SCF) iteration: in the first cycle of iteration, a trial MO for  $\psi_1$  is assumed to obtain  $E_G^{(1)}$  and  $\hat{F}^{(1)}$ . In the second cycle of iteration, we solve equation 8.36 for  $\hat{F}^{(1)}$  to find new MOs  $\psi_i^{(2)}$  ( $i = 1, 2$ ) and use  $\psi_i^{(2)}$  to generate  $E_G^{(2)}$  and  $\hat{F}^{(2)}$ . In the third cycle of iteration, equation 8.36 is solved for  $\hat{F}^{(2)}$  to obtain new MOs  $\psi_i^{(3)}$  ( $i = 1, 2$ ) and hence  $E_G^{(3)}$  and  $\hat{F}^{(3)}$ . If such an iteration is repeated  $n$  times, the state energies at various cycles of iteration satisfy the following relationship [3]

$$E_G^{(1)} \geq E_G^{(2)} \geq \dots \geq E_G^{(n-1)} \geq E_G^{(n)} \quad (8.38)$$

owing to the variation principle. When the energy difference between the last two iterations is negligibly small, the SCF iteration is said to be converged. In such a case, no further iteration could improve the wavefunction. In our discussion, the MOs  $\psi_i$  and the orbital energies  $e_i$  ( $i = 1, 2$ ) are assumed to be those determined from a converged SCF iteration for the state  $\Phi_G$ .

From equation 8.27 the orbital energies  $e_1$  and  $e_2$  are given by

$$e_1 = \langle \psi_1 | \hat{h} + 2\hat{J}_1 - \hat{K}_1 | \psi_1 \rangle = h_1 + 2J_{11} - K_{11} = h_1 + J_{11} \quad (8.39)$$

$$e_2 = \langle \psi_2 | \hat{h} + 2\hat{J}_1 - \hat{K}_1 | \psi_2 \rangle = h_2 + 2J_{12} - K_{12} \quad (8.40)$$

Thus,  $e_1$  is the effective potential exerted on an electron in the MO  $\psi_1$  of  $\Phi_G$ . If an extra electron is placed in the MO  $\psi_2$  of  $\Phi_G$ , that electron would feel the effective potential given by  $e_2$ . In all the electronic states of 8.3, the molecular geometry is assumed to be the same so that the relative stability of those states can be examined by simply comparing their electronic energies.

The electronic energies of the singlet ground state  $\Phi_G$  and the triplet state  $\Phi_T$  are determined by the form of the wavefunctions. The expressions of  $\Phi_G$  and  $\Phi_T$  are given by equations 8.34 and 8.41, respectively.

$$\Phi_T = \frac{1}{\sqrt{2}} \begin{vmatrix} \psi_1(1) & \psi_1(2) \\ \psi_2(1) & \psi_2(2) \end{vmatrix} = \frac{1}{\sqrt{2}} [\psi_1(1)\psi_2(2) - \psi_2(1)\psi_1(2)] \quad (8.41)$$

A bit of arithmetic leads to the form of the energies

$$\begin{aligned} E_G &= \langle \Phi_G | \hat{H} | \Phi_G \rangle \\ &= 2h_1 + J_{11} = 2e_1 - J_{11} \end{aligned} \quad (8.42)$$

$$\begin{aligned} E_T &= \langle \Phi_T | \hat{H} | \Phi_T \rangle \\ &= h_1 + h_2 + J_{12} - K_{12} = e_1 + e_2 - J_{11} - J_{12} \end{aligned} \quad (8.43)$$

The electronic energies of the configurations  $\Phi_1$  and  $\Phi_2$  are the same and are evaluated in an analogous way via a knowledge of the state functions

$$\Phi_1 = \frac{1}{\sqrt{2}} \begin{vmatrix} \psi_1(1) & \psi_1(2) \\ \bar{\psi}_2(1) & \bar{\psi}_2(2) \end{vmatrix} = \frac{1}{\sqrt{2}} [\psi_1(1)\bar{\psi}_2(2) - \bar{\psi}_2(1)\psi_1(2)] \quad (8.44)$$

$$\Phi_2 = \frac{1}{\sqrt{2}} \begin{vmatrix} \bar{\psi}_1(1) & \bar{\psi}_1(2) \\ \psi_2(1) & \psi_2(2) \end{vmatrix} = \frac{1}{\sqrt{2}} [\bar{\psi}_1(1)\psi_2(2) - \psi_2(1)\bar{\psi}_1(2)]$$

which leads to

$$\begin{aligned} E_1 &= \langle \Phi_1 | \hat{H} | \Phi_1 \rangle \\ &= E_2 = \langle \Phi_2 | \hat{H} | \Phi_2 \rangle \\ &= h_1 + h_2 + J_{12} = e_1 + e_2 - J_{11} - J_{12} + K_{12} \end{aligned} \quad (8.45)$$

Unlike the states  $\Phi_G$  and  $\Phi_T$ , however, the configurations  $\Phi_1$  and  $\Phi_2$  are not eigenfunctions of the so-called total spin angular momentum operator  $\hat{S}^2$  [4]. The singlet excited state  $\Phi_S$  is given by the linear combination

$$\Phi_S = \frac{1}{\sqrt{2}}(\Phi_1 - \Phi_2) \quad (8.46)$$

which does satisfy this requirement. From equation 8.44 it is easy to show the relationship

$$\langle \Phi_1 | \hat{H} | \Phi_2 \rangle = -(\psi_1 \psi_2 | \psi_1 \psi_2) = -K_{12} \quad (8.47)$$

which leads to the electronic energy of the singlet excited state  $\Phi_S$

$$E_S = \langle \Phi_S | \hat{H} | \Phi_S \rangle = h_1 + h_2 + J_{12} + K_{12} = e_1 + e_2 - J_{11} - J_{12} + 2K_{12} \quad (8.48)$$

One state wavefunction describing the triply degenerate triplet state is given by equation 8.41, and the other two are as follows:

$$\Phi'_T = \frac{1}{\sqrt{2}} \begin{vmatrix} \bar{\psi}_1(1) & \bar{\psi}_1(2) \\ \bar{\psi}_2(1) & \bar{\psi}_2(2) \end{vmatrix} = \frac{1}{\sqrt{2}} [\bar{\psi}_1(1)\bar{\psi}_2(2) - \bar{\psi}_2(1)\bar{\psi}_1(2)] \quad (8.49)$$

$$\Phi''_T = \frac{1}{\sqrt{2}}(\Phi_1 + \Phi_2) \quad (8.50)$$

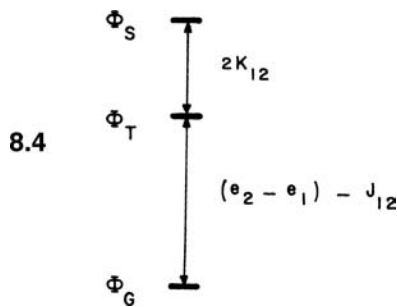
The MOs  $\psi_1$  and  $\psi_2$  are occupied by up-spin electrons in  $\Phi_T$ , but by down-spin electrons in  $\Phi'_T$ . It can be easily shown that the electronic energy of  $\Phi'_T$  or  $\Phi''_T$  is the same as that of  $\Phi_T$

$$E_T = \langle \Phi_T | \hat{H} | \Phi_T \rangle = \langle \Phi'_T | \hat{H} | \Phi'_T \rangle = \langle \Phi''_T | \hat{H} | \Phi''_T \rangle \quad (8.51)$$

Collecting the above results together,

$$\begin{aligned} E_T - E_G &= (e_2 - e_1) - J_{12} \\ E_S - E_T &= 2K_{12} \end{aligned} \quad (8.52)$$

Consequently, if  $(e_2 - e_1) - J_{12} > 0$ , the relative stability of the ground, the triplet, and the singlet excited states is given as in 8.4. Thus, with electron-electron



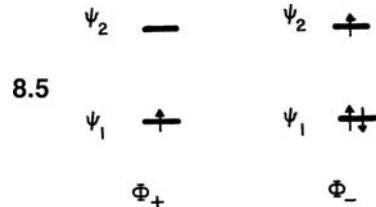
repulsion explicitly taken into consideration, the excitation energy is not simply given by the orbital energy difference  $(e_2 - e_1)$ . Since  $K_{12} > 0$ , the triplet state is always more stable than the singlet excited state.

## 8.6 IONIZATION POTENTIAL AND ELECTRON AFFINITY

The ionization potential (IP) and the electron affinity (EA) of a molecule M are defined as the energies required for the ionization processes



As indicated in 8.5, we may construct the cation state  $\Phi_+$  and the anion state  $\Phi_-$  by using the MOs  $\psi_1$  and  $\psi_2$  obtained from the ground state  $\Phi_G$ . The electronic



energies of those ionic states are evaluated via construction of the state wavefunctions using equation 8.13.  $\Phi_+ = \psi_1(1)$ , and  $\Phi_-$  is given by the determinant made up of the MOs  $\psi_1$ ,  $\bar{\psi}_1$  and  $\psi_2$ . Thus, we find

$$E_+ = \langle \Phi_+ | \hat{H} | \Phi_+ \rangle = h_1 = e_1 - J_{11} \quad (8.54)$$

$$\begin{aligned} E_- &= \langle \Phi_- | \hat{H} | \Phi_- \rangle \\ &= 2h_1 + h_2 + J_{11} + 2J_{12} - K_{12} \\ &= 2e_1 + e_2 - J_{11} \end{aligned} \quad (8.55)$$

and, combining with equation 8.42,

$$E_+ - E_G = -e_1 = \text{IP} \quad (8.56)$$

$$E_G - E_- = -e_2 = \text{EA} \quad (8.57)$$

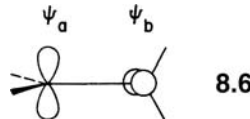
In general, for the electron configuration in 8.2, the ionization potential associated with an electron removal from an occupied MO  $\psi_i$  ( $i = 1, 2, 3, \dots, n$ ) is given by  $-e_i$ . This is known as Koopmans' theorem [5]. The energy of an unoccupied MO  $\psi_i$  ( $i = n+1, n+2, \dots$ ) refers to the potential exerted on an extra electron placed in that orbital. Thus, the energy required to remove such an electron from an unoccupied MO  $\psi_i$  (i.e., the electron affinity) is given by  $-e_i$ . These simple results are obtained because of the implicit assumptions that the electrons not involved in the ionization process are not perturbed and that the molecular geometry does not relax in the ionic states. Photoelectron spectroscopy (Section 7.5) yields experimental values of the ionization potentials associated with each occupied MO. Thus, Koopmans' theorem provides a direct comparison between theory and experiment, although its applicability is limited because of the assumptions employed to obtain it.

## 8.7 ELECTRON DENSITY DISTRIBUTION AND MAGNITUDES OF COULOMB AND EXCHANGE REPULSIONS

We noted in Section 8.3 that, for two MOs  $\psi_i$  and  $\psi_j$ , there are two kinds of electron-electron repulsions to consider, namely, the Coulomb repulsion  $J_{ij}$  and the

exchange repulsion  $K_{ij}$ . The electron density distributions associated with  $\psi_i$  and  $\psi_j$  are given by  $\psi_i\psi_i$  and  $\psi_j\psi_j$ , respectively. As noted earlier, these electron densities lead to  $J_{ij}$  (equation 8.18). On the other hand, it is the overlap density distribution  $\psi_i\psi_j$  that defines  $K_{ij}$  (equation 8.19).

The magnitude of  $K_{ij}$  is small unless the overlap density (not overlap integral)  $\psi_i\psi_j$  is large, in some region of space. Consider for example the two  $p$  orbitals  $\psi_a$  and  $\psi_b$  arranged perpendicular to each other as shown in **8.6**. Since the large amplitude

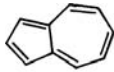


region of  $\psi_a$  does not coincide with that of  $\psi_b$ , the overlap density  $\psi_a\psi_b$  is small in all regions compared with the “diagonal” density  $\psi_a\psi_a$  or  $\psi_b\psi_b$ . Thus in **8.6**, the exchange repulsion  $K_{ab}$  is substantially smaller than the Coulomb repulsion  $J_{ab}$ . Further ramifications of this are pursued in Section 10.3. Given two MOs  $\psi_i$  and  $\psi_j$ , the magnitudes of  $J_{ij}$  and  $K_{ij}$  will satisfy the relationship [1]

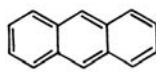
$$J_{ij} \geq K_{ij} \geq 0 \quad (8.58)$$

where the equality  $J_{ij} = K_{ij}$  arises when  $\psi_i$  and  $\psi_j$  are identical.

Another example that illustrates the effect of the overlap density  $\psi_i\psi_j$  upon the magnitude of  $K_{ij}$  involves two conjugated hydrocarbons. Listed in Table 8.1 are the experimental values of the first IP, the EA, the first singlet excitation energy ( $E_S - E_G$ ) and the first triplet excitation energy ( $E_T - E_G$ ) for azulene **8.7** and anthracene **8.8** [6]. For simplicity of notation, the highest occupied molecular orbital (HOMO) and lowest unoccupied molecular orbital (LUMO) of **8.7** and **8.8** are denoted by the



**8.7**



**8.8**

subscripts 1 and 2, respectively. According to Koopmans' theorem, the IP and EA values of **8.7** and **8.8** are related to their HOMO and LUMO energies as

$$\begin{aligned} e_2 &= -EA \\ e_1 &= -IP \end{aligned} \quad (8.59)$$

Despite the fact that the HOMO and LUMO energies of the two molecules are virtually identical, azulene is blue but anthracene is colorless (i.e.,  $E_S - E_G = 1.8$  and 3.3 eV for **8.7** and **8.8**, respectively). To explore the cause of this difference we note from equations 8.42 and 8.48 that the singlet excitation energy is given by

$$E_S - E_G = e_2 - e_1 - J_{12} + K_{12} \quad (8.60)$$

In addition, the magnitudes of  $J_{12}$  and  $K_{12}$  are estimated as follows:

$$J_{12} = e_2 - e_1 - (E_T - E_G) = -EA + IP - (E_T - E_G) \quad (8.61)$$

$$K_{12} = (E_S - E_T)/2 = (E_S - E_G)/2 - (E_T - E_G)/2 \quad (8.62)$$

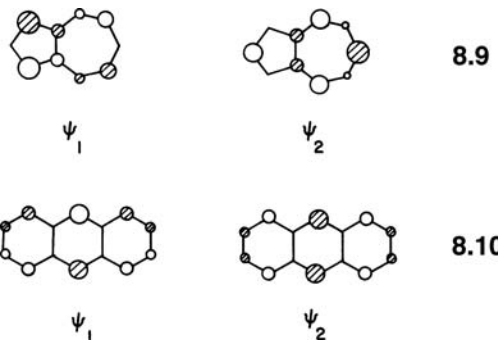
The  $J_{12}$  and  $K_{12}$  values derived in this way are listed in Table 8.1, which reveals that the  $J_{12}$  values of azulene and anthracene are nearly the same. Therefore, the difference in

**TABLE 8.1** The Ionization Potentials, Electron Affinities, and Excitation Energies of Azulene and Anthracene

Quantity <sup>a</sup>	Molecule	
	Azulene	Anthracene
IP	7.4	7.4
EA	0.7	0.6
$E_S - E_G$	1.8	3.3
$E_T - E_G$	1.3	1.8
$J_{12}$	5.4	5.0
$K_{12}$	0.25	0.75

<sup>a</sup>All the quantities are given in electron volts.

the  $(E_S - E_G)$  values of the two molecules originates largely from the fact that the  $K_{12}$  value of azulene is substantially smaller than that of anthracene. (Note that  $E_S - E_G$  is approximated by  $2K_{12}$ . Between **8.7** and **8.8**, the difference in  $E_S - E_G$  is 1.5 eV, and that in  $2K_{12}$  is 1.0 eV.) The nodal properties of the HOMO and LUMO in the two molecules are schematically depicted in **8.9** and **8.10**. They show that the large



amplitude regions of the HOMO coincide with those of the LUMO in anthracene, while this is not the case for azulene. Therefore, the overlap density  $\psi_1\psi_2$  of azulene is small in most regions, compared with that of anthracene. This leads to a smaller exchange repulsion  $K_{12}$ , and therefore a smaller  $E_S - E_G$ , for azulene than for anthracene [6].

## 8.8 LOW VERSUS HIGH SPIN STATES

According to **8.4**, the triplet state  $\Phi_T$  may become more stable than the singlet ground state  $\Phi_G$  if  $(e_2 - e_1) - J_{12} < 0$ , that is, when the orbital energy difference  $(e_2 - e_1)$  is small compared with the Coulomb repulsion  $J_{12}$ . Using equations 8.39 and 8.40, this may be expressed in terms of the difference in the core potentials

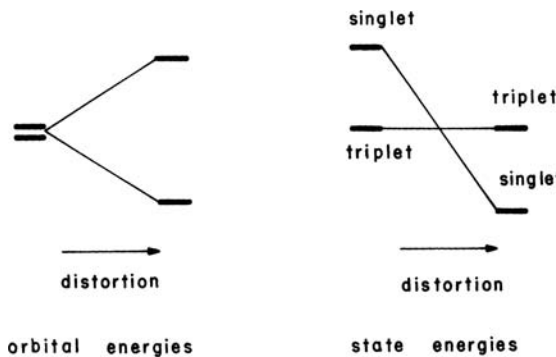
$$(E_T - E_G) = (h_2 - h_1) - J_{11} + J_{12} - K_{12} \approx h_2 - h_1 - J_{11} \quad (8.63)$$

where we have approximated the energy difference by making use of the relationship  $J_{12} \geq K_{12}$ . This shows that the high spin state  $\Phi_T$  becomes more stable than the low spin state  $\Phi_G$  when the core-potential difference  $(h_2 - h_1)$  is

smaller than the electron–electron repulsion  $J_{\parallel}$  resulting from the orbital double occupancy (i.e., electron pairing) in  $\psi_1$ . When the MOs  $\psi_1$  and  $\psi_2$  are degenerate,  $(h_2 - h_1)$  vanishes so that the high spin is more stable than the low spin state. This is a special case of Hund's first rule, that out of a collection of atomic states, the one with the highest spin multiplicity lies lowest in energy. It means in the molecular case, for example, that the lowest energy (or ground) electronic state of the oxygen molecule with the configuration  $(\pi_g)^2$  of Figure 6.3 will be a triplet, paramagnetic molecule.

The diffuseness of an orbital can play an important role in setting the energy difference between high and low spin states. When orbitals are contracted, the magnitude of  $J_{12}$  will be large, thereby making high spin states energetically preferred. An example of this behavior can be found in comparing the first row transition metal series which uses  $3d$  atomic orbitals versus their second and third row transition metal counterparts. The  $4d$  and  $5d$  elements have a  $d$  orbital core which serves to screen the valence  $d$  electrons from the nucleus. This is, of course, not present for the first row transition metal series so the  $3d$  atomic orbitals are much more contracted than their  $4d$  or  $5d$  counterparts. The Coulomb repulsion integrals associated with  $3d$  electrons are consequently larger, and hence high spin situations are more common for compounds of the first row transition elements. A similar case occurs for the first row elements in the Periodic Table compared to the others. The  $2p$  valence orbitals are more contracted than other  $np$  ( $n > 2$ ) valence orbitals, so the  $J_{12}$  terms are larger for the first row elements.

In Sections 7.1 and 7.2, the MOs of linear and bent  $AH_2$  were developed. There are six valence electrons in  $CH_2$  and so the  $\pi_u$  set is half-filled in a linear geometry. At a bent geometry  $2a_1$  is the HOMO and  $b_1$  is the LUMO for the ground singlet state. The energy gap between the  $2a_1$  and  $b_1$  levels is strongly dependent on the HCH angle, as can be seen from Figure 7.1. For reasons discussed in Section 7.3 the  $2a_1$  orbital is stabilized as the HCH angle decreases and  $b_1$  remains at constant energy. Therefore, in the triplet state for  $CH_2$  where  $b_1$  and  $2a_1$  are singly occupied, some of the driving force for bending is lost. Based on this orbital rationale, it is expected that the triplet state of  $CH_2$  should be less bent than its singlet analog. The result of an ab initio calculation on several electronic states of  $CH_2$  is discussed in Section 8.10. The relative stability of various electronic states as a function of molecular geometry is a general problem approachable only by direct calculation. Given a pair of degenerate levels and two electrons at the level of discussion here, the triplet state is always more stable than the singlet. Whether there is some other lower energy structure where this degeneracy is removed, and whether a singlet state lies lowest in energy (8.11), are difficult to probe qualitatively (see Section 8.10 for further discussion).



8.11

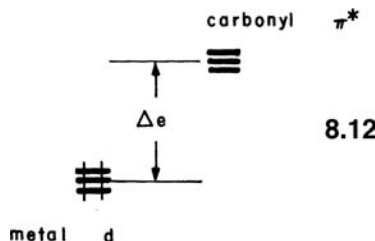
## 8.9 ELECTRON-ELECTRON REPULSION AND CHARGED SPECIES

As already noted, an important part of the orbital energy arises from electron-electron repulsion. The effective potential for an electron in the MO  $\psi_1$  of  $\Phi_+$  (8.5),  $e_1^+$ , is given by

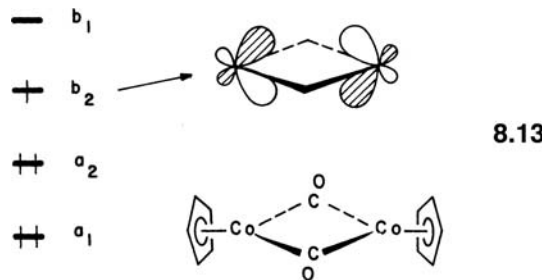
$$e_1^+ = h_1 = e_1 - J_{11} < e_1 \quad (8.64)$$

where  $e_1$  is the effective potential for an electron in the MO  $\psi_1$  of  $\Phi_+$  (8.3). Thus, removal of an electron lowers the orbital energy by an amount  $J_{11}$ , or equivalently, addition of an electron raises the orbital energy.

As an indication of the importance of charge on the energy levels of molecules, we look at the variation in carbonyl stretching vibrational frequencies in the series  $Mn(CO)_6^+$ ,  $Cr(CO)_6$ , and  $V(CO)_6^-$ . All are low spin  $d^6$ , isoelectronic molecules. The orbital details of how carbon monoxide bonds to a transition metal are reserved for Section 15.1. For this bonding, the acceptor behavior of the carbonyl  $\pi^*_{CO}$  level (8.12) plays an important role. As the extent of donation from metal  $d$  to



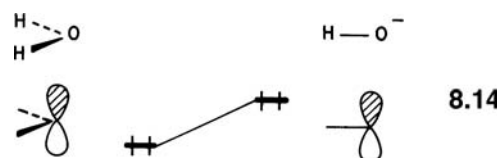
carbonyl  $\pi^*_{CO}$  increases, the carbonyl vibrational frequency becomes lowered. The mixing between these two sets of orbitals is intimately linked to their energy separation,  $\Delta e$ . If we imagine assembling one of these carbonyls from  $M^\pm$  (or  $M$ ) and six COs, the carbonyl levels will remain fixed in energy for all members of this series, but the location of the metal levels will depend on the charge. From what we have said earlier, their energy will decrease in the order  $|H_{\mu\mu}(M^+)| > |H_{\mu\mu}(M)| > |H_{\mu\mu}(M^-)|$ , leading to  $\Delta e$  values which decrease in the same order. Metal  $d \rightarrow \pi^*_{CO}$  donation will then increase in the order  $M^+ < M < M^-$  and the negative ion should have the lowest vibrational frequency. Experimentally,  $Mn(CO)_6^+$ ,  $Cr(CO)_6$ , and  $V(CO)_6^-$  have vibrational frequencies ( $t_{1u}$ ) of 2094, 1984, and  $1843\text{ cm}^{-1}$ , respectively [7]. A quantitative determination of the population of  $\pi^*_{CO}$  is given in Figure 15.5. A similar effect is seen upon reduction of the organometallic molecule,  $Co_2(\eta^5-C_5Me_5)_2(\mu-CO)_2$  [8]. One electron enters the  $b_2$  orbital of 8.13, a level



which is metal-metal antibonding but which contains no CO character. On reduction, the Co-Co distance accordingly increases by  $0.034\text{ \AA}$ . However, this is accompanied by a decrease in the Co-CO bond length of  $0.024\text{ \AA}$ . Clearly, a simple

one-electron orbital picture will not rationalize this result. What happens in fact is that the metal-located levels rise in energy on addition of the extra electron, and interaction with the  $\pi^*_{CO}$  levels increases as the energy separation  $\Delta e$  (of 8.12) decreases. This leads to a contraction of the Co–CO distance and a decrease in the CO stretching vibrational frequencies of about  $80\text{ cm}^{-1}$ .

Orbital energy also depends on core potential. The HOMOs of  $\text{H}_2\text{O}$  and  $\text{HO}^-$  are oxygen  $2p$  orbitals as shown in 8.14. The HOMO of  $\text{HO}^-$  is raised with respect to that of  $\text{H}_2\text{O}$  due to the loss of an atom that provides attractive potential. As a result,  $\text{OH}^-$  is more basic and nucleophilic.



## 8.10 CONFIGURATION INTERACTION [9]

So far it has been implicitly assumed that each electronic state of a molecule is represented by a single configuration (i.e., Slater determinant). This approach is known as the Hartree–Fock (HF) or SCF method, and the Slater determinant is called the HF wavefunction. In general, an electronic state of a molecule is better described if a linear combination of many configurations is used as its state wavefunction (i.e., multiconfiguration wavefunction). Physically, this process allows dynamic electron correlation (or, simply, electron correlation) to take place. Electron correlation refers to the fact that electrons of opposite spins also have a tendency to stay apart from each other to reduce their electrostatic repulsion. In HF theory, electron correlation is neglected because it assumes that each electron moves independently of all the electrons in the average field provided by them, that is, electrons of opposite spins are allowed to occupy the same space at the same time. Electron correlation, an energy lowering effect by definition, is incorporated into wavefunctions when they are expressed as linear combinations of many configurations. Computationally, the correlation energy of a multiconfiguration wavefunction is defined as its energy lowering relative to the energy of the corresponding HF configuration (precisely speaking, with respect to the energy of the HF-limit wavefunction, i.e., the best possible wavefunction in terms of a Slater determinant).

As an example of constructing a multiconfiguration wavefunction, consider two electron configurations  $\Phi_\mu$  and  $\Phi_\nu$  which are orthonormal, that is,

$$\begin{aligned}\langle \Phi_\mu | \Phi_\mu \rangle &= \langle \Phi_\nu | \Phi_\nu \rangle = 1 \\ \langle \Phi_\mu | \Phi_\nu \rangle &= 0\end{aligned}\tag{8.65}$$

so that their expectation values are given by

$$\begin{aligned}E_\mu &= \langle \Phi_\mu | \hat{H} | \Phi_\mu \rangle \\ E_\nu &= \langle \Phi_\nu | \hat{H} | \Phi_\nu \rangle\end{aligned}\tag{8.66}$$

Assuming that the interaction energy  $\langle \Phi_\mu | \hat{H} | \Phi_\nu \rangle$  between  $\Phi_\mu$  and  $\Phi_\nu$  is nonzero, configuration interaction (CI) wavefunctions  $\Psi_i^{\text{CI}}$  ( $i = 1, 2$ ) may be written as a linear

combination of the two configurations  $\Phi_\mu$  and  $\Phi_\nu$

$$\Psi_i^{\text{CI}} = d_{\mu i} \Phi_\mu + d_{\nu i} \Phi_\nu \quad (8.67)$$

where  $d_{\mu i}$  and  $d_{\nu i}$  are the mixing coefficients. We demand these CI wavefunctions to be normalized to unity (i.e.,  $\langle \Psi_i^{\text{CI}} | \Psi_i^{\text{CI}} \rangle = 1$ ) and also to be eigenfunctions of the molecular Hamiltonian  $\hat{H}$ :

$$\hat{H} \Psi_i^{\text{CI}} = E_i^{\text{CI}} \Psi_i^{\text{CI}} \quad (8.68)$$

Then the state energies  $E_i^{\text{CI}}$  ( $i = 1, 2$ ) are determined by solving the secular equation

$$\begin{vmatrix} E_\mu - E_i^{\text{CI}} & \langle \Phi_\mu | \hat{H} | \Phi_\nu \rangle \\ \langle \Phi_\mu | \hat{H} | \Phi_\nu \rangle & E_\nu - E_i^{\text{CI}} \end{vmatrix} = 0 \quad (8.69)$$

in an exactly analogous way to the generation of MOs from atomic orbitals in Section 1.3.

As a practical example of CI wavefunctions, let us consider how to improve the singlet ground state  $\Phi_G$  of **8.3**. The obvious question is to determine what configurations can mix with  $\Phi_G$ . First, we examine the interaction between  $\Phi_G$  and  $\Phi_1$ . Note that the MOs used in constructing  $\Phi_1$  are obtained from a closed-shell configuration  $\Phi_G$ , and  $\Phi_1$  differs from  $\Phi_G$  only in one MO. In such a case, the interaction  $\langle \Phi_G | \hat{H} | \Phi_1 \rangle$  vanishes according to Brillouin's theorem [10], which states that the HF wavefunction does not interact with its singly excited configurations. This can be shown as follows:

$$\begin{aligned} \langle \Phi_G | \hat{H} | \Phi_1 \rangle &= \langle \psi_1 | \hat{h} | \psi_2 \rangle + (\psi_1 \psi_1 | \psi_1 \psi_2) \\ &= \langle \psi_1 | \hat{h} | \psi_2 \rangle + \langle \psi_1 | \hat{J}_1 | \psi_2 \rangle \end{aligned} \quad (8.70)$$

Because of the relationship,

$$\langle \psi_1 | \hat{J}_1 | \psi_2 \rangle = \langle \psi_1 | \hat{K}_1 | \psi_2 \rangle = (\psi_1 \psi_1 | \psi_1 \psi_2) \quad (8.71)$$

equation 8.70 can be rewritten as

$$\begin{aligned} \langle \Phi_G | \hat{H} | \Phi_1 \rangle &= \langle \psi_1 | \hat{h} + 2\hat{J}_1 - \hat{K}_1 | \psi_2 \rangle \\ &= \langle \psi_1 | \hat{F} | \psi_2 \rangle = e_2 \langle \psi_1 | \psi_2 \rangle = 0 \end{aligned} \quad (8.72)$$

Similarly,  $\langle \Phi_G | \hat{H} | \Phi_2 \rangle = 0$ . Thus, the singlet excited configuration  $\Phi_S$  (equation 8.46) cannot mix into  $\Phi_G$ . The only configuration of **8.3** that can mix with  $\Phi_G$  is the doubly excited configuration  $\Phi_E$ , since

$$\langle \Phi_G | \hat{H} | \Phi_E \rangle = (\psi_1 \psi_2 | \psi_1 \psi_2) = K_{12} > 0 \quad (8.73)$$

Therefore, the CI wavefunction  $\Psi_i^{\text{CI}}$  ( $i = 1, 2$ ) may be written as

$$\Psi_i^{\text{CI}} = d_{Gi} \Phi_G + d_{Ei} \Phi_E \quad (8.74)$$

and the state energies  $E_i^{\text{CI}}$  ( $i = 1, 2$ ) of these CI wavefunctions  $\Psi_i^{\text{CI}}$  are obtained from

$$\begin{vmatrix} E_G - E_i^{\text{CI}} & K_{12} \\ K_{12} & E_E - E_i^{\text{CI}} \end{vmatrix} = 0 \quad (8.75)$$

Without loss of generality, it may be assumed that  $E_1^{\text{CI}} < E_2^{\text{CI}}$ . Then if the energy difference between  $\Phi_G$  and  $\Phi_E$  is substantially greater than the interaction energy  $K_{12}$  between them, we obtain the following results

$$\begin{aligned} \Psi_1^{\text{CI}} &\cong \Phi_G + \frac{K_{12}}{E_G - E_E} \Phi_E \\ E_1^{\text{CI}} &\cong E_G + \frac{(K_{12})^2}{E_G - E_E} \end{aligned} \quad (8.76)$$

Thus  $E_1^{\text{CI}}$  is lower in energy than  $E_G$ , and a better description of the singlet ground state is given by  $\Psi_1^{\text{CI}}$ , the leading configuration of which is  $\Phi_G$ . In  $\Psi_1^{\text{CI}}$ ,  $\Phi_E$  mixes into  $\Phi_G$  with a negative mixing coefficient since the interaction energy  $\langle \Phi_G | \hat{H} | \Phi_E \rangle = K_{12}$  is positive.

It is important to consider these results from the viewpoint of MO occupation. In the HF wavefunction  $\Phi_G$ , the MO  $\psi_1$  is doubly occupied, and the excited configuration  $\Phi_E$  is made up of the unoccupied MO  $\psi_2$ . The CI wavefunction  $\Psi_1^{\text{CI}}$ , which is a linear combination of  $\Phi_G$  and  $\Phi_E$ , should be normalized to unity. This makes the occupancy of  $\psi_1$  smaller than 2, and that of  $\psi_2$  greater than zero, in  $\Psi_1^{\text{CI}}$ . In essence, CI calculations incorporate electron correlation effects by slightly depopulating the occupied MOs and slightly populating the unoccupied MOs.

For qualitative discussions of chemical problems, one of the most important uses of CI wavefunctions arises when we deal with potential energy surfaces for chemical reactions. Let us suppose that the MOs  $\psi_1$  and  $\psi_2$  in 8.3 are functions of a reaction coordinate  $q$  as shown in Figure 8.1a, and the symmetry properties of these MOs are different throughout the reaction coordinate. Thus, Figure 8.1a is a typical example of a symmetry-forbidden thermal reaction. (To make our example more concrete,  $\psi_1$  and  $\psi_2$  of Figure 8.1a might be considered as, for example,  $\psi_2$  and  $\psi_3$  of Figure 5.8 which describes one geometrical possibility for the  $H_2/D_2$  exchange

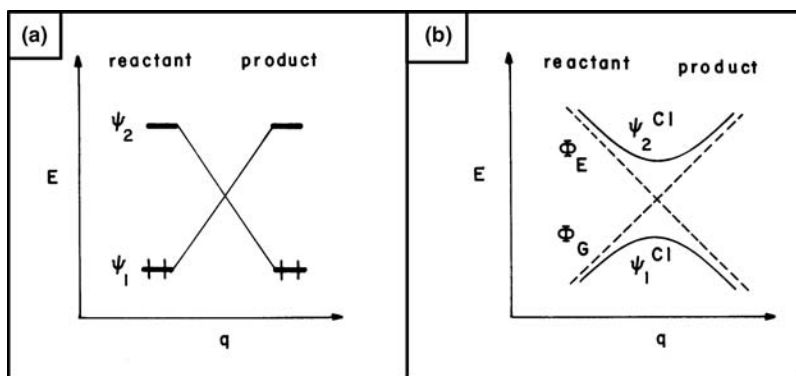


**FIGURE 8.1**

Orbital and state energy correlation diagrams of a typical symmetry-forbidden thermal reaction, where  $q$  refers to an appropriate reaction coordinate: (a) orbital energy and (b) state energy.

reaction.) The energies of the states resulting from the configurations  $(\psi_1)^2$  and  $(\psi_2)^2$  (i.e.,  $\Phi_G$  and  $\Phi_E$  respectively) vary as shown by the dashed lines in Figure 8.1b. The energies of the CI wavefunctions  $\Psi_1^{\text{CI}}$  and  $\Psi_2^{\text{CI}}$ , which are obtained by solving equation 8.75, behave as shown by the solid lines. This is another example of the noncrossing rule discussed in Section 4.7. The symmetry-forbidden nature of the reaction is indicated by the presence of a barrier between reactant and product in the potential energy surface for the state  $\Psi_1^{\text{CI}}$ .

We note that near the reactant site where  $E_G < E_E$ ,  $\Psi_1^{\text{CI}}$  is given by

$$\Psi_1^{\text{CI}} \cong \Phi_G + \frac{K_{12}}{E_G - E_E} \Phi_E \quad (8.77)$$

At the transition state where  $E_G = E_E$ ,  $\Psi_1^{\text{CI}}$  is expressed as

$$\Psi_1^{\text{CI}} = \frac{\Phi_G - \Phi_E}{\sqrt{2}} \quad (8.78)$$

Finally, near the product site where  $E_G > E_E$ ,  $\Psi_1^{\text{CI}}$  is written as

$$\Psi_1^{\text{CI}} \cong \Phi_E + \frac{K_{12}}{E_E - E_G} \Phi_G \quad (8.79)$$

Consequently, the new wavefunction  $\Psi_1^{\text{CI}}$  provides a continuous transformation from a wavefunction predominantly  $\Phi_G$  to one predominantly  $\Phi_E$  in character as the reaction proceeds.

As a practical example of configuration interaction, let us examine the result of an ab initio calculation on methylene,  $\text{CH}_2$ , summarized in Figure 8.2 [11]. An orbital description of the configurations leading to those states of Figure 8.2 is given in **8.15** for bent  $\text{CH}_2$  and in **8.16** for linear  $\text{CH}_2$ . For simplicity, other low-lying filled levels are not shown, and the Slater determinants resulting from the various electron configurations are denoted by parentheses. At any nonlinear geometry, there are two states of  ${}^1\text{A}_1$  symmetry. The upper state mixes into the lower one stabilizing

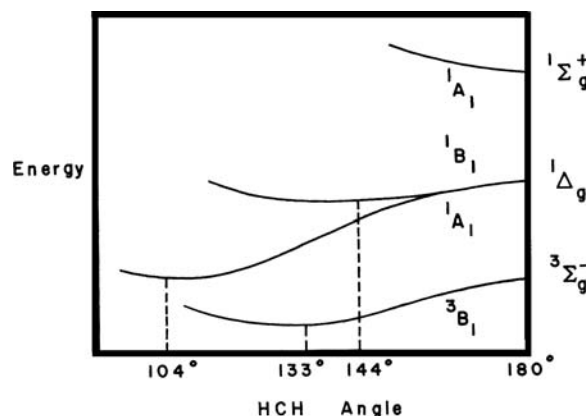
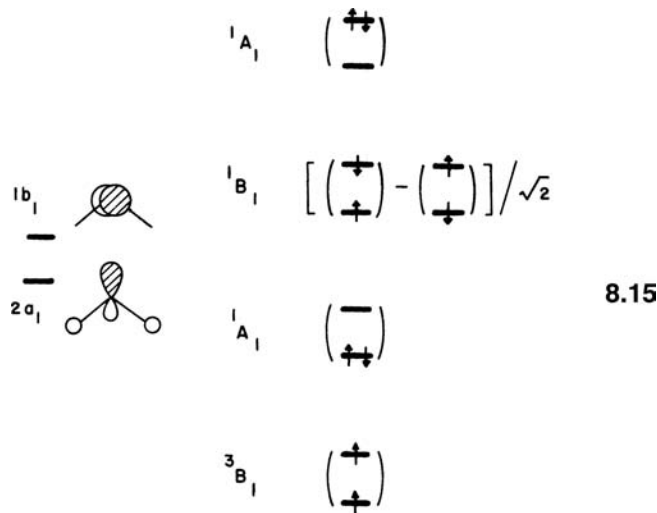
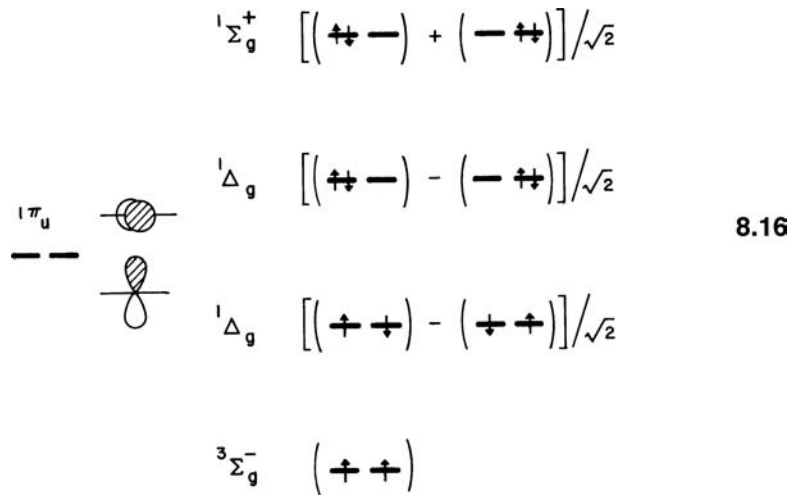


**FIGURE 8.2**

Calculated state energies of carbene  $\text{CH}_2$  as a function of the HCH valence angle.



the latter, and this in turn complicates the task of evaluating the singlet-triplet energy difference. For linear  $\text{CH}_2$ , each of the  ${}^1\Sigma_g$  and  ${}^1\Delta_g$  states is represented by a linear combination of two configurations of identical energy. It is not obvious from the orbital representations of 8.16 why the two components of the  ${}^1\Delta_g$  state should be



the same in energy. Let us represent the two atomic  $p$  orbitals of 8.16 by  $\phi_a$  and  $\phi_b$ . Then, it can be easily shown that the electronic energy of the upper  ${}^1\Delta_g$  is given by

$$E({}^1\Delta_g) = 2h_a + J_{aa} - K_{ab} \quad (8.80)$$

while that of the lower  ${}^1\Delta_g$  state is given by

$$E({}^1\Delta_g) = 2h_a + J_{ab} + K_{ab} \quad (8.81)$$

In deriving equations 8.80 and 8.81, we employed the relationships that  $h_b = h_a$ , and  $J_{bb} = J_{aa}$ . Consequently, the degeneracy of the two  ${}^1\Delta_g$  states requires that

$$J_{aa} - K_{ab} = J_{ab} + K_{ab} \quad (8.82)$$

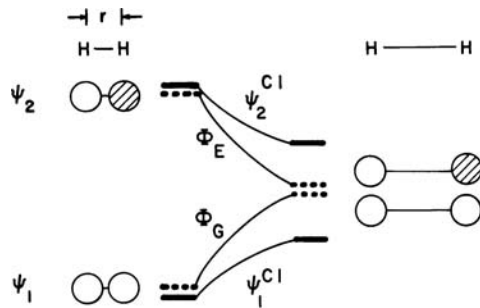
This is the case, [12] although we will not show the proof.

Figure 8.2 shows that the  $^1B_1$  state has an optimum HCH angle in the same region as the  $^3B_1$  state, while the molecule in these two states is significantly less bent than that in the lower  $^1A_1$  state. It is easy to understand this observation based on the Walsh diagram for  $\text{SH}_2$  shown in Figure 7.5. In both  $^1B_1$  and  $^3B_1$  states, the  $2a_1$  and  $b_1$  orbitals are singly occupied. On the other hand, the lower  $^1A_1$  state is dominated by the configuration that has the  $2a_1$  level doubly occupied and the  $b_1$  level empty. As noted in Figure 7.5 the  $2a_1$  level is lowered upon bending, but the  $b_1$  level is energetically invariant to bending. In general, those systems that have two closely spaced orbitals of different symmetry but only two electrons in them are referred to as diradicals [13]. Without elaborate calculations it is difficult to predict whether the ground electronic state of a diradical will be a singlet or triplet, but we can establish trends using the singlet–triplet energy differences from Walsh diagrams and a detailed knowledge of how orbitals are perturbed during geometrical distortion. In Section 7.4. we discussed why the HAH valence angle of  $\text{H}_2\text{S}$  is smaller than that of  $\text{H}_2\text{O}$ . As the HAH angle decreases, the stabilization of the  $2a_1$  level is greater for  $\text{H}_2\text{S}$  than  $\text{H}_2\text{O}$ . Similarly, with respect to a linear geometry, the  $^1A_1$  state is stabilized more for  $\text{SiH}_2$  than  $\text{CH}_2$ . In fact, for  $\text{SiH}_2$  and  $\text{GeH}_2$ , the  $^1A_1$  state is 22.8 and 23.2 kcal/mol, respectively, more stable than the  $^3B_1$  state [14]. In  $\text{CH}_2$  the  $^1A_1$  state is 9.0 kcal/mol higher in energy than  $^3B_1$  [15]. One should also recall that  $J_{12}$  (where 1 and 2 refer to the  $2a_1$  and  $b_1$  molecular orbitals) will be larger for  $\text{CH}_2$  than in  $\text{SiH}_2$  and  $\text{GeH}_2$  because the  $2p$  atomic orbital is more contracted than other  $np$  ( $n > 2$ ) orbitals. Thus, the triplet state is stabilized more in a relative sense for  $\text{CH}_2$ . For a quantitative understanding of diradical systems, configuration interaction is of vital importance. The  $\text{H}_2/\text{D}_2$  exchange, rectangular versus square planar cyclobutadiene,  $\text{Cr}(\text{CO})_5$ , and  $\text{Fe}(\text{CO})_4$  dynamics are all diradical situations. What we have learned from  $\text{CH}_2$  is applicable to all of them.

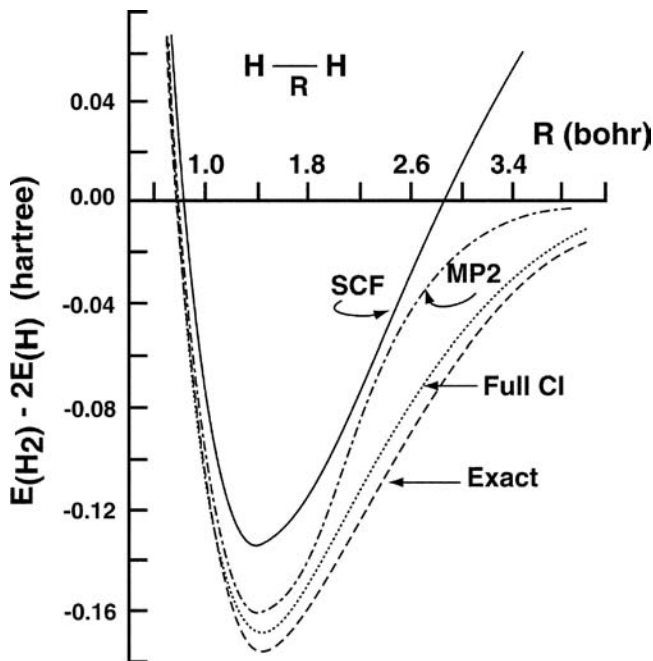
## 8.11 TOWARD MORE QUANTITATIVE TREATMENTS

Accurate calculations of the potential energy surface of a given chemical species allow one to identify various minimum-energy structures and evaluate their relative energies along with the energy barriers of their interconversion. For this purpose, calculations should be carried out using extensive AO basis sets and with electron correlation taken into consideration. In this section, we discuss several important issues associated with calculations at correlated levels, that is, at calculations beyond the HF description.

Figure 8.3 compares the potential energy curves of  $\text{H}_2$  calculated as a function of the  $\text{H} \cdots \text{H}$  distance with various computational methods [16]. As depicted in 8.17,



8.17

**FIGURE 8.3**

Relative total energy of H<sub>2</sub> as a function of internuclear distance. The SCF, MP2, and full CI calculations use a 6–31G\*\* basis set, and the exact calculation refers to the work by Kolos and Wolniewicz [22].

the bonding and antibonding levels of H<sub>2</sub> become closer in energy as the internuclear distance is increased. Consequently, the two electronic states  $\Phi_G = (\psi_1)^2$  and  $\Phi_E = (\psi_2)^2$  become closer in energy and hence configuration interaction between them becomes increasingly important. With a HF calculation, the MOs  $\psi_1$  and  $\psi_2$  cannot become degenerate even at a very large H · · · H distance. As discussed in Section 8.6,  $\psi_1$  is associated with an effective potential generated by one electron, but  $\psi_2$  with one generated by two electrons. H<sub>2</sub> dissociates into two H· radicals, not into H<sup>-</sup> and H<sup>+</sup> ions. Figure 8.3 shows that at large H · · · H distances the energy of the HF (labeled as SCF) wavefunction is higher than that of two H atoms. In other words, the HF wavefunction does not predict the correct dissociation products. This difficulty arises from the fact that the HF wavefunction, being constructed with one doubly occupied orbital, cannot describe the “diradical” state of two H atoms. In general, such a failure of a HF wavefunction in describing the dissociation of a molecule into open shell fragments is known as the HF catastrophe. Figure 8.3 shows that calculations at correlated levels lead to correct dissociation products. Nevertheless, it is important to note from Figure 8.3 that all wavefunctions, including the HF one, predict a similar equilibrium H · · · H distance and a similar curvature of the potential energy around the minimum distance. This observation is general for closed-shell molecules and provides a basis for why HF calculations can often be used to study their minimum energy structures and vibrational spectra. However, correlated levels of theory are frequently necessary when one studies transition states where there is significant bond breaking.

There are many ways of including electron correlation in electronic structure calculations [16,17]. In most CI calculations, various configurations are generated using the MOs  $\phi_i$  derived from a HF calculation, and the AO coefficients  $c_{\mu i}$  of the MOs  $\phi_i$  are not further optimized. Excited configurations that will interact with the ground state configuration  $\Phi_G$  are generated from  $\Phi_G$  by replacing occupied MOs with unoccupied MOs. In a full CI calculation, all possible excited configurations resulting from a given HF configuration  $\Phi_G$  are included. However, full CI calculations are practically impossible to carry out except for small molecules so that most CI calculations are based on truncated number of configurations. In

the multiconfiguration self-consistent field (MCSCF) method, [16,17] a state wavefunction is expressed as a linear combination of a small number of configurations  $\Phi_v$  ( $v = 1, 2, \dots, p$ )

$$\Psi^{\text{MCSCF}} = d_1\Phi_1 + d_2\Phi_2 + \dots + d_p\Phi_p \quad (8.83)$$

Then both the coefficients  $d_v$  of the configurations and the AO coefficients  $c_{\mu i}$  of the MOs  $\phi_i$  making up the configurations are optimized. In other words, an MCSCF calculation employs improved MOs and hence improved configurations to construct a state wavefunction. As a result, an MCSCF calculation with a small number of configurations can achieve the accuracy of what a regular CI calculation provides using a large number of configurations.

CI calculations are not the only method of improving the HF energy of a system. In Møller–Plesset perturbation theory [16], a perturbation expansion of the correlation energy is obtained by writing the total Hamiltonian  $\hat{H}$  as

$$\hat{H} = \hat{H}_0 + \hat{V} \quad (8.84)$$

The “unperturbed” Hamiltonian  $\hat{H}_0$  is defined as a sum of the Fock operators for all the occupied MOs (see equation 8.24),

$$\hat{H}_0 = \sum_{\mu=1}^n \left( \hat{h}(\mu) + \sum_{j=1}^n [2\hat{J}_j(\mu) - \hat{K}_j(\mu)] \right) \quad (8.85)$$

and the perturbation  $\hat{V}$  is defined as the difference between the true electron repulsion and the electron repulsion obtained by the HF method, namely,

$$\hat{V} = \sum_{\mu < v} \frac{1}{r_{\mu v}} - \sum_{\mu=1}^n \sum_{j=1}^n [2\hat{J}_j(\mu) - \hat{K}_j(\mu)] \quad (8.86)$$

(In our calculations for the correction of the HF energy, the geometry of a molecule is kept constant. Thus, the nuclear–nuclear repulsion is omitted from our consideration in writing down the total Hamiltonian  $\hat{H}$ .) Given the HF wavefunction  $\Phi_G$  and its energy  $E_G$  associated with the total Hamiltonian  $\hat{H}$ ,

$$\hat{H}\Phi_G = E_G\Phi_G \quad (8.87)$$

The wavefunction  $\Phi_G$  is also an eigenfunction of the Hamiltonian  $\hat{H}_0$

$$\hat{H}_0\Phi_G = E_0^{(0)}\Phi_G \quad (8.88)$$

where  $E_0^{(0)}$  is the sum of all the occupied orbital energies

$$E_0^{(0)} = \langle \Phi_G | \hat{H}_0 | \Phi_G \rangle \sum_{i=1}^n 2e_i \quad (8.89)$$

Thus,  $\Phi_G$  is the zeroth-order wavefunction (i.e.,  $\Phi^{(0)}$ ), and  $E_0^{(0)}$  is the zeroth-order energy. In Møller–Plesset perturbation theory the total energy is expanded as

$$E = E_0^{(0)} + E_0^{(1)} + E_0^{(2)} + E_0^{(3)} + E_0^{(4)} + \dots$$

The first-order energy  $E_0^{(1)}$  is given by

$$E_0^{(1)} = \langle \Phi_G | \hat{V} | \Phi_G \rangle = \sum_{i=1}^n \sum_{j=1}^n (2J_{ij} - K_{ij}) = V_{ee} \quad (8.90)$$

so that the sum of the zeroth- and first-order energies is equal to the HF energy,

$$E_0^{(0)} + E_0^{(1)} = E_G \quad (8.91)$$

and the total energy is rewritten as

$$E = E_G + E_0^{(2)} + E_0^{(3)} + E_0^{(4)} + \dots \quad (8.92)$$

Therefore, the correction to the HF energy starts with the second-order energy  $E_0^{(2)}$ ,

$$E_0^{(2)} = \sum_i \frac{\langle \Phi_G | \hat{V} | \Phi_{ab}^{rs} \rangle^2}{E_0^{(0)} - E_i^{(0)}} \frac{\langle \Phi_G | \hat{V} | \Phi_{ab}^{rs} \rangle^2}{E_0^{(0)} - E_i^{(0)}} \quad (8.93)$$

where  $E_i^{(0)}$  is the energy of a doubly excited configuration  $\Phi_{ab}^{rs}$ , which results from  $\Phi_G$  when the occupied orbitals  $\phi_a$  and  $\phi_b$  are replaced with the unoccupied orbitals  $\phi_r$  and  $\phi_s$ . The expressions for the third- and fourth-order energies are more complex. In Figure 8.3, the potential curve labeled as MP2 means that the HF energy was corrected by Møller–Plesset perturbation theory up to the second order. This is a utilitarian technique for electron correlation; the calculations require modest amounts of computation times relative to the HF method. This is often, however, just a starting point for more sophisticated treatments which are directed toward getting quantitative details right. Notice in Figure 8.3 that while  $H_2$  dissociates correctly at the MP2 level, nonetheless, the potentials from 2.2 to 3.4 bohr lie much higher in energy than the full CI or exact solutions but all three are quite close in energy around the minimum energy structure. Møller–Plesset perturbation theory itself has problems when a molecule is not well described by a single determinate wavefunction; here, for example, an MCSCF type of approach will yield more satisfactory results.

In the application of electronic structure calculations, one often needs to calculate the relative energies of molecules of different sizes. In electronic structure calculations for any realistic chemical system, one is forced to adopt approximate schemes (e.g., in the choice of AO basis sets and CI wavefunctions). For calculated relative energies to be meaningful, approximate schemes should be equally good for molecules with different number of electrons. For example, consider a dimer composed of two identical but noninteracting monomers. Such a dimer is well approximated by one in which two monomers are separated by a large distance. Because the monomers do not interact, it is required that the energy of the dimer be twice the energy of the monomer. When an approximate scheme for total energy calculation satisfies this requirement, it is said to be size-consistent [16]. The HF method, Møller–Plesset perturbation theory, and full CI are all size consistent. However, truncated CI is not size consistent. This can be readily illustrated by considering CI calculations with doubly excited configurations for a dimer of two noninteracting  $H_2$  molecules. For the case of two isolated monomers, the CI wavefunction of each monomer contains double excitations within the monomer so that both monomers have double excitations simultaneously. However, the CI

wavefunction of the noninteracting dimer exclude the possibility that both monomers are both doubly excited because this amounts to a quadruple excitation in the dimer.

---

## 8.12 THE DENSITY FUNCTIONAL METHOD [18,19]

---

The density functional (DF) method of electronic structure calculations is based on the fact that the ground state of a many-electron system is completely determined by its electron density. When compared with correlated ab initio methods, the density functional method can be applied to much larger systems than those approachable by traditional ab initio methods. The density functional method has long been employed in studying electronic structures of solid-state systems and has become a widely applicable, advanced computational method in chemistry. In this section, we briefly comment on the concepts of DF theory and compare them with those of HF theory.

The essential aspects of DF and HF theories can be summarized as follows [20]: The total energy of a system is determined by its wavefunction  $\Phi$  in HF theory, and by its total electron density  $\rho$  in DF theory.

$$\text{HF} : E = E(\Phi) \quad (8.94\text{a})$$

$$\text{DF} : E = E(\rho) \quad (8.94\text{b})$$

The total energy is an expectation value of the total Hamiltonian  $\hat{H}$  in HF theory, while it is decomposed into three density-dependent terms in DF theory (i.e., a kinetic energy term  $T(\rho)$ , a Coulomb energy term  $U(\rho)$ , and a many-body term  $E_{\text{xc}}(\rho)$  which contains all exchange and electron correlation effects).

$$\text{HF} : E = \langle \Phi | \hat{H} | \Phi \rangle \quad (8.95\text{a})$$

$$\text{DF} : E = T(\rho) + U(\rho) + E_{\text{xc}}(\rho) \quad (8.95\text{b})$$

The state wavefunction  $\Phi$  is described by a Slater determinant using one-electron functions  $\psi_i$  ( $i = 1, 2, \dots, n$ ) in HF theory, and the total density  $\rho$  is decomposed into single-electron densities, which originate from one-electron functions  $\psi_i$  in DF theory.

$$\text{HF} : \Phi = \hat{A} \psi_1 \bar{\psi}_1 \psi_2 \bar{\psi}_2 \cdots \psi_n \bar{\psi}_n \quad (8.96\text{a})$$

$$\text{DF} : \rho = \sum_{i=1}^n 2\psi_i \bar{\psi}_i \quad (8.96\text{b})$$

The total energy assumes a minimum upon variation of the wavefunction in HF theory, and upon the variation of the total electron density in DF theory.

$$\text{HF} : \frac{\partial E}{\partial \Phi} = 0 \quad (8.97\text{a})$$

$$\text{DF} : \frac{\partial E}{\partial \rho} = 0 \quad (8.97\text{b})$$

Equation 8.97a,b lead to one-electron eigenvalue equations, that is, the Fock equation in HF theory and the Kohn–Sham equation in DF theory.

$$\text{HF} : [\hat{h}(\mathbf{r}) + \hat{V}_c(\mathbf{r}) + \hat{V}_x^i(\mathbf{r})]\psi_i(\mathbf{r}) = e_i\psi_i(\mathbf{r}) \quad (8.98\text{a})$$

$$\text{DF} : [\hat{h}(\mathbf{r}) + \hat{V}_c(\mathbf{r}) + \hat{V}_{xc}(\mathbf{r})]\psi_i(\mathbf{r}) = e_i\psi_i(\mathbf{r}) \quad (8.98\text{b})$$

In these expressions the coordinates of an electron,  $\mathbf{r} = (x, y, z)$ , are explicitly shown. In this notation, the distance between two electrons located at coordinates  $\mathbf{r} = (x, y, z)$  and  $\mathbf{r}' = (x', y', z')$  is given by  $1/|\mathbf{r} - \mathbf{r}'|$ . The Fock equation (i.e., equation 8.98a) is expressed slightly differently from what we discussed in Section 8.3 in order to compare the difference between HF and DF theories.  $\hat{h}(\mathbf{r})$  is the core-Hamiltonian (equation 8.6), and the Coulomb repulsion  $V_c(\mathbf{r})$  is given by

$$V_c(\mathbf{r}) = \sum_{j=1}^n 2\hat{J}_j(\mathbf{r}) = \sum_{j=1}^n 2 \int \frac{\psi_j(\mathbf{r}')\psi_j(\mathbf{r}') d\mathbf{r}'}{|\mathbf{r} - \mathbf{r}'|} \quad (8.99)$$

(see equation 8.24). The difference between HF and DF theories lies in the terms  $V_x^i(\mathbf{r})$  and  $V_{xc}(\mathbf{r})$ . The definition of the exchange operator in equation 8.21 can be rewritten as

$$\begin{aligned} \hat{K}_j(\mathbf{r})\psi_i(\mathbf{r}) &= \left( \int \frac{\psi_j(\mathbf{r}')\psi_i(\mathbf{r}') d\mathbf{r}'}{|\mathbf{r} - \mathbf{r}'|} \right) \psi_j(\mathbf{r}) \\ &= \left( \int \frac{\psi_j(\mathbf{r}')\psi_i(\mathbf{r}')\psi_j(\mathbf{r})\psi_i(\mathbf{r}) d\mathbf{r}'}{|\mathbf{r} - \mathbf{r}'|} \right) / \psi_i(\mathbf{r}) \end{aligned} \quad (8.100)$$

Provided that  $\hat{K}_j(\mathbf{r})$  acts on  $\psi_i(\mathbf{r})$ ,  $\hat{K}_j(\mathbf{r})$  can be expressed as

$$\hat{K}_j(\mathbf{r}) = \left( \int \frac{\psi_j(\mathbf{r}')\psi_i(\mathbf{r}')\psi_j(\mathbf{r})\psi_i(\mathbf{r}) d\mathbf{r}'}{|\mathbf{r} - \mathbf{r}'|} \right) / \psi_i(\mathbf{r})\psi_i(\mathbf{r}) \quad (8.101)$$

Therefore the exchange operator  $V_x^i(\mathbf{r})$  is written as

$$\begin{aligned} V_x^i(\mathbf{r}) &= -\sum_{j=1}^n \hat{K}_j(\mathbf{r}) \\ &= -\sum_{j=1}^n \left( \int \frac{\psi_j(\mathbf{r}')\psi_i(\mathbf{r}')\psi_j(\mathbf{r})\psi_i(\mathbf{r}) d\mathbf{r}'}{|\mathbf{r} - \mathbf{r}'|} \right) / \psi_i(\mathbf{r})\psi_i(\mathbf{r}) \end{aligned} \quad (8.102)$$

This operator depends on the orbital  $\psi_i(\mathbf{r})$  on which it acts and contains information of all wavefunctions from the entire system. For instance, the  $V_x^i(\mathbf{r})$  operator is highly nonlocal. The corresponding term in DF theory is the exchange-correlation operator  $\hat{V}_{xc}(\mathbf{r})$ . This operator contains exchange as well as electron correlation effects (see below) and does not depend on the orbital on which it acts.

The HF equations solve the exact Hamiltonian (i.e., the molecular Hamiltonian) with approximate many-body wavefunctions (i.e., Slater determinants). As discussed earlier, HF-based methods converge to the exact solution through systematic improvements in the form of many-body wavefunctions such as CI wavefunctions. Approximations in DF theory are introduced only in the exchange-correlation operator  $\hat{V}_{xc}(\mathbf{r})$ . Thus, the DF equations solve an approximate many-body Hamiltonian with exact wavefunctions. DF theory approaches the exact solution

by improving the exchange-correlation operator  $\hat{V}_{xc}(\mathbf{r})$ . The latter is related to the total exchange-correlation energy  $E_{xc}(\rho)$  and the total density  $\rho(\mathbf{r})$  as

$$\hat{V}_{xc}(r) = dE_{xc}(\rho)/d\rho \quad (8.103)$$

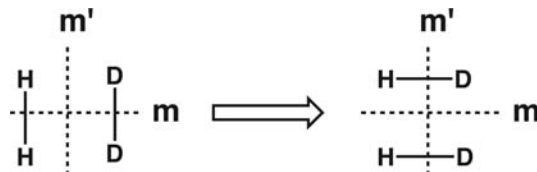
so it is determined by specifying the functional forms of  $E_{xc}(\rho)$ . The most common approximation to  $E_{xc}(\rho)$  is the local density approximation (LDA)

$$E_{xc}^{\text{LDA}}(\rho) = E_x^{\text{LDA}}(\rho) + E_c^{\text{LDA}}(\rho) \quad (8.104)$$

The first term represents the exchange energy, and the second term the correlation energy. The errors introduced in the  $E_x^{\text{LDA}}(\rho)$  term are corrected by adding a nonlocal correction term  $E_x^{\text{NL}}(\rho)$ . Discussion of how these terms depend on the total density  $\rho(\mathbf{r})$  is beyond the scope of this book. Some methods combine the density functional exchange functional with the Hartree–Fock exchange term and are known as hybrid functional methods. This is an area of very active research where many formulations have been proposed. A very popular one is the B3LYP hybrid functional. Unfortunately there is no a priori way at present to determine which functional will be best for a given problem. We note in passing that the eigenvalues and shapes of MOs from LDA calculations bear a close resemblance to those obtained from one-electron calculations [21].

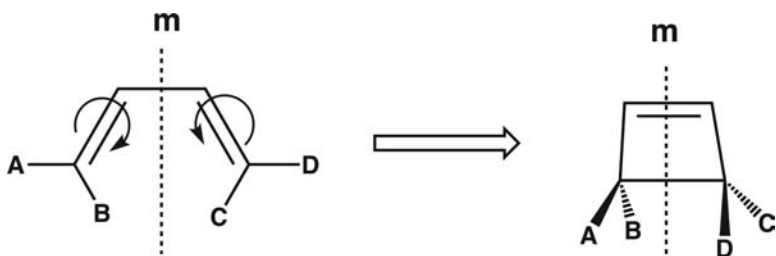
## PROBLEMS

- 8.1.** Consider the determinantal (i.e., Hartree–Fock) wavefunction  $\Psi(1, 2, 3, 4)$  for a four-electron system. How are the following wavefunctions related to  $\Psi(1, 2, 3, 4)$ ?
- $\Psi(2, 1, 3, 4)$
  - $\Psi(2, 4, 3, 1)$
- 8.2.** Consider the orbital energies (i.e., the eigenvalues of the Fock operator) for a closed-shell electron configuration of a  $2n$ -electron system. If the optical energy gap associated with the excitation  $\phi_k \rightarrow \phi_m$  were to be approximated by the orbital energy difference  $e_m - e_k$ , then the excitation energy is very much overestimated. Explain why this is the case.
- 8.3.** Consider the orbital energies from DF theory calculations for a closed-shell electron configuration of a  $2n$ -electron system. Thus, if the optical energy gap associated with the excitation  $\phi_k \rightarrow \phi_m$  were to be approximated by the orbital energy difference  $e_m - e_k$ , then the excitation energy is now very much underestimated. To correct this deficiency, the hybrid functional DF theory method employs functional in which some amount of the Hartree–Fock potential is mixed into the DF theory functional. Explain why this approach can lead to a better description of the optical energy gap.
- 8.4.** Consider the reaction  $\text{H}_2 + \text{D}_2 \rightarrow 2 \text{HD}$  examined in Chapter 5 (see Figure 5.5). Assuming that the two symmetry elements (i.e., the mirror planes of symmetry  $m$  and  $m'$ ) remain conserved throughout the reaction, construct the state correlation diagram and discuss whether the reaction is symmetry allowed or symmetry forbidden.

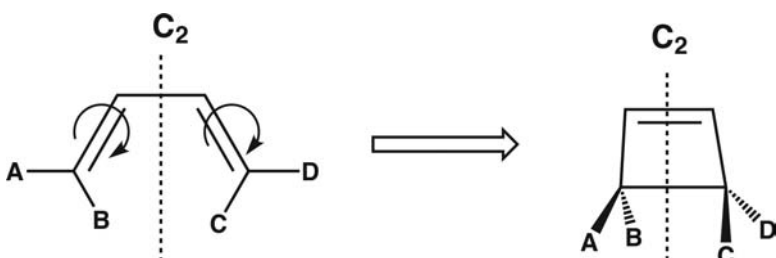


- 8.5.** Construct the orbital and state correlation diagrams for the disrotatory electrocyclic reaction of *cis*-1,3-butadiene to cyclobutene assuming that the mirror plane of symmetry

$m$  is conserved throughout the reaction, and discuss whether the reaction is symmetry-allowed or symmetry-forbidden.



- 8.6. Construct the orbital and state correlation diagrams for the conrotatory electrocyclic reaction of *cis*-1,3-butadiene to cyclobutene assuming that the twofold rotation symmetry  $C_2$  is conserved throughout the reaction, and discuss whether the reaction is symmetry-allowed or symmetry forbidden.



## REFERENCES

1. C. C. J. Roothaan, *Rev. Mod. Phys.*, **23**, 69 (1951).
2. K. Ruedenberg, *J. Chem. Phys.*, **66**, 375 (1977).
3. I. G. Csizmadia, *Theory and Practice of MO Calculations on Organic Molecules*, Elsevier, New York (1976).
4. R. L. Liboff, *Introductory Quantum Mechanics*, Holden-Day, San Francisco (1980).
5. T. Koopmans, *Physica*, **1**, 104 (1933).
6. J. Michl and E. W. Thulstrup, *Tetrahedron*, **32**, 205 (1976).
7. D. M. Adams, *Metal Ligand and Related Vibrations*, St. Martins Press, New York (1968).
8. L. M. Cirjak, R. E. Ginsberg, and L. S. Dahl, *Inorg. Chem.*, **21**, 940 (1982).
9. I. Shavitt, in *Methods of Electronic Structure Theory*, H. F. Schaefer, editor, Plenum, New York (1977), Chapter 6.
10. L. Salem, *The Molecular Orbital Theory of Conjugated Systems*, Benjamin, New York (1966).
11. S. V. O'Neil, H. F. Schaefer, and C. F. Bender, *J. Chem. Phys.*, **55**, 162 (1971).
12. W. T. Borden, in *Diradicals*, W. T. Borden, editor, John Wiley & Sons, New York (1982), Chapter 1.
13. L. Salem and C. Rowland, *Angew. Chem., Int. Ed.*, **11**, 92 (1972).
14. H. H. Michels and R. H. Hobbs, *Chem. Phys. Lett.*, **207**, 389 (1993); J. Karolczak, W. W. Harper, R. S. Grev, and D. J. Clouthier, *J. Chem. Phys.*, **103**, 2839 (1995).
15. H. F. Schaefer, III, *Science*, **231**, 1100 (1986).
16. A. Szabo and N. S. Ostlund, *Modern Quantum Chemistry*, McGraw-Hill, New York (1982).
17. A. C. Hurley, *Electron Correlation in Small Molecules*, Academic Press, New York (1976).
18. J. K. Labanowski and J. W. Andzelm, editors, *Density Functional Methods in Chemistry*, Springer-Verlag, New York (1991).
19. R. G. Parr and W. Yang, *Density-Functional Theory of Atoms and Molecules*, Oxford University Press, New York (1989).

20. E. Wimmer, in *Density Functional Methods in Chemistry*, J. K. Labanowski and J. W. Andzelm, editors, Springer-Verlag, New York (1991) Chapter 2; F. Jensen, *Introduction to Computational Chemistry*, 2nd edition, John Wiley & Sons (2007), Chapter 6; C. J. Cramer, *Essentials of Computational Chemistry*, 2nd edition, John Wiley & Sons (2004), Chapter 8; R. M. Martin, *Electronic Structure*, Cambridge University Press (2004), Chapters 6–9; W. Koch and M. C. Holthausen, *A Chemist's Guide to Density Functional Theory*, 2nd edition, Wiley-VCH (2001).
21. R. Stowasser and R. Hoffmann, *J. Am. Chem. Soc.*, **121**, 3414 (1999).
22. W. Kolos and L. Wolniewicz, *J. Chem. Phys.*, **49**, 404 (1968).

# Molecular Orbitals of Small Building Blocks

---

## 9.1 INTRODUCTION

---

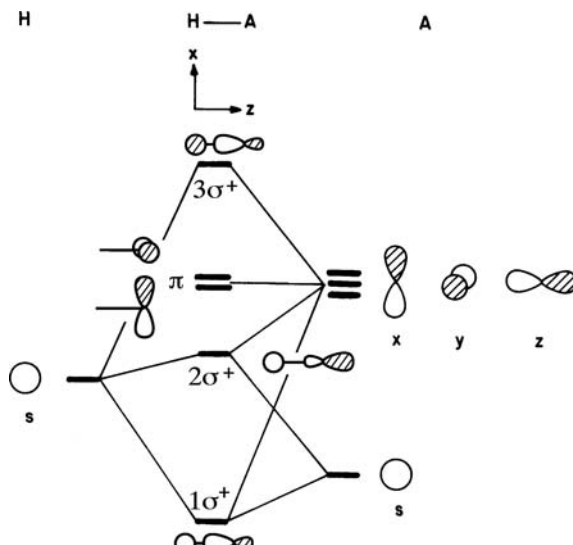
In Section 7.5, we found it convenient to construct the molecular orbitals (MOs) of  $\text{AH}_2$  by symmetry adaptation of bond orbitals. This analysis can easily be extended to other systems. Some bond orbitals may already transform as an irreducible representation of the molecular point group. It is usually only degenerate bond orbitals that require symmetry adaptation in constructing MOs. Of course, bond orbitals of the same symmetry can and will interact with each other, but these are details that for the most part will not be of concern in our qualitative analysis. In the following, we will first derive the MOs of  $\text{AH}$ , pyramidal  $\text{AH}_3$ , and tetrahedral  $\text{AH}_4$  based upon the appropriate orbital interaction diagrams, and then analyze those MOs in terms of bond orbitals. As in 7.4b, the hydrogen s orbital may be assumed to lie energetically in between the s and p orbitals of A. For convenience, the bond orbitals of  $\text{AH}$ ,  $\text{AH}_3$ , and  $\text{AH}_4$  may be constructed by assuming  $sp^3$  hybridization on A.

---

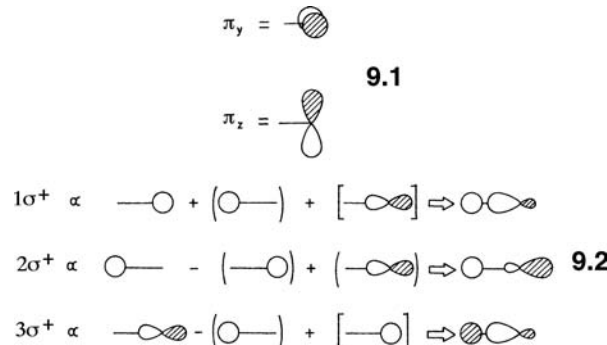
## 9.2 THE AH SYSTEM

---

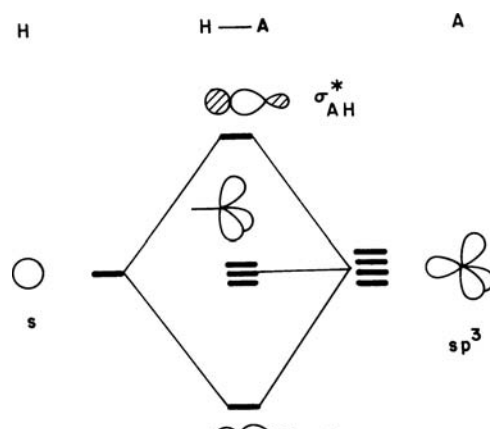
The interaction diagram for the orbitals of A and H is shown in Figure 9.1. The  $p_x$  and  $p_y$  orbitals of A do not overlap with the hydrogen s orbital, and so become the  $\pi$  set of nonbonding orbitals (9.1) for AH. According to the perturbation treatment of Chapter 3,  $1\sigma^+$ ,  $2\sigma^+$ , and  $3\sigma^+$  are derived as shown in 9.2. In this MO description,

**FIGURE 9.1**

An orbital interaction diagram for AH.

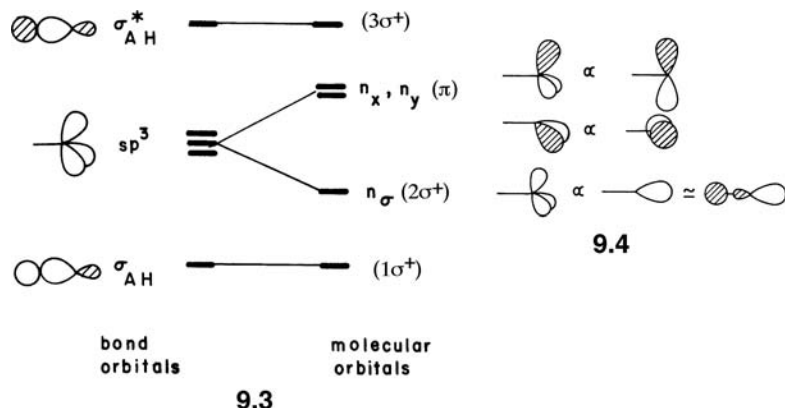


the second-order orbital mixing represented by brackets is essential for creating the orbital hybridization on A. One has the familiar three orbital pattern at work;  $1\sigma^+$  and  $3\sigma^+$  are the most bonding and antibonding HA combinations, respectively, possible. The middle orbital,  $2\sigma^+$ , is nonbonding and hybridized away from the HA region of space. The bond orbitals of AH that result from combining the  $sp^3$  hybrid orbitals of A with a hydrogen s orbital are shown in Figure 9.2. One  $sp^3$  hybrid orbital interacts with hydrogen s to form the  $\sigma_{AH}$  and  $\sigma_{AH}^*$  levels, and the remaining three

**FIGURE 9.2**

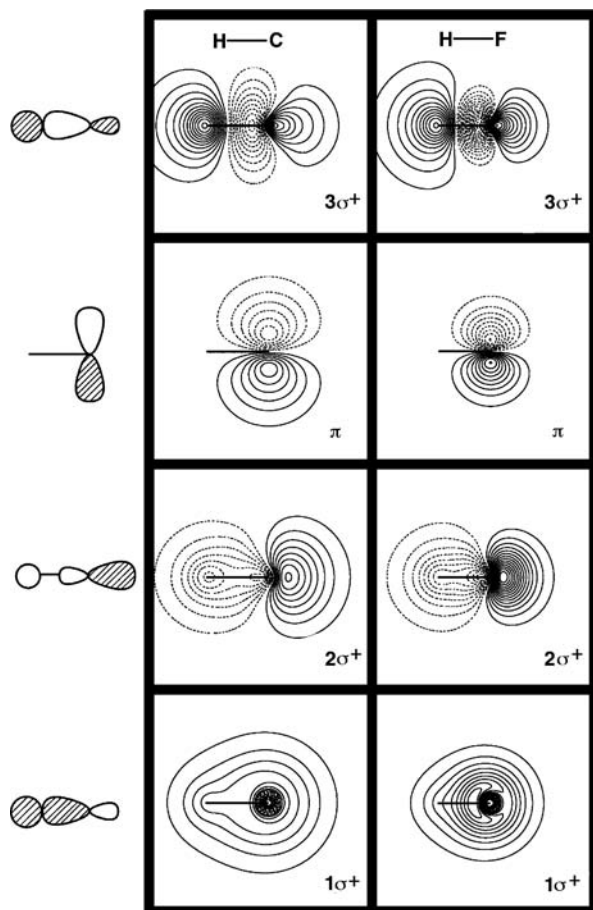
An orbital interaction diagram for AH using the bond orbital approach.

hybrid orbitals become nonbonding orbitals on A. Note that the bond orbitals  $\sigma_{AH}$  and  $\sigma_{AH}^*$  are already symmetry adapted (i.e., transform as one of the irreducible representations of the  $C_{\infty v}$  point group), and thus are similar in character to the corresponding MOs  $1\sigma^+$  and  $3\sigma^+$ , respectively. The three  $sp^3$  nonbonding orbitals of A are not symmetry adapted in this sense, but a linear combination of them may be constructed as described in Section 4.5 to produce a set of symmetry-adapted MOs. Let us recall the vector decomposition of a hybrid orbital as exemplified in Section 6.2, and, for convenience of a graphical presentation, let us represent a hybrid orbital by showing only the large front lobe for the  $sp^3$  hybrids. Then the MOs  $n_x$ ,  $n_y$ , and  $n_\sigma$  may be approximated by the three  $sp^3$  nonbonding orbitals as shown in 9.3.



Consequently, the bond orbitals and MOs of AH are correlated as indicated in 9.4. Notice the splitting of the three  $sp^3$  hybrid orbitals into a degenerate pair and a single nondegenerate orbital, a result demanded by group theory. The  $\sigma^+$  combination is the fully symmetric combination of the hybrids and the degenerate  $\pi$  set follows the familiar prescription shown in 9.3 and 9.4. The  $\pi$  sets in 9.3 and 9.4 are exactly identical. From the delocalized LCAO approach, the  $2\sigma^+$  molecular orbital has an atomic coefficient on hydrogen, whereas, the  $\sigma^+$  combination of hybrids does not. This is due to the neglect of nondegenerate mixing with  $\sigma_{AH}$  and  $\sigma_{AH}^*$  (Figure 9.2). In this example, one could have just as easily started with  $sp^2$  hybridization on A. The  $\sigma_{AH}$  and  $\sigma_{AH}^*$  combinations are formed from the one  $sp^2$  hybrid pointed toward the hydrogen atom. Taking symmetry-adapted combinations of the other two hybrids yield a symmetric combination identical to  $2\sigma^+$  and an antisymmetric combination that simplifies to an atomic  $p$  orbital on A, one member of the  $\pi$  set. The remaining  $p$  atomic orbital (AO) in this  $sp^2$  hybridization scheme is, of course, the other component of the  $\pi$  set. An even easier bond orbital derivation for the orbitals of HA starts with  $sp$  hybridization at A. The combinations with the hydrogen s orbital give the same bonding/antibonding orbitals. Now one has an  $sp$  hybrid and two  $p$  AO's on A to represent the three nonbonding orbitals. The symmetry labels shown are correct, but is  $2\sigma^+sp^3$ ,  $sp^2$ , or  $sp$  hybridized on A? The amount of s character on A in  $2\sigma^+$ , as we shall see below, depends upon where A lies in the Periodic Table. That is,  $1\sigma^+$ ,  $2\sigma^+$ , and  $3\sigma^+$  always intermix in the bond orbital approach to yield a varying ratio of s/p character on A as well as s character on H.

The orbital derivation of AH was constructed assuming that the electronegativity of H and A are approximately equal. There are, of course, two other possible situations, which, following the derivation of  $AH_2$  in Section 7.1, will create MOs with identical shapes, however, their weights at each center will not necessarily be the same. Figure 9.3 shows contour plots of the wavefunctions for HC and HF. These are calculations using STO-3G basis sets. The positive and negative values of

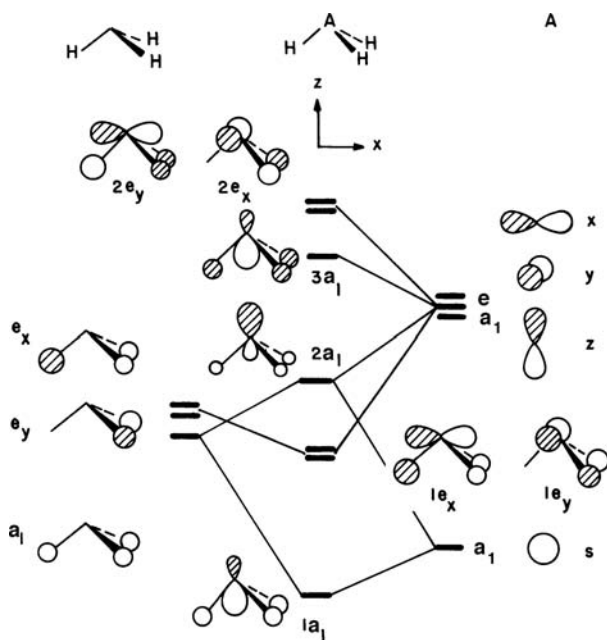
**FIGURE 9.3**

Contour plots of the wavefunctions for CH and HF. Only one component for the  $\pi$  sets is shown.

the wavefunctions are denoted by solid and dashed lines. The absolute value of each contour is one-half of the value of the contour before it proceeding from the nuclear regions outward. The gross similarity between the MOs of HC and HF underscore the idea that these orbitals do not change their shapes when the heavy atom is changed. The most obvious difference lies in the relative sizes of the AOs on carbon versus those for fluorine. Since fluorine is much more electronegative, the AOs are more contracted (e.g., compare the  $p$  AOs in the  $1\pi$  set). The three  $\sigma^+$  MOs for CH are more delocalized between C and H as implied by the interaction diagram in Figure 9.1. HF on the other hand corresponds to case 7.4c and so  $1\sigma^+$  is primarily F s. There is little  $sp$  hybridization in  $2\sigma^+$ , whereas, this feature is clearly present in CH. Finally, note that the amplitude on H for the  $3\sigma^+$  MO is much greater for FH than it is for CH, a result demanded again by the electronegativity differences.

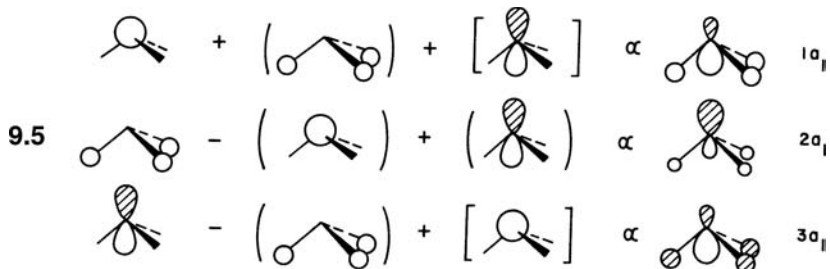
### 9.3 SHAPES OF $AH_3$ SYSTEMS

The interaction between the fragment orbitals of  $H_3$  and the AOs of the central atom, A, shown in Figure 9.4 gives rise to the MOs of pyramidal  $AH_3$  [1–4]. The  $p_x$  and  $p_y$  AOs on the A atom overlap and hence interact with the  $H_3$  combination of  $e$  symmetry. A simple two-orbital interaction results. The  $1e_x$  and  $2e_x$  orbitals are the in-phase and out-of-phase combinations of  $e_x$  and  $p_x$ , respectively. Likewise,  $1e_y$  and  $2e_y$  are the in-phase and out-of-phase combinations of  $e_y$  and  $p_y$ , respectively. The  $1a_1$ ,

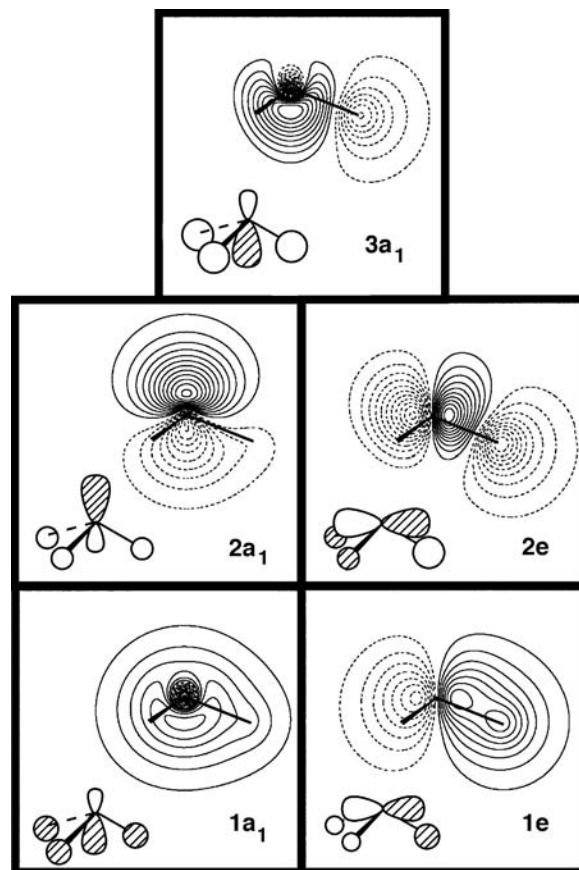
**FIGURE 9.4**

An orbital interaction diagram for pyramidal AH<sub>3</sub>.

2a<sub>1</sub>, and 3a<sub>1</sub> molecular orbitals in Figure 9.4 are derived from the three orbital interaction between s and p<sub>z</sub> on A with the H<sub>3</sub> combination of a<sub>1</sub> symmetry. The construction is illustrated in 9.5. A pattern in common exists for the three a<sub>1</sub>



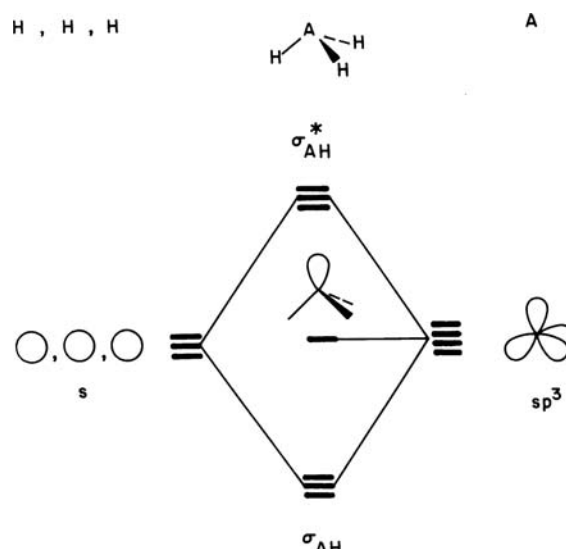
MOs we saw for AH<sub>2</sub> (7.8), AH (9.2), and AH<sub>3</sub> (9.5). The lowest and highest MOs of the three are always hybridized toward the hydrogen(s). The middle, nonbonding MO is concentrated on A and hybridized away from the hydrogen(s). This is a characteristic feature that we see again for the hypervalent molecules in Chapter 14 and the transition metal building blocks in Chapters 17–19. Whenever two different atomic orbitals on one center combine with an ensemble of hydrogen s or ligand σ donor orbitals, a maximally bonding combination at low energy and a maximally antibonding combination at high energy is produced. A nonbonding orbital at moderate energy is left behind, which is hybridized away from the surrounding hydrogens (or ligands). Contour plots of the valence molecular orbitals associated with NH<sub>3</sub> are given in Figure 9.5. The technical details are identical with those in Figures 9.3 and only the 1e<sub>x</sub> and 2e<sub>x</sub> components of the e sets have been plotted. Stylized representations of the molecular orbitals are drawn out on the lower left side of each plot. The hybridization in 2a<sub>1</sub> is quite clear. There is much greater density (number of contours) on the top half of the molecule as compared to the region around the hydrogen atoms. The composition of 3a<sub>1</sub>, primarily a hydrogen s combination with nitrogen p mixed in an antibonding fashion, is in accord with our expectations of what this MO should look like given the greater electronegativity of

**FIGURE 9.5**

Contour plots of the valence molecular orbitals in  $\text{NH}_3$ . Only one member of each  $e$  set is shown.

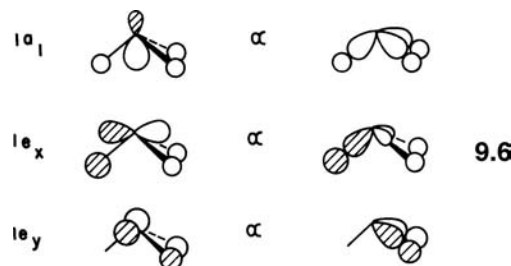
nitrogen. It can be seen that the mixing of nitrogen s character produces hybridization toward the hydrogens in  $1a_1$  and  $3a_1$  as anticipated by 9.5.

Formation of the bond orbitals of pyramidal  $\text{AH}_3$  is shown in Figure 9.6. The bond orbitals  $\sigma_{\text{AH}}$  and  $\sigma_{\text{AH}}^*$  are not symmetry adapted since triply degenerate species

**FIGURE 9.6**

An orbital interaction diagram for pyramidal  $\text{AH}_3$  in the bond orbital approach.

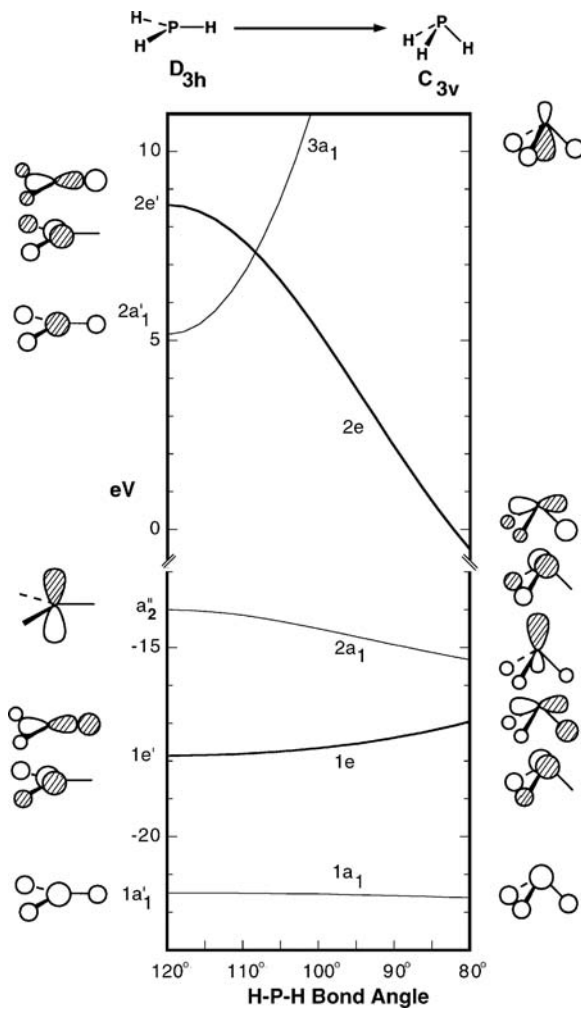
are not allowed in the C<sub>3v</sub> point group. The main features of the MOs, 1a<sub>1</sub>, 1e<sub>x</sub>, and 1e<sub>y</sub>, are well approximated by the standard linear combinations in this case of the three σ<sub>AH</sub> orbitals as in 9.6. Similarly, the 3a<sub>1</sub>, 2e<sub>x</sub>, and 2e<sub>y</sub>, MOs are approximated in terms of the symmetry-adapted combinations of the three σ<sub>AH</sub><sup>\*</sup> orbitals. The sp<sup>3</sup> nonbonding



orbital is already symmetry adapted and similar in description to the 2a<sub>1</sub> MO except for the absence of hydrogen s character. We could build this in by allowing it to interact with 1a<sub>1</sub> and 3a<sub>1</sub> symmetry-adapted combinations in a fashion identical to that used for the σ<sup>+</sup> set in the previous section. The energy of the nonbonding orbital does not change much as a result of this extra orbital mixing and remains concentrated on A. The degeneracy associated with the three σ<sub>AH</sub> and σ<sub>AH</sub><sup>\*</sup> bond orbitals is broken after symmetry-adapted combinations are taken. The 1a<sub>1</sub> combination of σ<sub>AH</sub> is more stable than the 1e set since the latter contains appreciable s character on the A atom, whereas, the 1e set contains exclusively p character on A. Recall that atomic s orbitals lie lower in energy than p.

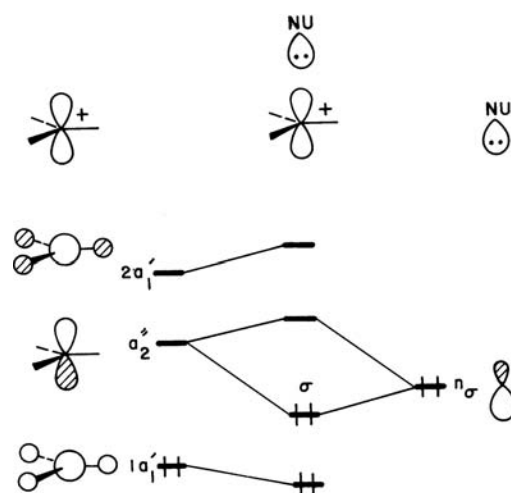
The MOs of trigonal planar AH<sub>3</sub> were already constructed by reference to the orbitals of H<sub>3</sub> and A in Figure 4.6. During the course of the trigonal planar to pyramidal (i.e., D<sub>3h</sub> → C<sub>3v</sub>) distortion, the MO levels of AH<sub>3</sub> vary as shown in Figure 9.7. This Walsh diagram is derived from extended Hückel calculations for the PH<sub>3</sub> molecule. There is a break in the energy scale from about -14 eV to ~0 eV. Let us use geometrical perturbation theory to analyze these results. Several trends in Figure 9.7 are immediately obvious. The 1a<sub>1</sub> level is stabilized slightly upon pyramidalization since overlap between the hydrogen s orbitals increases. In other words at small H—P—H angles ε<sup>(1)</sup> is negative. In the 1e' and 2e' levels, the magnitude of the overlap integral between the hydrogen s and p orbitals of P decreases upon pyramidalization, see Figure 1.5. Thus, the P—H bonding 1e' set rises in energy since ε<sup>(1)</sup> is positive, and the P—H antibonding 2e' set correspondingly falls in energy since ε<sup>(1)</sup> is negative. Recall that a similar situation occurred for the b<sub>2</sub> orbitals on bending in H<sub>2</sub>S (see Section 7.3). The steeper slope associated with 2e is derived from the fact that there are larger atomic coefficients in 2e (this is an antibonding orbital) than there are in the 1e set. This, in turn, creates a larger value in absolute magnitude for  $\tilde{S}_{ii}$  in 2e as compared to 1e. From first-order energy considerations, we expect both the 2a'<sub>1</sub> and 1a'<sub>1</sub> levels to go down slightly in energy and a<sub>2</sub>' to remain unchanged in energy. This clearly does not occur. Upon pyramidalization, both 2a'<sub>1</sub> and a<sub>2</sub>' become orbitals of a<sub>1</sub> symmetry so the two may mix together. As a result 2a'<sub>1</sub> is destabilized greatly on pyramidalization and a<sub>2</sub>' is stabilized. This orbital mixing will be examined in more detail below. For now, we note that the mixing of 2a'<sub>1</sub> into a<sub>2</sub>' is always larger than the mixing of 1a'<sub>1</sub> into a<sub>2</sub>' regardless of the identity of A. The rationale for this is precisely identical to the 1σ<sub>g</sub><sup>+</sup> — π<sub>u</sub> — 2σ<sub>g</sub><sup>+</sup> situation for bending in AH<sub>2</sub> discussed in Section 7.3.

Figure 9.7 shows that a six-electron AH<sub>3</sub> system such as CH<sub>3</sub><sup>+</sup> and BH<sub>3</sub> should be planar. The HOMO, 1e', of such a species is destabilized upon pyramidalization. The LUMO is the p orbital of A, which lies perpendicular to the molecular plane. Such an empty orbital, concentrated on one atomic center, is a powerful electron acceptor and is responsible for the Lewis acid character in boranes and carbocations.

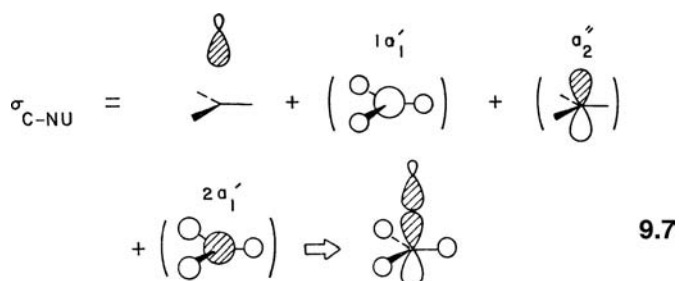
**FIGURE 9.7**

Walsh diagram for pyramidalization in  $\text{PH}_3$ . Notice the break in the energy scale.

Let us consider a nucleophilic addition to a carbocation  $\text{CH}_3^+$  by representing a nucleophile, Nu, by a filled nonbonding hybrid orbital  $n_\sigma$ . Figure 9.8 shows how  $n_\sigma$  is stabilized, primarily by  $a_2'$ , yielding the C—Nu bonding orbital  $\sigma$ . The resultant  $\sigma$  level is derived as in 9.7. If the hydrogen atoms distort away from the incoming nucleophile,

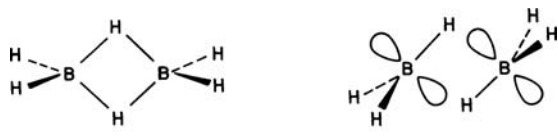
**FIGURE 9.8**

An orbital interaction diagram for the addition of a nucleophile to  $\text{CH}_3^+$ .



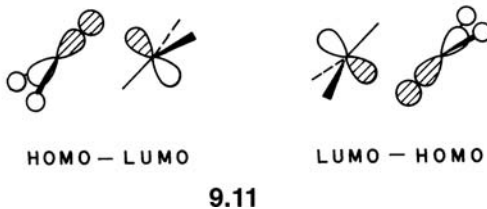
antibonding between the hydrogen s components in the  $a_1$  orbitals and  $n_\sigma$  is decreased. Furthermore, bonding between the hydrogen s components in the  $a_1$  orbitals and  $a_2''$  is increased. So as shown in 9.8, the  $\sigma$  orbital is further stabilized if the carbon configuration becomes tetrahedral. In another, equivalent context the orbital interaction shown in Figure 9.8 serves to transfer electron density from  $n_\sigma$  to  $a_2''$ , which induces the geometrical response (i.e., pyramidalization) of the CH<sub>3</sub> moiety since the 2a<sub>1</sub> MO is stabilized on pyramidalization (see Figure 9.7).

It is of interest to consider the formation of diborane, B<sub>2</sub>H<sub>6</sub>, 9.9, in terms of the HOMO and LUMO of two BH<sub>3</sub> fragments. The most stable arrangement of two BH<sub>3</sub> units in the incipient stage of dimerization is given by 9.10, which maximizes the extent of the two HOMO-LUMO interactions 9.11. On dimerization, a



9.9

9.10



pyramidalization occurs at each BH<sub>3</sub> unit. This takes place via a mechanism exactly analogous to the one considered in Figure 9.8. Here, electron transfer takes place from one component of the 1e' orbital (9.11). One would predict that decreasing the B–H distance for the bridging borohydride bonds should smoothly result in pyramidalization at boron.

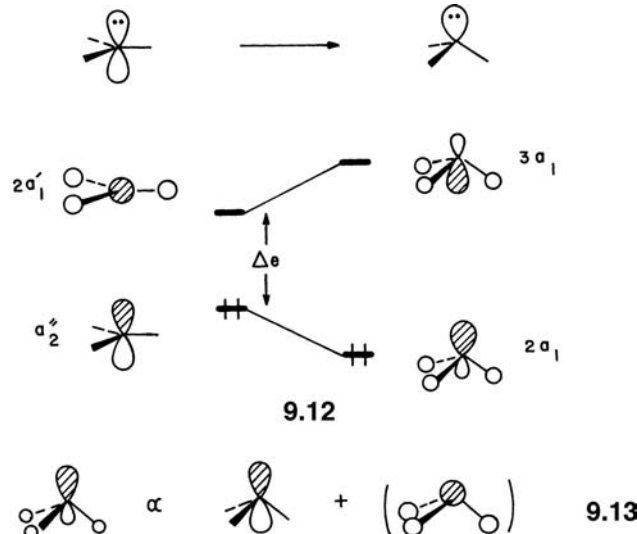
Figure 9.7 shows that an eight-electron AH<sub>3</sub> system such as CH<sub>3</sub><sup>-</sup> or NH<sub>3</sub> should be pyramidal since now the  $a_2''$  orbital is filled and it is markedly stabilized upon pyramidalization. The resultant HOMO in the new geometry (2a<sub>1</sub>) resembles an sp<sup>3</sup> nonbonding orbital. The potential energy diagram for pyramidal inversion in an eight-electron AH<sub>3</sub> system will be one where the two mirror image pyramidal geometries are minima and the planar species is a transition state that interconnects

**TABLE 9.1** The R—A—R Bond Angles and Inversion Barriers for Some R<sub>3</sub>A Molecules

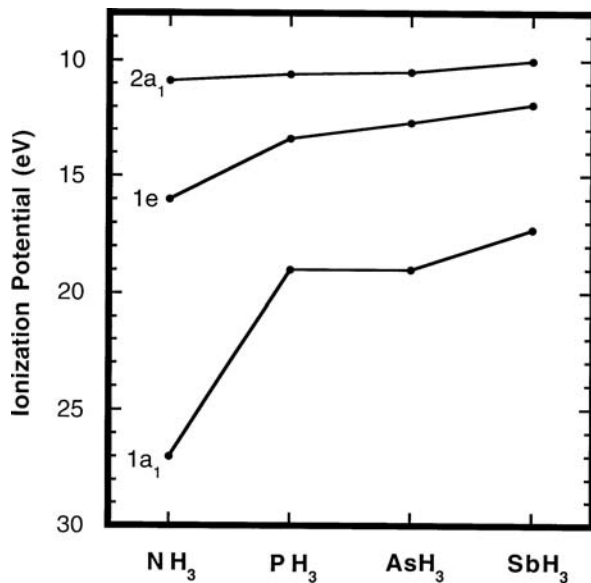
A	H <sub>3</sub> A		Me <sub>3</sub> A C—A—C	F <sub>3</sub> A F—A—F	A	H <sub>3</sub> A	
	H—A—H	ΔE <sub>inv</sub> <sup>a</sup>				H—A—H	ΔE <sub>inv</sub> <sup>a</sup>
N	107.2°	5.7	110.9°	102.4°	C	120.0°	0.0
P	93.4°	34.7	98.8°	97.2°	Si	112.7°	3.7
As	92.0°	39.7	96.2°	95.5°	Ge	112.4°	3.8
Sb	91.5°	44.9	94.2°	94.3°	Sn	110.6°	7.0
Bi	90.5°	60.5	97.1°	94.8°			

<sup>a</sup>C<sub>3v</sub> to D<sub>3h</sub> inversion barriers in kcal/mol.

them. The inversion barrier is, of course, the energy difference between the pyramidal and planar structures. The magnitude of the barrier is dictated by the slope of 2a<sub>1</sub> in Figure 9.7; a steeper slope will yield a larger inversion barrier. Calculations [5] have consistently shown that upon decreasing the electronegativity of A, the pyramidal inversion barrier, ΔE<sub>inv</sub>, increases and the HAH valence angle decreases. Table 9.1 presents several sets of data related to this for the eight-electron R<sub>3</sub>A series where A runs down the group 15 column of the Periodic Table. The H<sub>3</sub>A inversion barriers along with the F—A—F bond angles for the H<sub>3</sub>A and Me<sub>3</sub>A molecules are from microwave and electron diffraction measurements [7]. These observations are analogous to the corresponding ones in eight-electron AH<sub>2</sub> systems (Section 7.4.), and may be rationalized in terms of **9.12**. Geometry perturbation arguments point to the HOMO, 2a<sub>1</sub>, of pyramidal AH<sub>3</sub> as being constructed by the mixing of 2a'<sub>1</sub> into a''<sub>2</sub> (**9.13**). This orbital mixing stabilizes the



2a<sub>1</sub> level with respect to a''<sub>2</sub>. The magnitude of the stabilization is inversely proportional to the energy gap, Δe, between the a''<sub>2</sub> and 2a'<sub>1</sub> levels [4]. For exactly the same reasons as those discussed in Section 7.4B, the a''<sub>2</sub> and 2a'<sub>1</sub> levels of planar AH<sub>3</sub> are raised and lowered in energy, respectively, as one goes down the Periodic Table for the group 15 elements. In other words, the a''<sub>2</sub> MO is raised in energy since the central atom is becoming less electronegative (see the state averaged ionization potential for the valence p AOs in **2.9**). For the N 2s and 2p AOs have comparable sizes but for the rest of the atoms in this series the valence ns AOs become

**FIGURE 9.9**

A plot of the vertical ionization potentials for the group 15 hydrides.

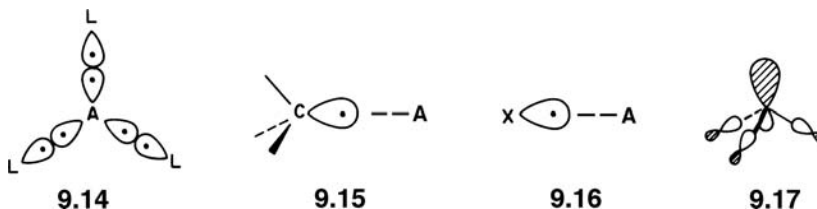
increasingly more contracted compared to the  $np$  AOs. The overlap then between the central  $ns$  AO and the hydrogen  $s$  orbitals decrease on going down the column, which results in the stabilization of the  $2a_1'$  LUMO. Therefore, a smaller energy gap  $\Delta e$ , a larger inversion barrier, and a smaller HAH angle are found in eight-electron AH<sub>3</sub> systems as A becomes less electronegative. There is an interesting (and yet unexplained) inversion on going from Me<sub>3</sub>Sb to Me<sub>3</sub>Bi that is also present for F<sub>3</sub>Bi (and I<sub>3</sub>Bi [7]) but not H<sub>3</sub>Bi.

The vertical ionization potentials for the NH<sub>3</sub> to SbH<sub>3</sub> series [8] are plotted in Figure 9.9. The 1a<sub>1</sub> – 1e energy differences going from NH<sub>3</sub> to SbH<sub>3</sub> are identical to the situation found for the 1a<sub>1</sub> – 1b<sub>2</sub> energy separations in the group 16 AH<sub>2</sub> molecules, see Figure 7.10, or for the valence s-p energy gaps for the atoms in 2.9. What is different is that for AH<sub>2</sub> the b<sub>1</sub> HOMO is found progressively at a lower ionization potential going down the column. On the other hand, for AH<sub>3</sub> the 2a<sub>1</sub> MO is at a nearly constant ionization potential. The energy of the b<sub>1</sub> MO is invariant with respect to the H—A—H bond angle. However, the 2a<sub>1</sub> MO decreases in energy when the H—A—H angle decreases (Figures 7.5 and 9.7). Since the H—A—H bond angle decreases going down the column for the group 15 molecules, there are two competing effects. The electronegativity decreases, which lowers the ionization potential, while the bond angle decreases, which should raise it. The net effect is one of near cancellation in the AH<sub>3</sub> series.

The above discussion also provides a rationale for the computational results that seven-electron AH<sub>3</sub> radicals with a first-row atom A (e.g., CH<sub>3</sub> and NH<sub>3</sub><sup>+</sup>) are planar, but those with a second-row atom (e.g., SiH<sub>3</sub>, GeH<sub>3</sub>, and SnH<sub>3</sub>) are pyramidal [9]. The a<sub>2</sub>' level is now only singly occupied and is of lower energy in the pyramidal geometry. However, the subjacent level, doubly degenerate and completely filled, is of lower energy at the planar geometry. A pyramidal structure is expected only if the energy lowering associated with a<sub>2</sub>' is substantial. This occurs for AH<sub>3</sub> systems containing a second-row atom A with a smaller electronegativity, and hence a smaller  $\Delta e$  value than their first-row counterparts. The results [9] for AH<sub>3</sub> are listed on the right side of Table 9.1. As expected from the arguments given above, the H—A—H angles are larger and the inversion barriers are smaller for the seven electron compounds compared to their eight electron counterparts. Furthermore, proceeding down the column for these group 14 molecules, the H—A—H bond angles become smaller and the inversion barriers larger, just like their group 15, eight-electron, counterparts.

## 9.4 $\pi$ -BONDING EFFECTS OF LIGANDS

Let us consider  $AL_n$  ( $n = 1, 2, 3, \dots$ ) systems in which L refers to a “ligand,” an atom or a group, that contains more than just a single s orbital. In most cases, L contributes one electron in a sigma fashion to A as shown in 9.14 for planar  $AL_3$ . The hybrid

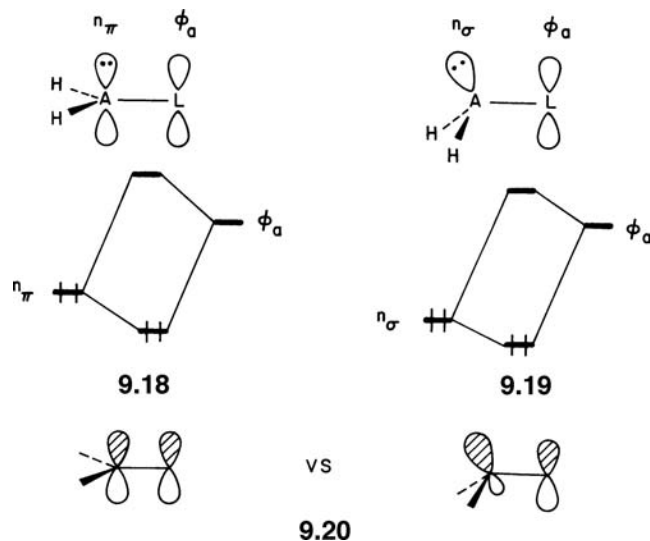


orbital used by L may be the  $sp^3$  hybrid of an alkyl group in 9.15 or the  $sp$  hybrid of a halogen atom in 9.16. The local symmetry of the hybrid orbitals in 9.15 or 9.16 is the same as that for a hydrogen s orbital. Thus, the way the atomic orbitals of A overlap with the ligand orbitals is the same whether the ligand carries a single s orbital or a directed (hybridized) orbital of this type. As a result, the overall shape and symmetry of the valence, A-centered orbitals of  $AL_n$  are the same as those of  $AH_n$ . The very important result is that the MOs of  $AH_n$  developed so far can be used to discuss the structures of  $AL_n$  systems where L is an arbitrary group (or groups). For example, the orbital of  $N(CH_3)_3$  corresponding to the  $2a_1$  orbital of pyramidal  $AH_3$  is that shown in 9.17. The hybrid orbitals on the methyl groups simply take the place of hydrogen s orbitals with the same relative phase as that for the  $2a_1$  MO. There are two layers of detail that should be taken into account when dealing with groups other than hydrogen. First one should consider any electronegativity changes on going from hydrogen to L. Secondly, any  $\pi$  interactions that exist between L and A need to be turned on. It is normally prudent to carry out the perturbations in the order given. Electronegativity changes bring about alterations in the  $\sigma$  system of the molecule, whereas,  $\pi$  bonding is a smaller perturbation, which can easily be added in a secondary step. Let us pursue this construction for the eight-electron  $AH_3$  case.

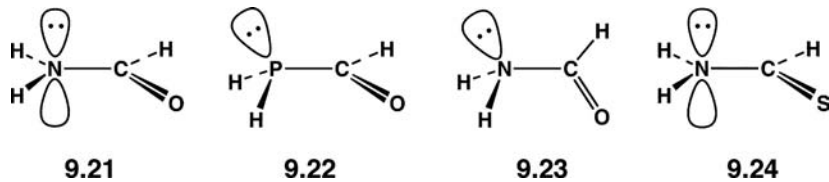
A very electronegative atom substituted at A causes all orbitals to decrease in energy (see Section 6.4), especially those that have appreciable orbital character associated with the electronegative substituent. There is a direct relationship between the energy lowering and the coefficients on the atoms that are made more electronegative. Consider the level ordering of planar,  $D_{3h}$   $AH_3$  in Figure 9.7. Replacement of the hydrogens by fluorine atoms would cause all of the MO levels to shift downward except for  $a''_2$  (in reality the  $a''_2$  orbital would also be slightly stabilized because of the increased Coulombic attraction by the electronegative fluorine atoms—see Section 8.9). The effect of  $\pi$  bonding between the central atom and the fluorine ligands as we shall shortly see will be to raise  $a''_2$  in energy. Consequently, the energy gap  $\Delta e$  in 9.12 will be smaller for  $NF_3$  than for  $NH_3$ . This suggests an explanation for the computational result that the  $NF_3$  inversion barrier is larger (78.5 kcal/mol) and the F—N—F valence angle is smaller ( $102.4^\circ$ —see Table 9.1) than the corresponding value for  $NH_3$  ( $106.7^\circ$ ) [10]. The  $NF_3$  inversion barrier of 78.5 kcal/mol via a  $D_{3h}$  structure is larger than the first bond dissociation energy of 57 kcal/mol so that bond breaking is energetically favored over distortion to the  $D_{3h}$  geometry. Instead inversion proceeds by a “T-shaped” transition state of  $C_{2v}$  symmetry [5]. The energy of the  $2a'_1$  MO in the  $D_{3h}$  structure is now so low in energy that it can effectively mix with one component of the  $1e'$  set. Therefore, the motion for inversion in  $NF_3$ , as well as the other group 15 fluorides, involves the

enlargement of one F—A—F bond angle. This couples the  $2a_1$  MO with  $1e_x$  (see Figure 9.4).

When the external ligand L is an atom or a group that possesses  $\pi$ -bonding capabilities it is convenient to separate the effects due to  $\sigma$  and  $\pi$  bonding. To do this, we first develop the valence orbitals around the central atom A, neglecting the  $\pi$ -bonding capabilities of L, and then introduce the  $\pi$ -bonding effects of L as a perturbation. As an example, consider  $H_2A-L$  where L stands for a group with a  $\pi$ -acceptor orbital  $\phi_a$  (e.g., an empty  $p$  orbital of  $BH_2$ , that of an electropositive metal such as Li, or a  $\pi_{CO}^*$  orbital of a carbonyl group), which can engage in  $\pi$  interaction with the nonbonding orbital (analogous to  $a''_2$ ) of A. The  $\pi$  interactions ( $n_\pi - \phi_a$ ) and ( $n_\sigma - \phi_a$ ) that occur in planar and pyramidal  $H_2A-L$  are shown in 9.18 and 9.19,



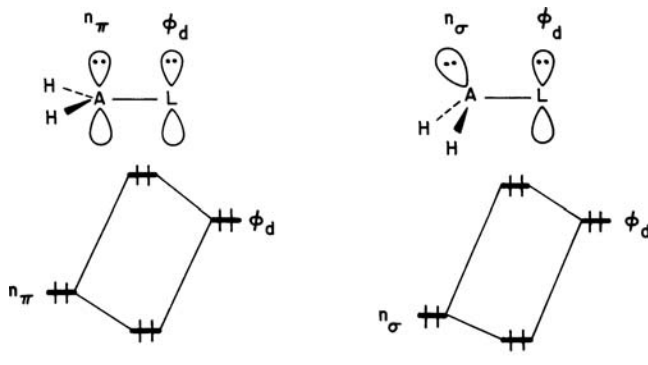
respectively. The stabilization of the nonbonding orbital on A is governed by the  $\pi$  overlap between the  $n$  and  $\phi_a$  orbitals and by the energy gap  $\Delta e$  between them. As can be seen from 9.20, the overlap  $\langle n_\pi | \phi_a \rangle$  in 9.18 is greater than the overlap  $\langle n_\sigma | \phi_a \rangle$  in 9.19. Since the  $n_\pi$  level of  $AH_2$  is higher in energy than the  $n_\sigma$  level, the energy gap  $\Delta e$  is smaller in 9.18. Therefore, in terms of both overlap and energy gap considerations, the stabilization of  $n_\pi$  in 9.18 is greater than that of  $n_\sigma$  in 9.19. Such a  $\pi$  interaction can stabilize the planar structure over the pyramidal one if it is larger than the competing  $\sigma$ -effect, described above, responsible for the pyramidal geometry of eight-electron  $AH_3$  molecules. As shown for the ground state geometries in 9.21 and 9.22, this is the case for  $H_2A-L$  with a first-row A atom but not for



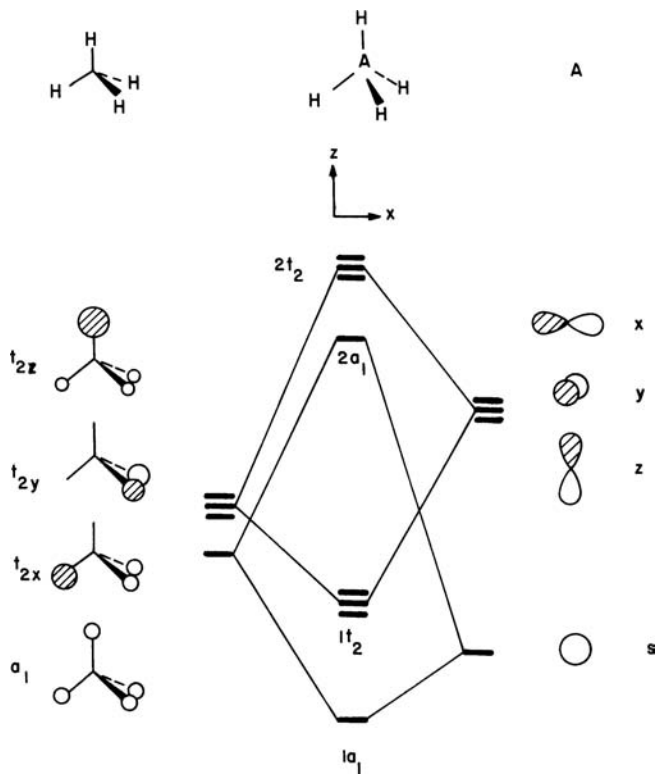
$H_2A-L$  when a second-row A atom is present. For the case of the heavier A atom, although the energy gap  $\Delta e$  between  $n_\pi$  and  $\phi_a$  is small, the  $\langle n_\pi | \phi_a \rangle$  overlap is small too because of the longer A—L bond and more diffuse valence orbitals. In addition, recall that the inversion barrier of  $AH_3$  is much larger for a second-

row atom compared to one from the first-row. As a result the  $(n_\pi - \phi_a)$  interaction in **9.18** is not large enough to make  $\text{H}_2\text{A-L}$  planar when A comes from the second row [11,12]. It should be noted that the nitrogen center of **9.21** becomes pyramidal when the  $\pi$  interaction is cut off by rotation around the N—L bond as depicted in **9.23**. Thus, rotation about the C—N bond in amides or thioamides, **9.24**, is intimately coupled with inversion at the amide nitrogen [13]. The greater  $\pi$  acceptor capability of C=S compared to C=O leads to a stiffer out of plane wagging potential for the amino group in **9.24** compared to **9.21** and so thioformamide has a larger rotational barrier [13]. Likewise, rotation about the C—C bond in the enolate ion  $^-:\text{CH}_2\text{CH}=\text{O}$  and that about the C—N bond in  $^-:\text{CH}_2\text{NO}_2$  are calculated to be complicated by inversion at the carbanion center [14]. A similar situation occurs for the species  $\text{N}(\text{SiH}_3)_3$  which has a planar  $\text{NSi}_3$  skeleton, and  $\text{P}(\text{SiH}_3)_3$  which has a pyramidal  $\text{PSi}_3$  skeleton [11]. Here the acceptor orbital  $\phi_a$  is one component of the 2e orbitals of  $\text{SiH}_3$  (see Figure 9.4 and Section 10.5).

Consider now a molecule of the form  $\text{H}_2\text{A-L}$ , where L is a group with a  $\pi$ -donor function,  $\phi_d$  (e.g., halogen atoms, a  $\text{NH}_2$  or OR group, etc.). The result is opposite to that described above for the acceptor case. Here the effects of  $\pi$  and  $\sigma$  bonding work in the same direction (most  $\sigma$  donor groups contain an electronegative atom, e.g., N, O, Cl), and the barrier to inversion around the atom A is greater than that in the parent  $\text{AH}_3$  system. As shown in **9.25** and **9.26**, the interaction between the nonbonding orbital of A and the donor orbital of L is a destabilizing two-orbital-four



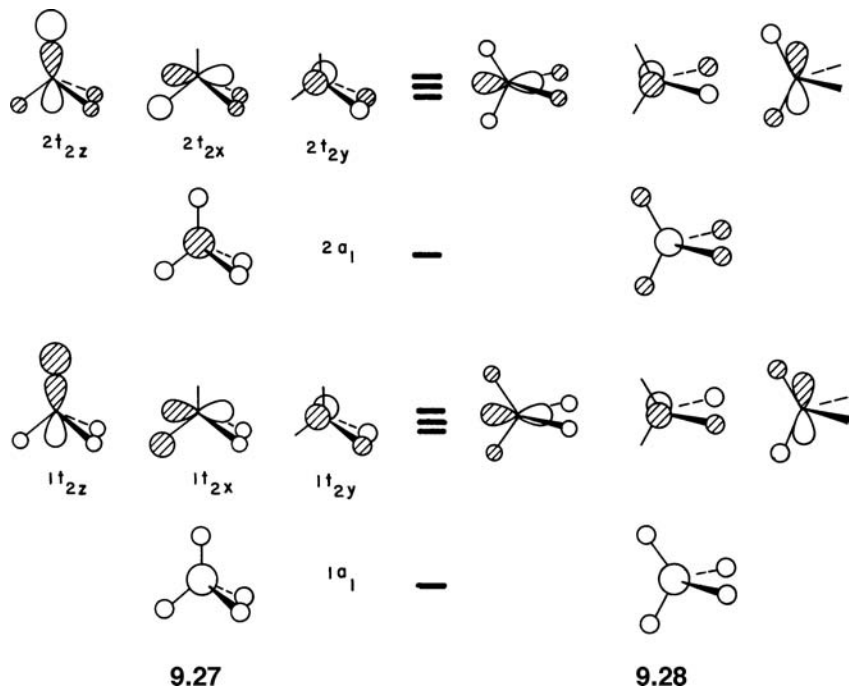
electron one. The destabilization is greater at the planar structure **9.25** since the overlap integral  $\langle n_\pi | \phi_d \rangle$  is greater than  $\langle n_\sigma | \phi_d \rangle$ . Therefore, the  $\pi$  interaction between the A and L centers increases the inversion barrier. The effect of  $\pi$  acceptors and donors on bending in  $\text{AH}_2$  (Section 7.3) can be understood in an identical fashion. This has a dramatic impact on not only the reactivity of carbenes but also the singlet-triplet energy difference (Section 8.10) [15]. Notice in the case of the singlet configuration that there is an acceptor orbital ( $b_2$ ) and a donor orbital ( $2a_1$ ) on the central atom. There is an interesting result, analogous to the observation concerning the planar skeleton of  $\text{N}(\text{SiH}_3)_3$ , in silicon–oxygen chemistry [16]. The average value of the Si—O—Si angle in silicates ( $\sim 149^\circ$ ) lies between the linear and tetrahedral extremes. There is also evidence from the variety of angles known in such species that the bending around the oxygen is rather soft. Both of these observations may be interpreted in terms of Si—O  $\pi$  bonding, which best stabilizes the linear geometry while  $\sigma$  effects best stabilize a considerably nonlinear geometry.

**FIGURE 9.10**

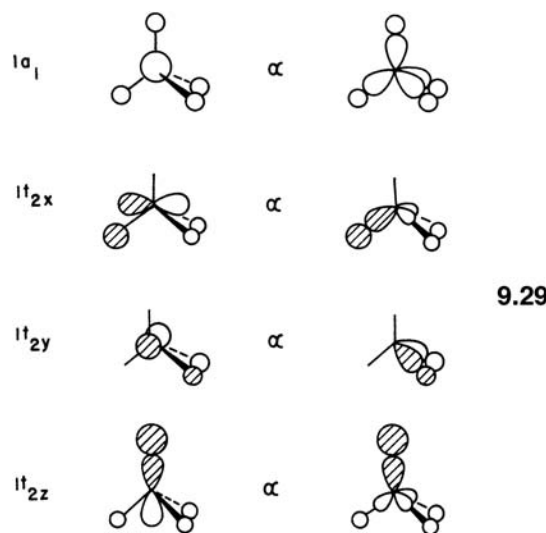
An orbital interaction diagram for tetrahedral AH<sub>4</sub>.

## 9.5 THE AH<sub>4</sub> SYSTEM

The orbital interaction diagram between H<sub>4</sub> and A is shown in Figure 9.10. The triply degenerate MOs of tetrahedral H<sub>4</sub> are an alternative representation of those shown in Figure 5.6. The orbital interaction diagram of Figure 9.10 leads to the MOs of tetrahedral AH<sub>4</sub> shown in 9.27. The  $a_1$ ,  $t_{2x}$ ,  $t_{2y}$ , and  $t_{2z}$  orbitals of H<sub>4</sub> combine in-phase with the  $s$ ,  $p_x$ ,  $p_y$ , and  $p_z$  orbitals of A to form the  $1a_1$ ,  $1t_{2x}$ ,  $1t_{2y}$ , and  $1t_{2z}$  MOs.



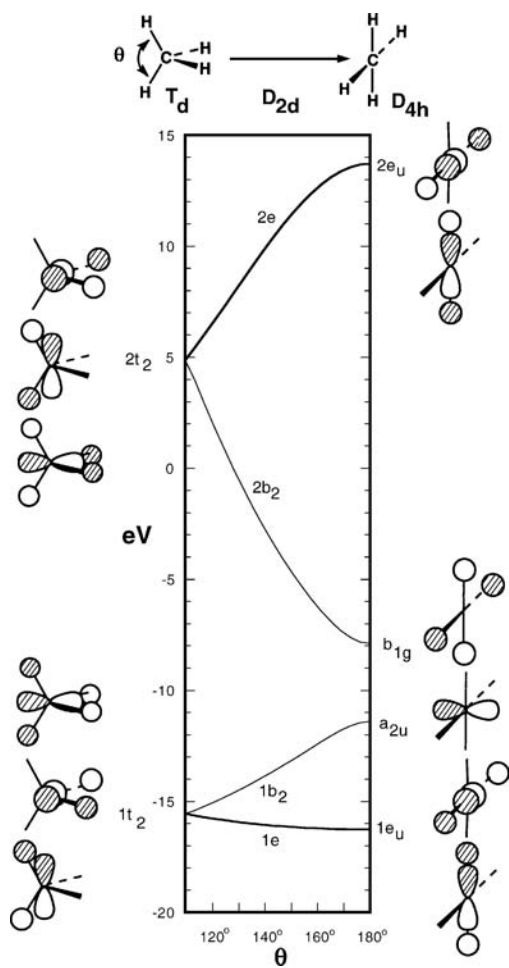
Likewise, the antibonding combination between the sets of fragment orbitals produces the  $2a_1$ ,  $2t_{2x}$ ,  $2t_{2y}$ , and  $2t_{2z}$  MOs. With the MOs of tetrahedral  $H_4$  chosen as in Figure 5.6, the MOs of  $AH_4$  are given by 9.28. We note that the triply degenerate MOs  $1t_2$  or  $2t_2$  of 9.28 can be expressed as linear combinations of the corresponding MOs of 9.27. Such linear combinations among a set of degenerate MOs do not lift the degeneracy, as already pointed out in Section 7.4. One could take four  $sp^3$  hybrid orbitals of A and interact them with the hydrogen s orbitals to form four  $\sigma_{AH}$  and four  $\sigma_{AH}^*$  orbitals. But these sets of four bond orbitals cannot all lie at the same energy (as we shall see in the next section from the PE spectra of  $CH_4$  and  $SiH_4$  molecules). Symmetry adaptation of the four  $\sigma_{AH}$  bond orbitals directly leads to the  $1a_1$ ,  $1t_{2x}$ ,  $1t_{2y}$ , and  $1t_{2z}$  MOs as indicated in 9.29. Similarly, the  $2a_1$ ,  $2t_{2x}$ ,  $2t_{2y}$ , and  $2t_{2z}$  MOs can be well approximated by suitable linear combinations of the



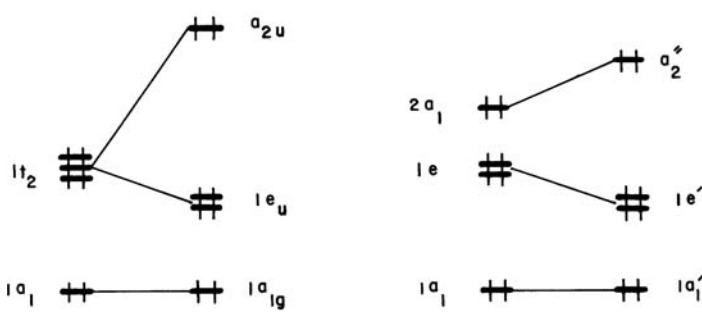
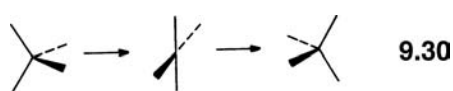
four  $\sigma_{AH}^*$  orbitals. Thus, symmetry adaptation of the bond orbitals directly leads to the delocalized MOs of tetrahedral  $AH_4$  and, of course the totally symmetric  $a_1$  combination no longer lies at the same energy as the  $t_2$  set.

Figure 9.11 shows a Walsh diagram for opening two H—C—H angles in methane from the tetrahedral geometry ( $\theta = 109.47^\circ$ ) to the square plane ( $\theta = 180.0^\circ$ ). During the  $T_d \rightarrow D_{4h}$  distortion, two members of the  $1t_2$  set are stabilized,  $e^{(1)} < 0$ , since overlap between the  $p$  orbital on A and the two hydrogen s orbitals is increased and these are bonding MOs. But the third member is destabilized,  $e^{(1)} > 0$ , since all bonding between the  $p$  orbital of A and the hydrogen s orbitals is lost. This leads to the  $1e_u$  and  $a_{2u}$  levels, respectively. For identical reasons, two members of the antibonding  $2t_2$  set are destabilized and the third member is lowered in energy, yielding the  $2e_u$  and  $b_{1g}$  levels. For the moment, we show the  $a_{2u}$  level lying below  $b_{1g}$  in Figure 9.11, but we note that the relative ordering of the two orbitals depends upon the electronegativity difference between A and H (or L) as will be discussed later. The  $1a_1$  and  $2a_1$  orbitals (not shown in Figure 9.11) do not change much in energy since they are constructed from s AO on the central atom and the surrounding hydrogens and this overlap does not change much during the course of the deformation.

In eight-electron  $AH_4$  systems such as  $CH_4$  and  $NH_4^+$ , the HOMO of a square planar structure is the totally nonbonding  $a_{2u}$  level. Thus, according to Figure 9.11, an eight-electron  $AH_4$  molecule prefers to be tetrahedral. The tetrahedral configuration of  $AH_4$  may in principle be inverted as shown in 9.30. However, the barrier for this inversion is exceedingly large compared with that for the pyramidal inversion in

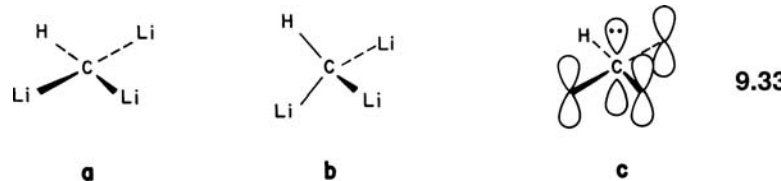
**FIGURE 9.11**

A Walsh diagram for bending two H—C—H bond angles in methane from the tetrahedral structure to the square planar one.

**9.31****9.32**

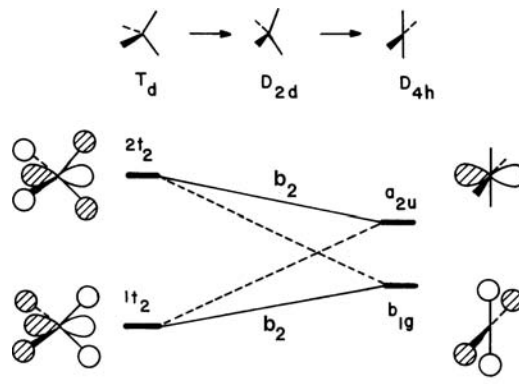
eight-electron  $\text{AH}_3$  systems. For example, the energy difference between  $T_d$  and  $D_{4h}$  geometries in  $\text{CH}_4$  is estimated to require about 131 kcal/mol from very high level calculations [17], in sharp contrast to the pyramidal inversion barrier of about 6 kcal/mol in  $\text{NH}_3$  [5]. This observation may be understood by reference to **9.31** and **9.32**. What is largely responsible for the inversion barrier in  $\text{AH}_3$  is the conversion of a nonbonding electron pair in a hybrid orbital ( $2a_1$ ) into a pair in a pure  $p$  orbital. In contrast, the inversion of  $\text{AH}_4$  requires the conversion of a bonding electron pair ( $1t_2$ ) into a nonbonding electron pair in a  $p$  AO. This also brings up an interesting point concerning the square planar geometry for methane. Since the  $a_{2u}$  orbital is a pure  $p$  AO on carbon, pyramidalization should, just as in the eight electron  $\text{AH}_3$  case, be stabilizing. The  $a_{2u}$  MO becomes hybridized on going to a  $C_{4v}$  geometry by mixing with the higher lying  $2a_{1g}$  MO. This is indeed the case, the  $C_{4v}$  structure is 26 kcal/mol more stable than the  $D_{4h}$  one [17]. However, the actual structure for stereomutation of methane is predicted to be a pyramidal singlet carbene complexed to a hydrogen molecule with  $C_s$  symmetry. This structure is 1 kcal/mol lower in energy than the  $C_{4v}$  one. The  $\text{H}_2$  unit is bound to the carbene by 13 kcal/mol but this structure is less stable than  $\text{CH}_3^+$  and  $\text{H}^+$  by 3 kcal/mol [17]. So stereomutation of methane without bond rupture is not likely to occur.

A square planar carbon configuration can be achieved only if the HOMO  $a_{2u}$  is substantially stabilized by good  $\pi$ -acceptor ligands. For example, di- and trolithiomethane are calculated to have a planar structure **9.33a** only 2.5 and 3.5 kcal/mol, respectively, higher than the tetrahedral structures **9.33b** [18]. As indicated in **9.33c**,



the low-lying empty  $p$  orbitals of Li stabilize the two electrons in the  $a_{2u}$  orbital. Similarly, the eight-electron  $\text{Li}_2\text{O}$  is not bent like  $\text{H}_2\text{O}$  but linear in structure. However,  $\text{Cs}_2\text{O}$  is bent although it is isoelectronic with  $\text{Li}_2\text{O}$  [19], because the magnitude of  $\pi$  overlap associated with the  $p$  orbital of a heavier element is much weaker. Recall from Section 9.4 that the nitrogen center of  $\text{H}_2\text{NCH=O}$  is planar while the phosphorus center of  $\text{H}_2\text{PCH=O}$  is pyramidal.

As the electronegativity of A in an  $\text{AH}_4$  molecule is decreased, the  $p$  orbital of A is raised in energy and the A–H distance tends to increase. Furthermore, the  $1t_2$  set becomes more concentrated on the hydrogens, and  $2t_2$  more concentrated on A. Consequently, in a square planar  $\text{AH}_4$  molecule with an electropositive atom,  $b_{1g}$  may become lower in energy than  $a_{2u}$ . As shown in **9.34** there is actually an avoided crossing between the two MOs which eventually become  $a_{2u}$  and  $b_{1g}$  at the  $D_{4h}$



9.34

geometry. At intermediate geometries they both have  $b_2$  symmetry and can intermix. In fact, the HOMO of a square planar  $\text{BH}_4^-$ ,  $\text{SiH}_4$ , or  $\text{PH}_4^+$  molecule is calculated to be the  $b_{1g}$  level [20]. One important consequence of such a level ordering is that  $\text{AL}_4$  systems with electronegative ligands such as halogens or alkoxides should have a lower barrier for configuration inversion at A than  $\text{CH}_4$ . This comes about because the HOMO  $b_{1g}$  carries electron density only on the ligand atoms, and will be stabilized by electronegative atoms. In addition, electronegative atoms carry nonbonding electron pairs. A two-orbital-two-electron stabilization results via interaction with the central atom  $p$  orbital ( $a_{2u}$ ) of the planar structure as depicted in 9.35. Square planar oxygen is known in the solid-state structure of



9.35

$\text{NbO}$  and  $\text{TiO}$  [21]. Here the square planar geometry is stabilized by the presence of  $\pi$ -acceptor Nb (or Ti)  $d$  orbitals. Likewise, molecules in which  $a_{2u}$  is empty are expected to be more stable at the square planar rather than tetrahedral or  $C_{4v}$  pyramidal geometry. Examples include  $\text{BH}_4^+$ ,  $\text{CH}_4^{2+}$ , or the doubly excited state of  $\text{CH}_4$  in which  $a_{2u}$  is empty and  $b_{1g}$  is filled [22]. We will return to this problem of tetrahedral-square planar- $C_{4v}$  pyramidal structure interconversion in Chapter 14, where  $\text{AL}_4$  molecules with more than eight electrons are considered.

Actually a  $C_{2v}$  structure for  $\text{CH}_4^{2+}$  has been found from high-level calculations [23] to be 1 kcal/mol more stable than the  $D_{4h}$  one. It structurally resembles a methylene dication coordinated to an  $\text{H}_2$  ligand. The H—H distance was found to be 1.03 Å [23], which is elongated compared to the hydrogen molecule at 0.74 Å and the C—H distance (to the  $\text{H}_2$  group) was 1.28 Å. It is instructive to look more closely at the bonding in this structure from the perspective of a  $\text{CH}_2^{2+}$  species coordinated to  $\text{H}_2$ . This is done for the ground state structure of  $\text{CH}_4^{2+}$  in Figure 9.12a. Here the  $b_1$  and  $2a_1$  frontier orbitals of the  $\text{CH}_2^{2+}$  fragment are

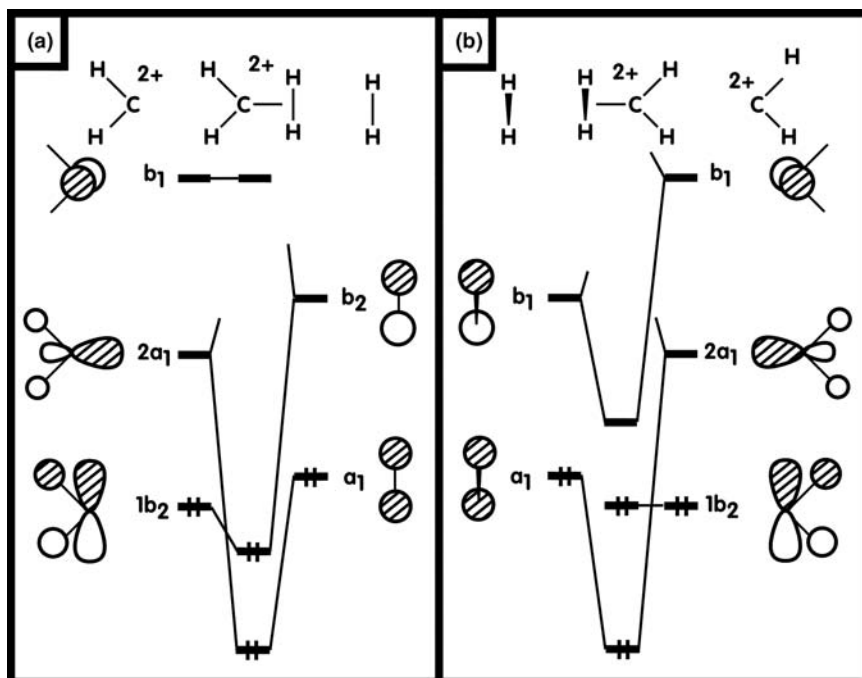


FIGURE 9.12

An orbital interaction diagram for  $\text{CH}_4^{2+}$  (a) in the ground state and (b) a rotational transition state, where  $\text{H}_2$  lies perpendicular to the  $\text{CH}_2$  plane.

empty. The  $2a_1$  fragment orbital interacts and stabilizes the filled  $\sigma$  orbital of  $H_2$ . The  $b_1$  fragment orbital is left nonbonding since the  $H_2$  and  $CH_2^{2+}$  units lie in a common plane in this structure. So electron density from the filled  $H_2 \sigma$  orbital is now delocalized over three centers and the  $2a_1$  fragment orbital becomes partly occupied. A  $CH_2^{2+}$  molecule with four valence electrons is predicted to be linear (see Section 7.3). Here the  $H-C-H$  angle closes down to  $124.1^\circ$ . It lies midway between the value expected ( $180^\circ$ ) for an isolated  $CH_2^{2+}$  molecule and that ( $90^\circ$ ) for the square planar compound as a consequence of the partial occupation of  $2a_1$ . But there is also a  $\pi$  interaction between the filled  $C-H$  bonding orbital,  $1b_2$ , and the empty  $H_2 \sigma^*$  orbital. This would be called back-donation by some and the  $2a_1\text{-}H_2 \sigma$  interaction, forward-donation. Back-donation here takes electron density from the  $CH_2^{2+}$  unit and places it in  $H_2 \sigma^*$ . The structural consequence of this is to elongate the  $H-H$  bond and shorten the  $C-H$  bonds (to the  $H_2$  ligand). Thus, if back-donation were made more important, then the  $D_{4h}$  geometry for  $CH_4^{2+}$  where the  $H-H$  bond is completely broken would become the ground state. Now suppose one rotates the  $H_2$  ligand by  $90^\circ$  to another  $C_{2v}$  structure, which is analyzed in Figure 9.12b. The  $H_2 \sigma$  orbital is involved in the same interaction and is stabilized by an identical amount since the  $2a_1$  fragment acceptor orbital is cylindrically symmetrical. In other words, the  $2a_1\text{-}H_2 \sigma$  overlap is identical in both conformations. What is different is that now  $H_2 \sigma^*$  has  $b_1$  symmetry and it interacts with the empty  $b_1$  fragment orbital on  $CH_2^{2+}$ . The bonding combination is not filled so this has no energetic impact. There is no longer any back-donation. As a consequence this structure was found [23] to be 13 kcal/mol higher in energy than the ground state one. The  $H-H$  distance was much smaller  $-0.90\text{ \AA}$  and the  $C-H$  distance (to  $H_2$ ) of  $1.43\text{ \AA}$  was longer than that found in the ground state. So the absence of back-donation makes the  $H_2$  ligand less strongly bound. Now with two more electrons, the  $b_1$  fragment orbital on  $CH_2$  is filled and its interaction with  $H_2 \sigma^*$  is strongly stabilizing so the  $H-H$  bond is broken and the tetrahedral geometry becomes the ground state. This brings up the result [17] mentioned previously for planar  $CH_4$ . A  $CH_2$  fragment will have  $2a_1$  filled and  $b_1$  empty. Therefore,  $H_2 \sigma$  can only interact in a stabilizing fashion with  $b_1$ , which precisely corresponds to the geometry found in the calculations. There is no back-donation so the  $H-H$  distance is again rather short at  $0.88\text{ \AA}$  [17]. We shall return to a related problem, the coordination of  $AH_3^+$  to  $H_2$ , in Section 14.3.

## 9.6 THE $AH_n$ SERIES—SOME GENERALIZATIONS

There are many connections between the molecular orbitals of the  $AH_n$  series that we have studied here and in Chapter 7. One could build a generalized orbital interaction consisting of the  $s$  and three  $p$  AOs on A. When symmetry adapted combinations of the  $n$  (where  $n \leq 4$ )  $s$  AOs on the hydrogen atoms are made,  $n A-H$  (delocalized) stabilized bonding MOs are produced. There will also be  $n A-H$  antibonding orbitals at high energy. Left behind are  $4-n$  nonbonding MOs, which are localized on the central atom. Thus, when  $n=2$ , there are two bonding and antibonding A-H orbitals. Left behind are the two nonbonding MOs (the  $1\pi_u$  set for linear molecules or  $2a_1$  and  $b_1$  for bent ones—see Section 7.1). One rule of thumb that we will use extensively is that a stable molecule (in a thermodynamic sense) will be one where all bonding MOs are filled. The nonbonding orbitals will be filled in this case if the central atom is electronegative; they lie at low energies. Therefore, a total of  $2 \times [(n) + (4 - n)] = 8$  electrons will lead to a stable molecule.

This is a very roundabout way to derive the eight electron rare-gas rule. As we will see in Section 14.1 an extension of this offers a particularly simple way to view the so-called hypervalent molecules and electron counting in organometallic molecules in later chapters.

Another way to view the AH<sub>n</sub> series can be developed as follows: in tetrahedral AH<sub>4</sub> the four atomic orbitals of A find a one-to-one match with the four orbitals of tetrahedral H<sub>4</sub>. Consequently four bonding and four antibonding MOs are produced. One hydrogen atom can be removed from AH<sub>4</sub> to produce pyramidal AH<sub>3</sub>. This produces a nonbonding orbital localized on A. The three bonding and three antibonding MOs of AH<sub>3</sub> have an essentially identical composition to their counterparts in AH<sub>4</sub>. Likewise, in AH<sub>2</sub> two hydrogen atoms have been removed which creates two A-centered nonbonding orbitals. Two A—H bonding and two A—H antibonding orbitals that are remnants of those in AH<sub>4</sub> remain. In AH there are three A-centered nonbonding orbitals and only one A—H bonding and one A—H antibonding MO. Therefore, each time a hydrogen atom is removed from a bonding orbital, this MO will rise in energy. This can be dramatically illustrated for the AH<sub>n</sub> series by photoelectron spectroscopy. Figure 9.13 presents the relevant

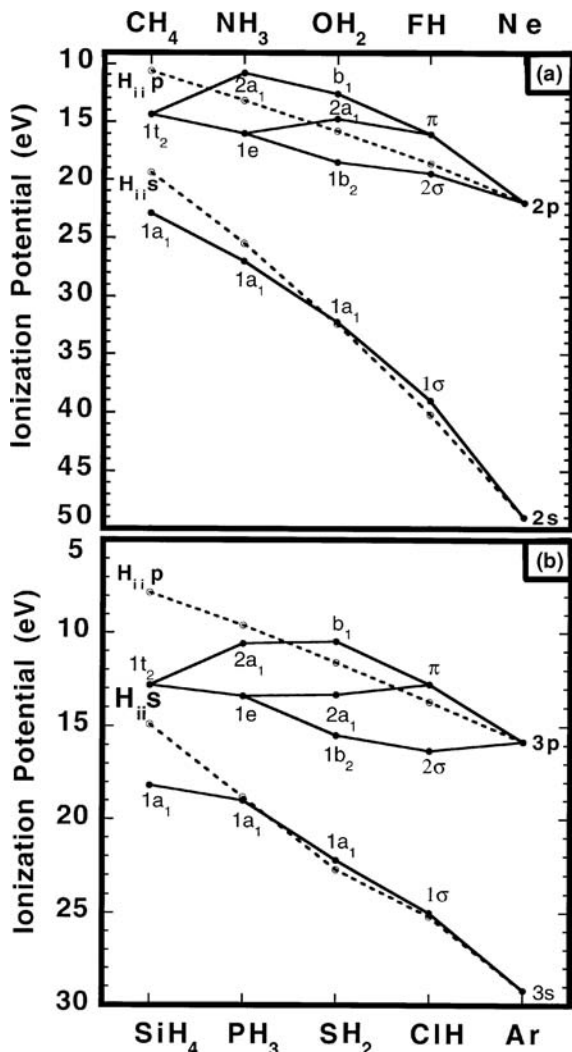


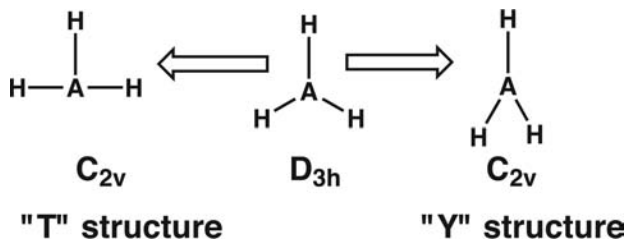
**FIGURE 9.13**

Plot of the vertical ionization potentials for the eight electron AH<sub>4</sub>, AH<sub>3</sub>, AH<sub>2</sub>, AH, and A series. First row molecules are plotted in (a) and second row ones in (b). The dotted line indicates the state averaged ionization potentials for the A atoms.

data [24] in terms of a graph. Figure 9.13a plots the vertical ionization potentials of CH<sub>4</sub>, NH<sub>3</sub>, H<sub>2</sub>O, HF, and Ne. Figure 9.13b does the same for the SiH<sub>4</sub> to Ar series from the second row of the Periodic Table. Notice that the energy scale is more expanded in Figure 9.13b than it is in Figure 9.13a. On going from CH<sub>4</sub> to NH<sub>3</sub> (or SiH<sub>4</sub> to PH<sub>3</sub>) one member of the  $t_{1g}$  set is destabilized to become the nonbonding  $2a_1$  MO. Now the electronegativity of N is much greater than that of C so the bonding  $1e$  set lies lower in energy than  $t_{1g}$  and, of course,  $1a_1$  in NH<sub>3</sub> is lower in energy than  $1a_1$  in CH<sub>4</sub>. In other words, using electronegativity perturbation theory considerations (Section 6.4)  $\epsilon^{(1)} < 0$  for these transformations. On going from NH<sub>3</sub> to H<sub>2</sub>O one member of the N—H bonding  $1e$  set is destabilized to create the nonbonding  $2a_1$  MO. Finally going from H<sub>2</sub>O to HF, the  $1b_2$  A—H bonding MO is not destabilized, but is actually stabilized by 1 eV on going to the nonbonding  $2\sigma$  MO in HF. However, this is much less than the stabilization on going from  $1a_1$  to  $1\sigma$  (6.8 eV) which is due to the increased electronegativity of F compared to O. Note that on moving from the nonbonding but hybridized  $2a_1$  orbital in PH<sub>3</sub> to the  $b_1$  MO in H<sub>2</sub>S, solely a  $p$  AO on S, the ionization potential decreases. This does not quite happen for the NH<sub>3</sub> to H<sub>2</sub>O transformation because the electronegativity difference between N and O is much larger than that between P and S, see Figure 2.4. A feeling of the energetic impact of electronegativity on the MO energies can be appreciated by plotting the state-averaged ionization potentials for the central atoms (from 2.9). These are the dashed lines in Figure 9.13. One might think that since these are a measure of the energy of an electron in an atomic orbital associated with an atom, then it should be easy to tell how much stabilization ensues when the hydrogen atoms interact with the central atom. In part this is true, but then only in a qualitative sense. In CH<sub>4</sub> and SiH<sub>4</sub> the  $1a_1$  and  $t_{1g}$  MOs are stabilized by a healthy amount with respect to the s and  $p$   $H_{ii}$ s of C and Si. But then the  $H_{ii}$  values for the s valence orbitals are almost coincident with the  $1a_1$  (and  $1\sigma$ ) MOs for the remaining molecules. Certainly on going from the left to the right of this series, the lowest MO becomes increasingly concentrated on the central atom since it becomes more and more electronegative compared to hydrogen. But this is not the whole story. Note that the  $b_1$  and  $\pi$  MOs for both rows have ionization potentials that are lower in energy than their  $H_{ii}$   $p$  AO atomic counterparts, yet these MOs are precisely a  $p$  AO on the central atom! The reason for this is increased electron-electron repulsion in the molecules compared to the atoms. Consider the oxygen atom, which has a  $s^2p^4$  electron configuration. The state averaged ionization potential then is one where four electrons are arranged in some (high spin) manner around three  $p$  AOs. So the average electron occupancy per  $p$  AO is  $<2$ . Contrast this situation with the  $b_1$  MO in H<sub>2</sub>O. Here the  $b_1$  MO of course is occupied with two electrons and these electrons are paired. So there is a greater Coulomb repulsion energy, and pairing the electrons in  $b_1$  also raises their energy (see Sections 8.8 and 8.9). Consistent with this explanation is that the differences are smaller for the second row (see Figure 9.13b). Here the orbitals on the central atoms are more diffuse so the differences in Coulomb repulsion and the pairing energies are smaller. The dashed lines for the  $p$  AOs do nicely divide bonding from nonbonding regions and both dashed lines do reflect the electronegativity perturbations brought about by the different atoms. But to emphasize again the value of Figure 9.13 we have here an experimental demonstration of the conversion of bonding into nonbonding MOs by removal of hydrogen atoms. This reductive approach for determining the valence orbitals of AH<sub>n</sub> species will be extended greatly when we discuss the ML<sub>n</sub> transition metal fragment series. Very similar patterns will emerge.

**PROBLEMS**

**9.1.** a. Construct a Walsh diagram for the distortion shown below.



- b. Predict what electron count(s) are viable for either  $C_{2v}$  geometry.  
 c. The optimum geometry for  $\text{LiH}_3$  is calculated to be the  $C_{2v}$  "T" structure. Use the Jahn-Teller theorem to show that it anticipates the distortion from  $D_{3h}$  to this structure.  
 d. Predict the reaction path for the rearrangement shown below.



**9.2.** Explain the following experimental facts:

$\text{H}-\text{A}-\text{H}$  angles:  $\text{CH}_3^-$ ,  $105^\circ$ ;  $\text{NH}_3$ ,  $106.7^\circ$ ;  $\text{OH}_3^+$ ,  $110^\circ$ .

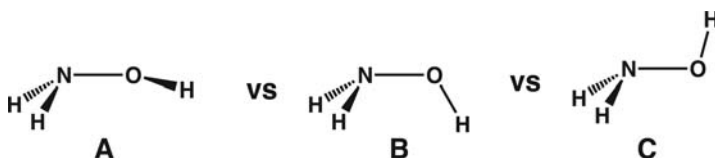
$\text{H}_3\text{A}$  inversion barriers:  $\text{CH}_3^-$ , 8 kcal/mol;  $\text{NH}_3$ , 5.8 kcal/mol;  $\text{OH}_3^+$ , 2 kcal/mol.

**9.3.**  $\text{CH}_4^{2+}$  is a known molecule but its structure has not been established by experiment. The structure as determined by high-level calculations was discussed in Problem 7.5. In this problem, we study possible geometries derived from a "gedankenexperiment" using the Jahn-Teller theorem and constructing Walsh diagrams using geometric perturbation theory.

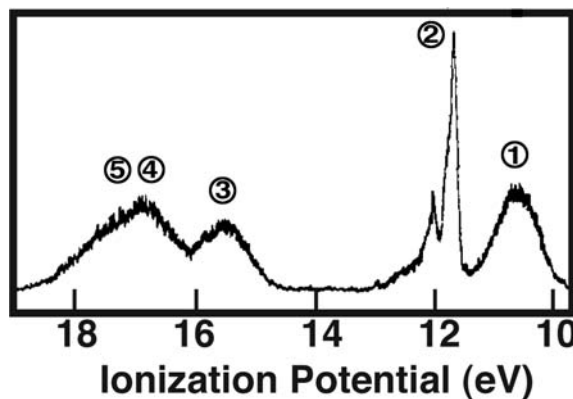
- a. The MOs of tetrahedral  $\text{AH}_4$  are drawn out in **9.27** and **9.28**. For  $\text{CH}_4^{2+}$  the orbital occupancy will be  $(1a_1)^2(1t_2)^4$ . Use the Jahn-Teller theorem and the normal modes for an  $\text{AB}_4$  tetrahedral molecule in Appendix III to predict possible geometries for  $\text{CH}_4^{2+}$ .  
 b. Construct Walsh diagrams for all of the possible distortions and predict possible stable structures.

**9.4.** We see in Section 21.5 that a  $\text{R}_3\text{P}-\text{Au}$  fragment has very similar bonding properties compared to a hydrogen atom! Construct an orbital interaction diagram for  $\text{H}_3\text{P}-\text{Au}$  by interacting the HOMO of  $\text{PH}_3$  (which has an ionization potential of 10.0 eV) with the s and p AOs of Au (s and p  $H_{ii} = -10.9$  and  $-5.6$  eV, respectively). The d AOs of Au lie at a very low energy and to a first approximation will not mix too heavily into the other MOs. Draw out the resultant MOs and indicate the orbital occupancy.

**9.5.** a. There are three possible geometries for hydroxylamine as shown below. Using the ideas from **9.26** determine the relative order of stabilities for these three conformations.



- b.** The photoelectron spectrum of hydroxylamine is shown below as adapted from Reference [25]. Using the PE spectral data for water in Figure 7.9 and ammonia in Figure 9.9 assign the five ionizations for  $\text{NH}_2\text{OH}$ .




---

## REFERENCES

---

1. B. M. Gimarc, *Molecular Structure and Bonding*, Academic Press, New York (1979).
2. A. D. Walsh, *J. Chem. Soc.*, 2266, 2288, 2296, 2301, 2306, 2318, 2321, 2325, 2330, 2260, (1953).
3. C. C. Levin, *J. Am. Chem. Soc.*, **97**, 5649 (1975).
4. B. M. Gimarc, *J. Am. Chem. Soc.*, **95**, 1417 (1973); A careful, rigorous treatment may be found in M. Atanasov and D. Reinen, *J. Am. Chem. Soc.*, **105**, 5450 (2001).
5. D. A. Dixon and D. S. Marynick, *J. Am. Chem. Soc.*, **99**, 6101 (1977); P. Schwerdtfeger, P. D. W. Boyd, T. Fischer, P. Hunt, and M. Liddell, *J. Am. Chem. Soc.*, **116**, 9620 (1994); P. Schwerdtfeger, L. J. Laakkonen, and P. Pykkö, *J. Chem. Phys.*, **96**, 6807 (1992).
6. J. Moc and K. Morokuma, *Inorg. Chem.*, **33**, 551 (1994).
7. P. Helminger, F. C. De Lucia, W. Gordy, H. W. Morgan, and P. A. Staats, *Phys. Rev.*, **9**, 12 (1974); K. Kijima and T. Tanaka, *J. Mol. Spectrosc.*, **89**, 62 (1981); M. Carlotti, G. DiLionardo, and L. Fusina, *J. Mol. Spectrosc.*, **102**, 310 (1983); W. Jeerzembeck, H. Büger, L. Constantin, L. Margules, J. Demaison, J. Breidung, and W. Thiel, *Angew. Chem. Int. Ed.*, **41**, 2550 (2002); B. Beagley and A. R. Medwid, *J. Mol. Struct.*, **38**, 229 (1977); J. Molnár, M. Kolonits, M. Hargittai, R. J. M. Konings, and A. S. Booij, *Inorg. Chem.*, **35**, 7639 (1996).
8. A. W. Potts and W. C. Price, *Proc. R. Soc. Lond. A*, **326**, 181 (1972).
9. T. A. Claxton and N. A. Smith, *J. Chem. Phys.*, **52**, 4317 (1970); F. Matthias, T. Ziegler, and P. v. R. Schleyer, *Organometallics*, **15**, 1477 (1996).
10. D. S. Marynick, *J. Chem. Phys.*, **73**, 3939 (1980).
11. K. Mislow, *Trans. N. Y. Acad. Sci.*, **35**, 227 (1973).
12. D. E. Dougherty, K. Mislow, and M.-H. Whangbo, *Tetrahedron Lett.*, **2321** (1979); J. R. Damewood, Jr. and K. Mislow, *Monatshefte für Chemie*, **111**, 213 (1980).
13. V. J. Klimkowski, H. L. Sellers, and L. Schafer, *J. Mol. Struct.*, **54**, 299 (1979); K. B. Wiberg and P. R. Rablen, *J. Am. Chem. Soc.*, **117**, 2201 (1995); K. B. Wiberg, P. R. Rablen, D. J. Rush, and T. A. Keith, *J. Am. Chem. Soc.*, **117**, 4261 (1995).
14. S. Wolfe, H. B. Schlegel, I. G. Csizmadia, and F. Bernardi, *Can. J. Chem.*, **53**, 3365 (1975); P. G. Mezey, A. Kresge, and I. G. Csizmadia, *Can. J. Chem.*, **54**, 2526 (1976); See also A. M. El-Nahas and P. v. R. Schleyer, *J. Comp. Chem.*, **15**, 596 (1994) for a number of related examples.
15. R. A. Moss, W. Guo, D. Z. Denny, K. N. Houk, and N. G. Rondan, *J. Am. Chem. Soc.*, **103**, 6164 (1981); P. H. Mueller, N. G. Rondan, K. N. Houk, J. F. Harrison, D. Hooper, B. H. Willen, and J. F. Lieberman, *J. Am. Chem. Soc.*, **103**, 5049 (1981); N. G. Rondan, K. N. Houk, and R. A. Moss, *J. Am. Chem. Soc.*, **102**, 1770 (1980).

16. G. V. Gibbs, E. P. Meagher, M. B. Newton, and D. K. Swanson, *Structure and Bonding in Crystals*, Vol. I, M. O'Keeffe and A. Navrotsky, editors, Academic Press, New York p. 195. (1981).
17. M. J. M. Pepper, I. Shavitt, P. v. R. Schleyer, M. N. Glukhovtsev, R. Janocheck, and M. Quack, *J. Comp. Chem.*, **16**, 207 (1995).
18. T. Clark and P. v. R. Schleyer, *J. Am. Chem. Soc.*, **101**, 7747 (1979); K. Sorger and P. v. R. Schleyer, *J. Mol. Struct. (Theochem)*, **338**, 317 (1995).
19. A. F. Wells, *Structural Inorganic Chemistry*, 4th edition, Clarendon, Oxford (1975).
20. M.-B. Krogh-Jespersen, J. Chandrasekhar, E.-U. Wurthwein, J. B. Collins, and P. v. R. Schleyer, *J. Am. Chem. Soc.*, **102**, 2263 (1980).
21. J. K. Burdett and T. Hughbanks, *J. Am. Chem. Soc.*, **106**, 3101 (1984).
22. J. B. Collins, P. v. R. Schleyer, J. S. Binkley, J. A. Pople, and L. Radom, *J. Am. Chem. Soc.*, **98**, 3436 (1976).
23. M. W. Wong and L. Radom, *J. Am. Chem. Soc.*, **111**, 1155 (1989).
24. A. W. Potts and W. C. Price, *Proc. R. Soc. Lond. A.*, **326**, 165, 181 (1972).
25. K. Kimura and S. Katsumata, *J. Chem. Phys.*, **67**, 1225 (1977)

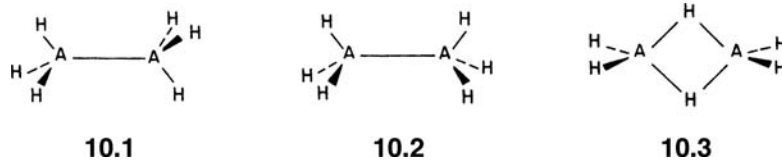
# Molecules with Two Heavy Atoms

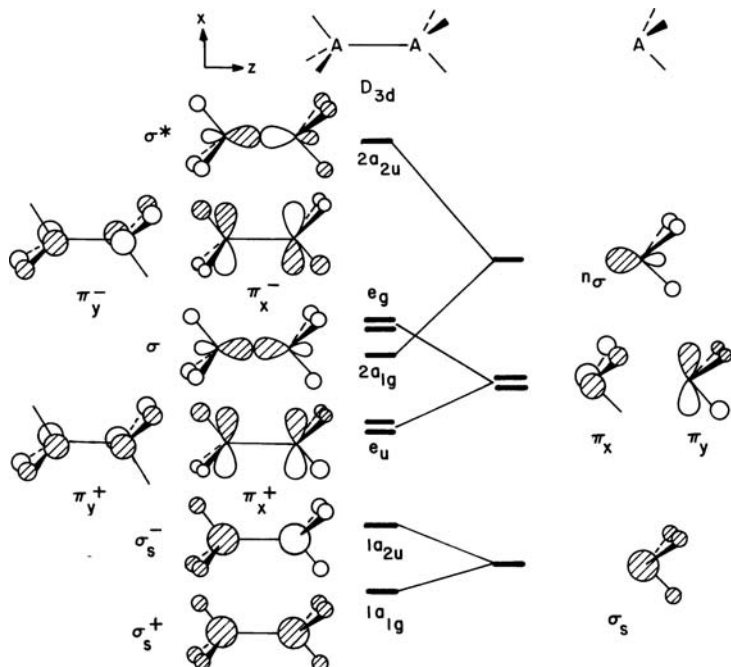
## 10.1 INTRODUCTION

In the previous chapters, the molecular orbitals (MOs) of  $AH_n$  systems were analyzed in some detail. These orbitals are convenient building blocks in constructing the MOs of large molecules such as  $A_2H_6$ ,  $A_2H_4$ , and so on, which may be envisaged as being made up of  $AH_n$  fragments. Extension to the series  $A_2L_{2n}$  is also straightforward and covers a good bit of organic and main group chemistry. For instance, the MOs of  $C_2H_6$  can be easily constructed from the MOs of two  $CH_3$  fragments. It is important to realize that the use of such molecular fragments implies nothing concerning their existence as stable chemical species. They are just conceptual building blocks convenient for analyzing the properties of large molecules [1]. The MOs of molecular fragments are often referred to as *fragment orbitals*. In this chapter, the structural properties of several molecules are examined by constructing their MOs in terms of the appropriate fragment orbitals.

## 10.2 $A_2H_6$ SYSTEMS [2]

Molecules of formula  $A_2H_6$  include ethane  $C_2H_6$  and diborane  $B_2H_6$ . Important structures of ethane are the staggered and eclipsed conformations, 10.1 and 10.2, respectively. Diborane adopts the bridged structure 10.3, as noted in Section 9.3. The



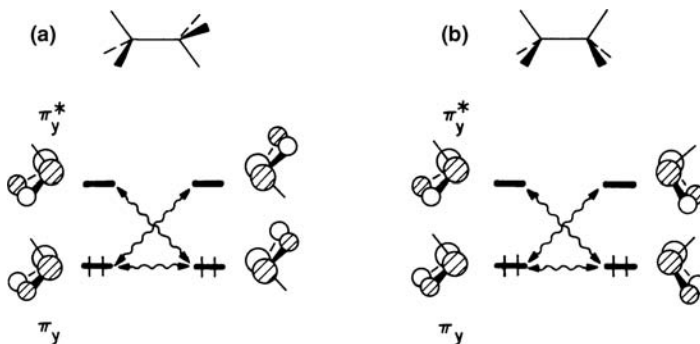
**FIGURE 10.1**

Construction of the MOs of staggered A<sub>2</sub>H<sub>6</sub> in terms of the orbitals of two pyramidal AH<sub>3</sub> fragments.

interaction between the orbitals of two pyramidal AH<sub>3</sub> fragments, shown in Figure 10.1, leads to the MOs of staggered A<sub>2</sub>H<sub>6</sub> depicted on the left-hand side of Figure 10.1. For simplicity, the A—H antibonding orbitals of AH<sub>3</sub> are not included in Figure 10.1. On the right-hand side of this figure are the 1a<sub>1</sub>, 1e, and 2a<sub>1</sub> orbitals of a pyramidal AH<sub>3</sub> fragment (developed in Section 9.3). They are denoted as σ<sub>s</sub>, π, and n<sub>σ</sub>, respectively, as convenient descriptors of the bonding type. To a reasonably good first approximation, one only needs to carry out degenerate perturbation theory to yield the resultant molecular orbitals; in other words, we only need to take positive and negative—bonding and antibonding—combinations. Thus, the 1a<sub>1g</sub> and 1a<sub>2u</sub> MOs are primarily the in-phase and out-of-phase combinations of the two σ<sub>s</sub> fragment orbitals, respectively, while the 2a<sub>1g</sub> and 2a<sub>2u</sub> MOs are primarily the in-phase and out-of-phase combinations of the two n<sub>σ</sub> fragment orbitals, respectively. The π<sub>x</sub><sup>+</sup> and π<sub>x</sub><sup>-</sup> MOs (e<sub>u</sub> and e<sub>g</sub>, respectively) are largely given by the in-phase and out-of-phase combinations of the two π<sub>x</sub> fragment orbitals. Likewise, the π<sub>y</sub><sup>+</sup> and π<sub>y</sub><sup>-</sup> MOs are largely given by the in-phase and out-of-phase combinations of the two π<sub>y</sub> fragment orbitals. Note that the splitting for the n<sub>σ</sub> fragment orbitals is larger than that for σ<sub>s</sub> and π. This is due to a larger overlap between the n<sub>σ</sub> orbitals. They are hybridized toward each other and overlap in a σ (as opposed to π) sense.

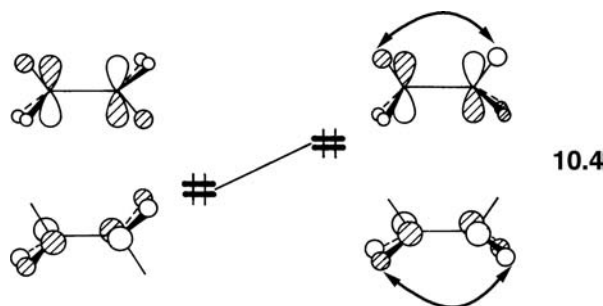
With 14 electrons, the highest occupied molecular orbital (HOMO) of staggered ethane, e<sub>g</sub>, is doubly degenerate and completely filled. The energy of eclipsed ethane differs from that of the staggered conformer, since the magnitudes of the orbital interactions between two CH<sub>3</sub> groups are different in the two conformations. Figure 10.2 shows the π<sub>y</sub> and π<sub>y</sub><sup>\*</sup> (the antibonding analog of π<sub>y</sub>) orbitals of two CH<sub>3</sub> groups in the staggered and eclipsed arrangements [3]. Each conformation gives rise to one destabilizing interaction (π<sub>y</sub>—π<sub>y</sub>), which is a two-orbital-four-electron situation since π<sub>y</sub> is filled. There are also two stabilizing interactions (π<sub>y</sub>—π<sub>y</sub><sup>\*</sup>) and (π<sub>y</sub><sup>\*</sup>—π<sub>y</sub>).

From the diagram in Figure 10.2, it can be seen that 1–4 H—H overlap in the (π<sub>y</sub>—π<sub>y</sub>) interaction is smaller in the staggered conformation. Thus the total overlap between the two π<sub>y</sub> orbitals is smaller, and the magnitude of the destabilizing (π<sub>y</sub>—π<sub>y</sub>) interaction is smaller in the staggered conformation. The 1–4 H—H overlap from the

**FIGURE 10.2**

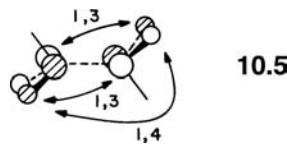
Frontier orbital interactions between the two  $\text{AH}_3$  fragments in staggered and eclipsed  $\text{A}_2\text{H}_6$ : (a) staggered and (b) eclipsed.

$(\pi_y - \pi_y^*)$  interaction is negative but the stronger I–2 C–C overlap is positive. It is also clear from the figure that in the staggered conformation the I–4 H–H overlap is less negative. Since the total overlap between the  $\pi_y$  and  $\pi_y^*$  is greater, with a correspondingly larger  $(\pi_y - \pi_y^*)$  stabilization in the staggered conformation, this geometry is predicted to be more stable than the eclipsed conformer. The same conclusion is reached by considering the  $\pi$ -type interactions associated with the  $\pi_x$  and  $\pi_x^*$  orbitals of two  $\text{CH}_3$  groups because  $\pi_x$  and  $\pi_x^*$  are degenerate with  $\pi_y$  and  $\pi_y^*$ , respectively. Consequently, the HOMO of ethane is lower in energy (less destabilized) in staggered ethane, as shown in 10.4, compared to the eclipsed conformation. As the double-headed

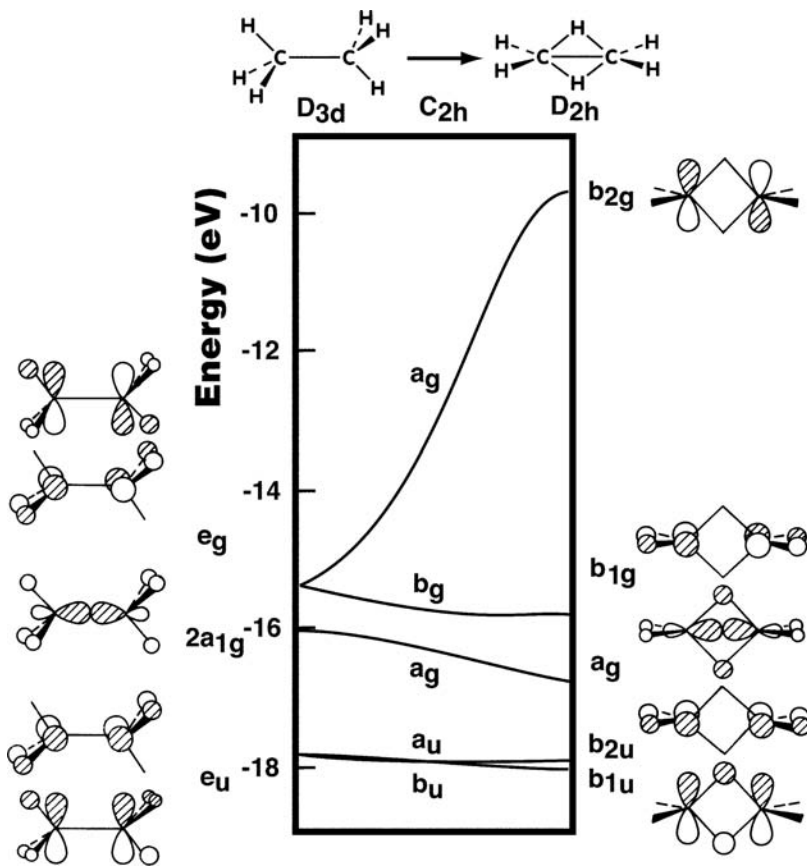


arrow indicates, there is more I–4 H–H antibonding in the eclipsed structure. The rotational barrier in ethane has been determined to be 2.93 kcal/mol [4].

With respect to ethane, diborane ( $\text{B}_2\text{H}_6$ ) has two electrons less so the electron occupancy in Figure 10.1 is  $(1a_{1g})^2(1a_{2u})^2(e_u)^4(2a_{1g})^2(e_g)^2$ . In other words, the HOMO of a staggered ethane-like  $\text{B}_2\text{H}_6$  structure would result in the  $e_g$  MO being half-filled and this signals a first-order Jahn–Teller instability. Figure 10.3 shows a Walsh diagram, computed at the extended Hückel level, for going from the staggered to bridged structure (i.e., 10.1 → 10.3) [5]. Only five of the most important valence orbitals are shown. The  $\pi_y^-$  level, one component of  $e_g$ , is lowered in energy since the antibonding I–3 and I–4 interactions in this MO (see 10.5) are reduced. But what is equally important is that the nonbridging H–B–H angle increases from  $110^\circ$  to  $120^\circ$ .



which increases the overlap between the hydrogens and the  $p_y$  atomic orbital on each boron atom (see Figure 1.5 and Section 9.3). On the other hand, the  $\pi_x$  component of  $e_g$  is raised in energy since bonding between A and H is lost upon the distortion. The

**FIGURE 10.3**

A Walsh diagram for going from a staggered  $A_2H_6$  structure to a bridged one for some of the valence molecular orbitals.

degeneracy of  $e_g$  in staggered diborane is therefore lifted upon distortion to a bridged structure; the  $b_{1g}$  HOMO is stabilized and the  $b_{2g}$  lowest unoccupied molecular orbital (LUMO) is considerably destabilized. The  $2a_{1g}$  MO is slightly stabilized on going to the bridged structure. The two bridging hydrogen s atomic orbitals (AOs) overlap to a greater extent with the hybrids on the central atoms. Finally, nothing much happens with the  $e_u$  set. For the  $\pi_y^+$  component of  $e_u$  the 1,3- and 1,4-interactions described above act in an opposite way, since the relevant overlaps are now positive whereas the H—B—H bond angle change will still be stabilizing. For the  $\pi_x^+$  component bonding to four hydrogens is lost while bonding to the two bridging hydrogens is not only retained is amplified. In short, the **10.1**  $\rightarrow$  **10.3** distortion relieves the Jahn–Teller instability associated with the staggered  $D_{3d}$  structure. This conclusion is also valid when there are three electrons to fill the HOMO level of the  $D_{3d}$  structure as in  $C_2H_6^+$ . In this case the  $\pi_x^-$  level ( $a_g$  at the intermediate  $C_{2h}$  geometry) is singly occupied (Figure 10.3) during the **10.1**  $\rightarrow$  **10.3** distortion, and the driving force for the distortion is reduced compared with the case of  $B_2H_6$ . Therefore,  $C_2H_6^+$  is predicted to have a  $C_{2h}$  structure (**10.6**), intermediate between **10.1** and **10.3** [6a], whereas  $C_2H_6^{2+}$  has the diborane, **10.3**, structure as a minimum [6b].



Diborane is two electrons short of a saturated compound like ethane. In the bond orbital approach, two three-center–two-electron bonds (**10.7**) are considered to be formed between the bridging hydrogens and the borons. A very careful and lucid approach using this basis has been given by Trinquier and Malrieu [7]. A perplexing question concerns the B–B bond order. One might naively think that since the C–C bond order in ethane is one, when two electrons are taken out, then the B–B bond order will be zero. A valence bond expansion of **10.7** reveals that the B–H interactions are stronger, but the direct B–B interaction cannot be neglected. In terms of MOs, the filled orbitals used for the two three-center two-electron bonds are the  $a_g$  and  $b_{1u}$  levels in Figure 10.3. One can see in them the essence of the  $a_1'$  level in the cyclic  $H_3$  system (Figure 7.6), here taken as linear combinations ( $a_g$  is the plus combination and  $b_{1u}$  is the negative one). The  $b_{2g}$  orbital corresponds clearly to one component of the  $e'$  set in  $H_3$ . We return to the electronic structure of diborane from a different perspective in Section 10.3.

### 10.3 12-ELECTRON $A_2H_4$ SYSTEMS

Some structures of interest for  $A_2H_4$  molecules are shown in **10.8**. Pyramidalization at each atomic center A leads the planar structure **10.8a** to the anti structure **10.8c**, and the perpendicular structure **10.8b** to the gauche structure **10.8d**. The orbital interaction between two  $AH_2$  units in Figure 10.4 using degenerate perturbation theory gives rise to the MOs of planar  $A_2H_4$  shown on the left-hand side of the figure. The splitting of the  $AH_2$  fragment orbitals (Section 7.1) follows the magnitude of the

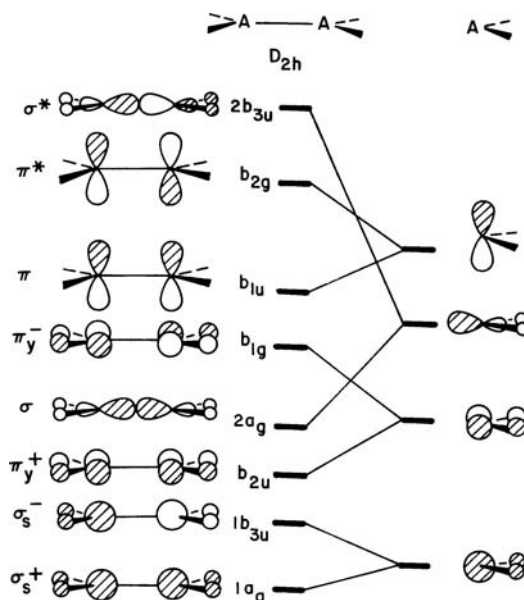
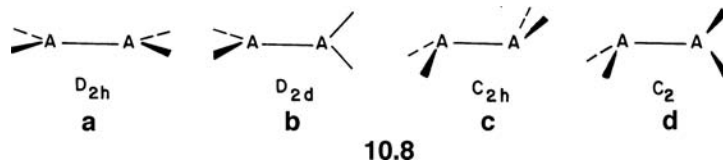
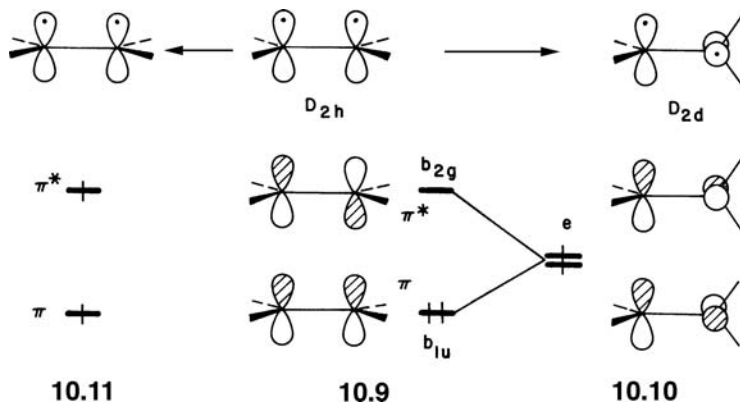


**FIGURE 10.4**

Construction of the MOs of planar  $A_2H_4$  in terms of the orbitals of two  $AH_2$  fragments.

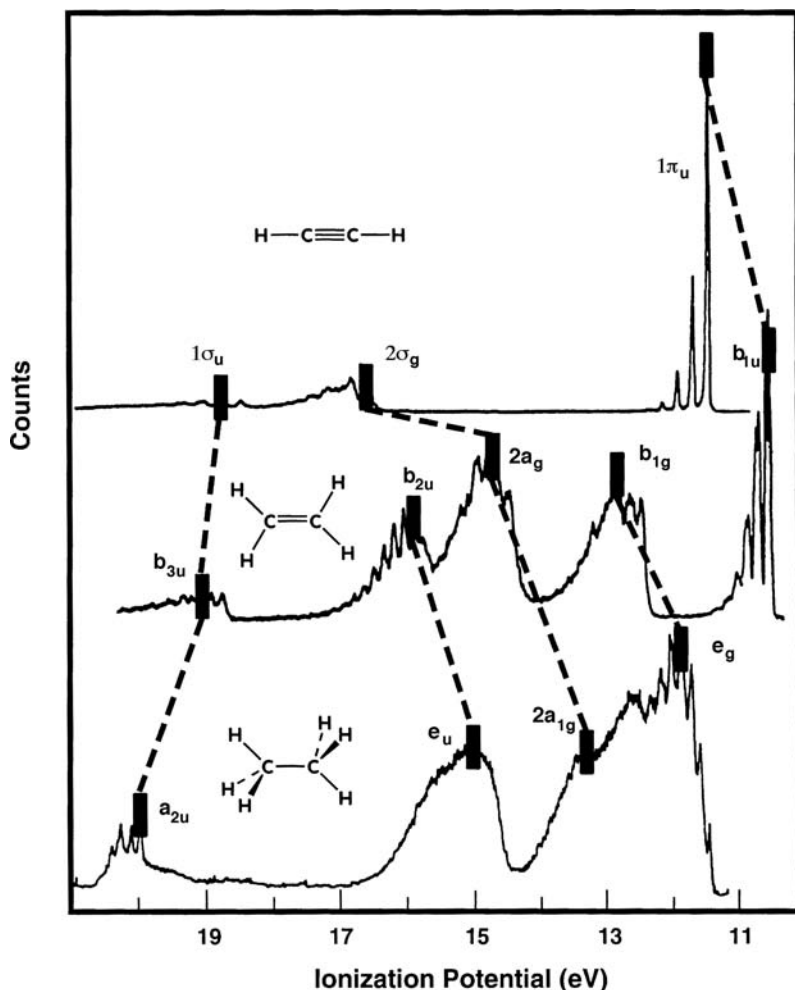
overlap turned on between the fragment orbitals. Using the maxim that the overlap varies  $\sigma > \pi$ , it is easy to see that the  $\sigma/\sigma^*$  ( $2a_g/2b_{3u}$ ) MOs are split to a much greater extent than the  $\pi/\pi^*$  ( $b_{1u}/b_{2g}$ ) or  $\pi_y^+/\pi_y^-$  ( $b_{2u}/b_{1g}$ ) sets. Furthermore, there is greater  $\pi/\pi^*$  splitting than that for  $\pi_y^+/\pi_y^-$ , since in the latter the fragment orbitals are delocalized in the A—H region which leads to a smaller inter-fragment overlap, whereas, the  $\pi/\pi^*$  combination is localized exclusively on the A atoms. This also explains the small  $\sigma_s^+/\sigma_s^-$  ( $1a_g/1b_{3u}$ ) splitting. These are MOs primarily involved with A—H bonding. There is also some second-order mixing primarily with the  $\sigma_s^-$  combination into  $\sigma_s^+$  since they have the same symmetry which serves to keep  $\sigma_s^-$  from rising to a high energy.

With 12 electrons as in C<sub>2</sub>H<sub>4</sub>, the  $\pi$  and  $\pi^*$  levels become the HOMO and LUMO of planar A<sub>2</sub>H<sub>4</sub>, respectively. At a given A—A distance,  $\pi$  bonding in the lower of these two levels is maximized when A<sub>2</sub>H<sub>4</sub> is planar. It is the occupation of this level that leads to planar 12-electron A<sub>2</sub>H<sub>4</sub> systems when A is from the first or second row of the periodic table, but the anti structure is preferred for heavier A atoms, as we see later. Occupation of the  $\pi$  orbital is also responsible for the large barrier to rotation around the C=C double bond (approximately 65 kcal/mol in C<sub>2</sub>H<sub>4</sub>) in alkenes [8], since  $\pi$  bonding is completely lost upon rotation as shown in going from **10.9** to **10.10**. Some of electronic states of importance for a 12-electron A<sub>2</sub>H<sub>4</sub> system are then the ground state **10.9**, the twisted triplet state, **10.10** and the excited triplet state **10.11** where rotation around the A—A bond has not taken



place. Inspection of the HOMOs in **10.10** and **10.11** shows the diradical state **10.10** to be more stable than the ( $\pi \rightarrow \pi^*$ ) excited state. Thus, the ( $\pi \rightarrow \pi^*$ ) excitation in alkenes provides a driving force for twisting around the C=C bond to a perpendicular structure. This is why cis-trans isomerization occurs in alkenes upon ( $\pi \rightarrow \pi^*$ ) excitation [8]. We also return in more depth to the excited states of olefins in Section 10.4.

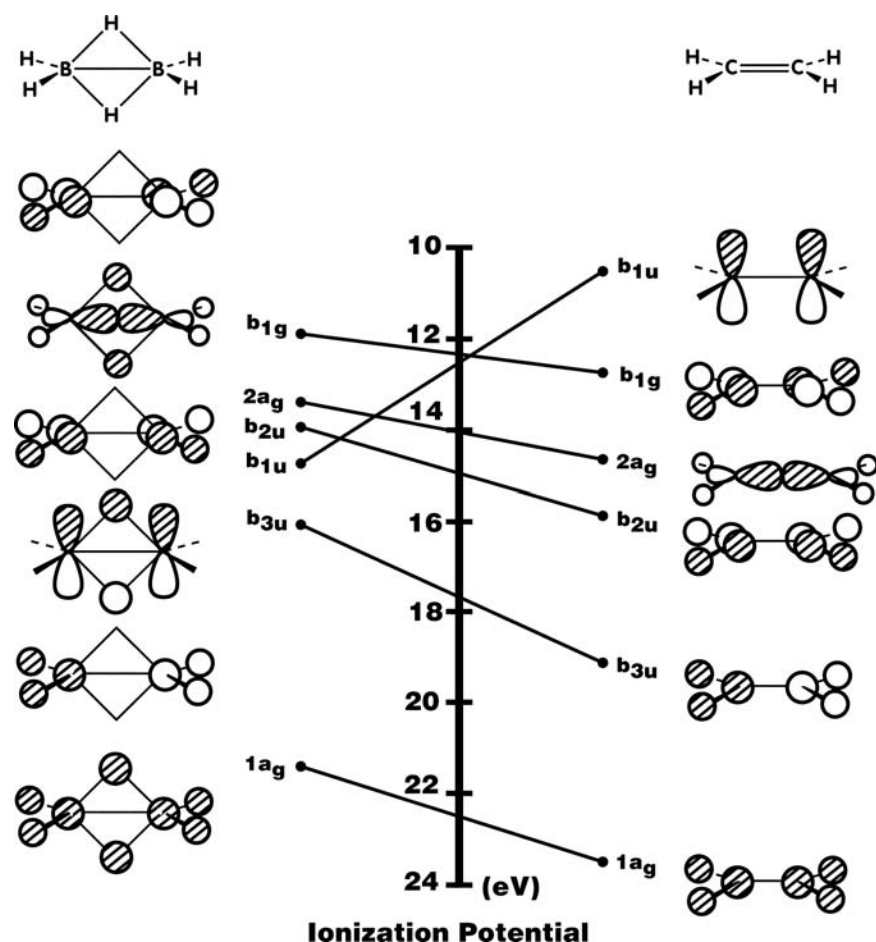
There are some interesting connections between the A<sub>2</sub>H<sub>4</sub> and A<sub>2</sub>H<sub>6</sub> orbitals. Figure 10.5 shows a correlation between the photoelectron spectra for C<sub>2</sub>H<sub>6</sub> with C<sub>2</sub>H<sub>4</sub> and C<sub>2</sub>H<sub>2</sub> [9]. The heavy bars indicate vertical transitions. The MOs of C<sub>2</sub>H<sub>6</sub> and C<sub>2</sub>H<sub>4</sub> are simply those from Figures 10.1 and 10.4, respectively. It is a trivial matter to construct the MOs of C<sub>2</sub>H<sub>2</sub> from two HA fragments (see Figure 9.1 for the orbitals of HA). The important geometrical change to remember is that the C—C bond length decreases from 1.531 to 1.330 to 1.203 Å on going from ethane (C<sub>2</sub>H<sub>6</sub>) to ethylene (C<sub>2</sub>H<sub>4</sub>) to acetylene (C<sub>2</sub>H<sub>2</sub>). Consequently,  $\pi$  overlap increases going from ethylene to acetylene and thus the ionization potential increases going from  $b_{1u}$  to  $1\pi_u$ . For the same reason, increasing  $\sigma$  overlap causes the ionization potential of  $2a_{1g} < 2a_g < 2\sigma_g$ . Now the ionization potentials associated with the  $a_{2u}$ ,  $b_{3u}$ , and  $1\sigma_u$  series behave in the opposite manner. This is consistent with the form of the MOs in

**FIGURE 10.5**

The correlation of the PE spectra of acetylene, ethylene, and ethane adapted from Reference [9].

that although they are primarily C—H  $\sigma$  bonding, they are also C—C  $\sigma$ -antibonding. A reason why the ionization potentials do not decrease more on going from ethane to acetylene is that the C—H bond length decreases (1.096 to 1.076 to 1.061 Å for ethane, ethylene, and acetylene, respectively). This will cause an increase in the C—H  $\sigma$  overlap. A final detail concerns itself with the  $\pi^-_y$  and  $\pi^+_y$  series of MOs. From Figures 10.1 and 10.4, it can be seen that these are primarily C—H  $\sigma$  bonding orbitals that overlap in a weaker  $\pi$  sense in the C—C region of the molecule. One then might think that ionization potential of  $b_{2u}$  for ethylene will be larger than the  $e_u$  set in ethane since the  $\pi$  bonding increases. This is indeed the case, but obviously not for the right reason since the  $\pi$  antibonding analog,  $b_{1g}$ , in ethylene also has a larger ionization potential than the  $e_g$  set in ethane. What dominates in both series is that the H—C—H bond angle increases from 109.5° in ethane to 119° in ethylene. The overlap between the  $p$  AO on carbon and the  $s$  AOs on the hydrogens increase (see Figure 1.5). Therefore, these MOs are stabilized on going from ethane to ethylene. The set of experimental data presented in Figure 10.5 are explained consistently and coherently in terms of orbital interactions.

As a second example of how experimental data can be understood based on orbital interactions, we consider the correlation between the PE spectra of ethylene and diborane [10]. This is shown in Figure 10.6. One could imagine that two protons are added across the C—C double bond of ethylene to form  $\text{C}_2\text{H}_6^{2+}$  which is isoelectronic to diborane. There is a large electronegativity perturbation at work

**FIGURE 10.6**

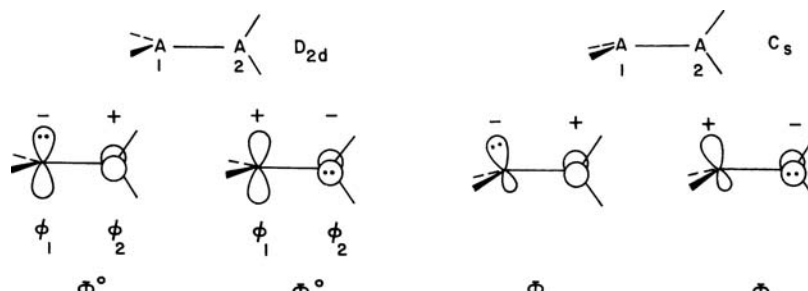
A correlation of the ionization potentials for ethylene and diborane.

here. Since boron is much less electronegative than carbon, those MOs which do not combine with the bridging hydrogen s AOs will be shifted up in energy (to lower ionization potentials). This does indeed occur for  $b_{3u}$ ,  $b_{2u}$ , and  $b_{1g}$  orbitals. The  $1a_g$  and particularly the  $2a_g$  MOs are not raised in energy as much, since the symmetric combination of hydrogen s AOs interacts with and stabilizes the orbitals. It would appear that the  $2a_g$  MO interacts more with the bridging hydrogens. This is consistent with the idea that the energy gap from hydrogen s to  $2a_g$  is smaller than that to the  $1a_g$  MO. The strongest interaction to the bridging hydrogens is found in the  $b_{1u}$  MO. As Figure 10.6 shows, this MO actually is stabilized on going from ethylene to diborane. It is the spatial extent of the  $b_{1u}$  orbital above and below the A<sub>2</sub>H<sub>4</sub> plane that maximizes overlap with the two bridging hydrogen s AOs. The picture from this correlation of photoelectron spectra points to a very large perturbation of the  $\pi$  orbital of ethylene on diprotonation to diborane. Certainly C—C  $\pi$  bonding is lost, however, not much stabilization occurs in  $2a_g$  (or  $1a_g$ ). This is consistent with the idea that direct B—B  $\sigma$  bonding is present in diborane, as pointed out in Section 10.2.

### 10.3.1 Sudden Polarization [11]

A perpendicular ( $D_{2d}$ ) A<sub>2</sub>H<sub>4</sub> molecule with 12 electrons is a typical diradical system (see Sections 8.8 and 8.10) **10.10**, with the triplet state lying very close in energy to

the singlet state. An alternative to the diradical state is obtained by asymmetrically occupying the  $p$  orbitals  $\phi_1$  and  $\phi_2$  with two electrons as shown in 10.12. The resulting electron configurations  $\Phi_1^\circ$  and  $\Phi_2^\circ$  are strongly dipolar because of the



formal positive and negative charges created on adjacent atoms. In general, strongly dipolar electron configurations, such as  $\Phi_1^\circ$  and  $\Phi_2^\circ$  obtained as an alternative to a nonpolar diradical configuration, are referred to as zwitterionic configurations.  $\Phi_1^\circ$  and  $\Phi_2^\circ$  are equivalent but differ in the way the two  $p$  orbitals are doubly occupied. Because of electron–electron repulsion arising from the orbital double occupancy (see Section 8.8),  $\Phi_1^\circ$  and  $\Phi_2^\circ$  are less stable than the diradical state. As the atomic centers  $A_1$  and  $A_2$  are equivalent, the state functions appropriate for perpendicular  $A_2H_4$  are given by linear combinations of  $\Phi_1^\circ$  and  $\Phi_2^\circ$ , namely,

$$\begin{aligned}\Psi_1^0 &= \frac{\Phi_1^\circ - \Phi_2^\circ}{\sqrt{2}} \\ \Psi_2^0 &= \frac{\Phi_1^\circ + \Phi_2^\circ}{\sqrt{2}}\end{aligned}\quad (10.1)$$

Since these states have equal weights on  $\Phi_1^\circ$  and  $\Phi_2^\circ$  they have equal electron densities on the two carbon atoms and hence no charge polarization. As noted in Section 8.10,  $\Psi_1^0$  is more stable than  $\Psi_2^0$  by  $-2K_{12}$ , where

$$K_{12} = \langle \Phi_1^0 | \hat{H} | \Phi_2^0 \rangle = (\phi_1 \phi_2 | \phi_1 \phi_2) \quad (10.2)$$

The exchange integral  $K_{12}$  originates from the overlap density distribution  $\phi_1 \phi_2$  and is extremely small in magnitude (e.g., 1–2 kcal/mol in perpendicular  $C_2H_4$ ) [11], because  $\phi_1$  lies in the nodal plane of  $\phi_2$  and vice versa. Consequently, the energy difference between the two states  $\Psi_1^0$  and  $\Psi_2^0$  is expected to be small. The relative stability of these two states is reversed in a large-scale CI calculation, although the energy difference between the two still remains very small [12]. Similarly, a large-scale CI calculation shows that the singlet diradical state is only slightly more stable than the triplet diradical state against the prediction of Hund's rule. In the following, we neglect the effect of a large-scale CI calculation on the relative stability of  $\Psi_1^0$  and  $\Psi_2^0$  because it is only the small energy difference between the two states that matters in our discussion.

Let us introduce a slight geometry perturbation to make the  $A_1$  and  $A_2$  sites nonequivalent. As an example, one may consider a slight pyramidalization at  $A_1$  as shown in 10.13. Three and four electron pairs around a given atom tend to make

that center planar and pyramidal, respectively. A<sub>1</sub> becomes a carbanion and A<sub>2</sub> a carbocation. Thus, Φ<sub>1</sub> is more stable than Φ<sub>1</sub><sup>0</sup>, that is,

$$E_1 < E_2 \quad (10.3)$$

where

$$\begin{aligned} E_1 &= \langle \Phi_1 | \hat{H} | \Phi_1 \rangle \\ E_2 &= \langle \Phi_2 | \hat{H} | \Phi_2 \rangle \end{aligned} \quad (10.4)$$

If the extent of the pyramidalization at A<sub>1</sub> is small, it is valid to use the following approximation

$$\langle \Phi_1 | \hat{H} | \Phi_2 \rangle = \langle \Phi_1^0 | \hat{H} | \Phi_2^0 \rangle = K_{12} \quad (10.5)$$

Therefore, with the condition that

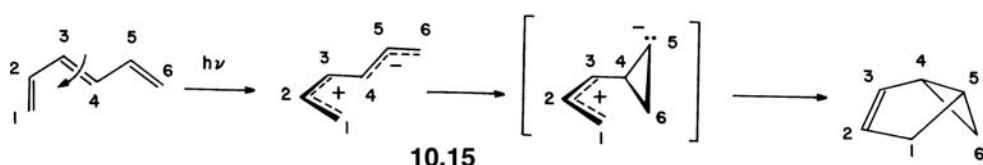
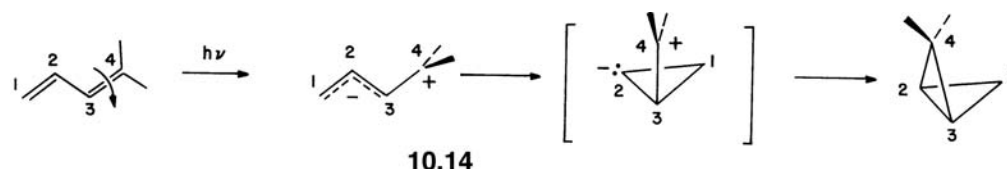
$$K_{12} \ll E_2 - E_1 \quad (10.6)$$

the state functions appropriate for 10.13 are given by

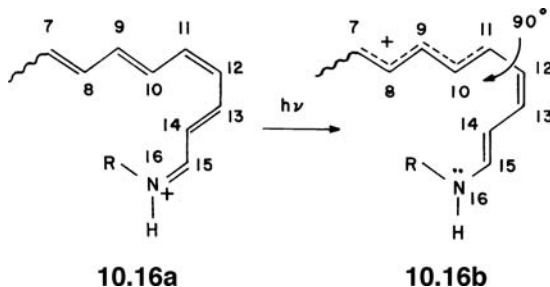
$$\begin{aligned} \Psi_1 &\cong \Phi_1 + \frac{K_{12}}{E_1 - E_2} \Phi_2 \\ \Psi_2 &\cong \Phi_2 + \frac{K_{12}}{E_2 - E_1} \Phi_1 \end{aligned} \quad (10.7)$$

Since K<sub>12</sub> is very small in a perpendicular structure, equation 10.7 is valid when the energy difference E<sub>2</sub> - E<sub>1</sub> is small, that is, when the extent of pyramidalization at A<sub>1</sub> is small. Now the state Ψ<sub>1</sub> is strongly zwitterionic since Φ<sub>2</sub> is only a small component. Namely, the electron density is concentrated on the pyramidal center A<sub>1</sub> and diminished on the planar center A<sub>2</sub>. Similarly, the state Ψ<sub>2</sub> shows zwitterionic character in which the electron density is concentrated on the planar center A<sub>2</sub>.

The above discussion shows that a small geometry perturbation can induce a strong charge polarization. This kind of phenomenon is generally referred to as a sudden polarization [11]. It has been postulated to occur in photochemical cyclization of conjugated dienes and trienes [13]. The stereospecificity observed in these reactions can be explained by a zwitterionic intermediate containing an allyl anion moiety which in turn undergoes a conrotatory ring closure to a substituted cyclopropyl carbanion. Finally, collapse of the zwitterion leads to a bicyclic product. As examples, 10.14 shows the photochemical conversion of a 1,3-butadiene to a



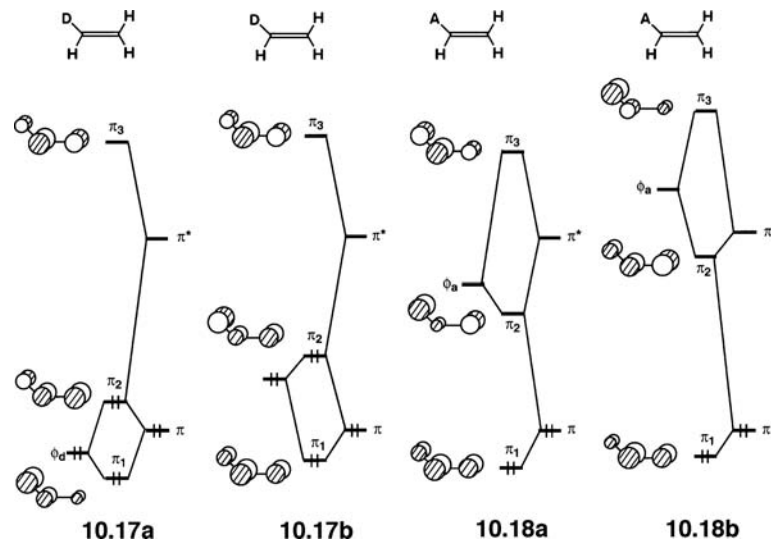
bicyclo[1.1.0]butane, and **10.15** that of a *cis,trans*-1,3,5-hexatriene to a bicyclo[3.1.0]hexene. In the above diene and triene, twisting of the C<sub>3</sub>—C<sub>4</sub> bonds generates the appropriate initial zwitterions. A similar charge polarization is thought to occur in retinal, **10.16a**. The primary excitation of the retinal skeleton [14] involves rotation



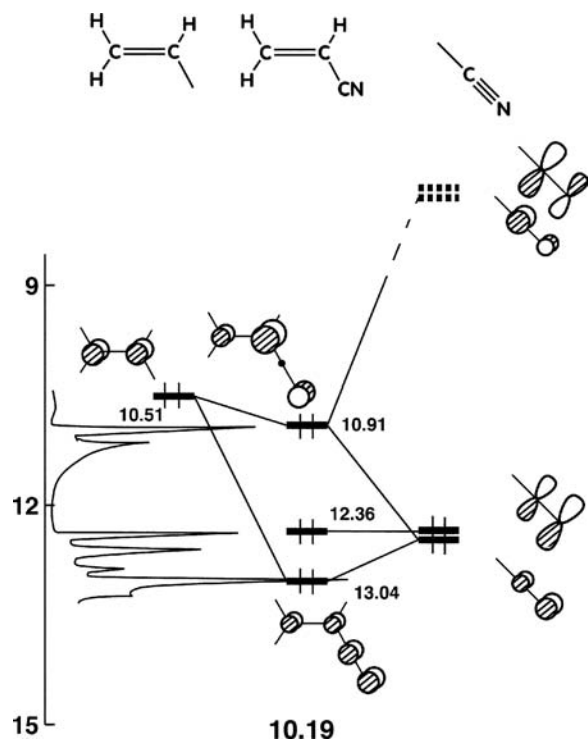
around the C<sub>11</sub>—C<sub>12</sub> bond leading to the all-trans form. At the halfway point of this rotation, the retinal skeleton is transferred into two pentadienylic moieties (i.e., the 7–11 and 12–16 fragments). Since these fragments are nonequivalent, charge polarization occurs in the excited state. Owing to the positive charge on the protonated imino group, a negative charge moves toward the 12–16 fragment (which therefore becomes neutral), and a positive charge toward the 7–11 fragment. This is shown in **10.16b**. The net result of excitation is the transformation of a photon into an electrical signal, as the positive charge migrates from the 12–16 to the 7–11 fragment. This sudden polarization is considered to be crucial for the mechanism of vision [11,15]. One might also consider the situation in the 12 electron aminoborane, H<sub>2</sub>N—BH<sub>2</sub>. The ground state is a flat,  $C_{2v}$ , structure which is consistent with strong N—B  $\pi$  bonding. Rotation around the B—N bond is accompanied by pyramidalization at the more electronegative NH<sub>2</sub> center [16]. The zwitterionic transition state for rotation, analogous to  $\Psi_1$ , now lies much lower in energy than the twisted triplet state because of the electronegativity stabilization for the lone pair on the N atom.

### 10.3.2 Substituent Effects [17]

Consider now an alkene with a  $\pi$  donor D or a  $\pi$  acceptor A on the C=C bond as shown in **10.17** and **10.18**, respectively. As usual, the C=C bond is described by the  $\pi$  and

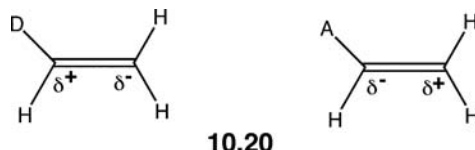


$\pi^*$  orbitals. For simplicity, we describe a  $\pi$  donor by a filled orbital  $\phi_d$  and a  $\pi$  acceptor by an empty orbital  $\phi_a$ . **10.17a** represents a case in which  $\phi_d$  lies below  $\pi$ . In **10.17b**,  $\phi_d$  lies above  $\pi$  but much closer to  $\pi$  than  $\pi^*$ . **10.18a** shows a case in which  $\phi_a$  lies below  $\pi^*$  but much closer to  $\pi^*$  than  $\pi$ . Finally, **10.18b** represents a case in which  $\phi_a$  lies above  $\pi^*$ . By employing the rules of orbital mixing in Chapter 3, the  $\pi_1$ ,  $\pi_2$ , and  $\pi_3$  MOs of **10.17a–10.18b** can be easily derived. Summarized also in **10.17a–10.18b** are the relative weights of these MOs on the vinyl carbon atoms and donor or acceptor substituent (represented by a single  $\rho$  atomic orbital for simplicity) of these MOs. It is noted from **10.17a** and **10.17b** that, for a  $\pi$ -donor substituted alkene, the HOMO has less weight but the LUMO has more weight on the carbon bearing the substituent. Thus, electron density is built up on the  $\beta$  carbon. In contrast, **10.18a** and **10.18b** show that, for a  $\pi$ -acceptor substituted alkene, the HOMO has more weight but the LUMO has less weight on the carbon bearing the substituent. In other words, electron density is now removed from the  $\beta$  carbon. To be sure, the situations displayed in **10.17a–10.18b** are quite idealized. The PE spectrum [9] and corresponding interaction diagram for acrylonitrile are shown in **10.19**. The  $\pi$ -acceptor cyano group contains not only a pair of empty  $\pi^*$

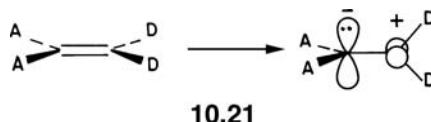


orbitals, but also a pair of filled  $\pi$  orbitals. As shown by **10.19**, the MO analogs to  $\pi_1$  in **10.18a** (or **10.18b**) is stabilized by only about 0.4 eV. This is relative to the ionization potential in ethylene itself. A significant portion of the stabilization is “carried” by the filled CN  $\pi$  MO. It is stabilized by 1.28 eV compared to the in-plane CN  $\pi$  MO (which to a first approximation is unperturbed by the vinyl group). But these are details that can easily be built into the basic structures offered by **10.17a–10.18b**. In all cases, the resulting form of the orbitals resembles that of the allyl system. For the donor-substituted cases the  $\pi_2$ , “nonbonding,” level is occupied and, like the allyl anion, electron density is concentrated on the donor and  $\beta$ -vinyl carbon atoms. The opposite occurs with an acceptor-substituted alkene which is analogous to an allyl cation. Consequently, the charge densities of the C=C bonds in

$\pi$ -donor and  $\pi$ -acceptor substituted alkenes are expected to polarize as shown in **10.20**, a result consistent with  $^{13}\text{C}$  NMR chemical shifts in substituted



alkenes [18]. Notice that the increase or decrease of electron density at the  $\beta$ -vinyl carbon is not due solely to the donation or acceptance of electron density by an electron donor or acceptor, respectively, which would be given by “electron pushing” arguments developed from resonance structure perspective. By second-order orbital mixing,  $\pi^*$  mixes into  $\pi$  to polarize the charge distribution in  $\pi_1$  (and  $\pi_2$ ). The charge polarization effect of a  $\pi$  donor is opposite to that of a  $\pi$  acceptor. Thus, when both  $\pi$  donors and  $\pi$  acceptors are substituted on opposite ends of the C=C double bond, the charge distribution of the C=C bond is strongly polarized. Thus  $\pi$  bonding is weak in the planar structure of **10.21**, while the zwitterionic



state of the perpendicular structure is stabilized significantly by the  $\pi$  acceptors at the anion site and by the  $\pi$  donors at the cation site. For the perpendicular structure of **10.21**, the zwitterionic state becomes more stable than its alternative, diradical state. Consequently, the rotational barrier around the C=C bond is substantially reduced. For example, the C=C rotational barrier of **10.21** is less than 8 kcal/mol for A =  $-\text{COCH}_3$  and D =  $-\text{N}(\text{CH}_3)_2$  [19].

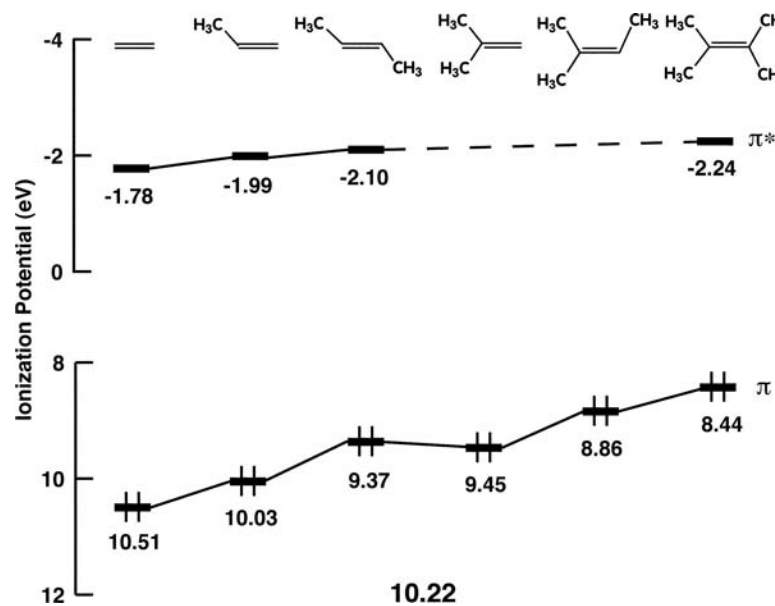
The strength of  $\pi$  acceptors and donors is an important concern in organic chemistry. Table 10.1 lists some  $\pi$  ionization potentials for three representative series of substituted olefins. The ionization potential of halogen-substituted olefins decreases; the  $\pi$  orbital is pushed to higher energy, since halogens with their lone pairs are good  $\pi$  donors. An upper-row halogen X has a shorter C–X bond and has a larger overlap between the  $\pi$  orbital of C=C and the  $p_\pi$  orbital of X, which is expected to push the  $\pi$  level to a larger extent. However, the ionization potential decreases as the halogen X is changed from Cl to Br to I. This is due to electronegativity perturbation. Namely, an upper-row halogen is more electronegative and hence lowers the  $\pi$  level, thereby decreasing the ionization potential.

A methoxy substituent (in the middle column of Table 10.1) is an excellent  $\pi$  donor. The  $\pi$  ionization potential decreases by 1.46 eV relative to ethylene. It can be seen from Figure 10.1, for example, that the  $\pi_x$  and  $\pi_y$  groups of  $\text{CH}_3$  can

**TABLE 10.1** Ionization Potentials (eV) for the  $\pi$ MO in Some Substituted Olefins of the Form X–CH=CH<sub>2</sub> [9,20]

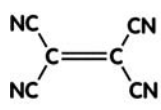
X	$\pi$	X	$\pi$	X	$\pi$
H	10.51	OMe	9.05	CH <sub>2</sub> F	10.56
Cl	10.2	CH <sub>3</sub>	10.03	CH <sub>2</sub> Cl	10.34
Br	9.9	SiMe <sub>3</sub>	9.86	CH <sub>2</sub> Br	10.18
I	9.1	GeEt <sub>3</sub>	9.2	Si(OMe) <sub>3</sub>	11.0
		SnBu <sub>3</sub>	8.6	SiCl <sub>3</sub>	10.7

act as  $\pi$  donors. We discuss this aspect in greater detail in Section 10.5. For now note that this is consistent with the  $\pi$  ionization potential being lowered by 0.47 eV on going from ethylene to propene. This destabilization of the  $\pi$  orbital is quite constant for the series of methyl-substituted olefins in **10.22** [9,21]. Alkyl substitution greatly enhances the susceptibility of a double bond toward

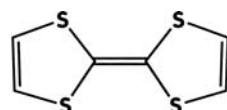


electrophilic attack, which is understandable because it raises the HOMO level. However, the thermodynamic stability of an olefin is also increased with alkyl substitution [22]. Thus in this example, the stability of the HOMO does not coincide with that of the total energy. Analysis of the  $\pi$ -type orbital interactions in alkyl-substituted olefins indicates that the net result of conjugation between double bond and methylene units is destabilizing, as is that between two methylene units (see Figure 10.2a), but the former is less destabilizing [22]. The energies associated with unoccupied MOs can be experimentally measured by electron transmission spectroscopy (ETS). The ETS values are associated with the  $\pi^*$  orbitals of ethylene and methyl-substituted ethylenes are shown in **10.22** [23]. The filled  $\text{CH}_3 \sigma_\pi$  orbital also destabilizes  $\pi^*$ , but to a lesser degree, primarily because the  $\sigma_\pi - \pi^*$  energy gap is much less than the  $\sigma_\pi - \pi$  gap.

It is clear from the middle column in Table 10.1 that for the AR<sub>3</sub> (A=Si, Ge, Sn) series the strength of the  $\pi$  donors increases dramatically on going down the periodic table; the SnBu<sub>3</sub> group is a very strong  $\pi$  donor indeed. We reserve a more detailed discussion of this phenomena, as well as, what occurs in the right-hand column of the table for Section 10.5. Nevertheless, it is important to note the effect of the C—A  $\sigma$ -bond (A=Si, Ge, Sn). Owing to the difference in the electronegativities of C and A, this bond is polarized as C<sup>δ-</sup>—A<sup>δ+</sup>. The partial negative charge on the carbon bearing the AR<sub>3</sub> substituent has the effect of raising the  $\pi$  level and hence lowering the ionization potential. One compound with an extraordinarily low-lying  $\pi^*$  MO is tetracyanoethylene, **10.23a**, (TCNE). The  $\pi^*$  orbital was measured to lie at +2.88 eV and the  $\pi$  orbital at 11.79 eV [24]. A very destabilized  $\pi$  orbital exists in tetrathiafulvalene, **10.23b** (TTF). Its  $\pi$  ionization potential has been measured at 6.83 eV [25]. TTF is then a superb electron donor and TCNE is an excellent electron acceptor. Mixing them together creates a charge transfer salt, TTF<sup>δ+</sup>TCNE<sup>δ-</sup>, in which there occurs a partial



10.23a

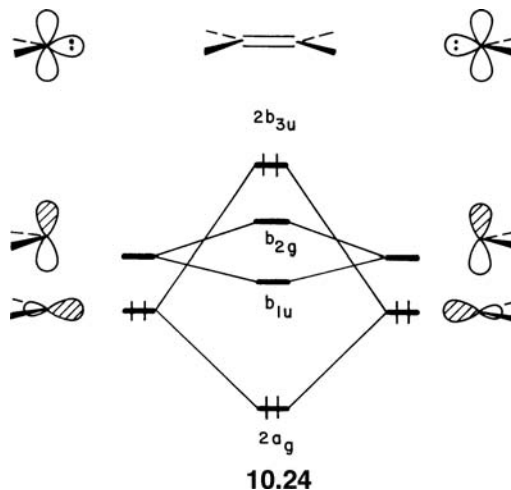


10.23b

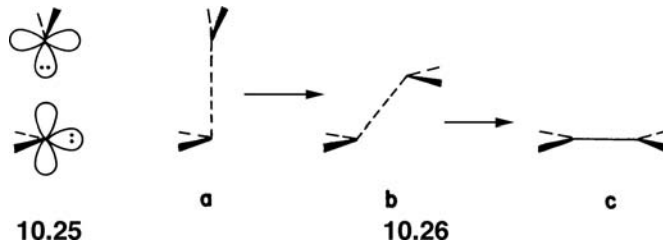
charge transfer from the  $\pi$  orbital of TTF to the  $\pi^*$  level of TCNE. The  $\text{TTF}^{\delta+}$  and  $\text{TCNE}^{\delta-}$  ions form stacks in the solid state, and this forms the basis of organic conducting materials, which is more fully covered in Chapter 13.

### 10.3.3 Dimerization and Pyramidalization of $\text{AH}_2$

Ethylene,  $\text{CH}_2=\text{CH}_2$ , may be obtained as a dimerization product of singlet carbene,  $\text{CH}_2$ . The least-motion approach [26], which maintains  $D_{2h}$  symmetry in this reaction, is symmetry forbidden as shown by the MO correlation-interaction diagram in 10.24. The least-motion approach is energetically unfavorable since it

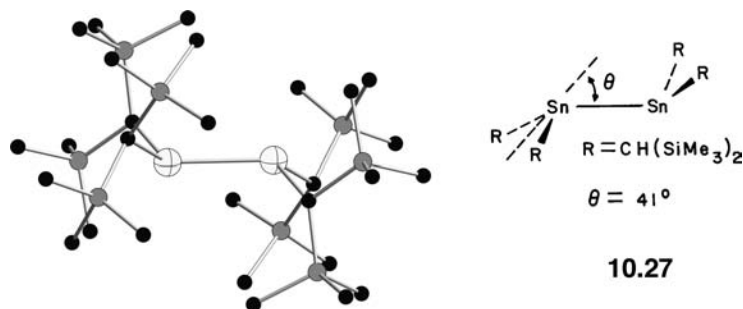


10.24



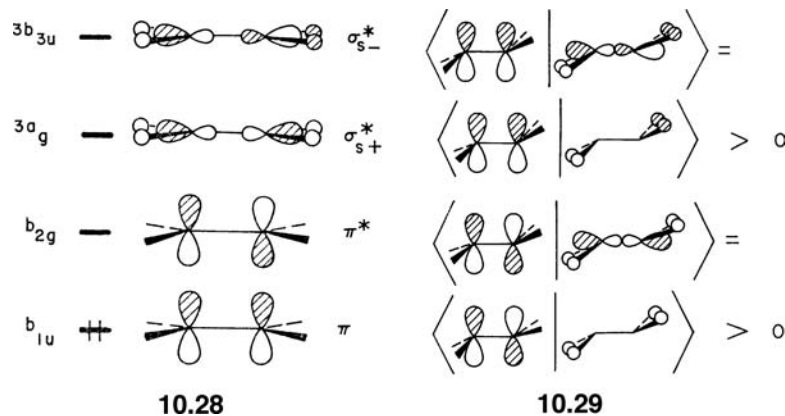
maximizes the HOMO–HOMO interaction (a two-orbital–four-electron destabilization) and minimizes the HOMO–LUMO interactions (a two-orbital–two-electron stabilization). Two  $\text{CH}_2$  units can approach in a more energetically favorable way such that the HOMO of one  $\text{CH}_2$  unit is directed toward the LUMO of the other as shown in 10.25. As the dimerization progresses, two  $\text{CH}_2$  units gradually tilt away from this perpendicular arrangement to become planar  $\text{CH}_2=\text{CH}_2$ . This is

illustrated in **10.26**. As the atomic number of A increases in 12-electron A<sub>2</sub>H<sub>4</sub> systems, the stability of the anti, C<sub>2h</sub> structure, **10.8c** (**10.26a**), increases relative to that of the planar, D<sub>2h</sub> structure, **10.8a** (**10.26c**). Thus, C<sub>2</sub>H<sub>4</sub> and Si<sub>2</sub>H<sub>4</sub> are planar while Ge<sub>2</sub>H<sub>4</sub> and Sn<sub>2</sub>H<sub>4</sub> have the anti structure [27,28]. Although Si<sub>2</sub>H<sub>4</sub> is planar, the potential energy surface for the planar to anti distortion is calculated to be very soft. Experimentally, Sn<sub>2</sub>R<sub>4</sub> [R=—CH(SiMe<sub>3</sub>)<sub>2</sub>] is found to have the anti structure shown in **10.27** [27]. In addition, this geometry is also found for

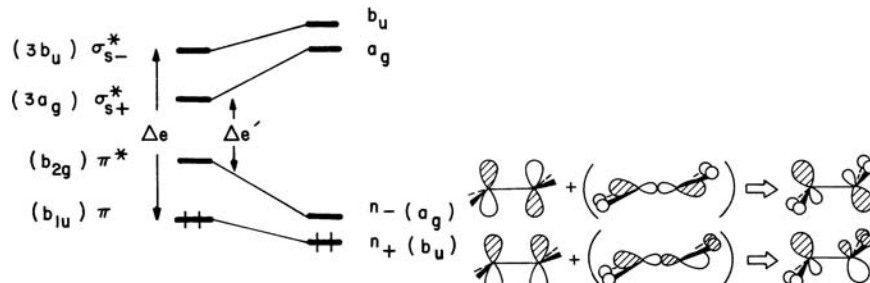
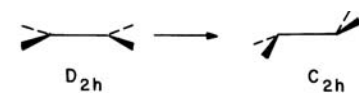


isoelectronic species such as Ge<sub>2</sub>P<sub>4</sub><sup>8-</sup> and Ge<sub>2</sub>As<sub>4</sub><sup>8-</sup> present in a crystalline environment with Ba<sup>2+</sup> counterions [29]. A number of 12-electron A<sub>2</sub>R<sub>4</sub> structures have been obtained [28]. For A=Si, the pyramidal angle,  $\theta$ , is normally 0° but with sterically bulky R groups it can be as much as 10°. For A=Ge,  $\theta$ =12–36° and in A=Sn,  $\theta$ =21–64° [28].

We use two different approaches to view this interesting problem. The interested reader should explore alternative explanations by Trinquier and Malrieu [30] that also have strong merits with which to view these interesting molecules. Our first approach uses an argument similar to that employed in Section 9.3 to view the pyramidalization of eight-electron AH<sub>3</sub> systems. The MOs of A<sub>2</sub>H<sub>4</sub> that result from the in-phase and out-of-phase combinations of  $\sigma_s^*$  on each AH<sub>2</sub> (i.e.,  $\sigma_{s+}^*$  and  $\sigma_{s-}^*$ ), omitted in Figure 10.4 for simplicity, are shown in **10.28** together with the  $\pi$  and  $\pi^*$  levels. Let us consider how  $\pi$  and  $\pi^*$  of planar A<sub>2</sub>H<sub>4</sub> mix with the  $\sigma_{s+}^*$  and  $\sigma_{s-}^*$  levels during the planar to anti distortion. In the anti structure, the overlap between  $\pi$  and  $\sigma_{s-}^*$  (both are of  $b_u$  symmetry) and that between  $\pi^*$  and  $\sigma_{s+}^*$  (both are of  $a_g$  symmetry) are nonzero, see **10.29**.



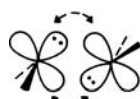
Consequently, orbital mixing occurs between  $\pi$  and  $\sigma_{s-}^*$  and between  $\pi^*$  and  $\sigma_{s+}^*$  on pyramidalization. An orbital correlation diagram is shown in **10.30**, where the  $n_+$  and  $n_-$  orbitals of anti A<sub>2</sub>H<sub>4</sub> are derived as in **10.31**. Owing to this orbital mixing,



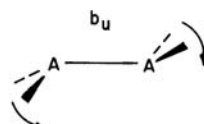
10.31

the  $\pi$  and  $\pi^*$  levels are lowered upon the planar to anti distortion. From second-order perturbation theory the stabilization of  $\pi$  is inversely proportional to the energy gap  $\Delta e$ , and that of  $\pi^*$  to  $\Delta e'$ . With an increase in the atomic number of A, the orbitals of A become more diffuse. Thus  $\sigma$  antibonding in A—H is reduced in  $\sigma_{s+}^*$  and  $\sigma_{s-}^*$ , so these levels are lowered in energy. In addition, the  $\pi$  and  $\pi^*$  levels are raised in energy because of the electronegativity of A decreases. Most importantly, the energy gap between  $\pi$  and  $\pi^*$  becomes quite small, since  $\pi$ -overlap in A—A is reduced by increasing diffuseness of the  $p$  atomic orbitals on A. The planar to anti distortion in a 12-electron  $A_2H_4$  system is therefore a second-order Jahn–Teller distortion, which becomes increasingly stronger upon going down a column in the periodic table.

The electronic structure of anti  $A_2H_4$  may also be described in terms of the dimerization of two  $AH_2$  units as shown in 10.26 and 10.32. The structure of 10.27 may



10.32



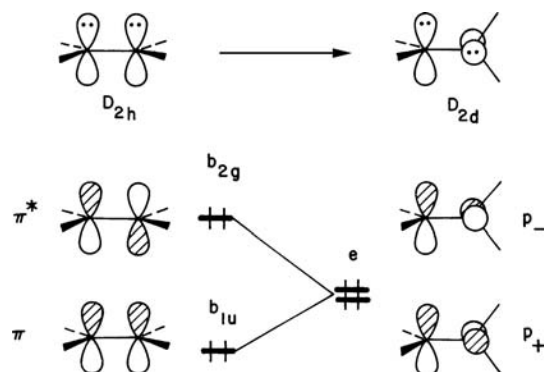
10.33

then be regarded as a stannylenes caught in the act of dimerization. When  $AH_2$  units cannot achieve strong  $\pi$  bonding because of a long A—A bond, they adopt an anti structure so as to maximize their mutual HOMO–LUMO interactions. It is noted from 10.30 that the HOMO–LUMO gap becomes smaller upon  $D_{2h} \rightarrow C_{2h}$  distortion, and thus the corresponding second-order Jahn–Teller instability should actually increase. In the  $C_{2h}$  point group,  $\Gamma_{a_g} \times \Gamma_{b_u} = \Gamma_{b_u}$  so that a distortion mode of  $b_u$  symmetry such as 10.33 would bring 10.26b toward 10.26a. There must be a whole range of geometries from 10.26b to 10.26a for 12-electron  $A_2L_4$  systems of third and fourth row A atoms.

#### 10.4 14-ELECTRON $AH_2BH_2$ SYSTEMS

With 14 valence electrons, the HOMO of planar  $AH_2AH_2$  is the  $\pi^*$  level in Figure 10.4. On rotation around the A—A bond overlap between the  $p$  AOs

is decreased so  $\pi^*$  is lowered in energy as shown in 10.34. Furthermore, this stabilization is greater than the amount of energy that the  $\pi$  level is destabilized.



10.34

The total stabilization decreases as the A—A  $\pi$  overlap decreases. The HOMO of perpendicular AH<sub>2</sub>AH<sub>2</sub> is further stabilized by pyramidalization at each center A. This reduces the  $D_{2d}$  symmetry of the perpendicular geometry to  $C_2$  in the resulting gauche structure. The orbital correlation diagram in Figure 10.7 reveals that  $\sigma_{s+}^*$  mixes into  $p_+$  to give  $n_+$ , and  $\sigma_{s-}^*$  mixes into  $p_-$  to give  $n_-$ . This has precisely the same features as the pyramidalization of A<sub>2</sub>H<sub>4</sub> to give the anti,  $C_{2h}$  structure in 10.30.

The relative stability of the gauche and anti conformations in AH<sub>2</sub>AH<sub>2</sub> may be examined in terms of the interactions leading to the generation of their HOMOs. As far as each center A is concerned, a 14-electron AH<sub>2</sub>—AH<sub>2</sub> molecule can be regarded as an 8-electron AH<sub>2</sub>—L (or L—AH<sub>2</sub>) derivative. The HOMO of AH<sub>2</sub>L is the nonbonding orbital  $n_\sigma$ , and that of anti or gauche AH<sub>2</sub>AH<sub>2</sub> is mainly composed of  $n_\sigma$  from each center A. The  $n_\sigma$  and  $\pi_{AH_2}^*$  orbitals of each AH<sub>2</sub> unit are arranged in anti

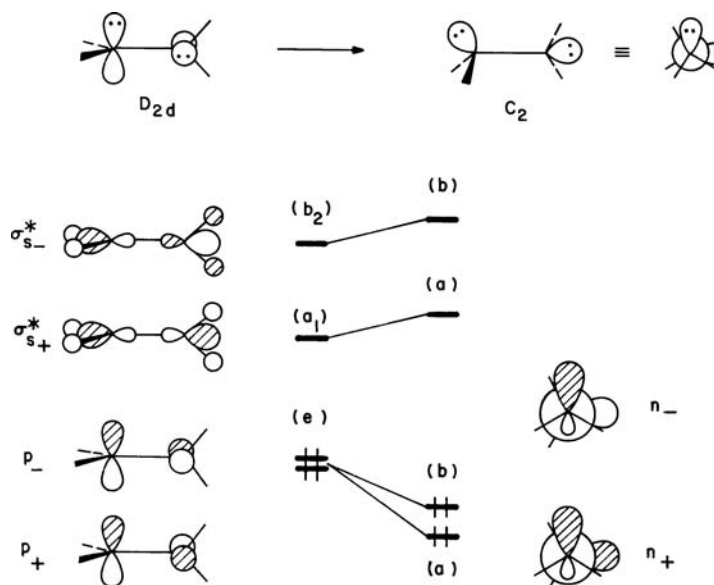
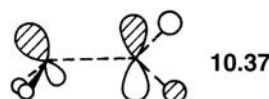
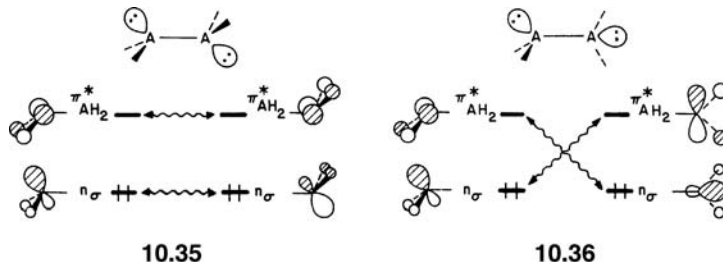


FIGURE 10.7

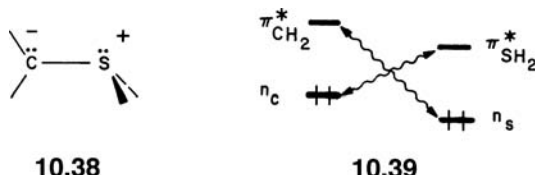
Correlation of the MO levels of bisected and gauche A<sub>2</sub>H<sub>4</sub>.

and gauche conformations in **10.35** and **10.36**, respectively. The overlap between the two  $n_{\sigma}$  levels is substantial in the anti conformation, but essentially nonexistent



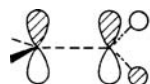
in the gauche conformation. Therefore, the destabilizing interaction between the two  $n_{\sigma}$  orbitals is negligible in the gauche geometry. Further, the gauche conformation provides a nonzero overlap between the  $n_{\sigma}$  and  $\pi_{\text{AH}_2}^*$  orbitals, thereby leading to the  $(n_{\sigma} - \pi_{\text{AH}_2}^*)$  stabilizing interaction, **10.37**. Both effects lead to the preference of the gauche conformation over the anti conformation in a 14-electron  $\text{AH}_2\text{AH}_2$  system such as hydrazine,  $\text{NH}_2\text{NH}_2$ . If the A—A distance of  $\text{AH}_2\text{AH}_2$  is large, as in diphosphine,  $\text{PH}_2\text{PH}_2$ , then the interaction between the two  $n_{\sigma}$  orbitals is weak even in the anti conformation so that the energetic variation of the HOMO is not an important factor governing the conformational preference. In such a case, the anti conformation becomes comparable in energy to, or may even become more stable than, the gauche conformation [31,32]. Be aware that we have conveniently singled out the  $(n_{\sigma} - \pi_{\text{AH}_2}^*)$  interaction as stabilizing the gauche conformation. The A—H bonding counterpart,  $\pi_{\text{AH}_2}$ , will also interact with  $n_{\sigma}$ . This is a two orbital-four electron destabilizing interaction which is maximized at the gauche geometry and minimized in the anti structure. Therefore, it does not cost much energy to rotate from one gauche structure to another by way of the anti conformation. On the other hand, rotation through a syn geometry will require a far greater activation energy [31]. In the syn geometry the four A—H bonds eclipse each other, and the two filled  $n_{\sigma}$  orbitals maximize their overlap at this geometry.

A sulfonium ylide  $\text{H}_2\text{S}^+ - \text{CH}_2^-$ , **10.38**, is an example of a 14-electron  $\text{AH}_2\text{BH}_2$ - system. Since the valence orbitals of sulfur are more diffuse than those of carbon, the

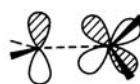


$\pi_{\text{SH}_2}^*$  level lies lower in energy than in  $\pi_{\text{CH}_2}^*$  level. Based solely upon the ionization potentials of sulfur and carbon, one might expect the nonbonding orbital of sulfur ( $n_s$ ) to lie higher in energy than that of carbon ( $n_c$ ). However, orbital levels are lowered and raised upon introducing formal positive and negative charges, respectively (Section 8.9). This effect raises the  $n_c$  level above  $n_s$  in sulfonium ylides [33] and consequently makes the carbanion center more nucleophilic than the sulfonium ion center. Therefore, the relative orderings of the  $n_s$ ,  $\pi_{\text{SH}_2}^*$ ,  $n_c$ , and  $\pi_{\text{CH}_2}^*$  may be approximated as in **10.39**. The energy gap between  $n_c$  and  $\pi_{\text{SH}_2}^*$  is small compared with that between  $n_s$  and  $\pi_{\text{CH}_2}^*$ . This gives rise to a strong  $(n_c - \pi_{\text{SH}_2}^*)$  interaction in the gauche conformation. The interaction is further enhanced if the carbanion center

becomes planar, because the  $\rho$  orbital of a planar carbanion center is closer in energy to  $\pi_{\text{SH}_2}^*$  and overlaps better with  $\pi_{\text{SH}_2}^*$  as shown in **10.40**. Thus a sulfonium ylide is



10.40



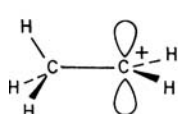
10.41

expected to have a planar carbanion center, thereby leading to a bisected structure **10.38** [33]. This structure is also found for aminophosphine ( $\text{PH}_2\text{NH}_2$ , isoelectronic with  $\text{H}_2\text{S}^+-\text{CH}_2^-$ ) derivatives which have a planar nitrogen center and exist in this bisected geometry [31,34].

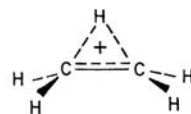
We have focused here upon the  $\pi_{\text{SH}_2}^*$  fragment orbital as a  $\pi$  acceptor. An empty  $d$  orbital on sulfur also plays the same role, as shown in **10.41**. Which is a more accurate picture, that in **10.40** or **10.41**? The symmetry of the ( $n_{\text{C}} - \pi_{\text{SH}_2}^*$ ) interaction is the same as that of the ( $n_{\text{C}} - d_{\text{S}}$ ) interaction, so there is no making a choice short of a calculation. Unfortunately, this does not provide a clear-cut answer, either. Inclusion of  $d$ -type functions is essential for a proper quantitative description of the structure and energetics of a molecule such as  $\text{H}_2\text{S}^+-\text{CH}_2^-$ . In such a calculation, however, electron density transferred to the  $d$ -type functions is not significant. In other words,  $d$ -type functions act as polarization functions to accurately tailor the wavefunctions but are not important in the customary sense of  $\rho_{\pi} - d_{\pi}$  bonding as depicted in **10.41**. We shall return to the question of  $d$  acceptor functions in Section 5 where some definitive experimental information exists and supports the thesis that  $d$  AOs simply are not used in these types of molecules.

## 10.5 AH<sub>3</sub>BH<sub>2</sub> SYSTEMS

A 12-electron system C<sub>2</sub>H<sub>5</sub><sup>+</sup> may adopt a classical structure **10.42** or a nonclassical one **10.43**. To probe the transition between the two possibilities, we first consider the

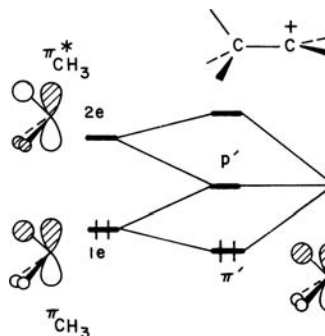


10.42

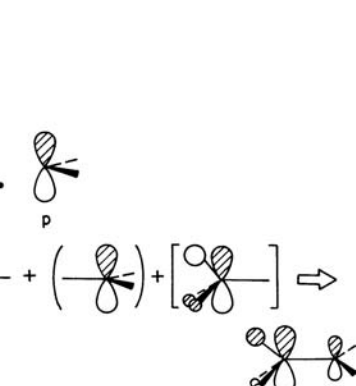


10.43

orbital interaction between the CH<sub>3</sub> and CH<sub>2</sub><sup>+</sup> units in **10.44**. The  $1a_1$  and  $1b_2$  orbitals of the CH<sub>2</sub><sup>+</sup> fragment will interact with  $1a_1$  and one component of  $1e$  on CH<sub>3</sub>, respectively, to form in-phase and out-of-phase combinations which are filled. The

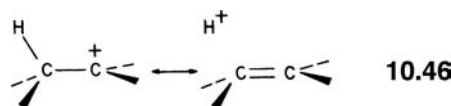


10.44

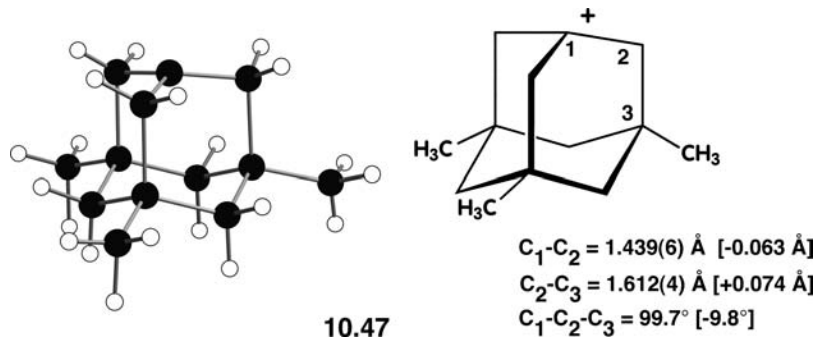


10.45

$2a_1$  level of  $\text{CH}_2^+$  will interact strongly with the  $2a_1$  level of  $\text{CH}_3$  to form a filled  $\sigma$  and empty  $\sigma^*$  MO. This pattern is like that found for  $\text{C}_2\text{H}_6$  (see Figure 10.1) and  $\text{C}_2\text{H}_4$  (see Figure 10.4). A difference from that in  $\text{C}_2\text{H}_6$  and  $\text{C}_2\text{H}_4$  comes from the interaction between the  $b_1$  fragment orbital (i.e., the  $p$  orbital on  $\text{CH}_2$ ,  $p_{\text{CH}_2}$ ) and the other components of  $1e$  and  $2e$  on  $\text{CH}_3$  ( $\pi_{\text{CH}_3}$  and  $\pi_{\text{CH}_3}^*$ , respectively) which overlap in a  $\pi$  manner (10.44). This is a typical three-orbital problem; according to the interaction diagram in 10.44, the  $\pi_{\text{CH}_3}$  level is perturbed by  $\pi_{\text{CH}_3}^*$  and  $p_{\text{CH}_2}$ . The resultant  $\pi_{\text{CH}_3}$  MO is stabilized by mixing the  $p_{\text{CH}_2}$  fragment orbital into it in a bonding way and there is a further polarization by the second-order mixing of some  $\pi_{\text{CH}_3}^*$  character into it, as shown in 10.45. Electron density from filled  $\pi_{\text{CH}_3}$  is transferred to the empty  $p_{\text{CH}_2}$  via  $\pi$  overlap. Since the  $\pi_{\text{CH}_3}$  orbital is C—H bonding, this interaction weakens the C—H bonds. To a lesser extent the in-phase mixing of  $\pi_{\text{CH}_3}^*$  with  $p_{\text{CH}_2}$  also increases C—C bonding and decreases C—H bonding. It is the C—H bond trans or periplanar to the carbocation  $p$  orbital that is preferentially weakened since the coefficients in  $\pi_{\text{CH}_3}$  and  $\pi_{\text{CH}_3}^*$  are largest for this hydrogen. This may also be seen quite clearly from the bond orbital descriptions of the  $\pi_{\text{CH}_3}$  and  $\pi_{\text{CH}_3}^*$  orbitals (see 9.6). Thus, the MO picture of 10.45 is analogous in nature to the concept of hyperconjugation, 10.46,



where the weakened C—H bond and C—C  $\pi$  bond formation is highlighted by the resonance structure on the right-hand side. The experimental “proof” for C—H hyperconjugation in carbocations (mostly on a kinetic or thermodynamic basis) is very well-known. What is also clear using 10.44 as a model is that C—C hyperconjugation is also possible and this will lead to the same structural distortions. In other words, the  $\pi_{\text{CH}_3}$  and  $\pi_{\text{CH}_3}^*$  fragment orbitals can be replaced by ones where the  $s$  AO on hydrogen has been replaced by an  $sp^3$  hybrid from the alkyl group that is added. A beautiful example of this exists in the experimental structure of 10.47 [35]. The numbers in brackets indicate how much the geometrical variables differ from

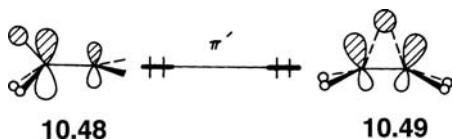


standard values compiled in a large database of closely related hydrocarbons. Therefore, the  $C_1-C_2$  bond lengths are  $0.063 \text{ \AA}$  shorter than normal as a consequence of increased  $\pi$  bonding at the expense of a  $0.074 \text{ \AA}$   $C_2-C_3$  bond lengthening. The  $C_1$  atom moves downward, causing the  $C_1-C_2-C_3$  bond angle to decrease from the normal tetrahedral value by  $9.8^\circ$ . This motion serves to increase the  $\pi$  overlap between the  $p$  AO on  $C_1$  and the  $C_2-C_3$   $\sigma$  bond.

Using the  $\pi_{\text{CH}_3}$  fragment orbital or its substituted analogs as a  $\pi$ -donor is common occurrence. Returning to the middle column of Table 10.1 notice that the ionization potential for the  $\pi$  orbital in propene is lowered by  $0.48 \text{ eV}$  relative to ethylene. This is due to  $\pi_{\text{CH}_3}$  mixing with and destabilizing  $\pi$ . From the composition of  $\pi_{\text{CH}_3}$  and  $\pi_{\text{CH}_3}^*$  in 10.44, it is understandable why the  $\pi$  ionization potential

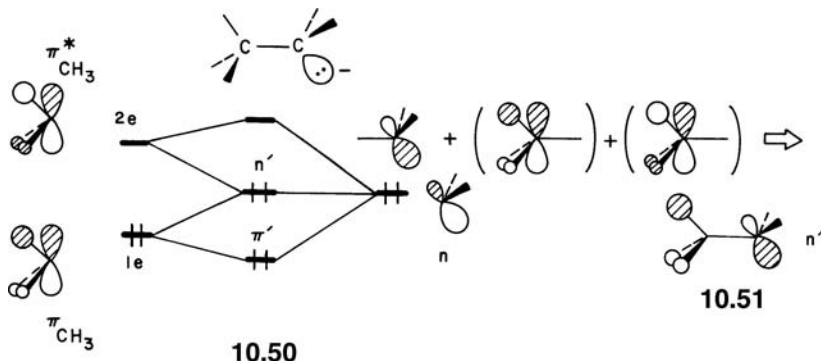
decreases moving down the column in Table 10.1. The central atom becomes more electropositive going from C to Si to Ge to Sn. Hence, the fragment orbital analogs to  $\pi_{\text{CH}_3}$  will move up in energy, becoming closer to the energy of the  $\pi$  orbital of the vinyl group. Furthermore, this electronegativity change causes  $\pi_{\text{CH}_3}$  to be more concentrated on the central atom so that its overlap with  $\pi$  becomes larger. The net effect is that moving down the column in the periodic table there will be a larger interaction between  $\pi_{\text{CH}_3}$  and  $\pi$  and so  $\pi$  will become more destabilized.

An electron-deficient group tends to migrate into an electron-rich region; we have seen this for  $\text{H}_3^+$  in Section 7.4C. So, the orbital correction in **10.45** facilitates the structural change which takes **10.42** to **10.43**. Along this distortion path, the  $\pi'$  level stays relatively constant in energy as shown in **10.48** to **10.49**. Alternatively, one may view the bridged, nonclassical structure as a protonated ethylene. As a



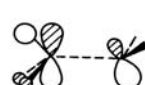
proton attacks ethylene, the empty s orbital of the proton will interact with the  $\pi$  orbital of ethylene. Maximum overlap occurs when the proton is centered over the carbon–carbon bond. This interaction directly leads to **10.49**. The stability difference in the  $\text{C}_2\text{H}_5^+$  isomers, **10.42** and **10.43**, is calculated to be very small even at a computational level beyond ab initio SCF MO calculations [36]. The orbital shape of **10.49** is topologically equivalent to the filled  $a'_1$  in the cyclic form of  $\text{H}_3^+$ . The  $\pi^*$  level of this protonated ethylene “complex” and the C–H antibonding analog of **10.49** are similar to the empty  $e'$  set in  $\text{H}_3^+$ . Exactly, the same pattern evolves from the transition state for 1,2-alkyl shifts in carbocations. The migrating alkyl group possesses a hybrid orbital that overlaps with the  $\pi$  level in the same way as the hydrogen s orbital does in **10.49**.

Consider an  $\text{AH}_3\text{BH}_2$  molecule with two more electrons. The interaction diagram for a 14-electron system,  $\text{CH}_3\text{CH}_2^-$ , is shown in **10.50** for the staggered structure. It is not

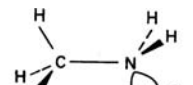


much different from that presented for  $\text{CH}_3\text{CH}_2^+$  in **10.44**. The major difference, of course, is that in the absence of a strong  $\pi$ -acceptor group we should expect that  $\text{RCH}_2^-$  assumes a pyramidal geometry. We now focus our interest on the middle level of this three-orbital pattern. There is still significant  $\pi$ -type overlap of  $n_\sigma$  with  $\pi_{\text{CH}_3}$  and  $\pi_{\text{CH}_3}^*$ . The form of  $\pi'$  is basically the same as that given in **10.44**. In the HOMO,  $n'$ , the  $n_\sigma$  orbital combines out-of-phase with  $\pi_{\text{CH}_3}$  but in-phase with  $\pi_{\text{CH}_3}^*$  so that methyl hydrogen character is enhanced at the expense of methyl carbon character (see **10.51**). As a result, the hydrogen atom in the C–H bond anti-periplanar to  $n_\sigma$  has more weight and hence a greater charge accumulation. Charge transfer from  $n$  to  $\pi_{\text{CH}_3}^*$ , arising from the  $(n_\sigma - \pi_{\text{CH}_3}^*)$  interaction, **10.52**, weakens

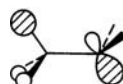
primarily the C—H bond antiperiplanar to  $n_{\sigma}$ . The same phenomenon is also observed in methylamine, **10.53**. The presence of a C—H bond antiperiplanar to a nitrogen nonbonding orbital  $n_{\sigma}$  is signaled by a characteristic infrared band in the C—H stretching region, known as the Bohlmann band [37].



10.52



10.53

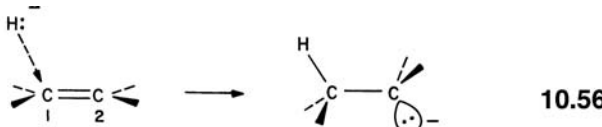


10.54

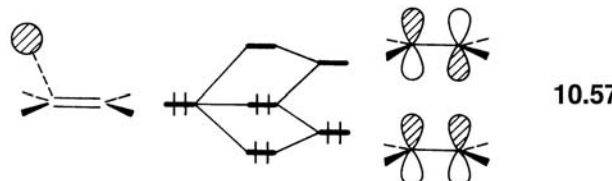


10.55

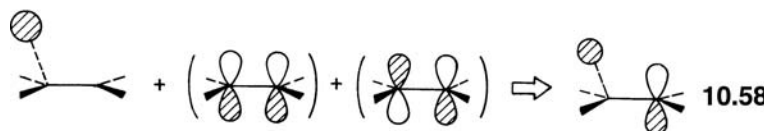
As in the case of staggered  $\text{CH}_3\text{CH}_2^-$ , the HOMO of an eclipsed structure, where the C—C bond has been rotated by  $60^\circ$ , can be easily derived. The HOMOs of the staggered and eclipsed structures are compared in **10.54** and **10.55**, respectively. The HOMO of  $\text{CH}_3\text{CH}_2^-$  lies lower in the staggered structure since it avoids antibonding between the two large orbital lobes present in **10.55**. Thus, the staggered geometry is energetically favored over the eclipsed one. In connection with nucleophilic addition reactions to multiple bonds, it is of interest to consider  $\text{CH}_3\text{CH}_2^-$  as derived from a nucleophilic addition of  $\text{H}^-$  to ethylene (**10.56**). The orbital interaction diagram in **10.57** leads to the HOMO as shown in **10.58**.



10.56



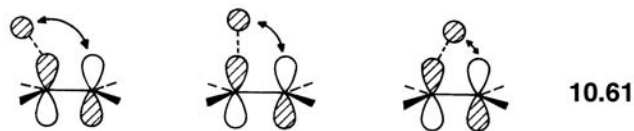
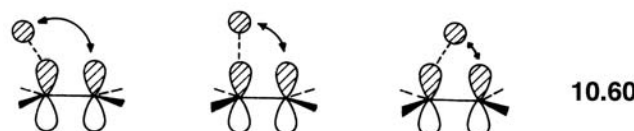
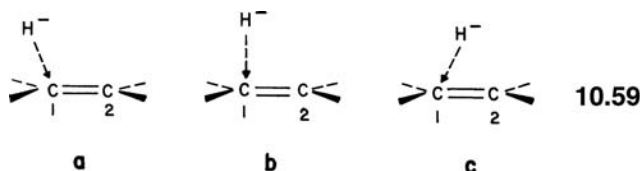
10.57



10.58

Note that p orbital character is reduced on  $\text{C}_1$  but enhanced on  $\text{C}_2$ , that is, carbanion character develops on  $\text{C}_2$  at the expense of weakening  $\pi$  bonding between  $\text{C}_1$  and  $\text{C}_2$ . The HOMO of **10.58** is further stabilized upon pyramidalization at the  $\text{C}_1$  and  $\text{C}_2$  centers. As expected from **10.54** and **10.55**, this distortion should favor an anti-periplanar arrangement of the developing lone pair on  $\text{C}_2$  to the newly forming bond at  $\text{C}_1$ . The hydride in **10.56** directly attacked ethylene  $\text{C}_1$ . It will make little sense to have the hydride attack between the  $\text{C}_1$ — $\text{C}_2$  bond as was predicted for the approach of an electrophile (e.g.,  $\text{H}^+$ ) toward ethylene. Such a path maximizes hydrogen s-ethylene  $\pi^*$  overlap which in the present case (see **10.57**) constitutes a two orbital-four electron destabilization. The stabilizing term, hydrogen s mixing with ethylene  $\pi^*$ , is zero by symmetry when the path of the hydride bisects the  $\text{C}_1$ — $\text{C}_2$  bond. There are still a large range of paths that can be considered allowing for the fact that the hydride should

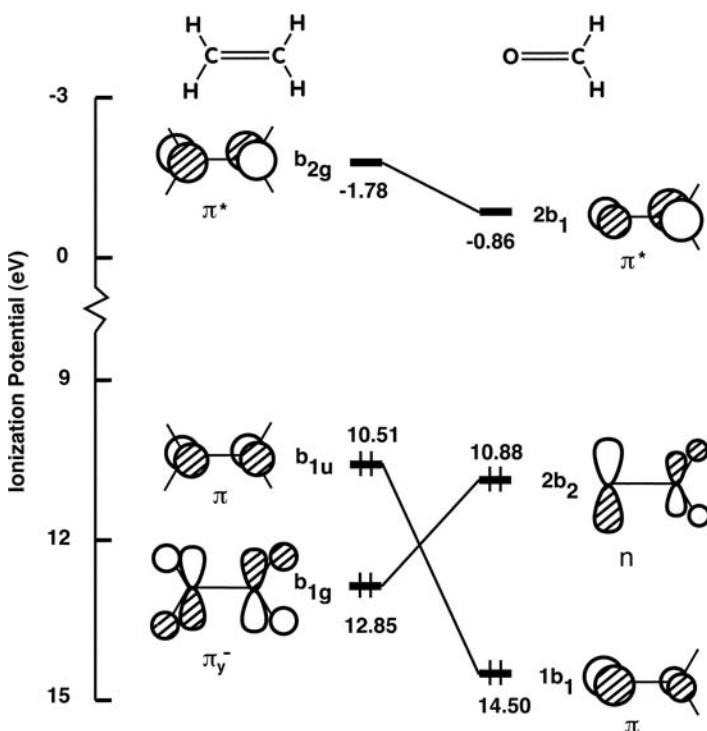
directly attack  $\text{C}_1$ . Three geometries are illustrated in 10.59. Again the favored path minimizes overlap between hydrogen s and ethylene  $\pi$  and maximizes overlap between hydrogen s and ethylene  $\pi^*$ . For the former case the three possibilities are shown



in 10.60. The smallest overlap occurs in geometry 10.59a where the overlap between hydrogen s and ethylene  $\pi$  (as indicated by the double-headed arrow in 10.60a) is minimized. Thus, the two orbital–four electron interaction is least destabilizing in 10.60a and most destabilizing in 10.60c. As shown in 10.61 the overlap between hydrogen s and ethylene  $\pi^*$  is maximized at 10.59a since now the 1,3-overlap between hydrogen s and the  $p$  atomic orbital at  $\text{C}_2$  is negative. Hence the two orbital–two electron interaction is most stabilizing in 10.61a and least stabilizing in 10.61c. Consequently, the hydride is expected to approach ethylene  $\text{C}_1$  at an oblique angle when the overlap between the reactants becomes appreciable. It can be easily seen that this is nothing more than a restatement of the linear versus bent  $\text{H}_3^-$  problem. For the same reasons that mandate a linear  $\text{H}_3^-$  geometry over a bent one, the  $\text{H}^- +$  ethylene system prefers to adopt an oblique  $\text{H}-\text{C}_1-\text{C}_2$  angle along the reaction path. Furthermore, the hydrogen s–ethylene  $\pi^*$  interaction results in charge transfer from the filled hydride s orbital to the empty ethylene  $\pi^*$  orbital. As shown in Section 9.3 this may be made more stabilizing by pyramidalization at  $\text{C}_1$  and  $\text{C}_2$ , a process that occurs as the reaction proceeds.

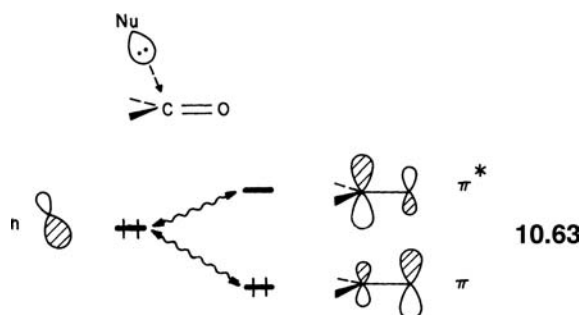
Now the reaction path and rationale for it can readily be extended to any reaction where a nucleophile attacks a  $\pi$  bond. The lone pair HOMO of a nucleophile ( $n$ ) plays the same role and is topologically analogous to the hydride s orbital. However, a nucleophile does not normally react with ethylene itself. The destabilization between  $n$  and ethylene  $\pi$  is not compensated by the stabilization between  $n$  and  $\pi^*$ . Perturbations that bring about the following two changes will render the nucleophilic attack more favorable: One is to provide a low-lying  $\pi$  HOMO and a  $\pi$  LUMO so as to decrease the energy gap between  $n$  and  $\pi$  LUMO and increase that between  $n$  and  $\pi$  HOMO. The other is to increase the orbital coefficient of the carbon under nucleophilic attack (i.e.,  $\text{C}_1$  in 10.56) in the  $\pi$  LUMO but decrease it in the  $\pi$  HOMO. Such an orbital polarization decreases the overlap between  $n$  and  $\pi$  HOMO. All of these modifications can be achieved either by having a  $\pi$ -acceptor substituent at  $\text{C}_2$  (see 10.18a) or by substituting a more electronegative atom for  $\text{C}_2$  in 10.56 (see Section 6.4). Consider the electronegativity perturbation going from  $\text{CH}_2=\text{CH}_2$  to  $\text{CH}_2=\text{O}$ . With reference back to equations 6.11 and 6.12 for the topologically equivalent  $\text{C}_2^{2-}$  to CO transformation, the  $e^{(1)}$  terms for  $\pi$  and  $\pi^*$  are both negative (stabilizing). On the other hand, the  $e^{(2)}$  for  $\pi$  is also negative but that

for  $\pi^*$  is positive. So, the  $\pi$  orbital is stabilized more than that for  $\pi^*$ . This is strikingly documented in the PE [9] and ETS [23] results for  $\text{CH}_2=\text{CH}_2$  and  $\text{CH}_2=\text{O}$ . As shown in 10.62, the  $\pi$  orbital is stabilized by 4 eV on going from  $\text{CH}_2=\text{CH}_2$  to  $\text{CH}_2=\text{O}$ . The  $\pi^*$  orbital, however, is stabilized by only 0.9 eV. Notice that the HOMO for  $\text{CH}_2=\text{O}$  is not the  $\pi$  MO. Two hydrogens are removed on going from a



10.62

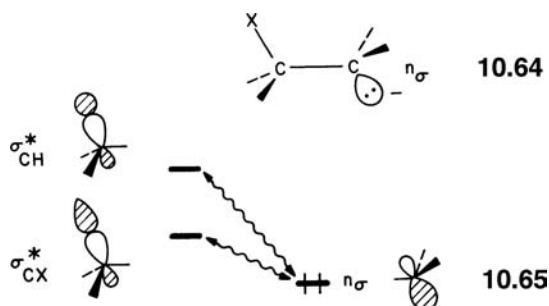
$\text{CH}_2$  group to an O atom. While this electronegativity perturbation is indeed stabilizing,  $\sigma$  bonding between C and H is lost. Thus, the  $b_{1g}$  C—H  $\sigma$  bonding combination is destabilized and becomes an orbital that is primarily nonbonding and localized on the O atom. As shown in 10.62 (and 6.8) going from  $\text{CH}_2=\text{CH}_2$  to  $\text{CH}_2=\text{O}$  not only lowers  $\pi$  and  $\pi^*$  but also polarizes these orbitals so that  $\pi$  is concentrated at the more electronegative oxygen atom and  $\pi^*$  is concentrated on carbon. Consequently, the stabilizing ( $n - \pi^*$ ) and destabilizing ( $n - \pi$ ) interactions are increased and decreased, respectively, compared to ethylene and the resultant reaction path will take into account these two interactions as illustrated in 10.63. Notice that the nucleophile still prefers an oblique approach and the carbon center



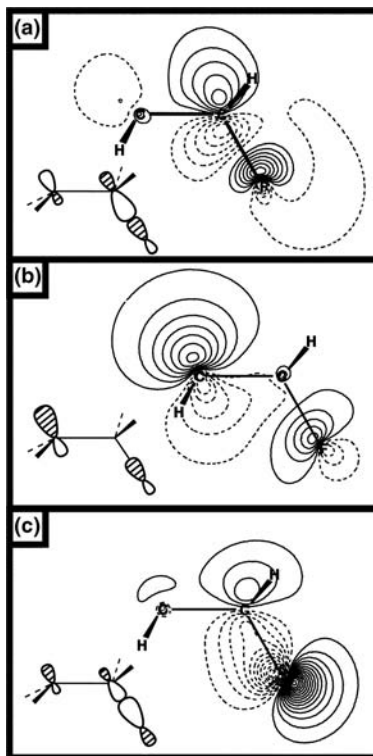
10.63

will pyramidalize for the same reasons as discussed for the ethylene case [38]. A crystallographic mapping of the reaction path for nucleophilic attack on carbonyl containing compounds has been provided [39,40]. There exist a large number of X-ray structures where a nucleophilic center is forced to be in close proximity to a carbonyl group. This may occur as a result of intra- and/or intermolecular contacts. The geometry around the nucleophile and carbonyl group is then adjusted to correspond to the energetically most favorable situation. Consequently, these X-ray structures effectively chart the path of least energy for the reaction. The features of the reaction that we have discussed are experimentally found; namely, as the nucleophile begins to appreciably interact with the carbonyl carbon it does so with an oblique Nu—C—O angle as shown in **10.63**. Furthermore, the carbonyl carbon center becomes progressively more pyramidal as the Nu—C distance decreases [39,40]. Cyclic amino-ketones of various ring sizes were also used to provide another experimental model of this reaction. There is a transannular interaction between the lone pair of the amino group and the carbonyl carbon of the ketone in these compounds that can be gauged by the geometry determined by X-ray diffraction. What is novel here is that the PE spectra can also be obtained so that an experimental plot of the orbital energies (via Koopmans' theorem) versus the C···N distance can be made [41]. As anticipated by the three-orbital problem outlined in **10.63**, the  $\pi$  orbital is stabilized as the C···N distance decreases and the  $n$  orbital is destabilized. Most importantly it is not destabilized greater than, or to the same extent as,  $\pi$  is stabilized since  $n$  is also stabilized by  $\pi^*$ .

Let us now return to the CH<sub>3</sub>CH<sub>2</sub><sup>-</sup> system. Of the three methyl hydrogens in CH<sub>3</sub>CH<sub>2</sub><sup>-</sup>, the one in the C—H bond antiperiplanar to  $n_\sigma$  carries the highest charge density as already pointed out (see **10.54**). Therefore using electronegativity perturbation theory arguments, this hydrogen is the preferred site for substitution by an electronegative ligand X, and an anti structure **10.64** is expected for XCH<sub>2</sub>CH<sub>2</sub><sup>-</sup>. Furthermore, due to the electronegativity perturbation provided by



X, the  $\sigma^*_{CX}$  orbital is found lower in energy than  $\sigma^*_{CH}$ . Therefore,  $\sigma^*_{CX}$  is closer in energy to  $n_\sigma$  as indicated in **10.65**. The  $\sigma^*_{CX}$  orbital is also more concentrated at carbon than is  $\sigma^*_{CH}$ . This is again due to electronegativity differences. Consequently, the overlap of  $\sigma^*_{CX}$  with  $n_\sigma$  is expected to be larger than that between  $\sigma^*_{CH}$  and  $n_\sigma$ . Thus, both the energy gap and overlap factors favor the ( $n_\sigma - \sigma^*_{CX}$ ) interaction over ( $n_\sigma - \sigma^*_{CH}$ ). The  $n_\sigma - \sigma^*_{CX}$  interaction is a stabilizing two orbital–two electron one. The  $n_\sigma$  orbital also combines with  $\sigma_{CX}$  or  $\sigma_{CH}$  depending upon the conformation. This is a four electron–two orbital destabilizing interaction. The reader may easily verify from electronegativity reasons that the ( $n_\sigma - \sigma_{CX}$ ) interaction is smaller and less destabilizing than the ( $n_\sigma - \sigma_{CH}$ ) one. The anti structure is again predicted to be the more stable conformation. Of course what

**FIGURE 10.8**

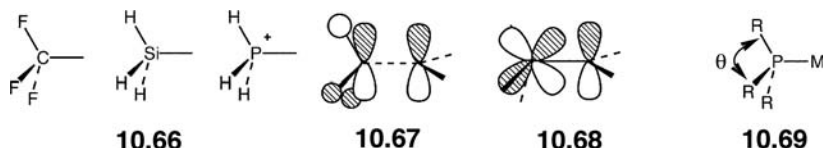
Contour plots of the three-orbital combination in the 2-fluoroethyl carbanion. These are ab initio calculations at the 3-21G level.

we really have here is a classic three-orbital picture with  $\sigma^*_{CX}$ ,  $\sigma_{CX}$ , and  $n_\sigma$ . Contour plots of the three resultant MOs for  $\text{FCH}_2\text{CH}_2^-$  are given in Figure 10.8. The  $\sigma_{CF}$  MO is primarily localized on the fluorine atom with a small amount of  $n_\sigma$  character mixed in a bonding manner (Figure 10.8c). The  $\sigma^*_{CF}$  MO (Figure 10.8a) is primarily localized on the carbon atom and some  $n_\sigma$  mixes into the orbital in an antibonding manner. The middle MO (Figure 10.8b) is primarily  $n_\sigma$ . The shape of this MO is consistent with  $\sigma_{CF}$  and  $\sigma^*_{CF}$  mixing into it in an antibonding and bonding manner, respectively. There is then approximate cancellation of electron density at the central carbon atom.

The picture we have developed for the optimum conformation in  $\text{XCH}_2\text{CH}_2^-$  contains all of the elements that determine the stereochemistry of  $E2$  (and  $EI_{cb}$ ) elimination reactions [42,43]. In an alkyl halide, the C—H bond antiperiplanar to the C—X bond is attacked by a base. At the transition state for an  $E2$  process, substantial negative charge is developed at the carbon atom that is being deprotonated. In orbital terms, orbital of the weakened C—H bond has a larger weight on the carbon and is similar in shape to  $n_\sigma$  in **10.64**, which is the intermediate for an  $EI_{cb}$  process. The favorable interaction with  $\sigma^*_{CX}$  is, of course, maximized at an antiperiplanar conformation. The interaction also transfers electron density from the carbon atom being deprotonated to the  $\sigma^*_{CX}$  orbital. Therefore, the C—X bond is weakened. Ultimately, the C—X and C—H bonds are totally broken and the  $\pi$  orbital of ethylene is formed.

The importance of the  $\sigma^*_{CX}$  fragment orbital acting as a  $\pi$ -acceptor group is a very pervasive effect and one that we shall see several other times. Notice from the third column in Table 10.1, the  $\pi$  ionization potential is increased from that in propene when a  $\text{CH}_3$  group is replaced by a  $\text{CH}_2\text{F}$  (0.53 eV),  $\text{CH}_2\text{Cl}$  (0.31 eV), and  $\text{CH}_2\text{Br}$  group (0.15 eV). This is certainly consistent with the  $\sigma^*_{CX}$  orbital mixing in and stabilizing the  $\pi$  MO. The  $(n_\sigma - \sigma^*_{\text{AH}_3})$  interaction in  $\text{AH}_3\text{BH}_2$  can be

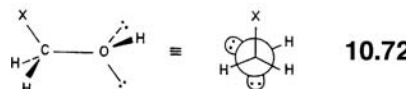
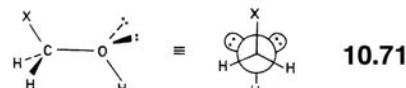
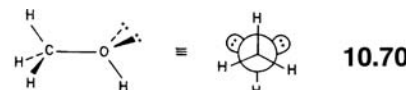
enhanced by lowering the energy of the  $\pi_{\text{AH}_3}^*$  level. Given by a few examples in **10.66**, the  $\pi_{\text{AH}_3}^*$  level is lowered by substituting electronegative ligands for



hydrogens, by moving down a column in the periodic table for A (the overlap between  $p$  atomic orbital on A and hydrogen s becomes smaller), and by introducing a formal positive charge on AH<sub>3</sub>. Therefore, the AH<sub>3</sub> group becomes a  $\pi$ -acceptor. This in part explains why in Table 10.1 the  $\pi$  ionization potentials increase markedly when Si(OMe)<sub>3</sub> or SiCl<sub>3</sub> groups are substituted on ethylene. In the phosphonium ylide,  $^+\text{PH}_3 - \text{CH}_2^-$ , the  $\pi_{\text{PH}_3}^*$  level is low in energy and the ( $n_\sigma - \pi_{\text{PH}_3}^*$ ) interaction (**10.67**) is maximized by having a planar carbanion center [33]. Similarly, the nitrogen center of N(SiMe<sub>3</sub>)<sub>3</sub> is found to be planar [44], which maximizes overlap between the lone pair on nitrogen with  $\pi_{\text{SiC}}$ . The siloxane molecule, H<sub>3</sub>Si—O—SiH<sub>3</sub> has a Si—O—Si angle of 147° and an inversion barrier of  $\sim 100 \text{ cm}^{-1}$  in contrast to normal ethers where the C—O—C angles are  $\sim 109^\circ$  and the inversion barriers are  $\sim 2\text{--}4 \text{ kcal/mol}$  [45]. The traditional explanation for the stability of phosphonium ylides and planarity of the carbanion center has been ascribed to the intervention of  $d$  orbitals on phosphorus (or  $d$  orbitals on silicon for N(SiMe<sub>3</sub>)<sub>3</sub> and H<sub>3</sub>Si—O—SiH<sub>3</sub>) in **10.68**. The ( $\sigma^* \pi - p_\pi$ ) interaction shown in **10.67** is topologically equivalent to the ( $d_\pi - p_\pi$ ) interaction in **10.68**. When electronegative groups (e.g., RO, F, etc.) are substituted at phosphorus, the  $\pi_{\text{PH}_3}^*$  level is lowered in energy and becomes a better  $\pi$  acceptor since it is more localized on phosphorus. The same argument applies to the  $d$  orbital model; when the effective charge at phosphorus becomes larger, the  $d$  AOs drop in energy. So, how can one tell the difference? Calculations obviously can play an important role; however, one must take care with the problems associated with population analysis. Nevertheless, all modern day computations have consistently pointed to the lack of involvement of  $d$  AOs in the bonding for these compounds and the importance of  $\sigma^* \pi$  [46]. But this is not exclusively a theoretical providence either. Orpen and Connelly [47] have investigated a large number of transition metal–phosphine complexes, **10.69**. The strength of the M—P  $\pi$ -bonding can be varied progressively in a number of ways and the magnitude can be conveniently gauged by the M—P bond lengths. In the  $d_\pi$  model the  $d$  AOs on phosphorus are expected to have little if any influence on the geometry of the PR<sub>3</sub> group. This is not the case for the  $\sigma^* \pi$  model. As can be seen from the phase relationships in **10.67** a greater involvement of  $\sigma^* \pi$  will elongate the P—R bonds and the R—P—R angle,  $\theta$  in **10.69**, will decrease because of the antibonding between P and R. Indeed, this is precisely what [47] happens and it furnishes excellent experimental evidence for the  $\sigma^* \pi$  model. There is also good spectroscopic evidence in siloxanes which is consistent with the  $\sigma^* \pi$  but not  $d_\pi$  bonding models [48]. The picture in **10.68** is simply wrong and should not be used. We shall see in Chapter 14 that the use of  $d$  AOs on P and S for the so-called hypervalent molecules is also incorrect. It should be noted from Figure 9.4 that there are two degenerate  $\pi_{\text{PH}_3}^*$  orbitals. We have focused upon the 2e<sub>x</sub> component, as shown in Figure 9.4. Rotation of the methylene group in H<sub>3</sub>P<sup>+</sup>—CH<sub>2</sub><sup>−</sup> by 90° causes  $n_\sigma$  to interact with the 2e<sub>y</sub> component. Since the two acceptor orbitals on PH<sub>3</sub> are degenerate, the overlap of  $n_\sigma$  to them is equivalent. In reality this only needs to be a 30° rotation. At any intermediate geometry,  $n_\sigma$  will interact with a linear combination of 2e<sub>x</sub> and 2e<sub>y</sub>. Therefore, even if there is strong  $\pi$  bonding in **10.67**, the barrier to rotation about the P—C bond is quite small [33,49].

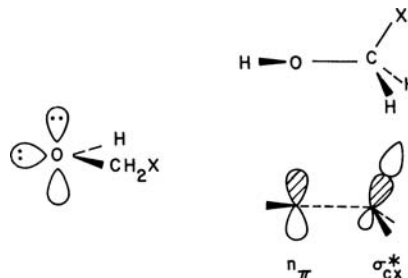
## 10.6 AH<sub>3</sub>BH SYSTEMS

An example of a 14-electron AH<sub>3</sub>BH system is methanol, CH<sub>3</sub>OH. Its stable conformation **10.70** has the three electron pairs of CH<sub>3</sub> staggered with respect to those of OH in the bond orbital description. With a modified methyl group XCH<sub>2</sub>,



in which X refers to an electronegative atom or group (e.g., X = halogen, OH, or NH<sub>2</sub>), XCH<sub>2</sub>—OH gives rise to two staggered conformational possibilities **10.71** and **10.72**. In the anti conformation **10.71**, each hybrid lone pair of oxygen is antiperiplanar to an adjacent  $\sigma^*_{\text{CH}}$  orbital. In the gauche conformation **10.72**, one lone pair of oxygen is antiperiplanar to a  $\sigma^*_{\text{CH}}$  orbital while another is antiperiplanar to the  $\sigma^*_{\text{CX}}$  orbital. The  $\sigma^*_{\text{CX}}$  level is closer in energy to the oxygen lone pair,  $n_{\text{O}}$ , than  $\sigma^*_{\text{CH}}$ ; therefore, the ( $n_{\text{O}} - \sigma^*_{\text{CX}}$ ) interaction is favored over the ( $n_{\text{O}} - \sigma^*_{\text{CH}}$ ) interaction. This makes the gauche conformation more stable in XCH<sub>2</sub>—OH. This bond orbital description is a straightforward application of the XCH<sub>2</sub>CH<sub>2</sub><sup>-</sup> problem.

In the MO description of the problem, the oxygen lone pairs of XCH<sub>2</sub>OH are represented by the  $n_{\pi}$  and  $n_{\sigma}$  orbitals (**10.73**) [50,51]. The  $n_{\pi}$  level lies higher lying in

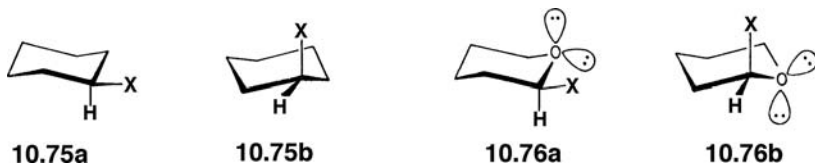


10.73

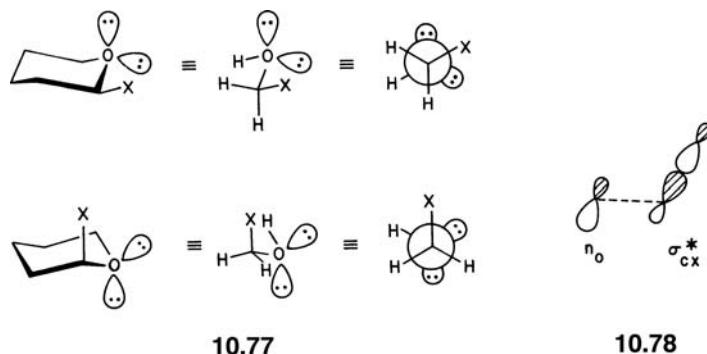
10.74

energy than  $n_{\sigma}$ . See, for example, the ionization potential difference between  $b_1$  and  $2a_1$  in Figure 7.9 for H<sub>2</sub>O; in ethanol and other alcohols the  $n_{\pi} - n_{\sigma}$  energy difference is also around 3 eV [9]. Of the possible interactions between these two lone pairs and the  $\sigma^*_{\text{CX}}$  and  $\sigma^*_{\text{CH}}$  orbitals of XCH<sub>2</sub>, the ( $n_{\pi} - \sigma^*_{\text{CX}}$ ) interaction is the most favorable one in terms of the energy gap. This interaction is maximized when the X—C—O—H dihedral angle  $\theta$  is 90° as indicated in **10.74**. The presence of the ( $n_{\pi} - \sigma^*_{\text{CH}}$ ), ( $n_{\sigma} - \sigma^*_{\text{CX}}$ ), and ( $n_{\sigma} - \sigma^*_{\text{CH}}$ ) interactions, which attain their maximum stabilization at  $\theta$  values other than 90°, makes the actual  $\theta$  value smaller than 90°. With the bond orbital description, the gauche conformation of XCH<sub>2</sub>OH is predicted by simply requiring one hybrid lone pair of oxygen to be antiperiplanar to  $\sigma^*_{\text{CX}}$ . In specifying various conformations of low-symmetry molecules containing OH groups, we find it convenient to adopt a bond orbital description.

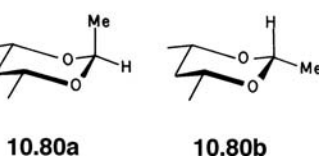
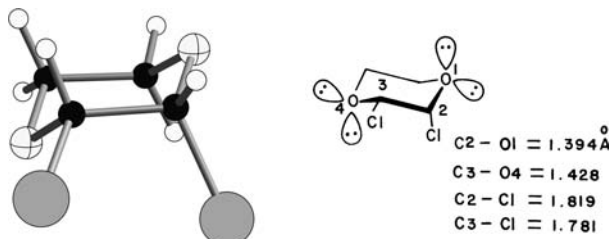
A monosubstituted cyclohexane prefers an equatorial conformation **10.75a** since its alternative, an axial conformation **10.75b**, leads to unfavorable 1,3-diaxial interactions.



The conformational preference for the equatorial over the axial structure is diminished significantly in a tetrahydropyran ring which has an electronegative ligand  $\text{X}$  attached at a carbon adjacent to the oxygen (**10.76**). This kind of preferential stabilization of the axial over the equatorial conformation, known as the anomeric effect [51–54], can be readily explained. The equatorial and axial conformations of 2-X-tetrahydropyran **10.76** are simply equivalent to the anti and gauche conformations, respectively, of  $\text{XCH}_2\text{OH}$ , as depicted in **10.77**.

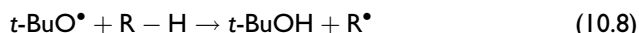


Besides this conformational preference, an  $(n_{\text{O}} - \sigma^*_{\text{CX}})$  interaction brings about an important bond length change. The  $(n_{\text{O}} - \sigma^*_{\text{CX}})$  interaction, **10.78**, is bonding between carbon and oxygen so that the C—O bond is strengthened and hence shortened. It also leads to charge transfer into  $\sigma^*_{\text{CX}}$  which weakens and hence lengthens the C—X bond. Consider, for example, the C—O and C—Cl bond lengths in *cis*-2,3-dichloro-1,4-dioxane, **10.79** [53]. The  $\text{C}_2$ —Cl bond is axial and is antiperiplanar to a lone pair of  $\text{O}_1$ . The  $\text{C}_3$ —Cl bond is equatorial and is not



antiperiplanar to either lone pair of O<sub>4</sub>. Consequently, the C<sub>2</sub>—O<sub>1</sub> bond is shorter than O<sub>4</sub>—C<sub>3</sub>, while the C<sub>2</sub>—Cl bond is longer than C<sub>3</sub>—Cl.

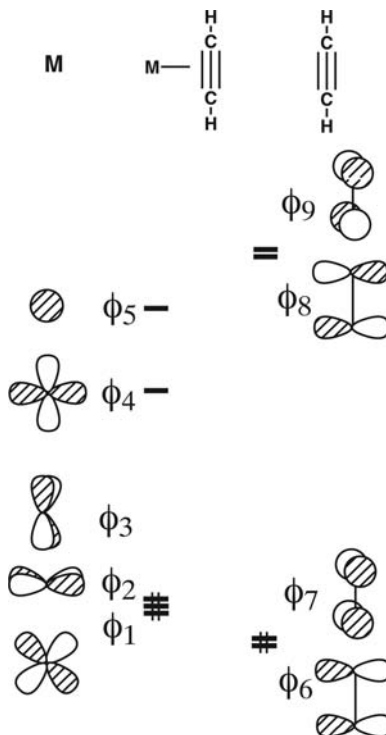
Two conformationally locked 1,3-dioxanes are shown in **10.80**, where **10.80a** has each oxygen lone pair antiperiplanar to the C<sub>2</sub>—H bond while **10.80b** has no oxygen lone pair antiperiplanar to the C<sub>2</sub>—H bond. Thus, the C<sub>2</sub>—H bond is weaker in **10.80a** than in **10.80b**. For the hydrogen abstraction of equation 10.8, the C<sub>2</sub>—H bond of **10.80a** is found to have a rate constant larger than that of **10.80b** by



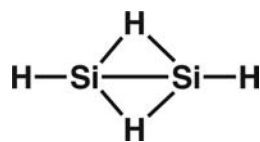
about an order of magnitude [55]. A similar observation has been noted for the cleavage of the tetrahedral intermediate in the hydrolysis of esters and amides [56,57]. Specific cleavage of a carbon–oxygen and a carbon–nitrogen bond in the tetrahedral intermediate is allowed only if the other two heteroatoms (oxygen or nitrogen) each provide a lone pair oriented antiperiplanar to the leaving O-alkyl or N-alkyl group. In general, determination of molecular reactivities by the relative orientation of the bond being broken or made and lone pairs on heteroatoms attached to the reaction center is known as stereoelectronic control [52,56,57].

## PROBLEMS

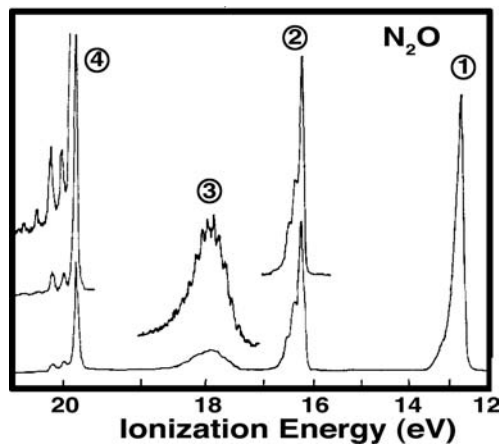
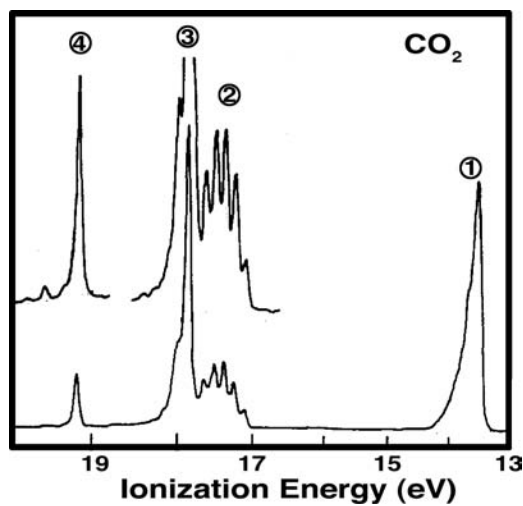
- 10.1.** Consider a transition metal with orbitals  $\phi_1 - \phi_5$ , as shown below, interacting with the  $\pi$  and  $\pi^*$  MOs of an acetylene,  $\phi_6 - \phi_9$ . Use intermolecular perturbation theory to determine the energy corrections and the mixing coefficients (write out the formulae) and carefully draw the resultant orbitals.



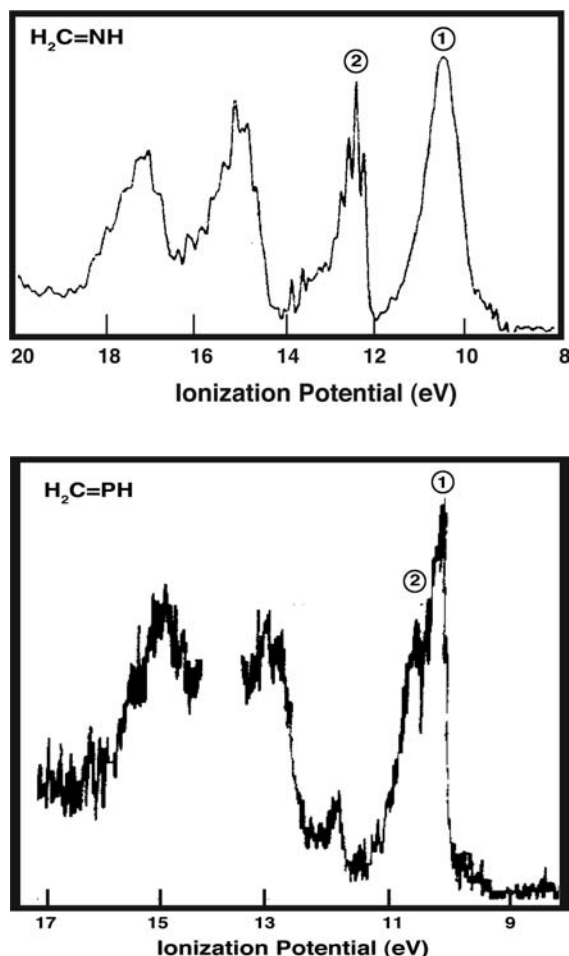
- 10.2.** The silicon analog of ethylene has been prepared in the gas phase. A number of structures have been considered for it including a di-bridging species as shown below. Develop the MOs for this structure using the  $\sigma$ ,  $\sigma^*$ ,  $\pi$ , and  $\pi^*$  orbitals of a HSiSiH fragment (analogs to acetylene) with the two bridging H s AO.



- 10.3.** a. Construct the orbitals of a  $D_{\infty h}$  B–A–B molecule where B is more electronegative than A. Draw out the resultant shapes.  
 b. Use geometric perturbation theory to predict the energies and shapes of the MOs on bending to a  $C_{2v}$  geometry.  
 c. Predict the geometry for  $\text{B}_2\text{C}$ ,  $\text{CN}_2$ ,  $\text{CO}_2$ ,  $\text{OF}_2$ , and  $\text{F}_3^-$  using Walsh's rules.
- 10.4.** The photoelectron spectra of  $\text{CO}_2$  and  $\text{N}_2\text{O}$  are shown below as adapted from Reference [58]. Assign the four ionizations in each spectrum paying close attention to the shape of each ionization, the area under the peaks, and your results from Problem 10.3.



- 10.5.** The  $\text{Sb}_3^{7-}$  molecule exists! Let us make the assumption that the Sb s AOs like at low energy and are core-like. Form an interaction diagram with the p AOs using an  $\text{Sb}_2$  unit interacting with an Sb atom. Be clever—use the easiest way to do this. Indicate the electron occupancy and draw out the MOs. Determine the Sb–Sb bond order.
- 10.6.** The PE of  $\text{H}_2\text{C}=\text{NH}$  and  $\text{H}_2\text{C}=\text{PH}$  are shown below—adapted from Reference [59]. Both molecules have short lifetimes in the gas phase so the resolution of the spectra is marginal. Using the data for ethylene from Figure 10.5, make assignments for the first two ionizations.

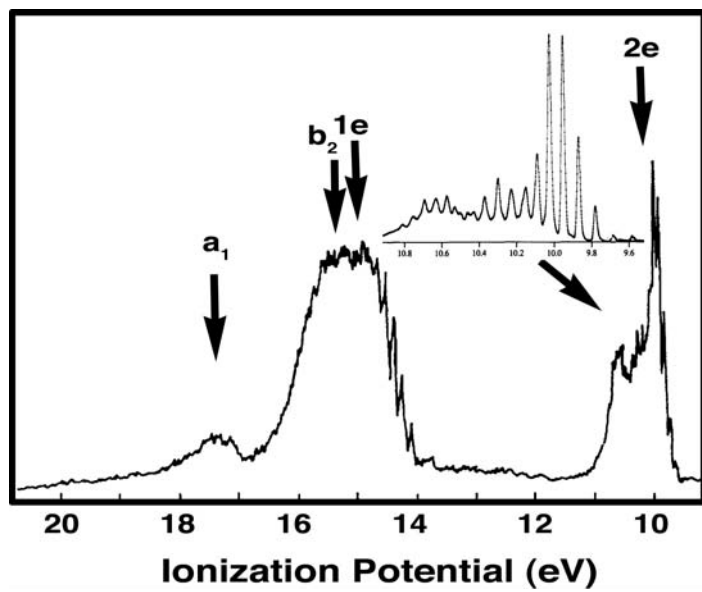


- 10.7.** In the early 1970s, ionization data from the photoelectron spectra of  $(\text{H}_3\text{A})_2\text{S}$  and  $(\text{H}_3\text{A})_3\text{P}$ , where  $\text{A} = \text{C}, \text{Si}$ , along with a number of other compounds were used to support the thesis that empty  $d$  AOs on Si were chemically important. The ionization energies are listed below. Provide orbital arguments for the PE data for these two sets of compounds that do not use  $d$  AOs on Si.

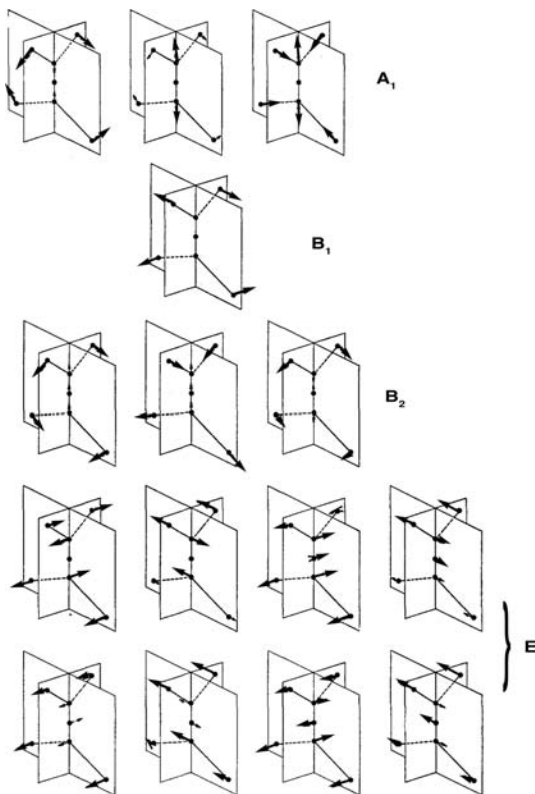
$\text{H}_3\text{A}-\text{S}-\text{AH}_3$			$(\text{H}_3\text{A})_3\text{P}$		
A	C	Si	A	C	Si
$b_1$	8.7	9.6	$a'_1$	8.6	9.3 eV
$a_1$	11.2	11.0	e	11.3	10.6 eV
$b_2$	12.6	11.7			

- 10.8.** We developed the  $\pi$  orbitals for allene in Problem 7.3. A slightly more complete treatment would use the  $b_1$ ,  $2a_1$ , and  $1b_2$  MOs of  $\text{CH}_2$  and interact these two sets with a central C atom.

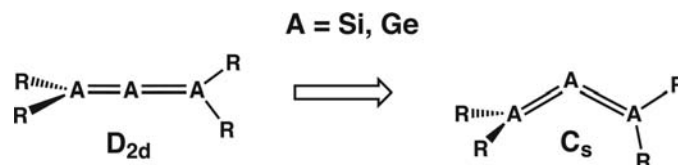
- Construct this interaction diagram and draw out the resultant MOs.
- The photoelectron spectrum of allene is given below—as adapted from Reference [60]. The assignments should match your interaction diagram!



The shape of the ionization from the 2e MO (the inset shows this peak at a higher resolution) is quite peculiar. Suggest a reason for this behavior. For this you need to have the normal modes of allene. These are shown below. Note: the  $b_1$  mode involves a torsion around the C–C–C axis. The rest of the modes involve bending and stretching.



- c. Heavy-atom analogs of allene have been prepared. Their structures are unusual in that the A–A–A bond angles range from  $136^\circ$  to  $122^\circ$ . Using the arguments around **10.30** as a guide, describe a second-order Jahn–Teller approach toward understanding why these molecules bend as shown below.




---

## REFERENCES

---

1. M.-H. Whangbo, H. B. Schlegel, and S. Wolfe, *J. Am. Chem. Soc.*, **99**, 1296 (1977).
2. B. M. Gimarc, *Molecular Structure and Bonding*, Academic Press, New York (1979).
3. J. P. Lowe, *J. Am. Chem. Soc.*, **92**, 3799 (1970); J. P. Lowe, *J. Am. Chem. Soc.*, **96**, 3759 (1974).
4. S. Weiss and G. Leroi, *J. Chem. Phys.*, **48**, 962 (1968) the electronic origin of the barrier continues to be a hotly debated subject; F. Weinhold, *Angew. Chem. Int. Ed.*, **42**, 4188 (2003); F. M. Bickelhaupt and E. V. Baerends, *Angew. Chem. Int. Ed.*, **42**, 4183 (2003); V. Pophristic and L. Goodman, *Nature*, **411**, 565 (2001).
5. B. M. Gimarc, *J. Am. Chem. Soc.*, **95**, 1417 (1973).
6. M. Iwasaki, K. Toriyama, and K. Nunome, *J. Am. Chem. Soc.*, **103**, 3591 (1981); H. M. Sulzbach, D. Graham, J. C. Stephens, and H. F. Schaefer, III, *Acta Chem. Scand.*, **51**, 547 (1997). G. A. Olah and M. Simonetta, *Acta Chem. Scand.*, **104**, 330 (1982); P. v. R. Schleyer, A. J. Kos, J. A. Pople, and A. T. Balaban, *Acta Chem. Scand.*, **104**, 3771 (1982).
7. G. Trinquier and J.-P. Malrieu, *J. Am. Chem. Soc.*, **113**, 8634 (1991); G. Trinquier, J.-P. Malrieu, and I. Garcia-Cuesta, *J. Am. Chem. Soc.*, **113**, 6465 (1991).
8. L. Salem, *Electrons in Chemical Reactions*, John Wiley & Sons, New York (1982); A. Lifschitz, S. H. Bauer, and E. L. Resler, *J. Chem. Phys.*, **38**, 2056 (1963); N. J. Turro, *Modern Molecular Photochemistry*, Benjamin/Cummings, Menlo Park (1978); J. Michl and V. Bonacic-Koutecky, *Electronic Aspects of Organic Photochemistry*, John Wiley & Sons, New York (1990). This is a tough number to experimentally or theoretically determine, yet everyone is in agreement on its physical origin. Contrast this with the barrier in ethane where every theoretical technique—from extended Hückel on up—gets the right magnitude but the physical origin remains controversial (see Reference [4]).
9. K. Kimura, *Handbook of He(I) Photoelectron Spectra of Fundamental Organic Molecules*, Japan Soc. Press, Tokyo (1981).
10. C. R. Brundle, M. B. Robin, H. Basch, M. Pinsky, and A. Bond, *J. Am. Chem. Soc.*, **92**, 3863 (1970).
11. L. Salem, *Acc. Chem. Res.*, **12**, 87 (1979).
12. R. J. Buenker and S. D. Peyerimhoff, *Chem. Phys.*, **9**, 75 (1976); B. Brooks and H. F. Schaefer, *J. Am. Chem. Soc.*, **101**, 307 (1979).
13. W. G. Dauben, M. S. Kellogg, J. I. Seeman, N. D. Wietmeyer, and P. H. Wendschuh, *Pure Appl. Chem.*, **33**, 197 (1973).
14. P. Hamm, M. Zurek, T. Röschinger, H. Patzelt, D. Oesterhelt, and W. Zinth, *Chem. Phys. Lett.*, **263**, 613 (1996) and references therein.
15. L. Salem, and P. Bruckmann, *Nature*, **258**, 526 (1975); an excellent overview of the current state of affairs may be found in I. Schapiro, P. Z. El-Khoury, and M. Olivucci, *Handbook of Computational Chemistry*, J. Leszczynski, editor, Springer Science, pp. 1360–1404 (2012).
16. R. M. Minyaev, D. J. Wales, and T. R. Walsh, *J. Phys. Chem.*, **101**, 1384 (1997).
17. L. Libit and R. Hoffmann, *J. Am. Chem. Soc.*, **96**, 1370 (1974); I. Fernandez and G. Frenking, *Chem. Eur. J.*, **12**, 3617 (2006).

18. G. C. Levy, R. L. Lichter, and G. L. Nelson, *Carbon-13 Nuclear Magnetic Resonance Spectroscopy*, 2nd edition, John Wiley & Sons, New York (1980), pp. 81–86.
19. I. Wennerbeck and J. Sandstrom, *Org. Magn. Reson.*, **4**, 783 (1972); L. M. Jackman, in *Dynamic Nuclear Magnetic Resonance Spectroscopy*, L. M. Jackman and F. A. Cotton, editors, Academic Press, New York, p. 203 (1975);
20. W. von Niessen, L. Åsbrink, and G. Bieri, *J. Electron Spectrosc. Relat. Phenom.*, **26**, 173 (1982); R. S. Brown and F. S. Jørgensen, in *Electron Spectroscopy*, Vol. **5**, C. R. Brundel and A. D. Baker, editors, Academic Press, New York p. 2–123. (1984).
21. D. M. Mintz and A. Kuppermann, *J. Chem. Phys.*, **71**, 3499 (1979).
22. M.-H. Whangbo and K. R. Stewart, *J. Org. Chem.*, **47**, 736 (1982); I. Fernandez and G. Frenking, *Chem. Eur. J.*, **12**, 3617 (2006).
23. K. D. Jordan and P. D. Burrow, *Acc. Chem. Res.*, **11**, 341 (1978).
24. H. Bock and H. Stafast, *Tetrahedron*, **32**, 855 (1976); K. N. Houk and L. L. Munchausen, *J. Am. Chem. Soc.*, **98**, 937 (1976).
25. R. Gleiter, F. Schmidt, D. O. Cowan, and J. P. Ferraris, *J. Electron Spectrosc. Relat. Phenom.* **2**, 207 (1973).
26. R. Hoffmann, R. Gleiter, and F. B. Mallory, *J. Am. Chem. Soc.*, **92**, 1460 (1970).
27. T. Fjeldberg, A. Haaland, M. F. Lappert, B. E. R. Schilling, R. Seip, and A. J. Thorne, *J. Chem. Soc., Chem. Commun.*, 1407 (1982); D. E. Goldberg, D. H. Harris, M. F. Lappert, and K. M. Thomas, *J. Chem. Soc., Chem. Commun.*, 261 (1976); P. J. Davidson, D. H. Harris, and M. F. Lappert, *J. Chem. Soc., Dalton Trans.*, 2269 (1976).
28. N. C. Norman, *Polyhedron*, **12**, 2431 (1993); M. Driess and H. Grützmacher, *Angew. Chem. Int. Ed.*, **35**, 828 (1996).
29. B. Eisenmann and H. Schaefer, *Z. Anorg. Allg. Chem.*, **484**, 142 (1982).
30. G. Trinquier, and J.-P. Malrieu, *J. Phys. Chem.*, **94**, 6184 (1990); J.-P. Malrieu, and G. Trinquier, *J. Am. Chem. Soc.*, **111**, 5916, (1989); G. Trinquier, *J. Am. Chem. Soc.*, **112**, 2130 (1990); G. Trinquier, *J. Am. Chem. Soc.*, **113**, 144 (1991); H. Jacobsen, and T. Ziegler, *J. Am. Chem. Soc.*, **116**, 3667 (1994).
31. A. H. Cowley, D. J. Mitchell, M.-H. Whangbo, and S. Wolfe, *J. Am. Chem. Soc.*, **101**, 5224 (1979).
32. A. H. Cowley, M. J. S. Dewar, D. W. Goodman, and M. C. Padolina, *J. Am. Chem. Soc.*, **96**, 2648 (1974).
33. D. J. Mitchell, S. Wolfe, and H. B. Schlegel, *Can. J. Chem.*, **59**, 3280 (1981).
34. P. Forti, D. Damiami, and P. G. Favero, *J. Am. Chem. Soc.*, **95**, 756 (1973); G. Trinquier and M. T. Ashby, *Inorg. Chem.*, **33**, 1306 (1994); A. E. Reed and P. von R. Schleyer, *Inorg. Chem.*, **27**, 3969 (1988); P. V. Sudhakar and K. Lammertsma, *J. Am. Chem. Soc.*, **113**, 1899 (1991).
35. T. Laube, *Acc. Chem. Res.*, **28**, 399 (1995) and references therein.
36. K. Raghavachari, R. A. Whiteside, J. A. Pople, and P. v. R. Schleyer, *J. Am. Chem. Soc.*, **103**, 5649 (1981); M. W Wong, J. Baker, R. H. Nobes, and L. Radom, *J. Am. Chem. Soc.*, **109**, 2245 (1987).
37. J. Skolik, P. J. Krueger, and M. Wieworowski, *Tetrahedron*, **24**, 5439 (1968); F. Bohlmann, *Chem. Ber.*, **91**, 2157 (1958); D. Kost, H. B. Schlegel, D. J. Mitchell, and S. Wolfe, *Can. J. Chem.*, **57**, 729 (1979).
38. A. J. Stone and R. W. Erskine, *J. Am. Chem. Soc.*, **102**, 7185 (1980).
39. F. H. Allen, O. Kennard, and R. Taylor, *Acc. Chem. Res.*, **16**, 146 (1983).
40. H.-B. Bürgi and J. D. Dunitz, *Structural Correlation*, VCH Weinheim (1994); H.-B. Bürgi and J. D. Dunitz, *Acc. Chem. Res.*, **16**, 153 (1983); H.-B. Bürgi, J. D. Dunitz, and E. Sheffer, *Acta Crystallogr., Sect. B*, **30**, 1517 (1974).
41. P. Rademacher, *Chem. Soc. Rev.*, 143 (1995).
42. J. P. Lowe, *J. Am. Chem. Soc.*, **94**, 3718 (1972); F. M. Bickelhaupt, E. J. Baerends, N. M. M. Nibberling, and T. Ziegler, *J. Am. Chem. Soc.*, **115**, 9160 (1993); N. T. Anh and O. Eisenstein, *Nouv. J. Chim.*, **1**, 61 (1977).
43. T. H. Lowry and K. S. Richardson, *Mechanism and Theory in Organic Chemistry*, 3rd edition, Harper & Row, New York (1987).
44. K. Hedberg, *J. Am. Chem. Soc.*, **77**, 6491 (1955).

45. J. Koput, *J. Phys. Chem.*, **99**, 15847 (1995).
46. D. G. Gilheany, *Chem. Rev.*, **94**, 1339 (1994); A. E. Reed and P. v. R. Schleyer, *J. Am. Chem. Soc.*, **112**, 1434 (1990) and references therein.
47. A. G. Orpen and N. G. Connelly, *J. Chem. Soc., Chem. Commun.*, **1310** (1985); A. G. Orpen and N. G. Connelly, *Organometallics*, **9**, 1206 (1990).
48. J. A. Tossell, J. H. Moore, K. McMillan, and M. A. Coplan, *J. Am. Chem. Soc.*, **113**, 1031 (1991); S. G. Urquhart, C. C. Turci, T. Tyliszczak, M. A. Brook, and A. P. Hitchcock, *Organometallics*, **16**, 2080 (1997) and references therein.
49. H. Lischka, *J. Am. Chem. Soc.*, **99**, 353 (1977) and references therein.
50. O. Eisenstein, N. T. Anh, Y. Jean, A. Devaquet, J. Cantacuzene, and L. Salem, *Tetrahedron*, **30**, 1717 (1974).
51. S. Wolfe, M.-H. Whangbo, and D. J. Mitchell, *Carbohydr. Res.*, **69**, 1 (1979); G. A. Jeffrey, J. A. Pople, and L. Radom, *Carbohydr. Res.*, **25**, 117 (1972).
52. A. J. Kirby, *The Anomeric Effect and Related Stereoelectronic Effects at Oxygen*, Springer-Verlag, New York (1983).
53. C. Romers, C. Altona, H. R. Buys, and E. Havinga, *Top. Stereochem.*, **4**, 39 (1969).
54. I. V. Alabugin and T. A. Zeidan, *J. Am. Chem. Soc.*, **124**, 3175 (2002).
55. A. L. J. Beckwith and C. J. Easton, *J. Am. Chem. Soc.*, **103**, 615 (1981).
56. P. Deslongchamps, *Tetrahedron*, **31**, 2463 (1975).
57. P. Deslongchamps, *Stereoelectronic Effects in Organic Chemistry*, Pergamon, Oxford (1983).
58. D. W. Turner and D. P. May, *J. Chem. Phys.*, **46**, 1156 (1967).
59. S. Lacombe, D. Gonbeau, J.-L. Cabioch, B. Pellerin, J.-M. Denis, and G. Pfister-Guillouzo, *J. Am. Chem. Soc.*, **110**, 6964 (1988) and J. B. Peel and G. D. Willett, *J. Chem. Soc., Faraday Trans. 2*, 1799 (1975).
60. P. Baltzer, B. Wannberg, M. Lundqvist, L. Karlsson, D. M. P. Holland, M. A. MacDonald, and W. von Niessen, *Chem. Phys.*, **196**, 551 (1995).

# Orbital Interactions through Space and through Bonds

---

## 11.1 INTRODUCTION

---

In the previous chapters, we showed how to construct the orbitals of a molecule in terms of orbital interaction diagrams. Many structural and reactivity problems can be rationalized using arguments based on the shape and energy of the frontier orbitals. Thus a primary purpose of an orbital interaction diagram is to identify and characterize these orbitals and to understand the nature of those orbital interactions that control the nodal properties of the frontier orbitals. The magnitude of an orbital interaction depends not only on through-space, direct interaction but also on through-bond, indirect interaction [1–4]. In the following text, structural and reactivity problems of organic molecules that utilize these concepts will be examined.

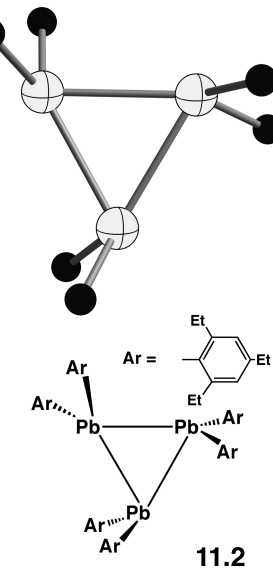
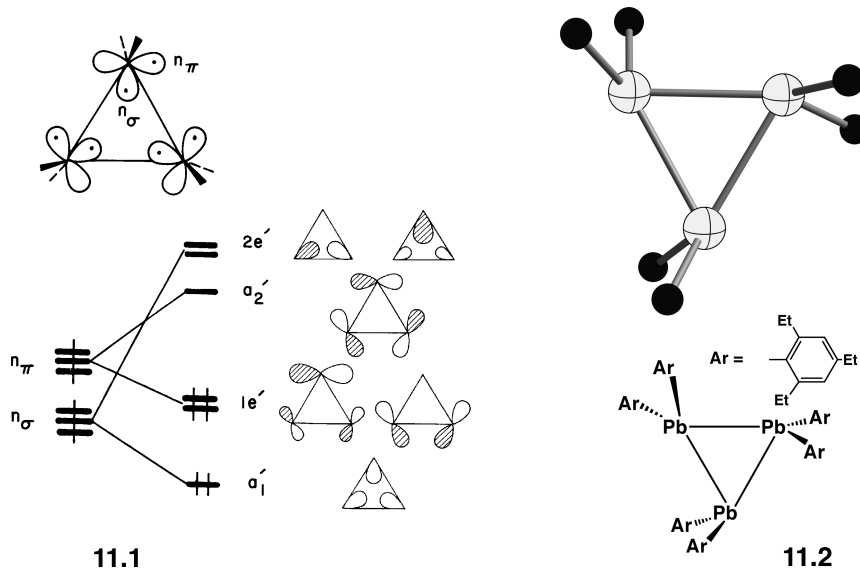
---

## 11.2 IN-PLANE $\sigma$ ORBITALS OF SMALL RINGS

---

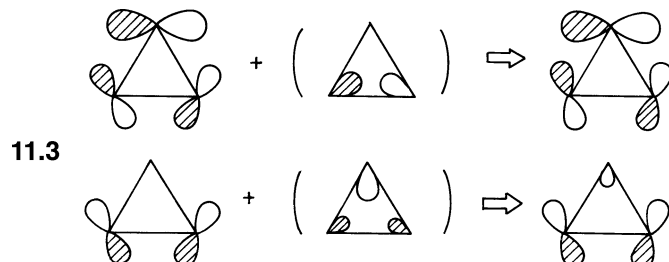
### 11.2.1 Cyclopropane

In Section 5.2, we derived the orbitals of triangular  $H_3$ , and in Section 5.7 the tangential  $\pi$  orbitals of cyclopropenium. As shown in 11.1, cyclopropane may be considered as made up of three methylene units [5–7]. Each  $CH_2$  unit uses its  $1a_1$  and  $b_2$  orbitals for C—H  $\sigma$  bonding. The remaining  $2a_1$  and  $b_1$  orbitals,  $n_\sigma$  and  $n_\pi$ ,



respectively, are used to form the C—C  $\sigma$  bonds in the cyclopropane ring [8]. In terms of the  $n_\sigma$  and  $n_\pi$  orbitals of each methylene unit, the in-plane  $\sigma$  MOs of cyclopropane can be constructed as discussed in earlier chapters. Taking symmetry-adapted linear combinations of the three  $n_\sigma$ , radial orbitals result in the formation of the  $a'_1$  and  $2e'$  orbitals. The  $a'_1$  combination is strongly bonding and  $2e'$  is strongly antibonding. The  $1e'$  and  $a'_2$  orbitals result from the combination of the three  $n_\pi$ , tangential orbitals. Since the orbitals are not directly pointed at one another, the overlap is not strong as that in the radial set. Consequently, the  $1e'$  and  $a'_2$  combinations lie at moderate energies. Following the arguments given in Sections 8.8 and 8.10, the singlet-triplet energy gap for  $AH_2$  molecules increases as going down Group 4 in the Periodic Table, with the singlet state (two electrons in  $2a_1$ ) being more stable. It is not surprising that the structure of a substituted cyclo-triplumbane [9] is not  $D_{3h}$  but rather  $C_{3h}$ , 11.2, where “cycloaddition” of the three  $PbR_2$  units has been arrested. This is exactly analogous to the situation for the heavy-atom  $H_4A_2$  analogs discussed in Section 10.3.C.

The pattern in 11.1 is derived exclusively by symmetry considerations. Since the  $2e'$  and the  $1e'$  sets have the same symmetry, the two may mix together as shown in 11.3 and 11.4. This intermixing is rather strong [10]. Using some reasonable parameters for the interaction energies, it can be shown that the resonance integral which links the  $1e'$  and  $2e'$  sets is  $-3.38\text{ eV}$  and that the energy separation between them is small,  $5.0\text{ eV}$  [10]. Consequently  $\sim 20\%$  of  $2e'$  mixes into  $1e'$  in 11.3. This is a



rather large number; perhaps it has been overestimated. The important point is that this mixing cannot be totally ignored. The reader should carefully examine the way that the  $1e'$  and  $2e'$  combinations mix with each other. They do so to provide greater bonding in 11.3 and more antibonding in 11.4. This can be shown clearly from the plot of the MOs shown in Figure 11.1. This intermixing for the antisymmetric member of  $1e'$  serves to redirect the  $p$  AOs associated the bottom two  $\text{CH}_2$  units

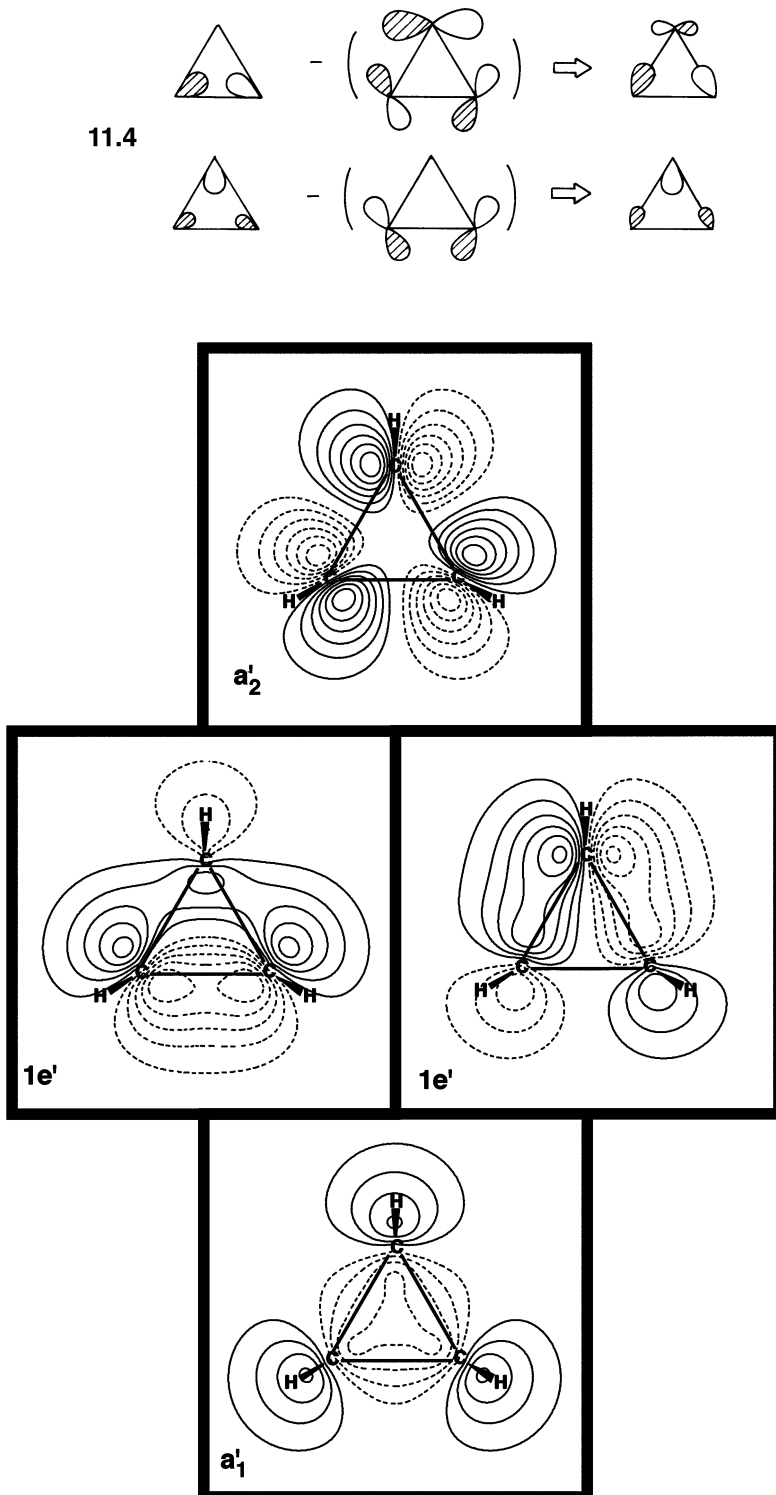


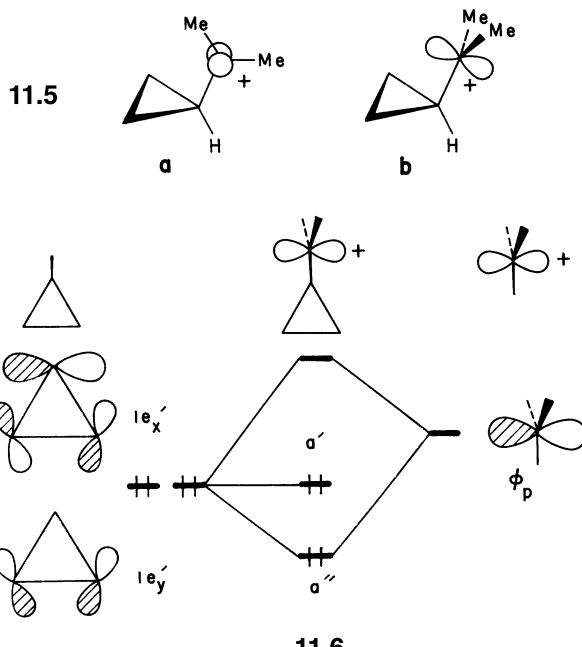
**FIGURE 11.1**

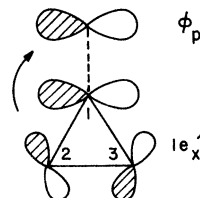
A plot of the STO-3G wavefunctions at the HF level for the three occupied ( $a'_1$  and  $1e'$ ) and lowest unoccupied ( $a'_2$ ) molecular orbitals. The solid and dashed contour lines refer to positive and negative values, respectively, of the wavefunction.

more along the C—C internuclear axis. The intermixing in the symmetric member of  $l e'$  serves primarily to provide amplitude on the top  $\text{CH}_2$  unit. Both of these features are evident in the contour plots of the  $l e'$  sets shown in Figure 11.1. Also plotted at the bottom of the figure is the product of the totally symmetrical combination of radial functions,  $a'_1$ . Maximal electron density is built up in the center of the cyclopropane ring and not along the internuclear C—C axis. This is purely a result of symmetry. One can construct hybrid combinations which lie along the C—C axis and are completely equivalent to the delocalized  $a'_1$  MO [10]. It is also clear for the plots of the  $l e'$  set that these MOs are not aligned along the C—C axis. This causes loss of overlap and yields C—C bond energies that are smaller than typical values for alkanes. The formation of  $\sigma$  bonds which lie off from the internuclear axis, so-called banana bonds, is the MO equivalent of ring strain. Notice also at the top of Figure 11.1 the presence of a low-lying C—C  $\sigma^*$  combination with  $a'_2$  symmetry. As indicated in 11.1, it is a combination exclusively comprised of the radial  $p$  AOs.

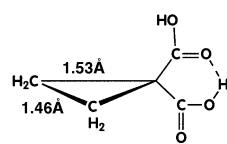
The in-plane  $\sigma$  orbitals of Figure 11.1 (occupied by three electron pairs) describe the three C—C bonds of a cyclopropane ring, so that the  $a'_1$  and  $l e'$  orbitals are each doubly occupied. The  $l e'$  set lies at a high energy compared to most C—C  $\sigma$  orbitals. They are composed primarily of carbon  $p$  character. Furthermore as indicated earlier, the orbitals are not directed toward each other on the internuclear axis as is the case in other cycloalkanes with larger dimensions. Therefore, the  $l e'$  set behaves as a good electron donor for a cyclopropyl substituent. For the same reasons, the  $a'_2$  orbital lies lower in energy compared to most C—C  $\sigma^*$  orbitals and can serve as an electron-acceptor orbital. Therefore, with respect to the plots in Figure 11.1, the antisymmetric member of the  $l e'$  set can be used as a  $\pi$ -donor function and  $a'_2$  as a  $\pi$ -acceptor. Then the cyclopropane ring is electronically like a vinyl group with its  $\pi$  and  $\pi^*$  orbitals. We shall now look briefly at two examples of this property in cyclopropane.

The three C—C bonds of cyclopropane are equivalent since both of the  $l e'$  pair of orbitals are occupied. The two components, however, have different capabilities of interaction with a ring substituent. For example, the dimethylcyclopropyl carbocation is more stable in the bisected conformation 11.5a than in 11.5b. In fact, the rotational barrier between the two, as determined by NMR methods, is very large ( $\sim 14 \text{ kcal/mol}$ ) [11]. As shown in 11.6, this arises simply because the carbocation





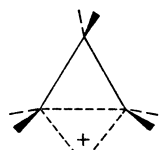
11.7



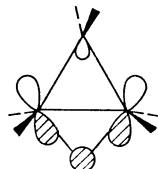
11.8

$p$  orbital,  $\phi_p$ , interacts effectively only with the  $l_{e'_x}$  orbital [12]. The resulting ( $\phi_p - l_{e'_x}$ ) interaction is of the charge-transfer type and leads to electron density removal from the  $l_{e'_x}$  orbital as shown in 11.7. A direct structural consequence of this interaction is that, since electron density is removed from  $l_{e'_x}$ , there is a reduction in the antibonding between C2 and C3 and in the bonding interactions between Cl and C2 and between Cl and C3. As a result, a good electron acceptor such as  $-CR_2^+$ ,  $-C\equiv N$  or  $-CO_2R$  strengthens the C2—C3 bond while weakening the Cl—C2 and Cl—C3 bonds. The most direct demonstration of this phenomenon comes from crystal structures [13]. A typical example is shown in 11.8.

Protonation of cyclopropane seems to occur via edge attack as shown in 11.9 [14]. This may be understood by considering the interaction of one component



11.9



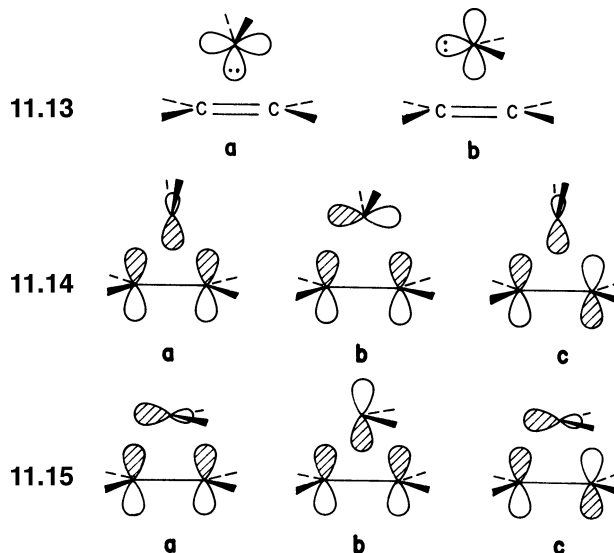
11.10

of the highest occupied molecular orbital (HOMO) ( $l_{e'}$ ) with the empty  $l_s$  orbital of the proton (11.10). Notice that the form of 11.10 is not much different from the bridged isomer of  $C_2H_5^+$  (see 10.49) where the bridging hydrogen s orbital interacts with the  $\pi$  orbital of ethylene. 11.9 is another example of closed three-center-two-electron bonding. Bicyclo[3.1.0]hexyl tosylates undergo solvolysis at a much faster rate than cyclohexyl tosylates [15]. Labeling studies in the first set of compounds have shown that the resulting cation in 11.11 has  $C_{3v}$  symmetry. In other words, each methine carbon possesses a formal  $1/3$  positive charge and there is a formal bond order of  $1/3$  between each nonadjacent methine carbon. A bonding orbital is formed,



which resembles the  $y$  component of  $l_{e'}$  and leads to the delocalization of the positive charge in 11.11. The form of the orbital is shown in 11.12. Note that it is the equatorial tosylate isomer in 11.11 that exhibits increased reactivity. The C—OTs  $\sigma^*$  orbital is then ideally situated for overlap with the filled  $l_{e'_y}$  level of the cyclopropane portion. It is this interaction which facilitates loss of the tosylate anion in the solvolysis reaction.

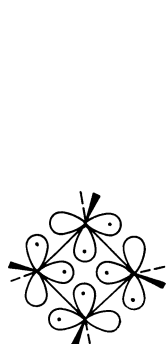
Let us examine the attack of a singlet carbene on ethylene which proceeds to give cyclopropane [16]. Shown in 11.13 are two possible approaches that a carbene might undertake. In 11.13a, the methylene and ethylene molecules approach each



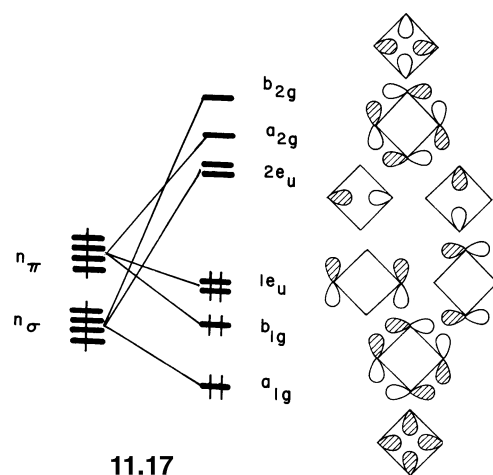
other maintaining  $C_{2v}$  symmetry. This is the least-motion reaction pathway. In **II.13b** methylene approaches the C—C double bond in a sideways manner. At some point along the reaction path, the methylene group must rock itself into an upright position. The important interactions in this problem are the destabilizing interaction between the filled hybrid on methylene,  $n_s$ , and the filled  $\pi$  orbital of ethylene,  $\pi_{CC}$  ( $n_s - \pi_{CC}$ ) as well as the stabilizing interactions between the empty  $p$  AO on methylene,  $n_\pi$ , with filled  $\pi_{CC}$  ( $n_\pi - \pi_{CC}$ ) and between filled  $n_s$  and the empty  $\pi^*$  orbital of ethylene,  $\pi^{*CC}$ , ( $n_s - \pi^{*CC}$ ). In the least-motion attack, **II.13a**, the orbitals associated with the  $(n_s - \pi_{CC})$ ,  $(n_\pi - \pi_{CC})$ , and  $(n_s - \pi^{*CC})$  interactions are arranged spatially as in **II.14a**, **II.14b**, and **II.14c**, respectively. It is clear that in this geometry, both of the stabilizing interactions vanish because of symmetry;  $n_\pi$  and  $\pi_{CC}$  have  $b_2$  symmetry while  $\pi_{CC}$  and  $n_s$  have  $a_1$  symmetry. Therefore, the overlap between the two fragments in **II.14b** and **II.14c** is zero. In the non-least-motion attack **II.13b**, the orbitals associated with the  $(n_s - \pi_{CC})$ ,  $(n_\pi - \pi_{CC})$ , and  $(n_s - \pi^{*CC})$  interactions are arranged as in **II.15a**, **II.15b**, and **II.15c**, respectively. Here neither of the stabilizing interactions vanishes, since the symmetry is lowered to  $C_s$  and all four relevant orbitals have  $a'$  symmetry. The most important aspect is that the stabilizing  $(n_\pi - \pi_{CC})$  interaction has maximal overlap, at this geometry (**II.15b**), while the destabilizing  $(n_s - \pi_{CC})$  interaction is diminished in magnitude (**II.15a**). Consequently, the initial approach of a carbene to ethylene is predicted to undergo a non-least-motion approach such as **II.13b** where the methylene unit rocks itself upward after substantial C—C bond formation has occurred [16]. Notice the connection here to the cycloetriplumbane example, **II.2**, in the previous section and the dimerization of two carbenes in Section 10.3.C.

### 11.2.2 Cyclobutane

By analogy with the Walsh construction of the MOs in cyclopropane, cyclobutane may be constructed from four methylene units (**11.16**) [17]. For convenience, the molecule will be considered to have a square planar rather than puckered structure.

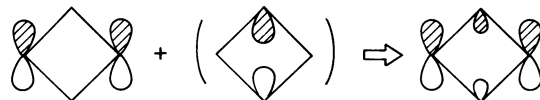


11.16

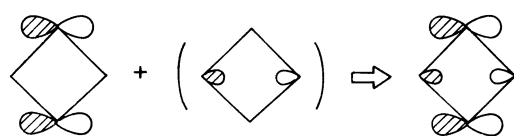


11.17

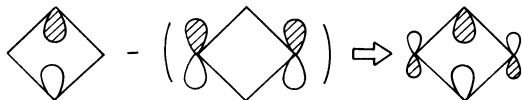
In terms of the  $n_s$ , radial, and  $n_\pi$ , tangential orbitals of each methylene, the  $\sigma$  MOs of cyclobutane are obtained by extending the results of Sections 5.3 and 5.7. This construction from group theoretical combinations alone is summarized in 11.17. The  $a_{1g}$ ,  $2e_u$ , and  $b_{2g}$  orbitals arise largely from the four  $n_s$  orbitals as shown on the right side of 11.17. The  $a_{1g}$  combination is strongly bonding while  $b_{2g}$  is strongly antibonding. The  $2e_u$  set is weakly antibonding. The  $b_{1g}$ ,  $1e_u$ , and  $a_{2g}$  symmetry-adapted combinations arise from the four  $n_\pi$  orbitals. The pattern is different than that presented by the radial set. The  $b_{1g}$  orbital is bonding and  $a_{2g}$  is the antibonding equivalent, however, the  $1e_u$  set is now weakly bonding. The  $2e_u$  and  $1e_u$  orbitals in 11.17 have the same symmetry, and so they mix together as shown in 11.18 and 11.19. The  $2e_u$  set mixes into  $1e_u$  to create an MO which is more



11.18

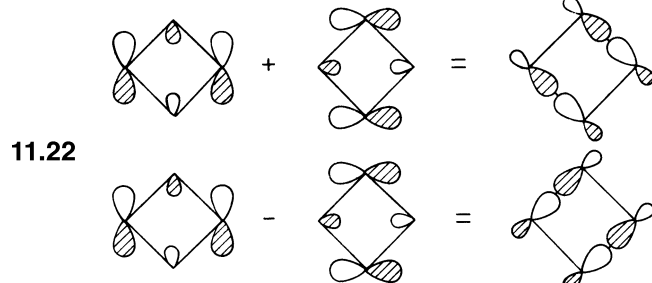
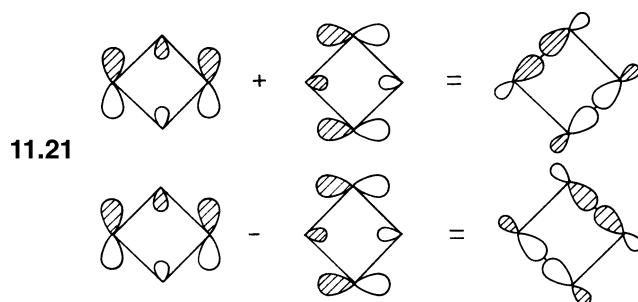
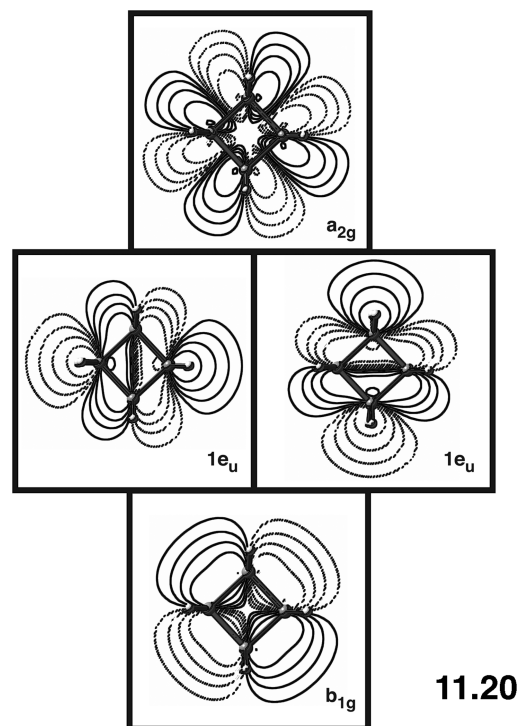


11.19



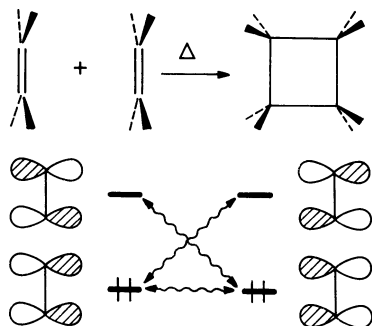
C—C  $\sigma$  bonding (11.18). In 11.19 the  $1e_u$  combination mixes into  $2e_u$  to create MOs that are more antibonding. Contour plots of  $b_{1g}$  and  $a_{2g}$  which are derived exclusively from the tangential set of methylene fragment orbitals are presented in 11.20. The wavefunctions were derived from the B3LYP hybrid functional with a 3-21G basis. Just as in the MOs of cyclopropane, these are a very good  $\pi$ -donor and acceptor orbitals. The  $1e_u$  set is also displayed in 11.20. One can clearly see the

mixing between the tangential and radial sets of fragment orbitals that is diagrammed in 11.18. Because of the flexibility allowed in the description of degenerate sets of orbitals, the  $1e_u$  set of 11.18 may be combined to give the alternative set of 11.21. Similarly the  $2e_u$  pair of 11.19 may be manipulated to give the orbitals of 11.22. What has been done is to create localized bond orbital equivalents of these



degenerate sets. With four electron pairs, the four  $\sigma$ -bonding orbitals  $a_{1g}$ ,  $b_{1g}$ , and  $1e_u$  are occupied and the four C—C  $\sigma$  bonds of cyclobutane result.

Consider now the concerted dimerization of ethylene. The frontier orbital interactions of this reaction are the  $(\pi_{CC} - \pi_{CC})$ ,  $(\pi_{CC} - \pi^*_{CC})$ , and  $(\pi^*_{CC} - \pi^*_{CC})$  interactions shown in 11.23. The one destabilizing interaction  $(\pi_{CC} - \pi_{CC})$  has a nonzero overlap as can be seen readily by inspection. The two stabilizing interactions



11.23

$(\pi_{CC} - \pi^*_{CC})$  and  $(\pi^*_{CC} - \pi^*_{CC})$  have an overlap of zero. Therefore, as two ground-state ethylene molecules approach each other in a least-motion way (11.23), a strongly repulsive barrier is encountered. The orbital correlation diagram for this reaction is shown in Figure 11.2. On the reactant side, forming linear combinations of the  $\pi_{CC}$  orbitals of two ethylenes lead to the  $\pi_+$  and  $\pi_-$  MOs, while the two  $\pi^*_{CC}$  orbitals lead to the  $\pi^*_+$  and  $\pi^*_-$  MOs. In the initial stage of the dimerization, the overlap between two ethylenes is weak so that  $\pi_+$  and  $\pi_-$  lie far below the  $\pi^*_+$  and  $\pi^*_-$  levels, and  $\pi_+$  and  $\pi_-$  are occupied. Of the  $\sigma$  orbitals of cyclobutane described earlier, only those related to the  $\pi_+$ ,  $\pi_-$ ,  $\pi^*_+$ , and  $\pi^*_-$  levels by symmetry are shown in Figure 11.2. Not all the occupied MOs of the reactant lead to occupied orbitals in

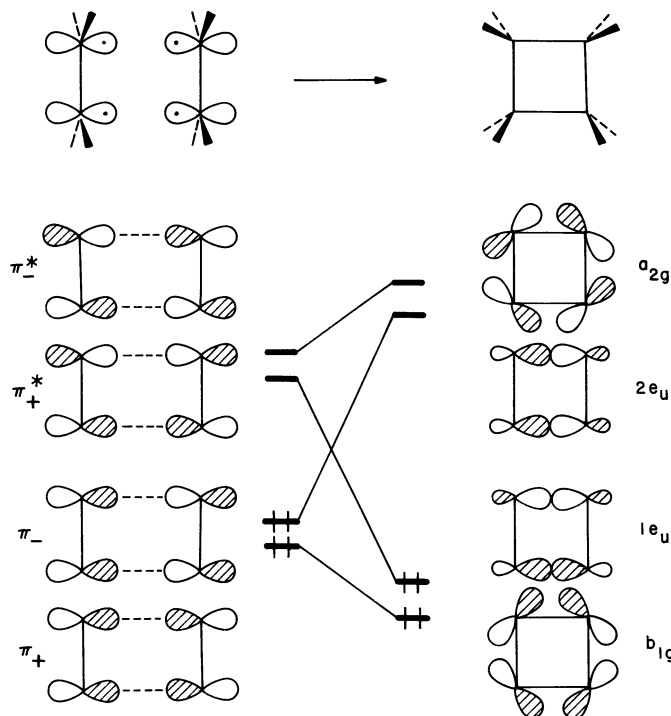
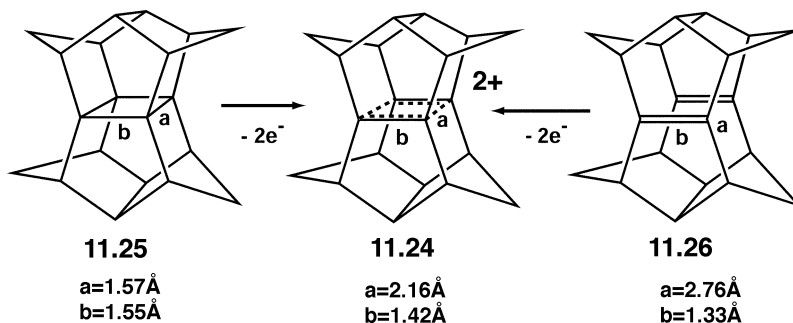


FIGURE 11.2

An orbital correlation diagram for the concerted dimerization reaction of ethylene.

the product. In particular,  $\pi_-$  is destabilized and correlates with one component of the empty  $2e_u$  set in cyclobutane (see 11.21). Antibonding between the two ethylenes increases as the distance between them decreases. However, in the  $\pi_+^*$  combination C—C  $\sigma$ -bonding is turned on so it ultimately becomes one component of the filled  $1e_u$  set in cyclobutane (see 11.20). Also notice that since  $\sigma$  overlap is stronger than  $\pi$  overlap,  $b_{1g}$  lies lower and  $a_{2g}$  higher in energy than the  $\pi_-$  and  $\pi_+^*$  combinations, respectively. A filled and an empty MO cross so the reaction is said to be symmetry-forbidden. A high activation barrier is associated with the reaction and the reaction path cannot be the one associated with the synchronous formation of both C—C  $\sigma$  bonds. In fact femtosecond studies of this reaction have shown [18] that it proceeds by way of a tetramethylene diradical, that is, this is a two-step reaction where one C—C  $\sigma$  bond is formed first and then diradical intermediate collapses to form the second C—C  $\sigma$  bond.

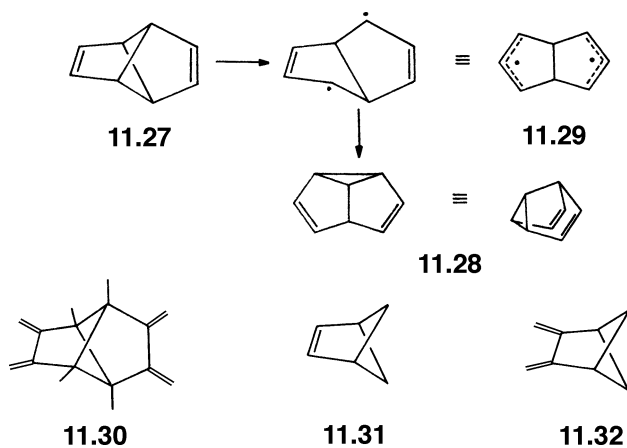
Suppose one removed two electrons from the situation displayed in Figure 11.2; the expectation would be that the structure should collapse without barrier to a “cyclobutane-like” structure. Only the  $\pi_+$  combination is filled, and this becomes stabilized when  $\sigma$ -bonding is turn on. Now there are two C—C bonds formed but there are only a total of two electrons to put in them so each has a formal bond order of one-half and a long C—C distance is to be expected. This is precisely the case [19] in compound 11.24 which is obtained by the removal of two electrons from 11.25 or 11.26. Because the  $\pi$  bonds are forced into close proximity by the caged structure in 11.26, the two  $\pi$  ionizations are split by 1.9 eV [19]. The decrease of the



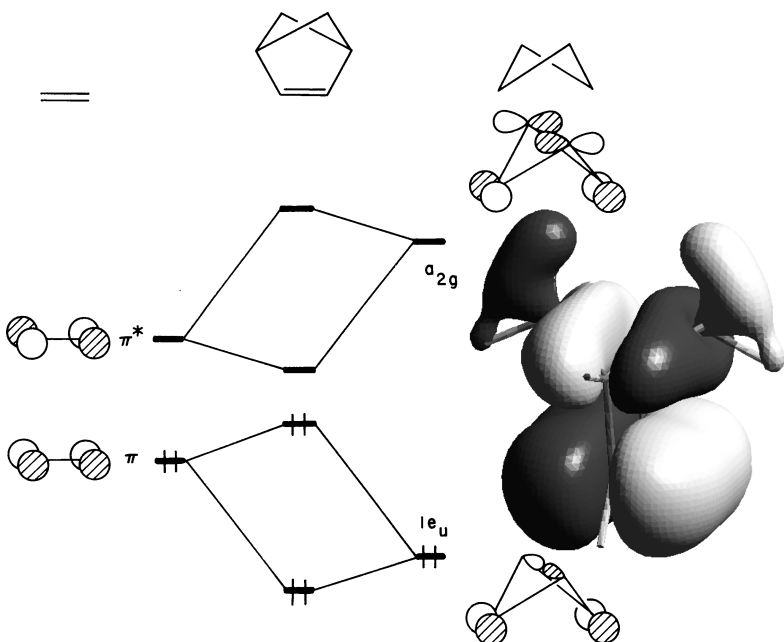
C—C distance  $a$  by 0.60 Å and increase in distance  $b$  by 0.09 Å on going from 11.26 to 11.24 is a consequence of the development of  $\sigma$ -bonding and the loss of  $\pi$ -bonding, respectively. The decrease in the  $b$  distance and increase in the  $a$  distance on going from 11.25 to 11.24 is likewise readily explained by the increase in  $\pi$ -bonding and decrease in  $\sigma$ -bonding, respectively.

The reader should carefully compare the correlation diagram for ethylene dimerization here with the  $H_2 + D_2$  reaction in Figure 5.5. The two correlation diagrams are very similar, as they should be, since in this instance the spatial distributions of  $\pi$  and  $\pi^*$  are similar to those of  $\sigma_g^+$  and  $\sigma_u^+$ , respectively, in  $H_2$ . These two reactions are probably the premier examples of symmetry-forbidden reactions. A related symmetry-allowed example is the concerted cycloaddition of ethylene and butadiene, the Diels–Alder reaction. We shall not cover the orbital symmetry rules for organic, pericyclic reactions. There are several excellent reviews that the reader should consult [20,21]. But it should be pointed out that the orbital symmetry rules have stereochemical implications in terms of the reaction path and products formed. The development of these rules by Woodward and Hoffmann revolutionized the way organic chemists think about reactions. We shall return to some reactions related to ethylene dimerizations in later chapters where a transition metal  $ML_n$  unit is inserted between two methylene units of the olefins.

Tricyclooctadiene **11.27** readily rearranges to semibullvalene **11.28** at room temperature. The experimental evidence for this reaction is consistent with the

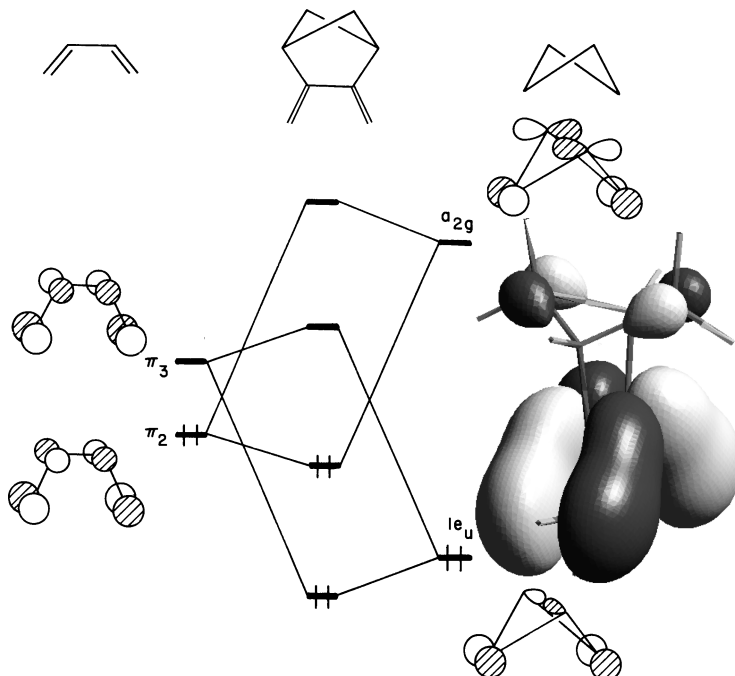


formation of the diradical **11.29**. However, a similar molecule, **11.30**, is found to be quite stable. Note that **11.27** contains a cyclobutane ring 1,3-bridged by two ethylene units, and **11.30** contains the same four-membered ring but is 1,3-bridged by two butadiene units. This difference between **11.27** and **11.30** can be studied in terms of the simplified model systems **11.31** and **11.32**, respectively [22]. The frontier orbital interactions between the ethylene and cyclobutane units in **11.31** are shown in Figure 11.3. It is easy to see that the HOMO–lowest unoccupied molecular orbital (LUMO) gap of **11.31** is smaller than that for ethylene itself because of interaction with the cyclobutane ring. The  $\pi$  orbital overlaps with one component of the filled  $1e_u$  set on the cyclobutadiene portion and is destabilized, whereas  $\pi^*$  is stabilized by the empty  $a_{2g}$  orbital. The HOMO of **11.31** is displayed on the right side of the figure where the molecule has been rotated approximately 45° from the plane



**FIGURE 11.3**

A simplified orbital interaction diagram for **11.31**. A plot of the HOMO is shown on the right side of this figure. Here the MO is displayed at a value of 0.05 a.u. where the black and gray surfaces correspond to positive and negative, respectively, values of the wavefunction. This surface was obtained from an ab initio HF calculation at the 3-21G level.

**FIGURE 11.4**

A simplified orbital interaction diagram for 11.32. On the right side of the figure is a plot of the HOMO with the same details as given in Figure 11.3.

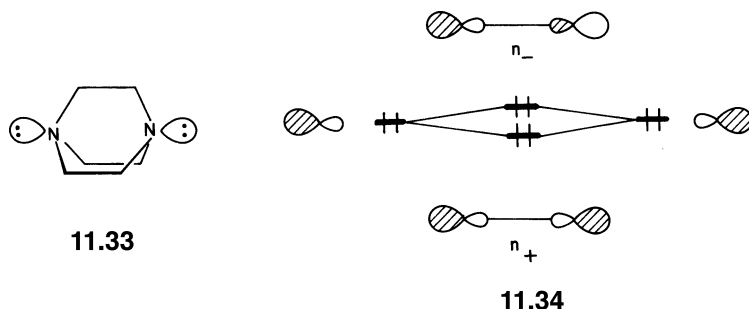
of the paper. The black and gray surfaces correspond to positive and negative regions, respectively, of the wavefunction. The involvement of the cyclobutane  $1e_u$  portion and its antibonding to ethylene  $\pi$  is obvious in this picture. From this contour surface, it appears that there is substantial mixing between ethylene  $\pi$  and cyclobutane  $1e_u$ . Since both fragment orbitals are filled this is a destabilizing interaction. The opposite effect occurs with the butadiene unit of 11.32. The frontier orbital interactions between the butadiene and cyclobutane units in 11.32 are shown in Figure 11.4. The HOMO–LUMO gap of 11.32 is enhanced with respect to that of butadiene. Now the HOMO of butadiene,  $\pi_2$ , is of correct symmetry to be stabilized by  $a_{2g}$  on the cyclobutane fragment and the LUMO,  $\pi_3$ , is destabilized by one component of the  $1e_u$  set. Again a plot of the HOMO is given on the right side of the Figure. There is a minor technical detail here. A lower lying filled orbital of  $a_{2g}$  on the cyclobutane portion of the ring also mixes with  $\pi_2$  on the butadiene fragment. The result then is that  $\pi_2$  is the middle member of this three-orbital pattern. There is cancellation of the coefficients at the two methine carbons which are connected to the butadiene. Notice that these different results for the two molecules emerge as a direct consequence of the nodal properties of the  $\pi$  orbitals of the ethylene and butadiene fragments. A molecule with a small energy gap between the HOMO and LUMO is susceptible to a distortion that allows orbital mixing between them (i.e., a second-order Jahn–Teller distortion). According to Figure 11.3, the LUMO of 11.31 has some contribution of  $a_{2g}$  which is antibonding between the carbon atoms of the cyclobutane ring. Thus any asymmetrical distortion of 11.31 that allows the mixing of the LUMO into the HOMO would effectively weaken the bonding between the carbon atoms of the cyclobutane ring. This is consistent with the cleavage of a C–C bond in 11.27 to produce the diradical 11.29. Since the HOMO–LUMO gap in 11.32 is predicted to be quite large, the driving force for an analogous second-order distortion is lost. Although 11.30 should have approximately the same strain energy as 11.27, nonetheless it is thermally more stable [22]. Notice also that the interaction with the cyclobutane fragment is repulsive in Figure 11.3 for 11.31 but is net attractive in Figure 11.4 for 11.32. We shall return to this prediction in the Chapter 12 when we discuss bond localization in benzene.

## 11.3 THROUGH-BOND INTERACTION

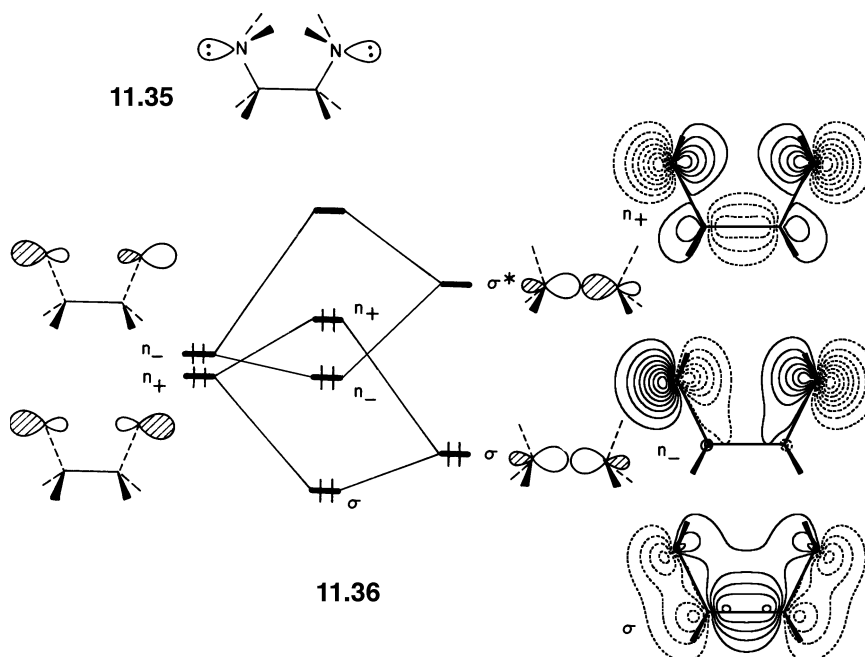
### 11.3.1 The Nature of Through-Bond Coupling

Conceptual fragmentation of a molecule allows us to readily construct its MOs in terms of linear combinations of fragment orbitals [1–4]. How a given molecule should be fragmented depends on the simplicity of the resulting orbital interaction picture. Given a pair of orbitals located on two molecular fragments, direct through-space interaction between them leads to two energy levels described in the usual in-phase and out-of-phase combinations. Typically, the in-phase combination is lower in energy than the out-of-phase one. However, this level ordering is not always found to be correct if the fragment orbitals involved further interact with the orbitals of a third fragment. We encountered this very situation for the intermixing between  $\sigma$ -bonding and lone-pair orbitals in N<sub>2</sub> in Section 6.5.

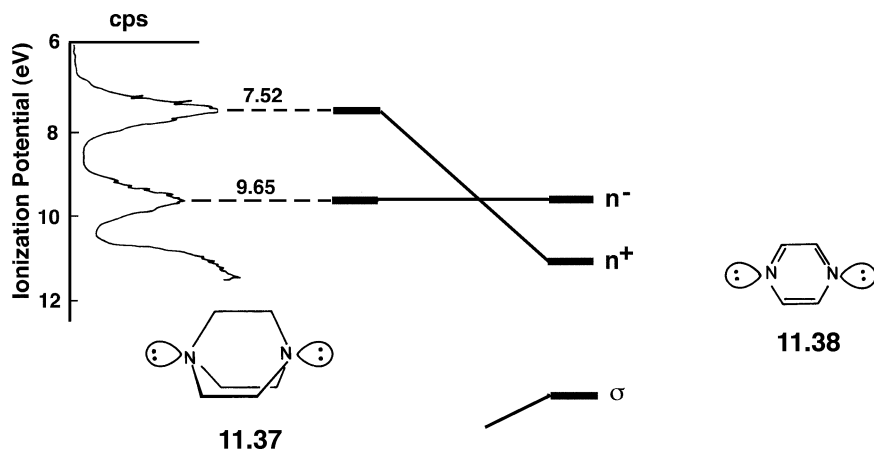
As another example, let us consider the two lone-pair levels in diazabicyclooctane **11.33**. The direct, through-space interaction between the hybrid lone pairs of nitrogen leads to the symmetry-adapted levels  $n_+$  and  $n_-$  shown in **11.34**. Because



of the large distance between the two hybrid lone pairs, the overlap between the two hybrids will be very small and, thus, the energy difference between  $n_+$  and  $n_-$  is expected to be small. However, both calculation and experiment show a large splitting between the  $n_+$  and  $n_-$  levels. The first two bands in the photoelectron spectrum of **11.33** have maxima at 7.52 and 9.65 eV to which  $n_+$  and  $n_-$  are the major contributors [23,24]. Thus, rather than being split by a small through-space interaction as anticipated by **11.34**, the two lone pairs are in fact separated by an enormous 2.13 eV. This seemingly unphysical splitting (and a counterintuitive level ordering, as we shall see) is due to the fact that each hybrid lone-pair orbital of nitrogen cannot be considered in isolation. They do interact with the  $\sigma$  and  $\sigma^*$  orbitals associated with the intervening C—C bonds. This kind of indirect effect is called through-bond interaction. The essence of through-bond interaction for the diazabicyclooctane system can be analyzed by a simplified molecule, 1,2-diaminoethane, which has been forced into the *syn*-eclipsed conformation given by **11.35**. Shown in **11.36** are the interactions of the  $n_+$  and  $n_-$  orbitals along with the C—C  $\sigma$  and  $\sigma^*$  orbitals. Initially the  $n_+$  and  $n_-$  combinations are not split much in energy because of the long distance and consequently small overlap between them. Compared with the through-space 1,4-interaction between the nitrogen centers, the 1,2-interactions ( $n_+ - \sigma$ ) and ( $n_- - \sigma^*$ ) are strong. As a result, the energy of the  $n_+$  and  $n_-$  levels are raised and lowered, respectively, by the  $\sigma$  and  $\sigma^*$  levels. This leads to a large splitting between the levels which we can still describe approximately as  $n_+$  and  $n_-$ . Contour plots using ab initio MO calculations at the HF 3-21G level on 1,2-diaminoethane are presented on the right side of **11.36** for the  $\sigma$ ,  $n_-$ , and  $n_+$  MOs. The mixing between  $n_+$  and  $\sigma$  is quite evident from these plots. The mixing of  $\sigma^*$  into  $n_-$  is not nearly so obvious and, in fact, the strength of both interactions are not the same. There is a much smaller energy gap between  $n_+$  and  $\sigma$  than that

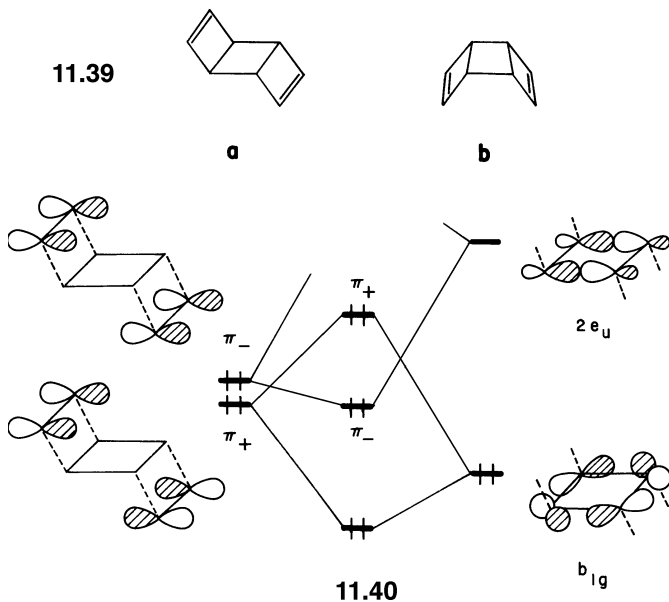


between  $n_-$  and  $\sigma^*$ . Therefore, the  $n_+ - \sigma$  interaction is much stronger in general for these types of through-bond conjugation [25]. Notice also from 11.36 that the  $n_-$  MO is predicted to lie lower in energy than the  $n_+$  combination. Returning now to diazabicyclooctane, 11.33, the two lowest ionizations show vibrational fine structure [23,24]. The PE spectrum of 11.33 is reproduced in 11.37. Comparison of the

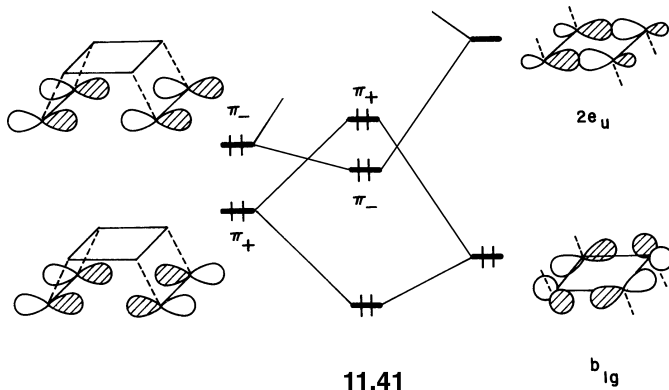


vibrational fine structure with the normal vibrational coordinates [26] of 11.33 shows that the vibrational frequencies of the bands centered at 7.52 and 9.65 eV are primarily associated with C—C stretching and CNC bending, respectively [24]. In addition, analysis of the overlap populations of the C—C and C—N bonds in 11.33 and its cation suggests that electron removal from  $n_+$  and  $n_-$  should mainly induce C—C stretching and CNC bending deformations of the molecular frame of 11.33, respectively [24]. Consequently, the  $n_+$  and  $n_-$  levels are responsible for the bands centered at 7.52 and 9.65 eV, respectively [24], namely,  $n_+$  lies higher in energy than  $n_-$ . A closely related example is the pyrazine molecule, 11.38. The  $n_+$  combination of the nitrogen lone pairs has been experimentally shown to lie 1.72 eV higher in energy than the  $n_-$  combination [27].

Competition between through-space and through-bond interactions often gives rise to interesting results. For example, let us consider tricyclo-3,7-octadiene which can adopt either the *anti* or the *syn* structure shown in **11.39a** and **11.39b**, respectively. In the *anti* structure the through-space interaction between the



double bonds is negligible. However, photoelectron studies of **11.39** reveal that the difference between the first and second ionization potentials ( $\Delta IP$ ), which is a measure of the extent the  $\pi$  levels are split, is larger in the *anti* than in the *syn* structure ( $\Delta IP = 0.97$  and  $0.36\text{ eV}$  for **11.39a** and **11.39b**, respectively) [28]. As shown in **11.40**, the through-space interaction in **11.39a** is small so that  $\pi_+$  is only slightly lower than  $\pi_-$ . Following our discussion of Section 11.2.B, the in-plane  $\sigma$  orbitals of the cyclobutane ring that can interact with  $\pi_+$  and  $\pi_-$  are the  $b_{1g}$  and  $2e_u$  levels, respectively, shown in **11.40**. Due to the through-bond interactions ( $\pi_+ - b_{1g}$ ) and ( $\pi_- - 2e_u$ ), the  $\pi_+$  and  $\pi_-$  levels are raised and lowered, respectively. Because of the high energy associated with  $2e_u$ , the stabilization of  $\pi_-$  is expected to be small. But there is still a large energy difference between the two  $\pi$  orbital combinations. The through-space interaction of **11.39b** is large as shown in **11.41**, which gives rise to a large splitting between  $\pi_+$  and  $\pi_-$ , with  $\pi_+$  below  $\pi_-$ . This level ordering is altered by the through-bond interactions ( $\pi_+ - b_{1g}$ ) and ( $\pi_- - 2e_u$ ). What determines the magnitudes of these interactions in **11.39a** or **11.39b** are the 1,2-interactions of the double-bond carbon atoms with the cyclobutane ring. Thus,

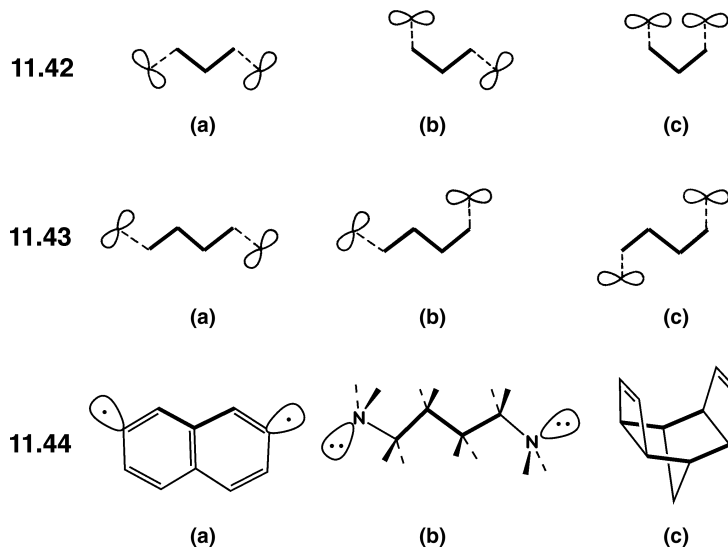


the through-bond interactions are nearly the same in magnitude in **11.39a** and **11.39b**. Consequently, the raising of  $\pi_+$  and the lowering of  $\pi_-$  by the through-bond interactions in **11.39b** lead to an effectively smaller gap between  $\pi_-$  and  $\pi_+$ , compared with the corresponding value of **11.39a**. In other words, the greater through-space interaction in the *syn* isomer induces a smaller  $\Delta\text{IP}$  value because of the opposing effect of through-bond interaction.

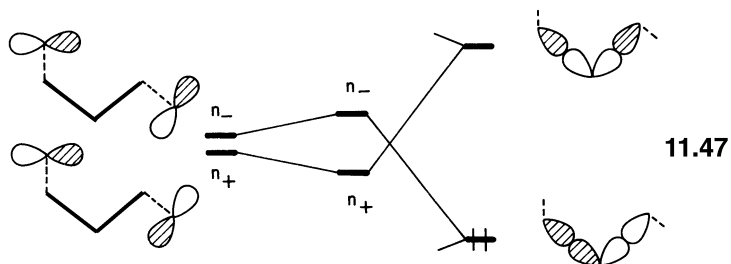
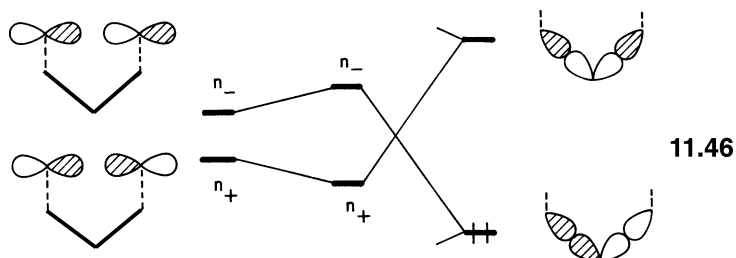
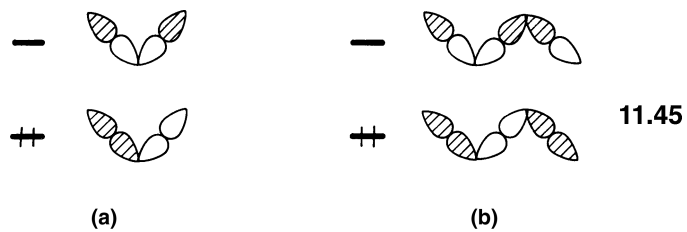
### 11.3.2 Other Through-Bond Coupling Units

As discussed earlier, the concept of through-bond interaction arises when a molecule is regarded as being composed of three fragments. Two of these fragments typically carry lone-pair orbitals, radical  $p$  orbitals or double-bond  $\pi$  orbitals, the in-phase and out-of-phase combination of which lead to the frontier orbitals of the whole molecule. The energy ordering of these combinations is affected by the 1,2 interactions associated with the remaining fragment, a through-bond coupling unit. Our discussion of Section 3.1 was limited to through-bond interactions occurring via three intervening  $\sigma$  bonds. It is instructive to examine how through-bond interactions are affected by the length of the coupling unit. Through-bond coupling is thought to be a very important mechanism for long-range electron transfer in donor/acceptor molecules [29].

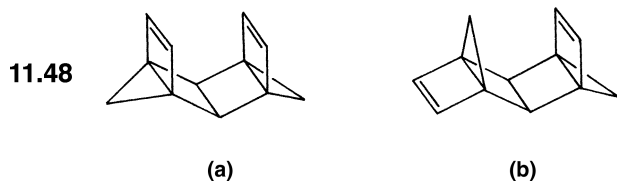
Schematically shown in **11.42** and **11.43** are two  $p$  orbitals coupled via the  $\sigma$  bond framework of four and five single bonds, respectively. The 1,2-interactions



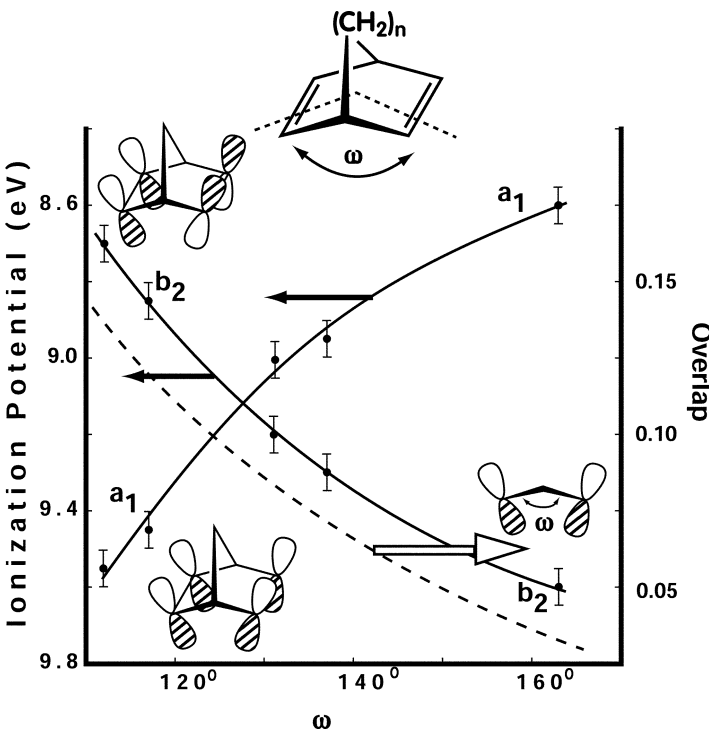
associated with both ends of each coupling unit are indicated by dashed lines. Thus **11.42a** is a simplified representation of, for example, 2,7-dehydronaphthalene, **11.44a**; **11.43a** is analogous to the extended conformation of 1,3-diaminopropane **11.44b**; and the coupling of the  $\pi$  orbitals in the basketane precursor **11.44c** can be represented by **11.42c**. In the examples of **11.44** the  $\sigma$ -bond framework involved in the through-bond coupling (i.e., the coupling unit) is highlighted by a thickened line. For simplicity, we may represent each  $\sigma$  bond of a coupling unit by  $\sigma$  and  $\sigma^*$  bond orbitals. Then the HOMO and LUMO of the coupling unit are approximated by the most antibonding combination of the  $\sigma$  orbitals and by the most bonding combination of the  $\sigma^*$  orbitals, respectively, as summarized in **11.45** [30]. By considering only the 1,2-interactions with these frontier orbitals, through-bond interactions in **11.42** and **11.43** can be easily estimated. For example, in **11.42c**, the through-space



and through-bond interactions reinforce each other as shown in **11.46**. In **11.42b**, the through-space interaction is negligible but the through-bond interaction is as strong as that in **11.42c** to a first approximation (see **11.47**). Consequently, the energy gap between  $n_+$  and  $n_-$  is larger in **11.42c** than in **11.42b**. This conclusion remains valid when the  $p$  orbitals of **11.44** and **11.45** are replaced by hybrid lone-pair orbitals or by double-bond  $\pi$  orbitals. Photoelectron studies show that the  $\Delta E$  values of **11.48a** and **11.48b** are 1.26 and 0.44 eV, respectively [31], consistent with the analysis given earlier. The magnitude of the through-space interaction decreases sharply with the distance between the interacting groups.



However, the magnitude of a through-bond interaction attenuates slowly with increasing the length of its coupling unit. This is due to the fact that a through-bond interaction is governed primarily by the 1,2-interactions associated with both ends of a coupling unit. In the HOMO and LUMO of a coupling unit, the weights on both ends diminish slowly as the length of a coupling unit increases. A striking experimental example of the interplay between through-space and through-bond conjugation has been found in the ionization potentials of the  $\pi$ -bonds for a series of bicyclic dienes [32]. The results are presented in Figure 11.5. The

**FIGURE 11.5**

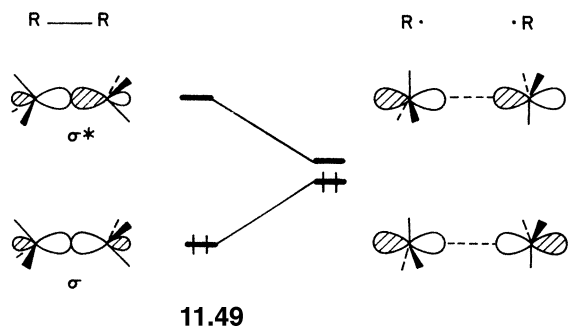
The ionization potentials for the  $a_1$  and  $b_2$   $\pi$ -bond combinations as a function of the angle between the  $\pi$ -bonds,  $\omega$ . The dashed line refers to the overlap between the  $\pi$  orbitals as a function of  $\omega$ .

two  $\pi$  orbitals overlap each other by through-space interaction to form a bonding,  $a_1$ , and an antibonding,  $b_2$ , combination. These MOs are explicitly drawn out for norbornadiene ( $n=1$ ) on the left side of the graph. As the number of methylene groups in the bridging chain increases, the angle between the two  $\pi$ -bonds,  $\omega$ , increases. This reaches a maximum for  $n=\infty$  which is modeled by 1,4-cyclohexadiene. When  $\omega$  increases, the overlap between the  $\pi$ -bonds decreases. This is plotted by the dashed line in Figure 11.5. Therefore, one would expect that  $a_1$  should rise and  $b_2$  to decrease in energy as  $\omega$  increases. If only through-space interaction was present, the  $a_1$  and  $b_2$  MOs should be close in energy for  $n=\infty$  and be degenerate at  $\omega=180^\circ$ . This clearly does not happen. The  $a_1$  combination rises above  $b_2$  in energy when  $\omega$  is larger than  $130^\circ$  and in fact there is a larger splitting of  $a_1$  and  $b_2$  on the right side of the graph compared to the left side. The reason for this is that the through-bond conjugation to  $a_1$  is particularly strong and reasonably constant throughout this series [32]. In other words, if the curve given by the  $a_1$  combination were to be uniformly lowered by at least 1 eV (it has been estimated to be 1.6 eV [32]), then the resultant curves for the  $a_1$  and  $b_2$  MOs would correspond to those given solely by through-space interaction.

## 11.4 BREAKING A C—C BOND

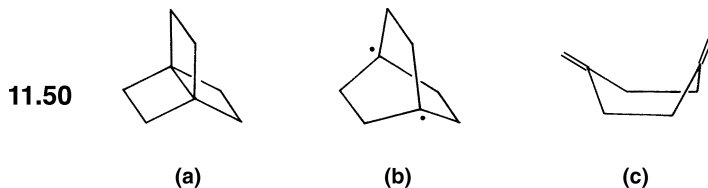
In previous chapters, we discussed the ways reagents attack organic substrates (e.g., nucleophilic substitution, addition reactions, and elimination reactions). Let

us examine some interesting ways that C—C  $\sigma$  bonds can be broken in a homolytic manner which, in turn, lead to unusual predictions concerning reaction paths or intermediate structures. We start this discussion with a simple example of homolytic C—C bond  $\sigma$  cleavage in an alkane. A correlation diagram for this process is displayed in 11.49. The  $\sigma$  bonding level between the two alkyl groups

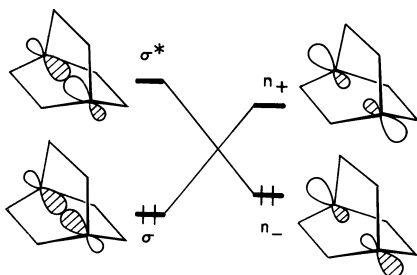


rises in energy as the C—C bond distance increases and  $\sigma^*$  is stabilized. When the distance between the two radicals is large, the overlap between the two  $p$  orbitals is negligible so we again have a typical diradical situation of two closely spaced orbitals with two electrons to put in them [33]. We will sidestep the issue of how to correctly describe the electronic states (see Section 8.10) that are created on the product side of **11.49**, but note that the  $\sigma$  level at no time crosses  $\sigma^*$  along the reaction path.

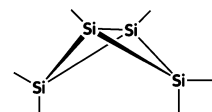
**11.50a** is an example of a class of molecules called propellanes. The strain energy of the molecule has been estimated to be about 90 kcal/mol [34] so one might think that the molecule may not exist. The central C—C  $\sigma$  bond is expected to



be extraordinarily weak and its rupture to the diradical **11.50b** should require little, if any, activation energy. Yet an amide derivative of **11.50a** has been isolated at  $-30^{\circ}\text{C}$  [35]. It decomposes, presumably via **11.50b**, with an activation energy of 22 kcal/mol. Density functional and ab initio calculations with a high level of CI [36] on **11.50** give **11.50c** to lie 58 kcal/mol lower in energy than **11.50a**. Furthermore, the diradical **11.50b** was found to be about 8 kcal/mol lower in energy than propellane **11.50a**! The computed barrier for the **11.50a** to **11.50b** “bond stretching” reaction was computed to be 19 kcal/mol in good agreement with experiment. Thus, the central C—C bond in **11.50a** has in essence a “negative” bond dissociation energy and yet there is an appreciable activation energy for the simple bond-stretching motion. The reason behind the unexpectedly high activation energy associated with this homolytic cleavage is outlined in **11.51** [37]. In diradical **11.50b** the through-bond interaction provided by the



11.51



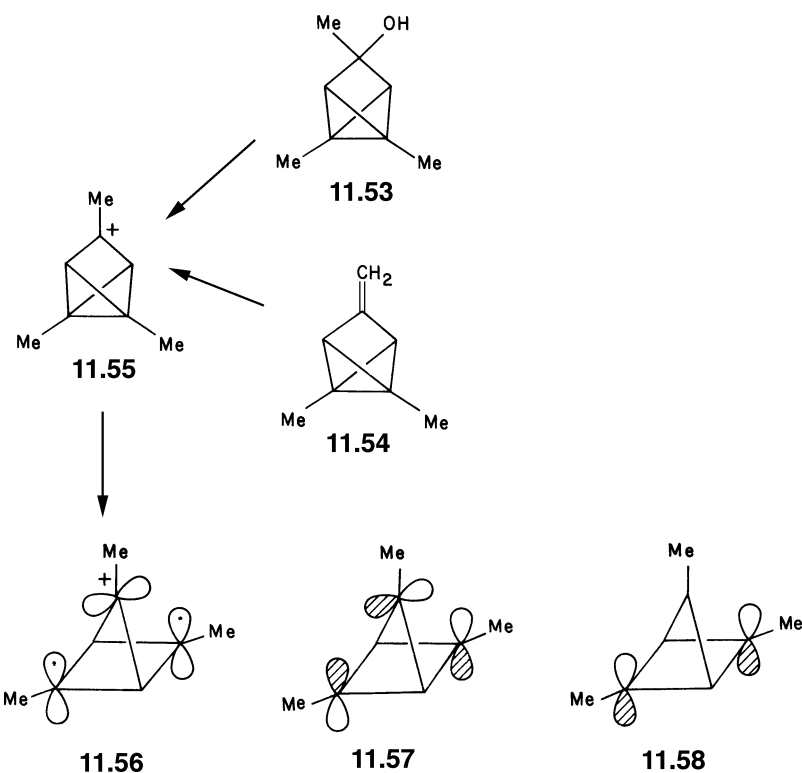
11.52

three C—C  $\sigma$  bonds parallel to the two  $p$  orbitals ensures that the  $n_-$  level lies below  $n_+$ , with a large splitting between them. This is identical to the lone pair-splitting problem in diaza[2.2.2]bicyclooctane, **11.33**. By correlating orbitals that have the same symmetry in **11.51** (a mirror plane which bisects the C—C linkage), one can see that this reaction is symmetry-forbidden. Therefore, **11.50a** is separated from singlet **11.50b** by a sizable barrier.

When two or more stable conformations of a molecule, related to each other by a simple bond stretching, differ in their electronic configuration, this is called bond-stretch isomerization. In the **11.50a** → **11.50b** bond-stretch isomerization, the singlet diradical is actually not stable. It undergoes a symmetry-allowed fragmentation to 1,4-bismethylenecyclohexane, **11.50c** with a tiny activation barrier of 0.3 kcal/mol [36]. It should be emphasized that one cannot gauge, in general, whether or not a molecule can distort along the reaction path thus intermixing the HOMO and LUMO and obliterating the reaction barrier. This can only be investigated by detailed computations at a high level.

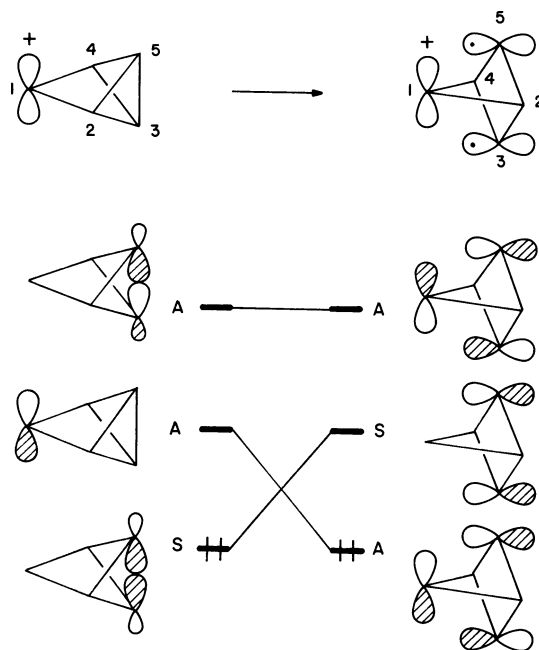
Another interesting example of bond-stretch isomerism is given by the tetrasilabicyclobutane,  $\text{Si}_4\text{H}_6$ , **11.52**. Derivatives of this compound have been shown to undergo a facile ring inversion reaction with an estimated activation energy of only 15 kcal/mol [38]. Initial computations [39] indicated the possibility of “closed” and “open” isomers where the Si—Si bond lengths were found to be 2.38 and 2.91 Å, respectively [40]. One might think that in the “open” form or the transition state for inversion which would have a flat  $D_{2h}$  structure, the in-phase  $\text{SiH}_2 \sigma_\pi$  combination would again destabilize the  $n_+$  hybrid combination above the  $n_-$  one. But this is not the case. The  $\text{SiH}_2$  also has a low-lying  $\sigma_{\pi^*}$  fragment orbital and following the material in Section 10.4, this orbital will play a dominant role. The symmetric  $\sigma_{\pi^*}$  combination will serve to mix into  $n_+$  and stabilize it. Thus,  $n_+$  stays below  $n_-$  as the Si—Si  $\sigma$  bond is broken [39,40]. For the parent  $\text{Si}_4\text{H}_6$  compound, the “open” form of **11.52** was found to be stable and no minimum was found for the closed form [40]. Replacement of the hydrogen atoms on the bridgehead positions by methyl or *t*-butyl groups stabilize the “closed” form relative to the “open” one, however, it remains to be seen whether or not a discrete “open” minimum will be found at a high computational level. This brings up an important caveat when considering the existence of bond-stretch isomers or any other two structures that can be readily interconverted by a simple motion. The existence of two minima on the potential energy surface is not a necessary condition. It may well be that only one of the minima actually exists. This is particularly true when the two structures are interconverted by a symmetry-allowed motion, but it also can be the case when the motion is symmetry-forbidden (particularly when the two isomers differ by large energy amounts).

There are other ways to stabilize a diradical. Solvolysis of **11.53** or protonation of **11.54** initially generates the carbocation **11.55** [41]. The central C—C bond in the bicyclobutane portion of the molecule is again weakened by strain and so bond-stretch isomerization of **11.55** to **11.56** should be possible. Now the antisymmetric combination of the two  $p$  orbitals which form the diradical is markedly stabilized by a through-space interaction with the empty  $p$  orbital on the carbocation. This is illustrated in **11.57**. The symmetric combination, **11.58**,

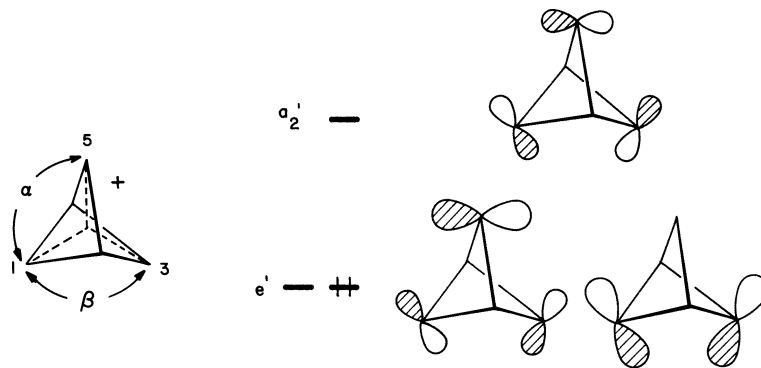


cannot interact with the carbocation  $p$  orbital. So there is a large splitting between filled **11.57** and empty **11.58**. A correlation diagram for the **11.55** → **11.56** interconversion in the parent compound  $C_5H_5^+$  is illustrated in Figure 11.6 [42]. On the left side are the  $\sigma$  and  $\sigma^*$  orbitals of the C—C bond which will be broken along with the  $p$  orbital at C1. These orbitals are classified as being symmetric (S) or antisymmetric (A) with respect to a mirror plane which contains C1, C2, and C4 and bisects the C3—C5 bond. The right side of this figure displays the relevant three orbitals of diradical **11.56**. A bond-stretch process that conserves this mirror plane is symmetry-forbidden. Calculations at all levels [43,44] indicate that the “closed” bond-stretch isomer (analogous to **11.55**) is less stable than the “open” form (**11.56**). All experimental evidence [43,45] is also consistent with this, so the through-space interaction provided by **11.57** does indeed greatly stabilize this diradical.

Let us now consider in more detail how the **11.55** → **11.56** rearrangement is likely to proceed. A measure of how much the C3—C5 bond is stretched can be given by the angles  $\alpha$  and  $\beta$ , as defined in **11.59**. Implicit in the correlation diagram of Figure 11.6 was that  $\alpha = \beta = 140^\circ$  for the “closed” isomer and  $90^\circ$  for the “open” one. Conservation of the mirror plane requires that  $\alpha = \beta$  for all points along

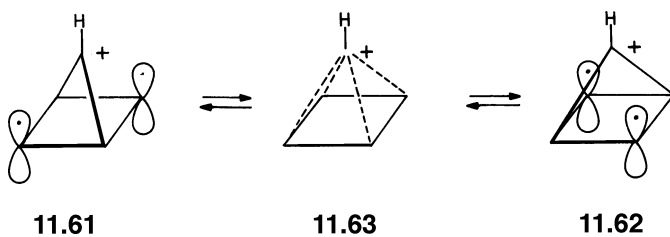
**FIGURE 11.6**

A simplified correlation diagram for bond-stretch isomerization in  $C_5H_5^+$ .

**11.59****11.60**

the reaction path. When  $\alpha = \beta = 120^\circ$ , the geometry of the molecule is  $D_{3h}$ . The three MOs used in Figure 11.6 then transform as  $a'_2$  and  $e'$  symmetry, **11.60**. This is the geometry where the HOMO—LUMO crossing occurs. The  $e'$  set is half-filled and there must be a non-least-motion way to avoid it. This requires that  $\alpha$  and  $\beta$  in **11.59** will vary at different rates along the true minimum energy reaction path. The potential energy surface has the shape shown in Figure 7.7. The coordinates along two edges of the triangle in this figure are  $\alpha$  and  $\beta$ . Structures A, B, and C are three possible (equivalent) “open” isomers in  $C_5H_5^+$ . The transition state(s) that interconnects them, D, is actually the “closed” bond-stretch isomer. Finally the high-energy point E at the center of this surface represents the Jahn–Teller unstable structure where  $\alpha = \beta = 120^\circ$ .

There is something more unusual about the electronic structure of the “open” isomer, redrawn in **11.61**. A bond-switching process converts **11.61** into **11.62** by way of **11.63**. This is a symmetry-allowed reaction [42]. Notice that the symmetry

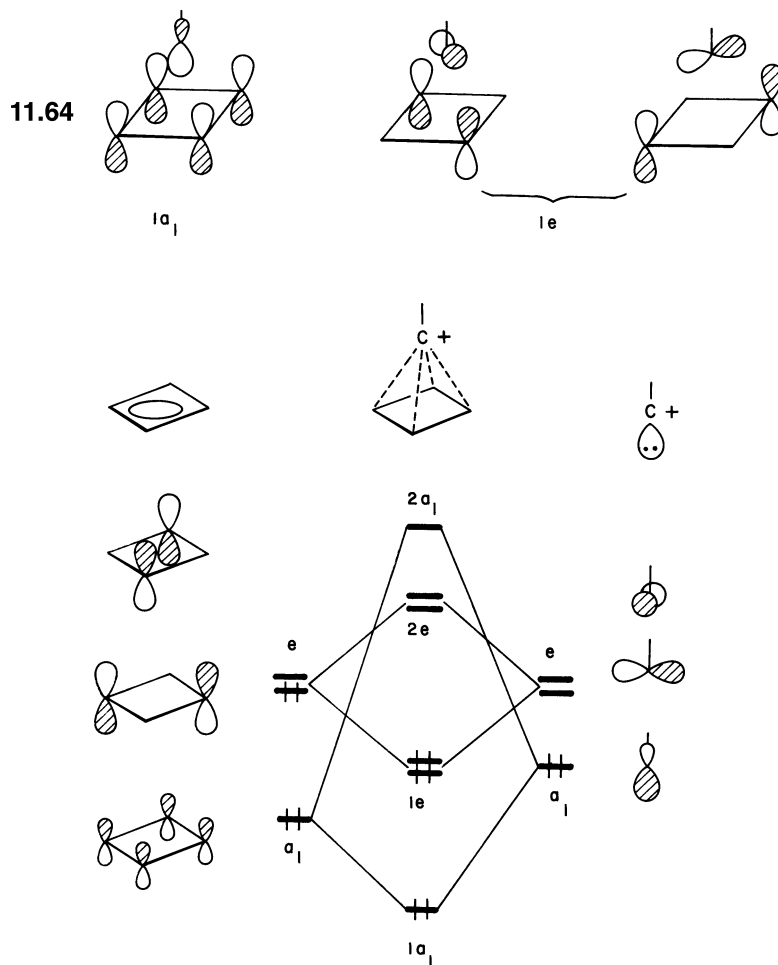


11.61

11.63

11.62

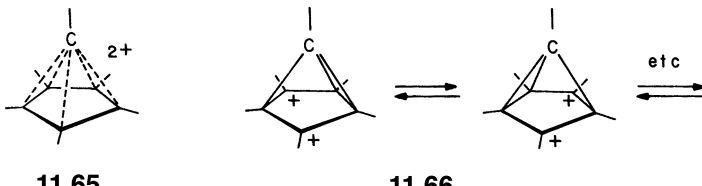
of 11.61 and 11.62 is  $C_{2v}$  while that in 11.63 is  $C_{4v}$ . All experimental evidence on derivatives of  $C_5H_5^+$  indicates that the symmetry of the parent cation is  $C_{4v}$  rather than  $C_{2v}$  [43,45]. In other words, 11.63 is the minimum energy structure of this stabilized diradical, not 11.61. This is also the case for the  $Si_5H_5^+$  congener [46]. The bonding in 11.63 is best described in terms of the interaction diagram in Figure 11.7. On the left side are the  $\pi$  orbitals of cyclobutadiene (see Sections 5.3 and 5.7) and on the right are the fragment orbitals for  $CH^+$  (see Section 9.2). The fragment orbitals are given symmetry labels consistent with the  $C_{4v}$  symmetry of the molecule. Both fragment orbitals of  $a_1$  symmetry combine to produce a bonding ( $1a_1$ ) and antibonding ( $2a_1$ ) MO. Likewise the  $e$  set on both fragments overlap substantially to produce a bonding ( $1e$ ) and antibonding ( $2e$ ) set. The highest  $\pi$  level of cyclobutadiene (not shown in the Figure) remains nonbonding. There are a total of six electrons in these valence orbitals which fill the  $1a_1$  and  $1e$  levels. These filled bonding MOs are shown in 11.64.

**FIGURE 11.7**

An orbital interaction diagram for  $C_5H_5^+$ . The fragment orbitals are labeled according to the  $C_{4v}$  symmetry of the molecule. The highest energy  $C_4H_4 \pi$  orbital has been left off for simplicity.

It can be seen that  $l_{a_1}$  and one member of the  $l_e$  set correspond to symmetry-adapted combinations of the two C—C  $\sigma$  bonds between the apical C—H unit and the four-membered ring as were explicitly drawn out in the classical structures of **11.61** or **11.62**. The other member of the  $l_e$  set is then identical to the lowest (filled) orbital of Figure 11.6. So this delocalized picture in Figure 11.7 suggests that there is actually little difference between **11.61** (and **11.62**) and **11.63**. In fact, **11.61** and **11.62** can be regarded as resonance structures which contribute to the electronic structure of the  $C_5H_5^+$  isomer with  $C_{4v}$  symmetry. Such delocalized pictures of cage molecules will form the basis of Chapter 22. The  $C_{4v}$  structure **11.63** of  $C_5H_5^+$  is not unusual when viewed in the context of cage and cluster molecules in general. There are clearly four equivalent C—C distances between the apical carbon and the remaining four basal carbon atoms and a total of six electrons in the bonding MOs (**11.64**). Therefore, one can view each apical–basal interaction as containing 1.5 electrons. In other words, this is another example of electron-deficient bonding. Two-center-two-electron bonding between the apical and basal carbons is not going to be an energetically favorable situation. There would then be eight electrons in the interaction diagram of Figure 11.7. The extra two electrons will need to be placed in the antibonding  $2e$  set.

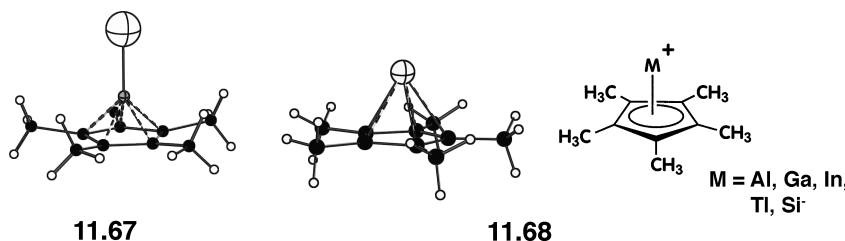
A number of other carbocations similar to  $C_5H_5^+$  have been studied, the most notable being  $C_6Me_6^{2+}$ . It has been demonstrated [47,48] that the structure of this cation is  $C_{5v}$ , **11.65**, rather than a rapidly equilibrating series of classical structures, **11.66**, where a bond-switching process permutes three two-center-two-electron bonds around the five-membered ring. An orbital interaction diagram for **11.65**



11.65

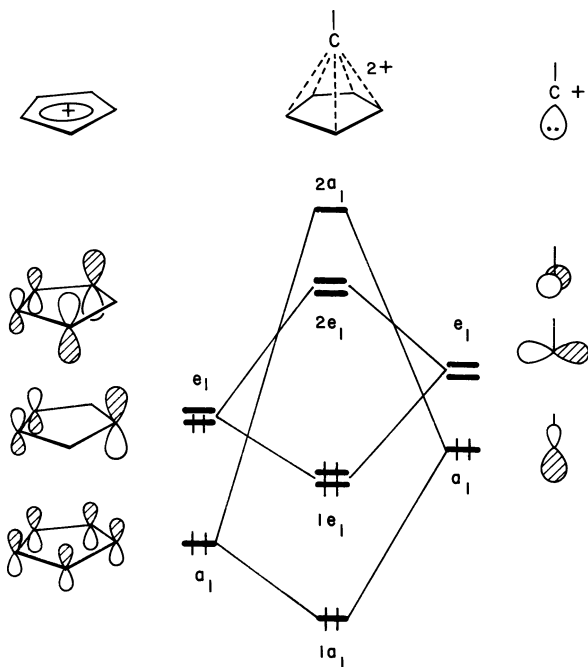
11.66

where all methyl groups have been replaced by hydrogen atoms is shown in Figure 11.8. The  $\pi$  orbitals of a cyclopentadienyl cation have been taken from Sections 5.6 and 5.7. The bonding in  $C_6H_6^{2+}$  has several features in common with  $C_5H_5^+$ . Again the three fragment orbitals of the  $CH^+$  “capping” unit find good matches in overlap and energy with the three lowest  $\pi$  orbitals in the cyclopentadienyl cation fragment. Three bonding MOs ( $l_{a_1} + l_{e_1}$ ) are produced. Six electrons nicely fill these orbitals to produce a stable structure. A compound with two more electrons,  $C_6H_6$ , cannot have this  $C_{5v}$  structure because the antibonding  $2e_1$  is half-filled. The intracluster bonding between the apical CH unit and the five basal carbons is again electron-deficient. This bonding motif is not that unusual. The structure [49] of  $(C_5Me_5)B-Br^+$  is shown in **11.67**. In fact there are a series of  $C_5Me_5-M^+$  compounds given by **11.68**,



11.67

11.68

**FIGURE 11.8**

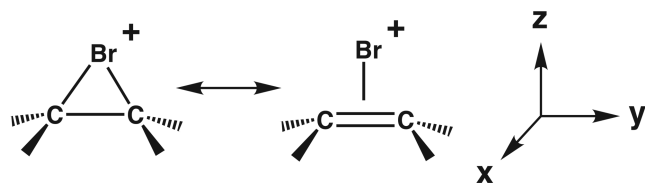
An orbital interaction diagram for  $C_6H_6^{2+}$ . The fragment orbitals are labeled according to the  $C_{5v}$  symmetry of the molecule.

where  $M = Al, Ga, In$ , and  $Tl$  along with  $C_5Me_5-Si$ . These molecules have all been structurally categorized [50] and have the  $C_{5v}$  structure implied by 11.68. Considering that there is one lone pair on the  $M$  atom which takes the place of the  $C-H$  bond in  $C_6H_6^{2+}$ , 11.68 is, therefore, isoelectronic to  $C_6H_6^{2+}$ .

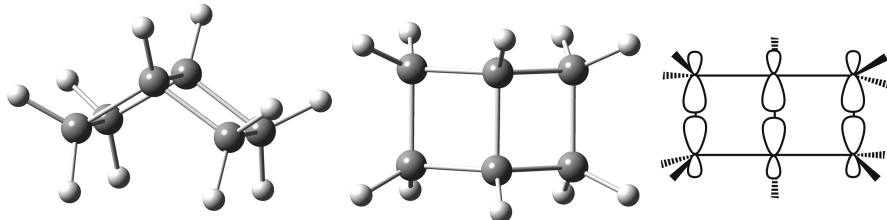
The pattern we have presented here for  $C_5H_5^+$  and  $C_6H_6^{2+}$  can be extended to any type or number of capping units and any size of carbocyclic ring [51]. A stable electronic configuration is achieved when there are six intracluster electrons partitioned between the capping unit and carbocyclic ring. The  $C_{4v}$  structure of  $C_5H_5^+$  and even the existence of  $C_6H_6^{2+}$  may be unsettling to organic chemists. We have noted earlier that such “unusual” arrangements fit in to quite a general pattern when considered in the wider context of cage and cluster molecules. In fact,  $C_5H_5^+$  and  $C_6H_6^{2+}$  are a small subset of fully categorized compounds that have identical shapes and bonding features. We shall return to  $C_5H_5^+$  and  $C_6H_6^{2+}$  to explore these relationships in the later chapters.

## PROBLEMS

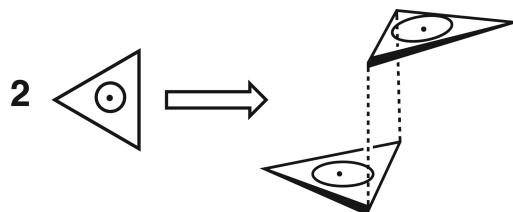
- 11.1.** The mechanism for the electrophilic addition of bromine to olefins has been known for a very long time. It consists of two steps where a cyclic bromonium ion serves as an intermediate. In 1951, M. J. S. Dewar offered an MO argument for the bonding in this compound which in turn led to the Dewar-Chatt-Duncanson model of metal-olefin bonding which we will discuss extensively in Chapter 19. His argument was that there are two important resonance structures associated with the bromonium ion as shown below. The structure on the left side is a molecule where there are two  $C-Br$   $\sigma$  bonds. The structure on the right side is a  $\pi$  complex. Let us work through what the  $\pi$  complex is composed of by interacting the  $\pi$  and  $\pi^*$  orbitals of ethylene with the s and p AOs of  $Br^+$  (using the coordinate system shown below). Fill the MOs with the correct electron count. Finally write out the perturbation theory equations for the MOs in each case and draw out the resultant MOs.



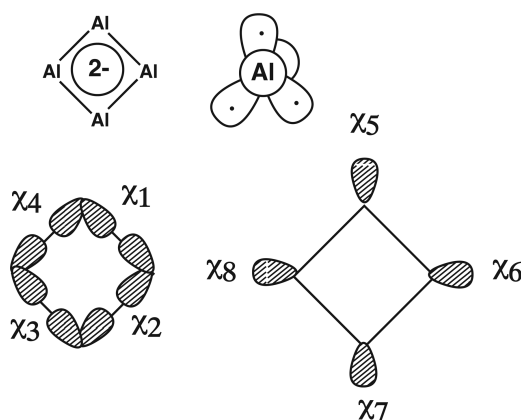
- 11.2.** A side and top view of bicyclo[2.2.0]hexane is shown below. Given  $sp^3$  hybrids shown on the right side, determine the MOs and relative energies for the  $\sigma$  and  $\sigma^*$  orbitals.  
Hint: remember that in terms of overlap  $\sigma > \pi$ .



- 11.3.** There is a somewhat novel idea that two cyclopropenium radicals can be held together in a very loose (i.e., long bond lengths) complex as shown below. Show how the bonding in this complex comes about using the  $\pi$  orbitals of each cyclopropenium radical.



- 11.4.** A  $D_{4h}$   $\text{Al}_4^{2-}$  structure has been proposed for a compound observed in the gas phase when lasers vaporize Al metal and  $\text{Na}_2\text{CO}_3$ . One could describe the bonding in this molecule using  $sp^2$  hybrids for the Al—Al  $\sigma$  bonds,  $\chi_1$ — $\chi_4$ , and the lone pairs,  $\chi_5$ — $\chi_8$ . The remaining  $p$  AO s are used for the  $\pi$  orbitals. Form SALCs of them (you ought to be able to do this without resorting to the whole procedure) and order them in energy. As a convention let the two mirror planes passing through the Al atoms be  $\sigma_v$  and those passing through the Al—Al bonds,  $\sigma_d$ . Likewise the two  $C_2$  axis passing through the atoms are  $C_2'$  and those passing through the bonds are  $C_2''$ .



Listed below is an extended Hückel calculation for this molecule. The  $e_u$  lone pair set lies at a high energy. What has happened?

---

**Al<sub>4</sub><sup>2-</sup> Cartesian Coordinates**


---

	Name	No.	x	y	z
POS	AL-I-1	1	1.841000	0.000000	0.000000
POS	AL-I-2	2	0.000000	-1.840000	0.000000
POS	AL-I-3	3	0.000000	1.840000	0.000000
POS	AL-I-4	4	-1.840000	0.000000	0.000000

---

**Molecular Orbitals**

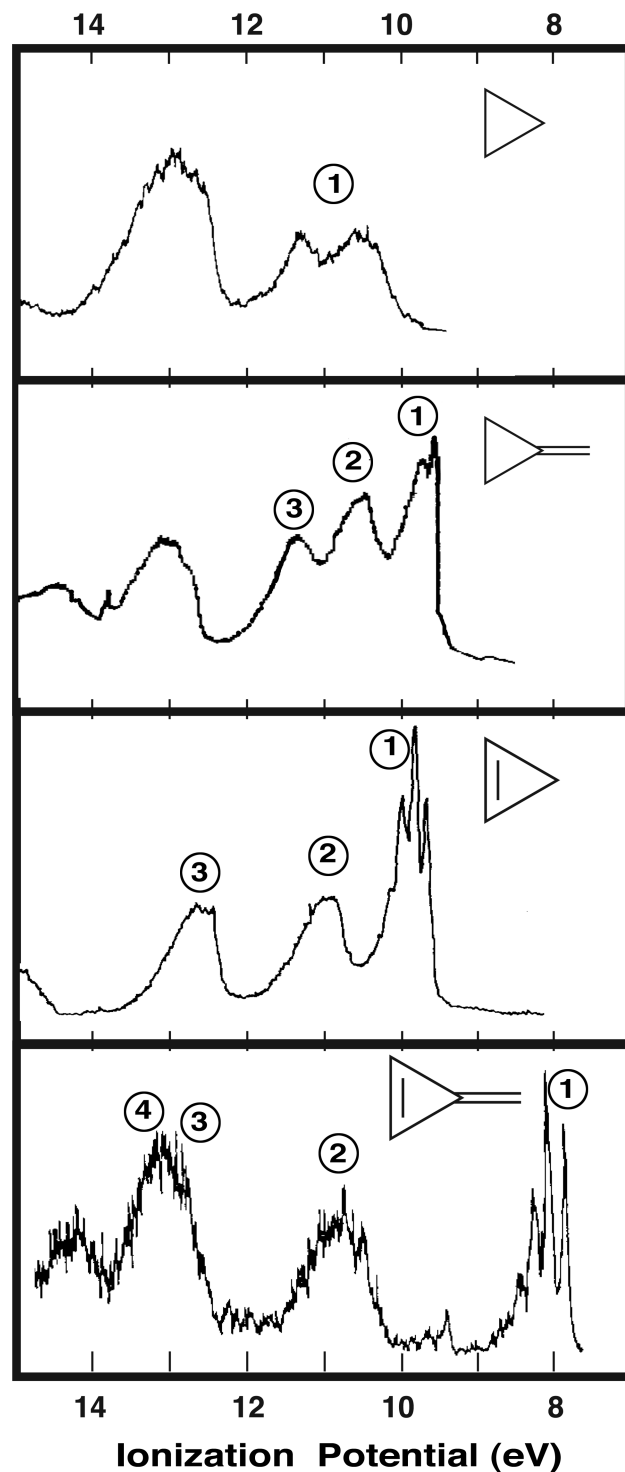
		1	2	3	4	5	6	7	8	9	10	11	12
	eigenvalues (eV)	-16.878	-12.432	-12.432	-8.281	-8.244	-8.167	-6.850	-6.097	-6.097	-5.815	-5.815	-2.929
AL-I-1	s	1	-0.3517	-0.5295	0.0000	0.0000	0.0000	0.3274	-0.1731	0.0000	0.0000	0.1215	0.0000
	P <sub>x</sub>	2	0.0076	-0.1042	0.0000	0.0000	0.0000	0.4111	-0.4008	0.0000	0.0000	0.6792	0.0000
	P <sub>y</sub>	3	0.0000	0.0000	0.2620	0.0000	0.4008	0.0000	0.0000	0.0000	0.0000	0.0000	0.3073
	P <sub>z</sub>	4	0.0000	0.0000	0.0000	0.3982	0.0000	0.0000	0.0000	0.7360	0.0000	0.0000	0.6578
AL-I-2	s	5	-0.3518	0.0000	-0.5293	0.0000	0.0000	-0.3272	-0.1732	0.0000	0.0000	0.0001	0.1216
	P <sub>x</sub>	6	0.0000	-0.2621	0.0000	0.0000	-0.4007	-0.0001	0.0001	0.0000	0.0000	-0.3070	0.0000
	P <sub>y</sub>	7	-0.0076	0.0000	0.1043	0.0000	0.0001	0.4107	0.4011	0.0000	0.0000	0.0000	-0.6795
	P <sub>z</sub>	8	0.0000	0.0000	0.0000	0.3984	0.0000	0.0000	0.0000	-0.0001	0.7358	0.0000	-0.6581
AL-I-3	s	9	-0.3518	0.0000	0.5293	0.0000	0.0000	-0.3272	-0.1732	0.0000	0.0000	0.0001	-0.1216
	P <sub>x</sub>	10	0.0000	-0.2621	0.0000	0.0000	0.4007	-0.0001	0.0001	0.0000	0.0000	-0.3070	0.0000
	P <sub>y</sub>	11	0.0076	0.0000	0.1043	0.0000	0.0001	-0.4107	-0.4011	0.0000	0.0000	0.0000	-0.6795
	P <sub>z</sub>	12	0.0000	0.0000	0.0000	0.3984	0.0000	0.0000	0.0000	-0.0001	-0.7358	0.0000	-0.6581
AL-I-4	s	13	-0.3518	0.5292	0.0000	0.0000	0.0000	0.3273	-0.1730	0.0000	0.0000	-0.1217	0.0000
	P <sub>x</sub>	14	-0.0076	-0.1042	0.0000	0.0000	0.0000	-0.4109	0.4006	0.0000	0.0000	0.6797	0.0000
	P <sub>y</sub>	15	0.0000	0.0000	0.2622	0.0000	-0.4007	0.0000	0.0000	0.0000	0.0000	0.3072	0.0000
	P <sub>z</sub>	16	0.0000	0.0000	0.0000	0.3984	0.0000	0.0000	0.0000	-0.7354	0.0000	0.0000	0.6585

---

		13	14	15	16
		5.411	19.479	19.479	88.979
AL-I-1	s	1	0.0000	0.0000	1.0276
	P <sub>x</sub>	2	0.0000	0.0000	-0.6655
	P <sub>y</sub>	3	-0.9285	-0.9058	0.0000
	P <sub>z</sub>	4	0.0000	0.0000	0.0000
AL-I-2	s	5	-0.0007	-1.0271	-0.0005
	P <sub>x</sub>	6	-0.9278	0.0012	-0.9075
	P <sub>y</sub>	7	-0.0005	-0.6649	-0.0003
	P <sub>z</sub>	8	0.0000	0.0000	0.0000
AL-I-3	s	9	0.0007	1.0271	-0.0005
	P <sub>x</sub>	10	0.9278	-0.0012	-0.9075
	P <sub>y</sub>	11	-0.0005	-0.6649	0.0003
	P <sub>z</sub>	12	0.0000	0.0000	0.0000
AL-I-4	s	13	0.0000	0.0000	-1.0266
	P <sub>x</sub>	14	0.0000	0.0000	-0.6642
	P <sub>y</sub>	15	0.9270	-0.9085	0.0000
	P <sub>z</sub>	16	0.0000	0.0000	0.0000

---

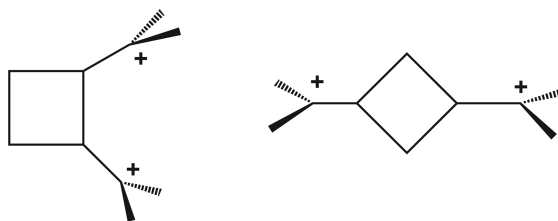
**11.5.** Assign the ionizations indicated in the PE spectra for cyclopropane, methylenecyclopropane, cyclopropene, and methylenecyclopropene.



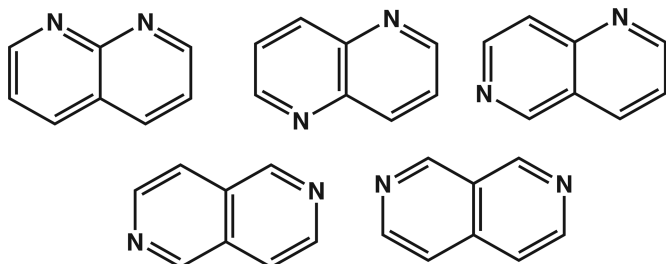
**11.6.** If you have not done so, please do Problem 3.7. There are two sets of  $\sigma$  symmetry-adapted linear combinations that were constructed in this problem.

- Combine the sets that have the same symmetry.

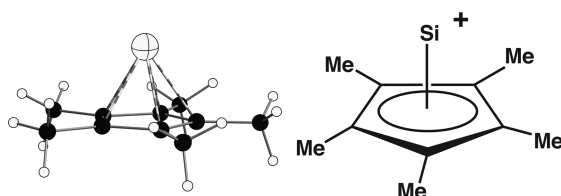
- b. Suppose one could make the bismethylenecyclobutane dication. There are two isomers shown below. Using 11.16 as a guide evaluate the stability of each structure.



- 11.7. Evaluate the symmetric ( $n_s$ ) versus antisymmetric ( $n_A$ ) lone-pair energy ordering for the diazanaphthalenes drawn as follows.



- 11.8. The remarkable compound shown below was recently prepared and structurally categorized by an X-ray structure [50]. Construct an orbital interaction diagram for this compound taking the  $\pi$  MOs of cyclopentadienyl anion and interacting them with the valence AOs of  $\text{Si}^{2+}$ . Hint: there are no  $d$  AOs on Si!



## REFERENCES

1. R. Hoffmann, *Acc. Chem. Res.*, **4**, 1 (1971).
2. R. Gleiter, *Angew Chem. Int. Ed.*, **13**, 696 (1974); R. Gleiter and G. Haberhauer, *Aromaticity and Other Conjugation Effects*, Wiley-VCH, Weinheim (2012).
3. M. N. Paddon-Row, *Acc. Chem. Res.*, **15**, 245 (1982).
4. J. W. Verhoeven, *Rec. J. Roy. Neth. Chem. Soc.*, **99**, 369 (1980); E. I. Brodskaya, G. V. Ratovskii, and M. G. Voronkov, *Russ. Chem. Rev.*, **62**, 919 (1993); H. Bock and B. G. Ramsey, *Angew. Chem. Int. Ed.*, **12**, 734 (1973).
5. R. Hoffmann, *XXIIIrd International Congress of Pure and Applied Chemistry*, Vol. **2**, Butterworths, London (1971), p. 233.
6. W. L. Jorgensen and L. Salem, *The Organic Chemist's Book of Orbitals*, Academic Press, New York (1973).
7. R. Gleiter, *Topics Current Chem.*, **86**, 199 (1979).
8. A. D. Walsh, *Trans. Faraday Soc.*, **45**, 179 (1949); E. Honneger, E. Heilbronner, A. Schmelzer, and W. Jian-Qi, *Isr. J. Chem.*, **22**, 3 (1982).

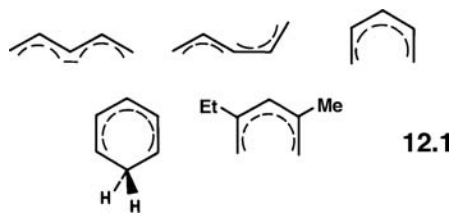
9. F. Stabenow, W. Saak, H. Marsmann, M. Weidenbruch, *J. Am. Chem. Soc.*, **125**, 10172 (2003).
10. E. Honegger, E. Heilbronner, and A. Schmelzer, *Nov. J. Chim.*, **11**, 519 (1982).
11. D. S. Kabakoff and E. Namanworth, *J. Am. Chem. Soc.*, **92**, 3234 (1970).
12. W. J. Hehre, *Acc. Chem. Res.*, **8**, 369 (1975).
13. M. A. M. Meester, H. Schenk, and C. H. MacGillavry, *Acta Cryst.*, **B27**630 (1971).
14. C. J. Collins, *Chem. Rev.*, **69**, 543 (1969).
15. S. Winstein and J. Sonnenberg, *J. Am. Chem. Soc.*, **83**, 3235, 3244 (1961).
16. R. Hoffmann, *J. Am. Chem. Soc.*, **90**, 1475 (1968); N. G. Rondan, K. N. Houk, and R. A. Moss, *J. Am. Chem. Soc.*, **102**, 1770 (1980); P. H. Mueller, N. G. Rondan, K. N. Houk, J. F. Harrison, D. Hooper, B. W. Willen, and J. F. Leibman, *J. Am. Chem. Soc.*, **103**, 5049 (1981); R. A. Moss, W. Guo, D. Z. Denney, K. N. Houk, and N. G. Rondan, *J. Am. Chem. Soc.*, **103**, 6164 (1981).
17. R. Hoffmann and R. B. Davidson, *J. Am. Chem. Soc.*, **93**, 5699 (1971).
18. S. Pederen, J. L. Herek, and A. H. Zewail, *Science*, **266**, 159 (1994).
19. H. Prinzbach, G. Gescheidt, H.-D. Martin, R. Herges, J. Heinze, G. K. Surya Prakash, and G. A. Olah, *Pure Appl. Chem.*, **67**, 673 (1995) and references therein.
20. R. B. Woodward and R. Hoffmann, *The Conservation of Orbital Symmetry*, Academic Press, New York (1970).
21. T. L. Gilchrist and R. G. Storr, *Organic Reactions and Symmetry*, Cambridge University Press, London (1972); A. P. Marchand and R. E. Lehr, editors, *Pericyclic Reactions*, Vol. **1** and **2**, Academic Press, New York (1977); I. Fleming, *Frontier Orbitals and Organic Chemical Reactions*, Wiley, London (1976); K. N. Houk, *Acc. Chem. Res.*, **8**, 361 (1975); Nguyen Trong Anh, *Die Woodward-Hoffmann-Regeln und ihre Anwendung*, Verlag Chemie, Weinheim (1972).
22. W. L. Jorgensen and W. T. Borden, *J. Am. Chem. Soc.*, **95**, 6649 (1973).
23. P. Bischof, J. A. Hashmall, E. Heilbronner, and V. Hornung, *Tetrahedron Lett.* 4025 (1969).
24. E. Heilbronner and K. A. Muszkat, *J. Am. Chem. Soc.*, **92**, 3818 (1970).
25. K. K. Baldridge, T. R. Battersby, R. Veron Clark, and J. K. Siegel, *J. Am. Chem. Soc.*, **119**, 7048 (1997).
26. P. Bruesch, *Spectrochim. Acta*, **22**, 861, 867 (1966); P. Bruesch and Hs. H. Gunthard, *Spectrochim. Acta*, **22**, 877 (1966).
27. K. A. Muszkat and J. Schaublin, *Chem. Phys. Lett.*, **13**, 301 (1972).
28. R. Gleiter, E. Heilbronner, M. Heckman, and H.-D. Martin, *Chem. Ber.*, **106**, 28 (1973).
29. L. A. Curtiss, C. A. Naleway, and J. R. Miller, *J. Phys. Chem.*, **99**, 1182 (1995) and references therein.
30. J. W. Verhoeven and P. Pasman, *Tetrahedron*, **37**, 943 (1981).
31. H.-D. Martin and R. Schwesinger, *Chem. Ber.*, **107**, 3143 (1974).
32. E. Heilbronner, *Israel J. Chem.*, **10**, 142 (1972); R. Hoffmann, E. Heilbronner, and R. Gleiter, *J. Am. Chem. Soc.*, **92**, 706 (1970).
33. W. T. Borden, editor, *Diradicals*, Wiley, New York (1982).
34. M. D. Newton and J. M. Schulman, *J. Am. Chem. Soc.*, **94**, 4391 (1972).
35. P. E. Eaton and G. H. Temme, *J. Am. Chem. Soc.*, **95**, 7508 (1973).
36. E. R. Davidson, *Chem. Phys. Lett.*, **284**, 301 (1998).
37. W.-D. Stohrer and R. Hoffmann, *J. Am. Chem. Soc.*, **94**, 779 (1972).
38. S. Masamune, Y. Kabe, and S. Collins, *J. Am. Chem. Soc.*, **107**, 5552 (1985).
39. W. W. Schoeller, T. Dabisch, and T. Busch, *Inorg. Chem.*, **26**, 4383 (1987).
40. J. A. Boatz and M. S. Gordon, *Organometallics*, **15**, 2118 (1996).
41. V. I. Minkin, N. S. Zefirov, M. S. Korobov, N. V. Averina, A. M. Boganov, and L. E. Nivorozhkin, *Zh. Org. Khim.*, **17**, 2616 (1981).
42. W.-D. Stohrer and R. Hoffmann, *J. Am. Chem. Soc.*, **94**, 1661 (1972).

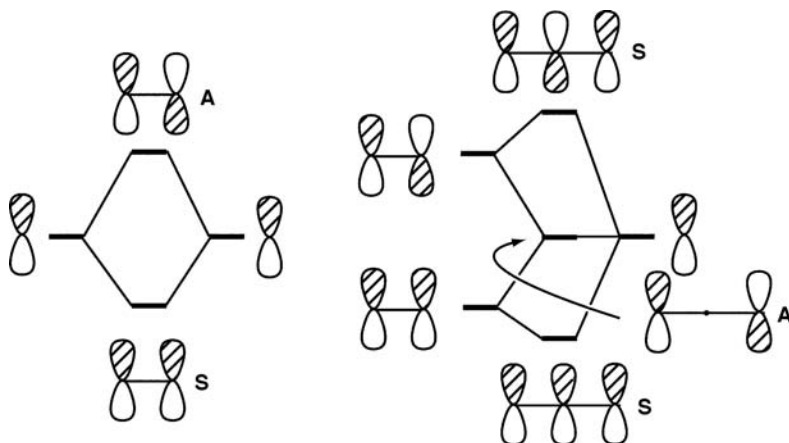
43. H. Schwartz, *Angew. Chem.*, **93**, 1046 (1981); *Angew. Chem. Int. Ed. Engl.*, **20**, 991 (1981); V. I. Minkin and R. M. Minyaev, *Usp. Khim.*, **51**, 586 (1982) Eng. Trans., **51**, 332 (1982); N. S. Lokbani, K. Costuas, J.-F. Halet, and J.-Y. Saillard, *J. Mol. Struct. (Theochem.)*, **571**, 1 (2001).
44. J. Feng, J. Leszczynski, B. weiner, and M. C. Zerner, *J. Am. Chem. Soc.*, **111**, 4648 (1989); M. N. Glukhovtsev and P.V.R. Schleyer, *Mendeleev Commun.*, **100** (1993).
45. G. Maier, H. Rang, and H. O. Kalinowski, *Angew. Chem. Int. Ed.*, **28**, 1232 (1989).
46. A. A. Korkin, V. V. Murashov, J. Leszcznshi, and P. V. R. Schleyer, *J. Phys. Chem.*, **99**, 17742 (1995).
47. H. Hogewe and P. W. Kwant, *Acc. Chem. Res.*, **8**, 413 (1975).
48. H. Hogewe and E. M. G. A.van Kruchten, *J. Org. Chem.*, **46**, 1350 (1981).
49. C. Dohmeier, R. Koppe, C. Robl, and H. Schnockel, *J. Organomet. Chem.*, **487**, 127 (1995).
50. A Haaland, K.-G. Martinsen, S. A. Shlykov, H. V. Volden, C. Dohmeier, and H. Schnöckel, *Organometallics*, **14**, 3116 (1995) and references therein; P. Jutzi, A. Mix, B. Rummel, W. W. Schoeller, B. Neumann, and H.-G. Stammmer, *Science*, **305**, 849 (2004).
51. E. D. Jemmis and P. V. R. Schleyer, *J. Am. Chem. Soc.*, **104**, 4781 (1982).

# Polyenes and Conjugated Systems

## 12.1 ACYCLIC POLYENES

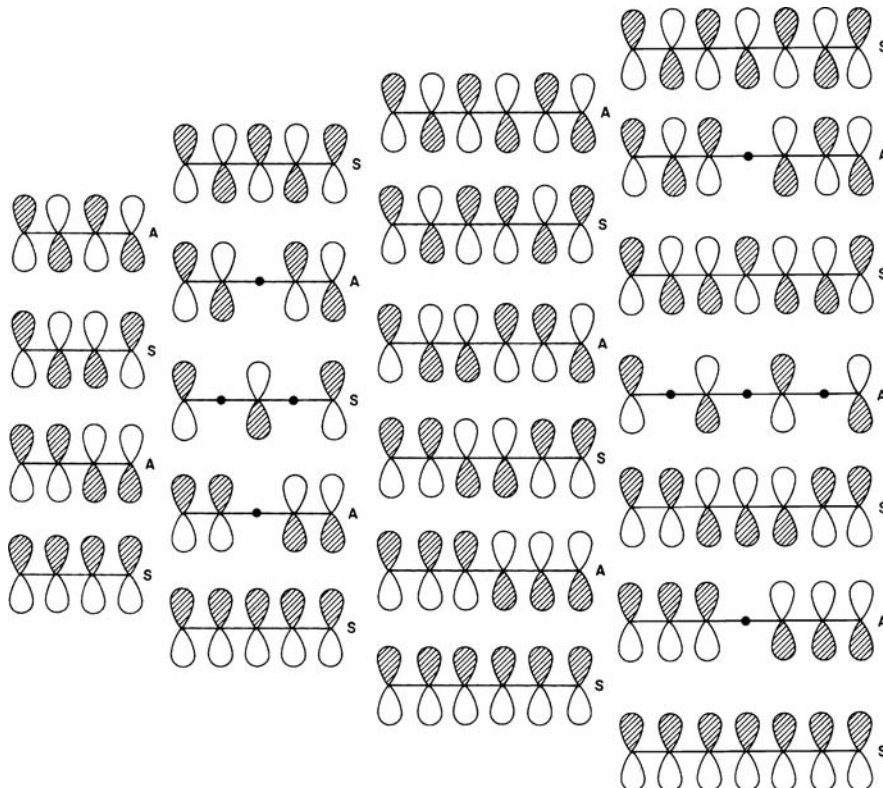
Here we will build up in general the  $\pi$  orbitals of a conjugated chain of  $N$  carbon atoms. We can start from the simple case of ethylene shown in Figure 12.1 and add on an extra orbital to get to allyl. We will not spend any time describing how the form of these orbitals actually come about since this three orbital problem is identical to the  $H_3$  problem in Sections 3.3 and 4.8. The result is a low-energy orbital bonding between each pair of adjacent atoms, a higher energy nonbonding orbital with a node at the central atom and a higher lying orbital which is antibonding between both pairs of adjacent atoms. One could easily continue in this vein, for example, the orbitals of butadiene could be constructed from two ethylenes and pentadienyl from the union between the allyl system and ethylene. These orbital interactions are straightforward and will not be further elaborated here. Figure 12.2 shows the orbitals of the lowest few polyenes which may be built up in a similar way. Although we have drawn the carbon backbone in a straight line for simplicity, these orbitals are applicable to real systems with perhaps very different geometries. For example, the pentadienyl orbitals apply to all the species given in 12.1. There are some general rules which guide us in their derivation:



**FIGURE 12.1**

The  $\pi$  orbitals of ethylene, assembled from two  $\text{CH}_2$  units on the left side. On the right side, the  $\pi$  orbitals of allyl, assembled from the corresponding orbitals of ethylene and a  $\text{CH}_2$  group.

- As their energy increases, the orbitals alternate in parity with respect to a mirror plane which is perpendicular to and bisects the  $\pi$  system. The lowest energy orbital is always symmetric with respect to this plane.
- The number of nodes perpendicular to the chain increases by one on going from one orbital to the one next highest in energy. The lowest energy orbital always has zero nodes (bonding between each pair of adjacent atoms) and the highest energy orbital always has nodes between every adjacent pair (i.e., it is antibonding between all such pairs).
- Nodes must always be symmetrically located with respect to the central mirror plane.

**FIGURE 12.2**

The  $\pi$  orbitals of the first few linear chain polyenes. No attempt has been made to represent the different orbital coefficients. The orbitals are labeled either symmetric or antisymmetric with respect to the mirror symmetry which bisects the length of the chain.

4. In systems with an odd number of atoms, the antisymmetric levels always have a node at the central carbon atom.

In Section 12.2 we use simple Hückel theory to quantify these results.

## 12.2 HÜCKEL THEORY

In this section we use simple Hückel theory to quantify the results summarized in Section 12.1. Conjugated  $\pi$  systems in carbon compounds represent one of the few areas where simple algebraic expressions may be easily derived for the orbital energies and wavefunctions. The basis of Hückel's approach is very simple indeed. All the  $\pi$  orbitals are antisymmetric with respect to reflection in the plane of the molecule, while the  $\sigma$  type orbitals by definition are symmetric with respect to this symmetry operation. Thus there is no overlap between the  $\sigma$  and  $\pi$  sets. So one can treat the  $\pi$  orbitals alone when using a one-electron theory as implicitly assumed in Section 12.1. In this approach, interactions are ignored between  $p_\pi$  orbitals located on atoms which are not directly linked via the  $\sigma$  framework, and the overlap integrals between all pairs of  $p_\pi$  orbitals, whether directly linked or not, are set equal to zero. The energy of each carbon  $p_\pi$  orbital before interaction (Coulomb integral) is put equal to  $\alpha$  ( $= e_i^0$ ) and the interaction energy between two adjacent  $p_\pi$  orbitals equal to  $\beta$  ( $= H_{ij}$ ), the resonance integral. The secular equations (Section 1.3) describing the interaction of the two  $p_\pi$  orbitals in ethylene are given by equation 12.1

$$\begin{aligned} (\alpha - e)c_{1i} + \beta c_{2i} &= 0 \\ \beta c_{1i} + (\alpha - e)c_{2i} &= 0 \end{aligned} \quad (12.1)$$

where  $e$  is the energy of the resulting molecular orbital and  $c_{1i}$  and  $c_{2i}$  are the coefficients of the atomic orbitals on atoms 1, 2, in MO  $\psi_i = c_{1i}\chi_1 + c_{2i}\chi_2$ . The secular determinant is then

$$\begin{vmatrix} \alpha - e & \beta \\ \beta & \alpha - e \end{vmatrix} = 0 \quad (12.2)$$

with roots

$$e = \alpha \pm \beta \quad (12.3)$$

for the energies of the two MOs  $\psi_i$ ,  $\alpha$  and  $\beta$  are both negative so the plus sign refers to the bonding level and the minus sign to the antibonding one. Substitution of  $e = \alpha + \beta$  into either of the equation 12.1 gives the relationship  $c_{1i} = c_{2i}$  and substitution of  $e = \alpha - \beta$  gives  $c_{1i} = -c_{2i}$ . Because interatomic overlap has been neglected, the normalization condition is very simple and leads directly to the numerical values for (equation 12.4)

$$1 = \int \psi_i^* \psi_i d\tau = c_{1i}^* c_{1i} \int \chi_1^* \chi_1 d\tau + c_{2i}^* c_{2i} \int \chi_2^* \chi_2 d\tau = c_{1i}^2 + c_{2i}^2 \quad (12.4)$$

the orbital coefficients (equation 12.5).

$$\begin{aligned} \psi_{\text{bonding}} &= \frac{1}{\sqrt{2}}(\chi_1 + \chi_2) \\ \psi_{\text{antibonding}} &= \frac{1}{\sqrt{2}}(\chi_1 - \chi_2) \end{aligned} \quad (12.5)$$

This is the most simple type of one-electron model, and we could imagine with a very basic form of the wavefunctions and a two-parameter form for the energies. In principle, it is then a straightforward matter to generate the energy levels and orbital coefficients for any conjugated system, whether acyclic, cyclic, polycyclic, or generally complex, by solution of the relevant determinant. Equation 12.6 shows the secular determinant for allyl **12.2**. Since atoms 1 and 3 are not directly



$$\begin{vmatrix} \alpha - e & \beta & 0 \\ \beta & \alpha - e & \beta \\ 0 & \beta & \alpha - e \end{vmatrix} = 0 \quad (12.6a)$$

connected, a zero appears in the 1, 3 and 3, 1 positions of the secular determinant. The MOs  $\psi_i = c_{1i}\chi_1 + c_{2i}\chi_2 + c_{3i}\chi_3$  of **12.2** satisfy the normalization condition

$$1 = c_{1i}^2 + c_{2i}^2 + c_{3i}^2 \quad (12.6b)$$

Figure 12.3a shows the orbital energies obtained by solving equation 12.6a as well as the orbital coefficients determined from equation 12.6b and the secular equations leading to equation 12.6a. The orbital energies and orbital coefficients of the MOs of 1,3-butadiene, obtained in an analogous manner, are shown in Figure 12.3b. The orbitals of these species may also be derived along exactly analogous lines to those

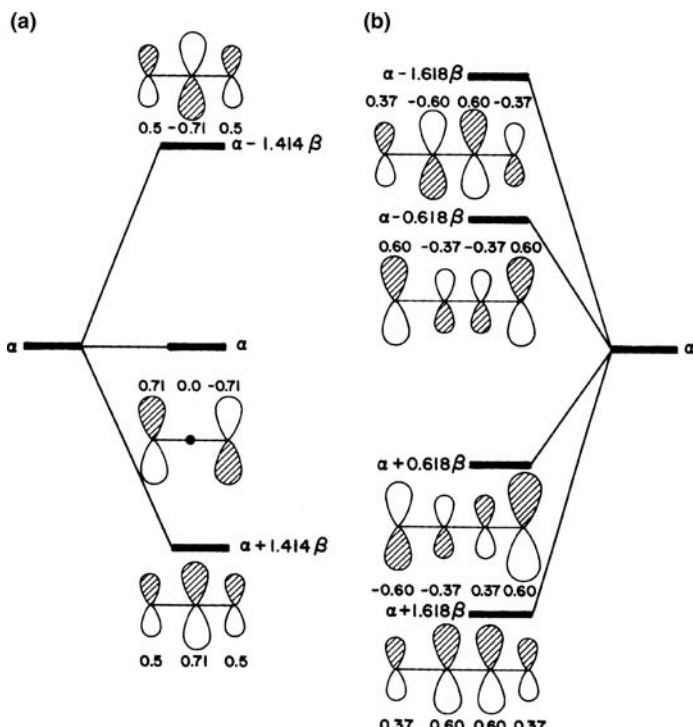


**FIGURE 12.3**

The Hückel  $\pi$  energy levels and coefficients of the (a) allyl and (b) butadiene systems.

used for the linear  $H_4$  problem of Section 5.5. Similarly the pattern for linear  $H_3$  looks just like that for allyl.

Simple functions describe both the energy levels and orbital coefficients for these acyclic systems. The energy of the  $j^{\text{th}}$  MO for a system with  $N p_{\pi}$  orbitals is given by

$$e_j = \alpha + 2\beta \cos \frac{j\pi}{N+1} \quad (12.7)$$

The orbital coefficient for the  $r^{\text{th}}$  atomic orbital in molecular orbital  $\psi_j$  where  $j$  runs from 1 to  $N$ , is given by

$$c_{rj} = \left( \frac{2}{N+1} \right)^{1/2} \sin \left( \frac{rj\pi}{N+1} \right) \quad (12.8)$$

The corresponding functions for cyclic systems are described in Section 12.3. The energy levels and orbital coefficients for more complex systems are to be found in the mammoth compilation of Streitweiser and Coulson [4].

One can see by equation 12.7 that as the number of orbitals in the chain increases, the energy of the highest energy molecular orbital increases to the limiting value of  $\alpha - 2\beta$  when  $N$  is very large and that of the lowest energy MO decreases to a limit of  $\alpha + 2\beta$ . This is not only present in the Hückel model, but it is in any other as well including those where overlap is explicitly considered since nonnearest neighboring overlap decreases exponentially with distance. This systematic evolution of MOs is nicely illustrated from the  $\pi$  orbital energies derived from photoelectron (PE) and electron transmission spectroscopy (ETS) results of linear polyenes. The ionization potentials for the  $\pi$  orbitals and electron affinities for the first few polyenes are shown in Figure 12.4a. The box drawn for  $\pi_4$  and  $\pi_5$  in hexatriene indicates their approximate range of values. It is clear that the  $\pi$  and  $\pi^*$  orbitals spread out in energy but it is already apparent from even this small series that there are exponential limits to the highest and lowest MOs as previously suggested.

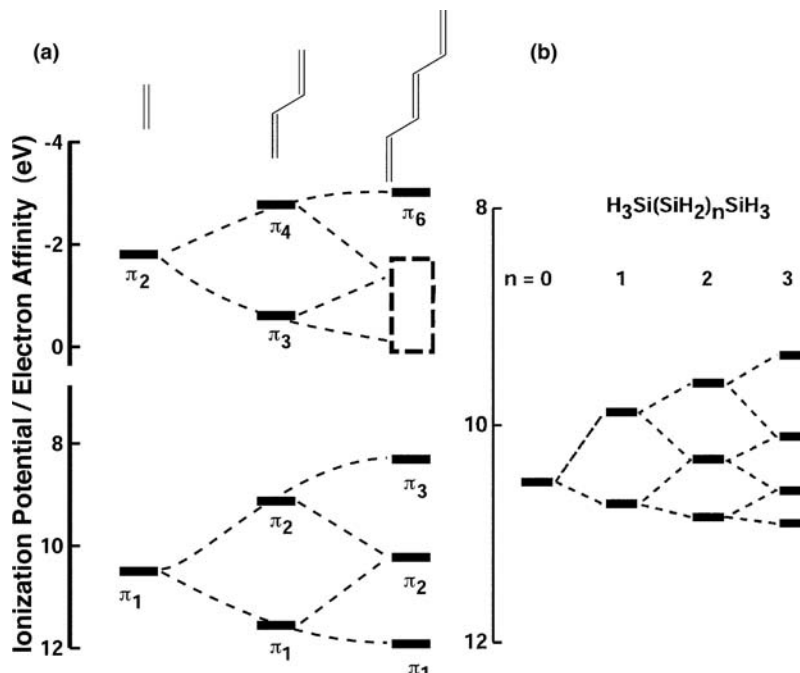


**FIGURE 12.4**

(a) The ionization potentials and electron affinities of the  $\pi$  molecular orbitals in linear polyenes. (b) A correlation of the Si–Si  $\sigma$  ionization potentials for linear polysilanes.

Furthermore, Figure 12.4a demonstrates that the  $\pi$  bonds in these polyenes are not completely localized. Interaction (overlap) between them does indeed exist and this can be quantified [3] by a resonance integral,  $\beta_{\pi-\pi}$ , which is  $\sim 1.2$  eV. This property has important technological ramifications. As we shall see in Chapter 13, doped long-chain polyenes (e.g., polyacetylene) can have electrical conductivities almost as high as copper does, and in their undoped states, they have remarkable nonlinear optical properties. Their uses in electronic devices and light emitting diodes have just begun to have a bright future. The Hückel treatment briefly outlined here need not be confined to the  $\pi$  systems of polyenes. One can also consider the interaction between  $\sigma$  orbitals in a similar vein. Figure 12.4b shows how the analogous  $\sigma$ -MOs spread out in the first few linear polysilanes [6]. This is a result exactly analogous to its polyene  $\pi$  counterpart. However, it is apparent that the interaction between the  $\sigma$  orbitals is not nearly as strong as that between the  $\pi$  orbitals in polyacetylene. Using the observed ionization potentials for several polysilanes, a resonance integral,  $\beta_{\sigma-\sigma} = \sim 0.5$  eV, about one-third the  $\beta_{\pi-\pi}$  value in polyenes, has been obtained [7].

## 12.3 CYCLIC SYSTEMS

Just as the  $\pi$  orbitals of the linear three- and four-atom chains formed molecular orbital patterns identical to those of linear  $H_3$  and  $H_4$  in Chapter 5, so there is a one-to-one correspondence between the orbitals of cyclic polyenes and those derived for cyclic  $H_n$  units. Figure 12.5 shows the orbitals of cyclic  $C_3$ – $C_6$  systems for comparison. There are several patterns which emerge:

1. The number of nodes increases by one on going from one orbital to the one next highest in energy, as in the linear case. The lowest energy orbital has no nodes; each degenerate pair of orbitals has the same number of nodes.
2. The lowest energy orbital is always nondegenerate. All other orbitals come as degenerate pairs except in even-membered rings where the highest

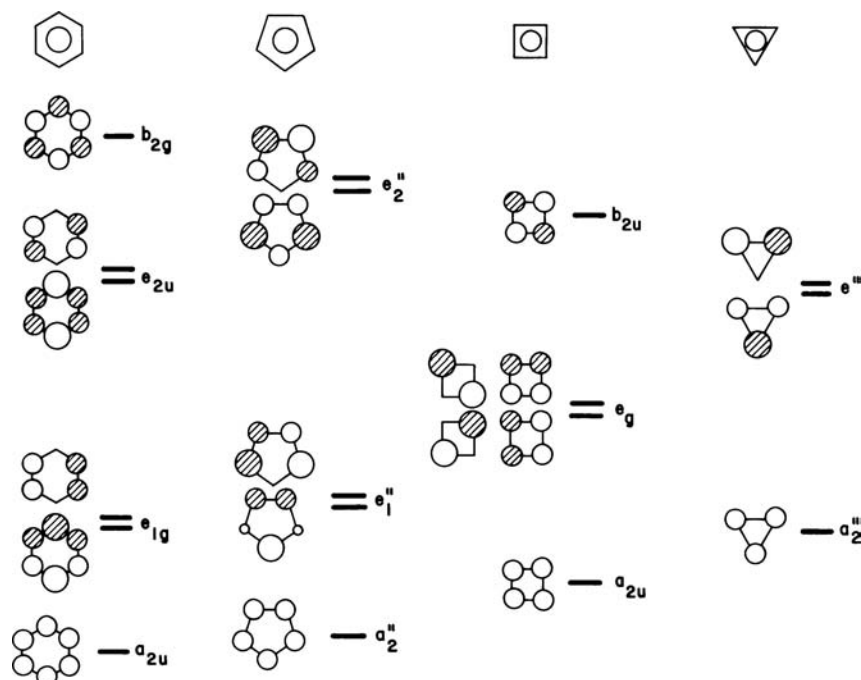
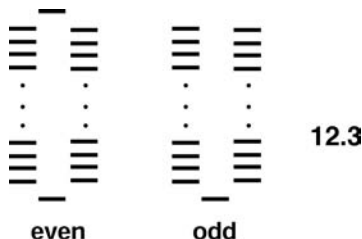


**FIGURE 12.5**

A top view of  $\pi$  orbitals for the first few cyclic polyenes.

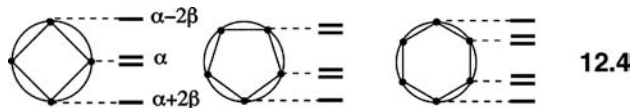
energy orbital is also nondegenerate. The resultant pattern of energy levels is then given in 12.3. In group theoretical terms for a cyclic  $N$  atom ring there are  $N$  orbitals, each corresponding to a different representation of the cyclic group of order  $N$ , as we will see as follows.



Algebraically, the levels of the cyclic polyenes may be derived using simple Hückel theory. The general result is given in equation 12.9 for the energy of the  $j$ th level for a cyclic system containing  $N$  atoms

$$e_j = \alpha + 2\beta \cos \frac{2j\pi}{N} \quad (12.9)$$

where  $j = 0, \pm 1, \pm 2, \dots, \pm N/2$  for even  $N$ , and  $j = 0, \pm 1, \pm 2, \dots, \pm(N-1)/2$  for odd  $N$ . The very simple form of this equation leads to a useful mnemonic for remembering the energy levels of these molecules. Draw a circle of radius  $2\beta$  and inscribe an  $N$ -vertex polygon such that one vertex lies at the 6 o'clock (bottom) position. The points at which the two figures touch define the Hückel energy levels as in 12.4. The energies for square cyclobutadiene are trivial; the middle two orbitals



lie at zero  $\beta$  and the highest MO must be at  $\alpha - \beta$  (which is also true for any even-membered cycle). There are obvious geometric ways to determine the energy associated with other MOs. The situation for cyclopentadienyl and benzene are also illustrated in 12.4. This construction is called a Frost circle. The form of the coefficients of the  $p^{\text{th}}$  atomic orbital in the wavefunction with an energy set by equation 12.9 is given by equation 12.10

$$\psi_j = \sum_{p=1}^N c_{pj} \chi_p = \frac{1}{\sqrt{N}} \sum_{p=1}^N \left[ \exp \left( \frac{2\pi i j(p-1)}{N} \right) \right] \chi_p \quad (12.10)$$

Here  $i$  is the square root of  $-1$ . As in equation 12.9,  $j$  runs from  $0, \pm 1, \pm 2, \dots$ . We shall see below, and, very importantly, in Chapter 13, that this complex form of the wavefunction is very useful. It is interesting to see where this expression comes from. Group theory provides the answer. The molecular point group of, for example, benzene is  $D_{6h}$ . However, the group  $C_6$  is the simplest one we can use to generate the  $\pi$  orbitals of the molecule. Table 12.1 shows its character table. The reducible representation for the basis set of six  $\pi$  orbitals is

$E$	$C_6$	$C_3$	$C_2$	$C_3^2$	$C_6^5$	(12.11)
$\Gamma_p$	6	0	0	0	0	

**TABLE 12.1** Character Table for the  $C_6$  Group

$C_6$	E	$C_6$	$C_3$	$C_2$	$C_3^2$	$C_6^5$	$\varepsilon = \exp(2\pi i/6)$
A	+1	+1	+1	+1	+1	+1	
B	+1	-1	+1	-1	+1	-1	
$E_1$	+2	$\varepsilon + \varepsilon^*$	$-\varepsilon^* - \varepsilon$	-2	$-\varepsilon - \varepsilon^*$	$\varepsilon^* + \varepsilon$	
$E_2$	+2	$-\varepsilon^* - \varepsilon$	$-\varepsilon - \varepsilon^*$	+2	$-\varepsilon^* - \varepsilon$	$-\varepsilon - \varepsilon^*$	

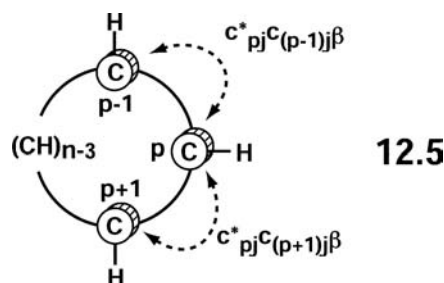
which reduces to  $a + b + e_1 + e_2$ , that is, two nondegenerate orbitals and two degenerate pairs as shown in Figure 12.5. Now symmetry-adapted linear combinations may be generated using the characters of Table 12.1 and equation 4.37. They become [with  $\varepsilon = \exp(2\pi i/6)$ ]

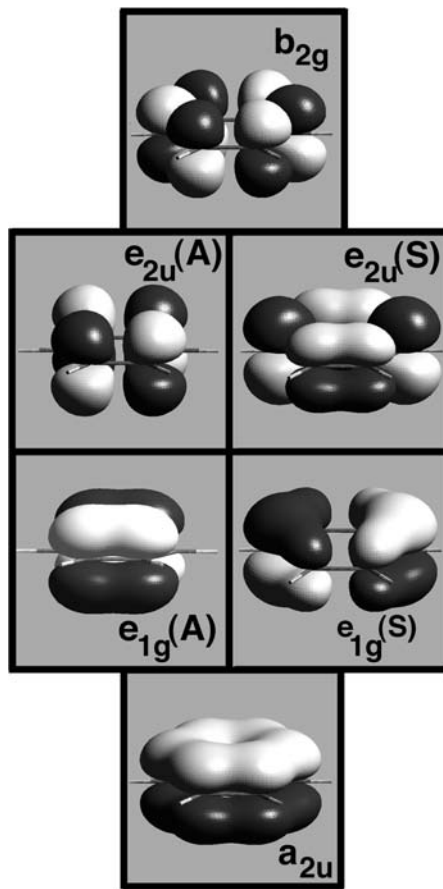
$$\begin{aligned}\psi(a) &\propto \chi_1 + \chi_2 + \chi_3 + \chi_4 + \chi_5 + \chi_6 \\ \psi(b) &\propto \chi_1 - \chi_2 + \chi_3 - \chi_4 + \chi_5 - \chi_6 \\ \psi(e_1) &\propto \chi_1 + \varepsilon \chi_2 - \varepsilon^* \chi_3 - \chi_4 - \varepsilon \chi_5 + \varepsilon^* \chi_6 \\ \psi(e_1)' &\propto \chi_1 + \varepsilon^* \chi_2 - \varepsilon \chi_3 - \chi_4 - \varepsilon^* \chi_5 + \varepsilon \chi_6 \\ \psi(e_2) &\propto \chi_1 - \varepsilon \chi_2 - \varepsilon^* \chi_3 + \chi_4 - \varepsilon^* \chi_5 - \varepsilon \chi_6 \\ \psi(e_2)' &\propto \chi_1 - \varepsilon \chi_2 - \varepsilon^* \chi_3 + \chi_4 - \varepsilon \chi_5 - \varepsilon^* \chi_6\end{aligned}\quad (12.12)$$

which are identical to the form of the functions from equation 12.10, without the normalization constant, for this case. Thus the exponential in equation 12.10 represents the character of the  $j^{\text{th}}$  irreducible representation of the cyclic group of order  $N$ . Note that the complex description of the orbitals only shows up in equation 12.12 for the degenerate molecular levels. These may be rewritten in a simpler way. A linear combination of the wavefunctions of a pair of degenerate orbitals (e.g.,  $j = +1, -1$  or  $j = +2, -2$ , and so on.) produces two new orbitals which are equivalent in every respect. We can recast the functions of equation 12.10, by making use of the trigonometric identity  $\exp(ix) = \cos(x) + (i)\sin(x)$ . The result is given by equation 12.13.

$$\begin{aligned}\psi_{j'} &= \frac{1}{2} (\psi_j + \psi_{-j}) = \frac{1}{2\sqrt{N}} \sum_{p=1}^N \left[ \cos \frac{2\pi j(p-1)}{N} \right] \chi_p \\ \psi_{j''} &= \frac{1}{2i} (\psi_j - \psi_{-j}) = \frac{1}{2\sqrt{N}} \sum_{p=1}^N \left[ \sin \frac{2\pi j(p-1)}{N} \right] \chi_p\end{aligned}\quad (12.13)$$

The resultant six molecular orbitals are plotted in Figure 12.6. These are three-dimensional plots of the boundary surface associated with one value of the wavefunction. The dark and light shapes represent positive and negative values, respectively. It is very clear from the plots that the number of nodes perpendicular to the molecular framework increase from zero for  $a_{2u}$  to one for each member of the  $e_{1g}$  set to two for  $e_{2u}$  and finally three for the  $b_{2g}$  molecular orbital. One can also see from this plot how the form of the  $\pi$  orbitals could be easily constructed by the union of two allyl fragments. Let us return, however, to equation 12.10 and see how this wavefunction simply leads to the energies of equation 12.9. From 12.5 it is easy to see that the energy of the orbital is given by equation 12.14



**FIGURE 12.6**

Three-dimensional plots of the  $\pi$  molecular orbitals in benzene. The MOs are displayed at a value of  $0.05 e^{1/2}$ , where the black and gray surfaces correspond to positive and negative, respectively, values of the wavefunction. These are ab initio calculations with a 3-21 G basis set.

$$e_j = \langle \psi_j | H^{\text{eff}} | \psi_j \rangle = \alpha + \beta \sum_p [c_{pj}^* c_{(p+1)j} + c_{pj}^* c_{(p-1)j}] \quad (12.14)$$

which represents the sum of all the interactions of each atom with its two nearest neighbors. Substitution of  $c_{pj}$  from equation 12.10 leads to

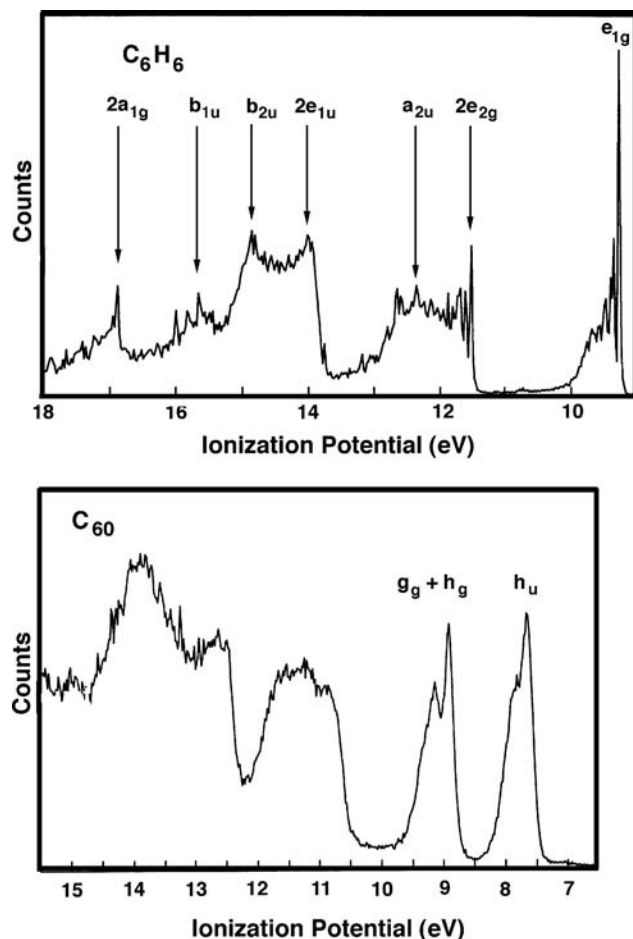
$$e_j = \alpha + \beta \sum_p \left( \frac{1}{\sqrt{N}} \exp \frac{-2\pi ij(p-1)}{N} \cdot \frac{1}{\sqrt{N}} \exp \frac{2\pi ij(p-1)}{N} \right) \left[ \exp \frac{2\pi ij}{N} + \exp \frac{-2\pi ij}{N} \right] \quad (12.15)$$

The term in parenthesis is equal to  $1/N$ , and the term in brackets is expressible as a simple cosine function. So

$$e_j = \alpha + \beta \sum_{p=1}^N \frac{1}{N} \left( 2 \cos \frac{2\pi j}{N} \right), \quad j = 0, \pm 1, \pm 2 \dots \quad (12.16)$$

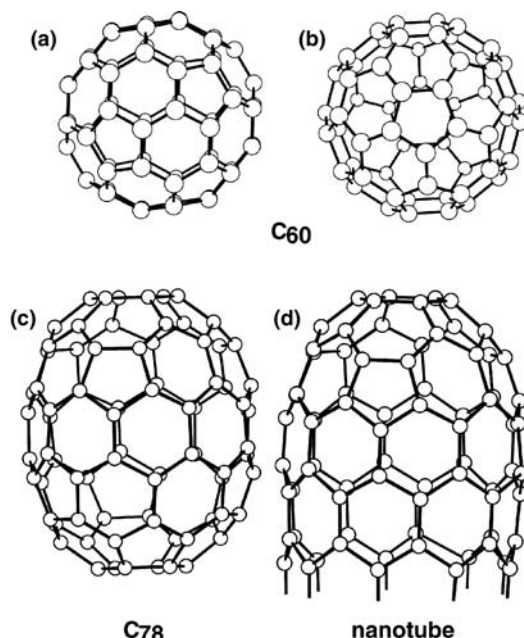
and, since there are  $N$  atoms in the ring,

$$e_j = \alpha + \beta \cos \frac{2\pi j}{N}, \quad j = 0, \pm 1, \pm 2 \dots \quad (12.17)$$

**FIGURE 12.7**

(a) The PE spectra of benzene and  
(b)  $C_{60}$ .

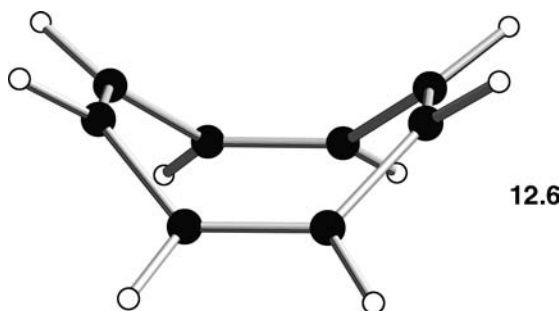
The number of electrons present in these cyclic systems has an important bearing on their stability, structure, and properties. In particular, we might expect that some sort of stability would exist for those systems where all bonding and nonbonding orbitals (where they exist) are completely filled with electrons. This leads to Hückel's  $4n + 2$  rule, nothing more than recognition of the special stability of a closed shell of electrons. From 12.3, we can see that after the first, lowest level, the orbitals always occur in pairs. If  $n$  pairs of these levels are occupied by electrons, a total of  $2n + 1$  orbitals will be filled for a total of  $(4n + 2)$  electrons ( $n = 0, 1, 2$ , etc.). The cases we shall come across most frequently are cyclobutadiene<sup>2-</sup>, cyclopentadienyl<sup>-</sup>, benzene, and cycloheptatriene<sup>+</sup> which all have  $n = 1$ . Cyclooctatetraene<sup>2-</sup> is an example with  $n = 2$ . Such species with  $4n + 2 \pi$  electrons are said to be aromatic systems. The PE spectrum of benzene is shown in Figure 12.7a. The ionizations of the  $e_{1g}$  and  $a_{2u}$   $\pi$  orbitals are found at 9.25 and 12.38 eV, respectively [8]. Notice that there is a high-lying  $e_{2g} \sigma$  set which lies between the ionizations from the  $\pi$  manifold. From electron transmission spectroscopy [9] the  $e_{2u}$  and  $b_{2g}$   $\pi$  MOs are at -1.15 and -4.85 eV, respectively. Let us consider the perturbation in the  $\pi$  manifold of MOs that ensues when the two ends of hexatriene are joined together to form benzene. The lowest  $\pi$  level in hexatriene (see Figure 12.2) is, of course, bonding between the two ends, so the ionization potential increases from 11.9 [10] to 12.38 eV for the  $a_{2u}$  level. The second  $\pi$  MO of hexatriene is antisymmetric with respect to the two ends, so the ionization potential decreases on going to benzene from 10.26 to 9.25 eV. Finally  $\pi_3$  is symmetric between the two ends, so it is stabilized from 8.29 to 9.25 eV. Notice that the  $e_{1g}$  set

**FIGURE 12.8**

The structures of  $C_{60}$  (a and b),  $C_{78}$  (c) and a nanotube (d).

of benzene lies precisely in the middle of  $\pi_2$  and  $\pi_3$  of hexatriene, just as one would expect from the nodal properties of the  $\pi$  orbitals in hexatriene and benzene. One could examine the perturbation of the  $\pi$  orbitals that results by fusing cyclic polyenes. For example, the electronic structure of graphite can be constructed from the  $\pi$  orbitals of benzene. We shall leave this for Chapter 13. Fusing five- and six-membered rings together produces a curved surface which can close upon itself to produce fullerenes. The archetypal example is  $C_{60}$  whose structure was first proposed in 1985 [11]. The geometry is shown from two perspectives in Figure 12.8a,b. The view in Figure 12.8a highlights the way five- and six-membered rings have been joined together. Figure 12.8b shows the cluster along one fivefold rotation axis. The molecule has icosahedral symmetry. The addition of a “belt” of benzene rings produces many other examples. The smallest member is  $C_{78}$  which is shown in Figure 12.8c. If this belt is extended in width, nanotubes (Figure 12.8d) are created. The photoelectron spectrum of  $C_{60}$  is shown in Figure 12.7b. The first two ionizations at 7.6 and 9.0 eV have been assigned to  $\pi$  ionizations from MOs of  $h_u$  and  $g_g + h_g$  symmetry [12]. In other words, these ionizations correspond to five and nine MOs, respectively. The construction of the  $\pi$  orbitals in  $C_{60}$  is most readily accomplished by the union of 12  $C_5$  rings [13]. The highest occupied levels then strongly resemble the  $e'_1$  set in the cyclopentadienyl polyene (Figure 12.5). There are antibonding interactions between the cyclopentadienyl units, so the  $h_u + g_g + h_g$  orbitals lie high in energy compared to the occupied MOs of benzene. The lowest unoccupied molecular orbital (LUMO) ( $t_{1u}$  symmetry) is also derived from cyclopentadienyl  $e''_1$ , so it lies at low energy compared to typical antibonding  $\pi$  MOs. Its electron affinity is +2.66 eV, that is, 3.81 eV lower than the  $e_{2u}$  set in benzene.  $C_{60}$  is then a good electron donor, as well as, an excellent electron acceptor.

In cyclic  $4n$   $\pi$  electron systems, a degenerate pair of  $\pi$  levels will be half-filled. Consequently the molecule with all electrons paired will become either nonplanar or at least distort to a nonsymmetrical structure as anticipated for a Jahn–Teller instability. Cyclooctatetraene,  $C_8H_8$ , is one such example of the first type. The molecule (12.6) is tub-shaped [14a] and the four double bonds have minimal conjugation to each other. It requires  $\sim 16$  kcal/mol [b] for cyclooctatetraene to



attain a planar,  $D_{8h}$  geometry. Cyclobutadiene is an example of the second type. This orbital problem is just like that of  $H_4$  and is shown in Figure 12.9a. From the viewpoint of the orbital energies derived from a one-electron Hamiltonian, the situation is of the first-order Jahn–Teller type where the molecule distorts so as to remove the orbital degeneracy. To be precise, however, one should note that  $e_g \otimes e_g = a_{1g} + a_{2g} + b_{1g} + b_{2g}$ , includes no degenerate representation. Thus from the viewpoint of the symmetry of state wavefunctions, no degenerate states are found, so the molecule is technically stable against a first-order Jahn–Teller distortion. There are modes of  $b_{1g}$  and  $b_{2g}$  symmetry (see Appendix III) which distort square cyclobutadiene to a rectangle (Figure 12.9a) or a diamond (Figure 12.9b), respectively. Strictly speaking, therefore, the distortion in cyclobutadiene is really of the second-order Jahn–Teller type. The result for the  $b_{1g}$  distortion is an opening up of a HOMO–LUMO gap and an overall stabilization of occupied orbitals on going to the rectangle. An exactly analogous result is shown in Figure 12.9b for the  $b_{2g}$  distortion to a diamond or rhomboid geometry. Note that we have chosen different ways to write the wavefunctions of the degenerate nonbonding  $\pi$  set in the two cases in order to make the results easier to understand. Here on distortion, the antibonding 1,3-interaction is decreased for one component and increased for the other on distortion. Clearly, the  $b_{1g}$  distortion should create a stronger driving force and ground-state cyclobutadiene is indeed rectangular.

Planar  $4n \pi$  systems are said to be antiaromatic. The stability of aromatic compounds and the lack thereof in antiaromatic ones has been an important concept in organic chemistry [5]. There are a number of interesting points to be made in the context of this stabilization and destabilization. Addition of two extra electrons to

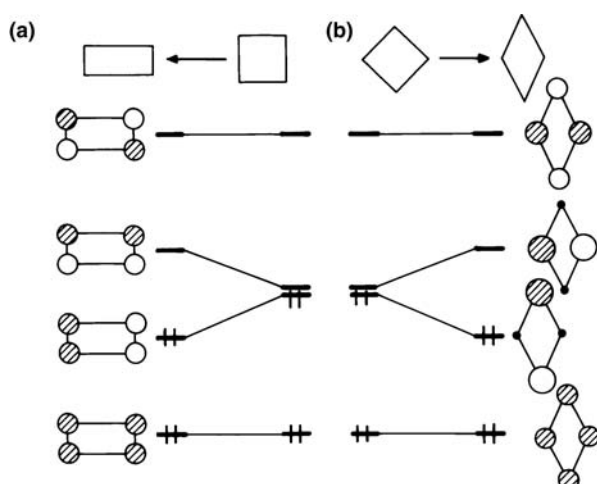
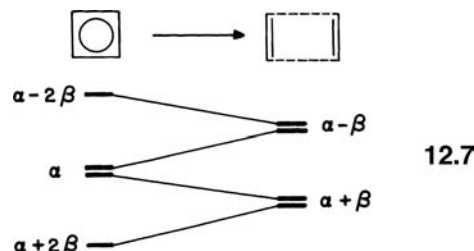


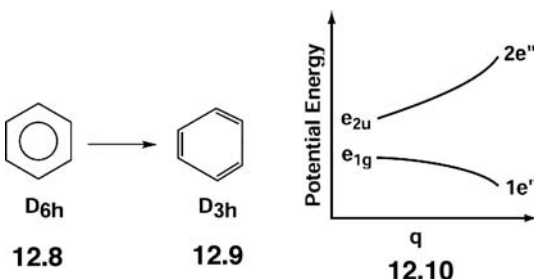
**FIGURE 12.9**

Relief of the Jahn–Teller instability in singlet square cyclobutadiene by distortion to (a) a rectangle and (b) a diamond.

cyclobutadiene leads, overall, to no increase in orbital stabilization, since these electrons enter a nonbonding orbital. In fact, Coulomb repulsion may lead overall to a destabilizing effect. However, on distortion to the rectangle, for  $C_4H_4^{2-}$  two electrons in this nonbonding orbital are destabilized. Quantitatively this is shown at the Hückel level in 12.7 where the distortion has gone all the way to two double bonded units. Cyclobutadiene itself has the same  $\pi$  energy as two ethylene segments



but the dianion loses  $2\beta$  of  $\pi$  energy on distortion. In other words, the zero HOMO–LUMO gap in the  $4n \pi$  molecule signals a Jahn–Teller type of distortion and also increases reactivity by having a high-lying HOMO and/or a low-lying LUMO. A valence bond calculation put the resonance energy for delocalizing four  $\pi$  electrons in a square cyclobutadiene to be stabilizing by 22 kcal/mol [16]. What is perhaps more perplexing is the state of affairs in benzene. It has been recognized as early as 1959 [17] that as the size of cyclic polyenes become larger, the tendency to produce a localized, alternating double single-bond structure, becomes greater within the Hückel approximation. However, there is good theoretical and experimental evidence that this does not occur in structures as large as  $C_{18}H_{18}$  [18]. There is a gigantic amount of information that benzene has a delocalized,  $D_{6h}$ , shape, 12.8, rather than an alternating,  $D_{3h}$  one, 12.9. It is this delocalized geometry that is



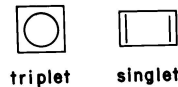
for many the nexus of the aromaticity—thermodynamic stability concept. Yet consider the following:  $H_6$  with a  $D_{6h}$  structure certainly does not exist as a stable molecule. It is a transition state structure [19] which lies 67 kcal/mol above three essentially isolated  $H_2$  molecules arranged in a  $D_{3h}$  manner. The six MOs of  $H_6$  (see Figures 5.10 and 5.11) are topologically identical to the  $\pi$  MOs of benzene (Figure 12.5). Therefore, it has been argued [20] that the  $\pi$  orbitals of benzene favor the distortion from 12.8 to 12.9. The sigma system in benzene favors 12.8 strongly over 12.9 and this factor dominates over the  $\pi$  orbital effect. There are a number of ways to come to this conclusion [20]; 12.10 can express the essence of them where the orbital energy of the HOMO and LUMO in benzene are plotted as a function of the distortion coordinate which takes the  $D_{6h}$  structure to a  $D_{3h}$  one. The important point is that the HOMO,  $e_{1g}$ , and the LUMO,  $e_{2u}$  both become  $e''$  in symmetry when the distortion proceeds and so they can and will mix with each other to produce the  $1e''$  and  $2e''$  MOs. The  $1e''$  set is filled and, therefore, the distortion is stabilizing in terms of these two MOs in the  $\pi$  system. In fact, this is nothing more than an

application of the second-order Jahn-Teller theorem. In the cross-product of  $e_{1g} \otimes e_{2u}$  there is a mode of  $b_{2u}$  symmetry. The normal modes of a six-membered ring are given in Appendix III, and one can easily see that the  $b_{2u}$  mode carries **12.8** into **12.9**. Part of the early controversy associated with this idea stemmed from the fact that the distortion coordinate,  $q$ , in **12.10** is not unique. More recent accurate calculations [21] of the second derivative of the energy with respect to the  $b_{2u}$  coordinate show in fact that the  $e_{1g}$  set is unstable with respect to the distortion. Furthermore, it has been experimentally shown [22] that the  $b_{2u}$  mode in the  $^1A_{1g}$  ground state of benzene has a smaller frequency than the same mode in the  $^1B_{2u}$  excited state. This can be shown [23] to be consistent with the notion that the  $\pi$  system is unstable with respect to localization. On going to the excited state, an electron is removed from the  $\pi$  system which prefers to distort, so the potential associated with the deformation should stiffen. Finally several molecules have been recently synthesized [24] which are tris-annelated. In each case one can show that the localization is one traced back to the stabilization that through-bond conjugation brings in Figure 11.4 and (probably more importantly) the destabilization shown in Figure 11.3. The double bonds prefer to be exocyclic rather than endocyclic with respect to the annelated rings. The connection between aromaticity and thermodynamic stability will always be problematic, for no other reason that a reference state is difficult to categorize. Derivations of aromaticity based upon magnetic criteria are perhaps more secure [25].

For cyclobutadiene, there is another interesting possibility which we have explored before with the case of methylene in Section 8.8. Is it possible to produce a stable structure by allowing the two highest energy electrons of the  $4n$  species to separately occupy the orthogonal pair of degenerate orbitals with their spins parallel? The result would be a triplet diradical species as in **12.11**. For such an electronic



12.11



12.12

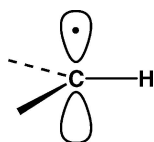
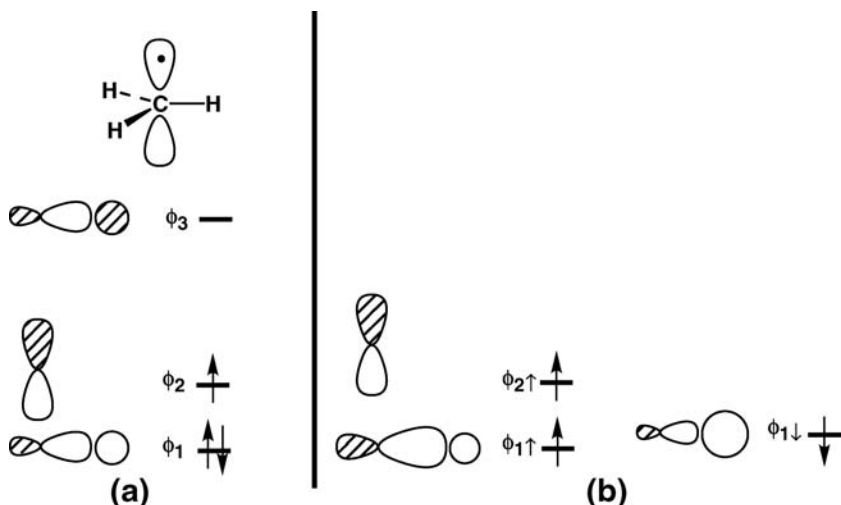
configuration there would be no obvious tendency from the orbital picture of Figure 12.9 to distort away from the square planar structure. So there exists the possibility of two structures (**12.12**) dependent on the spin state of the molecule. Experimental evidence [26] indicates a distorted structure for the singlet state but no experimental information is available for the structure of the diradical (triplet) state [27]. The discussion in Chapter 8 leads us to expect that the triplet should be more stable than the singlet at the square planar geometry because of more favorable two-electron energy terms. Results of calculations which include configuration interaction indicate [16,27] a reversal of this energy ordering with the singlet state  $\sim 10$  kcal/mol more stable than the triplet. The explanation for this behavior, called dynamic spin polarization is the subject of Sections 12.4 and 12.5 in this text. Examples [28] of square singlet species with  $4n + 2 = 6\pi$  electrons, which are therefore stable at this geometry, include the chalcogenide ions  $A_4^{2+}$  ( $A = S, Se, Te$ ),  $P_4^{2-}$  and the derivative  $S_2N_2$  which we shall examine in Section 12.4.

## 12.4 SPIN POLARIZATION

In a  $\pi$  radical system **12.13**, the C—H bond lies on the nodal plane of the carbon  $p_\pi$  orbital which carries some unpaired spin density. As depicted in Figure 12.10a, the

**FIGURE 12.10**

A C-H sigma bonding orbital  $\phi_1$ , the  $p_\pi$  orbital  $\phi_2$ , and the sigma antibonding orbital  $\phi_3$ : (a) in the absence of spin polarization and (b) in the presence of spin polarization. The up- and down-spin arrows are used in (b) to indicate the up- and down-spin spatial orbitals, respectively.



12.13

local electronic structure around the carbon center of **12.13** can be described in terms of the  $\sigma_{\text{CH}}$  and  $\sigma_{\text{CH}}^*$  orbitals ( $\phi_1$  and  $\phi_3$ , respectively) of the C—H bond and the  $p_\pi$  orbital ( $\phi_2$ ) of the carbon atom. To a first approximation, the up- and down-spin electrons in  $\sigma_{\text{CH}}$  are considered to have an identical spatial function so that no unpaired spin density occurs on the hydrogen atom. However, electron spin resonance (ESR) studies of  $\pi$  radical systems show a small amount of unpaired spin density on the hydrogen atoms [29]. To explain this observation, we recall that the up-spin electrons of the orbitals  $\phi_1$  and  $\phi_2$  stabilize the system by  $-K_{12}$ , where  $K_{12}$  is the exchange integral between  $\phi_1$  and  $\phi_2$ . The down-spin electron of  $\phi_1$  and the up-spin electron of  $\phi_2$  leads to the Coulomb repulsion  $J_{12}$ . Thus the energy of **12.13** can be lowered by enhancing  $K_{12}$  and reducing  $J_{12}$ . The exchange integral  $K_{12}$  is the self repulsion associated with the overlap density  $\phi_1\phi_2$  (see Chapter 8). As an example, consider the exchange and overlap integrals associated with  $p_x$  and  $p_z$  orbitals on a given atom. The exchange repulsion integral associated with the two orbitals is positive, because all the overlapping regions lead to a positive value (indicated by shading in Figure 12.11a). On the other hand, the overlap integral between the two orbitals is zero because the positive number from the shaded overlapping regions (indicated by shading in Figure 12.11b) is canceled out by the negative number resulting from the unshaded overlapping regions. In Figure 12.10a, the  $\phi_1$  orbital is an in-phase combination of C  $sp^2$  and H 1s orbitals, and the  $\phi_3$  orbital is an out-of-phase combination between them. At the carbon center, the  $p_\pi$  orbital is closer to the C  $sp^2$  hybrid than to the H 1s orbital so that the overlap density  $\phi_1\phi_2$  (and thus the exchange integral) is increased by increasing the weight of C  $sp^2$  in the up-spin orbital  $\phi_{1\uparrow}$ . Due to the normalization condition, this requires a reduction of the weight of H 1s in  $\phi_{1\uparrow}$ . These changes are accommodated by mixing  $\phi_3$  into  $\phi_1$ , that is,

$$\phi_{1\uparrow} = \frac{\phi_1 + \lambda\phi_3}{\sqrt{1+\lambda^2}} \quad (12.18)$$

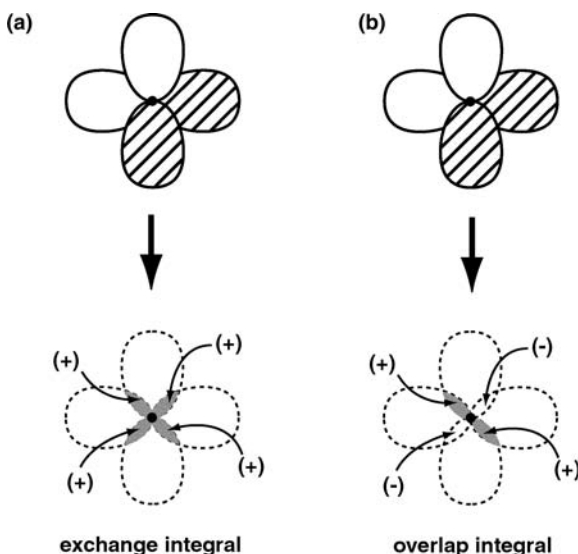


**FIGURE 12.11**

The signs of (a) the exchange repulsion integral and (b) the overlap integral associated with the overlapping regions of the  $p_x$  and  $p_z$  orbitals on a given atom. The shaded regions where the two AOs overlap lead to a positive value of the integral, and the unshaded regions to a negative value.

where  $\lambda$  is a small positive mixing coefficient ( $0 < \lambda \ll 1$ ). The Coulomb repulsion  $J_{12}$  is the repulsion between the charge density distributions  $\phi_1\phi_1$  and  $\phi_2\phi_2$ .  $J_{12}$  can be reduced by decreasing the weight of C  $sp^2$  in the down-spin orbital  $\phi_{1\downarrow}$  (which requires a reduction of the weight of H 1s in  $\phi_{1\downarrow}$ ). This can be achieved by mixing  $\phi_3$  into  $\phi_1$  as follows:

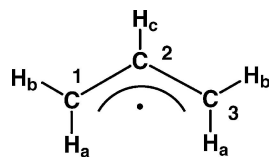
$$\phi_{1\downarrow} = \frac{\phi_1 - \kappa\phi_3}{\sqrt{1 + \kappa^2}} \quad (12.19)$$

where  $\kappa$  is a small positive mixing coefficient ( $0 < \kappa \ll 1$ ). As a consequence, the spatial functions of  $\phi_{1\uparrow}$  and  $\phi_{1\downarrow}$  are modified as depicted in Figure 12.10b. The net consequence of this mixing is that the hydrogen atom has more down-spin density than up-spin density, resulting in a small amount of unpaired down-spin density on the hydrogen. In other words, the up-spin electron in the carbon  $p_\pi$  orbital polarizes the distribution of the up- and down-spin electrons in the C—H bond. Such a phenomenon is known as spin polarization. It should be noted from Figure 12.10b that the up-spin level  $\phi_{1\uparrow}$  lies lower in energy than the down-spin level  $\phi_{1\downarrow}$ , because  $\phi_{1\uparrow}$  has the exchange interaction with  $\phi_{2\uparrow}$  while  $\phi_{1\downarrow}$  does not. (Our discussion of spin polarization was simplified by neglecting the Coulomb repulsion between  $\phi_{2\uparrow}$  and  $\phi_{1\uparrow}$  as well as that between  $\phi_{1\uparrow}$  and  $\phi_{1\downarrow}$ . To reduce the Coulomb repulsion between  $\phi_{2\uparrow}$  and  $\phi_{1\uparrow}$ , it is necessary to polarize  $\phi_{1\uparrow}$  as in  $\phi_{1\downarrow}$ . However, to reduce the Coulomb repulsion between  $\phi_{1\uparrow}$  and  $\phi_{1\downarrow}$ , their overlap density  $\phi_1\phi_1$  should be decreased. This happens when these orbitals are oppositely polarized. In addition, the Coulomb repulsion  $\phi_{1\uparrow}$  and  $\phi_{1\downarrow}$  is larger than that between  $\phi_{2\uparrow}$  and  $\phi_{1\uparrow}$ , as described in Chapter 8. Thus the Coulomb repulsion between  $\phi_{1\uparrow}$  and  $\phi_{1\downarrow}$  has a stronger spin polarization effect than does the Coulomb repulsion between  $\phi_{2\uparrow}$  and  $\phi_{1\uparrow}$ . We will employ the simplified approach described earlier in our later discussion of spin polarization.)

In a  $\pi$  radical system, the amount of unpaired down-spin density ( $\rho_H$ ) on a hydrogen atom, and hence the hyperfine splitting constant ( $a_H$ ) of the hydrogen atom in a ESR spectrum of the compound, is proportional to the amount of unpaired up-spin density ( $\rho_C$ ) on the carbon atom to which the hydrogen atom is attached [30]. In other words,

$$a_H = Q\rho_C \quad (12.20)$$

where  $Q$  is the proportionality constant. The allyl radical **12.14** provides another example of spin polarization. The  $\pi$  electronic structure of this radical is typically



12.14

described as shown in Figure 12.12a, where the bonding level  $\pi_1$  is doubly occupied and the nonbonding level  $\pi_2$  is singly occupied. This simple picture suggests that the C2 atom does not have unpaired spin density, so the Hc atom would not participate in the hyperfine spin–spin interaction. However, ESR studies of **12.14** show that a substantial amount of down-spin density exists on the C2 atom [31]. This is explained by considering the spin polarization in the up- and down-spin electrons in the  $\pi_1$  level induced by the up-spin electron in  $\pi_2$ . As in the case of **12.13**, the energy of **12.14** is lowered by enhancing the exchange integral  $K_{12}$  between  $\pi_{1\uparrow}$  and  $\pi_{2\uparrow}$ , that is, by increasing the overlap density  $\pi_1\pi_2$ . The main contributions to  $\pi_1\pi_2$  come from the terms involving the atomic orbital products  $\chi_1\chi_1$  and  $\chi_3\chi_3$ . (Here the  $\pi$  MOs are expressed as  $\pi_i = c_{1i}\chi_1 + c_{2i}\chi_2 + c_{3i}\chi_3$ .) To enhance the overlap density

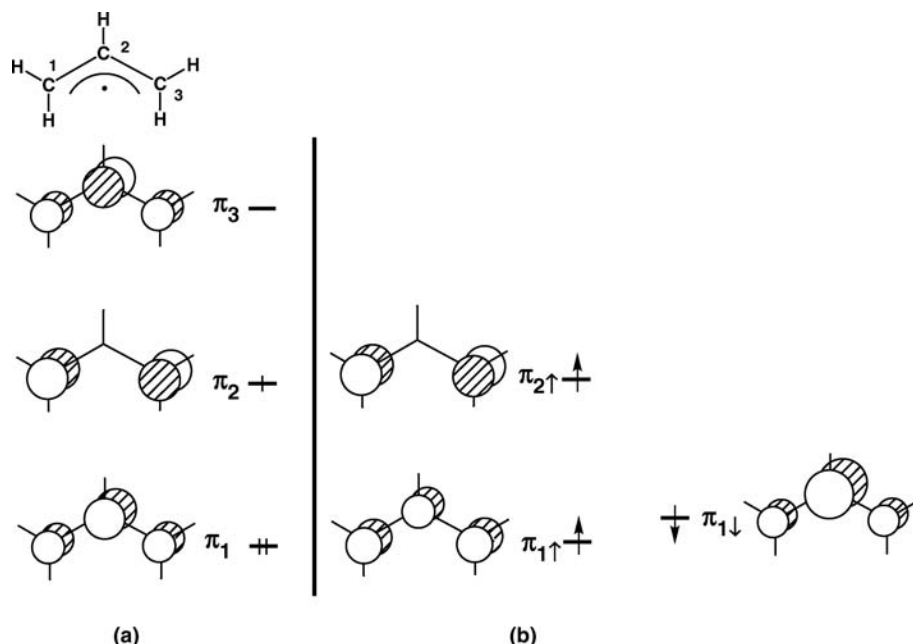


FIGURE 12.12

The bonding pi orbital  $\pi_1$ , the nonbonding pi orbital  $\pi_2$ , and the antibonding pi orbital  $\pi_3$  of an allyl radical: (a) in the absence of spin polarization and (b) in the presence of spin polarization. The up- and down-spin arrows are used in (b) to indicate the up- and down-spin spatial orbitals, respectively.

$\pi_1\pi_2$ , we increase the coefficients of the C1 and C3 atoms, and decrease the coefficient of the C2 atom, in the up-spin orbital  $\pi_{1\uparrow}$  by orbital mixing,

$$\pi_{1\uparrow} = \frac{\pi_1 + \lambda\pi_3}{\sqrt{1 + \lambda^2}} \quad (12.21)$$

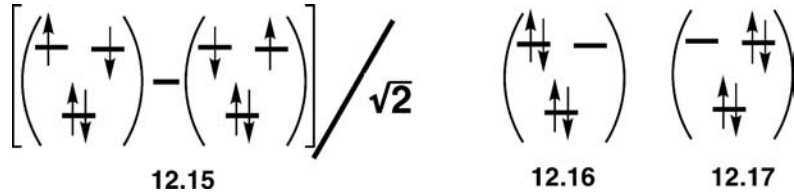
where  $\lambda$  again is a small positive mixing coefficient. The Coulomb repulsion  $J_{12}$  between the orbitals  $\pi_{1\downarrow}$  and  $\pi_{2\uparrow}$  is the repulsion between the charge density distributions  $\pi_1\pi_1$  and  $\pi_2\pi_2$ . This repulsion is also dominated by the terms involving the atomic orbital products  $\chi_1\chi_1$  and  $\chi_3\chi_3$ . To reduce  $J_{12}$ , we decrease the coefficients of C1 and C3 and increase the coefficient of C2 in the down-spin orbital  $\pi_{1\downarrow}$  by orbital mixing,

$$\pi_{1\downarrow} = \frac{\pi_1 - \kappa\pi_3}{\sqrt{1 + \kappa^2}} \quad (12.22)$$

where  $\kappa$  is a small positive mixing coefficient. The resulting spatial functions of  $\pi_{1\uparrow}$  and  $\pi_{1\downarrow}$  are depicted in Figure 12.12b, which shows that the C2 atom has more down-spin density than up-spin density thus leading to unpaired down-spin density on C2.

## 12.5 LOW- VERSUS HIGH-SPIN STATES IN POLYENES

For square cyclobutadiene, the lowest lying singlet state is described by the electron configuration **12.15**, in which the degenerate orbitals are singly occupied with opposite spins. The alternative singlet state configurations **12.16** and **12.17**,



in which one of the degenerate orbitals is doubly occupied, are higher in energy than **12.15** due to the pairing energy resulting from the orbital double occupancy (see Chapter 8). The singlet configuration **12.15** and the triplet configuration **12.11** are similar in energy because the degenerate orbitals are not doubly occupied in both cases. An exchange interaction exists between the two electrons of the degenerate orbitals in the triplet configuration **12.11**, but not in the singlet configuration **12.15**. Thus one might consider the triplet state to be the ground state. However, the triplet state is less stable than the singlet state, because the singlet configuration **12.15** interacts with other higher-lying singlet configurations (e.g., **12.16**, **12.17**, and so on.) to produce a lower-lying singlet state. The stabilization of the singlet state relative to the triplet state in a diradical is a consequence of the double (or dynamical) spin polarization effect (see below) [28,32,33]. As pointed out earlier, configuration interaction calculations show [16,27] the singlet state to be more stable by approximately 10 kcal/mol. In general, high-level configuration interaction calculations are needed to determine the relative stabilities of the singlet and triplet states of a diradical.

In discussing the relative stability of the singlet and triplet states of a diradical system, it is convenient to define their energy difference as follows (for further discussion see Section 24.4.1):

$$\Delta E = {}^1E - {}^3E \equiv J \quad (12.23)$$

where  ${}^1E$  and  ${}^3E$  refer to the total energies of the singlet and triplet states, respectively. The energy difference  $\Delta E$  is commonly written as  $J$  in describing the magnetic properties of compounds with unpaired spins, where  $J$  is called the spin-exchange parameter.  $J$  is positive when the triplet state is the ground state, and negative when the singlet state is the ground state. In general, the term  $J$  can be written as [34,35]

$$J = J_F + J_{AF} \quad (12.24)$$

where the “ferromagnetic” term  $J_F$  favors the triplet state (i.e.,  $J_F > 0$ ), and the “antiferromagnetic” term  $J_{AF}$  favors the singlet state (i.e.,  $J_{AF} < 0$ ). Given that two electrons of identical spin are accommodated in orbitals  $\phi_1$  and  $\phi_2$ , the  $J_F$  term is given by the exchange integral  $K_{12}$  between them, that is,

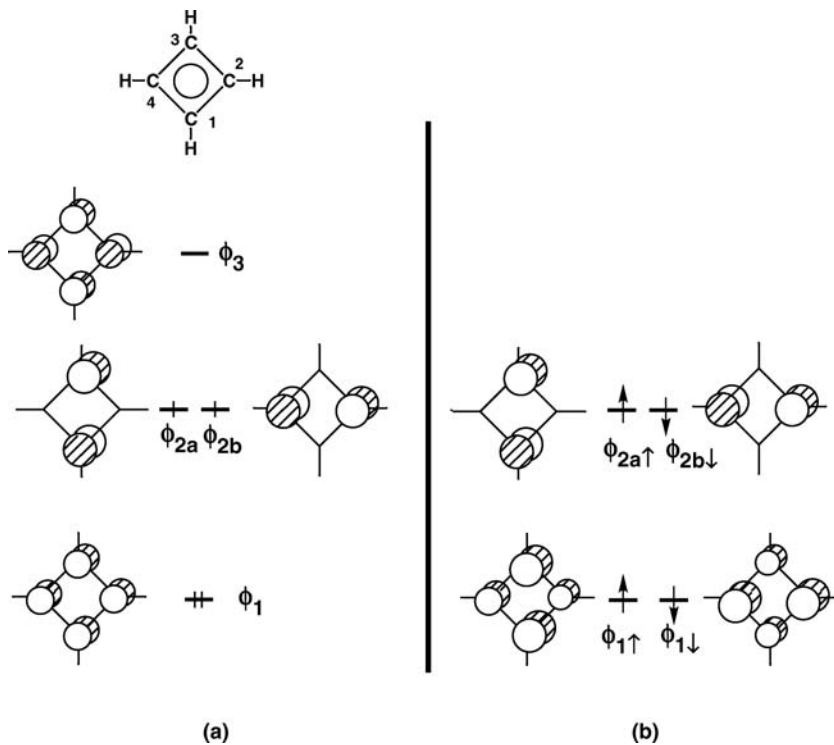
$$J_F = 2K_{12} \quad (12.25)$$

As mentioned earlier,  $K_{12}$  is the self-repulsion involving the overlap density  $\phi_1\phi_2$  and increases with the overlap density  $\phi_1\phi_2$ . When the orbitals  $\phi_1$  and  $\phi_2$  interact, their energies are split by  $\Delta e$ , which is proportional to the overlap integral  $S_{12}$  between the orbitals  $\phi_1$  and  $\phi_2$ . The antiferromagnetic term  $J_{AF}$  is essentially proportional to  $-(\Delta e)^2$  (see Section 24.4.) so that

$$J_{AF} \propto -(\Delta e)^2 \propto -(S_{12})^2 \quad (12.26)$$

Consequently, to have the triplet state as the ground state, it is necessary to enhance the exchange integral  $K_{12}$  and minimize the overlap integral  $S_{12}$ . The optimum case is to have  $S_{12} = 0$  and  $K_{12} > 0$ . For example, this condition holds for the two orthogonal  $p$  orbitals of an atom as depicted in Figure 12.11. To have the singlet state as the ground state, it is necessary to reduce the exchange integral  $K_{12}$  (i.e., to reduce the overlap density distribution  $\phi_1\phi_2$ ) and enhance the overlap integral  $S_{12}$ .

As discussed in Section 12.4, when a given molecule has more up-spin electrons than down-spin electrons, its total energy is lowered by allowing the spatial functions of up- and down-spin electrons to differ (e.g., unrestricted Hartree–Fock calculations [36]) compared with the case when they are forced to be identical. A diradical has two unpaired spins, and each unpaired spin induces spin polarization in the occupied orbitals. Dynamic spin polarization is said to be additive if the spin polarization effects of the unpaired spins reinforce, and competitive if they cancel. The ground state of a diradical is expected to be the state that leads to additive dynamic spin polarization. As an example, consider the spin polarization in square cyclobutadiene. With the orbital representation shown in Figure 12.13a, the two degenerate orbitals  $\phi_{2a}$  and  $\phi_{2b}$  do not have coefficients on common atoms, that is, the two orbitals are said to be disjointed [39]. A diradical with disjoint degenerate orbitals is called a disjoint diradical. (Obviously, with the alternative representation of Figure 12.5, the two degenerate orbitals have coefficients on common atoms. However, their linear combinations lead to disjoint orbitals.) The overlap density between the two disjoint orbitals is negligible and consequently so is the exchange integral between them. In addition, the overlap integral between the two disjoint orbitals is zero. Thus, in terms of the exchange and overlap integrals, it is difficult to predict which state of cyclobutadiene, singlet or triplet, is more stable.

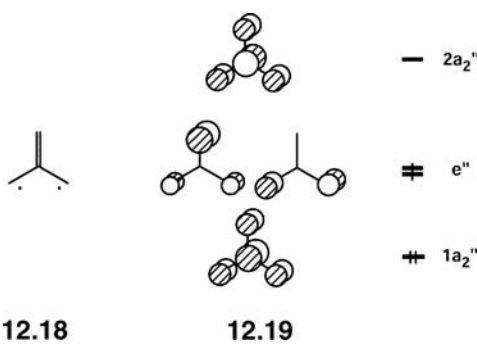
**FIGURE 12.13**

The bonding pi orbital  $\phi_1$ , the nonbonding pi orbitals  $\phi_{2a}$  and  $\phi_{2b}$ , and the antibonding pi orbital  $\phi_3$  of square planar cyclobutadiene: (a) in the absence of spin polarization and (b) in the presence of spin polarization. The up- and down-spin arrows are used in (b) to indicate the up- and down-spin spatial orbitals, respectively.

Figure 12.13b shows the spin polarization expected for the up- and down-spin electrons of the bonding orbital  $\phi_1$  in the singlet state. Consider the spin polarization induced by the up-spin electron in  $\phi_{2a\uparrow}$ . To enhance the exchange integral between  $\phi_{2a\uparrow}$  and  $\phi_{1\uparrow}$ , the up-spin orbital  $\phi_{1\uparrow}$  should increase the coefficients on C1 and C3, but decrease the coefficients on C2 and C4, using the orbital mixing  $\phi_1 + \lambda\phi_3$  ( $0 < \lambda \ll 1$ ). To reduce the Coulomb repulsion between  $\phi_{2a\uparrow}$  and  $\phi_{1\downarrow}$ , the down-spin orbital  $\phi_{1\downarrow}$  should decrease the coefficients on C1 and C3, but increase the coefficients on C2 and C4, using the orbital mixing  $\phi_1 - \kappa\phi_3$  ( $0 < \kappa \ll 1$ ). Likewise, the down-spin orbital  $\phi_{2b\downarrow}$  has the tendency to enhance the exchange integral between  $\phi_{2b\downarrow}$  and  $\phi_{1\downarrow}$  and reduce the Coulomb repulsion between  $\phi_{2b\downarrow}$  and  $\phi_{1\uparrow}$ . The down-spin electron of  $\phi_{2a\uparrow}$  reinforces the spin polarization induced by the up-spin electron of  $\phi_{2b\downarrow}$ . Namely, the singlet state leads to additive dynamic spin polarization. In the triplet state, the two unpaired spins of the degenerate levels have opposing spin polarization effects, so that no spin polarization takes place in  $\phi_{1\uparrow}$  and  $\phi_{1\downarrow}$ . That is, the triplet state leads to competitive dynamic spin polarization. Thus, the singlet state is predicted to be the ground state for square cyclobutadiene.

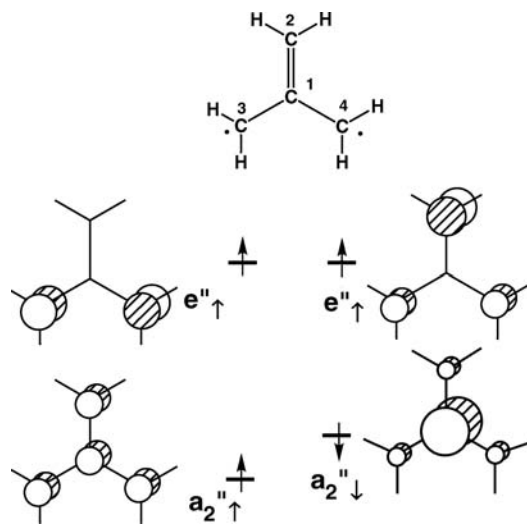
## 12.6 CROSS-CONJUGATED POLYENES

The molecules examined so far are conjugated in a linear sense, that is, double bonds are added at the ends of a polyene chain or the chains are tied together so that resonance structures can be drawn that propagate along the chain. Suppose, however, that a polyene is joined to the middle of an existing chain. These polyenes are said to be cross-conjugated and can have unusual properties because of their orbital topology. The simplest example is trimethylenemethane, **I2.18**. The neutral molecule has four  $\pi$  electrons and a resonance structure cannot be written



exclusively in terms of alternating single and double C—C bonds. As shown in **12.18**, only one C—C double bond can be drawn and the remaining two carbon atoms must each have one localized  $\pi$  electron. The  $\pi$  MOs are trivial to construct. In  $D_{3h}$  symmetry the  $p_\pi$  AOs from the outer three methylene groups generate combinations of  $a_2''$  and  $e''$  symmetry that we have seen time again. The  $a_2''$  combination interacts with the  $p$  AO on the central carbon to produce the  $1a_2''$  and  $2a_2''$  MOs in **12.19**. The  $e''$  combinations remain nonbonding. As shown in **12.19**, it is the  $e''$  set which contains two electrons. The two members of  $e''$  always have coefficients on common atoms no matter which linear combination of them is taken. Namely, **12.18** is a non-disjoint system [37]. The overlap density between the nondisjoint orbitals is substantial while the overlap integral between them is zero. Consequently, for the  $D_{3h}$  geometry of **12.18**, the triplet state is expected to be more stable than the singlet state. Indeed the triplet state is found to be more stable by 16.1 kcal/mol [38]. Let us now examine this from the viewpoint of spin polarization. As can be seen from Figure 12.14, additive dynamic spin polarization occurs when the two unpaired electrons in  $e''$  are parallel so that the triplet state should be the ground state.

The cyclobutadiene and trimethylenemethane examples suggest that for a disjoint diradical, the singlet state leads to additive dynamic spin polarization and, hence, should be the ground state. For a nondisjoint diradical, the triplet state provides additive dynamic spin polarization and hence should be the ground state. Several qualitative theories have been proposed for how to design high-spin molecules [39–42]. A very active area of research concerns itself with the preparation of molecules with high-spin states and characterization of their magnetic properties [35,43–47].

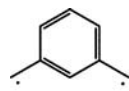
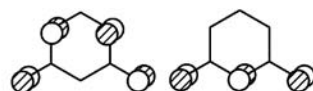


**FIGURE 12.14**

The bonding pi orbital  $\phi_1$ , the nonbonding pi orbitals  $\phi_{2a}$  and  $\phi_{2b}$ , and the antibonding pi orbital  $\phi_3$  of trigonal planar trimethylenemethane in the presence of spin polarization. The up- and down-spin arrows are used to indicate the up- and down-spin spatial orbitals, respectively.

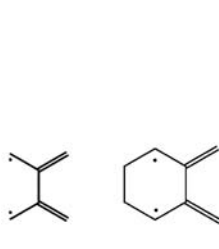
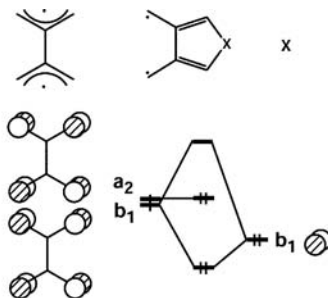
The singlet state of trimethylenemethane, **12.18**, is expected to be Jahn-Teller distorted to a structure where one C—C bond is shorter than the other two, that is, a reflection of the localized structure in **12.18**. On the other hand, another structure can be obtained for the singlet state where one methylene group has been rotated by 90°. This  $C_{2v}$  structure is thought to lie about 2 kcal/mol lower in energy [38]. Just like cyclobutadiene, the addition of two electrons forms a stable species, since the extra two electrons go into the nonbonding  $e''$  set. The stability of trimethylenemethane dianion and its relationship to  $C_4H_4^{2-}$  has suggested to some that it is aromatic. More recent calculations [48] have challenged this idea.

While trimethylenemethane has been known for some time, it was first prepared in 1966 [49]. There is a diradical which was prepared by Schlenk in 1915 [50]. It is a tetraphenyl derivative of **12.20**. The two MOs of relevance for Schlenk's hydrocarbon are shown in **12.21**. Notice that the  $a_2$  MO corresponds to

**12.20****12.21**

the nonbonding MO of the heptatrienyl system (Figure 12.2) while  $b_1$  corresponds to the nonbonding MO in the pentadienyl radical. Both MOs have appreciable amplitude on the methylene  $p$  AOs so they are nondisjoint. As expected, the triplet is 9.6 kcal/mol more stable than the singlet state [51].

Another cross-conjugated molecule which has been studied for sometime is tetramethyleneethane, **12.22** where two allyl radicals have been joined at the middle. When the allyl units are oriented perpendicular to each other, they are

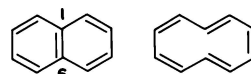
**12.22****12.23****12.24****12.25**

noninteracting so each nonbonding  $\pi$  orbital can either be combined or left alone. The situation is very reminiscent of that in twisted ethylene (Section 10.3.). The overlap density between the two nonbonding orbitals is negligible, and so is the overlap integral between them. Thus it is difficult to predict whether the ground state is singlet or triplet. A similar situation arises when the two allyl groups are forced into planarity, because the overlap integral and the overlap density between the two nonbonding allyl orbitals should be practically zero. Planar tetramethyleneethane is a pseudo disjoint system, so one might expect its ground state to be singlet. However, the spin polarization induced by an unpaired spin in one allyl fragment affects primarily the spin distribution of the same fragment. Thus a weak reinforcement of spin polarization results even for the singlet state. Recently, it was found for **12.23** [52], a close analog of **12.22**, that the singlet and triplet states are practically the same in energy. Forcing the two allyl groups into planarity and taking linear combinations of the nonbonding  $\pi$  MOs simply produces MOs of  $b_1$  and

$a_2$  symmetry, **12.24**. An interesting perturbation that has been explored [53] is to join two ends of the allyl unit by an electronegative atom or group that contains one  $p_{\pi}$  AO to form 3,4-dimethylene heterocycles. As indicated by **12.25**, the  $b_1$  combination interacts with the  $p_{\pi}$  AO of X to form bonding and antibonding combinations. The splitting between the two allyl nonbonding combinations is, therefore, increased which causes the singlet state to be stabilized over triplet (see Section 8.8). This indeed has been experimentally found to be the case; the ground state is decidedly the singlet one when X = O, S, and NR [53].

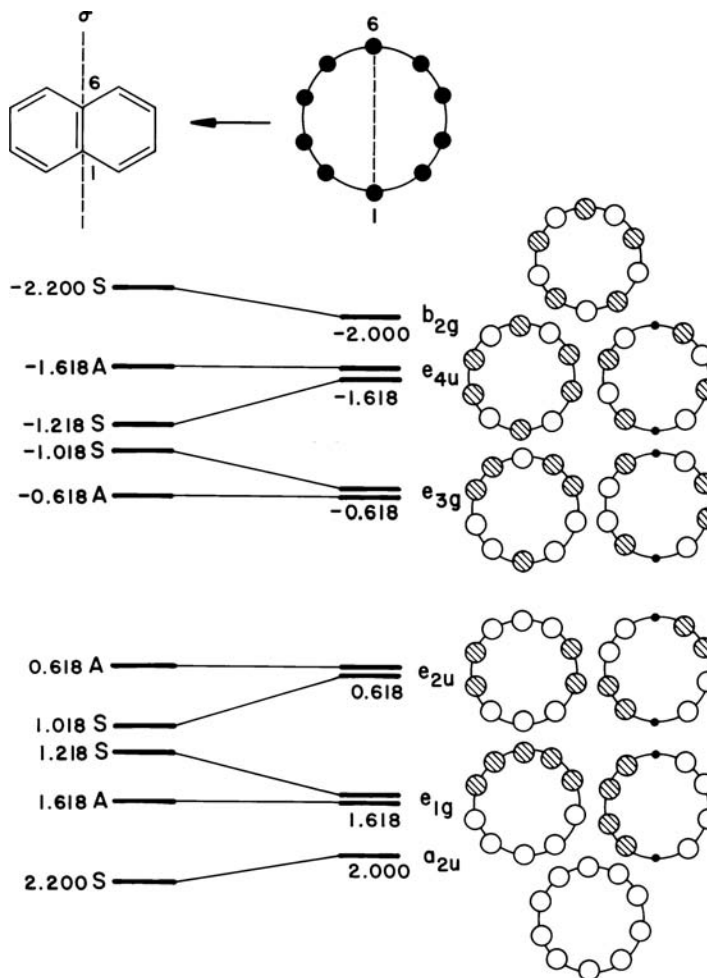
## 12.7 PERTURBATIONS OF CYCLIC SYSTEMS

The orbitals of Section 12.6 may be used to understand the orbital structures of other systems. Just as the orbitals of cyclobutadiene can be generated by linking together the end atoms of butadiene in a way analogous to that shown by Figure 5.4, the orbitals of naphthalene, **12.26**, may be derived by linking together pairs of atoms in the cyclic 10-annulene, **12.27**, as in Figure 12.15. Whether an orbital goes up or



12.26

12.27

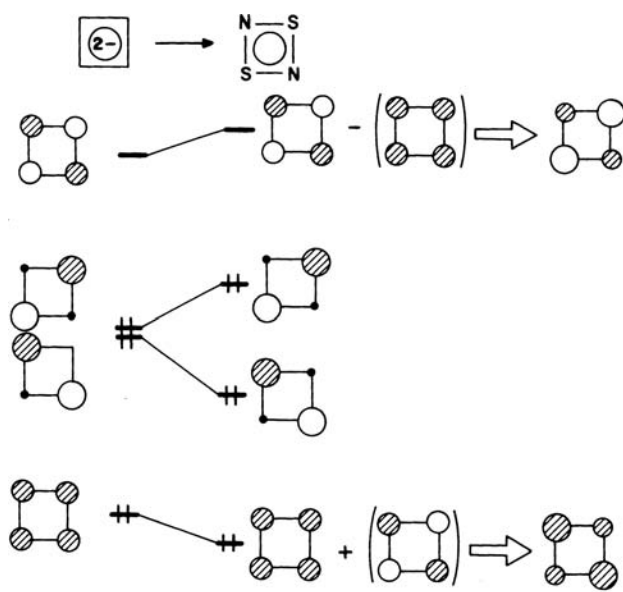
**FIGURE 12.15**

Generation of the  $\pi$  energy levels of naphthalene by linking together a pair of atoms of 10-annulene. The energies are given in units of  $\beta$  and no attempt has been made to represent the actual AO coefficients.

down in energy during the process depends upon the relative phases of the coefficients on the linking pair of atoms in that orbital. Notice that some orbitals remain unchanged in energy in the naphthalene case. They are the orbitals with nodes running through the pair of atoms C1 and C6 (**12.26**) and one partner of each degenerate pair is of this type. The new orbital energies may be derived numerically using first-order perturbation theory, as shown very nicely in Heilbronner and Bock's book [3]. With reference to equations 3.2, 3.4, and 3.6, the perturbation is simply one of increasing the value of  $H_{\mu\nu}$  from zero to  $\beta$  for the interaction integral linking the orbitals  $\mu$  and  $\nu$  located on the atoms between which a bond is to be made. Recall that within the Hückel approximation, overlap integrals between orbitals on different atoms are ignored. This leads to all  $\delta S_{\mu\nu} = 0$ , all  $\delta H_{\mu\nu} = 0$  for both  $\mu = \nu$  and  $\mu \neq \nu$  except for the one case (let us call this  $\delta H_{\kappa\lambda}$ ) that involves the bond formation itself. So in equations 3.4 and 3.6,  $\hat{H}_{ii} = c_{\kappa i}^0 \beta c_{\lambda i}^0$  and  $\hat{S}_{ii} = 0$  leading to  $e_i^{(1)} = c_{\kappa i}^0 \beta c_{\lambda i}^0$ . So the largest energy changes will be associated with the largest products of orbital coefficients  $c_{\kappa i}^0 c_{\lambda i}^0$ . This has guided our qualitative picture in Figure 12.15. Thus, in  $a_{2u}$  there is bonding between C1 and C6 so that MO goes down in energy on forming naphthalene. On the other hand, the highest orbital,  $b_{2g}$ , is antibonding between these carbons and so the MO rises in energy. For the remaining  $e$  sets, the wavefunctions can be chosen so that one member always contains a nodal plane across carbons C1 and C6. Therefore, one member of the  $e$  set remains unperturbed while the other is either stabilized or destabilized in energy.

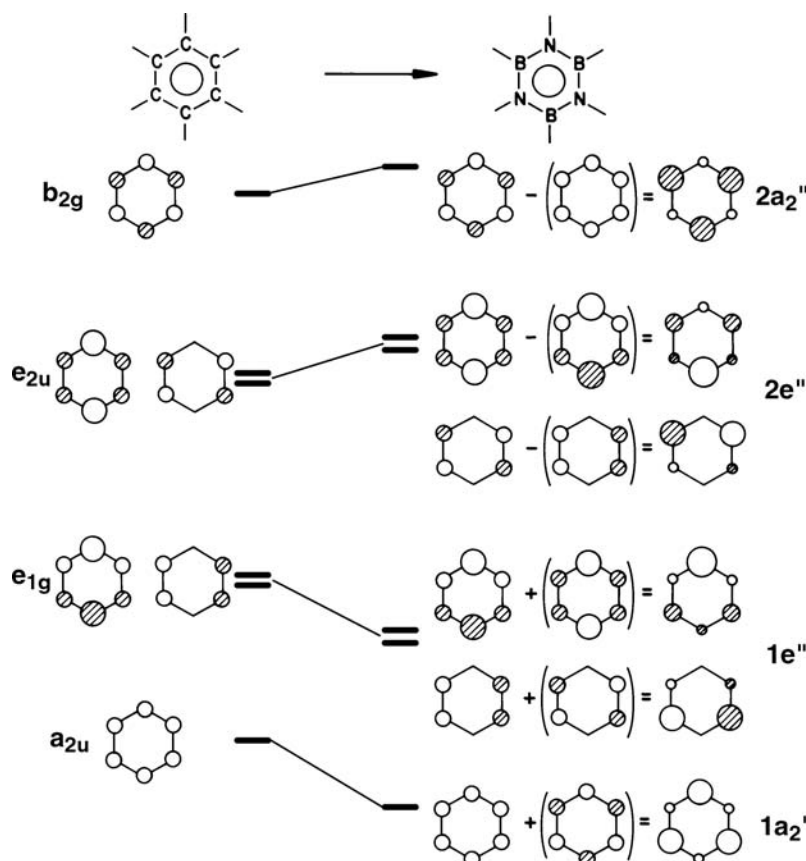
Another perturbation of these orbitals occurs when the atoms of the carbon framework are replaced with others of different electronegativity. Figure 12.16 shows how the  $\pi$  orbitals of  $S_2N_2$  are derived from those of cyclobutadiene<sup>2-</sup>. The lower symmetry removes the degeneracy of the middle pair of orbitals and these two new orbitals are either pure sulfur or pure nitrogen in character. We will leave it as an exercise for the reader to use the same perturbation theoretic ideas as employed for  $H_3$  in Figure 6.6 to generate these level shifts and the form of the new wavefunctions. With a total of six  $\pi$  electrons, the HOMO is a pure sulfur  $p$  orbital which lies above the mean value of N and S  $p$  atomic energies.

In a very similar vein, Figure 12.17 shows the construction of the orbitals for "inorganic benzene," the borazine molecule  $B_3N_3H_6$ . The degenerate benzene levels are not split apart in energy because the molecule has  $D_{3h}$  symmetry. However, the



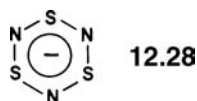
**FIGURE 12.16**

Generation of the  $\pi$  orbitals of  $S_2N_2$  from those of cyclobutadiene. For simplicity, we assume here that the electronegativity of carbon lies midway between that of sulfur and nitrogen. As a result, the old and new level patterns have a symmetry about the midpoint.

**FIGURE 12.17**

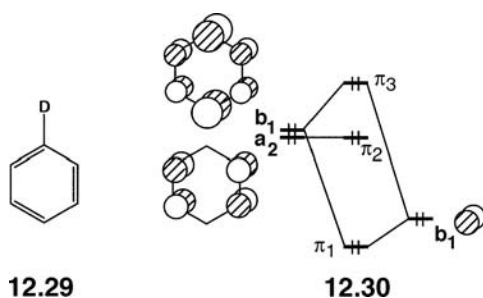
Generation of the  $\pi$  orbitals of borazine from those of benzene. For simplicity, we have assumed that the electronegativity of carbon lies midway between those for boron and nitrogen.

three higher energy orbitals contain more boron character than nitrogen character while the opposite is true for the three lower energy orbitals. This is a result clearly in keeping with an electronegativity perturbation on benzene, as is shown pictorially in the figure. With a total of six  $\pi$  electrons, this collection of orbitals is filled through  $1e''$ . The electronegativity of carbon lies almost exactly between that of boron and nitrogen (see Figure 2.4). Therefore, the  $e^{(1)}$  corrections will be close to zero for this perturbation. As shown in Figure 12.17,  $b_{2g}$  can mix into and stabilize  $a_{2u}$ . Experimentally this is the case. The ionization potential corresponding to the  $a_{2u}$  MO in benzene increases from 12.38 to 12.83 eV [54]. The ionization potential associated with the  $e_{1g}$  set increases somewhat more, from 9.25 to 10.14 eV. This is consistent with the fact that the  $e_{1g}-e_{2u}$  energy gap is smaller than the  $a_{2u}-b_{2g}$  one and consequently  $e^{(2)}$  is more stabilizing in the former case. Notice that the  $t_{ji}^{(1)}$  terms work out so that the  $1a_2''$  and  $1e''$  MOs are concentrated on the more electronegative nitrogen atoms and most of the density in  $2a_2''$  and  $2e''$  is associated with the less electronegative boron atoms.  $S_3N_3^-$  (12.28) has an analogous orbital pattern but has a total of 10  $\pi$  electrons. For this species, the levels are filled through  $2e''$ .



This is a feature of sulfur–nitrogen compounds in general—occupation of the lowest-energy orbital (as in  $\text{S}_2\text{N}_2$ ), or lowest-energy pair of orbitals (as in  $\text{S}_3\text{N}_3^-$ ) which lie above the midpoint of the  $\pi$  energy diagram. The molecule  $\text{S}_3\text{N}_3^-$  is isoelectronic with the planar  $\text{P}_6^{4-}$  unit in  $\text{Rb}_4\text{P}_6$  [55]. In this species (isoelectronic with  $\text{C}_6\text{H}_6^{4-}$ ), the P–P distances (2.15 Å) are longer than a typical P=P distance ( $\sim$ 2.0 Å) but slightly shorter than a typical P–P distance ( $\sim$ 2.2 Å).

There are many examples in organic chemistry where acceptor or donor substituents are positioned on the arene. Consider the simplified situation for the perturbation of the  $e_{1g}$  set in benzene by a donor group, 12.29. In the  $C_{2v}$  symmetry of the resultant molecule, the  $e_{1g}$  orbitals now have  $b_1$  and  $a_2$  symmetry.



12.29

12.30

For simplicity, the donor function will be represented by one  $p_\pi$  AO. The positioning of the relevant energy levels is indicated in 12.30 where we have taken into account the fact that most donor functions lie lower in energy than the  $e_{1g}$  set. As shown by 12.30 the  $a_2$  member is left nonbonding. We shall call this MO  $\pi_2$ . On the other hand, the  $b_1$  member of the  $e_{1g}$  set has the correct symmetry to interact with the donor AO. The energy level pattern for donor-substituted arenes is, therefore, relatively straightforward. A bonding combination between the  $b_1$  fragment orbitals,  $\pi_1$ , is produced. The antibonding combination,  $\pi_3$ , is largely arene-based and the  $\pi_2$ – $\pi_3$  energy gap is then a reflection of the strength of the donor substituent. The available experimental data [8,57] is consistent with this picture. Table 12.2 lists the ionization potentials associated with  $\pi_1$ ,  $\pi_2$ , and  $\pi_3$  for a series of donor-substituted arenes. The  $\text{NH}_2$ , OH, and SH substituents are all strong  $\pi$ -donor substituents and, therefore, the ionization potentials associated with  $\pi_3$  are lowered by 0.8 to over 1.1 eV with respect to the  $e_{1g}$  set in benzene. The amino substituent is definitely a stronger  $\pi$ -donor than hydroxyl and this is certainly born out for many reactivity patterns in organic chemistry. This is also consistent from a perturbation

TABLE 12.2 Ionization Potentials for Some Donor-Substituted Arenes

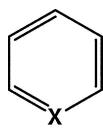
D	$\pi_3$	$\pi_2$	$\pi_1$	D	$\pi_3$	$\pi_2$	$\pi_1$
H	9.24	9.24	—				
$\text{NH}_2$	8.10	9.21	10.80	$\text{NMe}_2$	7.45	9.00	9.85
OH	8.67	9.36	11.50	$\text{OMe}$	8.42	9.21	11.02
SH	8.47	9.40	10.62	$\text{SMe}$	8.07	9.30	10.15
$\text{NHC(O)Me}$	8.46	9.35	10.75				
$\text{CH}_3$	8.83	9.36					
F	9.20	9.81	12.24				
Cl	9.10	9.69	11.69				
Br	9.02	9.65	11.21				
I	8.79	9.52	10.58				

theory perspective in that nitrogen is less electronegative than oxygen so its  $p_{\pi}$  AO must lie closer to the  $b_1$  fragment orbital and, therefore, it should destabilize  $\pi_3$  more. An acetamidyl group is not as strong of a  $\pi$ -donor as the amino substituent as shown by the  $\pi_3$  ionization potential since the lone pair on nitrogen is also delocalized into the carbonyl  $\pi^*$  system. Notice from Table 12.2 that the methyl group is a weak  $\pi$ -donor. The  $\pi_{\text{CH}_3}$  fragment orbital (see Section 10.5) is used here in exactly the same manner as the  $p_{\pi}$  AO in 12.30. This is also reflected in the larger  $\pi$ -donor ability displayed by the  $\text{NMe}_2$ ,  $\text{OMe}$ , and  $\text{SMe}$  groups on the right side of Table 12.2 compared to their parent substituents. In each case the ionization potential associated with  $\pi_3$  is smaller.

The series of halogen substituents offers a situation which is a little more complicated. The halogens are very electronegative. This is why the ionization potentials associated with  $\pi_2$  are all significantly larger than the  $e_{1g}$  set in benzene. (For the other substituents in Table 12.2,  $\pi_2$  does not vary by more than 0.1 eV.) This variation in  $\pi_2$  is most certainly due to the  $\sigma$  inductive effect associated with halogens which indirectly then by Coulombic forces stabilizes  $\pi_2$ . The  $\pi_3$  ionization potential for fluorine is almost identical to that of benzene itself. The ionization potential of the  $l_{\pi}$  set in HF should be a good model for the fluorine donor  $p_{\pi}$  AO in 12.30. It is at 16.06 eV; this is well below the 12.30 eV ionization for the lowest  $\pi$  level in benzene,  $a_{2u}$ . So the lowest  $b_1$  MO in fluorobenzene with an ionization potential of 16.31 eV most certainly corresponds to the fluorine lone pair orbital slightly stabilized by the benzene  $a_{2u}$  orbital. The next ionization at 12.24 eV is primarily benzene  $a_{2u}$  with some fluorine  $p_{\pi}$  mixed into it in an antibonding fashion. The  $b_1$  component of  $e_{1g}$  is then left basically unperturbed. Inspection of the rest of this series in Table 12.2 reveals that as the  $p_{\pi}$  AO of the donor moves to higher energy, the  $\pi_1$  and  $\pi_3$  ionization potentials become smaller as expected. The composition of  $\pi_1$  becomes more centered on the  $p_{\pi}$  AO of the halogen; however, the involvement with the lowest benzene  $\pi$  MO never becomes negligible (the ionization potentials corresponding to the lowest  $b_1$  MO are 14.68, 14.46, and 14.33 eV for  $X = \text{Cl}$ ,  $\text{Br}$ , and  $\text{I}$ , respectively). In this context, one should realize that for all cases in Table 12.2 the ionization of  $\pi_1$  is also going to be strongly affected by the interaction of benzene  $a_{2u}$  which will serve to destabilize  $\pi_1$  in contrast to simplified interaction displayed in 12.30.

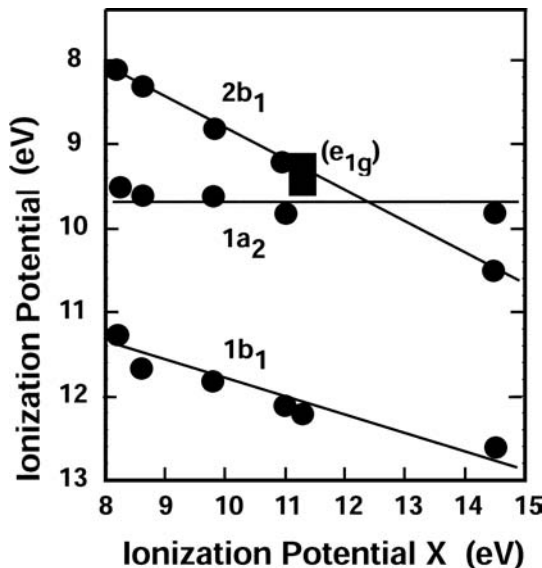
The intermolecular perturbation treatment outlined in Chapter 3 offers a straightforward way to show why electron density is increased at the two ortho and the para positions of a donor-substituted arene, whereas electron density is removed from these positions in an acceptor-substituted arene [56]. One can again use the  $b_1$  component of  $e_{1g}$ , but in order to create the polarization of the electron density, it is the second-order mixing of the  $b_1$  component of the empty  $e_{2g}$  set that is critical. The result is topologically identical to that developed for substituted olefins in Section 10.3. and will not be repeated here [56].

Another interesting series of perturbed benzene molecules is given by the heterocycles in 12.31, where  $X = \text{SiH}$ ,  $\text{N}$ ,  $\text{P}$ ,  $\text{As}$ , and  $\text{Sb}$  [58,59]. The vertical



12.31

ionization potentials,  $I_v$ , of the three  $\pi$  levels,  $1b_1$ ,  $1a_2$ , and  $2b_1$ , are plotted in Figure 12.18 versus the ionization potential for the  ${}^4\text{S}_{3/2} \rightarrow {}^3\text{P}_0$  states of  $X$ ,  $I_X$ . One can clearly see that there is a linear correlation for all three MOs with an equation of

**FIGURE 12.18**

A plot of the ionization potentials corresponding to the three  $\pi$  levels versus the ionization potential for  $X$  in some  $C_5H_5X$  heterocycles.

the form given in equation 12.27 where  $a$  and  $b$  are constants. The correlation coefficient for the  $1b_1$  and  $2b_2$  levels is 0.959 and 0.998, respectively.

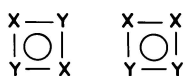
$$I_v = a + bI_X \quad (12.27)$$

The correlation is not as strong for the  $a_2$  MO. In particular the ionization potential for the  $e_{1g}$  set, given by the rectangle in Figure 12.18, deviates appreciably from the best-fit line. Neglecting this data point gives a correlation coefficient of 0.850. Consistent with the nodal structure of  $a_2$  (12.30), the ionization potential associated with this MO does not vary by more than 0.2 eV for the series and  $b$  is 0.045 in the linear-fit to equation 12.27. The small variation is consistent with inductive and Coulombic factors. The variation of the lowest  $\pi$  level,  $1b_1$ , and the HOMO,  $2b_2$ , is much more pronounced. In both cases the ionization potentials increase when the ionization potential of  $X$  increases, that is, as  $X$  becomes more electronegative. This is certainly understandable in terms of electronegativity perturbation theory. As shown in Section 6.4, the first-order correction to the energy,  $e_i^{(1)}$ , is given by equation 12.28. Here  $\delta\alpha$ , the change in the integral  $H_{\alpha\alpha} = \langle \chi_\alpha | H^{\text{eff}} | \chi_\alpha \rangle$  value for

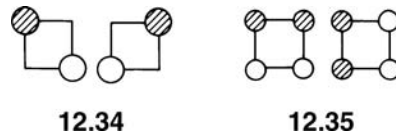
$$e_i^{(1)} = (c_{\alpha i}^0)^2 \delta\alpha \quad (12.28)$$

the perturbed atom, is of course directly related to a change in the ionization potential of  $X$  and  $c_{\alpha i}^0$  is the AO coefficient of the perturbed atom in MO  $\psi_i$ . Equations 12.27 and 12.28 then suggest that there should be a direct relationship between the changes in  $I_v$  and  $e_i^{(1)}$ . Specifically  $b$  in equation 12.27 should be close to  $(c_{\alpha i}^0)^2$  and, indeed, this is the case. Hückel theory gives  $c_{\alpha i}^0$  as 1/6 for  $1b_1$  and 1/3 for  $2b_2$ , respectively. The values of  $b$  are experimentally found to be 0.189 and 0.373 for the  $1b_1$  and  $2b_2$  MOs, respectively. These are very close to the values predicted from Hückel theory (0.166 and 0.333, respectively). The second-order corrections to the orbital energy can be shown to be less than  $\sim 0.2$  eV [58].

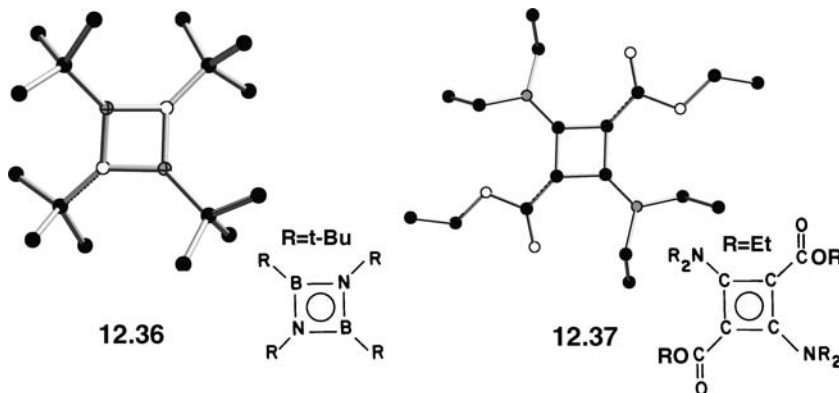
There are two obvious ways (12.32, 12.33) to reduce the symmetry of square cyclobutadiene by substitution with the aim of stabilizing the singlet structure. 12.32



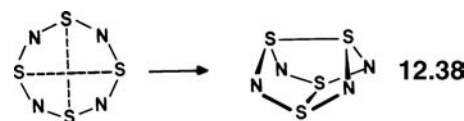
corresponds to the geometry of  $S_2N_2$  which we know exists but with two more electrons. What about the alternative structure **12.33**? The form of the wavefunctions in the substituted molecules gives us good clues as to the HOMO–LUMO gaps for the two possibilities. Recall that for the degenerate pair of cyclobutadiene orbitals we have some flexibility in the choice of the wavefunctions (see Figure 12.5). We will choose the degenerate pairs as in **12.34** and **12.35** which reflect the symmetry properties of **12.32** and **12.33**, respectively. In fact, the HOMO and



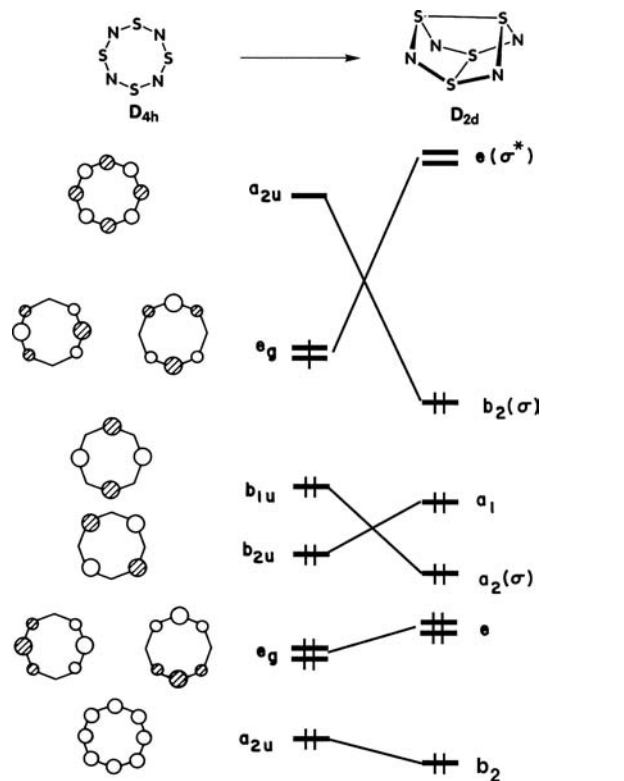
LUMO of the lower symmetry structures will look very much like these. The energies of the two functions **12.34** will differ by an amount which depends on the X/Y electronegativity difference alone, since these two orbitals are either completely X or completely Y located. The energies of **12.35** on the other hand are expected to be much like cyclobutadiene itself with a small gap between them. Both components of **12.35** are stabilized when X is more electronegative than Y in **12.33**. In addition to  $B_2N_2R_4$  (**12.36**) [60a] all cyclobutadienes containing  $\pi$ -donor and  $\pi$ -acceptor substituents which have been made (e.g., **12.37**) [60b] have a substitution pattern of the type **12.32**.



One interesting orbital derivation [32] is that of the unusual cradle-shaped molecule  $S_4N_4$  from the perturbed 8-annulene **12.38**. Just as on moving to  $S_2N_2$



from cyclobutadiene (Figure 12.19), the middle pair of orbitals of the 8-annulene split apart in energy on moving to  $S_4N_4$ , leading to the  $b_{2u}$  and  $b_{1u}$  levels of Figure 12.19. With a total of  $12\pi$  electrons, we expect either a triplet planar molecule with double occupancy of all the orbitals except the highest degenerate level, or a singlet species with some sort of distorted geometry. The latter will be necessary to remove the orbital degeneracy. One way this may be done (Figure 12.19) is to link two pairs of opposite atoms of the eight-membered ring as in **12.38**. This results in a dramatic stabilization of the highest energy  $\pi$ -type orbital (labeled  $a_{2u}$ );  $\sigma$  bonding is turned on between the S atoms. On the other hand, the phases between the S  $p_\pi$  AOs in the  $e_g$

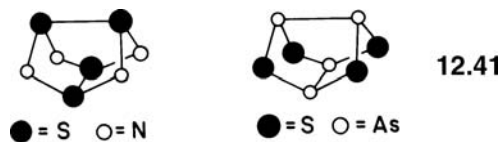
**FIGURE 12.19**

An orbital correlation diagram for the formation of the  $S_4N_4$  cage molecule. The  $\pi$  orbitals of planar  $S_4N_4$  may be obtained from those of the 8-annulene in a similar fashion to the generation of the levels of borazine in Figure 12.12.

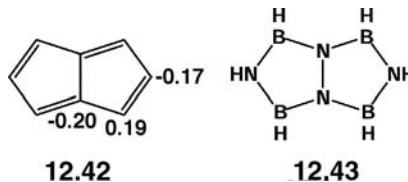
set are such that they are converted into  $\sigma$  antibonding MOs upon forming the bicyclic molecule. Therefore, this orbital set is considerably destabilized and a substantial HOMO–LUMO gap is generated. How the linking process occurs is an interesting question to answer. Just as in the derivation of naphthalene from 10-annulene, the largest orbital energy changes will be found when the coefficients on the linking atoms are largest. Since the  $a_{2u}$  orbital is an antibonding orbital, the largest coefficients will be associated with the least electronegative atom. The  $a_{2u}$  level is converted into a S–S  $\sigma$  bonding orbital **12.39** on forming the cradle. Likewise the  $b_{1u}$  level is converted into **12.40**.  $S_4N_4^{2+}$  has two fewer electrons. It is clear from

**12.39****12.40**

Figure 12.19 that the planar molecule will have a large HOMO–LUMO gap and that the bicyclic molecule will have a small one. Inspection of the levels of Figure 12.19 shows that while the  $b_{1u}$  orbital is stabilized, the two members of the  $e_g$  orbital are destabilized on bending the planar molecule.  $S_4N_4^{2+}$  is found as a planar species. In  $S_4N_4$  there is the unusual result of a two-coordinate nitrogen atom and three-coordinate sulfur. In the isoelectronic  $As_4S_4$  and  $As_4Se_4$  the chalcogen is now two coordinate (**12.41**) in accordance with the relative electronegativities of arsenic and chalcogen. In other words, the  $a_{2u}$  MO is concentrated more on As for these two compounds and, hence the formation of As–As  $\sigma$  bonds are preferred.



In Section 6.4, we saw how to predict the substitution pattern of molecules containing atoms of different electronegativity by making use of the charge distribution of the parent, unsubstituted molecule. The same approach may be used for polyenes containing inequivalent atoms. 12.42 shows the charge distribution of pentalene and 12.43 the “inorganic pentalene” made by replacing half of the carbon atoms with nitrogen and half with boron atoms. The more electronegative nitrogen



atoms occupy the sites of highest charge density in the unsubstituted analog. The idea that the most electronegative atoms should occupy sites of largest charge density is called the topological charge stabilization rule [62]. It is certainly grounded in an intuitive way with our notions about the electronegativity of atoms. It also relates to the first-order energy correction,  $e_i^{(1)}$ , in equation 12.28, since those atoms with largest coefficients coupled with atoms having the most negative values of  $\delta\alpha$  (the most electronegative ones) will provide the most stabilization. One can also recast a generalized Hückel solution [62,63] of the energy  $e_i$  associated with MO  $\psi_i$  as

$$e_i = \sum_{\mu} c_{\mu i}^2 \alpha_{\mu} + \sum_{\mu} \sum_{v \neq \mu} c_{\mu i} c_{v i} \beta_{\mu v} \quad (12.29)$$

where  $c_{\mu i}$  is the mixing coefficient of AO  $\chi_{\mu}$  in MO  $\psi_i$ ,  $\alpha_{\mu}$  is the Coulomb integral for  $\chi_{\mu}$  and  $\beta_{\mu v}$  is the resonance integral between  $\chi_{\mu}$  and  $\chi_v$ . The charge density  $q_{\mu}$  associated with  $\chi_{\mu}$  and bond order  $P_{\mu v}$  between  $\chi_{\mu}$  and  $\chi_v$  are defined by

$$q_{\mu} = \sum_i n_i c_{\mu i}^2 \quad (12.30)$$

and

$$P_{\mu v} = \sum_i n_i c_{\mu i} c_{v i} \quad (12.31)$$

where  $n_i$  ( $=2, 1, 0$ ) is the electron occupation number for MO  $\psi_i$ . The total energy,  $E$ , (at the Hückel level) can be written as follows [63].

$$E = \sum_{\mu} q_{\mu \mu} \alpha_{\mu} + \sum_{\mu} \sum_{v \neq \mu} P_{\mu v} \beta_{\mu v} \quad (12.32)$$

Recall that at the Hückel level all  $S_{\mu\nu}$  are set to zero (except when  $\mu = \nu$ ). If this restriction is lifted, then the charge densities and overlap populations become identical to those presented in equations 2.45 and 2.46, respectively. Namely

$$q_\mu = \sum_i n_i c_{\mu i}^2 + \frac{1}{2} \sum_{\nu \neq \mu} P_{\mu\nu} \quad (12.33)$$

and

$$P_{\mu\nu} = \sum_i n_i c_{\mu i} c_{\nu i} S_{\mu\nu} \quad (12.34)$$

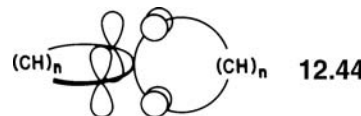
The total energy can then be expressed in a slightly more complicated way as

$$E = \sum_\mu q_{\mu\mu} H_{\mu\mu} + \sum_\mu \sum_{\nu \neq \mu} P_{\mu\nu} (H_{\mu\nu} - S_{\mu\nu} H_{\mu\mu}) \quad (12.35)$$

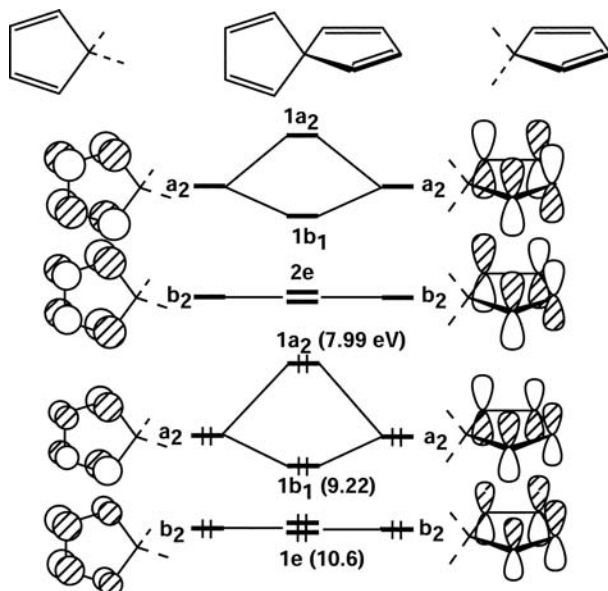
where  $H_{\mu\mu}$  and  $H_{\mu\nu}$  have the normal definitions associated with the Coulomb and resonance integrals. Equations 12.32 and 12.35 are very important. The first term is often called the site energy. It is maximized when the most electronegative atoms (ones with the smallest value of  $H_{\mu\mu}$ ) are located at positions where the charge density is largest. Hence, this provides a rationale for the topological charge stabilization rule [62]. The second term in equations 12.32 and 12.35 is called the bond energy term. It will be maximized when all bonding MOs or all bonding plus nonbonding MOs are filled. Thus, when antibonding MOs are occupied, they contribute a sizable negative number to  $P_{\mu\nu}$ , thereby reducing the bond energy term significantly. The use of these two factors offers an extremely simple yet accurate way to predict the structure of molecules and solids.

## 12.8 CONJUGATION IN THREE DIMENSIONS

Two acyclic polyene chains may be linked together by a single carbon atom to give a spiro-geometry as in 12.44 [1]. The overall symmetry of two planar polyenes that are connected by a single atom in this way is either  $D_{2h}$  or  $C_{2v}$ , depending upon whether the two ring sizes are identical or not. Take a case of  $C_{2v}$  symmetry. The  $\pi$

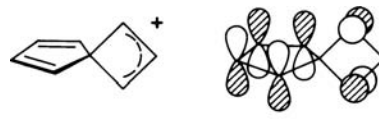
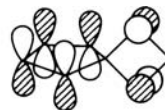


levels of the polyenes will then be of  $b_1$ ,  $b_2$ , or  $a_2$  symmetry. It can be shown by the insertion of the relevant phases in 12.44 that there will be a nonzero overlap only when two orbitals of  $a_2$  symmetry interact. Furthermore, there is a simple rule to tell whether this linking process results in a stabilization (to give a spiro-aromatic molecule) or a destabilization (to give a spiro-antiaromatic molecule). First of all  $4n$  systems are spiro-antiaromatic. This is easily shown by constructing the diagram (Figure 12.20) for spiro-nonatetraene. The HOMOs of both systems are of the correct symmetry and energy to interact with one another. Just as in the case of the repulsion of two ground state helium atoms with closed shells of electrons (Section 2.2), this two orbital-four-electron situation is, overall, a destabilizing one. Intrafragment mixing between the occupied and unoccupied sets of  $a_2$  orbitals will be very small; in the isolated fragments, they are orthogonal. It is also exceedingly reactive. The splitting between the bonding and antibonding combinations of the occupied  $a_2$  set has been determined [64] to be 1.23 eV by photoelectron

**FIGURE 12.20**

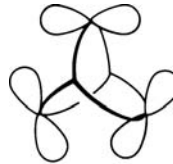
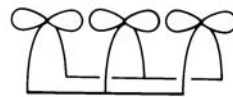
Assembly of the  $\pi$  orbital diagram for spiro-nonatetraene from those of two four-carbon fragments.

spectroscopy; the ionization potentials for the  $\pi$  MOs are given in parenthesis in Figure 12.20. The antibonding combination of  $a_2$   $\pi$  orbitals has a low ionization potential compared to most dienes. The interaction diagram for the spiro-octatrienyl cation, **12.45** can readily be constructed along the lines of Figure 12.20. The important difference is that now the  $a_2$  butadiene HOMO is stabilized by the LUMO of an allyl cation as shown in **12.46**.

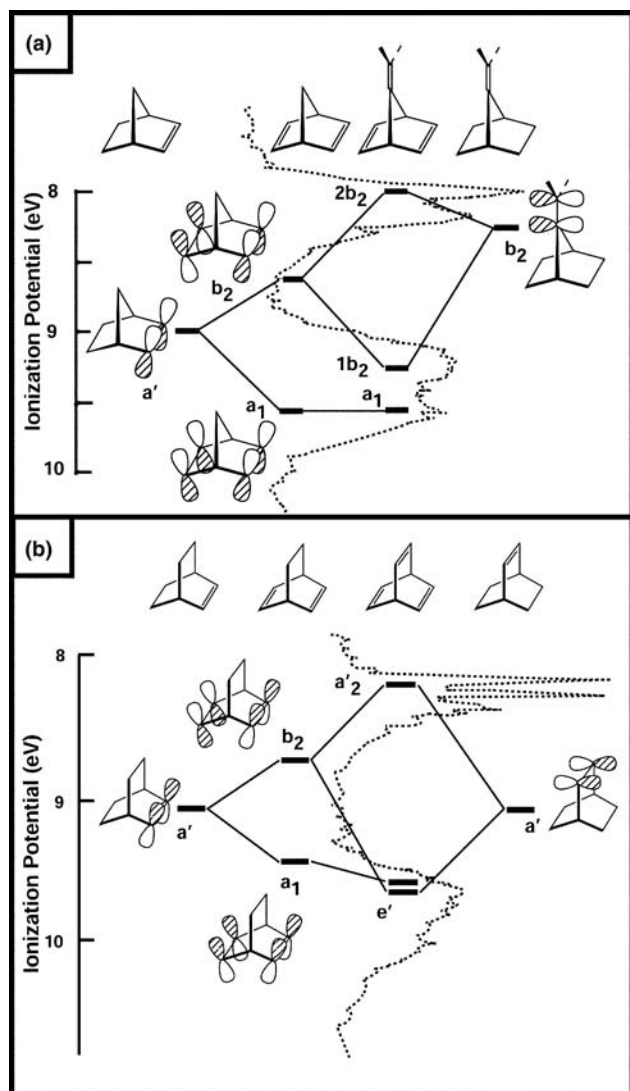
**12.45****12.46**

The nonbonding  $\pi$  level of allyl lies a low energy and consequently one expects that **12.45** should be stabilized. Calculations have shown this to be the case. The  $4n + 2 \pi$  electron systems will show this stabilizing feature. One needs to be careful here in that if the HOMO–LUMO gap is too large, then the stabilization may be negligible. The overlap in **12.44** is through-space and certainly not as large as that encountered between AOs on adjacent bonded atoms.

The potential for conjugation within polyene  $\pi$  “ribbons” has been examined for several other  $\pi$  topologies [1]. **12.47** and **12.48** illustrate two bicyclic motifs. Interaction diagrams can easily be constructed and generalized electron counting rules have been established [66]. The through-space conjugation mode in **12.47** is

**12.47****12.48**

called longicyclic. The experimental consequence of this interaction is represented here by the two examples from PE spectroscopy shown in Figure 12.21. Figure 12.21a constructs the  $\pi$  orbitals of 7-isopropylidenenorbornadiene. The actual PE spectrum [67] is displayed by the dotted line in this figure and the positions

**FIGURE 12.21**

The experimental construction of an orbital interaction diagram for (a) 7-isopropylidenenorbornadiene and (b) barralene. The actual PE spectrum for each compound is given in dotted lines.

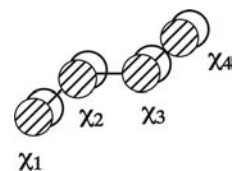
of all MOs correspond to experimental ionization potentials. The  $\pi$  orbital in norbornene is split into two on going to norbornadiene [68]. The bonding combination ( $a_1$ ) is separated from the antibonding combination ( $b_2$ ) by 0.58 eV. The  $\pi$  orbital (and  $\pi^*$ ) of the 7-isopropylidene function can interact with the  $b_2$   $\pi$  combination on the norbornadiene to form bonding ( $1b_2$ ) and antibonding ( $2b_2$ ) MOs. There are then three ionization potentials associated with the  $\pi$  orbitals: 9.54 ( $a_1$ ), 9.25 ( $1b_2$ ), and 7.97 ( $2b_2$ ) eV. Barralene (Figure 12.21b) presents a similar picture [69]. The  $\pi$  orbital of bicyclo[2.2.2]octene is split again by 0.58 eV on going to the  $a_1$  and  $b_2$  combinations of bicyclo[2.2.2]octadiene. The  $a_1$  MO is left nonbonding while the  $b_2$  combination combines in a bonding fashion with the third  $\pi$  orbital to form one member of the  $e'$  set of MOs. The antibonding combination then becomes the  $a'_2$  MO. The symmetry of barralene is  $D_{3h}$ . The  $e' - b_2$  splitting is considerable, and it is clear that the through-space overlap of  $\pi$  orbitals in both molecules is important. A more quantitative analysis of these interactions unfortunately becomes complicated [67,69]. Through-bond conjugation in norbornadiene and bicyclo[2.2.2]octadiene is very important in setting the  $a_1 - b_2$  energy gap (see Section 11.3 and Figure 11.5). There are also inductive effects when C—C double bonds are added to a structure

as well as geometry changes that prohibit a concrete dissection. Nevertheless, a  $\beta$  value in the range of 0.6 – 1.1 eV has been estimated [69] for barralene.

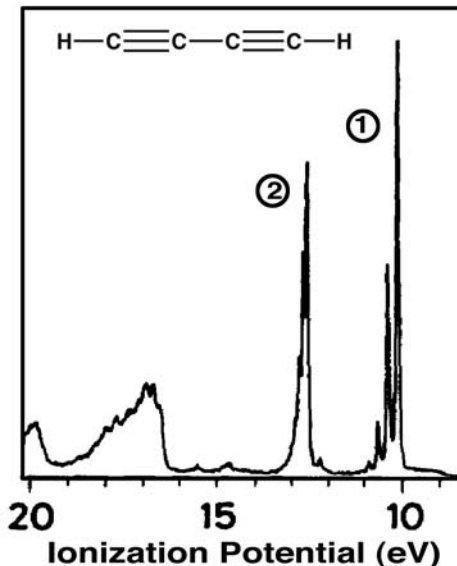
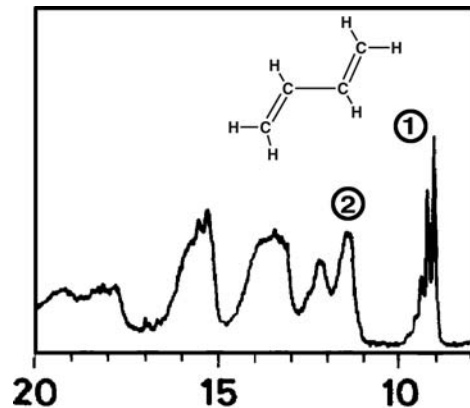
The through-space conjugation mode in **12.48** is called laticyclic. A number of systems have also been investigated here [66]. Definitive proof for this type of overlap has been harder to come by. However, at least one class of bicyclic hydrocarbons has been shown to have large  $\pi - \pi$  splittings [70] and more persuasively their radical cations have been shown to be delocalized by ESR spectroscopy [71].

## PROBLEMS

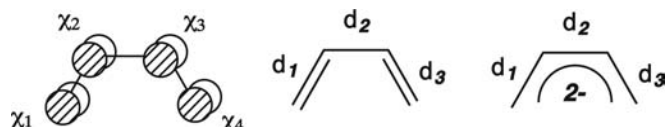
- 12.1. a.** Form the  $\pi$  orbitals of butadiene from the symmetry-adapted linear combination of  $p$  AOs shown below in  $C_{2h}$  symmetry. There is no need to normalize the wavefunctions but draw out the resultant combinations.



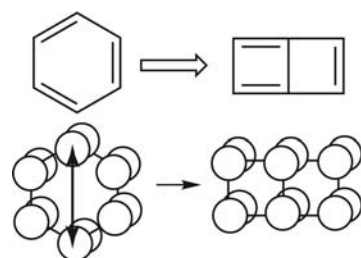
- b.** The photoelectron spectrum of transoid butadiene and 1,3-butadiyne adapted from are shown below. Assign peaks 1 and 2 in each compound



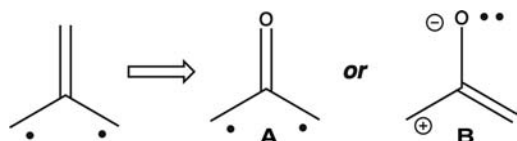
- 12.2.** a. Construct the  $\pi$  MOs of cisoid butadiene using the basis shown below. Draw the resultant orbitals and order them in terms of relative energy.  
 b. There are three bond lengths in butadiene which are also shown below. Use the MO occupations in (a) to determine the relative bond lengths.  
 c. Now consider butadiene dianion. What should happen to the relative bond lengths?



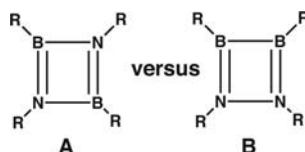
- 12.3.** The MOs of benzene can be used to form the MOs of the unusual hydrocarbon, 1,4-dehydrobenzene. By considering the perturbation of turning on  $\pi$  overlap between the  $p$  AOs on the 1 and 4 carbons, show what happens to the  $\pi$  orbitals of benzene in terms of first-order energy changes.



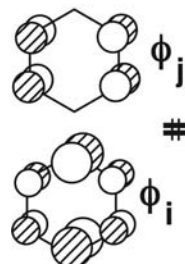
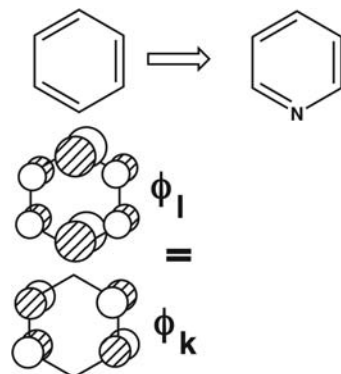
- 12.4.** a. The oxyallyl molecule has generated considerable experimental and theoretical interest. Conceptually, the  $\pi$  MOs for the molecule can easily be derived from the MOs of trimethylenemethane (**12.19**). Using electronegativity perturbation theory, show what happens to the  $\pi$  orbitals of trimethylenemethane going to the oxyallyl molecule.  
 b. There are two possible electronic states written in a valence bond way as "A" and "B". Using the results for the MOs write down the correct symbols for the two electronic states.



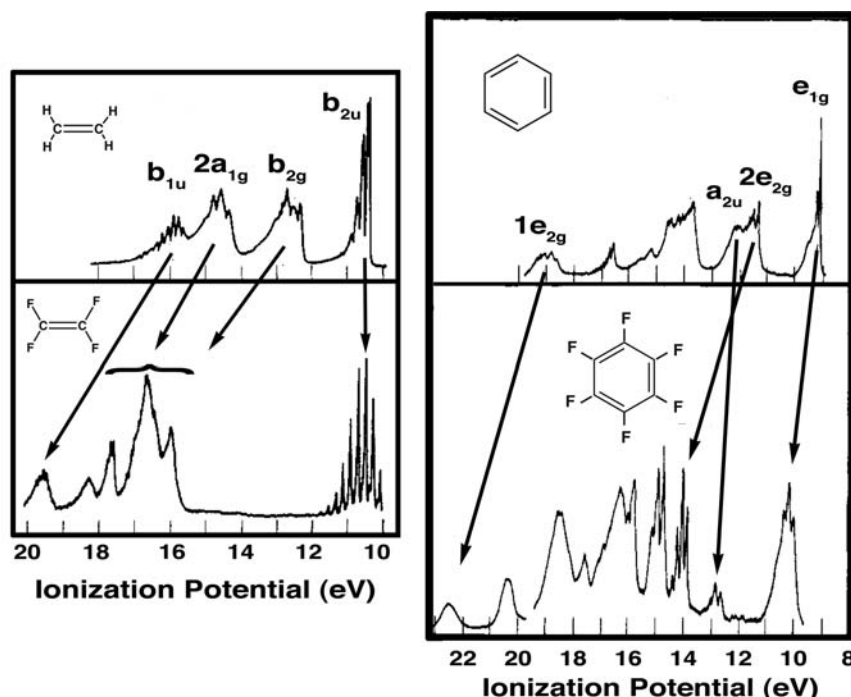
- 12.5.** There are two possible isomers for the heterocyclic analog of butadiene, **A** and **B**. Actually only **A** is found. Using electronegativity perturbation theory show why this is the case.



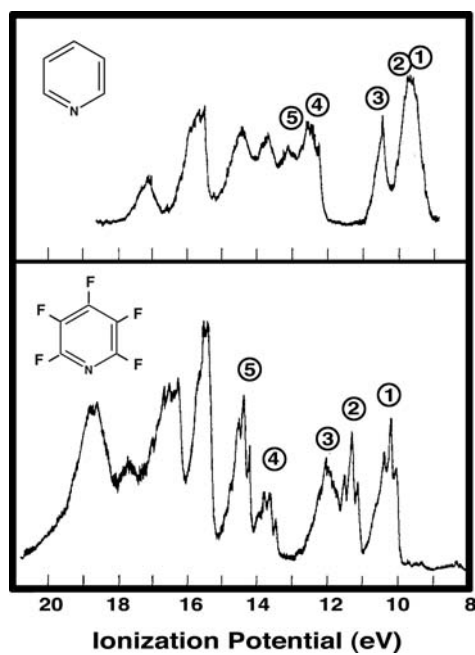
- 12.6. a.** Using the four MOs below determine the energy changes and the resultant MOs for the perturbation on going from benzene to pyridine.



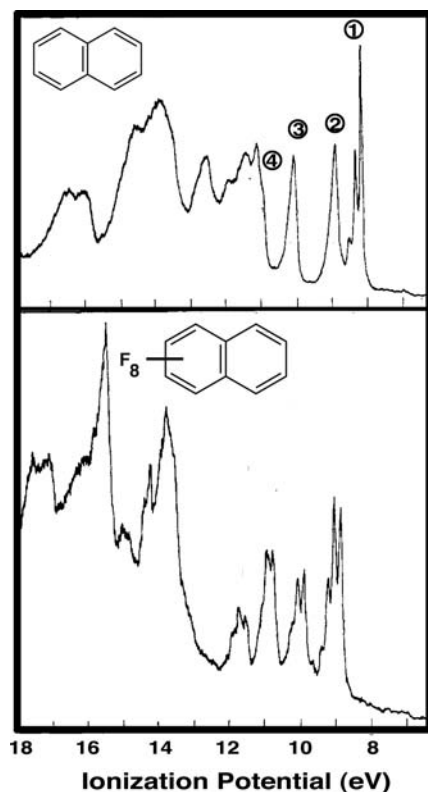
- b.** There is a useful technique in photoelectron spectroscopy, called the perfluoro effect, which can be used to assign ionizations. The idea is that  $\sigma$  and lone pair orbitals will be greatly stabilized in a perfluoro compound, whereas,  $\pi$  orbitals are not nearly perturbed as much. Typically ionizations from  $\sigma$  and lone pairs are increased by  $\sim 2 - 3$  eV, but those from  $\pi$  orbitals are increased only by 0.5 – 1.0 eV. Examples of this for ethylene and benzene are shown below as adapted from Ref. 72.



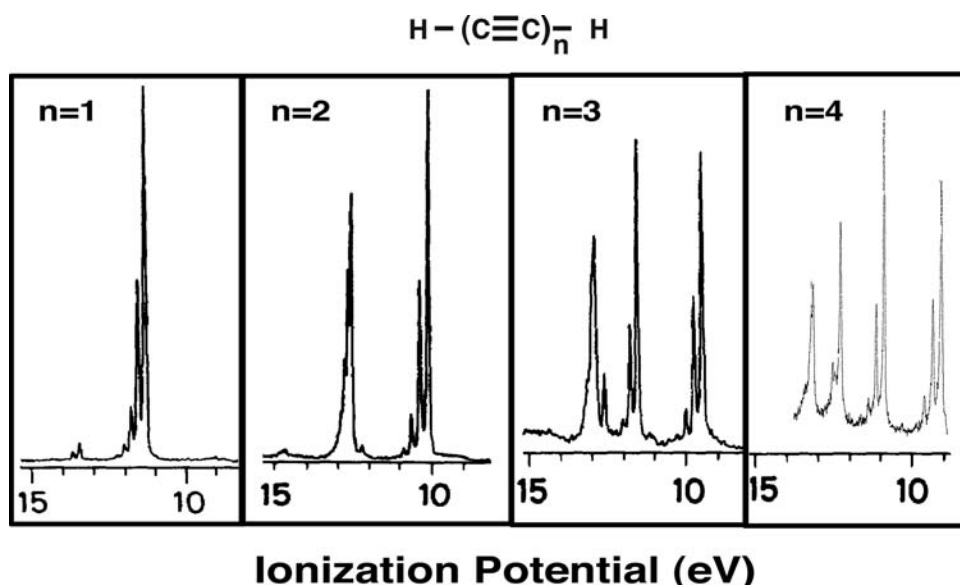
The photoelectron spectra of pyridine and pentafluoropyridine are shown below. Assign the first five ionizations (hint: one of the ionizations corresponds to a  $\sigma$  MO).



- I2.7.** a. Using Figure 12.15 as a guide draw out the shapes for the occupied  $\pi$  orbitals in naphthalene.  
 b. Below are the PE spectra for naphthalene and octafluoronaphthalene as adapted from Brundle, et al [73]. Assign the four ionizations to the MOs in (a) and correlate the IPs to the Hückel molecular orbital energies given in Figure 12.15. Use a  $\beta$  value of  $-2.2\text{ eV}$  and scale the  $\alpha$  value to give a best-fit to the experimental ionization potentials.



**12.8.** A portion of the PE spectra of a homologous series of poly-ynes is shown below (taken from Reference [72]). Construct a correlation diagram akin to Figure 12.4 for this series.




---

## REFERENCES

---

1. R. Gleiter and G. Haberhauer, *Aromaticity and Other Conjugation Effects*, Wiley-VCH, Weinheim (2012).
2. K. Yates, *Hückel Molecular Orbital Theory*, Academic Press, New York (1978).
3. E. Heilbronner and H. Bock, *The HMO-Model and its Application*, Wiley, New York (1976).
4. C. A. Coulson and A. Streitweiser, *Dictionary of  $\pi$ -electron Calculations*, Freeman, San Francisco (1965).
5. M. Beez, G. Bieri, H. Bock, and E. Heilbronner, *Helv. Chim. Acta*, **56**, 1028 (1973); K. D. Jordan and P. D. Burrow, *Acc.. Chem. Res.*, **11**, 341 (1978).
6. Y. Apelöig and D. Danovich, *Organometallics*, **15**, 350 (1996).
7. H. Bock and B. Solouki, *Chem. Rev.*, **95**, 1161 (1995).
8. K. Kimura, *Handbook of He(I) Photoelectron Spectra of Fundamental Organic Molecules*, Japan Scientific Societies Press, Tokyo (1981).
9. K. D. Jordan and P. D. Burrow, *Acc.. Chem. Res.*, **11**, 341 (1978).
10. M. Beez, G. Bieri, H. Bock, and E. Heilbronner, *Helv. Chim. Acta*, **56**, 1028 (1973).
11. H. W. Kroto, J. R. Heath, S. C. O'Brien, R. F. Curl, and R. E. Smalley, *Nature*, **318**, 162 (1985); A. D. J. Haymet, *J. Am. Chem. Soc.*, **108**, 319 (1986).
12. D. L. Lichtenberger, K. W. Nebesny, C. D. Ray, D. Huffman, and L. D. Lamb, *Chem. Phys. Lett.*, **176**, 203 (1991).
13. J. A. Lopez and C. Mealli, *J. Organomet. Chem.*, **478**, 161 (1994).
14. (a) K. H. Claus and C. Kruger, *Acta Crystallogr. Sect. C: Cryst. Struct. Commun.*, **44**, 1632 (1988). (b) D. A. Hrovat and W. T. Borden, *J. Am. Chem. Soc.*, **114**, 5879 (1992); C. D. Stevenson, E. C. Brown, D. A. Hrovat, and W. T. Borden, *J. Am. Chem. Soc.*, **120**, 8864 (1998); S. W. Staley, R. A. Grimm, and R. A. Sablosky, *J. Am. Chem. Soc.*, **120**, 3671 (1998) and references therein.
15. P. J. Garrett, *Aromaticity*, McGraw-Hill, New York (1971).
16. A. F. Voter and W. A. Goddard, III, *J. Am. Chem. Soc.*, **108**, 2830 (1986).

17. H. C. Longuet-Higgins and L. Salem, *Proc. Roy. Soc. (London)*, **A251**, 172 (1959).
18. C. H. Choi, M. Kertesz, and A. Karpen, *J. Am. Chem. Soc.*, **119**, 11994 (1997).
19. P. R. Taylor, A. Komornicki, and D. A. Dixon, *J. Am. Chem. Soc.*, **111**, 1259 (1989).
20. S. Shaik, A. Shurki, D. Danovich, and P. C. Hiberty, *J. Mol. Struct. (Theochem)*, **398–399**, 155 (1997), and references therein.
21. A. Gobbi, Y. Yamaguchi, G. Frenking, and H. F. Schaefer, III, *Chem. Phys. Lett.*, **244**, 27 (1995).
22. Y. Haas and S. Zilberg, *J. Am. Chem. Soc.*, **117**, 5387 (1995).
23. S. Shaik, S. Zilberg, and Y. Haas, *Acc. Chem. Res.*, **29**, 211 (1996); S. Shaik, A. Shurki, D. Danovich, and P. C. Hiberty, *Chem. Rev.*, **101**, 1501 (2001); R. S. Berry, *J. Chem. Phys.*, **35**, 2253 (1961).
24. H.-B. Bürgi, K. K. Baldridge, K. Hardcastle, N. L. Frank, P. Grantzel, J. Seigel, and J. Ziller, *Angew. Chem. Int. Ed.*, **34**, 1454 (1995); R. Rathore, S. V. Lindeman, A. S. Kumar, and J. K. Kochi, *J. Am. Chem. Soc.*, **120**, 6012 (1998).
25. P. von R. Schleyer, C. Maerker, A. Dransfeld, H. Jiao, and N. J. R. van E. Hommes, *J. Am. Chem. Soc.*, **118**, 6317 (1996).
26. D. W. Whitman and B. K. Carpenter, *J. Am. Chem. Soc.*, **102**, 4272 (1980).
27. S. Zilberg and Y. Haas, *J. Phys. Chem. A*, **102**, 10851 (1998); Y. Shiota, M. Kondo, and K. Yoshizawa, *J. Chem. Phys.*, **115**, 9243 (2001).
28. F. Kraus, J. C. Aschenbrenner, and N. Kerber, *Angew. Chem. Int. Ed.*, **42**, 4030 (2003); Y. Jung, T. Heine, P. V. R. Schleyer, and M. Head-Gordon, *J. Am. Chem. Soc.*, **126**, 3132 (2004).
29. J. E. Wertz and J. R. Bolton, *Electron Spin Resonance: Elementary Theory and Practical Applications*, McGraw-Hill, New York, (1972).
30. H. M. McConnell, *J. Chem. Phys.*, **24**, 764 (1956); H. M. McConnell and D. B. Chesnut, *J. Chem. Phys.*, **28**, 107 (1958).
31. R. W. Fessenden and R. H. Schuler, *J. Chem. Phys.*, **39**, 2147 (1963).
32. W. T. Borden and E. R. Davidson, *Acc. Chem. Res.*, **14**, 69 (1981); S.-Y. Chu, T.-S. Lee, and S.-L. Lee, *Chem. Phys. Lett.*, **91**, 17 (1982); H. Kollmar and V. Staemmler, *J. Am. Chem. Soc.*, **99**, 3583 (1977); H. Kollmar and V. Staemmler, *Theoret. Chim. Acta*, **48**, 223 (1978).
33. P. Karafiloglou, *J. Chem. Ed.*, **10**, 816 (1989).
34. O. Kahn, *Angew. Chem. Int. Ed.*, **24**, 834 (1985).
35. O. Kahn, *Molecular Magnetism*, Wiley-VCH, Weinheim (1993), Section 8.4.
36. J. A. Pople and D. L. Beveridge, *Approximate Molecular Orbital Theory*, McGraw-Hill, New York (1970).
37. W. T. Borden and E. R. Davidson, *J. Am. Chem. Soc.*, **99**, 4587 (1977).
38. P. G. Wenthold, J. Hu, R. R. Squires, and W. C. Lineberger, *J. Am. Chem. Soc.*, **118**, 475 (1996).
39. H. M. McConnell, *J. Chem. Phys.*, **39**, 1910 (1963).
40. H. M. McConnell, *Proc. Robert A. Welch Found. Conf. Chem. Res.*, **11**, 144 (1967).
41. A. Ovchinnikov, *Theoret. Chim. Acta*, **47**, 297 (1978).
42. R. Breslow, *Pure Appl. Chem.*, **54**, 927 (1982); R. Breslow and T. J. LePage, *J. Am. Chem. Soc.*, **109**, 6412 (1987).
43. H. Iwamura, *High-Spin Organic Molecules and Spin Alignment in Organic Molecular Assemblies*, Academic Press, New York (1990).
44. J. S. Miller, A. J. Epstein, and W. M. Reiff, *Chem. Rev.*, **88**, 201 (1988).
45. A. Caneschi, D. Gatteschi, and R. Sessoli, *Acc. Chem. Res.*, **22**, 392 (1989).
46. D. A. Dougherty, *Acc. Chem. Res.*, **24**, 88 (1991).
47. A. Rajca, *Chem. Rev.*, **94**, 871 (1994).
48. K. B. Wiberg, *J. Am. Chem. Soc.*, **112**, 4177 (1990).
49. P. Dowd, *J. Am. Chem. Soc.*, **88**, 2587 (1966).
50. W. Schlenk and M. Brauns, *Ber. Dtsch. Chem. Ges.*, **48**, 661, (1915).

51. P. G. Wentholt, J. B. Kim, and W. C. Lineberger, *J. Am. Chem. Soc.*, **119**, 1354 (1997).
52. K. Matsuda and H. Iwamura, *J. Am. Chem. Soc.*, **119**, 7412 (1997).
53. L. C. Bush, R. B. Heath, X. W. Feng, P. A. Wang, L. Maksimovic, A. I. Song, W.-S. Chung, A. B. Berinstain, J. C. Scaiano, and J. A. Berson, *J. Am. Chem. Soc.*, **119**, 1406 (1997).
54. B. P. Hollebone, J. J. Neville, Y. Zheng, C. E. Brion, Y. Wang, and E. R. Davidson, *Chem. Phys.*, **196**, 13 (1995).
55. W. Schmettow, A. Lipka, and H. G. von Schnerring, *Angew. Chem.*, **86**, 379 (1974). For  $C_6H_6^{4+}$  see M. Diefenbach and H. Schwarz, *Chem. Eur. J.*, **11**, 3058 (2005).
56. L. Libit and R. Hoffmann, *J. Am. Chem. Soc.*, **96**, 1296 (1977).
57. J. P. Maier and D. W. Turner, *J. Chem. Soc., Faraday Trans.*, **69**, 521 (1973).
58. C. Batich, E. Heilbronner, A. J. Ashe, III, D. T. Clark, U. T. Cobley, D. Kilcast, and I. Scanlan, *J. Am. Chem. Soc.*, **95**, 928 (1973).
59. For the PE spectra of di, tri and tetra-azines see R. Gleiter, E. Heilbronner, and V. Hornung, *Helv. Chim. Acta*, **55**, 255 (1972); R. Gleiter, M. Korbayashi, H. Neunhoeffer, and J. Spanget-Larsen, *Chem. Phys. Lett.*, **46**, 231 (1977).
60. (a) P. Paetzold, C. von Plotho, G. Schmid, R. Boese, B. Schrader, D. Bougeard, U. Pfeiffer, R. Gleiter and W. Schafer, *Chem. Ber.*, **117**, 1089 (1984). (b) H. J. Lindner and B. von Gross, *Chem. Ber.*, **107**, 598 (1974).
61. R. Gleiter, *Angew. Chem. Int. Ed.*, **20**, 444 (1981).
62. B. M. Gimarc, *J. Am. Chem. Soc.*, **105**, 1979 (1983).
63. G. J. Miller, *Eur. J. Chem.*, 523 (1998).
64. C. Batich, E. Heilbronner, and M. F. Semmelhack, *Helv. Chim. Acta*, **56**, 2110 (1973).
65. P. Bischof, R. Gleiter, and R. Haider, *J. Am. Chem. Soc.*, **100**, 1036 (1978).
66. M. J. Goldstein and R. Hoffmann, *J. Am. Chem. Soc.*, **93**, 6193 (1971).
67. E. Heilbronner and H.-D. Martin, *Helv. Chim. Acta*, **55**, 1490 (1972).
68. P. Bischof, J. A. Hashmall, E. Heilbronner and V. Hornung, *Helv. Chim. Acta*, **52**, 1745 (1969).
69. E. Haselbach, E. Heilbronner, and G. Schröder, *Helv. Chim. Acta*, **54**, 153 (1971).
70. W. Grimme, J. Wortmann, D. Frowein, J. Lex, G. Chen and R. Gleiter, *J. Chem. Soc., Perkin Trans. 2*, 1893 (1998).
71. A. M. Oliver, M. N. Paddon-Row, and M. C. R. Symons, *J. Am. Chem. Soc.*, **111**, 7259 (1989).
72. G. Bieri and L. Åsbrink, *J. Electron Spectrosc. Rel. Phenom.*, **20**, 149 (1980).
73. C. A. Brundle, M. B. Robin, and N. A. Kuebler, *J. Am. Chem. Soc.*, **94**, 1451 (1972), and references therein.

# Solids

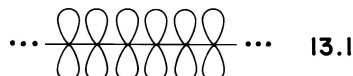
## 13.1 ENERGY BANDS

In the previous chapters, we have examined the orbitals of molecules of finite extent. In this chapter, we describe the case where there are, for all practical purposes, an infinite number of orbitals, namely, those of a solid—a giant molecule. We are exclusively concerned with crystalline materials, that is, those with a regularly repeating motif in all three dimensions. The results of earlier chapters, especially the previous one, will carry over quite naturally to this area. We take advantage of three factors:

1. The translational symmetry associated with the unit cell.
2. The symmetry present within the unit cell.
3. Perturbation theory principles within and between unit cells.

The global operational strategy is to develop the orbitals within the unit cell and then utilize cyclic boundary conditions to express the range of energies and associated wavefunctions of each starting orbital.

We start with a one-dimensional situation that of an infinite chain of carbon  $p_{\pi}$  orbitals (13.1). We actually know a lot about the form of the orbitals and their

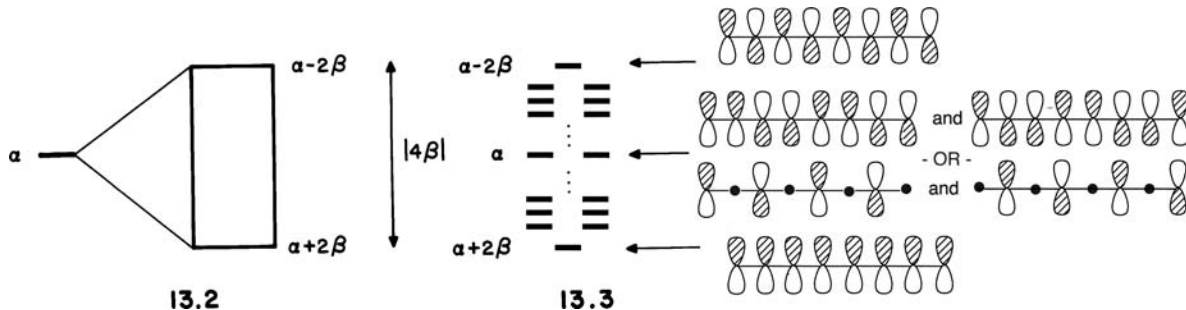


energies for the “infinite” polymer. From the results of Section 12.2, we know qualitatively what the orbitals of this chain will look like. Simple Hückel theory provided an analytic expression for the orbitals of such linear polyenes. Equation 13.1 gives the energy of the  $j^{\text{th}}$  level for an  $N$  atom (orbital) chain:

$$e_j = \alpha + 2\beta \cos \frac{j\pi}{N+1} \quad (13.1)$$

When  $N$  is very large, the lowest level ( $j=1$ ) will lie at  $e \approx \alpha + 2\beta$  where there are bonding interactions between all adjacent atom pairs. The highest energy level

$(j=N)$  will be at  $e \approx \alpha - 2\beta$  and contains antibonding interactions between all adjacent atom pairs. Between them lies a continuum of levels which we call an energy band with an energy spread of  $(\alpha - 2\beta) - (\alpha + 2\beta) = 4\beta$  (13.2, 13.3). In the middle



of this stack of levels at  $e = \alpha$  there is a nonbonding situation (13.3) which may be written in several different ways. This is analogous to the choice we had for the degenerate levels in the case of cyclic  $H_4$  (Chapter 5) or cyclobutadiene in Figure 12.5. The number of nodes increases as the energy increases, just as for the finite case and each is a degenerate combination. The general result when  $N$  is a very large number is the production of an energy band for each of the atomic orbitals (AOs) located on the atoms that make up the chain. This result is anticipated from group theory. If one inspects the group tables for the  $C_n$  groups in Appendix II, the fully symmetric irreducible representation,  $a$ , is of course always present. The resultant wavefunction,  $\psi(a)$  is given by

$$\psi(a) \propto \chi_1 + \chi_2 + \chi_3 + \chi_4 + \chi_5 + \chi_6 + \cdots + \chi_{N-3} + \chi_{N-2} + \chi_{N-1} + \chi_N$$

The phase of  $\chi$  remains the same on translation from one  $p$  AO (one unit cell) to another. When  $N$  is even then there is also a representation of  $b$  symmetry and, therefore,  $\psi(b)$  is given by

$$\psi(b) \propto \chi_1 - \chi_2 + \chi_3 - \chi_4 + \chi_5 - \chi_6 + \cdots + \chi_{N-3} - \chi_{N-2} + \chi_{N-1} - \chi_N$$

Now the phase of  $\chi$  changes on translation from one  $p$  AO (one unit cell) to another. These two unique solutions for  $\psi$  represent the lowest and highest energy solutions. All other irreducible representations come as  $e$  sets. Exactly in the middle of this "band" of molecular orbitals (MOs), the wavefunctions can be written as

$$\psi(e) \propto \chi_1 + \chi_2 - \chi_3 - \chi_4 + \chi_5 + \chi_6 - \cdots + \chi_{N-3} + \chi_{N-2} - \chi_{N-1} - \chi_N$$

and

$$\psi(e)' \propto \chi_1 - \chi_2 - \chi_3 + \chi_4 + \chi_5 - \chi_6 - \cdots + \chi_{N-3} - \chi_{N-2} - \chi_{N-1} + \chi_N$$

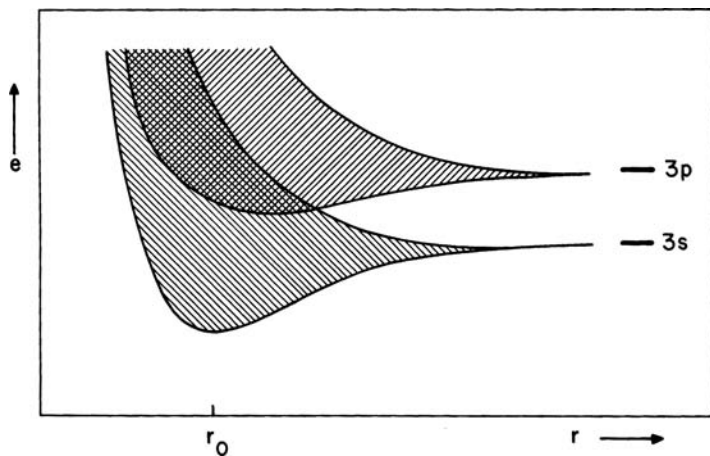
Taking the plus and minus combinations of these two members yields

$$\psi(e)'' \propto \chi_1 - \chi_3 + \chi_5 + \cdots + \chi_{N-3} - \chi_{N-1}$$

for the plus solution and

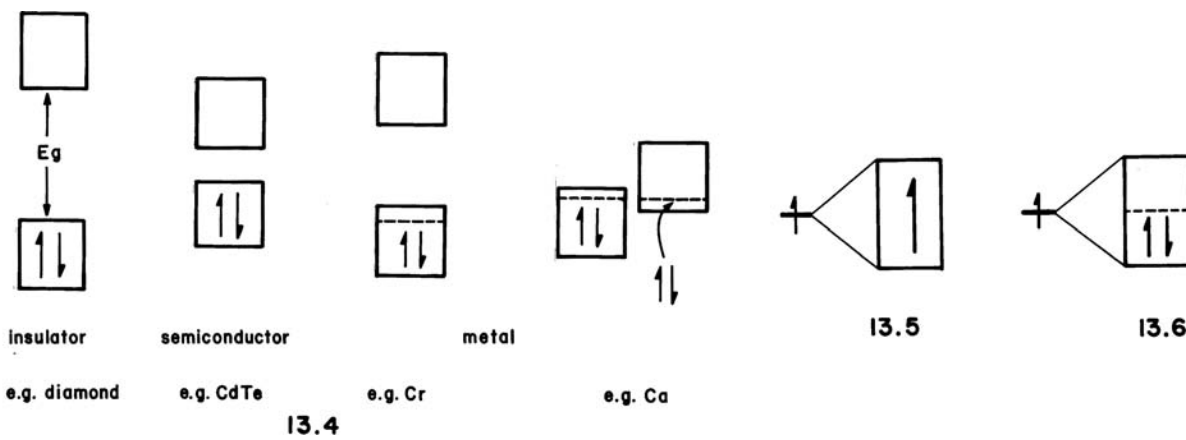
$$\psi(e)''' \propto \chi_2 - \chi_4 + \chi_6 + \cdots + \chi_{N-2} - \chi_N$$

for the negative one. These are equally valid representations of the  $e$  set. It is clear that only counting nearest-neighbor interactions, the  $\psi(e)$  set are rigorously nonbonding. We shall use the  $\psi(e)/\psi(e)'$  representations some times and the  $\psi(e)''/\psi(e)'''$  representations at others, depending on the nature of the problem.

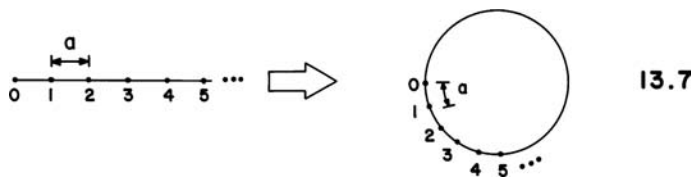
**FIGURE 13.1**

Energy levels for a crystalline solid of sodium atoms as a function of the separation  $r$  between adjacent sodium atoms. Notice how, as  $r$  decreases, the collection of  $s$  and  $p$  orbitals broaden into bands. At the equilibrium internuclear distance ( $r_0$ ) the  $s$  and  $p$  bands overlap.

In two and three dimensions a similar process occurs. The atomic energy levels of each of the atoms of, for example, elemental sodium are broadened into bands in the solid. The width of these bands depends upon the magnitude of the corresponding interaction integrals (the equivalent of the Hückel  $\beta$  for the  $p_{\pi}$  one-dimensional chain above) between the orbitals concerned. Figure 13.1 shows [1] how the energy levels for a crystalline solid of sodium atoms vary with internuclear distance. The shaded areas represent the energy bands formed from the valence  $3s$  and  $3p$  orbitals. Notice that the bottom of each band, at the equilibrium separation  $r_0$ , lies lower in energy than the corresponding atomic level at infinite separation (i.e., it is bonding) but the top of the band lies above this energy. Also notice that at large internuclear separation there are two separate "s" and "p" bands but as this distance decreases the two bands overlap (intermix). In general, the energetic relationship of the energy bands of a solid material and how many electrons are contained in each has an extremely important bearing on the properties of the system. If the highest occupied band (the valence band) is full then the solid is an insulator or semiconductor, depending on whether the energy gap,  $E_g$  (the band gap) between the valence band and the lowest empty band (conduction band) is respectively large or small (13.4). If the valence band is only partially full or full and empty bands overlap, then a typical metal results. For the notation used in 13.4, we imply that all the electrons in the occupied levels are paired. The case of 13.5 all levels of the band are singly occupied gives rise to a magnetic insulator. The energetic considerations that control the stability of the alternatives 13.5 and 13.6 are very similar indeed to those used in Section 8.8 to view high and low spin arrangements in molecules.



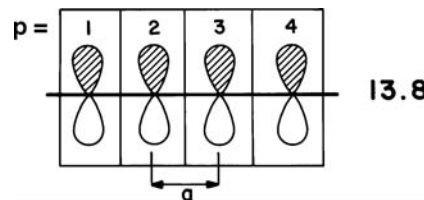
How are we going to represent in more general terms the complex situation of the giant molecule and handle this infinite collection of orbitals? We can make use of results from Chapter 12 and assume that the atoms in the very long one-dimensional chain behave as if they were embedded in a very big ring. Alternatively, we can imagine imperceptibly bending the very long chain and tying the end atoms together (13.7) to make a cyclic system, which is referred to as imposing cyclic boundary conditions. Surely, the overwhelming majority of the atoms of a real crystal are so far away from the edges that they do not know the difference. Obviously then our discussion will only be valid for macroscopic crystals, those where most of the atoms are “bulk” rather than surface atoms.



Now the values of the energy levels of the very long cyclic chain (with  $N$  atoms) are given from equation 12.9 as

$$e_j = \alpha + 2\beta \cos \frac{2j\pi}{N} \quad (13.2)$$

where  $j = 0, 1, 2, \dots, N$ . Since  $N$  is quite a large number, we can recast this equation to make it easier to handle. It was mentioned above that we only study crystalline materials in this book. These are systems where a fundamental building block of atoms is regularly repeated in three dimensions. In 13.8, we show a part of the

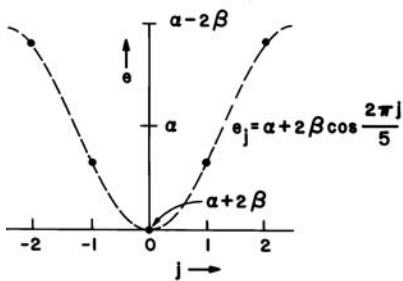


infinite one-dimensional chain of carbon 2p-orbitals with several unit cells outlined. The position of an arbitrary unit cell  $p$  is given by the vector  $\mathbf{R}_p = (p - l)a$ , where  $a$  is the length of the repeat unit cell. The latter contains the regularly repeating motif. We can define a new index  $k = 2\pi j/Na$  which runs from 0 to  $+\pi/a$  such that equation 13.2 now can be recast as

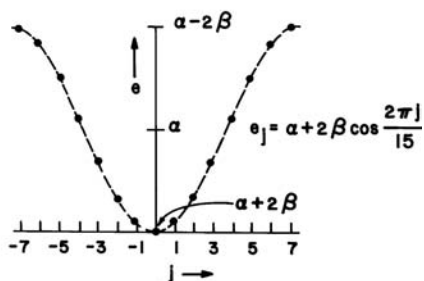
$$e(k) = \alpha + 2\beta \cos ka \quad (13.3)$$

Notice that by using  $k$  we have gotten rid of the  $j$  index and problematic  $N$ . Furthermore, there are, as we shall see, a range of values associated with  $k$  that yield unique solutions.

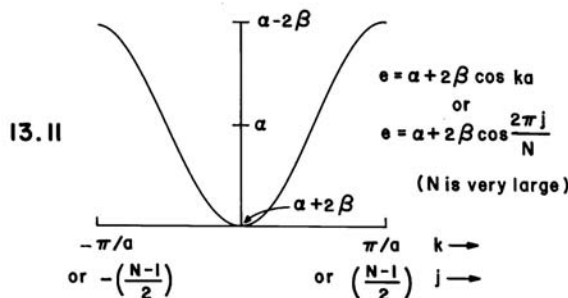
Let us show this result pictorially [2]. Using equation 12.10 we may plot out the energy levels of, for example,  $C_5H_5$  as shown in 13.9. The allowed values of  $j$  are 0,  $\pm 1$ , and  $\pm 2$ . The reader can show that substitution of values of  $|j|$  larger than 2 just



13.9



13.10



leads to duplication of the values we have already derived, that is, use of  $|j| > (N - 1)/2$  for  $N = \text{odd}$  (or  $N/2$  for  $N = \text{even}$ ) leads to redundant information. **13.10** shows an analogous plot for a ring containing 15 atoms. Here,  $j$  runs from 0 through  $\pm 1, \pm 2$ , and so on to  $\pm 7$ . Finally, **13.11** shows a diagram exactly analogous to those of **13.9** and **13.10** for the infinite system. Now  $k$  runs from 0 through  $-\pi/a$  or  $j$  from 0 through  $+(N - 1)/2$  where  $N$  is very large, just as in the finite case.

One important difference between the finite and infinite cases, of course, is that whereas  $j$  increases in discrete steps,  $k$  increases continuously. Also in a way closely similar to the behavior of  $e_j$  in the finite case, when  $|j| > (N - 1)/2$ , values of  $|k| > \pi/a$  lead to redundant information in the solid state. In the crystal, the region of  $k$  values between  $\pi/a$  and  $-\pi/a$  is referred to as the first Brillouin zone, usually just called the Brillouin zone. The point  $k = +\pi/a$  is called the zone edge and  $k = 0$  the zone center.

Since the diagram **13.11** has mirror symmetry about  $k = 0$  it will suffice just to use one-half of this diagram. We choose the right-hand half that corresponding to positive  $k$ . The index  $k$  is called the wavevector. The variation in energy as a function of the wavevector  $k$  is called the dispersion of the band. In three-dimensional situations, the vector nature of the wavevector becomes apparent and we write it as  $\mathbf{k}$ .

The wavefunctions describing the chain **13.7** may be generated by seeing how the wavefunctions of the finite ring change when  $N$  becomes large. As before we define  $\chi(r - \mathbf{R}_p)$  as the atomic orbital wavefunction located on the atom in the  $p^{\text{th}}$  unit cell, namely,  $\mathbf{R}_p = (p-1)a$ . From equation 12.10, the wavefunctions of the  $N$  atom chain are given by

$$\phi_j = \sum_{p=1}^N c_{pj} \chi(r - \mathbf{R}_p) = \frac{1}{\sqrt{N}} \sum_{p=1}^N \left\{ \exp \left[ \frac{2\pi i j(p-1)}{N} \right] \right\} \chi(r - \mathbf{R}_p) \quad (13.4)$$

Substitution of  $k = 2\pi j/Na$  leads to the expression

$$\phi(k) = \frac{1}{\sqrt{N}} \sum_{p=1}^N \{ \exp[ik(p-1)a] \} \chi(r - \mathbf{R}_p) \quad (13.5)$$

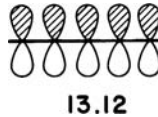
which may be rewritten as

$$\phi(k) = \frac{1}{\sqrt{N}} \sum_{p=1}^N \{\exp[ik\mathbf{R}_p]\} \chi(r - \mathbf{R}_p) \quad (13.6)$$

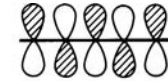
As we see in three dimensions the exponential in this equation needs to be written as a vector dot product  $\exp(i\mathbf{k} \cdot \mathbf{R}_p)$ . Just as the vector  $\mathbf{R}_p$  (with dimensions of length) maps out a direct space ( $x, y, z$  coordinates of points) with which we are familiar, so  $\mathbf{k}$  [with dimensions of  $(\text{length})^{-1}$ ] maps out a reciprocal space. The functions  $\phi(k)$  are called Bloch functions [3–5] and are nothing more than the symmetry adapted linear combination of atomic orbitals, under the action of translational symmetry and the cyclic boundary condition, just as the orbitals of equation 12.10 are the symmetry adapted linear combinations of orbitals under the action of the cyclic group of order  $N$ . In Section 12.3, we showed for the illustrative example of the  $\pi$  orbitals of benzene ( $N = 6$ ) that the exponential in equations 12.10 and 13.4 was just the character of the  $j^{\text{th}}$  irreducible representation of the cyclic group of order  $N$ . Similarly, the exponential in equations 13.5 and 13.6 is related to the character of the  $k^{\text{th}}$  irreducible representation of the cyclic group of infinite order, which, according to the picture of 13.7, we may replace with an (infinite) linear translation group. Just as the wavefunctions of equation 12.10 with different  $j$  are orthogonal to each other so the wavefunctions of equation 13.6 are orthogonal for different  $k$  values. At  $k = 0$  we can write, using equation 13.6,

$$\phi(k = 0) = \frac{1}{\sqrt{N}} [\cdots \chi(r) + \chi(r - a) + \chi(r - 2a) + \cdots] \quad (13.7)$$

where  $\chi(r)$  is some arbitrary orbital located on some atom in the chain;  $\chi(r - a)$  lies at a distance  $a$  along the chain (13.8),  $\chi(r - 2a)$  at a distance  $2a$ , and so on, from  $\chi(r)$ . The coefficients from equation 13.7 are all equal. This wavefunction is shown in 13.12 and of course extends all the way through the crystal. The normalization



13.12



13.13

constant of  $N^{-1/2}$  has been included as a result of the Hückel approximation of Section 12.2. We can easily calculate the energy associated with the wavefunction of equation 13.7 as

$$e(k = 0) = \langle \cdots \chi(r) + \chi(r - a) + \chi(r - 2a) + \cdots | H^{\text{eff}} | \cdots \chi(r) + \chi(r - a) + \chi(r - 2a) + \cdots \rangle \quad (13.8)$$

Using the same technique as in 12.5 for the molecular case

$$e(k = 0) = \frac{1}{N} [N(\alpha + 2\beta)] = \alpha + 2\beta \quad (13.9)$$

where

$$\alpha = \langle \chi(r - \mathbf{R}_p) | H^{\text{eff}} | \chi(r - \mathbf{R}_p) \rangle$$

and

$$\beta = \langle \chi(r - \mathbf{R}_p) | H^{\text{eff}} | \chi(r - \mathbf{R}_{p+1}) \rangle$$

This, of course, is the result from equation 13.3 too. Notice that  $N$ , although included in the expression for the wavefunction, has neatly dropped out of the expression for the energy. At  $k = \pi/a$  the wavefunction  $\phi(k)$  becomes

$$\begin{aligned}\phi(k = \pi/a) &= \frac{1}{\sqrt{N}} [\dots \chi(r)\exp(i\pi 0) + \chi(r-a)\exp(i\pi) + \chi(r-2a)\exp(2i\pi) + \dots] \\ &= \frac{1}{\sqrt{N}} [\dots \chi(r) - \chi(r-a) + \chi(r-2a) - \dots]\end{aligned}\quad (13.10)$$

which is shown in 13.13. The energy of this function can be readily seen to be equal to  $e(k = \pi/a) = \alpha - 2\beta$ . Since  $\beta < 0$ , the maximum bonding (and therefore maximum stabilization) is found at the zone center ( $k = 0$ ) and the maximum antibonding character at the zone edge ( $k = \pi/a$ ). This is in keeping with the form of the band dispersion of 13.11 and the qualitative picture of 13.3. For a general value of  $k$  equation 13.5 may be rewritten as

$$\phi(k) = \frac{1}{\sqrt{N}} [\dots \chi(r) + \chi(r-a)\exp(ika) + \chi(r-2a)\exp(2ika) + \dots] \quad (13.11)$$

which leads to a general expression for the energy

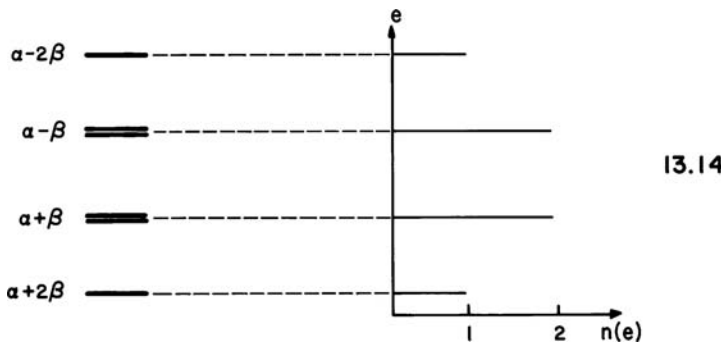
$$\begin{aligned}e(k) &= \langle \phi(k) | H^{\text{eff}} | \phi(k) \rangle \\ &= \left(\frac{1}{N}\right) N \{ \alpha + [\exp(ika) + \exp(-ika)]\beta \} \\ &= \alpha + 2\beta \cos ka\end{aligned}\quad (13.12)$$

With a given number of electrons per unit cell in the solid the levels, doubly occupied, will be filled from the lowest energy level to a certain energy  $e_F$ , called the Fermi level. Here, we assume that each level is doubly filled. The Fermi level corresponds to a specific value of  $k$ , called the Fermi vector,  $k_F$ . The total one electron energy per unit cell,  $E/N$ , is then obtained by integrating equation 13.13

$$\frac{E}{N} = \frac{a}{2\pi} \int_{-k_F}^{k_F} 2e(k) dk = \frac{2a}{\pi} \int_0^{k_F} e(k) dk \quad (13.13)$$

This is an exactly analogous equation to the energy sum over a discrete collection of levels in the molecular case. In the solid there are, however, a very large number of levels and electrons to occupy them. The total energy of equation 13.13, therefore, refers to the content of one unit cell. In many cases, there will be a nonintegral number of electrons per cell as a result of this choice. There will always be the same number of energy bands as there are atomic orbitals in the unit cell. Sometimes, however, the collection of bands arising from the three  $p$  orbitals on an atom are referred to collectively as “the  $p$  bands” or the levels derived from the five  $d$  orbitals as “the  $d$  bands.”

One of the important quantities in describing the electronic structure of a molecule or an extended system is the so-called density of states (DOS). In a molecule, there is a set of discrete levels as shown in 13.14 for the  $\pi$  orbitals of benzene. Thus, the number of allowed orbital levels with energy  $e$  (i.e., density of



states,  $n(e)$ ) is two if  $e$  refers to the doubly degenerate levels, one if  $e$  refers to the nondegenerate ones, and zero otherwise. Similarly, the density of states  $n(e)$  in an extended system is the number of allowed band orbital levels having an energy  $e$ . For the one-dimensional case,  $n(e)$  is known to be inversely proportional to the slope of the  $e$  versus  $k$  curve (equation 13.14) as shown in Figure 13.2b.

$$n(e) \propto \left[ \frac{\partial e(k)}{\partial k} \right]^{-1} \quad (13.14)$$

At  $k=0$  and  $\pi/a$  Figure 13.2a shows that the slope of this curve is zero and so  $n(e) \rightarrow \infty$ . Such features in  $n(e)$  at these points are called van Hove singularities. In two and three dimensions, the densities of states are invariably more complex, but do not usually display such singularities in  $n(e)$ .

The methodology we have just described is a natural extension of the molecular ideas discussed in previous chapters. This LCAO approach is called the tight-binding method by solid-state physicists. It exists in several different forms, each of which has an analog in the molecular area. We have used simple Hückel theory to derive the results in this section but more sophisticated ones and many-electron approaches are available. Much of the work in this area comes from solid-state physics.

**FIGURE 13.2**

(a) Dispersion [ $e(k)$ ] of a one-dimensional energy band formed by overlap of adjacent  $p_{\pi}$  orbitals. The orbitals are filled up to the dashed line, the Fermi level ( $e_F$ ). The corresponding  $k$  value is called  $k_F$ . (b) A density of states diagram appropriate to Figure 3.2a.

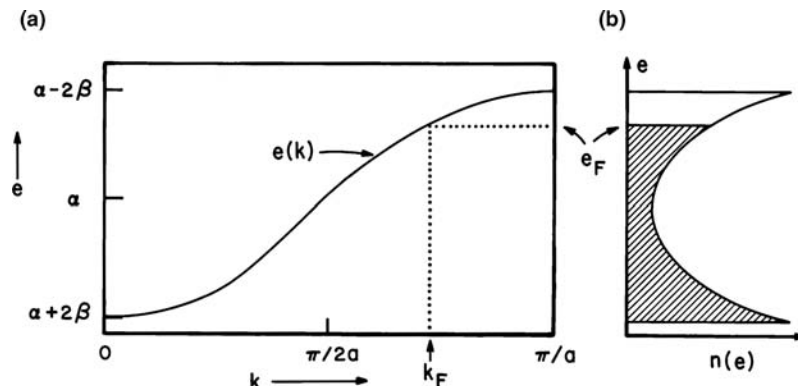
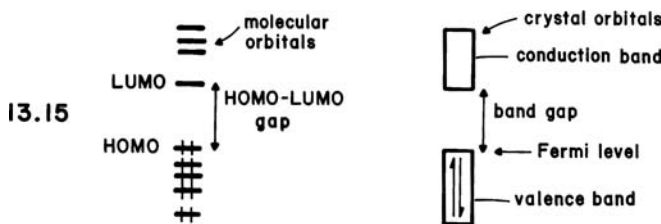


**TABLE 13.1** Approximate Analogs Between Molecular and Solid-State Terminology

Molecular	Solid-State
LCAO-MO	Tight-binding
Molecular orbital	Crystal orbital (band orbital)
HOMO	Valence band
LUMO	Conduction band
HOMO-LUMO gap	Band gap
Jahn-Teller distortion	Peierls distortion
High or intermediate spin	Magnetic
Low spin	Nonmagnetic

In Table 13.1 and 13.15, we compare some of the jargon used with its nearest molecular equivalent.



Equations 13.3 and 13.5 give the expressions for the simplest possible case, that of a one-dimensional chain containing a single orbital per unit cell. Most systems are more complex. Suppose that there are a set of atomic orbitals  $\{\chi_1, \chi_2, \dots, \chi_n\}$  contained in each unit cell. Then one can form a set of Bloch functions  $\{\phi_1(k), \phi_2(k), \dots, \phi_n(k)\}$ , given in general by

$$\phi_\mu(k) = \frac{1}{\sqrt{N}} \sum_{p=1}^N [\exp(ik\mathbf{R}_p)] \chi_\mu(r - \mathbf{R}_p) \quad (13.15)$$

where  $\mu = 1, 2, \dots, n$ . In such a case, the band orbitals  $\psi_j(k)$  ( $j = 1, 2, \dots, n$ ) are given by linear combinations of the Bloch functions as

$$\psi_j(k) = \sum_{\mu=1}^n c_{\mu j}(k) \phi_\mu(k) \quad (13.16)$$

where the mixing coefficients,  $c_{\mu j}$ , refer to how much an AO  $\mu$  in the unit cell mixes into crystal orbital  $j$  at a particular value of  $k$ . This is entirely analogous to the molecular case. An important difference is that  $c_{\mu j}$  for molecules is a real number, but in the solid state this is not necessarily so. The energy of such a band orbital  $e_j(k)$  is given by the usual expression

$$e_j(k) = \frac{\langle \psi_j(k) | H^{\text{eff}} | \psi_j(k) \rangle}{\langle \psi_j(k) | \psi_j(k) \rangle} \quad (13.17)$$

The variational theorem, when applied to this problem allows determination of the optimum values of the  $c_{\mu j}(k)$  and the generation of a secular determinant

$$\begin{vmatrix} H_{11}(k) - S_{11}(k)e(k) & H_{12}(k) - S_{12}(k)e(k) & \cdots & H_{1n}(k) - S_{1n}(k)e(k) \\ H_{21}(k) - S_{21}(k)e(k) & H_{22}(k) - S_{22}(k)e(k) & \cdots & H_{2n}(k) - S_{2n}(k)e(k) \\ \vdots & \vdots & \ddots & \vdots \\ H_{n1}(k) - S_{n1}(k)e(k) & H_{n2}(k) - S_{n2}(k)e(k) & \cdots & H_{nn}(k) - S_{nn}(k)e(k) \end{vmatrix} = 0 \quad (13.18)$$

where the interaction element  $H_{\mu\nu}(k)$  and the overlap integral  $S_{\mu\nu}(k)$  are defined in terms of the Bloch functions

$$\begin{aligned} H_{\mu\nu}(k) &= \langle \phi_\mu(k) | H^{\text{eff}} | \phi_\nu(k) \rangle \\ &= N^{-1} \sum_p \sum_q \{ \exp[ik(\mathbf{R}_q - \mathbf{R}_p)] \} \langle \chi_\mu(r - \mathbf{R}_p) | H^{\text{eff}} | \chi_\nu(r - \mathbf{R}_q) \rangle \end{aligned} \quad (13.19)$$

and

$$\begin{aligned} S_{\mu\nu}(k) &= \langle \phi_\mu(k) | \phi_\nu(k) \rangle \\ &= N^{-1} \sum_p \sum_q \{ \exp[ik(\mathbf{R}_q - \mathbf{R}_p)] \} \langle \chi_\mu(r - \mathbf{R}_p) | \chi_\nu(r - \mathbf{R}_q) \rangle \end{aligned} \quad (13.20)$$

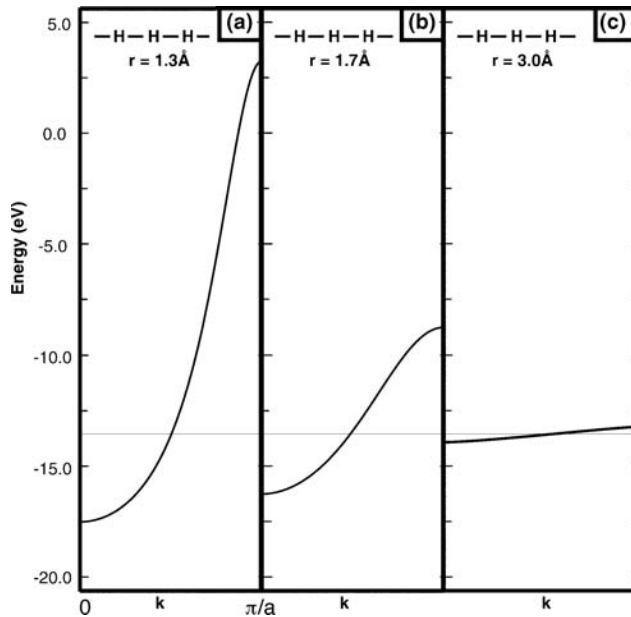
Equation 13.18 may be written in a shorthand way as

$$|H_{\mu\nu}(k) - S_{\mu\nu}(k)e(k)| = 0 \quad (13.21)$$

This is a very similar equation indeed to that in equation 1.31 derived for the molecular case. There the basis orbitals used were single atomic orbitals; here they are Bloch functions. In order to derive the energy levels of a molecule, equation 1.31 needs to be solved just once (in principle). For an extended solid-state system, equation 13.21 needs to be solved at several “ $k$  points” in order to map out the energy dispersion of the bands. Sometimes we will be able to derive simple algebraic solutions for  $e(k)$ , as shown above for a particularly simple example. These cases will utilize Hückel theory. This is adequate for our purposes since we are interested in qualitative explanations. The most important deficiency that everyone should recognize is that we have not included overlap in the normalization. The consequence is that, for example, the band and DOS plots in Figure 13.2 are symmetrical about the  $e = \alpha$  point. In other words, the bonding crystal orbitals are stabilized as much as their antibonding counterparts are destabilized. The Hückel approximation also uses one interaction energy,  $\beta$ , which is related to the value of the nearest neighbor overlap. In other words, all nearest neighbor interactions are the same, as if the nearest neighbor internuclear distances are identical, and all the rest are assigned a value of zero. Finally, the atoms are all identical so the starting orbital energy is given as  $\alpha$ . Actually the last two caveats can be relaxed a little, but as we shall see the solution becomes much more cumbersome.

Most often, as is the case too for almost all the molecules we have studied, we have to rely on a computational solution. We shall use extended Hückel theory, as outlined in Section 1.3, for these situations, but the qualitative results do carry over to other levels. In general a more realistic calculation, even at the extended Hückel level will

- I. take overlap into account explicitly so that antibonding orbitals will be more destabilized than the bonding ones are stabilized;

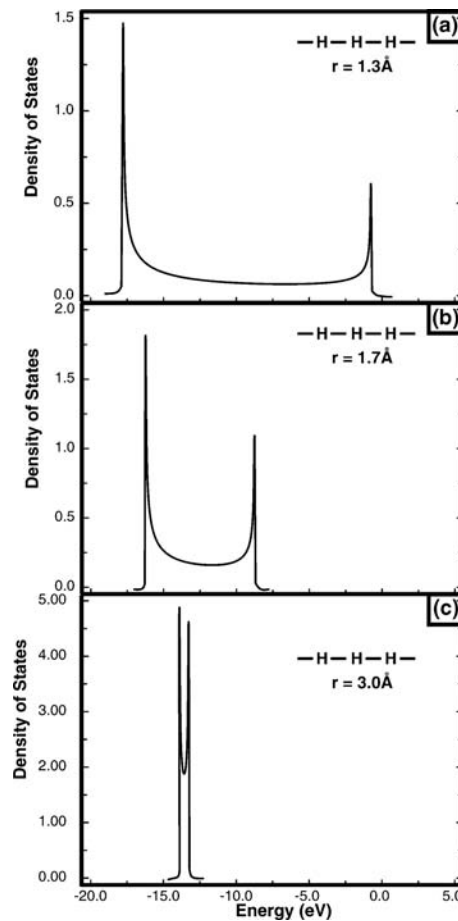
**FIGURE 13.3**

Band formed from a one-dimensional chain of hydrogen atoms where the unit cell contains one hydrogen atom. (a)–(c) represent the cases when the H–H distance is 1.30, 1.70, and 3.00 Å, respectively. The thin horizontal line represents the energy of an isolated H  $s$  AO.

2. create bands that spread out around a particular energy. This is set by what kind of orbital(s) is used, that is, it is determined by the overlap with other AOs and electronegativity factors *within* the unit cell;
3. determine the magnitude of the band dispersion by taking into account how much overlap there is between unit cells.

The  $\sigma$  overlap of H  $s$  AOs has the same functional form as the  $\pi$ -type overlap between  $p$  AOs. The picture we have constructed using Hückel theory in Figure 13.2 should be compared to that found for the hydrogen chain (one H  $s$  AO in each unit cell) in Figure 13.3 which uses an extended Hückel Hamiltonian and includes a specific calculation with use of overlap in the calculation. The three cases cover representative situations for when orbital overlap between unit cells is strong, moderate, and small—Figures 13.3a–c, respectively. Recall that the H–s overlap is dependent on the H–H distance in an exponential manner, see 1.1. Consequently as the distance between hydrogen atoms increases, the overlap and band dispersion quickly decreases. The thin horizontal line indicates the energy of an isolated hydrogen  $s$  AO. It is very clear that this does not lie in the middle of the band and that as the overlap increases the part between the top of the band to this line and the part between the bottom and the line becomes increasingly different. This result is just what one expects from the two-orbital molecular problem—see equations 2.8–2.11. The DOS curves associated with these three bands are shown in Figure 13.4. Note again the asymmetry brought upon by the inclusion of overlap. The most bonding states have a larger density than the most antibonding ones. This is a consequence of the fact that since the bonding states are stabilized less than the antibonding ones, there are more of the former in a given energy interval than in the latter. An equivalent way to put this is that, recalling equation 13.14, the slope at the bottom of the bands in Figure 13.3 is smaller than that at the top of the bands. If the band dispersion is small enough, then only a single peak will be found (of course, this depends upon the sampling size and the Gaussian line widths used in the calculation).

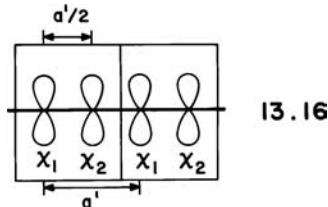
There is one more analytical tool that we shall occasionally use in the solid state. Section 2.3 discusses the partition of electron density using the Mullikan population analysis. An analogous treatment can be used for solids. The overlap population

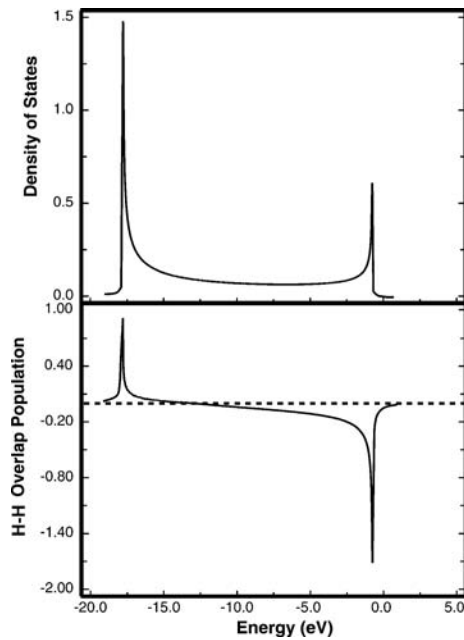
**FIGURE 13.4**

Density of states plots associated with Figure 13.3.

between two orbitals, or more frequently summed over two atoms, determines the electron density shared between the pair; it is given in equation 2.46. The crystal orbital overlap population (COOP) [6] is defined in an analogous manner except that the electron occupation number is made to be two for all crystal orbitals and the overlap population computed in a particular energy interval is weighted by the density of states in that region. Figure 13.5 shows the DOS for our hydrogen chain with an H–H distance of 1.3 Å for reference and the COOP curve is just below it. The H–H overlap population refers to that between adjacent hydrogen atoms. This shows that the orbitals around –17.0 eV are strongly bonding ones while those at –0.5 eV are strongly antibonding. Remember from our discussion of the two-orbital problem in Chapter 2, the coefficients in the antibonding combinations are much larger than those in the bonding counterparts, thus the peak at –0.5 eV is “taller” (in absolute magnitude) than the one at –17.0 eV even though there are more states per energy interval for the latter.

In 13.8, we chose a repeat unit for our calculation that contained a single orbital. If we choose a two-atom repeat unit as in 13.16 where  $a' = 2a$ , how does the result change?

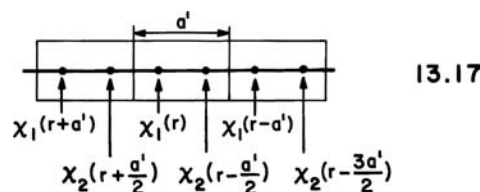


**FIGURE 13.5**

COOP curve for a chain of hydrogen atoms where the H–H distance was 1.3 Å. The corresponding DOS plot is given above it for reference.

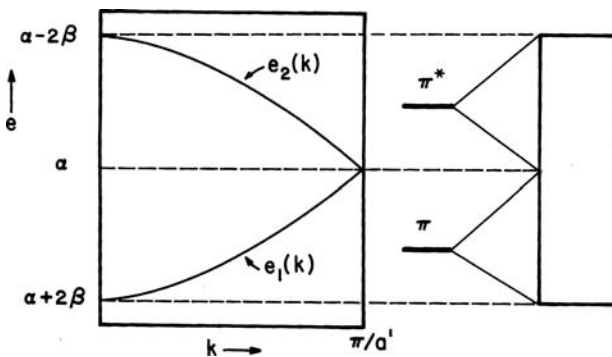
Any observable property will, of course, have the same calculated value. The  $e(k)$  versus  $k$  diagram will, however, be different since at each value of  $k$  there will be two energy levels, a direct result of the fact that there are now two orbitals per unit cell. Let us return to the Hückel model. To tackle this problem a secular determinant is set up, just as for the ethylene molecule of Section 12.2 but where from equation 13.19 the values of  $H_{ij}$  now depend upon  $k$ . As before, a considerable simplification of the problem can be made by using the Hückel approximation. First, we need to develop Bloch functions for each of the two orbitals in the unit cell. As shown in 13.16, we shall locate  $\chi_1$  and  $\chi_2$  on the left- and right-hand side atoms of any given unit cell. Starting with  $\chi_1(r)$ , this orbital is sent to  $\chi_1(r - a')$  by a translation  $a'$  and to  $\chi_1(r + a')$  by a translation  $-a'$  (13.17). Then using equation 13.5

$$\phi_1(k) = \frac{1}{\sqrt{N}} [\cdots + \chi_1(r + a') \exp(-ika') + \chi_1(r) + \chi_1(r - a') \exp(ika') + \cdots] \quad (13.22)$$



Note that  $\chi_2$  and  $\chi_1$  are translationally separated by  $a'/2$ . Since the orbitals  $\chi_1(r)$ ,  $\chi_1(r + a')$ , and  $\chi_1(r - a')$  are not nearest neighbors in the chain, all interaction integrals between orbitals located on them are zero in the Hückel approximation. This means that the energy of  $\phi_1(k)$ ,  $H_{11}(k)$ , evaluated as  $\langle \phi_1(k) | H^{\text{eff}} | \phi_1(k) \rangle$  is simply equal to  $\alpha$ . A similar expansion occurs for  $\chi_2(r)$

$$\begin{aligned} \phi_2(k) = & \frac{1}{\sqrt{N}} \left[ \cdots + \chi_2\left(r + \frac{a'}{2}\right) \exp\left(\frac{-ika'}{2}\right) + \chi_2\left(r - \frac{a'}{2}\right) \exp\left(\frac{ika'}{2}\right) \right. \\ & \left. + \chi_2\left(r - \frac{3a'}{2}\right) \exp\left(\frac{3ika'}{2}\right) + \cdots \right] \end{aligned} \quad (13.23)$$

**FIGURE 13.6**

Dispersion behavior of the two-orbital problem of 13.16. Also shown is the identification of the lower and upper halves of this diagram with the energetic behavior of the  $\pi$  and  $\pi^*$  levels of the diatomic unit contained in the unit cell of 13.16.

Just as before,  $H_{22}(k) = \alpha$  (within the Hückel approximation). Unlike the diagonal elements,  $H_{12}(k)$  does contain nearest neighbor interactions and exhibits a  $k$  dependence

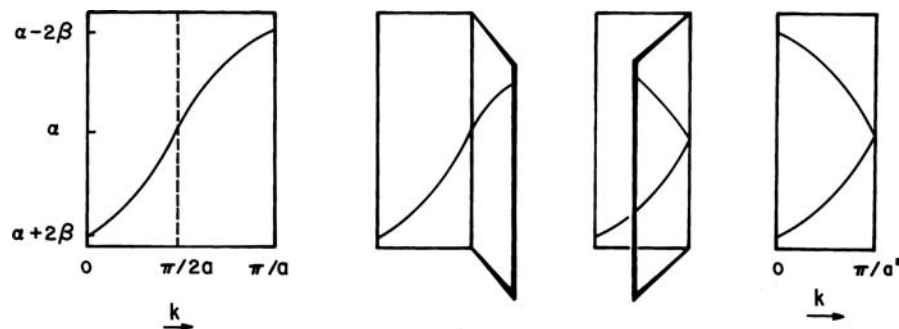
$$\begin{aligned} H_{12}(k) &= \langle \phi_1(k) | H^{\text{eff}} | \phi_2(k) \rangle \\ &= N \times \frac{1}{N} \times \left[ \exp\left(\frac{ika'}{2}\right) + \exp\left(-\frac{ika'}{2}\right) \right] \\ &= 2\beta \cos\left(\frac{ka'}{2}\right) \end{aligned} \quad (13.24)$$

According to the Hückel approximation  $S_{11}(k) = S_{22}(k) = I$  and  $S_{12}(k) = 0$ . Consequently from equation 13.18, the secular determinant becomes

$$\begin{vmatrix} \alpha - e(k) & 2\beta \cos\left(\frac{ka'}{2}\right) \\ 2\beta \cos\left(\frac{ka'}{2}\right) & \alpha - e(k) \end{vmatrix} = 0 \quad (13.25)$$

The lower energy root is  $e_1(k) = \alpha + 2\beta \cos(ka'/2)$  and the higher energy root is  $e_2(k) = \alpha - 2\beta \cos(ka'/2)$ . These results are shown graphically in Figure 13.6. Remembering that  $a'$  in 13.16 is twice the magnitude of  $a$  in 13.8 the relationship between Figures 13.6 and 13.2 is straightforward. The  $e(k)$  versus  $k$  diagram of the two-atom cell is just that of the one-atom cell but the levels have been folded back along  $k = \pi/2a$  (Figure 13.7). Now, there are two orbitals for each value of  $k$ .

The orbitals at various values of the energy in Figure 13.6 are exactly those shown in 13.3. At the zone center are found the most bonding and most antibonding levels and at the zone edge the nonbonding levels. Figure 13.6 also shows another way of generating these energy bands by starting off from the  $\pi$  and

**FIGURE 13.7**

"Folding back" of the dispersion curve for the one orbital cell to give the dispersion curve for the two orbital cell.

$\pi^*$  levels of a diatomic unit (located at  $e = \alpha + 2\beta$  and  $e = \alpha - 2\beta$ , respectively). First, we write

$$\begin{aligned} \text{for } \pi & \quad \xi_1(r) = \frac{1}{\sqrt{2}} \left[ \chi_1(r) + \chi_2 \left( r - \frac{a'}{2} \right) \right] \\ \text{for } \pi^* & \quad \xi_2(r) = \frac{1}{\sqrt{2}} \left[ \chi_1(r) - \chi_2 \left( r - \frac{a'}{2} \right) \right] \end{aligned} \quad (13.26)$$

Using the same notation as before we can construct Bloch functions as

$$\begin{aligned} \phi'_1(k) &= \frac{1}{\sqrt{N}} [\cdots + \xi_1(r + a') \exp(-ika') + \xi_1(r) + \xi_1(r - a') \exp(ika') + \cdots] \\ \phi'_2(k) &= \frac{1}{\sqrt{N}} [\cdots + \xi_2(r + a') \exp(-ika') + \xi_2(r) + \xi_2(r - a') \exp(ika') + \cdots] \end{aligned} \quad (13.27)$$

Using the Hückel approximation, we can readily evaluate  $H_{11}(k)$  and  $H_{22}(k)$  as

$$\begin{aligned} H_{11}(k) &= \langle \phi'_1(k) | H^{\text{eff}} | \phi'_1(k) \rangle \\ &= \left( \frac{1}{N} \right) N \left\{ \alpha + \beta + \frac{1}{2} \beta [\exp(ika') + \exp(-ika')] \right\} \\ &= \alpha + \beta + \beta \cos ka' \\ H_{22}(k) &= \langle \phi'_2(k) | H^{\text{eff}} | \phi'_2(k) \rangle \\ &= \left( \frac{1}{N} \right) N \left\{ \alpha - \beta - \frac{1}{2} \beta [\exp(ika') + \exp(-ika')] \right\} \\ &= \alpha - \beta - \beta \cos ka' \end{aligned} \quad (13.29)$$

$H_{12}(k)$  may be evaluated analogously as

$$\begin{aligned} H_{12}(k) &= \langle \phi'_1(k) | H^{\text{eff}} | \phi'_2(k) \rangle \\ &= \left( \frac{1}{N} \right) N \left\{ \alpha + \beta + \frac{1}{2} \beta [\exp(ika') - \exp(-ika')] \right\} \\ &= i\beta \sin ka' \end{aligned} \quad (13.30)$$

Similar evaluation of  $H_{21}(k)$  leads to  $-i\beta \sin ka'$ , that is,  $H_{21}(k) = H_{12}^*(k)$ . The secular determinant then becomes

$$\begin{vmatrix} \alpha + \beta + \beta \cos ka' - e(k) & i\beta \sin ka' \\ -i\beta \sin ka' & \alpha - \beta - \beta \cos ka' - e(k) \end{vmatrix} = 0 \quad (13.31)$$

Notice that it is  $H_{12}(k)$  and  $H_{12}^*(k)$  that go into the off-diagonal positions of this equation. Solution of the secular determinant leads to

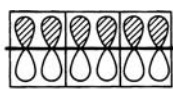
$$[\alpha - e(k)]^2 - \beta^2 (1 + \cos ka')^2 - \beta^2 \sin^2 ka' = 0 \quad (13.32)$$

and therefore

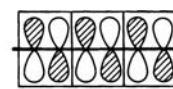
$$e(k) = \alpha \pm 2\beta \cos \frac{ka'}{2} \quad (13.33)$$

which is the same result as before. Notice that the value of  $H_{12}$  in equation 13.31 is identically zero at  $k = 0$  and also at  $k = \pi/a'$ . At these points the upper and lower bands are then, respectively, pure  $\phi'_1(k)$  and  $\phi'_2(k)$  in character since there is no mixing between them. Equation 13.27 requires that, at  $k = 0$ , the coefficient of  $\xi_\mu(r - \mathbf{R}_p)$  is  $\exp(i k \mathbf{R}_p) = +1$ . In other words the contents of the unit cell, the  $\pi$  and

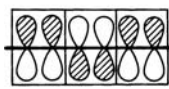
$\pi^*$  orbitals, are translated from one unit cell to the next with the same phase. Thus, the  $\pi$  orbitals are combined as in **13.18** which is bonding between unit cells. Note



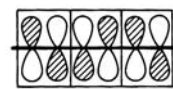
13.18



13.19

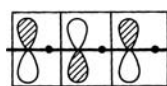


13.20

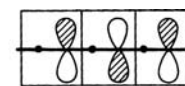


13.21

that this function is not only intercell bonding but is intracell bonding too. At the same time the  $\pi^*$  orbitals are combined as in **13.19** which is antibonding between cells. As a consequence, the function that results is both intracell and intercell antibonding. At the  $k = \pi/a'$  point the coefficient of  $\xi_\mu(r - \mathbf{R}_p)$  is now  $(-1)^p$ , and the phases of the orbital combinations within the unit cell alternate in sign upon translation to the next unit cell and so on. This gives rise to the combination of  $\pi$  orbitals in **13.20** which is intracell bonding but intercell antibonding. Similarly, the  $\pi^*$  levels combine to give a function (**13.21**) which is intracell antibonding but intercell bonding. Going from **13.18** to **13.20** then causes the band to rise in energy from left to right in the  $e(k)$  versus  $k$  plot (see Figure 13.6), whereas, the opposite occurs with the  $\pi^*$  band. Whether the band “runs” up or down depends upon the topology of the orbital within the unit cell; the direction of the band can easily be determined by an evaluation of the intercell overlap at the zone edge and center. Obviously, **13.20** and **13.21** have the same energy and the top of the  $\pi$  band and bottom of the  $\pi^*$  band touch at this point. As noted before, functions that are equally good for this degenerate pair may be obtained by taking a linear combination of **13.20** and **13.21**. The result is shown in **13.22** and **13.23**. The results of **13.18** to **13.21** were anticipated already in **13.3**. One can just as easily take



13.22

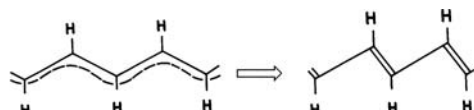


13.23

three or four  $p$  AOs per unit cell which then will give rise to three or four bands. The bands which, starting from the lowest, run up from left to right, then up from right to left and so on in a ladder manner. It is important to realize that the colligative properties—the total energy, DOS, and COOP plots, and so on do not change when the unit cell is doubled, tripled, and so on. Then why bother? Doubling the unit cell, as we discuss in Section 13.2, prepares us for further geometric distortions or electronegativity perturbations.

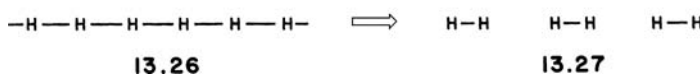
## 13.2 DISTORTIONS IN ONE-DIMENSIONAL SYSTEMS

The polymeric material of **13.24**, polyacetylene, with one  $p_\pi$  orbital per atom has a  $\pi$ -band structure which is identical to the one we have spent so much time discussing in Section 13.1. With one  $p_\pi$  electron per atom this band is half-full and if the electrons



13.24

13.25

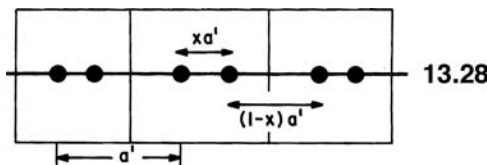


13.26

13.27

are paired (**13.6**) the system should be metallic. Polyacetylene itself does not have the regular structure indicated in **13.24** but is a semiconductor with a band gap of about 1.5 eV and exhibits the bond alternation shown in **13.25** where the C—C double bonds are about 0.07–0.09 Å shorter than the single bonds [7]. Likewise, elemental hydrogen does not consist of chains like **13.26** with formally one electron associated with each hydrogen atom; a half filled band in Figure 13.3a. At normal pressures, it undergoes a pairing distortion (**13.27**) to give isolated H<sub>2</sub> molecules and is, of course an insulator. We would like to know why this occurs, furthermore, when electrons are removed from polyacetylene, the material becomes a quite good metal. The band gap and perhaps the driving for distortion disappear. Application of extreme pressure causes molecular hydrogen to “polymerize” probably to a three-dimensional structure more complicated than that given by **13.26**. It undergoes a transition to a metallic state [8,9].

Let us see how  $e(k)$  varies for polyacetylene. Now, the distances between one atom and its two neighbors (**13.28**) are not the same [ $(1-x)a'$  and  $xa'$  where  $x < 1/2$ ].



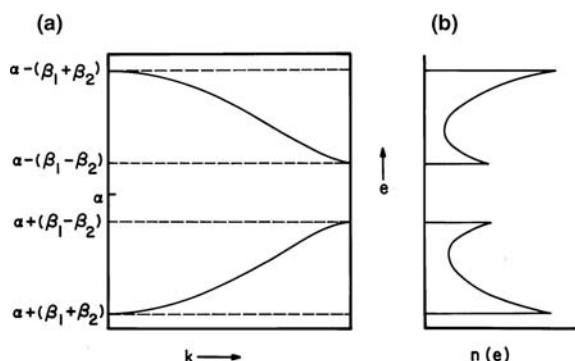
In addition to giving rise to different values of  $R_p$  in equation **13.6**, different values of the resonance integrals will also be found.  $\beta_1$  and  $\beta_2$  may be assigned to the interaction integrals between two neighboring orbitals separated by  $xa'$  and  $(1-x)a'$ , respectively. Since  $xa'$  is smaller than  $(1-x)a'$  we note that  $|\beta_1| > |\beta_2|$ . Note also that  $\beta_1$  and  $\beta_2 < 0$  for the case of  $p_{\pi}$  orbital overlap. The secular determinant then becomes

$$\begin{vmatrix} \alpha - e(k) & \beta_1 \exp(ikxa') + \beta_2 \exp[-ik(1-x)a'] \\ \beta_1 \exp(-ikxa') + \beta_2 \exp[ik(1-x)a'] & \alpha - e(k) \end{vmatrix} = 0 \quad (13.34)$$

Note that as in equation **13.31** one off-diagonal element is the complex conjugate of the other. Solution of this determinant leads to

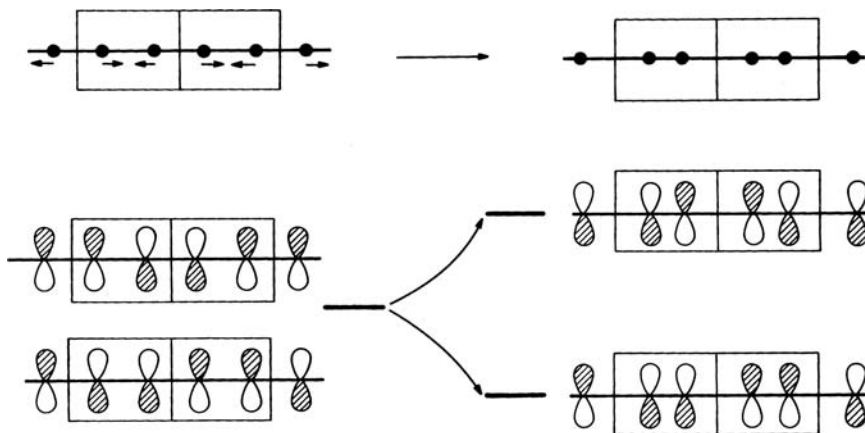
$$e(k) = \alpha \pm (\beta_1^2 + \beta_2^2 + 2\beta_1\beta_2 \cos ka')^{1/2} \quad (13.35)$$

Notice that any dependence on  $x$  has disappeared from the cosine term. We take the lower energy level  $e_1(k)$  as equation **13.35** with the negative root and the higher energy level  $e_2(k)$  as equation **13.35** with the positive root. At  $k=0$ ,  $e_1(k=0)=\alpha + (\beta_1 + \beta_2)$  and  $e_2(k=0)=\alpha - (\beta_1 + \beta_2)$ . At  $k=\pi/a'$ ,  $e_1(k=\pi/a')=\alpha + (\beta_1 - \beta_2)$  and  $e_2(k=\pi/a')=\alpha - (\beta_1 - \beta_2)$ . The  $e(k)$  versus  $k$  diagram which results is shown in Figure 13.8a for the case where  $|\beta_1| > |\beta_2|$ . The corresponding density of states



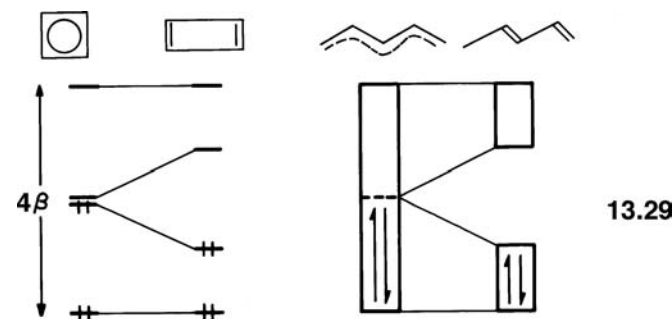
**FIGURE 13.8**

(a) Dispersion behavior of the two orbitals contained in the unit cell of **13.28** where the internuclear distances along the chain are not uniform. (b) The corresponding density of states.

**FIGURE 13.9**

Generation of the form of the new wavefunctions at  $k = \pi/a'$  as a result of the distortion shown in 13.28.

picture is shown in Figure 13.8b. For small distortions  $\beta_1 + \beta_2 \approx 2\beta$ . The important result is a splitting of the degeneracy at the zone edge. The form of the new wavefunctions is easy to derive and is given in Figure 13.9. In the previous chapters, we have emphasized how symmetrical structures on distortion may either open up a gap or increase an existing energy gap between the highest occupied molecular orbital (HOMO) and lowest unoccupied molecular orbital (LUMO). In the case of the nonalternating polyene of 13.24 with one electron per atom the  $\pi$  band of Figure 13.2 is half-full, there is no HOMO–LUMO gap, and the situation is reminiscent of the case of singlet cyclobutadiene of Chapter 12. In the alternating case of 13.25, the lower band of Figure 13.8 is full and the upper empty. Thus, the energetic stabilization on distortion of the symmetrical structure to one with bond alternation is really the solid-state analog of a Jahn–Teller distortion [4,5,10]. It is called a Peierls distortion and the situation is compared with that of cyclobutadiene in 13.29. A Peierls



distortion to open a band gap is always a possibility in a one-dimensional band, but this is not always the case for two-dimensional or three-dimensional bands. Furthermore, it is not always clear what electron counts energetically favor a geometric distortion even in a one-dimensional system.

Let us approach this dimerization problem from a slightly different, more qualitative, approach using this time the pairing distortion in a hydrogen chain as a model. The solid line in Figure 13.10 shows the undistorted, 13.27, hydrogen chain. The lower band in the  $e(k)$  versus  $k$  plot consists of  $H_2\sigma$  orbitals. The band runs up going from left to right; there is maximal bonding between  $H_2\sigma$  orbitals at  $k = 0$  and maximal antibonding at  $k = \pi/a$ . On the other hand, the  $H_2\sigma^*$  band runs down going from left to right; at  $k = 0$  there is maximal antibonding between unit cells and the  $k = \pi/a$  solution is maximally bonding

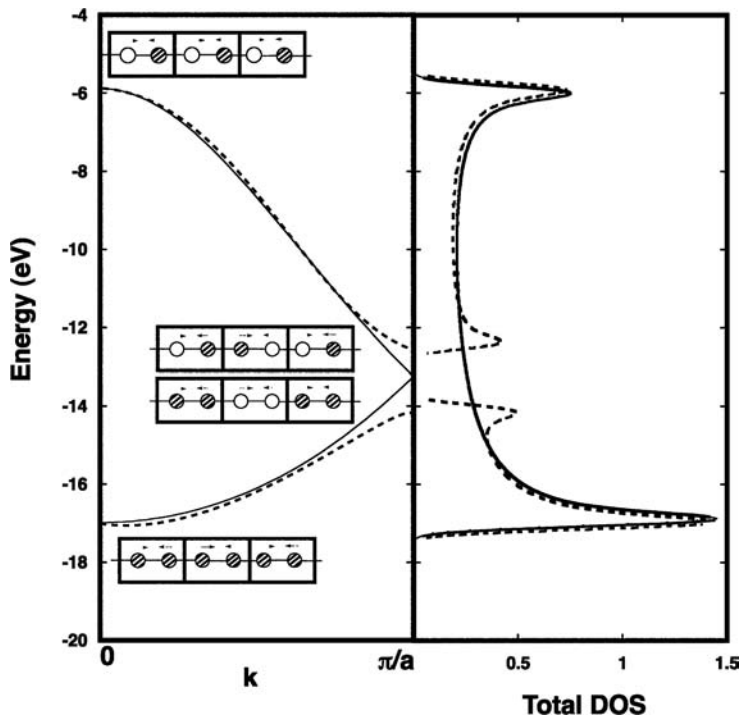


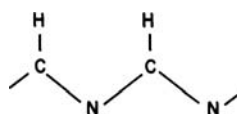
FIGURE 13.10

Plots of  $e(k)$  versus  $k$  and DOS for a hydrogen chain. The solid lines refer to 13.26 where all H–H nearest neighbor distances are equal. The dashed lines are for the paired situation in 13.27.

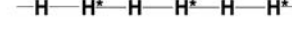
between unit cells. All of this is, course, topologically equivalent to the  $\pi/\pi^*$  combinations in 13.18–13.21. When the pairing distortion occurs, as we have defined it, the two hydrogens within the unit cell move closer. Overlap between the s AOs increases. On the other hand the H–H intercell distance increases so that corresponding overlap decreases. What happens to the bands is then easy to predict and is given by the dashed line in Figure 13.10. For the  $\sigma$  solution at  $k = 0$  the gain in intracell overlap is stabilizing since the two s AOs have the same phase, however, this is compensated by the loss of intercell overlap which raises the energy since there is also intercell bonding. Exactly, the converse occurs for the  $\sigma^*$  solution at  $k = 0$ . So, the net result is that both bands stay at nearly the same energy around  $k = 0$ . One can argue that the variation of the overlap between two s AOs as a function of internuclear separation is exponential (see 1.11)—not linear. So, the gain in intracell overlap is a little larger than the intercell overlap. This is why the dashed line is slightly lower for the  $\sigma$  band and a little higher for  $\sigma^*$ . But the largest effect occurs for the two bands around the  $k = \pi/a$  region. Here increased intercell bonding and the loss of intercell overlap which is antibonding for the  $\sigma$  band causes it to be stabilized. Exactly, the opposite occurs for the  $\sigma^*$  band; it rises in energy. A gap is created, shown nicely by the dashed line in the DOS plots. For a hydrogen chain, the lower band is completed filled if the electron spins are paired and, consequently the paired solution for  $H_2$  is the more stable one. What if electrons were removed from the  $H_2$  chain? Those electrons come from the highest energy region of the  $\sigma$  band—right around the  $k = \pi/a$  solution. The driving force for the distortion is lost or at least greatly diminished. The same occurs in polyacetylene. The  $\pi$  orbitals around  $k = \pi/a$  are the ones that are stabilized the most. The potential here is probably much smaller since the underlying  $\sigma$  framework prefers the nonalternating solution—just as in benzene. The intercalation of electron acceptors (halogens,  $PF_5$ , etc.) into polyacetylene solids causes electrons to be removed from the  $\pi$  band and it becomes a good metal—signaling that the  $\pi$  band is indeed partially occupied. A bronze solid results with a conductivity of  $200 \Omega^{-1} \text{ cm}^{-1}$ . The mechanistic details for electron conduction in polyacetylene, as well as, other one-dimensional materials are beyond the scope of this book [11]. The most

popular mechanism [12] today views pristine polyacetylene as primarily the alternate structure given by **13.25**, however, there are also defects, called solitons. These are long, odd-numbered segments of the polyene chain which are nonalternating and give rise to an ESR signal. Their energy signature puts them right in the middle of the polyacetylene band gap. This is precisely what one would expect for a neutral odd-membered polyene ribbon. The highest filled MO has one electron at an energy of  $\alpha$  using the Hückel approximation. There is good theoretical validation for the formation of solitons [13]. It is these polyene radicals, which are oxidized to become cations, that are mobile in the presence of an electric field.

There are ways, other than geometrical, for stabilizing a half-filled band in polyacetylene or the hydrogen chain. In Chapter 12, we saw that altering the electronegativity of two carbon atoms in cyclobutadiene relative to the other two, split the degeneracy of the nonbonding set and the driving force to the rectangular geometry was lost. **13.30** and **13.31** are two possible related examples in the solid state. The first is known but, as yet, poorly characterized, the second is purely hypothetical where an electronegativity perturbation has lowered the  $H_{ii}$  for the hydrogens with an asterisk by 2.0 eV. **13.30** is

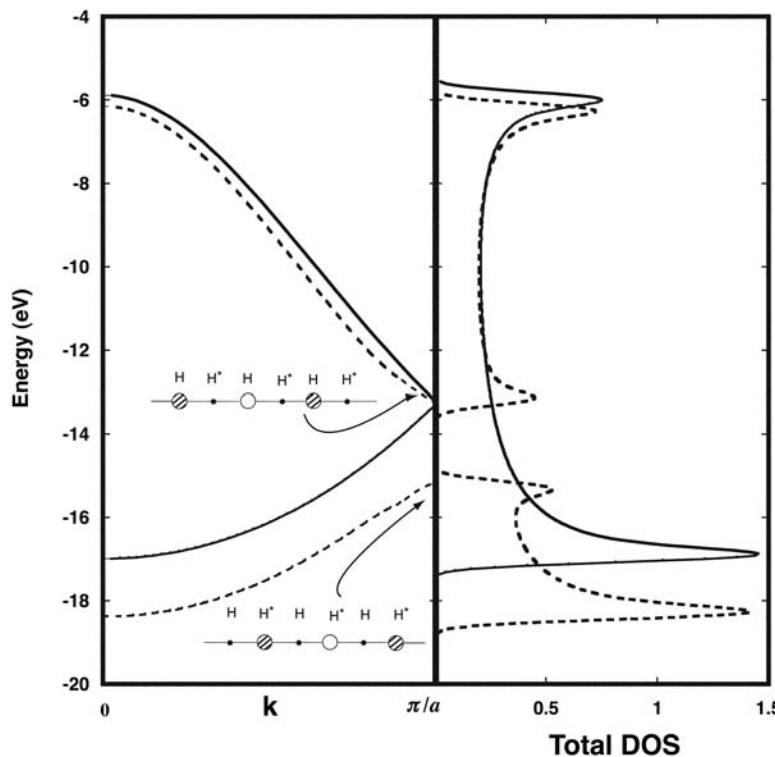


13.30



13.31

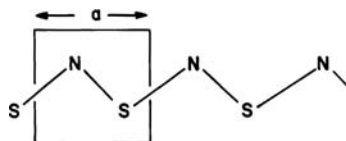
isoelectronic with polyacetylene but the electronegativity difference ensures that the  $\pi$  bands will not touch at the zone edge. (We examine this case in detail below.) Figure 13.11 shows the situation for **13.31**. The solid line for the  $e(k)$  versus  $k$  and DOS plots refer again to the unperturbed hydrogen chain. The dashed lines show what happens to **13.31**. The dashed line indicates the perturbed solution. Using the electronegativity perturbation ideas from equations 6.6 and 6.7, it is easy to see what happens at the zone edge. Recall from **13.3** that the exact middle of our one-dimensional band consists of a degenerate set and one can just as easily use plus

**FIGURE 13.11**

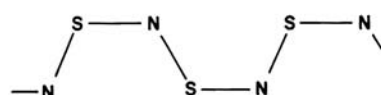
Plots of  $e(k)$  versus  $k$  and DOS for an unperturbed hydrogen chain (solid lines) and for the perturbed system where the  $H_{ii}$  for every other hydrogen atom was lowered by 2.0 eV.

and minus linear combinations of them. These two MOs form the  $k = \pi/a$  solutions for the two bands when the unit cell is doubled (Figure 13.7) and these are explicitly drawn inside of the  $e(k)$  versus  $k$  plot for our perturbed hydrogen chain. The upper member is unperturbed;  $e^{(1)} = e^{(2)} = 0$  because the atomic coefficients on the perturbed (starred) hydrogen atoms ( $c_{\alpha i}^0$  in equation 6.7) are zero. Whereas, for the lower band the coefficients on the starred hydrogens are maximized and so this point is stabilized greatly;  $\delta\alpha < 0$  and  $e^{(1)} < 0$ . A large gap is created in the absence of a pairing distortion. For the  $k = 0$  solutions, the lower and upper bands are stabilized with  $e^{(1)} < 0$ , however they also intermix. The energetic consequence of this is that  $e^{(2)} < 0$  for the lower band, but  $e^{(2)} > 0$  for the upper band. It is also easy to see that the intermixing will serve to build up electron density on the starred hydrogens (at  $k = 0$  and the regions around it) for the lower band; however, the reverse occurs in the upper band. Here, the coefficients on the unstarred hydrogens become large. Logically, the situation here is little different from what we developed in Section 6.4 for the  $\pi$  orbitals on going from  $C_2^{2-}$  to CO. Certainly the  $\pi$  and  $\pi^*$  bands in polyacetylene can be perturbed in the same way to derive the orbitals for a polyorgano-nitrile, **13.30**.

Electronically intermediate between the polyacetylene example with one  $\pi$  electron per center and the planar analog of the sulfur chain with two such electrons per center is the  $(SN)_x$  polymer with three  $\pi$  electrons per SN atom pair [10]. Let us approach this problem from the Hückel perspective. The band structure of the trans isomer **13.32** is shown in Figure 13.12 where we have chosen a unit cell containing



13.32



13.33

two atoms. It is easy to understand in a qualitative manner. With two  $\pi$  orbitals per cell there will be two  $\pi$  bands. The splitting at the zone edge in  $(SN)_x$ , absent in the polyacetylene example of Figure 13.6, is due to the different atomic  $p_\pi$  ( $\alpha_S$  and  $\alpha_N$ , respectively) energies of the two atoms, sulfur and nitrogen. We show this in the following way. The secular determinant of equation 13.22 which described a degenerate interaction becomes in  $(SN)_x$

$$\begin{vmatrix} \alpha_N - e(k) & 2\beta \cos \frac{ka'}{2} \\ 2\beta \cos \frac{ka'}{2} & \alpha_S - e(k) \end{vmatrix} = 0 \quad (13.36)$$

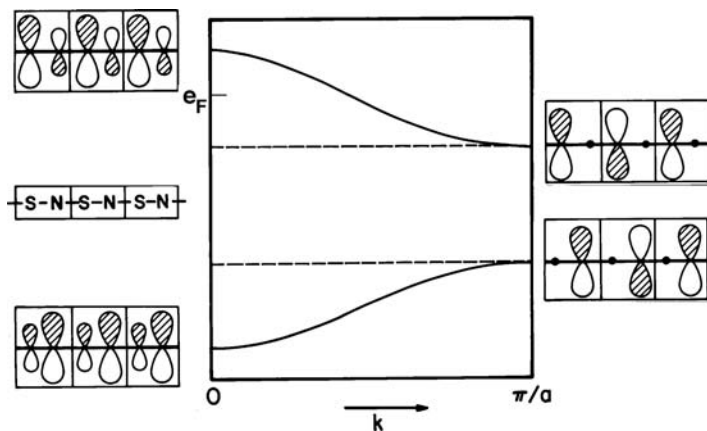


FIGURE 13.12

Dispersion behavior of the  $\pi$  orbitals of polymeric  $(SN)_x$ . With three  $\pi$  electrons per SN unit the upper band is half-full and so the material is metallic.

This describes a nondegenerate interaction between the levels  $\alpha_S$  and  $\alpha_N$ . Using the ideas of Section 3.2, the energies of the two bands become

$$e_1(k) \cong \alpha_N + \frac{4\beta^2 \cos^2 ka'/2}{\alpha_N - \alpha_S} \quad (13.37)$$

and

$$e_2(k) \cong \alpha_S - \frac{4\beta^2 \cos^2 ka'/2}{\alpha_N - \alpha_S} \quad (13.38)$$

At  $k = \pi/a'$  the two energies are simply  $\alpha_N$  and  $\alpha_S$ , and the form of orbitals just as in **13.22** and **13.23** which are now nondegenerate. With three  $\pi$  electrons per cell the upper  $\pi$  band is half-full and the Peierls type of distortion is expected. The actual structure of  $(SN)_x$  is in fact an isomer of **13.32**, that given in **13.33**. Since the repeat unit is now four atoms, the band structure is somewhat more complex. (Essentially the levels of Figure 13.12 are folded back as in Figure 13.7). We shall look at a related compound in Section 13.3. The overall result though is very similar with a similar prediction of a Peierls instability. Instead of distorting to remove this instability, however,  $(SN)_x$  remains a metal with a half-filled band. It has been suggested that a Peierls distortion is inhibited by interactions between chains of the polymer. This is a very striking material, one composed of sulfur and nitrogen only, which has a copper-like luster and is metallic. When there are only two  $\pi$  electrons per unit cell (as in **13.30**) then the symmetrical structure is now an insulator and does not suffer from a Peierls instability.

### 13.3 OTHER ONE-DIMENSIONAL SYSTEMS

Our discussion so far has focused on polyacetylene, the hydrogen chain and related examples. The broad results, however, are transferable to many other systems. For a band describing a chain of  $p_\sigma$  orbitals the  $e(k)$  versus  $k$  diagram will look a little different. The phase factor at  $k=0$  requires (equation 13.6) all the atomic coefficients equal to +1 (**13.34**). This is the point where maximum



$k=0$

$k=\pi/a$



13.35

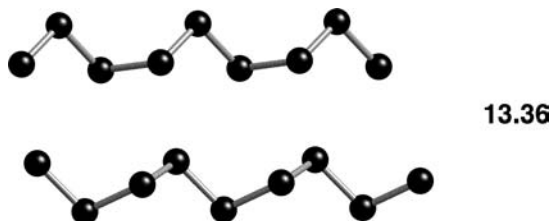
destabilization occurs. So

$$e(k) = \alpha - 2\beta \cos ka \quad (13.39)$$

At  $k = \pi/a$  the phase difference between adjacent orbitals is  $-1$  and maximum bonding results. Apart from this rather simple difference the band structure is identical to our earlier example. The bands run down from left to right in the  $e(k)$  versus  $k$  diagram. Now, of course,  $\beta$  represents  $p_\sigma - p_\sigma$  rather than  $p_\pi - p_\pi$  interactions. Consequently, the band spread in an absolute sense is larger since  $p_\sigma$  overlap is larger than  $p_\pi$  overlap, that is,  $|\beta_\sigma| > |\beta_\pi|$ .

A band made up of  $z^2$  orbitals on each atomic center (in this case a transition metal) in a linear chain will also look very similar to that of Figure 13.2 with  $\beta$  now

describing  $z^2-z^2$  interactions. The crystal orbital at  $k=0$  is shown in 13.35. We shall explicitly consider examples where transition metal  $d$  AOs are used in the later chapters. A realistic situation will be one where there is more than one AO per atom in the unit cell. This does not affect the results too much. Of course, the band widths will differ since intercell overlap will not be the same for  $s$ ,  $p$ , or certainly  $d$  AOs. There is one detail that presents a complication. At certain places in the Brillouin zone the bands can mix with each other. A good example is given by one of the elemental phases of sulfur. At normal temperatures and pressures sulfur consists of a number of cyclic compounds. At high pressures chain structures predominate. For example, the structure (showing two strands) at 5.8 GPa is given in 13.36. There are six valence electrons so each sulfur atom must form two  $\sigma$  bonds and this then leaves two lone pairs on each atom. The sulfur chain wraps itself in a helical manner,



presumably to minimize adjacent lone pair interactions. Rather than dealing with the geometrical complexities of this structure, for illustrative purposes we shall just consider a linear sulfur chain. The details of the calculation are shown in Figure 13.13. On the left-hand side of the figure is the  $e(k)$  versus  $k$  plot. We take the  $z$  axis as that lying along the S-S chain. There are three bands shown (rather than four), since the  $x$  and  $y$   $p$  AOs are degenerate and so this gives two bands which are also degenerate. The lowest band is, of course sulfur  $s$  in character. Of the  $p$  bands, the one that “runs” up must be the sulfur  $x$  and  $y$  bands, analogous to the polyacetylene  $\pi$  band and the band running “down” must be sulfur  $z$ , analogous to 13.34. Notice that the band dispersions are just what one would expect: the  $x,y$  bands have the smallest—

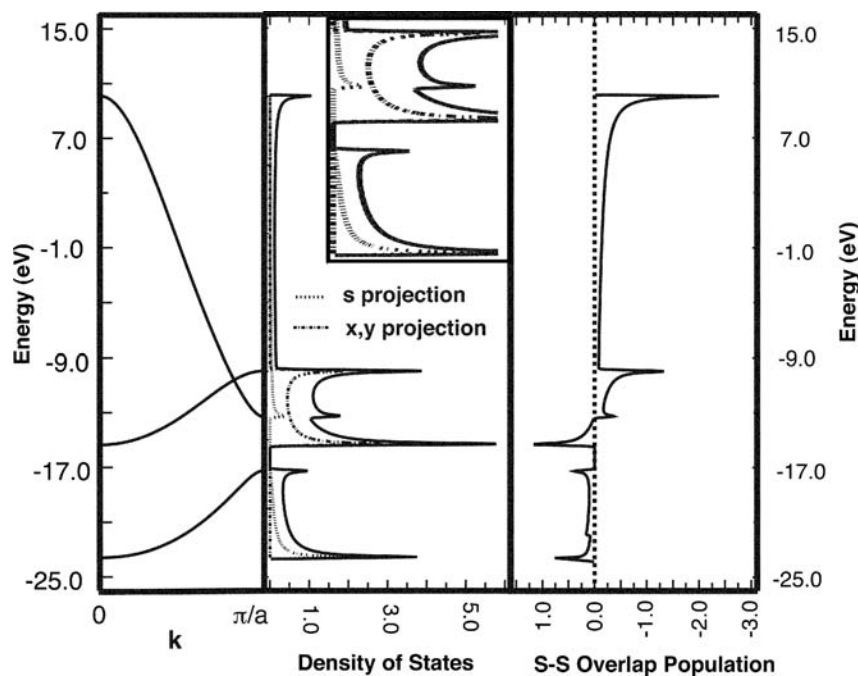
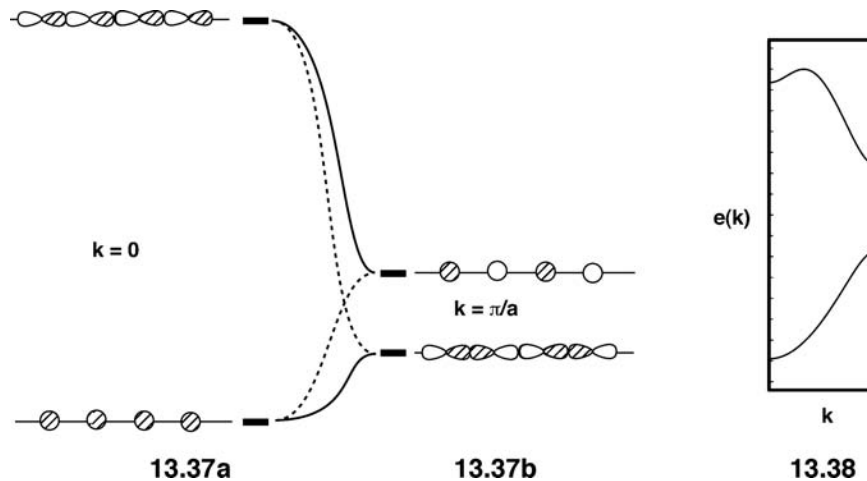


**FIGURE 13.13**

Plots of  $e(k)$  versus  $k$ , DOS and S-S COOP for a one-dimensional, linear chain of sulfur atoms. An expansion of the DOS around the  $s$  region is given in the box at the top.

they have intercell overlap of the  $\pi$  type; the sulfur s band is next with a  $\sigma$  overlap and finally the z band has the largest dispersion—the intercell  $\sigma$  overlap here is greater than that between the s AOs. The shape of the DOS plots in the middle panel of Figure 13.13 is a nice reflection of the sum of the three one-dimensional bands. But here is where things get more complicated. One can in a calculation project out any AO character from the total DOS. So, the projection of the x and y character in the DOS is given by the dot-dashed line in Figure 13.13. It is, as expected, that portion of the DOS from about  $-16$  to  $-10$  eV which corresponds to the  $x,y$  bands. The projection of the sulfur s character, the dotted line, starts at about  $-24$  eV, but then it dies out and becomes zero at the top of what we called the s band at about  $-17$  eV! The s character “reappears” at about  $-13$  eV which is the bottom of the p band. The opposite occurs with the projection of z character. At the top of the band, about 10 eV, it is solely z in character, whereas, there is no z character at the bottom of the band, about  $-13$  eV. What has occurred is diagrammed in 13.37. At the  $k = 0$  point, the lower band is totally s in character and intercell bonding. The upper band is totally z and is



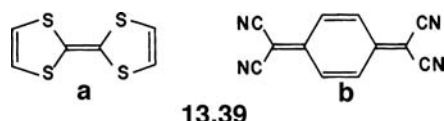
antibonding. The s band rises in energy and the z band is stabilized as  $k$  becomes larger. This is reflected by the dashed lines in 13.37. At the  $k = 0$  point, 13.37a, the two crystal orbitals have different symmetry upon translation along the chain. The s crystal orbital is symmetric, where the z is antisymmetric. The opposite is true for the  $k = \pi/a$  point, 13.37b. But at any intermediate value of  $k$  the two have the same symmetry and they cannot cross each other. This is just a solid-state analog of the noncrossing rule in molecular systems (Section 4.7). The upper band mixes in and stabilizes the lower band and the converse occurs with the lower band. The reader can easily verify this by drawing out the solution for the two bands at the  $k = \pi/2a$  point. For this problem, the determinant at the Hückel level can be written as in equation 13.40

$$\begin{vmatrix} \alpha_s + 2\beta_{ss} \cos(ka) - E & 2i\beta_{sz} \sin(ka) \\ -2i\beta_{sz} \sin(ka) & \alpha_z + 2\beta_{zz} \cos(ka) - E \end{vmatrix} = 0 \quad (13.40)$$

Here,  $\alpha_s$  and  $\alpha_z$  are the starting energies of the s and z AOs. There are three resonance integrals;  $\beta_{ss}$  and  $\beta_{zz}$  for s-s and z-z interactions, respectively, and  $\beta_{sz}$  for the interaction between s and adjacent z AOs. The s/p mixing is even stronger for a carbon chain; see 13.38 as expected for first versus second row elements. An interesting corollary is that the bottom of the lower band is bonding, as well as, the top. The s-s COOP curve for the “s” band in Figure 13.13 nicely shows this. The upper “p” band is antibonding at the bottom and top. Notice that the s-s overlap

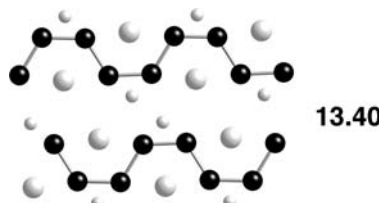
population is negative at  $-13\text{ eV}$ . The band constitution shown by **13.37** does not occur in every instance. The extent of mixing depends on the  $s-p$  energy difference and the magnitude of the  $\beta$ 's. When the  $s-p$  energy difference is large and the  $\beta$ 's are small the "s" band remains  $s$  and the "p" band remains  $p$ . The structure of Group 2 and 12 elements is, of course, three dimensional, but the salient features are those we have studied for the one-dimensional chain [16]. For Ca and Sr with the  $s^2$  configuration, the "s" band is totally filled and there is substantial  $s/p$  mixing so the situation is analogous to that shown in **13.37**. When pressure is applied, the unit cell volume decreases which creates a greater overlap between the  $s$  and  $p$  AOs. One normally would expect that the band dispersion increases (see Figure 13.1) and thus, the top of the "s" band goes up in energy while the bottom of the "p" band decreases. But this does not occur. The top of the "s" band is bonding so an increase in overlap will cause it to be stabilized. The bottom of the "p" band is antibonding so an increase in overlap causes it to go up in energy. The  $s-p$  band gap increases with increasing pressure and so the measured conductivity decreases. The opposite occurs for Zn and Cd with a  $d^{10}s^2$  configuration (the  $d$  AOs lie at very low energies and do not hybridize with the  $s$  and  $p$  AOs). Consequently, the top of the  $s$  band is  $s-s$  antibonding and it is destabilized upon application of pressure. The bottom of the  $p$  band is  $p-p \sigma$  bonding and, therefore it is stabilized when the pressure is increased. The net result is that the band gap decreases and conductivity increases with increasing pressure.

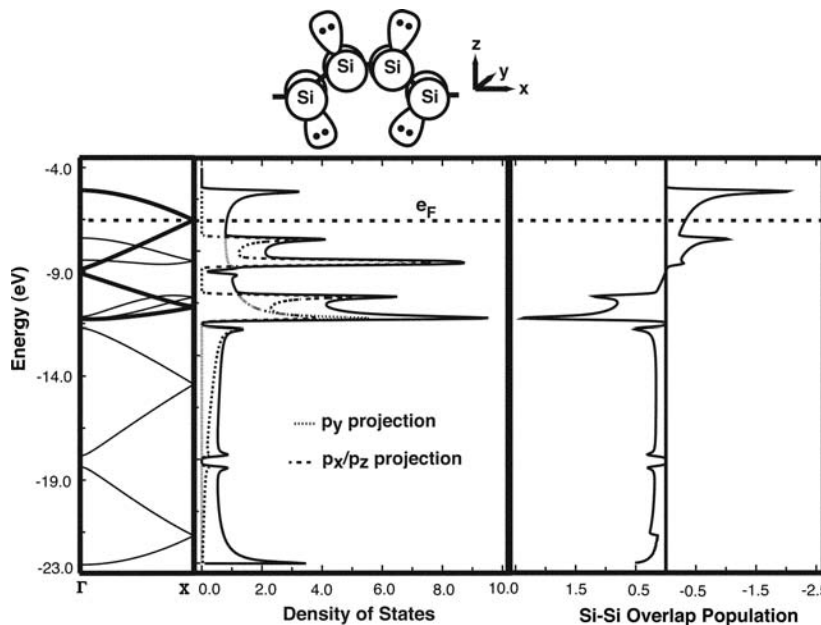
Many other one-dimensional examples exist [17], with perhaps very different chemical compositions, but which are understandable in an exactly analogous way [18]. One particularly important series are the organic metals made by stacking planar molecules on top of one another [19]. Tetrathiofulvalene (TTF) shown in **13.39a** is one example. The tetramethylated derivative (TMTTF) and its selenium



analog (TMTSF) are two others. Stacked conductors containing these units may be made in an exactly analogous way to the one-dimensional examples described above.  $(\text{TTF})\text{Br}_{\sim 0.73}$ , for example, has a conductivity parallel to the chain axis of about  $400\Omega^{-1}\text{ cm}^{-1}$ . Here, the orbital involved in forming the one-dimensional band is not localized on a single atom as in tetracyanoplatinate but is delocalized over the organic unit. In  $(\text{TTF})\text{Br}$ , where this band is exactly half-filled, discrete  $(\text{TTF})_2^{2+}$  dimers are found with an exactly analogous explanation to the one for the dimerization of the H atom chain (**13.26** to **13.27**). 7,7,9,9-Tetracyano- $\rho$ -quinodimethane (TCNQ) is another example of an organic metal (**13.39b**). The system  $[\text{H}(\text{CH}_3)_3\text{N}]^+(\text{I}^-)_{1/3}(\text{TCNQ})^{2/3-}$  has a conductivity of  $\sim 20\Omega^{-1}\text{ cm}^{-1}$ . Note that TTF forms a cationic but TCNQ an anionic chain. Although this is a simple description of the electronic problem here, these systems are, in fact, somewhat more complex than we have intimated.

A little more complicated compound but isoelectronic to  $\text{SN}_x$  is  $\text{BaMg}_{0.1}\text{Li}_{0.9}\text{Si}_2$ , prepared by Wengert and Nesper [20]. Its structure is shown in **13.40**. Here, the black spheres are Si and the grey ones correspond to Ba (large) and Li along with Mg (small).



**FIGURE 13.14**

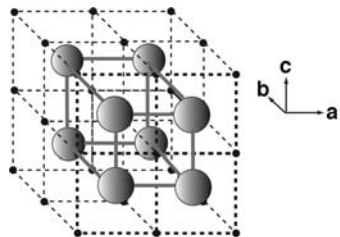
Plots of  $e(k)$  versus  $k$ , DOS and Si-Si COOP for  $\text{Si}_4^{6-}$ . The dashed line indicates the position of the Fermi level.

Let us forget for a moment the Mg doping for Li. The formula is then  $\text{BaLiSi}_2$ . One certainly anticipates complete, or nearly so, donation of electron density from the electropositive atoms to Si. One then can consider this as  $\text{Si}_2^{3-}$  (isoelectronic to SN) or since the repeat unit is double the formula unit to  $\text{Si}_4^{6-}$ . How are we then going to partition the 22 electrons? An easy way to sort this out is to use eight electrons for the Si—Si  $\sigma$  bonds. Each Si atom also has a lone pair ( $n$ ) in the plane of the Si chain, as shown at the top of Figure 13.14. This leaves six electrons for the  $\pi$  system in the  $\text{Si}_4^{6-}$  unit. The calculated results for this compound are illustrated in Figure 13.14. The  $e(k)$  versus  $k$  plot is beginning to look like a “spaghetti” diagram, but we can still unravel most of the details quite readily. Here  $k=0$  and  $\pi/a$  is labeled  $\Gamma$  and X, respectively. The lowest four bands correspond to the Si—Si  $\sigma$  bonds. One could construct them using the bond orbital approach, for example, by taking two  $sp^2$  hybrids on each Si atom and forming symmetry adapted combinations. The Si—Si bonding combinations are then translated at the  $\Gamma$  and X points to determine the slope of the bands. Notice that this group is just a Si—Si  $\sigma$  bond which has been folded back twice. The COOP curve shows these to be Si—Si bonding throughout, as expected, and which lie below the Fermi level. They are clearly seen as the two wide bands with x and z character in the DOS plot. The four  $\pi$  bands are highlighted as the bold lines in the  $e(k)$  versus  $k$  plot. It again is a  $\pi$  band that has been doubled twice. The shape of each is topologically identical to the  $\pi$  orbitals of butadiene (Figure 12.3). The bands and their associated dispersion can be determined by using the phase factors for the  $\Gamma$  and X points. We leave this as an exercise for the reader. For  $\text{BaLiSi}_2$  then the highest  $\pi$  band is empty and this is met at the  $k=X$  point by the third filled  $\pi$  band. Should not there be a Peierls distortion? For one thing, one-tenth of the Li atoms have been replaced by Mg, therefore, the Fermi level for the real compound lies a little higher in energy and this will serve to dampen the Peierls distortion (the upper band is pushed up more than the lower one is stabilized because of overlap—just like a molecular system). Secondly, there are strong interactions between the Si and alkali/alkaline atoms, which will stabilize a non-alternate system, since the alkali (alkaline) atoms strongly repel each other. Finally, in Figure 13.14 are the four bands which represent the four lone pairs in the unit cell.

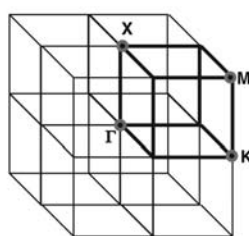
They are high in energy, in the vicinity of the  $\pi$  bands, are below the Fermi level and do not have much dispersion.

## 13.4 TWO- AND THREE-DIMENSIONAL SYSTEMS

So far we have concentrated on one-dimensional systems, but this approach is readily extended in principle to two and three dimensions. We shall illustrate the three-dimensional case with a simple example where each unit cell contains one s AO. The natural structure to look at is simply the linking together of chains of atoms along the  $x$ ,  $y$ , and  $z$  directions. This gives rise to the simple cubic structure of 13.41. It is easy to



13.41



13.42

generate the  $k$  dependence of the energy in this case using the Hückel approximation as given by equation 13.41 where we specify values of  $k$  in terms of the three Cartesian

$$e(k_a, k_b, k_c) = \alpha + 2\beta_a \cos k_a a + 2\beta_b \cos k_b b + 2\beta_c \cos k_c c \quad (13.41a)$$

directions. When the interactions along the three directions are identical, that is,  $\beta_a = \beta_b = \beta_c = \beta$ , we obtain

$$e(k_a, k_b, k_c) = \alpha + 2\beta[\cos k_a a + \cos k_b b + \cos k_c c] \quad (13.41b)$$

The energy dependence is simply the sum of three perpendicular systems each given by equation 13.3. It is problematical to display the energy dependence upon  $k_a$ ,  $k_b$ , and  $k_c$  simultaneously, but what can be done is to present slices through the  $e(k)$  surface as in Figure 13.15. Here the symbol  $\Gamma$  represents the center of the Brillouin zone, 13.42, where  $(k_a, k_b, k_c) = (0, 0, 0)$  ( $2\pi/a$ ), since we consider a cubic lattice for which  $a = b = c$ . The other unique points (in this case where all nearest neighbor distances are the same, that is, all three translation vectors are identical) given by M, K, and X

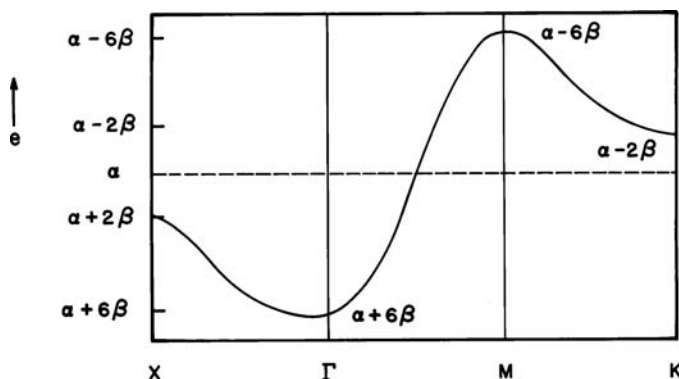


FIGURE 13.15

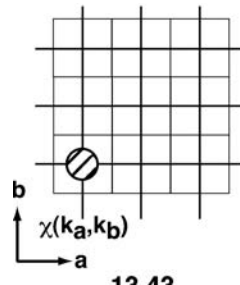
Dispersion behavior of the s orbitals of a simple cubic structure (13.41).

are represented by points in the Brillouin zone  $(k_a, k_b, k_c) = (1/2, 1/2, 1/2)(2\pi/a)$ ,  $(1/2, 1/2, 0)(2\pi/a)$  and  $(0, 0, 1/2)(2\pi/a)$ , respectively. Clearly because of the symmetry inherent in equation 13.41, the energies at  $(0, 0, 1/2)(2\pi/a)$ ,  $(0, 1/2, 0)(2\pi/a)$ , and  $(1/2, 0, 0)(2\pi/a)$  are equal. Also,  $e(k_a, k_b, k_c) = e(-k_a, -k_b, -k_c)$ . The points  $\Gamma$ , M, K, and so on, are called the symmetry points of the Brillouin zone. In general, however, the situation can become a bit more complicated. The three translation vectors need not be the same length, nor do they need to be orthogonal to each other. Frequently, they are symbolized by the vectors  $\mathbf{a}$ ,  $\mathbf{b}$ , and  $\mathbf{c}$  so the Bloch functions may be written as

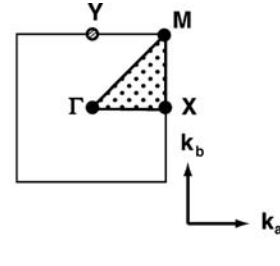
$$\phi(k_a, k_b, k_c) = \frac{1}{\sqrt{N}} \sum_m \sum_n \sum_p \exp(ik_a ma) \exp(ik_b nb) \exp(ik_c pc) \chi(\mathbf{r} - m\mathbf{a} - n\mathbf{b} - p\mathbf{c}) \quad (13.42)$$

following the development in equation 13.6. The  $m$ ,  $n$ , and  $p$  variables are just indices for the unit cell in the  $\mathbf{a}$ ,  $\mathbf{b}$ , and  $\mathbf{c}$  directions. Now the Brillouin zone may, in general, be specified by  $0 \leq k_a \leq \pi/a$ ,  $0 \leq k_b \leq \pi/b$  and  $0 \leq k_c \leq \pi/c$ , although in practice symmetry [21] may very well present a unique  $k$  space which is smaller than that given.

An illustrative example of a two-dimensional square lattice is given by 13.43 where there is one s AO per unit cell. The symmetry is tetragonal—the  $\mathbf{a}$  and  $\mathbf{b}$  vectors are



13.43



13.44

orthogonal and have the same length (rather than orthorhombic where the  $\mathbf{a}$  and  $\mathbf{b}$  vectors are still orthogonal but have different lengths). The unique portion of the Brillouin zone is represented by the dotted area in the triangle of 13.44 and the Bloch functions by

$$\phi(k_a, k_b) = \frac{1}{\sqrt{N}} \sum_m \sum_n \exp(ik_a ma) \exp(ik_b nb) \chi(\mathbf{r} - m\mathbf{a} - n\mathbf{b}) \quad (13.43a)$$

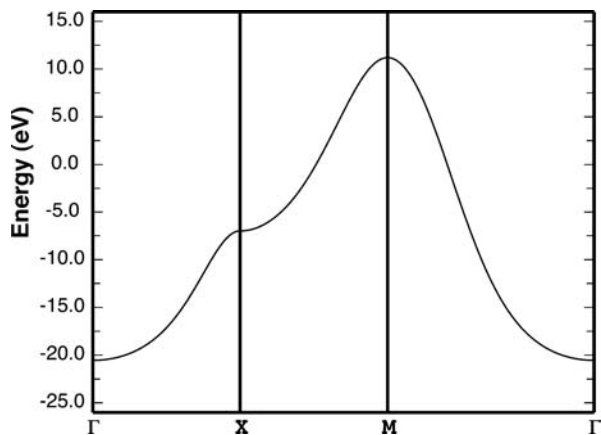
and the associated energy by

$$e(k_a, k_b) = \alpha + 2\beta_a \cos k_a a + 2\beta_b \cos k_b b \quad (13.43b)$$

directions. When the interactions along the two directions are identical, that is,  $\beta_a = \beta_b = \beta$ , we obtain

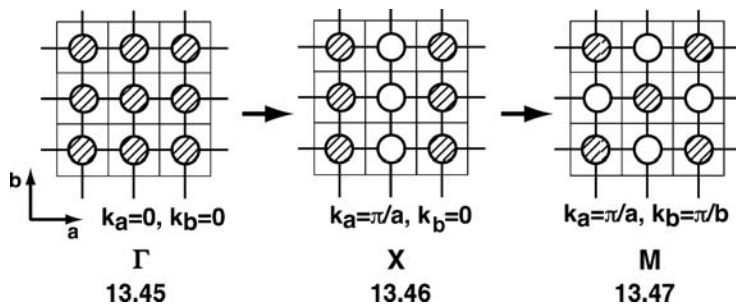
$$e(k_a, k_b) = \alpha + 2\beta[\cos k_a a + \cos k_b b] \quad (13.43c)$$

One could do calculations for each of the  $(k_a, k_b)$  points shown in 13.44 and in practice one does many more, but the representation of  $\phi$  in three dimensions (for one orbital or many sheets in three dimensions for a realistic compound) becomes problematic. There are two ways to represent the solutions. For the  $e(\mathbf{k})$  versus  $\mathbf{k}$

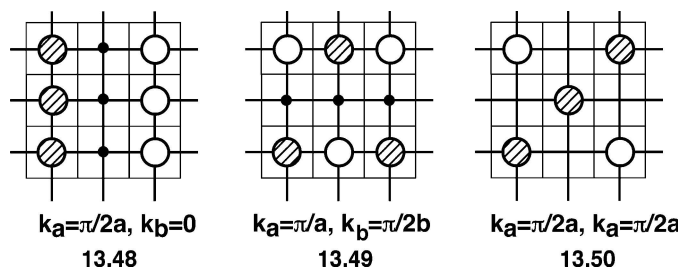
**FIGURE 13.16**

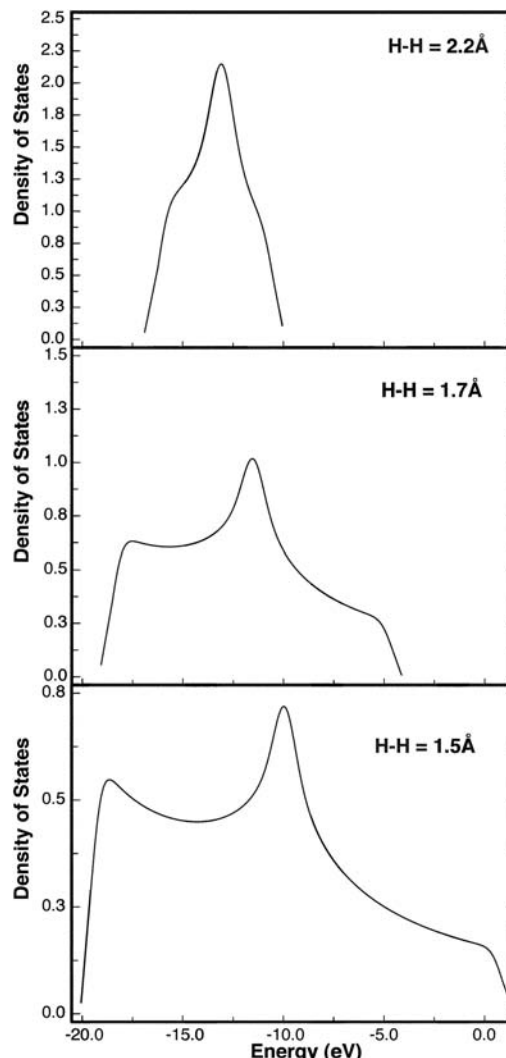
Plot of  $e(k)$  versus  $\mathbf{k}$  for a two-dimensional square lattice of hydrogen atoms with an H–H distance of 1.3 Å.

band structure plot the best one can do is to cover the range of  $\mathbf{k}$  values by going around the high symmetry points of the Brillouin zone. Extremes of the orbital energies should then be represented. In this case the “tour” in **13.44** runs from  $\Gamma$  to  $X$  to  $M$  and then back to  $\Gamma$ . A calculation of the bands for an H–H distance of 1.3 Å is shown in Figure 13.16. The orbitals can easily be constructed from the Bloch functions of equation 13.43 in a manner precisely analogous to that in the one-dimensional case. For the  $\Gamma$  point, the hydrogen s AO is translated with the same phase in both the  $a$  and  $b$  directions leading to the representation in **13.45**.



Obviously, the  $\Gamma$  point in this case represents the most bonding situation and, therefore, it lies lowest in energy. At the  $X$  point the phase of the s AO alternates in the  $a$  direction, but stays the same for the  $b$  direction, see **13.46**. Consequently, the band “runs up” going from  $\Gamma$  to  $X$ . At the  $M$  point (**13.47**) the phase of the s AO alternates in both directions. It then represents the most antibonding, the most destabilized solution to the Bloch equations. One can also easily write down intermediate solutions given by **13.48–13.50**. The situation in **13.48** is the halfway point on going from  $\Gamma$  to  $X$ , **13.49** is that for going from  $X$  to  $M$  and **13.50**

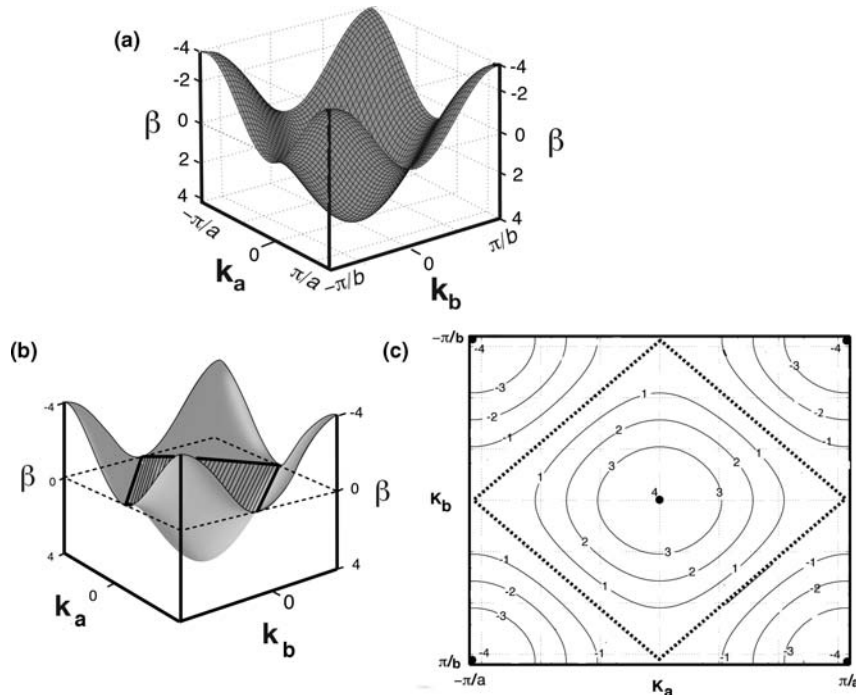


**FIGURE 13.17**

DOS curves for a square hydrogen net with different H–H distances.

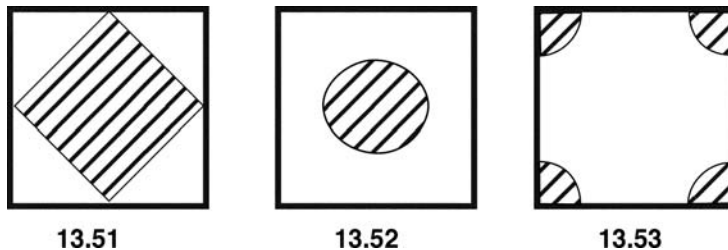
corresponds to the halfway point on returning from M to  $\Gamma$ . The reader should verify that the Y point in the Brillouin zone of **13.44** lies at an energy identical to that given by X. The band width which in this case is over 30 eV, of course, is greatly influenced by the intra-cell overlap—the magnitude of the H–H distance. The DOS plots which result from our tetragonal H net are shown in Figure 13.17 for various H–H distances. Again the shape of the DOS curves depends upon intercell overlap with the most common shape for two-dimensional systems being that for H–H = 1.7 Å. Notice the asymmetry induced by the inclusion of overlap; states toward the bottom of the band are more dense than those at the top of the band.

Let us return to the simple Hückel model from equation 13.41a where  $\beta_c = 0$  and  $\beta_a = \beta_b = \beta$ . Namely, there is no interaction along the c-direction so that we are dealing with a two-dimensional system. Then, a simple analytical solution results, which can be plotted in three dimensions for the full Brillouin zone. This is shown in Figure 13.18a. The minimum lies at the zone center with a value of  $4\beta$ . The  $(k_a, k_b) = (\pm 1/2, \pm 1/2)\pi/a$  points with energy values of  $-4\beta$  and four inflection points at  $0\beta$  which are located at  $(k_a, k_b) = (0, \pm 1/2)\pi/a$  and  $(\pm 1/2, 0)\pi/a$ . Suppose the electrons in this compound were paired. The band then would be exactly half full and any states lying below  $0\beta$  would be filled. This is illustrated in

**FIGURE 13.18**

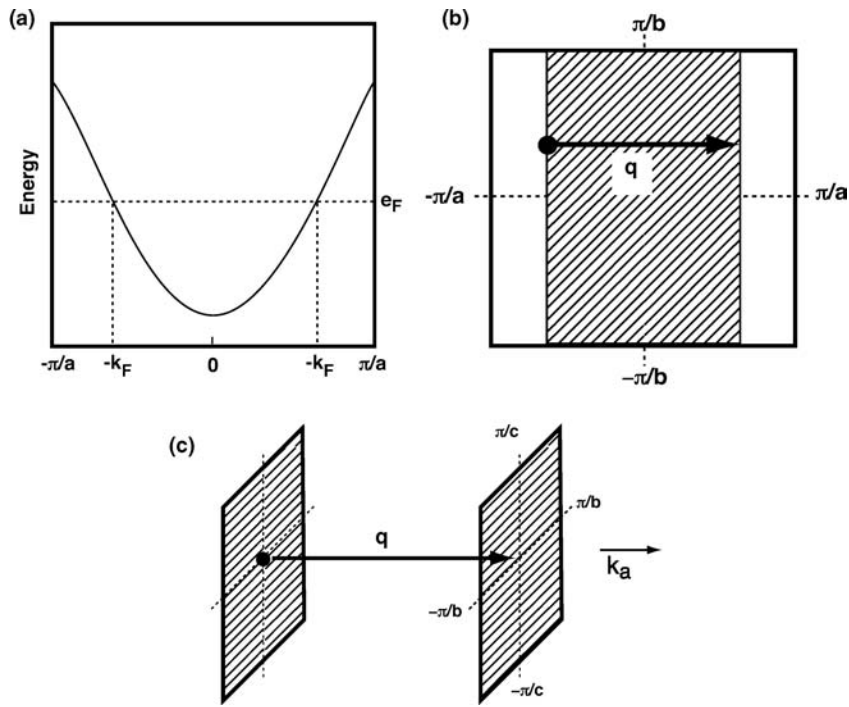
(a) Plot of the square hydrogen net using the Hückel approximation. (b) The shaded surface shows the band filling for the case when the electrons are paired. (c) A contour plot for this system where the units of the contours are given in units of  $\beta$ . The heavy dotted line corresponds to the half-filled case in (b).

Figure 13.18b by the shaded square which is embedded in the band structure. Figure 13.18c shows an equivalent way to plot this two-dimensional system. Here, the contours are in units of  $\beta$  and the dotted line corresponds to the situation for half-filling. The dotted line is then the boundary surface of  $(k_a, k_b)$  values that separate the  $(k_a, k_b)$  values leading to the unoccupied states from those leading to the occupied states. It is called the Fermi surface and it is of vital concern for the transport properties of a material. For a compound, where there is a gap between the highest occupied and lowest unoccupied states, there is no Fermi surface. For our hydrogen square net problem, the Fermi surface can be drawn as in 13.51. The shaded area indicates that portion of  $k$  values which



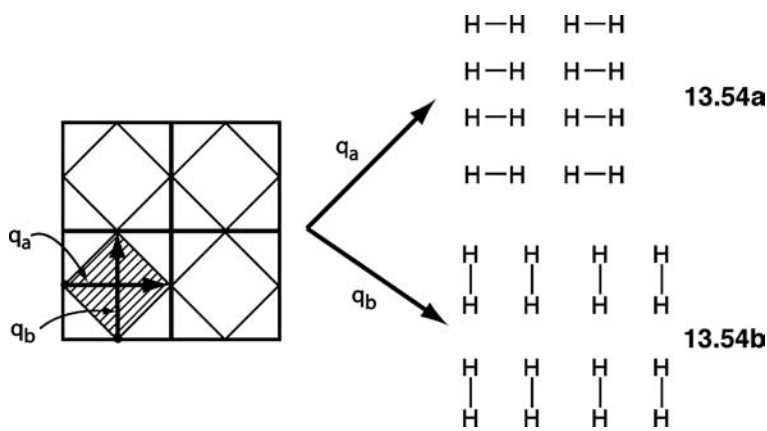
correspond to occupied states. Now, the shape of the Fermi surface is very sensitive to the electron count. If electrons are removed (see Figure 13.18; the Fermi level moves to lower energy, larger  $\beta$ ) then the surface given by 13.52 results. The addition of electrons to the two-dimensional hydrogen net changes the Fermi surface to that given by 13.53. The shape of the Fermi surface for a metal can, in principle, be determined experimentally and so there is another connection here between experiment and theory.

For a one-dimensional metallic system with a partially filled band as shown in Figure 13.19a, the orbitals of the wavevector region  $-k_f \leq k_a \leq k_f$  are occupied, and those of the remaining wavevector region are unoccupied. Thus, the

**FIGURE 13.19**

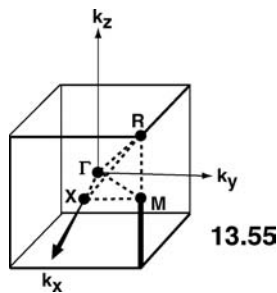
Representation of the Fermi surfaces in a one-dimensional (a), two-dimensional (b), and three-dimensional system with one crystal orbital in the unit cell. Here  $\mathbf{q}$  is the nesting vector.

occupancy of the band is given by the fraction  $f = 2k_f/(2\pi/a) = ak_f/\pi$ . If this one-dimensional band is represented in the two-dimensional space of  $k_a$  and  $k_b$  with  $\beta_b = 0$  (equation 13.43a), then the Fermi surface is given by two parallel lines, which are separated by the vector  $\mathbf{q} = 2k_f$  and are perpendicular to the chain direction, that is, the line from  $\Gamma = (0,0)$  to  $X = (1/2, 0)(\pi/a)$  (see Figure 13.19b). If the one-dimensional band is represented in the three-dimensional space of  $k_a$ ,  $k_b$ , and  $k_c$  with  $\beta_b = \beta_c = 0$  (equation 13.41a), then the Fermi surface is given by two parallel planes separated by the vector  $\mathbf{q} = 2k_f$  and perpendicular to the chain direction, namely, the line from  $\Gamma = (0,0,0)$  to  $X = (1/2, 0, 0)(\pi/a)$  (see Figure 13.19c). In the representation of the one-dimensional band in the one-dimensional space of  $k_a$ , the Fermi surface is given by the two points at  $-k_f$  and  $k_f$ , which are separated by  $\mathbf{q}$  (see Figure 13.19a). In all three representations of the one-dimensional Fermi surface, one piece of the Fermi surface, when translated by the vector  $\mathbf{q}$ , is superposed on the other piece of the Fermi surface. In such a case, the Fermi surface is said to be nested by  $\mathbf{q}$ . The presence of Fermi surface nesting signals that the metallic system has an electronic instability which can give rise to a periodic lattice distortion, known as a charge density wave (CDW), hence to a band gap opening at the Fermi level and to the removal of the nested Fermi surface [22]. The unit cell size of the CDW state resulting from a Fermi surface nesting is increased by a factor of  $1/f$  with respect to that of the metallic state. For example, the Peierls distortion for a one-dimensional system with half-filled metallic band (i.e.,  $f = 1/2$ ) is an example of a CDW. In an extended zone scheme, the Fermi surface of 13.51 for the half-filled two-dimensional square net can be represented as in 13.53, which shows that the two sets of parallel lines are simultaneously by the nesting vectors  $\mathbf{q}_a$  and  $\mathbf{q}_b$ , for which  $\mathbf{q}_a = (1/2)(2\pi/a)$  and  $\mathbf{q}_b = (1/2)(2\pi/b)$ . Thus, this Fermi surface nesting suggests a dimerization of the two-dimensional net either along the  $a$ -direction (13.54a) or along the  $b$ -direction (13.54b).



There is a relationship here to the Peierls distortion for one-dimensional materials discussed in Section 13.2 and the first-order Jahn–Teller distortion in the molecular domain (Section 7.4.B). We shall not cover the details of this phase distortion or the formation of charge density waves or spin density waves here, but direct the reader to a comprehensive treatment for chemists [22]. All of these are potential factors that may drive metallic states as represented in 13.3 into insulators. Predicting this behavior *a priori* is very difficult indeed.

Let us now consider a case of three  $p$  atomic orbitals on one atom per unit cell, now for a three-dimensional system. For simplicity, we use a cubic lattice with  $a = b = c$  using the traditional Cartesian coordinates. The  $x$ ,  $y$ , and  $z$  orbitals can be translated to form three bands in the Brillouin zone which is shown in 13.55. Here, the special points for  $(k_x, k_y, k_z)$  are:  $\Gamma = (0, 0, 0)$ ,  $X = (\pi/a, 0, 0)$ ,  $M = (\pi/a, \pi/a, 0)$ , and

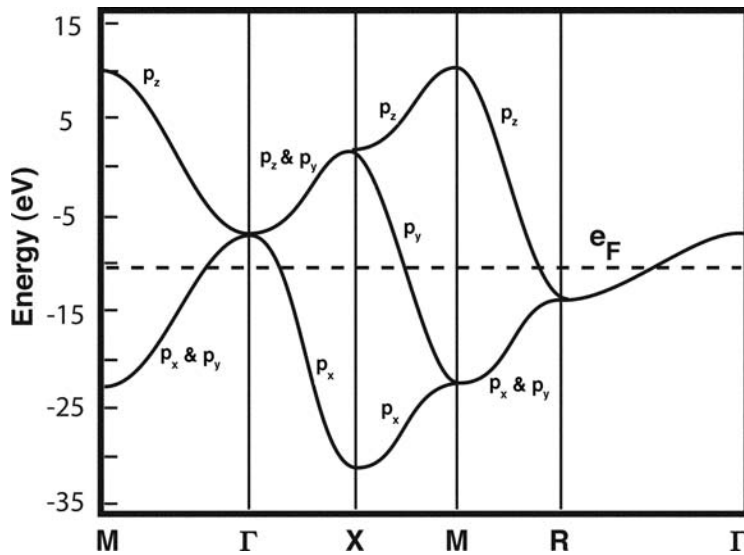


$R = (\pi/a, \pi/a, \pi/a)$ . Using a Hückel approximation for the  $\sigma$  and  $\pi$  interactions for each individual  $p$  atomic orbital in turn, the energy dispersion relations become

$$\begin{aligned} \text{For } p_x : e(k) &= \alpha + 2\beta_\sigma \cos k_x a + 2\beta_\pi \cos k_y a + 2\beta_\pi \cos k_z a \\ \text{For } p_y : e(k) &= \alpha + 2\beta_\pi \cos k_x a + 2\beta_\sigma \cos k_y a + 2\beta_\pi \cos k_z a \\ \text{For } p_z : e(k) &= \alpha + 2\beta_\pi \cos k_x a + 2\beta_\pi \cos k_y a + 2\beta_\sigma \cos k_z a \end{aligned} \quad (13.44)$$

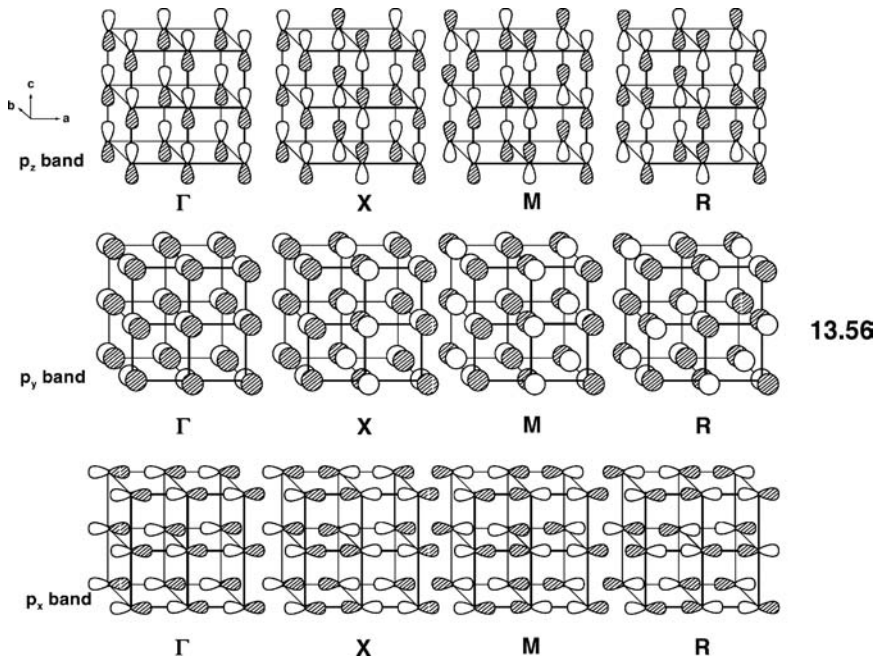
Here, the two resonance integrals are, of course, not equal since  $\sigma$  overlap is larger than  $\pi$  overlap  $-|\beta_\sigma| > |\beta_\pi|$ . Using specific values for the resonance integrals and  $\alpha$  leads to the  $e(\mathbf{k})$  versus  $\mathbf{k}$  plot in Figure 13.20 [23]. Notice the triple degeneracies at the  $\Gamma$  and  $R$  points.

The  $x$  and  $y$  bands are degenerate from  $M$  to  $\Gamma$  and  $M$  to  $R$  whereas,  $z$  and  $y$  are degenerate from  $\Gamma$  to  $X$ . Finally, all three bands are degenerate from  $R$  back to  $\Gamma$ . There is much symmetry at work here. It is easy, albeit tedious, to write down the

**FIGURE 13.20**

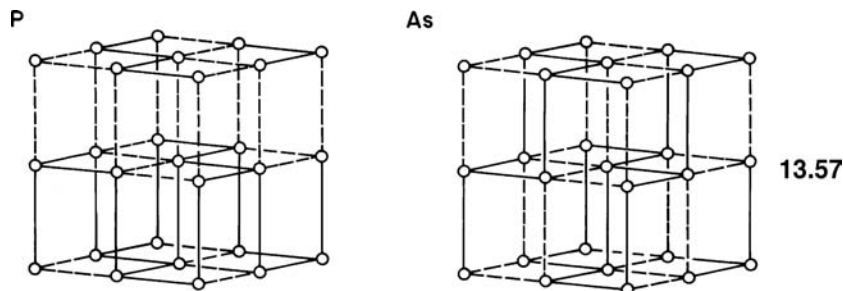
Band structure for a cubic lattice in which each has only three  $p$  atomic orbitals. The energies were evaluated (Reference [23]) using only nearest-neighbor  $\sigma$  and  $\pi$  interactions within the Hückel framework—see equation 13.44.

form of the crystal orbitals at each of the special  $k$  points. This is done in 13.56. Taking, for example, the  $z$  band, at the  $\Gamma$  point there is  $\sigma$  antibonding along the  $c$ -direction and  $\pi$  bonding along the other two directions. The same is true for the  $x$  and  $y$  bands which are  $\sigma$  antibonding along the one axis and  $\pi$  bonding along the other two. Hence, all three bands are degenerate at the  $\Gamma$  point. Within this group of



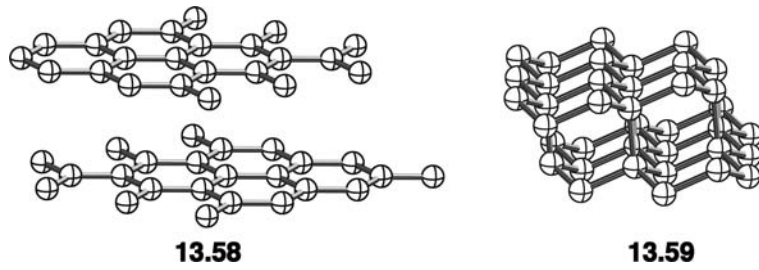
$k$  points, the  $x$  band is the most bonding one at  $X$ . It is both  $\sigma$  and  $\pi$  bonding. The  $z$  band at the  $M$  point is antibonding in all directions. The reader should carefully work through the shapes of these bands at the various  $k$  points. If this were a cube of phosphorus or another group 15 atom, then there would be five valence electrons. Two electrons in our approximation fill the  $s$  band which, of course, lies at lower energy than the three in Figure 13.20. There will also be varying amounts

of  $s/p$  mixing which has also been neglected. The three electrons per unit cell in Figure 13.20 fill up to the dashed horizontal line which indicates the Fermi level. A structural distortion—breaking some of the bonds and re-enforcing others—will occur. In fact each atom in the cube has six nearest neighbors. Exactly, half of these “bonds” are broken. Two out of several ways to accomplish this are illustrated in 13.57. The dashed lines indicate bonds that are broken. The geometric distortions lead to the structures of elemental black phosphorus and arsenic. Here, each atom

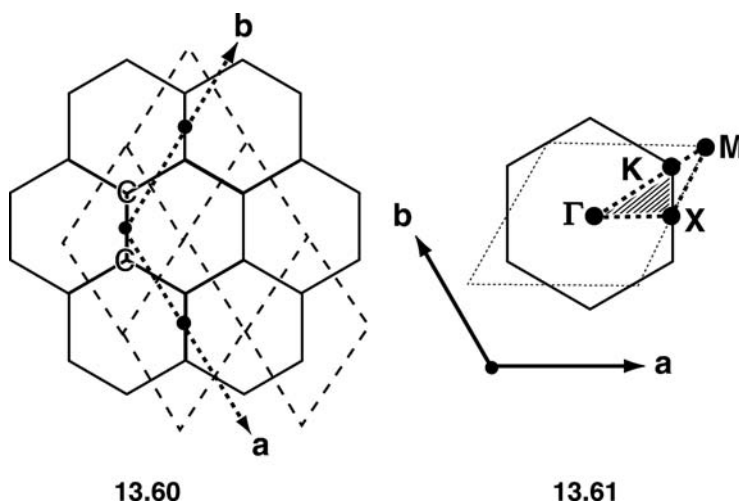


is now connected to three others in a pyramidal manner with a lone pair pointed away from the three neighbors. This is precisely analogous to the eight electron  $\text{AH}_3$  series in Section 9.3. On applying pressure to crystals of black phosphorus the simple cubic structure is re-produced rendering it metallic, a process similar to the one described earlier for hydrogen. Both the arsenic and black phosphorus structures are layer structures with no covalent bonds between the layers. Each atom is in a trigonal pyramidal coordination. There are two other ways to generate these structures which will be considered later.

Another very common layered structure is given by graphite, 13.58, one of the elemental forms of carbon. The other common structure is diamond, 13.59.



In diamond every carbon is four-coordinate, in other words one might consider that each carbon is  $sp^3$  hybridized and connected to four others via  $\sigma$  bonds. The compound is saturated, that is, there will be a large energy gap ( $\sim 5.5$  eV) between the filled  $\sigma$  bonding and the empty  $\sigma$  antibonding orbitals. The situation is quite different in graphite. Here, each carbon could be considered to be  $sp^2$  hybridized so there are three  $\sigma$  bonds around each carbon. Leftover is one  $p$  AO perpendicular to the molecular plane which can  $\pi$  bond to its three neighbors. Formally, there is one electron in each  $p_\pi$  AO just like in benzene. Therefore, the bonding between the graphite layers is weak which means that the sheer force needed for cleaving the adjacent sheets is small. This makes graphite an excellent lubricant (and gives it excellent writing properties). If we take one graphite sheet, namely, graphene, which exhibits many interesting properties [24], then we have a two-dimensional system where there are two carbon atoms in each unit cell. This is shown in 13.60. Several unit cells are sketched out by the rhomboid figures given by dashed lines. The  $a$  and  $b$



axis are not orthogonal to each other; they are hexagonal. The Brillouin zone is shown in 13.61. For a density of states plot one would evaluate the region of  $k$  space which is shaded and go from, say  $\Gamma$  to  $X$  to  $K$  and back to  $\Gamma$  for a plot of the band structure. However, the  $K$  point is one with  $k_a = 2\pi/3a$  and  $k_b = 2\pi/3b$  and the orbital mixing coefficients have both real and an imaginary components. This brings about complications when trying to visualize the phase relationship between the orbitals, so what we shall do instead is to extend the dispersion to the  $M$  point. The band structure for a single sheet of graphite is shown on the left-hand side of Figure 13.21. The two solid lines are the two  $\pi$  bands—each carbon in the unit cell contributes one  $p$  AO so these combine to form  $\pi$  and  $\pi^*$  combinations. The translational details are precisely the same as those presented for the tetragonal square net. At  $\Gamma$  the  $\pi$  and  $\pi^*$  combinations translate with the same phase in the  $a$  and  $b$  directions. Consequently, as shown on the right-hand side of Figure 13.21, the  $\pi$  band is totally bonding at this point, whereas,  $\pi^*$  is totally antibonding. At the  $X$  point translation in the  $a$  direction occurs with alternating phase and in the  $b$  direction with the same phase. Intercell bonding is turned on in the  $a$  direction for  $\pi^*$  so the band is stabilized. The opposite occurs for  $\pi$ . This same pattern occurs on going from  $\Gamma$  to  $M$ . At  $M$ , the phase is reversed on going from one unit cell to

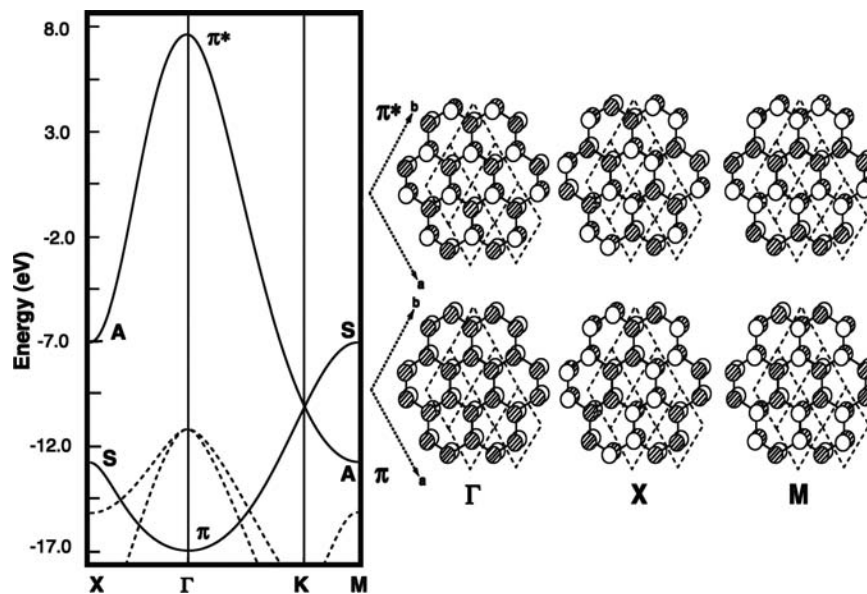
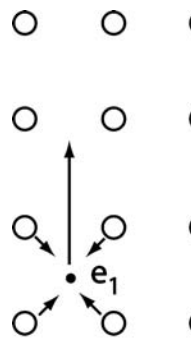


**FIGURE 13.21**

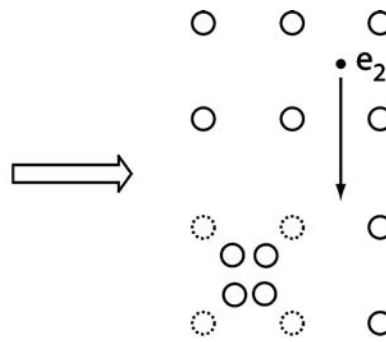
Plot of  $e(k)$  versus  $k$  for a single sheet of graphite is shown on the left-hand side where the solid line corresponds to the two  $\pi$  bands. The dashed line shows the two highest filled  $\sigma$  bands. The crystal orbitals for the  $\pi$  and  $\pi^*$  bands are explicitly drawn out for the three  $k$  points on the right-hand side.

another in both directions. Consequently, the  $\pi$  band rises to an even higher energy than at X and  $\pi^*$  falls to a greater extent. The result shown in the  $e(\mathbf{k})$  versus  $\mathbf{k}$  plot is that  $\pi$  and  $\pi^*$  cross each other, which occurs at the K point by symmetry. Notice that the crystal orbitals for the  $\pi$  band at the three special points are symmetric with respect to a mirror plane that runs parallel to the  $\mathbf{ab}$  bisector. On the other hand, the  $\pi^*$  combinations are antisymmetric with respect to this mirror plane. This occurs throughout the band structure in Figure 13.21 and, as a consequence, the  $\pi$  and  $\pi^*$  bands cross each other without mixing, so that the  $e(\mathbf{k})$  vs.  $\mathbf{k}$  relation around K is linear [25]. The Fermi level lies just at this crossing point so there is no gap between the occupied and unoccupied orbitals. The linear  $e(\mathbf{k})$  vs.  $\mathbf{k}$  relationship forms two cones merged at K; note that Figure 13.21 shows a cross-sectional view of them. These cones are known as Dirac cones, and the merged point as the Dirac point, because the electrons around K behave like relativistic particles described by the Dirac equation with zero mass [25]. The density of states (DOS) at the Dirac point is zero, so graphene is a zero DOS metal. Dirac cones are also found in a topological insulator (e.g.,  $\text{Bi}_{1-x}\text{Sb}_x$ ,  $\text{Bi}_2\text{Se}_3$ ,  $\text{Bi}_2\text{Te}_3$ , and  $\text{Sb}_2\text{Te}_3$ ) [26], which behaves as an insulator in its interior but whose surface is metallic because it has conducting states described by Dirac cones.

For a typical metal (see 13.4), the Fermi surface is sizable and the electrons at the Fermi level would be accelerated in a direction opposite to the applied electric field. However, this accelerated movement of the electrons is prevented by imperfections in crystallinity (e.g., vibrations and defects) and other electrons. At a high temperature thermal vibrations of the atoms in the solid state (from a group theoretical sense these vibrations have symmetry attributes and are called phonons) disturb the periodicity of the potential thereby scattering the electrons. As the temperature decreases the vibrations decrease and the conductivity rises, however, because the electrons have like charges, they repel each other and the conductivity reaches a finite value. For semiconductors, there is a small energy gap between the valence and conduction bands (13.4 and 13.15). Thermal (or photochemical) excitation can promote some electrons from the valence band to the conduction band, thereby producing hole and electron carriers in the valence and conduction bands, respectively. The amount of these carriers increases when the temperature is raised so conductivity will increase with increasing temperature. Impurities can be added (doping) to semiconductors to increase the number of mobile electrons or holes. Superconductivity is a phenomenon which occurs at low temperatures in some conductors. In this state, the electrons undergo a collective ordered transition where all electrical resistance disappears below a specific temperature ( $T_c$ ). There are many theories on how superconductivity arises; perhaps the most successful one is due to Bardeen, Cooper and Schrieffer—the BCS theory [27]. The key feature of the BCS theory is the coupling of the conducting electrons to the lattice vibration, the phonon. As illustrated in 13.62, a moving electron causes a slight, momentary lattice deformation around it. This momentary deformation affects the motion of a



13.62



13.63

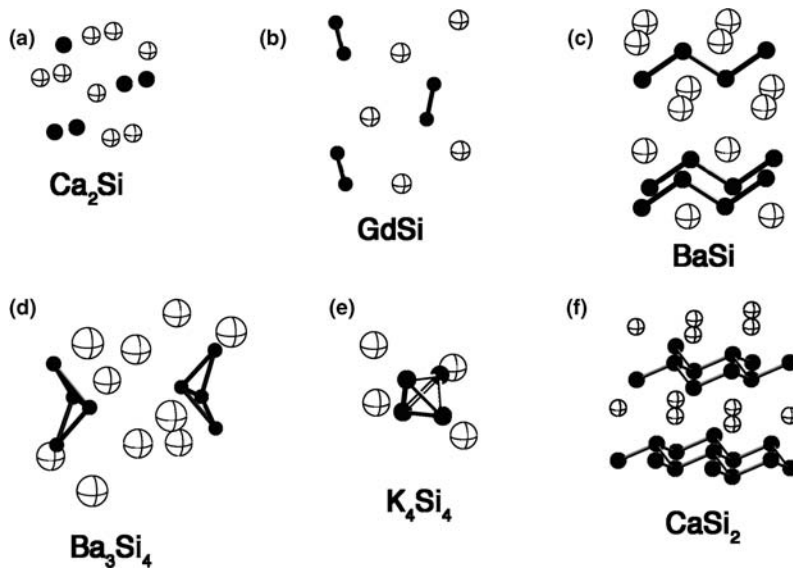
second electron moving in the opposite direction in the wake of the first, **I3.63**, such that the two electrons move as an entity as if bound together by an attractive force. Such pairs of electrons, known as Cooper pairs, are responsible for superconductivity. In the BCS theory, the phonon is responsible for the formation of Cooper pairs. The distance between the pair of electrons is called the coherence length. It normally is quite long—over several unit cells. There are, of course, many other conducting electrons between the Cooper pair we have constructed so if Cooper pairs are to form, they must all form together in a collective state. Notice that the BCS theory of superconductivity represents a breakdown of the Born–Oppenheimer approximation.  $\text{MgB}_2$  is a compound which has been known and actually available as a commercial reagent for some time. Recently, it was discovered to be a superconductor with  $T_c = 39 \text{ K}$  [28]. The structure of  $\text{MgB}_2$  is quite simple. The boron atoms form a two-dimensional layer exactly like that in graphite with the magnesium atoms sandwiched in between layers above and below the center of the hexagons. The usual way to think about this compound is that electropositive magnesium transfers its two electrons to the boron atoms, thus, making the boron layer isoelectronic to graphite. This is, however, not quite the case. It is thought that Mg to B charge transfer is not complete. This leaves the  $\pi$  band partly filled, but what is more important is that there are two  $\sigma$  bands in Figure I3.20. These are given by the dashed lines. There are two specific phonon modes which strongly couple to the two  $\sigma$  bands and give rise to the superconducting state [29]. It is thought that these bands lie high enough in energy so that they too are partially occupied. Furthermore, theory suggests [29] that there is a second superconducting state at lower temperature that is derived from the  $\pi$  electrons! It should be emphasized that superconductivity is an extremely fragile state. Substitution of other elements in  $\text{MgB}_2$ , for example, does not give rise to a superconductor.

---

## 13.5 ELECTRON COUNTING AND STRUCTURE

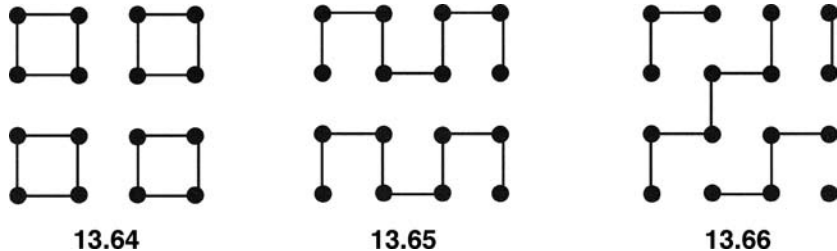
---

A common thread that runs throughout this book is that the electron count determines the structure for a compound. In the solid-state domain, this is a little more tricky since metastable phases are often isolated. Certainly metallic compounds where bands are partially occupied cannot be dealt with in a straightforward manner. There are a number of ways that chemists have related the electron count in a solid-state compound to its structure; perhaps the most simple one is an electron counting scheme for semiconductors and insulators called the Zintl–Klemm concept [30]. The idea here is that electropositive elements will donate all of their valence electrons to the more electronegative ones. The latter will then exist as isolated anions (e.g., the situation in  $\text{NaCl}$ ) or form bonds with each other to satisfy the octet rule. The Zintl–Klemm concept works well with electropositive elements from Groups 1–3 and the rare earth ions along with the main group elements. We have chosen a particularly simple set of binary silicides as examples to illustrate this approach. For  $\text{Ca}_2\text{Si}$ , the four electrons from the two calcium atoms are transferred to each silicon atom. Thus, we have  $\text{Si}^{4-}$  single atoms surrounded by  $\text{Ca}^{2+}$  cations. The structure of this compound is shown in Figure I3.22a, where the black spheres are Si and the white ones are Ca. The shortest Si—Si distances are  $4.80 \text{ \AA}$ , far too long for there to be any bonding. In  $\text{GdSi}$ , the most likely counting scheme would be  $\text{Gd}^{3+}$  which then leaves a narrow band of seven  $4f$  electrons with their spins unpaired (**I3.5**). So, silicon becomes  $\text{Si}^{3-}$  which then will pair with another  $\text{Si}^{3-}$  anion to form one Si—Si bond. The structure is shown in Figure I3.22b. Here, there is one short Si—Si distance at  $2.49 \text{ \AA}$  with the next shorter ones at a very long  $4.23 \text{ \AA}$ . In  $\text{BaSi}$  (Figure I3.22c), the  $\text{Si}^{2-}$  atoms need to form two bonds. There are a number

**FIGURE 13.22**

Structure of some binary silicides. In each case the Si atoms are presented by the black spheres and the other element by the white spheres.

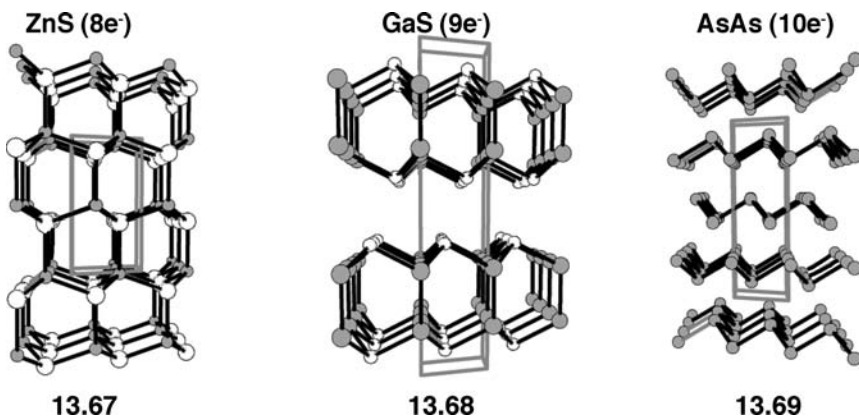
of ways to do this. One could have Si—Si double bonds. This is not likely since  $\pi$  bonding is relatively weak for second and higher rows in the periodic table. Alternatively, the structure could be built up from Si squares, **13.64** or “U” shaped polymers, **13.65** which is akin to the structure of  $\text{BaMg}_{0.1}\text{Li}_{0.9}\text{Si}_2$ , **13.40** or, finally, a “W” shaped polymer, **13.66**. These represent some of the two-dimensional



possibilities. The latter is the real structure (Figure 13.22c) where the Si—Si distances in the chain are 2.50 Å and the chains are separated by 5.04 Å. For  $\text{Ba}_3\text{Si}_4$ , a  $\text{Si}_4^{6-}$  unit gives a 22-electron count. This is 10 electrons short of an octet for each Si atom; therefore, five Si—Si bonds must form in some way. Figure 13.22d shows that individual  $\text{Si}_4^{6-}$  butterfly units are formed with four Si—Si distances of 2.34 Å and a central one of 2.29 Å. Figure 13.22e and f show two different structures that are formed for  $\text{Si}^-$ . According to the Zintl–Klemm concept,  $\text{Si}^-$  requires the formation of three bonds to each Si atom. Discrete  $\text{Si}_4^{4-}$  tetrahedra are present in  $\text{K}_4\text{Si}_4$ , whereas,  $\text{CaSi}_2$  adopts a structure akin to elemental phosphorus or arsenic (**13.57**). Elemental silicon requires four bonds to each Si atom and so the diamond rather than graphite structure exists. We must hasten to add that  $\pi$  bonding can and does exist for main group compounds. In the  $\text{BaMg}_{0.1}\text{Li}_{0.9}\text{Si}_2$  example, three out of four  $\pi$  bands are filled for the  $\text{Si}_4^{6-}$  unit cell (see Figure 13.14). A bit more complicated example is provided by  $\text{SrCa}_2\text{In}_2\text{Ge}$  [31]. Here the  $[\text{In}-\text{Ge}-\text{In}]^{6-}$  framework exists in a “W” polymer, **13.66** and possesses 16 electrons. This is eight electrons short of the Lewis octet rule so four bonds are needed to form. Two In–Ge  $\sigma$  bonds and two  $\frac{1}{2}$  In  $\sigma$  bonds are used on either side of the In–In bonds. This then leaves one  $\pi$  bond to be formed. Therefore, if the

$\text{In}_2\text{Ge}$  polymer uses  $sp^2$  hybridization, then the three  $p$  AOs will generate three  $\pi$  bands, two of which are filled. It should be clear to the reader that the *a priori* prediction of the structure of a solid-state compound will be tenuous at best and the Zintl–Klemm concept will be most frequently used for the analysis of a known structure rather than the reverse.

Returning to the diamond structure, zinc blende or wurtzite,  $\text{ZnS}$  has a total of eight electrons (the  $3d$  AOs on  $\text{Zn}$  are at much too low of an energy to be involved in bonding). It is, therefore, no surprise that both  $\text{Zn}$  and  $\text{S}$  are tetracoordinate. The structure is shown in 13.67, where the  $\text{S}$  atoms are the grey circles. We have seen in

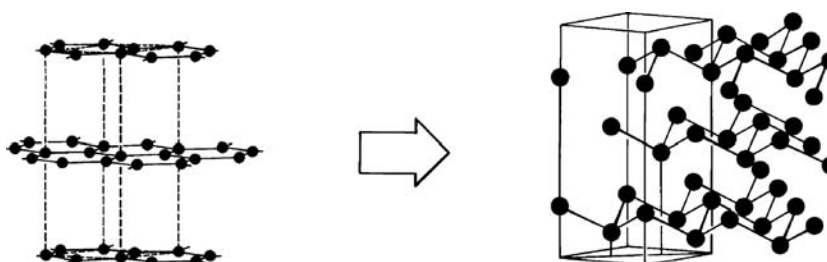


previous chapters that the addition of electrons to electronically saturated compounds causes bonds to elongate or even break. Such is the case here. The addition of one electron to give  $\text{GaS}$ , 13.68, causes every other layer to separate and shift laterally. The addition of another electron causes every layer to separate, 13.69, yielding again the phosphorus or arsenic structure.

A third way to derive the arsenic or phosphorus structure is as a distortion of another layer structure, namely, that of graphite (Figure 13.23). Three of the four electrons from each carbon atom in graphite are used in forming a  $\sigma$ -bonded network. This leaves one electron per carbon atom in a  $p_z$  orbital, perpendicular to the graphite plane, which may interact with its neighbors in a  $\pi$  sense. Crudely then, planar graphite is akin to  $\text{CH}_3$  or  $\text{BH}_3$  with one less valence electron. Both of these species are planar.  $\text{NH}_3$ ,  $\text{PH}_3$ , or  $\text{AsH}_3$  however, with five valence electrons are pyramidal, as described in Chapter 7, for very well-defined reasons. The driving force for pyramidalization in the solid-state analog is similar [32], but with the additional factor that  $\pi$ -antibonding between the lone pairs on adjacent As atoms is minimized upon pyramidalization.

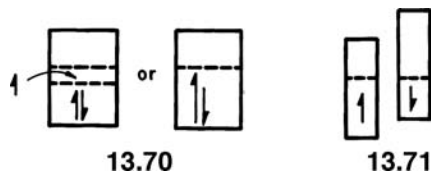
**FIGURE 13.23**

Relationship between the structures of graphite (left) and arsenic (right). Geometrically, puckering each sheet of graphite and shifting it relative to the one below it leads to the structure of arsenic.



## 13.6 HIGH-SPIN AND LOW-SPIN CONSIDERATIONS

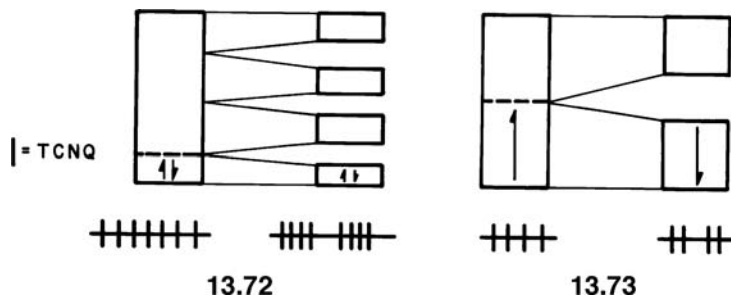
Just as in the molecular case, and discussed in detail in Chapter 8, there is always a choice to be made between filling all the lowest levels with electron pairs and the alternative of allowing some of the higher energy levels to be occupied by electrons with parallel spins. 13.5 and 13.6 showed two extreme cases where all the electrons in a band were either all spin unpaired or all spin paired. An intermediate situation shown in 13.70 is also of importance, where not all of the spins are unpaired. An example of this type, which, in addition to being metallic is magnetic, is found in the



13.71

body-centered cubic structure of elemental iron. There are about 1.5 unpaired electrons per atom. 13.71 depicts an alternative way of showing this result which emphasizes the lower energy of the up-spin band compared to the down-spin band. This is a result of the larger number of up-spin electrons and a concomitantly larger number of stabilizing exchange integrals between them, compared to the down-spin electrons. As in the molecular case, it is difficult to predict *a priori* whether magnetic or nonmagnetic states will be found in a given instance. One interesting observation which has an exact parallel with molecular chemistry is that a change of spin state is often associated with a change in structure. Just as high and low spin four-coordinate  $d^8$  molecules are tetrahedral and square planar, respectively (Section 16.4), so magnetic iron has the body-centered cubic structure but nonmagnetic iron crystallizes in the hexagonal close-packed arrangement.

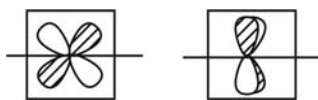
Another instance where spin state is important and has a direct bearing on structure is in one-dimensional systems. Just as in Section 13.2 where we showed how a half-filled band usually results in a pairing distortion, so similar reasoning suggests that a quarter-filled band should result in a tetramerization 13.72. However, if the distorted arrangement is magnetic then dimerization is the process that is favored 13.73. Again prediction of the mode of distortion is not at all easy.



The state of affairs shown in 13.73 is found for the  $(\text{MEM})^+(\text{TCNQ})_2^-$  species [ $(\text{MEM})^+$  = methyl ethyl morpholinium cation] where there is one electron per two TCNQ orbitals [4].

## PROBLEMS

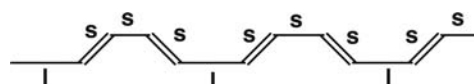
- 13.1. For the two examples below draw out the  $e(k)$  versus  $k$  plot and show the solution for three unit cells at the  $\Gamma$  and  $\pi/a$   $k$ -points.



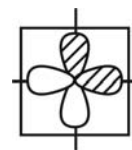
- 13.2. a.** Consider a polyacetylene conformer as shown below where all C–C distances are equal. Determine the size of the unit cell, draw the  $\pi$  bands and show the solutions for two unit cells at the  $\Gamma$  and  $\pi/a$   $k$ -points.



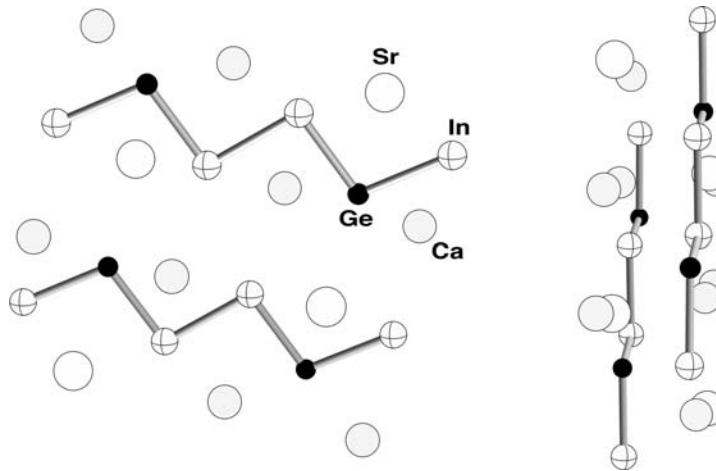
- b.** Distort the polymer as shown below where s and l stand for short and long bonds, respectively. Show what happens to the band structure at the  $\Gamma$  and  $\pi/a$   $k$ -points.



- 13.3.** Using 13.43–13.47 along with Figure 13.16 as a guide draw the  $e(k)$  versus  $k$  band structure and illustrate the solutions for the  $\Gamma$ ,  $X$ , and  $M$  points for the case when there are two orthogonal  $p$  AOs in a unit cell.

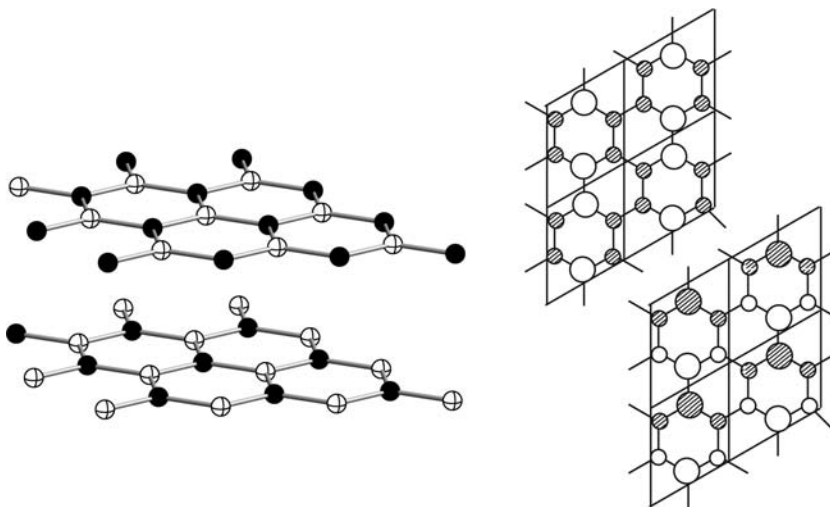


- 13.4.** The structure of  $\text{SrCa}_2\text{In}_2\text{Ge}$  consists of a one-dimensional ribbon of  $\text{In}_2\text{Ge}$  atoms surrounded by separate Sr and Ca cations. Two views are shown below.



- a.** Draw the band structure and the wavefunctions at the  $\Gamma$  and  $\pi/a$   $k$ -points for the  $\pi$  bands making the assumption that the electronegativity of In and Ge are the same. Show the position of the Fermi level.
- b.** In fact the  $p$  AOs of Ge are at  $-7.5$  eV while those for In are  $-5.6$  eV (2.9). Show what happens to the results in (a) when the Ge atoms are made more electronegative than In.

- 13.5.** Boron nitride has a layered structure just like graphite. There are again two  $\pi$  bands. Let us make the assumption that going from  $C_2$  to BN that  $|\delta\alpha_N| \approx |\delta\alpha_B|$ . The band structure of graphite is displayed in Figure 13.21 along with the solutions for the  $\Gamma$ , X, and M points. What happens to the two bands on going from graphite to BN? In other words one needs to evaluate the results at the  $\Gamma$ , X, and M points, as well as the K point. The real part of the K point solutions (they are a degenerate pair) are given below. Notice that the upper member is the bonding combination of  $e_{2u}$  and the lower one is the most antibonding combination of  $e_{1g}$  in benzene. Since they are a degenerate, it is best to take linear combinations of them.

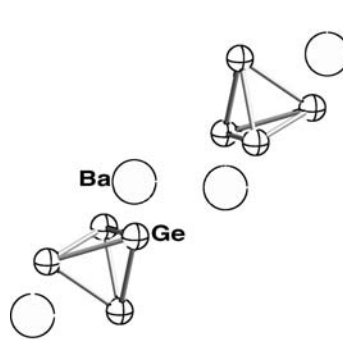


- 13.6.** Use the Zintl–Klemm concept to predict the structures for the following ternary compounds (hint: put the less electronegative atom from the anion surrounded by the more electronegative ones—why?).

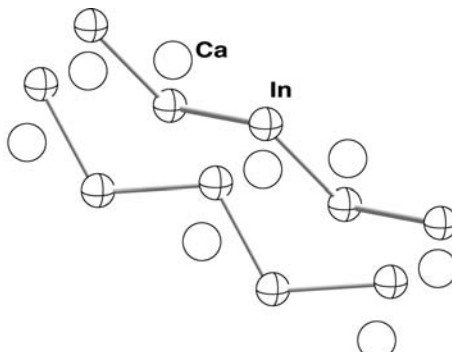
- $K_5TiO_4$
- $BaHgO_4$
- $K_4P_2Be$

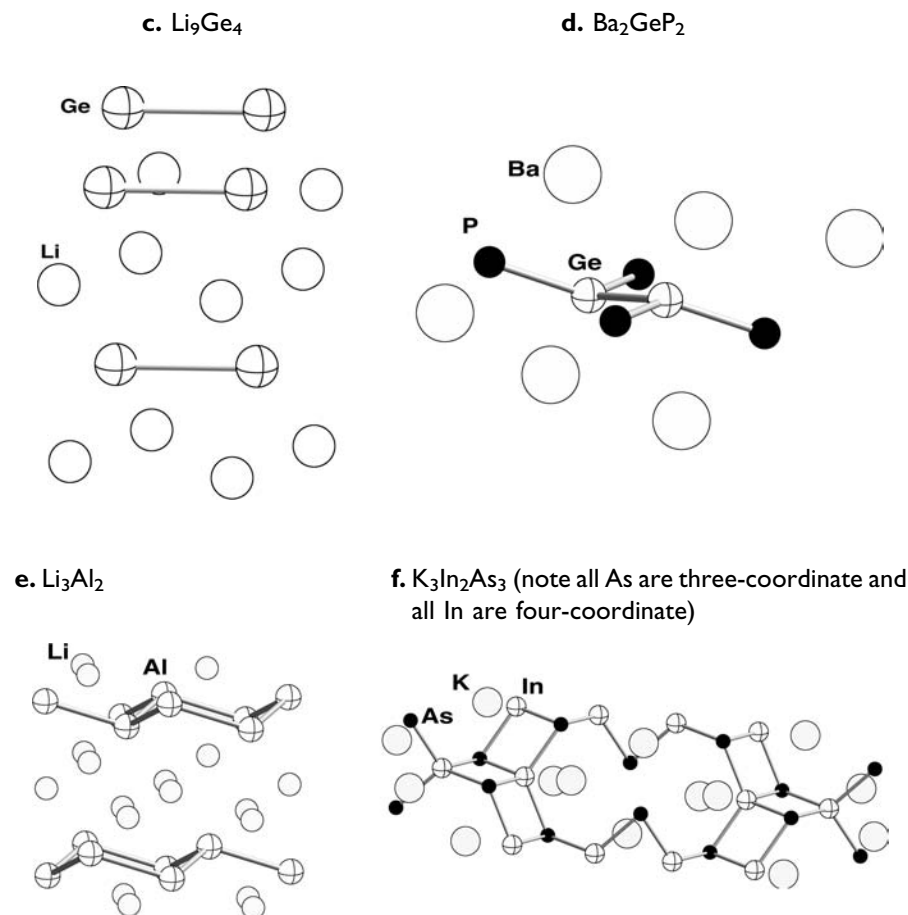
- 13.7.** Tell whether or not the structures below conform to the Zintl–Klemm counting rules.

a.  $Ba_2Ge_4$

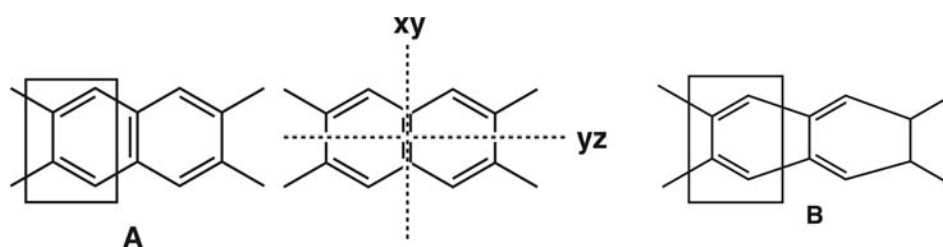


b.  $CaIn_2$



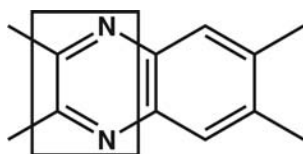


**13.8.** The hypothetical polymer polyacene fuses benzenoid rings on their edges in a linear manner to give the structure shown by **A** where all C—C bond lengths are identical.

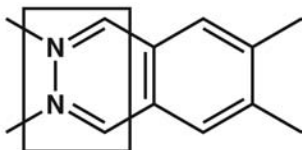


- Before we tackle this problem let us start with something easier. Suppose polyacene was distorted to **B**. Take the  $\pi$  orbitals of cisoid butadiene and form bands with them. Show the position of the Fermi level.
- The catch with structure **A** is that there is a  $yz$  mirror plane running along the propagation axis just as in **B**. The orbitals generated in both **A** and **B** must be either symmetric or antisymmetric with respect to this mirror plane. However, in **A** there are also mirror planes in the  $xy$  direction perpendicular to the propagation axis and the orbitals in **A** must be symmetric or antisymmetric with respect to them. This can be done by mixing the orbitals determined for **B**. Again show the position of the Fermi level.

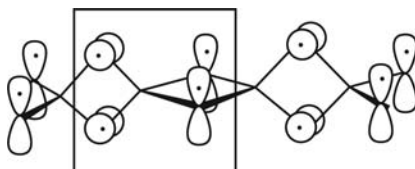
- c. Use electronegativity perturbation ideas to determine which of the two polydiacenes is more stable.



**versus**



- 13.9.** A very interesting, hypothetical molecule is shown below. This has the monomeric unit of a tetraradical and uses spiroconjugation. Draw out an  $e(k)$  versus  $k$  plot and show the form of the bands at the  $\Gamma$  and  $\pi/a$   $k$ -points.



## REFERENCES

1. J. C. Slater, *Introduction to Chemical Physics*, McGraw-Hill, New York (1939).
2. B. C. Gerstein, *J. Chem. Educ.*, **50**, 316 (1973).
3. N. W. Ashcroft and N. D. Mermin, *Solid State Physics*, Saunders, Philadelphia (1976).
4. M.-H. Whangbo, *Acc. Chem. Res.*, **16**, 95 (1983).
5. M.-H. Whangbo, in *Extended Linear Chain Compounds*, Vol. II, J. S. Miller, editor, Plenum, New York (1982).
6. R. Hughbanks and R. Hoffmann, *J. Am. Chem. Soc.*, **105**, 3528 (1983).
7. For an excellent review of polyacetylene and other one-dimensional conjugated polymers, see M. Kertesz, C. H. Choi, and S. Yang, *Chem. Rev.*, **105**, 3448 (2005).
8. G. W. Collins, L. B. Da Silva, P. Celliers, D. M. Gold, M. E. Foord, R. J. Wallace, A. Ng, S. V. Weber, K. S. Budil, and R. Cauble, *Science*, **281**, 1178 (1998); H. K. Mao and R. J. Hemley, *Science*, **244**, 1462 (1989).
9. For an excellent discussion of how the application of pressure modifies the geometric and electronic structure, see W. Gochala, R. Hoffmann, J. Feng, and N. W. Ashcroft, *Angew. Chem. Int. Ed.*, **46**, 3620 (2007).
10. M.-H. Whangbo and R. Hoffmann, *J. Am. Chem. Soc.*, **100**, 6093 (1978); M.-H. Whangbo, R. Hoffmann, and R. B. Woodward, *Proc. R. Soc., A* **366**, 23 (1979).
11. T. Giannachi, *Chem. Rev.*, **104**, 5037 (2004).
12. A. J. Heeger, S. Kivelson, J. R. Schrieffer, and W.-P. Su, *Rev. Mod. Phys.*, **60**, 781 (1988).
13. T. Bally, D. Hrovat, and W. T. Borden, *Phys. Chem. Chem. Phys.*, **2**, 3363 (2000).
14. The brand of perturbation theory that we have been using in this book has been extended to the solid state, see H. Tang, Ph. D. Dissertation, University of Houston (1995); D.-K. Seo, G. Papoian, and R. Hoffmann, *Int. J. Quantum Chem.*, **77**, 408 (2000).

15. O. Degtyareva, E. Gregoryanz, H. Mao, and R. Hemley, *Nat. Mater.*, **4**, 152 (2005).
16. J. K. Burdett, *Chem. Soc. Rev.*, 299 (1994).
17. See, for example, J. S. Miller, editor, *Extended Linear Chain Compounds*, Vol. I, Plenum, New York (1982).
18. H. Seo, C. Hotta, and H. Fukuyama, *Chem. Rev.*, **104**, 5005 (2004).
19. J.-L. Bredas, D. Beljonne, V. Coropceanu, and J. Cornil, *Chem. Rev.*, **104**, 4971 (2004).
20. S. Wengert and R. Nesper, *Inorg. Chem.*, **39**, 2861 (2000).
21. M. Lax, *Symmetry Principles in Solid State and Molecular Physics*, Wiley, New York (1973).
22. E. Canadell and M.-H. Whangbo, *Chem. Rev.*, **91**, 965 (1991); M.-H. Whangbo and E. Canadell, *J. Am. Chem. Soc.*, **114**, 9587 (1992); E. Canadell, M.-L. Doublet, and C. Iung, *Electronic Structures of Solids*, Oxford University Press (2012).
23. D.-K. Seo and R. Hoffmann, *J. Solid State Chem.*, **147**, 26 (1999).
24. K. S. Novoselov, A. K. Geim, S. V. Morozov, D. Jiang, Y. Zhang, S. V. Dubonos, I. V. Grigorieva, and A. A. Firsov, *Science* **306**, 666 (2004); K. S. Novoselov, Z. Jiang, Y. Zhang, S. V. Morozov, H. L. Stormer, U. Zeitler, J. C. Maan, G. S. Boebinger, P. Kim, and A. K. Geim, *Science* **315**, 1379 (2007).
25. P. R. Wallace, *Phys. Rev.* **71**, 622 (1947); G. W. Semenoff, *Phys. Rev. Lett.* **53**, 2449 (1984).
26. C. L. Kane and E. J. Mele, *Phys. Rev. Lett.* **95**, 146802 (2005); D. Hsieh, D. Qian, L. Wray, Y. Xia, Y. S. Hor, R. J. Cava and M. Z. Hasan, *Nature* **452**, 970 (2008); M. Z. Hasan and C. L. Kane, *Rev. Modern Phys.* **82**, 3045 (2010).
27. Some references for chemists may be found in A. Simon, *Angew. Chem. Int. Ed.*, **36**, 1788 (1997); R. J. Cava, *Chem. Commun.*, 5373 (2005).
28. J. Nagamatsu, N. Nakagawa, T. Muranaka, Y. Zenitani, and J. Akimitsu, *Nature*, **410**, 63 (2001).
29. H. J. Choi, D. Roundy, H. Sun, M. L. Cohen, and S. G. Louie, *Nature*, **418**, 758 (2002).
30. E. Zintl, *Angew. Chem. Int. Ed.*, **52**, 1 (1939); H. Schäfer, B. Eisenmann, and W. Müller, *Angew. Chem. Int. Ed.*, **85**, 742; *Angew. Chem. Int. Ed.*, **12**, 694 (1973).
31. Z. Xu and A. M. Guloy, *J. Am. Chem. Soc.*, **119**, 10541 (1997).
32. K. Yoshizawa, T. Yumura, and T. Yambe, *J. Chem. Phys.*, **110**, 11534 (1999).

# Hypervalent Molecules

---

## 14.1 ORBITALS OF OCTAHEDRALLY BASED MOLECULES

---

In many of the molecules studied so far, there were obvious ties between the orbital picture we presented and traditional ideas of electron pair bond formation. But not all molecules are susceptible to the elementary decomposition described in Chapter 7, which showed the correspondence between localized and delocalized bonding viewpoints. For example, the linear  $\text{H}_3^-$  molecule of Section 3.3 has a single pair of electrons located in a bonding orbital (**3.9**) and another pair in a nonbonding orbital (**3.10**). Clearly the two H—H “bonds” cannot be described as two-center-two-electron ones. In this case, the best description of the bonding situation is as a three-center orbital arrangement containing two bonding electrons. Such ideas are quite familiar to us in the realm of conjugated organic molecules. In benzene, for example, we consider a  $\pi$  network delocalized equally over all six carbon atoms of the molecule. With a total of six  $\pi$  electrons located as three bonding electron pairs and six C—C linkages, the C—C  $\pi$  bond order is  $\frac{1}{2}$ . One could use the same argument in  $\text{H}_3^-$ . The central hydrogen does not share four electrons with its neighbors. With reference to Figure 4.2, the two electrons in  $\psi_1$  are shared, whereas the two electrons in  $\psi_2$  are localized on the end hydrogen's. So one could write two resonance structures in  $\text{H}_3^-$ ; each structure contains one two-center-two-electron bond with a negative charge on the other end hydrogen atom. In  $D_{3h}$   $\text{H}_3^+$  there are certainly not three pairs of electrons, although one would normally draw its structure with three lines. In Figure 5.1, only  $\psi_1$  is filled with two electrons. Three resonance structures can be drawn, each containing one two-center-two-electron bond with a nonbonded  $\text{H}^+$ . Such considerations are so much a part of the chemist's background that we feel quite comfortable mixing localized (e.g., the benzene C—H and C—C  $\sigma$  linkages) and delocalized (e.g., benzene C—C  $\pi$  linkages) descriptions of bonding within the same molecule. In this chapter, we study some main group molecules (such as  $\text{SF}_4$  or  $\text{ClF}_3$ ) where, as in benzene, localized and delocalized

bonding descriptions may be concurrently used to describe different parts of the molecule. These molecules may also be viewed via a completely delocalized description. For some species such as  $\text{SF}_6$ , we have no choice but to use a delocalized description (as in  $\text{H}_3^-$ ) as opposed to six two-center-two-electron bonds unless higher energy  $d$  orbitals are included in the bonding picture. For “penta or hexavalent carbon” (e.g.,  $\text{C}_5\text{H}_5^+$  or  $\text{C}_6\text{H}_6^{2+}$  in Section 11.3 or  $\text{H}_3^+$ ) where such  $d$  orbital participation is unlikely on energy grounds, a delocalized picture is the only one we have.

First we generate the levels of an octahedral  $\text{AH}_6$  molecule since it illustrates several of the general features associated with these so-called hypervalent molecules—molecules with more than an octet of electrons around the central atom. Group theory plays an important role. Figure 14.1 shows the strikingly simple interaction diagram for  $\text{AH}_6$ , assembled from an A atom bearing valence  $s$  and  $p$  orbitals and six hydrogen  $1s$  orbitals. The ligand orbitals break down into three sets of  $a_{1g}$ ,  $e_g$ , and  $t_{1u}$  symmetry. The  $a_{1g}$  and  $t_{1u}$  combinations find symmetry matches with the  $s$  and  $p$  atomic orbitals (AOs) on the central atom to give bonding and antibonding combinations as shown in the figure. An important result is that the  $e_g$  pair finds no central atom orbitals with which to interact and remains completely ligand located and, therefore, rigorously A—H nonbonding. With a total of six valence electron pairs (e.g., for the hypothetical  $\text{SH}_6$  molecule), four occupy the A—H bonding orbitals and two are placed in this  $e_g$  nonbonding pair. So the molecule has six “bonds”—or we should really say, six “close contacts” but there are only four bonding electron pairs. In other words, there are eight electrons shared between A and the surrounding hydrogens. From this perspective, the Lewis octet rule remains intact. The form of these bonding orbitals is particularly interesting. The lowest energy level arises via the in-phase overlap of the central atom  $s$  and ligand  $s$  orbitals, but the triply degenerate  $t_{1u}$  set are three center-bonding orbitals just like the lowest energy orbital in  $\text{H}_3^-$  (3.9). The only difference arises from the fact that the central atom in  $\text{AH}_6$  has a  $p$  orbital, while the central hydrogen in  $\text{H}_3^-$  has only an

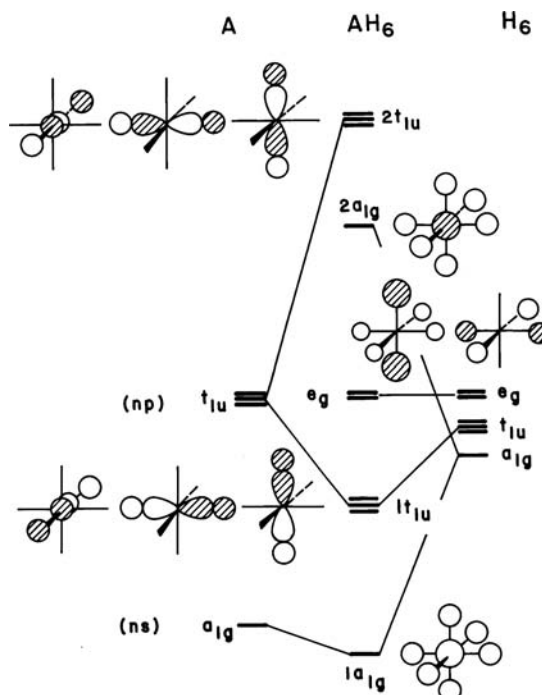
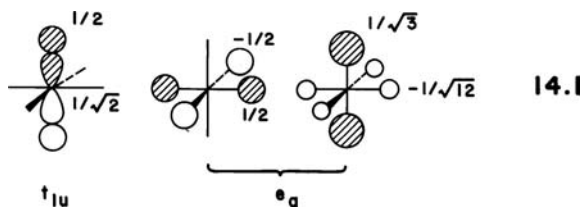


**FIGURE 14.1**

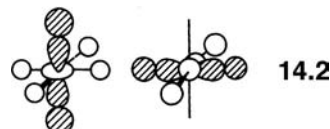
Assembly of the molecular orbital diagram of an octahedral  $\text{AH}_6$  molecule from the orbitals of A and of  $\text{H}_6$ .  $d$  orbitals are not included on A.

s orbital. The symmetry of the molecule leads to a single nonbonding, ligand-located orbital for  $\text{H}_3^-$  but in  $\text{AH}_6$  there is a doubly degenerate pair of ligand-based orbitals ( $e_g$ ). Just as in the case of  $\text{H}_3^-$ , electronic configurations with occupation of the nonbonding  $e_g$  pair lead to a buildup of electron density on the ligands. This is difficult to show in a general analytic way, but a simplification of this orbital picture will help. The Rundle–Pimentel scheme [1,2] neglects the involvement of the central atom s orbital, except as a storage location for one pair of electrons. This assumption is not so drastic of an approximation. We have discussed in numerous places (e.g., the table in 1.3 and discussion around it) that the valence s AO becomes increasingly more contracted than the  $p$  AOs due to screening effects and also to relativistic effects at the bottom row of the Periodic Table. Let us assume that the atomic sulfur  $3p$  and hydrogen  $1s$  orbitals have the same energy. Then the form of the wavefunctions for the  $t_{1u}$  and  $e_g$  orbitals are readily written down as in 14.1. Using these results



leads to a ligand density of seven electrons (where overlap between the ligand atomic orbitals has been neglected) and a central atom density of five electrons for the configuration  $(la_{1g})^2(t_{1u})^6(e_g)^4$ . With specific reference to  $\text{SH}_6$  this implies a transfer of one electron from the central atom to the ligands as a result of this electron-rich three-center bonding. The result suggests that the best stabilization will arise when the terminal atoms of such a structure are electronegative ones. This is in general true. For example,  $\text{SF}_6$  is known but  $\text{SH}_6$  is not. In a qualitative sense, we could have anticipated this result by inspection of the interaction diagram of Figure 14.1. If the ligands are electropositive, then the  $e_g$  set would lie at high energy and the compound would be expected to undergo oxidation very readily. Furthermore, electronegative ligands disfavor the disproportionation reaction,  $\text{AX}_n \rightarrow \text{AX}_{n-2} + 1/2\text{X}_2$ , because the X—X bond dissociation energies are small. Finally, many of these hypervalent molecules offer a sterically crowded environment around the central atom. Long A—X bonds (or small X atoms) are required. In this regard, fluorine is a favorite ligand for all three reasons and main group elements from the third and higher rows for the first and third reasons.

One way that has been used to produce a localized bonding picture for molecules of this type is to involve the higher energy valence shell  $d$  orbitals in bonding. In the  $O_h$  point group these transform as  $e_g + t_{2g}$  and the result of their inclusion is shown in 14.2. Now, of course, there are six bonding orbitals and the



rules of Chapter 7 would allow us to generate six localized two-center-two-electron orbitals. Group theory will not tell us whether the electron-rich Rundle–Pimentel model in Figure 14.1 is sufficient or  $d$  AOs on sulfur are needed. The only question concerning such a picture is one of magnitude. Just how important are these  $d$  orbitals energetically? This is no longer a controversial question; the involvement of, for example, the sulfur  $3d$  orbitals in the groundstate wavefunction for  $\text{SF}_6$  or other

hypervalent molecules is small and not important in a sense that chemists would recognize as a sign of chemical bonding (the variational principle always ensures that the addition of higher angular momentum functions, polarization functions, will lead to a lower energy solution for the wavefunction). This feature has been found to be true from many high-level calculations, including valence bond ones, on many molecules [3]. Unfortunately, general and higher level inorganic texts frequently still refer to the bonding in  $\text{SF}_6$  as using  $d^2sp^3$  hybridization at sulfur. This is simply wrong. In a sense using the term hypervalent [4] is also a misnomer since there are really only eight shared electrons for the molecule ( $\text{SH}_6$  or  $\text{SF}_6$  where F uses either a  $p$  AO or a hybrid to bond to the central atom), but we will continue to use it to refer to those situations where extra electrons reside in ligand-based, nonbonding orbitals.

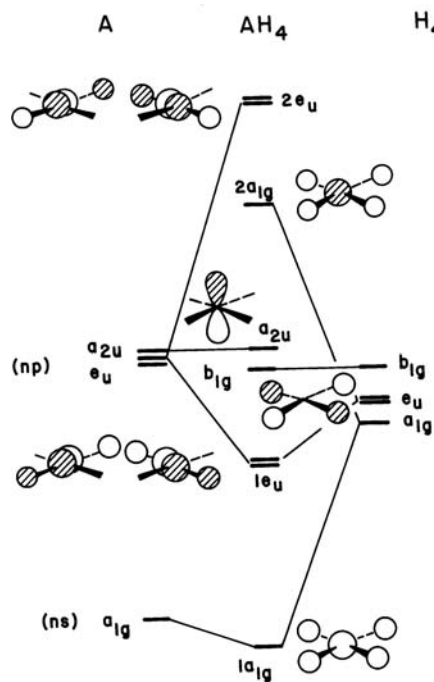
The hypothetical  $\text{SH}_6$  molecule (the arguments for  $\text{SF}_6$  will be similar) has one pair of electrons in the lowest energy  $a_{1g}$  orbital, three pairs of electrons in three-center bonding orbitals, and two pairs in nonbonding orbitals. With an extra pair of electrons, the  $2a_{1g}$  orbital is occupied, an orbital that is A—H antibonding. The highest occupied molecular orbital (HOMO) for  $\text{KrF}_6$  is shown in 14.3. Notice that there is little difference in the shape of this MO compared to that given by  $2a_{1g}$  in Figure 14.1. Now



there are only three bonding pairs for six bonds. The molecules  $\text{SbX}_6^{n-}$  ( $X = \text{Cl}, \text{Br}; n = 1, 3$ ) are known which differ in the occupancy of this  $a_{1g}$  orbital (it is empty for  $n = 1$ ). In nice verification of our description of the  $2a_{1g}$  orbital, the bond lengths are substantially shorter for  $n = 1$  compared to  $n = 3$ . (For  $X = \text{Cl}$ , bond lengths are 2.35, 2.65 Å; for  $X = \text{Br}$  they are 2.55 and 2.80 Å.) We will return to  $\text{AX}_6$  molecules with this electron count shortly.

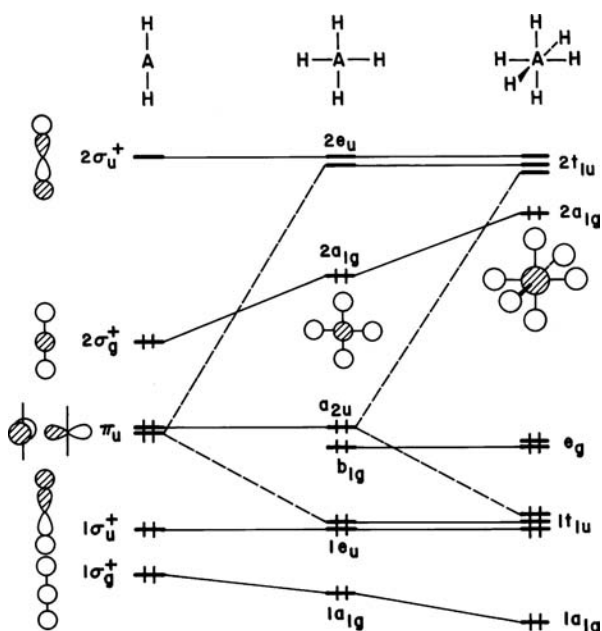
Figure 14.2 shows the analogous derivation of the level structure of the square planar  $\text{AH}_4$  molecule. Once again group theoretical considerations are very useful in its generation. The fully symmetric combination of ligand orbitals forms bonding and antibonding combinations with the central atom s AO. Analogous to  $t_{1u}$  in  $\text{AH}_6$ , the  $e_u$  set overlaps with two  $p$  AOs on the central atom. There are now two nonbonding orbitals; one is ligand located ( $b_{1g}$ ) and is the analog of the  $e_g$  pair in  $\text{AH}_6$  and the other is purely A located. This second orbital is a pure A  $p$  orbital which has a zero overlap with all of the ligand s orbitals. The level ordering for square-planar  $\text{AH}_4$  in Figure 14.2 is different from that discussed for square planar methane in Section 9.5. Here, the central main group atom will be surrounded by electronegative atoms. For the discussion in this chapter, the  $b_{1g}$  orbital is placed below  $a_{2u}$ , anticipating that a more realistic case would be an  $\text{AF}_4$  molecule. What electron counts will generate stable molecules? In Section 9.5 we discussed the situation for four and eight electrons. A compound with 10 electrons (e.g.,  $\text{SF}_4$ ) where  $a_{2u}$  is the HOMO should be stable. Indeed it is, but as we shall see later, the most favorable geometry is not  $D_{4h}$ . In analogy to our arguments concerning 14 electron  $\text{AX}_6$ , one might suspect that 12 electron  $\text{AX}_4$ , where  $2a_{1g}$  is occupied, might also be stable. This is true,  $\text{XeF}_4$  represents one such example.

Figure 14.3 shows the very interesting energetic correlation between the levels of linear  $\text{AH}_2$ , square planar  $\text{AH}_4$ , and octahedral  $\text{AH}_6$ . The orbitals that directly

**FIGURE 14.2**

Assembly of the molecular orbital diagram of a square  $\text{AH}_4$  molecule from the orbitals of A and  $\text{H}_4$ .

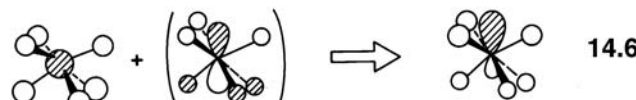
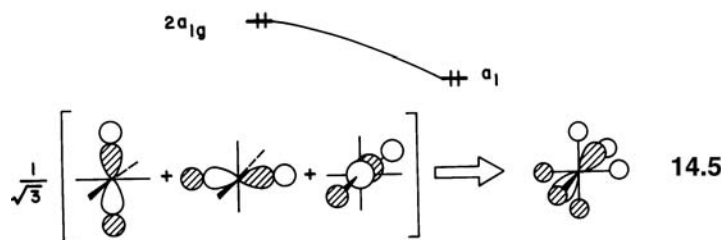
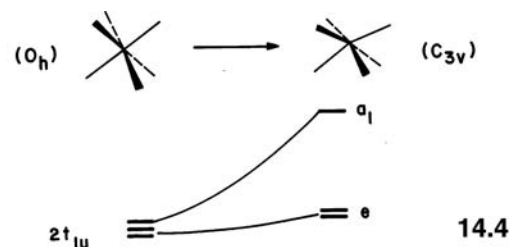
correlate between  $\text{AH}_2$  and  $\text{AH}_4$  are connected by a solid line. Two hydrogen atoms are added to  $\text{AH}_2$  and consequently there will be two additional valence orbitals in  $\text{AH}_4$ . One of these is derived from one component of the  $\pi_u$  set in  $\text{AH}_2$ . Bonding and antibonding combinations to  $\sigma_u^+$  from the  $\text{H}_2$  “fragment” are formed. This is indicated by dashed lines in Figure 14.3. The other orbital that is formed is  $b_{1g}$ . This is derived from the  $\sigma_g^+$  fragment orbital of  $\text{H}_2$ . It will mix with  $1\sigma_g^+$  and  $2\sigma_g^+$  in an antibonding and bonding manner, respectively. The reader should establish that the central atom s character cancels. Likewise, on going from  $\text{AH}_4$  to  $\text{AH}_6$  two extra molecular orbitals are created. One is derived from the  $a_{2u}$  orbital of  $\text{AH}_4$ , which

**FIGURE 14.3**

Correlation diagram for the molecular orbital levels of linear  $\text{AH}_2$ , square  $\text{AH}_4$ , and octahedral  $\text{AH}_6$ . The orbital occupancy is that expected for the  $\text{XeH}_n$  systems. Each time two hydrogen atoms are added to the system, two new orbitals are created. For example, on adding two H atoms to  $\text{AH}_2$ , a new ligand-located orbital ( $b_{1g}$  is produced). The dashed lines show how one component of  $\pi_u$ , along with one orbital combination from the added H give rise to two new orbitals.

combines with the  $\sigma_u^+$  orbital of  $H_2$  to give one component of the  $1t_{lu}$  and  $2t_{lu}$  orbitals. The other MO is derived from  $\sigma_g^+$  of  $H_2$ , and leads to one component of the  $e_g$  set. So once the orbital energies of  $AH_2$  have been decided upon, most of the resulting energies in  $AH_4$  and  $AH_6$  are set. We can also use this diagram to trace the similarities between  $XeF_2$ ,  $XeF_4$ , and  $XeF_6$ , the latter assumed to be octahedral. (We will return to its distorted structure below.) The usual assumption is made that the energetics of these molecules are dominated by the  $\sigma$  manifold. These species then have five, six, and seven  $\sigma$  pairs of electrons around the xenon atom, respectively. All three molecules are held together by three center bonds involving the central atom  $p$  orbital. The bonding contributed by the occupation of the deep lying orbital involving the central atom  $s$  orbital is canceled by occupation of its antibonding counterpart. The  $\sigma$ -bond order in all cases is thus equal to 2. All three species have two nonbonding orbitals. In  $XeF_6$  they are ligand located. In  $XeF_2$  they are central atom located. In  $XeF_4$  there is one orbital of each type. Clearly the nature of the electronic charge distribution is determined by the symmetry of the system in these cases.

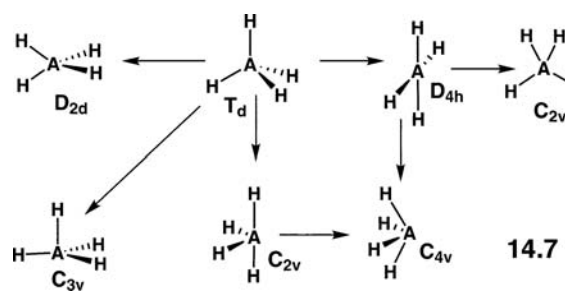
A prominent feature of Figure 14.3 is the decreasing HOMO–LUMO (lowest unoccupied molecular orbital) gap in  $AH_n$  as  $n$  increases. The HOMO becomes increasingly more destabilized by the surrounding ligands while the LUMO energy remains (to a first approximation) constant. In some  $AX_6$  molecules with this electronic configuration the octahedral geometry is unstable and the molecule distorts. Since the HOMO is of  $a_{lg}$  symmetry and the LUMO of  $t_{lu}$  symmetry, according to the second-order Jahn–Teller recipe of Chapter 7, the symmetry-lowering distortion  $O_h \rightarrow C_{3v}$  should lead to a larger HOMO-LUMO gap as shown in 14.4 [5]. If the driving force is large enough a static distortion will result. As with



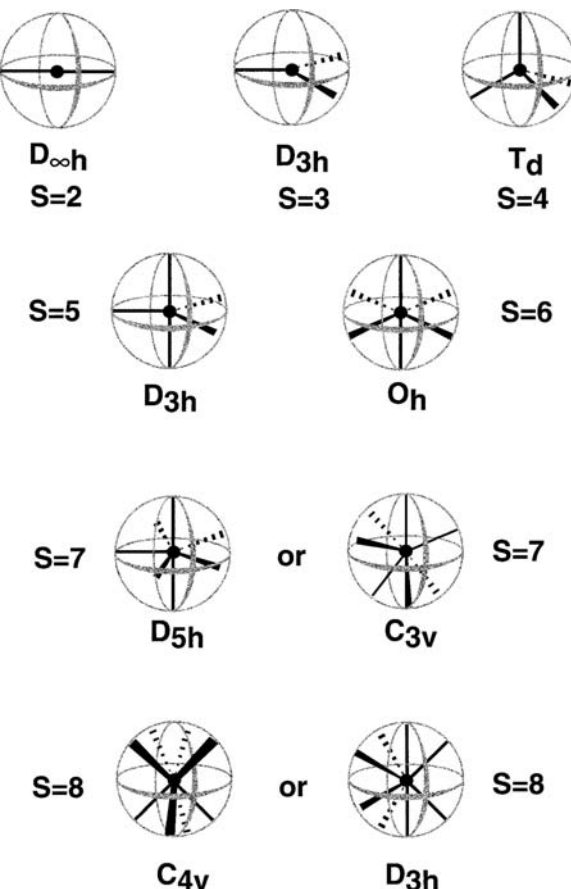
any degenerate set of orbitals we have a choice of how to write the wavefunctions. To see what happens in the distortion given by 14.4 we will write 14.5 as one component of a new  $2t_{lu}$  set by using a linear combination of the old functions. On distortion the  $2a_{lg}$  orbital and 14.5 mix together to give a hybrid orbital directed toward one face of the octahedron (14.6). As the distortion proceeds this orbital

becomes more and more like a lone pair. It is a complicated issue as to whether or not the driving force for this distortion is large enough to cause a distortion to a sterically more encumbered  $C_{3v}$  structure. Some species isoelectronic with  $XeF_6$  have a distorted structure while others have a regular octahedral geometry [6]. In molecules that fall into the second category their geometry is often discussed in terms of an inert pair of electrons. This chemically inert pair of electrons, often implied by the structures of complexes containing a heavy atom from the right-hand side of the Periodic Table, has long posed a problem for theorists. At present, the best explanation of the reluctance of the  $6s^2$  pair of electrons to enter into bonding is based on a relativistic effect [7], which manifests itself primarily as a contraction of s rather than p orbitals and is expected to be most important for heavy atoms. We will return to solid state compounds with octahedral units in them and an analogous electron count in the next section.

The problem that we need to address in this chapter is that hypervalent molecules frequently exhibit structures that are strongly distorted; consider the case of  $AH_4$  where some of the modes shown in 14.7 from the tetrahedral geometry were addressed in Section 9.5. Furthermore, molecules with five and more ligands

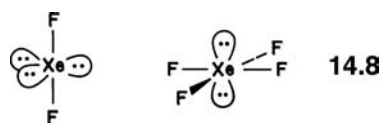


around the central atom result in even more indecision. It was easy to explore all of the geometrical space available to  $AH_2$  and  $AH_3$  molecules. Here we need a shortcut, a model which will offer clues as to which geometry(ies) to investigate. One such approach is given by the VSEPR (valence shell electron pair repulsion) scheme [8]. In this very useful approach for the prediction of the geometries of main group compounds the electron pairs (or in the more modern variant [9]—electron domains) in the valence shell of the central atom are considered to arrange themselves so as to minimize the electrostatic repulsions between them. In methane there are a total of four valence pairs (four electrons from the central carbon atom and one from each coordinated hydrogen atom). These arrange themselves in a tetrahedral geometry. Since each electron pair is a bond pair then the location of these pairs determines the position of the hydrogen atom ligands. The geometry of  $CH_4$  is tetrahedral as a result. In  $NH_3$  there are also a total of four valence electron pairs (five electrons from the central nitrogen atom and one from each coordinated hydrogen atom). Three out of the four are bond pairs and one is, by default, a lone pair.  $NH_3$  as a result has a pyramidal geometry with one lone pair envisaged as pointing out of the top of the pyramid. The resultant structure is one where the distances between points on a sphere are minimized. This is shown in Figure 14.4 for up to  $S = 8$ . Notice that for  $S = 7$  and 8 there is some ambiguity as to what structure will be favored [10]. This, of course becomes an even more serious problem for larger coordination numbers. We should also point out that the theoretical underpinnings of the VSEPR scheme have been, and remain, controversial. There are instances when it fails, a particularly spectacular example is given in the next chapter, and there have been attempts [9] to “patch things up.” We employ models frequently in (or perhaps, some might say, throughout) this book. For them to be useful they must be simple to apply and useful, but not necessarily accurate all of

**FIGURE 14.4**

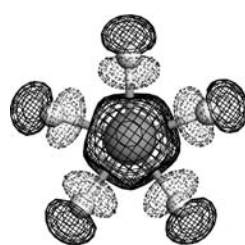
Lowest energy structures that maximize the distance between points on a sphere. The  $S$  numbers correspond to the total number of electron pairs within the VSEPR model.

the time. In fact when they do fail, they often lead us to interesting bonding situations. In  $XeF_6$  with a total of seven pairs we expect to observe an octahedral geometry with a lone pair occupying a seventh site. Therefore, either a  $C_{3v}$ , capped octahedron or a  $D_{5h}$  pentagonal bipyramidal should be formed. As mentioned earlier, the capped octahedron and octahedron are very close in energy, probably less than 2 kcal/mol in difference [6].  $BiF_7^{2-}$ ,  $IF_7$ , and  $XeF_7^+$  all exist as pentagonal pyramids and are highly fluxional [11].  $XeF_2$  and  $XeF_4$  present no problems for the VSEPR scheme. With five and six pairs of electrons, respectively, these molecules should have the structures shown in 14.8, based on a trigonal bipyramidal and octahedron, respectively. One of

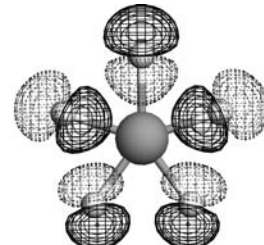


the tenets of the VSEPR model is that lone pair–lone pair repulsion > lone pair–bond pair repulsion > bond pair–bond pair repulsion. This is said [8,9] to be a consequence of the fact that a lone pair is closer to the nucleus and has a larger domain than a bond pair (the lone pair is attracted to one core while a bond pair is attracted to two). The structures in 14.8 put the lone pairs as far apart from each other as possible. What is remarkable is that both  $XeF_5^-$  and  $IF_5^{2-}$  exist [12]. With 14 electrons each they have a  $D_{5h}$  structure—all five fluorine atoms lie in the same

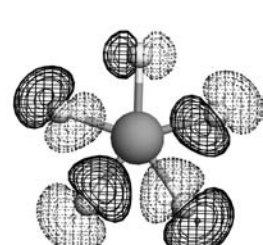
plane! The bonding in these molecules is a simple extrapolation of that in  $\text{AH}_6$  and  $\text{AH}_4$ : the central s AO forms bonding and antibonding combinations with the surrounding ligand orbitals. The latter is shown in 14.9 for  $\text{XeF}_5^-$ . The two in-plane  $p$  AOs on the central atom form bonding combinations with the surrounding ligands. The out-of-plane  $p$  AO is filled and remains nonbonding (neglecting  $\pi$



14.9



14.10



effects). This then leaves two nonbonding, ligand-based combinations, 14.10, which are also occupied for the seven filled MOs in this molecule. Notice in 14.10 that there are “tangential” fluorine lone pairs, which do mix slightly with the fluorine  $p$  AOs pointing directly at the xenon atom.

The levels of square pyramidal  $\text{AH}_5$  are easy to derive either from the square planar  $\text{AH}_4$  or octahedral  $\text{AH}_6$  units. Figure 14.5 shows a correlation diagram with the orbitals of both these species. Many of the orbitals have descriptions (and therefore energies) identical to those in  $\text{AH}_4$  and  $\text{AH}_6$  geometries if the axial/basal

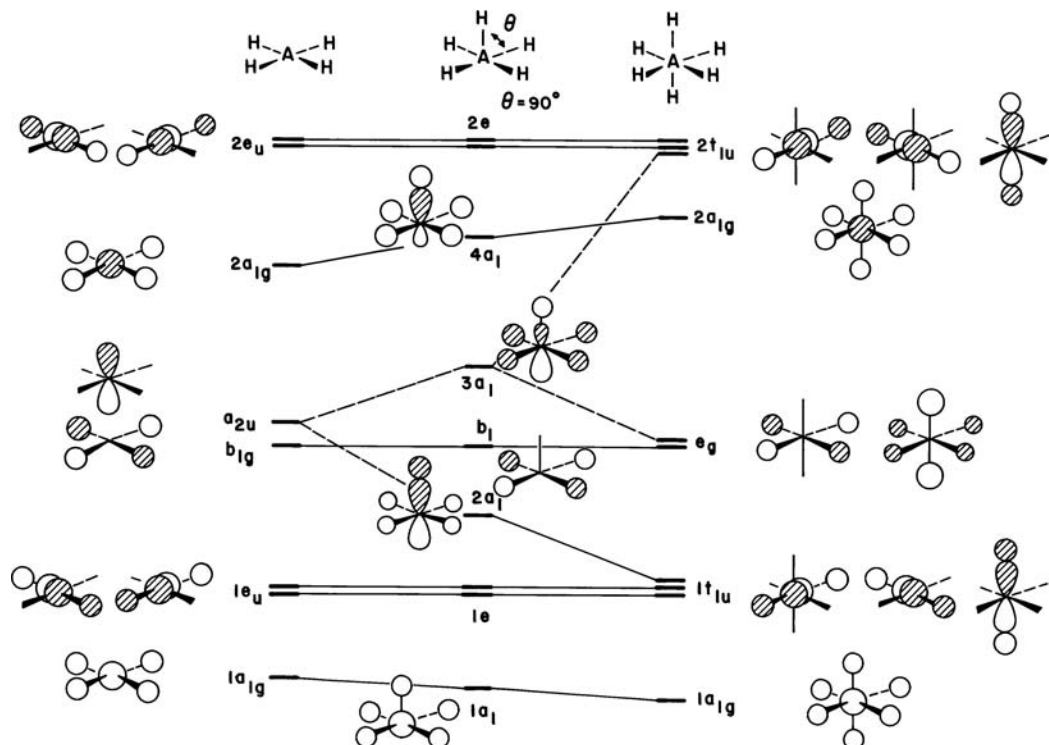
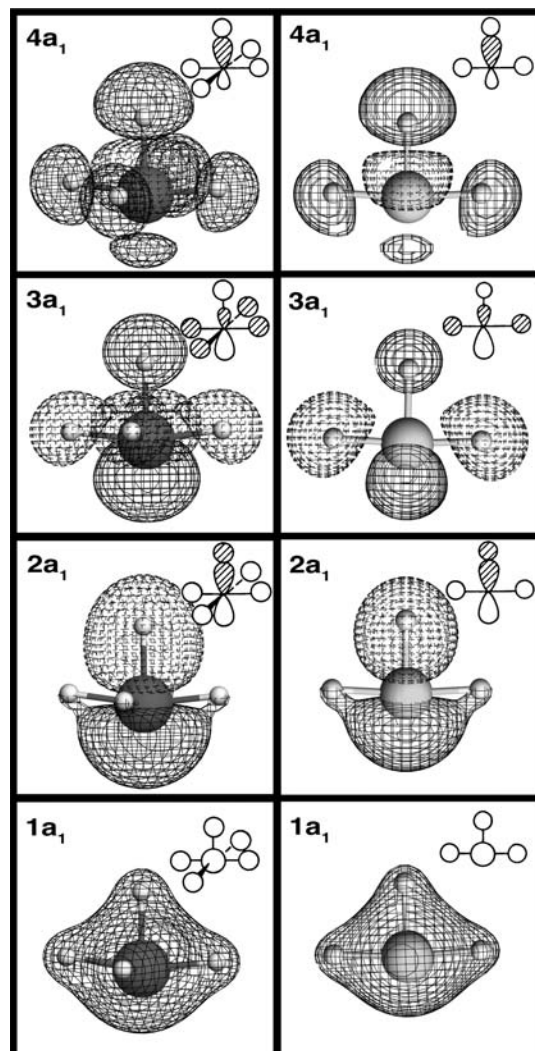


FIGURE 14.5

Correlation diagram for the molecular orbital levels of square  $\text{AH}_4$ , square pyramidal  $\text{AH}_5$  ( $\theta = 90^\circ$ ), and octahedral  $\text{AH}_6$ . As in Figure 14.3 we show the effect of the new orbitals by the use of dashed tie lines.

angle is set at  $90^\circ$ . The only orbitals that do have different energies are those with  $a_1$  symmetry. In this point group both the  $p_z$  and s orbitals transform as  $a_1$  (if we choose the z axis to lie parallel to the fourfold rotation axis of the square pyramid) and will therefore mix together to produce hybrid orbitals. The deepest lying  $a_1$  orbital,  $1a_1$ , is dominated by the central atom s rather than  $p$  character and so lies intermediate in energy between analogous orbitals in the square and octahedron. The next highest orbital,  $2a_1$ , although it contains some basal ligand character, is largely a bonding orbital between the central atom  $p_z$  and the axial ligand s orbital. Notice that it correlates to one component of the  $1t_{1u}$  set on going to  $\text{AH}_6$ . The  $3a_1$  orbital has a large contribution from central atom s and ligand orbitals (just like the  $2a_{1g}$  orbital of the  $\text{AH}_6$  unit) but also a significant contribution from the central atom  $p$  and axial ligand orbitals (just like the  $2t_{1u}$  orbital of the  $\text{AH}_6$  unit). It is an orbital intermediate in character between these two extremes. As a result of the  $sp$  mixing in this orbital a lone pair is created pointing toward the vacant sixth site of the square pyramid. The highest energy  $a_1$  orbital,  $4a_1$ , combines the roles of the  $2a_{1g}$  orbital of  $\text{AH}_4$ , antibonding between central s orbital and basal ligands, and the antibonding partner to the  $2a_1$  axial bonding orbital. This picture can only be an approximate one of course because of this intermixing between  $a_1$  orbitals. Plots of the  $1a_1$ – $4a_1$  MOs are given on the left side of Figure 14.6 for the hypothetical  $\text{BrH}_5$  molecule. For a real



**FIGURE 14.6**

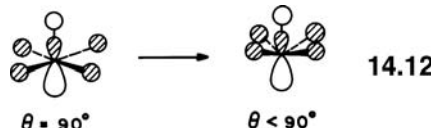
Plots of the  $1a_1$ – $4a_1$  MOs in  $\text{BrH}_5$  (left) and  $\text{ClH}_3$  (right).

example, such as  $\text{BrF}_5$ , there will be an additional complication in that the fluorine lone pairs will also mix into these orbitals, particularly  $2a_1$  and  $3a_1$ . Nevertheless, the essence of the orbital mixing in Figure 14.5 can still be clearly seen. The lowest and highest MOs are the maximal bonding and antibonding combinations from the surrounding hydrogen s AOs to the central atom. The  $2a_1$  orbital is primarily bonding between the central atom  $p$  AO and the apical hydrogen. Finally,  $3a_1$  is essentially nonbonding between the central atom and surrounding hydrogens. Recall from Figure 14.5 that this MO evolves into one member of the rigorously nonbonding  $e_g$  set. The level composition we have described thus leads to an approximate description for  $\text{BrF}_5$  of three center bonding (as in  $\text{XeF}_4$ ) for the four basal ligands plus a conventional two-center two-electron bond for the axial ligand. In accord with this picture the axial distance (two center bonding) is shorter than the basal ones (three center bonding) in  $\text{BrF}_5$  and  $\text{IF}_5$  (14.11) [13].  $\text{BrF}_5$  and  $\text{IF}_5$  do not have the square pyramid geometry with  $\theta = 90^\circ$



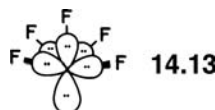
14.11

but exhibit a somewhat smaller value ( $85^\circ$  and  $82^\circ$ , respectively). The reason for this is easy to see by considering the energetics of the HOMO as a function of angle. Notice in 14.12 the phase of the central atom  $p_z$  orbital relative to the basal ligand



14.12

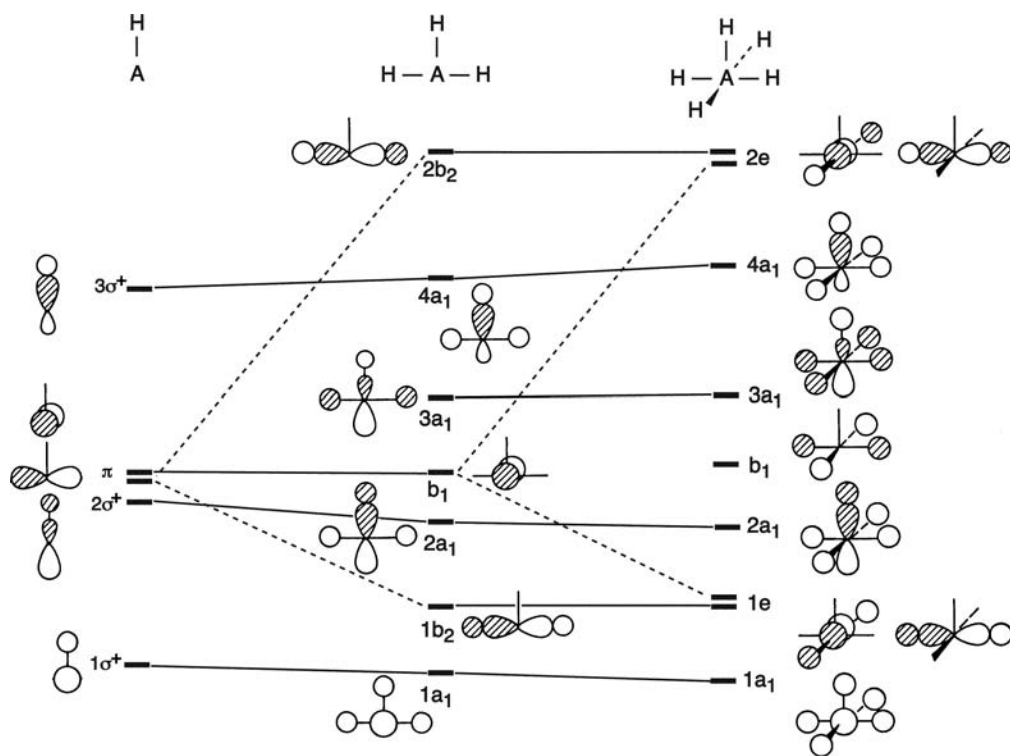
orbitals. At  $\theta = 90^\circ$  there is no overlap between these two orbital sets. A distortion to  $\theta > 90^\circ$  switches on an antibonding (destabilizing) interaction between these atomic orbitals, but a distortion to  $\theta < 90^\circ$  generates a stabilizing, bonding interaction. A distortion too far in this direction leads to repulsive, antibonding interactions between axial and basal ligand orbitals. The VSEPR explanation of this result is the following: In  $\text{BrF}_5$  there are six valence pairs, which point toward the vertices of an octahedron. Five vertices are occupied by ligands, the sixth position contains a lone pair, 14.13. One of the VSEPR rules [8,9], that lone pairs repel bonding pairs more



14.13

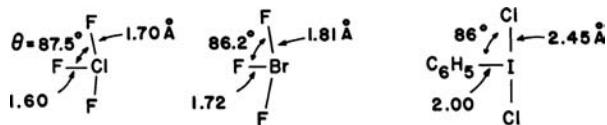
than bonding pairs repel each other, requires the basal ligand's bond orbitals to be pushed away from the lone pair leading to  $\theta < 90^\circ$ . We see here the orbital explanation of this rule.

The level structure of the T-shaped  $\text{AH}_3$  is readily derived from that for the square pyramid by the removal of a trans pair of ligands. Alternatively, it can be derived by the addition of two hydrogen s AOs to the well-known H–A molecule. Still yet another method would be to start from  $D_{3h}$   $\text{AH}_3$  and employ geometric

**FIGURE 14.7**

Correlation diagram for the molecular orbital levels of A—H, T-shaped  $\text{AH}_3$ , and square pyramidal  $\text{AH}_5$ . As in earlier figures we show the effect of the new orbitals by the use of dashed tie lines.

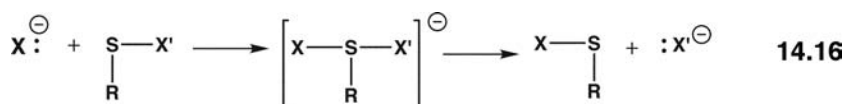
perturbation theory to develop the orbitals for the  $C_{2v}$  structure. This is done in Section 14.3. Here the former two approaches are shown in Figure 14.7. The orbitals of  $\text{AH}_5$  and  $\text{AH}_3$  are very similar. The nonbonding ligand-based  $b_1$  orbital of the square pyramid is replaced by a nonbonding, central-atom located orbital ( $b_1$ ). Notice that going from  $\text{AH}_5$  to  $\text{AH}_3$  two valence orbitals are removed (corresponding to  $\sigma_g$  and  $\sigma_u$  from the  $\text{H}_2$  unit which is lost). One of these is  $b_1$  in  $\text{AH}_5$ , which correlates with  $\sigma_g$ . The other is derived from one component from each of  $1e$  and  $2e$ . The nonbonding  $b_1$  orbital in  $\text{AH}_3$  is created (as shown by the dashed lines), and the  $\sigma_u$  orbital of  $\text{H}_2$  (not shown), on loss of the two hydrogen atoms. There are four orbitals of  $a_1$  symmetry in  $\text{AH}_3$ , just as in  $\text{AH}_5$ . While there is an obvious relationship between  $1\sigma^+$  in  $\text{AH}_2$ ,  $1a_1$  in  $\text{AH}_3$ , and  $1a_1$  in  $\text{AH}_5$ , there is also a strong resemblance between  $2\sigma^+$ ,  $2a_1$ , and  $2a_1$  (also between  $3\sigma^+$ ,  $4a_1$ , and  $4a_1$ ) in A—H,  $\text{AH}_3$ , and  $\text{AH}_5$ , respectively. The derivation of  $3a_1$  in  $\text{AH}_3$  from  $3a_1$  in  $\text{AH}_5$  is easy to see. An alternative way to look at this MO is that it is derived from the  $2e'$  set in  $D_{3h}$ —see Figure 4.6 (the  $2b_2$  orbital is the other member of the  $2e'$  set). An even more striking resemblance between the  $1a_1$ – $4a_1$  MOs in  $\text{AH}_3$  and  $\text{AH}_5$  is provided by the plots of these orbitals in  $\text{BrH}_5$  and  $\text{CH}_3$  in Figure 14.6. There is an almost one-to-one correspondence between the two sets. With a total of five pairs of electrons in  $\text{ClF}_3$  or  $\text{BrF}_3$  there are two ligands, trans to one another, attached to the central atom by three center bonding and one ligand attached by a conventional two-center-two-electron bond. We will return to the  $b_1$  and  $3a_1$  MOs shortly. Accordingly in these molecules the unique bond is the shorter one (14.14) [14]. Since the trans pair of atoms carries the highest charge in the



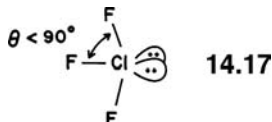
14.14

14.15

unsubstituted parent, (as we showed earlier for electron-rich three-center bonds) in derivatives such as **14.15** [15], the more electronegative ligands occupy these sites. Just as  $S_N2$  processes at tetrahedral carbon proceed through a transition state with a trigonal bipyramidal geometry, so the analogous substitution at sulfur in  $RSX$  compounds is calculated [16] to proceed through a T-shaped geometry. In **14.16** the  $RSXX'$  transition state has the electronegative halide ( $X$ ) atoms located in the arms of the T. The path for this reaction type has been probed by examining

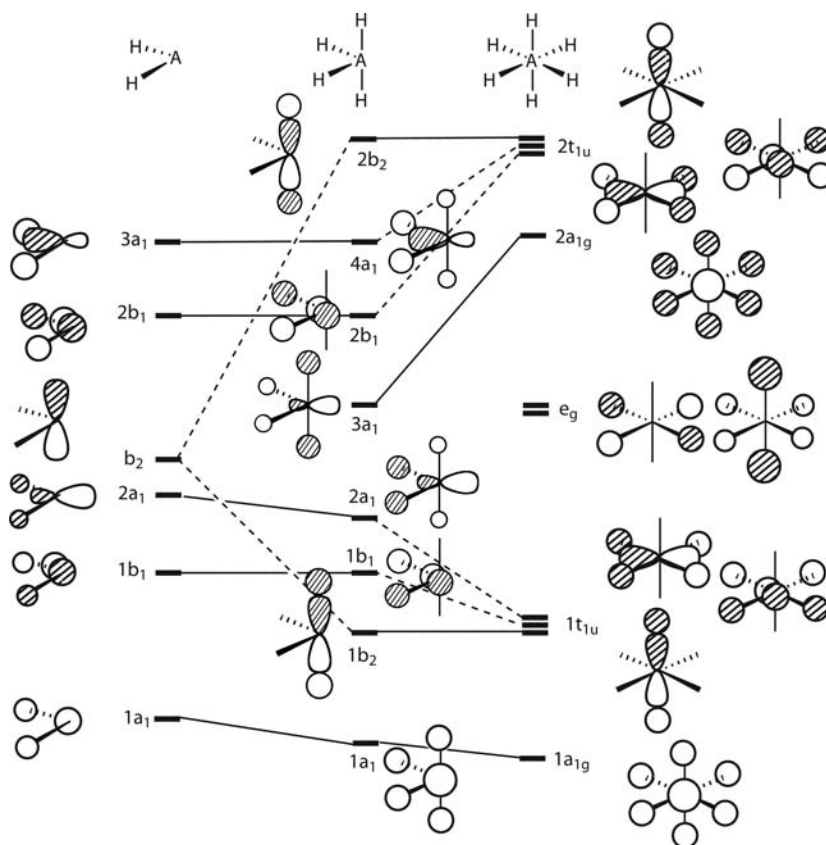


the X-ray structures of  $R_2S$  molecules where there exist close, nonbonded contacts to S from neighboring groups [17]. The geometries span a range of contacts where the neighboring group attacks along the side of a species with the lowest energy is the S—R bond, just like that given in **14.16**, leading up to a T-shaped transition state. The bending back of the trans ligands in **14.14** and **14.15** to give angles  $\theta < 90^\circ$  is explicable along exactly the same lines as the distortion of  $BrF_5$  in **14.12**. In VSEPR terms the argument is also similar to the one used for  $BrF_5$ .  $ClF_3$  contains five valence electron pairs that are arranged in the form of a trigonal bipyramidal (**14.17**). Placing two lone pairs in the trigonal plane and using the same argument concerning the



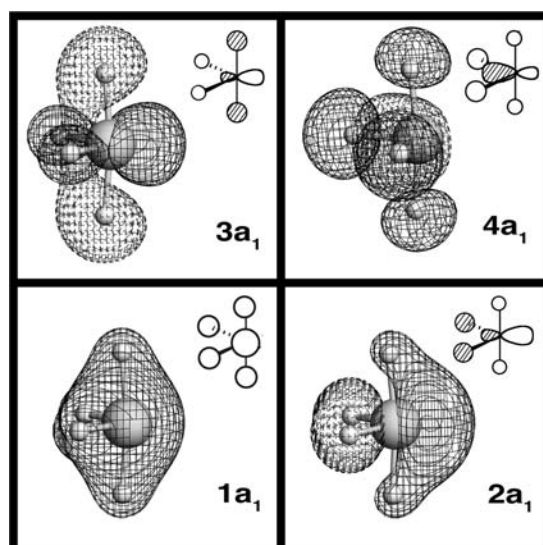
relative sizes of the repulsions between the bond pairs and lone pairs leads to the prediction of  $\theta < 90^\circ$ . But just where are those two lone pairs drawn in **14.17** from a localized (VSEPR) perspective in a delocalized picture? Linear combinations of them yield two orbitals of  $b_1$  and  $a_1$  symmetries. It is immediately apparent that they correspond to the  $b_1$  and  $3a_1$  molecular orbitals for  $AH_3$  in Figure 14.7. And just like the orbital argument in **14.12**, the nodal structure of the  $3a_1$  orbital favors  $\theta < 90^\circ$ .

Figure 14.8 shows an orbital derivation for the butterfly ( $C_{2v}$ ) structure of  $AH_4$  from that of  $AH_2$  and the trans addition of  $H_2$  or by the removal of a cis  $H_2$  unit from octahedral  $AH_6$ . The level pattern and description of the molecular orbitals are very similar to those of the square pyramidal  $AH_4$  and T-shaped  $AH_3$  geometries. It is easy to see that the  $b_2$  MO in  $AH_2$  forms bonding and antibonding combinations with  $\sigma_u^+$  from the  $H_2$  unit to give  $1b_2$  and  $2b_2$ , respectively. It is also easy to see the evolution of  $1b_1$  and  $2b_1$  into one member of the  $1t_{1u}$  and  $2t_{1u}$  sets, respectively. One component of  $e_u$  results from the middle of a three orbital pattern between  $1b_1$  and  $2b_1$  in  $AH_4$  and  $\sigma_u^+$  from the  $H_2$  unit. The  $a_1$  combinations again are problematic. The evolution of  $1a_1$  and  $3a_1$  in  $AH_2$  is reasonably straightforward; however, there actually is a good bit of intermixing between all four combinations. The  $2a_1$  and  $4a_1$  MOs in  $AH_4$  evolve into one member of  $1t_{1u}$  and  $2t_{1u}$ , but it is not so obvious how  $3a_1$  in  $AH_4$  comes about. Plots of these

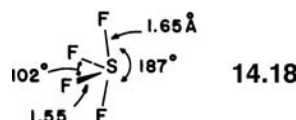
**FIGURE 14.8**

Correlation diagram for the molecular orbital levels of an  $\text{AH}_4$  unit with the butterfly ( $\text{SF}_4$ ) geometry, with those of  $\text{C}_{2v}$   $\text{AH}_2$  and octahedral  $\text{AH}_6$ . As in earlier figures the effect of the extra orbitals is indicated by the use of dashed tie lines.

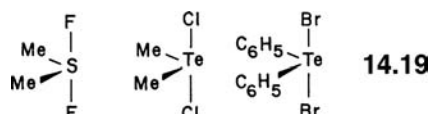
molecular orbitals are displayed in Figure 14.9. Notice the resemblance to the plots in Figure 14.6. The  $1a_1$  and  $4a_1$  are again the maximal bonding and antibonding MOs. The  $2a_1$  is primarily bonding now to the two equatorial hydrogens. The  $3a_1$ , which is very similar to the  $3a_1$  orbitals in  $\text{BrH}_5$  and  $\text{ClH}_3$ , is largely nonbonding. As in the cases of  $\text{ClF}_3$  and  $\text{BrF}_5$  the energetic behavior of the HOMO,  $3a_1$ , in  $\text{SF}_4$  allows understanding of the angular geometry [18] of the molecule, **14.18**. The distortion away from the ideal structure runs, as in all of

**FIGURE 14.9**

Plots of the  $a_1$  MOs in  $\text{SH}_4$ .



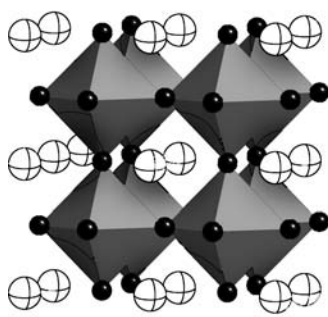
these molecules, counter to steric reasoning. Also the site preference problem is a similar one to  $\text{ClF}_3$  and  $\text{BrF}_5$ . In  $\text{SF}_4$  the electronic description of one pair of trans ligands attached by three center bonding, and two other ligands attached by the two-center–two-electron bonds, leads to the prediction of the three center sites for electronegative atoms in substituted sulfuranes as found in the examples of 14.19. The bond lengths of 14.18 are in accord with this picture too.



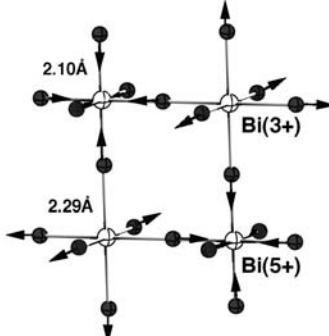
The orbital correlation diagrams of Figures 14.3, 14.5, 14.7, and 14.8 were used to highlight the orbital relationships between many  $\text{AH}_n$  species. As an exercise the reader should work through explicit orbital interaction diagrams for the compounds in terms of interacting an  $\text{AH}_n$  fragment with one or two hydrogen atoms. One could also consider what happens, in orbital terms, when a hydrogen atom is removed from  $\text{AH}_6$  to give a square pyramidal  $\text{AH}_5$  molecule. That is a method that will be extensively used for the derivation of the valence orbitals of  $\text{ML}_n$  fragments in later chapters.

## 14.2 SOLID-STATE HYPERVALENT COMPOUNDS

There are many solid-state compounds where the coordination number around a main group atom is 6 (or greater). These are generally oxides, where the main group atom from the right side of the Periodic Table is surrounded by six oxygen atoms. One such example is given by  $\text{BaBiO}_3$ . The structure is patterned after many  $\text{AMO}_3$  perovskites, where A is a very electropositive atom, typically from the first–third rows, and M is a wide variety of transition metal or main group atoms. The M atoms form  $\text{MO}_6$  octahedra and the oxygen atoms are two-coordinate. The octahedron are linked together in three directions by corner sharing. A representation of the high temperature (820 K) structure [19] for  $\text{BaBiO}_3$  is given in 14.20. The large open circles are barium atoms and the small black ones are oxygen. There are three lower



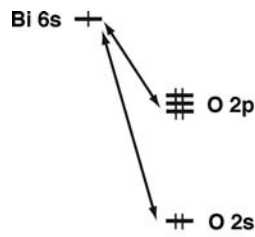
14.20



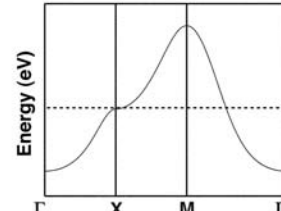
14.21

temperature phases that differ in that the “ $\text{BiO}_6$ ” octahedra twist and turn about their axes [19]. In terms of electron counting, using the procedure in Section 13.5,

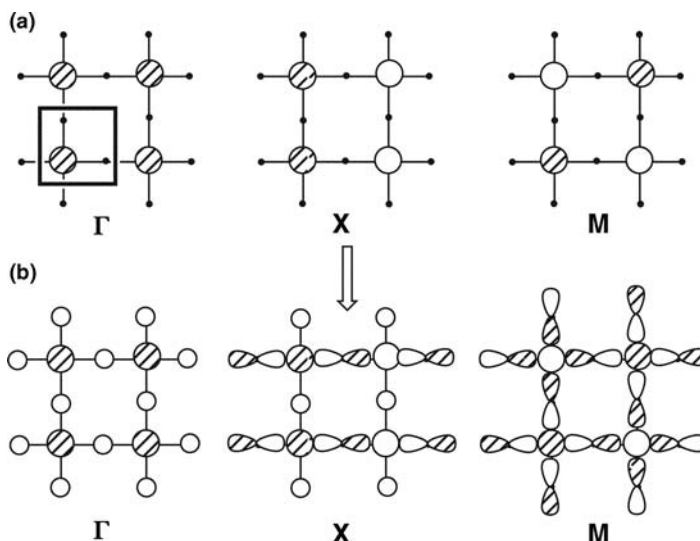
we will have  $\text{Ba}^{2+}$  and  $3\text{O}^{2-}$  (recall that oxygen is much more electronegative than bismuth) so this leaves Bi in the 4+ oxidation state. What this would mean is that the highest filled orbital around each Bi atom would be a Bi s AO with surrounding oxygen AOs mixing with it in an antibonding fashion. In other words, the local electronic environment would be akin to  $\text{XeF}_6$  with one less electron. But the real situation, even in the high temperature phase, is more complicated. The oxygen atoms move in the direction shown in 14.21 so that half of the bismuth atoms have shorter Bi—O distances ( $2.10\text{ \AA}$ ), while the others have longer ones ( $2.29\text{ \AA}$ ). In a formal sense then one could say that the  $\text{Bi}^{4+}$  oxidation state was unstable with respect to disproportionation to  $\text{Bi}^{3+}$ , which have the long Bi—O bonds and  $\text{Bi}^{5+}$  with the short bonds. This has all of the hallmarks of a Peierls distortion. For this to occur there must be a reasonable Bi 6s bandwidth. In Chapter 13, there were numerous examples where the width of the band is determined by intracell overlap. Consider a 2-D analog of undistorted  $\text{BaBiO}_3$  where each unit cell has only a Bi 6s AO. The crystal orbital for the  $\Gamma$ , X, and M points is given in Figure 14.10a. The black square outlines one  $\text{BiO}_2$  unit cell which is translated in a horizontal and vertical direction by the same amount. Since the Bi—Bi distances are very long, one might expect that the band would have no dispersion. The symmetry of the crystal orbital at  $\Gamma$  allows oxygen s to mix in as shown in Figure 14.10b. Remember that the Bi s AO lies above the oxygen AOs so this interaction will be an antibonding one. For the M point oxygen p mixes with Bi s and at X both oxygen s and p mix as shown in Figure 14.9b. So the Bi s AO is destabilized by the oxygen AOs throughout the Brillouin zone, but that destabilization is not uniform. It is difficult to predict, *a priori*, the magnitude of the Bi s—O s versus Bi s—O p overlap. But what is certainly true is that the energy gap between Bi s and O s, 14.22, is much greater than that between Bi s



14.22

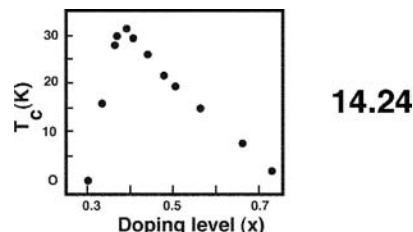


14.23

**FIGURE 14.10**

(a) Solutions for translating the Bi 6s AO at the  $\Gamma$ , X, and M points for a square  $\text{BiO}_2$  net. One unit cell is given by the square box at the  $\Gamma$  point. (b) The addition of O s and p AOs at each of the special  $k$  points.

and O  $p$ . Consequently, the Bi  $s$  crystal orbital is destabilized less by O  $s$  than O  $p$ . It is the energy denominator in the orbital interaction energy that sets up the dispersion in the Bi  $s$  band. The net result for the  $e(k)$  versus  $k$  plot, **14.23**, is a familiar one. It is identical to the square hydrogen net problem worked out in Section 13.4 and consequently, the DOS plot will also be the same. The Fermi level is given by the dotted line in **14.23** for Bi $^{4+}$ ; the band is half-full if the spins are paired. This sets the stage for the Peierls distortion shown in **14.21**. For a one-dimensional Bi—O chain, it is easy to see how this distortion will open up a gap. The lower Bi  $s$  band will be concentrated on the Bi atoms with long bonds, that is, the Bi $^{3+}$  sites and the upper band concentrated on the Bi atoms with short bonds – Bi $^{5+}$ . We leave this to the reader to work out the relevant details. For a 2-D model like that in Figure 14.10 one will need to quadruple the unit cell. So there will be four Bi  $s$  bands. But the overall result for it as well as that for the 3-D case will be the same. Removing or adding electrons from the  $s$  band should diminish the driving force for this distortion. One way to do this is to “dope” K $^+$  ions for Ba $^{2+}$ . A series of compounds with a stoichiometry  $\text{Ba}_{1-x}\text{K}_x\text{BiO}_3$  have been prepared [20]. As mentioned previously for the high temperature structure [19] with  $x=0$ , one Bi site has Bi—O distances of 2.10 Å and the other 2.29 Å. When  $x=0.04$  one Bi site has four short Bi—O bonds at 2.11 Å and two long at 2.22 Å while the other Bi site has four long Bi—O bonds of 2.23 Å and two short at 2.11 Å. In other words, the two kinds of Bi atoms are becoming more alike. At  $x=0.37$  bond length alternation has ceased and Bi—O = 2.14 Å [20]. Furthermore, this material is a superconductor. The temperature for the onset of superconductivity,  $T_c$ , is very sensitive to the level of doping, an example is given in **14.24** for the  $\text{Ba}_{1-x}\text{K}_x\text{BiO}_3$  system [21]. The highest  $T_c$  is  $\sim 33$  K with

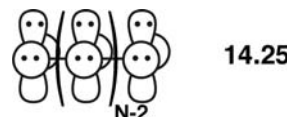


$x \approx 0.4$ . This is a remarkably high temperature. Other ways to dope  $\text{BaBiO}_3$  have been found to create superconductors as well. One example is the substitution of Pb for Bi, another is the removal of some of the oxygen atoms. In both cases electrons are removed from the parent material. We see in Chapter 16 a very analogous situation for the copper oxide superconductors where the addition or removal of electrons from a half-filled copper  $d$  band creates a superconducting state. As mentioned in the previous chapter, BCS theory is perhaps the most popular one for the mechanism behind superconductivity. At the heart of this is the coupling between electron motion and phonons (nuclear motion). The frequency associated with the critical phonon scales with  $T_c$ , and consequently, inversely to the masses of the vibrating nuclei. Replacing  $^{16}\text{O}$  with  $^{18}\text{O}$  then should decrease  $T_c$  in the BCS model for these compounds. This is experimentally found to be true and the isotope effect was found to be very large [22]. The motion of the oxygen atoms in **14.21** creates large charge fluctuations at Bi; it is tempting to think that this might be important for superconductivity in these materials.

We have seen that hypervalent compounds frequently have unusual geometries and this is also true in the solid-state area. The usual Zintl–Klemm counting rules that were presented in Section 13.5 have been extended to electron-rich phases [23]. The basic premise is that these compounds have an occupied valence  $s$  AO, which lies at a low energy with respect to the  $p$  AOs. Consequently, the

bonding will be derived from the main group  $p$  AOs. The most likely candidates are then derived from elements in columns 13–17 and rows 4–6 of the Periodic Table. Notice that this is quite different from the oxides we have just discussed where the main group valence orbitals lie high in energy with respect to surrounding ligand orbitals. The idea here is that with normal electron counts, the Zintl–Klemm leads to the formation of two center–two electron A–A bonds or long A–A distances where no electrons are shared. If electrons are added, then it may be possible to form more condensed structures. A trivial example would be a chain of  $\text{Br}_2$  or  $\text{I}_2$  molecules. When electrons are added,  $\text{Br}_3^-$  or  $\text{I}_3^-$ , as well as, higher oligomers are formed.

Within the Rundle–Pimentel model the bonding in  $\text{Br}_3^-$ ,  $\text{I}_3^-$ ,  $\text{XeF}_2$ , or any 22 electron  $\text{A}_3$  molecule can be expressed in terms of the A–A bonding as shown on the left side of Figure 14.11. A fully bonding and fully antibonding MO are produced along with a rigorously nonbonding one (remember that we are making the approximation that the s AOs do not overlap greatly with the  $p$  AOs and, therefore, can be neglected). The addition of A units creates a bonding pattern exactly like that between  $p$  AOs that overlap in a  $\pi$ -type fashion (see Figure 12.2 and the discussion around it). The middle diagram shows what happens for an  $\text{A}_5$  molecule. For any  $\text{A}_n$  molecule ( $n \geq 3$ ) the lowest MO is antisymmetric (A) with respect to the central mirror plane and the symmetry alternates on going to the next higher MO. The number of nodes between the A–A bonds also increases by one on going to higher energy. When  $n$  is an odd number there will also be a totally nonbonding orbital, just as in the linear polyenes (Figure 12.2) using the Hückel approximation, with a relative energy of  $0\beta$ . These features are presented for  $\text{A}_5$  in the middle of Figure 14.11. On the right side is the situation for  $\text{A}_N$  where  $N$  is a very large number. The total number of electrons, which will be stable for this  $\text{A}_N$  chain in the A–A  $\sigma$  region is  $2\left[\frac{(N-1)}{2} + 1\right] = N + 1$ . Now recall that there are two sets of lone pairs in  $p$  AOs, 14.25, plus one “lone pair” in an s AO around each A atom. Therefore,



the total number of electrons is  $N + 1 + 4N + 2N = 7N + 1$ . So there are  $7 + 1/N = 7$  electrons per A atom in the infinite chain. A band structure and density of states

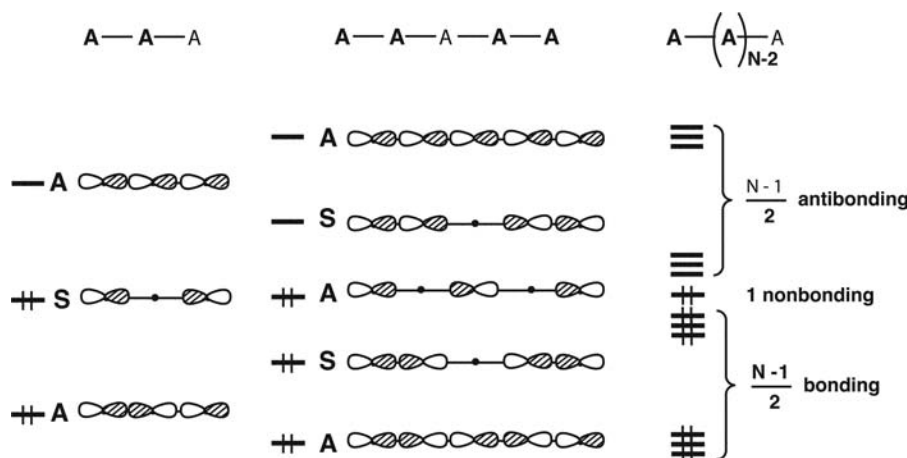
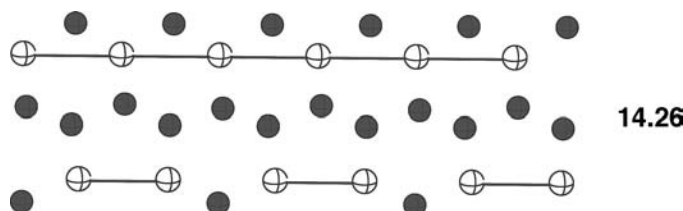


**FIGURE 14.11**

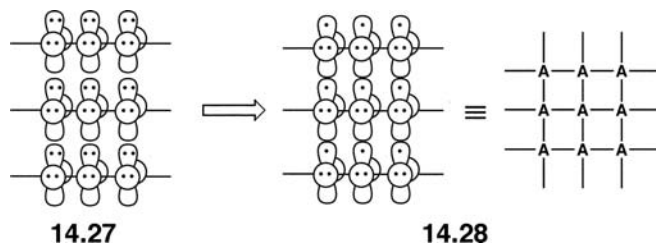
Building up the molecular orbitals of a chain consisting of  $p$  AOs interacting in a  $\sigma$  fashion for three (a), five (b), and infinite (c) chains. S and A refer to the MOs being symmetric or antisymmetric, respectively, to the central mirror plane of the molecule.

plot is basically the same as that given in Figure 13.13, for a linear sulfur chain except for two important details. First, especially for fifth and sixth row atoms, the s band will lie lower in energy than that shown. More importantly, as was extensively discussed in Section 6.3,  $s-p$  mixing is less important in the third row than it is in the second and this is a trend that continues as one goes down the rows in the Periodic Table. For the compounds that we are interested in, Figure 13.13 needs to be modified in that there is little, if any,  $s-p$  mixing. As a consequence the top of the “s” band is still s and, importantly, the bottom of the p band is p—p bonding between the A atoms. With seven electrons per A atom the p band is half-full. Surely, this signals a Peierls instability; yes and no. A dimerization opens a band gap and creates “classic” A—A single bonds and A—A no-bonds just like the dimerization of a hydrogen chain. On the other hand, because of the small  $s-p$  mixing, the bottom portion of the p band is A—A bonding and this will resist the tendency to dimerize. The net result is a delicate balance [23]. Clearly, in  $\text{Br}_2$  or  $\text{I}_2$  the result is dimerization. The case of  $\text{Li}_2\text{Sb}$  [24] is not so clear. The structure of this compound, shown in 14.26, consists of  $\text{Sb}_2^{4-}$  dimers (the Sb and Li atoms are given by the white and black circles, respectively) where the Sb—Sb distances in the dimer is 2.97 Å and clearly a nonbonded 3.56 Å between them. However, there are also  $\text{Sb}^{2-}$

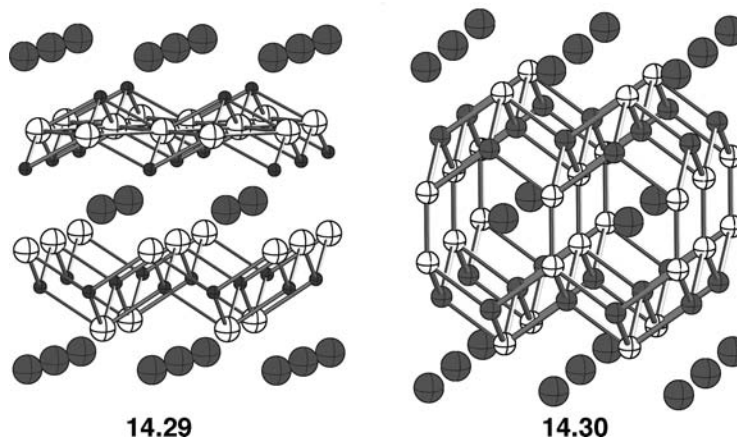


chains where the Sb—Sb distances are 3.26 Å. This is about half-way between the two center–two electron dimers and the nonbonded distances. But as we saw in Section 13.5, the six electron  $\text{A}_n$  chains are either kinked in a “zig-zag” fashion or further twisted to form helices. So should the  $\text{Sb}^{2-}$  chains be linear here? The answer is yes. We showed in the previous section that  $\text{XeF}_2$  or any other 22 electron molecule will be linear (within the VSEPR model there are five electron pairs and consequently is a trigonal bipyramidal, 14.8). The same is true for the higher oligomers. Thus, the linear —Sb—Sb— portion of  $\text{Li}_2\text{Sb}$  is consistent with our “hypervalent” description while the other chain is dimerized into a “classical” arrangement. The two must be very close in energy.

The optimal electron count for a square net can be determined in a straightforward manner [23], as follows. We have shown that the hypervalent linear chain is one which has seven electrons per A atom. Bringing an infinite number of parallel chains together generates 14.27. Recall that there is one electron in a p AO that runs along each chain. Therefore, removing one electron from the in-plane lone pair on

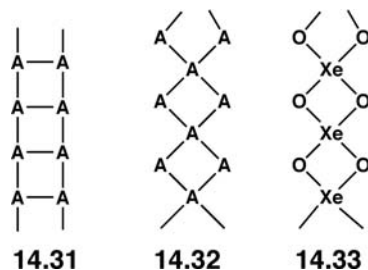


each A atom will generate a hypervalent bonding pattern in **14.28**. So a total of six electrons per A atom creates a hypervalent square net. Let us examine a couple of cases.  $\text{CaBe}_2\text{Ge}_2$  [25], **14.29**, can be viewed as having tetrahedral and square pyramidal  $\text{Be}^{2+}$  cations (small, dark circles), isolated  $\text{Ca}^{2+}$  cations (large dark circles), and two types of Ge atoms (large white circles). The square pyramidal Ge atoms we

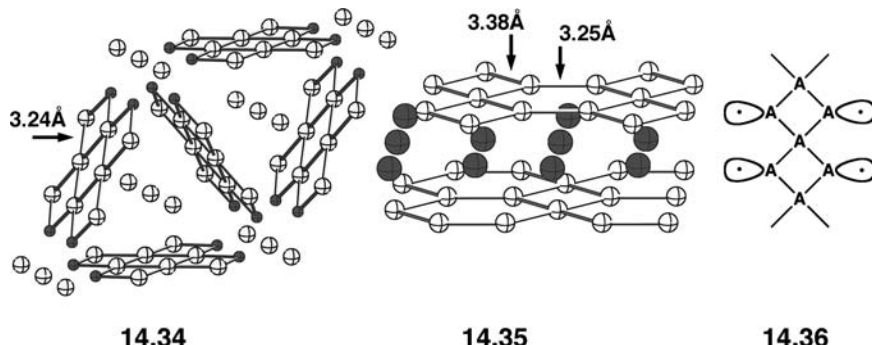


could count as being electron precise  $\text{Ge}^{4-}$  and this then means that the Ge atoms making up the square sheets are  $\text{Ge}^{2-}$ , which is precisely the electron count anticipated by **14.28**. The Ge—Ge distances here are  $2.84 \text{ \AA}$ . **14.30** shows the structure for  $\text{SrCd}_2\text{Ge}_2$ . This structure is called the  $\text{ThCr}_2\text{Si}_2$  type and it is very common. If the cadmium atoms (small dark circles) are considered to be  $\text{Cd}^{2+}$ ,  $\text{Sr}^{2+}$  (large dark circles) and the square pyramidal  $\text{Ge}^{4-}$  as before, Then the other germanium site must again be  $\text{Ge}^{2-}$  which in this case dimerizes with Ge—Ge distances of  $2.54 \text{ \AA}$ . Is this a Ge—Ge double bond? The structure [26] of  $\text{BaGe}_2$  (with  $\text{Ge}^-$ ) consists of isolated  $\text{Ge}_4^{4-}$  tetrahedra where there must be a Ge—Ge single bond—the bond lengths here are  $2.54 \text{ \AA}$ . We bring up structure **14.30** for several reasons. Whereas  $\pi$  bonding is common and quite strong for the second row elements, we have seen in many places (see in particular Section 10.3C) that  $\pi$  bonding for the third row is very weak and so it must be negligible for the third and higher rows. The bond distance between atoms may be more of a function of electrostatic and crystal packing effects than of bond order. Although the electron counting in **14.29** and **14.30** are identical their structures are totally different. Yet the energy difference between the structures must be small [27].  $\text{BaZn}_2\text{Sn}_2$  and  $\text{BaMg}_2\text{Pb}_2$  both have structures [25] analogous to **14.29** with group 14 square nets and, as mentioned, there are many structures analogous to **14.30**, for example,  $\text{BaMg}_2\text{Si}_2$  or  $\text{BaMg}_2\text{Ge}_2$ . The situation for  $\text{BaMg}_2\text{Sn}_2$  [28] is a combination of the two; it is called an intergrowth structure. If one removes either the top or bottom alkaline atom sheet in **14.29** and replaces it with **14.30**, this produces the  $\text{BaMg}_2\text{Sn}_2$  structure. The Sn—Sn distances in the square sheets of  $\text{BaZn}_2\text{Sn}_2$  are  $3.32 \text{ \AA}$  and in  $\text{BaMg}_2\text{Sn}_2$  they are even longer at  $3.46 \text{ \AA}$ . This can be compared to  $\text{KSn}$  where there are  $\text{Sn}_4^{4-}$  tetrahedra with Sn—Sn single bond distances of  $2.96$  and  $2.98 \text{ \AA}$  [29].

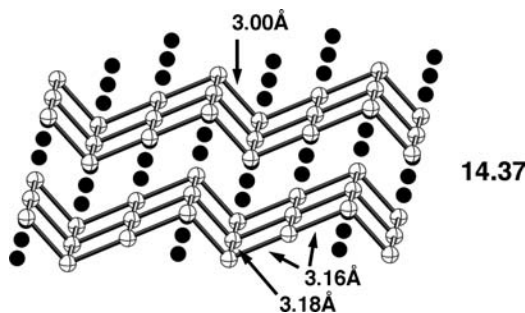
With six electrons in a square net there also exist several ways to generate Peierls distortions [23]. Several were diagramed in **13.67–13.69**. Each case generates “classical” structures where all of the atoms are two-coordinate and, therefore, follow the Zintl–Klemm formalism. Ladder structures, **14.31**, can also form where the A atoms still are at a six electron count [23]. A diamond chain of vertex sharing



squares, **14.32**, gives a further alternative. There is a simple way to figure out the appropriate electron count for this case. In the previous section, we showed that  $\text{XeF}_4$  molecule was stable at the square planar geometry. The analogous electron count for a 1-D polymer is then for a  $\text{XeO}_2$  unit cell to yield **14.33**. The  $\text{A}_3$  unit cell should, therefore, have  $8 + 12 = 20$  electrons.  $\text{LaGaBi}_2$  [30], **14.34**, presents an interesting, complicated compound that contains the structural element in **14.32**.

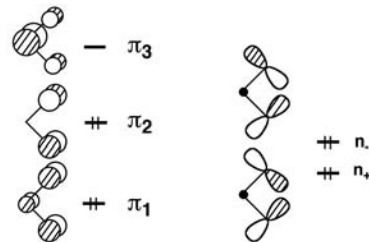
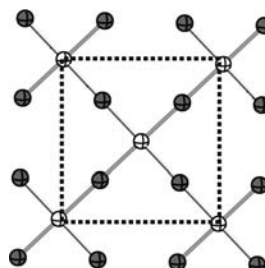


For convenience the positions of the La atoms are not shown. The small dark circles are Ga atoms and the larger open circles are Bi atoms. There are isolated  $\text{Bi}^{3-}$  atoms. The  $\text{Ga}_2\text{Bi}_3$  planar nets can be further dissected [30] into  $\text{Ga}_6$  hexagons connected to  $\text{Bi}_3^{5-}$  chains with 20 valence electrons analogous to **14.32**. The Bi—Bi distance of  $3.24 \text{ \AA}$  is somewhat longer than in elemental Bi with a structure analogous to **13.57** where the Bi—Bi (single bond) distance is  $3.09 \text{ \AA}$ . The electron counting in the  $\text{Ga}_6$  hexagons can also be deciphered [30] so the total electronic structure of  $\text{LaGaBi}_2$  with all of its complexity can be understood without recourse to a computation. But now consider  $\text{Ba}_2\text{Bi}_3$  [31] which, on the surface of things should be much more simple. Now the structure of the isoelectronic  $\text{Sr}_2\text{Bi}_3$  is quite different and there are a series of  $\text{Sr}_{2-x}\text{Ba}_x\text{Bi}_3$  compounds where the structure continuously evolves [32]. Let us take  $\text{Ba}_2\text{Bi}_3$  or the isostructural  $\text{Ba}_2\text{Bi}_2\text{Sb}$ , shown in **14.35**. There are again  $\text{Bi}_3^{5-}$  square planar diamond chains which are now linked in a perpendicular fashion to form 2-D nets. The Bi—Bi distances of  $3.38 \text{ \AA}$  are a little long compared to that in **14.34**. The optimal electron count is easy to extrapolate from **14.33**. As shown in **14.36** each divalent A atom has an in-plane and out-of-plane lone pair. To connect these A atoms to become trivalent, one needs to remove two electrons per  $\text{A}_3$  unit or, in other words, each  $\text{A}_3$  unit cell must have  $20 - 2 = 18$  electrons. But counting  $2\text{Ba}^{2+}$  gives  $\text{Bi}_3^{4-} = 19$  electrons! There is one electron per unit cell too many. Electronic structure calculations show [31] that the “extra” electron partially stays in Ba valence orbitals and Bi—Bi antibonding states. Another structure, which contains hypervalent Sn, is given by the “simple” binary compound,  $\text{LiSn}$ , **14.37** [33]. Recall that  $\text{KSn}$  exists as electron precise tetrahedra with Sn—Sn distances of  $2.98$  and  $2.96 \text{ \AA}$ .



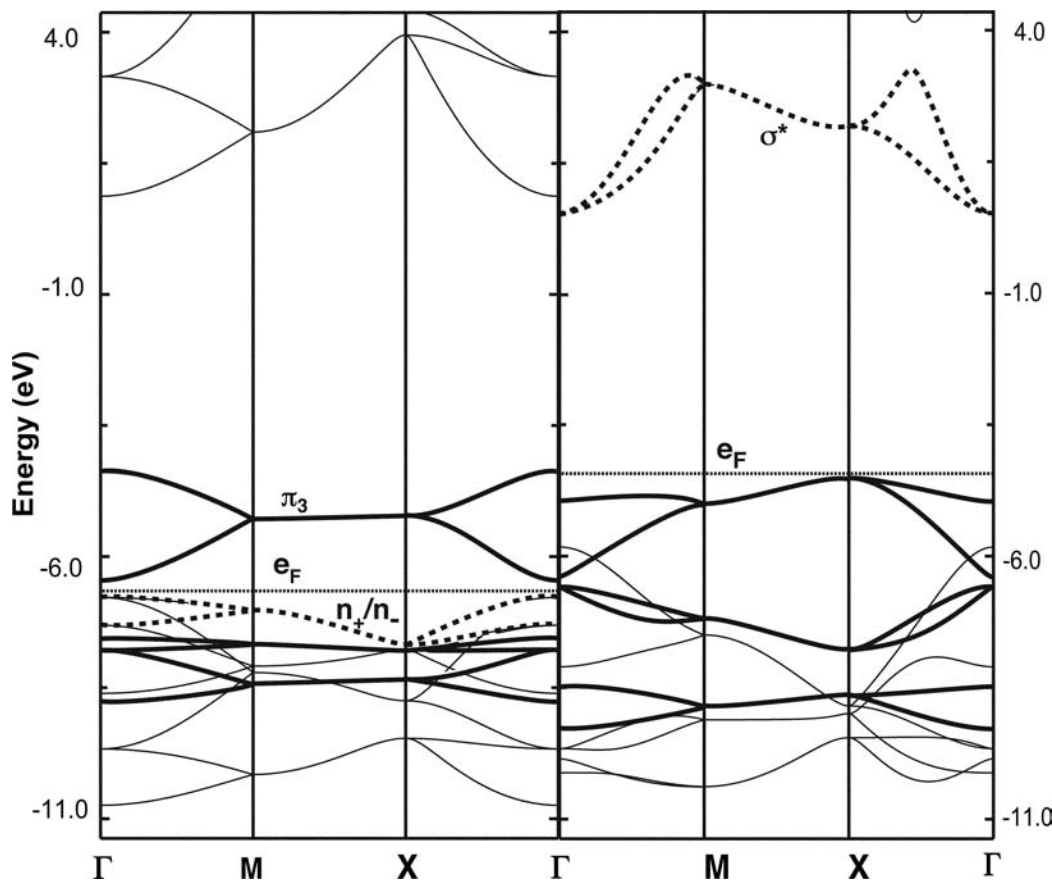
Here one has 2-D sheets of Sn (the open circles). Instead of six electrons per Sn atom and forming planar sheets, there is one less electron on average per Sn atom and the sheets are buckled. We will not work through the details here [34], suffice it to say that a rationale analysis can be given for why a lower electron count than normal is preferred for this type of structure.

In the examples that have been presented we have primarily used electron counting to “understand” the electronic structure. While the electron count frequently cannot predict the geometric structure, nature offers too many viable alternatives; we have used the latter along with the assignment of some “standard” oxidation states in our survey of hypervalent compounds. We present a cautionary note as a final case. There are a number of isostructural  $\text{RE}_2\text{AX}_2$  compounds [35,36] where RE is a rare earth element (La, Ce, Yb, Gd, etc.), A is Mg, Sc, Cd, or with one more electron, Al or In, and X is either Si or Ge. Let us take one example,  $\text{La}_2\text{CdGe}_2$  [36]. The usual way that we have been counting electrons would be to assign RE as a  $3+$  cation, and so the resulting  $\text{CdGe}_2^{6-}$  unit would normally be viewed as  $\text{Cd}^{2+}$  leaving  $2\text{Ge}^{4-}$ . The Ge atoms are not isolated and the electronegativity difference between Ge and Cd is not gigantic—there must be some covalency, thus, one might reasonably expect two electron bonds between Cd and Ge. An attractive structure to consider would be given by 14.38, where the open and dark circles are Cd and Ge atoms, respectively. Here the  $\text{CdGe}_2^{6-}$  unit cell forms a square planar lattice where the  $\text{Ln}^{3+}$  cations would lie above the  $\text{Cd}_4\text{Ge}_4$  squares. For reasons that will become apparent in a minute, the size of the



14.40

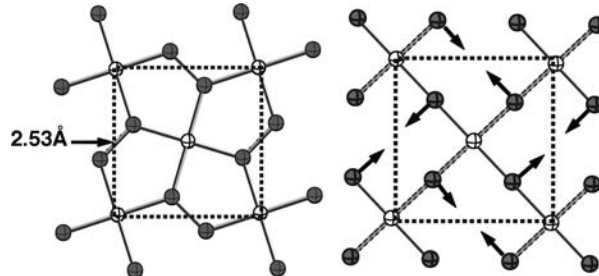
unit cell has been doubled (the unit cell is indicated by the dotted lines) to give  $\text{Cd}_2\text{Ge}_4^{12-}$ . The extended Hückel band structure for 14.38 (without the La atoms) is given on the left side of Figure 14.12. There are four bands, not shown, at around  $-16 \text{ eV}$  which are symmetry adapted combinations of the four Ge s AOs. These bands do not have much dispersion; there is not much bonding to the Cd s and  $p$  AOs. This leaves 12 Ge  $p$  AOs which are filled. The dotted line in Figure 14.12 shows the Fermi level,  $e_F$ . Indeed, if one looks carefully (avoiding degeneracies at the special

**FIGURE 14.12**

Plots of  $e(k)$  versus  $k$  for  $\text{Cd}_2\text{Ge}_4^{12-}$  at the geometry given by 14.38 (left) and 14.41, the experimental structure (right). The Fermi level is given by a dotted line and the  $\pi$  bands are drawn with thick lines. Two of the in-plane Ge lone pair combinations are given by the dashed lines (left) which then become  $\sigma^*$  combinations (right).

points) there are 12 bands from the bottom up to the top of the Fermi level. For each Ge atom one  $p$  AO will be used to form  $\sigma$  bonds to the Cd atoms and the other two AOs in a formal sense are Ge lone pairs. The  $p$  AO perpendicular to the coordination plane will create a network of  $\pi$  orbitals by overlap with a Cd  $p$  AO. 14.39 shows the combinations for a  $\text{CdGe}_2^{6-}$  unit cell.  $\pi_1$  and  $\pi_2$  can be identified with the in-phase and out-of-phase combinations of the two Ge “lone pairs.”  $\pi_3$  is primarily the Cd  $p$  AO. Doubling  $\pi_1-\pi_3$  gives six  $\pi$  bands in the  $e(k)$  versus  $k$  plot on the left side of Figure 14.12. The  $\pi$  bands are indicated by thick lines. Notice that the two bands derived from  $\pi_3$  are empty and a narrow gap ensues between filled and empty orbitals. There is also a  $p$  AO, which corresponds to an in-plane lone pair on the Ge atom. 14.40 shows the two combinations for a  $\text{CdGe}_2^{6-}$  unit cell, and of the four bands in Figure 14.12, two are shown as dashed lines. Notice that there is little dispersion associated with these bands; this is a consequence of the fact that they are essentially nonbonding with respect to the Cd AOs. The six bands above  $\pi_3$  (some of which are not shown) are concentrated on Cd and are  $s/p$   $\sigma$ -antibonding to the Ge AOs. The bonding picture developed here from the band structure nicely agrees with the oxidation state assignments as  $\text{Cd}^{2+}$  and  $\text{Ge}^{4-}$ . The only new feature has come about by the allowance of  $\sigma$  and  $\pi$  overlap between Cd and Ge. But this is not the structure of  $\text{La}_2\text{CdGe}_2$  [36] nor any of the other  $\text{RE}_2\text{AX}_2$

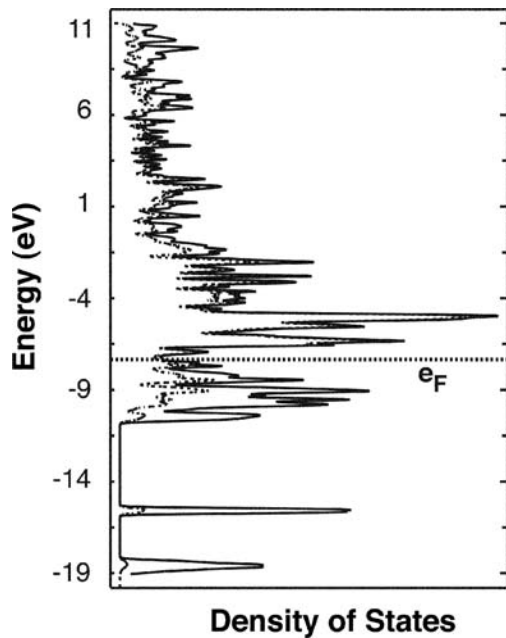
phases [35,36]. The real structure is given by 14.41. Here again the RE cations lie above and below the coordination plane. Now X—X bonds are formed; in other



14.41

14.42

words, for  $\text{La}_2\text{CdGe}_2$  instead of “isolated”  $\text{Ge}^{4-}$  atoms, Ge—Ge bonds at a normal, 2.53 Å distance are formed. One is tempted then to assign the oxidation states in  $\text{CdGe}_2^{6-}$  as being Cd(0) and two  $\text{Ge}^{3-}$  which dimerizes to form  $\text{Ge}_2^{6-}$ . The square planar Cd atoms would have an  $s^2$  configuration akin to  $\text{XeF}_4$ . We shall see that this description is also wrong! The motion shown in 14.42 shows how Ge—Ge  $\sigma$  bonds are formed, starting with the structure in 14.38. Each  $\text{CdGe}_4$  unit rotates by  $27.9^\circ$ . The resultant band structure diagram is shown on the right side of Figure 14.12. Nothing much happens to the six  $\pi$  bands, shown by the thick lines. However, major changes occur in the rest of the band structure. In particular, the two bands, labeled  $n_+/n_-$  with the dashed line on the left side of the Figure, become the two  $\text{Ge}-\text{Ge} \sigma^*$  bands. As shown on the right side of the Figure they are shifted, of course, to much higher energies. (It is also clear that the upper band undergoes avoided crossings with the Cd-based bands.) The  $n_+/n_-$  bands not only are raised in energy, but the electrons associated with them are dumped into the two  $\pi_3$  bands. This repositioning of the Fermi level by shifting bands is a very common phenomenon for reactions on metal surfaces. It should be noted that the two  $n_+/n_-$  bands on the left side lie lower in energy than the two  $\pi_3$  bands on the right. By itself this does not create a stabilizing distortion. However, it is the formation of Ge—Ge  $\sigma$  bonds that creates the driving force for the distortion in 14.42. This is hard to show; there is much intermixing between the two other in-plane lone pairs with the Ge—Cd  $\sigma$  orbitals. In fact, two of the four Ge s bands (not shown in the Figure) are shifted from  $\sim -16$  to  $\sim -18$  eV. The bonding picture that is developed for  $\text{La}_2\text{CdGe}_2$  is then one where, if oxidation state formalism is to be used, the Cd(0) oxidation state does not imply an  $s^2$  configuration, but rather  $p^2$  since  $\pi_3$  is filled. But this does not make good sense either;  $\text{Gd}_2\text{MgGe}_2$  [36] is isostructural and a  $p^2$  configuration for Mg(0) seems suspicious. The authors [36a] report a  $2\text{Gd}^{3+}\text{Mg}^{2+}\text{Ge}^{6-}(2\text{e}^-)$  formulation. In other words, the extra two electrons are added to the top of the Fermi level. What we have left out in  $\text{La}_2\text{CdGe}_2$  is the La atoms. A full 3-D calculation, which includes La, of the DOS is presented in Figure 14.13. The dashed line shows the projection of La (valence  $d$ ,  $s$ , and  $p$  character) to the total DOS. Without the La atoms included in the 2-D calculation there was a large band gap; see the right side of Figure 14.12. In Figure 14.13 the Fermi level (the dotted line) is embedded in a region of states that have significant La composition. In other words, La-based bands overlap and are dispersed by Ge  $p$  AOs so that they extend into the Ge  $p$  region and are partially filled. The resulting compound is then predicted to be metallic, and it is, albeit a rather poor one. This picture of the partial occupation of La orbitals or Gd orbitals in  $\text{Gd}_2\text{MgGe}_2$  is also derived from higher level density functional calculations [36b].

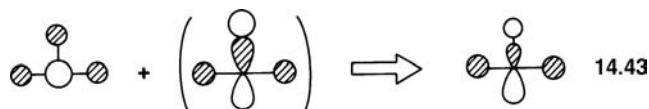
**FIGURE 14.13**

Density of states plot for  $\text{La}_2\text{CdGe}_2$  obtained at the extended Hückel level. The dashed line indicates the projection of La valence  $s$ ,  $p$ , and  $d$  levels. The Fermi level is marked by the dotted line.

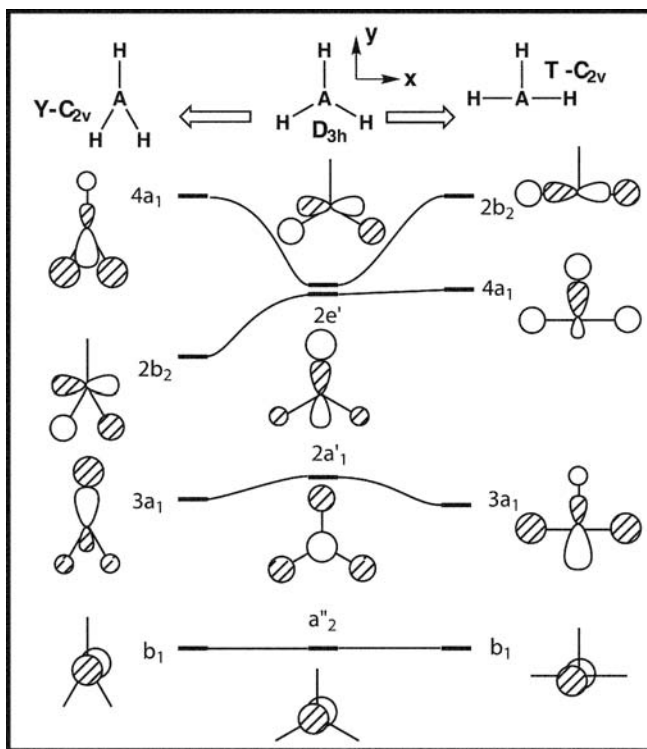
Furthermore, in the  $\text{RE}_2\text{InGe}_2$  compounds [35] there is yet another electron to be placed in this region. The assignment of oxidation states is a very tricky matter in these and analogous compounds [37]. Oxidation states, electron counting, and the extrapolation of electron counting to the bonding in a compound need not always go hand-in-hand. Arguments concentrating on oxidation state and bond order tend to produce much more heat than light.

### 14.3 GEOMETRIES OF HYPERVALENT MOLECULES

We have already mentioned the predictions of the VSEPR approach in the area of molecular geometry. Here we will not exhaustively treat all possible geometric excursions away from a symmetric structure in orbital terms but will show slices through the potential energy surface along some selected distortion coordinates. The right side of Figure 14.14 shows the connection between the levels of the planar  $\text{AH}_3$  molecule of  $D_{3h}$  symmetry and the corresponding levels of the T-shaped  $C_{2v}$  planar geometry. With a total of five valence electron pairs the  $2a'_1$  orbital of the  $D_{3h}$  structure is occupied. This orbital is rapidly stabilized on bending toward the T-shaped structure since it strongly mixes with the  $y$  component (see the top of Figure 14.14 for the coordinate system) of the  $2e'$  LUMO in the  $D_{3h}$  structure as shown in 14.43. From a geometric perturbation theory perspective,  $e^{(1)} = 0$ , but  $e^{(2)} < 0$ . To evaluate the first-order mixing correction to the wavefunction it is



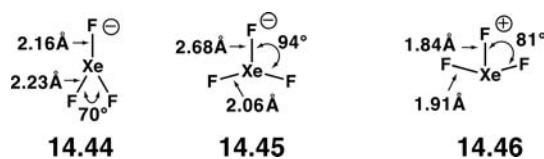
necessary to determine the overlap between  $2a'_1$  and  $2e'$  upon distortion. The overlap between the two as shown in 14.43 is positive; it is the mixing between the H s AOs in  $2a'_1$  and the  $p$  AO in  $2e'$  that determines this. Since the  $2e'$  set lies higher in

**FIGURE 14.14**

Idealized Walsh diagram for the degenerate H—A—H bending modes in a  $D_{3h}$   $AH_3$  molecule. The A—H bonding MOs,  $1a'_1$  and  $1e'$ , lie at lower energies and are not shown in the figure.

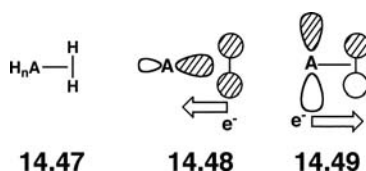
energy than  $2a'_1$ , the mixing coefficient will be positive, as shown. Octet molecules have an empty  $2a'_1$  orbital and are stable with respect to such a distortion. Molecules with five valence pairs, where this orbital is occupied, should then be unstable at the  $D_{3h}$  geometry and distort to a  $C_{2v}$  arrangement. The distortion of the  $D_{3h}$  to  $C_{2v}$  geometry for  $ClF_3$  may be envisaged as a second-order Jahn–Teller instability of the trigonal structure with this electronic configuration. A distortion coordinate of  $a'_1 \otimes e' = e'$  will allow the HOMO and the one component of the LUMO to strongly mix, as shown in 14.43. The first excited electronic state of  $NH_3$  in planar ( $D_{3h}$ ) and has the configuration  $\dots (1e')^4 (1a''_2)^1 (2a'_1)^1$ . With only one electron in this  $2a'_1$  orbital, therefore, the geometry remains trigonal and does not distort to the  $C_{2v}$ , T-shaped structure. However, examples where the second-order driving force is greater, for example, the excited state for  $PH_3$ , and so on (see Chapters 9.3 and 9.4), a T-shaped structure is favored. Furthermore,  $NF_3$ , as well as, other eight electron  $AF_3$  molecules do not undergo pyramidal inversion via a  $D_{3h}$  transition state. The electronegativity of fluorine puts the orbital analogous to  $2a'_1$  below the  $a''_2$  MO at the putative  $D_{3h}$  transition state. As a consequence the true transition state is then distorted to the  $C_{2v}$  T-shape [38]. What is also clear from the left side of Figure 14.14 is that distortion to a  $C_{2v}$  geometry with a Y-shape should also be possible. Apparently this is the case. For  $ClF_3$  experiment (14.14) and theory [39] predict the T-shaped structure to be the ground state. A Y-shaped structure has been found to be the transition state for axial-equatorial F exchange [39].

Experiments on the reaction of  $F^-$  with  $XeF_2$  in the gas phase result in the production of  $XeF_3^-$  amongst other species [40]. This compound now has 12 valence electrons. A singlet electronic state would pair two electrons in the  $2e'$  set for a  $D_{3h}$  geometry. This will be unstable; it is a first-order Jahn–Teller problem where calculations [40] show that both Y and T geometries, 14.44 and 14.45, respectively, represent more stable structures. This is precisely analogous to the



$\text{H}_3^-$  potential energy surface in Figure 7.7 (see Sections 7.4.A and 7.4.C). The Y structure was found to be about 14.5 kcal/mol more stable than the T [40]. In other words, with respect to Figure 14.14, if the x component of the  $2e'$  set is filled, then distortion to the Y shape will stabilize  $2b_2$ . The  $e^{(1)}$  correction is negative since overlap is lost in an antibonding orbital. On the other hand, if the two electrons are in the y component of  $2e'$ , then it is stabilized again by the  $e^{(1)}$  correction, however, the  $e^{(2)}$  correction is positive because of the mixing with the  $2a'_1$  MO. This is presumably why the Y structure is more stable than the T one. **14.44** and **14.45** are remarkable structures. All of the MOs in Figure 14.14 are filled except the top one. Yet the molecule requires 0.84 eV to dissociate one Xe—F bond to  $\text{XeF}_2$  and  $\text{F}^-$  [40]. The geometric features of  $\text{XeF}_3^-$  are also unusual. All of the Xe—F bonds are long in comparison to  $\text{XeF}_2$  or  $\text{XeF}_4$  which have Xe—F bond lengths of 2.00 and 1.95 Å, respectively. This is in line with the occupation of an additional antibonding orbital. Notice in **14.44** that the unique, equatorial bond is the shorter one in line with the occupation of the  $2b_2$  MO. Exactly the opposite is true for **14.45**, which is consistent with  $4a_1$  being occupied. The crystal structure [41] of  $\text{XeF}_3^+$  with two less electrons is given in **14.46**. It is instructive to note the differences from **14.45**. In **14.46** the HOMO is the  $3a_1$  MO so that, as mentioned previously, the two axial bonds are longer and the F atoms bend back towards the equatorial F so that in  $3a_1$  the F lone pairs overlap better with the Xe p AO. For **14.45** it is the occupation of  $4a_1$  that not only creates exactly the opposite pattern of Xe—F distances, but also, causes the axial F ligands to move in exactly the opposite direction. The phase of the Xe p AO in the  $4a'_1$  MO (see Figure 14.14) is such that now it is energetically favorable for the axial groups to bend away from the equatorial one. It is difficult to use the VSEPR approach to rationalize the geometry and relative energies of **14.44** and **14.45**. A three center–four electron bonding model also is not applicable. On the other hand, all of the geometrical features fit in nicely with a consideration of the HOMO in these species.

The situation for the very electron rich  $\text{XeF}_3^-$  is mirrored for the very electron-deficient  $\text{BeH}_3^+$ . With four valence electrons at the  $D_{3h}$  geometry, the  $1e'$  set is half full. A first-order Jahn–Teller distortion results in T and Y structures. Calculations [42] have shown that the Y geometry is the ground state. The unique H—Be—H bond angle is only 24.8°! The structure is really  $\text{HBe}^+$  coordinated to  $\text{H}_2$ . The bond dissociation energy was about 25 kcal/mol and the coordinated H—H distance was found to be 0.753 Å, this is a little longer than that in  $\text{H}_2$  itself (0.741 Å). The bonding in  $\text{BeH}_3^+$  can easily be described in terms of the interaction between  $\text{HBe}^+$  and  $\text{H}_2$ . Referring back to the orbitals of AH (Figure 9.1), the  $1\sigma$  orbital could be associated with the two-center–two-electron Be—H bond. The  $2\sigma$  orbital then interacts with and stabilizes  $\text{H}_2\sigma_g^+$ . The formation of  $\text{H}_2$  complexes is something that we have seen before. The simplest was the “coordination” of  $\text{H}_2$  to  $\text{H}^+$  (Figure 5.1). The interaction between the  $\text{H}^+$ ’s AO and  $\text{H}_2\sigma_g^+$  is, of course stronger than in the present case. The H—H distance elongates to 0.872 Å. We have also seen (Figure 9.12) the same pattern emerge in  $\text{CH}_4^{2+}$  that can be viewed as a complex between  $\text{CH}_2^{2+}$  and  $\text{H}_2$ . There is another bonding component in this case—with  $\text{H}_2\sigma_u^+$ . Let us generalize at this point in anticipation of another series of molecules that we will encounter shortly. There are two possible constituents in the bonding of an  $\text{AH}_n$  unit to  $\text{H}_2$ , **14.47**. The first is the overlap of  $\text{H}_2\sigma_g^+$  with a cylindrically symmetric orbital on the  $\text{AH}_n$  fragment, **14.48**. Electron density is shifted



from the H—H bonding region toward A. If there is a filled orbital on  $AH_n$  of the correct symmetry, it can interact with  $H_2 \sigma_u^+$ , 14.49. Electron density then flows in the opposite direction, which again weakens the coordinated H—H bond since it is H—H antibonding. We shall also see this exact pattern in the next chapter for  $H_2$  complexes to transition metals, as well as, olefin- $ML_n$  compounds.

The Walsh diagram for the  $D_{4h} \rightarrow C_{4v}$  distortion of  $SH_4$ , shown in Figure 14.15, is easy to derive. It was briefly discussed in Section 9.5 and has obvious ties with the pyramidalization of planar  $AH_3$  (shown in Figure 9.7) and the bending of linear  $AH_2$  (shown in Figure 7.5). A prominent feature is the strong coupling between  $a_{2u}$  and  $2a_{1g}$  orbitals on bending. With five electron pairs,  $SF_4$  should be unstable at the planar geometry in a second-order Jahn–Teller sense. The situation is reminiscent of that of  $NH_3$  or better yet,  $PH_3$ , and the pyramidal structure will be stabilized with respect to the planar one. For  $SF_4$  (or hypothetical  $SH_4$ ) with this configuration the  $C_{4v}$  geometry is a possible candidate for the ground-state structure. We have shown that  $SF_4$  actually exists in a  $C_{2v}$  geometry (14.18). The relationship between the  $C_{4v}$

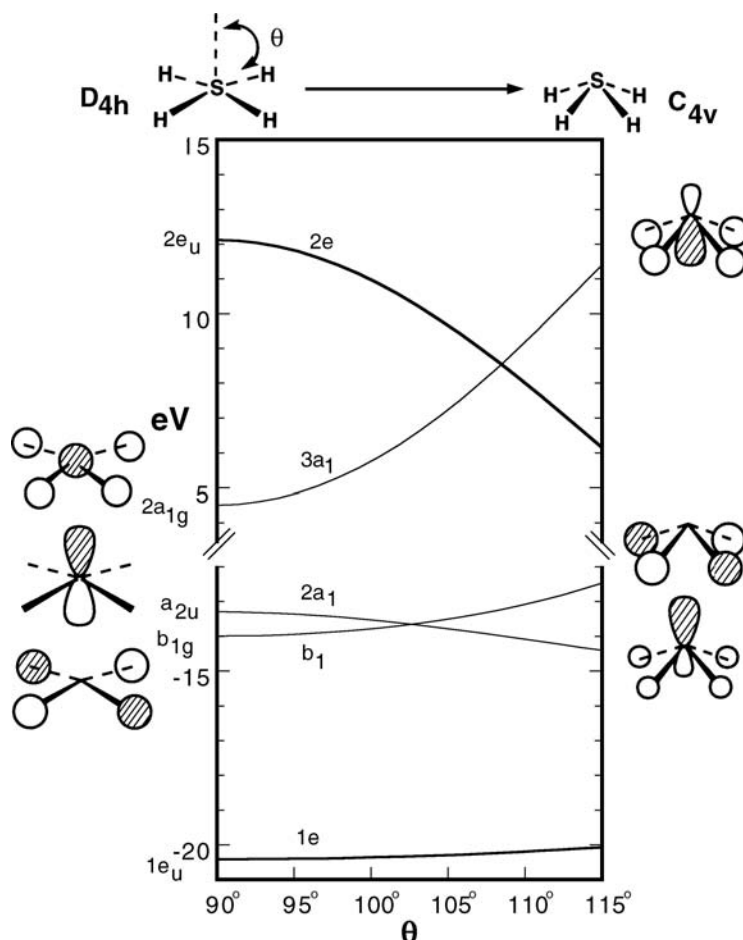
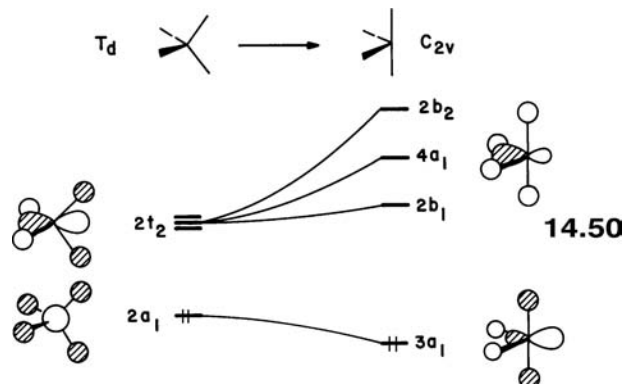


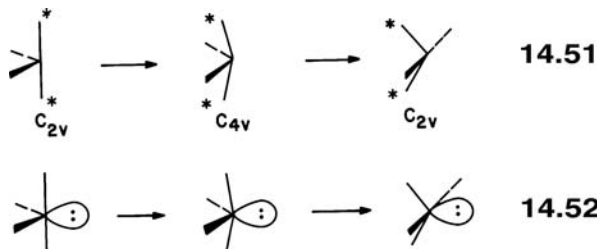
**FIGURE 14.15**

Walsh diagram for the pyramidalization of square  $SH_4$ .

and  $C_{2v}$  structures for these molecules with five pairs of electrons is one that will shortly be explored.  $\text{XeF}_4$  with six valence pairs will be more stable at the planar structure since here the HOMO,  $2a_1g$  is destabilized on pyramidalization. (The same argument can be used to rationalize the planar rather than pyramidal first excited electronic state of  $\text{NH}_3$ .) Use of second-order Jahn–Teller ideas at the tetrahedral geometry leads to a different geometry, the butterfly structure of **14.18**. **14.50** shows how the HOMO ( $2a_1$ ) and LUMO ( $2t_2$ ) may couple together during a  $t_2$  distortion, which leads to the observed structure of  $\text{SF}_4$ . Whether the  $C_{2v}$  or  $C_{4v}$

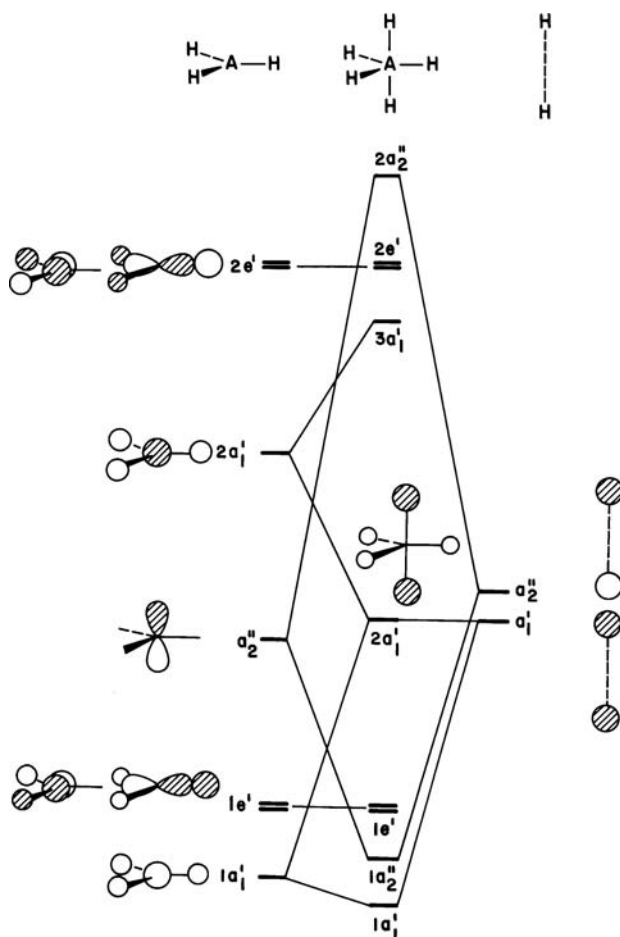


structure lies lower in energy is very difficult to predict. Numerical calculations [43] suggest that the  $C_{4v}$  structure is the lower energy isomer for the (hypothetical)  $\text{SH}_4$  molecule but the  $C_{2v}$  structure [44] is the lower energy isomer for  $\text{SF}_4$  (as observed [18]). The energetic juxtaposition of these two structures leads to a ready pathway for the isomerization of  $\text{SF}_4$  (**14.51**). Notice that the initially axial ligands (of the



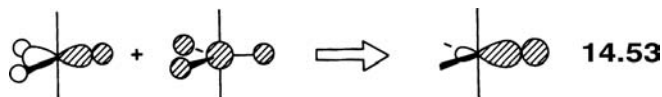
VSEPR trigonal bipyramidal) labeled with asterisks become the equatorial ligands after rearrangement. This process is just the Berry pseudorotation process for five coordinate molecules (which we describe more fully below) but with a lone pair occupying the fifth coordinate position **14.52**. The Berry process (or rather a ligand interchange process consistent with it) has been verified for  $\text{SF}_4$  by nuclear magnetic resonance (NMR) studies [45]. There are experimental complications with measuring the barrier, but calculations [44] have shown that the Berry psuedorotation process, shown in **14.52**, is the lowest energy reaction pathway with a barrier height (the relative energy of the  $C_{4v}$  species) of 8.1 kcal/mol.

Main group five-coordinate molecules are found either as trigonal bipyramidal molecules (e.g.,  $\text{PF}_5$ ) or as square pyramidal species (e.g.,  $\text{BrF}_5$ ). Geometrically they are quite close and slight modifications of the bond angles takes one form to the other. The levels [46] of the  $\text{AH}_5$  trigonal bipyramidal are built up in Figure 14.16 from the  $\text{AH}_3$  trigonal plane plus a pair of axial hydrogen ligands. In the five-electron pair molecule the HOMO is a nonbonding orbital. Its origin is best seen as a three orbital interaction pattern between  $1a'_1$  and  $2a'_1$  on the  $\text{AH}_3$  unit and the symmetric combination of  $\text{H}_2$  orbitals. Of the three MOs that are produced, the lowest,  $1a'_1$ , is fully bonding between the A s orbital and the surrounding

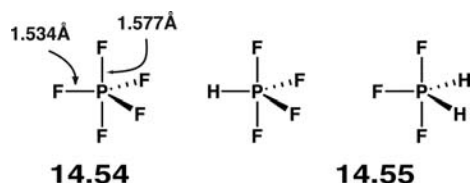
**FIGURE 14.16**

Assembly of the molecular orbital diagram for trigonal bipyramidal  $\text{AH}_5$  from the levels of A and of trigonal planar  $\text{AH}_3$  and those of  $\text{H}_2$ .

hydrogens while the highest MO,  $3a_1'$ , is maximally antibonding. The middle orbital,  $2a_1'$ , is rigorously nonbonding. It is primarily the  $\text{H}_2 a_1'$  combined with  $2a_1'$  and  $1a_1'$  on  $\text{AH}_3$  in a bonding and antibonding manner, respectively. An even simpler way to view the bonding here would be to consider that the equatorial ligands are attached by conventional two-center–two-electron bonds. We could imagine  $sp^2$  hybrid orbitals bonding to H s AOAs as being constructed from the  $1a_1'$  and  $1e'$  orbitals as shown in 14.53 (and  $2a_1'$  along with  $2e'$  as the antibonding analogs).

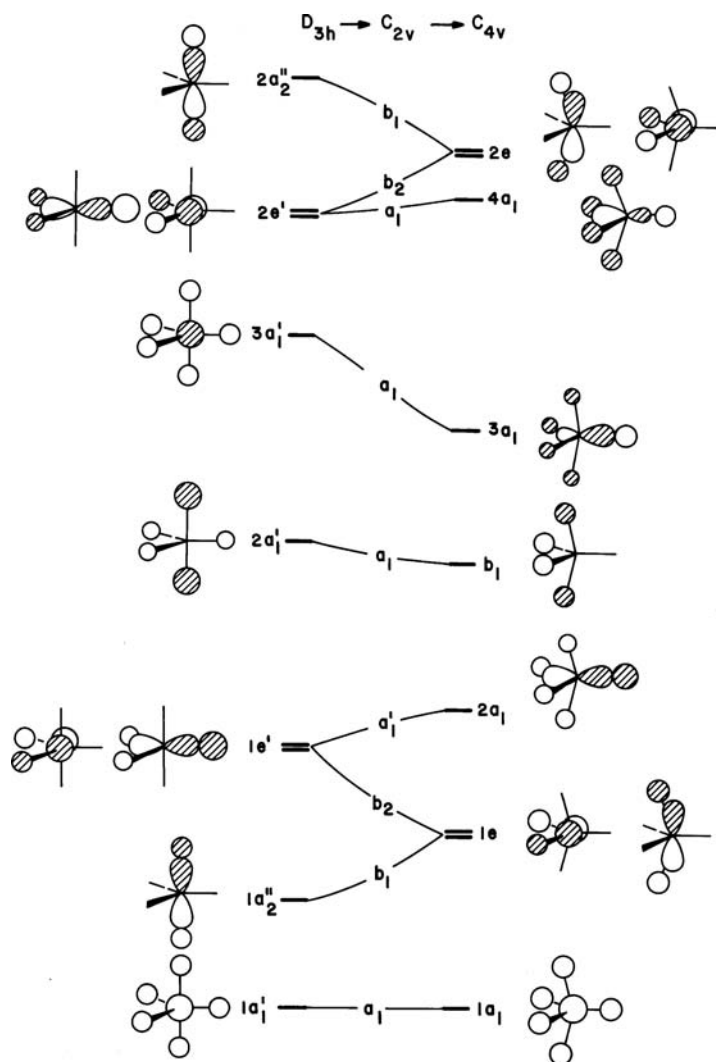


The axial ligands are clearly attached by three-center–four electron bonds in this molecule. The remaining p AO on A ( $a_2''$ ) overlaps with the antisymmetric combination of H s orbitals; the bonding combination is filled. The symmetric combination of H s AOAs is then left filled and nonbonding. As a result the axial linkages are longer than the equatorial ones in  $\text{PF}_5$ , 14.54 [46]. Recall that one of the results of



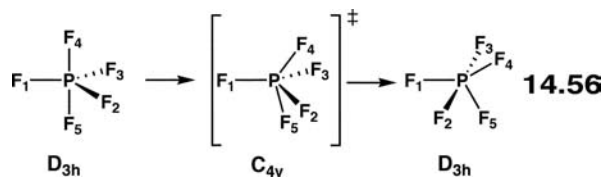
electronegativity perturbation theory was that the  $e^{(1)}$  stabilization is largest in absolute magnitude when the orbital mixing coefficients are the largest (equation 12.28). In accord with this principle, the larger coefficients at the axial positions in the  $2a_1'$  HOMO insures that electronegative substituents preferentially reside in the axial positions. **14.55** [47] shows two of many examples. But why do 10 electron trigonal bipyramidal species form so readily from the third and higher rows of the Periodic Table? Compounds of this type do exist where the central atom is carbon, for example, but they are compounds which have special ligands that force this geometry to occur [48]. It has been a common, but incorrect, assumption that third and higher row elements use a *d* AO to stabilize the  $2a_1'$  MO—the topology of the ligand set ideally matches a  $z^2$  AO. A number of valid hypothesis have been proposed. One argument, actually from a valence bond perspective [49], has been that the  $2a_1'$  fragment orbital for  $AH_3$  in Figure 14.16 is lower in energy for say  $A = Si$  compared to  $C$  (we have used this argument before in Section 9.3) and this is the stabilizing feature in the HOMO. So consequently, electron rich bonding at a trigonal bipyramidal geometry is more favored for  $SiH_5^-$  than it is for  $CH_5^-$ . An equally persuasive argument [50] is that  $Si-R$  distances are longer than  $C-R$ . Whether one has a minimum or a transition state for  $Cl_2SiR_3^-$  depends largely on the steric factors associated with  $R$ .

Figure 14.17 shows the orbital correlation diagram connecting the square pyramidal and trigonal bipyramidal structures. Comparison of the occupied levels

**FIGURE 14.17**

Walsh diagram for the distortion of trigonal bipyramidal  $AH_5$  ( $D_{3h}$ ) to the square pyramidal geometry ( $C_{4v}$ ) via a  $C_{2v}$  structure.

for five valence pairs of electrons shows little energetic preference for either structure.  $\text{PF}_5$  itself has the trigonal bipyramidal structure but with a low energy rearrangement pathway via the square pyramidal geometry. Thus, facile rearrangement of  $\text{PF}_5$  occurs via the Berry pseudorotation process (3.7 kcal/mol) [51] **14.56**. After an excursion to the square pyramidal structure and back, axial and



equatorial sites of the trigonal bipyramidal have been exchanged. In **14.56**  $\text{F}_4$  and  $\text{F}_5$  bend over the  $\text{F}_2\text{-P-F}_3$  face. There are two other faces that will generate trigonal bipyramidal structures with a different permutation of the numbered ligands. There are a total of 20 minima and 30 transition states. The full potential energy surface has been mapped [51].

It is interesting at this point to mention the structures that have been calculated for the  $\text{CH}_5^\pm$  ions.  $\text{CH}_5^-$  is predicted to be unstable with respect to dissociation but the most stable geometry of the ion with this stoichiometry is the trigonal bipyramidal  $\text{S}_{\text{N}}2$  transition state [42].  $\text{CH}_5^+$  on the other hand is an “electron-deficient” species and was initially observed in mass spectra. Most of the experimental work on this compound has been carried out in the gas phase. Its structure, or lack thereof, has generated some excitement [52]. It is calculated [53] to have the lowest energy geometry shown in **14.57**, and as previously indicated may be regarded as being isoelectronic with  $\text{H}_3^+$ . A  $\text{CH}_3^+$  unit provides the  $2a_1$  LUMO

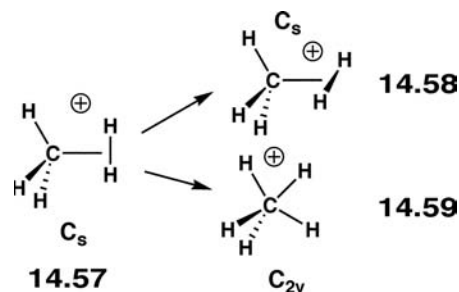
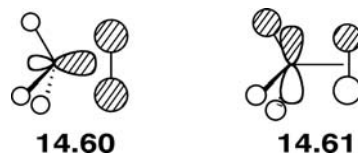


(Figure 9.4), which interacts with  $\text{H}_2 \sigma_g^+$ , **14.60**. One component of the  $1e$  HOMO in  $\text{CH}_3^+$  interacts with  $\sigma_u^+$ , **14.61**. This is a specific example of the  $\text{H}_2$  bonding



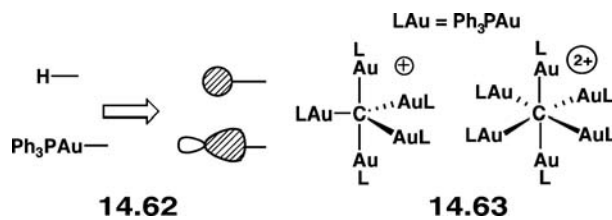
model presented in **14.47–14.59**. The “forward donation” of electron density from  $\text{H}_2$  to  $\text{CH}_3^+$  is given by **14.60**; while the “back donation” of electron density from  $\text{CH}_3^+$  to  $\text{H}_2$  is shown in **14.61**. The  $2a_1$  orbital is cylindrically symmetric, so the overlap of  $\text{H}_2 \sigma_g^+$  with it upon rotation from **14.57** to **14.58** is constant. Furthermore, at the geometry given by **14.58** the  $\text{H}_2 \sigma_u^+$  simply overlaps with the other component of  $1e$  (in reality this is only a  $30^\circ$  rotation) to an equal extent. Recall that any linear combination of the two members of an  $e$  set are equally valid,

**TABLE 14.1** Calculated Number of Electrons Transferred from and to  $\text{H}_2 \sigma_g^+$  and  $\sigma_u^+$  in  $\text{AH}_5^+$

A	$\sigma_g^+$	$\sigma_u^+$	$r_{\text{H}-\text{H}} (\text{\AA})$
C	-0.84	+0.15	0.988
Si	-0.29	+0.02	0.777
Ge	-0.22	+0.02	0.772

therefore, constant back donation to  $\text{H}_2 \sigma_u^+$  will occur irrespective of the rotation angle. The bottom line is that there is essentially no energy difference between **14.57** and **14.58**. The most sophisticated calculations put the energy difference at 0.08 kcal/mol. The H—H bond, as we shall shortly see, has been weakened considerably so that it requires only 0.97 kcal/mol to reach **14.59**. Both values are below the zero point energy. Thus, the molecule really has no structure associated with it at any temperature.

The relative amounts of forward and back donation are, of course, not the same. Both do work in the same way, in that the bonding between the “coordinated”  $\text{H}_2$  unit and carbon is increased when the two bonding modes are of increased importance at the expense of a weaker H—H bond. When **14.60** is turned on, electron density from the H—H bonding region is shifted towards carbon. Thus, the H—H bond becomes weaker and longer. The same result occurs with **14.61**. Electron density flows from the  $\text{CH}_3^+$  unit to the H—H region which is now antibonding. Numerical results [54] using a hybrid density functional for the  $\text{AH}_5^+$  series, where A = C, Si, and Ge, are presented in Table 14.1. For all  $\text{AH}_5^+$  the amount of forward donation greatly exceeds back donation. On going from C to Si and Ge, the  $2a_1'$  MO in  $\text{AH}_3^+$  becomes more diffuse and overlaps less with the  $\text{H}_2 \sigma_g^+$  MO (it also lies higher in energy and so the energy gap also becomes larger). Consequently there is also less forward donation as one goes down the column and the H—H bond becomes stronger. This is consistent with the experimental facts [55] that while rotation of the  $\text{H}_2$  unit in  $\text{SiH}_5^+$  is facile, permutation with the other hydrogens (presumably via **14.59** where the H—H bond is broken) is not. The addition of more protons to  $\text{CH}_5^+$  creates more coordinated  $\text{H}_2$  units [56]. For example,  $\text{CH}_6^{2+}$  presumably exists as  $C_{2v}(\text{H}_2)_2\text{CH}_2^{2+}$  and  $\text{CH}_7^{3+}$  as  $C_{3v}(\text{H}_2)_3\text{CH}^{3+}$ . These molecules can be viewed as examples of electron-deficient bonding where “closed” structures exist rather than “open” geometries for the electron rich cases. An interesting series of exceptions to this structural pattern have been synthesized. There is a relationship, called the isolobal analogy, which is covered fully in Chapter 21 that equates different fragments. In this case a hydrogen with its s AO is electronically like a  $\text{Au}(\text{PPh}_3)$  fragment that has an s/p hybridized (mainly s in character) valence orbital also with one electron associated with it, see **14.62**. Both of the compounds in **14.63** have been structurally categorized [57].



The trigonal bipyramidal and octahedral structures are thought to be a consequence of an “aurophilic” effect, that is, there are attractive Au—Au interactions which are thought [58] to be due to a combination of relativistic and electron correlation effects.

---

## PROBLEMS

---

- 14.1.** Listed below are the results of an extended Hückel calculation on  $\text{PH}_5$  at the trigonal bipyramidal geometry. (a) Draw out the MOs. (b) The overlap populations are listed. Which of the P—H bonds are weaker? (Note for the calculation all P—H bonds were set to the same length.) Also listed are the gross population of all of the atoms. This uses the Mullikan population analysis, that is, the gross population (electrons) for atom A is defined as;

$$P_A = \sum_{\Psi} n(\text{occ})_{\Psi} \left[ \sum_{\mu} P_{\mu\mu} + \frac{1}{2} \sum_{\mu \neq \nu} P_{\mu\nu} \right]$$

where  $n(\text{occ})_{\Psi}$  is the occupation number of the MO  $\Psi$ . Predict which positions more electronegative atoms will prefer.

---

### Cartesian Coordinates

---

	Name	No.	x	y	z
POS	P-0-0	1	0.000000	0.000000	0.000000
POS	H-1-0	2	0.000000	0.000000	1.420000
POS	H-2-0	3	0.000000	0.000000	-1.420000
POS	H-3-0	4	0.000000	1.420000	0.000000
POS	H-4-0	5	1.230000	-0.710000	0.000000
POS	H-5-0	6	-1.230000	-0.710000	0.000000

---

### Molecular Orbitals

		1	2	3	4	5	6	7	8	9
		-22.291	-18.276	-17.871	-17.871	-11.167	9.320	9.321	20.408	23.380
P-0-0	s	1	0.6015	0.0000	0.0000	-0.0182	-0.0009	0.0000	1.4456	0.0000
	$p_x$	2	0.0000	0.0000	-0.5730	0.0000	0.0000	1.2440	0.0000	0.0000
	$p_y$	3	0.0000	0.0000	0.0000	-0.5730	0.0000	1.2440	0.0000	0.0010
	$p_z$	4	0.0000	0.5484	0.0000	0.0000	0.0000	0.0000	0.0000	1.4999
H-1-0	s	5	0.1808	0.3659	0.0000	0.0000	0.6134	0.0004	0.0000	-0.5659
H-2-0	s	6	0.1808	-0.3659	0.0000	0.0000	0.6134	0.0004	0.0000	-0.5659
H-3-0	s	7	0.1798	0.0000	0.0000	-0.4319	-0.4023	-1.0598	0.0000	-0.5996
H-4-0	s	8	0.1797	0.0000	-0.3741	0.2160	-0.4024	0.5304	-0.9181	-0.5983
H-5-0	s	9	0.1797	0.0000	0.3741	0.2160	-0.4024	0.5304	0.9181	-0.5983

---

### Population Between Atoms

---

	P-0-0	H-1-0	H-2-0	H-3-0	H-4-0
H-1-0	0.5910				
H-2-0	0.5910	0.0249			
H-3-0	0.7212	-0.0867	-0.0867		
H-4-0	0.7211	-0.0867	-0.0867	0.0184	
H-5-0	0.7211	-0.0867	-0.0867	0.0184	0.0184

---

### Gross Population of Atom

---

P-0-0	4.311526
H-1-0	1.263495
H-2-0	1.263495
H-3-0	1.053759
H-4-0	1.053863
H-5-0	1.053863

---

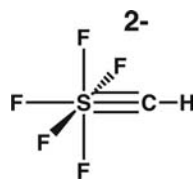
**14.2.** Draw out an orbital interaction diagram for an  $\text{AH}_4$  molecule at a square pyramidal geometry by interacting the  $\text{H}_5$  symmetry-adapted linear combinations (SALCs) with the s and  $p$  AOs on A.

**14.3. a.** Use electronegativity perturbation theory to show how the orbital change in energy and shape on going from  $\text{SH}_3^+$  to  $\text{SF}_3^+$ .

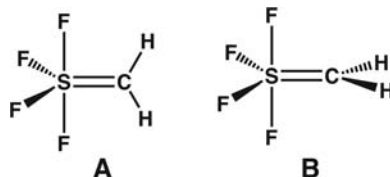
b. We are now going to use the important orbitals of  $\text{SF}_3^+$  and interact them with  $\text{C}^-$  (important means those MOs that are important to S—C bonding) to produce the molecule  $\text{F}_3\text{S}\equiv\text{CH}$ . A derivative of this molecule is actually known and contains a very short S—C bond.

**14.4. a.** For the  $\text{F}_5\text{S}\equiv\text{CH}^{2-}$  molecule shown below draw out an orbital interaction diagram for interacting the most important orbitals of a  $\text{F}_5\text{S}^+$  unit with  $\text{CH}^{3-}$ .

b. There are two different S—F bonds in this molecule. On the basis of your interaction diagram, which should be longer than the other(s).

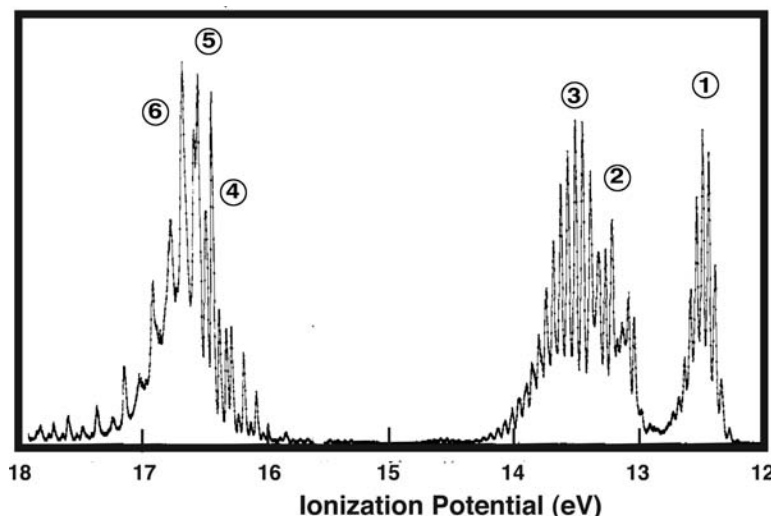


**14.5. a.**  $\text{F}_4\text{S}=\text{CH}_2$  is a known, stable molecule. Two geometries, **A** and **B**, are drawn below. Interact the *important*  $\text{CH}_2$  orbitals with those of  $\text{SF}_4$  and determine which geometry is more favorable.



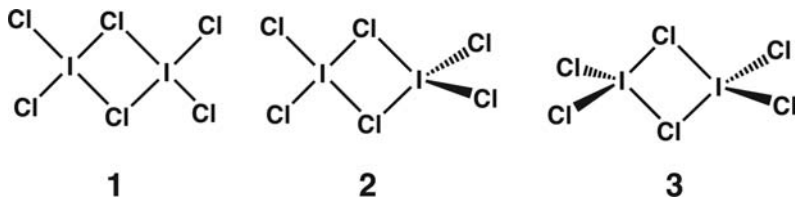
b. On the basis of your answer (and knowing that S—C  $\pi$  bonding is quite strong), predict what geometrical change should occur in the  $\text{SF}_4$  unit as the  $\text{CH}_2$  group rotates.

**14.6.** The photoelectron spectrum of  $\text{SO}_2$  as adapted from Reference [59] is shown below. Assign the six ionizations.



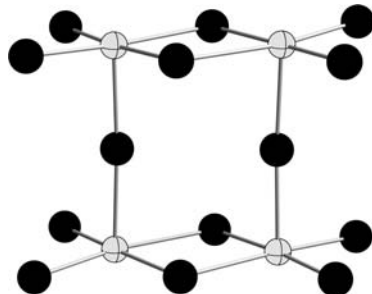
**I4.7.** Use the VSEPR rules to predict the following structures:

- The structure of a compound recently prepared was formulated as  $[\text{BrF}_6][\text{Sb}_2\text{F}_{11}]$ . As indicated by the formula, there are two separate species and both compounds by NMR results contain an even number of electrons. Predict the structures.
- Shown below are three possible structures for  $\text{I}_2\text{Cl}_6$ . Which structure should be the most stable?

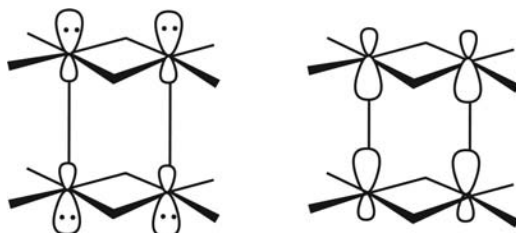


- Which of the above structures is predicted to be the most stable for  $\text{Hg}_2\text{Br}_6^{2-}$ ?
- What is the predicted structure for  $(\text{C}_6\text{F}_5)_2\text{Xe}_2\text{Cl}^+$  where Cl is the central atom flanked on either side by Xe?
- $\text{FCIO}_2$  (Cl is the central atom).
- $\text{NSF}$  (S is the central atom).
- $\text{Me}_2\text{TeBr}_2$  (Te is the central atom).
- $\text{OIF}_5$  (I is the central atom).
- $\text{SO}_2^-$ .
- $\text{BrO}_3\text{F}$  (Br is the central atom).

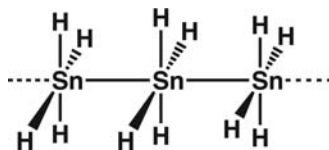
**I4.8.** The structure of  $\text{Se}_4\text{Br}_{14}^{2-}$  is shown below. There is an electron counting dilemma here. If we set the two bridging bromides as  $\text{Br}^-$  then each  $\text{Se}_2\text{Br}_6$  unit has 54 electrons.



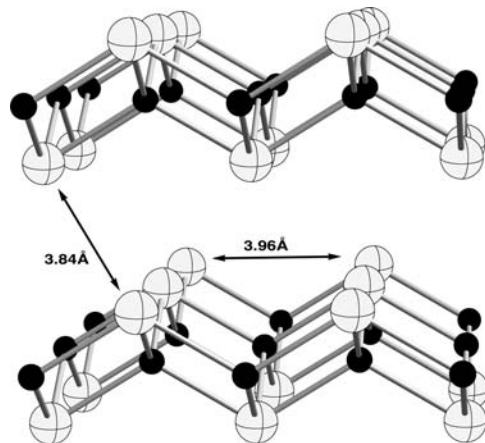
Counting each Br—Se bond as a two-center two-electron one with a full complement of lone pairs around the Br atoms gives 48 electrons. However,  $\text{Se}_2\text{Br}_6$  has 54 electrons so each Se must have 3 “extra” electrons. One might reasonably think that there should be an orbital at each Se hybridized away from the  $\text{Se}_2\text{Br}_6$  plane as shown below. This leaves hybrids at Se pointed in the opposite direction with four electrons to interact with the bridging Br p AOs (for the sake of simplicity let the s AOs of the bridging Br atoms be doubly occupied and core-like). Form SALCs of the Se hybrids. Construct an orbital interaction diagram with the Se SALCs and Br p AOs and indicate the orbital occupancy.



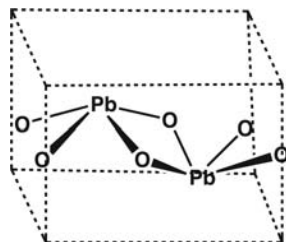
- 14.9.** Consider a hypothetical chain of square planar  $\text{SnH}_4$  units. Let us take a  $\text{Sn}-\text{Sn}$  distance of  $3\text{\AA}$  which is slightly longer than a typical  $\text{Sn}-\text{Sn}$  single bond.



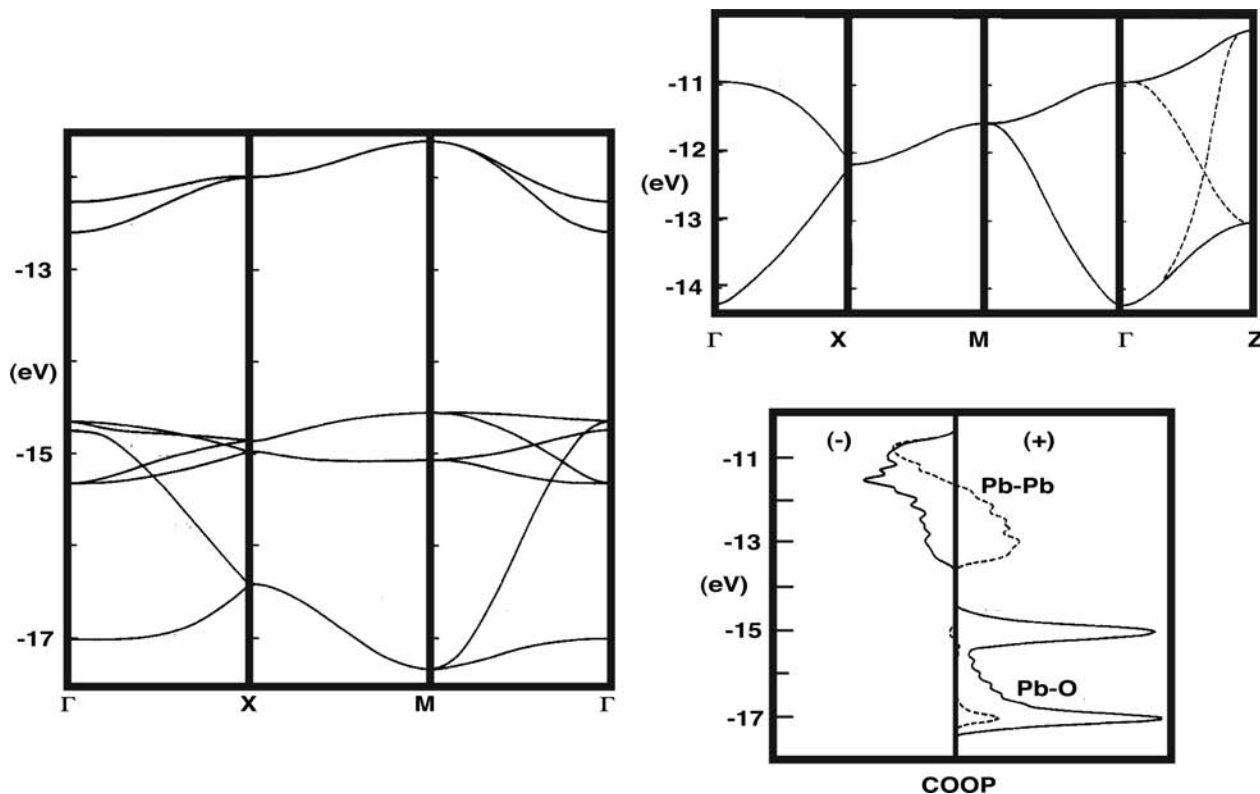
- Draw out all eight orbitals in the  $\text{SnH}_4$  unit cell and order them in energy.
  - Draw out the expected band structure for this material and draw out the crystal orbitals at the  $k = \Gamma$  and  $\pi/a$  points.
- 14.10.** There are two crystal modifications for  $\text{PbO}$ . We will take the simpler one,  $\alpha\text{-PbO}$ .



This is a layered compound. Notice that each oxygen is coordinated in a tetrahedral fashion, while the lead atoms are square pyramidal. There are two Pb and O atoms in the unit cell:

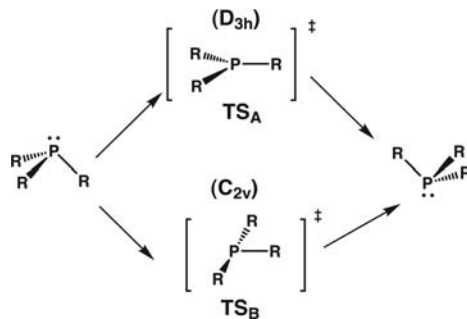


- Draw the orbital environment around Pb for eight orbitals (just consider a  $sp$  hybridized orbital at each of the four oxygen atoms that point toward Pb). Indicate which orbitals are filled.
- The band structure (adapted from Reference [60]) for one layer of  $\alpha\text{-PbO}$  is shown below on the left side. All of these bands are filled. There are two bands much lower in energy and are not shown. What are the two bands at highest energy?



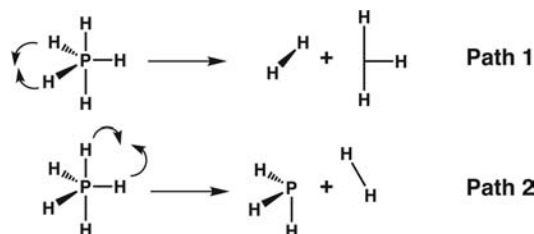
- c. The three-dimensional band structure results are plotted for the top two bands are shown above on the right side. There is considerably more dispersion. The COOP curves for Pb—O (solid line) and Pb—Pb overlap population (between layers, dashed line) are also shown above on the right side. Show that your results from (a) are in agreement with the Pb—O COOP curve. The region from about  $-13.5$  to  $-10.5$  eV show negative Pb—O overlap populations. What does this imply about the composition of the two bands in this region? Comment on the interlayer Pb—Pb overlap population in this energy range.

- 14.11.** Construct an orbital interaction diagram for a “T”-shaped  $\text{AH}_3$  unit by interacting a  $D_{\infty h}$   $\text{AH}_2$  fragment with a hydrogen atom. Draw out the orbital shapes.
- 14.12.** Normally phosphines, amines and other eight electron  $\text{AR}_3$  molecules undergo pyramidal inversion via a  $D_{3h}$  transition state ( $\text{TS}_A$  below). There are instances, however, when an alternative path via a  $C_{2v}$  transition state ( $\text{TS}_B$ ) is favored. An example is provided by  $\text{PF}_3$  where  $\text{TS}_B$  lies 56 kcal/mol lower in energy than  $\text{TS}_A$ , whereas, the situation is reversed for  $\text{PH}_3$  ( $\text{TS}_A$  is favored by 121 kcal/mol). Show by means of a Walsh diagram going from  $\text{TS}_A$  to  $\text{TS}_B$  why this is the case.



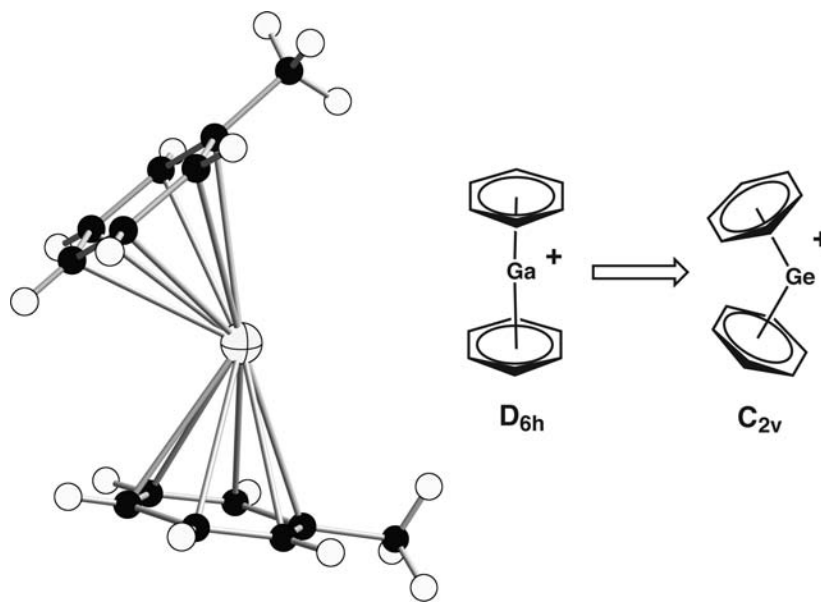
- 14.13.** The decomposition of  $\text{PX}_5$  to  $3\text{X}_2$  has been known for sometime. The first reported example was in 1833 [61]! The mechanism of the reaction is not

known with any certainty. The purpose of this exercise is to illustrate some of the problems associated with proposing a mechanism. First of all, the reaction proceeds smoothly in nonpolar solvents, which suggests that ionic intermediates (e.g.,  $\text{PX}_4^+ + \text{X}^-$ ) are probably not formed. Secondly, no evidence has been encountered for the existence of free radicals. This suggests that some kind of concerted reaction may be a possibility. Two potential least-motion pathways are shown below. Draw an orbital correlation diagram for each and show why both should engender a high activation barrier.

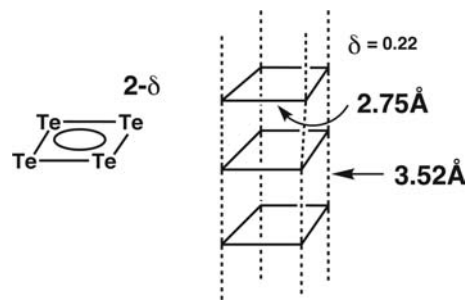


**14.14.** A number of  $(\eta^6\text{-arene})_2\text{Ga}^+$  molecules have been prepared. One example from Reference [62] is shown below.

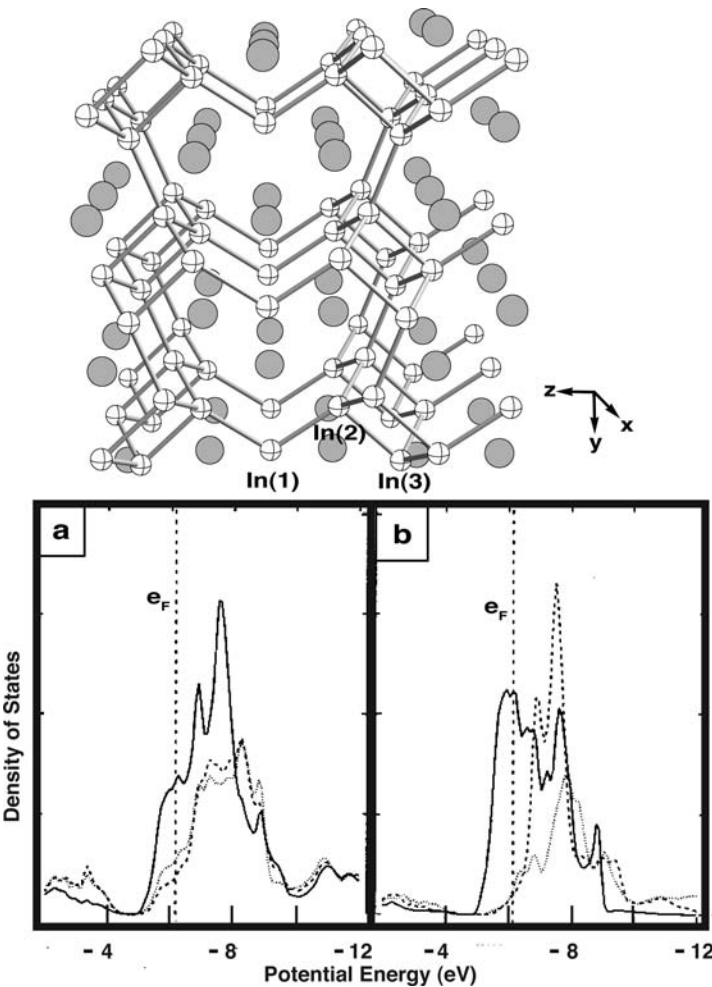
- Construct the MOs for  $(\eta^6\text{-benzene})_2\text{Ga}^+$  at the  $D_{6h}$  geometry using the  $\pi$  orbitals of benzene and the valence AOs of Ga.
- Draw a Walsh diagram for bending to a  $C_{2v}$  geometry.



**14.15.** A novel  $\text{Te}_4$  polymer has recently been prepared by Ahmed et al. [63]. An electron precise compound has the formula  $\text{Te}_4^{2+}$  and is a semiconductor. The material (shown below)  $\text{Te}_4^{1.78}$  is a good metal and, in fact, undergoes a superconducting transition at 7.2 K. The orbitals of  $D_{4h}\text{ Te}_4^{2+}$  are easy to derive. Look back at Problem 11.4 where the orbitals of  $\text{Al}_4^{2-}$  were constructed. There is one important difference here— $\pi$  bonding in  $\text{Te}_4^{2+}$  is going to be much weaker, therefore the MO sequence in terms of energy will be:  $2e_u > 1b_{2u} > 1e_g > 1e_u > 1a_{2u}$ . Sketch out the band structure for these orbitals from  $\Gamma$  to  $\pi/a$  and show where the Fermi level is likely to be, given the experimental data, for these two compounds.



**14.16.** Seo and Corbett [64] reported the structure and bonding of  $\text{Sr}_3\text{In}_5$ . The structure consists of ladders of  $\text{In}_4$  squares arranged in a staircase fashion linked by two-coordinate In atoms. The structure and several density of states projections around the Fermi level are shown below:



Here  $\text{In}(1)$  is two-coordinate while  $\text{In}(2)$  and  $\text{In}(3)$  are four-coordinate (there are two  $\text{In}(2)$  and  $\text{In}(3)$  sites for every single  $\text{In}(1)$  atom). As the density of states plots show, this compound is metallic. A plot of the In populations is shown on the left side where the solid line, dashed line and dotted line refers to the  $\text{In}(1)$ ,  $\text{In}(2)$ , and  $\text{In}(3)$  atoms, respectively. The DOS plot on the right side shows the projected contributions to the  $x$  (solid line),  $y$  (dashed), and  $z$  (dotted)  $p$  AO's of the In atoms. How does this compound fit into the Zintl-Klemm counting scheme? What do the crystal orbitals around the Fermi level look like?

---

**REFERENCES**

---

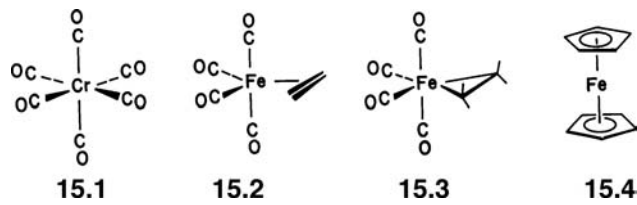
1. R. E. Rundle, *J. Am. Chem. Soc.*, **85**, 112 (1963).
2. G. C. Pimentel, *J. Chem. Phys.*, **19**, 446 (1951).
3. D. L. Cooper, T. P. Cunningham, J. Gerratt, P. B. Karadakov, and M. Rainmondi, *J. Am. Chem. Soc.*, **116**, 4414 (1994); E. Magnusson, *J. Am. Chem. Soc.*, **112**, 7940 (1990), see, for an extensive review of previous calculations; A. E. Reed and P. von R. Schleyer, *J. Am. Chem. Soc.*, **112**, 1434 (1990).
4. For a historical perspective on the term hypervalent, see W. B. Jensen, *J. Chem. Ed.*, **83**, 1751 (2006).
5. M. Atanasov and D. Reinen, *J. Am. Chem. Soc.*, **124**, 6693 (2002).
6. M. Kaupp, Ch. Van Wüllen, R. Franke, F. Schmitz, and W. Kutzelnigg, *J. Am. Chem. Soc.*, **118**, 11939 (1996); D. A. Dixon, W. A. de Jong, K. A. Peterson, K. O. Christe, and G. J. Schrobilgen, *J. Am. Chem. Soc.*, **127**, 8627 (2005).
7. K. S. Pitzer, *Acc. Chem. Res.*, **12**, 271 (1979).
8. R. J. Gillespie, *Molecular Geometry*, Von Nostrand-Rheinhold, London (1972).
9. R. J. Gillespie and E. A. Robinson, *Angew. Chem. Int. Ed.*, **35**, 495, (1996); R. J. Gillespie and P. L. A. Popelier, *Chemical Bonding and Molecular Geometry*, Oxford University Press, Oxford (2001).
10. For larger clusters, see, for example, K. D. Bell, R. S. Berry, R. E. Kunz, F.-Y. Len, A. Proykova, and D. J. Wales, *Science*, **271**, 5251 (1996).
11. G. W. Drake, D. A. Dixon, J. A. Sheehy, J. A. Boatz, and K. O. Christe, *J. Am. Chem. Soc.*, **120**, 8392 (1998) and references therein.
12. K. O. Christe, E. C. Curtis, D. A. Dixon, H. Mercier, J. C. P. Sanders, and G. J. Schrobilgen, *J. Am. Chem. Soc.*, **113**, 3351 (1991); K. O. Christe, W. W. Wilson, G. W. Drake, D. A. Dixon, J. A. Boatz, and R. Z. Gnann, *J. Am. Chem. Soc.*, **120**, 4711 (1998).
13. A. G. Robiette, R. H. Bradley, and P. N. Prier, *Chem. Commun.*, 1567 (1971).
14. D. F. Smith, *J. Chem. Phys.*, **21**, 609 (1953); D. W. Magnusson, *J. Chem. Phys.*, **27**, 223 (1957).
15. E. M. Archer and T. G. D. van Schalkwyk, *Acta Crystallogr.*, **6**, 88 (1953).
16. I. Minkin and R. M. Minyaev, *Zh. Org. Khim.*, **13**, 1129 (1977), Eng. trans., **13**, 1039 (1977).
17. R. E. Rosenfield, Jr., R. Parthasarathy, and J. D. Dunitz, *J. Am. Chem. Soc.*, **99**, 4860 (1977).
18. W. M. Tolles and W. D. Gwinn, *J. Chem. Phys.*, **36**, 1119 (1962); K. Kimura and S. H. Bauer, *J. Chem. Phys.*, **39**, 3172 (1963).
19. B. J. Kennedy, C. J. Howard, K. S. Knight, Z. Zhang, and Q. Zhou, *Acta Crystallogr.*, **62B**, 537 (2006).
20. L. F. Schneemeyer, J. K. Thomas, T. Siegrist, B. Batlogg, L. W. Rupp, R. L. Opila, R. J. Cava, and D. W. Murphy, *Nature*, **335**, 421 (1988).
21. Y. Y. Wang and P. D. Han, *Phys. Rev. B*, **67**, 24505 (2003).
22. D. G. Hinks, D. R. Richards, B. Drabowski, D. T. Marx, and A. W. Mitchell, *Nature*, **335**, 419 (1988).
23. G. A. Papoian and R. Hoffmann, *Angew. Chem. Int. Ed.*, **39**, 2408 (2000).
24. W. Mueller-Wiking, *Z. Naturforsch. B*, **32**, 357 (1977).
25. B. Eisenmann, N. May, W. Müller, H. Schäfer, *Z. Naturforsch.*, **27b**, 1155 (1972).
26. J. T. Vaughey, G. J. Miller, S. Gravelle, E. A. Leon-Escamilla, and J. D. Corbett, *J. Solid State Chem.*, **133**, 347 (1997).
27. For calculations on the energy difference see C. Zheng, *J. Am. Chem. Soc.*, **115**, 1047 (1993).
28. B. Eisenmann and H. Schäfer, *Z. Anorg. Allg. Chem.*, **403**, 163 (1974).
29. I. F. Hewaidy, E. Busmann, and W. Klemm, *Z. Anorg. Allg. Chem.*, **328**, 283 (1964).
30. M. G. Morgan, M. Wang, W. Y. Chan, and A. Mar, *Inorg. Chem.*, **42**, 1549 (2003).
31. S. Ponou and T. F. Fässler, *Inorg. Chem.*, **43**, 6124 (2004).
32. S.-J. Kim, S. Ponou, and T. F. Fässler, *Inorg. Chem.*, **47**, 3594 (2008).

33. W. Müller and H. Schäfer, *Z. Naturforsch.*, **28b**, 246 (1973).
34. A. Ienco, R. Hoffmann, and G. Papoian, *J. Am. Chem. Soc.*, **123**, 2317 (2001).
35. V. I. Zaremba, D. Kaczorowski, G. P. Nychyporuk, U. C. Rodewald, and R. Pöttgen, *Solid State Sci.*, **6**, 1301 (2004).
36. (a) W. Choe, G. J. Miller, and E. M. Levin, *J. Alloys Compd.*, **329**, 121 (2001). (b) Wang, Tang and Guloy, *unpublished observations*.
37. M.-H. Whangbo, C. Lee, and J. Köhler, *Angew. Chem. Int. Ed.*, **45**, 7465 (2006).
38. P. Schwerdtfeger, P. D. W. Boyd, T. Fischer, P. Hunt, and M. Liddell, *J. Am. Chem. Soc.*, **116**, 9620 (1994).
39. J. J. Lehman and E. Goldstein, *J. Chem. Ed.*, **73**, 1096 (1996).
40. I. H. Krouse, C. Hao, C. E. Check, K. C. Lobring, L. S. Sunderlin, and P. G. Wenthold, *J. Am. Chem. Soc.*, **129**, 846 (2007).
41. P. Boldrini, R. J. Gillespie, P. R. Ireland, and G. J. Schrobilgen, *Inorg. Chem.*, **13**, 1690 (1974).
42. J. B. Collins, P. v. R. Schleyer, J. S. Binkley, J. A. Pople, and L. Radom, *J. Am. Chem. Soc.*, **98**, 3436 (1976); M. Jungen and R. Ahlrichs, *Mol. Phys.*, **28**, 367 (1974).
43. C. J. Marsden and B. A. Smart, *Aust. J. Chem.*, **47**, 1431 (1994).
44. M. Mauksch and P. v. R. Schleyer, *Inorg. Chem.*, **40**, 1756 (2001).
45. W. G. Klemperer, J. K. Kreiger, M. D. McCreary, E. L. Muettterties, D. D. Traficante, and G. M. Whitesides, *J. Am. Chem. Soc.*, **97**, 7023 (1975).
46. K. W. Hansen and L. S. Bartell, *Inorg. Chem.*, **4**, 1775 (1965); R. Hoffmann, J. M. Howell, and E. L. Muettterties, *J. Am. Chem. Soc.*, **94**, 3047 (1972).
47. M. F. Klapdor, H. Beckers, W. Poll, and D. Mootz, *Z. Naturforsch.*, **52b**, 1051 (1997).
48. J. C. Martin, *Science*, **221**, 509 (1983); K. Akiba, M. Yamashita, Y. Yamamoto, and S. Nagase, *J. Am. Chem. Soc.*, **121**, 10644 (1999).
49. G. Sini, G. Ohanessian, P. C. Hiberty, and S. S. Shaik, *J. Am. Chem. Soc.*, **112**, 1408 (1990).
50. A. P. Bento and F. M. Bickelhaupt, *J. Org. Chem.*, **72**, 2201 (2007).
51. A. Caligiana, V. Aquilanti, R. Burel, N. C. Handy, and D. P. Tew, *Chem. Phys. Lett.*, **369**, 335 (2003).
52. X. Huang, A. B. McCoy, J. M. Bowman, L. M. Johnson, C. Savage, F. Dong, and D. J. Nesbitt, *Science*, **311**, 60 (2006).
53. K. C. Thompson, D. L. Crittenden, and M. J. T. Jordan, *J. Am. Chem. Soc.*, **127**, 4954 (2005); S. X. Tian and J. Yang, *J. Phys. Chem. A*, **111**, 415 (2007) and references therein.
54. E. del Rio, M. I. Menendez, R. Lopez, and T. L. Sordo, *Chem. Commun.*, 1779 (1997).
55. D. W. Boo and Y. T. Lee, *J. Chem. Phys.*, **103**, 514 (1995).
56. G. A. Olah and G. Rasul, *Acc. Chem. Res.*, **30**, 245 (1997) and references therein.
57. A. Görling, N. Rösch, D. E. Ellis, and H. Schmidbaur, *Inorg. Chem.*, **30**, 3986 (1991); H. Schmidbaur, *Chem. Soc. Rev.*, **24**, 391 (1995).
58. P. Pykkö and T. Tamm, *Organometallics*, **17**, 4842 (1998).
59. D. M. P. Holland, M. A. MacDonald, M. A. Hayes, P. Baltzer, L. Karlsson, M. Lundqvist, B. Wannberg and W. von Niessen, *Chem. Phys.*, **188**, 317 (1994).
60. G. Trinquier and R. Hoffmann, *J. Phys. Chem.*, **88**, 6696 (1984).
61. E. Mitscherlich, *Ann. Phys. Chem.*, **29**, 221 (1833).
62. J. M. Slattery, A. Higelin, T. Bayer and I. Krossing, *Angew. Chem. Int. Ed.*, **49**, 3228 (2010).
63. E. Ahmed, J. Beck, J. Daniels, T. Doert, S. J. Eck, A. Heerwig, A. Isaeva, S. Lindin, M. Ruck, W. Schnelle and A. Stankowski, *Angew. Chem. Int. Ed.*, **51**, 8106 (2012).
64. D. K. Seo and J. D. Corbett, *J. Am. Chem. Soc.*, **123**, 4512 (2001).

# **Transition Metal Complexes: A Starting Point at the Octahedron**

## **15.1 INTRODUCTION**

Apart from a brief digression on hypervalent molecules in Chapter 14, we have only considered molecules with coordination numbers one through four. The geometries, or more precisely, the angles around the central atom of these  $AH_n$  building-block fragments were small in number and fell into rather well-defined classes. We have also utilized a small “basis set” of atomic  $s$  and  $p$  orbitals to describe their bonding. In the transition metal field, coordination numbers of two through eight are common. There are also a richer variety of structural types that are found for these molecules. Many times it is not at all obvious as to whether a compound should be viewed as a member of one class or another. To make matters worse, the coordination number of a metal, particularly, in the organometallic domain is not always uniquely defined. For example  $\text{Cr}(\text{CO})_6$ , **15.1**, is clearly an octahedron.



There are two alternatives for ethylene- $\text{Fe}(\text{CO})_4$ . One might consider it as a trigonal bipyramidal, **15.2**, or as an octahedral complex, **15.3**. Related to this issue is whether one regards the compound as an olefin–metal (**15.2**) or metallacyclopropane (**15.3**).

*Orbital Interactions in Chemistry*, Second Edition.

Thomas A. Albright, Jeremy K. Burdett, and Myung-Hwan Whangbo.

© 2013 John Wiley & Sons, Inc. Published 2013 by John Wiley & Sons, Inc.

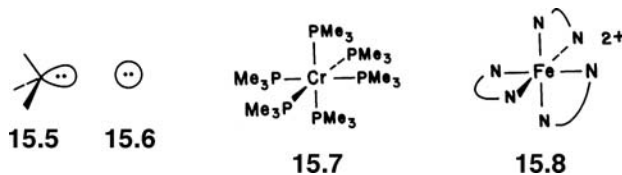
complex. In fact, there are two basic geometries for an  $ML_5$  complex: the trigonal bipyramidal and square pyramid. If we insist that the ethylene ligand in ethylene-Fe( $\text{CO}$ )<sub>4</sub> occupies one coordination site, it falls into the trigonal bipyramidal class. But many  $ML_5$  compounds geometrically lie somewhere between the idealized trigonal bipyramidal and the square pyramid. Ferrocene, **15.4**, is another common example of the coordination number problem. Is it two coordinate, as shown in **15.4**, or ten coordinate? In actual fact, it is better described as a six-coordinate octahedron! We see in Chapters 20 and 21 that the cyclopentadienyl group effectively utilizes three coordination sites.

Part of this complexity is a result of the fact that the metal utilizes five  $d$  as well as its  $s$  and  $p$  atomic functions to bond with the surrounding ligands, but the reader should not despair. Our focus will naturally be concentrated on the metal-based orbitals. However, all nine atomic  $s$ ,  $p$ , and  $d$  functions will rarely be needed. As in the preceding chapters, those relationships, and there are many of them, that bridge the worlds of organic/main group chemistry to inorganic/organometallic chemistry will be highlighted. Actually, structural diversity is an added bonus. Different vantage points can be exploited when a problem is analyzed. Changes in structure can certainly modify reactivity, so too will oxidations or reductions and fine-tuning the electron density at the metal by varying the electronic properties of the ligands. All of this makes life more interesting to the chemist.

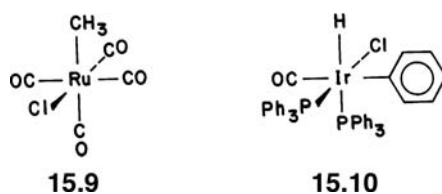
This chapter and the next introduce the use of  $d$  orbitals in transition metal complexes. First of all, we build up the orbitals of octahedral  $ML_6$  and square planar  $ML_4$  complexes. These molecular levels will be used to develop the orbitals of  $ML_n$  fragments, which are the topic of Chapters 17–20, hence considerable time will be spent on this aspect. How the octahedral splitting pattern and geometry are modified by the numbers of electrons and the electronic nature of the ligands is also undertaken.

## 15.2 OCTAHEDRAL $ML_6$

Let us start with octahedral  $ML_6$ . For the moment L will be a simple a donor ligand. In other words, L has one valence orbital that is pointed toward the metal and there are two electrons in it. Examples are the lone pair of a phosphine, amine, alkyl group, **15.5**, or even the  $s$  orbital of a hydride, **15.6**. Some  $ML_6$  examples are Cr(PMe<sub>3</sub>)<sub>6</sub>, **15.7**, or the



tris(ethylenediamine)Fe<sup>2+</sup> complex, **15.8** (here the ethylenediamine group is H<sub>2</sub>NCH<sub>2</sub>CH<sub>2</sub>NH<sub>2</sub>). What we are initially concerned with are the metal-ligand  $\sigma$  orbitals;  $\pi$  bonding is reserved for the next section. In this regard, the pattern that is constructed will not change much for Cr(CO)<sub>6</sub>, **15.1**, CH<sub>3</sub>Ru(CO)<sub>4</sub>Cl, **15.9**, or even the more complicated **15.10**. The  $\pi$  and  $\pi^*$  levels of CO and the phenyl group in



**15.10** along with the chlorine lone pairs can be introduced into the electronic picture at a later stage of the analysis. While the symmetry of **15.9** and **15.10** is low, there is an effective pseudosymmetry that the transition metal experiences in the  $\sigma$  levels which is octahedral. What is important in **15.7–15.10** is that there are six lone pairs directed toward the metal in an octahedral arrangement which brings us back to the ubiquitous L groups. They will be utilized throughout the remaining chapters when we want to present a generalized treatment of a problem.

Figure 15.1 illustrates one approach to construction of the molecular orbitals (MOs) of  $ML_6$ . The nine atomic orbitals of a transition metal are shown on the left side of the interaction diagram. Notice, in particular, that the d functions are drawn in their familiar form and correspond to the coordinate system at the top center of the

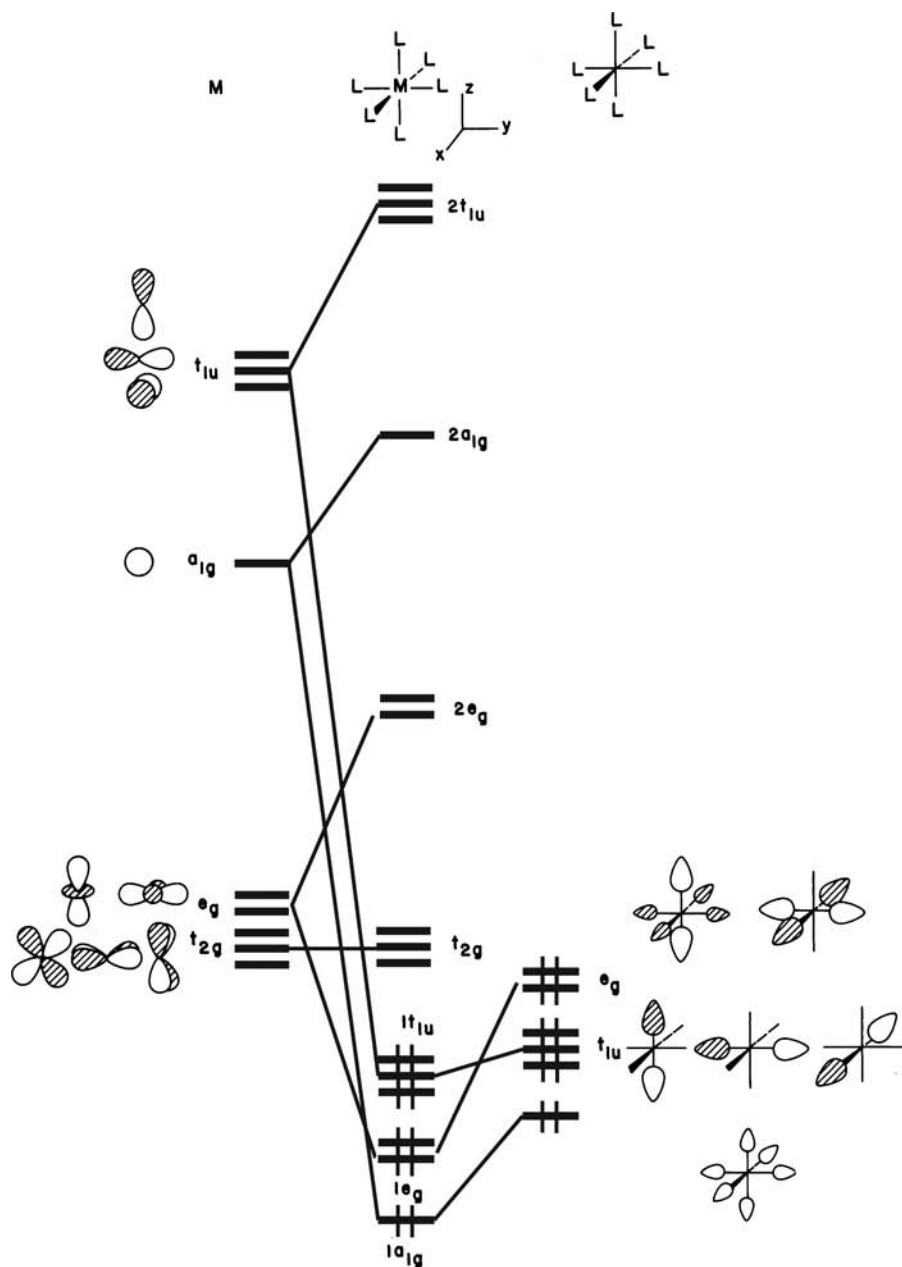


**FIGURE 15.1**

Development of the molecular orbitals of an octahedral  $ML_6$  complex where L is an arbitrary  $\sigma$  donor ligand.

figure. The  $z^2$  (or more precisely the  $3z^2 - r^2$ ) and  $x^2 - y^2$  functions<sup>1</sup> are of  $e_g$  symmetry and  $xy, yz, xz$  transform as a  $t_{2g}$  set. At higher energies lie the metal s and p levels. Recall that we are concerned only with the valence levels, so that the inner shells of s and p electrons on the metal are neglected. The symmetry-adapted linear combinations of the ligand orbitals are shown on the right side of Figure 15.1. There are six and their relative ordering is set by the number of nodes within each member (see Section 14.1). There is none in  $a_{1g}$ ,  $t_{1u}$  has one, and  $e_g$  contains two nodes. The  $a_{1g}$  and  $t_{1u}$  combinations match with metal s and p so they are stabilized, yielding the molecular levels  $1a_{1g}$  and  $1t_{1u}$ . The  $e_g$  ligand set is stabilized by metal  $z^2$  and  $x^2 - y^2$  that gives the molecular  $1e_g$  levels. The ordering of these M—L bonding orbitals is exactly the same as that for  $AH_6$  (Section 14.1) with the exception that  $1e_g$  was left nonbonding in the main group system. In this case, the  $z^2$  and  $x^2 - y^2$  d orbitals have an excellent overlap with the  $e_g$  ligand set, and there is a small energy gap between them. Hence, the  $1e_g$  combination is stabilized greatly. Notice that it lies lower in energy than the  $1t_{1u}$  set. The central atom s and p atomic orbital (AO) set is well separated from the “ligand”  $a_{1g}$ ,  $t_{1u}$ , and  $e_g$  sets in  $ML_6$ , unlike the case of  $AH_6$ . Here, the six M—L bonding orbitals are concentrated at the ligands. There are also six corresponding M—L antibonding levels:  $2e_g$ ,  $2a_{1g}$ , and  $2t_{1u}$  which are heavily weighted on the metal atom. Left behind is  $t_{2g}$  on the metal. It is nonbonding when L is a  $\sigma$  donor; however, it will play an important role when the ligands have functions that can enter into  $\pi$  bonding with the metal. Inspection of Figure 15.1 shows that an octahedral compound is likely to be stable when  $t_{2g}$  is either completely filled or empty. The latter case is more likely for transition metals that are electropositive. For the former, one can think of the six electrons in  $t_{2g}$  as three sets of lone pairs that are localized on the metal. Together with the 12 electrons from the M—L bonding levels creates a situation where 18 valence electrons are associated with the metal.

Notice that in Figure 15.1, the metal AO's lie at a higher energy than the ligand donor functions. This is normally the case and will be a view that we shall take for the rest of the book. An actual plot of the state averaged d and s ionization potentials for the first-row transition metals [I] is given in Figure 15.2. As expected, the ionization

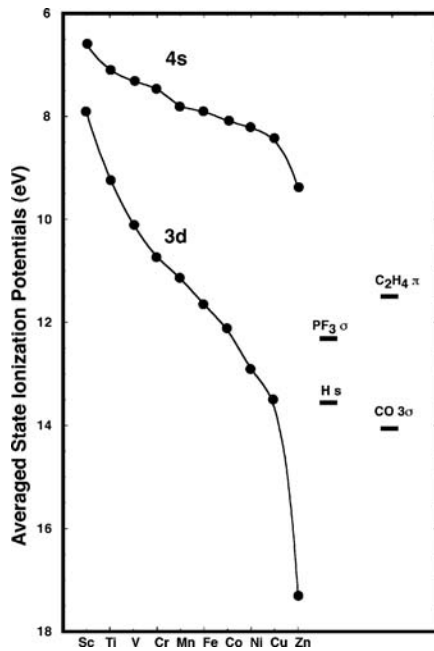


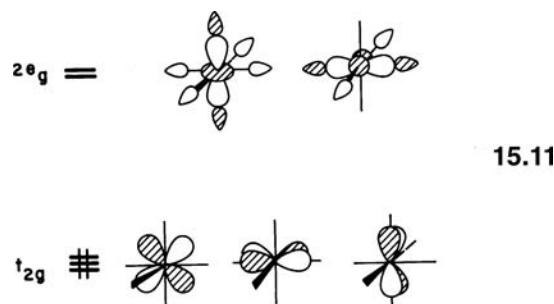
**FIGURE 15.2**

Plot of the s and d transition metal state-averaged ionization potentials. The vertical ionization potentials for some common ligands are on the right side.

<sup>1</sup> In the rest of this book, we refer to the nd AO's as  $z^2$ ,  $x^2 - y^2$ ,  $xz$ ,  $yz$ , and  $xy$ . The  $(n + 1)s$ ,  $(n + 1)p$  AO's are given as s, x, y, and z.

potentials increase on going from left to right in the periodic table, as the metal becomes more electronegative. For the second and third transition metal rows, the  $4d$  and  $5d$  orbital energies level off from Nb to Pd and Re to Pt [1a]. The leveling effect is due to the partial shielding of the  $nd$  electrons by the  $(n+1)s$  electrons. For the first transition metal row, the  $3d$  AOs are more contracted and not appreciably shielded by the  $4s$  electrons. The  $H_{ii}$  values for the  $4p$  AOs lie about 4.5 eV higher than the  $4s$  AOs (for an internally consistent set of  $d$ ,  $s$ , and  $p$   $H_{ii}$  values for the transition metals see [1b]). Notice that the  $3d$  AOs for Zn sink to a very low energy. They become core-like and it is controversial whether or not they (along with the  $4d$  and  $5d$  AOs in Cd and Hg, respectively) are significantly involved in the bonding to surrounding ligands. Vertical ionization potentials for a few common ligands are plotted on the right side of Figure 15.2. The absolute values are not critical for our qualitative discussions of the bonding in  $\text{ML}_n$  complexes. The important point is that in general the ligand orbitals used in  $\sigma$  bonding to the metal are close to, and probably a little lower in energy than, the valence metal  $d$  AOs. There certainly will be electronegativity factors that are discussed in this chapter, as well as, the following ones that create bonding, structural, and reactivity differences. The  $4d$  and  $5d$  AOs for the second- and third-row elements are more diffuse and have similar radial extent to the  $(n+1)s$  and  $(n+1)p$  AOs. On the other hand, the  $3d$  AOs for the first row are quite contracted due to the absence of  $(n-1)d$  AOs. This will also create variations.

As seen for the octahedral splitting pattern in Figure 15.1, it is the highest occupied molecular orbital ( $\text{HOMO}$ ),  $t_{2g}$ , and the lowest unoccupied molecular orbital ( $\text{LUMO}$ ),  $2e_g$ , which are the focus of our attention in the rest of this book. They are shown in 15.11. The energy gap between  $t_{2g}$  and  $2e_g$  is a function of the ligand  $\sigma$  donor strength



(in the absence of  $\pi$  effects). Raising the energy of the ligand lone pairs causes the energy gap between ligand  $e_g$  and the metal  $d$  set to diminish. Consequently, there is a stronger interaction; the antibonding  $2e_g$  set is destabilized so the  $t_{2g}$ – $2e_g$  energy gap increases. Overlap between the ligand lone pairs and metal  $e_g$  can also play an obvious role. Thus, a strong  $\sigma$  donor set of ligands creates a sizable energy gap between the molecular  $t_{2g}$  and  $2e_g$  levels. This ensures a singlet ground state (all the six electrons reside in  $t_{2g}$  for an 18-electron complex), which is called a low-spin situation 15.12, by inorganic chemists. This is the case for nearly all organometallic

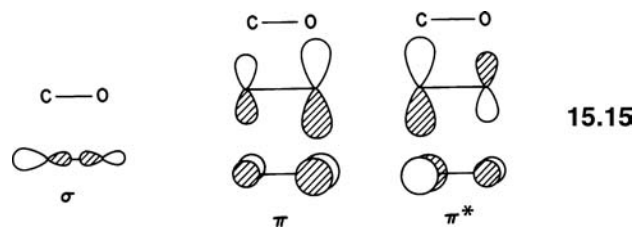


compounds. Classical coordination complexes, where  $L = \text{NH}_3, \text{H}_2\text{O}$ , halogen, and so on, sometimes behave differently. The  $t_{2g}-2e_g$  splitting is not so large because the ligands are very electronegative. Therefore, the ground state may be one that contains some spins unpaired—an intermediate spin system, **15.13**, or a maximum of unpaired spins—a high-spin system, **15.14**. The energy balance between these spin states can be formulated in the same terms as the singlet-triplet situation for organic diradical; see methylene, for example, in Section 8.8 where the  $b_2-2a_1$  energy gap was small. For coordination compounds, the  $t_{2g}-e_g$  splitting is in delicate balance with the spin pairing energies, consequently, the high-spin–low-spin energy difference is often very tiny. A change of spin states can even be induced by cooling the sample or application of mechanical stress! This is particularly true for the first transition metal row where the  $3d$  AOs are contracted and, hence, the electron–electron repulsion energy for putting two electrons in the same orbital is large (see Section 8.8). Putting more than 18 electrons into the molecular orbitals of  $\text{ML}_6$  in Figure 15.1 will cause problems. The extra electrons will be housed in  $2e_g$  which is strongly M–L antibonding. We would expect that the compounds will distort so as to lengthen the M–L distances or perhaps one or two M–L bonds might completely break. An example of this is bombardment of  $\text{Cr}(\text{CO})_6$  (an 18-electron complex) with electrons in a solid Ar matrix [2a]. Instead of isolating the 19-electron  $\text{Cr}(\text{CO})_6^-$ , the major product was found to be a 17-electron  $\text{Cr}(\text{CO})_5$  complex. But remember for the classic coordination complexes  $2e_g$  is not greatly destabilized. Electron counts at the metal which exceed 18 are possible, and population of  $2e_g$  with unpaired electrons (**15.13** and **15.14**) is frequent;  $\text{Ni}(\text{OH}_2)_6^{2+}$ , where there are two unpaired electrons in  $2e_g$ , is a well-known example. This is not to say that there will be no structural changes that accompany the population of  $2e_g$ . Structural data [2b] exist for low-spin  $\text{Co}(\text{NH}_3)_6^{3+}$  and high-spin  $\text{Co}(\text{NH}_3)_6^{2+}$ . In the former complex, the  $t_{2g}$  set is filled and  $e_g$  is empty. The Co–N bond length is  $1.94\text{\AA}$ . In the latter complex, the  $e_g$  set contains two electrons. The Co–N bond length increases to  $2.11\text{\AA}$ . When there are less than 18 electrons associated with the metal, the  $t_{2g}$  set is partially filled. This signals a Jahn–Teller (Section 7.4) or some other geometrical distortion (for a low-spin complex), which lowers the symmetry of the molecule. We will return to this problem in greater depth after substituent effects of the ligands are covered.

What will become obvious, in the next chapters, is that the primary valence orbitals that we will use are derived from  $t_{2g}, 2e_g$ , and sometimes  $2a_{1g}$  in Figure 15.1. Therefore, our basis set of orbitals will never be larger than five or six. Those orbitals are concentrated on the metal and they lie at intermediate energies. They will be the HOMOs and LUMOs in any transition metal complex. When the octahedral symmetry is perturbed by removing a ligand or distorting the geometry, the  $2a_{1g}$  and  $2t_{1u}$  orbitals may be utilized. For example, metals or  $p$  may mix into the members of  $e_g$  or  $t_{2g}$ . In other words,  $2t_{1u}$  and  $2a_{1g}$  provide a mechanism for the hybridization of the valence orbitals.

### 15.3 $\pi$ -EFFECTS IN AN OCTAHEDRON

How does the picture in Figure 15.1 change when  $\pi$  functions are added to the surrounding ligands? Let us start by replacing one of the generalized donor ligands in  $\text{ML}_6$  by a carbonyl group that yields an  $\text{ML}_5\text{CO}$  complex. CO is isoelectronic to  $\text{N}_2$ . A detailed discussion of the perturbations encountered on going from  $\text{N}_2$  to CO was given in Section 6.4. We briefly review the results. The few molecular orbitals of CO that are needed for this analysis are shown in **15.15** and contour plots of these MOs are displayed in Figure 6.8. The  $\sigma$  orbital is derived from  $2\sigma_g^+$  in  $\text{N}_2$ . It is hybridized



at carbon and will act as the  $\sigma$  donor function in a transition metal complex. Notice that the hybridization of electron density at carbon makes the CO ligand bind to the metal at the carbon end. There are also two orthogonal  $\pi$  and  $\pi^*$  levels. In  $N_2$ , they were  $\pi_u$  and  $\pi_g$ , respectively. These  $\pi$  sets intermix with the perturbation to CO so that the  $\pi$  level becomes more heavily weighted at the electronegative oxygen atom. On the other hand,  $\pi^*$  becomes concentrated at carbon. As mentioned previously, the  $\sigma$  donor orbital of CO along with the five  $\sigma$  levels of the  $L_5$  grouping produce a splitting pattern in  $ML_5CO$  analogous to that in Figure 15.1. The two members of  $2e_g$ , for example, will not be at precisely the same energy. That will depend on the relative  $\sigma$  donor strength of CO compared to whatever L is; however, there will be a close correspondence. What does change is the  $t_{2g}$  levels as shown in Figure 15.3.

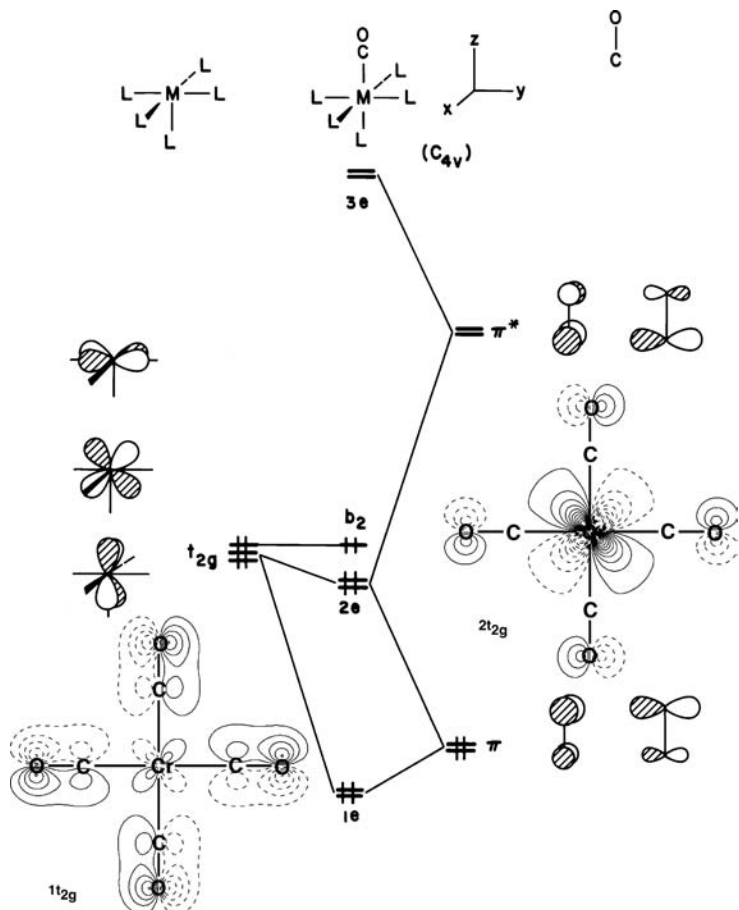
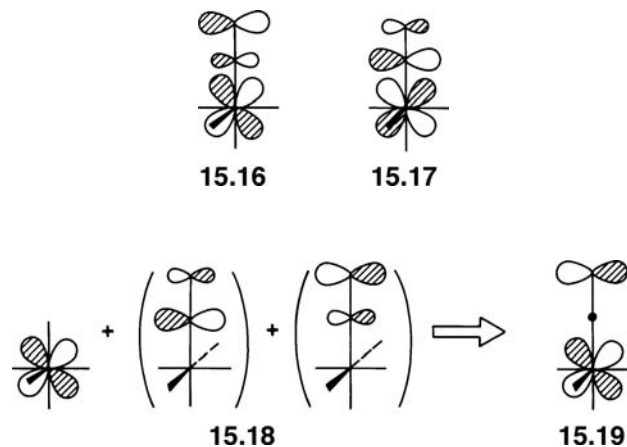


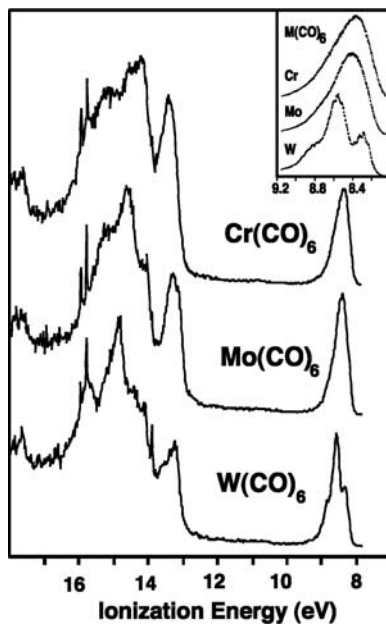
**FIGURE 15.3**

Interaction diagram for the  $\pi$  components in an  $ML_5CO$  complex where L is an arbitrary  $\sigma$  donor.

Two members of  $t_{2g}$ ,  $xz$  and  $yz$  (see the coordinate system at the top of this figure), have the correct symmetry to interact with  $\pi$  and  $\pi^*$  of CO. They become an e set in the reduced  $C_{4v}$  symmetry of the complex. The third component,  $xy$ , is left nonbonding. What results from this interaction is a typical three-level pattern, which is exactly the same as in the linear  $H_3$  (Section 3.3) or allyl (Section 12.1) systems. At low energy, the orbital labeled 1e in Figure 15.3, is primarily  $\pi$  with some  $xz$  and  $yz$  mixed in a bonding fashion. One component of 1e is shown in 15.16. At high energy 3e is primarily CO  $\pi^*$ , antibonding to  $xz$  and  $yz$ ; 15.17 shows one component. The middle level, 2e, is slightly more complicated. It is represented by metal  $xz$  and  $yz$  perturbed by CO  $\pi$  and  $\pi^*$ . Since  $\pi^*$  and  $\pi$  lie at, respectively, higher and lower energy than metal  $t_{2g}$ , 2e contains CO  $\pi^*$  mixed in a bonding way to  $xz$  and  $yz$  while CO  $\pi$  mixes in an antibonding fashion. This is expressed by 15.18 for the component of 2e in the  $yz$  plane. The net result, 15.19, shows cancellation of

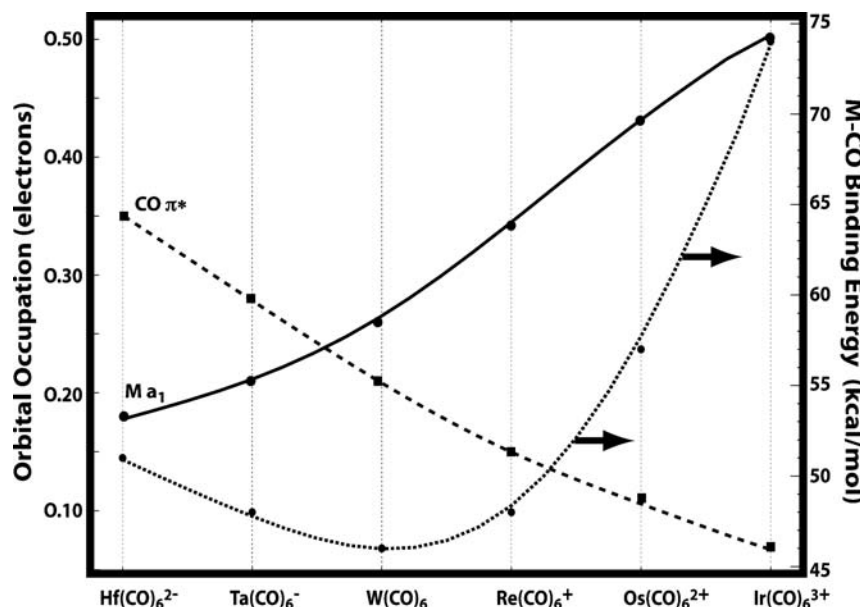


electron density at the carbon and reinforcement at oxygen. Contour plots at the ab initio 3-21G level of one component in  $1t_{2g}$  and  $2t_{2g}$  for  $Cr(CO)_6$  are also shown in Figure 15.3. The node at the carbons does *not* indicate that the  $\pi$  bonding from Cr to CO is negligible. It is a natural consequence of the mixing in 15.18. In actual fact, the interaction of CO  $\pi^*$  to metal  $xz$ ,  $yz$  is larger than that to CO  $\pi$ . CO is overall a  $\pi$  acceptor in that there is a net drift of electron density from metal  $t_{2g}$  to the carbonyl group. In essence, we are saying that the interaction of  $xz$  and  $yz$  to CO  $\pi^*$  is greater than that to CO  $\pi$ . This is due to overlap factors. Recall that there is a larger AO coefficient at carbon in  $\pi^*$  than there is in  $\pi$  and this creates the larger overlap to the  $xz$ ,  $yz$  set. It is also important to realize that energetically it is the 1e levels in Figure 15.3, which are stabilized the most. The stabilization in 2e with respect to  $t_{2g}$  will be relatively small. This can also be deduced experimentally. Figure 15.4 shows the He(I) photoelectron spectra for  $Cr(CO)_6$ ,  $Mo(CO)_6$ , and  $W(CO)_6$ <sup>3</sup>. The multiple overlapping ionizations greater than around 14 eV correspond to the CO  $\pi$  and  $\sigma$  ( $a_{1g}$  and  $e_g$ ) combinations. The one peak between 12 and 13 eV is thought to arise from ionizations from the  $t_{1u}$  combinations of CO  $\sigma$  to the metal ( $n + 1$ )  $p$  AOs (see  $1t_{1u}$  in Figure 15.1). The peaks around 8.5 eV are most interesting. These correspond to ionizations from the  $2t_{2g}$  set.  $W(CO)_6$  is split into two peaks because of spin-orbit coupling effects in W. Notice that there is very little difference in the ionization potentials; the metals have similar electronegativity and overlap with CO  $\pi^*$ . A detailed analysis [3] of the vibrational fine structure present in especially  $W(CO)_6$  shows that the W—CO bond is weakened upon ionization to the  $^2T_{2g}$  state. It is estimated that the W—C distance increases by approximately 0.1 Å. This is only consistent with the fact that CO is overall a  $\pi$  acceptor and that there is a net

**FIGURE 15.4**

He(I) photoelectron spectra for  $\text{Cr}(\text{CO})_6$ ,  $\text{Mo}(\text{CO})_6$ , and  $\text{W}(\text{CO})_6$ .

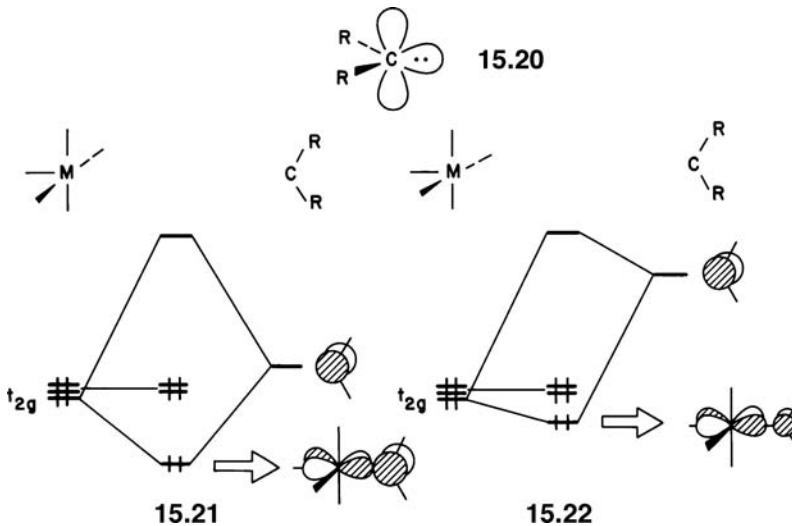
drift of electron density from metal  $t_{2g}$  to the carbonyl group. The M—CO bonding is synergistic; that is, electron density from the filled  $\sigma$  level (15.15) is transferred to empty metal  $s$ ,  $p$ , and two of the five  $d$  orbitals. Likewise, electron density from the other three  $d$  AOs, the filled metal  $t_{2g}$  set is transferred to the empty CO  $\pi^*$ . This synergism is nicely displayed by DFT calculations at the BP86 level for a series of 18-electron (all MOs through  $t_{2g}$  are filled in Figure 15.1)  $\text{M}(\text{CO})_6$  complexes by Frenking and coworkers [4]. One CO ligand was removed from each molecule, and the M—CO bonding was analyzed in terms of an energy and population analysis. Some of the results are shown in Figure 15.5. The occupation of CO  $\pi^*$  (the dashed line) falls on going from  $\text{Hf}(\text{CO})_6^{2-}$  to  $\text{Ir}(\text{CO})_6^{3+}$ . This is due to charging and electronegativity effects at the metal. In  $\text{Hf}^{2-}$ , the metal  $d$  orbitals are high in energy

**FIGURE 15.5**

$\pi^*$  orbital occupation for one CO ligand (dashed line) and the metal  $a_1$  orbital occupation for an  $\text{M}(\text{CO})_5$  fragment that interacts with CO (solid line) in a series of 18-electron  $\text{M}(\text{CO})_6$  complexes. The calculated M—CO bond energy with the scale on the right side of the plot is given by the dotted line.

and consequently close to CO  $\pi^*$  so there is a strong interaction and considerable electron density is transferred from metal to CO  $\pi^*$ . Going to Ir<sup>3+</sup> causes the metal  $d$  energies to fall and the metal  $d$ -CO  $\pi^*$  gap increases. There is then not so much mixing. We shall see in Chapter 17 that the metal  $a_1$  orbital (the solid line) in Figure 15.5 is primarily metal  $z^2$  with some  $s$  and  $p$  mixed in to hybridize it toward the missing CO ligand. Its energy will vary with respect to charging and electronegativity in the same way as metal  $t_{2g}$  does. Consequently, on the left side of Figure 15.5, the gap between metal  $a_1$  and  $\sigma$  CO is large so there is not much interaction. However, the gap becomes smaller moving to the right and the occupation of metal  $a_1$  becomes larger. The calculated M—CO bond energy, given by the dotted line with the energy scale listed on the right side of the plot, is a reflection of both interactions. A minimum value of the bond energy is obtained in the middle of this series and it peaks at either end where one of the two interactions is maximized. A statistical analysis has been made of over 20,000 X-ray structures that contain CO bonded to a transition metal [5]. As expected, when the M—C bond distance decreases, the C—O distance elongates. The gradient of these curves is different on going from one metal to the next which as a consequence of the differing importance of donation from CO  $\sigma$  which does not change the C—O distance as strongly as donation into  $\pi^*$  does.

When the ligand has only one  $\pi$  acceptor function, one component of  $t_{2g}$  is stabilized. A case in point is the carbene ligand, **15.20**; it has a filled  $\sigma$  donor and empty  $\pi$  acceptor function (Section 8.8) which is available for bonding to one member of the  $t_{2g}$  set. When the energy gap and overlap to  $t_{2g}$  is favorable, there



is a strong interaction, **15.21**. A good bit of electron density is transferred from metal  $t_{2g}$  to the carbene. The carbene carbon becomes nucleophilic (alternatively one could imagine that those two electrons originally came from a carbanionic group and are partially donated to an empty member of  $t_{2g}$ ). When the interaction is not so strong—this occurs when the metal is more electronegative or there are other  $\pi$  acceptor ligands so that the energy gap between the metal  $t_{2g}$  and the carbene  $p$  AO is large—the situation in **15.22** is obtained. The carbene carbon remains electrophilic [3]. Two computational examples illustrate this situation. Figure 15.6 shows the contour plots for the resultant  $\pi$  and  $\pi^*$  orbitals in two carbene complexes. These are DFT calculations at the B3LYP level with a double-zeta basis. On the left side of the figure, there are the two MOs for a prototypical carbene,  $\text{CH}_2\text{Cr}(\text{CO})_5$ , of the type first prepared by Fischer. It is apparent in Figure 15.6a that the  $\pi$  orbital

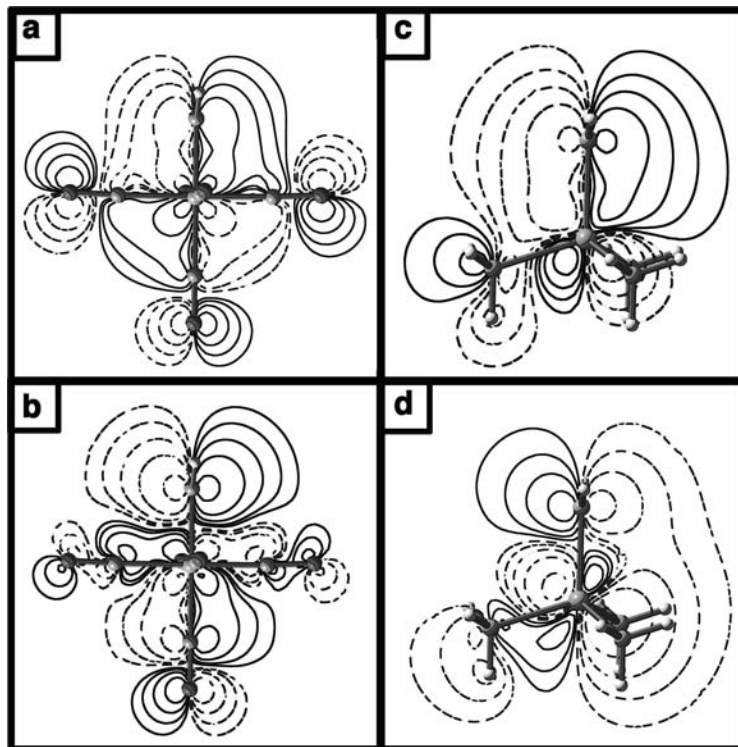
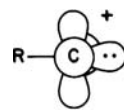


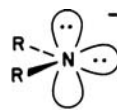
FIGURE 15.6

Contour plots of the  $\pi$  and  $\pi^*$  orbitals in  $\text{CH}_2\text{Cr}(\text{CO})_5$ , (a) and (b), respectively, along with the corresponding orbitals in  $\text{CH}_2\text{Ta}(\text{CH}_3)_3$ , (c) and (d), respectively.

has significant CO  $\pi^*$  character built into it. Thus, the coefficient on the carbene carbon is small, contrasted with the situation in  $\pi^*$ , see Figure 15.6b. It is the large coefficient in the LUMO that makes the carbene electrophilic. We are not aware of a simple nucleophilic carbene based on octahedral coordination, but there are excellent examples prepared by Schrock which are tetrahedral or five coordinate complexes. The  $\pi$  and  $\pi^*$  MOs are shown in Figure 15.6c and d, respectively. The example here is  $\text{CH}_2\text{Ta}(\text{CH}_3)_3$ . We shall see in the next chapter that the three analogs to the octahedral  $t_{2g}$  set lie higher in energy and are not rigorously nonbonding to the ligand  $\sigma$  set. The result is then analogous to that given by 15.21. There is a large coefficient on the carbene carbon in the filled  $\pi$  MO, Figure 15.6c, and a smaller one in  $\pi^*$ , Figure 15.6d. Thus,  $\text{CH}_2\text{Ta}(\text{CH}_3)_3$  is expected to be a good nucleophile at the carbene carbon. Related to the carbenes are carbyne ligands, 15.23. Now there are two orthogonal  $\pi$  acceptor functions and one hybrid  $\sigma$  donor.



15.23



15.24

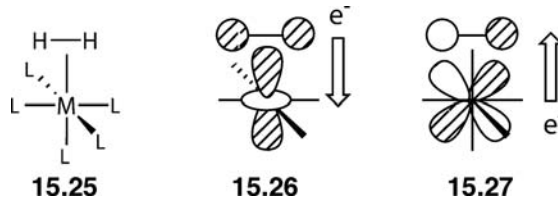
Taking the ligand to be positively charged stresses the analogy to the carbene case. The two  $t_{2g}$  derived metal orbitals interact with the empty  $p$  AOs on the carbyne. Consequently, there is a sizable splitting between the stabilized  $t_{2g}$  members and the one that is left nonbonding [7]. A good  $\pi$  donor ligand will contain a high-lying filled  $\pi$  orbital. It will destabilize one or two components of  $t_{2g}$ . Examples of  $\pi$  donor ligands are amido groups, 15.24, or the halogens where there are two filled  $p$  orbitals. Many ligands have both  $\pi$  acceptor and  $\pi$  donor functions, for example, the  $\pi^*$  and  $\pi$  orbitals in CO, N<sub>2</sub>, NO, and RNC. A detailed theoretical investigation of  $\pi$  acceptor

**TABLE 15.1** Calculations of a Series of L—W(CO)<sub>5</sub> Complexes

L	BE (kcal/mol)	D (e <sup>-</sup> )	BD (e <sup>-</sup> )	Method
<sup>+</sup> NO	109	0.12	0.38	CCSD(T)
CH <sub>2</sub>	91	0.31	0.28	CCSD(T)
CO	46	0.46	0.25	B3LYP
C <sub>2</sub> H <sub>2</sub>	33	0.54	0.22	B3LYP
C <sub>2</sub> H <sub>4</sub>	28	0.50	0.18	B3LYP
N <sub>2</sub>	24	0.13	0.13	B3LYP
NH <sub>3</sub>	36	0.27	-0.02	B3LYP
OH <sub>2</sub>	26	0.25	-0.01	B3LYP
PM <sub>3</sub>	44	0.53	0.13	BP86
PCl <sub>3</sub>	29	0.40	0.20	BP86
H <sub>2</sub>	16	0.35	0.13	CCSD(T)

BE is the bond dissociation energy, D is the number of electrons donated from the lone pair of the ligand to W(CO)<sub>5</sub>, and BD is the number of electrons donated from the W(CO)<sub>5</sub> to the ligand  $\pi^*$ .

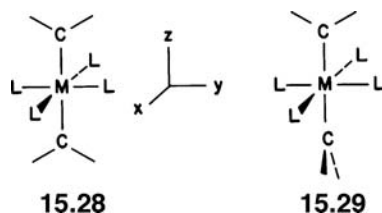
and donor effects for several ligands has been given by Ziegler and Rauk [8]. A more recent extensive survey has been undertaken by Frenking and coworkers [9]. Their computational results are given in Table 15.1, which are both coupled cluster, CCSD (T) and hybrid DFT at the B3LYP and BP86 levels for a series of L-W(CO)<sub>5</sub> compounds. Here BE is the energy required to dissociate L from L-W(CO)<sub>5</sub>. D and BD are derived from a population analysis where the former measured the amount of electron donation from the ligand  $\sigma$  orbital to W(CO)<sub>5</sub> and BD is the amount of backdonation from the W(CO)<sub>5</sub> “t<sub>2g</sub>” set to the ligand in a  $\pi$  fashion. For the isoelectronic series <sup>+</sup>NO, CO, and N<sub>2</sub>, CO is by far the strongest  $\sigma$  donor ligand because of energy gap and overlap factors. The 3 $\sigma$  MO lies highest in energy and has the largest coefficient on the coordinated atom because of electronegativity. On the other hand, <sup>+</sup>NO is the best  $\pi$  acceptor ligand. The  $\pi^*$  MO lies much lower in energy. The calculated binding energy is a balance of both factors. It appears that the major source of bonding in <sup>+</sup>NO is via  $\pi^*$ , whereas, NH<sub>3</sub> and OH<sub>2</sub> (and probably better yet, <sup>-</sup>CH<sub>3</sub>) only use the  $\sigma$  system. Notice that the two phosphines have a significant amount of backbonding associated with them. This is *not* due to M—P d <sub>$\pi$</sub> —d <sub>$\pi$</sub>  bonding as has been unfortunately claimed in many inorganic textbooks. Referring back to **10.67–10.69** and the discussion around them, the PR<sub>3</sub> group has a low-lying set of  $\sigma^*$  orbitals which are used as  $\pi$  acceptors rather than d AOs on phosphorus. We emphasize that this has been experimentally established [10] for a series of metal phosphine complexes. The last entry, the dihydrogen ligand, merits some discussion. Depending on the metal and the type of surrounding ligands, metal—H<sub>2</sub> complexes, **15.25**, can be isolated [11]. The bonding can be described in a fashion



similar to the bonding in M—CO complexes. Electron donation occurs from H<sub>2</sub>  $\sigma$  to an empty metal-centered orbital. In the case of an octahedral complex, the metal orbital will be one member of the 2e<sub>g</sub> set, **15.26**. Backdonation is represented by **15.27** where electron density from one component of the metal t<sub>2g</sub> set flows into H<sub>2</sub>  $\sigma^*$ . The balance between donation and backdonation is given by whether the

surrounding ligands are  $\sigma$  donors, for example,  $\text{PR}_3$  or  $\pi$  acceptors [12]. In 15.26, electron density is removed from the H—H bonding orbital; in 15.27 electron density increases in the H—H antibonding orbital. Consequently, when metal–hydrogen bonding increases, the H—H bonding energy decreases with an increase in the H—H distance. At some point, the H—H interaction becomes small enough so that the complex may be viewed as a metal dihydride rather than a dihydrogen complex. Hence, there is a spectrum of H—H distances from  $\sim 0.8$  to  $1.5\text{ \AA}$  that have been found for the dihydrogen ligand [11].

The substitution of two or more  $\pi$  acceptor ligands at the metal will stabilize two or all the three members of the metal  $t_{2g}$  set. For example, in  $\text{Cr}(\text{CO})_6$ , symmetry-adapted linear combinations of the 12  $\pi^*$  levels yields one of  $t_{2g}$  symmetry. Therefore, metal  $xz$ ,  $yz$ , and  $xy$  are stabilized. An interesting problem arises when there are two  $\pi$  acceptor ligands, say trans to one another, and each ligand has only one acceptor function. A hypothetical case is a trans  $(\text{R}_2\text{C})_2\text{ML}_4$  complex [13]. The particular question to be addressed is the  $D_{2h}$  conformation, 15.28, more stable than the  $D_{2d}$  form, 15.29 for an 18-electron complex? The  $\sigma$  levels in 15.28 and 15.29



will be at identical energies. The splitting pattern will strongly resemble that for an octahedron in Figure 15.1. The difference lies in the way the empty  $p$  functions of the carbene backbond to the metal  $t_{2g}$  set. In the  $D_{2h}$  conformation of 15.28, both carbenes lie in the  $yz$  plane so both the  $p$  orbitals will interact with metal  $xz$ . In the  $D_{2d}$  geometry of 15.29, the carbenes are orthogonal. One  $p$  function will overlap with  $xz$  and the other with  $yz$ . Figure 15.7 illustrates these differences in  $\pi$  bonding by means

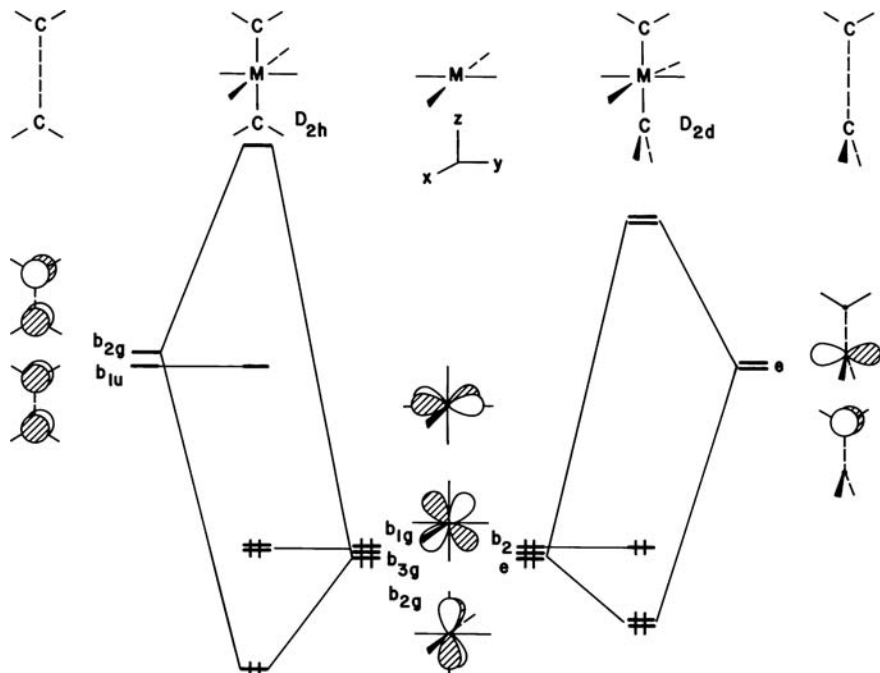


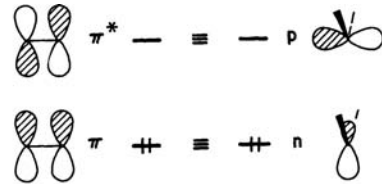
**FIGURE 15.7**

Interaction diagrams for two possible conformations in a trans- $(\text{R}_2\text{C})_2\text{ML}_4$  complex. Only the  $\pi$  interactions are illustrated.

of interaction diagrams. Let us start with the  $D_{2h}$  geometry. In-phase and out-of-phase combinations of the carbene  $p$  functions are taken on the left side of the figure. They are of  $b_{1u}$  and  $b_{2g}$  symmetry, respectively. They will be nearly degenerate in energy since the carbenes are far from each other. The  $b_{2g}$  combination has the same symmetry and will overlap with metal  $xz$ . That metal orbital will then be stabilized greatly with respect to  $xy$  and  $yz$ , which are left nonbonding. Notice also that the in-phase combination,  $b_{1u}$ , of carbene  $p$  orbitals is left nonbonding. In the  $D_{2d}$  geometry of 15.29, the carbene functions transform as an  $e$  set—see the right side of Figure 15.7. They will stabilize metal  $xz$  and  $yz$ . It is clear that the interaction in the  $b_{2g}$  combination of the  $D_{2h}$  geometry will be greater than that in  $e$  for the  $D_{2d}$  case. But will it be twice as large? In that case, the energy difference between the two conformations will be zero. It turns out, and can be proven by perturbation theory arguments [13, 14], that if the energy difference between the carbene  $p$  and the metal  $d$  levels is large, the stabilization in  $b_{2g}$  is twice as large as that in the  $e$  set. However, as the energy difference becomes smaller,  $b_{2g}$  is stabilized by less than twice as much as  $e$ . Therefore, the  $D_{2d}$  conformation becomes more stable than the  $D_{2h}$  one. Two computational examples illustrate this. DFT calculations [15] on  $(CH_2)_2PtCl_4$  gave the  $D_{2d}$  structure to be 3.5 kcal/mol more stable than the  $D_{2h}$  geometry. Here, the energy gap between the carbene  $p$  and metal “ $t_{2g}$ ” combinations are large. On the other hand, in  $(CH_2)_2W(CO)_4$  the  $D_{2h}$  geometry is over 250 kcal/mol higher in energy than the  $D_{2d}$  one. This result is a general one: if two good acceptors have a choice, they will choose to interact with orthogonal donor functions. A “real” case occurs in *trans*-bis-ethylene–ML<sub>4</sub> complexes. There are two 18-electron complexes which have been shown [16] to have structure 15.30. There is also an isoelectronic dioxygen complex which has an equivalent geometry [17]. Exactly the same story occurs here. The ethylene ligand has a filled  $\pi$  and empty  $\pi^*$  orbital pointed at the



15.30

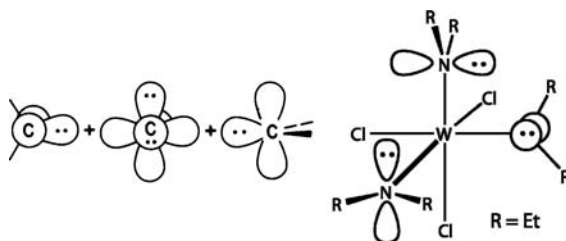


15.31

metal. This is topologically equivalent to the situation in a carbene, as indicated in 15.31. In 15.30, the two acceptor  $\pi^*$  functions backbond to orthogonal members of the metal  $t_{2g}$  set and, therefore, this geometry is more stable than one with the ethylenes oriented parallel to each other. The actual mechanism of rotation about the ethylene–metal bond in 15.30 is complicated by another electronic factor [18,19]; it is easier to see what happens in the bis-carbene complex and so we will describe what happens in that situation. Starting from the  $D_{2d}$  geometry, 15.29, rotation of both CR<sub>2</sub> units in the same direction will cause little change in the energy. This is a consequence of the fact that the  $xz$  and  $yz$  donor functions are degenerate. At 15.29 or the rotamer where both methylene groups are twisted by 90°, the two  $p$  orbitals interact with  $xz$  and  $yz$ . At intermediate geometries they will interact with linear combinations of  $xz$  and  $yz$ . Recall that any linear combination of a degenerate set yields an equivalent set, so the two stabilized metal orbitals will stay at constant energy. From another point of reference one could say that the ML<sub>4</sub> group is freely rotating with the CR<sub>2</sub> units fixed in space, orthogonal to each other. This is a little bit of an oversimplification that depends on the size of the R groups and L. In 15.29, the carbenes eclipse the M–L bonds, so there may be a steric preference for rotation by 45° to a staggered geometry. The reader should note that removing two electrons from the (R<sub>2</sub>C)<sub>2</sub>ML<sub>4</sub> complex will produce a stable

16-electron system. However, as shown in Figure 15.7, those two electrons would come from the  $xy$  orbital in the  $D_{2d}$  conformation. The  $e$  set is probably stabilized enough to give a ground state singlet. In the  $D_{2h}$  geometry,  $xy$  and  $yz$  are degenerate so a triplet state is predicted.

There are many other systems where two acceptors interact with orthogonal donors. One way to view allene is by the union of two carbenes with a central carbon atom, 15.32. The four electrons in the central carbon will artificially be placed in the two  $p$  orbitals. The  $D_{2d}$  geometry then maximizes  $\pi$  bonding if the two carbene

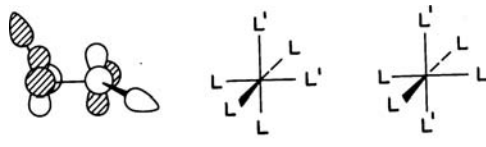


15.32

15.33

functions are orthogonal. With three  $\pi$  acceptors, one would expect that a fac arrangement would be most stable where each  $\pi$  acceptor is arranged in a way to interact with one member of the  $t_{2g}$  set. There is a closely related example. The structure of  $(Et_2N)_3WCl_3$  has been determined [20]. The amido group (in this case  $Et_2N$ ) is considered to be a  $\pi$  donor, so that there are now two electrons in the  $p$  AO, see 15.24, that can participate in  $\pi$  bonding. We shall see in the next chapter that this molecule possesses an empty  $t_{2g}$  set at the metal. The experimental geometry is shown in 15.33. The  $NR_2$  groups are oriented so that each lone pair interacts with a different member of the  $t_{2g}$  set. Using amido groups brings up a corollary to the “busy orbital” rule, namely, with the  $t_{2g}$  set filled and the presence of  $\pi$  donors, the most favored geometry is now one that uses the least number of  $t_{2g}$  orbitals. In other words, if one put an additional four electrons in the orbital interaction diagrams in Figure 15.7, the least destabilizing one will be the  $D_{2h}$  geometry. Notice that if one had only two more electrons to add in Figure 15.7, the  $D_{2h}$  conformation could have a singlet ground state and would be more stable than the  $D_{2d}$  structure with a triplet state.

This phenomenon of acceptor orbitals maximizing their interaction to orthogonal donors need not be restricted to  $\pi$  bonding. Arguments can be constructed for the orientation of  $\sigma$  bonds as well. Take  $F_2O_2$  as being divided into two  $F^+$  atoms with empty hybrids pointed at  $O_2^{2-}$ . Now  $O_2^{2-}$  has four more electrons than  $N_2$  (see Section 6.3). Therefore,  $\pi_g$  is totally filled and provides an orthogonal donor set to bond to  $F^+$  (see 15.34). Both members of  $\pi_g$  in the  $O_2^{2-}$  core are then stabilized when the  $F-O-O-F$  dihedral angle is  $90^\circ$ . That is a more stabilizing arrangement than



15.34

15.35

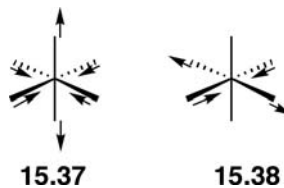
15.36

the case when the dihedral angle is  $0^\circ$  or  $180^\circ$  (a cis or trans structure), in which only one  $\pi_g$  function is stabilized. Likewise, for the transition metal complexes in 15.35 and 15.36 consider  $L'$  to be a better  $\sigma$  donor than  $L$ . In 15.35 the donor functions

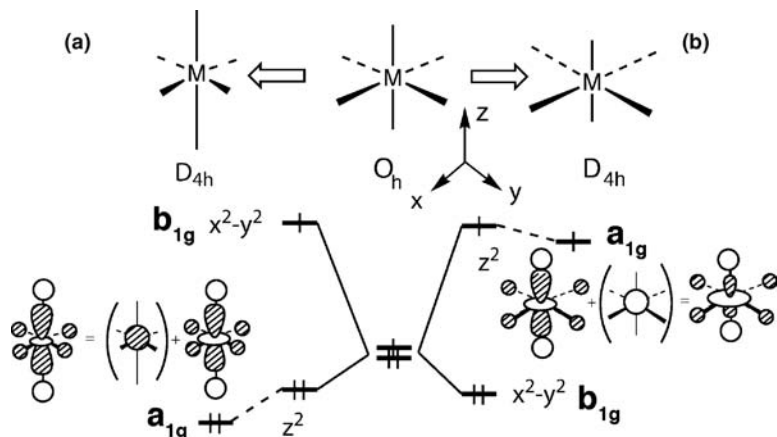
interact with  $z^2$  and  $x^2 - y^2$ , that is, both members of  $e_g$  (see Figure 15.1). In 15.36, only  $z^2$  will stabilize them. It is easy to see that 15.35 will energetically be preferred. For the reverse situation, when  $L'$  is a weaker  $\sigma$  donor than L, the same preference is predicted. The stronger  $\sigma$  donors interact only with the  $x^2 - y^2$  component of  $e_g$  in 15.36. In 15.35 they interact with both. One should be cautious in pushing this argument too far in predicting cis and trans energy differences for octahedral complexes. Steric effects and other electronic factors (most notably of the  $\pi$  type) can overrule the arguments that have been constructed here.

## 15.4 DISTORTIONS FROM AN OCTAHEDRAL GEOMETRY

By far the most common geometry for a six-coordinate complex is the octahedron, but it is worthwhile to consider some of the alternative geometries that are conceivable for  $ML_6$  complexes. The octahedron is a special geometry for an 18-electron count. As shown in Figure 15.1, it is seen that there are a total of 12 electrons housed in six strong M—L bonding orbitals— $1a_{1g}$ ,  $1e_g$ , and  $1t_{1u}$ . The remaining six electrons are localized at the metal (barring  $\pi$  effects) and are nonbonding. That is, they are directed in space away from the M—L bonding regions (see 15.11). We see in Chapter 16 that most transition metal complexes are of the 18-electron type and so it is not unusual to find that this geometry is so pervasive in nature. Of course, another way to view this is from a valence shell electron repulsion (VSEPR) model [21]. Consider the ligands again as Lewis bases. The optimal way to position six bases around a sphere (the transition metal) is in an octahedral arrangement. This minimizes steric interactions, as well as lone-pair repulsions (or repulsions between the electron density in the M—L bonds) between the ligands. But what happens when there are more than 18 electrons around the transition metal complex? As mentioned in Section 15.1, the  $2e_g$  set (see Figure 15.1) will be partially filled. The complex will either adopt a higher spin state or distort. The unequal occupation of the  $2e_g$  set signals a first-order Jahn–Teller distortion (see Section 7.4A). We first discuss the classic example of Cu(II) where there are three electrons in  $2e_g$ . This  $d^9$  configuration leads to an electronic state of  ${}^2E_g$  symmetry. The symmetric direct product of  $E_g$  is  $A_{1g} + E_g$ . For a nonzero first-order term a vibration of symmetry species  $a_{1g}$  or  $e_g$  is required. A vibration of  $a_{1g}$  symmetry does not lower the symmetry (see Appendix III for the normal modes of an octahedron), but a vibration of  $e_g$  symmetry will lower the symmetry of the molecule and split the energy of the two members of the  $2e_g$  set. 15.37 and 15.38 show two  $e_g$  modes for the octahedron, which lead to bond lengthening and shortening. Following the



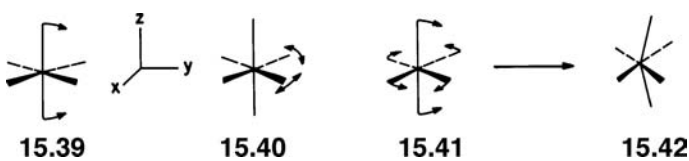
distortion in 15.37 reduces the point symmetry to  $D_{4h}$ . Let us initially examine this motion which is called a tetragonal (or axial) elongation. Four M—L bonds become shorter and two are longer. Figure 15.8a shows what happens to the two members of the  $2e_g$  set [22]. There is increased overlap between the metal d and the ligand  $\sigma$  orbital (here represented by an s AO for simplicity) for the four short bonds so the

**FIGURE 15.8**

Two members of the  $2e_g$  set undergo a tetragonal elongation in (a) and tetragonal compression in (b). The solid tie lines show the effect of the first-order changes in energy. The dashed lines indicate the effect of a second-order in energy mixing with the  $s$  AO at the metal and the corresponding first-order corrections are drawn for the mixing of the  $s$  AO at the metal.

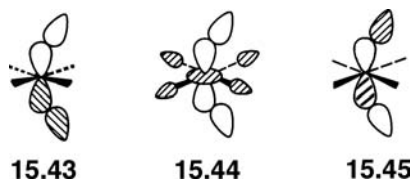
$x^2-y^2$  member of  $2e_g$  rises in energy. Overlap between the ligand and  $z^2$ , is, however, diminished and so this MO is stabilized. Therefore, this  $D_{4h}$  distortion creates an  $^2B_{1g}$  state which according to the Jahn-Teller theorem, should be more stable than the  $^2E_g$  state. But it is equally valid to move the ligands in the direction opposite to that given in 15.37. This is called a distortion with tetragonal compression (or axial flattening). Since now there are four long and two short bonds, exactly the opposite occurs energetically to the members of  $2e_g$ .  $x^2-y^2$  is stabilized whereas  $z^2$  is destabilized. An electronic state of  $^2A_{1g}$  is created. Therefore, there must be a state crossing on going from one geometry to the other. This treatment uses only the first-order corrections to the energy, equation 7.2, or using the Jahn-Teller methodology, the first three terms of equation 7.8. But this is not the whole story. In the reduced  $D_{4h}$  symmetry, metal  $s$  and  $z^2$  have the same symmetry ( $a_{1g}$  in  $D_{4h}$ ) and consequently they can mix in second order (equation 7.3) that will always stabilize  $z^2$ . The dashed lines indicate this in Figure 15.8. The first-order corrections to the wavefunctions in each case are also drawn. It is easy to see that the two distortions are not energetically equivalent. Two electrons are stabilized in  $z^2$  for the tetragonal elongation in (a), whereas only one electron is stabilized for the compression mode in (b). If all the ligands are the same, the distortion found is always that of (a). The magnitude of the distortion varies. Some systems appear only to be distorted a little away from the symmetrical structure. For others, the bond length differences are quite large. The bond lengths in  $\text{CuBr}_2$ , for example, are two at  $3.18\text{\AA}$  and four at  $2.40\text{\AA}$ . There are many examples of square planar Cu(II), the extreme case of this two long-four short distortion. We explore this in some depth in Chapter 16. But life is not always so simple. An equally valid distortion mode is given by 15.38. This is the other component of the  $e_g$  normal mode. One can also take any linear combination of them. Ultimately, a “Mexican-hat” potential energy surface (see Figure 7.7) is generated [23,24]. Square planar coordination is also a feature of low-spin  $d^8$  chemistry. It is understandable in Jahn-Teller terms by recognizing the presence of the  $^1E_g$  state of the  $d^8$  configuration so that there is one less electron than that given in Figure 15.8.

Low-spin  $\text{ML}_6$  complexes with electron counts of 14–16 valence electrons in the levels of Figure 15.1 are also the most likely cases where distortions from an octahedron will be found [25]. We shall first examine two typical distortions [26–29]. The first is a decrease of one trans L–M–L angle from  $180^\circ$ , as shown by 15.39. In the second, the cis L–M–L angle is varied, 15.40, in either direction

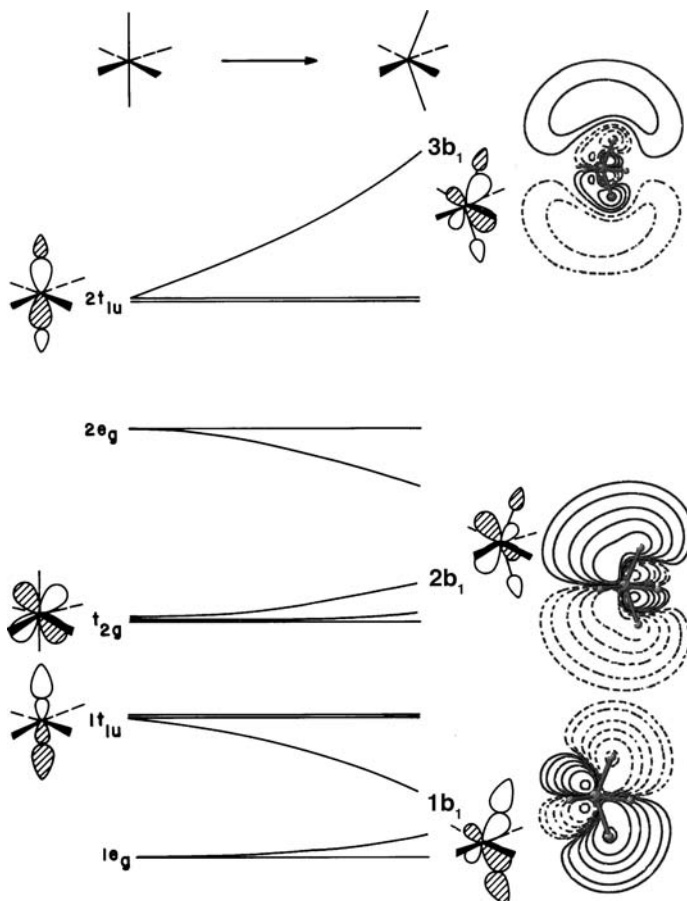


from  $90^\circ$ . A combination of both types of deformation, as shown in 15.41, takes an octahedron to a bicapped tetrahedron, 15.42.

Let us start with 15.39 where all ligands are solely  $\sigma$  donating. The symmetry of the complex is lowered along this distortion coordinate, as it is in any distortion from octahedral symmetry. Orbitals that were formerly orthogonal now mix. This is a necessary and complicating feature that is to be analyzed in some detail. Let us sidestep that issue for a moment and see what will happen to the splitting pattern of our octahedron in Figure 15.1 solely on the basis of overlap changes. In other words, we only concern ourselves with first-order energy changes using geometric perturbation theory. It is easy to see that those orbitals that contain metal  $z$  and  $z^2$  will be perturbed. The metal  $s$  orbital is spherical. Therefore, any ligand angular distortion will keep a constant overlap with it. The net result is that the  $z$  component of  $1t_{1u}$  in Figure 15.1 and  $z^2$  in  $1e_g$  will rise in energy to the first order since these are bonding orbitals and overlap to the lone pairs of the ligands is lost—see 15.43 and 15.44. Likewise, the corresponding member of  $2t_{1u}$  and  $2e_g$  will fall in energy since they are antibonding orbitals. For convenience, we have rotated our coordinate system for

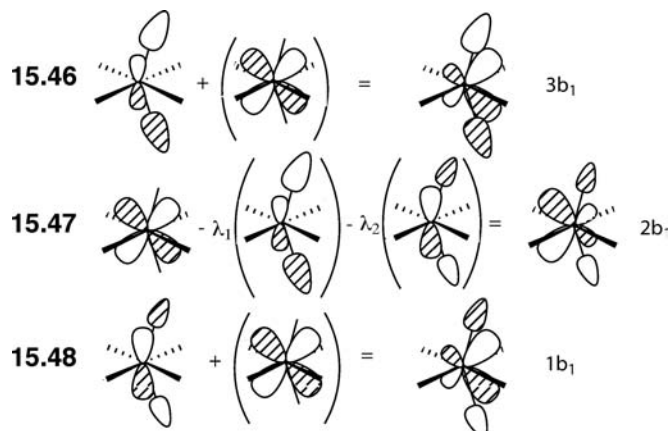


the octahedron by  $45^\circ$  to that in 15.39. The components of the important  $t_{2g}$  set will now be  $x^2-y^2$ ,  $xz$ , and  $yz$ . Let us concentrate on  $yz$ . At the octahedron, it was orthogonal, of course, to the  $z$  component of  $1t_{1u}$  and  $2t_{1u}$ . However, the symmetry of the molecule is reduced to  $C_{2v}$  with the distortion in 15.39. Both  $yz$  and 15.43 are of  $b_1$  symmetry so they will intermix along with the antibonding analog of 15.43, 15.45. There are a number of ways within the framework of perturbation theory to see how they intermix; let us use geometric perturbation theory. The three orbitals of interest to us are shown on the left side of Figure 15.9. When the L–M–L angle is less than  $180^\circ$ , the three orbitals intermix so there is a second-order correction to the energy. Since  $1t_{1u}$  and  $t_{2g}$  lie quite close in energy, the second-order stabilization is large in absolute magnitude (larger than the first-order correction). The lowest molecular level,  $1b_1$ , will be stabilized upon bending. Recall that the nonvanishing matrix element that determines the mixing sign will be derived from the overlap of  $yz$  with the lone pair hybrids in 15.43 and 15.45. The first-order correction to the wavefunction will then be given by 15.46. (Notice that  $S_{ij}$  here is a positive number). The  $yz$  orbital here mixes strongly in a bonding way to the lone pairs. Another, valence bond, way to look at this result is that  $1b_1$  contains a hybrid orbital at the metal. Since metal  $d$  AOs lie at a lower energy and overlap better than the  $p$  set, more  $d$  character in the hybrid will produce an orbital that is more stabilized. A contour plot of the  $1b_1$  MO for  $WH_6$  (from a DFT calculation) is shown on the right side of the Walsh diagram in Figure 15.9. The amount of  $d$  character in this orbital is very large. Let us work

**FIGURE 15.9**

Walsh diagram for bending one trans L—M—L angle in a  $\text{ML}_6$  complex.

through  $2b_1$  in some detail. As shown in 15.47, 15.43 mixes into  $yz$  (since it is at lower energy) in an antibonding fashion. The  $\tilde{S}_{ij}$  for  $\langle yz | 15.45 \rangle$  is negative so the

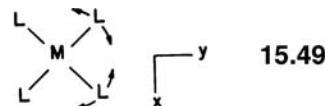


sign of the mixing coefficient is also negative. Therefore, 15.45 mixes into  $yz$  in-phase. The mixing coefficients in 15.47 will be in the order  $\lambda_1 < \lambda_2$ . In 15.43, the orbital is concentrated on the lone-pair hybrids, and 15.45 is more heavily weighted on metal  $z$ . Irrespective of this detail  $2b_1$  becomes hybridized by the mixing of both orbitals in a direction away from the two ligands that bend. This is clear in the

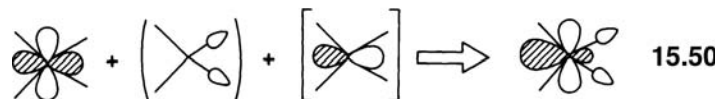
contour plot for  $2b_1$  for  $\text{WH}_6$  in the figure. Since **15.43** mixes more strongly into  $yz$  than does **15.45**,  $2b_1$  will be destabilized along the ordinate of Figure 15.9. Finally the  $3b_1\text{MO}$ , **15.48**, mixes  $yz$  into it in a way that is strongly antibonding to the lone pairs, so the orbital rises in energy. It becomes a hybrid orbital which is hybridized toward the ligands. This exercise is unusual in that the absolute magnitudes of the first-order energy changes are smaller than those in the second order. This is certainly not the norm. Here, the situation arises because the interaction between the metal  $d$  with the ligands is so much stronger than that with metal  $p$ . But the reader should be fully aware that this three-orbital perturbation problem is conceptually the same as bending  $\text{AH}_2$  (Section 7.3) and pyramidalization of  $\text{AH}_3$  (Section 9.2). In those two cases, the nonbonding level (which started as an atomic  $p$  orbital), as well as here, hybridizes out away from the bending. The lowest orbital is always stabilized greatly and the highest, destabilized. The hybridization is in the opposite direction so that the former is the most bonding and the latter the most antibonding combination.

It was previously pointed out that overlap factors cause the  $z^2$  component of  $1e_g$  to rise in energy and  $2e_g$  to fall. This is also indicated in Figure 15.9. A low-spin 16-electron  $\text{ML}_6$  complex would then be stabilized by this distortion. At the octahedral geometry, all levels are doubly occupied up to  $t_{2g}$ . For a 16-electron complex, there will be 4 electrons in  $t_{2g}$ . The downward slope of  $1b_1$  overrules the one component of  $1e_g$  that rises in energy. Notice also that since  $2b_2$  goes up in energy a HOMO-LUMO gap is created for a distorted 16-electron complex. Notice also that this distortion will be stabilizing for a complex with only 12-electron ( $t_{2g}$  is empty). We shall pursue the ramifications of this shortly.

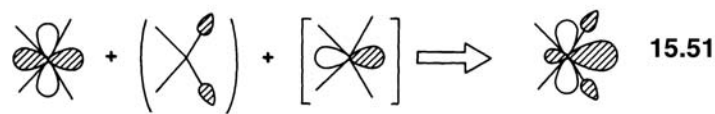
An analysis of bending for two cis ligands in **15.40** can be constructed along the same lines. A convenient top view of this distortion is presented in **15.49**. Here,



15.49



15.50



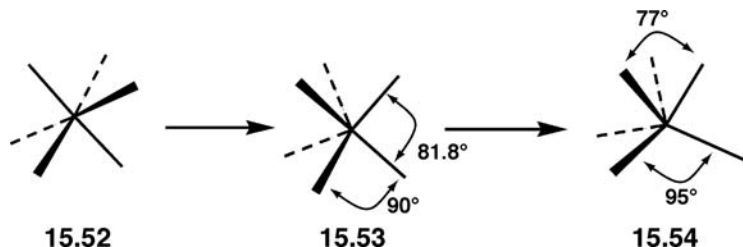
15.51

the  $y$  component of  $1t_{1u}$  and  $2t_{1u}$  mix with the  $x^2 - y^2$  component of  $t_{2g}$ . It is apparent that when the L–M–L angle changes from  $90^\circ$  some  $x^2 - y^2$  character will mix into  $1t_{1u}$  in a way to increase the M–L bonding. In the  $x^2 - y^2$  component of  $t_{2g}$ , there will be a small amount of ligand lone pair and metal  $y$  character mixed in. This is shown in **15.50** when the L–M–L angle becomes less than  $90^\circ$  and in **15.51** when it is larger than  $90^\circ$ . Energetically, the distortion in both directions will stabilize one member of  $1t_{1u}$  and destabilize  $x^2 - y^2$  in  $t_{2g}$ . The reader should realize that this is a considerably simplified treatment, especially the analysis of the cis angle distortion. The symmetry of the molecule is lowered from  $O_h$  to  $C_{2v}$ . Metal  $x^2 - y^2$  and  $y$  are of  $a_1$  symmetry. So too are  $s$  and  $z^2$ . Therefore,  $1a_{1g}$ ,  $2a_{1g}$ , and the  $z^2$  components  $1e_g$  and  $2e_g$  (see Figure 15.1) also become  $a_1$  functions. They will mix into **15.50** and **15.51**. That is certainly a complicating factor, but adds little to the final result.

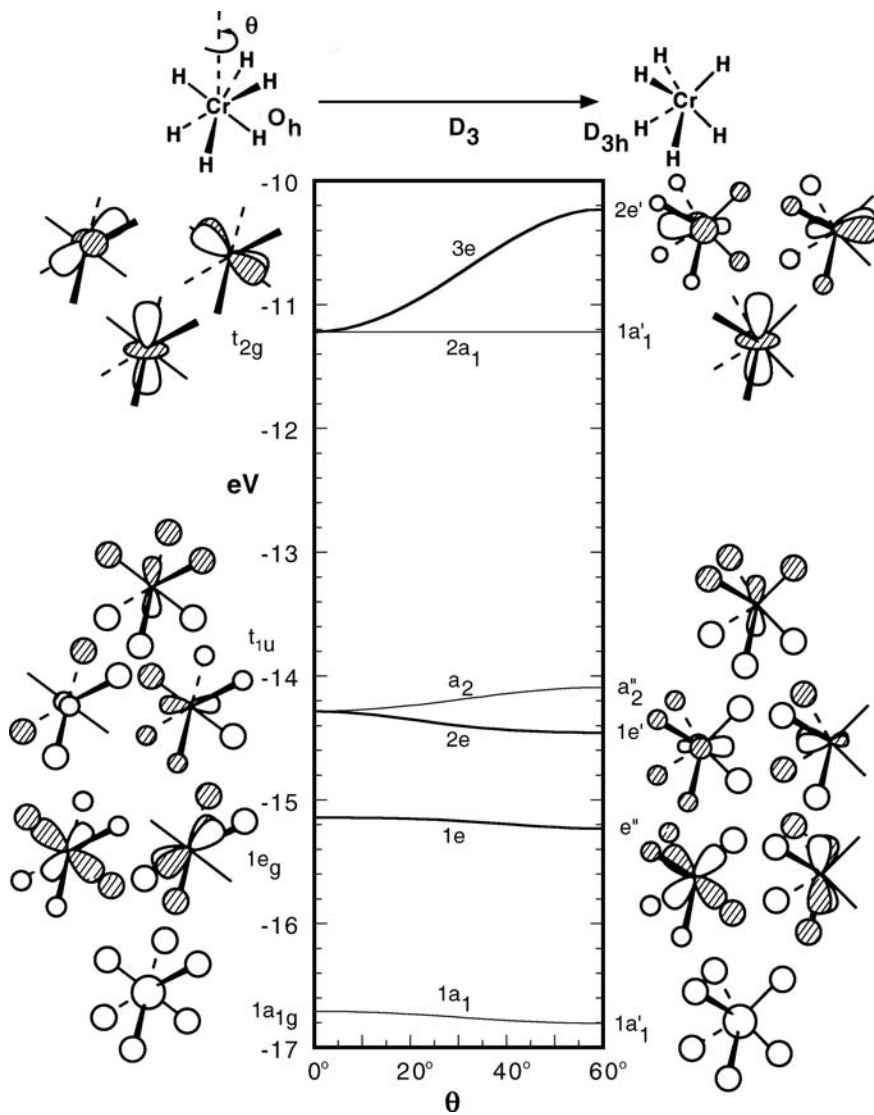
These cis and trans L–M–L angle distortions split the degeneracy of the  $t_{2g}$  set. In both cases, one component is destabilized. Recall that  $\pi$  acceptors or  $\pi$  donors will

also create an energy difference between the members of  $t_{2g}$ . What happens to the  $\pi$  overlap as a function of angular changes can easily be established [26,27]. Normally, a 16-electron  $ML_6$  molecule will utilize both  $\pi$  effects and angular changes together so that one member of  $t_{2g}$  lies appreciably higher in energy than the other two. Thus, while low-spin 16-electron complexes are unusual, their stability is understandable and there is a growing body of them in the literature [26–28].

Let us return again to the octahedral splitting pattern in Figure 15.1. Our discussion of the cis and trans distortions in 16-electron (and 14 electron) complexes hinged on the mixing of  $t_{2g}$  into one component of  $t_{1u}$  which stabilizes the latter. Then, what will happen to a 12-electron complex where  $t_{2g}$  is empty? The VSEPR approach is very clear—the octahedron with six bond pairs is certainly the most stable geometry. This is certainly the case for, say,  $WF_6$  or any other molecule where the surrounding ligands are electronegative. The  $t_{2g}$ – $t_{1u}$  gap is large since electronegative ligands will place  $t_{1u}$  at a low relative energy. On the other hand, consider the ligands to be  $H^-$  or  $CH_3^-$ . Now the  $t_{2g}$ – $t_{1u}$  gap is small and a second-order Jahn–Teller distortion is a possibility [30]. This leads to many possible paths. For  $CrH_6$  ab initio calculations located 19 additional stationary points and in  $VH_6$  nine other structures were found [30]. In both cases, the octahedron was the least stable structure! A common deformation mode available to an octahedron is called the Bailer twist [25]. Three *fac* ligands rotate with respect to the other three *fac* ligands to produce a trigonal prismatic structure. A Walsh diagram for this motion is shown in Figure 15.10 for the hypothetical  $CrH_6$  molecule. This has been calculated at the extended Hückel level with a rigid rotation angle,  $\theta$ . The lowest six MOs are filled in  $CrH_6$ , so consequently the HOMO is the  $t_{1u}$  set and the LUMO is  $t_{2g}$  in the figure. It is important to realize that a rotation from the octahedron to the trigonal prism, 15.52 to 15.53, brings a close contact between the three eclipsing M–L



bonds. Another way to express this is that while the top and bottom three L–M–L angle stay constant at  $90^\circ$ , the remaining three angles are reduced to  $81.8^\circ$ . Rotating about the threefold axis of the octahedron,  $\theta$ , reduces the symmetry first to  $D_3$  then to  $D_{3h}$  at the trigonal prism. In either symmetry group,  $t_{1u}$  becomes  $e + a_2$  or  $e' + a_2''$  and the  $t_{2g}$  set transforms to  $e + a_1$  or  $e' + a'_1$  symmetry. Therefore, the upper  $e$  set, derived from  $t_{2g}$  will mix in and stabilize the lower  $e$  set derived from  $t_{1u}$ . We have, of course, just seen two examples of this when one component of the  $t$  sets intermix and provide a stabilizing distortion. One can see from the right side of Figure 15.10 that  $a_2''$  is filled and  $a'_1$  is empty. They can mix with each other by a distortion to  $C_{3v}$  symmetry. That is on going from 15.53 to 15.54, the top three ligands move closer together and the bottom three splay out. High-quality DFT calculations on  $W(CH_3)_6$  have shown that 15.54 is about 88 kcal/mol more stable than the octahedron [31].  $W(CH_3)_6$  was prepared and reported by Wilkinson and coworkers, 23 years earlier. In accordance to VSEPR reasoning, it was tacitly assumed to be octahedral. An experimental determination of the structure is not a trivial exercise.  $W(CH_3)_6$  is a low melting, pyrophoric (and explosive) solid. But, nevertheless, its structure was determined [32] and, indeed, corresponds to the  $C_{3v}$  model. The averages of the two sets of

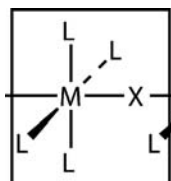
**FIGURE 15.10**

Extended Hückel calculation for the Bailer twist in  $\text{CrH}_6$ .

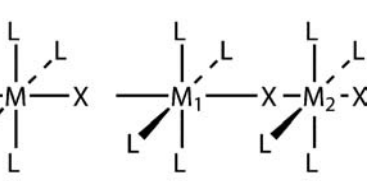
angles are given in 15.54. This is a very crowded geometry. Calculations [31] show this structure to be only about 5 kcal/mol more stable than the trigonal prism, 15.53. For  $\text{WH}_6$  the differences are larger [30,31]. The octahedron and trigonal prism are predicted to be around 158 and 37 kcal/mol, respectively, less stable than  $C_{3v}$ , 15.54. The  $C_{3v}$  structure is predicted to be even more distorted with angles of  $62^\circ$  and  $115^\circ$ .  $\text{WH}_6$  has been isolated in a neon matrix [33] and the IR spectrum of it is consistent with a  $C_{3v}$  structure. An even more unusual structure has been predicted [30,31] to lie only slightly higher energy, namely, a  $C_{5v}$  molecule shaped like an umbrella! There have been VSEPR attempts [21,34] to rationalize the  $C_{3v}$  or trigonal prismatic structures within the context of polarization by core electrons. But these efforts still have problems with an umbrella structure or some of the other cases of low electron count  $\text{ML}_n$  transition metal complexes. On the other hand, a valence bond perspective [35], where one maximizes the  $d$  character in the M—L hybrids is a conceptually simple solution that is complementary to the second-order Jahn–Teller arguments given here.

## 15.5 THE OCTAHEDRON IN THE SOLID STATE

Probably, the most common structural unit in the solid state is the octahedron. We start at the most simple one-dimensional class and first look at vertex-shared examples with a  $\text{ML}_4\text{X}$  formula unit, 15.55. Here, L is a two electron  $\sigma$  donor and the bridging atom, X, contains s and p AOs. The band structure for this polymer is easy



15.55



15.56

to construct. Figure 15.11 shows the metal d portion. The coordinate system here corresponds to that used in Figure 15.1. As shown, the  $xy$  and  $x^2-y^2$  bands have the wrong symmetry for there to be an interaction with an orbital on the bridging atom and the metal atoms are too far apart for there to be any reasonable M–M overlap. So those two bands are flat. Notice that  $xy$  is one component of  $t_{2g}$ , whereas,  $x^2-y^2$  is strongly M–L antibonding. It is one component of the  $e_g$  set, thus, it lies at high energy. At the  $k=0$  ( $\Gamma$ ) point the other two members of  $t_{2g}$  are also nonbonding with respect to the bridging atom. On the other hand, at  $k=\pi/a$  ( $X$ ) the x and z AOs of the bridging atom do overlap with metal  $xz$  and  $yz$ . They do so in an antibonding way (the two bands which are concentrated on X will be bonding to metal d and, therefore, stabilized at this  $k$  point). So the  $xz$  and  $yz$  bands “run up” and stay degenerate. The  $z^2$  band is a little different. Its energetic positioning relative to  $x^2-y^2$

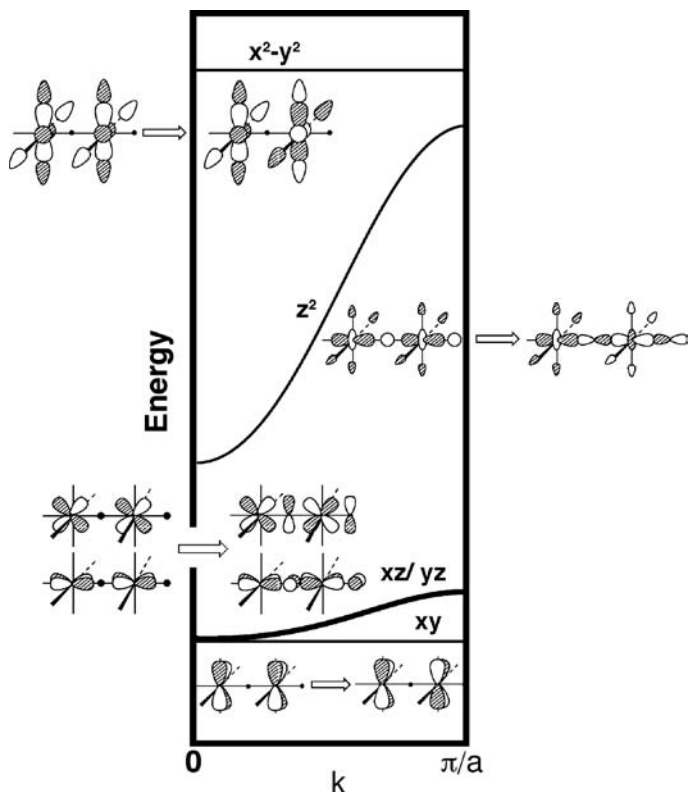
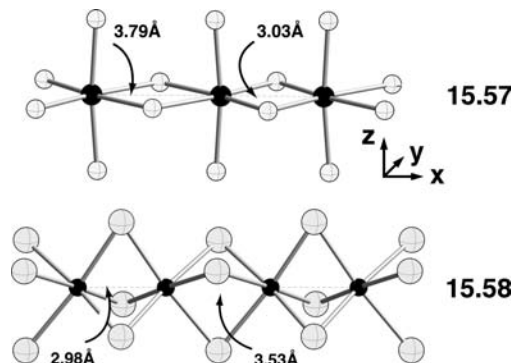


FIGURE 15.11

Idealized band structure diagram for a one-dimensional  $\text{ML}_4\text{X}$  polymer where L is a  $\sigma$  donor and the bridging atom X possesses s and p AOs.

depends on whether L is a better (as in the case used here) or poorer  $\sigma$  donor than X. The important point is that the  $z^2$  band has significant dispersion. At the  $k=0$  point, it is antibonding to the s AO of X and at  $k=\pi/a$ , it is antibonding to the y AO of X. Since the p AOs of X lie higher in energy (closer to the metal d) and overlap better with metal d, the  $k=\pi/a$  solution lies at a higher energy than  $k=0$  does. This is precisely analogous to the picture that we developed for the bismuth oxides in Figure 14.9 and 14.22 and 14.23. An important lesson from Figure 15.11 is that the energetic position of the band depends on intracell interactions and that band dispersion need not be exclusively dependent on intercell overlap. We shall shortly return to 15.55 where there is a total of 12 electrons around each metal. In 15.55, where  $L=NR_3$ ,  $X=Cl$  or Br, and  $M=Pt_{3+}$  there are a total of seven electrons in Figure 15.11. Therefore, the  $z^2$  band (pairing the electrons) is half-full. This signals a Peierls distortion precisely analogous to the bond alternation in polyacetylene that was covered in Section 13.2. We see in Section 17.4 that doubling the unit cell folds the  $z^2$  band into two and the distortion in 15.56 splits the two at  $k=\pi/a$  [36]. Here,  $M_1$  essentially has square planar coordination while  $M_2$  is octahedral. We will return to this problem in Chapter 17.

A one-dimensional chain can also be constructed when octahedra share edges. An example is provided by  $NbCl_4$ , 15.57. Here there is one electron in the  $t_{2g}$  so



again there will be one band which is half-full and a pairing distortion is expected. The actual situation is slightly more complicated [36]. The three bands in the non-alternating structure overlap with each other. Taking two octahedra as the unit cell results in the band structure on the left side of Figure 15.12. Here, the + and - superscripts simply refer to plus and minus combinations of the members of the  $t_{2g}$  set on each metal of the dimeric unit cell. For convenience, we have switched the coordinate system so that  $xz$ ,  $yz$  along now with  $x^2-y^2$  (instead of  $xy$ ) are  $t_{2g}$ . The dispersion for the  $e(k)$  plot on the left is again caused by differences in overlap with the bridging Cl atom AOs. We will leave it up to the reader to ascertain whether the bands “run up” or “run down” in energy [36]. The Fermi level,  $e_F$ , given by the dashed line is one that cuts across two bands. The distortion in the real structure, 15.57, is one that moves both Nb atoms closer together. The middle panel in the figure is one where the Nb atoms have each moved 0.1 Å toward each other. Overlap between the two  $xz$  orbitals cause the + combination to be stabilized and the - one to be destabilized. Since this is  $\delta$  type overlap between the two metals, the two bands do not split much in energy. The  $yz$  combinations have  $\pi$  overlap and they are split more. Finally, overlap between  $x^2-y^2$  is of the  $\sigma$  sort and so it is split the most. The  $e(k)$  vs.  $k$  plot on the right shows a distortion of 0.2 Å toward each other. Now the  $(x^2-y^2)^+$  band has been stabilized enough so that it is completely full. An alternating  $\sigma$  bond has formed along the chain. Octahedra can also share faces in a chain. A completely

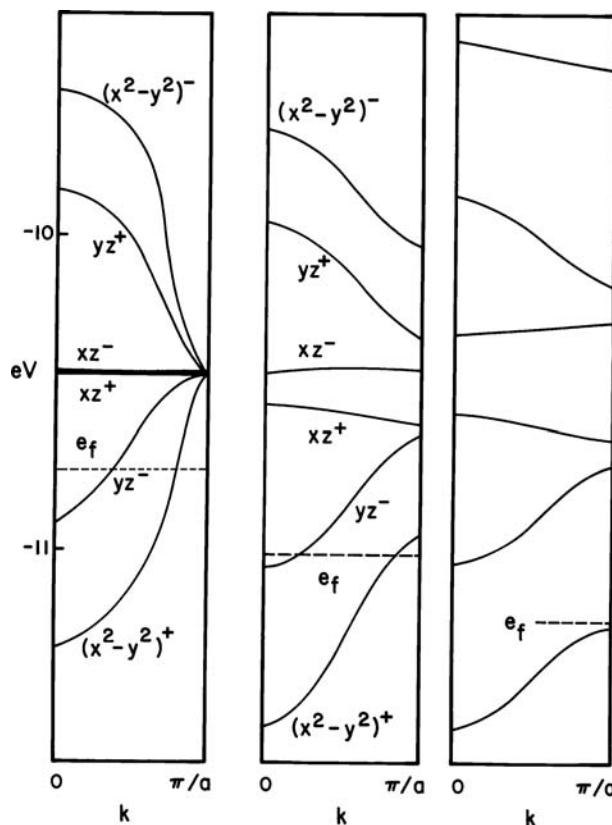
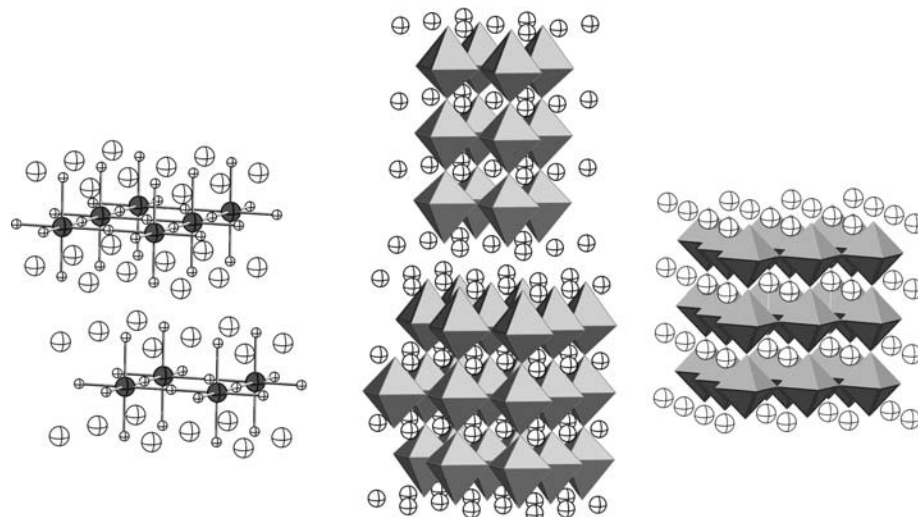


FIGURE 15.12

Plots of  $e(k)$  for a chain of  $\text{Nb}_2\text{Cl}_8$  dimers in the " $t_{2g}$ " region. The bands are labeled using the coordinate system in 15.57 where the + and - superscripts refer to the plus and minus combinations of metal  $d$  AOs. The middle panel occurs when the two Nb atoms are moved 0.1 Å toward each other and in the right panel they have been moved 0.2 Å. The Fermi level in each case is given by the dashed line.

analogous structure is given by  $\text{ZrI}_3$  [37], 15.58. There is again formally one electron in the  $t_{2g}$  set of the octahedral and so these can pair to form alternating Zr—Zr  $\sigma$  bonds.

Octahedra which propagate in two dimensions are also very common, particularly the metal oxides. The Ruddlesen–Popper series have a stoichiometry of  $\text{A}_{n+1}\text{M}_n\text{O}_{3n+1}$ , where A is generally an electropositive atom and n is the number of octahedra that comprise the 2-D slab. 15.59 is the  $n=1$  case for the classic  $\text{La}_2\text{CuO}_4$  or  $\text{K}_2\text{CuF}_4$  compounds. Here, the black balls are the Cu atoms and the O



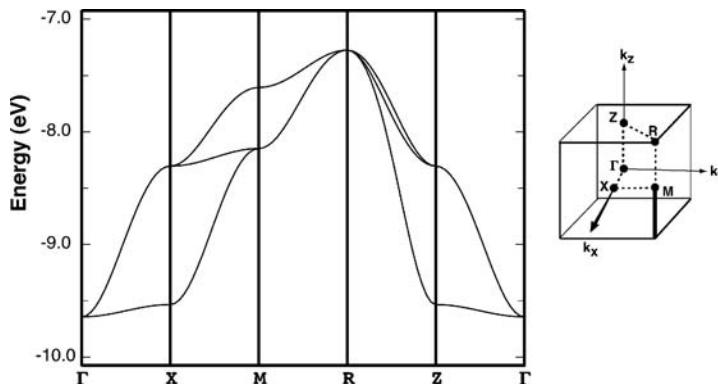
15.59

15.60

15.61

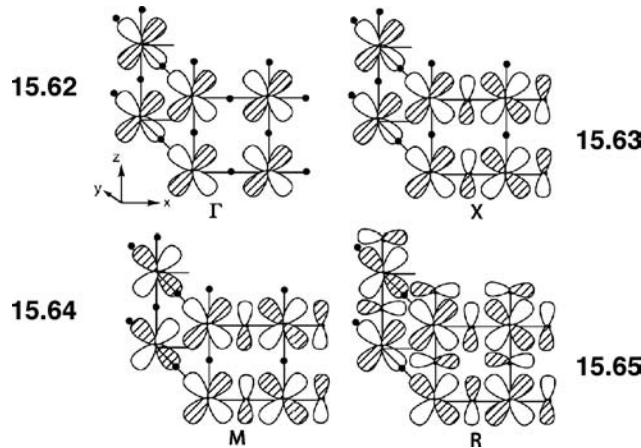
**FIGURE 15.13**

Plot of  $e(k)$  for the  $t_{2g}$  bands of  $\text{TiO}_3^{2-}$ . A diagrammatic representation of the first Brillouin zone and the special points is shown on the right side.



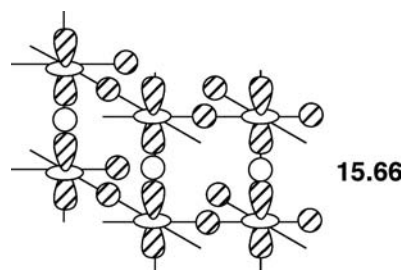
or F atoms are given by the small open spheres. The cations are represented by the large open circles. We shall have more to say about the former compound in the chapter. For now, we note that there are in a formal sense nine  $d$  electrons present at each Cu atom in both materials. Therefore, one might expect that a first-order Jahn–Teller distortion should occur yielding a tetragonally elongated structure. This is, indeed, the case. **15.60** represents the structure for  $\text{Sr}_{1.15}\text{Ca}_{2.25}\text{Mn}_3\text{O}_{10}$  where the slab now consists of three octahedra. Notice that the cations position themselves both within the slab of octahedra and between them. In this case, there are formally three electrons associated with each Mn atom. The infinite layer compound is represented in **15.61**. They are called perovskites and have a stoichiometry of  $\text{AMO}_3$ . A multitude of examples exist where the electron count on the metal ranges anywhere from zero to 10  $d$  electrons.

We shall use **15.61** as a starting point where the A atoms are considered to donate all of their valence electrons to the  $\text{MO}_3$  octahedral core. Figure 15.13 shows the band structure for  $\text{TiO}_3^{2-}$  ( $\text{BaTiO}_3$  is a real example) in the  $t_{2g}$  region. A schematic of the first Brillouin zone is shown on the right side. Let us use one member of the  $t_{2g}$  set,  $xz$ , as an example. At  $\Gamma$  ( $k_x = k_y = k_z = 0$ )  $xz$  is translated with the same phase in all three directions. This is shown in **15.62**. Notice that there is no AO at any of the oxygen atoms that has the right symmetry to interact with the  $xz$



combinations. The reader can easily verify that the same is true for  $yz$  and  $xy$  (the coordinate system is indicated by **15.62**). Therefore, all the three solutions to the Bloch equations are at the same energy. On going to  $X$  ( $k_x = \pi/a$ ;  $k_y = k_z = 0$ ), **15.63**

shows that oxygen  $z$  can combine with  $xz$  along the  $x$  direction and it does so in an antibonding way. So the  $xz$  band rises in energy going from  $\Gamma$  to  $X$ . The same occurs with  $xy$ , so these bands remain as a degenerate pair. On the other hand,  $yz$  remains nonbonding to all oxygen AOs. The form of the  $M$  ( $k_x = \pi/a$ ;  $k_y = \pi/b$ ;  $k_z = 0$ ), solution for  $xz$  is given by 15.64. One might think that it should lie at the same energy as the  $X$  point, but there is weak Ti—Ti antibonding and so this band rises ever so slightly. Finally at the  $R$  ( $k_x = \pi/a$ ;  $k_y = \pi/b$ ;  $k_z = \pi/c$ ), solution, 15.65, there is maximal  $\pi$  antibonding between  $xz$  and the oxygen  $p$  AOs. This solution lies at the highest energy and is degenerate, in fact, with the other two members of  $t_{2g}$ . One might think that the  $e_g$  set for Ti  $d$  lies at a much higher energy. The actual gap is not so clearly determined [39]. As 15.66 shows it is the oxygen  $s$  AOs that keep  $z^2$  at high energy.



If there is a weak (or negligible) interaction between them, then the  $z^2$  and  $x^2-y^2$  bands for  $\Gamma$  are at essentially the same energy as the three  $t_{2g}$  members (actually the  $e_g$  set lies slightly lower because of Ti—Ti bonding if O  $s$  is neglected). Figure 15.14 gives the full DOS and Ti—O COOP curve for our  $TiO_3^{2-}$  perovskite model. The peak associated with the oxygen  $s$  AOs at around  $-32$  eV is not shown. The oxygen  $p$  AOs are found from  $-17$  to  $-14.5$  eV. Some Ti  $d$ ,  $s$ , and  $p$  character mixes into them in a bonding fashion. One can easily see this feature from the COOP curve.

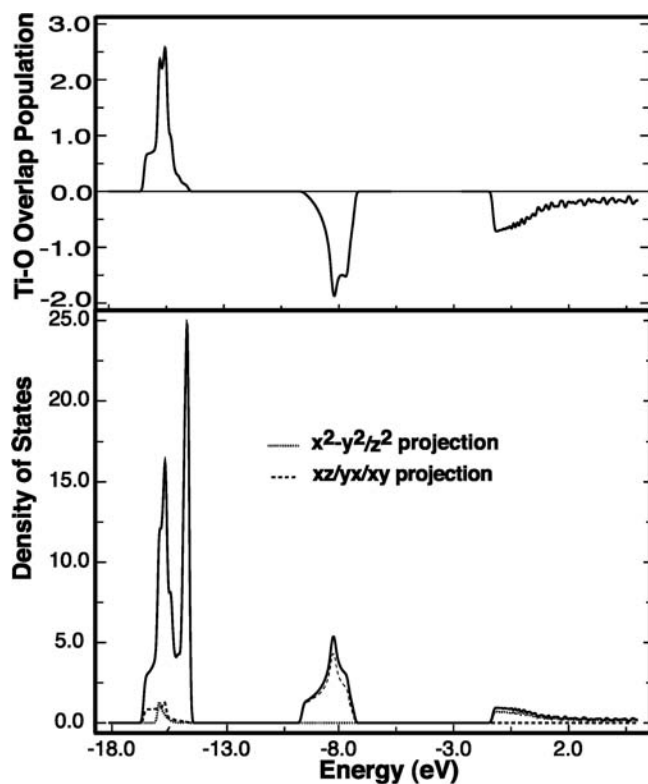
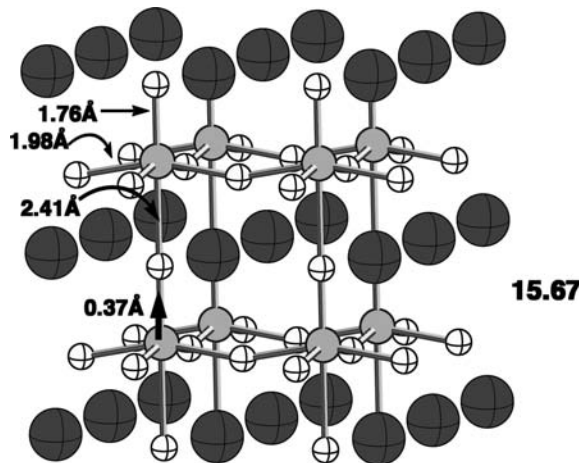


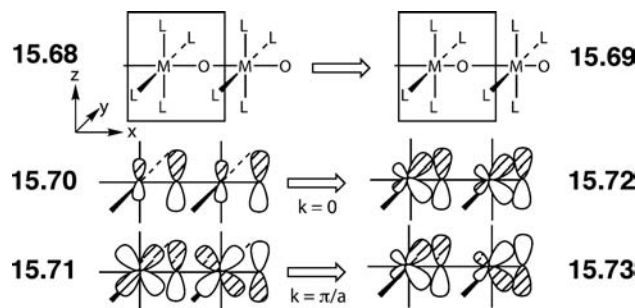
**FIGURE 15.14**  
DOS and Ti—O COOP plots for  $TiO_3^{2-}$  at the EHT level.

At approximately  $-15\text{ eV}$  is a tall, thin peak. This corresponds to oxygen  $p$  combinations that do not find a symmetry match to Ti orbitals. The  $t_{2g}$  states of Ti are found from  $-10$  to  $-7.5\text{ eV}$ , and the  $e_g$  states of Ti from  $-1$  to  $2\text{ eV}$  and above. As one can see from the COOP plot some oxygen  $p$  mixes into them in an antibonding fashion. In the  $t_{2g}$  levels, it is Ti—O  $\pi$  antibonding, whereas, in  $e_g$  it is  $\sigma$  antibonding. For  $\text{TiO}_3^{2-}$  the oxygen  $p$  states are the highest filled ones and so the band gap to the Ti “ $t_{2g}$ ” ones is very large, nearly  $6\text{ eV}$ .  $\text{BaTiO}_3$  is an insulator.

There is much symmetry at work in this example. However, many perovskites are distorted in a number of ways to a lower symmetry. We shall look at one common variant where the metal moves from an idealized octahedron, toward one of the oxygen vertices. An example is provided by  $\text{PbTiO}_3$ , **15.67**.

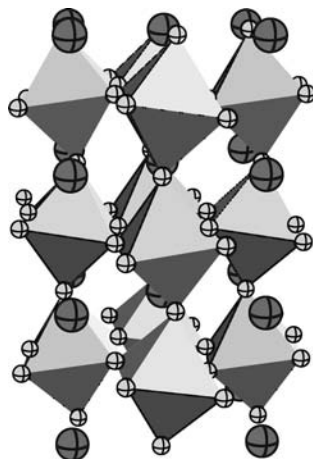
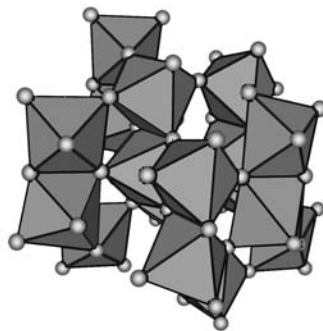


Here the Ti atoms move  $0.37\text{ \AA}$  as shown by the arrow and the Ti—O bond distances differ in this direction by a large amount,  $0.65\text{ \AA}$ ! The other Ti—O bonds at  $1.98\text{ \AA}$  are typical distances for Ti—O single bonds, so the short  $1.76\text{ \AA}$  bonds are certain to have multiple bond character while the very long  $2.41\text{ \AA}$  distances might be considered to be no bond at all. Rather than examining this specific distortion, let us take a more transparent case by returning to the one-dimensional  $\text{ML}_4\text{O}$



chain, **15.68**. Here, L again is a two-electron  $\sigma$  donor and the electron count that we are interested in will leave the metal “ $t_{2g}$ ” (and, of course  $e_g$ ) set empty. The distortion is a simple one; the oxygen atoms all move in the same direction so that, as shown in **15.69**, the unit cell dimensions stay the same, but the intracell M—O distance becomes shorter than the intercell one. For the symmetrical structure the form of the  $k=0$  solution of the oxygen z AO's is given in **15.70**. By symmetry metal z will mix into this solution and will do so in a bonding manner. If the oxygen atoms are slipped, then metal xz can mix also in a bonding way. Just as L—M—L bending in **15.46**, this will stabilize the band at  $k=0$ . An analogous situation occurs for the

$k = \pi/a$  solution. In this instance, only metal  $xz$  can mix with oxygen  $z$  in the symmetrical structure, **15.71**. Upon distortion metal  $z$  can mix so that the metal–oxygen overlap increases and this will also stabilize the orbital. Consequently, the entire oxygen  $z$  band is stabilized. Notice that the oxygen  $y$  band is degenerate with  $z$ , so the electronic driving force for this distortion is large. The metal  $xz$  and  $xy$  bands, on the other hand, have oxygen  $z$  and  $y$  mixed into them in an antibonding way, and so this distortion destabilizes these bands. So the **15.68** to **15.69** distortion is stabilizing for low electron count compounds. One can easily see that slipping the metal atoms to the oxygen vertices creates an identical pattern. But the situation for the real three-dimensional perovskite compounds is more complicated. The metal often moves toward an edge or a face of the octahedron. This has been also shown to result in increased metal–oxygen  $\pi$  bonding [40]. Furthermore, the octahedra are frequently twisted and turned. An example showing this is given in **15.74**, which is a

**15.74****15.75**

low temperature polymorph of  $\text{CaTiO}_3$ . These distortions, particularly those which move the metal way from the center of the octahedron will create a dipole moment within the unit cell. If the dipole moments lie in the same direction, the crystal becomes polarized, ferroelectric. There are many important real-world applications for compounds of this type. The interplay between electronic and electrostatic (the size match between  $A$  and  $M$ ) factors in  $\text{AMO}_3$  perovskites is complex [40–42]. An ideal cubic perovskite, in which the  $M\text{—O—M}$  bonds are linear with  $A$  located at the center of each  $M_8$  cube (hence forming a  $\text{AO}_{12}$  polyhedron), is possible when the tolerance factor [41]

$$\tau = (r_O + r_A)/\sqrt{2}(r_O + r_M)$$

is 1 (here  $r_A$  and  $r_M$  are the ionic radii of the  $A$  and  $M$  cations, respectively, with  $r_O$  as that of the  $\text{O}^{2-}$  anion). In most cases, the  $A$  cations are small so that  $\tau < 1$ , and the  $A\text{—O}$  bonds are too long to keep the ideal cubic structure. Thus, the  $A$  cation moves away from the center of the  $M_8$  cube, accompanied by the bending of the  $M\text{—O—M}$  bonds and the rotation of the  $\text{MO}_6$  octahedra, to form a lower-coordinate  $\text{AO}_n$  polyhedron ( $n < 12$ ) with short  $A\text{—O}$  bonds. The distortion of the ideal cubic perovskite toward a noncentrosymmetric ferroelectric structure requires another local instability besides  $\tau < 1$ , namely, the second-order Jahn–Teller (SOJT) instability of the  $A$ - and/or  $M$ -site cation [42]. As found for  $\text{PbTiO}_3$  [43],  $\text{PbVO}_3$  [44], and  $\text{BiCoO}_3$  [45], moving the  $A$  cation toward the center of one  $M_4$  face leads to a tetragonal ferroelectric structure with space group  $\text{P}4\text{mm}$ . The  $M$  cations move

away from the approaching A cations such that the coordinate environment of each M cation becomes more similar to an  $MO_5$  square pyramid with shortened axial M—O bond. In  $PbTiO_3$ ,  $PbVO_3$ , and  $BiCoO_3$ , the  $s^2$  A-site cations  $Pb^{2+}$  and  $Bi^{3+}$  are susceptible to an SOJT distortion, which mixes the empty  $6p$  orbital of A into the filled  $6s^2$  orbital of A hence forming a lone pair on A. In  $PbTiO_3$ , the M-site cation  $Ti^{4+}$  ( $d^0$ ) is also susceptible to an SOJT distortion, which mixes the empty  $Ti\ 3d$  orbitals into the filled  $2p$  orbitals of the O atom of the axial Ti—O bond. Thus, in  $PbTiO_3$ , the need to make short Pb—O bonds and the SOJT instabilities of both  $Pb^{2+}$  and  $Ti^{4+}$  ions cooperate to give rise to the observed ferroelectric distortion. Another type of the A-cation displacement from the center of the  $M_8$  cube is the movement toward one corner of the  $M_8$  cube along the body-diagonal direction (i.e., the  $C_3$  rotational axis) to form a noncentrosymmetric ferroelectric trigonal structure with space group  $R3c$ , as found for  $BiFeO_3$  [46]. In  $BiFeO_3$ , the M-site cation  $Bi^{3+}$  ( $s^2$ ) undergoes an SOJT distortion forming a lone pair on  $Bi^{3+}$ , and the need to make short Bi—O bonds and the SOJT instability of  $Bi^{3+}$  ions cooperate to cause the observed ferroelectric distortion.

In general it is not possible to *a priori* determine how a perovskite will distort, what will be the most stable structure or under what conditions of temperature and pressure will favor the formation of one polymorph over another. But there are some common threads that can be exploited when one thinks about the electronic structure of these materials in a qualitative sense. We have emphasized the relationship between the details of the electronic structure in the unit cell and how this carries over to the compound itself, for example, the functional form and relative energy of the “ $t_{2g}$ -like” states. Figure 15.15 shows the density of states for the mineral anatase,  $TiO_2$ . The structure of anatase is much more complicated than the previous cases that we investigated. A polyhedral representation of anatase is shown in 15.75. Here, the small spheres represent the oxygen atoms. The Ti atoms are not at the center of octahedra, furthermore, the octahedra are both corner-shared and edge-shared compared to our idealized  $BaTiO_3$  perovskite example in 15.6 in which the octahedra are only corner-shared. The reader should carefully compare the DOS of idealized  $TiO_3^{2-}$  in Figure 15.14 to that of  $TiO_2$  in Figure 15.15. There are more similarities than differences. There are the same three groups of peaks in Figure 15.15 that represent the oxygen  $p$ , Ti “ $t_{2g}$ ” and Ti “ $e_g$ ” states going from low energy to high. There is even the sharp peak (approximately –15 eV) in the oxygen  $p$  AO region that is reproduced here. To be sure, the “ $t_{2g}$ ” region is more

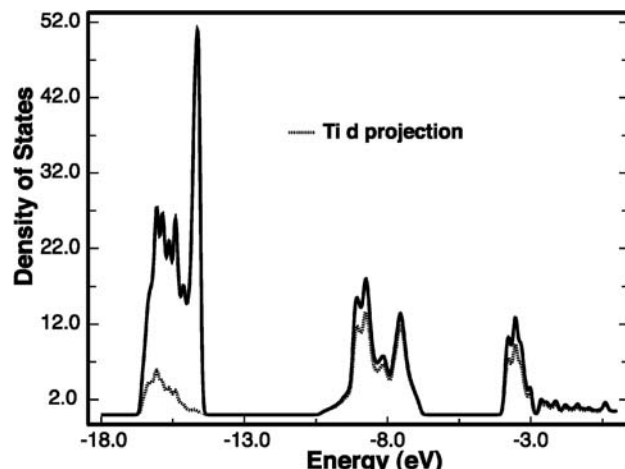
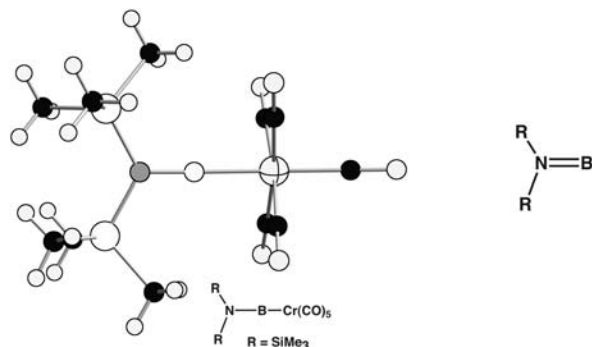


**FIGURE 15.15**  
DOS for anatase  $TiO_2$ .

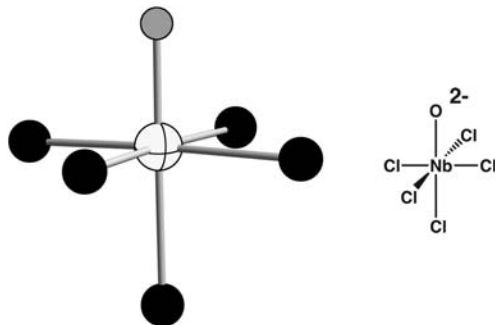
spread out and the “ $e_g$ ” levels lie at lower energies in  $\text{TiO}_2$  but given that the much greater complexity in the structure of **15.75** compared to **15.71**, the similarity of the two DOS curves is encouraging. In this vein, it is usually possible to provide a rough sketch of the DOS and associated COOP curves if one has some knowledge about the electronic structure in the unit cell and how much band dispersion (in a very rough sense) is likely to occur. The same cannot be said about the  $e(k)$  plots of the band structure. While one-dimensional or high-symmetry situations (e.g., Figure 15.13) can be constructed in a qualitative sense without the aid of a computer, the band structure of a distorted perovskite similar to that in **15.74** or  $\text{TiO}_2$  in **15.75** would prove to be too much of a challenge. We have avoided a discussion how to determine the Fermi level (i.e., the highest-occupied level) in the solid-state structures or even how many levels are filled in our octahedral molecular examples. The topic of how to do electron counting is one of the main ones covered in the next chapter.

## PROBLEMS

- 15.1.** A number of transition metal complexes have been prepared using the aminoborylene ligand,  $\text{R}_2\text{N}=\text{B}$ . An example from Reference [47] of a  $\text{Cr}(\text{CO})_5$  complex is shown below. This immediately suggests that the aminoborylene ligand somehow resembles CO. Compare and contrast the two ligands.

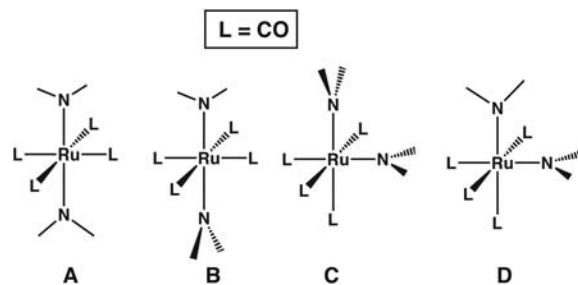


- 15.2.** The  $\text{Cl}_5\text{NbO}^{2-}$  complex has been known for sometime. Using Figure 15.3 as a guide, show the bonding between niobium and oxygen. We will treat electron counting extensively in the next chapter. For now count the ligands as  $\text{Cl}^-$  and  $\text{O}^{2-}$ .

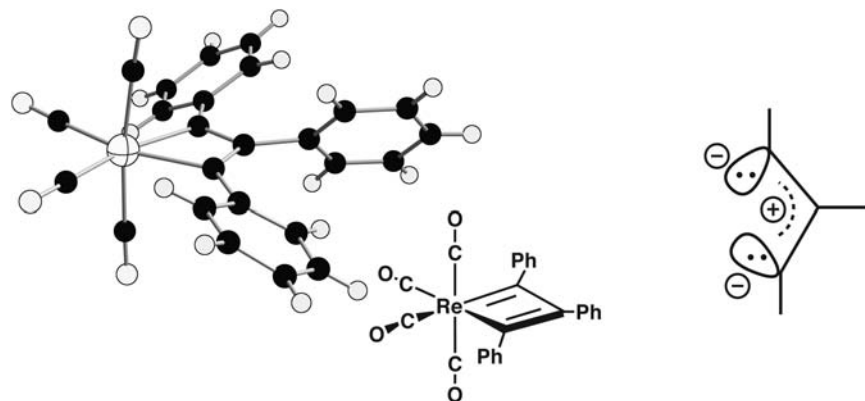


- 15.3.** The M—O bond length for the entire series of  $\text{M}(\text{H}_2\text{O})_6^{2+}$  from the first transition row is known. They are M=Ca (2.40 Å), Sc (2.31), Ti (2.25), V (2.18), Cr (2.24), Mn (2.28), Fe (2.18), Co (2.12), Ni (2.15), Cu (2.16), and Zn (2.19 Å). All of these complexes (except Ca, Sc, Cu, and Zn) are high spin. Comment on what the M—O bond length changes show.

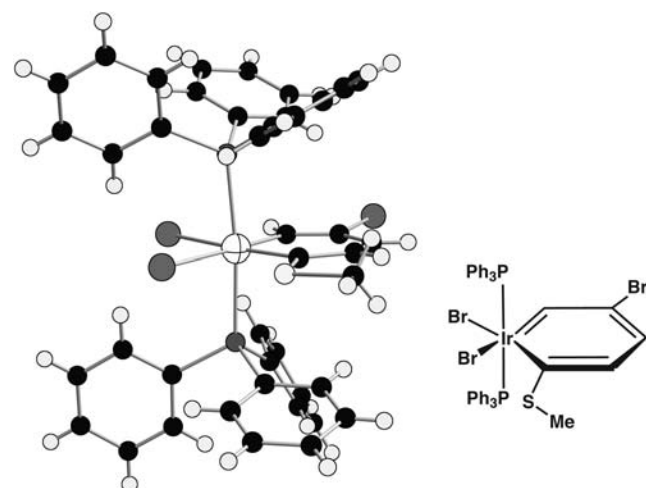
**15.4.** Consider the four geometries for  $\text{Ru}(\text{NMe}_2)_2(\text{CO})_4$  shown below. The electron count here is the same as in  $\text{Cr}(\text{CO})_6$ . Make an estimate of the stability order (hint:  $\text{NMe}_2$  is expected to be a stronger donor than  $\text{CO}$ ; why?).



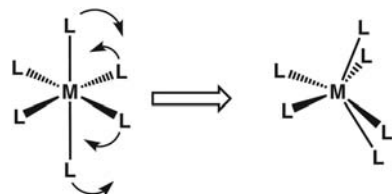
**15.5.** The structure below from Reference [48] is an example of a metallacyclobutadiene. There is little, if any, bond alternation here in contrast to cyclobutadiene itself. Using Figure 15.3 again as a guide draw an interaction diagram to illustrate the  $\pi$  bonding in this molecule. Count the bisdehydropropenyl system as anionic which makes the electron count around Re to have six  $d$  electrons.



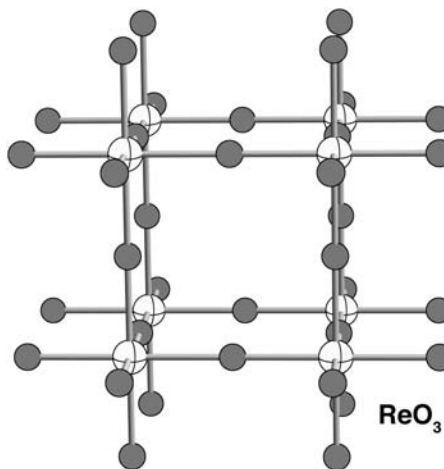
**15.6.** There are also a number of metallabenzenes which have been prepared. One example is given in Reference [49]. Draw out a similar orbital interaction diagram using a bisdehydropentadienyl anion. The Ir atom then has again six  $d$  electrons.



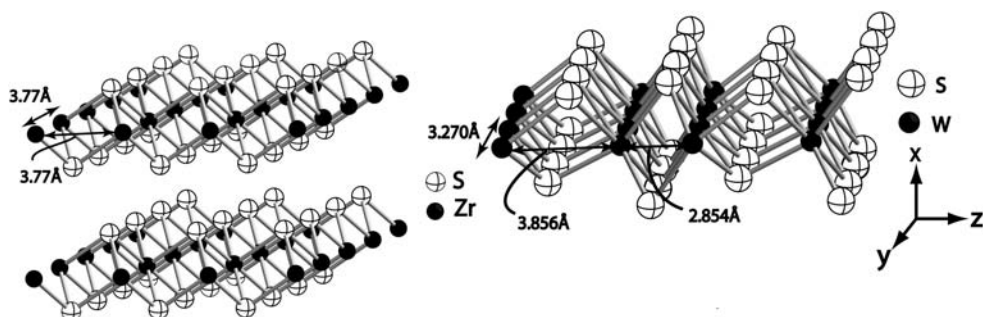
- 15.7.** Draw a Walsh diagram for the distortion from an octahedron to a bicapped tetrahedron ( $C_{2v}$ ) for the  $t_{1u}$  and  $t_{2g}$  MOs.



- 15.8.**  $\text{ReO}_3$  has a cubic perovskite structure. Sketch the DOS and corresponding Re–O COOP curve and indicate the position of the Fermi level. For the purposes of electron counting, count oxygen as  $\text{O}^{2-}$ .



- 15.9.** The structure of  $\text{ZrS}_2$  is shown below. It is a layered structure where face-shared Zr octahedra spread out in two dimensions. The closest Zr–Zr contact is the same in both directions, 3.77 Å. There is something different in  $\text{WS}_2$ . It has the same layered structure but the W–W distances within the layer are not all the same. As shown below, the W–W distances in front of and in back of the plane of the paper are all 3.270 Å. On the other hand, the W–W distances along the plane of the paper alternate (3.856 and 2.854 Å). First draw the DOS curve for  $\text{WS}_2$  in the *undistorted*  $\text{ZrS}_2$  structure. Show the position of the Fermi level counting sulfur as  $\text{S}^{2-}$ . Then draw the DOS and Fermi level for the W  $d$  region going to the real structure. Use the coordinate system the right to identify any orbitals in your drawing.



---

## REFERENCES

---

1. (a) J. B. Mann, T. L. Meek, E. T. Knight, J. L. Capitani, and L. C. Allen, *J. Am. Chem. Soc.*, **122**, 5132 (2000); (b) P. Macchi, D. M. Proserpio, and A. Sironi, *Organometallics*, **16**, 2101 (1997).
2. (a) P. A. Breeze, J. K. Burdett, and J. J. Turner, *Inorg. Chem.*, **20**, 3369 (1981) and references therein; (b) N. E. Kime, and J. A. Ibers, *Acta Crystallogr.*, **B25**, 168 (1969); T. Barnet, B. M. Craven, N. E. Kime, and J. A. Ibers, *Chem. Commun.*, 307 (1966).
3. J. L. Hubbard and D. L. Lichtenberger, *J. Am. Chem. Soc.*, **104**, 2132 (1982); D. L. Lichtenberger and G. E. Kellogg, *Acc. Chem. Res.*, **20**, 379 (1987).
4. A. Diefenbach, F. M. Bickelhaupt, and G. Frenking, *J. Am. Chem. Soc.*, **122**, 6449 (2000).
5. R. K. Hocking and T. W. Hambley, *Organometallics*, **26**, 2815 (2007).
6. R. J. Goddard, R. Hoffmann, and E. D. Jemmis, *J. Am. Chem. Soc.*, **102**, 7667 (1980); W. A. Nugent, R. J. McKinney, R. V. Kasowski, and R. A. Van-Catledge, *Inorg. Chim. Acta*, **65**, L91 (1982).
7. N. M. Kostic and R. F. Fenske, *Organometallics*, **1**, 489 (1982); U. Schubert, D. Neugebauer, P. Hofmann, B. E. R. Schilling, H. Fischer, and A. Motsch, *Chem. Ber.*, **114**, 3349 (1981).
8. T. Ziegler and A. Rauk, *Inorg. Chem.*, **18**, 1755 (1979).
9. A. W. Ehlers, S. Dapprich, S. F. Vyboishchikov, and G. Frenking, *Organometallics*, **15**, 105 (1996); A. Kovacs and G. Frenking, *Organometallics*, **20**, 2510 (2001); G. Frenking, K. Wichmann, N. Fröhlich, J. Grobe, W. Golla, D. Le Van, B. Krebs, and M. Läge, *Organometallics*, **21**, 29221 (2002).
10. A. G. Orpen and N. G. Connelly, *J. Chem. Soc. Chem. Commun.*, 1310 (1985); A. G. Orpen and N. G. Connelly, *Organometallics*, **9**, 1206 (1990).
11. G. J. Kubas, *Metal Dihydride and (-Bond Complexes*, Kluwer Academic, New York (2002).
12. D. S. Nemcsok, A. Kovacs, V. M. Rayon, and G. Frenking, *Organometallics*, **21**, 5803 (2002).
13. M. M. L. Chen, Ph.D. Dissertation, Cornell University (1976); N. Rösch and R. Hoffmann, *Inorg. Chem.*, **13**, 2656 (1974).
14. J. K. Burdett and T. A. Albright, *Inorg. Chem.*, **18**, 2112 (1979).
15. T. A. Albright, personal communications.
16. E. Cormona, J. M. Marin, M. L. Poveda, J. L. Atwood, R. D. Rogers, and G. Wilkinson, *Angew. Chem.*, **94**, 467 (1982); J. W. Byrne, H. V. Blaser, and J. A. Osborn, *J. Am. Chem. Soc.*, **97**, 3871 (1975).
17. B. Shevrier, Th. Diebold, and R. Weiss, *Inorg. Chim. Acta*, **19**, L57 (1976).
18. C. Bachmann, J. Demuynck, and A. Veillard, *J. Am. Chem. Soc.*, **100**, 2366 (1978).
19. T. A. Albright, R. Hoffmann, J. C. Thibeault, and D. L. Thorn, *J. Am. Chem. Soc.*, **101**, 3801 (1979).
20. S. Dietz, V. Allured, and M. Rakowski DuBois, *Inorg. Chem.*, **32**, 5418 (1993).
21. R. J. Gillespie and P. L. A. Popelier, *Chemical Bonding and Molecular Structures*, Oxford University Press, Oxford (2001).
22. J. K. Burdett, *Inorg. Chem.*, **20**, 1959 (1981).
23. I. B. Bersuker, *The Jahn–Teller Effect*, University Press, Cambridge (2006).
24. H. Stratemeier, B. Wagner, E. R. Krausz, R. Linder, H. H. Schmidtke, J. Pebler, W. E. Hatfield, L. ter Haar, D. Reinen, and M. A. Hitchman, *Inorg. Chem.*, **33**, 2320 (1993).
25. S. Alvarez, D. Avnir, M. Llunell, and M. Pinsky, *New J. Chem.*, **996** (2002).
26. P. Kubacek and R. Hoffmann, *J. Am. Chem. Soc.*, **103**, 4320 (1981).
27. J. L. Templeton, P. B. Winston, and B. C. Ward, *J. Am. Chem. Soc.*, **103**, 7713 (1981).
28. M. Kamata, K. Hirotsu, T. Higuchi, K. Tatsumi, R. Hoffmann, T. Yoshida, and S. Otsuka, *J. Am. Chem. Soc.*, **103**, 5772 (1981).
29. R. Hoffmann, J. M. Howell, and A. R. Rossi, *J. Am. Chem. Soc.*, **98**, 2484 (1976).
30. S. K. Kang, H. Tang, and T. A. Albright, *J. Am. Chem. Soc.*, **115**, 1971 (1993).
31. M. Kaupp, *J. Am. Chem. Soc.*, **118**, 3018 (1996); see also M. Kaupp, *Angew. Chem. Int. Ed.*, **40**, 3534 (2001) for a review.

32. V. Pfennig and K. Seppelt, *Science*, **271**, 626 (1996); see also K. Seppelt, and B. Roessler, *Angew. Chem. Int. Ed.*, **39**, 1259 (2000); S. Kleinhenz, V. Pfennig, and K. Seppelt, *Chem. Eur. J.*, **4**, 1687 (1998); B. Roessler, V. Pfennig, and K. Seppelt, *Chem. Eur. J.*, **7**, 3652 (2001) for related material.
33. X. Wang and L. Andrews, *J. Am. Chem. Soc.*, **124**, 5636 (2002).
34. R. J. Gillespie, I. Bytheway, T.-H. Tang, and R. F. W. Bader, *Inorg. Chem.*, **35**, 3954 (1996).
35. C. Landis, T. K. Firman, D. M. Root, and T. Cleveland, *J. Am. Chem. Soc.*, **120**, 1842 (1998).
36. M.-H. Whangbo and M. J. Fossee, *Inorg. Chem.*, **20**, 113 (1981).
37. A. Lachgar, D. G. Dudis, and J. D. Corbett, *Inorg. Chem.*, **29**, 2242 (1990).
38. R. Chen, M. Greenblatt, and L. A. Bendersky, *Chem. Mater.*, **13**, 4094 (2001).
39. J. K. Burdett and S. A. Gramsch, *Inorg. Chem.*, **33**, 4309 (1994).
40. R. A. Wheeler, M.-H. Whangbo, T. Hughbanks, R. Hoffmann, J. K. Burdett, and T. A. Albright, *J. Am. Chem. Soc.*, **108**, 2222 (1986).
41. M. W. Lufaso and P. M. Woodward, *Acta Crystallogr.*, **B60**, 10 (2004).
42. E. J. Kan, H. J. Xiang, C. Lee, F. Wu, J. L. Yang, and M.-H. Whangbo, *Angew. Chem. Int. Ed.*, **49**, 1603 (2010).
43. A. Sani, M. Hanfland, and D. Levy, *J. Solid State Chem.*, **167**, 446 (2002).
44. A. A. Belik, M. Azuma, T. Saito, Y. Shimakawa, and M. Takano, *Chem. Mater.*, **17**, 269 (2005).
45. A. A. Belik, S. Iikubo, K. Kodama, N. Igawa, S. Shamoto, S. Niitaka, M. Azuma, Y. Shimakawa, M. Takano, F. Izumi, and E. Takayama-Muromachi, *Chem. Mater.*, **18**, 798 (2006).
46. A. Palewicz, R. Przenioslo, I. Sosnowska, and A. Hewat, *Acta Crystallogr. B*, **63**, 537 (2007).
47. H. Braunschweig, M. Colling, C. Kollann, H. G. Stammler, and B. Neumann, *Angew. Chem., Int. Ed.*, **40**, 2298 (2001).
48. C. Lowe, V. Shklover, and H. Berke, *Organometallics*, **10**, 3396 (1991).
49. G. R. Clark, P. M. Johns, W. R. Roper, and L. J. Wright, *Organometallics*, **27**, 451 (2008).

# Square Planar, Tetrahedral $ML_4$ Complexes and Electron Counting

---

## 16.1 INTRODUCTION

---

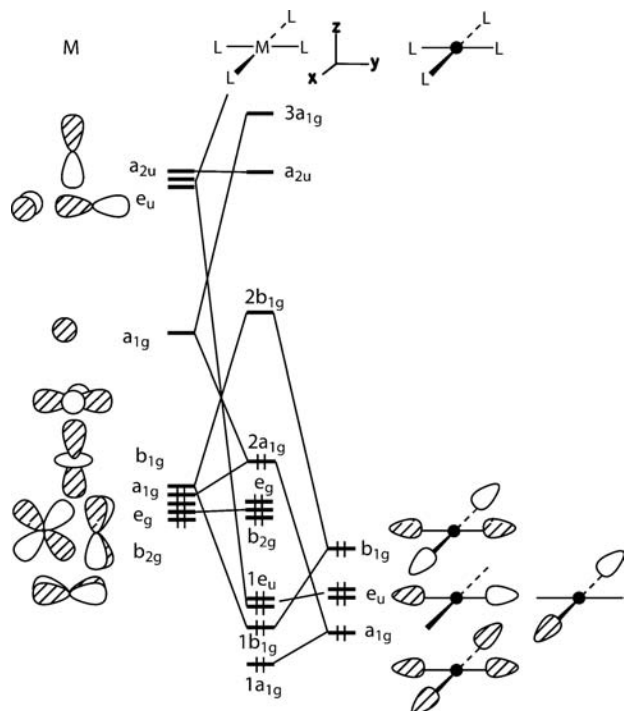
This chapter is a continuation of the last in that the orbitals of our other molecular building block, a square planar  $ML_4$  complex, are developed. This is a little more complicated than the octahedral case; however, we shall need to use the orbitals of both extensively in subsequent chapters. From the octahedral and square planar splitting patterns, a generalized bonding model can be constructed for transition metal complexes. This, in turn, leads to the topic of electron counting. Finally, we examine one distortion that takes a square planar molecule to a tetrahedron and two examples from the solid state.

---

## 16.2 THE SQUARE PLANAR $ML_4$ MOLECULE

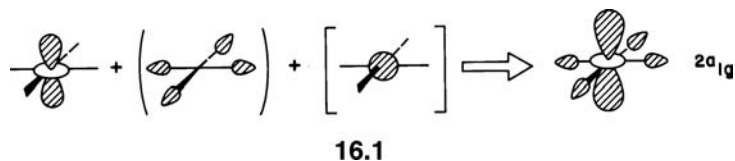
---

We shall again develop the molecular orbitals for a  $D_{4h}$   $ML_4$  complex in a generalized way where the ligands, L, as before represent two-electron  $\sigma$  donors. Figure 16.1 constructs the molecular orbitals (MOs) for this system. In the left side of the figure are the metal s, p, and d levels. In the right side are presented the symmetry-adapted combinations of the four ligand lone pairs. These were developed in some depth for the  $D_{4h}$   $H_4$  system (Section 5.3). Basically, the  $b_{1g}$  lone-pair combination is stabilized by metal  $x^2 - y^2$  and  $e_u$  by metal x and y (see the coordinate system at the top center

**FIGURE 16.1**

Orbital interaction diagram for a square planar,  $D_{4h}$   $ML_4$  complex.

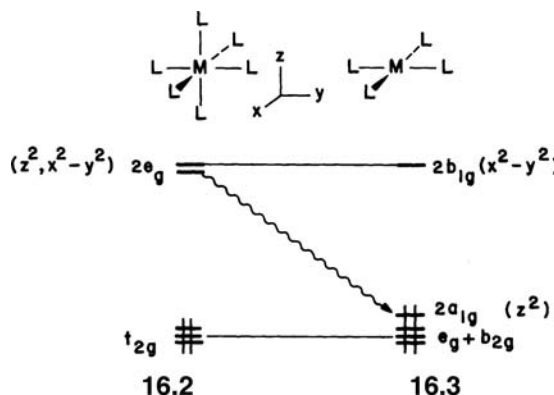
of Figure 16.1). The  $a_{1g}$  combination overlaps with and is stabilized by metal  $z^2$  and s. Here, again is another three-orbital pattern. The molecular level  $1a_{1g}$  is mainly lone-pair  $a_{1g}$  mixed in a bonding way with metal  $z^2$  and s. There is a fully antibonding analog, labeled  $3a_{1g}$ , which consists primarily of metal s character. The middle level,  $2a_{1g}$ , is chiefly  $z^2$  antibonding to the lone-pair  $a_{1g}$  combination. Metal s is also mixed into  $2a_{1g}$  in a bonding fashion to the lone pairs. The net result is sketched in 16.1. Metal  $x^2 - y^2$  is destabilized by the  $b_{1g}$  combination yielding molecular  $2b_{1g}$ , and likewise, metal x and y are destabilized by  $e_u$ . What is left as nonbonding in Figure 16.1 is metal  $xy$ ,  $b_{2g}$ :



16.1

metals  $xz$  and  $yz$ ,  $e_g$ ; and metal z,  $a_{2u}$ . While the resultant level splitting pattern looks complicated at first glance, it is quite simple to construct. Notice that there are four levels,  $b_{2g} + e_g + 2a_{1g}$ , which are primarily metal in character and lie at moderate energy. We have called  $2a_{1g}$  a nonbonding orbital because of the pattern in 16.1. The bonding of metal s to the lone pairs counterbalances the  $z^2$  antibonding and keeps  $2a_{1g}$  at low energy. The reader should recall that the orbital is predominantly  $z^2$  in character and, therefore, is often termed  $z^2$ . Along with these four nonbonding levels are four M—L bonding ones,  $1a_{1g} + e_u + 1b_{1g}$ . So, there will be a total of eight molecular orbitals that lie at low-to-moderate energies and are well separated from the antibonding combinations. In other words, a stable complex will be one wherein these eight bonding and nonbonding levels are filled for a total of 16 electrons. This is a different pattern from that in the octahedral system where 18 electrons represented a stable species.

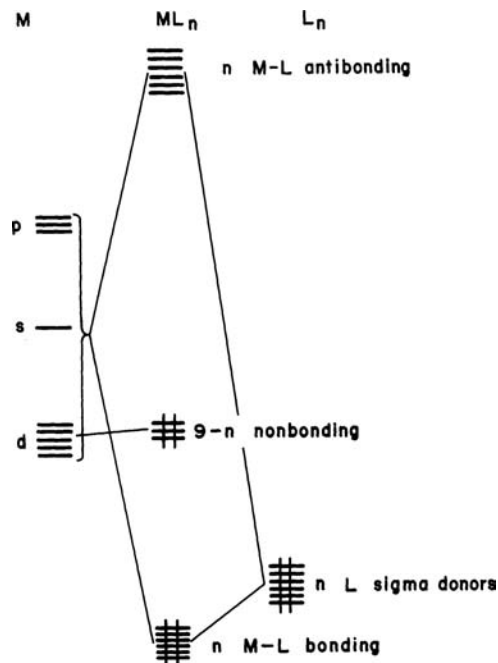
It is instructive to see what is behind this 16–18 electron difference in the two types of complexes. First of all, there are two less ligand-based orbitals for  $ML_4$  compared to  $ML_6$ . Compare Figure 15.1 with Figure 16.1. One of the  $e_g$  and one of the  $t_{1u}$  lone-pair contributions are lost in  $ML_4$ . Secondly, when the two trans ligands in  $ML_6$  are removed, the  $z^2$  component of  $2e_g$  is stabilized considerably, yielding  $2a_{1g}$ . Pictorially, this is shown in 16.2 and 16.3. So, the  $ML_4$  complex gains one metal



nonbonding orbital over that in  $ML_6$  and loses two M—L bonding orbitals. The net result is that there is one less valence level or two less electrons in the stable square planar complex. Notice also in Figure 16.1 that there is one high lying orbital of  $a_{2u}$  symmetry that is also left nonbonding. This orbital, primarily metal z, is clearly too high in energy to be filled. In the octahedral  $ML_6$  system, it was one member of the  $2t_{1u}$  set. Our chief concern will be with the metal-based orbitals at moderate energy. As 16.2 and 16.3 indicate, there is a close correspondence between the splitting patterns in  $O_h$   $ML_6$  and  $D_{4h}$   $ML_4$ . Four orbitals are identical in the two systems. It is only the  $z^2$  component of  $2e_g$  in  $ML_6$  that becomes  $2a_{1g}$  in  $ML_4$  that is modified. The way in which  $\pi$  acceptors or  $\pi$  donors modify 16.3 can be followed in a way that is identical to that for  $ML_6$  in Section 15.3. Therefore, we do not spend any further time on this issue. The correspondence suggests that there may be a general pattern for any  $ML_n$  complex. This, along with electron counting, is the topic of concern in the next section.

### 16.3 ELECTRON COUNTING

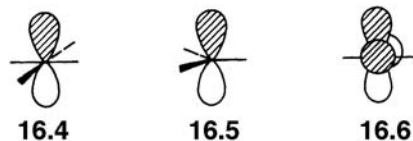
Most stable, diamagnetic transition metal complexes possess a total of 18 valence electrons. We covered some exceptions to this in Chapter 15 and the square planar  $ML_4$  situation presents possibilities for another. But, apart from these, the overwhelming majority of compounds are of the 18 valence electron type. In other words, the number of nonbonding electrons at the metal plus the number of electrons in the M—L bonds, which we have formally assigned to the ligands, should total 18. Yet, another way of putting this is that there are 18 electrons associated with the metal. The derivation of this rule can be constructed in a number of ways. A transition metal will have five  $nd$  (where  $n$  is the principal quantum number), three  $(n+1)p$ , and one  $(n+1)s$  atomic orbitals (AOs), which form bonding combinations to the surrounding ligands or remain nonbonding. These nine AOs will then house 18 electrons. This is true for most geometries, but it can be seen that when all of the ligands lie in a plane containing the transition metal one  $p$  AO (perpendicular to this plane) cannot take part in the interactions.

**FIGURE 16.2**

Generalized orbital interaction diagram for a  $\text{ML}_n$  complex where the ligands are arranged in a spherical manner around the transition metal.

The 18-electron rule is therefore nothing but a restatement of the Lewis octet rule. The extra 10 electrons are associated with the five  $d$  orbitals. A more elaborate way to express this is shown in Figure 16.2. The orbitals of any  $\text{ML}_n$  complex can be developed in a way that is analogous to what we have done for  $\text{ML}_6$ ,  $\text{ML}_4$ , and the  $\text{AH}_n$  series. Figure 16.2 does so for a generalized transition metal system. There are  $n$  ligand-based lone pairs illustrated at the lower right of this figure. Symmetry-adapted linear combinations of the  $n$  ligand orbitals will normally find matches with  $n$  of the nine metal-based AOs. This produces  $n$  M—L bonding and  $n$  M—L antibonding MOs. Left behind are  $9-n$  nonbonding orbitals that are localized at the metal. These  $9-n$  nonbonding levels will be primarily metal  $d$  in character since the metal AOs start out with the  $d$  set lower in energy than  $s$  and  $p$ . Furthermore,  $d$  AOs are more nodded than the  $s$ - or  $p$ -type functions, so that, it is more likely for the ligand set to lie on or near the nodal plane of  $d$ -based functions. (The glaring exception to this generalization occurs when the metal and ligands lie in a common plane.) There are, therefore, a total of  $n + (9 - n) = 9$  valence levels at low-to-moderate energies that constitute bonding and nonbonding interactions and 18 electrons can be housed in them.

The square planar system was different (Figure 16.1) in that one  $p$  orbital at the metal, **16.4**, found no symmetry match. There are four metal orbitals primarily of



$d$  character at moderate energies, and **16.4**, which lies at an appreciably higher energy. It is unreasonable to expect that two electrons should be placed in **16.4**, and therefore, stable square planar  $\text{ML}_4$  complexes have 16 valence electrons. A trigonal  $\text{ML}_3$  complex will also have one empty metal  $p$  orbital, **16.5**, and a stable complex will thus be of the 16-electron type. Examples of these two cases are very common in

inorganic chemistry. Linear  $ML_2$  compounds have two nonbonding  $p$  AOs, **16.6**, so here, a 14-electron complex will be stable. Compounds of this type are more rare. Two examples are  $M(CO)_2^+$  salts, where  $M = Ag$  and  $Au$  [1].

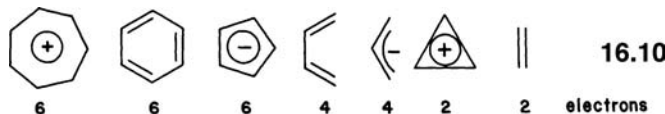
This sort of generalized interaction diagram in Figure 16.2 can be extended to main group compounds where the  $d$  orbitals on the central atom have been neglected. The 6-electron, trigonal  $BR_3$ , and other electron deficient compounds are then related in an obvious way to 16-electron square planar  $ML_4$  and trigonal  $ML_3$  complexes. In the hypervalent  $AH_6$  and  $AH_4$  molecules (Section 14.1), there are two and one “ligand” combinations, respectively, which do not match in symmetry the central atom’s  $s$  and  $p$  set. For example, the electron count at the central atom in  $SH_6$  is still 8, although the total number of electrons is 12 (there are, however, violations of this rule, see discussion in Chapter 14). This can also happen, albeit with much less frequency, for transition metal complexes [2]. An example discussed shortly is tris(acetylene) $W(CO)$  that appears to be a 20-electron complex. However, here one occupied acetylene  $\pi$  combination does not find a symmetry match with the metal AOs, and so, the compound is in reality an 18-electron system.

This brings up the mechanics of electron counting. The convention that we shall use is to treat all ligands as Lewis bases. Listed in **16.7** are some typical two-electron  $\sigma$  donors groups. In **16.8** are listed some two-electron  $\sigma$  donors that also have one or two  $\pi$  acceptor functions. We covered the CO and  $CR_2$  cases explicitly in

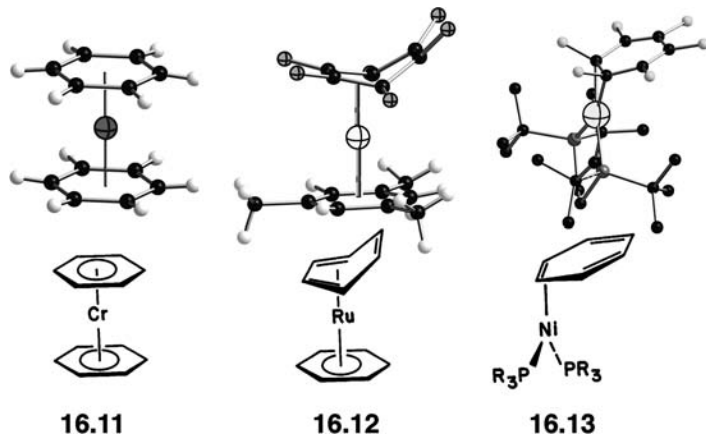
$NR_3$ , $PR_3$ , $CH_3^-$ , $SIR_3^-$ , $H^-$	<b>16.7</b>
$CO$ , $CNR$ , $SO_2$ , $CR_2$ , $NO^+$ , $CR^+$	<b>16.8</b>
$NR_2^-$ , $Cl^-$ , $OR^-$ , $SR_2$ , $NR^2-$ , $O^{2-}$	<b>16.9</b>

Section 15.2. For the purposes of electron counting, it does not matter what the strength of  $\pi$  bonding really is between the metal and ligand. The ligands are counted only in so far as their  $\sigma$  donating numbers. The ligands in **16.9** are two-electron  $\sigma$  donors with  $\pi$  donor functions. The ways that electrons are assigned to the ligands in **16.7–16.9** are only conventions. One could just as well have had alkyl groups and hydrides as one-electron, neutral ligands. Exactly, the same electron count at the metal will be obtained. What changes is the oxidation state at the metal—the number of electrons that are formally assigned to the metal. The nitrosyl ( $NO$ ) group is a particularly difficult case. Counting it as a cationic system stresses the analogy to the isoelectronic  $CO$  group. The  $M-NO$  coordination mode is then expected to be linear. Indeed, there are many examples of this type, but there are also compounds where the  $M-N-O$  angle is appreciably less than  $180^\circ$ . A detailed discussion of this distortion is reserved for Section 17.5. The point is that with a bent geometry, the nitrosyl can be considered as an anionic four-electron donor. The “extra” two electrons are housed in an  $NO$ -based  $\pi^*$  orbital (which causes the nitrosyl group to bend; recall the ammonia inversion problem in Section 9.2), and only partial  $\pi$  back donation occurs to an empty metal orbital.

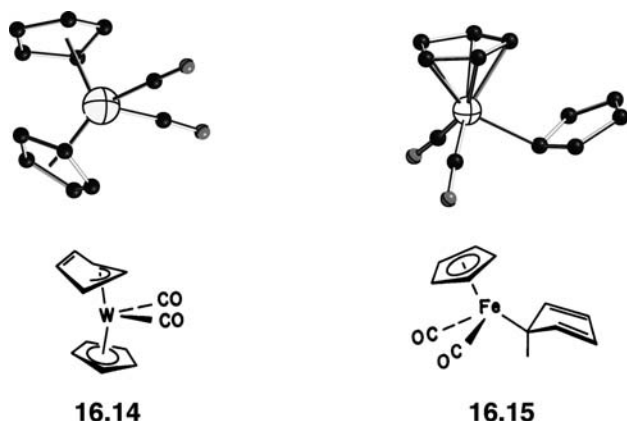
Polyenes are also considered as Lewis bases. They are counted such that all their bonding and nonbonding levels are occupied. Some representative examples are given in **16.10**. Listed below each structure is the number of electrons donated to the metal. Some care, however, must be used to establish the connectivity of these



polyenes to the metal. The benzene ligand will donate its six  $\pi$  electrons to the metal only if all six-carbon atoms are bonded to the metal atom. A shorthand notation to denote this is the hapto number. In this example, it would be called an  $\eta^6$  complex. Bis(benzene)chromium, **16.11**, contains two  $\eta^6$  benzene ligands; all Cr-C distances are equivalent [3]. In a derivative of **16.12** [4], the hexafluoro arene ring is  $\eta^4$  and the mesitylene is  $\eta^6$ . In other words, two Ru-C distances are much longer than that found for the other ten. The hexafluoro derivative [5] of **16.13** contains an  $\eta^2$  benzene ligand. In the  $\eta^4$  case, a total of four  $\pi$  electrons and



in the  $\eta^2$  example two  $\pi$  electrons are donated to the metal. Likewise, the two cyclopentadienyl ligands will donate a total of 12  $\pi$  electrons if both are  $\eta^5$  in  $Cp_2W(CO)_2$ . As we shall shortly see, this will put a total of 20 electrons shared between the metal and surrounding ligands. This is two electrons too many and so one cyclopentadienyl donates four electrons with an  $\eta^3$  geometry, the upper Cp in **16.14**, [6] while the lower Cp stays at an  $\eta^5$  geometry. In  $Cp_2Fe(CO)_2$ , **16.15** [7],



one Cp is  $\eta^1$  and donates two electrons while the other remains  $\eta^5$ . An isoelectronic situation would put both Cp ligands at  $\eta^3$ . Presumably, this is the transition state for the exchange reaction between the two Cp ligands. Thus, the connectivity of the polyene to the metal must be carefully established. Alternatively, one can assign an 18- or 16-electron count at the metal, and this sets the coordination mode of the

Polyene. The portion of the polyene that is not bonded to the metal bends out of the plane defined by the coordinated carbons in a direction away from the metal [8]. This stereochemical feature has been highlighted in the drawings of **16.11–16.15** along with the actual slippage of the metal over the coordinated portion of the polyene. Thus, a fairly detailed geometrical prediction can be made for polyene metal complexes on the basis of electron counting.

The number of  $d$  electrons (the electrons housed in the  $9-n$  nonbonding levels of Figure 16.2) assigned to the metal is determined by adding the number of charges at the ligands and subtracting this sum from the total charge on the molecule. This gives the formal charge or oxidation state at the metal. Finally, the number of  $d$  electrons is then equal to the number of  $d$  electrons at the metal in the zero oxidation state minus the oxidation state (formal charge) assigned to the metal. **16.16** lists the number of  $d$  electrons for the transition metals in their zero oxidation state. Notice that this is not the atomic electron configuration. In other words,

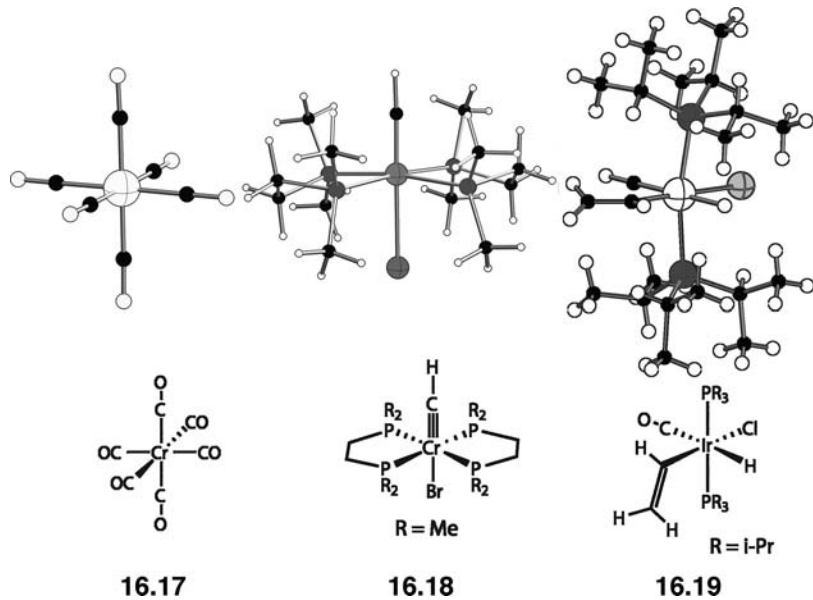
$d^4$	$d^5$	$d^6$	$d^7$	$d^8$	$d^9$	$d^{10}$	$d^{10} s^1$
Ti	V	Cr	Mn	Fe	Co	Ni	Cu
Zr	Nb	Mo	Tc	Ru	Rh	Pd	Ag
Hf	Ta	W	Re	Os	Ir	Pt	Au

### 16.16

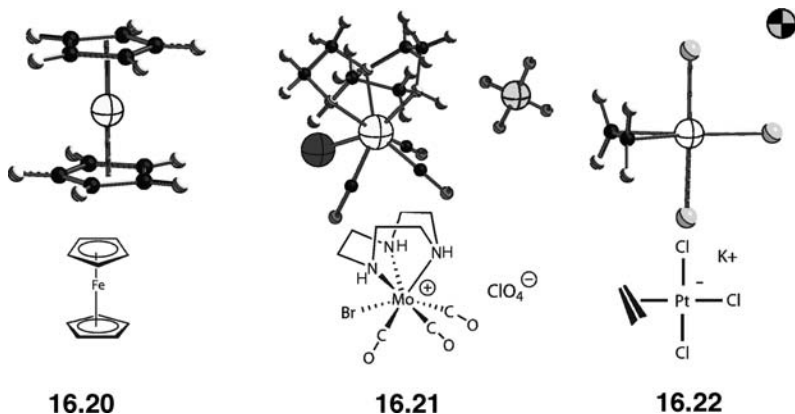
$Ti(0)$  is  $d^4$  rather than the atomic configuration  $3d^24s^2$ . The total number of electrons associated with the metal, that is, the number of electrons in the  $nM-L$  bonding and  $9-n$  nonbonding orbitals (see Figure 16.2), is equal to the number of  $d$  electrons plus the number of electrons that have been donated in a  $\sigma$  fashion by the ligand set.

We want to be very clear here. The assignment of an oxidation state at the metal rests on the charges assigned to the surrounding ligands, and this is entirely arbitrary. The most simple ligand, hydrogen, could be regarded as a hydride like it is in **16.7**, a proton (and metal hydrides are frequently acidic) or something in between. Thus, our decision of the oxidation state at the metal is subjective. But sometimes, this is a source of great controversy [9]. In our formulation,  $\sigma M-L$  bonds are counted while  $M-L\pi$  bonds are not. Many would object to this. Our use of electron counting is focused primarily upon setting up an interaction diagram where the weaker perturbations (e.g.,  $M-L\pi$  bonding) are explicitly examined. Clearly, the coordination of Lewis acids to a transition metal does not correspond to the ligand electron counting schemes in **16.7–16.9**. For example, when  $Me_3Al$  coordinates to an organometallic complex, the bonding pattern is certainly not one where two electrons are transferred from the ligand to the metal, on the contrary, the reverse—two electrons from the metal are transferred to the ligand. Consequently, the formal oxidation state at the metal would be increased by one. There are generalized ways of handling these situations that shall not be covered here [10].

A few simple examples should make this electron counting rule clearer. In  $Cr(CO)_6$ , **16.17** [11], the CO groups donate two  $\sigma$  electrons each for a total of 12 electrons. The charge on the molecule and each CO is zero, so Cr is in the zero oxidation state, that is, it is a  $d^6$  complex (see **16.16**). The total number of electrons associated with Cr is  $6 + 12 = 18$ . In The Fischer carbyne complex [12], **16.18**, the carbyne ligand is taken to be a cationic 2-electron  $\sigma$  donor (see **16.8**) and Br is counted as an anionic two-electron donor (**16.9**). Together with the four phosphine



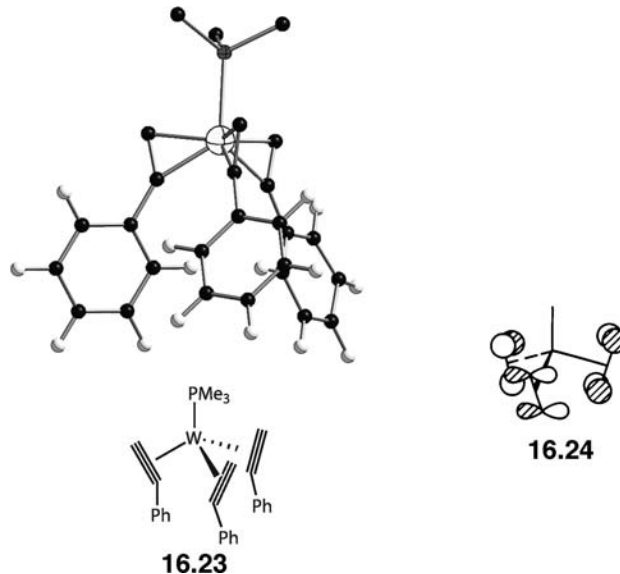
groups makes for a total of 12 electrons from the ligand set, which are donated to the metal. The molecule is neutral, and the total charge on the ligand set is zero; therefore, the metal is  $\text{Cr}(0)$ ,  $d^6$ . Again, there is a total of  $6 + 12 = 18$  electrons associated with the metal. In 16.19 [13], the hydride, chloride, and vinyl groups are anionic. The CO and two phosphines are neutral, so 12 electrons are donated with a net charge of  $-3$ . The complex is neutral, so this is  $\text{Ir}^{3+}$ ,  $d^6$ . This is yet another 18-electron complex. In a qualitative level, the orbital pattern and filling is just that for the generic  $\text{ML}_6$  example in Figure 15.1, namely, there are six  $\text{M}-\text{L}$   $\sigma$  bonding levels filled. All three examples here are  $d^6$ , so the  $t_{2g}$  set is also filled. One can easily take into account the two  $\pi$  bonds in 16.18 by a second set of interactions along the lines given in Figure 15.3. The compounds given by 16.20 and 16.21 are also 18-electron systems. In ferrocene [14], 16.20, the cyclopentadienyl ( $\text{Cp}$ ) ligands are  $\eta^5$  and counted as a six- $\pi$ -electron  $\text{Cp}^-$  (see 16.10). The metal is then  $d^6 - \text{Fe}^{2+}$ . We shall see in Chapter 20 that the splitting pattern for the  $d$  AOs in ferrocene strongly resembles those in an octahedron. Electron counting then tells us that the lower



three  $d$  orbitals are filled. Finding the oxidation state for 16.21 [15] is a little more complicated. There are a neutral trisamine and three carbonyls, a  $\text{Br}^-$  ligand, and a

positive charge associated for the molecule. The oxidation state is then  $\text{Mo}^{2+}$ ,  $-d^4$  and  $4 + 6 + 6 + 2 = 18$  electrons. **16.21** is seven-coordinate and so whatever the splitting pattern one finds here, there should be two  $d$  MOs at low energy, which are filled. In **16.22** [16], there are three  $\text{Cl}^-$  and one neutral ethylene ligands, yielding a total of 8 electrons donated to the metal. The charge on the molecule is  $-1$ , so the oxidation state at Pt is given by  $-1 - (-3) = +2$ .  $\text{Pt}^{2+}$  is  $d^8$  (see **16.16**); therefore, it is an  $8 + 8 = 16$ -electron complex. Notice that the geometry around **16.22** is, as expected from the previous section, square planar. The compounds provided in **16.11**, **16.12**, and **16.14–16.16** all have 18 electrons. The reader should work through these examples. Special attention should be given to **16.12**. One benzene ring is  $\eta^4$ —a four- $\pi$ -electron donor—and the other is  $\eta^6$ —a six-electron donor. But suppose each benzene was  $\eta^6$ . Then, the molecule would be a 20-electron complex. The extra two electrons would enter a M—L antibonding orbital in the generalized scheme of Figure 16.2 (in this case a Ru  $d$ -benzene  $\pi$  antibonding orbital). Clearly, this is expected to be an energetically unfavorable situation. This is not quite true for this special case, and we shall return to the bonding in metallocenes in Section 20.3. **16.13** is an example of a 16-electron trigonal complex. The two coordinated carbons lie in the  $\text{NiP}_2$  plane. A viable alternative to this geometry would be an 18-electron complex where the benzene was  $\eta^4$ . The benzene must distort to something like that given in **16.12** and can be regarded as the equivalent of two olefins coordinated to Ni. We shall see in the next section that tetrahedral complexes are stable at the 18-electron count, and so, the Ni—bisphosphine must rotate by  $90^\circ$  from that in **16.13** to achieve a tetrahedral geometry.

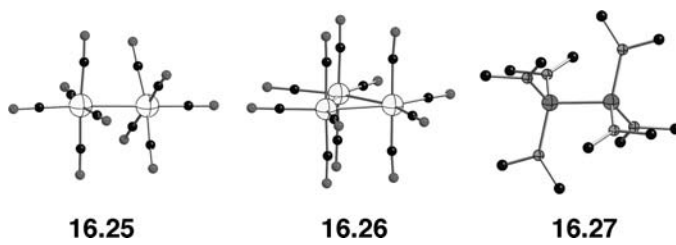
A practical consideration that must be kept in mind when counting electrons is that the ligand donor orbitals must find a metal function with which to overlap. There are a few “high symmetry” situations where this is not followed. The tris(acetylene)-W molecule, **16.23**, is one example [17]. The acetylene ligand carries



two orthogonal  $\pi$  orbitals. Let us consider that one  $\pi$  orbital at each acetylene is pointed directly at the tungsten atom. This will create an  $a_1 + e$  set of “radial”  $\pi$  orbitals. The three orthogonal  $\pi$  orbitals are of  $a_2 + e$  symmetry—a tangential set (see the Walsh model for cyclopropane in Section 11.2). The  $a_1$  and two  $e$  set of  $\pi$

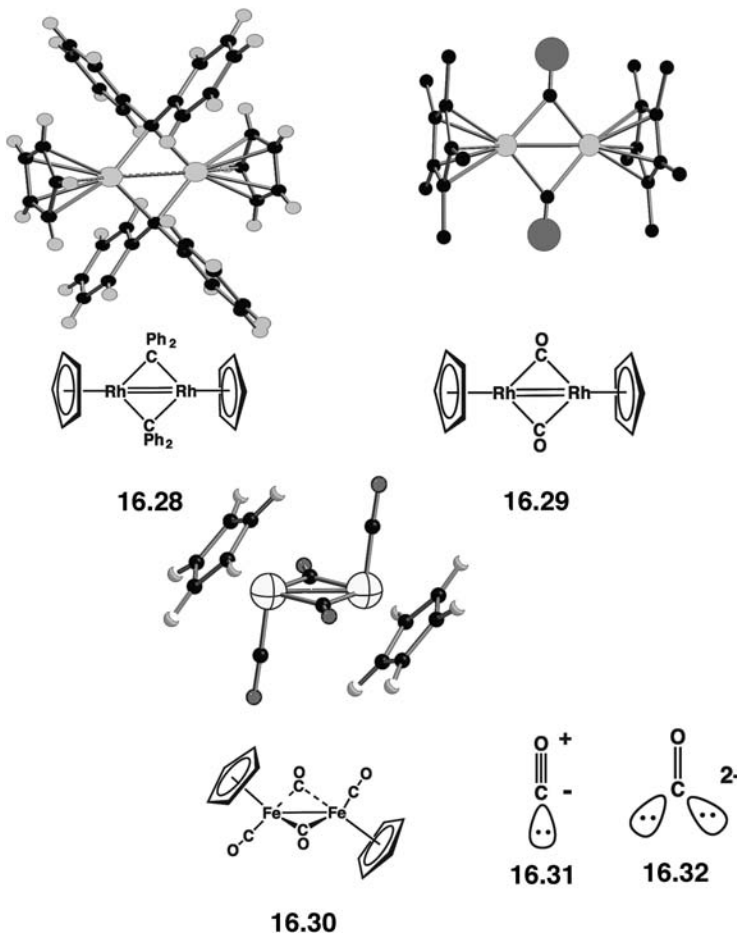
donor orbitals find overlap with tungsten *s*, *p*, and *d* AOs; however, no function on tungsten matches the  $a_2$  combination **16.24** (an *f* AO would overlap with **16.24**). Therefore, the three acetylenes donate a total of 10 electrons, making **16.23** an 18-electron complex. This is analogous to our treatment of main-group hypervalent molecules. We shall see several other examples where symmetry dictates unusual electron counts in later chapters.

Transition metal complexes that have metal–metal bonds pose special problems in electron counting. There are two ways, in general, to approach this problem. One can, just as we have done before, concentrate on the electron count around each metal. If there are fewer than 18 electrons, then one or more nonbonding *d* electrons can be used with one or more nonbonding *d* electrons on a neighboring metal(s) to form two-center-two-electron bonds for each pair shared. Alternatively, one could do a “global” electron count for all of the metals. The resultant electron sum subtracted from 18 times the number of metals tells us the number of shared electrons and half this amount gives the number of metal–metal bonds. A couple of examples will suffice to show the general principles.

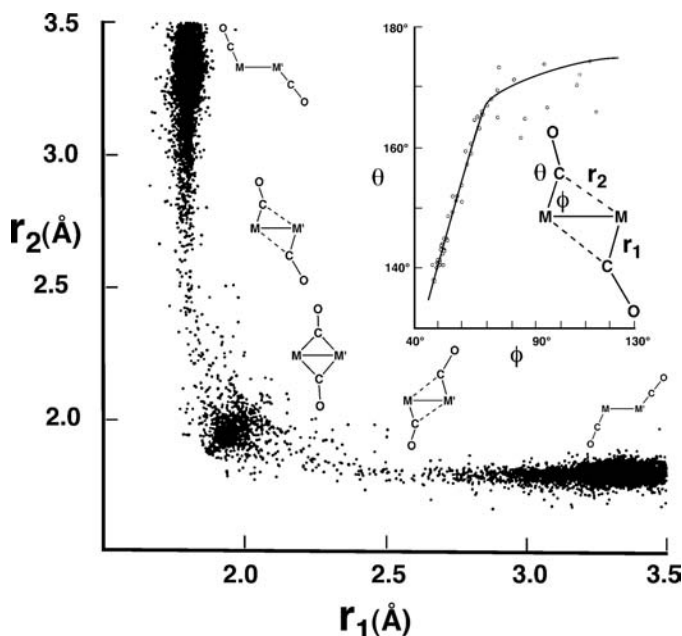


For  $\text{Mn}_2(\text{CO})_{10}$  [18], **16.25**, each Mn is formally  $d^7$ . There are 10 electrons donated by the five CO ligands that would give a 17-electron count at each metal. However, one electron from each Mn is shared with the other. In other words, there is a two-center-two-electron,  $\sigma$  bond formed between the two metal atoms. Obviously, the two electrons are shared equally so each metal attains an 18-electron configuration. In a formal way, each Mn contributes one electron to the Mn–Mn bond that leaves six nonbonding electrons just as in any other 18-electron  $\text{ML}_6$  complex. The octahedral environment for each Mn is clear from **16.25**, and one might expect a splitting pattern very similar to that presented for  $\text{ML}_6$  in Figure 15.1. This is a point that we shall return to in the next chapter. Alternatively, one could count this as  $(2 \times 7) + (10 \times 2) = 34$  electrons. But,  $18 \times 2 = 36$  electrons are needed. Thus, there are  $36 - 34 = 2$  electrons shared or one Mn–Mn bond. In  $\text{Os}_3(\text{CO})_{12}$  [19], **16.26**, there are four carbonyls around each Os. The compound is neutral, so each  $d^8 \text{Os}^0$  has  $4 \times 2 + 8 = 16$  electrons around it. Two electrons are needed to bring the metals up to an 18-electron count; thus, there must be two bonds to each Os. Indeed there are; the molecule has  $D_{3h}$  symmetry. In a global context  $(3 \times 8) + (12 \times 2) = 48$  electrons, but 54 electrons are need. Therefore, 6 electrons need to be shared, which yield three Os–Os bonds. One must be careful in assigning bond orders even in an idealized sense. The ethane-like molecule,  $\text{W}_2(\text{NMe}_2)_6$  [20], **16.27**, has three  $\text{NMe}_2^-$  ligands. Therefore, each  $\text{W}^{3+}$ , is  $d^3$ , so the electron count at each metal is only  $3 \times 2 + 3 = 9$ . Clearly, there cannot be a W–W bond order of nine that leads to the 18-electron count! There are only three nonbonding W electrons to form W–W bonds. Thus, the W–W bond order is three. This brings up the interesting point of what can be the highest bond order between two metals. There are a reasonable number of dimers with a quintuple bond that have been prepared [21]. A M–M bond order of six has been proposed for  $\text{Mo}_2$  and  $\text{W}_2$  [22], and this appears to be the maximum.

Each Rh atom in **16.28** [23] is formally Rh(I),  $d^8$ . We are counting the bridging carbene ligands as neutral two-electron donors (as in **16.8**). Discounting the Rh—Rh



bonding, there are a total of 16 electrons associated with each metal. Sharing two electrons from the neighboring metal will bring each Rh atom up to an 18-electron count. A Rh—Rh double bond is then postulated for this molecule. An identical situation is found for **16.29** (this is really the pentamethyl-Cp derivative [24]) where we have counted the bridging carbonyls as two-electron  $\sigma$  donors. So, again a Rh-Rh double bond is predicted. Bridging groups in transition metal dimers and clusters are often times a source of confusion and controversy. The problem stems from an ambiguity of how to partition the electrons between the metals and bridging groups. Another example is presented in **16.30** [25]. Counting the bridging carbonyl as a neutral, two-electron donor, **16.31**, just as we have done for terminal carbonyls implies that each iron is Fe(I) —  $d^7$ . There will be a total of 10 electrons supplied by the ligands, so the total electron count is 17 and the formation of a single Fe—Fe bond is required to attain an 18-electron configuration. This way of counting the bridging carbonyls implies that they are three-center-two-electron bonds. An alternative and certainly reasonable way to handle the bridging carbonyls is to insist that they are “ketonic.” That is, they make two-center-two-electron bonds to each iron. This implies the dianionic formulation, **16.32**, and each iron is then  $\text{Fe}^{3+}$  —  $d^5$ . The ligand set now donates 12 electrons, so there is an electron count of 17 at each iron and again an 18-electron system will be created with an Fe—Fe single bond. Both methods of electron counting lead to the same conclusion, namely, an 18-electron configuration is attained by the formation of a metal–metal bond. This is

**FIGURE 16.3**

Structure correlation plots for the bridging—terminal carbonyl exchange. The plots have been adopted from References [27,28].

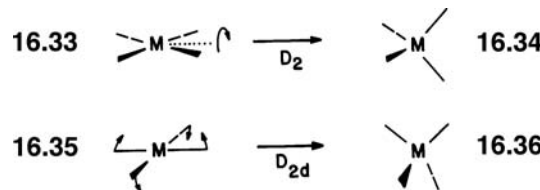
certainly an oversimplification. There are actually a number of occupied metal–metal bonding and antibonding orbitals in **16.30**. The number of occupied bonding levels will exceed the number of occupied antibonding levels by one; however, it is not at all true that each metal–metal orbital carries the same weight toward the total iron–iron overlap population. The bridging carbonyls significantly perturb the electronic environment of the metal-centered orbitals [26]. The situation here is exactly analogous to the one discussed for diborane in Section 10.2. What is different in the transition metal world is that the energy difference between a pair of carbonyl ligands migrating from a bridging to a terminal position normally is a low energy process. Figure 16.3 shows the structural variations found from X-ray studies of many metal carbonyls [27,28]. The clusters of structures at the lower right and upper left of the figure correspond to terminal carbonyls, and the clump of structures at the lower left to the bridging cases. The important point is that there is a smooth continuum of semi-bridging structures in between. This is consistent with the existence of a low energy path for pair-wise rearrangement from terminal to bridging geometries. Angular variations for a smaller set of structures are plotted in the upper right of Figure 16.3. There is a fairly large variation of the M–C–O angles in the terminal side of the structures ( $\phi > 80^\circ$ ), which is consistent with low-frequency carbonyl bending motions, but upon going to a semi-bridging coordination, there is a strong, linear correlation between the two angles.

The only difference that is created in the two ways of counting electrons for **16.30** is that different oxidation states for iron are obtained and, of course, the number of  $d$  electrons formally assigned to the metal changes. That is just a formalism. There is really no right or wrong way to partition the electrons associated with the metal. One hopes that the methods used to assign electrons for the ligands in these complexes will lead to an oxidation state (charge) at the metal that approaches reality. But, this is probably an unreasonable expectation. Treating each ligand in **16.7–16.10** as a Lewis base does offer a practical advantage. What we are really saying is that the  $\sigma$  donor orbitals of the ligands lie at lower energy than the metal  $d$  levels—see Figure 16.2. This is normally the case. Furthermore, the number of  $d$  electrons assigned will then correspond to those contained with the  $9-n$  nonbonding levels of Figure 16.2. For example, in  $\text{Cr}(\text{CO})_6$ , there are

three “nonbonding” levels—the  $t_{2g}$  set of Figure 15.1.  $\text{Cr}(\text{CO})_6$  is counted as being  $d^6$  so those six electrons are housed in  $t_{2g}$ . A  $d^4 \text{ML}_6$  complex will possess four electrons in  $t_{2g}$ , and so on.

## 16.4 THE SQUARE PLANAR-TETRAHEDRAL $\text{ML}_4$ INTERCONVERSION

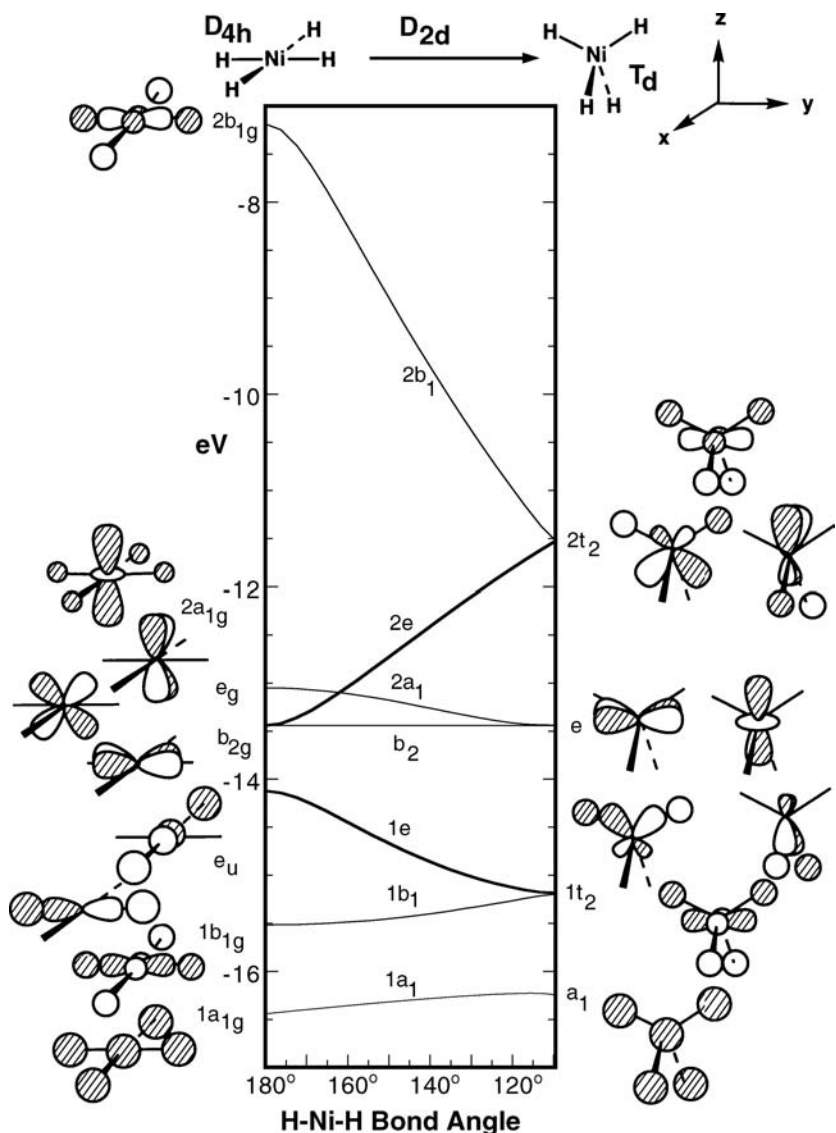
In the first section of this chapter, we built up the orbitals of a square planar  $\text{ML}_4$  complex. An alternative geometry would be a tetrahedral species. There are two basic ways to convert a square planar complex into a tetrahedral one. The 16.33 to 16.34 interconversion involves twisting one pair of cis ligands about an axis



shown in 16.33. That will conserve  $D_2$  symmetry along all points that interconnect 16.33 with 16.34. In the other path, the two trans L—M—L angles are decreased, as shown in 16.35, ultimately yielding the tetrahedron, 16.36. This conserves  $D_{2d}$  symmetry. The elements of this latter pathway have actually been developed in Section 15.4, so we shall briefly explore this distortion. A Walsh diagram for a model  $\text{NiH}_4$  is presented in Figure 16.4. In the left side are the metal-centered, valence orbitals of a square planar  $\text{ML}_4$  system, which have been taken from Figure 16.1. Upon going to the tetrahedron, overlap between  $x^2 - y^2$  and the ligand lone pairs are decreased. Therefore, the  $1b_{1g}$  level is destabilized via a first-order correction to the energy since this orbital is strongly M—L bonding. Likewise, the first-order correction to the energy for the  $2b_{1g}$  molecular orbital is negative (stabilizing) upon reduction of the two trans L—M—L angles since this orbital is strongly M—L antibonding. The  $e_u$  (only the lower, bonding combination is shown in Figure 16.4) and  $e_g$  sets upon distortion have the same symmetry, and therefore, they are allowed to mix in second order. The lowest,  $1e$ , is greatly stabilized by the mixing with  $e_g$ . We have seen this phenomenon before in Section 15.4 for angular distortions in the octahedron. It is always energetically advantageous to mix metal  $d$  character into an orbital that contained only metal  $p$  bonding to the ligand set. The  $e_g$  set ( $xz, yz$ ) is consequently destabilized and meets  $x^2 - y^2$  at the tetrahedral geometry to form a  $t_2$  set. The rationale for the destabilization is identical to that developed for the distortion in 15.39 (see Section 15.4). The ligands move into a position where overlap to  $xz$  and  $yz$  is turned on. The ligand lone pairs mix with  $e_g$  in an antibonding manner; thus,  $xz$  and  $yz$  are destabilized. This is abated somewhat by mixing in some metal  $x$  and  $y$  character. The result is that the metal-centered functions become hybridized away from the ligands. The reader should note that metal  $z$  is mixed in a bonding way to the ligand lone pairs in both  $2b_{1g}$  and  $1b_{1g}$ . For clarity, this is not shown in Figure 16.4.

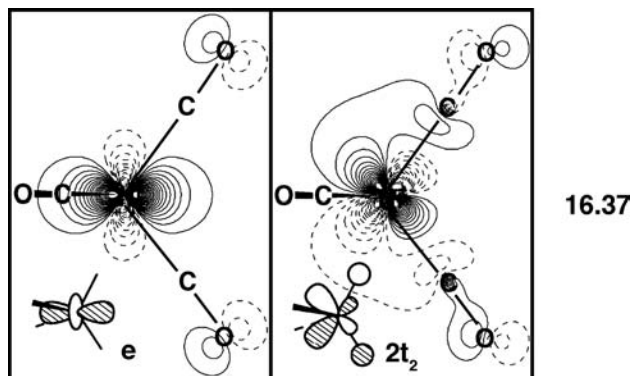
The  $2a_{1g}$  level at the square planar geometry is mainly  $z^2$  with some antibonding from the lone pairs (see 16.1). This distortion moves the ligands into the nodal planes of  $z^2$ . Therefore,  $2a_{1g}$  is stabilized; it becomes one partner of an  $e$  set, along with  $xy$  that is unperturbed along the rearrangement path.

The  $e$  set at the tetrahedron has the same role as  $e_g$  and  $b_{2g}$  in the square plane and  $t_{2g}$  in the octahedron, namely they will participate in  $\pi$  bonding to the

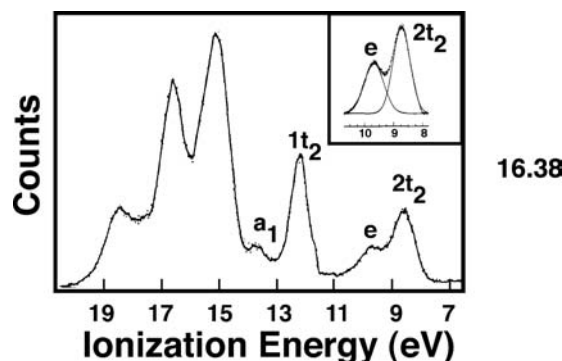
**FIGURE 16.4**

Walsh diagram at the extended Hückel level for the square planar to tetrahedron distortion in  $\text{NiH}_4$ .

surrounding ligands. The  $2t_2$  set is moderately antibonding and lies at higher energies. A contour plot of one member in each set for  $\text{Ni}(\text{CO})_4$  at the ab initio HF level is shown in 16.37. The  $z^2$  component of the  $e$  set shows the features typical of



interaction between metal  $d$ , CO  $\pi$ , and CO  $\pi^*$ , and shown in detail in Figure 15.3. The density at the carbonyl carbons is quite low. For the  $yz$  component of  $t_2$ , one can clearly see the antibonding between CO  $\sigma$  and metal  $d$ . The He(I) photoelectron



spectrum of  $\text{Ni}(\text{PF}_3)_4$  is shown in 16.38 (adapted from Reference [29]). The Mullikan symbols refer to the orbitals in the right side of Figure 16.4. This is a  $d^{10}$  molecule, so  $2t_2$  is the HOMO. The  $e$  set lies 1.0 eV lower in energy. The four Ni—P bonding orbitals are given by the  $1t_2$  and  $a_1$  ionizations. The next two bands at 16.0 and 17.5 eV have been assigned to be associated with fluorine lone-pair combinations and the peak at 19.4 eV with the P—F  $\sigma$  bonds. The first two ionizations from  $\text{Ni}(\text{CO})_4$  are shown along with their Gaussian deconvolutions [30] in the inset at the upper right corner of 16.38. The splitting between the  $2t_2$  and  $e$  ionizations is again 1.0 eV. This is consistent with the idea that the  $\sigma$  donating and  $\pi$  accepting ability of  $\text{PF}_3$  is very similar to that of CO. The metal  $d$  ionizations in  $\text{Ni}(\text{PF}_3)_4$  are 1.0 eV larger in energy than those in  $\text{Ni}(\text{CO})_4$  presumably because of the electronegativity of the fluorine atoms.

Before we discuss the actual dynamics of the square planar to tetrahedral interconversion, it is instructive to compare the two endpoint geometries. Returning to Figure 16.4 in the square planar system, the very high lying  $2b_{1g}$  level makes it obvious that a singlet  $d^8$  complex (where  $2a_{1g}$  is the HOMO) will be a stable species. At the tetrahedral side, a  $d^8$  system will have four electrons in  $2t_2$ . Consequently, a high spin (triplet) situation is required for a stable species. Notice in the right side of Figure 16.4 and 16.37 that the three members of  $t_2$  have M—L antibonding character. At the square planar geometry, only  $2a_{1g}$  is slightly antibonding. As a result, we expect weaker (and therefore longer) M—L distances for high spin  $d^8$  compounds compared to their low spin, square planar counterparts. This is often found to be true. Table 16.1 lists some examples. With two electrons more, it is clear

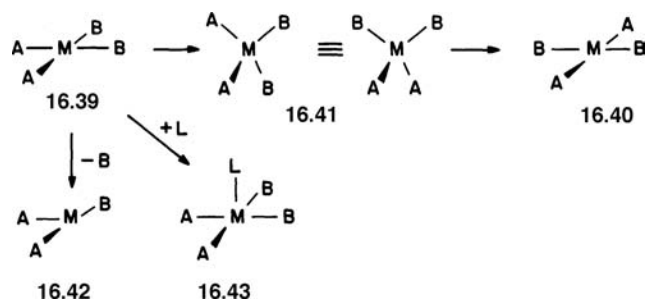
TABLE 16.1 Mean Nickel–Ligand Distances ( $\text{\AA}$ )

	Square Planar	Tetrahedral
Ni–N ( $\text{sp}^2$ )	1.68	1.96
Ni–P	2.14	2.28
Ni–S	2.15	2.28
Ni–Br	2.30	2.36

Source: Taken from K. W. Muir, *Molecular Structure by Diffraction Methods*, Vol. I, the Chemical Society, London (1973), p. 580.

from the relative energies of  $2b_{1g}$  vs.  $t_2$  in Figure 16.4 that the tetrahedral form will be much more stable. Notice that this is a saturated 18-electron  $d^{10} \text{ML}_4$  complex. In the tetrahedral geometry, the ligands are arranged in a spherical manner around the transition metal. The generalized orbital pattern in Figure 16.2 is appropriate. But what about complexes with fewer valence electrons? A  $d^0$  complex will strongly favor the tetrahedron. The four electrons in the  $1e$  set make a strong preference for the tetrahedron. Thus,  $\text{TiCl}_4$  and the overwhelming majority of  $d^0 \text{ML}_4$  complexes [31] are tetrahedral. For a  $d^2$  complex, inspection of Figure 16.4 shows that a triplet state will be most likely be favored (particularly for the first transition metal row where spin pairing energies are large because of contracted  $3d$  AOs). Again, the tetrahedron will be strongly favored as is found computationally for  $\text{Cr}(\text{CH}_3)_4$  [32], and there are a number of structurally categorized examples with more complicated ligands. There will be a first order Jahn–Teller distortion for the singlet. We find for  $\text{Cr}(\text{CH}_3)_4$  that there are four C–Cr–C angles of  $113.0^\circ$  and two at  $94.8^\circ$ . With four  $d$  electrons, for example  $\text{Fe}(\text{CH}_3)_4$ , a singlet tetrahedron is found to be most stable with C–Fe–C angles ranging from  $109.3^\circ$ – $109.5^\circ$ . On the other hand, a high spin complex will be more stable at the square plane with the  $d$  occupation  $(b_{2g})^1(e_g)^2(2a_{1g})^1$ . Indeed, the known molecules have this geometry and are high spin [31]. With six  $d$  electrons, things are more difficult. At the tetrahedron, there will be two electrons in  $2t_2$  and, therefore, a first order Jahn–Teller distortion is expected. In a square planar geometry, the HOMO is the  $e_g$  set and the LUMO is  $2a_{1g}$  that is expected to lie only slightly higher in energy, so a second order Jahn–Teller distortion is expected. Some of the distortion modes for a tetrahedral molecule are shown in 14.7. A  $C_{2v}$  “sawhorse” or “butterfly” structure has been suggested [32], but it is found [33] that singlet  $\text{Ni}(\text{CH}_3)_4$  adopts a  $D_{2d}$  type of deformation from the tetrahedron where two C–Ni–C angles are much smaller than  $109.5^\circ$  and the other four are larger.

A number of  $d^8$  square planar complexes undergo a cis-trans isomerization process, 16.39 to 16.40 [34]. Of interest to us in this section is to probe the direct



pathway via the tetrahedral structure 16.41; however, there are at least two alternative paths that we come back to in the next two chapters. One ligand may dissociate yielding a cis T-shaped intermediate 16.42. It can rearrange to a trans T-shaped structure, and interception by ligand B gives 16.40. Another path involves association of an external ligand, L, which yields the five-coordinate intermediate 16.43. Rearrangement of 16.43 followed by expulsion of L gives 16.40. So, the dynamics of the cis-trans interconversion are complicated by several competing pathways. Returning to the direct route for interconversion, there are two reaction paths that are possible: the so-called twist mechanism given in 16.33 and the spread path in 16.35. Structural correlation studies on many  $d^9 \text{ML}_4$  complexes reveal that

the spread mechanism is favored [39]. A schematic illustration for a thermal process is given in 16.44 for a  $d^8$  complex. The correlation of orbitals has been taken from

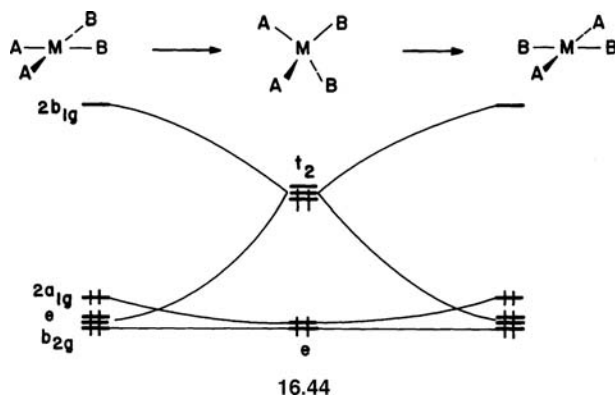
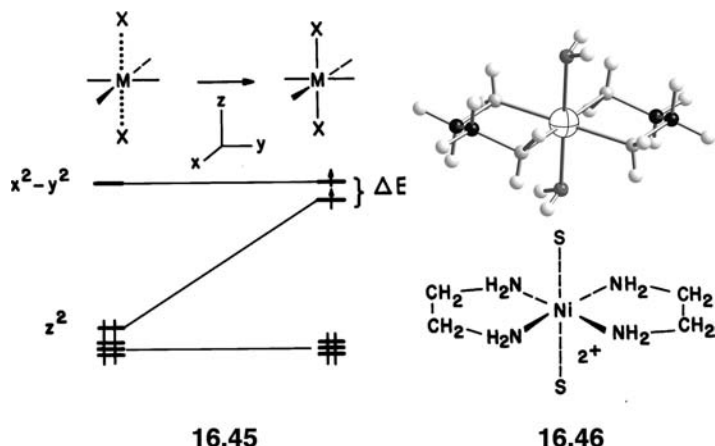


Figure 16.4. Although the symmetry of the two square planar and tetrahedral complexes is lower than  $D_{4h}$  and  $T_d$ , respectively, the essential details of the splitting patterns will remain very close to the idealized cases. The important feature in 16.44 is that the cis-to-trans interconversion via a tetrahedron should be a high-energy process. It is symmetry forbidden under thermal conditions [35]. Hybrid DFT (B3LYP) calculations on  $NiF_4^{2-}$  and  $PtF_4^{2-}$  (with triple zeta valence and a set of polarization functions on each atom) give the singlet tetrahedral state to be 38 and 79 kcal/mol higher in energy for  $NiF_4^{2-}$  and  $PtF_4^{2-}$ , respectively, than the square planar singlet state. For  $PtF_4^{2-}$ , the triplet tetrahedral state is still 52 kcal/mol higher in energy than square planar singlet. But, in  $NiF_4^{2-}$ , the triplet tetrahedral state is 5 kcal/mol lower in energy than the singlet square planar structure. This again illustrates the large spin pairing energy for first-row transition metals. There is not much difference in a qualitative sense between this rearrangement and the  $H_2 + D_2$  reaction (Section 5.4) or the dimerization of two olefins (Section 11.3). In all three cases, a critical point, a high energy cusp, is reached on the potential energy surface. A path of lower or at least different symmetry will be followed. In this case, dissociative or associative paths represent viable alternatives. However, the isomerization can proceed via an excited state species. For example, photochemical excitation of the cis compound populates the  $2b_{1g}$  orbital. The excited state singlet complex can undergo intersystem crossing to a triplet state. This may then relax to a tetrahedral geometry that decays back to the square planar ground-state singlet with either cis or trans geometry. In this context, it is easy to see why  $d^8 ML_4$  complexes adopt a wide variety of geometries on the square planar to tetrahedral reaction path [34]. On the other hand, almost all of the  $d^8$  molecules are either square planar (and have a singlet state) or tetrahedral (and are triplets) with few structures in between. The one-electron picture in 16.44 is a very crude representation of the photochemical processes. State correlation diagrams have been constructed, which more clearly show the relative energies of the molecule as a function of the electronic and geometrical configurations. Furthermore, the actual details of the spin-state change have been neglected here [35]. In principle, the singlet-triplet interconversion can occur thermally [35,36] and this accounts for yet another mechanism of the cis-trans equilibrium for square planar complexes.

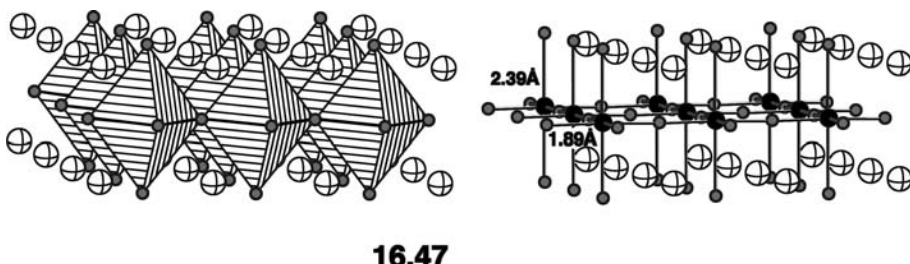
Another interesting isomerization process can take place between square planar and octahedral systems in coordination compounds. 16.45 shows how the  $z^2/x^2-y^2$  separation changes as two trans ligands are brought closer to the square plane. When  $\Delta E$  is small enough then a high spin  $d^8$  species is formed, as



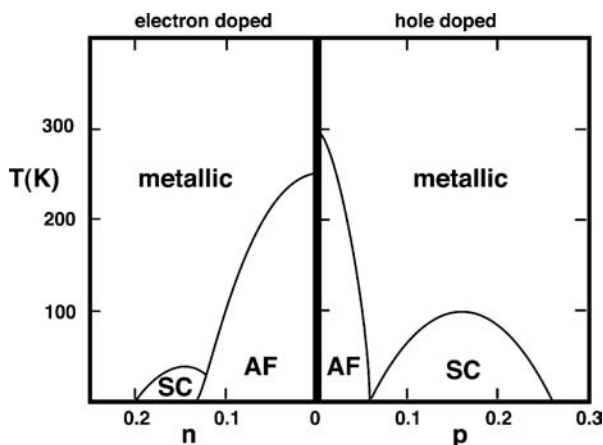
indicated in the right side of **16.45**. This is, of course, just the reverse process, **16.2** to **16.3**, which we have discussed in the first section of this chapter. The Lifschitz salts,  $\text{Ni}(\text{ethylenediamine})_2^{2+}$  (**16.46**), are either paramagnetic and octahedral with two donor solvent molecules,  $\text{H}_2\text{O}$  for example, occupying the axial sites, or square planar and diamagnetic (with noncoordinated solvent molecules) [37]. Which species is actually found depends critically on crystallization conditions. The diamagnetic  $d^8$  species has  $z^2$  as the HOMO that points toward the fifth and sixth coordination positions of the octahedron. As the solvent molecules are brought closer to Ni,  $z^2$  is greatly destabilized by the symmetric combination of donor lone pairs. One should recall that the symmetric combination of solvent lone pairs is, in turn, stabilized. Furthermore, the antisymmetric combination will be stabilized by metal  $z$ . There is a delicate balance between the two molecular extremes of **16.45**, especially since it involves a spin-state change and two-electron energy terms as well.

## 16.5 THE SOLID STATE

The discovery of a high temperature cuprate superconductor by Bednorz and Müller in 1986 [38] generated a renaissance in solid state chemistry. The parent compound,  $\text{La}_2\text{CuO}_4$ , in fact, is an antiferromagnetic (AFM) insulator. Its structure is given in **16.47**. Here, the small gray spheres are oxygen atoms, and the large open spheres are



the La atoms. The polyhedral view highlights the fact that this is a layered structure with  $\text{La}^{3+}$  cations sandwiched between the layers. The coordination at copper is, however, not a typical vertex-shared octahedron. It is an example of a tetragonally elongated structure, which was discussed in Section 15.4. Each copper is surrounded

**FIGURE 16.5**

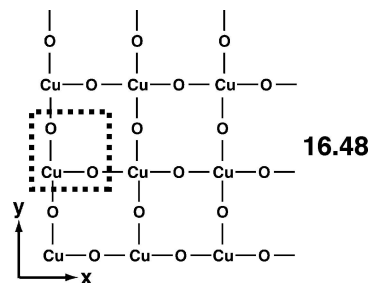
Three regions associated with the electrical transport in the copper oxide superconductors, where SC and AF refer to superconducting and antiferromagnetic insulating states, respectively.

by four oxygen atoms with short Cu—O distances of  $1.89\text{ \AA}$  that form the planes. Oxygen atoms lie on either side of the Cu—O plane with very long,  $2.39\text{ \AA}$ , distances. In terms of electron counting, we have  $2\text{La}^{3+}$  and  $4\text{O}^{2-}$ , so this leads to  $\text{Cu}^{2+}$ ,  $d^9$ . The electronic structure within the unit cell is then given by that on the left side of Figure 15.8. The Cu  $x^2-y^2$  crystal orbitals, each with one electron, will spread out into a band. We show how this happens in a moment. So, if the electrons are paired then the band will be half filled (13.6). This half-filled band then can lead to metallic behavior. But, this is not the case at room temperature and below. The on-site repulsion for two electrons occupying the same site is large, so the compound is an AFM insulator, in which each  $\text{Cu}^{2+}$  site has a local magnetic moment and the moments of adjacent  $\text{Cu}^{2+}$  sites are antiferromagnetically coupled. Thus, there is an energy gap between the highest occupied and the lowest unoccupied energy states. There are two ways to alter this electronic situation by chemical doping. One can substitute, for example,  $\text{Sr}^{2+}$  or  $\text{K}^+$  for  $\text{La}^{3+}$ . So, less electrons are transferred, that is, holes are introduced into the half-filled band. Alternatively, one can add electrons into this band;  $\text{Nd}_{2-x}\text{Ce}_x\text{CuO}_4$  and  $\text{Pr}_{2-x}\text{Ce}_x\text{CuO}_4$  are examples. Here, Nd and Pr are  $3+$  cations (the  $f$  electrons stay on the cation and are not involved in the bonding), whereas Ce is a  $4+$  cation. The dependence of their transport properties on temperature and composition is shown in Figure 16.5. On the horizontal scale,  $n$  is the number of electrons added per formula unit and  $p$  is the number of electrons taken away (or holes added). The AF region is the insulating AFM domain and the SC region is the area where superconductivity is found. The metallic regime can be further subdivided, but that is not our concern here. So far, there is no consensus as to what mechanism is responsible for the Cooper-pair formation that makes these cuprates superconductors. Nevertheless, there are three universal features that all known copper oxide superconductor share:

1. All have a two-dimensional  $\text{CuO}_2$  plane where the Cooper pairs (see Section 13.4) are formed.
2. The electron count for the parent compound is  $d^9$ , in other words, the half-filled  $x^2-y^2$  band is the source for Cooper pair formation.
3. Electrons are either added or taken away from the parent compound to drive it into a superconducting state.

There are certainly other universal factors, but these three are of primary interest to chemists.

The most simple system that contains these features is the two-dimensional  $\text{CuO}_2^{2-}$  sheet. In fact, compounds like this exist [39]. A view from the top is given in 16.48 where the unit cell is enclosed by the dashed lines and the coordinate system



is displayed on the lower left side. This is a tetragonal system where the two translation vectors,  $\mathbf{a}$  and  $\mathbf{b}$ , are equivalent. The energy versus  $k$  plot is shown in Figure 16.6. Here,  $\Gamma$  refers to  $k_x = k_y = 0$ , X to  $k_x = \pi/a$  and  $k_y = 0$ , and M to  $k_x = k_y = \pi/a$ . There are two oxygen s bands around  $-33$  eV that are not shown in the plot. The lowest six bands in Figure 16.6 are mainly oxygen p AOs. The next four bands are primarily copper d. This is confirmed by examining the copper projection in the DOS curve. The COOP curve for the Cu—O overlap population shows that, as expected, the primarily oxygen states are Cu—O bonding. For the four copper d bands, there is not much dispersion since the oxygen p AOs (with the exception of  $z^2$ ) will mix in an  $\pi$  antibonding way. The highest band in Figure 16.6 is primarily  $\text{Cu } x^2-y^2$ . Now whether this band is 60% Cu and 40% O or the reverse is not so important and will depend on the exact computational details. The plots in Figure 16.6 are created at the extended Hückel level. What is important is that it is  $\text{Cu } x^2-y^2$  strongly antibonding to oxygen; notice the large negative peak in the COOP curve in this energy region. It is this band that is half-filled for  $\text{CuO}_2^{2-}$ . The dispersion here has absolutely nothing to do with intercell Cu—Cu (or O—O) overlap, although this occasionally has been claimed in the literature. The distances are on the order of  $3.8\text{ \AA}$  for these compounds. The composition of the band and understanding its dispersion can be derived in a fashion strictly analogous to that presented for  $\text{BaBiO}_3$  in Section 14.2. One can easily draw out the solutions for the

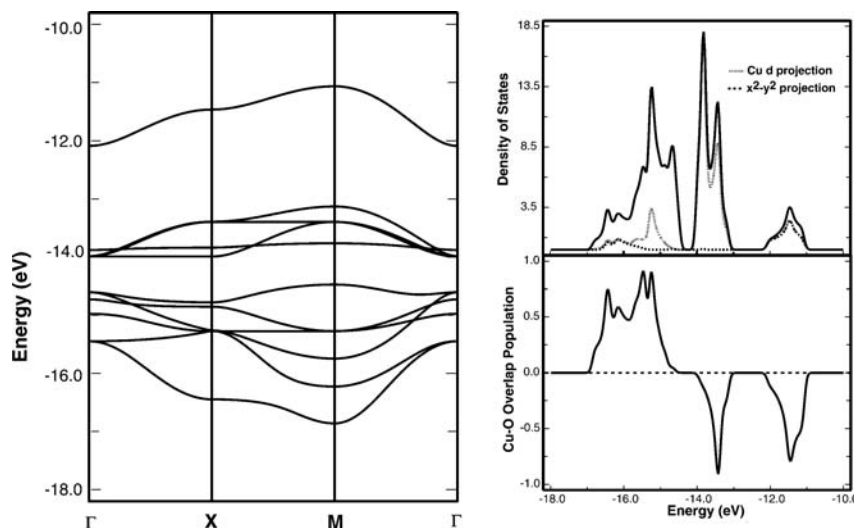
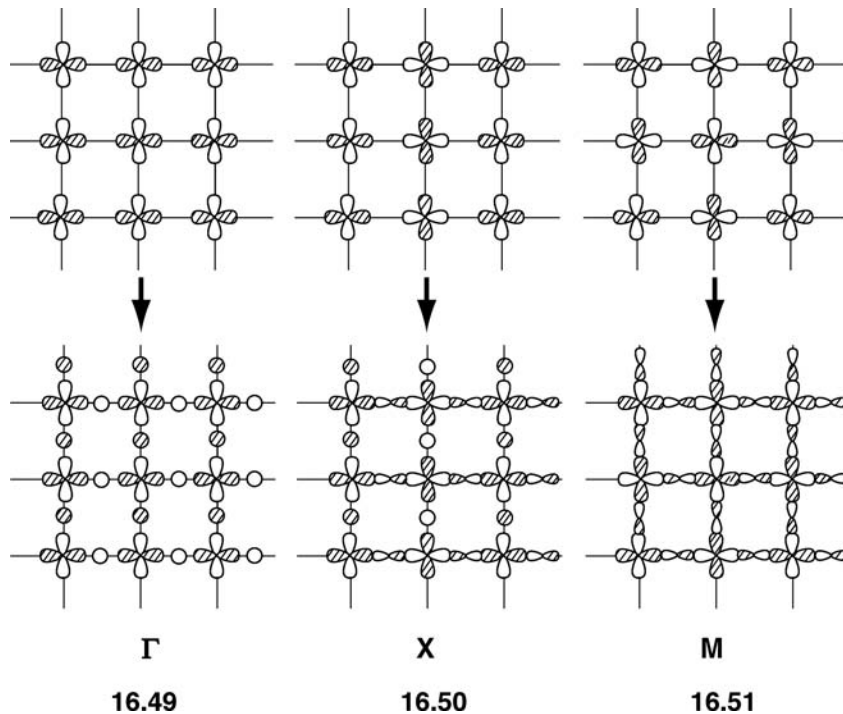


**FIGURE 16.6**

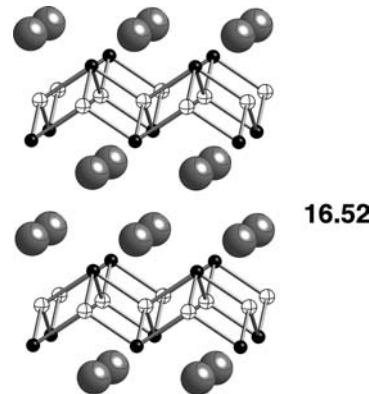
On the left side is the  $e(k)$  versus  $k$  plot for the tetragonal  $\text{CuO}_2^{2-}$  system. In the right side is plotted the corresponding DOS curve and below it the COOP plot for the Cu—O overlap population.

$x^2-y^2$  Bloch functions at the  $\Gamma$ , X, and M points. One then completes the process by drawing the oxygen s and p AOs that can overlap to the  $x^2-y^2$  AOs both within and between unit cells. Furthermore,  $x^2-y^2$  and the oxygen AOs must be antibonding. This is illustrated in 16.49–16.51. At the  $\Gamma$  point (16.49), only oxygen s can interact.



On the other hand, at M (16.51), only oxygen p AOs can overlap with the  $x^2-y^2$  crystal orbitals. At the X point, half the interactions are with oxygen s and the other half with oxygen p. Since the oxygen p AOs lie higher in energy than oxygen s, the p AOs have a smaller energy gap to the Cu d AOs and therefore will destabilize Cu d AOs more. The consequence of this is a  $\sim 1$  eV dispersion of the  $x^2-y^2$  band that rises in energy on going from  $\Gamma$  to X to M. We return to a nearly analogous picture in the next chapter with an examination of  $\text{YBa}_2\text{Cu}_3\text{O}_7$ .

A common structural motif of solids with formula  $\text{AMX}$  is given in 16.52. The



large gray spheres are cations (e.g., Li, Na, Cs), the white spheres are generally first-row transition metals (e.g., Mn, Fe), and the black spheres are pnictides (e.g., P, As).

The MX layers are separated by two rows of A cations; thus, each layer is electronically isolated from adjacent ones. These compounds display interesting magnetic phenomena, and several are superconducting. A closely related structure is the so-called ThCr<sub>2</sub>Si<sub>2</sub> type. There are over 600 AM<sub>2</sub>X<sub>2</sub> compounds that have been structurally categorized [40]. Here, half of the cations that separate the layers have been removed and every other layer has been translated by one-half of a unit cell. The pnictide atoms from different layers can then be very close (see 14.30), and inter-layer bonding is turned on [41]. We shall take an elementary example, NaMnP, to examine. The metal atoms, Mn, are tetrahedrally coordinated to four pnictides, P. The phosphorus atoms have a square pyramidal geometry; the valence orbitals are shown in Figure 14.14. Sodium is much more electropositive than Mn or P; thus, it will donate its electron to form MnP<sup>-</sup> layers. We count phosphorus as being P<sup>3-</sup> and so this leaves Mn<sup>2+</sup> that is d<sup>5</sup>. The DOS along with a COOP curve for the Mn—P overlap population in MnP<sup>-</sup> is presented in Figure 16.7. The states at -13.1 eV and below correspond to the phosphorus p AO s, and one can see from the COOP plot that they are Mn—P bonding. The sharp peak at -13.1 eV is primarily associated with the lone-pair orbital perpendicular to the layer (see 2a<sub>1</sub> in Figure 14.14). The states from -9.8 -12.0 eV are Mn d in character. As expected from the splitting pattern for a tetrahedron, there are two groups. The “e” orbitals, z<sup>2</sup> and xy using the z axis as being perpendicular to the layer, correspond to the two sharp peaks at -11.6 and -11.7 eV and are nonbonding to phosphorus. The states from -9.7 and lower (and extended into the “e” states) correspond to the “t<sub>2</sub>” set. These are

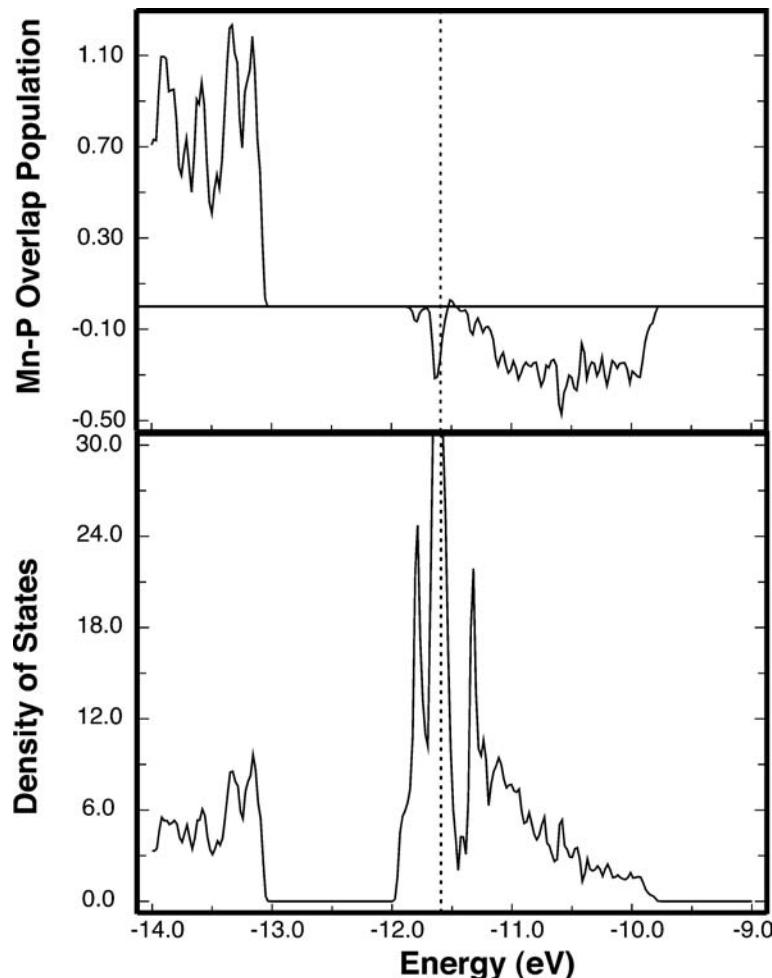
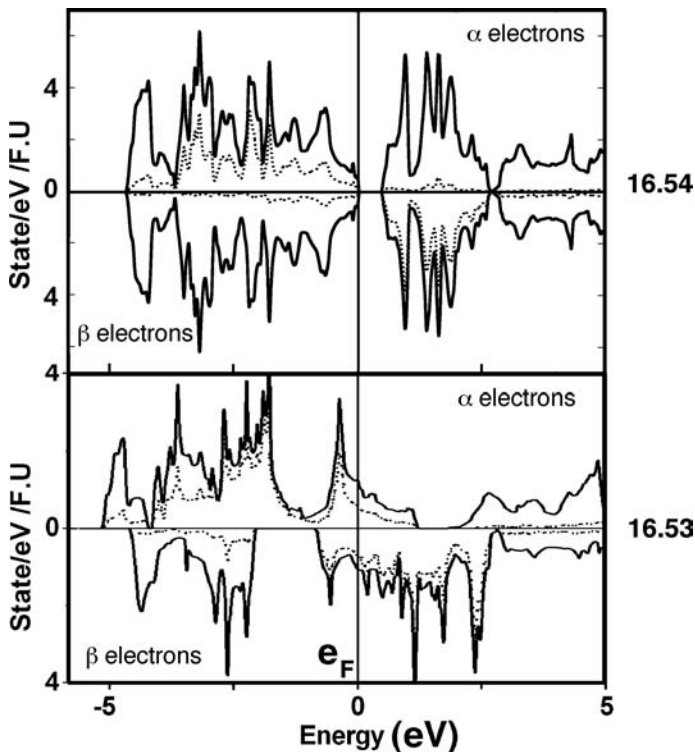


**FIGURE 16.7**

DOS and COOP plots for a single layer of MnP<sup>-</sup> with the geometry given in 16.52. These are calculations using an extended Hückel Hamiltonian. The dotted line indicates the Fermi level for a nonmagnetic metallic state.

weakly Mn—P antibonding. The Mn—Mn distances are 3.12 and 4.42 Å. These are much too long for any significant overlap, so the dispersion of the “ $t_2$ ” states is due to differences in Mn—P bonding. Around  $-19$  eV are the states associated with phosphorus s and above  $-7$  eV are Mn s and p; these are not shown in the DOS plot. The Fermi level is given by the dotted line in the DOS and COOP curves. This corresponds to pairing the electrons, so “e” is nearly filled and the “ $t_2$ ” is empty. But as we have discussed previously in this chapter, first-row transition metals have a large spin pairing energy and certainly with a  $d^5$  configuration, an AFM or ferromagnetic (FM) ordering is also possible. By using the full-potential linearized augmented plane wave (FP LAPW) method, spin-polarized density-functional theory calculations were carried out for the FM and AFM states of NaMnP, in which the  $\alpha$  (up-spin) and  $\beta$  (down-spin) electrons are allowed to have different spatial orbitals. The resultant DOS plots are given in 16.53 for the FM state. There are certainly some differences that are found in this more rigorous calculation. The dotted lines indicate the Mn d contribution to the DOS. The states from  $\sim 2.0$  eV and up for the  $\alpha$  electrons and  $\sim 2.6$  eV and up for the  $\beta$  electrons are Na s states in character. The range of Mn d and P p states is about 6 eV in the FP LAPW calculation that is close to that in Figure 16.7 at the extended Hückel level. The FP LAPW calculation gives much more mixing between Mn d and P p, and there is no gap between the two groups for the  $\alpha$  electrons as there is in Figure 16.7. But, there is a gap of comparable

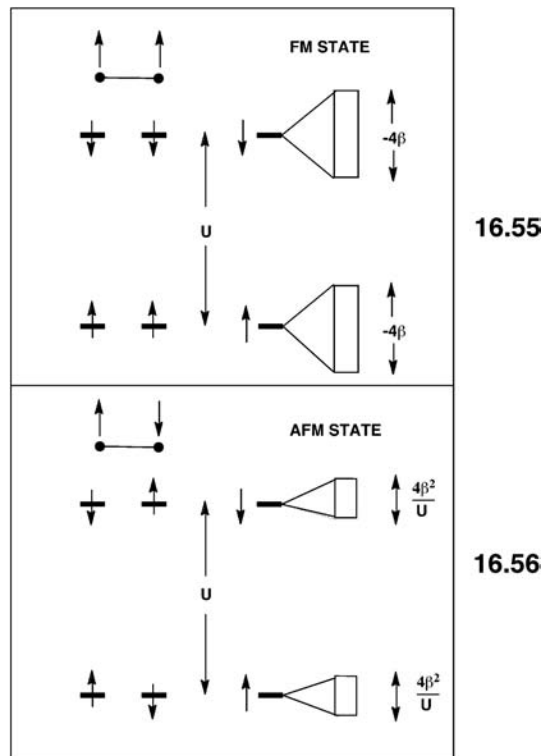


magnitude for the  $\beta$  electrons. What is clear from 16.53 is that the mainly Mn d states from  $\sim -2.2$  to 1.3 eV are almost all filled for the  $\alpha$  electrons, whereas the Mn d region for the  $\beta$  electrons, from  $\sim -1.0$  to 2.6 eV, is almost empty, that is, our prediction of high spin Mn  $d^5$  was not far off. This also predicts that NaMnP should be metallic; the Fermi level,  $e_F$ , lies within an appreciable number of states for both the  $\alpha$  and  $\beta$  electrons. But, this is not in agreement with experiment that shows it to be an AFM insulator [42]. For NaMnP, the AFM state is calculated to be 0.45 eV per formula unit more stable than the FM state, in agreement with experiment [42]. One must be a little careful about using the terms FM and AFM. Our references

before were concerned mainly with the electron spin arrangement within the unit cell. But, in reality, it is the net property of the crystal that is determined. If the spins from one unit cell are aligned antiparallel to the ones in the adjacent unit cells, then an AFM ordering is achieved. This is in fact what is occurring in NaMnP and related compounds. The corresponding DOS plots for the AFM state are reproduced in **16.54**. Again, the projection of Mn  $d$  is given by the dotted line. At a given  $\alpha$ -spin Mn site, essentially all of the Mn  $d$   $\alpha$  states are occupied whereas the Mn  $d$   $\beta$  states are empty and lie just above the Fermi level. Furthermore, there is a gap of  $\sim 0.5$  eV at the Fermi level, so the compound is an insulator. The reason for this difference between the FM versus AFM states has to do with the fact that in the AFM state the Mn  $d$  bands are more narrow than those in the FM arrangement (for more details, see Section 24.2.3). One can see this most clearly for the  $\beta$  spins in **16.53** versus that in **16.54**. A simple argument (for more details, see Section 24.2.3) can be used to illustrate this situation [43,44]. For simplicity, let us consider a one-dimensional chain with one orbital per site and use the Hückel approximation. Recall from Eq. 13.3 and the material around it that the energies associated with the Bloch functions are

$$e(k) = \alpha + 2\beta \cos ka$$

where  $\beta$  is the nearest-neighbor interaction energy so that the bandwidth is given by  $4|\beta|$ . In spin-polarized density functional calculations for magnetic states, the up- and down-spin states of each spin site are split by the on-site repulsion  $U$ . In the FM state, the neighboring spin sites have the same spin, so that the up-spin state is lower in energy than the down-spin state at every spin site (the left side of **16.55**). The interactions between adjacent spin sites take place only between the same spin states, so that the interactions between the up-spins are degenerate interactions and so are those between the down-spins. Thus, the bandwidth associated with the FM state is  $-4\beta$  for the up-spin as well as for the down-spin bands as shown in the right side of **16.55**. Note that the up- and down-spin bands will overlap if  $-4\beta$  is greater than  $U$ , resonance integral between orbitals on adjacent sites. For the AFM



ordering, the initial  $\alpha$  (or  $\beta$ ) states do not have the same energy (as they do in the FM case). But, in the AFM state, adjacent spin sites have opposite spins so that the interactions between adjacent spin sites become nondegenerate interactions with energy separation of  $U$  (left side of **16.56**), so that the strength of the interaction between adjacent spin sites is given by  $\beta^2/U$ . Therefore, in the AFM state, the width of the up- and down-spin bands is given by  $4\beta^2/U$  (right side of **16.56**). Since  $\beta^2/U$  is smaller than  $-\beta$  in magnitude, the AFM state has a smaller bandwidth than does the FM state. Typical values of  $U$  range from about 2–5 eV, and we have seen that the metal  $d$  bandwidths for these types of systems are at a maximum 1 or 2 eV. The taking an extreme position,  $U=2$  eV and  $\beta=-0.5$  eV, then leads to bandwidths of 2 versus 0.5 eV for the FM and AFM cases, respectively. In the AFM case, the bands are separated by 1.5 eV. Clearly, this is a very simplified argument. For example, if overlap was included, then not only would the AFM bands broaden, but the gap would also be reduced. There are certainly other electron–electron factors at work here, but the essence of this situation is neatly described by **16.55** and **16.56**.

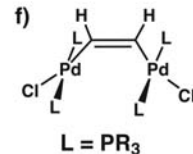
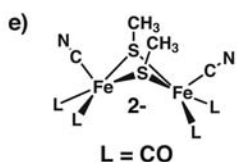
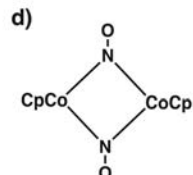
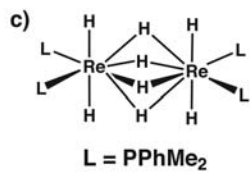
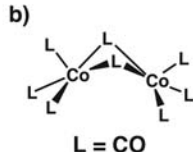
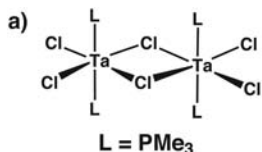
Another case of AFM spin order is found for  $\text{SrFeO}_2$ . Its structure is precisely like that of  $\text{SrCuO}_2$  in **16.48** with  $\text{Sr}^{2+}$  cations lying on either side of the  $\text{FeO}_2^{2-}$  sheets [45]. We now have Fe in the +2 oxidation state, so it is  $d^6$ . Detailed calculations [44] have shown that the electronic configuration at Fe is approximately given by  $(z^2)^2(xz, yz)^2(xy)^1(x^2 - y^2)^1$ . In other words, one has high spin iron sites that are antiferromagnetically coupled, as opposed to a FM ordering or a nonmagnetic state with a  $(z^2)^2(xz, yz)^4(xy)^0(x^2 - y^2)^0$  electron configuration. This latter configuration might well be the ground state for a compound containing a second- or third-row transition metal where the spin pairing energies are not so large because their  $d$  AOs are more diffuse.  $\text{SrCuO}_2$  and  $\text{La}_2\text{CuO}_4$  are the compounds with one electron per unit cell in the  $x^2 - y^2$  band and are antiferromagnetic insulators.

## PROBLEMS

**16.1.** Determine the electron count and approximate structure for the compounds listed below:

- a.  $\text{CpRe(O)(CH}_3)_2$
- b.  $\text{PtH(CN)(PPh}_3)_2$
- c.  $\text{CpRe(NO)(PMMe}_3)\text{CH}_2^+$
- d.  $\text{Ru(CO)}_2(\text{SO}_2)(\text{PPh}_3)_2$
- e.  $\text{CpRh(benzene)}$
- f. (cyclooctatetraene) $\text{Fe(CO)}_3$
- g.  $\text{CpRuCl(CO)(PPh}_3)$
- h.  $\text{CpW(CO)}_3\text{I}$
- i.  $(\text{Me}_3\text{Si})\text{Ta(N-}t\text{-Bu})(\text{NMe}_2)_2$
- j.  $\text{Cp}_2\text{Zr(Cl)(N=CMe}_2)$
- k.  $\text{CpRuH}(\pi\text{-allyl})(\text{MeC}\equiv\text{CMe})^+$
- l.  $\text{O}_2\text{Os}(\text{N-}t\text{-Bu})_2$

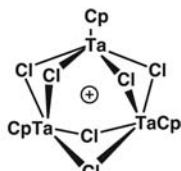
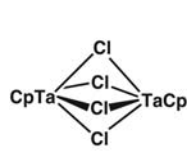
**16.2.** Determine the M—M bond order for the following compounds:



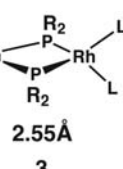
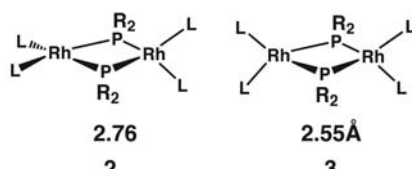
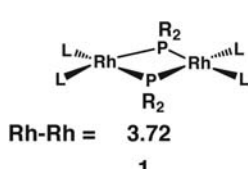
**16.3.** Predict what value for  $x$  will yield a stable species:

- $Mn(CO)_4(NO)_x$
- $\eta^5\text{-CpCr}(NO)_2Cl_x$
- $(\eta^4\text{-C}_4\text{H}_4)\text{Fe}(\text{CO})_x$
- $(\eta^5\text{-Cp})_2\text{WH}_x$
- $W(\text{PPh}_3)_3\text{H}_x$

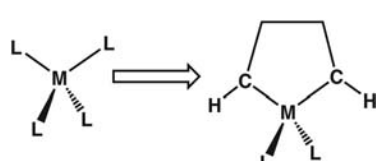
**16.4.** Figure out the Ta—Ta bond order for the two compounds below.



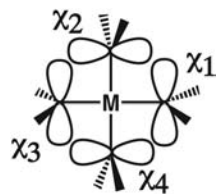
**16.5.** The three isomeric rhodium dimers shown below have very different Rh—Rh bond lengths. Explain this feature.



**16.6.** Show how the level splitting for a tetrahedron is modified when a biscarbene is substituted for two of the ligands.



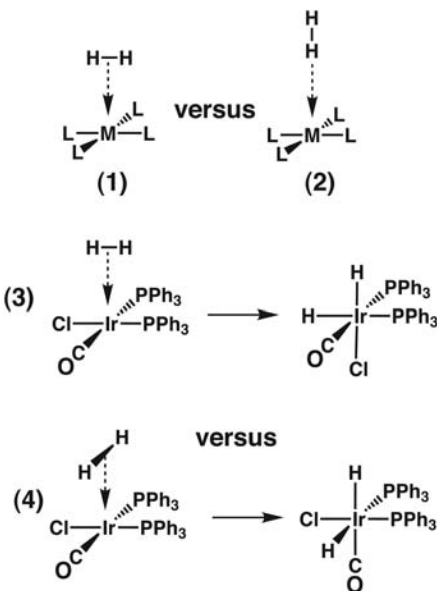
**16.7. a.** Form SALCs of the four carbene  $p$  AOs using  $\chi_1-\chi_4$  as a basis.



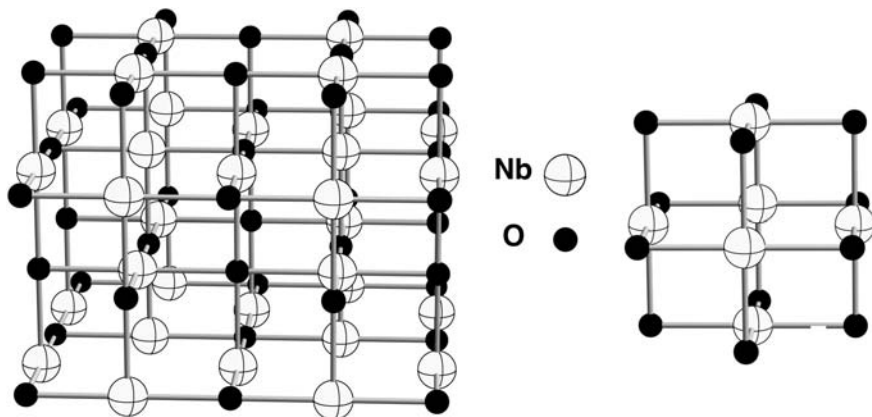
- b.** Use the splitting pattern for a square planar complex and construct an orbital interaction diagram with the SALCs from (a). Place the carbene orbitals between metal  $z^2$  and  $x^2-y^2$ . What electron count(s) should be stable?

**16.8.** The hydrogenation of olefins catalyzed by transition metals is a very important industrial reaction. The initial step in the catalytic cycle is the addition of  $H_2$  to a square planar complex to form an octahedral metal dihydride. There are two possible ways that  $H_2$  can approach a  $d^8$   $ML_4$  complex. These are shown in reactions (1) and (2).

- a. Show the most critical interactions between  $H_2$  and  $ML_4$  at the early stages of the reactions, that is, when the orbital interactions are strong, but not large enough so that there are significant geometrical changes in the two reactants.
- b. Indicate on the basis of these interactions why reaction (1) is preferred over (2).
- c. For  $C_{11}Ir(CO)(PPh_3)_2 + H_2$ , there are two possible reaction paths that could be taken. These are listed as reactions (3) and (4). Notice that the two products are isomers of each other. It turns out that only the product from reaction (4) is formed. Show why the pathway leading to this product is preferred to that from (3).



**16.9.** Below are two different representations for the  $NbO$  structure. Notice that both niobium and oxygen are square planar! The  $Nb-O$  and  $Nb-Nb$  bond lengths are  $2.10\text{\AA}$  and  $2.97\text{\AA}$ , respectively. Draw the DOS for the Nb 5d AOs and label the peaks. Along side of the DOS, draw the COOP curve for the  $Nb-Nb$  overlap population. Indicate the position of the Fermi level.




---

## REFERENCES

---

1. P. K. Hurlburt, J. J. Rack, S. F. Dec, O. P. Anderson, and S. H. Strauss, *Inorg. Chem.*, **33**, 373 (1993); H. Willner, J. Schaebs, G. Hwang, F. Mstry, R. Jones, J. Trotter, and F. Aubke, *J. Am. Chem. Soc.*, **114**, 8972 (1992).
2. R. Hoffmann and J. Lauher, *J. Am. Chem. Soc.*, **98**, 1729 (1976); R. D. Rogers, R. V. Bynum, and J. L. Atwood, *J. Am. Chem. Soc.*, **100**, 5238 (1978); A. Davidson and S. S. Wreford, *Inorg. Chem.*, **14**, 703 (1975); J. Silvestre, T. A. Albright, and B. A. Sosinsky, *Inorg. Chem.*, **20**, 3937 (1981); S.-Y. Chu and R. Hoffmann, *J. Phys. Chem.*, **86**, 1289 (1982); R. M. Laine, R. E. Moriarity, and R. Bau, *J. Am. Chem. Soc.*, **94**, 1402 (1972); R. B. King, *Inorg. Chem.*, **7**, 1044 (1968); J. K. Burdett, *Molecular Shapes*, John Wiley & Sons, New York (1980), pp. 224–225; J. T. Anhaus, T. P. Lee, M. H. Schofield, and R. R. Schrock, *J. Am. Chem. Soc.*, **112**, 1642 (1990).
3. E. Keulen and F. Jellinek, *J. Organomet. Chem.*, **5**, 490 (1966); A. Haaland, *Acta Chem. Scand.*, **19**, 41 (1965).
4. A. Martin, A. G. Orpen, A. J. Seeley, and P. L. Timms, *J. Chem. Soc., Dalton Trans.*, 2251 (1994).
5. K.-R. Porschke, R. Goddard, C. Kopiske, C. Kruger, A. Rufinska, and K. Sevogel, *Organometallics*, **15**, 4959 (1996).
6. G. Huttner, H. H. Brintzinger, L. G. Bell, P. Friedrich, V. Bejenke, and D. Neugebauer, *J. Organomet. Chem.*, **145**, 329 (1978).
7. M. J. Bennett, F. A. Cotton, A. Davison, J. W. Faller, S. J. Lippard, and S. M. Morehouse, *J. Am. Chem. Soc.*, **88**, 4371 (1966).
8. R. Hoffmann and P. Hofmann, *J. Am. Chem. Soc.*, **98**, 598 (1976).
9. See, for example, S. Alvarez, R. Hoffmann, and C. Meali, *Chem. Eur. J.*, **15**, 8358 (2009).
10. G. Parkin in *Comprehensive Organometallic Chemistry*, III, Vol. 1, R. Crabtree and M. Mingos, editors, Elsevier, Amsterdam (2007) pp. 1–57; G. Parkin, *Organometallics*, **25**, 4744 (2007).
11. L. J. Ferrugia and C. Evans, *J. Phys. Chem., A*, **109**, 8834 (2005).
12. C. Menoret, A. Spasojevic-de Bire, N. Q. Dao, A. Couson, J.-M. Kiat, J. D. Manna, and M. D. Hopkins, *J. Chem. Soc., Dalton Trans.*, 3731 (2002).
13. M. Schulz and H. Werner, *Organometallics*, **11**, 2790 (1992).
14. F. Takusagawa and T. F. Koetzle, *Acta Crystaollogr., Sect. B*, **35**, 1074 (1979).
15. P. Chaudhari, K. Weghardt, Y.-H. Tsai, and C. Kruger, *Inorg. Chem.*, **23**, 427 (1984).
16. R. A. Love, T. F. Koetzle, G. J. B. Williams, L. C. Andrews, and R. Bau, *Inorg. Chem.*, **14**, 2653 (1975).
17. K. W. Chiu, D. Lyons, G. Wilkinson, M. Thornton-Pett, and M. B. Hursthouse, *Polyhedron*, **2**, 803 (1983).
18. R. Bianchi, G. Gervassio, and D. Marabello, *Inorg. Chem.*, **39**, 2360 (2000).

19. M. R. Churchill and B. G. deBoer, *Inorg. Chem.*, **16**, 878 (1977).
20. M. H. Chisholm, F. A. Cotton, M. Extine, and B. R. Stults, *J. Am. Chem. Soc.*, **98**, 4477 (1976).
21. T. Nguyen, A. D. Sutton, M. Brynda, J. C. Fettinger, G. L. Long, and P. P. Power, *Science*, **310**, 844 (2005); Y. C. Tsai, H.-Z. Chen, C.-C. Chang, J.-S. K. Yu, G.-H. Lee, Y. Wang, and T.-S. Kuo, *J. Am. Chem. Soc.*, **131**, 12534 (2009).
22. B. O. Roos, A. C. Borin, and L. Gagliardi, *Angew. Chem. Int. Ed.*, **46**, 1469 (2007).
23. P. Schwab, J. Wolf, N. Mahr, P. Steinert, U. Herber, and H. Werner, *Chem. Eur. J.*, **6**, 4471 (2000).
24. M. Green, D. R. Haulley, J. A. K. Howard, P. Louca, and F. G. A. Stone, *Chem. Commun.*, 757 (1983).
25. A. Mitschler, B. Rees, and M. S. Lehmann, *J. Am. Chem. Soc.*, **100**, 3390 (1978).
26. M. Benard, *Inorg. Chem.*, **18**, 2782 (1979).
27. P. Macchi, L. Garlaschelli, and A. Sironi, *J. Am. Chem. Soc.*, **124**, 14173 (2002).
28. R. H. Crabtree and M. Levin, *J. Am. Chem. Soc.*, **25**, 805 (1986); G. K. Anderson and R. J. Cross, *Chem. Rev.*, **9**, 185 (1980).
29. J. G. Brennan, J. C. Green, C. M. Redfern, and M. A. MacDonald, *J. Chem. Soc., Dalton Trans.*, 1907 (1990); P. J. Bassett, B. R. Higginson, D. R. Lloyd, N. Lynaugh, and P. J. Roberts, *J. Chem. Soc., Dalton Trans.*, 2316 (1974).
30. J. E. Reutt, L. S. Wang, Y. T. Lee, and D. A. Shirley, *Chem. Phys. Lett.*, **126**, 399 (1986).
31. J. Cirera, P. Alemany, and S. Alvarez, *Chem. Eur. J.*, **10**, 190 (2004).
32. J. Cirera, E. Ruiz, and S. Alvarez, *Inorg. Chem.*, **47**, 2871 (2008); T. A. Albright, unpublished calculations.
33. M. Carnes, D. Buccella, J. Y.-C. Chen, A. P. Ramirez, N. J. Turro, C. Nuckolls, and M. Steigerwald, *Angew. Chem. Int. Ed.*, **48**, 290 (2009); T. A. Albright, unpublished calculations.
34. S. Keinan and D. Avnir, *Inorg. Chem.*, **40**, 318 (2001); G. Klebe and F. Weber, *Acta Cryst.*, **B50**, 50 (1994).
35. E. A. Halevi and R. Knorr, *Angew. Chem. Int. Ed.*, **94**, 307 (1982); E. A. Halevi and R. Knorr, *Angew. Chem. Int. Ed., Suppl.* 622 (1982) and references therein.
36. A. G. Starikov, R. Minyaev, and V. I. Minkin, *Chem. Phys. Lett.*, **459**, 27 (2008).
37. A. F. Wells, *Structural Inorganic Chemistry*, 4th edition, Clarendon Press, Oxford (1975), pp. 964–967.
38. J. G. Bednorz and K. A. Müller, *Angew. Chem. Int. Ed.*, **27**, 735 (1988).
39. T. Siegrist, S. M. Zahurak, D. W. Murphy, and R. S. Roth, *Nature*, **334**, 231 (1988).
40. G. Just and P. Paufler, *J. Alloys Compd.*, **232**, 1 (1996).
41. R. Hoffmann and C. Zheng, *J. Phys. Chem.*, **89**, 4175 (1985).
42. W. Bronger, P. Müller, R. Höppner, and H.-U. Schuster, *Z. Anorg. Allgem. Chem.*, **539**, 175 (2004).
43. D. Dai, H. Xiang, and M.-H. Whagbo, *J. Comput. Chem.*, **29**, 2187 (2008).
44. H. J. Xiang, S.-H. Wei, and M. H. Whangbo, *Phys. Rev. Lett.*, **100**, 167207 (2008); W. L. Huang, *J. Comput. Chem.*, **30**, 2684 (2009).
45. Y. Tsujimoto, C. Tassel, N. Hayashi, T. Watanabe, H. Kageyama, K. Yoshimura, M. Takano, M. Ceretti, C. Ritter, and W. Paulus, *Nature*, **450**, 1062 (2007).

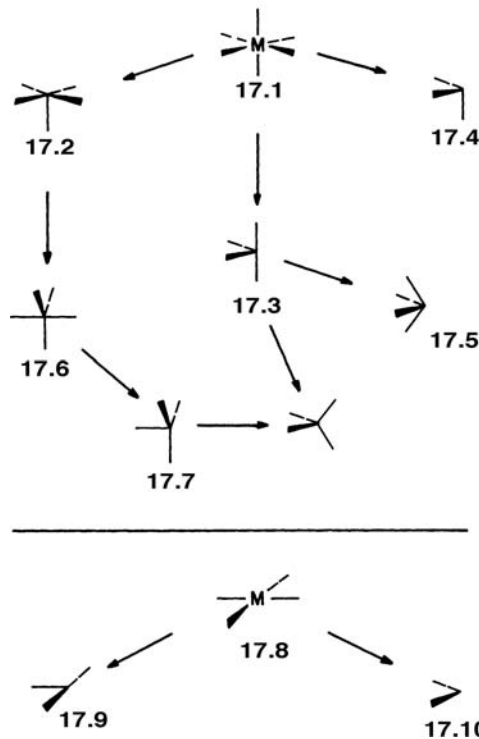
# Five Coordination

## 17.1 INTRODUCTION

Throughout this book, we have stressed one technique for understanding the molecular orbitals of complicated molecules, namely, their construction from the valence orbitals of smaller subunits. In the organometallic area, this is particularly useful since the molecules consist of an  $ML_n$  unit bonded to some organic ligand. For this purpose, we need to build up a library of valence orbitals for common  $ML_n$  fragments, where  $n = 2–5$  and L is a generalized two-electron  $\sigma$  donor ligand. We could do this by interacting an ensemble of  $L_n$  functions with a transition metal, just as was carried through for the octahedron (Section 15.1) and square plane (Section 16.1) cases. However, an easier method [1–3] starts with the valence, metal-centered orbitals of the octahedron and square plane. One or more ligands are then removed. This is illustrated in Chart 17.1. The valence orbitals of a  $C_{4v}$   $ML_5$  fragment, 17.2, can easily be derived by taking those of  $ML_6$ , 17.1, and considering the perturbation induced by removing one ligand. A  $C_{2v}$   $ML_4$  species, 17.3, is derived by removing two cis ligands from  $ML_6$ , and removal of three fac ligands will yield the  $C_{3v}$   $ML_3$  fragment, 17.4. We shall be primarily concerned with the geometry perturbation on going from 17.1 to 17.2 in this chapter. Now, those fragments, 17.2–17.3, can be distorted to give fragments of other types. For example, the  $C_{2v}$   $ML_4$  fragment can easily be distorted to a  $C_{4v}$  structure, 17.5, or a tetrahedron. Likewise, we find it useful to generate the levels of 17.6 from those of the square pyramid.

Once the orbitals of a trigonal bipyramid have been derived, they can be used in turn to establish the orbitals of a  $C_{3v}$   $ML_4$  fragment like 17.7 which may then be distorted to a tetrahedron, and so on. Thus, the reductive approach illustrated in Chart 17.1 offers many ways to interrelate the orbitals of different systems. The fragments are interesting molecules in their own right, and we shall spend some time with their structure and dynamics. Our other starting point is the square plane, 17.8.

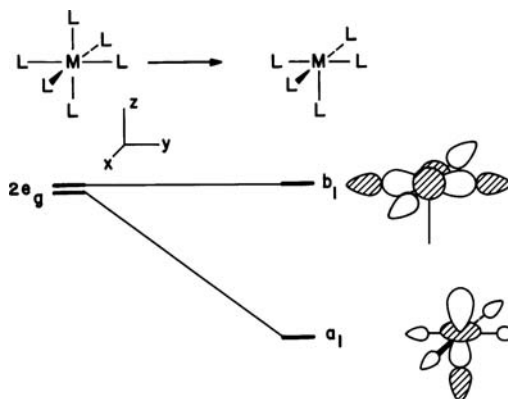
CHART 17.1



Removal of one ligand gives a  $C_{2v}$   $ML_3$  fragment, 17.9. We shall see in Section 18.1 that the orbital structure of 17.9 is very similar to that of the  $C_{4v}$   $ML_5$  fragment, 17.2. Removing two cis ligands from 17.8 gives 17.10, with orbitals similar to those of 17.3. This correspondence between different  $ML_n$  fragments is an important way to simplify and unify organometallic chemistry and forms a common thread running through Chapters 18–20.

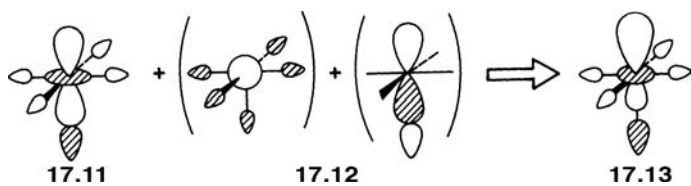
## 17.2 THE $C_{4v}$ $ML_5$ FRAGMENT

On the left of Figure 17.1 are listed the metal-centered  $d$  blocks of orbitals for octahedral  $ML_6$ . In Section 15.1 (see Figure 15.1), we established that there is a lower group of three levels,  $xz$ ,  $yz$ , and  $xy$ , using the coordinate system at the top of Figure 17.1, which have  $t_{2g}$  symmetry. These are filled for a saturated ( $18$  electron)  $d^6$  complex. At much higher energy is the  $2e_g$  set. It will be empty in most organometallic examples and consists of  $x^2 - y^2$  and  $z^2$  antibonding to the ligand lone pairs. When one ligand is removed from the octahedron [1], to a first approximation, the  $t_{2g}$  set is left unaltered. The resultant levels are labeled as  $e + b_2$  in the  $C_{4v}$  point group of the fragment. No hybridization or energy change is introduced because the lone pair of the missing ligand is orthogonal to  $t_{2g}$ . The same is true for the  $x^2 - y^2$  component of  $2e_g$ . Suppose that the ligand removed from  $\text{Cr}(\text{CO})_6$  was  $\text{CO}$ —a  $\pi$  acceptor [4]. Then, the  $xz$  and  $yz$  components of  $t_{2g}$  would rise slightly in energy and  $xy$  is left untouched. Consequently, a relatively small energy gap will be introduced between  $e$  and  $b_2$ . The major perturbation occurs with the  $z^2$  component of  $2e_g$ . That orbital, labeled  $a_1$ , will be greatly stabilized. Removing the ligand loses one strong antibonding interaction between metal  $z^2$  and the ligand. The  $a_1$  level also becomes hybridized by mixing some s

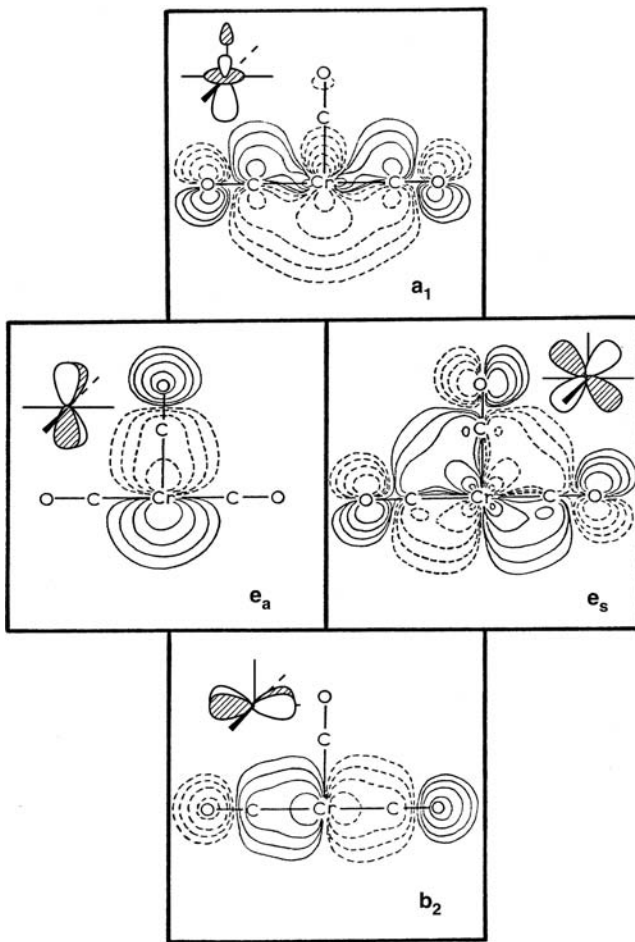
**FIGURE 17.1**

Orbital correlation diagram for the octahedron to square pyramid conversion. Only the *d* orbital part of the diagram is shown. Note the rehybridization of *z*<sup>2</sup> toward the empty coordination site.

and *z* characters in a way that reduces the antibonding between the metal and surrounding ligands. The origin of this hybridization in *a*<sub>1</sub> is not much different from that in the variation of cis and trans L–M–L angles in ML<sub>6</sub> (Section 15.3). We shall outline one way to view the resultant hybridization. The O<sub>h</sub> ML<sub>6</sub> to C<sub>4v</sub>, ML<sub>5</sub> conversion involves a reduction of symmetry. The 2*a*<sub>1g</sub> orbital (see Figure 15.1) and the *z* component of 2*t*<sub>1u</sub> lie close in energy to 2e<sub>g</sub>. Both orbitals also will have *a*<sub>1</sub> symmetry upon loss of the CO ligand. Consequently, they mix into the *z*<sup>2</sup> component of 2e<sub>g</sub>, **17.11** (in first order), in a way that reduces the antibonding between the metal and its surrounding ligands. Recall that 2*a*<sub>1g</sub> and 2*t*<sub>1u</sub> lie at higher energy than 2e<sub>g</sub>; thus, they mix



into **17.11** in a bonding manner. This is diagrammed in **17.12**. Notice that it is the phase relationship shown for the metal *s* and *z* in **17.12** to the ligand lone pairs in **17.11** that sets the mixing sign. 2*a*<sub>1g</sub> and 2*t*<sub>1u</sub> are, after all, concentrated at the metal. Therefore, the largest interorbital overlap will occur between the atomic components of **17.12** at the metal and the lone pairs in **17.11**. The resultant orbital, **17.13**, is stabilized further by this mixing process, and it becomes hybridized out away from the remaining ligands, toward the missing one. The *a*<sub>1</sub> orbital is empty for a d<sup>6</sup> fragment. It obviously will play a crucial role when real molecules are constructed from the ML<sub>5</sub> fragment. Its directionality and the fact that it lies at moderate energy make it a superlative σ-accepting orbital. An MO plot at the extended Hückel level of this orbital in Cr(CO)<sub>5</sub> is shown at the top of Figure 17.2. Notice the distinct hybridization out toward the missing carbonyl. Returning to Figure 17.1,

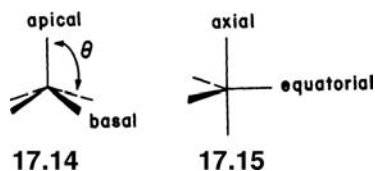
**FIGURE 17.2**

Contour plots at the extended Hückel level of the five important valence orbitals in  $\text{Cr}(\text{CO})_5$ . The plots for  $e_a$  and  $b_2$  are 0.5 Å from the Cr atom and parallel to the  $yz$  plane (see Figure 17.1).

below  $a_1$  lies a nest of three “ $t_{2g}$  like” orbitals that are utilized for  $\pi$  bonding,  $xz$ ,  $yz$  ( $e$  symmetry), and  $xy$  ( $b_2$ ). Plots of these three MOs for  $\text{Cr}(\text{CO})_5$  are also shown in Figure 17.2. The antisymmetric component of the  $e$  set,  $e_a$ , and the  $b_2$  orbital are plotted in a plane parallel to the  $yz$  plane at a distance of 0.5 Å from the Cr atom. It is very clear that these three MOs have large amounts of CO  $\pi^*$  character mixed into them. How much  $\pi^*$  mixes into these levels is certainly a question of methodology and parameterization (basis set choices, etc.). Looking back to the plots in Chapters 15 and 16 using DFT and HF methods would suggest somewhat less involvement of CO  $\pi^*$ . But, rather than being concerned with exact quantitative matters, we shall take a more qualitative, global view. Before we use the  $\text{ML}_5$  unit as a building block for larger molecules, it is instructive to examine it as a molecule in its own right.

### 17.3 FIVE COORDINATION

We have looked at the orbital properties of the main group  $\text{AH}_5$  molecules in Chapter 11. Two basic structures are known, the square pyramid (17.14) and the trigonal bipyramidal (17.15). The ideal square pyramid has  $C_{4v}$  symmetry. As a result,



there are two different ligand sites, apical and basal, and there is one angular degree of freedom,  $\theta$ . The ideal trigonal bipyramidal has  $D_{3h}$  symmetry, so there are again two different ligand sites, equatorial and axial. A whole spectrum of geometries between the two extremes is also found in practice. The interconversion of the two geometries can occur via the Berry pseudorotation process that shall be examined shortly.

The energy levels of the square pyramid [5] with  $\theta = 90^\circ$  have been derived in Section 17.1. First, we see how they change in energy as the angle  $\theta$  varies. This is done in the Walsh diagram for  $\text{FeH}_5^+$  at the extended Hückel level in Figure 17.3. Notice that this model is free from any  $\pi$  effects. As  $\theta$  increases from  $90^\circ$ , the  $\sigma$  overlap of the basal ligands with  $z^2$  and  $x^2 - y^2$  decreases (Figure 17.3); they become less antibonding and lowered in energy. In other words, the first-order correction to the energy in both cases is negative using geometric perturbation theory. A plot of the  $z^2$  MO at the B3LYP DFT level for  $\text{FeH}_5^+$  is also shown on the upper right side of the figure. Concurrently,  $\sigma$  interaction with the  $xz, yz$  pair of orbitals is turned on, so these levels are pushed to higher energy. Such a geometry change also changes the shape of these metal  $d$ -based orbitals since they become hybridized with the  $(n+1)p$  metal orbitals. This is shown for the pair of  $e$  MOs on the right side of Figure 17.3. A plot of the  $yz$  component of the  $e$  set for  $\text{FeH}_5^+$  is shown in the middle right side of the figure. We have seen this  $d-p$  mixing previously in Section 15.4 for a related angular geometry change. The resulting hybridization out away from the ligands is entirely analogous to this previous case. From a geometrical perturbation theory perspective, there is no change in the energy to first order since at  $\theta = 0^\circ$ , the  $e$  set is

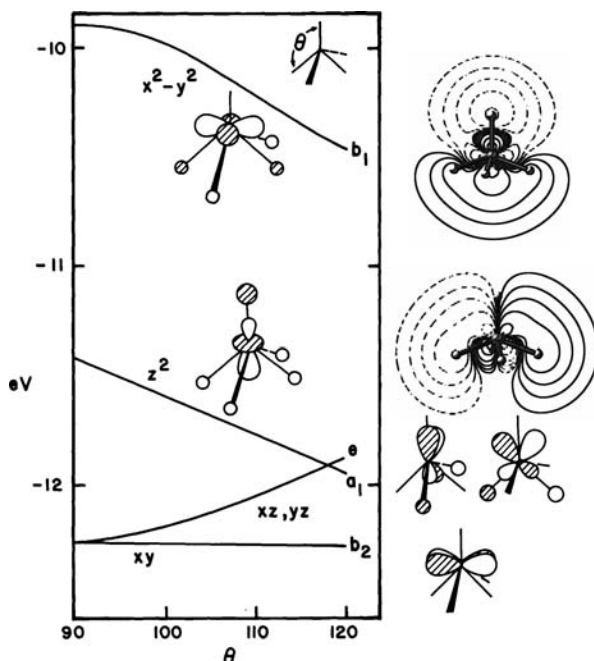


**FIGURE 17.3**

Orbital correlation diagram for the metal  $d$  orbitals on bending a square pyramid.

**TABLE 17.1** Some Apical–M–Basal Bond Angles,  $\theta$ , in Square Pyramidal Molecules as a Function of Electronic Configuration

Compound	$d^n$	$\theta$ (degrees)	CCDC Entry <sup>a</sup>
Nb(OR) <sub>2</sub> Cl <sub>3</sub>	$d^0$	102.7	ZEQTEU
Ta(NR <sub>2</sub> ) <sub>5</sub>	$d^0$	104.2	AKINAJ
Ti(OMe)(porp) <sup>b</sup>	$d^2$	107.2	BULXIP
Mo(SR) <sub>5</sub> <sup>-</sup>	$d^2$	107.8	DIZMEE
Re(CO) <sub>3</sub> (PR <sub>3</sub> ) <sub>2</sub> <sup>+</sup>	$d^6$	93.3	PIWWEX
Ir(porp)(CH <sub>2</sub> - <i>p</i> -tol)	$d^6$	92.1	VOFDAW
Ru(PPh <sub>3</sub> ) <sub>3</sub> (CO) <sub>2</sub>	$d^8$	105.1	POWCUZ
Ni(CN) <sub>5</sub> <sup>3-</sup>	$d^8$	100.2	EDCRCN
Zn(NR <sub>3</sub> ) <sub>4</sub> Cl <sup>+</sup>	$d^{10}$	104.2	MENLAS
Cd(porp)(pyr)	$d^{10}$	107.4	JITDOG
Fe(porp)(imid) <sup>c</sup>	hs $d^6$	101.7	KIMGAO
Fe(porp)(imid)CO	ls $d^6$	89.1	FATWUS

<sup>a</sup>Cambridge Crystallographic Data Center entry.

<sup>b</sup>porp = porphyrin.

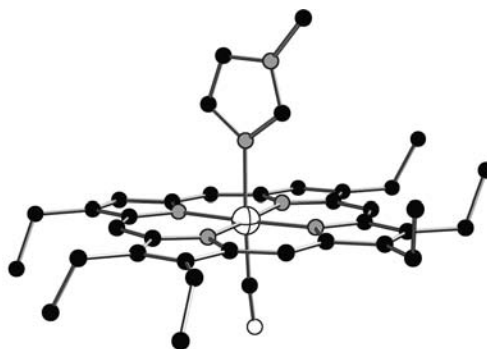
<sup>c</sup>imid = imidazole.

purely  $xz$  and  $yz$ . However, when the metal  $x$  and  $z$  are introduced into this  $e$  set, they bring in the ligand  $s$  AOs in a bonding manner, and the latter make antibonding with the  $e$  set hence destabilizing it. Notice that the ligand-based  $e$  set will then be stabilized upon increasing  $\theta$ . Finally, the  $b_2$  orbital stays at a constant energy and remains nonbonding with respect to the ligand  $\sigma$  donors.

Since the  $d$  orbital energies of the  $ML_5$  square pyramid change significantly with the angle  $\theta$ , the details of the geometry of such species will depend upon the number of  $d$  electrons and how the orbitals are occupied. Table 17.1 is a collection of some representative square pyramidal molecules where  $\theta$  is the averaged apical–metal–basal bond angle. The  $d^0$ – $d^2$  molecules are expected to have  $\theta > 90^\circ$  since, as just mentioned, the ligand-based  $e$  set is stabilized upon bending. The first four entries in Table 17.1 illustrate this with  $\theta = 102.7^\circ$ – $107.8^\circ$ . There are three  $d^0$  Ta(CH<sub>2</sub>R)<sub>5</sub> molecules that have been structurally determined:  $\theta = 111.1^\circ$  for R=H [6],  $\theta = 110.7^\circ$  for R=Ph [7], and  $\theta = 111.0^\circ$  for R=*p*-tol [8]. Furthermore,  $\theta = 113.6^\circ$  for the  $d^1$  Mo(CH<sub>3</sub>)<sub>5</sub> [6]. Low spin  $d^6$  species are expected to be close to a flat pyramid ( $\theta = 90^\circ$ ) since  $xz$  and  $yz$  (filled for a  $d^6$  system) rise in energy as  $\theta$  increases. The two examples in Table 17.1 are in fact close to this estimate. We shall shortly cover the dynamics associated with  $d^6$  Cr(CO)<sub>5</sub> in some detail. The computed gas-phase structure is one where  $\theta = 92^\circ$  [9]. Low spin  $d^8$  species where  $z^2$  is occupied are more distorted ( $\theta > 90^\circ$ ). This is a trend found in general, and the examples of Table 17.1 are typical of complexes with this electron count. The  $x^2 - y^2$  orbital is also stabilized upon increasing  $\theta$ ; thus, it is tempting to argue that the larger values of  $\theta$  for the two  $d^{10}$  complexes in Table 17.1 can be attributed to the occupation of  $x^2 - y^2$ . But, it is also true that the  $d$  AOs of Zn and Cd lie at very low energies, see Figure 15.2, and, therefore bonding between the  $d$  AOs and the ligand  $\sigma$  donor functions is expected to be minimal. A better example is given by high spin  $d^8$  complexes that have the electronic configuration  $(xy)^2(xz/yz)^4(z^2)^1(x^2-y^2)^1$ . An example of great importance is deoxyhemoglobin where the iron atom in a heme unit lies in a site of square pyramidal coordination. There are four such heme units, connected to peptide chains, in hemoglobin [10]. Commensurate with the high spin  $d^6$  electronic configuration,  $\theta$ , is larger than  $90^\circ$ . A model given in the second to last entry in Table 17.1 is shown in **17.16**. On the coordination of O<sub>2</sub>, the iron atom becomes six coordinate and the spin state changes to low spin. Both of these



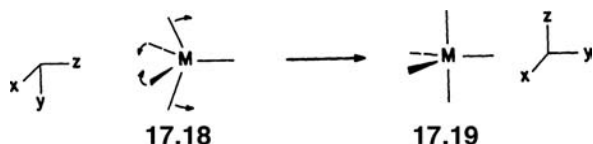
17.16



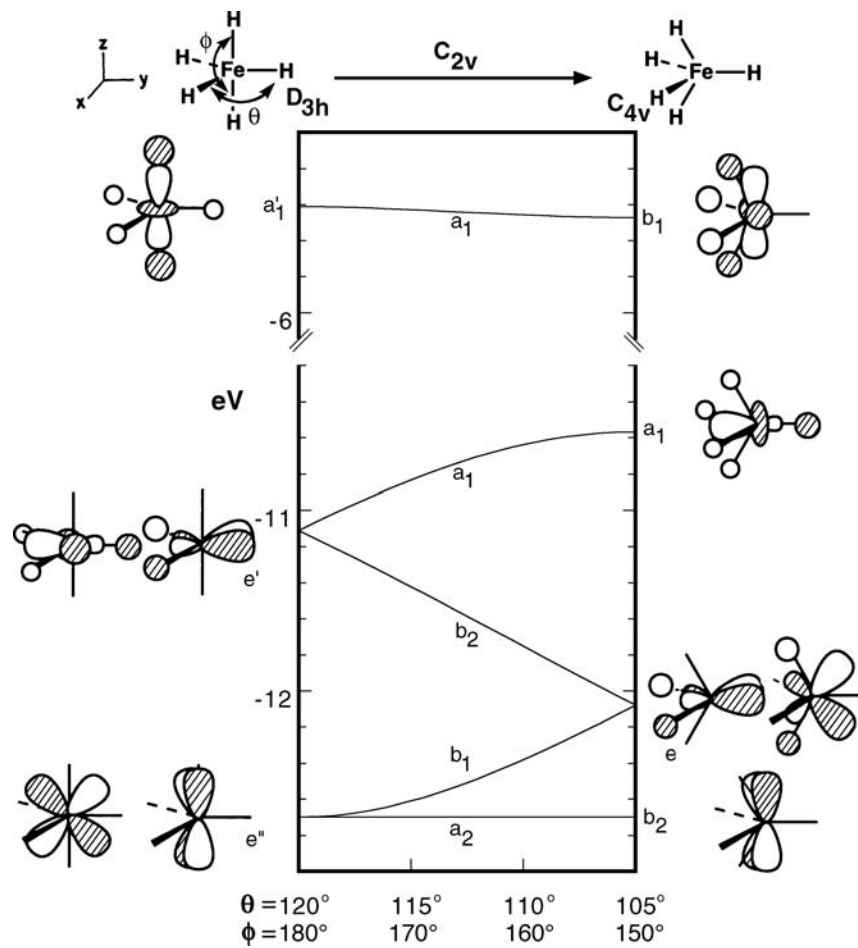
17.17

factors lead to a  $\theta$  angle of about  $90^\circ$  in oxyhemoglobin. Thus, the stereochemical change on oxygenation leads to a considerable movement of the iron atom and, of course, the imidazole ring attached to it in the apical position of the square pyramid shown in a model where CO (rather than  $O_2$ ) is used as the sixth ligand in 17.17. Connected to the imidazole ring is the organic peptide part of the molecule. The deformations induced in this framework by the movement on going to 17.17 have been suggested to be important for the triggering of the important cooperative peptide reorganization process upon oxygen binding of one heme unit. Such movement exposes the other heme groups, so that attack by further  $O_2$  molecules is facilitated.

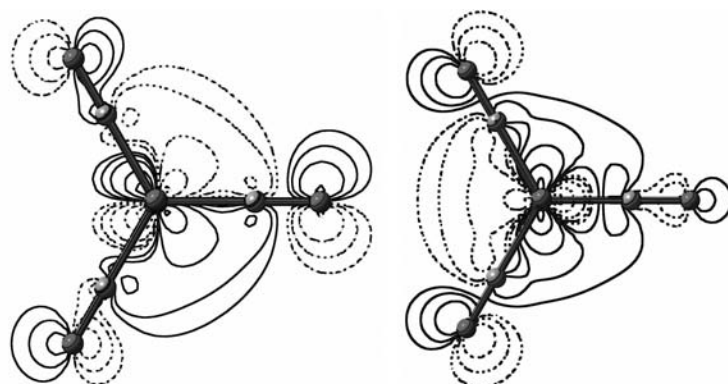
Just as the electronic configuration is very important in determining the geometry along the deformation coordinate 17.14, so too is it important in influencing the relative stabilities of the square pyramid and trigonal bipyramidal along the related coordinate 17.18. A minor complication arises in that the obvious



axis choice in the two molecules is different (17.18 versus that in 17.19) so that the  $z^2$  orbital of the trigonal bipyramidal becomes the  $x^2 - y^2$  orbital of the square pyramid. The molecule, of course, does not know about  $x$ ,  $y$ ,  $z$  axes; these labels are there to identify orbitals. Figure 17.4 shows the Walsh diagram that correlates the orbitals for the two geometries. On the far right, the orbitals of a square pyramid are listed for a geometry with  $\theta \sim 90^\circ$ . The basic motion that is followed in Figure 17.4 takes the square pyramid (17.18) to a trigonal bipyramidal (17.19), by decreasing one trans L-M-L angle in the  $yz$  plane,  $\phi$ , and decreasing two equatorial angles in the  $xy$  plane. Using the coordinate system at the upper left side of Figure 17.4, the  $xz$ ,  $b_2$ , level for the square pyramid is unchanged along this pathway. It becomes one member of the  $e''$  set at the trigonal bipyramidal geometry. The other member of  $e''$  is derived from  $yz$ . As the one trans L-M-L angle is increased, the ligands move into the node of  $yz$ , causing this orbital to be stabilized. (This also results in the loss of hybridization with metal  $y$ .) The  $xz$  orbital of the square pyramid is destabilized. As the equatorial L-M-L angles in the  $xy$  plane are increased, the lone pair on the ligand increases its antibonding interaction with  $xy$ . This is reduced somewhat by increased mixing of metal  $x$  character. Ultimately, at the trigonal bipyramidal geometry, this orbital lies at moderate energy and is substantially hybridized out away from the ligands in the  $xy$  plane. A contour plot in the  $xy$  plane of this MO for  $Fe(CO)_5$  is given in 17.20 from a

**FIGURE 17.4**

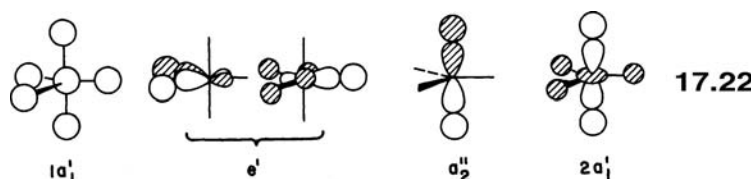
A Walsh diagram (at the extended Hückel level) for the metal  $d$  orbitals that connect square pyramidal,  $C_{4v}$ , and trigonal bipyramidal,  $D_{3h}$ , geometries.

**17.20****17.21**

computation using the B3LYP hybrid functional. Along with the hybridization, note the large involvement of CO  $\pi^*$  particularly with the carbonyl ligand on the right side of the molecule. What happens to the two highest levels of the square pyramidal and trigonal bipyramidal geometries of Figure 17.4 is more difficult to describe. The  $z^2$

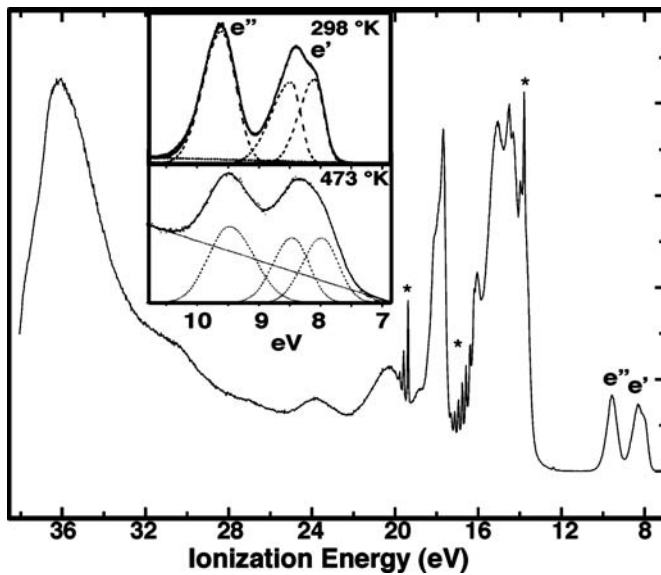
and  $x^2 - y^2$  “character” of these two levels switch. One way we can trace this intermixing is by noting that the symmetry of the molecule is  $C_{2v}$  at a geometry intermediate between the two extremes. The three orbitals that we have just examined are of  $a_2 + b_1 + b_2$  symmetry. The two higher orbitals are both of  $a_1$  symmetry. They can, and will, intermix along the reaction path. Starting from the square pyramidal side, the  $z^2$  orbital will mix some  $x^2 - y^2$  character into it until, at the trigonal bipyramidal structure, it is predominantly  $x^2 - y^2$ . (Remember that we have changed the coordinate system. It would become an  $x^2 - z^2$  orbital if we had stayed with the axis system in 17.18.) Two ligands in the  $xy$  plane move into the nodal plane of this  $x^2 - y^2$  function. Furthermore, metal  $y$  mixes into the orbital in a bonding way to the three ligands in the  $xy$  plane. Therefore, this level is stabilized, and it becomes the other member of the  $e'$  set at the trigonal bipyramidal geometry. A contour plot of this MO in  $\text{Fe}(\text{CO})_5$  is displayed in 17.21. Again note the substantial  $\pi^*$  involvement for the two CO ligands on the left side of the molecule. The two members of the  $e'$  set in the trigonal bipyramidal are ideally hybridized and lie at moderately high energies, so they make excellent interactions with  $\pi$  acceptor orbitals that lie in the  $xy$  plane. We shall see several ramifications of this fact later on. The highest  $d$ -based orbital at the square pyramid that one would normally call  $x^2 - y^2$  mixes some  $z^2$  character into itself. At the trigonal bipyramidal geometry, it is primarily  $z^2$ , antibonding to the surrounding ligands. There is some metal  $s$  character in this orbital that reduces the antibonding interactions with the ligands in the  $xy$  plane.

The level structure for the valence levels of the trigonal bipyramidal is worth studying with some care. At low energy, there is an  $e''$  orbital, a pure metal  $d$  combination, which is orthogonal to the ligand lone pairs. At intermediate energy are two hybridized metal functions of  $e'$  symmetry. At higher energy,  $a_1$  is fully metal–ligand antibonding. What has been left off this diagram are the five metal–ligand bonding orbitals (17.22). Except for  $2a_1$  (and the  $z^2$  orbital in Figure 17.4), these are



exactly analogous to the orbitals of the  $\text{AH}_5$  main group compound (see the left side of Figure 14.17). We have introduced a strong mixing with metal  $d$  orbitals, so that  $e'$  in 17.22 is a mixture of  $x^2 - y^2$  and  $xy$  character as well as  $x$  and  $y$  at the metal. The  $e'$  set displayed in Figure 17.3 are the nonbonding components of this three-orbital pattern. Likewise, the nonbonding  $2a_1$  orbital of  $\text{AH}_5$  will now find a perfect symmetry match with metal  $z^2$ . The  $2a_1$  level in 17.22 is the bonding component, and  $a_1$  shown at the upper left of Figure 17.4 is the antibonding partner.

We shall take a short aside here to examine the photoelectron spectrum of  $\text{Fe}(\text{CO})_5$ . This is a trigonal bipyramidal molecule in the gas phase and as a crystalline solid. The formal oxidation state is  $\text{Fe}(0)$ , and so, the molecule is a  $d^8$  complex that means that it should have the electron configuration  $(e'')^4(e')^4$  by the inspection of the level ordering on the left side of Figure 17.4. The photoelectron spectrum of this compound has been studied a number of times [11–14]. The 40 eV photoelectron spectrum of  $\text{Fe}(\text{CO})_5$  [11] is given in Figure 17.5. The asterisks correspond to ionizations from free CO. The peaks at 8.5 and 9.8 eV have been assigned to ionizations from the  $e'$  and  $e''$  MOs, respectively. The peaks from 14.1 to 16.5 eV are thought to originate from CO  $1\pi$ - and  $3\sigma$ -based orbitals (see Figure 6.7 for the orbitals of CO), and those from 17.9 to 20.0 eV are derived

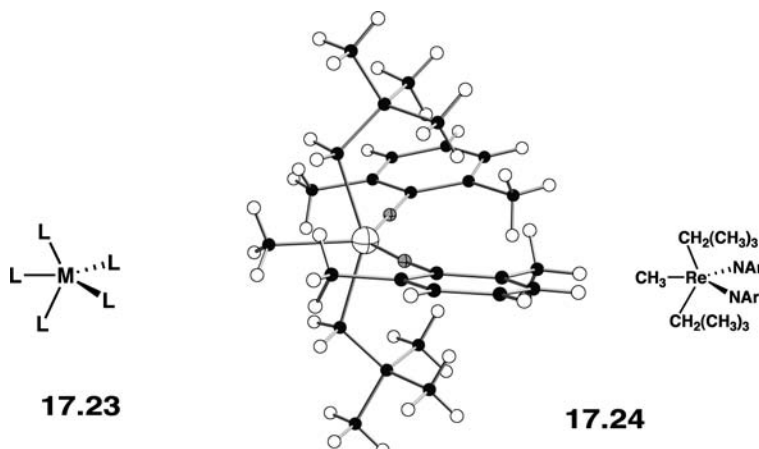
**FIGURE 17.5**

The 40 eV photoelectron spectrum of  $\text{Fe}(\text{CO})_5$  taken from Reference [11]. The asterisks show the positions of peaks due to free CO. The two insets at the top center of the figure are expansions of the low energy regions at two temperatures and are taken from Reference [12].

from CO  $2\sigma$  [14]. What is intriguing about the PE spectrum is that the band associated with the  $e'$  set is decidedly asymmetrical. An expansion of the two lowest ionizations is shown [12] in the two insets at the top of the figure. The  $e'$  ionization can be deconvoluted into two peaks. The reason for this lies in the fact that the  ${}^2\text{E}'$  state of  $[\text{Fe}(\text{CO})_5]^+$  ion, resulting from the ionization, is Jahn–Teller unstable (see Section 7.4.A). The symmetric direct product yields possible distortions of  $a'_1$ ,  $a'_2$ , and  $e'$  symmetry. The normal modes for a trigonal bipyramidal are shown in Appendix III. It is the  $e'$  normal mode that can split the degenerate state into two. An elegant analysis [12] of this shows that a motion like that in Figure 17.4 to  $C_{2v}$  symmetry will split the  ${}^2\text{E}'$  state into  ${}^2\text{B}_2$  and  ${}^2\text{A}_1$  (a single electron occupies either  $b_2$  or  $a_1$  upon distortion to  $C_{2v}$ ). Now, the  ${}^2\text{E}''$  ion is also Jahn–Teller unstable and the symmetric direct product also points to the same vibrational mode of  $e'$  symmetry as creating two states of  ${}^2\text{B}_1$  and  ${}^2\text{A}_2$  symmetry. One can see from Figure 17.4 that the  $b_2$ – $a_1$  splitting is large upon deformation as opposed to that for the  $b_1$ – $a_2$  set and this in turn leads to a larger electronic state difference for the former. The inset in Figure 17.5 also shows that the Jahn–Teller splitting in the  ${}^2\text{E}'$  state becomes larger as the temperature is raised. At 298 K, it is 0.38 eV and this increases to 0.47 eV at 473 K [12]. At higher temperatures, the mean vibrational distribution maximizes at larger nuclear displacements from the  $D_{3h}$  geometry and, therefore, the splitting between the two electronic states becomes larger.

From Figure 17.4, we can comment on the preferred geometries of  $\text{ML}_5$  compounds as a function of  $d$  electron configuration. Recall that there is a slight favoring of the  $D_{3h}$  trigonal bipyramidal geometry for what would be the  $d^0$  configuration from our discussion of main group stereochemistry in Section 14.3 in accordance with the VSEPR model. But, here there is strong  $d$  orbital involvement in the bonding. Notice in 17.22 that the  $a_2''$  orbital has only metal  $p$  character. If the axial–M–axial angle is decreased from  $180^\circ$ , then metal  $yz$  can mix into this molecular orbital and this will be a powerful driving force for distortion. The most obvious way to do this is along the Berry pseudorotation coordinate going from 17.19 to the square pyramid 17.18. Indeed, the first two entries in Table 17.1 are examples, as well as, the  $\text{TaR}_5$  compounds mentioned previously.

But what about bending the two axial ligands in the opposite direction, toward one of the equatorial ligands to give a  $C_{2v}$  structure, **17.23**? In fact, this structure is



computed to be the transition state for apical–basal exchange in  $TaH_5$  and  $TaMe_5$  [15]. These two molecules are square pyramids in their ground states, and are much more stable than the trigonal bipyramidal. Ward and coworkers have elegantly examined what electronic factors can be used to stabilize structure **17.23** [16].  $\pi$  donors that are oriented so that their  $p$  AOs lie parallel to the axial–metal–axial axis will be stabilized by the empty metal  $xz$  and  $yz$  orbitals. When the two axial ligands are bent back, then the  $yz$  orbital mixes with metal  $z$  to produce an orbital hybridized toward the two  $\pi$  donors, and consequently, the latter are stabilized more. A real example (and there are several [16]) is given by **17.24** [17]. There are three anionic alkyl groups along with two imido groups that are counted as having  $-2$  charge. **17.24** is then  $Re^{7+} - d^0$ . The axial  $C-Re-C$  angle is only  $147.7^\circ$ . A  $d^1$  or  $d^2$  (low spin) complex from the examination of Figure 17.3 must be a square pyramid. Two  $d^2$  examples are given in Table 17.1, and  $d^1$   $Mo(CH_3)_5$  [16] is another. A high spin  $d^2$  complex is expected to be a trigonal bipyramidal with the  $(e'')^2$  configuration. Figure 17.3 indicates that for  $d^3$  and  $d^4$  complexes, the trigonal bipyramidal should be favored even more since the  $yz$  component of  $e''$  rises in energy on distortion away from this structure. There are many examples of  $d^4$  compounds that show this, for example, several  $MnCl_5^{2-}$  salts. For  $d^5$  and  $d^6$ , a square pyramid (with  $\theta \sim 90^\circ$  from Figure 17.3) is expected. For  $d^7$ , we need to weigh a two-electron stabilization along the  $D_{3h} \rightarrow C_{4v}$  coordinate against a one-electron destabilization. The  $D_{3h}$  geometry, however, is Jahn–Teller unstable. In low temperature matrices where low spin  $d^5$ ,  $d^6$ , and  $d^7$  pentacarbonyls have been made [18], these compounds have square pyramidal geometries. The  $d^6$  case is particularly interesting since the level pattern for the  $D_{3h}$  and  $C_{4v}$  structures suggests the singlet and triplet states might have different geometries. The situation therefore is very similar to that for cyclobutadiene in Chapter 12 and just like the tetrahedral/square planar problem discussed for four-coordinate  $d^8$  molecules in Chapter 16. The  $d^6$  singlet state is unstable at the  $D_{3h}$  geometry since the  $e'$  orbital would be half-full but is stabilized on distortion to a  $C_{4v}$  or  $C_{2v}$  geometry. Computations [19] have shown that the  $C_{4v}$  square pyramid is the most stable singlet for  $M(CO)_5$  where  $M = Cr$ ,  $Mo$ , and  $W$  and  $\theta = 90.8^\circ - 89.6^\circ$ . This is also consistent with the two experimental structures cited in Table 17.1. A  $D_{3h}$  trigonal bipyramidal has been computationally found to be stable for the triplet state [20] that lies about 15 kcal/mol above the singlet  $C_{4v}$  state. Molecules with a  $d^8$  or  $d^9$  configuration exist either as trigonal bipyramids or square pyramids with plenty

in-between that define the Berry pseudorotation pathway (**17.18** to **17.19**)<sup>[21]</sup>. In other words, there is a very soft potential associated with this at, especially the 18 electron,  $d^8$  count so that the structure in the solid state is set by inter- and intramolecular nonbonded contacts.

The substitution of one group for another in a molecule is a ubiquitous reaction in chemistry. In the transition metal/organometallic worlds, this most often requires a prior dissociation of a coordinated ligand and then rapid attack of an external nucleophile. The dissociative step may be thermally or photochemically activated. In this context, the photolysis of  $M(CO)_6$ ,  $M = Cr$ , Mo, and W, to yield  $M(CO)_5$  is of fundamental importance. There is a beautiful collaboration between ultrafast spectroscopy [22] and theory [9,23], which has considerably expanded our knowledge of this reaction. We shall review the situation for  $M = Cr$ , which for Mo and W is quite similar. Recall that  $Cr(CO)_6$  is a  $d^6$  molecule, so the HOMO (see Figure 15.1) is  $t_{2g}$ . The LUMO is not  $2e_g$ ; the CO  $\pi^*$  sets will lie at lower energy. These transform as  $t_{1u} + t_{2u} + t_{1g} + t_{2g}$  where all but the last are nonbonding with respect to the metal. On the other hand,  $2e_g$  is strongly Cr–C antibonding. So, the lowest excited state is one where an electron from  $t_{2g}$  is promoted to the  $t_{1u}$  set of CO  $\pi^*$ <sup>[24]</sup>, which has the electronic state symmetry  $^1T_{1u}$ . This is shown on the left side of Figure 17.6. This is called a metal to ligand charge transfer (MLCT) state. This state, along with

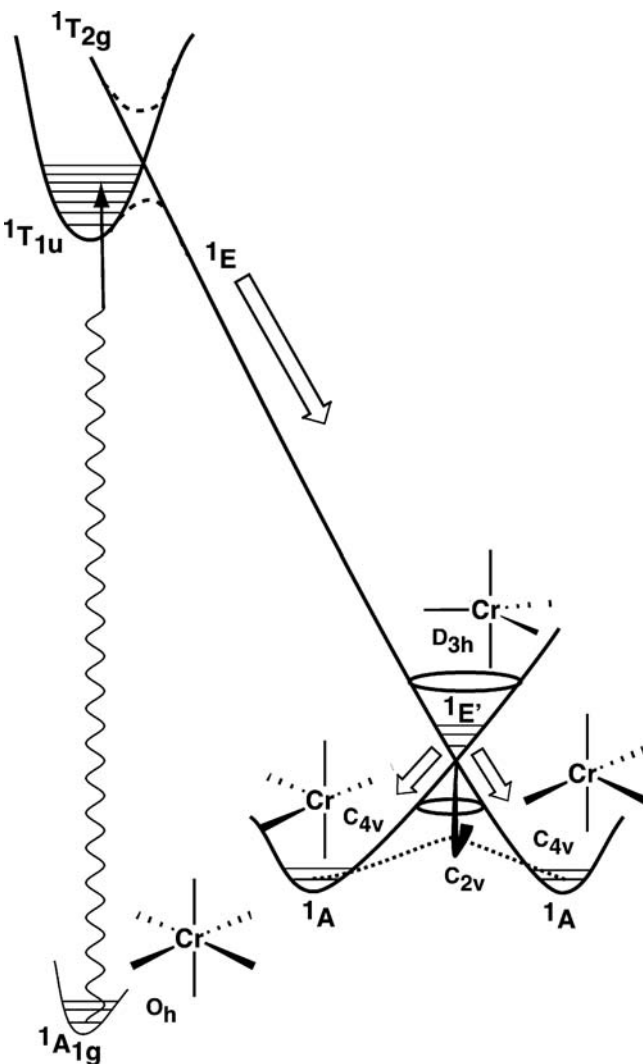
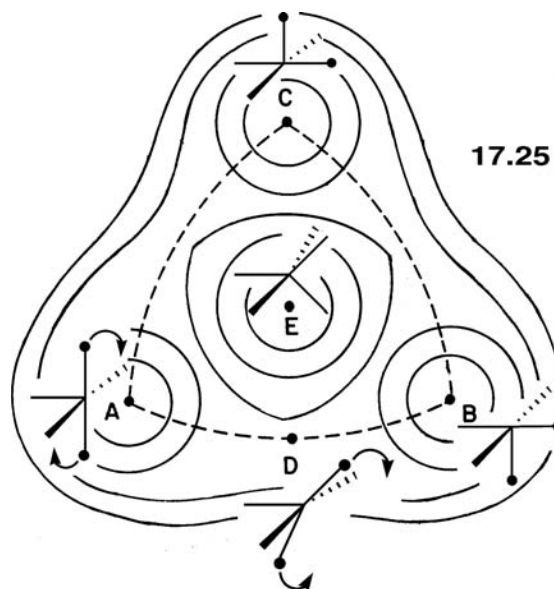


**FIGURE 17.6**

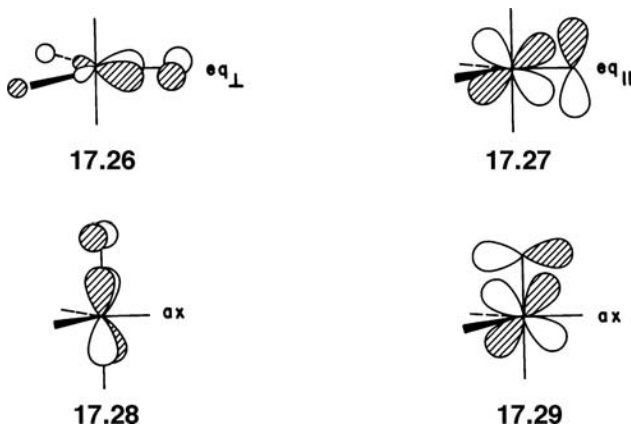
An electronic state correlation diagram for removing one carbonyl ligand from  $Cr(CO)_6$ . The vertical energy axis is not drawn to scale.

other MLCT states, is bound with respect to Cr–CO dissociation. Promotion of an electron from  $t_{2g}$  to  $2e_g$ , however, produces a strongly dissociative  $^1T_{2g}$  electronic state. A distortion to  $C_{4v}$  by removing a CO ligand allows the formation of an avoided crossing between the two states (both have E symmetry). At an excitation of 270 nm, the lifetime of the  $^1T_{1u}$  state was measured to be 12.5 fs. There are in fact other MLCT states that also undergo this crossing with very similar lifetimes. The strongly dissociative state of  $^1E$  symmetry has a lifetime of 18 fs and ejects the carbonyl ligand with a mean square velocity of about 1200 m/s! The  $\text{Cr}(\text{CO})_5$  molecule falls into a Jahn–Teller unstable cone ( $^1E'$ ) where it has  $D_{3h}$  symmetry and a lifetime of 40 fs. Finally, it passes through the conical intersection to the square pyramidal  $C_{4v}$  ground state ( $^1A$ ). But, the dynamics do not stop here. The surface on the lower right of Figure 17.6 is the familiar threefold Jahn–Teller surface, which we encountered in Figure 7.7. The potential surface for the thermal rearrangement of this molecule is similar in form to that for  $\text{H}_3^-$  and  $\text{C}_5\text{H}_5^+$  described earlier. An idealized representation of it is given in 17.25. When the  $\text{Cr}(\text{CO})_5$  molecule is at the Jahn–Teller unstable  $D_{3h}$  geometry, it can distort in three ways to form structures A, B, or C in 17.25. There is more than enough

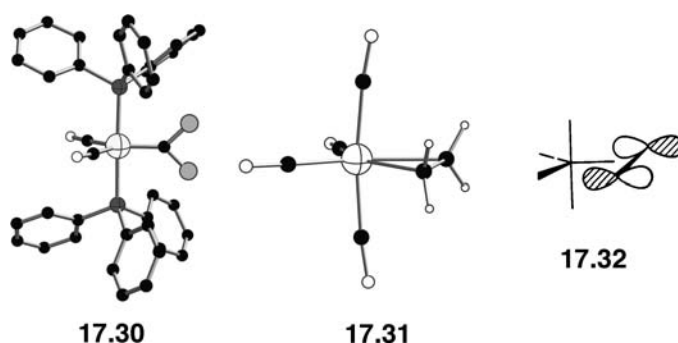


kinetic energy to send, let us say the molecule in structure A, to structure B. However, it does not do so via the least-motion path that would climb back to the trigonal bipyramidal, E. As the arrows associated with A show, there is a peculiar bending motion that sends  $\text{Cr}(\text{CO})_5$  to a structure with  $C_{2v}$  symmetry, D. The  $C_{2v}$  structure has been calculated to lie 9.3 kcal/mol above the  $C_{4v}$  minimum [9]. The  $D_{3h}$  species is 23.1 kcal/mol above  $C_{4v}$  [9]. The  $\text{M}(\text{CO})_5$  molecules are very strong electrophiles that only can be studied in the gas phase or at low temperatures in an inert matrix. There are, however, a growing number of  $d^6$  molecules that are more robust. The important fact is that, unless they are triplets, they will behave in an analogous fashion, avoiding the  $D_{3h}$  geometry. Table 17.1 presents two examples. Here, structures A, B, and C are minima and D along with the two other symmetry related structures are transition states. Can this be reversed? Indeed, there are several ways to do this and the interested reader is directed elsewhere for the electronic dissection of this coordination geometry [25].

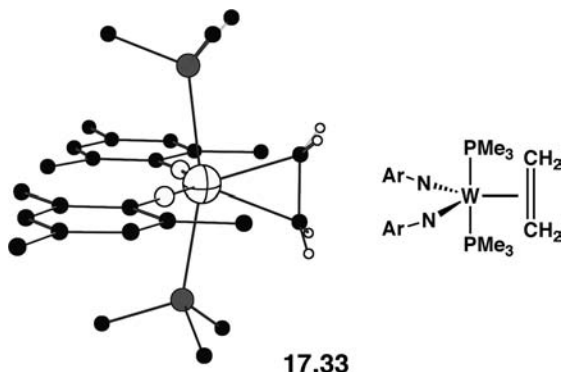
As mentioned previously within the same molecule, there are two symmetry inequivalent linkages (and therefore sites), axial and equatorial in the trigonal bipyramidal (**17.15**) and apical and basal in the square pyramid (**17.14**). The patterns for  $\pi$  bonding [5] can be constructed following the procedure used for the octahedron. For the trigonal bipyramidal, there are four symmetry-allowed interactions shown in **17.26–17.29**. Three involve interaction with the  $e''$  orbitals and one interaction with the  $e'$  orbitals (see the left side of Figure 17.4). **17.28** and **17.29** are equivalent by symmetry. Since the  $e'$  orbitals are hybridized away from the ligands as described above and shown in **17.20**, the  $\pi$ -type overlap of a ligand orbital with  $e'$  in **17.26** is significantly larger than any of the other interactions, that is,  $eq_{\perp} > eq_{||} \gg ax$ . However, it is important to realize that



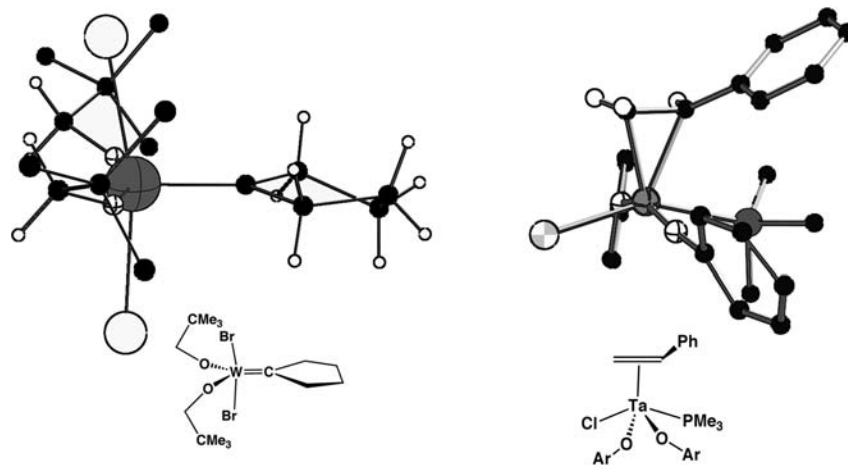
just because the  $eq_{\perp}$  interaction is larger than  $ax$ ,  $\pi$ -bearing ligands will not always prefer the  $eq_{\perp}$  site. The site preferences depend on the number of electrons and on whether the ligand is a  $\pi$  acceptor or donor. For a  $\pi$  acceptor ligand, a  $d^8$  system will prefer the  $eq_{\perp}$ , and  $d^2$  systems, the  $eq_{||}$  arrangement. An example of the  $d^8$  case is provided by the molecule Ru( $PPh_3$ )<sub>2</sub>(CO)<sub>2</sub>CF<sub>2</sub> (**17.30**) [26]. The CF<sub>2</sub> carbene ligand has an empty  $p$  AO—a superlative  $\pi$  acceptor orbital orthogonal to the CF<sub>2</sub> plane.



Therefore, the carbene is oriented in a sterically most demanding position to take advantage of the interaction shown in **17.26**. Another example is provided by Os(CO)<sub>4</sub>(ethylene) [27], **17.31**, where the ethylene ligand is a  $\pi$  acceptor via its  $\pi^*$  orbital, **17.32**. In fact, all  $d^8$  (olefin)ML<sub>4</sub> complexes have this conformation. We shall explore the consequences of this further in Chapters 19 and 21. An interesting molecule is provided by **17.33** [28]. Each imido group has a formal charge of -2 so we have a  $d^2$  molecule. The imido  $p$  AO lone pairs will push the  $xz$  orbital of what

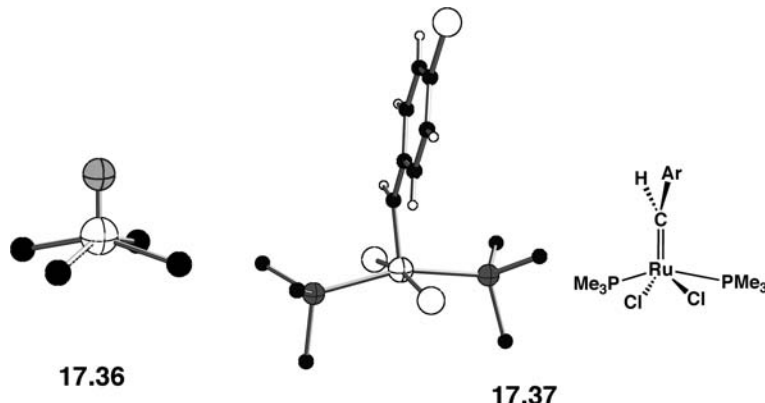


was the metal  $e''$  set (see the left side of Figure 17.4) above  $yz$ . Therefore, metal  $yz$  is filled and will interact with the empty  $\pi^*$  orbital on ethylene as long as the olefin is oriented in the  $eq_{||}$  direction. Consider another carbene complex, **17.34** [29].



This is formally a  $W^{4+} - d^2$  system, if the  $CR_2$  carbene group is treated as a neutral two-electron donor with an empty  $p$  orbital, a superlative  $\pi$  acceptor along the lines of **15.21**. This again presupposes a trigonal bipyramidal geometry and that the  $yz$  component of  $e''$  on the left side of Figure 17.4 is filled and significantly stabilized with respect to the  $xz$  component. Another way to view **17.34** would be the carbene has both the  $\sigma$  orbital and the  $p$  AO filled. It then is an di-anionic fragment yielding a  $d^0$ ,  $W^{4+}$  complex. After all, this is an early transition metal and the carbene complexes in this area are decidedly nucleophilic at carbon as opposed the electrophilic ones represented by **17.30**. But, recall that  $d^0$  molecules are square pyramids rather than trigonal bipyramids. The  $Br-W-Br$  angle is  $167^\circ$ —not too far from what is expected for two axial groups in a trigonal bipyramidal, but the  $O-W-O$  angle is opened much wider than the expected  $120^\circ$  to  $159^\circ$ . Thus, **17.34** could easily be viewed as a square pyramid with the carbene ligand at the apical site and  $\theta \sim 98^\circ$ . A related example with an olefin at the apical position is given by **17.35** [30]. Here, the  $Cl-Ta-P$  angle is  $151^\circ$  and the  $O-Ta-O$  angle is  $159^\circ$ . Referring back to the lower left side of Figure 17.3, notice that  $xy$ ,  $xz$ , and  $yz$  are close in energy. In **17.34** (using the  $xz$  plane to correspond to the plane of the paper),  $xy$  and  $yz$  orbitals at the metal will overlap with the lone pair  $\pi$  donor orbitals at the two alkoxides ligands and be destabilized. That leaves metal  $yz$  as the orbital to overlap with the carbene  $p$  AO. The same affair occurs in **17.35**. The

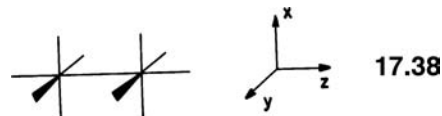
alkoxides use  $xy$  and  $xz$  for  $\pi$  bonding that leaves the filled  $yz$  orbital to backbond to the olefin  $\pi^*$  orbital. Two unequivocal cases of square pyramidal coordination are given by **17.36** [31] and **17.37** [32]. In **17.36**,  $\text{OVCl}_4^-$ , the oxo group is counted as di-anionic,



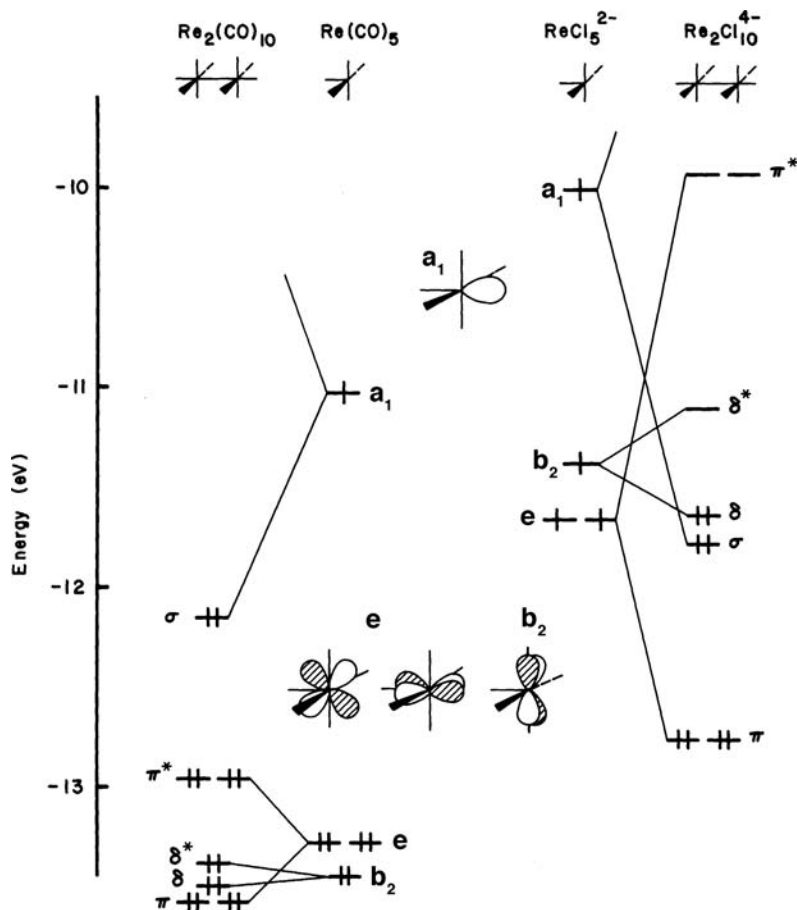
so this is a  $d^0$  complex with oxygen in the apical site. It uses the two-oxygen  $p$  AOs to  $\pi$  bond to metal  $xz$  and  $yz$ . **17.37** has a  $d^6 \text{Ru}^{2+}$ , so the electron count is set at 16, the same as in  $\text{Cr}(\text{CO})_5$  that we have just discussed. The P–Ru–P angle was  $161^\circ$  while the Cl–Ru–Cl angle was  $168^\circ$ . **17.34**, **17.35**, and **17.37** illustrate cases where the  $\pi$  acceptor orbital is in the apical position and is orthogonal to the basal–metal–basal plane that contains the stronger set of  $\pi$  donors. As a consequence, there will be a barrier to rotate the apical group about the metal-apical axis.

## 17.4 MOLECULES BUILT UP FROM $\text{ML}_5$ FRAGMENTS

In this section, the valence  $C_{4v}$   $\text{ML}_5$  fragment orbitals are used to build up the orbitals of more complex units. First, we look at the level structure [33,34] of a simple dimer,  $\text{M}_2\text{L}_{10}$  (**17.38**). The  $\text{ML}_5$   $d$  orbitals neatly partition into  $\sigma$  ( $z^2$ ),  $\pi$  ( $xz, yz$ ), and  $\delta$  ( $x^2 - y^2$ ,  $xy$ ) types in this geometry. The details of the resulting orbital diagrams, however,

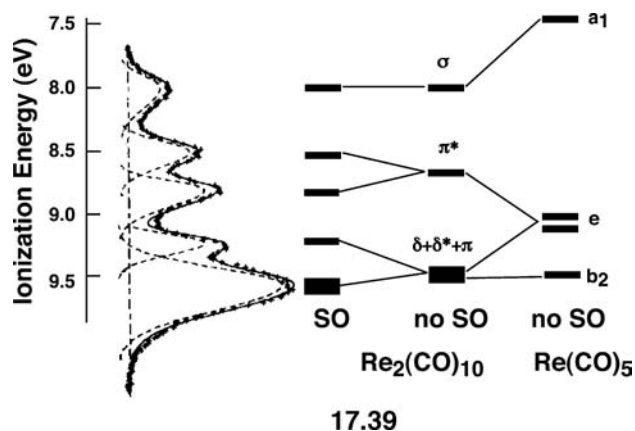


depend crucially on the identity of the ligands L. Let us look at the two cases,  $L = \text{Cl}$  and  $L = \text{CO}$ , typical simple  $\pi$  donor and acceptor ligands, respectively. Recalling that  $\pi$  donors destabilize and acceptors stabilize the “ $t_{2g}$ ” orbitals (Chapter 15) and that although  $xy$  may interact with four ligand  $\pi$  orbitals,  $xz$  and  $yz$  may only interact with three, we end up with a two above one level arrangement for  $\text{M}(\text{CO})_5$  and a one above two arrangement for  $\text{MCl}_5$ . These are shown at the middle of Figure 17.7. The  $x^2 - y^2$  level is at very high energy being destabilized by the four basal ligands and is not shown in this figure. Since  $xy$ ,  $xz$ , and  $yz$  are destabilized by the lone pairs on Cl, these levels are energetically closer to the  $z^2$  hybrid orbital for  $\text{ReCl}_5^{2-}$  than in  $\text{Re}(\text{CO})_5$ . These factors are important in understanding the differences in the orbital pictures that result when two  $\text{MCl}_5$  or two  $\text{M}(\text{CO})_5$  units are brought together. The metal–metal distance in  $\text{Re}_2(\text{CO})_{10}$  of  $3.04 \text{ \AA}$  is much longer than the corresponding distance ( $2.22 \text{ \AA}$ ) in  $\text{Re}_2\text{Cl}_8\text{X}_2^{2-}$  ( $X = \text{H}_2\text{O}$ ). As a result, all of the metal–metal interactions are stronger in the halide. Because of this fact and the other points we have just noted,  $d^7 \text{Re}_2(\text{CO})_{10}$  has a single  $\sigma$  bond between the two metal atoms but  $\text{Re}_2\text{Cl}_8\text{X}_2^{2-}$  has a quadruple bond

**FIGURE 17.7**

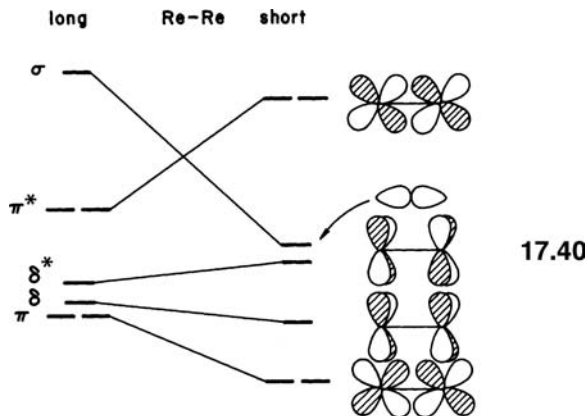
Interaction diagrams for two  $M_2\text{L}_{10}$  systems. Notice how the  $\pi$  levels in  $\text{Re}(\text{CO})_5$  lie lower energy than in  $\text{ReCl}_5^{2-}$ , a direct result of the  $\pi$  acceptor and donor nature of the ligands, respectively. Combined with a shorter metal–metal distance in the halide, the final-level diagrams are quite different.

made up of one  $\delta$ , one  $\sigma$ , and two  $\pi$  components as shown in Figure 17.7. Just how close do the extended Hückel calculations in Figure 17.7 correspond to the experimental situation? The photoelectron spectrum for  $\text{Re}_2(\text{CO})_{10}$  is shown in 17.39 [35,36].

**17.39**

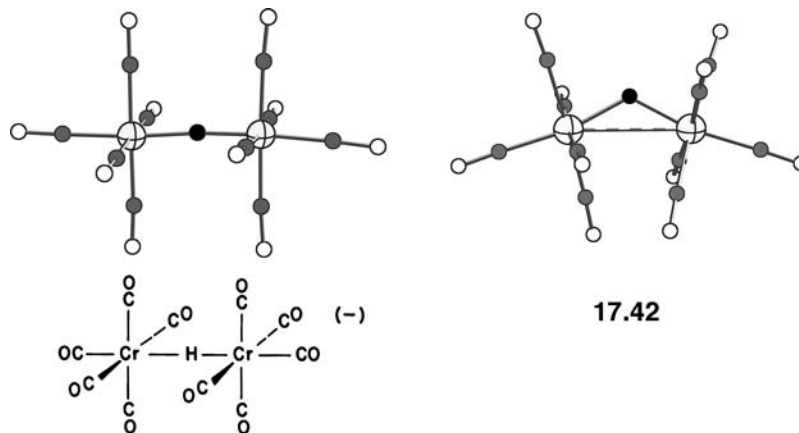
On the right side are the approximate ionization potentials for a  $\text{Re}(\text{CO})_5$ . These are then split in the same manner as in Figure 17.7 to generate the  $\delta$ ,  $\delta^*$ ,  $\pi$ ,  $\pi^*$ , and  $\sigma$  MOs. An important detail is that the  $\pi$  and  $\pi^*$  orbitals are further split into two by spin–orbit coupling effects. This can be analyzed [35] along with other examples containing the  $\text{Re}(\text{CO})_5$  group to give the fitting in 17.39. The peak with largest ionization potential is

comprised of  $\delta$ ,  $\delta^*$ , and the lower component of  $\pi$ . It has roughly three times the area of the other four peaks. The bonding picture in Figure 17.7 closely matches that in **17.39** with the exception that the orbital energies from the calculation are about 4 eV lower than those given by Koopmans' theorem from experiment. How can we increase the bond order between the two  $ML_5$  fragments for the case of  $L =$  acceptor? By shortening the M–M distance, the relevant orbitals change in energy in the obvious way shown in **17.40**. For the case of 10 electrons (a  $d^5$  metal), a formal triple bond is predicted ( $\pi^4\delta^2\delta^{*2}\sigma^2$ ). Indeed,  $Cp_2M_2(CO)_4$  species ( $M = Cr, Mo, W$ ),



isoelectronic with the unknown  $V_2(CO)_{10}$  molecule, with this electron configuration have very short metal–metal distances. As we will see later  $Cp$  is equivalent to three coordinated ligands.

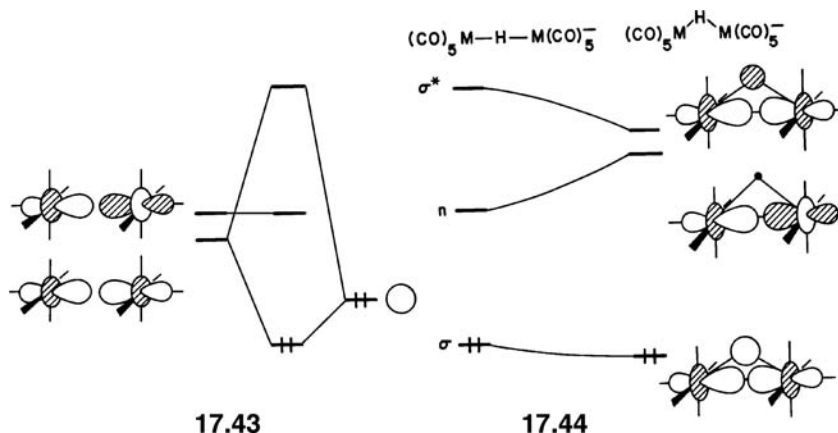
There are a number of molecules having the formula  $H(ML_5)_2$ , where  $M =$  a  $d^7$  metal, that pose an interesting structural feature. One might think of them as being derived from reacting the 18 electron  $H-Cr(CO)_5$  molecule, for example, with the 16 electron  $Cr(CO)_5$  to give **17.41** [37], which in this case contains a linear Cr–H–Cr bonding arrangement. One might consider this as being the interaction of



**17.41**

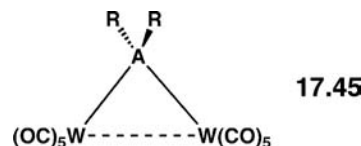
a Lewis base (the hydride portion of the molecule  $HCr(CO)_5$ ) with the Lewis acid,  $Cr(CO)_5$ . These compounds can also be prepared by protonating the M–M  $\sigma$  bond in  $M_2L_{10}$  dimers. A structural analog,  $HW_2(CO)_{10}^-$ , is shown in **17.42** [38]. Here, the W–H–W angle is  $123.4^\circ$  and there are, in fact, many isoelectronic compounds with intermediate M–H–M angles. In both cases, we have a three-center–two-electron bond; **17.41** is certainly an example of an “open” one, but then is **17.42**

an example of a “closed” three-center–two-electron bonding arrangement like we have seen many times before in previous chapters? The point of contention here is whether there is metal–metal bonding or not in molecules where the M–H–M bond angle is acute [39]. The energy levels of a linear  $\text{H}(\text{ML}_5)_2$  complex may be derived in a very simple way by adding the hydrogen 1s orbital to the orbital picture produced by the two  $a_1$  orbitals of the  $\text{ML}_5$  units set at a very long metal–metal distance expected in a molecule of this type. In other words, this is just the symmetry-adapted combination of the two  $a_1$  hybrids. The hydrogen s AO will form a bonding and antibonding combination with the symmetric member to form the  $\sigma$  and  $\sigma^*$  MOs in 17.43. The antisymmetric combination of  $a_1$  hybrids stays nonbonding. There are two electrons, so the  $\sigma$  MO is the only one filled of the



three. The simplest way to view the distortion leading to a structure like that in 17.42 is to gradually move the metal atoms closer together (and thereby increase their interaction) and, at the same time, move the hydrogen atom off the M–M axis. The result is shown in 17.44 for the pertinent orbitals. The unoccupied out-of-phase  $z^2$  orbital combination (metal–hydrogen nonbonding) goes to higher energy as the metal atoms increase their overlap, and the corresponding bonding combination experiences stabilization. At the same time, however, the hydrogen 1s orbital moves toward a node in the  $\text{ML}_5 z^2$  hybrid orbital and overlap is reduced. These two factors operate energetically in opposite directions. This means that the bending motion is rather soft, and a variety of geometries are observed. If the distortion 17.44 proceeds further, the orbital pattern and bonding picture becomes very similar to that of triangular  $\text{H}_3^+$  (Section 5.2) and other “closed” three-center–two-electron species. But, there are other arguments as to why the M–H–M bending potential is so soft and there are electron density portioning schemes that shed doubt on the existence of metal–metal bonding [39]. We should make it clear that the argument for the existence of M–M bonding does not imply a bond order of two-thirds, which must be the case in  $\text{H}_3^+$ , but rather that there is some evidence for an attractive M–M interaction. The W–W distance in 17.42 is indeed quite long—3.34 Å. The W–W distance in the linear  $(\text{CO})_5\text{W}=\text{W}(\text{CO})_4=\text{W}(\text{CO})_5^{2-}$  molecule which has a W–W bond order of one-half, is considerably shorter, 2.79 Å. (The reader should note that the two end  $\text{W}(\text{CO})_5$  units have symmetric and antisymmetric combinations of the  $a_1$  hybrids like that in 17.43. The middle  $\text{W}(\text{CO})_4$  fragment has only an empty  $z^2$  orbital that can interact with the symmetric  $a_1$  combination. The bonding MO is filled and the other two are empty.) As illustrated in 17.44, if M–M bonding is turned on then the axial C–M–H angle should be less than 180°. In 17.42 it is 169.0°, whereas in 17.41 it is 175.8°, close to the expected 180°. Perhaps more persuasive for the existence of some, albeit small, W–W bonding in

**17.42** comes from a series of structures given by **17.45**. The W–W distance varies from 3.37 to 3.12 Å for A=Ge, Si, and C. These molecules also can be considered



to have three-center–two-electron bonds (this is a bit of an over-simplification since the  $sp$  hybrid of the  $AR_2$  group acts in the same way as the  $s$  AO of H but the empty orthogonal  $p$  AO on  $AR_2$  can form a bonding combination to the antisymmetric combination of the two  $yz$  orbitals) and their W–W distances fall within the range given by **17.42**. What is consistent with some W–W bonding in these molecules is that the addition of two electrons makes the W–W distance much longer. It was found to be 4.61 Å when  $AR_2 = PH_2^-$  and 4.84 Å for  $AR_2 = I^-$ . The question of a bond or no bond is almost as old as chemistry itself. Often, these arguments generate more heat than light. We take a perhaps more liberal rather than absolutist view of these matters.

Another problem that may be tackled in the same way as the bridging hydride case is that of a bridging halide that contains  $s$  and  $p$  orbitals. Figure 17.8 shows a diagram, analogous to **17.43** for this particular case. Now, both symmetric and antisymmetric  $z^2$  hybrid combinations of the two  $ML_5$  units find suitable partners on the bridging halide. The diagram has been constructed to emphasize the larger  $\sigma$ - than  $\pi$ -type interactions in this unit. The scheme shown in Figure 17.8 gives rise to a collection of six closely spaced orbitals derived from weak  $\pi$  overlap of the “ $t_{2g}$ ”

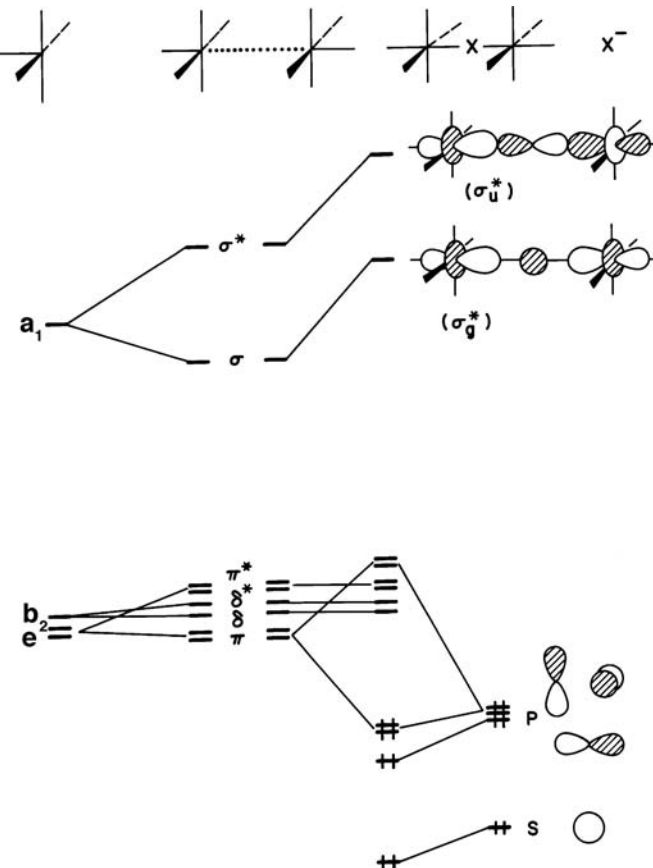
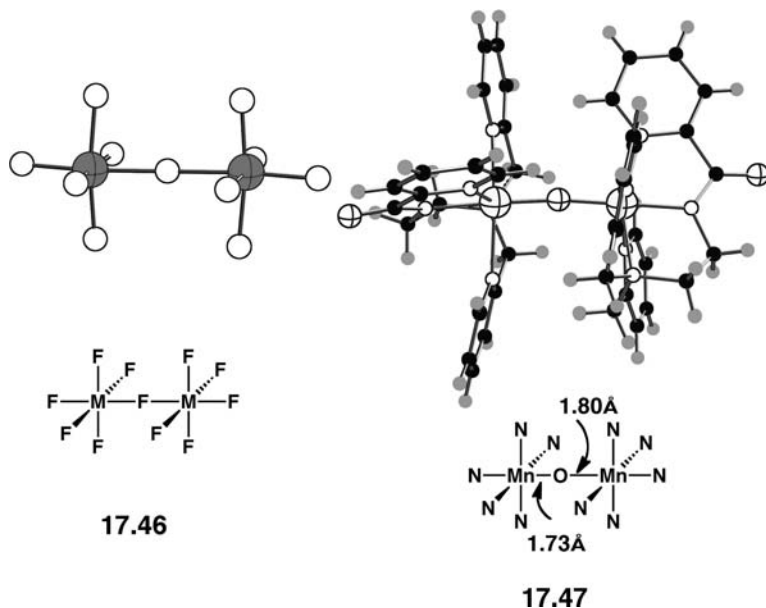


**FIGURE 17.8**

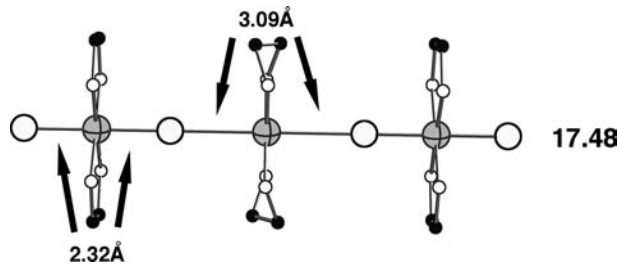
Generation of the level diagram for an  $XM_2L_{10}$  species by allowing the valence  $s$  and  $p$  orbitals of X to interact with the orbitals of the  $M_2L_{10}$  unit.

orbital sets of the two square pyramids with the bridging ligand orbitals. Two  $d^4$  metals, with a total of eight electrons occupying this collection of six orbitals, are then expected to lead to a paramagnetic situation. If the  $\pi$  interaction between the  $\text{ML}_5$  units and the bridging ligand is large, then the situation changes. The result is a much stronger destabilization of the  $(\text{ML}_5)_2$  level labeled  $\pi$  than shown in the middle of Figure 17.8. With a total of eight  $d$  electrons, a sizable HOMO–LUMO gap opens up and a diamagnetic species is formed. This is the case [40] for the molecule  $\text{Cp}(\text{CO})_2\text{Cr}=\text{S}=\text{Cr}(\text{CO})_2\text{Cp}$ , isoelectronic with  $(\text{CO})_5\text{Cr}=\text{S}=\text{Cr}(\text{CO})_5$ . The good  $\pi$  contribution to the Cr–S linkages suggests the description  $\text{Cp}(\text{CO})_2\text{Cr}=\text{S}=\text{Cr}(\text{CO})_2\text{Cp}$  for this molecule.

Sometimes, in these  $\text{XM}_2\text{L}_{10}$  units, the M–X–M bridge is linear; otherwise, it is bent. We are particularly interested in a different type of distortion, the distortion of the symmetric structure to an asymmetric one by slipping the bridging halide towards one of the metal atoms. We have already discussed this type of distortion in the solid state for  $d^0$  metal-oxide compounds where the bridging oxygen atom slips closer to one metal. This is because M–O  $\pi$  bonding is enhanced, see 15.68–15.73. In the following discussion, we concentrate on bridging halides where  $\pi$  bonding is considerably weaker. Examples of this are molecules of the type  $\text{M}_2\text{X}_{11}$ , 17.46.  $\text{Ti}_2\text{F}_{11}^{3-}$  is a



$d^0-d^0$  dimer and the bridging fluorine atom is symmetrically placed with Ti–F distances of 1.97 Å [41]. This is the structure observed for  $\text{Cr}_2\text{F}_{11}^{3-}$  (Cr–F = 1.92 Å) [42], which is high spin  $d^2-d^2$  ( $\delta$ ,  $\delta^*$ , and  $\pi^*$  filled with one electron in each MO in Figure 17.8).  $\text{Cr}_2\text{F}_{11}^{5-}$  (Cr–F = 1.90 Å) [43], high spin  $d^3-d^3$  ( $\delta$ ,  $\delta^*$ ,  $\pi^*$ , and  $\pi$  filled), along with many other metal halide dimers are also symmetrically bridged. Unfortunately,  $\text{Cr}_2\text{F}_{11}^{6-}$  high spin  $d^3-d^4$ , or other isoelectronic  $\text{M}_2\text{X}_{11}$  compounds have not been synthesized. We think that the bridging halide will be asymmetrically bonded to the two metals. A closely related example is given by 17.47 [44]. This is a high spin  $d^3-d^4$  system where the bridging oxygen atom is much closer to the left Mn atom that then might be counted as  $\text{Mn}^{4+}-\text{d}^3$ , so the Mn atom on the right has the +3 oxidation state— $d^4$ . This is one of a number of mixed valence compounds. The orbital occupation here puts one electron in each MO up to and including  $\sigma_g^*$ . This pattern also extends to solid-state polymers. The polymeric analog of 17.46,  $\text{CrF}_5$ , is symmetrically bridged with Cr–F distances of 1.95 Å [45]. On the other hand, there are a number of  $\text{Pt}^{2+}/\text{Pt}^{4+}$  salts that have an alternating structure. One example is shown in 17.48 [46] where there are two ethylenediamine ligands around each Pt.



In Section 15.5, we discussed the structure and bonding in  $d^0$  perovskites that have the formula  $\text{AMO}_3$  and the idealized structure given in 15.61. In 17.48, the orbital occupation corresponds to that in the dimer where there is filling of all MOs through  $\sigma_g^*$ . So, a clue to understanding this particular motion lies in the energetic behavior of the  $\sigma_g^*$  and  $\sigma_u^*$  orbitals of Figure 17.8. It is difficult to predict *a priori* whether  $\sigma_g^*$  or  $\sigma_u^*$  lies higher in energy, but we see that for our purposes it is not important. Let us assume that  $\sigma_g^*$  is lower than  $\sigma_u^*$  at the symmetric geometry, see the middle of Figure 17.9. A Walsh diagram at the extended Hückel level plots here the energies of these two MOs as a function of the Cr-bridging Cl bond distance on the left side, keeping the Cr-Cr distance constant. As the bridging Cl moves to the left or right, the center of symmetry is lost and  $\sigma_g^*$  and  $\sigma_u^*$  orbitals mix together. The top orbital always goes up in energy, and the bottom orbital drops in energy as a result of this orbital intermixing (Figure 17.9). The change in the nature of the  $\sigma_g^*$  and  $\sigma_u^*$  orbitals on distortion is an interesting one [15]. The higher energy orbital at the symmetrical

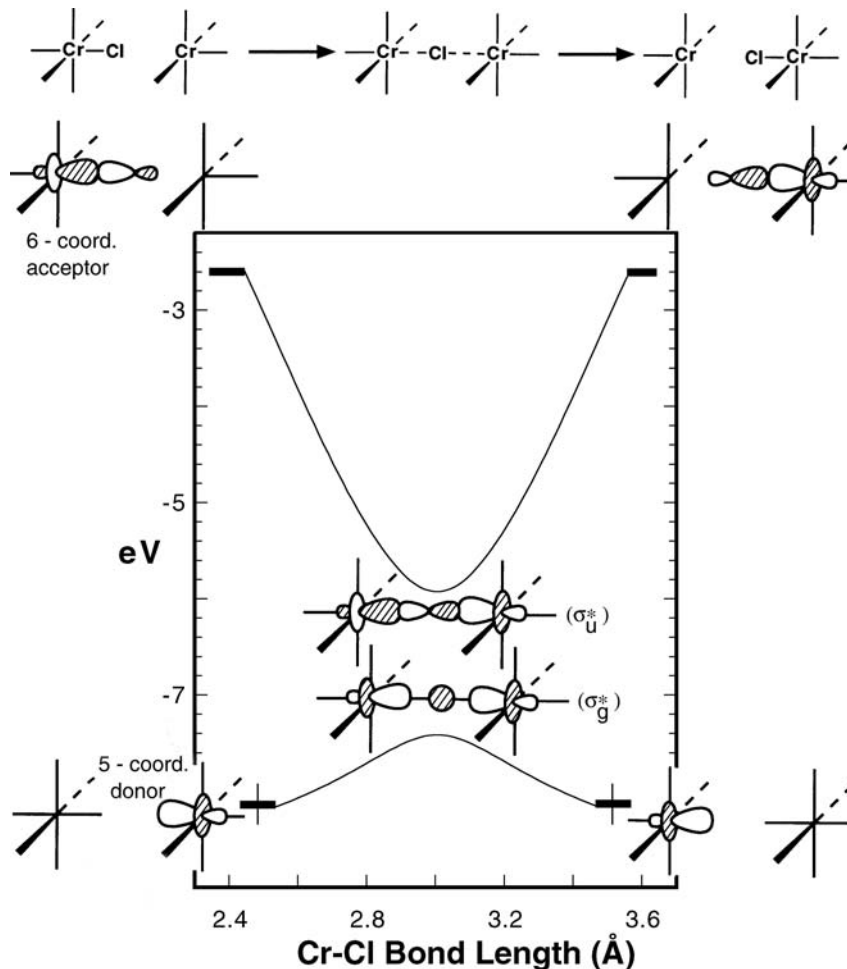
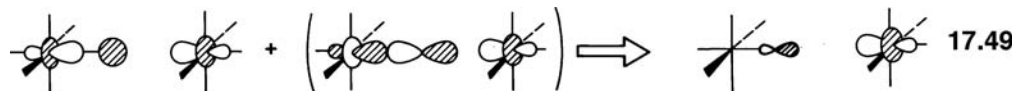


**FIGURE 17.9**

Walsh diagram at the extended Hückel level for the  $\sigma_g^*$  and  $\sigma_u^*$  orbitals in  $\text{Cr}_2\text{Cl}_{11}^{6-}$  as the bridging Cl atom is moved off center.

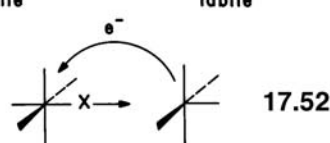
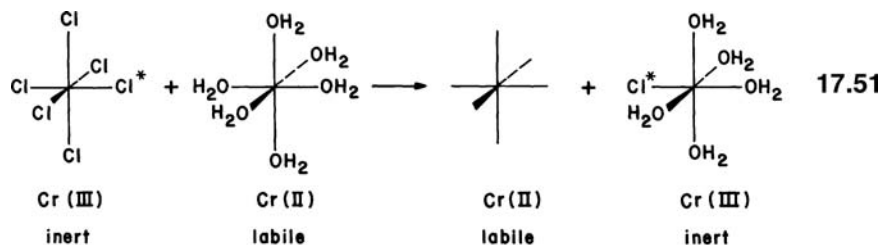
structure ends up as a  $\sigma$  antibonding orbital (one of the  $e_g$  pair) on the now approximately octahedral unit, and the lower energy orbital becomes a pure  $z^2$  hybrid orbital located on the  $\text{ML}_5$  square pyramidal fragment. Figure 17.9 shows this pictorially for both the left and right distortions of the bridging atom or alternatively as the bridging atom is moved from one side of the bridge to the other.

Let us work with the example on the left side of Figure 17.9. As the bridging halide moves toward the metal atom  $\sigma_u^*$  mixes (17.49) into  $\sigma_g^*$  in a way to reduce the antibonding interaction between the metal atom on the left and the bridging atom ( $z^2$  in  $\sigma_u^*$  is bonding to the halide s orbital in  $\sigma_g^*$  and the halide z in  $\sigma_u^*$  is bonding to metal  $z^2$  in  $\sigma_g^*$ ). The resultant orbital cancels amplitude on the left  $\text{ML}_5$



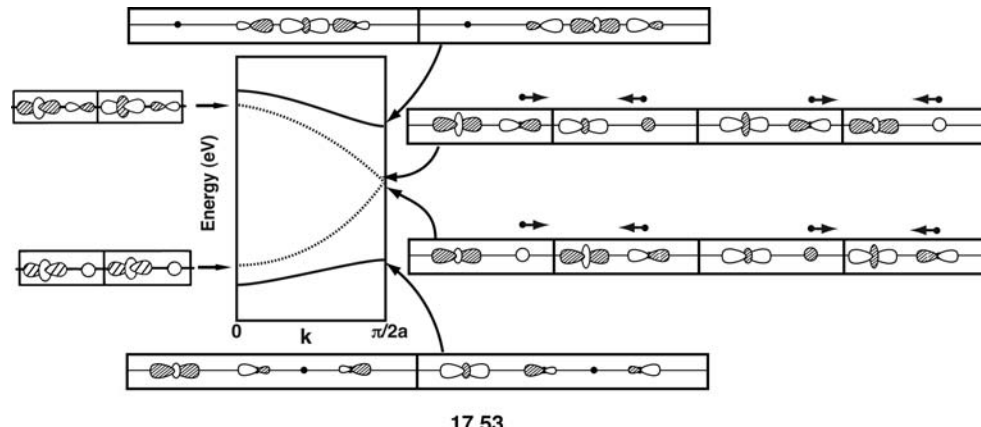
unit and reinforces it on the right  $\text{ML}_5$  unit. Now,  $\sigma_g^*$  must mix into  $\sigma_u^*$  with the opposite phase relationships. The result, shown in 17.50, has reinforced amplitude at the left  $\text{ML}_5$  fragment and canceled amplitude at the right  $\text{ML}_5$ . If  $\sigma_u^*$  lies below  $\sigma_g^*$  in Figure 17.9, exactly the same results are obtained. We shall continue with the ordering of  $\sigma_g^*$  below  $\sigma_u^*$ . With one or two electrons in the  $\sigma_g^*$  orbital, this simple result indicates that such species will be unstable at the symmetrical structure and should distort to the asymmetric arrangement. This is a typical example of a second-order Jahn–Teller distortion. For the case of two electrons, the electronic ground state is  ${}^1\Sigma_g^+$  and the lowest excited singlet state is of symmetry  ${}^1\Sigma_u^+$ . The distortion mode that will lower the energy of the system via a second-order Jahn–Teller mechanism is of symmetry  $\sigma_g \otimes \sigma_u = \sigma_u$ , that is, the asymmetric motion of the central atom. The  $\text{Mn}^{3+}/\text{Mn}^{4+}$  compound in 17.47 with one electron in  $\sigma_g^*$  is one example showing this distortion. With two electrons in the  $\sigma_g^*$  orbital, the classic series of  $\text{Pt}^{2+}/\text{Pt}^{4+}$ -mixed valence compounds are found (17.48). Both of these examples are mixed valence compounds because, as we can see from Figure 17.9 at the asymmetric structure, the  $\sigma_g^*$  electron(s) are located on the five coordinate unit in  $\text{CrCl}_5^{3-}$  (and the analogous orbital for the square planar Pt case).

There are strong links between these mixed valence species and an important class of reactions—namely those arising via electron transfer [48]. The inner sphere redox behavior of the  $\text{Cr}^{2+}/\text{Cr}^{3+}$  system has been studied in great detail. By using labeled chloride ( $\text{Cl}^*$ ), it was cleverly shown that the redox process is associated with atom transfer (17.51) and that this occurs in the opposite direction to electron transfer, perhaps via the inner sphere complex (17.52). In 17.51, we use the terms



labile and inert to describe the kinetic stability of these complexes. Ligand substitution at  $\text{Cr}^{3+}$  is very slow, and so, the identity of the  $\text{CrCl}_5\text{Cl}^{3-}$  ion is preserved in solution. In contrast, ligand substitution at  $\text{Cr}^{2+}$  is fast, and so, the ion is best described as an aquo complex constantly exchanging water molecules with the solvent. After electron transfer, the coordination sphere around the old  $\text{Cr}^{2+}$  ion (new  $\text{Cr}^{3+}$  ion) is frozen since it is now the inert species in solution. The coordination sphere around the old  $\text{Cr}^{3+}$  ion (new  $\text{Cr}^{2+}$  ion) will rapidly be replaced by water. We can use the scheme of Figure 17.9 to see how this takes place in detail. On the left-hand side of the diagram, the electron is totally associated with the square pyramidal five-coordinate reductant,  $\text{Cr}^{2+}$ . As the X atom from the  $\text{Cr}^{3+}$  unit moves to the center of the bridge (a transition state from our discussion above), the orbital containing this electron has equal weight from both metal atoms. Technically, “half an electron” has been transferred at this point. As the bridging atom moves past the symmetric structure to the right-hand side of the bridge, then the electron transfer is now complete and  $\text{Cr}^{2+}$  and  $\text{Cr}^{3+}$  species are again produced. Thus, the electron transfer has proceeded in a smooth way initiated by the atom transfer. We stress that not all redox processes are this simple (many proceed by the outer sphere route where no species such as **17.52** occurs), but within the context of this electronic model, one can think about ways that the other ligands around the metal and the transferred halogen can perturb the rate of the reaction.

As we mentioned above, the  $\text{Pt}^{2+}/\text{Pt}^{4+}$  mixed valence compounds are in fact found as infinite chains. So, instead of the two orbitals,  $\sigma_g^*$  and  $\sigma_u^*$  of Figure 17.8, we have an energy band [49] shown in Figure 15.11. At the symmetric geometry, the  $z^2$  band is just half-full, signaling a Peierls-type distortion. The distortion exhibited in **17.48** requires that the unit cell be doubled so the  $z^2$  band is folded back as shown by the dotted line for the  $e(k)$  versus  $k$  plot in **17.53**.



17.53

The  $k = 0$  and  $\pi/2a$  solutions are explicitly shown. At  $k = 0$ , the very bottom of the  $z^2$  band corresponds to the  $\sigma_g^*$  type of orbital with a phase factor of +1 between adjacent cells, and the top of the  $z^2$  band at  $k = 0$  is the corresponding  $\sigma_u^*$  combination. The  $k = \pi/2a$  solutions have the form

$$\psi \propto (\chi_1 - \phi_1) + (\chi_2 + \lambda_2) - (\chi_3 - \phi_3) - (\chi_4 + \lambda_4) + (\chi_5 - \phi_5) + (\chi_6 + \lambda_6) + \dots \quad (17.1)$$

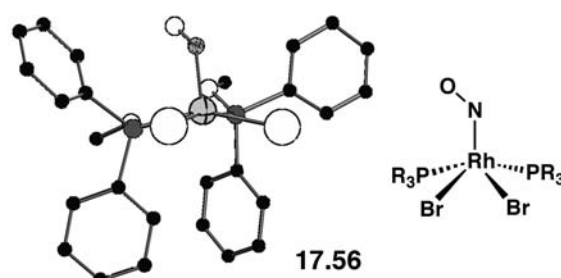
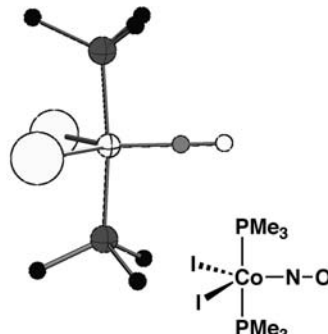
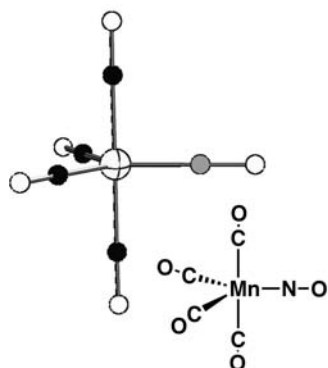
and

$$\psi' \propto (\chi_1 + \lambda_1) - (\chi_2 - \phi_2) - (\chi_3 + \lambda_3) + (\chi_4 - \phi_4) + (\chi_5 + \lambda_5) - (\chi_6 - \phi_6) + \dots \quad (17.2)$$

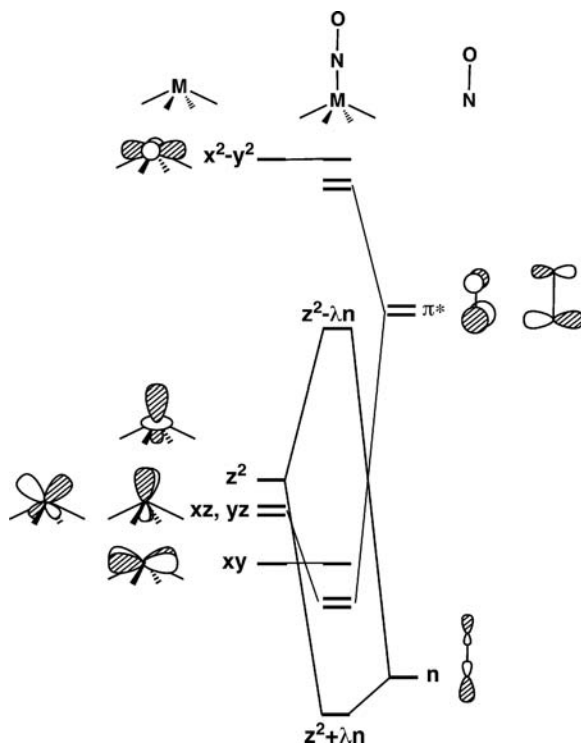
where  $\chi$ ,  $\lambda$ , and  $\phi$  represent the Pt  $z^2$ , Cl s, and Cl z contributions, respectively, and the subscripts refer to the numbering in the primitive unit cell. Just as the pair of orbitals of Figure 17.9 increased their separation as the bridge is made asymmetric, so the band of the infinite system splits into two on such a distortion. The upper and lower bands mix with each other, stabilizing the latter and destabilizing the former. The phases in **17.53** have been chosen so that the upper band at  $k = \pi/2a$  mixes in phase into the lower one. By adding equation 17.2 into equation 17.1, one can easily verify that the  $z^2$  coefficients at unit cell 1, 3, 5, . . . are reinforced and those at unit cell 2, 4, 6, . . . cancel. The lower band, of course, also mixes into the upper one, now out of phase. Subtracting equation 17.1 from equation 17.2 cancels the  $z^2$  coefficients at unit cell 1, 3, 5, . . . and increases them at 2, 4, 6, . . . The reader can easily derive the crystal orbitals at the  $k = 0$  point. The lower band has become the filled  $z^2$  combination on the Pt atoms that have long distances to the bridging Cl atoms. The upper band becomes localized on the Pt atoms that have the short Pt–Cl distance. Note that the stabilization results in a square planar environment for low spin  $d^8$   $\text{Pt}^{2+}$  and an octahedral environment for the low spin  $d^6$   $\text{Pt}^{4+}$  species, two typical geometries for these oxidation states. The application of pressure [50] causes the chains to become compressed. The Pt–Cl distances then become closer to each other, and the conductivity greatly rises.

## 17.5 PENTACOORDINATE NITROSYLS

Coordinated NO is found in two basic geometries in transition metal complexes, linear and bent, exemplified by the molecules **17.54**–**17.56** [51–53], as well as structures intermediate between the two. We shall concentrate on five-coordinate

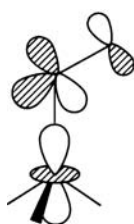


examples that may have a square pyramidal, trigonal bipyramidal, or an intermediate coordination environment. We are interested in understanding in broad terms when the MNO unit is linear and when it is bent [54,55]. We begin with a square pyramidal  $\text{ML}_4\text{NO}$  complex containing an apical nitrosyl group. Figure 17.10 shows the assembly of such a diagram in the obvious way, using the important frontier orbitals ( $n$ ,  $\pi^*$ ) of the

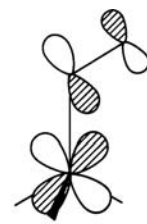
**FIGURE 17.10**

Construction of the important valence orbitals in a  $\text{ML}_5(\text{NO})$  molecule.

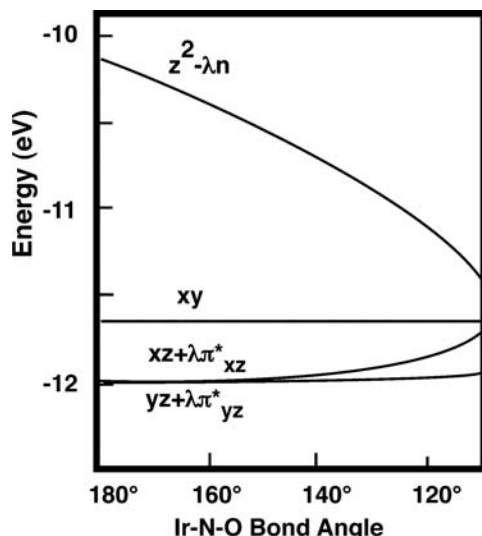
NO. On the left of Figure 17.10 are the orbitals of a square pyramidal ( $C_{4v}$ )  $\text{ML}_4$  unit. There are a couple of ways to derive these orbitals. One could start with the  $d$  orbitals of the square plane—see Figure 16.1 or the left side of Figure 16.4. Making the four ligands pyramidal leaves the  $xy$  orbital unchanged in energy. It stays totally nonbonding. The  $x^2 - y^2$  orbital is stabilized somewhat since some overlap to the ligands is lost. This also occurs in  $z^2$  except that metal  $s$  and  $z$  hybridize with  $z^2$  so that the orbital points out away from the ligands. The mechanism for this change is identical to that for pyramidalization in  $\text{AH}_3$  (Chapter 6). Finally,  $xz$  and  $yz$  are destabilized and somewhat hybridized. A close comparison of the  $\text{ML}_4$  orbitals and those of the  $C_{4v}$   $\text{ML}_5$  unit on the right side of Figure 17.3 shows that there is only one difference. Removal of the apical ligand in  $\text{ML}_5$  stabilizes the  $z^2$  orbital greatly and rehybridization occurs so that it is pointed toward the missing apical ligand. The  $z^2$  orbital is crucial for understanding the bending of NO. It finds a strong interaction with the lone-pair orbital of NO that has been labeled  $n$  on the right side of Figure 17.10. Bonding,  $z^2+\lambda n$ , and antibonding,  $z^2-\lambda n$ , MOs are created. Likewise,  $xz$  and  $yz$  interact with the  $\pi^*$  levels of NO to form bonding,  $xz/yz + \lambda\pi^*$ , and antibonding,  $xz/yz - \lambda\pi^*$ , combinations. When filling this manifold with electrons, we need to keep track, not only of the number of  $d$  electrons but in addition those which lie in the nitrosyl  $\pi^*$  levels. The sum of the two ( $m$ ) is given by a notation  $\{\text{MNO}\}^m$ . Figure 17.11 shows how the energy of these levels change as the MNO angle decreases from  $180^\circ$ . The  $z^2 - \lambda n$  level is stabilized quite dramatically. As shown in 17.57, there are two effects behind this.



17.57

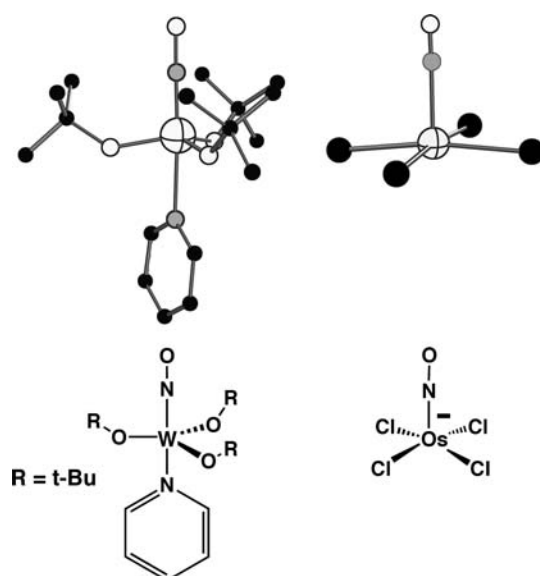


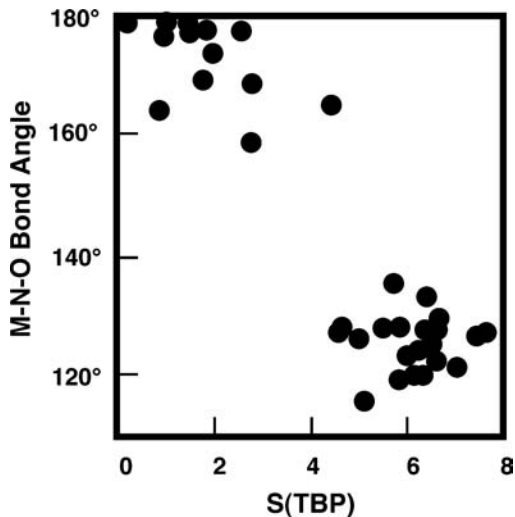
17.58

**FIGURE 17.11**

Energetic behavior of the metal  $d$  and nitrosyl  $\pi^*$  levels on bending the M–N–O unit. Adapted from Reference [54], the extended Hückel calculation refers to an iridium nitrosyl species.

The antibonding interaction with the nitrosyl lone pair ( $n$ ) is reduced on bending since now M, N, and O are not collinear. Using geometric perturbation theory, this loss of overlap between  $z^2$  and  $n$  creates a first-order change in energy that is negative. Concurrently, a bonding interaction between  $z^2$  and the nitrosyl  $\pi^*$  orbital is turned on. Within a perturbation theory construct, there is a second-order energy correction between  $z^2 - \lambda n$  and primarily  $xz - \lambda \pi^*_{xz}$  along with  $xz + \lambda \pi^*_{xz}$ . The interaction of one component of the nitrosyl  $\pi^*$  orbitals ( $\pi^*_{xz}$ ) with  $xz$  decreases on bending **17.58**, and  $xz + \lambda \pi^*_{xz}$  becomes less M–L  $\pi$  bonding and rises in energy, that is, there is a positive first-order energy correction. In a simple way, then, Figure 17.11 indicates two opposing factors influencing bending. Occupation of  $xz + \lambda \pi^*_{xz}$  favors linearity but the occupation of  $z^2 - \lambda n$  favors bending. There are several {MNO}<sup>4</sup> molecules. One example is given by **17.59** [56]. Here, the



**FIGURE 17.12**

Plot of the M–N–O bond angle versus the symmetry measure for a trigonal bipyramidal,  $S(\text{TBP})$  in molecules with a  $\{\text{MNO}\}^8$  electron configuration. The plot has been adapted from Reference [59].

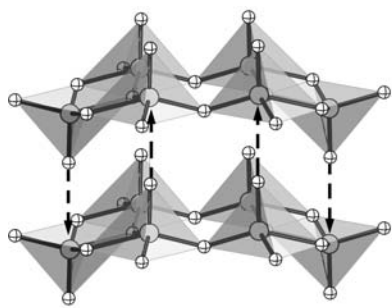
$xz/yz + \lambda\pi^*$  MOs are filled and  $xy$  is empty. All of these molecules have linear M–N–O bond angles as expected from Figure 17.11. For  $\{\text{MNO}\}^6$  systems where  $xy$  is the HOMO, the approach also definitely predicts a linear geometry. There are a number of molecules that confirm this. One example is provided by **17.60** [57]. Notice that **17.59** is a trigonal bipyramidal and **17.60** is a square pyramid in agreement with the Walsh diagram given in Figure 17.4. The placement of the excellent  $\pi$  acceptor ligand, NO, in the axial and apical positions, respectively, allows for maximal stabilization (note that the equatorial groups in **17.59** are bent away from the NO group so as to hybridize the  $xz/yz$  orbitals towards NO  $\pi^*$ ). For the  $\{\text{MNO}\}^8$  configuration  $z^2 - \lambda n$  is filled and inspection of Figure 17.11 suggests that bending should occur for the square pyramid. An example is provided by **17.56**. The M–N–O bending potential is drastically reduced, and linear nitrosyl molecules are quite common (see **17.54** and **17.55**) by changing the nature of the coordination geometry to the trigonal bipyramidal, which is beyond the scope of our discussion here [54]. Recall that the Berry pseudorotation path for the conversion of the trigonal bipyramidal to square pyramid is a soft potential for this electron count. There is way to quantify how far away a molecule is distorted from a trigonal bipyramidal (toward a square pyramid)[58]. This is called the symmetry measure,  $S(\text{TBP})$ , for a trigonal bipyramidal. A plot [59] of the M–N–O bond angle versus  $S(\text{TBP})$  for  $\{\text{MNO}\}^8$  molecules is given in Figure 17.12.  $S(\text{TBP}) = 0$  defines a perfect trigonal bipyramidal; however, any structure with  $S(\text{TBP}) \leq \sim 3$  is close to one. When  $S(\text{TBP}) \geq \sim 5$ , then it is close to a square pyramid. Figure 17.12 shows that molecules with a trigonal bipyramidal geometry have linear M–N–O bond angles or close to it, whereas square pyramids are strongly bent.

## 17.6 SQUARE PYRAMIDS IN THE SOLID STATE

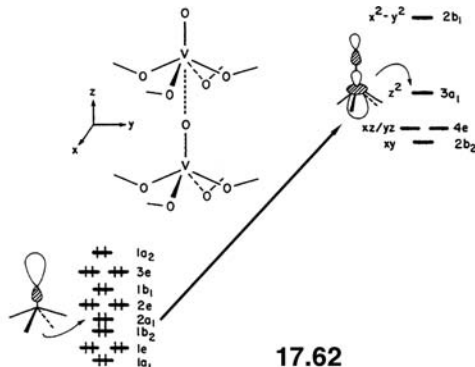
By far the most common coordination geometry in the solid state is the octahedron followed perhaps by the tetrahedron. Trigonal bipyramids are quite rare, but there are a significant number of materials that are built from square pyramids. In this section, we shall look at three compounds with different electron counts.

$\text{V}_2\text{O}_5$  is a solid-state compound with many catalytic and electronic uses including an electrode material for rechargeable lithium batteries. Its structure [60] is

somewhat complicated and has been described in a number of ways. The most useful perspective is that it consists of rows of edge-shared square pyramids, 17.61, which form a layered structure. There are double rows of “up” and “down” pointed



17.61



17.62

pyramids, and the registry of the layers is such that the apical oxygen from one layer is directly above or below the vanadium atom in an adjacent layer. The dashed arrows show several of these contacts in 17.61. The layers in graphite (Section 13.4) are held together by van-der-Waals forces, and it is easy to intercalate materials between the layers.  $V_2O_5$  also can be intercalated by, for example, Li, Na, or K that form a number of vanadium bronzes with varying degrees of electrical conductivity. The interest here is whether or not there remains some covalent bonding between the vanadium atoms in one layer and apical oxygen atoms from an adjacent layer. The distances are 2.79 Å, which are very long. The V–O distances to the basal oxygen atoms range from 1.78 to 2.02 Å, while that to the apical oxygen is even shorter, 1.58 Å. If any covalent interlayer interaction exists, the most likely source would be from the outer-pointing, filled hybrid on the apical oxygen atoms, and the empty  $z^2$  hybrid on vanadium. This is shown in 17.62. The DOS [61] for  $V_2O_5$  where the layers are separated by a very long 6.00 Å is shown in Figure 17.13a. The states from about –16.1 eV to the Fermi

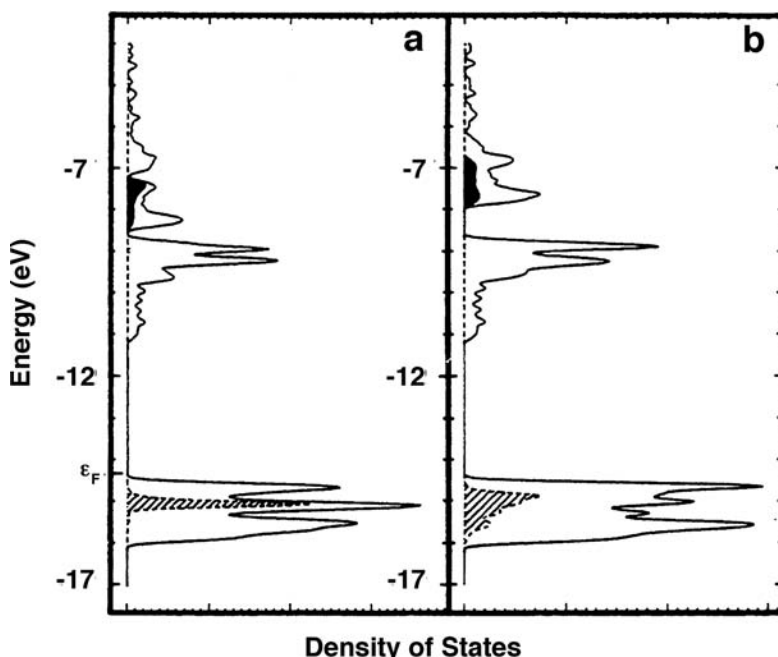
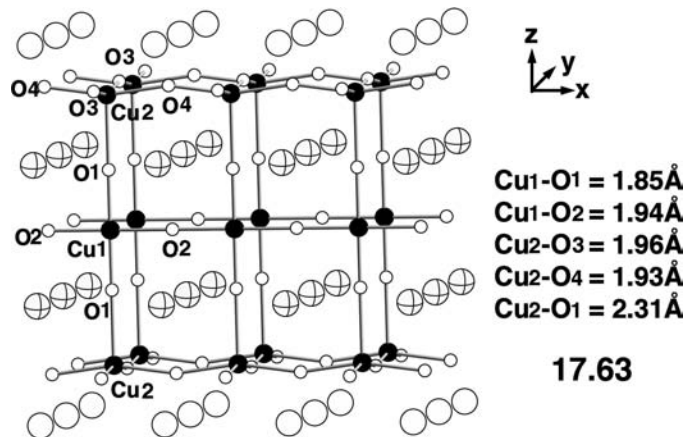


FIGURE 17.13

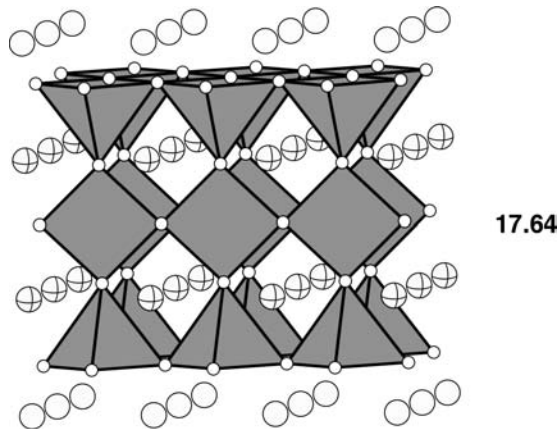
DOS for  $V_2O_5$  when the distance between the vanadium atoms of one layer and the apical oxygen atoms in an adjacent one is 6.00 Å in (a) and the experimental distance, 2.79 Å, in (b). The projection of the apical oxygen lone pair,  $2a_1$ , in 17.62 is given by the shaded area. The vanadium  $z^2$  projection is shown by the solid area. The Fermi level is indicated by  $\epsilon_F$ . The DOS plots are taken from Reference [61].

level at  $-14.4\text{ eV}$  correspond to the oxygen  $p$  AO region. The projection of the apical oxygen  $z$  AO is given by the shaded area. The narrow peak is consistent with its nonbonding nature. The region from  $-11.2$  to  $-8.5\text{ eV}$  consists primarily of vanadium  $xy$ ,  $xz$ , and  $yz$  (see 17.62). The  $z^2$  contribution is found in the dark area from about  $-7.2$  to  $-8.5\text{ eV}$ . Its dispersion is due to small mixing with the basal oxygen atoms. The  $x^2 - y^2$  levels lie above  $-7.1\text{ eV}$  and are greatly dispersed by  $\sigma$  bonding to oxygen. In Figure 17.13b, the interlayer distance was decreased to the experimental value of  $2.79\text{ \AA}$ . The states with oxygen  $z$  character have been stabilized, and there is much greater dispersion. The majority of the vanadium  $z^2$  levels are destabilized. Both of these facets are consistent with the establishment of covalent bonding between vanadium and oxygen. At the extended Hückel level [61], 0.05 electrons were transferred from the apical oxygen to vanadium as a result of this interaction. From an energetic perspective, this is worth  $4.5\text{ kcal/mol}$  per vanadium atom. Clearly, this is not a typical V–O single  $\sigma$  bond. One can use the Mullikan overlap population as a gauge. Again, at the extended Hückel level, the V–O basal overlap population was calculated to be 0.389, whereas the interlayer V–O population was 0.064. Coincidentally, the V–O overlap population to the apical oxygens within the layer was found to be 0.880. This large value is consistent with the strong  $\pi$  overlap that exists between oxygen  $x$  and  $y$  with vanadium  $xz$  and  $yz$ .

In 1988, Bednorz and Müller were awarded the Nobel Prize in Chemistry for the discovery of superconductivity in  $\text{La}_{2-x}\text{Sr}_x\text{CuO}_4$  with a  $T_c$  at  $35\text{ K}$  [62]. We have discussed the electronic structure of this material in Section 16.5. Chu and coworkers prepared a related compound,  $\text{YBa}_2\text{Cu}_3\text{O}_7$ , with a  $T_c = 92\text{ K}$  [63]. The structure of this compound is shown in 17.63. The environment around CuI is clearly a corner-shared square plane that runs along the  $x$ -axis to form a one-dimensional chain. On either side of this chain in the  $z$  direction lies a puckered



two-dimensional net of  $\text{CuO}_2$ . Thus, one has a layer of  $\text{Cu}_3\text{O}_7^{7-}$ , which is sandwiched on the top and bottom by an  $\text{Y}^{3+}$  layer, and  $\text{Ba}^{2+}$  cations are stuffed within the copper-oxygen layers. The  $\text{CuO}_2$  nets are connected to the square planes via O1. Thus, the Cu2 environment may be regarded as square pyramidal. The basal O–Cu2–O angles were  $164.4^\circ$ , or another way of putting this is that the Cu2 atoms lie  $0.32\text{ \AA}$  out of the O3/O4 plane. An alternative polyhedral view of this structure is then given in 17.64. How then should one view the copper oxidation states in the  $\text{Cu}_3\text{O}_7^{7-}$  layers? In principle, there are two possibilities: (1) three  $\text{Cu}^{2.33+}$  ions or (2) two  $\text{Cu}^{2+}$  and one  $\text{Cu}^{3+}$  ions. In other words, are we dealing with a delocalized or



a mixed valence case? If the latter is true, then one might expect that the CuI atoms in the chains are +3,  $d^8$ , so the copper  $d$  bands are filled up to the  $x^2 - z^2$  one (see the coordinate system in 17.63). The Cu2 atoms in the square pyramids then are  $d^9$ , so the two  $x^2 - y^2$  bands are exactly half-full (for an antiferromagnetic ordering) and present a situation exactly like that for the  $\text{CuO}_2^{2-}$  plane in Section 16.5. Extended Hückel calculations on  $\text{YBa}_2\text{Cu}_3\text{O}_7$  have shown [64] that the latter atomic distribution is indeed appropriate for the equilibrium structure at rest. Density of states plots for the energy region around the Fermi level is presented in Figure 17.14.

The left side shows the projection of the Cu2  $x^2 - y^2$  states where the dashed line corresponds to the copper contribution and the dotted line to the oxygen contribution. The panel on the right side shows the projection of the CuI  $x^2 - z^2$  states. On average, the Cu2  $x^2 - y^2$  bands lie lower in energy than CuI  $x^2 - z^2$ . The principal reason for this is that since the Cu2 atoms lie out of the plane of the surrounding four oxygen atoms in contrast to the situation for the CuI atoms, the  $\sigma$  overlap of the oxygen AOs to Cu2  $x^2 - y^2$  is diminished. As a result the Fermi level,  $\varepsilon_F$ , in Figure 17.14 lies right in the middle of the Cu2  $x^2 - y^2$  states. So, why should this material become metallic and superconducting when the planar  $\text{CuO}_2^{2-}$

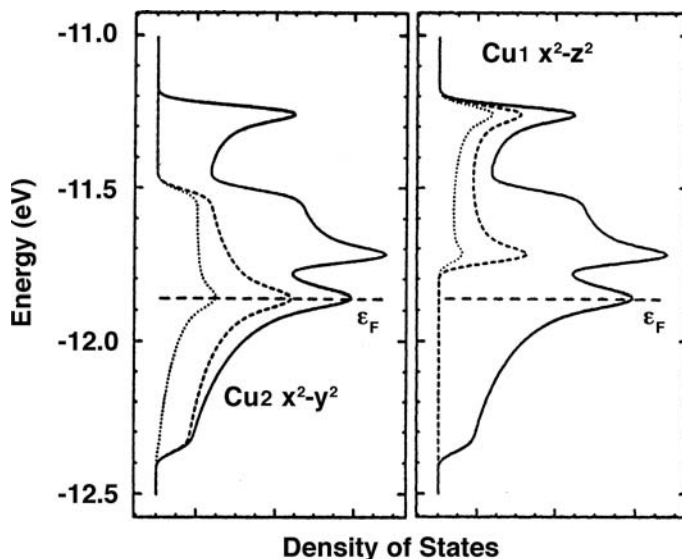
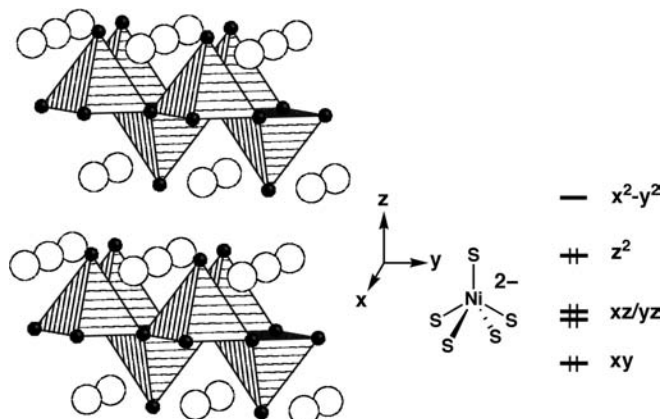


**FIGURE 17.14**

The density of states for the region around the Fermi level,  $\varepsilon_F$ , in  $\text{YBa}_2\text{Cu}_3\text{O}_7$ . The plots show the projection of copper and oxygen character by the dashed and dotted lines, respectively. The plots were adapted from Reference [64].

family needed to be doped with electrons or holes to achieve this condition (see Figure 16.5)? Notice that distance of O1 to Cu1 is very short while that to Cu2 is quite long. One can easily show that moving the O1 atoms along the z axis bringing them closer to the Cu2 atoms will cause the  $x^2 - z^2$  states at Cu1 to move to lower energy and become occupied and, thus, the  $x^2 - y^2$  Cu2 states become emptied. One could also consider vibrations of the O1 atoms in the x or y directions to create the same electronic situation. If the Cu2 atoms are displaced into the plane of the surrounding oxygen atoms, then the Cu2  $x^2 - y^2$  states will be raised in energy and again the electronic state moves towards that of the delocalized type for the three copper atoms. The dynamic features of the family of compounds related to  $\text{YBa}_2\text{Cu}_3\text{O}_7$  and its impact on superconductivity from a chemist's perspective may be found elsewhere [65].

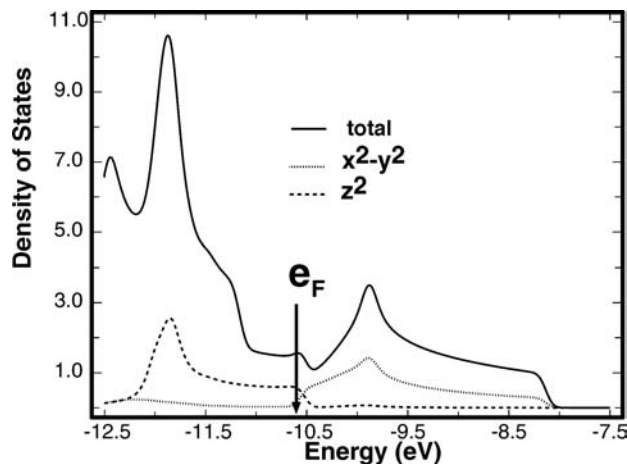
The structure [66] of  $\text{BaNiS}_2$  is very similar to that presented for  $\text{V}_2\text{O}_5$  except, as shown in 17.65, that there are Ba cations between the  $\text{NiS}_2$  layers and consequently there is no interlayer bonding present in this material. The  $\text{NiS}_2^{2-}$



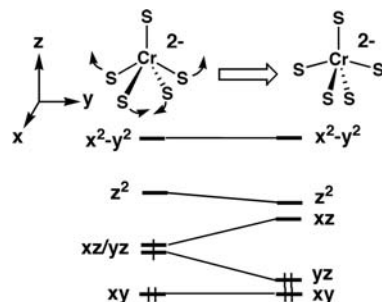
17.65

17.66

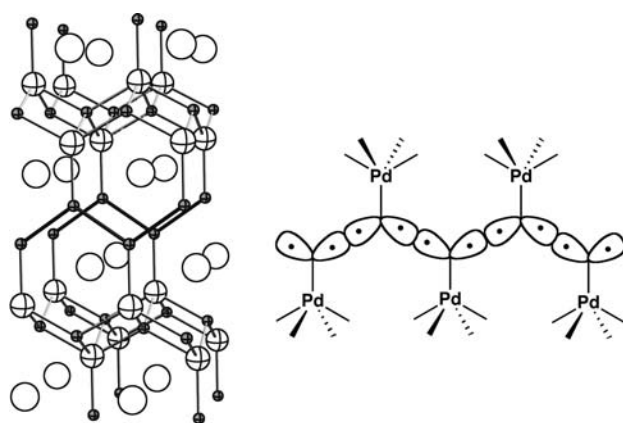
layer then makes the formal oxidation state of nickel to be +2, which is  $d^8$  in contrast to the  $d^0$  electron count in  $\text{V}_2\text{O}_5$ . There are some important structural differences, as well. The  $d$  AO splitting for a square pyramid, taken from the right side of Figure 17.4, is reproduced in 17.66. Since  $xz$ ,  $yz$ , and  $z^2$  are filled, the Ni–S basal and apical distances are nearly equal, 2.34 and 2.32 Å, respectively. The apical–Ni–basal angle is 109.1° (in  $\text{V}_2\text{O}_5$ , the average apical–V–basal angle is 106.6°). With the electronic formulation in 17.66, one might think that  $\text{BaNiS}_2$  is a semiconductor. The  $x^2 - y^2$  and  $z^2$  bands will spread out in a typical two-dimensional manner; the issue is to what extent this will occur. In actual fact,  $\text{BaNiS}_2$  is a metal [66]. The density of states around the Ni  $x^2 - y^2$  and  $z^2$  region is presented in Figure 17.15. The dispersion associated with the  $x^2 - y^2$  band was discussed in Chapter 16; see 16.49–16.51. The dispersion for  $z^2$  comes about in a very similar manner and is primarily due to differential  $\pi$  overlap with the basal sulfur atoms. The important point is that at the extended Hückel level, the two bands cross. This also occurs at much higher levels of theory [67]. Within this context, the metallic character of  $\text{BaNiS}_2$  is understandable. One might think that  $\text{BaCrS}_2$  would be metallic because of the low,  $d^4$  electron count at Cr. This is not the case [68]. With the  $d$  AO splitting pattern in 17.66, one might expect that the  $xz/yz$  set would be half filled leading to a metallic state as illustrated on the left side of 17.67. This is not the case. The structure of  $\text{BaCrS}_2$  is distorted a good bit

**FIGURE 17.15**

The density of states around the Fermi level,  $e_F$ , for  $\text{BaNiS}_2$  at the extended Hückel level.

**17.67**

from that in  $\text{BaNiS}_2$ . One basal S–Cr–S opens up from  $141.6^\circ$  to  $164.3^\circ$  while the other angle narrows to  $114.1^\circ$ . In other words, the coordination geometry around Cr is very close to that of a trigonal bipyramidal. Drawing from the Walsh diagram in Figure 17.4, 17.67 shows the correlation of orbitals going from the  $\text{BaNiS}_2$  structure to the  $\text{BaCrS}_2$  one. A gap is opened between the  $xy/yz$  set of orbitals and the  $xz$  states. As a result,  $\text{BaCrS}_2$  is a semiconductor [68]. The structure of  $\text{BaCoS}_2$  [69] is not much different from  $\text{BaNiS}_2$ . On the other hand an interesting structural variation is offered in  $\text{BaPdAs}_2$  [70], 17.68, with two less electrons. The basic

**17.68****17.69**

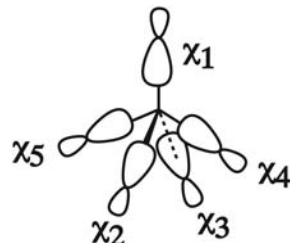
structure of  $\text{BaNiS}_2$  is kept except that the registry of the layers with respect to each other is shifted so that As–As bonds are formed. The As–As bond length in these zigzag chains is  $2.66\text{\AA}$  compared to  $2.52\text{\AA}$  for elemental As. An easy way to view their formation starts with  $\text{BaNiS}_2$ . The apical S lone pairs for this compound are filled. Of the three lone pairs, let us take the  $a_1$  combination (corresponding to the  $2a_1$  in 17.62) and one member of the  $e$  set ( $a p$  AO in the plane of what will become the As–As  $\sigma$  bonds) to form two hybrid orbitals at each apical As atom. In  $\text{BaPdAs}_2$ , consider that the two electrons removed come from these hybrids. After all, As is less electronegative than S, so these hybrids will lie at higher energy. As shown by 17.69, the apical As–As  $\sigma$  bonds then are constructed from coupling the radical pairs. There are a number of compounds with one less electron; an example is  $\text{LnNiGe}_2$  [71]. The situation here is not so clear cut; however, the majority of the electrons removed come from the  $\pi^*$  states associated with the apical Ge atoms (perpendicular to the plane in 17.69).

---

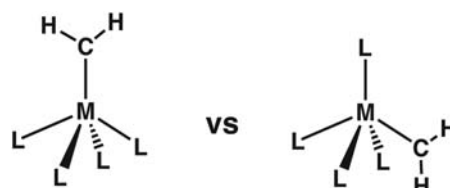
## PROBLEMS

---

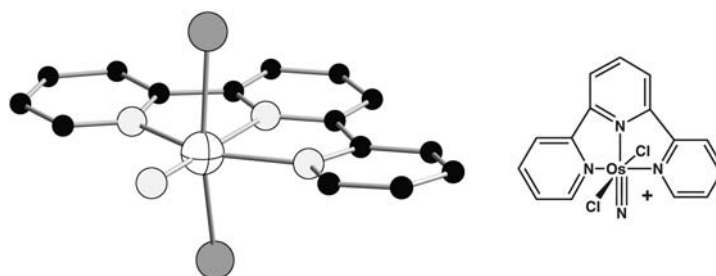
- 17.1.** a. Using  $x_1 - x_5$  form SALCs at the square-pyramidal geometry shown below.  
 b. Interact the SALCS with the  $s$ ,  $p$ , and  $d$  AOs of a transition metal. Draw the resultant orbitals.



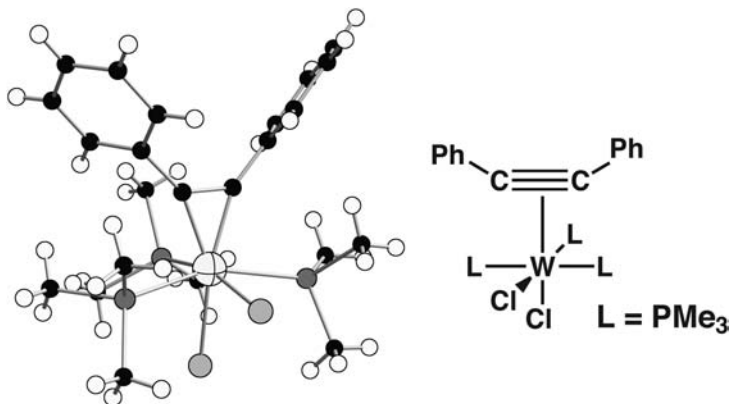
- 17.2.** A  $d^8$  square pyramidal  $(\text{CH}_2)\text{ML}_4$  complex could have the carbene positioned in the apical or basal site. Determine which would be more favorable.



- 17.3.** Pipes et al. [72] reported the preparation and structure of an unusual transition metal nitride. How many electrons are associated with the metal? What would be the level ordering and electron occupation for the Os  $d$  orbitals in this molecule?

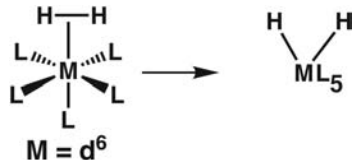


- 17.4.** Acetylene complexes are fairly common; however, Nielson et al. [73] reported the structure of a  $d^4$  tungsten complex, see below. Construct the important valence orbitals for this compound and indicate the orbital occupation.

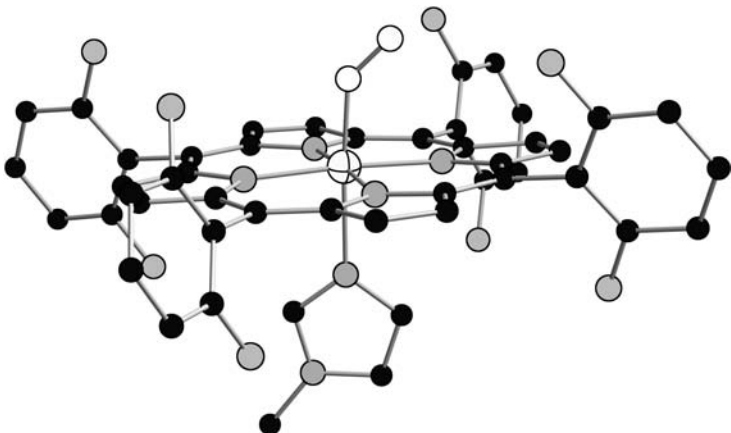


- 17.5.** We introduced the bonding for dihydrogen complexes in Chapter 15. In general when the ligands L are good  $\pi$ -acceptors and/or the metal M exists in a high oxidation state, then these complexes can be observed. On the other hand, if these conditions are not met then transition metal dihydrides are found.

- Describe why this occurs.
- Sometimes one can initially observe dihydrogen complexes that then rearrange into dihydride products. What is the activation barrier that interconnects them?



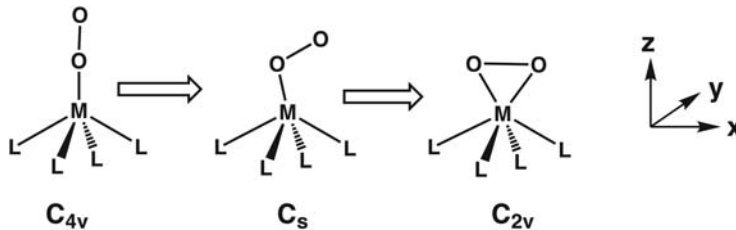
- 17.6.** Section 17.5 discusses the bending in metal nitrosyl complexes. In this problem, we are going to go one step further with M–O<sub>2</sub> complexes. The heme adducts of O<sub>2</sub> involve a low spin Fe–porphyrin, a model of which is shown below (in actual fact this is a nitrosyl complex).



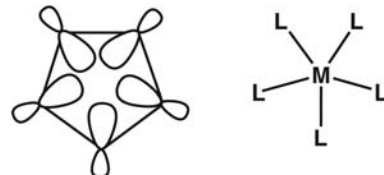
- Using Figures 17.10 and 17.11 as models, determine whether or not the O<sub>2</sub> complex should be bent. When O<sub>2</sub> initially reacts, the iron porphyrin is high spin and, of course so is O<sub>2</sub>. What should be the Fe–O–O bond angle in the initial adduct. You need to figure out what happens to  $\pi^* - xz$  and  $\pi^* - yz$ , and add these curves

to Figure 17.11. Perhaps the easiest way to figure out what MOs are occupied is to count the  $O_2$  ligand as being iso-electronic to CO or  $NO^+$ , that is, as  $O_2^{2+}$ .

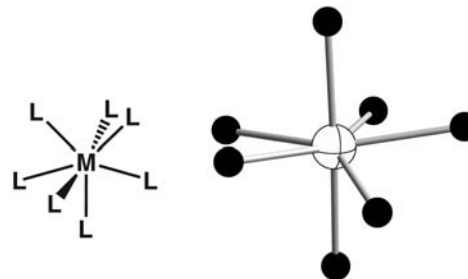
- b. If the  $M—O—O$  bending motion is continued, eventually the complex becomes an  $(\eta^2-O_2)ML_4$  complex as shown below. Carefully work out the metal d, as well as,  $\pi^* - xz$  and  $\pi^* - yz$  MOs for the  $C_{4v}$  and  $C_{2v}$  geometries. Then, draw a Walsh diagram for the reaction path from  $C_{4v}$  to  $C_s$  to  $C_{2v}$ . What electron counts favor the  $(\eta^2-O_2)ML_4$  structure?



- 17.7. a. Determine the five SALCs for five generic ligands arranged in a pentagonal planar manner. Use these to interact with a transition metal's s, d, and p AOs.



- b. Form the MOs for a pentagonal bipyramidal by interacting the orbitals in (a) with capping ligands. This is a common geometry for seven coordinate structures. An example provided below is from Reference 7 of Chapter 21. What other metal  $d^n$  electron counts should be stable at this geometry?



## REFERENCES

1. M. Elian and R. Hoffmann, *Inorg. Chem.*, **14**, 1058 (1975).
2. R. Hoffmann, *Science*, **211**, 995 (1981).
3. T. A. Albright, *Tetrahedron*, **38**, 1339 (1982).
4. D. E. Sherwood and M. B. Hall, *Inorg. Chem.*, **22**, 93 (1983).
5. A. R. Rossi and R. Hoffmann, *Inorg. Chem.*, **14**, 365 (1975).
6. B. Roessler, S. Kleinhenz, and K. Seppelt, *Chem. Commun.*, 1039 (2000).
7. S. Groysman, I. Goldberg, M. Kol, and Z. Goldschmidt, *Oranometallics*, **22**, 3793 (2003).
8. C. J. Piersol, R. D. Profleet, P. E. Fanwick, and I. P. Rothwell, *Polyhedron*, **12**, 1779 (1993).
9. M. J. Paterson, P. A. Hunt, M. A. Robb, and O. Takahashi, *J. Phys. Chem. A*, **106**, 10494 (2002).

10. M. F. Perutz, H. Muirhead, J. M. Cox, and L. C. G. Goaman, *Nature*, **219**, 131 (1968).
11. A. J. Yencha, S. Canton, J. D. Bozek, and N. Berrh, *Report Number LBNL/ALS-43727*, July 1, 2001.
12. J. L. Hubbard and D. L. Lichtenberger, *J. Chem. Phys.*, **76**, 2660 (1981).
13. Y. Harada, K. Ohno, and H. Mutoh, *J. Chem. Phys.*, **79**, 3251 (1983).
14. C. Angeli, G. Berthier, C. Rolando, M. Sablier, C. Alcaraz, and O. Dutuit, *J. Chem. Phys.*, **101**, 7907 (1997); R. Fukuda, M. Ehara, H. Nakatsuji, N. Kishimoto, and K. Ohno, *J. Chem. Phys.*, **132**, 84302 (2010).
15. S. K. Kang, H. Tang, and T. A. Albright, *J. Am. Chem. Soc.*, **115**, 1971 (1993).
16. T. R. Ward, H.-B. Bürgi, F. Gilardoni, and J. Weber, *J. Am. Chem. Soc.*, **119**, 11974 (1997).
17. M. R. Cook, W. A. Herrmann, P. Kiprof, and J. Takacs, *J. Chem. Soc., Dalton Trans.*, 797 (1991).
18. J. K. Burdett, *Coord. Chem. Rev.*, **27**, 1 (1978).
19. Y. Ishikawa and K. Kawakami, *J. Chem. Phys., A*, **111**, 9940 (2007).
20. J. Kim, T. K. Kim, J. Kim, Y. S. Lee, and H. Ihée, *J. Chem. Phys., A*, **111**, 4697 (2007).
21. S. Alvarez and M. Llunell, *J. Chem. Soc., Dalton Trans.*, 3288 (2000).
22. S. A. Trushin, W. Fuß, and W. E. Schmid, *Chem. Phys.*, **259**, 313 (2000); S. A. Trushin, K. Kosma, W. Fuß, and W. E. Schmidt, *Chem. Phys.*, **347**, 309 (2008); For early work see M. Poliakoff and J. J. Turner, *Angew. Chem., Int. Ed.*, **40**, 2809 (2001); M. Poliakoff, *Inorg. Chem.*, **15**, 2022, 2892 (1976) and references therein.
23. G. Worth, G. Welch, and M. J. Paterson, *Mol. Phys.*, **104**, 1095 (2006).
24. A. Rosa, E. J. Baerends, S. J. A. van Gisbergen, E. van Lenthe, J. A. Groenveld, and J. G. Snijders, *J. Am. Chem. Soc.*, **121**, 10356 (1999) and references therein.
25. I. E. Rachidi, O. Eisenstein, and Y. Jean, *New J. Chem.*, **14**, 671 (1990).
26. G. R. Clark, S. V. Hoskins, T. C. Jones, and W. R. Roper, *Chem. Commun.*, 719 (1983).
27. B. R. Bender, J. R. Norton, M. M. Miller, O. P. Anderson, and A. K. Rappe, *Organometallics*, **11**, 3427 (1992).
28. U. Radius, J. Sundermeyer, and H. Pritzkow, *Chem. Ber.*, **127**, 1827 (1994); U. Radius and R. Hoffmann, *Chem. Ber.*, **129**, 1345 (1996).
29. M. T. Youinou, J. Kress, J. Fischer, A. Aguero, and J. A. Osborn, *J. Am. Chem. Soc.*, **110**, 1488 (1988); See also, J. Kress, M. Wesolek, and J. A. Osborn, *J. Chem. Soc., Chem. Commun.*, 514 (1982).
30. J. R. Clark, P. E. Fanwick, and I. P. Rothwell, *Chem. Commun.*, 553 (1995).
31. A. Noll, S. Rabe, and U. Muller, *Z. Naturforsch.*, **54b**, 591 (1999).
32. P. Schwab, R. H. Grubbs, and J. W. Ziller, *J. Am. Chem. Soc.*, **118**, 100 (1996).
33. F. A. Cotton, C. A. Murillo, and R. A. Walton, editors. *Multiple Bonds Between Metal Atoms*, 3rd edition, Springer Science, New York (2005).
34. S. Shaik, R. Hoffmann, C. R. Fisel, and R. H. Summerville, *J. Am. Chem. Soc.*, **102**, 1194 (1980).
35. M. B. Hall, *J. Am. Chem. Soc.*, **97**, 2057 (1975).
36. Y. F. Hu, G. M. Bancroft, and K. H. Tan, *Inorg. Chem.*, **39**, 1255 (2000).
37. M. Grillone, F. Benetollo, G. Bombieri, and A. Del Pra, *J. Organomet. Chem.*, **575**, 193 (1999).
38. D. W. Hart, R. Bau, and T. F. Koetzle, *Organometallics* **4**, 1590 (1985).
39. P. Macchi, D. Donghi, and A. Sironi, *J. Am. Chem. Soc.*, **127**, 16494 (2005).
40. C. Mealli and L. Sacconi, *Inorg. Chem.*, **21**, 2870 (1982).
41. L. Q. Tang, M. S. Dadachov, and X. D. Zon, *Z. Kristallogr.*, **216**, 387 (2001).
42. Z. Mazej and E. Goresknik, *Eur. J. Inorg. Chem.*, 1795 (2008).
43. G. Ferey, J. Renaudin, A. Kozak, and Y. Mary, *Eur. J. Solid State Chem.*, **26**, 427 (1989).
44. O. Horner, E. Anxolabehere-Mallart, M. F. Charlot, L. Tchertanov, J. Guilhern, T. A. Mattioli, A. Bossac, and J. J. Girerd, *Inorg. Chem.*, **38**, 1222 (1999).
45. H. Shorafa and K. Seppelt, *Z. Anorg. Allg. Chem.*, **635**, 112 (2009).

46. N. Matsumoto, M. Yamashita, I. Ueda, S. Kida, *Mem. Fac. Sci. Kyushu U., Ser. C* **11**, 209 (1978).
47. N. Matsushita, F. Fukuhara, and N. Kojima, *Acta Crystallogr.*, **E61**, i123 (2005) and references therein.
48. J. K. Burdett, *Inorg. Chem.*, **17**, 2537 (1978); J. K. Burdett, *J. Am. Chem. Soc.*, **101**, 5217 (1979).
49. M.-H. Whangbo and M. J. Foshee, *Inorg. Chem.*, **20**, 113 (1981).
50. L. V. Interrante, K. W. Browall, and F. P. Bundy, *Inorg. Chem.*, **13**, 1158 (1974).
51. B. A. Frenz, J. H. Enemark, and J. A. Ibers, *Inorg. Chem.*, **8**, 1288 (1969).
52. O. Alnaji, Y. Peres, M. Dartiguenave, F. Dahan, and Y. Dartiguenave, *Inorg. Chim. Acta*, **114**, 151 (1986).
53. R. B. English, M. M. de, V. Steyn, and R. J. Haines, *Polyhedron*, **6**, 1503 (1987).
54. R. Hoffmann, M. M-L Chen, M. Elian, A. R. Rossi, and D. M. P. Mingos, *Inorg. Chem.*, **13**, 2666 (1974).
55. J. H. Enemark and R. D. Feltham, *Coord. Chem. Rev.*, **13**, 339 (1974).
56. M. Chisholm, F. A. Cotton, and R. L. Kelly, *Inorg. Chem.*, **18**, 116 (1979).
57. B. Czeska, K. Dehnicke, and D. Fenske, *Z. Naturforsch.*, **B38**, 1031 (1983).
58. M. Pinsky and D. Avnir, *Inorg. Chem.*, **37**, 5575 (1998).
59. S. Alvarez and M. Liunell, *J. Chem. Soc., Dalton Trans.*, 3288 (2000).
60. R. Enjalbert and J. Galy, *Acta Crystallogr.*, **C42**, 1467 (1986).
61. S. Seong, K. A. Yee, and T. A. Albright, *J. Am. Chem. Soc.*, **115**, 1981 (1993).
62. J. G. Bednorz and K. A. Müller, *Angew. Chem. Int. Ed.*, **27**, 735 (1988).
63. M. K. Wu, J. R. Ashburn, C. J. Torng, P. H Hor, R. L. Meng, L. Goa, Z. J. Huang, Y. Q. Wang, and C. W. Chu, *Phys. Rev. Lett.*, **58**, 908 (1987); P. H. Hor, L. Gao, R. L. Meng, Z. J. Huang, Y. Q. Wang, K. Forster, J. Vassiliou, C. W. Chu, M. K. Wu, J. R. Ashburn, and C. J. Torng, *Phys. Rev. Lett.*, **58**[911] (1987).
64. M.-H. Whangbo, M. Evain, M. A. Beno, and J. M. Williams, *Inorg. Chem.*, **26**, 1831 (1987); *Inorg. Chem.*, **26**, 1832 (1987).
65. M.-H. Whangbo and C. C. Torardi, *Acc. Chem. Res.*, **24**, 127 (1991) and references therein.
66. I. E. Grey and H. Steinfink, *J. Am. Chem. Soc.*, **92**, 5093 (1970).
67. L. F. Mattheiss, *Solid State Commun.*, **93**, 879 (1995); I. Hase, N. Shirakawa, and Y Nishihara, *J. Phys. Soc. Jpn.*, **64**, 2533 (1995).
68. O. Fuentes, C. Zheng, C. E. Check, J. Zhang, and G. Chancon, *Inorg. Chem.*, **38**, 1889 (1999).
69. M. C. Gelabert, N. E. Brese, F. J. DiSalvo, S. Jobic, P. Deniard, and R. Brec, *J. Solid State Chem.*, **127**, 211 (1996).
70. D. Johrendt, C. Lux, and A. Mewis, *Z. Naturforsch.*, **B51**, i213 (1991).
71. D. M. Proserpio, G. Chacon, and C. Zheng, *Chem. Mater.*, **10**, 1286 (1998).
72. D. W. Pipes, M. Bakir, S. E. Vitols, D. J. Hodgson, and T. J. Meyer, *J. Am. Chem. Soc.*, **112**, 5507
73. A. J. Nielson, P. D. W. Boyd, G. R. Clark, P. A. Hunt, M. B. Hursthouse, J. B. Metson, C. E. F. Rickard, and P. A. Schwerdtfeger, *J. Chem. Soc., Dalton Trans.*, **112**, 11531995.

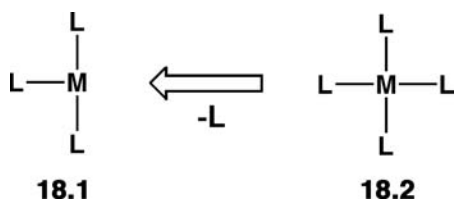
# The $C_{2v}$ $ML_3$ Fragment

## 18.1 INTRODUCTION

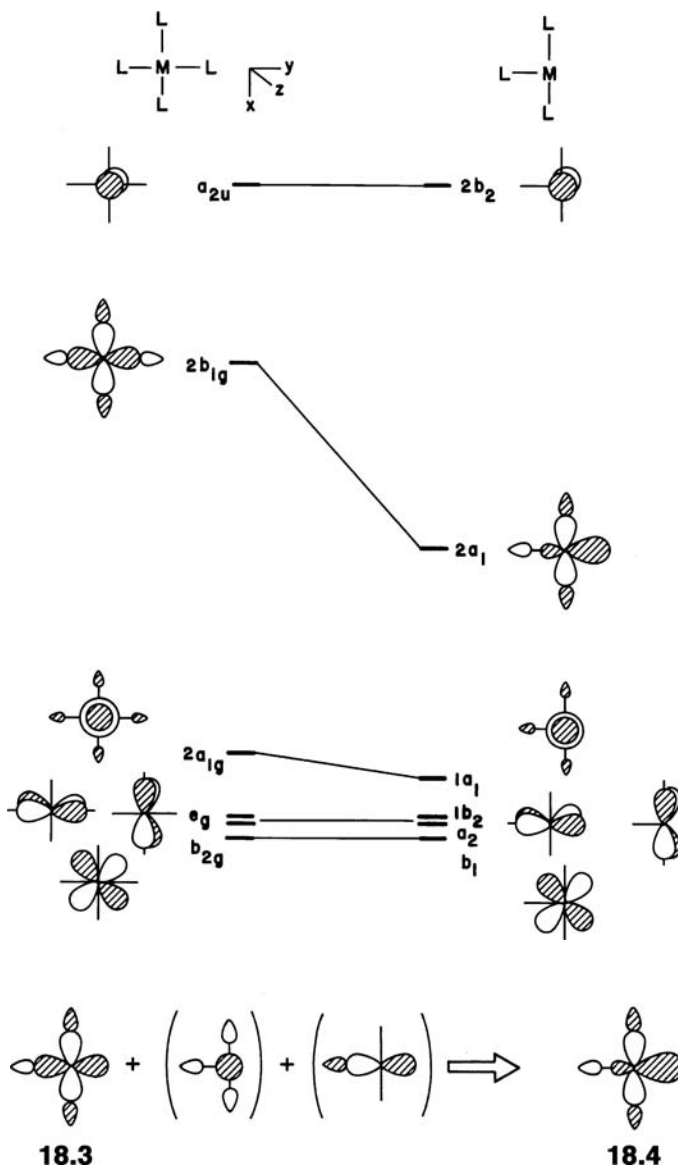
There is a strong electronic resemblance between the  $C_{4v}$   $ML_5$  fragment which was discussed in Section 17.1 and the “T-shaped”  $ML_3$  fragment which is covered here. That relationship will be probed further in Section 18.4. In Section 18.2 some examples are presented which use the  $C_{2v}$   $ML_3$  fragment.

## 18.2 THE ORBITALS OF A $C_{2v}$ $ML_3$ FRAGMENT

The valence orbitals of the T-shaped  $ML_3$  fragment, **18.1**, can be derived by removing one ligand from square planar  $ML_4$ , **18.2**. This is shown in Figure 18.1. The five  $d$

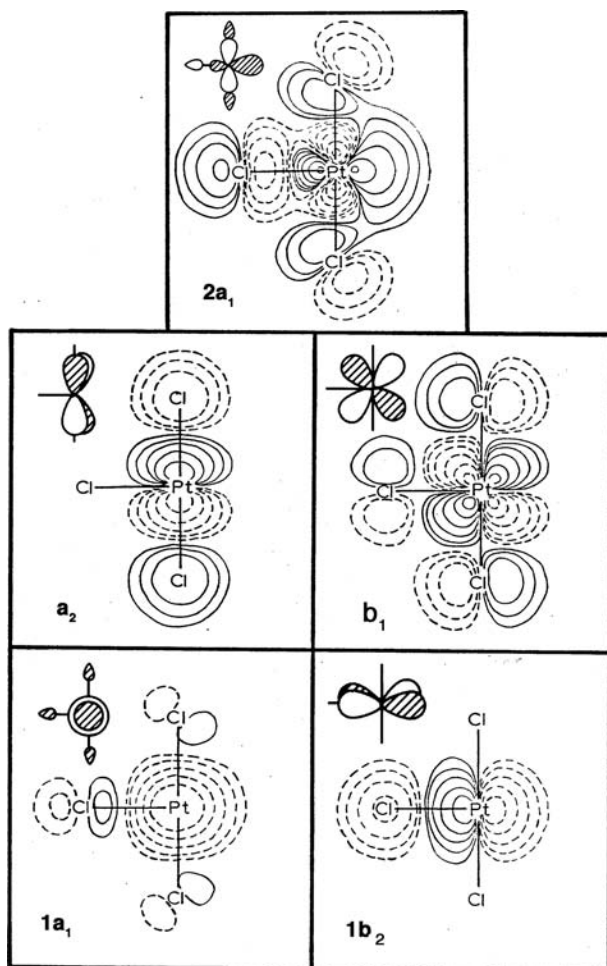


block and one  $p$  orbital of  $ML_4$  (see Section 16.2) are displayed from a top view on the left side of this figure. All of the orbitals are basically unperturbed when one ligand is removed except for  $x^2 - y^2$ ,  $2b_{1g}$ . This is stabilized greatly because one strongly antibonding interaction with a ligand lone-pair is removed. The orbital also becomes hybridized as some metal s and  $y$  character are mixed into **18.3** in a way which is bonding to the lone-pair hybrids in **18.3**. This hybridization comes about in a way

**FIGURE 18.1**

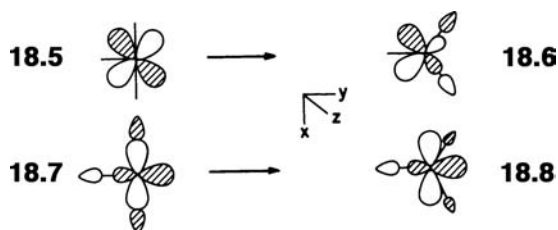
Construction of the orbitals of a  $C_{2v}$   $ML_3$  fragment from a square planar complex. The  $L$  ligands contain only  $\sigma$  donor hybrids.

that is analogous to the  $a_1$  hybrid in the  $C_{4v}$   $ML_5$  fragment (Section 17.2). The resultant orbital, **18.4**, is labeled  $2a_1$  in Figure 18.1. The  $2a_{1g}$  ( $z^2$ ) level will also be stabilized very slightly by removing one ligand. The reader should note that we have labeled each orbital in the  $ML_3$  fragment according to the  $C_{2v}$  point group. We want to emphasize, however, that one antibonding orbital is shifted to moderate energy and it becomes hybridized out toward the missing ligand. The rest of the levels remain basically unchanged, just as we saw for the square pyramidal  $ML_5$  fragment. We have also included the  $z$  atomic orbital (AO),  $2b_2$  in this figure. Occasionally this orbital will be utilized (just as it is in square planar complexes). However, it must be remembered that this orbital lies at a much higher energy than the others. Contour plots of the important valence orbitals in  $PtCl_3^-$  are presented in Figure 18.2. In this case the  $Cl^-$  ligands are  $\pi$  donors. Therefore, their  $p$  AOs interact with the  $d$  AOs on Pt in an antibonding way. This is particularly clear for the  $1a_2$ ,  $1b_2$ , and  $1b_1$  molecular orbitals. Note that even in the  $2a_1$  orbital which is strongly  $\sigma$  antibonding, there is still noticeable  $\pi$  antibonding.

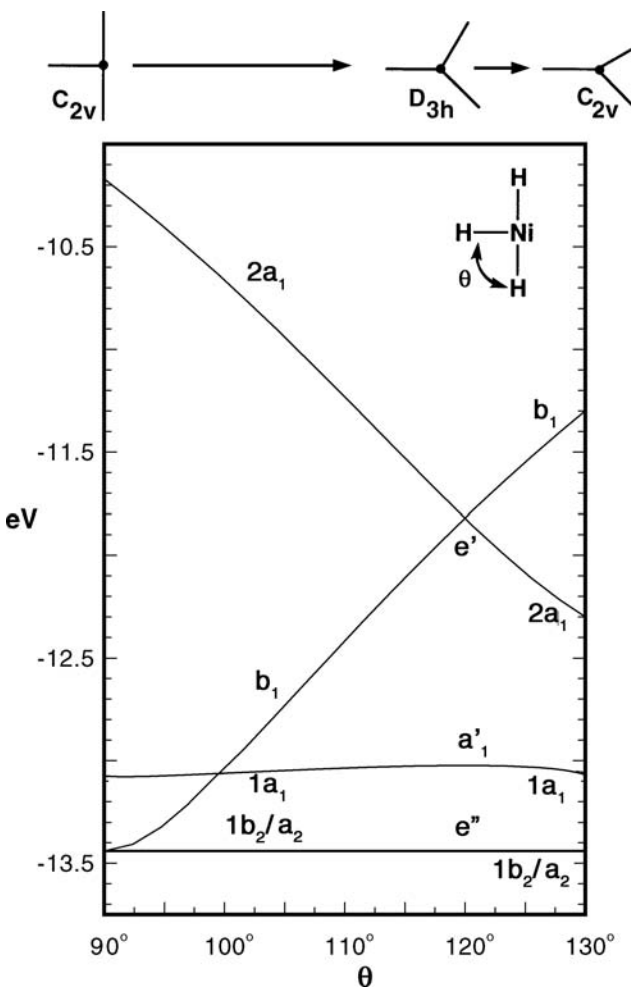
**FIGURE 18.2**

Contour plots of the valence  $d$  orbitals in the  $\text{PtCl}_3^-$  fragment at the extended Hückel level.

Next, it is interesting to examine what geometrical options are available to  $ML_3$  as a molecule itself. A surface that we explored in the main group area (Section 14.2) is the variation of one angle from a T-shaped through  $D_{3h}$  to a Y-shaped structure. This is done for  $ML_3$  in Figure 18.3. The orbitals listed on the left correspond to the  $C_{2v}$  T-shaped structure derived in Figure 18.1. The  $1a_2$ ,  $1b_2$ , and  $2b_2$  orbitals are orthogonal to the lone-pair functions of the ligands on all points of the distortion coordinate. The  $1a_1$  orbital is primarily metal  $z^2$  and s. Varying the H—Ni—H angle does not change the overlap of the ligand s AOs to them, so these four levels remain at constant energy. The  $b_1$  orbital, 18.5, is destabilized as the *trans* H—Ni—H angle



is decreased. Overlap between the ligands and metal  $xy$  is turned on and as seen in 18.6 this is an antibonding interaction (see Section 15.4 for a related case). The ligand-based level will be stabilized. The destabilization is somewhat abated because

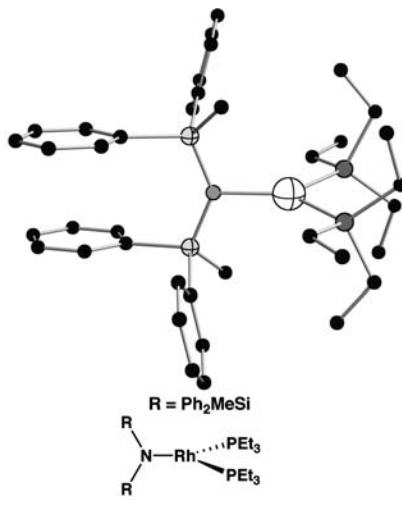
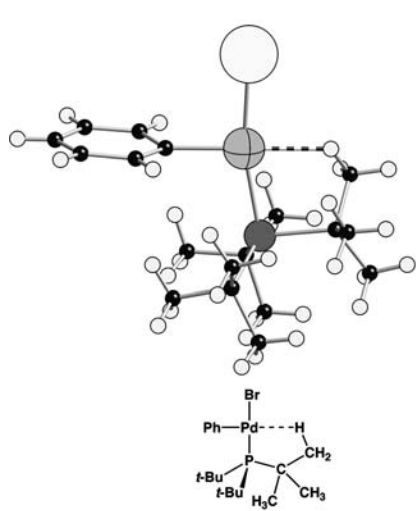
**FIGURE 18.3**

A Walsh diagram for the hypothetical  $\text{NiH}_3$  molecule obtained at the extended Hückel level. Note that at  $\theta = 120^\circ$  the symmetry of the molecule becomes  $D_{3h}$  and the orbitals at this point have been labeled accordingly.

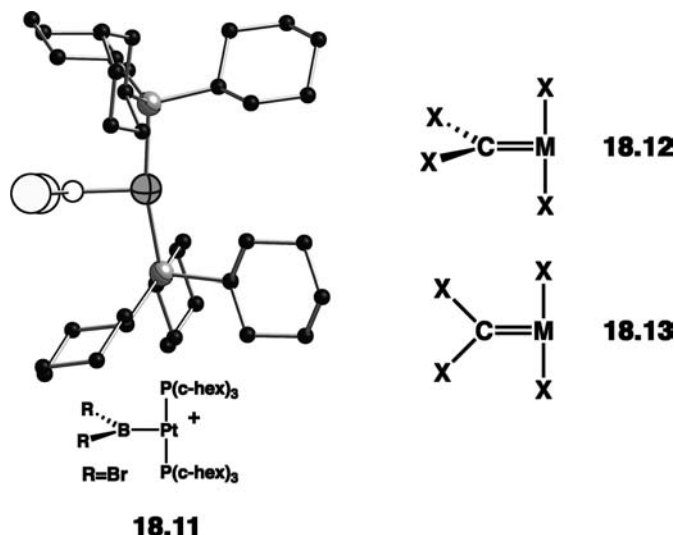
metal  $x$  character is also mixed into this level in a way that is bonding to the ligands. Conversely, the  $2a_1$  level, **18.7**, is stabilized. As shown in **18.8**, antibonding between the ligand hybrids and  $x^2 - y^2$  is diminished while bonding to metal  $y$  is turned on. When the three L—M—L angles are  $120^\circ$ , **18.6** and **18.8** meet and become an  $e'$  set. At this special point the symmetry of the molecule is  $D_{3h}$ . The orbitals have been labeled at the middle of Figure 18.3 to reflect this.

With 10  $d$  electrons in the valence levels of Figure 18.3, it is clear that a  $D_{3h}$  structure will be preferred. Remember that although  $b_1$  goes up in energy from the T geometry to  $D_{3h}$ , there is a lower ligand-based orbital of  $b_1$  symmetry which is stabilized (see, for example the situation in Figure 15.4). Thus the dominant factor is the stabilization of the HOMO,  $2a_1$ , which sets the  $D_{3h}$  geometry for these  $d^{10}$   $\text{ML}_3$  compounds. For example,  $\text{Pt}(\text{PPh}_3)_3$  and tris(ethylene nickel adopt this structure. Depending upon the steric constraints of the surrounding ligands, there is some latitude in the L—M—L bond angles that are observed [1], so distortions toward the T or Y structures are relatively soft for these 16-electron complexes. With one less electron the  $D_{3h}$  geometry is Jahn–Teller unstable. A distortion toward a T or Y geometry is expected. The P—Ni—P bond angles in one crystallographic modification of  $\text{Ni}(\text{PPh}_3)_3$  [2] are  $121.2^\circ$ ,  $118.5^\circ$ , and  $120.2^\circ$  while those in another are  $118.0^\circ$ ,  $121.7^\circ$ , and  $120.3^\circ$ . In  $\text{Ni}(\text{PPh}_3)_3^+$  the angles were found to be  $107.0^\circ$ ,  $110.9^\circ$ , and  $142.0^\circ$  [3]. In other words the  $d^9$  complex has opened to a T geometry.

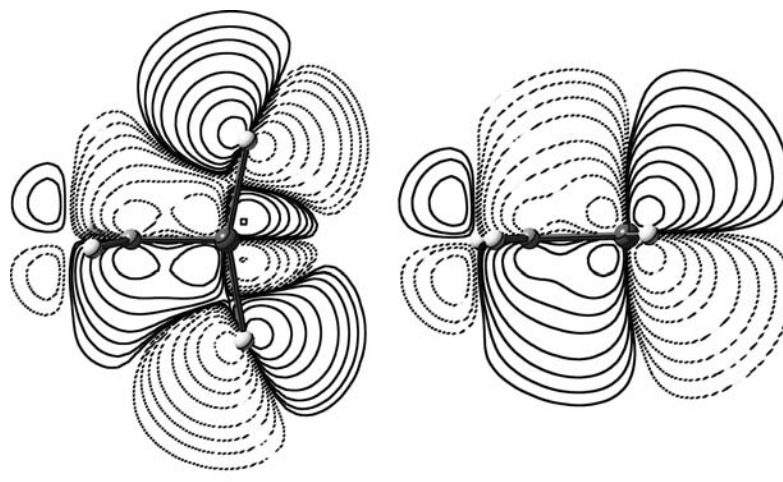
A  $d^8$ , 14-electron  $ML_3$  complex would have the lowest four levels filled in Figure 18.3. These are  $b_1 + a_2 + 1b_2 + 1a_1$  on the T side or  $a_2 + 1b_2 + 1a_1 + 2a_1$  at the Y geometry. At a  $D_{3h}$  structure there will be a degeneracy. The  $e'$  set will be half-filled which signals that either the complex must be high spin (a triplet) or it will undergo a Jahn–Teller distortion to the T or Y geometry. Most of these very reactive 14-electron complexes possess a T geometry where the vacant coordination site (see the radial extent of the  $2a_1$  orbital in Figure 18.2) is in fact occupied by a weak bonding interaction to a C–H bond [4]. For example, in **18.9** a C–H bond from



one of the *t*-butyl groups lies at a Pd–H distance of 2.18 Å [5]. This is called an agostic bond; it is another example of a three center, two-electron bond where in this case the C–H  $\sigma$  bond interacts with a low-lying empty metal orbital. Agostic bonds (from the Greek word “to hold close together”) are weak interactions, typically in the range of 10–15 kcal/mol. We shall see a number of instances where agostic bonding interactions take place here and in later chapters. The structure of  $(Ph_3P)_3Rh^+$  has been determined [6]. It is diamagnetic and approximately T-shaped (the P–Rh–P angles are 97.7°, 102.4°, and 159.4°). From Figure 18.3, one can see that the  $b_1$  orbital on going to the T structure is stabilized far more than the  $2a_1$  orbital is stabilized on going to the Y structure. This is consistent with the observation that there are far more  $d^8$   $ML_3$  complexes that have been structurally categorized with a T shape [7]. A Y structure is favored when there is a strong  $\pi$ -donor coordinated to the metal. In that case the  $b_1$  orbital will be destabilized by the  $p$  AO from the donor to become the LUMO (Figure 18.3), which makes  $2a_1$  the HOMO, so a Y geometry is favored. An example is given by **18.10** [8]. Here the N–Rh–P angles were found to be 133.7° while the P–Rh–P angle was 92.7°. Notice that the Si–N–Si plane is perpendicular to the P–Rh–P plane which is required for there to be overlap between the  $b_1$  orbital and the  $p$  AO from the  $\pi$ -donor. With one  $\pi$ -acceptor ligand, a  $d^8$   $ML_3$  will be most stable with the T structure. A number of boryl ( $-BR_2$ )-substituted complexes have been synthesized [9]. An example is provided by **18.11** [9]. Note that our prescription for electron counting in Chapter 16 makes the boryl ligand to be a two-electron  $\sigma$ -donor, that is,  $BR_2^-$ , so **18.11** is a  $Pt^{2+}$  complex. For a variety of R groups, the P–Pt–P angles range from 157.3°–171.8°. In all cases the R groups are bulky enough so that the  $BR_2$  plane lies perpendicular to the PtP<sub>2</sub> plane. This is certainly the sterically most favorable geometry and allows the metal  $b_1$

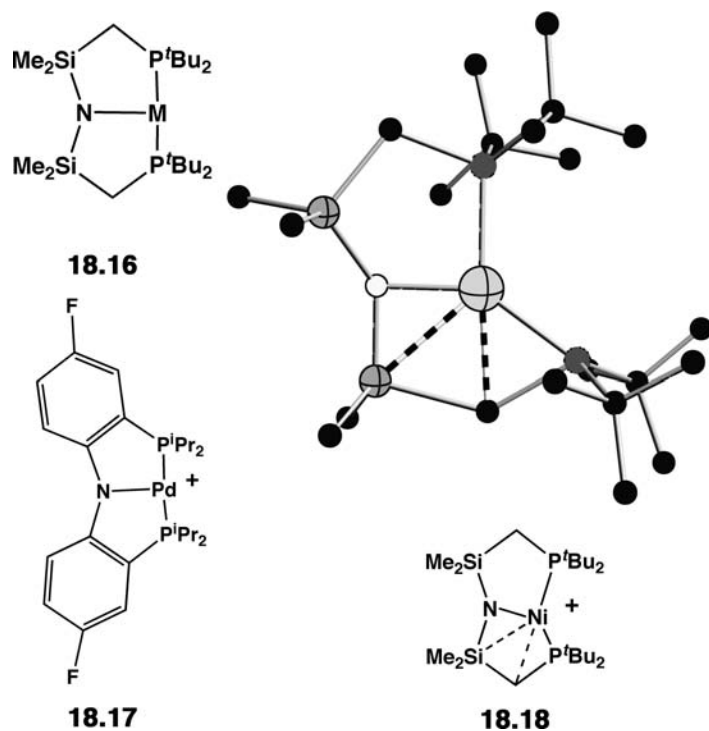


orbital to be stabilized by the empty  $p$  AO on boron. Reference back to Figure 18.3 indicates that when  $\theta$  is close to  $90^\circ$  (the P—Pt—P bond angle in **18.11** =  $180^\circ$ ),  $b_2$  is at about the same energy as  $b_1$  and, therefore, in the absence of steric effects there should be free rotation about the Pt—B bond. Andrews and coworkers [10] have reacted metal atoms with CX<sub>4</sub> at cryogenic temperatures to create a series of X<sub>2</sub>C=MX<sub>2</sub> molecules where X = F, Cl and M = Ni, Pd, and Pt. The IR spectra of these compounds have shown them to be metal–carbene complexes and the calculations [11a] indicate that there is substantial M—C  $\pi$  character [10]. B3LYP calculations on M = Pt and X = F with several high-level basis sets give either **18.12** or **18.13** to be the ground state with the other less than 1 kcal/mol at higher energy (the F—Pt—F angles in **18.12** and **18.13** were calculated to be  $159^\circ$  and  $168^\circ$ , respectively). The Y structure where  $b_1$  is empty and  $2a_1$  filled with F—Pt—F =  $78.5^\circ$  can only form a  $\pi$  bond with  $b_2$ . It lies about 42 kcal/mol higher in energy than the structures akin to **18.12** and **18.13** [11a]. Contour plots of the resulting Pt—C  $\pi$  orbital are shown in **18.14** and **18.15** for the



two rotamers. In each case one can see substantial delocalization. Therefore, this appears to be an ethylene analog, with a strong  $\sigma$  and  $\pi$  bond, where there is

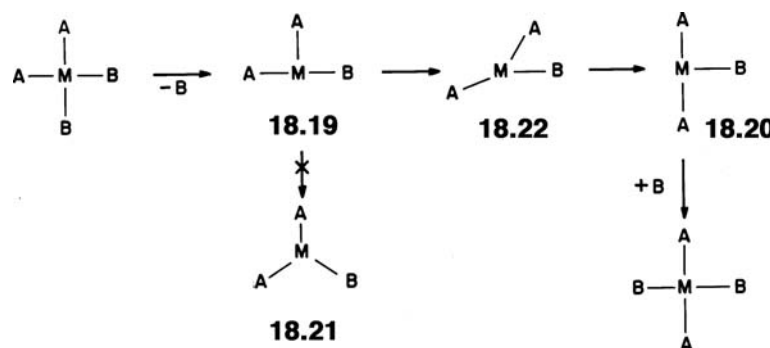
effectively free rotation about the double bond. There are a number of mer-tridentate ligands that generate unusual electronic environments by virtue of their geometric requirements. These so-called pincer ligands have been used to create a number of three-coordinate, T-shaped molecules. Caulton and coworkers have prepared the series given in **18.16** [12a]. With M = Ni the ESR spectrum strongly suggests that the singly occupied orbital is akin to  $2a_1$ . For M = Co the  $d^8$  molecule is a triplet. This is consistent with the idea that the pincer ligand will not allow the molecule to distort to a Y geometry. Referring back to Figure 18.3,  $\theta = 94.7^\circ$  and the amido group is now forced to lie in the CoP<sub>2</sub> plane. Therefore, the  $b_2$  orbital is strongly destabilized by the nitrogen lone-pair and it lies close enough to  $2a_1$  so that a triplet state is preferred, that is, the electron occupancy is  $(a_2)^2(b_1)^2(1a_1)^2(b_2)^1(2a_1)^1$ . For M = Fe, the metal is now  $d^7$ . Magnetic measurements show that S = 3/2 so that presumably the electron configuration is  $(a_2)^2(b_1)^2(1a_1)^1(b_2)^1(2a_1)^1$ . Returning to the  $d^8$  case, a (pincer)Pd<sup>+</sup> complex, **18.17**, has also been isolated [11b]. Remarkably,



this is also a high-spin, triplet molecule. High-spin organometallic compounds that contain second- or third-row transition metals are very rare; the valence d AOs are quite diffuse leading to small values for the exchange repulsions (see Section 8.8). High-level density functional theory (DFT) calculations on Pd<sup>+</sup>(PH<sub>3</sub>)<sub>2</sub>(NH<sub>2</sub>) which enforce  $C_{2v}$  symmetry and keep the NH<sub>2</sub> group in the PdP<sub>2</sub> plane yield a T-structure for both the triplet and singlet states [11a]. The triplet was found to be 12.3 kcal/mol more stable than the singlet. What is perhaps even more unusual is the **18.16**, M = Ni<sup>+</sup>,  $d^8$  complex. It is a ground-state singlet [12b] with the structure given by **18.18**. The  $C_{2v}$  structure analogous to **18.16** is calculated [12b] to be a triplet 7.5 kcal/mol higher in energy than the ground state, whereas, the analogous singlet state is higher in energy by 11.9 kcal/mol and is categorized to be a transition state. The dynamics associated with this molecule are quite complicated. The unusual distortion in the ground state allows the filled Si—C bond to overlap with empty  $2a_1$  (the  $b_2$  orbital is doubly occupied). Rather than forming an agostic C—H bond

elsewhere in the ligand (as in **18.9** and presumably made difficult in this instance for steric reasons), a Si—C agostic bond is formed.

There are a number of other connections that make these  $d^8$  systems interesting. First of all, in Section 16.4, one pathway for *cis-trans* square planar  $ML_4$  interconversion involved a  $d^8$ - $ML_3$  species, **18.19**. A rearrangement must take **18.19** to its trans isomer **18.20** which then may be intercepted to yield the *trans*- $ML_4$ .

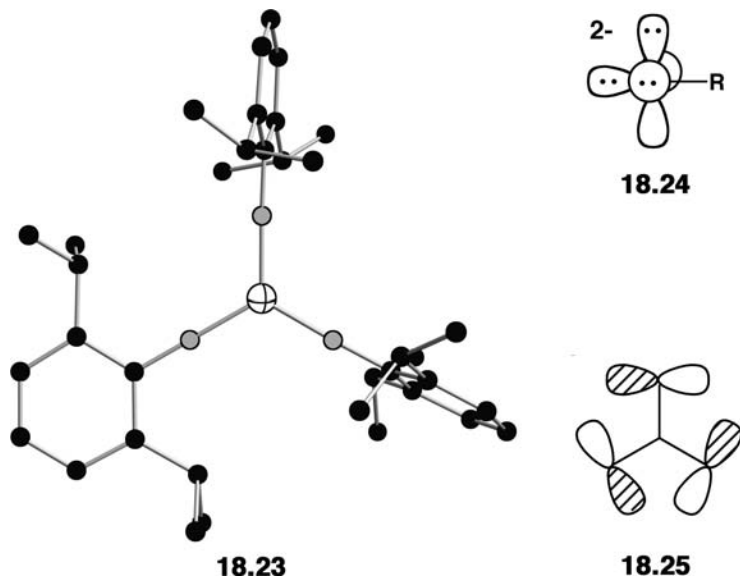


There are two ways that the rearrangement from **18.19** to **18.20** can occur. A geometrically obvious pathway would be to decrease the *trans* A—M—B angle in **18.19** to a trigonal species, **18.21**, where all angles around the metal are about  $120^\circ$ . However, as shown in Figure 18.3, this is energetically prohibitive (provided that there is no change of spin state). Instead the molecule must distort via the Y structure of **18.22** where the A—M—A angle has opened considerably and the *cis* A—M—B angle somewhat decreases. Relaxation of this Y arrangement yields the *trans*-T intermediate, **18.20**. In Section 19.5 we shall cover a reaction where a  $d^8$   $(CH_3)_3M$  intermediate with a T ground state rearranges to a Y geometry and undergoes reductive elimination to ethane and  $(CH_3)M$ . There are also interesting connections with problems we have discussed elsewhere. For example, in Section 17.3, the mechanism of the thermal and photochemical rearrangements in  $Cr(CO)_5$  was investigated. The reader should carefully compare the electronic details for the rearrangement of this  $d^6$   $ML_5$  species with  $d^8$   $ML_3$  case here. They are identical! A Mexican-hat surface like that given by Figure 7.7 occurs for each.

The valence shell electron repulsion (VSEPR) model clearly predicts that a  $d^0$   $ML_3$  molecule should be  $D_{3h}$ . When L is a good  $\sigma$ -donating ligand this is not the case [13,14]. The  $e''$  set at the  $D_{3h}$  geometry is empty. Pyramidalization of  $ML_3$  to  $C_{3v}$  causes  $e''$  to mix in and stabilize the M—L  $\sigma$  bonding  $e'$  orbitals (these are the fully metal  $d$  and  $p$  bonding to ligand  $\sigma$  analogous of **18.6** and **18.8**). From a valence-bond perspective [14], this mixing increases the amount of  $d$  character in the M—L  $\sigma$  bonds and, hence, is stabilizing. Consistent with this analysis is the fact that the  $d^0$  species  $Sc[N(SiMe_3)_2]_3$  [15],  $Y[CH(SiMe_3)_2]_3$  [16], as well as several other examples have  $ML_3$  cores that are  $C_{3v}$  despite the fact that the ligands are sterically very demanding. When L is very electronegative the  $e''-e'$  gap becomes large and the driving force for pyramidalization is lost. Thus,  $ScF_3$  and  $LaF_3$  are both  $D_{3h}$  [17] (for the same reason that  $WF_6$  and  $CrF_6$  are octahedral).

Rationalizing (or predicting) the shape of  $d^1-d^7$   $ML_3$  compounds becomes complicated and difficult for three reasons. First, there is not much of an energy difference in the five  $d$ -centered orbitals compared to that in the octahedron,

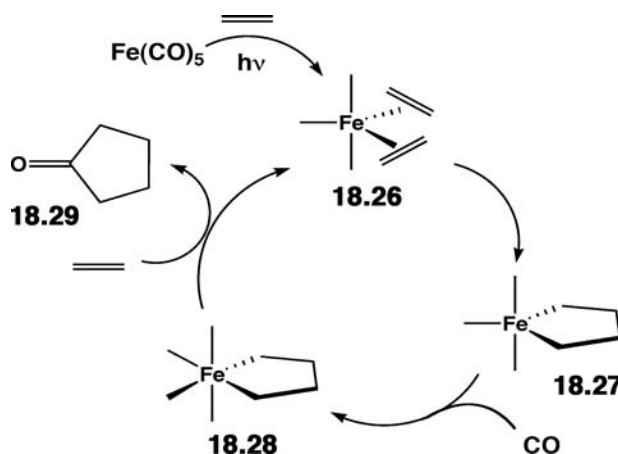
square plane, and so on. This, in turn means that the substitution of strong  $\pi$ -donors (recall that these will be electron-deficient molecules and, therefore,  $\pi$ -donor substitution is a quite common approach to stabilize these molecules) may, and often does, change the  $d$ -centered level ordering. Thirdly, the problem of spin state is always present for these intermediate electron count species. A careful dissection and analysis of these factors has been given by Alvarez [7,18], and we direct the readers to his work. We would like to point out that the presence of strong M—L  $\pi$  bonding in these molecules might tempt some to include  $\pi$  bonds in the electron count at the metal. This was assiduously avoided in our introduction to electron counting in Section 16.3 since it frequently can lead to unneeded confusion. An  $\text{ML}_3$  example is given by the  $d^2$   $\text{Os}(\text{N-Ar})_3$  [19] molecule shown in 18.23. The  $\text{NR}^{2-}$  group, of course, donates two  $\sigma$  electrons. It also has



two  $p$  AOs, 18.24, that can be used for  $\pi$  donation. If these interactions were used in the electron count, then 18.23 would possess 20 electrons. In fact it cannot use the symmetry-adapted combination 18.25 and, therefore the electron count, if one is going to use the  $\pi$  bonds, is 18. Exactly the same situation applies for a  $d^2$   $\text{W}(\text{OR})_2(\text{NR}')$  complex which also has a  $D_{3h}$  shape [20]. Referring back to the  $D_{3h}$  level ordering in the middle of Figure 18.3, the presence of these very strong  $\pi$ -donors destabilizes  $e''$  above  $a_1'$ , and as a consequence, both of these molecules are low-spin complexes.

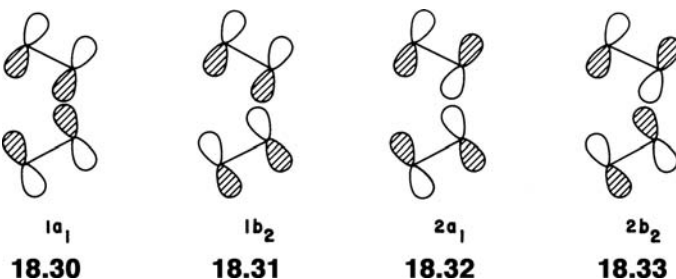
### 18.3 $\text{ML}_3$ -CONTAINING METALLACYCLES

In Section 11.2.B, we showed that the concerted or least-motion dimerization of two olefins requires excessively high activation energies. This is the classic case of a symmetry-forbidden reaction. A two-step reaction mechanism, or at least a different reaction path, has to be followed. In this section, a somewhat analogous reaction, the dimerization of two olefins in the presence of  $\text{Fe}(\text{CO})_5$  and CO [21], is investigated. An initial sequence in this reaction is the photosubstitution of CO by two olefins on  $\text{Fe}(\text{CO})_5$  which gives the 18-electron intermediate, 18.26. It rearranges to the 16-electron metallacyclopentane, 18.27, wherein one C—C and two Fe—C bonds

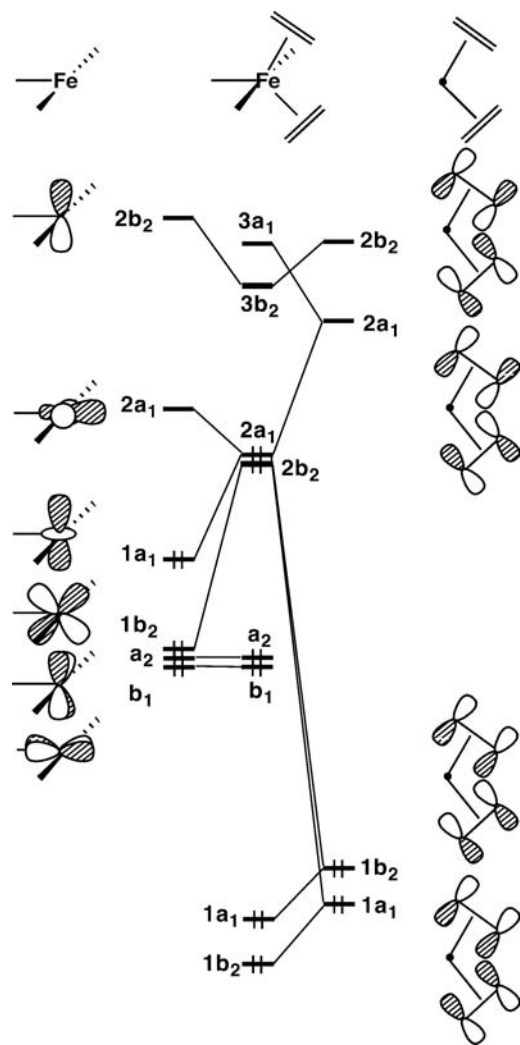


have been formed. Intermediate **18.27** is then trapped by CO, yielding the 18-electron metallacyclopentane, **18.28**. Finally, **18.28** presumably undergoes carbonyl insertion, addition of an olefin, reductive elimination and addition of the second olefin to regenerate **18.26** and cyclopentanone, **18.29**. The oxidative cycloaddition step, **18.26** to **18.27**, is the focus of our interest here. A careful theoretical study of the reaction has been carried out by Stockis and Hoffmann [22], and the reader should consult the original work for details on alternative reaction sequences, stereoselectivity questions, and so on. There have been a number of other investigations of the coupling of two coordinated olefins to form a metallacyclopentane [23–28]. The reader is cautioned that the exact details depend critically on the number of ligands, their geometrical disposition around the metal, as well as the number of electrons assigned to the metal. We shall return to the oxidative cycloaddition reaction again in Section 20.4 with a totally different ligand set and we shall see that there are many differences between the two reactions.

We start our analysis by building up the valence orbitals of **18.26** in terms of a  $C_{2v}$   $\text{Fe}(\text{CO})_3$  fragment and two ethylenes. Notice that the olefins lie in the equatorial plane. This, recall from **17.31** and **17.32**, is the electronically preferred way to orient olefins in a  $d^8$  trigonal bipyramidal complex. Symmetry-adapted linear combinations of the  $\pi$  and  $\pi^*$  levels of the ethylenes are shown in **18.30** to **18.33** from a top view.



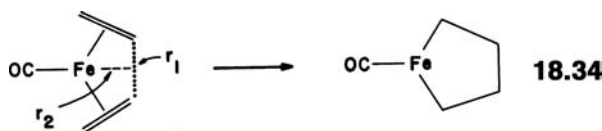
They are simply the in-phase and out-of-phase combinations and have been redrawn from a side view on the right side of Figure 18.4. The orbitals of a  $d^8$   $\text{Fe}(\text{CO})_3$  fragment are illustrated on the left side. Notice that there are two fragment orbitals of  $a_1$  symmetry on  $\text{Fe}(\text{CO})_3$  and two of  $b_2$  symmetry that interact with **18.30**–**18.33**. Consequently four molecular orbitals of  $a_1$  and four of  $b_2$  symmetry are formed from this union (only the lowest three of each type are explicitly shown in Figure 18.4). The molecular  $1a_1$  and  $1b_2$  orbitals are primarily **18.30** and **18.31** stabilized by the  $1a_1$

**FIGURE 18.4**

An orbital interaction diagram for bis-ethylene- $\text{Fe}(\text{CO})_3$ .

and  $1b_2$  fragment orbitals of  $\text{Fe}(\text{CO})_3$ , respectively. Molecular levels  $2a_1$  and  $2b_1$  are primarily  $\text{Fe}(\text{CO})_3$   $1a_1$  and  $1b_2$ . The ethylene  $\pi$  functions mix into these MOs in an antibonding fashion. Molecular  $2a_1$  and  $2b_2$  are kept at low energy because the  $2a_1$  and  $2b_2$  fragment orbitals of  $\text{Fe}(\text{CO})_3$  mix in second order very heavily into them. Molecular  $3a_1$  and  $3b_2$  consist primarily of the  $2a_1$  and  $2b_2$  fragment orbitals of  $\text{Fe}(\text{CO})_3$  antibonding to the ethylene  $\pi$  set and bonding to ethylene  $\pi^*$ . Not shown in Figure 18.4 are two very high lying molecular orbitals which are the ethylene set, **18.32** and **18.33**, mixed with  $2a_1$  and  $2b_2$  on  $\text{Fe}(\text{CO})_3$  in an antibonding way. Finally, the  $b_1$  and  $a_2$  orbitals on  $\text{Fe}(\text{CO})_3$  are left nonbonding. What we want to stress is that there is a distinct resemblance here to the splitting pattern of a trigonal bipyramidal (Section 17.3), that is, the ethylene and CO ligands are electronically similar. The  $a_2$  and  $b_1$  molecular levels correspond to  $e''$  in a  $D_{3h}$   $\text{ML}_5$  molecule. The  $2b_2$  and  $2a_1$  molecular orbitals are analogs of the  $e'$  set.

Two major geometrical parameters can be used to describe a reaction path for the oxidative coupling of **18.26** to the ferracyclopentane tricarbonyl, **18.27**. They are illustrated from a top view of the complex in **18.34**. Decreasing  $r_1$  causes



formation of the C—C  $\sigma$  and  $\sigma^*$  bonds in the ferracyclopentane. Increasing  $r_2$  maximizes formation of the two Fe—C  $\sigma$  and  $\sigma^*$  bonds. Figure 18.5 shows an idealized Walsh diagram for the orbital energy changes along this reaction path. Since the  $a_2$  and  $b_1$  levels are concentrated at the iron atom and are nonbonding to the two olefins, they remain unperturbed throughout the transformation. Let us carefully look at the other molecular orbitals from the bis-olefin side of the reaction. Molecular  $1a_1$  is concentrated on the ethylene  $\pi$  combination **18.30**. It is stabilized as  $r_1$  decreases becoming the C—C  $\sigma$  bond, shown on the lower right of Figure 18.5. The  $1b_2$  molecular orbital correlates to an Fe—C  $\sigma$  level of  $b_2$  symmetry, also illustrated at the lower right. Notice that the electron density on the olefinic carbons becomes greatly redistributed. This is a result of the other MOs of  $a_1$  and  $b_2$  symmetry mixing into  $1a_1$  and  $1b_2$ , respectively. The exact details are not important to this analysis [22]; however, one can easily see that  $1a_1$  is C—C bonding and  $1b_2$  is Fe—C bonding. The two very high lying MOs not shown in Figure 18.5 smoothly correlate to the C—C  $\sigma^*(b_2)$  and an Fe—C  $\sigma^*(a_1)$  combination. The other molecular orbitals behave in a more complicated way. Let us start with  $3a_1$  on the bis-olefin side of the reaction. It is primarily ethylene  $\pi^*$  antibonding to  $z^2-y^2$ . This is illustrated at the top left side of Figure 18.5. There is substantial density on the olefinic carbons, thus decreasing  $r_1$  stabilizes it. Molecular  $2a_1$  is concentrated heavily on the iron atom, shown also on the top left side. Recall that  $2a_1$  corresponds to one

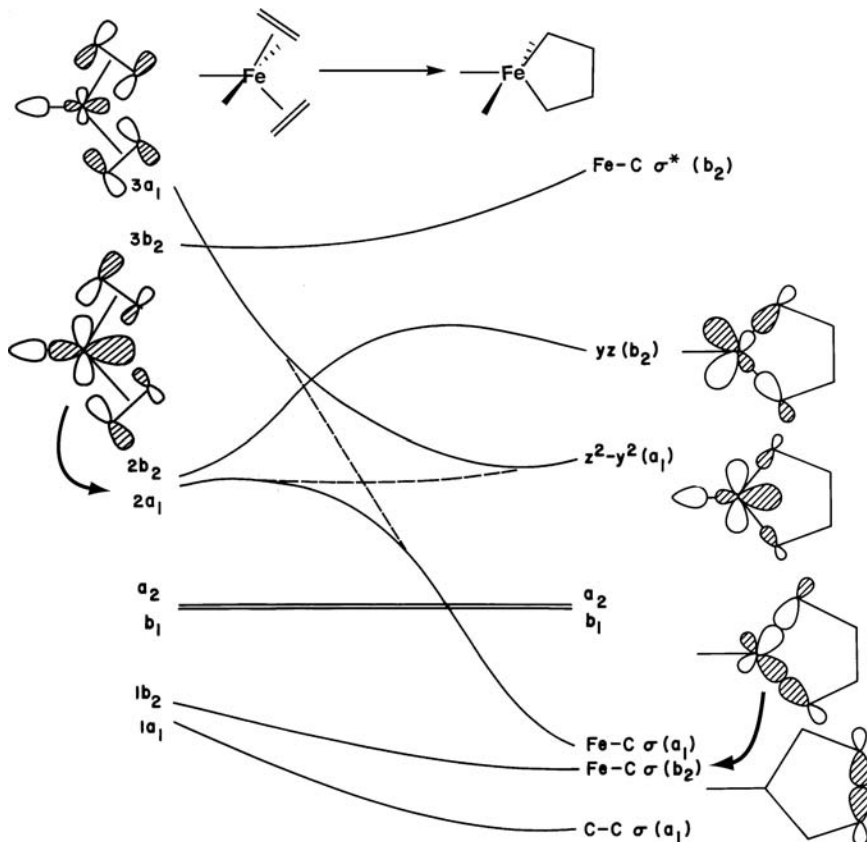


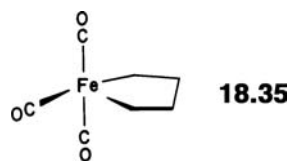
**FIGURE 18.5**

An idealized plot of the orbital energies for the oxidative coupling reaction, **18.26** to **18.27**.

member of the  $e'$  set in a trigonal bipyramidal splitting pattern. Decreasing  $r_1$  and increasing  $r_2$  increases the antibonding between the ethylene  $\pi$  and metal  $d$  functions, and therefore,  $2a_1$  initially rises somewhat in energy. Initially then  $3a_1$  attempts to correlate with the C—C  $\sigma$  or Fe—C  $\sigma$  level and  $2a_1$  with the nonbonding  $z^2-y^2$  or Fe—C  $\sigma^*$  orbital. But molecular orbitals of the same symmetry can never cross and what actually occurs is an avoided crossing (Section 4.7) between  $2a_1$  and  $3a_1$ . This is indicated by the dashed line in Figure 18.5, so  $2a_1$  becomes an Fe—C  $\sigma$  orbital and  $3a_1$  correlates to the nonbonding  $z^2-y^2$  (shown on the middle right side of the figure). Something similar happens to the molecular  $2b_2$  orbital. On the bis-olefin side it is primarily metal  $yz$  antibonding to the olefin  $\pi$  combination in **18.31**. The antibonding between the two olefinic carbons as  $r_1$  decreases makes this orbital rise in energy. An actual correlation to the  $\sigma^*$  C—C level is avoided by the  $3b_2$  molecular orbital and  $2b_2$  actually evolves into the  $yz$  nonbonding orbital shown also on the mid-right side of the figure.

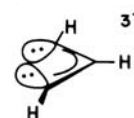
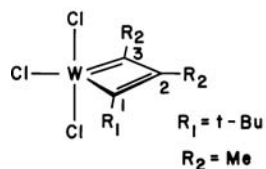
The important result of this exercise is that, given all of the avoided crossings along the reaction path and the complexity that the metal  $d$  functions add to the problem, the reaction is still symmetry-forbidden. The empty  $3a_1$  orbital on the bis-olefin side becomes filled and the filled  $2b_2$  level becomes empty. The reader should note that this is true only if  $z^2-y^2$  lies lower in energy than the  $yz$  orbital. One expects a trigonal bipyramidal splitting pattern on the ferracyclopentane side of the reaction.  $z^2-y^2$  and  $yz$  correspond to the  $e'$  set of  $D_{3h}$   $\text{ML}_5$ . However, we have clearly not shown these two molecular orbitals to be degenerate on the right side of Figure 18.5. The reason behind this lies in the relative  $\sigma$  donor strengths of the equatorial ligands. In the ferracyclopentane intermediate  $z^2-y^2$  is antibonding primarily to carbonyl  $\sigma$ , however in  $yz$  it is antibonding to two alkyl hybrid functions. The latter interaction is stronger (more destabilizing) for energy gap and overlap reasons. Therefore, we are left with the notion that this reaction path which maintains  $C_{2v}$  symmetry cannot be the correct one.

A number of routes can be envisioned which are symmetry-allowed [22]. The most plausible one involves twisting the equatorial carbonyl off from the  $y$  axis as the cyclization proceeds to form **18.35**. **18.35** is ready to coordinate an additional CO



ligand at the sixth coordination site to yield **18.28**. Moving the equatorial CO group lowers the symmetry to the molecule to  $C_s$ . The  $z^2-y^2$  and  $yz$  orbitals at the right of Figure 18.5 now have the same symmetry ( $a'$ ). At some point along the reaction path they undergo an avoided crossing, and therefore, the reaction becomes symmetry-allowed.

The preparation and study of metallacycles has been a subject of active investigation for organometallic chemists. We have just seen one example where metallacycle formation is a key step in a catalytic process and there are several others most notably, olefin metathesis. The metal acts as a geometrical and electronic template in these reactions. For unsaturated metallacycles there are interesting questions concerning delocalization [29]. Certain metal carbynes can react with acetylene to give metallacyclobutadienes as intermediates [30]. One such example of an insoluble molecule is the tungstenacyclobutadiene complex, **18.36** [31]. The compound is quite stable and not very reactive (in contrast to cyclobutadienes



with similar substituents). Its structure [31] shows relatively short W—Cl(C3) and Cl—C2(C3) bond lengths indicative of substantial delocalization. Furthermore, the Cl—C2—C3 bond angle is very oblique, 119°, so that the W—C2 distance is relatively short, 2.12 Å (compared to the W—Cl(C2) distances of 1.86 Å). Furthermore, the W—Cl—C2(W—C3—C2) angle is 78°, somewhat less than the idealized value of 90°. So the compound has distorted from a square to a rhombus. The electronic structure can be developed by interacting a bisdehydroallyl<sup>3-</sup> fragment, **18.37**, with WCl<sub>3</sub><sup>3+</sup>. The full interaction diagram is given in Figure 18.6 at a “square” geometry with  $C_{2v}$  symmetry. The complexity is deceiving; the interaction diagram is easily constructed because  $\sigma$ - and  $\pi$ -type orbitals are orthogonal. On the right side of this figure is the bisdehydroallyl fragment. There are two lone pairs (**18.37**) which are directed toward the two missing hydrogens of an

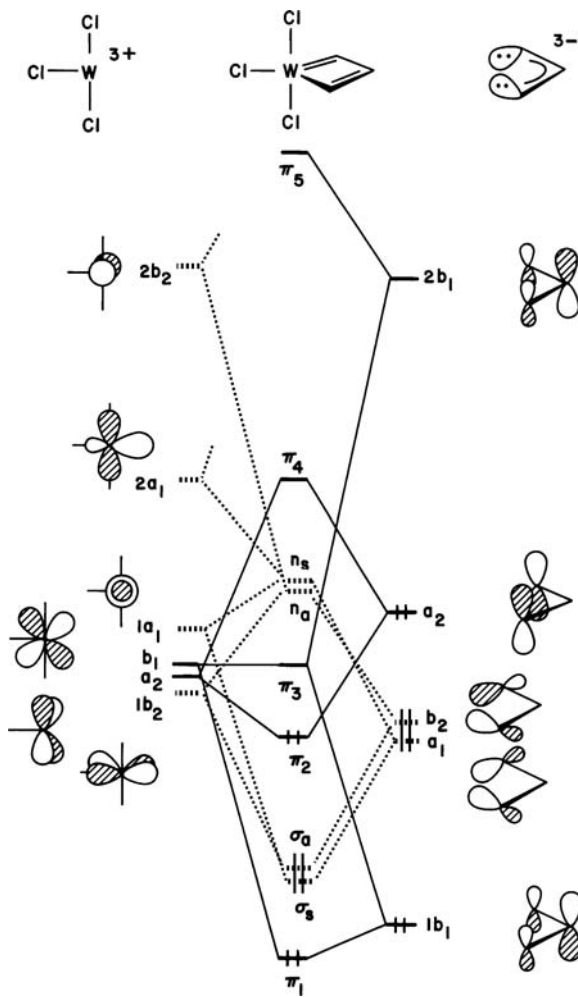


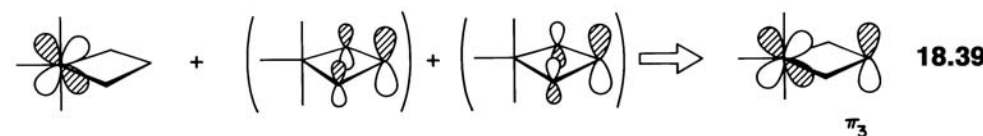
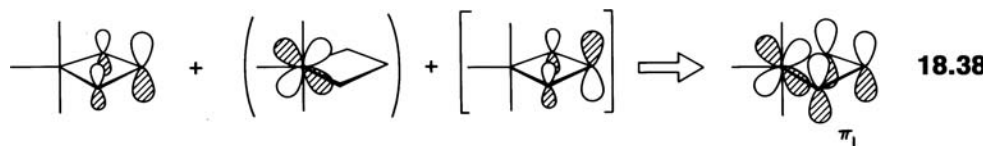
**FIGURE 18.6**

An orbital interaction diagram for the tungsten-metallacyclobutadiene complex **18.36** at a square geometry. The orbitals that contribute to the  $\sigma$  framework are indicated with dotted lines.

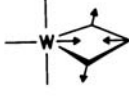
allyl anion. Linear combinations yield two fragment orbitals of  $a_1$  and  $b_2$  symmetry. There are also three  $\pi$  levels,  $1b_1 + a_2 + 2b_1$ . We have formally adjusted the electron count so that  $1b_1$  and  $a_2$  are filled as in the allyl anion. On the left side of the orbital interaction diagram are displayed the valence orbitals of the  $\text{Cl}_3\text{W}^{3+}$  fragment. Since halogens, like alkyl groups, are treated as anionic two-electron donors, the metal is  $\text{W}^{6+}$ . Therefore, the metal is formally  $d^0$ . There is a slight difference in the level ordering for this fragment (and this was also true for the  $\text{Fe}(\text{CO})_3$  case) from that in Figure 18.1. Our earlier treatment of the  $\text{ML}_3$  fragment ignored  $\pi$  effects so the  $b_1$ ,  $a_2$ , and  $1b_2$  levels were all at the same energy. This is not the case for the  $\text{WCl}_3^{3+}$  fragment since Cl is a  $\pi$  donor (see Figure 18.2). The ordering in Figure 18.6 is a reflection of this. All three chloro ligands destabilize  $b_1$ . The two *trans* chlorines destabilize  $a_2$  and only one interacts with  $1b_2$  (the  $\pi$  acceptor CO groups stabilize the  $d$  set so the level ordering in Figure 18.4 is opposite to that shown here).

As previously mentioned, the  $\pi$  and  $\sigma$  molecular orbitals remain orthogonal in this molecule. Figure 18.6 shows the  $\sigma$  component as dotted lines. The  $a_1$  and  $b_2$  lone-pairs of the bisdehydroallyl unit are stabilized primarily by  $1a_1$  and  $1b_2$  along with  $2a_1$  and  $2b_2$  on the metal. The resultant molecular orbitals are listed as  $\sigma_s$  and  $\sigma_a$  for mnemonic purposes in this figure. The molecular levels  $n_s$  and  $n_a$  are primarily  $\text{WCl}_3^{3+}$  fragment orbitals  $1a_1$  and  $1b_2$  antibonding to the lone-pair hybrids on the dehydroallyl fragment. The  $2a_1$  and  $2b_2$  fragment orbitals of  $\text{WCl}_3^{3+}$  also mix into these molecular orbitals.  $n_s$  and  $n_a$  then are hybridized and closely match the  $e'$  set in a trigonal bipyramidal  $\text{ML}_5$  complex.

Overlaying these  $\sigma$  orbitals are the  $\pi$  orbitals of the metallacyclobutadiene. Three fragment orbitals are of  $b_1$  symmetry. Let us start with the molecular level labeled  $\pi_1$ . It is composed, as shown in 18.38, by the in-phase combination of the



lowest allyl  $\pi$  level and metal  $b_1$ . Some allyl  $2b_1$  is mixed in second order. There is an obvious correspondence to the lowest  $\pi$  level in cyclobutadiene (Section 12.3). Likewise,  $\pi_3$ , which is illustrated in 18.39, corresponds to one of the nonbonding cyclobutadiene set. The other member would be the middle allyl  $\pi$  level,  $a_2$ . In this system, and this is part of the reason why the metallacycle is less reactive than cyclobutadiene, the allyl  $a_2$  orbital interacts with the  $a_2$  metal function. The bonding combination,  $\pi_2$  (see 18.40), is markedly stabilized and a healthy energy gap between



$\pi_2$  and  $\pi_3$  ensues. Finally,  $\pi_4$  and  $\pi_5$  are the antibonding analogs of **18.40** and **18.38**, respectively.

The  $\pi$  bonding in the metallacyclobutadiene can be improved still further by the rhomboid distortion indicated by the arrows in **18.41** (see Figure 12.9b for the related distortion in cyclobutadiene).  $\pi_1$  is stabilized as the W—C2 distance (see numbering system in **18.36**) becomes shorter. Overlap between metal  $b_1$ , and allyl  $1b_1$  increases. The LUMO,  $\pi_3$ , raises in energy, see **18.39**. As the C1—C3 distance increases,  $\pi_2$ , **18.40**, will also be stabilized because the antibonding between C1 and C3 is diminished and bonding is increased from C1 and C3 to the metal  $a_2$  orbital. Thus distortion to a rhomboid structure is stabilizing and actually increases  $\pi$  conjugation in the metallacyclobutadiene ring. So is **18.23** aromatic? Certainly in comparison to cyclobutadiene itself,  $\pi_2$  is at a decidedly lower energy than  $\pi_3$  is. There certainly is  $\pi$  delocalization. Computation of the magnetic properties associated with chemical shifts in **18.23** are in concurrence with the idea that that the molecule is aromatic [32]. On the other hand, there is a very low energy pseudorotation motion that leads to a square pyramid where the bisdehydroallyl unit spans apical and a basal position [11a]. The metallacycle here shows marked localization. If this structure is nonaromatic (or close to it), then how much stabilization does aromaticity afford the trigonal bipyramidal?

## 18.4 COMPARISON OF $C_{2v}$ $ML_3$ AND $C_{4v}$ $ML_5$ FRAGMENTS

The valence orbitals of a  $d^6$   $ML_5$  and  $d^8$   $ML_3$  fragment are explicitly shown in Figure 18.7. There is an obvious, direct correspondence between the  $e + b_2$  trio in  $ML_5$  and  $b_1 + 1b_2 + a_2$  in  $ML_3$ . The  $z^2$  fragment orbital in  $ML_5$  also resembles  $x^2 - z^2$ . Both orbitals are hybridized out away from the ligands and present the same symmetry

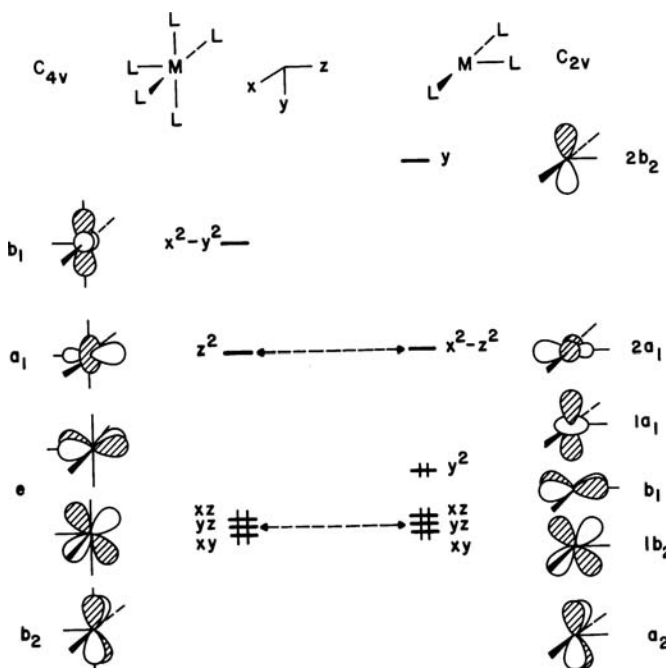
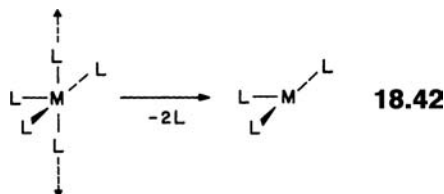


FIGURE 18.7

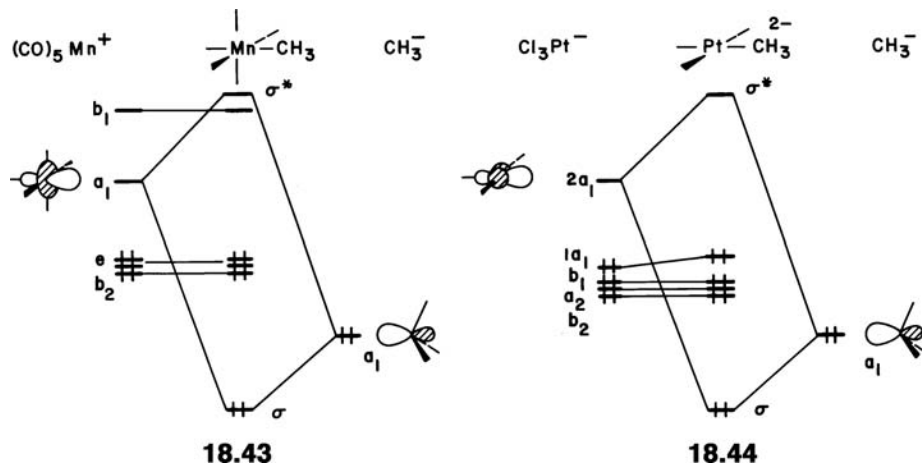
(a) The valence orbitals of a  $d^6$   $C_{4v}$   $ML_5$  and (b) a  $d^8$   $C_{2v}$   $ML_3$  fragment.

properties to an incoming probe ligand. (In this case both are of  $a_1$  symmetry, but what is important is that both have hybrid functions which are cylindrically symmetric.) The  $x^2 - y^2$  orbital in  $ML_5$  does not find a match in the  $ML_3$  fragment. However, it is an orbital that is strongly metal–ligand antibonding. It will not overlap to any significant extent with an additional, sixth ligand (that overlap would be of the  $d$  type). In the  $ML_3$  fragment  $y^2$  ( $1a_1$ ) and  $y$  ( $2b_2$ ) would also be essentially nonbonding to a fourth ligand which forms a square planar complex. In Section 16.1 (see 16.2 and 16.3), we saw that there was a relationship between the molecular orbitals of octahedral and square planar systems. Here we emphasize the correspondence between the orbitals of an  $ML_5$  fragment (forming an octahedral complex with a sixth ligand) and those of an  $ML_3$  fragment (forming a square planar complex with a fourth ligand). In this regard when two *trans* ligands are removed from an  $ML_5$  fragment, 18.42, the antibonding  $x^2 - y^2$



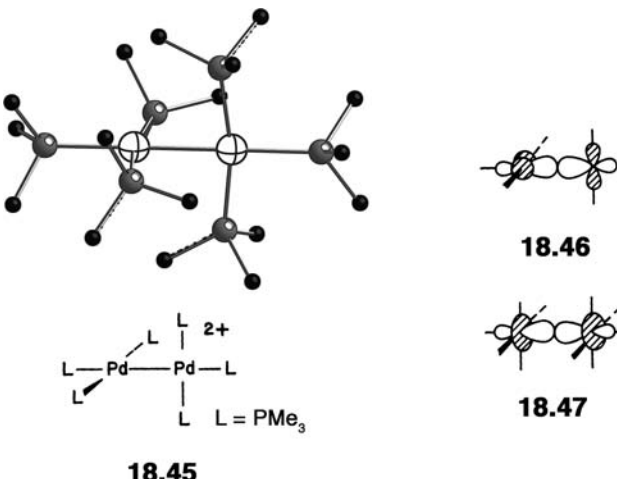
level is greatly stabilized. It becomes  $y^2$  in Figure 18.7 and is doubly occupied for a low spin  $d^8$  system. There is certainly some intermixing of  $x^2 - y^2$ ,  $z^2$ , and metal  $s$  that creates  $1a_1$  and  $2a_1$ . However, it should be clear that the  $ML_5$  and  $ML_3$  fragments have four analogous valence orbitals. In a  $d^6$   $ML_5$  and  $d^8$   $ML_3$  fragment, three are filled and one is empty. The extra two electrons in  $ML_3$  come from the nonbonding  $y^2$ ,  $1a_1$ . The three filled metal orbitals in each fragment are utilized for  $\pi$  bonding. The low-lying, empty fragment orbital in each will form a  $\sigma$  bond with a donor orbital from an extra ligand.

Let us see how this relationship works out in terms of some simple, representative examples. The molecular orbitals of  $CH_3Mn(CO)_5^+$  are developed in 18.43. The



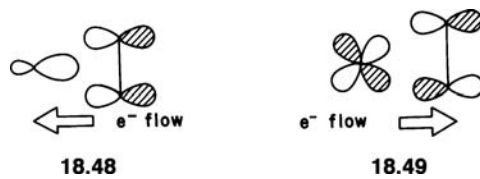
$a_1$  hybrid orbital on  $Mn(CO)_5^+$  interacts strongly with the lone-pair of the methyl group.  $\sigma$  and  $\sigma^*$  molecular orbitals are formed. The rest of the valence orbitals on  $Mn(CO)_5^+$  are left nonbonding to the sixth ligand so we have reconstructed the octahedral splitting pattern with three (filled) MOs lying below two. An orbital interaction diagram for  $Cl_3Pt(CH_3)^{2-}$  is given in 18.44. A square planar splitting pattern is restored. Notice that again the major perturbation between the fragment orbitals occurs between the hybrid orbital on  $Cl_3Pt^-$  and the lone-pair of the methyl

group that forms the  $\sigma$  and  $\sigma^*$  MOs. To be fair the  $1a_1$   $Cl_3Pt^-$  fragment orbital is destabilized slightly by the methyl lone-pair, but this is a minor effect (for overlap reasons) and the other three orbitals on  $Cl_3Pt^-$  are left rigorously nonbonding. A number of  $d^9-d^9$   $M_2L_6$  dimers exist; **18.45** is one such example [33] and

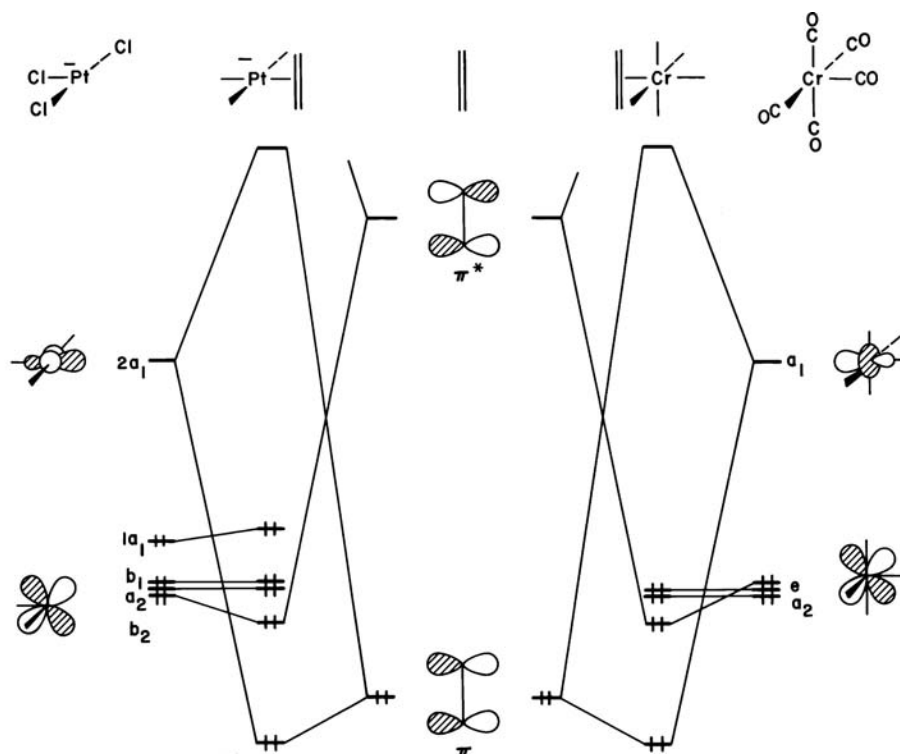


$Pt_2(CO)_2Cl_4^{2-}$  is another [34]. Each metal atom achieves a 16-electron count by the formation of a metal–metal single bond. It is a straightforward matter to build up the MOs of **18.45** from the union of two  $d^9$   $ML_3$  fragments. The  $2a_1$  hybrids form bonding ( $\sigma$ ) and antibonding ( $\sigma^*$ ) molecular orbitals. **18.46** shows the orbital that houses the two electrons from each singly occupied  $2a_1$  fragment orbital. There will also be eight closely spaced MOs which are filled. They are derived from the in-phase and out-of-phase combinations of  $1a_1$ ,  $b_1$ ,  $a_2$ , and  $b_2$  orbitals of the  $ML_3$  unit. The separation between bonding and antibonding partners will depend on the metal–metal separation. This distance is fairly large for the Pd–Pd single bond in **18.45** and the splitting is therefore small. The orbital pattern is not at all different from that derived for  $Re_2(CO)_{10}$  (see Section 17.4). The  $\sigma$  bond, **18.47**, has an obvious resemblance to **18.46** for the  $M_2L_6$  dimers.

The left side of Figure 18.8 builds up the molecular orbitals for Zeise's salt, ethylene-PtCl<sub>3</sub><sup>-</sup>. The ethylene  $\pi$  level is stabilized by the  $2a_1$  acceptor orbital. One member of the group of nonbonding metal functions, namely the  $b_2$  level, has the right symmetry to find a match with ethylene  $\pi^*$ . Consequently, the metal  $b_2$  orbital is also stabilized. This is the essence of the Dewar–Chatt–Duncanson model [35] for metal–olefin bonding. Charge from the filled ethylene  $\pi$  orbital is transferred to an empty metal hybrid orbital, **18.48**. There is also a backbonding component; charge is



transmitted from a filled metal  $d$  function to the empty ethylene  $\pi^*$  orbital. This pattern is also readily apparent for ethylene-Cr(CO)<sub>5</sub> on the right side of Figure 18.8. The ethylene  $\pi$  orbital is stabilized by  $a_1$  on Cr(CO)<sub>5</sub> and one component of the  $e$  set

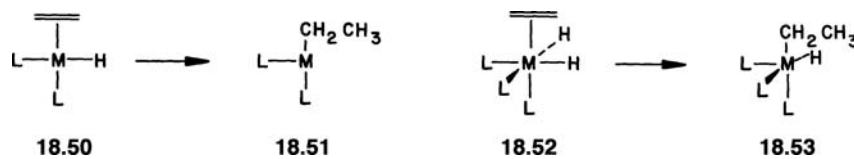
**FIGURE 18.8**

Orbital interaction diagrams for two olefin–metal complexes.

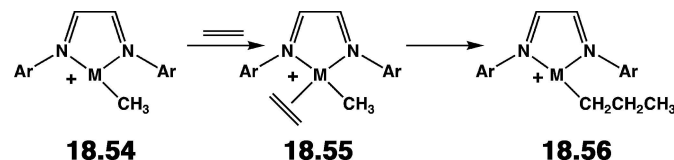
is stabilized by ethylene  $\pi^*$ . The amount of forward and back donation in **18.48** and **18.49** is not expected to be precisely the same in both complexes. We can say with some certainty that both effects will be important [36]. Computationally, this is a quantity which is difficult to pin down. It is sensitive to the method, parameters (basis set, and so on), and the exact details for partitioning electron density between the atoms. What we can do is to establish trends. If  $\pi$  acceptor groups are substituted on the ethylene, then the energies of  $\pi$  and  $\pi^*$  drop. This makes the **18.49** ( $b_2 + \pi^*$  or  $e + \pi^*$ ) interaction stronger since the energy gap between the fragment orbitals becomes smaller. The **18.48** interaction ( $a_1 + \pi$ ) must necessarily become smaller at the same time since the energy gap between  $a_1$  and  $\pi$  is larger. On the other hand substitution of  $\pi$  donors on the ethylene ligand causes **18.48** to become stronger and **18.49** weaker. With early transition metals the filled  $d$  AOs will be high in energy so the **18.49** component becomes more important at the expense of **18.48**. Late transition metals will have the converse situation.

Returning to Figure 18.8 notice that if the ethylene were rotated by  $90^\circ$  so that it lies in the  $PtCl_3$  plane, the interaction between  $\pi$  and  $2a_1$  remains the same. The  $2a_1$  fragment orbital is cylindrically symmetric. Now  $\pi^*$  interacts with  $b_1$  rather than  $b_2$ . The overlap of the two metal orbitals with  $\pi^*$  is similar. The same situation applies to (ethylene) $Cr(CO)_5$ . Rotation of ethylene by  $45^\circ$  causes  $\pi^*$  to interact with a combination of the two members of the  $e$  set. However, in both cases the  $\pi$  orbital interacts with a filled metal orbital [36] upon rotation. Therefore, the most stable orientations are those shown in Figure 18.8.

The analogy between the  $C_{2v}$   $ML_3$  and  $C_{4v}$ ,  $ML_5$  fragments can be carried much further. For example, the electronic features of the olefin insertion reaction [37,38], **18.50–18.51**, in  $d^8$  complexes are very similar to the catalytic olefin hydrogenation step for **18.52–18.53** for  $d^6$  molecules [38,39]. The olefin insertion reaction is



directly analogous to olefin polymerization reactions using late transition metals [40] (mainly  $d^8$ ) with the general structure given by **18.54**. Here the diimine ligand is counted as being a bidentate  $\pi$  donor. The Ar groups are very bulky aryl groups so



the olefin is forced to lie in the N<sub>2</sub>M plane, **18.55**. **18.55** then undergoes olefin insertion to yield a growing polymer, **18.56** [41]. There are a number of ways to view the electronic details associated with these reactions. Starting from **18.50** and **18.52** we shall use the hydride s AO and ethylene  $\pi$  fragment orbitals to combine with the orbitals of the metal. This is shown on the left side of Figure 18.9. The in-phase combination of H s and ethylene  $\pi$  interacts with an s AO at the metal whereas, the out-of-phase combination overlaps with  $x^2-y^2$ . The metal–ligand bonding

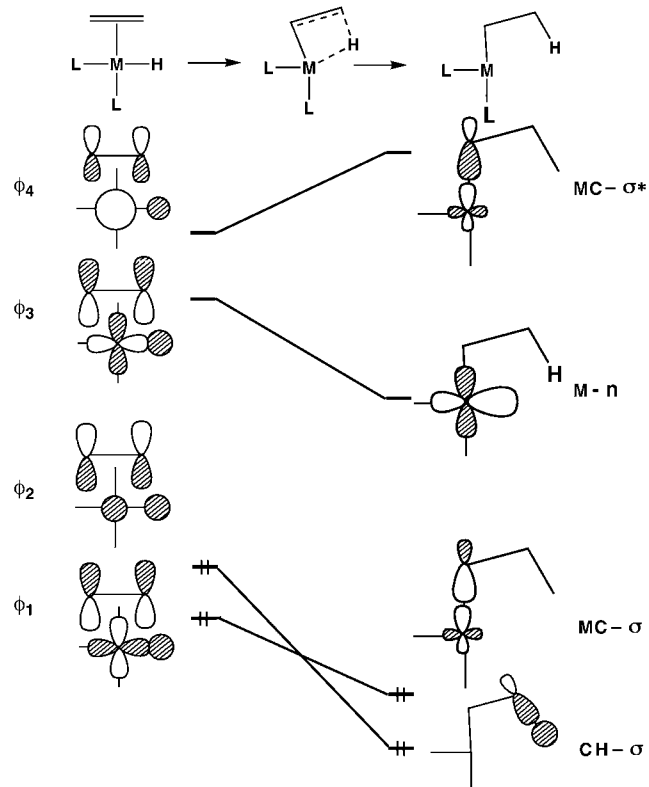


**FIGURE 18.9**

Idealized orbital correlation diagram for the olefin insertion reaction.

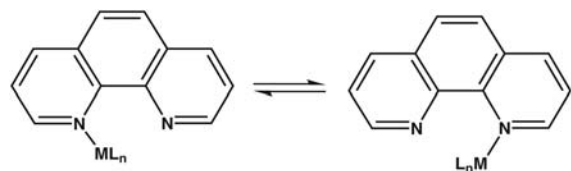
combinations are listed as  $\phi_1$  and  $\phi_2$  and the antibonding analogs as  $\phi_3$  and  $\phi_4$ . Along the reaction path the coordinated ethylene must slip and rotate to an  $\eta^1$  position and, of course the hydride ligand must migrate to the uncoordinated carbon atom of the ethylene. This is a very low symmetry process so there is much intermixing between the molecular orbitals along the reaction coordinate. Figure 18.9 is a highly idealized orbital correlation diagram for the reaction. Starting with  $\phi_2$  there is bonding between the hydride s AO and the  $p$  AO of the  $\beta$  carbon. The MO will be greatly stabilized; it ultimately evolves into the C—H  $\sigma$  orbital. On the other hand, the interaction between hydride s and carbon  $p$  in  $\phi_1$  is antibonding. But instead of increasing in energy  $\phi_2$  mixes into it with the opposite of the phase shown in Figure 18.9. Cancellation of hydride s character occurs and the orbital ultimately evolves into the M—C  $\sigma$  level.  $\phi_4$  mixes into  $\phi_3$  with the phase shown. Cancellation takes place with ethylene  $\pi$  and hydride s and so  $\phi_3$  becomes the nonbonding metal  $a_1$  orbital in the  $ML_3$  or  $ML_5$  product. Finally mixing  $\phi_3$  into  $\phi_4$  with the opposite phase yields the M—C  $\sigma^*$  MO. The analysis in Figure 18.9 does not show the genesis of the activation barrier for this reaction. In fact it is this olefin insertion step which is the rate-determining one for the reaction sequence of **18.54–18.56**. This should be sensitive to the strength of the metal–olefin bond. Bonding between metal  $d$  and ethylene  $\pi$  in particularly  $\phi_1$  is diminished greatly along the early portion of the reaction path. Therefore, a higher barrier will be reflected by a larger bond energy. This is indeed the case. The calculated barriers for the **18.55** to **18.56** step are 9.9, 16.2, and 25.3 kcal/mol for  $M = Ni$ , Pd and Pt, respectively [42]. The metal–ethylene binding energy, the exothermicity of the **18.54–18.55** step, was calculated to be 27.9, 31.7, and 43.6 kcal/mol for  $M = Ni$ , Pd, and Pt, respectively [42]. Of course the strength of the M—H bond is also important in setting the barrier size and this also runs in the order  $Ni < Pd < Pt$  [43]. The bond strengths are a reflection of the facts that the Ni  $d$  AOs are quite contracted and do not overlap with ligand orbitals as effectively as the  $4d$  and  $5d$  AOs. Also the relativistic contraction of the Pt  $6s$  AO also leads to a larger overlap with H s or C  $p$  AOs. What has been neglected in the analysis given in Figure 18.9 is the intervention of ethylene  $\pi^*$ . The mixing with ethylene  $\pi^*$  creates the node at the  $\beta$  carbon for  $\phi_2$ – $\phi_4$ . In fact a similar correlation diagram can be drawn using just  $\phi_1$ ,  $\phi_3$ , and  $\pi^*$  [37]. We shall return to the very related Ziegler–Natta polymerization in Chapter 20 where yet another analysis will be given. The electronic factors that modify the *trans* M—L bond length for octahedral  $L'ML_5$  complexes are identical to those in square planar  $L'ML_3$  [44]. These studies utilized extended Hückel, DFT, and ab initio techniques. The important lesson is that the basic electronic structure of these molecules, as set by their fragment orbitals, is expected to be invariant with respect to the computational technique.

---

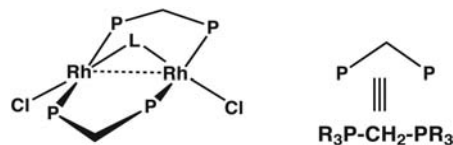
## PROBLEMS

---

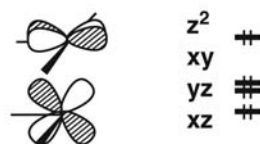
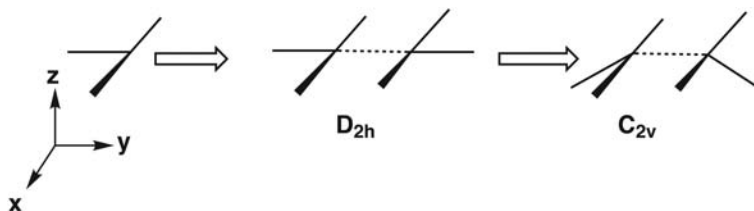
- 18.1.** A number of diazines can coordinate to  $d^6$ - $ML_5$  and  $d^8$ - $ML_3$  complexes. NMR studies have shown that the  $ML_n$  units can shift from one coordination site to another with low to moderate activation energies depending upon the diazine and  $ML_n$  unit. An example is provided by phenanthroline- $Cr(CO)_5$  and phenanthroline- $Pt(PEt_3)_2Cl^+$ . Develop a model for this rearrangement using the two nitrogen lone pairs for these cases and show why the activation energy in the Cr compound is high (18.9 kcal/mol), whereas that for the Pt complex is low (<9.5 kcal/mol).



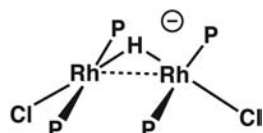
**18.2.** In this set of problems, we are going to study the bonding in a couple of so-called A-frame complexes, see below. The interested reader is referred to Reference [45] for many other examples.



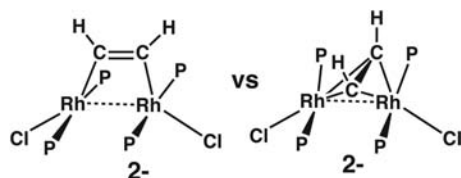
- a. We need to construct the most important valence orbitals for the Rh<sub>2</sub>(Me<sub>2</sub>PCH<sub>2</sub>PM<sub>2</sub>)Cl<sub>2</sub> fragment. There are five orbitals in the  $C_{2v}$ ML<sub>3</sub> unit. We use three of them to interact with the bridging L ligand. These are shown below. The  $z^2$  and  $xz$  orbitals will only be used for the purpose of electron counting. Combine two ML<sub>3</sub> fragments to form a  $D_{2h}$  M<sub>2</sub>L<sub>6</sub> dimer and then consider what occurs when the Cl—Rh—Rh angle are bent from 180° to ~150°.



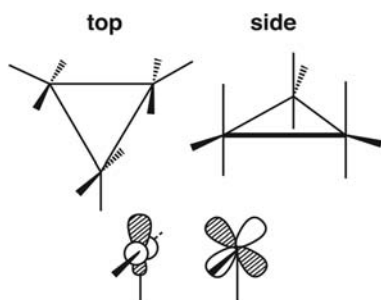
- b. Using the six fragment orbitals in (a) use L = H<sup>-</sup> to build up the important valence orbitals. What is the expected Rh—Rh bond order?



- c. Acetylenes can also be incorporated as a ligand in the A-frame structure. Taking the acetylene as a formal H<sub>2</sub>C<sub>2</sub><sup>2-</sup> fragment, construct interaction diagrams for the two orientations shown below? Which is more stable?



- 18.3.** Consider a hypothetical cyclopropane model,  $\text{Pd}_3\text{Cl}_9^{3-}$  shown from the top and side view below. Using the  $2a_1$  and  $b_2$  orbitals of  $\text{PdCl}_3^-$ , take symmetry-adapted combinations to form the MOs. This is not a stable molecule. In Chapter 19 we see a  $\text{M}_3\text{Cl}_9$  molecule at the same electron count which is a known molecule.



## REFERENCES

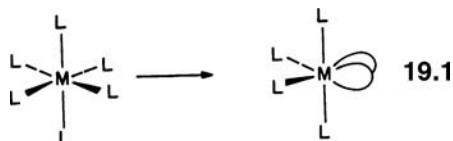
- M. Barrow, H. B. Bürgi, D. K. Johnson, and L. M. Venanzi, *J. Am. Chem. Soc.*, **98**, 2356 (1976); N. C. Baeziger, K. M. Dittemore, and J. R. Doyle, *Inorg. Chem.*, **13**, 805 (1974).
- D. G. Dick, D. W. Stephan, and C. F. Campana, *Can. J. Chem.*, **68**, 628 (1990).
- V. V. Saraev, P. B. Kraikivskii, I. Svoboda, A. S. Kuzakov, and R. F. Jordan, *J. Phys. Chem. A*, **112**, 12449 (2008).
- W. Baratta, S. Stoccero, A. Doppiu, E. Herdtweck, A. Zucca, and P. Rigo, *Angew. Chem. Int. Ed.*, **42**, 105 (2003) and references therein.
- J. P. Stambuli, C. D. Incarvito, M. Buhl, and J. F. Hartwig, *J. Am. Chem. Soc.*, **126**, 1184 (2004).
- Y. W. Yared, S. L. Miles, R. Bau, and C. A. Reed, *J. Am. Chem. Soc.*, **99**, 7076 (1977).
- S. Alvarez, *Coord. Chem. Rev.*, **193–195**, 13 (1999).
- P. Zhao, C. Krug, and J. F. Hartwig, *J. Am. Chem. Soc.*, **127**, 12066 (2005).
- H. Braunschweig, K. Radacki, and K. Uttinger, *Chem. Eur. J.*, **14**, 7858 (2008) and references therein.
- H.-G. Cho and L. Andrews, *J. Am. Chem. Soc.*, **130**, 15836 (2008); H. G. Cho, L. Andrews, B. Vlaisavljevich, and L. Gagliardi, *Organometallics*, **28**, 5623, 6871 (2009).
- (a) T. A. Albright, *private communications*; (b) O. Ozerov, *private communications*.
- (a) M. I. Ingleson, H. Fan, M. Pink, J. Tomaszewski, and K. G. Caulton, *J. Am. Chem. Soc.*, **128**, 1804 (2006); M. J. Ingleson, B. C. Fullmer, D. T. Buschhorn, H. Fan, M. Pink, J. C. Huffman, and K. G. Caulton, *Inorg. Chem.*, **47**, 407 (2008); (b) H. Fan, B. C. Fullmer, M. Pink, and K. G. Caulton, *Angew. Chem. Int. Ed.*, **47**, 9112 (2008).
- C. A. Jolly and D. S. Marynick, *Inorg. Chem.*, **28**, 2893 (1989).
- C. R. Landis, T. Cleveland, and T. K. Firman, *J. Am. Chem. Soc.*, **117**, 1859 (1995).
- J. S. Gotra, M. B. Hursthouse, and A. J. Welch, *J. Chem. Soc., Dalton Trans.*, 669 (1973).
- M. Westerhausen, M. Hartmann, and W. Schwartz, *Inorg. Chim. Acta*, **269**, 91 (1998).
- A. Haaland, K.-G. Martinsen, D. J. Shorokhov, G. V. Girichev, and V. I. Sokolov, *J. Chem. Soc., Dalton Trans.*, 2787 (1998) and references therein.
- A. A. Palacios, P. Alemany, and S. Alvarez, *Inorg. Chem.*, **38**, 707 (1999).

19. J. T. Anhaus, T. P. Kee, M. H. Schonfeld, and R. R. Schrock, *J. Am. Chem. Soc.*, **112**, 1642 (1990).
20. D. F. Eppley, P. T. Wolczanski, and G. D. Van Duyne, *Angew. Chem. Int. Ed.*, **30**, 584 (1991).
21. E. Weissberger and P. Laszlo, *Acc. Chem. Res.*, **9**, 209 (1976).
22. A. Stockis and R. Hoffmann, *J. Am. Chem. Soc.*, **102**, 2952 (1980).
23. R. G. Pearson, *Fortschr. Chem. Forsch.*, **41**, 75 (1973).
24. R. G. Pearson, *Symmetry Rules for Chemical Reactions*, Wiley, New York (1976).
25. P. S. Braterman, *J. Chem. Soc. Chem. Commun.*, 70 (1979).
26. R. J. McKinney, D. L. Thorn, R. Hoffmann, and A. Stockis, *J. Am. Chem. Soc.*, **103**, 2595 (1981).
27. Y. Wakatsuki, O. Nomura, H. Tone, and H. Yamazaki, *J. Chem. Soc., Perkin II*, 1344 (1980).
28. J. W. Lauher and R. Hoffmann, *J. Am. Chem. Soc.*, **98**, 1729 (1976).
29. See, for example, D. L. Thorn and R. Hoffmann, *Nouv. J. Chim.*, **3**, 39 (1979); J. R. Bleeke, *Chem. Rev.*, **101**, 1205 (2001) and references therein.
30. R. R. Schrock, *Adv. Synth. Cat.*, **349**, 41 (2007).
31. S. F. Pederson, R. R. Schrock, M. R. Churchill, and H. J. Wasserman, *J. Am. Chem. Soc.*, **104**, 6808 (1982).
32. F. Erdman, III, and D. B. Lawson, *J. Organomet. Chem.*, **690**, 4939 (2005).
33. W. Lin, S. R. Wilson, and G. S. Girolami, *Inorg. Chem.*, **33**, 2265 (1994).
34. A. Modinos and P. Woodward, *J. Chem. Soc., Dalton Trans.*, 1516 (1975).
35. J. Chatt and L. A. Duncanson, *J. Chem. Soc.*, 2939 (1953); M. J. S. Dewar, *Bull. Soc. Chim. Fr.*, **18**, C79 (1951); for an amusing historical perspective see M. J. S. Dewar and G. P. Ford, *J. Am. Chem. Soc.*, **101**, 783 (1979).
36. T. A. Albright, R. Hoffmann, J. C. Thibeault, and D. L. Thorn, *J. Am. Chem. Soc.*, **101**, 3801 (1979); P. J. Hay, *J. Am. Chem. Soc.*, **103**, 1390 (1981); T. Ziegler and A. Rauk, *Inorg. Chem.*, **18**, 1558 (1979); for more recent studies, see G. Frenking and N. Fröhlich, *Chem. Rev.*, **100**, 717 (2000) and references therein.
37. D. L. Thorn and R. Hoffmann, *J. Am. Chem. Soc.*, **100**, 2079 (1978); see also S. Creve, H. Oevering, and B. B. Coussenes, *Organometallics*, **18**, 1967 (1999).
38. For a review of the theoretical work on these reactions, see S. Niu and M. B. Hall, *Chem. Rev.*, **100**, 353 (2000).
39. A. Dedieu, *Inorg. Chem.*, **19**, 375 (1980); A. Dedieu, *Inorg. Chem.*, **20**, 2803 (1981); A. Dedieu and A. Strich, *Inorg. Chem.*, **18**, 2940 (1979).
40. For the initial experimental work, L. K. Johnson, C. M. Killian, and M. Brookhart, *J. Am. Chem. Soc.*, **117**, 6414 (1995).
41. For theoretical work, see A. Michalak and T. Ziegler, in *Computational Modelling of Homogeneous Reactions*, F. Mascras and A. Lledos, editors, Kluwer Academic Press (2002), pp. 57–78; R. D. J. Froese, D. G. Musaev, and K. Morokuma, *J. Am. Chem. Soc.*, **120**, 1581 (1998); D. G. Musaev, R. D. J. Froese, and K. Morokuma, *Organometallics*, **17**, 1850 (1998); K. Albert, P. Gisdakis, and N. Rösch, *Organometallics*, **17**, 1608 (1998); P. E. M. Siegbahn, S. Strömberg, and K. Zetterberg, *Organometallics*, **15**, 5542 (1996).
42. D. G. Musaev, R. D. J. Froese, and K. Morokuma, *New J. Chem.*, **21**, 1269 (1997); These values are very close to those obtained by S. Strömberg, K. Zetterberg, and P. E. M. Siegbahn, *J. Chem. Soc., Dalton Trans.*, 4147 (1997).
43. G. Ohanesian and W. A. Goddard, III, *Acc. Chem. Res.*, **23**, 386 (1990).
44. J. K. Burdett and T. A. Albright, *Inorg. Chem.*, **18**, 2112 (1979).
45. D. M. Hoffman and R. Hoffmann, *Inorg. Chem.*, **20**, 3543 (1981).

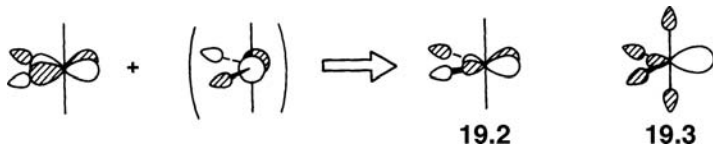
# The $ML_2$ and $ML_4$ Fragments

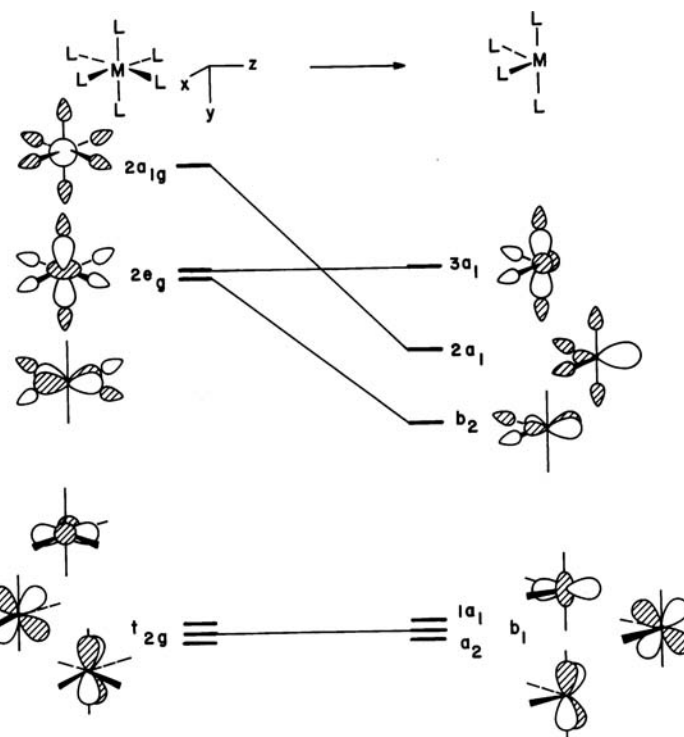
## 19.1 DEVELOPMENT OF THE $C_{2v}$ $ML_4$ FRAGMENT ORBITALS

The removal of two cis ligands from an octahedron generates the  $C_{2v}$   $ML_4$  fragment, 19.1 [1]. The lessons we have learned from the  $d^6C_{4v}$   $ML_5$  and  $d^8C_{2v}$   $ML_3$  fragments



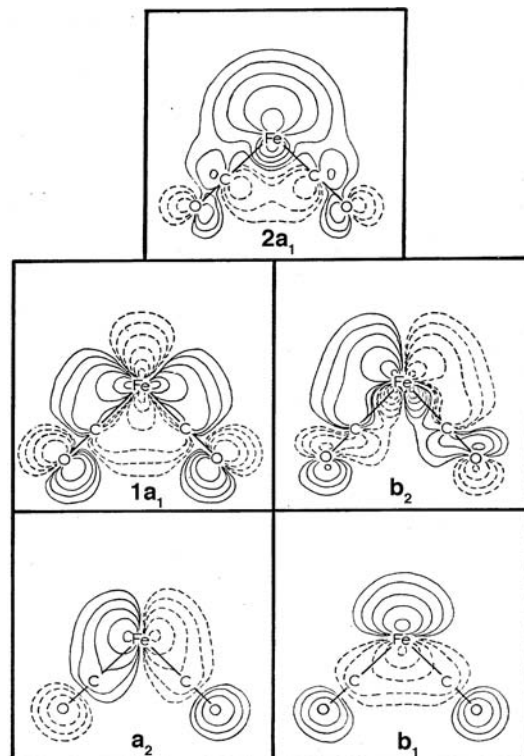
in the previous two chapters suggest that removal of these two ligands will create two empty hybrid orbitals for a  $d^6$  fragment at moderate energies that are directed toward the missing ligands. Figure 19.1 shows this decomposition. The three members of  $t_{2g}$  are not affected by the perturbation, nor basically is one member of the  $e_g$  set. The other member of  $e_g$ ,  $xz$  using the coordinate system at the top of this figure, and  $2a_{1g}$  are stabilized greatly. In both cases, a substantial portion of metal–ligand antibonding is removed. Both orbitals are also hybridized by mixing metal  $x$  and  $z$  into them since the symmetry of the molecule is lowered from  $O_h$  to  $C_{2v}$ . For the  $b_2$  case, the  $x$  component of  $2t_{1u}$  mixes in a bonding way with respect to the overlap between the metal function in one orbital and the ligand portion in the other, see 19.2. The  $2a_1$  orbital also is perturbed by metal  $z$  from the  $2t_{1u}$  set, yielding 19.3. The two empty hybrids of 19.1 generate  $b_2$  and  $a_1$  symmetry adapted orbitals that correspond to those in 19.2 and 19.3. The remainder of the octahedral



**FIGURE 19.1**

Construction of the valence orbitals of a  $C_{2v}$   $ML_4$  fragment from octahedral  $ML_6$ .

set is basically unperturbed. Note from Figure 19.1 that there has been some redistribution of  $d$  character in  $1a_1$  and  $3a_1$ . Most of this is due to changing the ligand field (the coordinate system has also been changed from that normally given for an octahedron so that the  $ML_4$  fragment orbitals are simpler combinations). The

**FIGURE 19.2**

Contour plots of the important valence orbitals in  $Fe(CO)_4$ . These are orbitals from an extended Hückel calculation that have been plotted in the  $xz$  plane (see Figure 19.1). The  $a_2$  and  $b_1$  MOs are plotted 1.5 Å from this plane in the  $y$  direction.

components of  $1a_1$  and  $3a_1$  intermix so that  $3a_1$  retains maximal antibonding to the ligands and  $1a_1$  remains nonbonding.

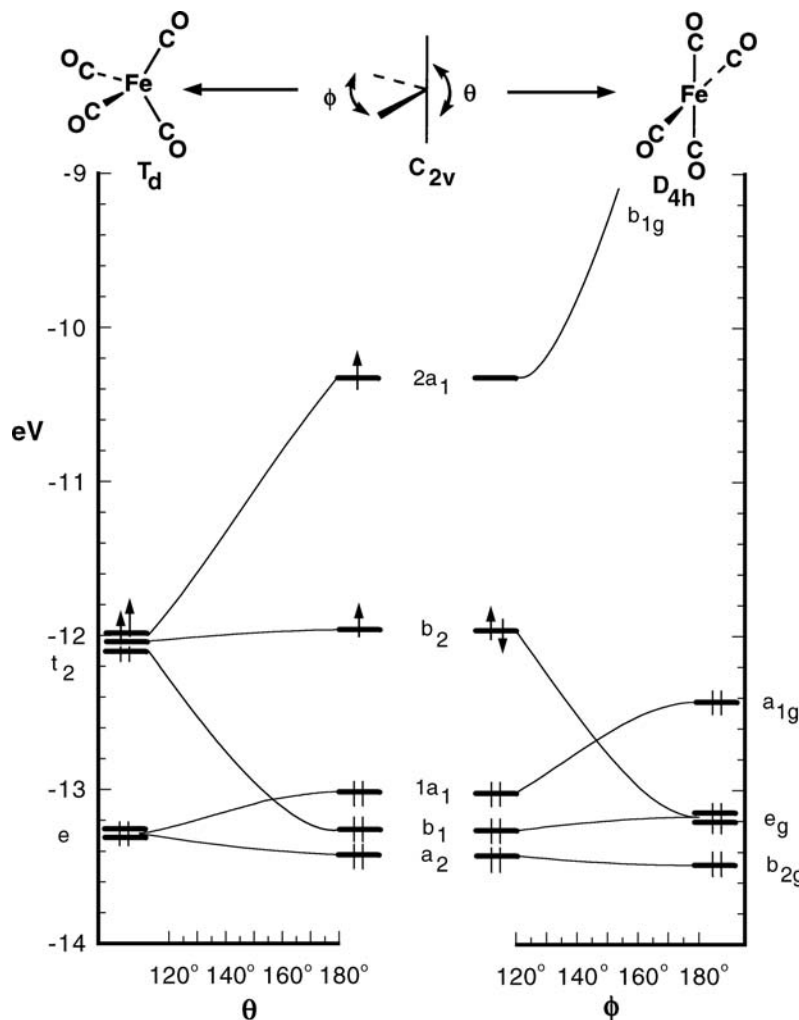
The composition of the six  $ML_4$  fragment orbitals depends not only on the electronegativity of the metal and the diffuseness of the metal  $d$  orbitals, and the nature of the L group is also critical. In Figure 19.2 the orbitals of  $\text{Fe}(\text{CO})_4$  are plotted at the extended Hückel level. The geometry is idealized from that in the octahedron parent so that one C—Fe—C angles is  $90^\circ$  while the other is  $180^\circ$ . Note that there is significant CO  $\pi^*$  character for all five orbitals (the  $3a_1$  molecular orbital, is not plotted). A  $d^6$   $M(\text{CO})_4$  fragment then will have  $1a_2$ ,  $1b_2$ , and  $1a_1$  filled. The  $d^6$   $M(\text{CO})_4$  fragment is set up to interact with either two external ligands or a single four-electron donor (say a cyclobutadiene or butadiene ligand; both cyclobutadiene-Cr(CO)<sub>4</sub> and butadiene-Cr(CO)<sub>4</sub> are well-known organometallic compounds) via its empty  $2a_1$  and  $b_2$  fragment orbitals. An octahedral-like splitting pattern will be restored. The hybridization of the  $b_2$  and  $2a_1$  orbitals is such that the wavefunctions extend outward toward the missing carbonyl ligands. It is these two MOs that form the dominant  $\sigma$  interactions with any incoming ligand.

## 19.2 THE Fe(CO)<sub>4</sub> STORY

An interesting situation arises with the addition of two electrons to  $\text{Cr}(\text{CO})_4$  to give  $\text{Fe}(\text{CO})_4$ . A low spin  $d^8$  species would have the  $b_2$  level filled. But there is not so great of an energy difference between  $b_2$  and the empty  $2a_1$  orbital. We are back again to the singlet–triplet energy difference we first encountered with methylene (Section 8.8). Actually, there are a number of similarities between  $\text{Fe}(\text{CO})_4$  and  $\text{CH}_2$  besides the spin multiplicity questions. Both species have orbitals of  $a_1$  and  $b_2$  (or  $b_1$ ) symmetry with a small energy difference between them. The singlet–triplet energy difference in each case is sensitive to the geometry. Figure 19.3 shows the essence of two distortion pathways that are of interest to us. The left side pertains to the triplet  $\text{Fe}(\text{CO})_4$  molecule. The  $b_1$  orbital as shown in 19.4 is destabilized, becoming one member of the  $t_2$  set on distortion to a tetrahedron. Another member of  $t_2$  is  $b_2$ , which does not

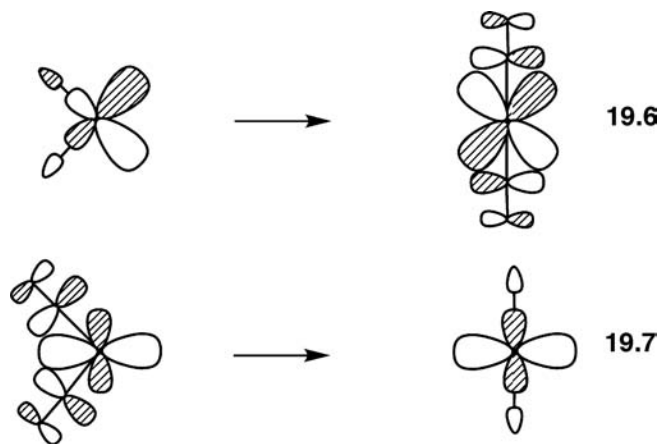


change energy much upon distortion to the tetrahedron. Finally,  $2a_1$  undergoes an avoided crossing with  $3a_1$ . There is also considerable interorbital mixing with  $1a_1$  so that ultimately  $2a_1$  becomes the third member of  $t_2$ , 19.5. The  $3a_1$  level is converted into a high-lying metal orbital of  $a_1$  symmetry. The  $a_2$  and  $1a_1$  MOs basically stay at constant energy yielding the  $e$  set. On the surface it seems that there should be no tendency for triplet  $\text{Fe}(\text{CO})_4$  to adopt a tetrahedral geometry. The one electron in  $2a_1$  that is stabilized certainly cannot overrule the two electrons in  $b_1$  that rise in energy. However, recall from related distortions (see, for example, Sections 15.4 and 16.4) that there is a bonding equivalent to 19.4 which is stabilized. This partially offsets the upward slope of  $b_1$ . The optimum geometry of triplet  $\text{Fe}(\text{CO})_4$  then lies somewhere between these two extremes. The exact details are still open to uncertainty [2]. Analysis of the IR spectra taken in various low temperature matrices gave C—Fe—C angles (as defined in Figure 19.3) of  $\theta = 145^\circ$  and  $\phi = 120^\circ$  with uncertainties of  $\pm 3^\circ$  [3]. On the theoretical side, density functional LDA calculations with nonlocal corrections [4] gave  $\theta = 147^\circ$  and  $\phi = 99^\circ$  and more recent hybrid density functional calculations [5]

**FIGURE 19.3**

Walsh diagrams for bending triplet  $\text{Fe}(\text{CO})_4$  toward a tetrahedron (left) and singlet  $\text{Fe}(\text{CO})_4$  to a square plane (right).

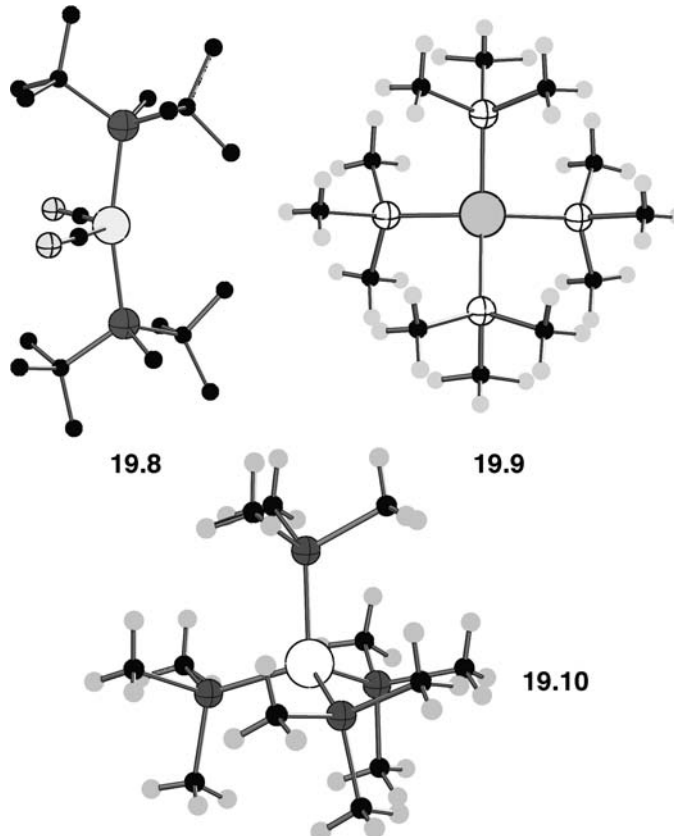
yielded a very similar structure with  $\theta = 152^\circ$  and  $\phi = 97^\circ$ . Turning to  $\text{Fe}(\text{CO})_4$  now with a singlet electronic configuration the right side of Figure 19.3 shows the distortion to a square planar structure. The hybridized  $b_2$  orbital is stabilized and becomes one member of  $e_g$ , 19.6. Antibonding between metal  $d$  and the ligands is reduced.



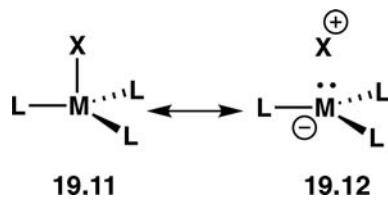
It also must lose its hybridization, but bonding to  $\text{CO} \pi^*$  is turned on. There is again a complicated intermixing between  $1a_1$ ,  $2a_1$ , and  $3a_1$  so that ultimately  $1a_1$  becomes

$a_{1g}$  ( $z^2$  using the normal coordinate system of a square plane),  $2a_1$  becomes  $a_{2u}$  ( $z$ ), and  $3a_1$  becomes  $b_{1g}$  ( $x^2 - y^2$ ). What is critical here is that at the  $C_{2v}$  structure  $1a_1$  has maximal bonding to  $\pi^*$ . This can readily be seen from the contour plot of it in Figure 19.2. On going to the square plane this is lost and antibonding to carbonyl  $\sigma$  is turned on, **19.7**, so this molecular orbital is destabilized. Therefore, the energetic behavior of  $b_2$  and  $1a_1$  cancel each other and the distortion is energetically a soft one. Ultrafast electron diffraction [6] of singlet Fe(CO)<sub>4</sub> has given a structure where  $\theta = 169 \pm 2^\circ$  and  $\phi = 125 \pm 3^\circ$ . Theory puts  $\theta = 168^\circ$  and  $\phi = 130^\circ$  for the LDA with nonlocal corrections [4] and  $\theta = 162^\circ$  and  $\phi = 112^\circ$  for the hybrid DFT ones [5]. So the structure is one between the butterfly  $C_{2v}$  geometry and the square plane. Certainly, on the basis of electron counting, one would expect a square planar complex for this 16-electron system. Indeed there are many other 16-electron complexes that are square planar (see Section 16.4); we return to this point shortly. The energy difference between singlet and triplet Fe(CO)<sub>4</sub> is not known with any certainty. Experimentally the triplet does lie lower in energy than the singlet [2]. On the theoretical front, a wide range of values exist (from  $-6$  to  $21$  kcal/mol) depending on the exact nature of the functional [7]. The most likely value, however, is around  $2\text{--}4$  kcal/mol. Not surprisingly, the singlet structure was calculated to be the most stable one for Ru(CO)<sub>4</sub> and Os(CO)<sub>4</sub> [4]. The addition of two more electrons fully populates  $2a_1$  and  $b_2$ . The structure of a complex such as Na<sub>2</sub>Fe(CO)<sub>4</sub> then lies very close to the tetrahedron [8].

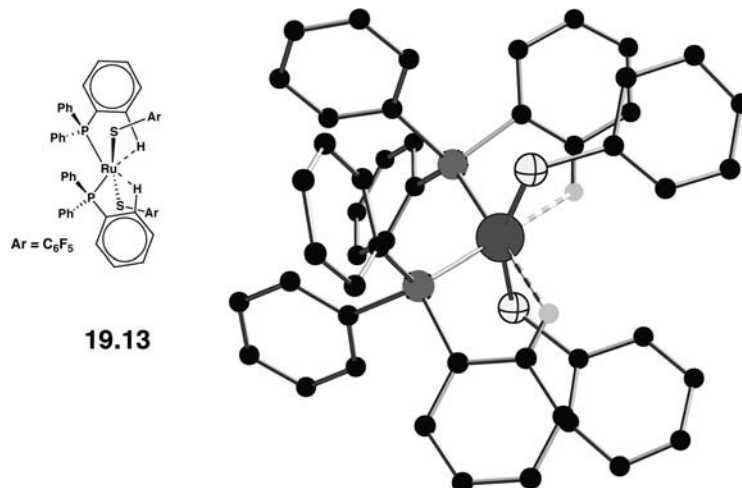
ML<sub>4</sub> complexes remain at the sawhorse geometry when two CO ligands are replaced by  $\sigma$ -donor phosphines, for example, Ru(CO)<sub>2</sub>[P(*t*-Bu)<sub>2</sub>Me]<sub>3</sub><sub>2</sub> [9], **19.8**. Here P—Ru—P =  $165.6^\circ$  and C—Ru—C =  $133.4^\circ$ . In other words, the loss of  $\pi$ -bonding in **19.7** is energetically more important than the gain in **19.6**. The structure with four phosphines can be considered to be one with an approximate



$D_{2d}$  distortion slightly away from a square plane. For example, in  $\text{Rh}(\text{PMe}_3)_4^+$  **19.9**, two P—Rh—P angles are  $148.3^\circ$  and  $151.4^\circ$  [10]. There are two other structures with different anions [11]; the P—Rh—P angles are  $139.5^\circ$  and  $144.3^\circ$  in one and  $151.3^\circ$  and  $155.8^\circ$  in the other. There are two independent molecules in the crystal of  $\text{Ir}(\text{PMe}_3)_4^+$ . The structure [12] is similar to that shown by **19.9** with sets of P—Ir—P angles of  $158.9^\circ$  and  $152.8^\circ$  along with  $160.4^\circ$  and  $158.5^\circ$ . These are typical of many  $d^8 \text{M}(\text{PR}_3)_4$  examples; all are close to a square planar geometry with a variety of P—M—P angles that signals a soft  $D_{2d}$  distortion path. On the other hand,  $\text{Co}(\text{PMe}_3)_4^+$ , **19.10**, is clearly tetrahedral. In one structure, the P—Co—P angles range from  $105.1^\circ$  to  $113.6^\circ$ , and in the other, the range is a little broader: from  $101.1^\circ$  to  $125.4^\circ$  [13]. There is one more basic coordination geometry for the  $d^8 \text{ML}_4$  complex, namely, the  $C_{3v}$  trigonal pyramid, **19.11**. The easiest way to see how this structure can be



stabilized is for X to be a very strong  $\sigma$ -donor so that resonance structure **19.12** is important which leaves the  $\text{ML}_3$  species to have a  $d^{10}$  16-electron count. There are several examples of this coordination mode [14]. What is quite interesting is the reaction mechanisms for phosphine exchange in Wilkinson's catalyst,  $(\text{Ph}_3\text{P})_3\text{Rh}(\text{Cl})$ , and related compounds [15]. It has been determined that there are two intramolecular routes. The ground state for these compounds is very close to the square plane. In one mechanism the molecule distorts to a transition state with a trigonal pyramid geometry akin to **19.11** (with  $X = \text{Cl}$ ). The other mechanism involves a distortion along the  $D_{2d}$  path to a crossing point between the singlet and triplet surfaces and then it collapses to a triplet tetrahedral intermediate. There is also a dissociative intermolecular route, which we discuss in Chapter 20. Finally, there are a few even lower electron count molecules that have the basic  $C_{2v}$  sawhorse structure. An example is provided by the 14-electron  $\text{Ru}(\text{C}_6\text{F}_5\text{S})_2(\text{PPh}_3)_2$ , **19.13** [16]. As indicated by the dashed bonds in the drawing, there are two agnostic Ru—Hbonds with



lengths of  $2.80$  and  $2.87 \text{ \AA}$ . Referring back to Figure 19.1, the  $2a_1$  and  $b_2$  MOs are empty. They have just the right symmetry properties and radial extent to interact with the two C—H bonds.

### 19.3 OLEFIN-ML<sub>4</sub> COMPLEXES AND M<sub>2</sub>L<sub>8</sub> DIMERS

The  $d^8C_{2v}$  ML<sub>4</sub> fragment presents an anisotropic electronic environment to a ligand. The three lower orbitals in Figure 19.1,  $a_2 + b_1 + 1a_1$ , are filled along with the higher lying  $b_2$  orbital. The asymmetry comes about from the  $b_2 - b_1$  difference. The  $b_2$  orbital lies at a higher energy and is hybridized toward the missing ligand(s). Therefore, it will be a better donor orbital than the  $b_1$ . Our probe ligand where this effect can nicely be illustrated is ethylene. In Section 17.3 we developed a rationale why olefins lie in the equatorial plane for  $d^8$  trigonal bipyramidal complexes rather than orienting themselves along the axial direction. We return to the problem here from a fragment orbital perspective. Figure 19.4 shows orbital interaction diagrams for ethylene–Fe(CO)<sub>4</sub> in the two possible orientations, 19.14 and 19.15.



In both conformations,  $1a_1$  and  $2a_1$  interact with the ethylene  $\pi$  level. That produces three molecular orbitals; the lower two shown in Figure 19.4 are filled. The middle level can be identified with the  $e'$  set in a trigonal bipyramidal splitting pattern and the lowest level is mainly ethylene  $\pi$  with some  $1a_1$  and  $2a_1$  character mixed into it in a bonding fashion. It is important that the overlap between these three fragment orbitals is essentially invariant to rotation. In other words, all are cylindrically symmetrical with respect to the Fe–olefin axis. Therefore, energies of the three molecular orbitals must also be constant as a function of rotation. The  $a_2$  Fe(CO)<sub>4</sub>

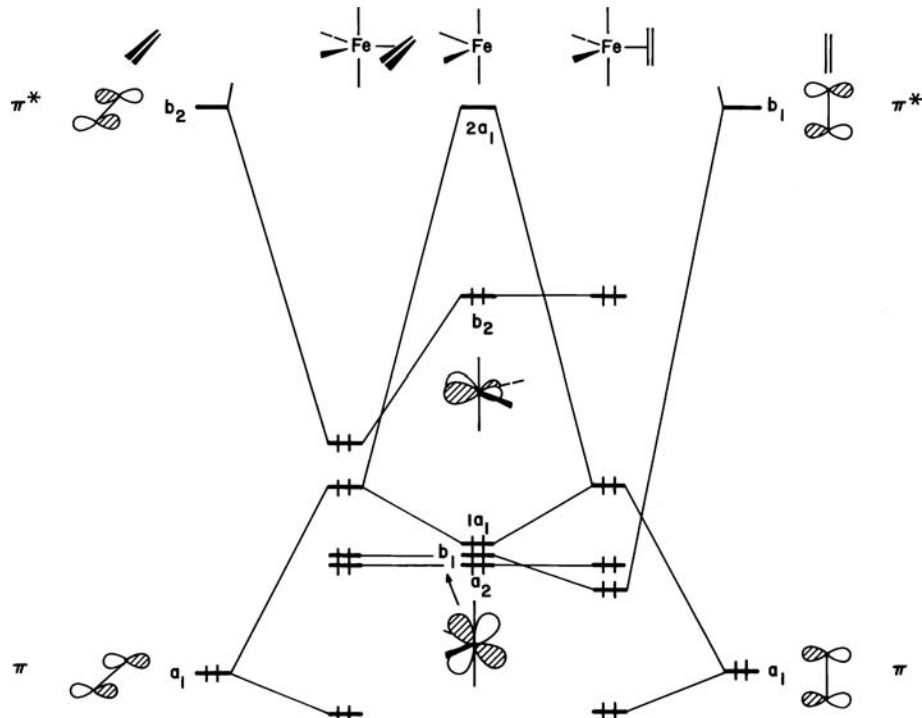
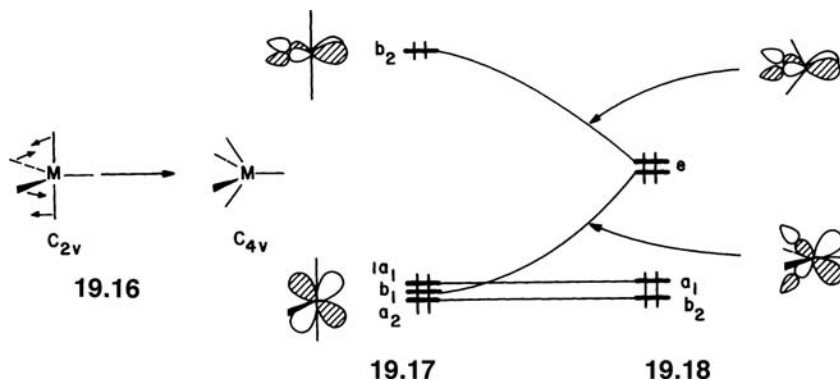


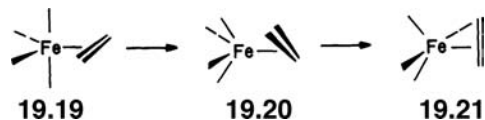
**FIGURE 19.4**

Interaction diagrams for ethylene–Fe(CO)<sub>4</sub> in two possible conformations.

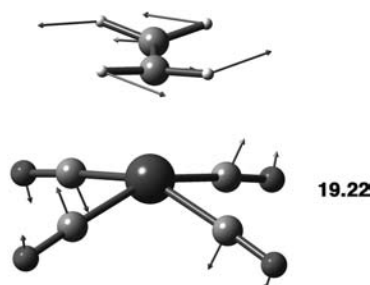
fragment orbital is nonbonding at conformations **19.14** and **19.15**. This leaves us with the  $b_1$ ,  $b_2$  pair of  $\text{Fe}(\text{CO})_4$  and ethylene  $\pi^*$ . In the conformation **19.14** as shown on the left side of Figure 19.4, the  $\pi^*$  orbital is of  $b_2$  symmetry. Its overlap with the  $\text{Fe}(\text{CO})_4$   $b_2$  fragment orbital is large, and the small energy gap between them creates a stable two-electron–two-orbital bonding situation. The filled bonding orbital can be identified with the other  $e'$  component of a trigonal bipyramidal complex, strongly backbonding to ethylene  $\pi^*$ . When the ethylene ligand is rotated by  $90^\circ$  to **19.15** the  $\pi^*$  orbital becomes of  $b_1$  symmetry. It then forms a bonding combination with the  $b_1$  fragment on  $\text{Fe}(\text{CO})_4$ . The  $b_2$   $\text{Fe}(\text{CO})_4$  level is left nonbonding. Which conformation is more stable? The real question is which of the two bonding combinations,  $b_2 + \pi^*$  in **19.14** or  $b_1 + \pi^*$  in **19.15**, is more stabilizing? The  $b_2$  level is closer in energy to  $\pi^*$  than  $b_1$  by virtue of the antibonding between metal  $d$  and the two equatorial lone pairs. Furthermore,  $b_2$  is hybridized (see **19.2**) out toward the ethylene, whereas  $b_1$  is not. The hybridization creates a larger overlap with  $\pi^*$ . Therefore, both energy gap and overlap factors make the  $b_2 + \pi^*$  interaction stronger than that for  $b_1 + \pi^*$ , and so conformation **19.14** with the olefin lying in the equatorial plane is of lower energy than **19.15** where ethylene is in the axial plane. Steric factors also reinforce this preference. The energy difference is actually calculated to be quite large—about 30 kcal/mol at the extended Hückel [17] and ab initio [18] levels. Indeed, all  $d^8$  olefin– $\text{ML}_4$  complexes adopt this geometry [19]. However, NMR measurements [20] have put the rotational barrier for  $d^8$  olefin– $\text{M}(\text{CO})_4$  complexes to be in the 10–15 kcal/mol range. Why is there so large a discrepancy? The energy and hybridization differences of  $b_1$  and  $b_2$  are at the heart of the barrier problem, but we have looked at a rigid rotation. There is a geometrical way to equivalence  $b_1$  and  $b_2$  by carrying out a pseudorotation motion, **19.16**. The arrows indicate the direction



the carbonyl ligands take going from the  $C_{2v}$  to a  $C_{4v}$  structure where both trans C–Fe–C angles are identical. As the two equatorial carbonyls move apart, the lone pairs move toward the node of the metal  $d$  component in  $b_2$ . Consequently, the  $b_2$  fragment orbital drops in energy, **19.17**. On the other hand, as the axial carbonyls move closer together, the lone pair hybrids overlap with the  $b_1$  fragment orbital in an antibonding way so the energy rises and hybridization is turned on. The  $b_2$  and  $b_1$  levels meet to form an  $e$  set at the  $C_{4v}$  structure, **19.18**. Now the ethylene  $\pi^*$ -acceptor orbital will not discriminate between the two fragment orbitals because they are members of an  $e$  set, and there should be free rotation at this geometry. The reaction path these complexes take is complicated. A coupled olefin rotation, pseudorotation path is followed from **19.19** to the square pyramidal structure, **19.20**, which serves as a transition state. It will cost energy

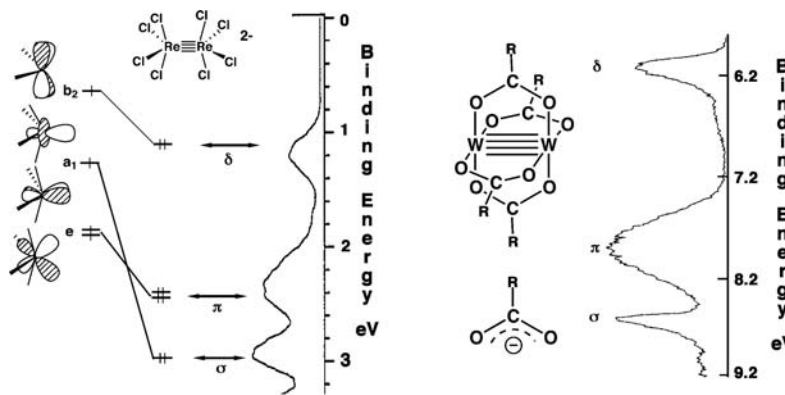


to attain **19.20**; notice in **19.17** and **19.18** that the energy of  $b_1$  rises and  $b_2$  becomes a poorer  $\pi$ -donor (it is stabilized less by  $\pi^*$ ). Continuing the rotation–pseudorotation motion in the same direction leads to the trigonal bipyramidal structure **19.21**. The equatorial and axial carbonyl groups have exchanged sites. In order for this to be the correct mechanism, equatorial–axial carbonyl exchange must be (and is from the NMR studies) present. Notice that a rigid rotation mechanism would not exchange equatorial and axial groups. B3LYP calculations [18b] put the barrier for ethylene–Os(CO)<sub>4</sub> at 11.6 kcal/mol. The transition state is shown in **19.22** where the arrows indicate the components of the transition state vector.



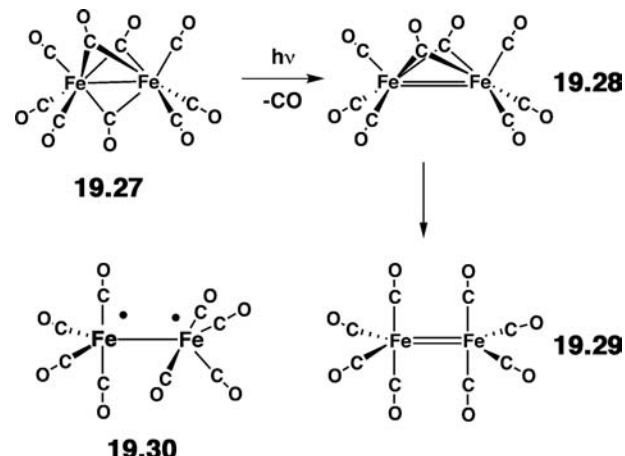
Here ethylene rotation is clearly coupled to pseudorotation. In the ground state of ethylene–Os(CO)<sub>4</sub> (analogous to **19.19**) the Os–C and C–C bond lengths are calculated to be 2.27 and 1.45 Å, respectively. Experimentally, these values were found to be 2.21 and 1.43 Å, respectively [21]. Upon going to the transition state, the Os–C distance increases to 2.39 Å and the C–C distance decreases to 1.40 Å. In other words, at the transition state, **19.22**, the interaction between the olefin and the Os(CO)<sub>4</sub> group decreases. This does not originate from the interaction between ethylene  $\pi$  and the  $a_1$  components on Os(CO)<sub>4</sub>. These are cylindrically symmetrical. It is the consequence of the fact that  $b_2$  drops lower in energy and is less hybridized so there is less back-donation to ethylene  $\pi^*$ . We return to other elements of these structures shortly. The reader should recall the structure of **17.33** and the discussion around it. This is a  $d^2$  W(PMe<sub>3</sub>)<sub>2</sub>(NAr)<sub>2</sub> fragment with a sawhorse geometry. The  $a_2$  orbital is destabilized by the two imido ligands, so the  $b_1$  and  $1a_1$  fragment orbitals are close in energy and will interact with the olefin  $\pi$  and  $\pi^*$  orbitals.  $1a_1$  (and also  $2a_1$ ) interacts with  $\pi$ . This leaves  $\pi^*$  to combine with  $b_1$ . Thus, the preferred orientation of the olefins is one where the olefin lies parallel to the two axial ligands, analogous to structure **19.15**.

Probably the quintessential transition metal dimer is Re<sub>2</sub>Cl<sub>8</sub><sup>2-</sup>. The discovery of the structure [22] brought a whirlwind of activity in the field of transition metal compounds with multiple M–M bonds [23]. Re<sub>2</sub>Cl<sub>8</sub><sup>2-</sup> has Re in the +3 oxidation state and, therefore, each ReCl<sub>4</sub><sup>-</sup> unit is  $d^4$ . These four  $d$  electrons couple to form one  $\sigma$ , two  $\pi$ , and one  $\delta$  bonds as shown in **19.23**. The overlap of  $\sigma > \pi \gg \delta$  insures that the MO ordering is given by that in **19.23**. The  $a_1$  and  $e$  set are hybridized out toward the



other  $\text{ReCl}_4^-$  unit. This hybridization in turn increases  $\sigma$  and  $\pi$  overlap so the Re—Re bonding becomes stronger. We have seen in several places before that the hybridization is a consequence of pyramidalization; in other words, at the square plane  $a_1$  and  $e$  are exclusively  $z^2$  and  $xz/yz$ . Consequently, as the Re—Re—Cl angle becomes larger, the Re—Re distance should and does decrease [24]. Since  $\delta^*$  and  $\pi^*$  lie at low energies, there is a very rich spectrum of electronic states associated with  $\text{Re}_2\text{Cl}_8^{2-}$  [25]. Using electrospray techniques, the photoelectron spectrum of  $\text{Re}_2\text{Cl}_8^{2-}$  has been obtained, **19.24** [26]. The very small binding energies are a result of the strong electrostatic repulsion in this molecule. A class of related neutral compounds is given by  $\text{M}_2(\text{carboxylate})_4$ . Carboxylates are anionic, **19.25**, so  $\text{W}_2(\text{carboxylate})_4$  may be regarded as two  $\text{W}^{2+}$ ,  $d^4$  square pyramidal units. The photoelectron spectrum for  $R = \text{CH}_3$  is presented in **19.26** [27]. The broad peak width associated with the ionization at about 8 eV assures that this corresponds to the  $\pi$  orbitals and surely ionization from the  $\sigma$  orbital should be larger than from the  $\delta$ . So, the assignment of the photoelectron spectrum in **19.26** is reasonable. Other derivatives have more complicated spectra [27]. Also, it is overly simplistic that the  $(\sigma)^2(\pi)^4(\delta)^2$  electronic configuration leads to a metal–metal bond order of four. A result of the very weak  $\delta$  bonding in these molecules is that in a multiconfigurational approach (see Section 8.11), states arising from the occupation of  $\delta^*$  heavily mix into the ground state. Therefore, the Re—Re bond order in  $\text{Re}_2\text{Cl}_8^{2-}$  is around 3.2 [25] where the “ $\delta$  bond” contributes a bond order of about 0.5.

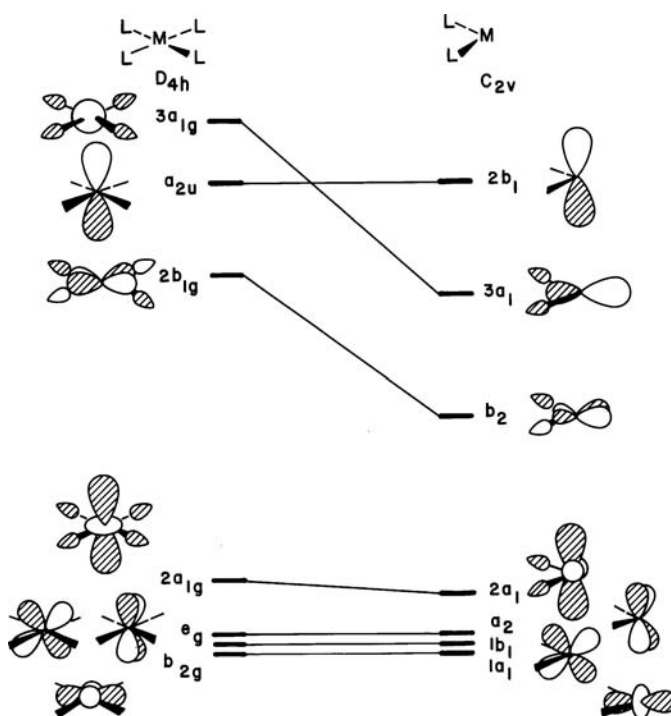
Along with  $\text{Fe}(\text{CO})_4$ , the Turner group has also studied the low temperature matrix isolation of  $\text{Fe}_2(\text{CO})_8$  by photolysis of  $\text{Fe}_2(\text{CO})_9$ , **19.27** [28]. Electron counting in **19.27** yields 17 electrons around each Fe, so an Fe—Fe bond should



be present. Photolysis removes one bridging CO. The resultant structure, **19.28**, then has  $C_{2v}$  symmetry. More recent computations [29] do find a structure analogous to this with CO stretching frequencies in the IR close to the experimental ones [28]. Another structure was observed which contains no bridging carbonyls and could be formed from **19.28**. It was tempting to assign this to the  $D_{2h}$  structure, **19.29**. With reference back to Figure 19.1 or 19.3, the  $2a_1$  fragments combine (with one electron each) to give the Fe—Fe  $\sigma$  bond and the  $b_2$  fragments create the  $\pi$  bond. So, **19.29** is the inorganic analog of ethylene. Unfortunately, the calculations [29] predict that **19.29** is about 10–15 kcal/mol higher in energy than **19.28**. A  $D_{2d}$  structure, **19.30**, is much lower in energy where there is a rotation by 90° around the Fe—Fe bond. Just as in ethylene (see Section 10.3), the  $\pi$  bond is broken and a triplet spin state is created. The energy difference between singlet **19.28** and triplet **19.30** is uncertain, but most likely **19.30** is about 10 kcal/mol more stable than **19.28**.

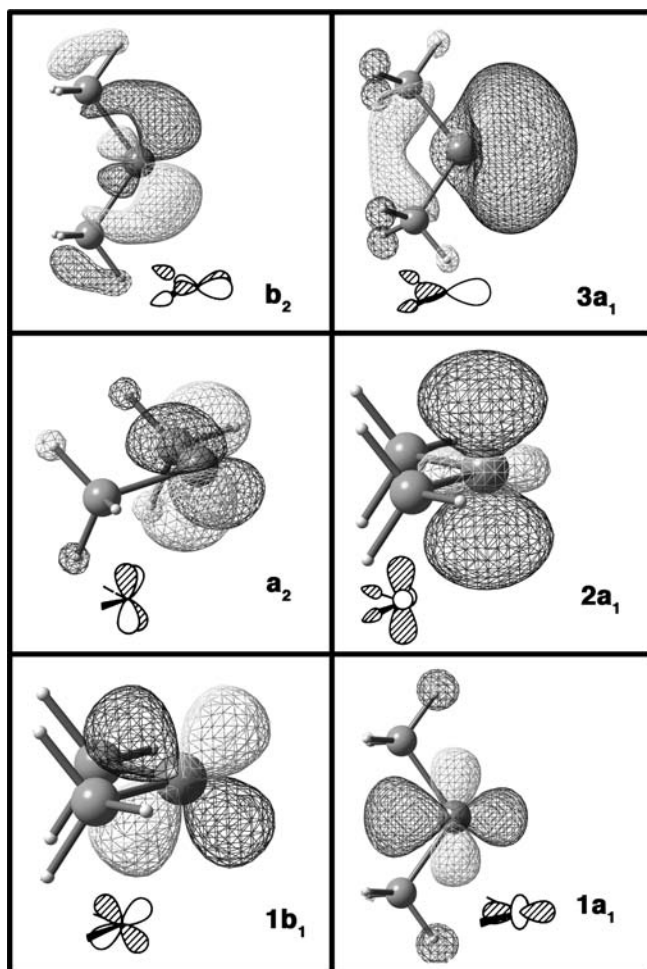
## 19.4 THE $C_{2v}$ ML<sub>2</sub> FRAGMENT

Figure 19.5 shows the derivation of the orbitals of a  $C_{2v}$  ML<sub>2</sub> fragment by removal of two cis ligands from a square planar ML<sub>4</sub> complex. The  $e_g$  and  $a_{2u}$  levels of the square plane are totally unaffected by the perturbation. The  $2a_{1g}$  and  $b_{2g}$  molecular orbitals intermix a little since the symmetry of each fragment orbital becomes  $a_1$ . But the major change comes from  $2b_{1g}$  and  $3a_{1g}$ . Both orbitals lose one-half of their antibonding character to ligand lone pairs and so they are stabilized considerably. Metal  $p$  character is also mixed into each in a way that is bonding to the remaining ligand lone pairs. Three-dimensional plots of these orbitals are given in Figure 19.6. These are taken from a B3LYP calculation on Pd(PH<sub>3</sub>)<sub>2</sub>. The hybridization in  $b_2$ , absent in  $1b_1$ , is very clear. Notice in the  $3a_1$  orbital that it still is primarily Pd s in



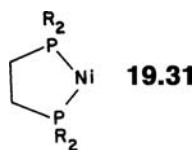
**FIGURE 19.5**

Derivation of the orbitals of a  $C_{2v}$  ML<sub>2</sub> fragment from the molecular orbitals of square planar ML<sub>4</sub>.

**FIGURE 19.6**

Contour surfaces for the important valence orbitals in  $\text{Pd}(\text{PH}_3)_2$  from a B3LYP calculation.

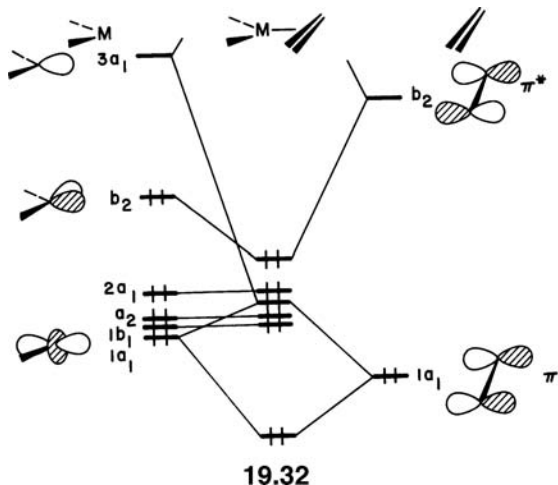
character. It is also apparent that  $2a_1$ ,  $a_2$ ,  $1b_1$ , and  $1a_1$  are almost exclusively Pd  $d$  in character with little or no involvement on P. Similar to the  $C_{4v}$   $\text{ML}_5$  and  $C_{2v}$   $\text{ML}_3$  fragments, there is a correspondence between the orbitals of  $C_{2v}$   $\text{ML}_2$  and  $\text{ML}_4$  (compare Figure 19.1 with 19.5). Both have a set of three  $d$ -based orbitals at low energy of  $a_1 + b_1 + a_2$  symmetry. There are two hybrid orbitals at higher energy that point away from the remaining ligands. They are of  $a_1$  and  $b_2$  symmetry and were derived by removal of two cis ligands. The  $\text{ML}_2$  unit has one additional orbital at low energy,  $2a_1$ , which corresponds to the high-lying, antibonding  $3a_1$  level in  $\text{ML}_4$ . Finally,  $\text{ML}_2$  has a high-energy metal  $p$  orbital,  $2b_1$ . This orbital along with  $2a_1$  is destabilized when two axial ligands are added to form a  $C_{2v}$   $\text{ML}_4$  fragment. This analogy then pairs a  $C_{2v}$   $d^6$   $\text{ML}_4$  fragment with a  $d^8$   $\text{ML}_2$  unit and  $d^8$   $\text{ML}_4$  with  $d^{10}$   $\text{ML}_2$ . A singlet ground state for  $d^{10}$   $\text{Ni}(\text{PH}_3)_2$  is guaranteed because the molecule is greatly stabilized by distortion to a nearly a linear,  $D_{\infty h}$  geometry. The  $b_2$  highest occupied molecular orbital (HOMO) goes down in energy, meeting the block of the other four  $d$  orbitals. This is then just a linear 14-electron system (see the discussion around 16.6). With the BP86 hybrid functional, singlet  $\text{Ni}(\text{PH}_3)_2$  is predicted to have a P—Ni—P angle of  $170^\circ$ . The P—Ni—P bond angle decreases to  $105^\circ$  for the triplet state. The singlet state is 33 kcal/mol more stable than the triplet [18b, 30]. One could envision a chelating bisphosphine (an example is provided by 19.31), where the P—Ni—P angle is forced to be less than  $180^\circ$ . The  $b_2$  level then is energetically close to



$3a_1$ , and a triplet state with one electron in  $b_2$  and the other in  $3a_1$  should become energetically more favorable. Indeed, this appears to be the case; with  $R = H$  for **19.31** the singlet and triplet were found to have a P—Ni—P angles of  $101^\circ$  and  $85^\circ$ , respectively. The triplet now lies only 12 kcal/mol higher in energy than the singlet. For  $\text{Ni}(\text{CO})_2$ , the situation is similar [31]. However, the interaction of the CO  $\pi^*$  orbitals with  $1a_1$  keep the C—Ni—C angle to be somewhat smaller. Experimentally this is found to be around  $145^\circ$ , but calculations show that there is computed to be only a 3 kcal/mol energy difference between this  $C_{2v}$  structure and the linear,  $D_{\infty h}$  one [31].

## 19.5 POLYENE-ML<sub>2</sub> COMPLEXES

The bonding and conformational preference of ethylene– $\text{Ni}(\text{PR}_3)_2$  is very similar to the case study of ethylene– $\text{Fe}(\text{CO})_4$ . The orbital interaction diagram for an “in-plane” conformation is shown in **19.32**. Ethylene  $\pi$  interacts with  $1a_1$  and  $3a_1$  to produce three molecular orbitals; the two filled lower ones are explicitly shown in

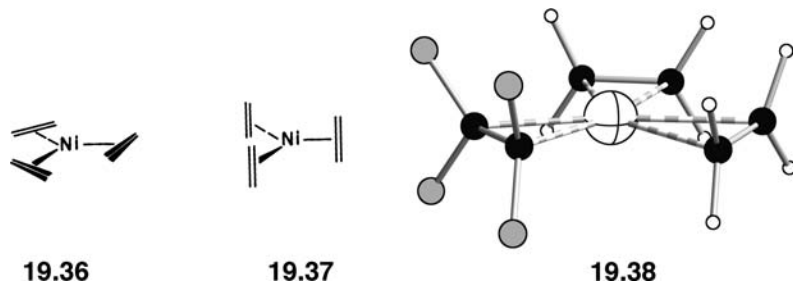


**19.32.** The  $1b_1$ ,  $a_2$ , and  $2a_1$  orbitals are nonbonding. This leaves us with  $b_2$  and ethylene  $\pi^*$ . They combine to form a strong bonding interaction. Rotation of the olefin to an “out-of-plane” geometry, **19.33**, will be energetically costly. At **19.33**, ethylene  $\pi^*$  has  $b_1$  symmetry and will stabilize the  $\text{ML}_2 b_1$  fragment orbital, **19.34**. We

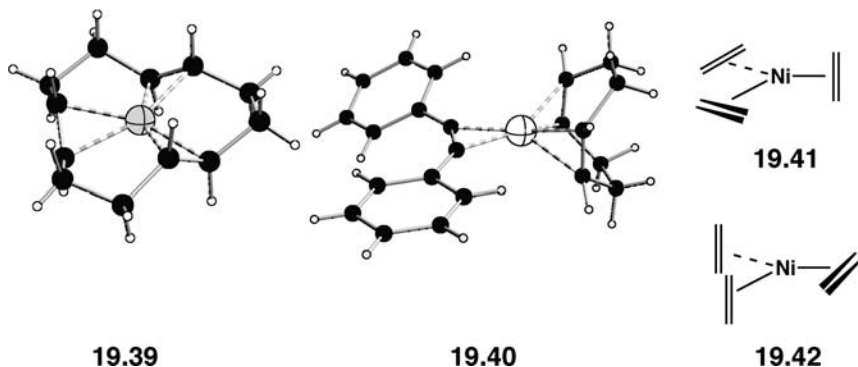


are again at a point where the  $b_2 + \pi^*$  combination in **19.35** for the in-plane conformer needs to be compared with the  $b_1 + \pi^*$  one, **19.34**, for the out-of-plane

geometry. For the same energy gap and overlap reasons as in ethylene– $\text{Fe}(\text{CO})_4$ , the interaction in **19.35** is much stronger than that in **19.34**. The  $a_1$  orbitals are cylindrically symmetric, so these molecular orbitals remain at constant energy during rotation. The actual barrier is quite high. It is calculated [18b] to be 19 kcal/mol at the B3LYP level for ethylene– $\text{Ni}(\text{PH}_3)_2$  because unlike ethylene– $\text{Fe}(\text{CO})_4$ , there is no good geometric way here to make the  $b_1$  orbital equivalent to  $b_2$ . Experimentally, there has not been a determination of the magnitude of the barrier; however, of the hundreds of crystal structure of olefin– $\text{ML}_2$  compounds, all have the in-plane geometry of **19.32**. The loss of backbonding to  $\pi^*$  upon rotation has other geometric consequences. For example, the predicted Pt–C bond length was 2.14 Å for the structure given in **19.32**. This is elongated by 0.18 Å on going to **19.33**. In a sense, these features should not surprise us too much. Consider ethylene to be a bidentate ligand. The in-plane conformation then corresponds to a 16-electron square planar system (one could either think of the olefin as a two-electron neutral donor or as a dianionic four-electron donor). The out-of-plane geometry would correspond to an unstable 16-electron tetrahedral complex (see Section 16.4). An extension of this analysis [32] also shows that the sterically much more encumbered structure, **19.36**, for triethylene–nickel is more stable than **19.37**. This has been determined to be experimentally true by a number of



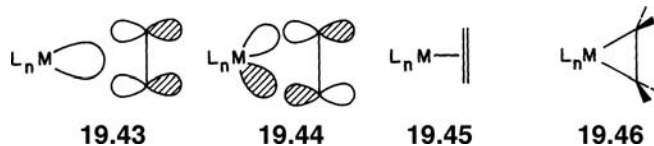
X-ray diffraction structures. An example is provided by  $(\text{C}_2\text{F}_4)\text{Ni}(\text{C}_2\text{H}_4)_2$ , **19.38** [33]. The energy difference between **19.36** and **19.37** is calculated to be huge—30 kcal/mol [34]. But this does not imply that the barrier to rotate about the Ni–ethylene bond is large. A number of X-ray structures show that all three olefins can be twisted from a common plane, as given by the structure of the cyclododeca-*triene*–Ni complex, **19.39** [35] or even rotating two olefins to an upright position, as



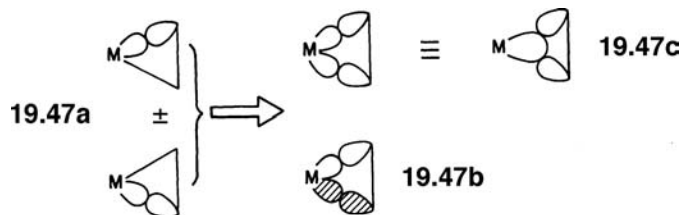
in the cyclooctadiene–Ni(diphenylacetylene) complex, **19.40** [36]. At the B3LYP level it requires only 3 kcal/mol to rotate to **19.41** and 9 kcal/mol to rotate two ethylene ligands to **19.42**. The destabilization in **19.37** is a consequence of the  $D_{3h}$  symmetry and orbital topology. Backbonding from Ni  $d$  to ethylene  $\pi^*$  is maximal in **19.36** because hybridization with Ni  $p$  is possible at this geometry. **19.41** and **19.42**

also have one or two  $\pi^*$  orbitals that can interact with the metal  $b_2$  fragment orbital akin to **19.35**. So again there is still appreciable stabilization through backbonding. It is only in **19.37** that, by symmetry, hybridization of  $d$  atomic orbitals (AOs) with metal  $p$  is not possible, so backbonding from Ni  $d$  to ethylene  $\pi^*$  is minimized in this series. It has been argued [34] that there is homoaromatic stabilization in **19.36**, which takes place between the ethylene carbons. These “nonbonded” distances are 2.90, 2.88, and 2.76 Å in **19.38**, which puts them at or inside the van der Waals radii for  $sp^2$  hybridized carbons. Furthermore, computation of the anisotropy of the induced current density [34] indicated that there is delocalization of electron density between the ethylenes in **19.36**. On the other hand, the negative Laplacian of the charge density [37] does not indicate any accumulation of electron density between the ethylene ligands in **19.36**. So what are we to believe? There is a frequent and recurring problem throughout chemistry—is there meaningful bonding between two atoms, in this case between the “nonbonded” ethylene carbons? An even more contentious problem lies in a determination of the bond order between atoms. In Section 19.3 we mentioned that a relatively clear-cut example,  $\text{Re}_2\text{Cl}_8^{2-}$ , can cause problems. In  $\text{B}_2\text{H}_6$ , is the B—B bond order one, as implied by examination of Figure 10.3, or is it closer to two from the perspective in Figure 10.6? There are a myriad of ways to get a handle on this issue and certainly, as evidenced by the discussion of **19.36**, this will lead to conflicting conclusions [38]. Perhaps, a better question is—does it make a difference? We now turn to a very old conundrum in the organometallic world.

In the last two chapters we have analyzed metal–olefin bonding in four different systems. Let us present a general argument that ties this discussion together and pursue some of its ramifications. Any  $\text{ML}_n$  fragment has an empty orbital of  $a_1$  symmetry, **19.43**. It interacts with the filled  $\pi$  orbital of the olefin. There is also a

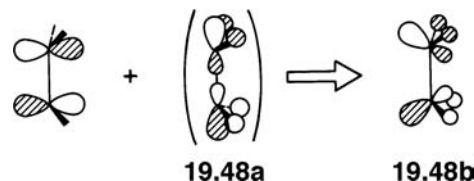


filled metal orbital of  $b_2$  (or  $b_1$ ) symmetry, **19.44**, available for backbonding to ethylene  $\pi^*$ . We have taken an olefin–metal representation, **19.45**, for these complexes and this is the essence of the Dewar–Chatt–Duncanson model of metal–olefin bonding [39]. But perhaps these molecules are viewed better as metallacyclopropane complexes, **19.46**. Putting this question in another way, is there any difference between the formulations of **19.45** and **19.46**? The metallacyclopropane model can be represented by the two localized metal–carbon  $\sigma$  bonds in **19.47a**. These are made symmetry correct by taking in-phase and out-of-phase combinations. The resultant orbitals, **19.47c** and **19.47b**, have  $a_1$  and  $b_2$



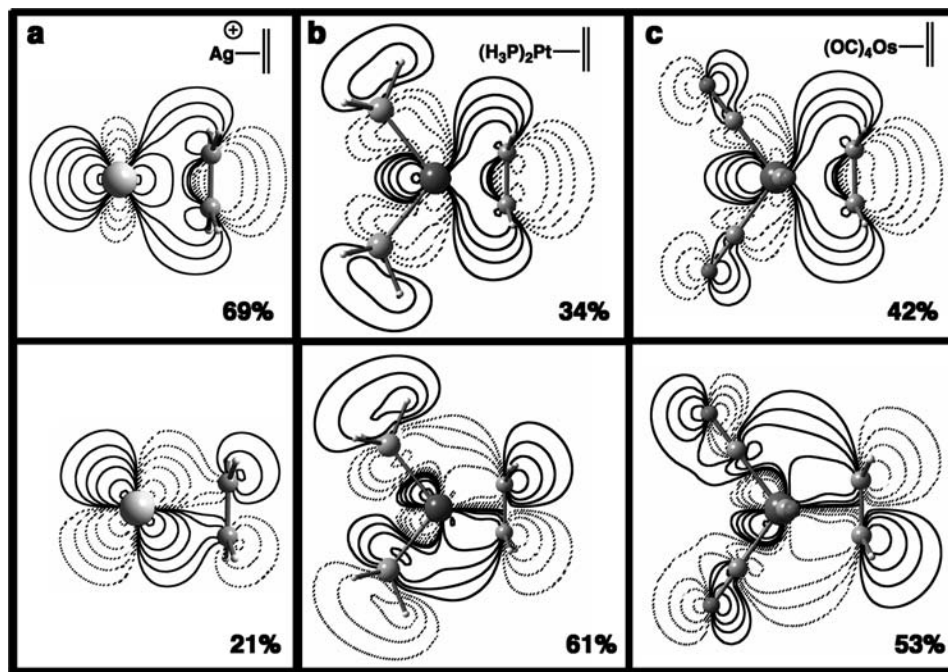
symmetry, respectively. Clearly, **19.47c** corresponds to **19.43** and **19.47b** to **19.44**. So, there appears to be no difference between the metal–olefin and metallacyclopropane structures. But a further consequence of the metallacyclopropane

formation is that one immediately expects the substituents on the olefinic carbons to be bent back from a plane containing the olefinic carbons and away from the metal. This is illustrated in **19.46**. Does the metal–olefin formulation lead to this distortion? When the hydrogens in ethylene are pyramidalized (see Section 10.3) a higher  $\sigma^*$  level, **19.48a**, mixes into  $\pi^*$  in a manner that the hydrogen s components are



bonding with respect to  $\pi^*$ . This hybridizes  $\pi^*$  in the sense shown by **19.48b**. The addition of carbon s character and tilting of the two orbitals as shown leads to better overlap with the filled metal  $b_2$  orbital. This mixing also lowers the energy of  $\pi^*$ , so the energy gap between it and metal  $b_2$  is smaller. Therefore, bending back the hydrogens makes the metal  $b_2 +$  ethylene  $\pi^*$  interaction, **19.44**, stronger. In terms of hybridization at carbon and bending back the hydrogens, there is no difference between the olefin–metal and metallacyclopropane representations.

What does change is the relative amount of  $a_1 + \pi$  versus  $b_2 + \pi^*$  interaction. A weaker  $b_2 + \pi^*$  interaction will diminish the tendency for the olefinic substituents to bend back. Notice that an increased  $a_1 + \pi$  interaction, **19.43**, will cause the C–C bond to lengthen as well as increased  $b_2 + \pi^*$  bonding, **19.44**. In the former case, electron density is shifted from the carbon–carbon ( $\pi$ ) bonding region toward the metal. For the latter case, electron density is transferred from the metal to a fragment orbital, which is carbon–carbon ( $\pi$ ) antibonding. The approach here is rooted in the delocalized LCAO approach. One could do a valence bond calculation on **19.45** and **19.46** for a given  $\text{ML}_n$  fragment to see which has the lower energy solution. In practice, the electronic structure will be a combination of the two valence bond forms and, therefore, calculations will be needed if this is to be a numerical evaluation. Is there a way to establish this on a qualitative level? Yes, if one is willing to return to the delocalized framework expressed in **19.43** and **19.44**. As the contribution of **19.44** increases, the solution becomes closer to the metallacyclopropane structure. There are several ways to accomplish this from a perturbation theory point of view that spring immediately to mind. As the metal becomes less electronegative (or there are electron donating groups on the surrounding ligands or there is a negative charge on the complex), the  $b_2$  orbital rises in energy and so the energy gap between it and  $\pi^*$  becomes smaller. The  $b_2 + \pi^*$  interaction becomes stronger. This situation can also easily be shown to weaken the  $a_1 + \pi$  interaction. A set of real examples from B3LYP calculations is shown in Figure 19.7. The plots on the top row show the MOs that correspond to the  $a_1 + \pi$  interaction, forward donation, and those for the bottom row are the  $b_2 + \pi^*$ , back donation MO. The orbital shapes are strikingly similar, especially for ethylene– $\text{Pt}(\text{PH}_3)_2$  and ethylene– $\text{Os}(\text{CO})_4$ . The numbers at the bottom right-hand corner of each MO come from an energy decomposition analysis [40]. One portion of this decomposition energy between the ethylene and  $\text{ML}_n$  fragments is given by the attractive orbital interaction term. This is listed as a percentage in the figure. For ethylene– $\text{Ag}^+$ , the  $a_1 + \pi$  interaction is dominant. Notice that the contours for the  $b_2 + \pi^*$  MO are primarily localized on the metal. This is certainly not the case for ethylene– $\text{Pt}(\text{PH}_3)_2$  and ethylene– $\text{Os}(\text{CO})_4$ . The  $b_2 + \pi^*$  interaction is more important. It has been argued [41] that ethylene– $\text{Os}(\text{CO})_4$  is a metallacyclopropane. Then so should ethylene– $\text{Pt}(\text{PH}_3)_2$ . Yet, the binding energy between ethylene and the  $\text{ML}_n$  fragments are vastly different: 62 kcal/mol for the Os compound and 20 kcal/mol for

**FIGURE 19.7**

Contour plots of the MOs corresponding to forward (top row) and back donation (bottom row) in three representative olefin complexes. The numbers indicate the percentage of the orbital energy stabilization from an energy decomposition analysis.

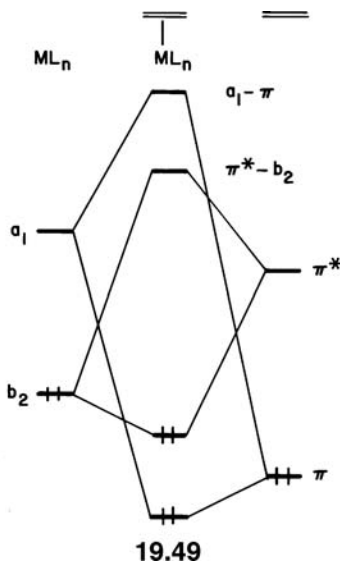
the Pt. One might think that the Os—C and Pt—C  $\sigma$  bond energies would not be too different. The bond dissociation energies for Os—CH<sub>2</sub><sup>+</sup> and Pt—CH<sub>2</sub><sup>+</sup> were computed to be 113 and 123 kcal/mol, respectively. Likewise the Os—H<sup>+</sup> and Pt—H<sup>+</sup> bond energies are 56 and 62 kcal/mol, respectively [42]. Another way to make the  $b_2 + \pi^*$  interaction more important is to substitute electronegative or  $\pi$  electron withdrawing groups on the olefin. This will cause the energy of the  $b_2 + \pi^*$  interaction to become more important, that is, the  $\pi^*$  orbital will drop in energy and consequently the  $b_2 - \pi^*$  energy gap will become smaller. This is shown for the three olefin–Pt(PH<sub>3</sub>)<sub>2</sub> complexes reported in Table 19.1. The  $\pi$  and  $\pi^*$  orbital energies (eV) are reported along with the amount of stabilization associated with the  $a_1 + \pi$  interaction,  $E_{a1}$ , and  $b_2 + \pi^*$  interaction,  $E_{b2}$  (kcal/mol). The percentages associated with the stabilization energies for R = H are almost identical to those in Figure 19.7b although the computation algorithm and basis sets were different. There is not much change in the  $a_1 + \pi$  interaction, but a huge change in  $b_2 + \pi^*$ . As the energy of  $\pi^*$  decreases,  $E_{b2}$  becomes increasingly attractive. This is precisely what we have

**TABLE 19.1** Calculated Orbital Energies for the  $\pi$  and  $\pi^*$  MOs (eV) and Stabilization Energies Along with the Bond Dissociation Energies (BDEs) (kcal/mol) for Three (C<sub>2</sub>R<sub>4</sub>)-Pt(PH<sub>3</sub>)<sub>2</sub> Complexes [43]

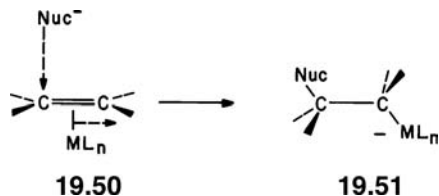
R	$\pi$	$\pi^*$	$E_{a1}$	$E_{b2}$	BDE
H	-7.58	+0.10	-47	-72	24
F	-8.27	-0.64	-51	-111	39
CN	-9.37	-5.10	-40	-120	31

predicted from the delocalized model. It is not clear how one could come to the conclusion that the structure **19.46** becomes increasingly more important from a valence bond context without resorting to **19.43** and **19.44**. Whether one writes these molecules as metallacyclopropanes with two M—C bonds or as metal olefins with one M—C bond is a matter of personal preference. We actually use the latter throughout this chapter (and in previous ones) while the former is most useful for us in Chapter 21. Also listed in Table 19.1 are the calculated [43] bond dissociation energies (BDEs), in kcal/mol. The tetrafluoroethylene and tetracyanoethylene complexes have higher BDEs than the ethylene– $\text{Pt}(\text{PH}_3)_2$ , however, certainly not by the amounts of greater  $E_{b2}$  interaction energies. This is a result of the fact that the BDE includes other terms: an energy preparation (the energy needed to distort the two fragments) and electrostatic and Pauli repulsion (two-orbital electron repulsion) terms. Thus, it is not a simple matter to trace bond dissociation energies to one factor alone.

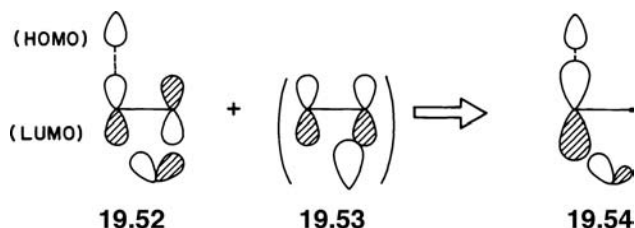
The relative amounts of forward and back donation can also play a role in reactivity questions. Take, for example, nucleophilic attack on an olefin–metal complex [44]. Our generalized bonding model for olefin–metal complexes is presented again in **19.49** (see **19.32**). The filled, lone-pair orbital of a nucleophile will seek



maximal bonding with the lowest unoccupied molecular orbital (LUMO) of olefin– $\text{ML}_n$ . This is shown in **19.49** as being the antibonding combination of  $\pi^*$  with metal  $b_2$ ,  $\pi^* - b_2$ . That orbital is concentrated on the olefinic portion of the molecule and, thus, a large overlap with an incoming nucleophile lone-pair orbital is expected. The antibonding  $a_1 - \pi$  level is normally at a higher energy, and it is concentrated at the metal. Nevertheless, one could utilize this orbital as an acceptor for the nucleophile as well. It is clear that the lower  $\pi^* - b_2$  is in energy (the less  $\pi^*$  interacts and is destabilized by  $b_2$ ), the greater will be its interaction with the attacking nucleophile. There are obvious ways to accomplish this by perturbations within the  $\text{ML}_n$  unit and substitutional factors at the olefin; however, it would seem that nucleophilic attack on olefin– $\text{ML}_n$  complexes should never proceed at a rate that is faster than on the uncoordinated olefin. The  $\text{ML}_n$   $b_2$  orbital will always destabilize  $\pi^*$  to some extent. Yet, a number of  $\text{ML}_n$  groups accelerate nucleophilic attack [44]. The point we have missed is that the  $\text{ML}_n$  group slips from an  $\eta^2$  position to  $\eta^1$  in the product, **19.50** to

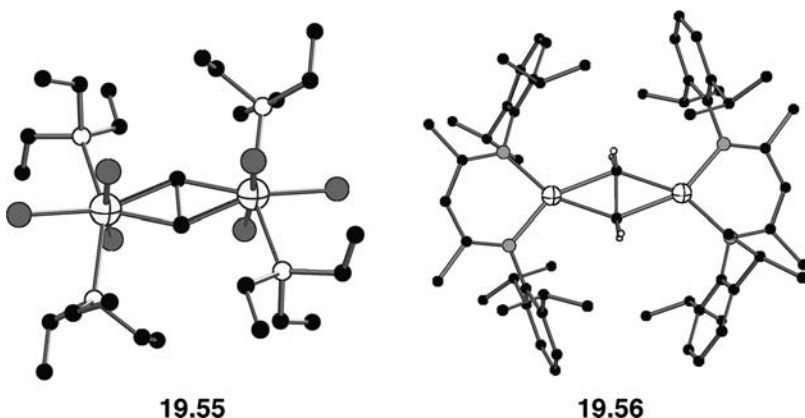


**19.51**, as the nucleophile attacks. It is this slipping motion that activates the olefin to a nucleophilic attack. Let us examine the form of the crucial HOMO–LUMO interaction between the nucleophile,  $\text{Nuc}^-$ , and olefin– $\text{ML}_n$  complex at some point intermediate between **19.50** and **19.51**. The HOMO lone pair of the nucleophile will still interact mainly with the  $\pi^* - b_2$  LUMO of the complex as shown in **19.52**. That stabilizes the lone pair. Slipping the  $\text{ML}_n$  group toward  $\eta^1$  lowers the local

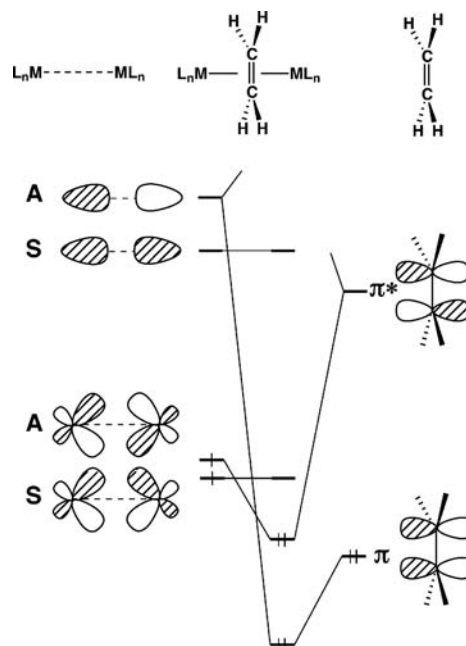
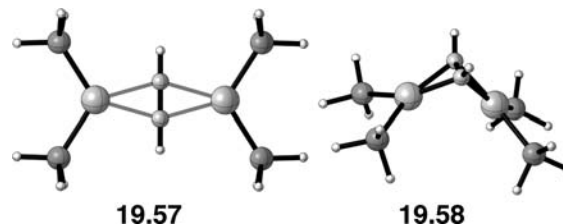


symmetry in the olefin–metal region and so the unoccupied  $a_1 - \pi$  orbital can also mix into **19.52**. It will do so in a way given by **19.53**, which is bonding to the incoming nucleophile. The resultant orbital is shown in **19.54**. There are two factors at work here. First,  $\pi^* - b_2$  is lowered by the slipping motion since the overlap between  $\pi^*$  and  $b_2$  is maximized at the  $\eta^2$  geometry. It is lowered further in energy by the first-order mixing of  $a_1 - \pi$ . Second, the mixing of **19.53** into **19.52** induces a polarization on the olefinic carbons (compare this to nucleophilic attack of olefin vs carbonyl compounds in Section 10.5). The atomic  $p$  coefficient at the carbon atom being attacked increases (see **19.54**). That results in a larger overlap between the LUMO and the lone-pair HOMO. Therefore, slipping from  $\eta^2$  to  $\eta^1$  activates attack by the nucleophile both by energy gap and overlap factors. This reaction type has been described here in a very general fashion. The number and kinds of ligands, the charge on the transition metal, and so on, will set the relative energies of  $\pi^* - b_2$  and  $a_1 - \pi$  and their composition. This, in turn, varies the extent of **19.52**–**19.53** intermixing and consequently the propensity toward nucleophilic attack [44].

There are a few structures where transition metals coordinate to both faces of an olefin. One example is given by the  $\text{Br}_3\text{Hf}(\text{PEt}_3)_2$  dimer, **19.55** [45]. The C—C distance here was found to be  $1.50 \text{ \AA}$  which is close to a typical C—C single bond

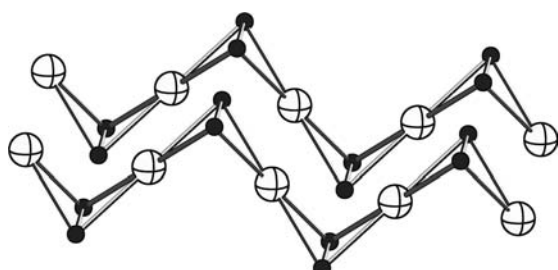


distance of 1.56 Å and certainly longer than a typical C—C distance in a coordinated olefin of 1.40–1.45 Å. Another example is provided by **19.56** [46] where ethylene is sandwiched between two Cr(diketiminate) units. Here, the C—C distance was found to be 1.48 Å. In **19.55** there are two  $\text{Hf}^{3+}$ ,  $d^1$   $\text{ML}_5$  units. Referring back to Figure 17.1, the  $b_2$  and the one component of the e set that lies in the  $\text{HfBr}_3$  plane are destabilized by the lone pairs on the bromine ligands. This leaves one electron in the e component which is orthogonal to the  $\text{HfBr}_3$  plane. In **19.56** the diketiminate ligand has a negative charge and so both metals are high spin  $d^5$  complexes. Referring back to Figure 19.5, the  $b_2$  orbital will be singly occupied. The bonding in both molecules can be constructed in general terms as shown in Figure 19.8. On the left are the symmetry-adapted combinations of the two metal components which have  $b_2$  and  $a_1$  symmetry. Each will be symmetric (S) and antisymmetric (A) with respect to the mirror plane that ethylene lies in. The two  $a_1$  components are empty and are derived from  $a_1$  in Figure 17.1 or  $3a_1$  in Figure 19.5. The A combination nicely overlaps with and stabilizes the  $\pi$  orbital of ethylene. The S combination of the  $b_2$  components overlaps with  $\pi^*$ . A sizable gap is formed with the S combination. Therefore, the two electrons pair in the bonding combination with  $\pi^*$ . Notice that in **19.55** the ethylene ligand lies in the plane of the phosphines, and in **19.56** it lies in the plane of the two  $\text{ML}_2$  units. This is precisely what is predicted from the bonding model in Figure 19.8, yet this is sterically the most encumbered geometry. If one substitutes an acetylene for the ethylene, then the analogous geometry, **19.57**, for acetylene– $[\text{Pt}(\text{PH}_3)_2]_2$  is very high in energy relative to the ground state, **19.58**. At

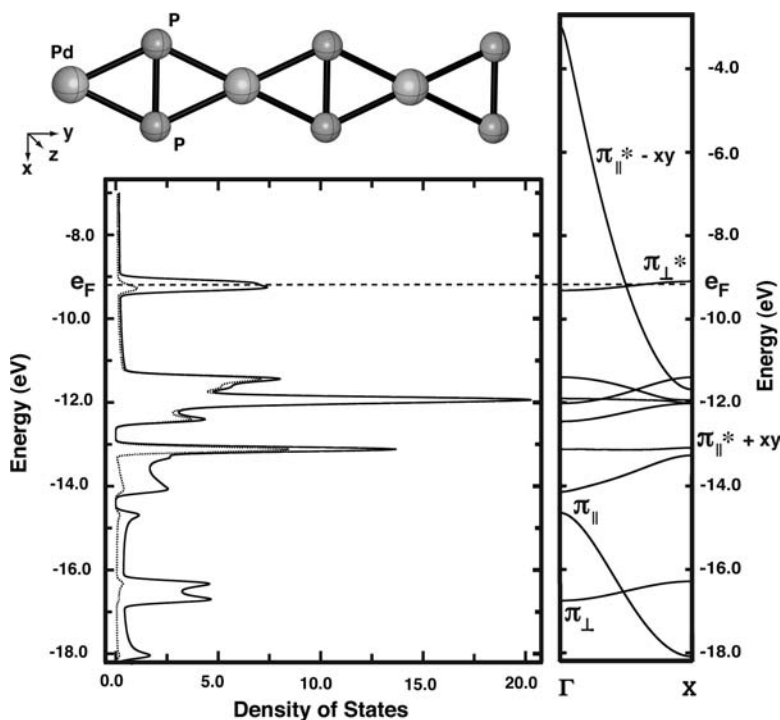
**FIGURE 19.8**

Generalized orbital interaction diagram for an olefin–( $\text{ML}_n$ )<sub>2</sub> complex.

the B3LYP level **19.57** lies 43 kcal/mol higher in energy than **19.58**. The acetylene ligand, of course, has two orthogonal  $\pi$  and  $\pi^*$  orbitals. In **19.57**, only one  $\pi/\pi^*$  set is used, whereas in **19.58** both sets can be employed. A variety of structures have been found where additional acetylene–Pt (or acetylene–Ni) units have been added on to **19.58** [47]. The ultimate structure would be a one-dimensional polymer with an acetylene–Pt unit cell [48]. There actually are a number of structures [48] with the formula  $K_2MX_2$  where  $M = Pt$  or  $Pd$  and  $X = P$  or  $As$  that have an analogous structure, **19.59**. The structure here is of  $K_2PdP_2$  where the K ions are not shown.

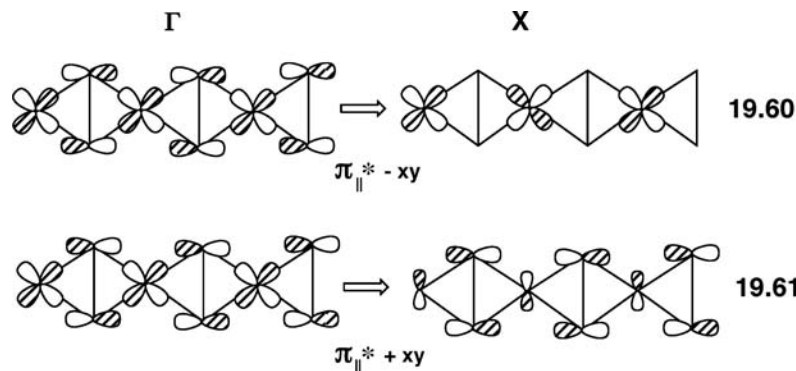
**19.59**

The P—P distance within each  $P_2$  unit is  $2.17\text{ \AA}$ . This is within the range of P—P distances for compounds with a single bond ( $\sim 2.22\text{ \AA}$ ). The P—P distances between  $PdP_2$  ribbons is  $4.19\text{ \AA}$  that is much too long to signal any bonding interaction. In terms of electron counting, the potassium atoms donate two electrons, which gives a  $PdP_2^{2-}$  chain. If the phosphorus dimers were treated as  $P \equiv P$  (and then isoelectronic to acetylene) the extra two electrons would need to be assigned to Pd. A chemically more reasonable scenario would be to use  $[P=P]^{2-}$  units (equivalent to ethylene). But then, why is the polymer kinked rather than flat as in the dimers, **19.55** and **19.56**? Let us start with a  $PdP_2$  model that is flat. Figure 19.9 shows the density of states and associated band structure for this compound. The dotted line in the DOS

**FIGURE 19.9**

DOS and band structure for a hypothetical  $PdP_2^{2-}$  one-dimensional ribbon. The structure and the coordinate system used are displayed at the upper left corner. The dashed lines indicate the position of the Fermi level and the dotted lines are the projection of Pd character in the DOS plot. The  $\pi_{||}$  and  $\pi_{\perp}$  symbols refer to the  $\pi$  orbitals in the plane and perpendicular to the plane of the one-dimensional ribbon, respectively.

plot shows the projection of Pd character. The region approximately from 11.2 to 12.6 eV represents the states associated with the four lower-lying Pd  $d$  orbitals:  $xz$ ,  $yz$ ,  $x^2 - y^2$ , and  $z^2$  using the coordinate system at the upper left side of the Figure. The Fermi level,  $e_F$ , lies in the middle of a narrow peak primarily of phosphorus character. This signals the likelihood of a Peierls distortion. The corresponding  $e(k)$  versus  $k$  plot is shown on the right side of Figure 19.9. The  $\pi_{\parallel}$  and  $\pi_{\perp}$  symbols refer to the  $\pi$  orbitals in the plane and perpendicular to the plane, respectively, in the one-dimensional ribbon. Therefore, at the Fermi level the  $\pi_{\perp}^*$  band is just the  $\pi^*$  combination of  $\text{P}_2$  perpendicular to the ribbon. Not surprisingly, this band has very little overlap with Pd and hence it has little dispersion. There are two bands which we need to examine in greater detail,  $\pi_{\parallel}^* - xy$ , 19.60, and  $\pi_{\parallel}^* + xy$ , 19.61. The latter is fully occupied and lies just below the Pd  $d$  block while the latter dips down below  $\pi_{\perp}^*$



and consequently is partially occupied. 19.61 is more heavily weighted on Pd and at the  $k=0$ ,  $\Gamma$ , point. This represents the backbonding from metal  $d$  to  $\pi^*$  in the Dewar–Chatt–Duncanson model. At the  $k=\pi/a$ ,  $X$ , point one expects that this band should rise to high energy. It does not; instead it undergoes a strongly avoided crossing with the  $\pi_{\parallel}^* - xy$  band. Likewise,  $\pi_{\parallel}^* - xy$  at  $\Gamma$  loses Pd–P  $\sigma$  antibonding on going to  $X$  and ultimately winds up in the Pd  $d$  block. Therefore,  $\pi_{\parallel}^* + xy$  remains flat and the  $\pi_{\parallel}^* - xy$  band along with  $\pi_{\perp}^*$  are both approximately half full. Density functional calculations [49] for  $\text{K}_2\text{PdP}_2$ , which employed the frozen-core projector augmented wave method, show features very similar to those in Figure 19.9, which were obtained at the extended Hückel level. By buckling the ribbon to the experimental structure creates a 28 kcal/mol per formula unit stabilization. The electronic driving force for lowering the energy can be understood in a number of ways. Doubling the unit cell for the band structure in Figure 19.9 folds back the bands in the manner discussed in Section 13.1 (see Figure 13.7 and the discussion around it). The upper part of the  $\pi_{\perp}^*$  band now has the same symmetry as the lower part of the  $\pi_{\parallel}^* - xy$ . They strongly mix upon bending and so a gap opens. At the density functional level, this amounts to an  $\sim 1.5$  eV gap. The lower part of  $\pi_{\parallel}^* - xy$  is greatly stabilized while the upper band of  $\pi_{\perp}^*$  is destabilized. A valence bond approach starts with  $\text{P}_2^{4-}$ , 19.62. There are three  $sp^3$  lone pair hybrids at each phosphorus atom.

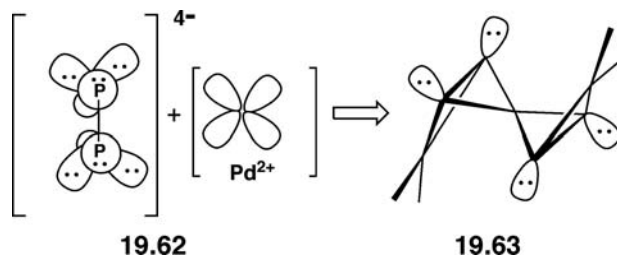
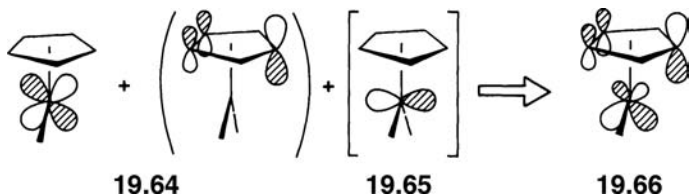


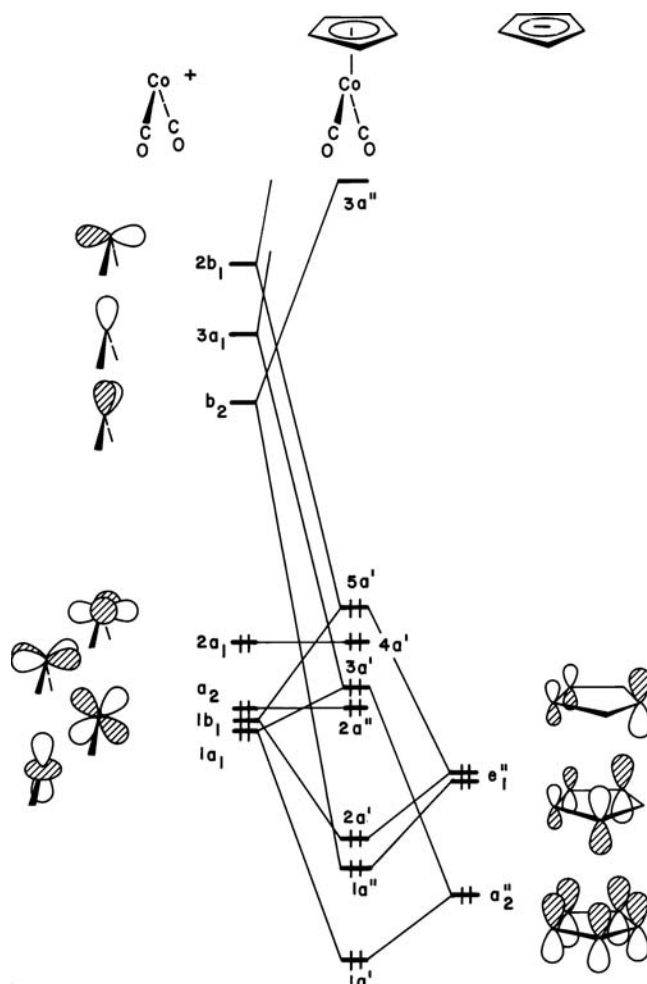
**TABLE 19.2** P—P Distances and Overlap Populations for Three Standard Molecules and K<sub>2</sub>PdP<sub>2</sub>

Compound	P—P Distance (Å)	P—P Overlap Population
P <sub>2</sub>	1.893	1.85
H <sub>2</sub> P <sub>2</sub>	2.048	1.21
H <sub>4</sub> P <sub>4</sub>	2.219	0.84
K <sub>2</sub> PdP <sub>2</sub>	2.166	0.84

The Pd<sup>2+</sup> atom has four empty hybrids made up with s, x, y, and xy character using the coordinate system at the top left of Figure 19.9. In other words, it has four empty sp<sup>2</sup>d hybrids. Two will be used to form two Pd—P σ bonds with two lone pairs on P<sub>2</sub><sup>4-</sup>. The structure then analogous to a metallacyclopropane is given in 19.63. So in K<sub>2</sub>PdP<sub>2</sub>, is the P—P bond order one? Table 19.2 reports P—P distances and P—P overlap populations for some standards and K<sub>2</sub>PdP<sub>2</sub> calculated at the extended Hückel level. The three standard molecules have P—P bond orders of three, two, and one. Using both P—P distances and overlap populations it appears that the P—P bond order in K<sub>2</sub>PdP<sub>2</sub> is close to one. This is consistent with the picture provided in 19.63. A compound with two more electrons also exists, K<sub>2</sub>PtS<sub>2</sub> [50]. The structure here has two more electrons and is a flat ribbon. Critically the S—S distance opens to 3.06 Å. This is certainly a nonbonding distance. From a valence bond point of view, the extra two electrons go into the P—P σ bond which breaks it. So there are two S<sup>2-</sup> bridging atoms connected to the Pd<sup>2+</sup> atoms. From a delocalized perspective, the additional two electrons fill the π<sub>||</sub>\*—xy and π<sub>⊥</sub>\* bands. When the S—S distance increases, the π\* interaction and Pd xy—P y overlap decreases, so the energy of the π<sub>||</sub>\*—xy and π<sub>⊥</sub>\* bands decreases which stabilizes the structure.

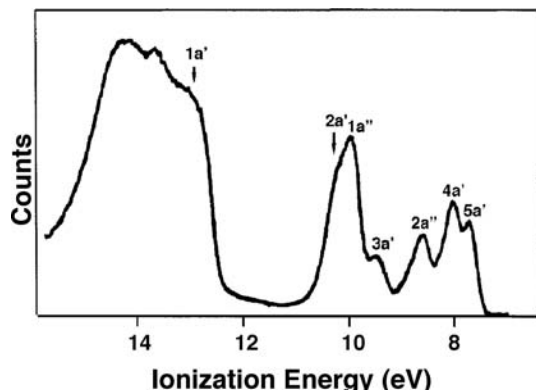
Let us move on to a more complicated polyene-ML<sub>2</sub> complex. An orbital interaction diagram for CpCo(CO)<sub>2</sub> [51] is presented in Figure 19.10. The Cp ligand has been treated as an anionic, six-electron donor. The three filled π orbitals that serve this function are displayed on the right side of the figure. This requires the metal to be formally Co<sup>+</sup>, d<sup>8</sup>, and with the two CO ligands an 18-electron count at the metal is achieved. The form of the resultant MOs is fairly easy to derive. The a<sub>2</sub>' orbital of Cp<sup>-</sup> interacts primarily with 1a<sub>1</sub> and 3a<sub>1</sub> on Co(CO)<sub>2</sub><sup>+</sup>. Two of the three composite MOs, labeled 1a' and 3a' in Figure 19.10, stay at low energy and are filled. The 2a<sub>1</sub> and a<sub>2</sub> fragment orbitals of Co(CO)<sub>2</sub><sup>+</sup> have δ symmetry with respect to Cp<sup>-</sup>. This means that they overlap with the two highest π\* orbitals of Cp (not shown in the figure, see Figure 12.10). However, the energy gap is quite large and the overlap is small since it is of the δ type, so the interaction is weak. Therefore, 2a<sub>1</sub> and a<sub>2</sub> are essentially nonbonding. One component of the e<sub>1</sub>'' set on Cp<sup>-</sup> interacts strongly with the empty b<sub>2</sub> fragment orbital of Co(CO)<sub>2</sub><sup>+</sup>. This generates the 1a'' and 3a'' MOs in the molecule. The former MO is filled and the latter is empty, see Figure 19.10. The other component of e<sub>1</sub>'' interacts primarily with 1b<sub>1</sub>. Notice that 1b<sub>1</sub> and e<sub>1</sub>'' are both filled, so the bonding, 2a', and antibonding, 5a', combinations are occupied. The composition of 5a' is primarily given by 1b<sub>1</sub> with e<sub>1</sub>'' mixed into it in an antibonding fashion, 19.64. Additionally, some 2b<sub>1</sub> character from the Co(CO)<sub>2</sub><sup>+</sup> fragment



**FIGURE 19.10**

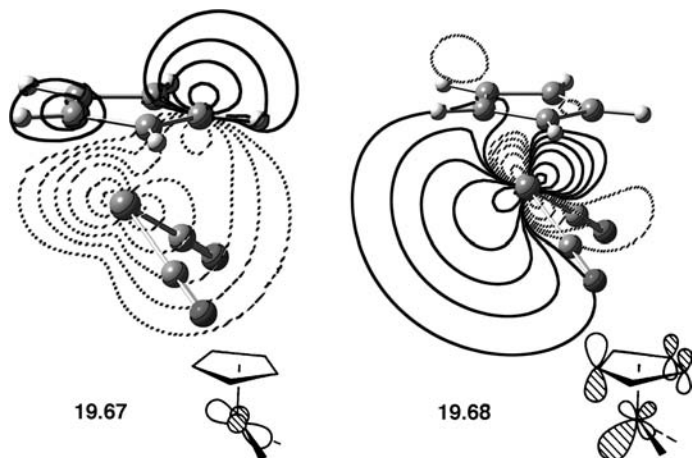
An orbital interaction diagram for  $\text{CpCo}(\text{CO})_2$  at the extended Hückel level.

mixes in second order with the phase relationship shown in **19.65** (bonding to  $e_1''$ ). The resultant MO, **19.66**, is heavily weighted on the metal and hybridized away from the Cp ligand. The reader may be puzzled as to why the  $b_1 - e_1''$  orbital,  $5a'$ , stays at such a low energy compared to the  $b_2 - e_1''$  analog,  $3a''$ . The  $b_2$  level is initially at a higher energy than  $1b_1$ . Furthermore, it is hybridized, whereas  $1b_1$  is not, which makes the overlap between  $b_2$  and  $e_1''$  larger than that between  $1b_1$  and  $e_1''$ . Another reason is the second-order mixing that  $2b_1$  offers. This keeps the energy of  $5a'$  low and  $b_2$  has no low-lying counterpart which accomplishes an analogous task. Nevertheless,  $5a'$  does lie at moderately high energies because of metal  $d$ —Cp  $\pi$  antibonding.  $\text{CpCo}(\text{CO})_2$  is consequently a strong base [52]. Puckering the Cp ligand to diminish this antibonding is energetically favorable for  $\text{CpCo}(\text{CO})_2$  [53] as well as for other 18-electron polyene– $\text{ML}_2$  complexes where an analogous situation occurs [54]. Alternatively, the  $\text{ML}_2$  unit can slip to a lower coordination number to relieve this antibonding interaction. The photoelectron spectrum of  $\text{CpCo}(\text{CO})_2$  [55] is shown in Figure 19.11. The first ionization potential of 7.59 eV is quite low. All assignments [56] have pointed to  $5a'$ , **19.66**, as being associated with this ionization. The assignments for the other six ionizations roughly agree with the order presented in Figure 19.10 but  $3a'$  and  $2a''$  along with  $2a'$  and  $1a''$  are inverted. Nonetheless, the details of the electronic structure in a complicated molecule with little symmetry can be understood and verified by experiment.

**FIGURE 19.11**

He(I) photoelectron spectrum of  $\text{CpCo}(\text{CO})_2$ . The assignments correspond to the orbitals in Figure 19.10.

Suppose the two electrons in  $5a'$  were removed, yielding a 16-electron complex, for example,  $\text{CpMn}(\text{CO})_2$ . Reference back to Figures 19.10 and 19.11 shows that the now empty  $5a'$  orbital lies fairly close in energy to the HOMO,  $4a'$ . Pyramidalization causes the two orbitals to mix [51], which lowers the energy of  $4a'$  and raises the energy of the empty  $5a'$ . The form of  $4a'$  and  $5a'$  at a pyramidal geometry is given by **19.67** and **19.68**, respectively. The stabilization of the HOMO,



**19.67**, causes the pyramidal geometry for  $\text{CpMn}(\text{CO})_2$  to be favored over a planar one. The LUMO, **19.68**, is beautifully hybridized to interact with the lone pair of a third carbonyl giving  $\text{CpMn}(\text{CO})_3$ —a well-known, 18-electron complex (see Section 20.1). There is an amusing antithetic relationship here between these organometallic  $\text{CpML}_2$  complexes and main group analogs. Consider the  $\text{Cp}$  unit to be one “ligand.” The 16-electron  $\text{L}'-\text{ML}_2$  ( $\text{L}' = \text{Cp}$ ) complexes are pyramidal, whereas six-electron compounds such as  $\text{CH}_3$  and  $\text{BR}_3$  are planar (see Section 9.3). Both classes, of course, have a low-lying LUMO and are strong Lewis acids. The addition of two electrons causes the  $\text{L}'-\text{ML}_2$  series to become planar (**19.68** is stabilized); however, eight-electron main group compounds such as  $\text{CH}_3^-$  and  $\text{NH}_3$  are pyramidal. Again both classes have a high-lying HOMO and are Lewis bases. The magnitude of the inversion barrier is predicted to be very sensitive to the nature of the auxiliary ligands [51]. When  $\text{L}$  is a  $\pi$ -acceptor, for example,  $\text{CO}$ , the inversion barrier is largest. DFT calculations [51] give the inversion barrier for  $\text{CpFe}(\text{CO})_2^+$  to be 10.5 kcal/mol. There is ample kinetic proof for the existence of an inversion barrier in a number of analogous complexes [57], and there are a number of 16-electron  $\text{CpML}_2$  complexes that have been isolated and have a pyramidal structure [58]. But there are three caveats to recognize in this area. First, the barrier may be very low or even

nonexistent when the auxiliary ligands are  $\sigma$  donors with little or no  $\pi$ -accepting capability. An example is given by  $\text{CpRu}(\text{NR}_3)_2^+$  complexes [58]. Second, the photolysis of  $\text{CpM}(\text{CO})_3$ ,  $\text{M} = \text{Mn, Re}$ , produces singlet  $\text{CpM}(\text{CO})_2$  which reacts without a barrier to produce  $\text{CpM}(\text{CO})_2(\text{solvent})$  without the observation of a discrete  $\text{CpM}(\text{CO})_2$  molecule [59]. Finally, the HOMO–LUMO splitting is small, so a triplet state with one electron in both orbitals is also viable [60]. In fact, a number of  $\text{CpFe}(\text{PR}_3)_2^+$  molecules have been isolated, have planar geometries and are, in fact, triplets [61]. The triplet state for  $\text{CpMn}(\text{CO})_2$  is predicted to be 10 kcal/mol more stable than the singlet [59]. For  $\text{CpFe}(\text{PH}_3)_2^+$ , this energy difference is 3 kcal/mol while in  $\text{CpFe}(\text{CO})_2^+$  the singlet is predicted to be more stable than the triplet by 3 kcal/mol [62].

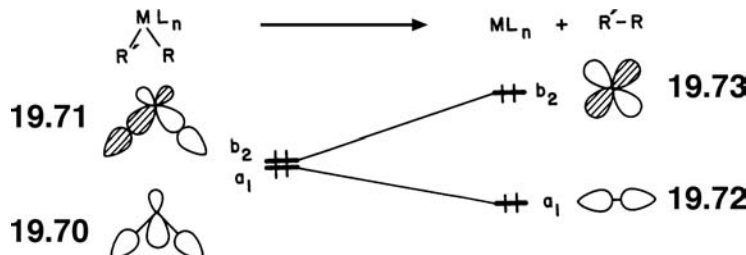
## 19.6 REDUCTIVE ELIMINATION AND OXIDATIVE ADDITION

In a reductive elimination reaction, a dialkyl transition metal complex decomposes into an alkane and a coordinatively unsaturated complex as shown in **19.69**. The reaction is



synthetically useful under catalytic and stoichiometric conditions [63], and the reverse reaction, oxidative addition of an unsaturated metal complex into a C–C or C–H bond, offers a way to functionalize alkanes. Consequently, there has been much research on the mechanistic aspects of the reaction in the academic and industrial communities. The electronic aspects of this reaction and its reverse have also been studied extensively [64]. The wide variety of metals, the number of ligands, and the electronic properties of the ligand set in **19.69** create a tremendous diversity in terms of reaction rates and even mechanistic details.

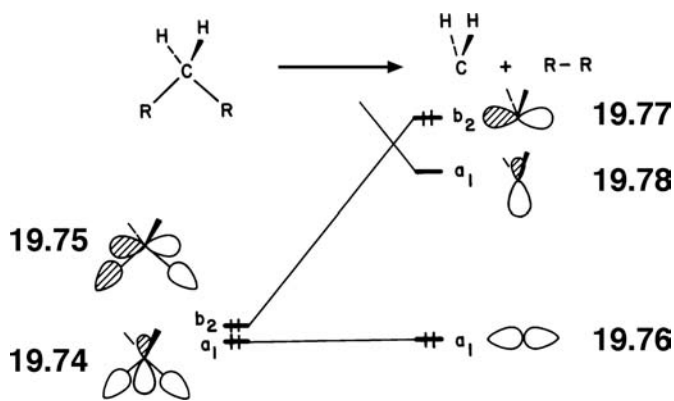
The discussion here starts in a very generalized sense with the reductive elimination reaction. There are four electrons in the two M–R bonds of **19.69**. We would formally assign them to the alkyl groups; hence, we assign the formal oxidation state of the metal to be  $\text{M}(\text{x}+2)$ . Two of the electrons are used to form the C–C bond in the alkane product of the reaction; the remaining two electrons become localized on the coordinately unsaturated metal complex making it have the metal oxidation state  $\text{x}$ . Linear combination of the two M–R bonds produces **19.70** and **19.71**. The splitting between **19.70** and **19.71** is expected to be small. Both



orbitals will be concentrated on the alkyl groups with some metal  $d$  and  $p$  character (**19.70** will also contain metal  $s$  character). As the reductive elimination reaction proceeds, **19.70** smoothly correlates to a  $\sigma$  C–C bond, **19.72**, while **19.71** evolves

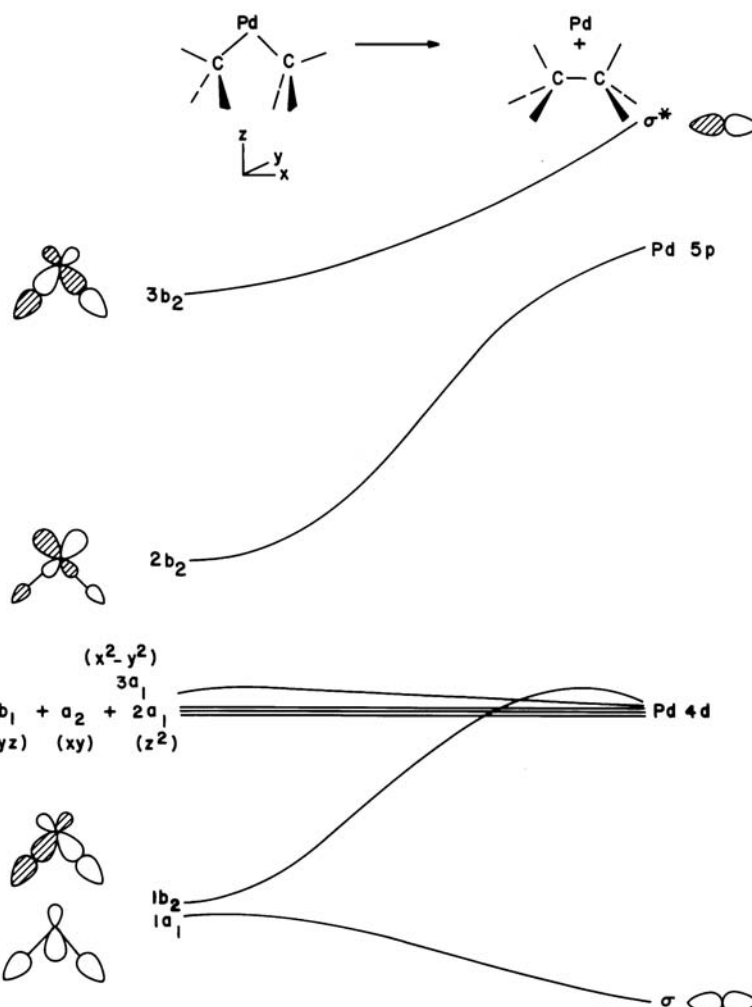
into a nonbonding metal  $d$  orbital, **19.73**. The metal plays two roles in this reaction: it serves as a geometrical template holding the two alkyl groups in close proximity, and it is a repository for the other two electrons. There is a crucial difference here in the latter role compared to organic and main group compounds.

Consider an analogous least-motion reaction for the reductive elimination process in  $\text{CH}_2\text{R}_2$  that yields  $\text{CH}_2$  and  $\text{R}-\text{R}$ . The MOs displayed in **19.74** and **19.75** are analogs of **19.70** and **19.71**, respectively. They have been labeled according to the  $C_{2v}$  symmetry of the molecule. A least-motion path then conserves  $C_{2v}$  symmetry. The  $a_1$  level, **19.74**, again becomes the  $\text{C}-\text{C} \sigma$  level, **19.76**, of the



resulting alkane. However, now the  $b_2$  orbital, **19.75**, correlates with a  $p$  orbital of  $\text{CH}_2$ , **19.77**. We know from Section 7.2 that the  $a_1$  level, **19.78**, of  $\text{CH}_2$  lies below  $b_2$  in energy. **19.78** evolved from an empty  $\sigma^*$  orbital, and therefore, the least-motion path for this reaction or the reverse—insertion of  $\text{CH}_2$  into a  $\text{C}-\text{C}$  bond—is symmetry forbidden. The  $\text{CH}_2$  group must undergo a sideways rocking motion as the two alkyl groups couple. The symmetry of the activated complex is lowered to  $C_s$ . An analogous pathway, the reaction of  $\text{CH}_2$  with ethylene to form cyclopropane, was covered in Section 11.2.1.

Returning back to the reductive elimination process for transition metal complexes, the evolution of **19.71–19.73** seems to be a bit mysterious. Originally, **19.71** is concentrated on the alkyl groups. One might think that this orbital should ultimately become the  $\sigma^*$  level of  $\text{R}'-\text{R}$ . At some point along the reaction path, electron density must be shifted from the alkyl groups toward the metal. We have conveniently left out a number of orbitals in this analysis, one of which serves to redistribute the electron density in **19.71**. **19.71** is crucial because its upward slope will figure heavily in setting the activation energy for the reaction [65]. Let us look at the decomposition of  $\text{MR}_2$  into a naked metal atom and  $\text{R}-\text{R}$ . Figure 19.12 shows this for  $\text{R}=\text{CH}_3$  and  $\text{M}=\text{Pd}$ . This is not a reaction that is likely to occur on thermodynamic grounds; however, it contains all of the elements present in a more realistic case. On the left side of this figure are the orbitals of  $\text{Pd}(\text{CH}_3)_2$ . They are identical with those derived for a  $\text{ML}_2$  fragment in Figure 19.5 except that they have been redrawn so that the  $\text{MR}_2$  “molecule” lies in the plane of the paper. The lower two  $\text{M}-\text{R} \sigma$  levels, which correspond to **19.70** and **19.71** ( $1a_1$  and  $1b_2$ , respectively), have also been included in the Walsh diagram. The  $1a_1$  orbital has been drawn very stylistically. It actually consists of metal  $s$ ,  $z$ ,  $x^2-y^2$ , and  $z^2$  bonding to the in-phase combination of alkyl lone-pair orbitals. There are now three orbitals of  $b_2$  symmetry:  $1b_2$  is concentrated on the alkyl groups bonding to metal  $x$  and  $xz$ ;  $2b_2$  corresponds to the  $b_2$  valence orbital in the  $\text{ML}_2$  fragment (see Figure 19.5); finally,  $3b_2$  is the fully antibonding analog of  $1b_2$ . There is also a block of

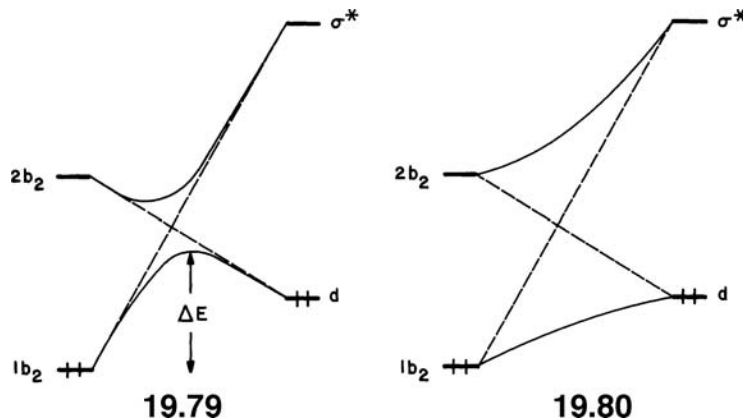
**FIGURE 19.12**

A Walsh diagram for reductive elimination in  $\text{Pd}(\text{CH}_3)_2$ .

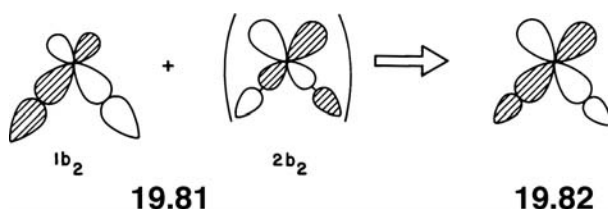
four nonbonding metal  $d$  orbitals,  $2a_1 + b_1 + a_2 + 3a_1$ , at moderate energy. A  $d^8$  complex like  $\text{Pd}(\text{CH}_3)_2$  will have  $3a_1$  as the HOMO and  $2b_2$  as the LUMO.

When the C—Pd—C angle decreases and the two methyl groups pivot toward each other, the energy of  $1a_1$  goes down. It smoothly correlates to the  $\sigma$  C—C bond of ethane. The  $1b_2$  level rises in energy; metal–carbon bonding is lost and some antibonding between the methyl groups is introduced until finally  $1b_2$  evolves into the Pd  $xz$  atomic orbital. Nothing much happens to the block of four metal  $d$  orbitals. They essentially stay nonbonding with respect to the methyl groups along the reaction path. The  $2b_2$  and  $3b_2$  levels behave differently. Initially,  $2b_2$  is primarily metal  $xz$ ; as the methyl groups move toward each other, antibonding between them and  $xz$  is diminished. Therefore,  $2b_2$  stays at relatively constant energy, or in a more realistic system it may even be stabilized. Ultimately it becomes a Pd  $x$  atomic orbital; consequently, it rises in energy. The  $3b_2$  MO behaves in a similar manner; it becomes the C—C  $\sigma^*$  orbital of ethane. The three  $b_2$  levels undergo avoided crossings. Let us concentrate only on  $1b_2$  and  $2b_2$ . There is a natural correlation between  $1b_2$  and  $\sigma^*$  along with  $2b_2$  descending to the metal  $d$  block. This is indicated by the dashed line in **19.79**. However, remember that two molecular orbitals of the same symmetry may never cross (Section 4.7). An avoided crossing occurs so that  $1b_2$  becomes metal  $xz$ . Another avoided crossing

takes place between  $2b_2$  and  $3b_2$  so that  $2b_2$  actually correlates to the Pd  $x$  AO, and  $3b_2$  becomes  $\sigma^*$ . For simplicity, we disregard the latter avoided crossing, and as

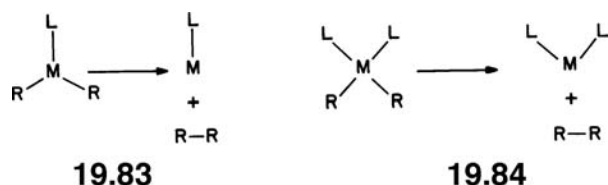


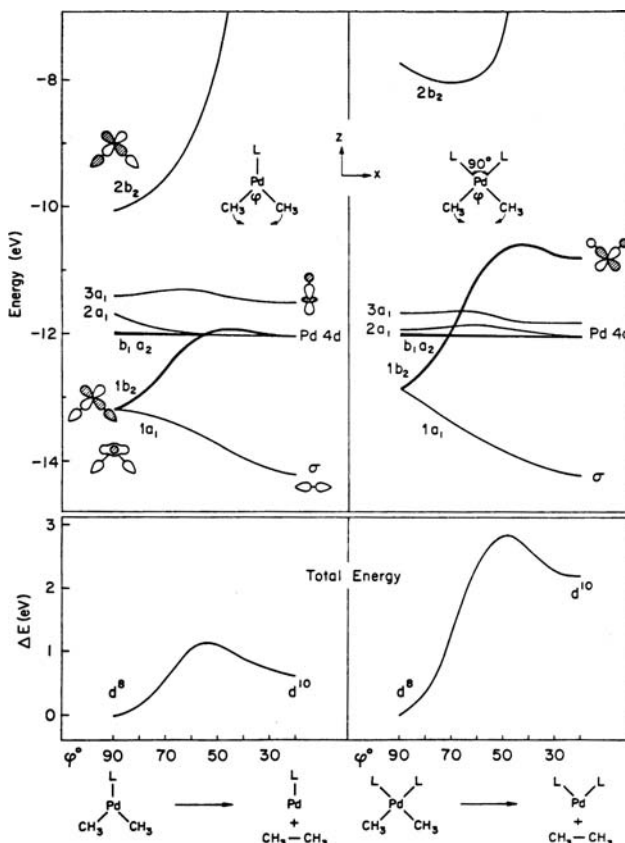
shown in **19.79**,  $2b_2$  will yield  $\sigma^*$ . The intermixing of  $1b_2$  and  $2b_2$  can be treated in a typical perturbation mode. The amount of mixing depends directly on the amount of overlap between the two unperturbed MOs that is introduced along the reaction path and inversely on the energy difference between the molecular orbitals. The quantity  $\Delta E$  in **19.79** is related to the origin of the activation barrier for reductive elimination considering only the changes in orbital energies. The situation shown in **19.80** is a weakly avoided crossing. There is not much intermixing between  $1b_2$  and  $2b_2$  until just before the crossing would have taken place. The pattern illustrated by **19.80** is indicative of a strongly avoided crossing. Here there is substantial intermixing between  $1b_2$  and  $2b_2$  all along the reaction path. The avoided crossing for  $\text{Pd}(\text{CH}_3)_2$  in Figure 19.12 lies somewhere between these two extremes and is complicated by the intermixing with  $3b_2$ . Nonetheless, there is significant  $1b_2$ ,  $2b_2$  mixing, and the phase relationship is given by the major components in both molecular orbitals—the methyl hybrids in  $1b_2$  and metal  $xz$  in  $2b_2$ . The  $2b_2$  MO lies above  $1b_2$ , and therefore, it mixes into  $1b_2$  in a net bonding manner, **19.81**. The resultant MO, **19.82**, contains increased metal  $xz$  and decreased methyl character.



The intermixing continues until  $1b_2$  becomes a pure metal  $xz$  orbital. The  $1b_2$  level will also mix into  $2b_2$  with the opposite phase relationship to that shown in **19.81**. Cancellation of metal  $x$  and  $xz$  character and reinforcement of methyl character occurs so that  $2b_2$  becomes  $\sigma^*$  (neglecting the influence of  $3b_2$ ).

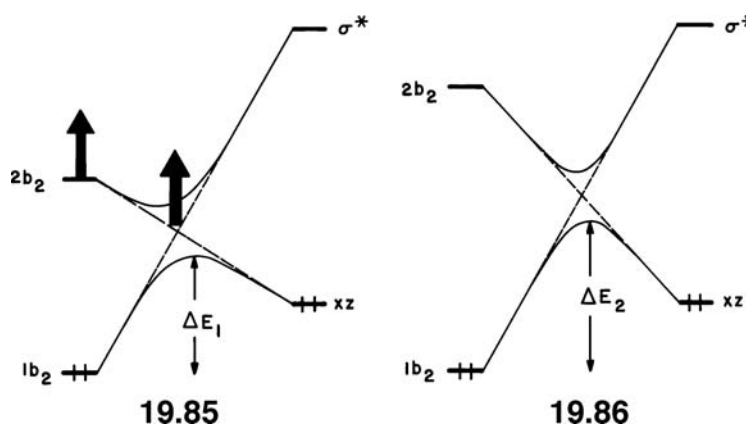
Let us now turn our attention to a couple of more realistic models, **19.83** and **19.84**, where in both cases the metal is  $d^8$  in the starting complex and L is an



**FIGURE 19.13**

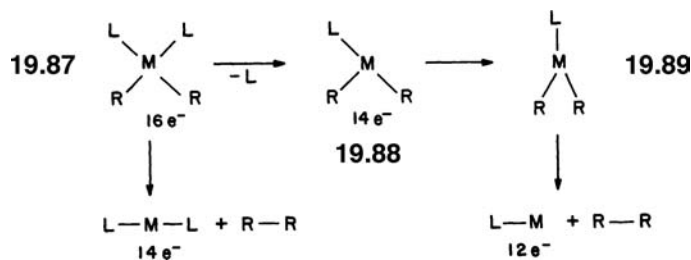
Walsh diagrams for reductive elimination in a three coordinate  $\text{L}-\text{Pd}(\text{CH}_3)_2$  and  $\text{L}_2\text{Pd}(\text{CH}_3)_2$  complex. For simplicity the L groups were taken to be  $\text{H}^-$  with their valence state ionization potentials adjusted to match the lone pair orbital of  $\text{PH}_3$ . Here,  $\phi$  is defined as the  $\text{C}-\text{Pd}-\text{C}$  angle; this was varied in concert with stretching the  $\text{Pd}-\text{C}$  bonds and rocking the methyl groups off from the  $\text{Pd}-\text{C}$  axis, toward each other. (Reprinted with permission from Reference [65a].)

arbitrary two-electron donor ligand (e.g.,  $\text{PPh}_3$ ). Walsh diagrams for these examples are displayed in Figure 19.13. On the left side is the case for the trigonal  $\text{L}-\text{MR}_2$  species. It is essentially identical to the  $\text{Pd}(\text{CH}_3)_2$  case in Figure 19.12. The extra ligand L with its donor orbital of  $a_1$  symmetry cannot mix into any of the crucial  $b_2$  orbitals (notice that  $2a_1$  and  $3a_1$  are destabilized slightly by the donor orbital of L). The calculated total energy for the reaction is plotted at the bottom left of Figure 19.13. The moderate activation energy is clearly due to the rise in energy of  $1b_2$ , counterbalanced by the stabilization in  $1a_1$ . The  $\text{L}_2\text{MR}_2$  system is plotted on the right side of this figure. First, the calculated total energy is much greater than that for  $\text{L}-\text{MR}_2$ . Notice that  $1b_2$  rises to a much higher energy in  $\text{L}_2\text{Pd}(\text{CH}_3)_2$ . The reason behind this change is that one combination of the ligand lone-pair hybrids has  $b_2$  symmetry. It destabilizes  $2b_2$  greatly and restores a square planar splitting pattern. Therefore,  $2b_2$  corresponds now to  $2b_{1g}$  in Figure 19.5. 19.85 shows the essential details of the avoided crossing in the  $\text{L}-\text{Pd}(\text{CH}_3)_2$  (or  $\text{Pd}(\text{CH}_3)_2$ ) model. Raising the energy of  $2b_2$  causes the intersection of the dashed lines in 19.85 to go up in energy. This is indicated by the arrows. The avoided crossing now corresponds to that given in 19.86 and is appropriate for the  $\text{L}_2\text{Pd}(\text{CH}_3)_2$  reaction on the right side of Figure 19.13. The  $1b_2$  level must rise to a higher energy before the avoided crossing occurs, and consequently the reaction requires a greater activation energy. However, there are two important qualifications that should be given for this analysis. First, there must be approximately the same intermixing of  $1b_2$  and  $2b_2$  along the reaction path in the two reactions. Second, the avoided crossing cannot be of the strongly avoided type since that would predict equal activation energies. These conditions are fulfilled in this example. One can also think of other complications. For example, the  $\text{L}-\text{Pd}-\text{L}$  angle in Figure 19.13 was kept at  $90^\circ$ . This is



unreasonable since the product of the reductive elimination for the  $\text{L}_2\text{Pd}(\text{CH}_3)_2$  case is the 14-electron  $\text{L}-\text{Pd}-\text{L}$  complex which is expected to be linear. Notice that the  $1b_2$  orbital on the product side lies at very high energy and this is the reason why the reaction is calculated to be very endothermic. Allowing the  $\text{L}-\text{Pd}-\text{L}$  angle to relax along the reaction path to  $180^\circ$  will stabilize  $1b_2$ ; it will merge with the block of other  $d$  orbitals. This also lowers the activation energy; however, it is still computed to be larger than that in the  $\text{L}-\text{Pd}(\text{CH}_3)_2$  system [65b].

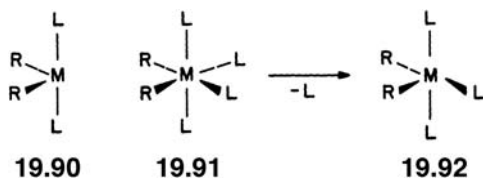
The theoretical prediction we made here is somewhat unusual. That is, reductive elimination from a 16-electron  $\text{L}_2\text{MR}_2$  complex, **19.87**, to the 14-electron



$\text{L}_2\text{M}$  species is less facile than reductive elimination from a 14-electron  $\text{LMR}_2$  complex, **19.88**, to a 12-electron  $\text{LM}$  intermediate. Moreover, we know something about the geometry and dynamics of **19.88** from Section 18.2. Inspection of Figure 18.3 and the discussion around it tells us that a 14-electron  $\text{LMR}_2$  complex will be stable at a “T” or “Y” structure. A trigonal geometry where the  $\text{L}-\text{M}-\text{R}$  and  $\text{R}-\text{M}-\text{R}$  angles are approximately equal is a high energy point on the potential surface. (Although the symmetry of  $\text{LMR}_2$  is likely to be lower than  $D_{3h}$ , the surface will still strongly resemble that in Figure 7.7; References [65–68] give some practical examples.) The Y structure, **19.89**, where the  $\text{R}-\text{M}-\text{R}$  angle is acute, will serve as the exit geometry for reductive elimination. The path from **19.87** to **19.89** has been experimentally demonstrated for a number of systems, for example,  $\text{Pd}^{2+}$ ,  $\text{Au}^{3+}$ , and  $\text{Pt}^{2+}$  [63]. The dissociation of a ligand from **19.87** to **19.88** must be an endothermic process. Therefore, a delicate balance exists for reductive elimination from **19.87** or **19.88** as well. If ligand dissociation becomes too endothermic, then direct reductive elimination from the four-coordinate **19.87** will be more favorable. For example, computations [66] suggest that reductive elimination of ethane from  $\text{L}_2\text{Pd}(\text{CH}_3)_2$  with  $\text{L}=\text{P}(\text{c-hex})_3$  proceeds via **19.88** but with  $\text{L}=\text{PMe}_3$ , the direct path from **19.87** is operative. If the avoided crossing between  $1b_2$  and  $2b_2$  is made to be more strongly avoided, then the direct pathway

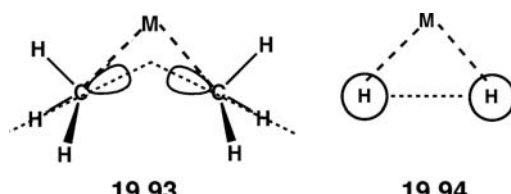
can be made more viable. An obvious way to do this is to make the metal more electronegative so the  $d$  AOs will lie at lower energy. Examples exist for  $\text{Ni}^{2+}$  complexes [63]. One can also see that the electronic nature of the auxiliary ligands determines the eventual choice of reaction paths. As  $L$  becomes a stronger donor, the  $2b_2$  orbital is increasingly destabilized and reductive elimination is rendered less facile. But replacing a phosphine with an olefin with strong electron withdrawing groups greatly lowers the barrier [67], which is consistent with stabilizing  $2b_2$ . Making the alkyl groups better  $\sigma$  donors will actually lower the activation energy. This is because the energy of  $1b_2$  (concentrated on the alkyl lone-pair functions) rises when  $R$  is a better  $\sigma$  donor. One must be a little careful here. The barrier for reductive elimination by either pathway is much larger for  $M = \text{Pt}$  than  $\text{Pd}$ . This is because the  $\text{Pt}-\text{C}$  bonds are stronger than  $\text{Pd}-\text{C}$  ones. There are a number of ways to rationalize this; a simple one is derived from a valence bond point of view [68]. The  $\text{M}-\text{C}$   $\sigma$  bonds are constructed from  $sp^3$  hybrids on carbon and  $sd$  hybrids from the metal  $s^1d^9$  state of the metal. For Pt, this is the ground state of the atom, but for Pd the  $d^{10}$  configuration is the ground state. It is the relativistic effect on the  $6s$  AO for Pt that causes this and in general makes the transition metal–carbon bonds of the third row more stable than their second row analogs. There are serious concerns [69] about the viability of a true 14-electron complex analogous to **19.88**. Of the complexes that have been isolated, all have an agostic bond occupying the fourth coordination site. **18.9** provides one example that we have seen before. The current thought is that a solvent molecule or an agostic bond stabilizes the 14-electron complex in its “resting state.” A low energy dissociation step then precedes the actual reductive elimination event for the dissociative mechanism.

The model that we have presented can easily be extended to other systems. In the past sections of this chapter we have highlighted the close resemblance between the orbitals of  $C_{2v}$   $\text{ML}_2$  and  $C_{2v}$ ,  $\text{ML}_4$  fragments. Our discussion in this chapter could have started from the orbitals of a  $d^6$   $\text{L}_2\text{MR}_2$  species, **19.90**. The orbital pattern and



occupation is equivalent to that for the  $d^8 \text{MR}_2$  system in Figure 19.12. One or two extra ligands could be added, and we would have come to an equivalent prediction: reductive elimination from the  $d^6$ , 18-electron  $\text{L}_4\text{MR}_2$  complex, **19.91**, requires a greater activation energy than that for the 16-electron  $\text{L}_3\text{MR}_2$  complex, **19.92** [65,70]. Here again, **19.92** rearranges from a “T” geometry to a “Y” one which then undergoes the reductive elimination step.

The reverse of reductive elimination, oxidative addition (**19.69**) might be thought to be just microscopic reverse of the paths that we have just covered. This is not exactly true for thermodynamic reasons. The reductive elimination reactions of  $(\text{PR}_3)_2\text{MR}_2$ ,  $\text{M} = \text{Pd}, \text{Pt}$ , are very exothermic by 20–40 kcal/mol (contrary to the total energy profiles in Figure 19.13). Certainly the reverse reaction cannot possibly take place. Nor is it likely that a 12-electron  $\text{M}(\text{PR}_3)$  can be generated as an intermediate. The  $\text{M}-\text{R}$  bond energies must be considerably larger to offset the large C–C or C–H bond energy along with the entropy cost (two particles into one) to make a viable oxidative addition. Furthermore, the geometry associated with the transition state for oxidative addition/reductive elimination certainly favors the latter for the coupling of two methyl groups. As shown in **19.93**, the two  $sp^3$  carbons



must have partial bonding to the metal atom and partial C—C bonding. In other words, the C—C bond must be partially broken and this requires severe geometrical constraints for the oxidative addition to a C—C  $\sigma$  bond. The addition to the H—H bond in  $H_2$ , as in 19.94, or the H—C bond in an alkane is expected to require lower activation energies even though the H—H and C—H bond energies are larger (104 and 98 kcal/mol, respectively) than that for a C—C bond (88 kcal/mol) since the s AO is spherical and can, therefore, retain overlap between two partners more effectively than a highly directional  $sp^3$  hybrid. Let us consider the addition of  $H_2$  to the 16-electron  $Fe(CO)_4$ . With reference back to Figures 19.1 and 19.3, the empty  $2a_1$  MO on singlet  $Fe(CO)_4$  will interact with and stabilize  $H_2 \sigma$ . Electron density from the H—H bonding region is delocalized towards Fe. The filled  $b_2$  orbital on  $Fe(CO)_4$  will overlap with  $H_2 \sigma^*$ . Electron density flows from  $Fe(CO)_4$  to the H—H antibonding region. Both interactions serve to weaken the H—H bond and strengthen the Fe—H ones. This is graphically illustrated in Figure 19.14. These

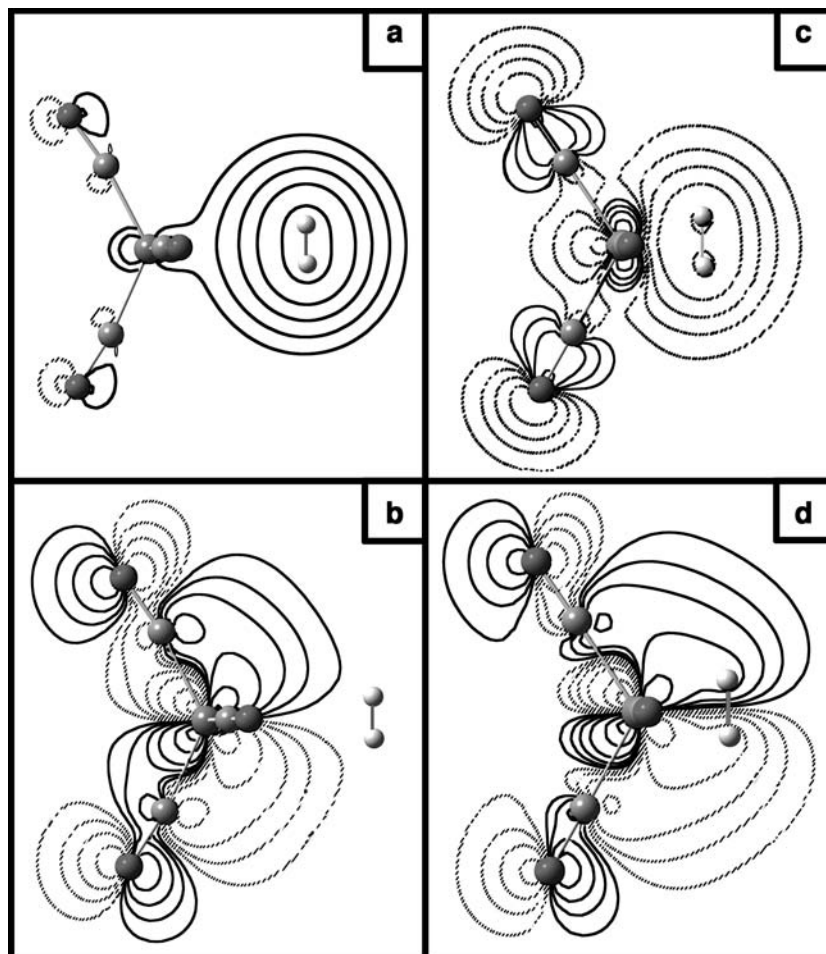
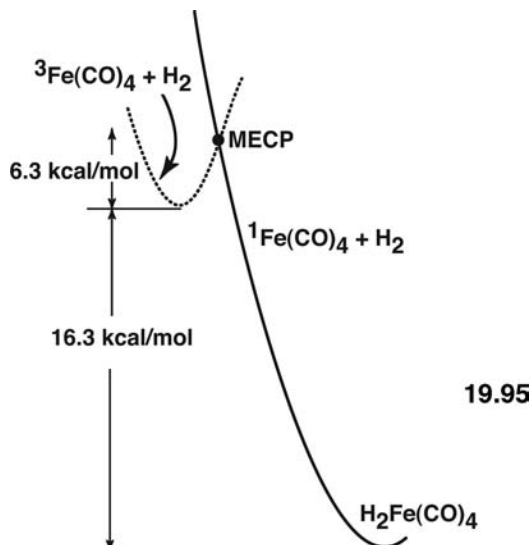


**FIGURE 19.14**

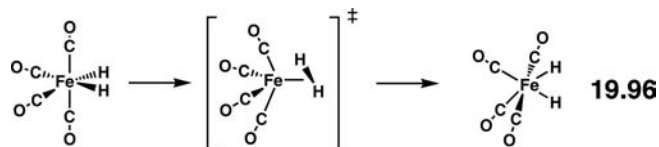
Contour plots from B3LYP calculations of the  $H_2 \sigma + Fe(CO)_4$   $2a_1$  MO in (a) and (c) along with  $H_2 \sigma^* + Fe(CO)_4$   $b_2$  MO in (b) and (d). The Fe to  $H_2$  midpoint distance was 3.0 Å in (a) and (b) while it was 1.75 Å in (c) and (d).

are contour plots of the two combinations at the B3LYP level where (a) and (b) were obtained when the Fe, midpoint of the H—H bond,  $r$ , was 3.0 Å. One can barely see any interaction between the  $\text{H}_2$  and the  $\text{Fe}(\text{CO})_4$  units. The situation is much different for  $r = 1.75$  Å as shown in (c) and (d). The electron density in (c) around the  $\text{Fe}(\text{CO})_4$  group originated from  $\text{H}_2 \sigma$ . In (d) the antibonding along the H—H axis is quite evident. Ultimately, at about  $r = 1.5$  Å, the H—H bond is totally broken and the  $\text{H}_2\text{Fe}(\text{CO})_4$  product lies  $\sim 19$  kcal/mol lower than the energy of the isolated reactants [5]. But remember that the ground state of  $\text{Fe}(\text{CO})_4$  is, in fact, the triplet. The  $\text{Fe}(\text{CO})_4$  molecule has one electron in  $2a_1$  and  $b_2$ . The interaction of  $2a_1$  with  $\text{H}_2 \sigma$  is a two orbital—three electron one while that between  $b_2$  and  $\text{H}_2 \sigma^*$  is of the two orbital—one electron kind. Furthermore, there is repulsion between  $\text{H}_2 \sigma$  and filled  $1a_1$  (see Figure 19.2). Thus, the attraction between the two reactants is diminished, and the potential energy surface is repulsive. So the comprehensive experimental and theoretical picture for this reaction [5] is the photochemical excitation of  $\text{Fe}(\text{CO})_5$  with concomitant CO loss (similar to that discussed for  $\text{Cr}(\text{CO})_6$  in Chapter 17) to give triplet  $\text{Fe}(\text{CO})_4$ . As shown in 19.95 the  ${}^3\text{Fe}(\text{CO})_4 + \text{H}_2$  complex must undergo a



spin state change through a minimum energy crossing point (MECP). The resultant  ${}^1\text{Fe}(\text{CO})_4 + \text{H}_2$  complex then decays without activation to the product. It is the MECP that creates an activation barrier for this reaction. The height of the MECP for oxidative addition of  $\text{H}_2$  to metal complexes ranges from minuscule to very significant depending on the single–triplet energy difference of the metal precursor [71].  $\text{H}_2$  addition to other singlet 16-electron  $\text{ML}_4$  complexes, which possess a butterfly type of structure, also do not have an intrinsic reaction barrier [72,73]. We previously covered dihydrogen complexes of the form  $(\text{H}_2)\text{ML}_5$ , see 15.25. The components of bonding, 15.26 and 15.27, are precisely the same as those discussed here. In fact, the H—H distances in these molecules vary from not much longer than an isolated  $\text{H}_2$  molecule to quite long ones where there certainly is no direct H—H bonding. The structure depends on the metal and L groups where substantial back-donation (15.27) via a high-lying metal  $t_{2g}$  set breaks the H—H bond. So are there instances where the metal–dihydrogen complex is an intermediate along the reaction path for oxidative addition? Our suspicion is that there is none; the overlap in 19.94 varies in a smooth and continuous fashion along a least-motion reaction path that varies  $r$  and the H—H distance. There is good evidence that the oxidative addition of a C—H bond, for example, methane, proceeds by way of an intermediate where the metal forms an agostic bond with the C—H group [64,72b,73]. Polytopal rearrangements

in  $\text{H}_2\text{ML}_n$  complexes may in fact rearrange via transition states possessing a dihydrogen ligand. An example is provided by  $\text{H}_2\text{Fe}(\text{CO})_4$  itself [74]. There is a low energy process that exchanges the two types of CO ligands. Calculations have shown [74] that the transition state for this process is one where an H—H bond is formed and rotated by  $45^\circ$  while the CO ligands undergo a pseudorotation motion, **19.96**. This is precisely what we have encountered for olefin rotation in



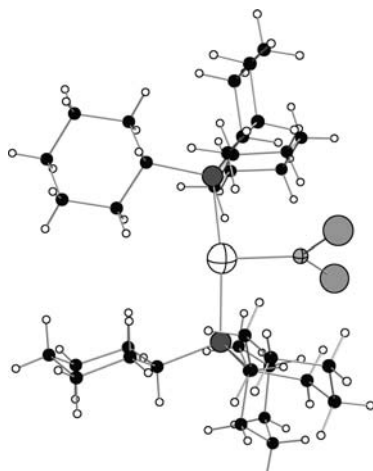
ethylene– $\text{Fe}(\text{CO})_4$ , **19.19–19.21**, and the electronic rationale is also identical. Topologically, the  $\text{H}_2 \sigma$  orbital is equivalent to ethylene  $\pi$ , and  $\text{H}_2 \sigma^*$  is equivalent to ethylene  $\pi^*$ . Their behavior when coordinated to a metal should be, and is similar. We will give more examples of unifying threads in subsequent chapters.

## PROBLEMS

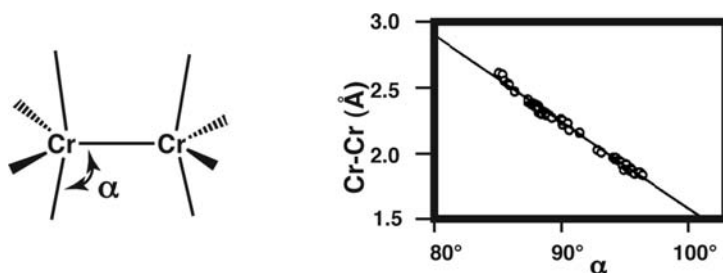
**19.1.** Interact the  $\pi$  orbitals of  $\text{Cp}^-$  with a  $C_{4v}$   $d^4 \text{V}(\text{CO})_4^+$  fragment and construct the important valence orbitals of  $\eta^5\text{-CpV}(\text{CO})_4$ .

**19.2.** There have been a number of very interesting ligands in the past few years. Here are two cases from the Braunschweig group:

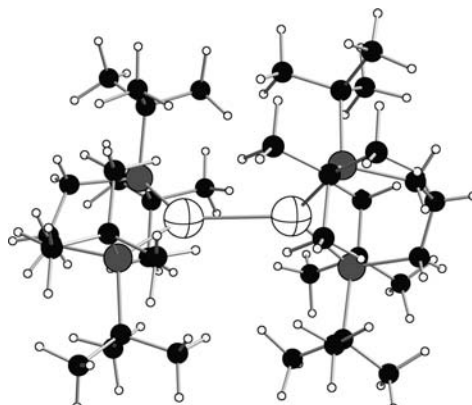
- a. Braunschweig et al. [75] reported the preparation of  $\text{Fe}(\text{CO})_4[\text{BN}(\text{SiMe}_3)_2]$ . No X-ray structure is available. A comparison of the  $\text{B}=\text{NR}_2$  ligand to CO was given in Problem 15.1. Make a prediction of the structure for  $\text{Fe}(\text{CO})_4(\text{B}=\text{NR}_2)$  and tell why this should be the case.
- b. Braunschweig et al. [76] reported the structure of a  $\text{BeCl}_2$  ligand coordinated to a  $\text{Pt}(\text{PR}_3)_2$ . Do the electron counting and construct an orbital interaction diagram to describe the bonding in this molecule. Experimentally the P—Pt—P bond angle was  $172.6^\circ$  instead of a more typical value of  $\sim 120^\circ$ . Why?



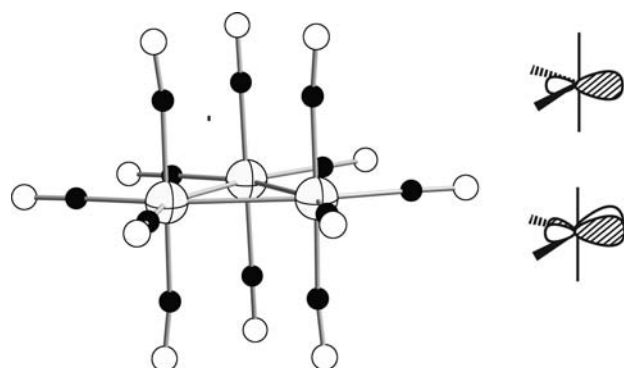
**19.3.** Dimers constructed from the  $C_{4v}$   $\text{ML}_4$  fragment were briefly discussed in Section 19.3. For a series of  $\text{Cr}^{2+}$  dimers it was found that the pyramidal angle,  $\alpha$ , defined below was strongly correlated to the Cr—Cr bond length. Describe orbitals why this should be the case.



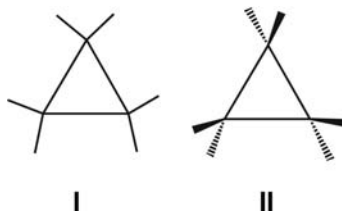
**19.4.** There are a number of  $\text{Pt}(\text{PR}_3)_2$  dimers, one example is given below consists of  $d^{10}$   $\text{Pt}(\text{PR}_3)_2$  fragments. How then can there be a Pt—Pt bond? Note that the Pt—Pt distance is 2.77 Å; normally, the Pt—Pt single bond distances in  $d^9-d^9$  dimers are 2.58–2.65 Å.



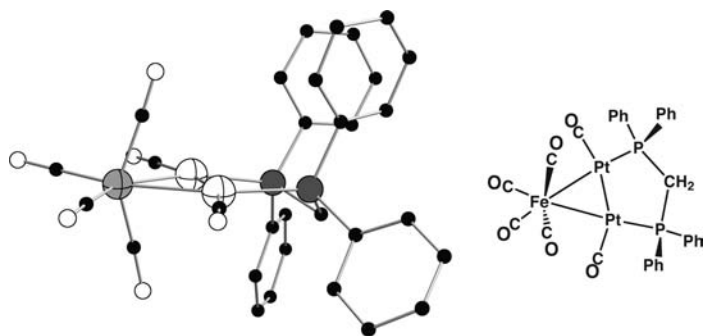
**19.5.** There are hundreds of 48-electron  $\text{M}_3\text{L}_{12}$  structures. One example is  $\text{Ru}_3(\text{CO})_{12}$ . Using the two important valence orbitals of the  $\text{Ru}(\text{CO})_4$  fragment, **19.2** and **19.3**, develop the Ru—Ru  $\sigma$  orbitals in  $\text{Ru}_3(\text{CO})_{12}$ .



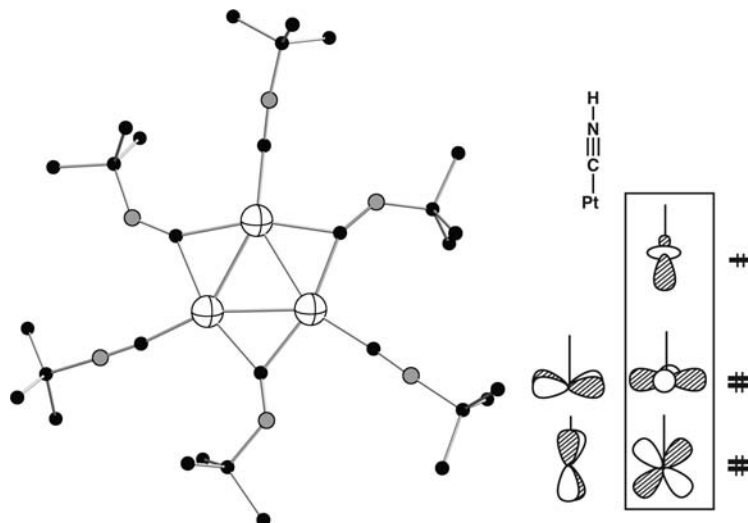
**19.6.** Chapter 19 stresses the similarity between the HOMO and LUMO of  $C_{2v}$   $d^8$   $\text{ML}_4$  and  $d^{10}$   $\text{ML}_2$  fragments. Yet there are to our knowledge no 42-electron  $\text{M}_3\text{L}_6$  compounds with either structure I or II.



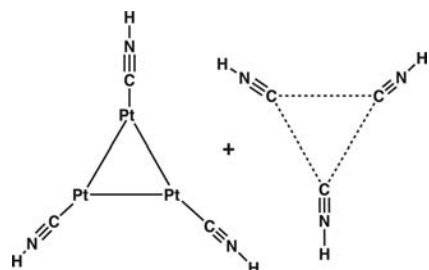
- a. Structure I corresponds to the orientation analogous to that found for  $M_3L_9$ . Show why the electronic structure is unfavorable here and in structure II.
- b. On the other hand, there are a few structures of the  $(ML_2)_2M'L_4$  type. One example is given by Braunstein et al. [77]. With respect to the answer in (a) show why this compound is stable.



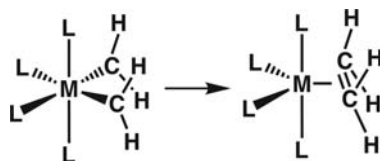
- c. There are 42-electron  $M_3L_6$  compounds but with a different geometry. One example by Green et al. [78] is  $Pt_3(CN-t-Bu)_6$ . The valence  $d$  orbitals of  $Pt(CN-t-Bu)$  are shown on the right side. Use the orbitals within the rectangular box to develop the orbitals of the  $Pt_3(CN-t-Bu)_3$  fragment.



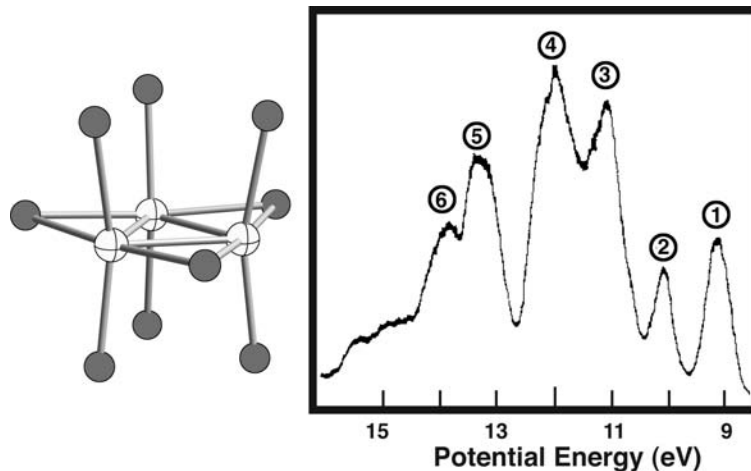
- d. Interact the  $Pt_3(CN-t-Bu)_3$  orbitals from (c) with the  $\sigma$  lone pairs and only the in-plane  $\pi^*$  orbitals of the three bridging *t*-butyl-isocnitrile ligands. Be careful to only use those interactions where the overlap between fragment orbitals is large.



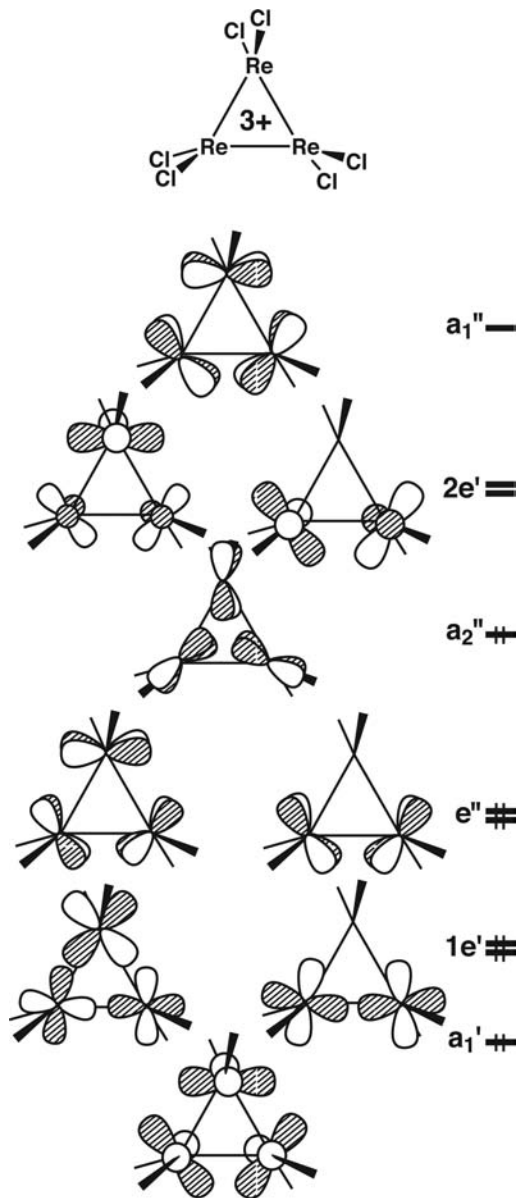
- 19.7.** Draw an orbital correlation diagram for the reaction shown below. Besides the  $\text{ML}_4$  d orbitals be sure to include the two lone pairs on the methylenes on the reactant side and the C—C  $\sigma$  bond on the product side along with their antibonding counterparts. Indicate what d-counts (if any) are likely to produce a facile reaction.



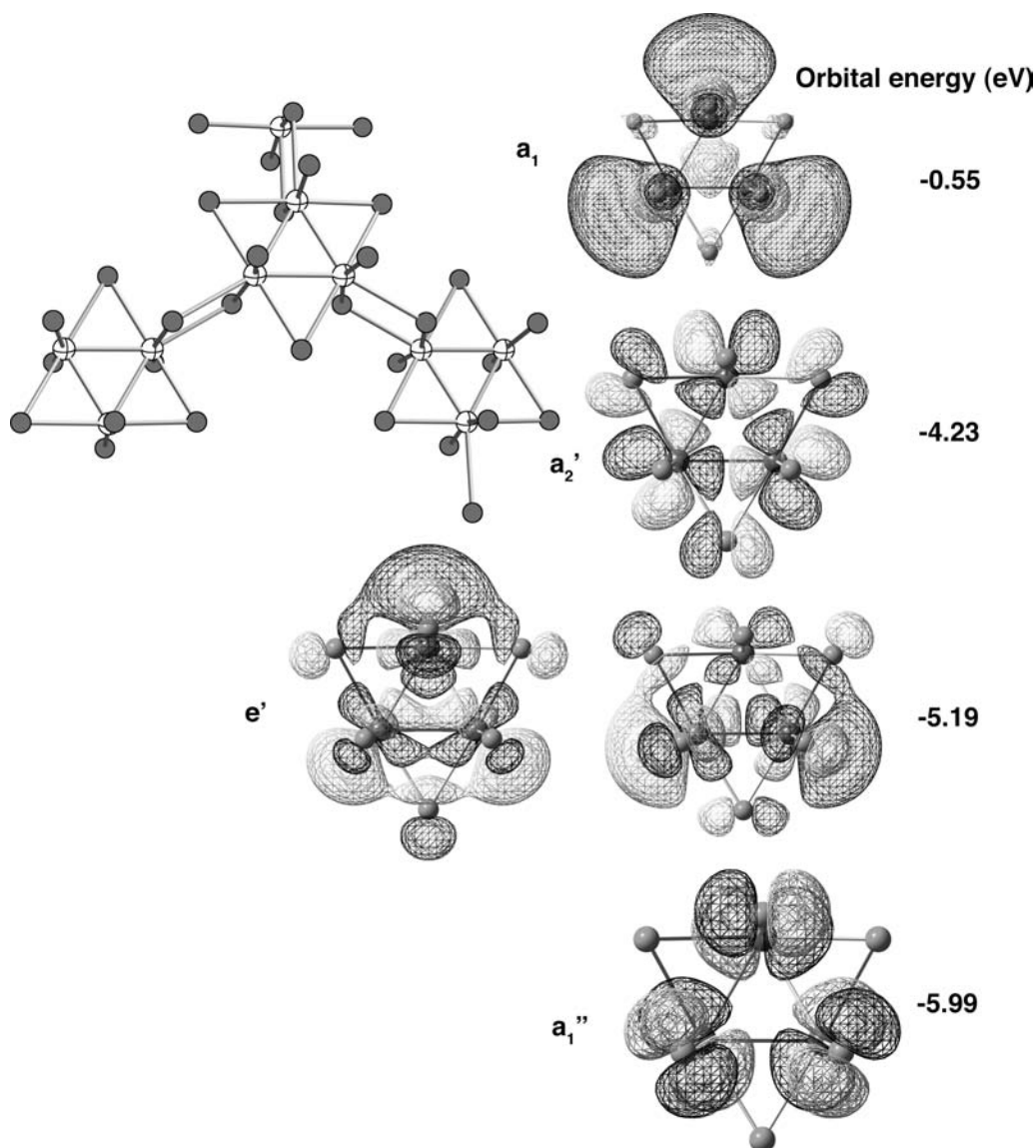
- 19.8.** The  $\text{Re}_3\text{Cl}_9$  cluster has been known for some time. The photoelectron spectrum of this molecule has been obtained [79] and reproduced below. There are six readily discernable peaks that correspond to around 23 MOs! Unraveling the nature of these ionizations is clearly a daunting task that relies heavily upon computations. One can see, however, the derivation of the first two ionizations.



- Determine the Re—Re bond order in this remarkable compound.
- Shown below is a partial listing of the orbitals of a  $\text{Re}_3\text{Cl}_6^{3+}$  fragment. Interact them with bridging the Cl  $p$  AOs to form the MOs of  $\text{Re}_3\text{Cl}_9$ . Which MOs correspond to the first two ionizations? A full listing of the assignments is given in the answers.



- c. The real structure for  $\text{Re}_3\text{Cl}_9$  in the solid state is more complicated. It consists of two-dimensional sheets where a terminal Cl ligand is also bonded to a Re atom in an adjacent  $\text{Re}_3\text{Cl}_9$  unit, as shown below. The  $\text{Re}-\text{Cl}$  bond lengths are long,  $2.67 \text{ \AA}$ , where the  $\text{Re}-\text{Cl}$  bond lengths for the terminal and bridging Cl atoms in the cluster are  $2.29$  and  $2.46 \text{ \AA}$ , respectively. Furthermore, there are several compounds with the composition  $\text{L}_3\text{Re}_3\text{Cl}_9$  where L is a two-electron donor including  $\text{Cl}^-$ . Explain the bonding of these three extra ligands to the cluster, and the solid state. The LUMOs of  $\text{Re}_3\text{Cl}_9$  are shown below.




---

## REFERENCES

---

1. M. Elian and R. Hoffmann, *Inorg. Chem.*, **14**, 1058 (1975); J. K. Burdett, *Inorg. Chem.*, **14**, 375 (1975); J. K. Burdett, *J. Chem. Soc., Faraday Trans. 2*, **70**, 1599 (1974).
2. For a review see M. Poliakoff and J. J. Turner, *Angew. Chem. Int. Ed.*, **40**, 2809 (2001).
3. B. Davies, A. McNeish, M. Poliakoff, and J. J. Turner, *J. Am. Chem. Soc.*, **99**, 7573 (1977); J. K. Burdett, *Coord. Chem. Rev.*, **27**, 1 (1978); M. Poliakoff and J. J. Turner, *J. Chem. Soc., Dalton Trans.*, 2276 (1974).
4. J. Li, G. Schrekenbach, and T. Ziegler, *J. Am. Chem. Soc.*, **117**, 486 (1995).
5. M. Besora, J.-L. Carreon-Macedo, A. J. Cowan, M. W. George, J. N. Harvey, P. Portius, K. L. Ronayne, X.-Z. Sun, and M. Towrie, *J. Am. Chem. Soc.*, **131**, 3583 (2009).
6. H. Ihee, J. Cao, and A. H. Zewail, *Angew. Chem. Int. Ed.*, **40**, 1532 (2001).
7. J.-L. Carreon-Macedo and J. N. Harvey, *Phys. Chem. Chem. Phys.*, **8**, 93 (2006) and references therein.

8. R. G. Teller, R. G. Finke, J. P. Collman, H. B. Chin, and R. Bau, *J. Am. Chem. Soc.*, **99**, 1104 (1977); S.-M. Kuang, Z.-Z. Zhang, Q.-G. Wang, and T. C. W. Mak, *J. Organomet. Chem.*, **558**, 131 (1998) and references therein.
9. M. Ogasawara, S. A. Macgregor, W. E. Streib, K. Folting, O. Eisenstein, and K. G. Caulton, *J. Am. Chem. Soc.*, **118**, 10189 (1996).
10. R. A. Jones, F. M. Real, G. Wilkinson, A. M. R. Galas, M. B. Hursthouse, K. M. A. Malik, *J. Chem. Soc., Dalton Trans.*, 511 (1980).
11. W. Clegg, M. R. J. Elsegood, A. J. Scott, T. B. Marder, C. Dai, N. C. Norman, N. L. Pickett, and E. G. Robins, *Acta Crystallogr., Sect. C: Cryst. Struct. Commun.*, **55**, 733 (1999); J. H. Rivers and R. A. Jones, *Chem. Commun.*, 4300 (2010).
12. M. G. Crestani, A. Steffen, A. M. Kenwright, A. S. Batsanov, J. A. K. Howard, and T. B. Marder, *Organometallics*, **28**, 2904 (2009).
13. N. Lu, N. C. Norman, A. G. Orpen, M. J. Quayle, P. L. Timms, and G. R. Whittell, *J. Chem. Soc., Dalton Trans.*, 4032 (2000); L. C. A.de Carvalho, M. Dartiguenave, Y. Dartiguenave, and A. L. Beauchamp, *J. Am. Chem. Soc.*, **106**, 6848 (1984).
14. D. Ostendorf, C. Landis, and H. Grützmacher, *Angew. Chem. Int. Ed.*, **45**, 5169 (2006).
15. J. Goodman, V. V. Grushin, R. B. Larichev, S. A. Macgregor, W. J. Marshall, and D. C. Roe, *J. Am. Chem. Soc.*, **132**, 12013 (2010).
16. R.-M. Catala, D. Cruz-Garritz, P. Sosa, P. Terreros, H. Torrens, A. Hills, D. L. Hughes, R. L. Richards, *J. Organomet. Chem.*, **359**, 219 (1989).
17. T. A. Albright, R. Hoffmann, J. C. Thibeault, and D. L. Thorn, *J. Am. Chem. Soc.*, **101**, 3801 (1979).
18. (a) J. Demuyck, A. Strich, and A. Veillard, *Nouv. J. Chim.*, **1**, 217 (1977). (b) T. A. Albright, *unpublished*.
19. For a review see, S. D. Ittel and J. A. Ibers, *Adv. Organomet. Chem.*, **14**, 33 (1976).
20. See, for example, L. Kruczynski, L. K. K. Li ShingMan, and J. Takats, *J. Am. Chem. Soc.*, **96**, 4006 (1974); S. T. Wilson, N. J. Coville, J. R. Shapley, and J. A. Osborn, *J. Am. Chem. Soc.*, **96**, 4038 (1974); J. A. Segal and B. F. G. Johnson, *J. Chem. Soc., Dalton Trans.*, 677, 1990 (1975).
21. C. Karunatilaka, B. S. Tackett, J. Washington, and S. G. Kukolich, *J. Am. Chem. Soc.*, **129**, 10522 (2007).
22. F. A. Cotton, N. F. Curtis, B. F. G. Johnson, and W. R. Robinson, *Inorg. Chem.*, **4**, 326 (1965); F. A. Cotton and C. B. Harris, *Inorg. Chem.*, **4**, 330 (1965).
23. F. A. Cotton, C. A. Murillo, and R. A. Walton, editors, *Multiple Bonds Between Metal Atoms*, 3rd Edition, Springer Science (2005).
24. F. Mota, J. J. Novoa, J. Losada, S. Alvarez, R. Hoffmann, and J. Silvestre, *J. Am. Chem. Soc.*, **115**, 6216 (1993).
25. L. Gagliardi and B. O. Roos, *Inorg. Chem.*, **42**, 1599 (2003); P. J. Hay, *J. Am. Chem. Soc.*, **104**, 7007 (1982) and references therein.
26. X.-B. Wang and L.-S. Wang, *J. Am. Chem. Soc.*, **122**, 2096 (2000).
27. D. L. Lichtenberger and J. G. Kristofzski, *J. Am. Chem. Soc.*, **109**, 3458 (1987); D. L. Lichtenberger, M. A. Lynn, and M. H. Chisholm, *J. Am. Chem. Soc.*, **121**, 12167 (1999).
28. S. C. Fletcher, M. Poliakoff, and J. J. Turner, *Inorg. Chem.*, **25**, 3597 (1986).
29. L. Bertini, M. Bruschi, L.de Gioia, and P. Fantucci, *J. Phys. Chem. A*, **111**, 12152 (2007).
30. R. Craciun, A. J. Vincent, K. H. Shaughnessy, and D. A. Dixon, *Inorg. Chem.*, **49**, 5546 (2010).
31. L. Manceron and M. E. Alikhani, *Chem. Phys.*, **244**, 215 (1999); M. Zhou and L. Andrews, *J. Am. Chem. Soc.*, **120**, 11499 (1998).
32. N. Rösch and R. Hoffmann, *Inorg. Chem.*, **13**, 2656 (1974).
33. J. A. K. Howard, J. L. Spencer, and S. A. Mason, *Proc. R. Soc. A*, **386**, 145 (1983).
34. R. Herges and A. Papafiliopoulos, *Angew. Chem. Int. Ed.*, **40**, 4671 (2001).
35. D. J. Brauer and C. Kruger, *J. Organomet. Chem.*, **44**, 397 (1972).
36. R. Goddard, B. Apotecher, and H. Hoberg, *Acta Crystallogr., Sect. C: Cryst. Struct. Commun.*, **43**, 1290 (1987).

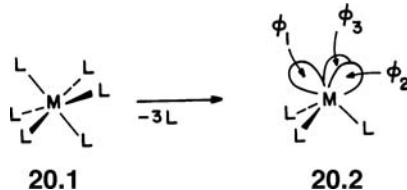
37. N. Hebben, H.-J. Himmel, G. Eickerling, C. Herrmann, M. Reiher, V. Herz, M. Presnitz, and W. Scherer, *Chem. Eur. J.*, **13**, 10078 (2007).
38. For a lively and instructive debate on the existence of a bond in one compound see, S. Alvarez, R. Hoffmann, and C. Mealli, *Chem. Eur. J.*, **15**, 8358 (2009); J. F. Berry, *Chem. Eur. J.*, **16**, 2719 (2010); S. Alvarez and E. Ruiz, *Chem. Eur. J.*, **16**, 2726 (2010).
39. M. J. S. Dewar, *Bull. Soc. Chim. Fr.*, **18**, C71 (1951); J. Chatt and L. A. Duncanson, *J. Chem. Soc.*, 2939 (1953); For a rather uncharitable discussion of one person's views on the name associated with this theory and the history around it, see M. J. S. Dewar and G. P. Ford, *J. Am. Chem. Soc.*, **101**, 783 (1979).
40. M. S. Nechaev, V. M. Rayon, and G. Frenking, *J. Phys. Chem. A*, **108**, 3134 (2008); C. Massera and G. Frenking, *Organometallics*, **22**, 2758 (2003).
41. B. R. Bender, J. R. Norton, M. M. Miller, O. P. Anderson, and A. K. Rappe, *Organometallics*, **11**, 3427 (1992).
42. K. K. Irikura and W. A. Goddard, III, *J. Am. Chem. Soc.*, **116**, 8733 (1994); G. Ohanessian and W. A. Goddard, III, *Acc. Chem. Res.*, **23**, 386 (1990).
43. F. Nunzi, A. Sgamellotti, N. Re, and C. Floriani, *J. Chem. Soc., Dalton Trans.*, 3487 (1999).
44. O. Eisenstein and R. Hoffmann, *J. Am. Chem. Soc.*, **103**, 4308 (1981); H. Fujimoto and N. Koga, *Tetrahedron Lett.*, 4357 (1982); see also the related case of nucleophilic substitution on Ir-allyl complexes, S. Sakaki, M. Nishikawa, and A. Ohyoshi, *J. Am. Chem. Soc.*, **102**, 4062 (1980); and coordinated carbon monoxide, S. Nakamura and A. Dedieu, *Theoret. Chim. Acta*, **61**, 587 (1982).
45. F. A. Cotton and P. A. Kibala, *Inorg. Chem.*, **29**, 3192 (1990).
46. W. H. Monillas, G. P. A. Yap, L. A. MacAdams, and K. H. Theopold, *J. Am. Chem. Soc.*, **129**, 8090 (2007).
47. I. Hyla-Kryspin, J. Koch, R. Gleiter, T. Klette, and D. Walther, *Organometallics*, **17**, 4724 (1998).
48. (a) D. J. Underwood, M. Nowak, and R. Hoffmann, *J. Am. Chem. Soc.*, **106**, 2837 (1984).  
(b) J. Huster and W. Bronger, *J. Less-Common Metals*, **119**, 159 (1986).
49. M.-H. Whangbo, *unpublished calculations*.
50. W. Bronger and O. Günther, *J. Less-Common Metals*, **27**, 73 (1972).
51. P. Hofmann, *Angew. Chem. Int. Ed.*, **89**, 551 (1977); T. R. Ward, O. Schafer, C. Daul, and P. Hofmann, *Organometallics*, **16**, 3207 (1997).
52. H. Werner and W. Hofmann, *Angew. Chem. Int. Ed.*, **89**, 835 (1977); W. Hofmann, W. Buchner, and H. Werner, *Angew. Chem. Int. Ed.*, **89**, 836 (1977); N. Dudeney, J. C. Green, P. Grebenik, and O. N. Kirehner, *J. Organomet. Chem.*, **252**, 221 (1983).
53. L. R. Byers and L. F. Dahl, *Inorg. Chem.*, **19**, 1760 (1979).
54. T. A. Albright and R. Hoffmann, *Chem. Ber.*, **111**, 1578 (1978); T. A. Albright, *J. Organomet. Chem.*, **198**, 159 (1980); T. A. Albright, R. Hoffmann, Y.-C. Tse, and T. D'Ottavio, *J. Am. Chem. Soc.*, **101**, 3812 (1979); L. J. Radonovich, F. J. Koch, and T. A. Albright, *Inorg. Chem.*, **19**, 3373 (1980); D. M. P. Mingos, *J. Chem. Soc., Dalton Trans.*, 602 (1977); D. M. P. Mingos, M. I. Forsyth, and A. J. Welch, *J. Chem. Soc., Dalton Trans.*, 1363 (1978); D. M. P. Mingos and A. J. Welch, *J. Chem. Soc., Dalton Trans.*, 1674 (1980); C. Mealli, S. Midollini, S. Moneti, L. Sacconi, J. Silvestre, and T. A. Albright, *J. Am. Chem. Soc.*, **104**, 95 (1982).
55. D. L. Lichtenberger, D. C. Calabro, and G. E. Kellogg, *Organometallics*, **3**, 1623 (1984).
56. R. Fukuda, M. Ehara, H. Nakatsuiji, N. Kishimoto, and K. Ohno, *J. Chem. Phys.*, **132**, 84302 (2010); X. Li, G. M. Bancroft, R. J. Puddephatt, Y.-F. Hu, and K. H. Tan, *Organometallics*, **15**, 2890 (1996); N. Dudeney, O. N. Kirchner, J. C. Green, and P. M. Maitlis, *J. Chem. Soc., Dalton Trans.*, 1877 (1984).
57. H. Brunner and T. Tsuno, *Acc. Chem. Res.*, **42**, 1501 (2009); C. H. Winter, A. M. Arif, and J. A. Gladysz, *J. Am. Chem. Soc.*, **109**, 7560 (1987); M. Brookhart, D. M. Lincoln, J. R. Volpe Jr., and G. F. Schmidt, *Organometallics*, **8**, 1212 (1989).
58. H. Aneetha, M. Jimenez-Tenorio, M. C. Puerta, P. Valerga, V. N. Sapunov, R. Schmid, K. Kirchner, and K. Mereiter, *Organometallics*, **21**, 5334 (2002); U. Kölle, J. Kossakowski, and G. Raabe, *Angew. Chem. Int. Ed.*, **29**, 773 (1990).

59. H. Yang, M. C. Asplund, K. T. Kotz, M. J. Wilkens, H. Frei, and C. B. Harris, *J. Am. Chem. Soc.*, **120**, 10154 (1998); C. R. Kemnitz, E. S. Ball, and R. J. McMahon, *Organometallics*, **31**, 70 (2012) and references therein.
60. P. Legzdins, W. S. McNeil, K. M. Smith, and R. Poli, *Organometallics*, **17**, 615 (1998) and references therein.
61. G. Argouarch, P. Hamon, L. Toupet, J.-R. Hamon, and C. Lapinte, *Organometallics*, **21**, 1341 (2002) and references therein.
62. K. Costuas and J.-Y. Saillard, *Organometallics*, **18**, 2505 (1999).
63. J. F. Hartwig, *Organotransition Metal Chemistry: From Bonding to Catalysis*, University Science Books, Sausalito, CA (2009), pp. 261–349; R. Crabtree, *The Organometallic Chemistry of the Transition Metals*, 4th Edition, Wiley, New York, NY (2005).
64. For a review see, S. Niu and M. B. Hall, *Chem. Rev.*, **100**, 353 (2000).
65. (a) R. Hoffmann, in *Frontiers of Chemistry*, K. J. Laidler, editor, Pergamon Press, New York (1982), pp. 247–263. (b) K. Tatsumi, R. Hoffmann, A. Yamamoto, and J. K. Stille, *Bull. Chem. Soc. Jpn.*, **54**, 1857 (1981); S. Kominya, T. A. Albright, R. Hoffmann, and J. K. Kochi, *J. Am. Chem. Soc.*, **98**, 7255 (1976); S. Kominya, T. A. Albright, R. Hoffmann, and J. K. Kochi, *J. Am. Chem. Soc.*, **99**, 8440 (1977).
66. V. P. Ananikov, D. G. Musaev, and K. Morokuma, *Organometallics*, **24**, 715 (2005); V. P. Ananikov, D. G. Musaev, and K. Morokuma, *Eur. J. Inorg. Chem.*, 5390 (2007).
67. M. Perez-Rodriguez, A. A. C. Braga, M. Garcia-Melchor, M. H. Perez-Temprano, J. A. Casares, G. Ujaque, A. R. de Lera, R. Alvarez, F. Maseras, and P. Espinet, *J. Am. Chem. Soc.*, **131**, 3650 (2009).
68. S. Moncho, G. Ujaque, A. Lledos, and P. Espinet, *Chem. Eur. J.*, **14**, 8969 (2008).
69. J. J. Low and W. A. GoddardIII, *Organometallics*, **4**, 609 (1986); J. J. Low and W. A. GoddardIII, *J. Am. Chem. Soc.*, **108**, 6115 (1986).
70. K. L. Bartlett, K. I. Goldberg, and W. T. Borden, *Organometallics*, **20**, 2669 (2001); A. Ariaafard, Z. Ejehi, H. Sadra, T. Mehrabi, S. Etaati, A. Moradzadeh, M. Moshtaghi, H. Nosrati, N. J. Brookes, and B. F. Yates, *Organometallics*, **30**, 422 (2011); G. S. Hill and R. J. Puddephatt, *Organometallics*, **17**, 1478 (1998).
71. J.-L. Carreon-Macedo and J. N. Harvey, *J. Am. Chem. Soc.*, **126**, 5789 (2004).
72. (a) S. A. Macgregor, O. Eisenstein, M. K. Whittlesey, and R. N. Perutz, *J. Chem. Soc., Dalton Trans.*, 291 (1998). (b) J. N. Harvey and R. Poli, *J. Chem. Soc., Dalton Trans.*, 4100 (2003).
73. P. E. M. Siegbahn, *J. Am. Chem. Soc.*, **118**, 1487 (1996); M.-D. Su and S.-Y. Chu, *Organometallics*, **16**, 1621 (1997); M.-D. Su and S.-Y. Chu, *Chem. Eur. J.*, **5**, 198 (1999).
74. C. Soubra, Y. Oishi, T. A. Albright, and H. Fujimoto, *Inorg. Chem.*, **40**, 620 (2001).
75. H. Braunschweig, C. Kollann, and U. Englert, *Angew. Chem. Int. Ed.*, **37**, 3179 (1998).
76. H. Braunschweig, K. Gruss, and K. Radacki, *Angew. Chem., Int. Ed.*, **48**, 4239 (2009).
77. P. Braunstein, J.-L. Richert, and Y. Dusausoy, *J. Chem. Soc., Dalton Trans.*, 3801 (1990).
78. M. Green, J. A. K. Howard, M. Murray, J. L. Spencer, and F. G. A. Stone, *J. Chem. Soc., Dalton Trans.*, 1509 (1977).
79. B. E. Burstyn, F. A. Cotton, J. C. Green, E. A. Seedon, and G. G. Stanley, *J. Am. Chem. Soc.*, **102**, 955 (1980).

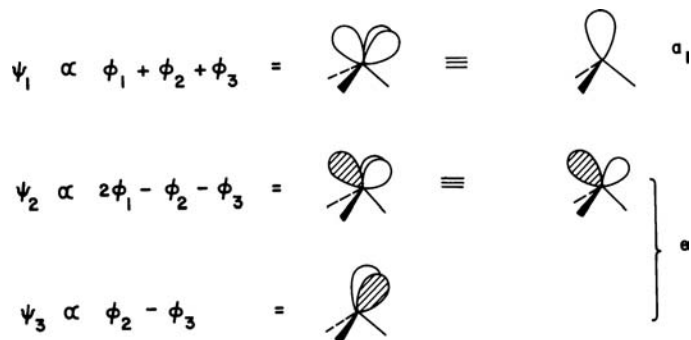
# **Complexes of $ML_3$ , $MCp$ and $Cp_2M$**

## **20.1 DERIVATION OF ORBITALS FOR A $C_{3v}$ $ML_3$ FRAGMENT**

Following the pattern established in the previous chapters, we can construct the valence orbitals of a  $C_{3v}$   $ML_3$  fragment by the removal of three fac ligands in an octahedral complex, **20.1–20.2**. Three empty hybrid orbitals will then be formed, labeled  $\phi_1$ ,  $\phi_2$ , and  $\phi_3$  in **20.2**. These point toward the missing ligands. If the original



octahedron was a  $d^6$ , 18-electron complex, then **20.2** will also possess three filled valence orbitals that closely correspond to the  $t_{2g}$  set (Section 15.2) of the octahedron. Recall that L is taken to be an arbitrary ligand with only  $\sigma$ -donating capability; therefore, the  $t_{2g}$  set in **20.1** is rigorously nonbonding. Those three orbitals will consequently remain unperturbed when the three fac ligands are removed. Alternatively one can easily establish that if the three ligands have  $\pi$  acceptor functions, then the three members of  $t_{2g}$  will raise in energy on going to **20.2** since  $\pi$  backbonding is lost. The three localized bond orbitals, illustrated in **20.2**, are highly directional. They are a convenient set to be used for conformational problems. Linear combinations of them form a set of symmetry-correct fragment orbitals. This is shown in **20.3**. One orbital of  $a_1$  symmetry and an e set are formed by the linear combinations (see Section 4.5). For  $\text{Cr}(\text{CO})_3$  the



20.3

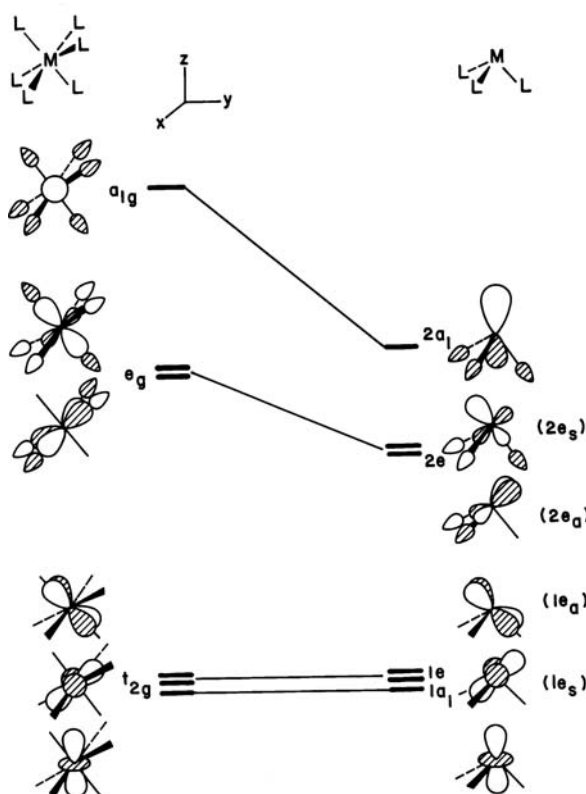
$a_1 + e$  triad in 20.3 is empty and a set of three orbitals of  $a_1 + e$  symmetry which are analogous to the  $t_{2g}$  set in  $\text{Cr}(\text{CO})_6$  are filled. In the  $\text{Fe}(\text{CO})_3$  fragment there are two more electrons. It becomes problematic whether they are associated with the  $a_1$  or  $e$  orbitals. In other words, does the  $a_1$  level lie energetically above or below the  $e$  set? The  $a_1$  orbital is the fully bonding combination of the  $\phi_1 - \phi_3$  hybrids and, therefore, one might think that this should lie at lower energy than the  $e$  set. However, linear combinations of orbitals do not directly point to an energy ordering. The  $a_1$  combination is, as we shall see, primarily metal  $s$  and  $p$  in character while the  $e$  set is predominately metal  $d$ . Since metal  $s$  and  $p$  lie above the  $d$  set, the  $a_1$  combination will lie at a higher energy than the  $e$  set. The situation is most clearly seen by looking carefully at what happens to the molecular orbitals of an octahedron when three fac ligands are removed. This is done in Figure 20.1 for the generalized  $\text{ML}_6$  to  $\text{ML}_3$  conversion. The  $t_{2g}$  and  $e_g$  sets, displayed on the left side of this figure, have a different composition from what we have previously used. This is simply due to a change of coordinate system, shown at the top center of Figure 20.1. The  $z$ -axis now coincides with a threefold rotational axis of the octahedron. The orbitals are exactly the same as those derived in Section 15.2; however, their atomic composition has changed. The members of  $t_{2g}$  become [1]

$$\begin{aligned} z^2 \\ \sqrt{\frac{2}{3}(x^2 - y^2)} - \sqrt{\frac{1}{3}}yz \\ \sqrt{\frac{2}{3}}xy - \sqrt{\frac{1}{3}}xz \end{aligned}$$

and the metal component of  $e_g$  is given by

$$\begin{aligned} \sqrt{\frac{1}{3}(x^2 - y^2)} + \sqrt{\frac{2}{3}}yz \\ \sqrt{\frac{1}{3}}xy + \sqrt{\frac{2}{3}}xz \end{aligned}$$

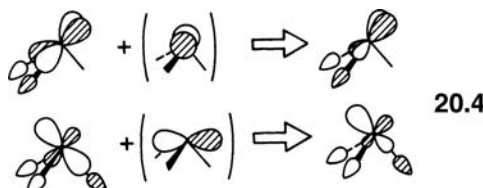
The members of the  $t_{2g}$  set that are predominately  $x^2 - y^2$  and  $xy$  have some  $yz$  and  $xz$  character, respectively, mixed into them so that they are reoriented to lie between the M-L bonds. The  $e_g$  set is mainly  $xz$  and  $yz$ . The  $xy$  and  $x^2 - y^2$  character mixed into them provides maximal antibonding to the ligand lone-pair functions. The intermixing of atomic functions is due to nothing more than our choice of a coordinate

**FIGURE 20.1**

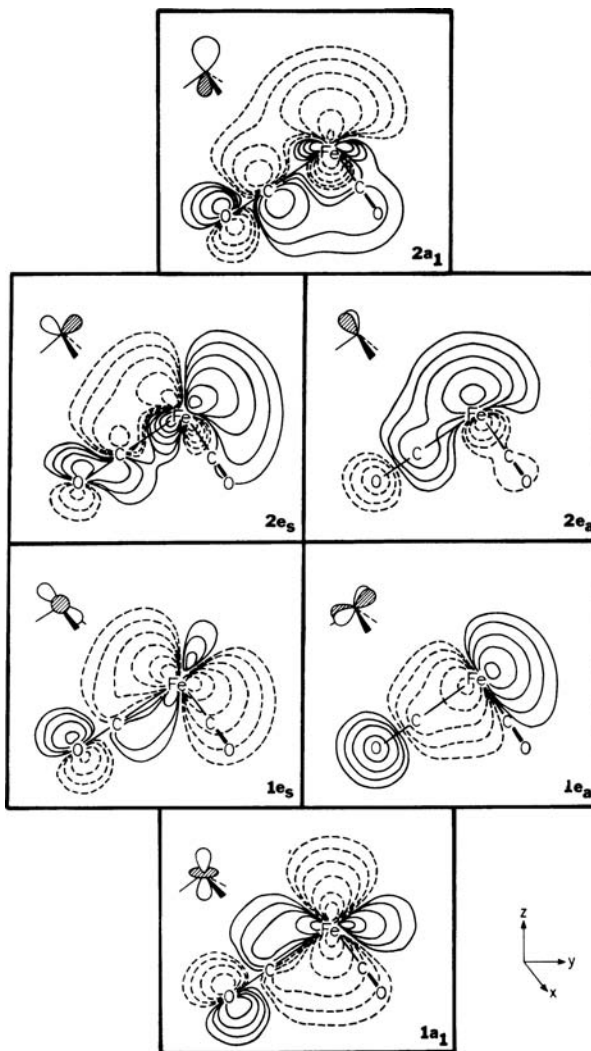
Derivation of the fragment orbitals for a  $C_{3v}$   $ML_3$  unit from an octahedron.

system. It is certainly not the normal one for an octahedron; however, it is the natural choice for a  $C_{3v}$   $ML_3$  unit.

When the three fac ligands are removed from  $ML_6$ , the  $t_{2g}$  set is unperturbed. The  $z^2$  component is labeled  $1a_1$  and the other two are listed as the  $1e$  set at the right of Figure 20.1. Contour plots at the extended Hückel level of these orbitals are also shown in Figure 20.2 for a  $Fe(CO)_3$  fragment. All of the orbitals have been plotted in the  $yz$  plane (see the coordinate system on the bottom right side of Figure 20.2) where the plane for the  $1e_a$  and  $2e_a$  orbitals was displaced by 1 Å along the  $x$  axis. Notice that  $1a_1$  and  $1e$  are strongly involved in  $\pi$  bonding to the CO ligands. They are transparently related to the octahedral  $t_{2g}$  set where  $\pi$  bonding to the ligands is maximal. The  $e_g$  set is stabilized considerably on going to  $ML_3$  since one-half of the antibonding from the ligand lone-pair hybrids to metal is lost. Because the symmetry of the molecule is lowered from  $O_h$  to  $C_{3v}$  some hybridization also comes into play. Metal  $x$  and  $y$  character mix into what was  $e_g$  in a way that is bonding to the remaining lone-pair functions; see 20.4. Another way to think about this hybridization is that reduction of the symmetry allows the higher



lying  $2t_{1u}$  set (see Figure 15.1) to mix into  $e_g$  in a bonding way. The resultant orbitals, labeled  $2e$  in Figure 20.1, are hybridized away from the remaining ligands. Figure 20.2

**FIGURE 20.2**

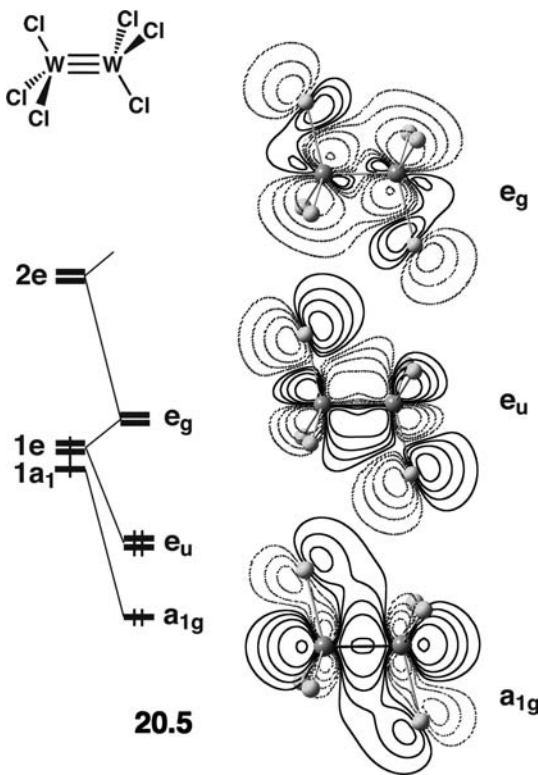
Contour plots at the extended Hückel level for the important valence orbitals in a  $Fe(CO)_3$  fragment. The  $1e_a$  and  $2e_a$  orbitals are plotted in the  $yz$  plane, displaced 1 Å along the  $x$  axis.

shows that the  $2e$  set is antibonding to  $CO\ \sigma$  as implied by 20.4, but  $CO\ \pi^*$  also mixes into the orbitals in a bonding manner. The  $a_{1g}$  orbital in  $ML_6$  also loses one-half of its antibonding when the ligands are removed. So that orbital,  $2a_1$  in Figure 20.1, is also lowered in energy and considerable metal  $z$  character mixes into it in a way that is bonding to the lone-pair hybrids on the remaining ligands. Inspection of Figure 20.2 also shows considerable  $CO\ \pi^*$  has mixed into it and this will further stabilize  $2a_1$ . The  $2a_1$  and  $2e$  molecular orbitals are readily identified as the  $a_1 + e$  set in 20.3 which were generated from the bond orbital approach. Notice that as anticipated  $2a_1$  lies at a higher energy than the  $2e$  combination. The level ordering for  $2e$  and  $2a_1$  is a natural consequence of the energetics of the constituent atomic orbitals on the metal. A  $d^8$   $Fe(CO)_3$  molecule would then have two electrons housed in  $2e$ .

The intermixing of  $x^2 - y^2$  with  $yz$  and  $xy$  with  $xz$  in the  $1e$  and  $2e$  sets can be derived along other lines [2]. It is also sensitive to the pyramidality of the  $ML_3$  fragment. That is most apparent by comparing the  $ML_3$  orbitals at an  $L-M-L$  angle of  $90^\circ$  in Figure 20.1 with those for a planar  $ML_3$  unit where  $L-M-L = 120^\circ$  at the middle

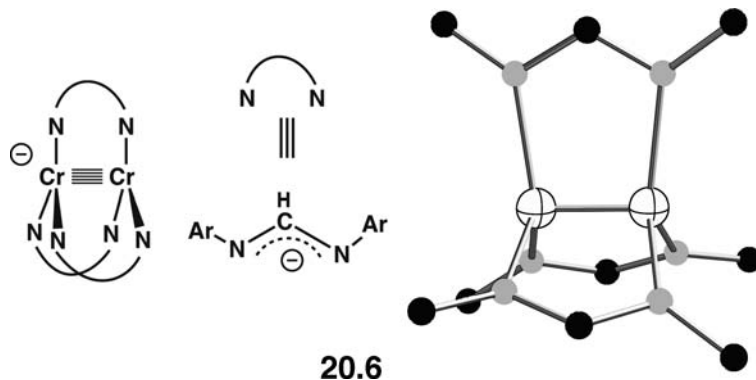
of Figure 18.3. Starting from the planar,  $D_{3h}$  species the  $a_2''$  orbital evolves into  $2a_1$  (Figure 20.1) upon pyramidalization. The perturbation is exactly analogous to the  $\text{AH}_3$  pyramidalization in Section 9.3. The  $a_2''$  level is stabilized and hybridized by the second-order mixing of a higher-lying metal s orbital. The  $a_1', z^2$ , level is also stabilized on pyramidalization since the ligand lone-pair functions move off from the torus, toward the nodal plane of  $z^2$  (see Figure 1.5). At the planar geometry the  $e'$  set consists exclusively of  $x^2-y^2$  and  $xy$  along with  $y$  and  $x$ , respectively (see **18.6** and **18.8**). The lower energy  $e''$  set is metal  $xz$  and  $yz$ . At the pseudo-octahedral geometry the  $2e$  set is mainly  $xz$  and  $yz$ , whereas the lower lying  $1e$  set consists of primarily  $x^2-y^2$  and  $xy$  character. In other words, pyramidalization induces an intermixing of the character in the two  $e$  sets and an avoided crossing occurs. So the exact composition of  $1e$  and  $2e$  is given only at the planar,  $D_{3h}$ , and pyramidal geometry when  $\text{L}-\text{M}-\text{L} = 90^\circ$ .

The molecular orbitals of  $\text{A}_2\text{H}_6$  were constructed in Figure 10.1 from two  $\text{AH}_3$  units. An analogous construction can easily be derived for the  $\text{M}_2\text{L}_6$  dimer. The example we used before to illustrate electron counting was  $\text{W}_2(\text{NMe}_2)_6$ , **16.27**. In **20.5** the two  $e$  sets and  $1a_1$  are used to construct the most important orbitals used in



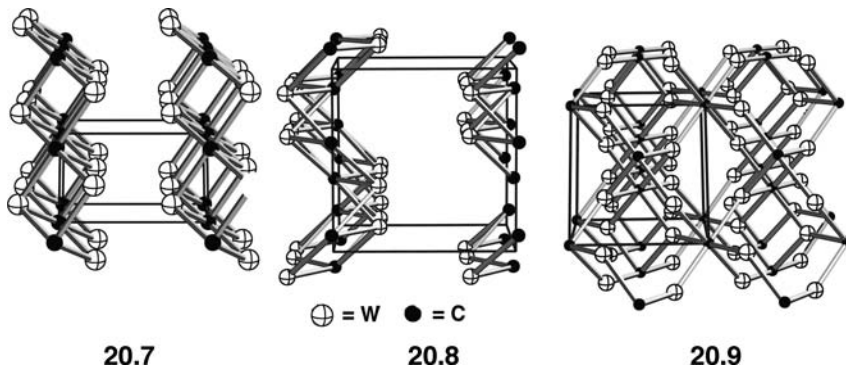
$\text{W}-\text{W}$  bonding for  $\text{W}_2\text{Cl}_6$ . These are  $\text{W}^{3+}$  fragments so there are three electrons in the  $1a_1 + 1e$  set. The two  $1a_1$  fragment orbitals combine to give the  $\text{W}-\text{W}$   $\sigma$  bonding orbital. A contour plot of the  $a_{1g}$  MO is illustrated on the bottom right side of **20.5**. The bonding combination of  $1e$ ,  $e_u$ , is predominately  $\pi$  in character. The B3LYP optimized structure for  $\text{W}_2\text{Cl}_6$  has a  $\text{W}-\text{W}-\text{Cl}$  angle of  $103.2^\circ$ . That is closer to the value where two trigonal  $\text{ML}_3$  units interact ( $\text{M}-\text{M}-\text{L} = 90^\circ$ ) than the pyramidal value of  $125.25^\circ$  (where the  $\text{L}-\text{M}-\text{L}$  angles are  $90^\circ$ ). Consequently  $e_u$  is mainly the metal  $xz/yz$  combination. One component is shown on the right side of **20.5**. The antibonding combination of the  $1e$  set,  $e_g$ , in fact has  $2e$  strongly mixed into it. As one can see from the contour diagram,  $e_g$  is  $\pi$  antibonding but also  $\delta$  bonding. It has predominately  $x^2-y^2/xy$  character. This brings up an interesting point: if the

$M-M-L$  angle can be held at  $90^\circ$ , then  $1e$  is, as previously mentioned,  $xz$  and  $yz$  and  $2e$  is  $x^2-y^2$  and  $xy$ . So  $e_u$  in **20.5** is  $\pi$  bonding and  $e_g$  is purely  $\delta$  bonding. So a  $d^5 ML_3$  fragment can dimerize to form a  $M_2L_6$  molecule with a  $M-M$  bond order of five. A molecule with just this electronic configuration has been prepared and is shown in **20.6** [3]. It has an incredibly short Cr—Cr distance of  $1.74\text{ \AA}$ . With one less electron the Cr—Cr bond length increases by  $0.08\text{ \AA}$  [3]. The

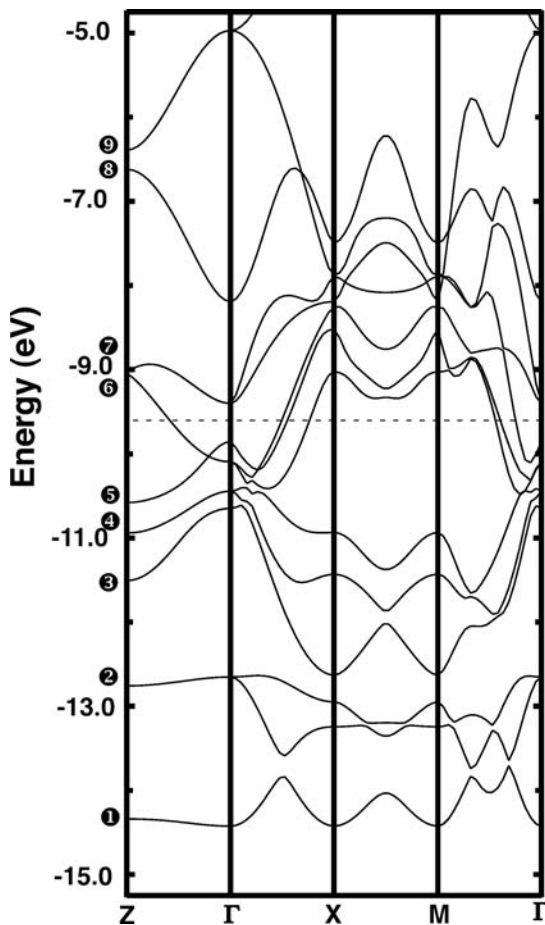


possible existence of a structure akin to **20.6** with a pentuple metal–metal bond was predicted almost 30 years earlier [4].

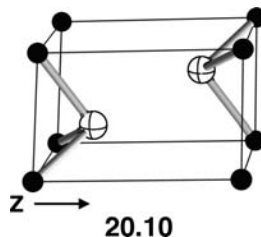
There are very few pyramidal  $ML_3$  molecules [5]; however, there are a number of  $M_2X$ , (where  $M = V, Cr, Nb, Mo, W, Co$ , and  $X = C$  or  $N$ ) solid-state materials, which possess this structural feature. We shall examine one compound,  $W_2C$ , which is part of the family of tungsten carbides that are of great industrial importance. There are several structures [6]; three of which are shown in **20.7**–**20.9**. All have pyramidal  $WC_3$  cores, where the angles around tungsten are close to



$90^\circ$ . It would appear that these are layered structures (in the case of **20.9**, there are a few carbon atoms between the layers). But this is certainly not the case in all three structures; the closest  $W-W$  contacts between the layers range from  $2.93$  to  $3.01\text{ \AA}$ . The corresponding distance in tungsten metal is  $2.78\text{ \AA}$ . Let us consider **20.7**; it is the simplest structure of the three. Each carbon atom is coordinated in an octahedral fashion to six tungsten atoms. If we allow for the existence of  $W-W$  bonds (at  $2.93\text{ \AA}$ ), then each tungsten is coordinated to three tungsten atoms from an adjacent layer and three from within the same layer. Thus each tungsten atom becomes nine-coordinate. The actual unit cell is shown in **20.10**. An  $e(k)$  versus  $k$  plot at the extended Hückel level is shown in Figure 20.3. The horizontal dashed line

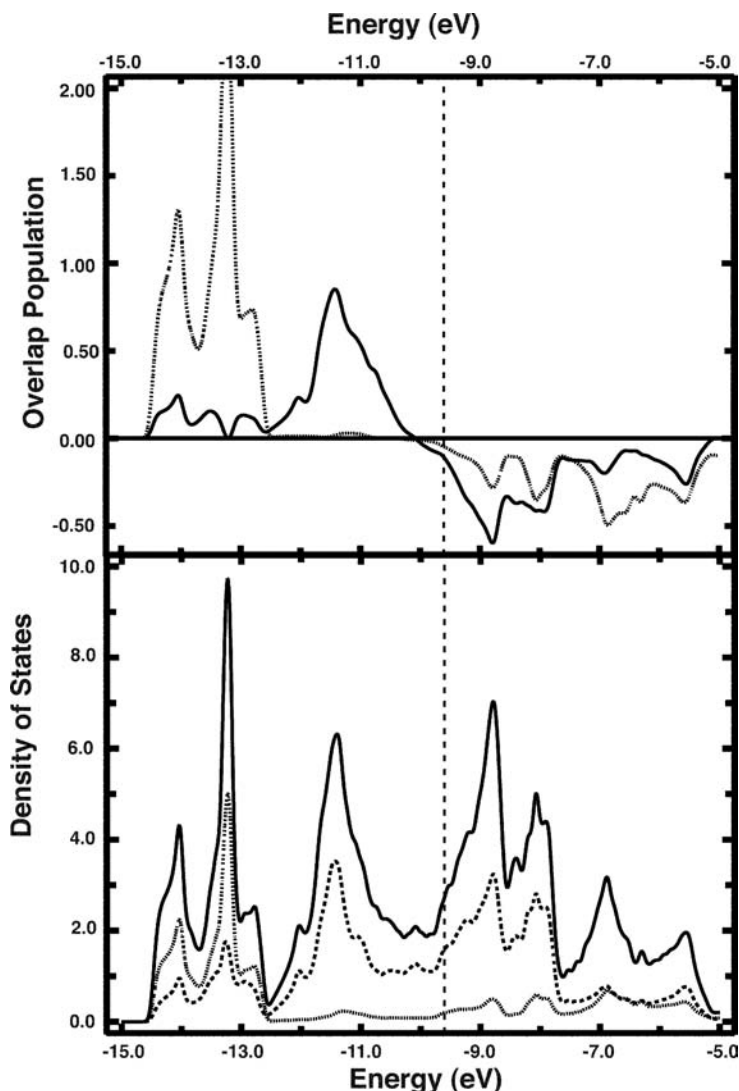
**FIGURE 20.3**

Band structure for  $W_2C$ . The horizontal dashed line indicates the position of the Fermi level. The special  $k$  points are  $(k_x, k_y, k_z)$  for  $\Gamma = (0, 0, 0)$ ;  $X = (0.5, 0, 0)$ ;  $M = (0.5, 0.5, 0)$ ;  $Z = (0, 0, 0.5)$ .

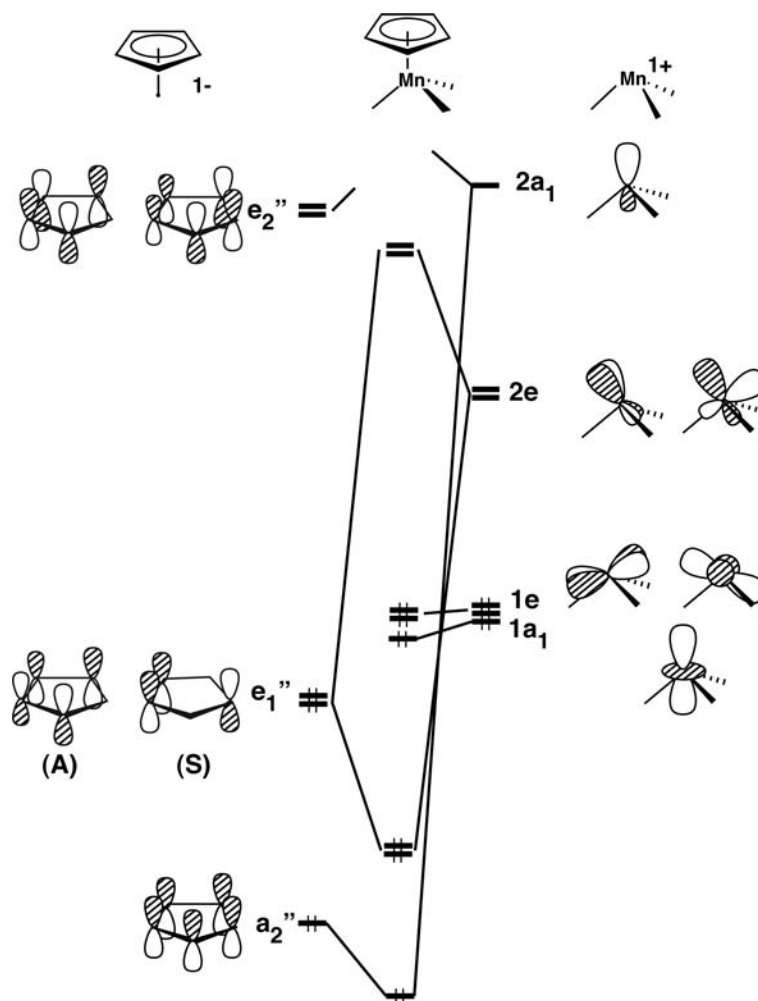


indicates the Fermi level, which cuts across three bands so the compound is expected to be, and is, a metal. There is a great deal of complexity that is offered by these bands with many avoided crossings. This is starting to resemble a “spaghetti diagram.” But one can still get very qualitative ideas about the nature of these bands. This is particularly true for the  $\Gamma$  to  $Z$  direction where a threefold axis of symmetry and a mirror plane perpendicular to it are retained. So our discussion is primarily devoted to this portion of the bands. Not shown in Figure 20.3 is a band at very low energy—around  $-24$  eV that is predominately carbon s in character. Band ① consists primarily of carbon z and ② contains carbon x and y. These are strongly bonding to W  $z^2$  and W  $x^2-y^2/xy$ , respectively. Since there are two tungsten atoms per unit cell (see 20.10) there will be bonding and antibonding combinations of the W d AOs. Bands ③ and ④ are the two W  $z^2$  combinations. Band ④ is the out-of-phase combination of the  $x^2-y^2/xy$  set (the positive combination is greatly destabilized by carbon x and y and can be identified with band ⑨). Bands ⑥ and ⑦

correspond to the two combinations of  $xz/yz$  and band ❸ is primarily W s, z, and  $z^2$ . So one can see the remnants of the ML<sub>3</sub> set from at least  $\Gamma$  to Z with 1a<sub>1</sub> and 1e at low energy and 2a<sub>1</sub> along with 2e at higher energies. The densities of states plot along with two COOP curves are displayed in Figure 20.4 for W<sub>2</sub>C. Again the dashed vertical line in each plot marks the position of the Fermi level. The projection of C AOs is given by the dotted line in the DOS plot. This lies predominately in the region from -14.6 to -12.7 eV. The W—C overlap population is given by the dotted line in the COOP plot and one can readily see that this energy region is strongly W—C bonding. This is totally consistent with our analysis of bands ❶ and ❷ in Figure 20.3. The energy region from -12.7 to  $\sim$  -10.0 eV is almost exclusively W d AOs that are W—W bonding. Those from  $\sim$  -10.0 to -7.8 are W—W antibonding. These energy regions correspond to bands ❸–❻ in Figure 20.3. Above this are states that are W—C antibonding and correspond to bands ❼ and ❼. The Fermi level lies in a region of heavily populated states. What is interesting is that it lies on the borderlines between W—W and W—C bonding and antibonding. In other words the maximum number of W—W and W—C bonding states are filled at this electron count

**FIGURE 20.4**

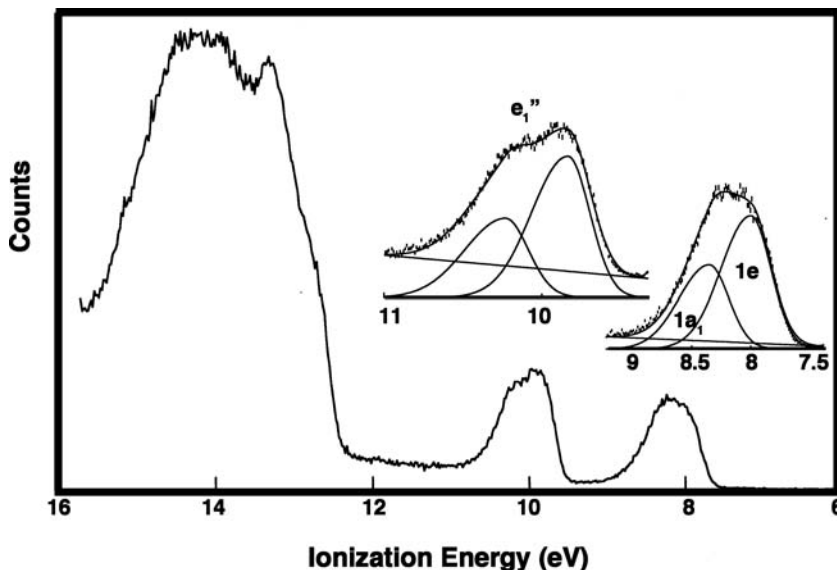
The COOP and DOS plots for W<sub>2</sub>C. The projection of C AOs and W  $z^2 + xz + yz$  are given by the dotted and dashed lines, respectively, in the DOS plot. The W—W and W—C overlap populations are given by the solid and dotted lines, respectively in the COOP plot. The vertical dashed line indicates the position of the Fermi level.

**FIGURE 20.5**

An orbital interaction diagram for  $\text{CpMn}(\text{CO})_3$ .

and therefore, this should be (and is) a stable stoichiometry in the W—C phase diagram.

An example where the  $\text{ML}_3$  valence orbitals are utilized is given by cyamantrene, cyclopentadienyl- $\text{Mn}(\text{CO})_3$ . An orbital interaction diagram is shown in Figure 20.5. The complex has been divided into cyclopentadienyl ( $\text{Cp}$ ) anion and  $\text{Mn}(\text{CO})_3$  cation fragments. The  $a_2''$  orbital of  $\text{Cp}^-$  and  $1a_1$  and  $2a_1$  from  $\text{Mn}(\text{CO})_3^+$  enter into a three orbital pattern. The lowest molecular level is primarily  $a_2''$  stabilized by  $1a_1$  and  $2a_1$ . The middle member is mainly  $1a_1$ . Some  $a_2''$  character mixes into the molecular orbital in an antibonding manner but the z AOs on the ring carbons lie approximately on the nodal cone of the Mn z<sup>2</sup> AO. Thus the overlap between  $a_2''$  and  $1a_1$  is small. Furthermore,  $2a_1$  mixes into this MO in second order (bonding with respect to  $a_2''$ ). So  $1a_1$  is essentially nonbonding. The  $e_1''$  set of  $\text{Cp}^-$  is stabilized greatly by  $2e$  on  $\text{Mn}(\text{CO})_3^+$ . Finally there is a weak interaction between the  $1e$  and  $e_2''$  levels. That stabilizes the  $1e$  set, but not by much. First of all, the overlap between  $1e$  and  $e_2''$  is primarily of the  $\delta$  type and consequently is much smaller than the predominately  $\pi$  type between  $e_1''$  and  $2e$ . Secondly, there are relatively high lying  $\sigma$  orbitals on the  $\text{Cp}$  fragment which overlap with and destabilize the  $1e$  set. Therefore, the  $1e$ - and  $1a_1$ -based molecular levels are not expected to be split apart significantly in energy. The photoelectron spectrum of  $\text{CpMn}(\text{CO})_3$ , given in Figure 20.6, shows this to be true [7]. The peak

**FIGURE 20.6**

The photoelectron spectrum of  $\text{CpMn}(\text{CO})_3$ .

at lowest ionization potential can be deconvoluted into two peaks with the first having roughly twice the peak area as the second. In other words, the  $1e$ -based MOs lie at slightly higher energy than  $1a_1$ . This is consistent with the interaction diagram in Figure 20.5. The second broad peak is associated with the Cp  $e_i''$  bonding to the  $2e$  set on  $\text{Mn}(\text{CO})_3$ . It is also resolved into two separate ionizations. There are a number of explanations for this splitting but by far the most likely reason is that the  $\text{Mn}(\text{CO})_3$  group, due to the tilting associated with the  $1e$  and  $2e$  sets, causes C—C bond length changes in the Cp ring which, in turn splits the energy of the  $e_i''$  set by 0.4 eV. The  $e_i''$  component which is symmetric with respect to the plane of the paper in Figure 20.5, labeled (S), is destabilized and the other member of  $e_i''$  which is antisymmetric, (A), is stabilized [7a]. There is one minor problem with this argument. Table 20.1 presents the first four ionization potentials for  $\text{CpMn}(\text{CO})_3$ ,  $\text{MeC}_5\text{H}_4\text{Mn}(\text{CO})_3$ , and  $\text{Me}_5\text{C}_5\text{Mn}(\text{CO})_3$  [7a]. The uncertainty in these measurements was  $\pm 0.05$  eV. The substitution of one methyl group for a hydrogen lowers the ionization potential for the  $1e + 1a_1$  set by 0.16 eV. On the other hand, the two members of the  $e_i''$  set are lowered by roughly three times as much, 0.33 and 0.29 eV. The same pattern emerges for the replacement of all five hydrogens with methyl groups. The  $1a_1 + 1e$  ionizations are lowered by 0.58 eV while the  $e_i''$  set is lowered by 1.19 eV. As discussed in Section 10.3.B, a methyl group possesses a C—H  $\sigma$  orbital that can interact with and destabilize a  $\pi$  orbital and this effect is much stronger than the inductive  $\sigma$ -donor effect of a methyl group. Thus the ionization

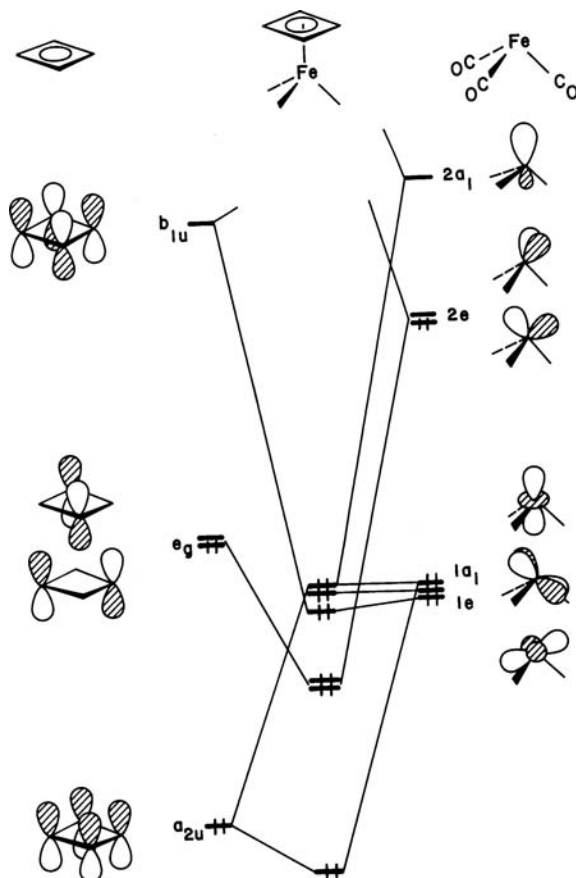
**TABLE 20.1** The First Four Ionization Potentials (eV) for Methyl-Substituted  $\text{CpMn}(\text{CO})_3$  Complexes

$\text{CpMn}(\text{CO})_3$	$\text{MeC}_5\text{H}_4\text{Mn}(\text{CO})_3$	$\text{Me}_5\text{C}_5\text{Mn}(\text{CO})_3$
8.05	7.89	7.46
8.40	8.23	7.82
9.90	9.57	8.72
10.29	10.00	9.09

Potential for the  $\pi$  orbital in ethylene is lowered by 0.48 eV on going to propene, see 10.22. So the results here are consistent with the idea that the coefficients in the  $\text{Cp}$   $\pi$  region are very small for the  $1e + 1a_1$  molecular orbitals. Therefore, if the  $e''_1$  is split so that (S) lies higher than (A), then the 0.33 eV (using Koopmans' theorem) destabilization of the (S) component is a result of the  $\pi$  donor effect of the methyl group which is substituted on the carbon atom that lies in the mirror plane of the  $\text{Cp}$  in Figure 20.5. The problem here is that the (A) member of  $e''_1$  has a node on this carbon so its ionization potential should be lowered only by the  $\sigma$  inductive effect of the methyl group. However, it is lowered within experimental error the same as the (S) member of  $e''_1$  is. Suppose the assignment of (S) and (A) for  $\text{CpMn}(\text{CO})_3$  is reversed. The prediction would be that the splitting of the  $e''_1$  set should become much smaller on going to  $\text{MeC}_5\text{H}_4\text{Mn}(\text{CO})_3$ . It does not. One might argue that the  $\text{Mn}(\text{CO})_3$  group might rotate from that in  $\text{CpMn}(\text{CO})_3$ . We will not belabor the point here but note that the conformational preference for the orientation of the  $\text{Mn}(\text{CO})_3$  group in  $\text{MeC}_5\text{H}_4\text{Mn}(\text{CO})_3$  will be the same and even stronger than in  $\text{CpMn}(\text{CO})_3$ . Therefore, the origin of the splitting in the  $e''_1$  set and how methyl substitution affects it remains an open question in our opinion.

Notice that the symmetry of  $\text{CpMn}(\text{CO})_3$  is only  $C_s$ . However, the “apparent” symmetry is higher. The astute reader will have recognized something very familiar about the orbital interaction diagram for  $\text{CpMn}(\text{CO})_3$  in Figure 20.5. There are three closely spaced, filled orbitals at moderate energies. The two lowest unoccupied orbitals are primarily metal  $2e$  antibonding to the  $e''_1$  set on  $\text{Cp}^-$ . Furthermore,  $2e$  is comprised of metal  $d$  antibonding to the carbonyl donor orbitals (see Figure 20.1). The octahedral splitting pattern has been restored. In other words, there is not much difference between the interaction diagram in Figure 20.2 and the one for  $\text{Cr}(\text{CO})_6$  (also a  $d^6 \text{ML}_6$  fragment) interacting with three carbonyls. The three carbonyl  $\sigma$  donor orbitals form symmetry-adapted linear combinations that are topologically analogous to the  $a''_2 + e''_1$  set of  $\text{Cp}^-$ . Replacement of a  $\text{Cp}^-$  fragment for three carbonyl ligands is a useful concept and is one that we shall extensively develop; however, it is important to realize that there are differences between the two fragments [8]. Perhaps the most important difference lies in the fact that the three carbonyl ligands are excellent  $\pi$  acceptors. To be sure, the  $\text{Cp}^-$  ligand does possess the  $e''_2$  set for metal backbonding, but its spatial extent does not allow for maximal overlap with  $1a_1$  and  $1e$  as is present for the  $\pi^*$  combinations on a fac carbonyl set. This brings up a final point about the molecular orbital description of  $\text{CpMn}(\text{CO})_3$ . It is obvious that there are six bonds to Cr in  $\text{Cr}(\text{CO})_6$  or any  $d^6 \text{ML}_6$  complex. The delocalized molecular orbital picture in Figure 15.1 also shows six filled M–L bonding orbitals. In  $\text{CpMn}(\text{CO})_3$  there will be three orbitals that are bonding between Mn and CO donor functions, not shown in Figure 20.5. There are also three filled molecular orbitals that are bonding between the  $\text{Cp}^- \pi$  set and the  $\text{Mn}(\text{CO})_3^+$  fragment. Therefore, it is conceptually useful to imagine that there are three bonds between Mn and Cp unit. The single line between Cp and Mn at the top center of Figure 20.6 does not imply a bond order of one between the two units. Rather, it indicates delocalized bonding between Mn and five carbons.

Actually the basic orbital pattern for any 18-electron polyene– $\text{ML}_3$  complex will be very similar to that found in  $\text{CpMn}(\text{CO})_3$ . Figure 20.7 illustrates the situation for cyclobutadiene– $\text{Fe}(\text{CO})_3$ . The  $e_g$  set on cyclobutadiene is stabilized by  $2e$  on  $\text{Fe}(\text{CO})_3$ . Likewise, the  $a_{2u}$  orbital is stabilized by the  $1a_1$  and  $2a_1$  levels on  $\text{Fe}(\text{CO})_3$ . Three metal-centered orbitals are left “nonbonding.” Notice that the two fragments have been partitioned to be neutral. The  $e_g$  set on cyclobutadiene and  $2e$  set on  $\text{Fe}(\text{CO})_3$  are each half-filled. It is reasonable to assume that  $e_g$  lies at a lower energy than  $2e$  (recall that the  $2e$  set is carbonyl  $\sigma$ -metal  $d$  antibonding). Therefore,

**FIGURE 20.7**

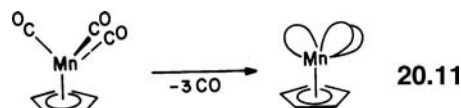
An orbital interaction diagram for cyclobutadiene–Fe(CO)<sub>3</sub>.

the electron density in the molecular orbitals that result from the union of these two fragment orbitals is more concentrated on the cyclobutadiene ligand. To take an extreme view, one could say that the two electrons in the 2e levels of Fe(CO)<sub>3</sub> are transferred to the  $e_g$  set located on the cyclobutadiene fragment, making it a six- $\pi$ -electron aromatic system. That is certainly an overstatement but it does point to the fact that electrophilic substitution reactions on the cyclobutadiene ligand are very common [9]. Electrophilic substitution on the Cp ligand for CpMn(CO)<sub>3</sub> is also facile and this reactivity has been used to support the concept of “metalloaromaticity” [10] for CpMn(CO)<sub>3</sub> and cyclobutadiene–Fe(CO)<sub>3</sub>. However, what is not clear in all cases is whether an electrophile directly attacks the polyene ring or attack occurs at the metal with subsequent migration of the electrophile to the polyene ring. From the interaction diagrams of Figures 20.5 and 20.7, it is clear that the molecular orbitals involving polyene  $\pi$ -metal  $d$  interactions are concentrated on the polyene portion of these molecules. That would favor direct attack by an electrophile on the polyene. However, there are also three occupied molecular orbitals in each complex that are the remnants of the octahedral  $t_{2g}$  set. Since these lie at relatively high energies and are concentrated at the metal, they too will overlap effectively and find a good energy match with the lowest unoccupied molecular orbital (LUMO) of an electrophile. This interaction, of course, leads to attack at the metal. Which reaction path occurs is sensitive to the metal, the electronic features of the ligands, and the steric bulk of the electrophile. One can also envision reaction paths wherein the electrophile LUMO interacts with a polyene  $\pi$ -based MO and metal “ $t_{2g}$ ” MO simultaneously.

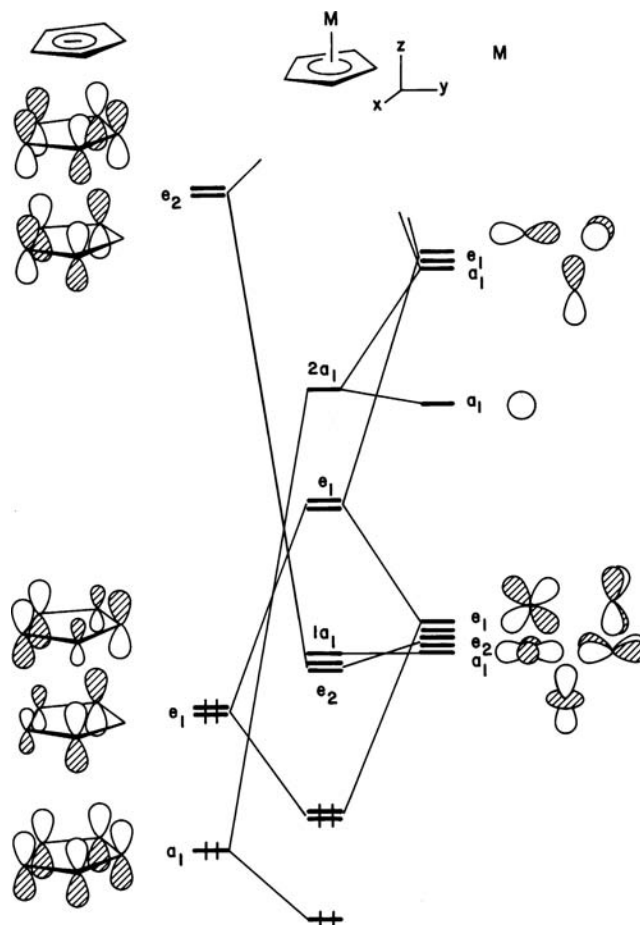
(an analogous situation was found for protonation of  $\text{H}_2\text{O}$  in Section 7.5). In other words, the electrophile directly attacks the polyene ring from the same side as the metal is coordinated.

## 20.2 THE $\text{CpM}$ FRAGMENT ORBITALS

Suppose the three carbonyl ligands are removed from  $\text{CpMn}(\text{CO})_3$ ; this generates the  $\text{CpMn}$  fragment, **20.11**. Three empty hybrid orbitals are produced which point toward the missing carbonyls. This is exactly the same pattern produced by the

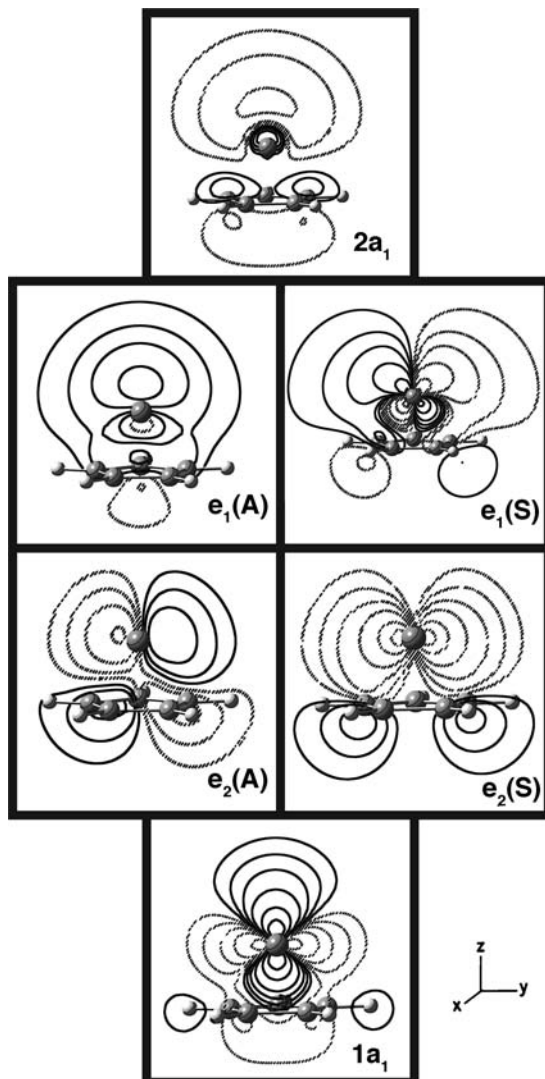


removal of three fac carbonyls from  $\text{Cr}(\text{CO})_6$ , see **20.2**. In other words, the  $\text{CpMn}$  fragment is expected to be very similar to  $\text{Cr}(\text{CO})_3$ . That result should not be too surprising. In Section 20.1 it was shown how a  $\text{Cp}^-$  ligand is topologically equivalent to three fac carbonyls. Therefore, replacing the carbonyls with  $\text{Cp}^-$  in  $\text{Cr}(\text{CO})_3$  generates  $\text{CpCr}^-$  which is isoelectronic to  $\text{CpMn}$ . The orbitals of an arbitrary  $\text{CpM}$  fragment are constructed in Figure 20.8 by interacting a  $\text{Cp}^-$  ligand with an M atom. The symmetry labels used for the orbitals of  $\text{Cp}^-$  and M correspond to the  $C_{5v}$



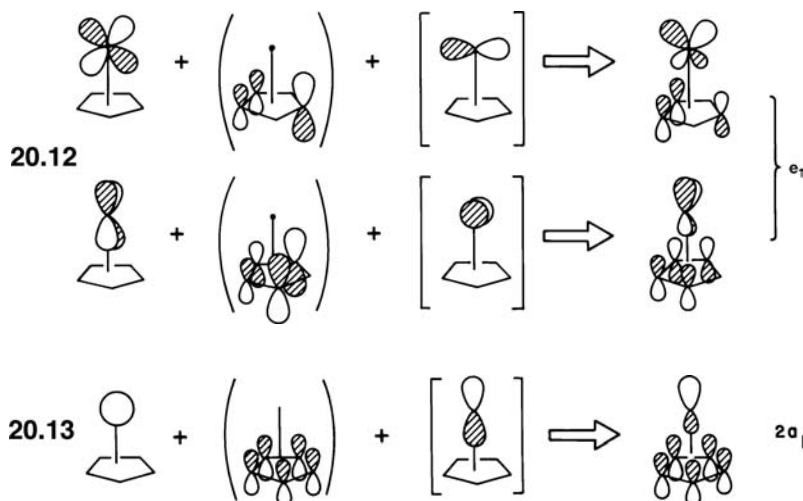
**FIGURE 20.8**

An orbital interaction diagram for the  $\text{MCp}$  fragment, which shows the orbital occupancy for the  $d^0$  case.

**FIGURE 20.9**

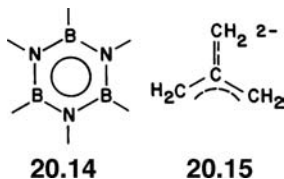
Contour plots at the B3LYP level for the important valence orbitals in MnCp fragment. The  $e_2(A)$  and  $e_1(A)$  orbitals are plotted in the  $yz$  plane, displaced 1 Å along the  $x$  axis.

symmetry of CpM. The lowest  $\pi$  level of  $Cp^-$ ,  $a_1$ , is stabilized by metal  $s$  and  $z$  (see coordinate system at the top of this figure). The  $e_1$  set on  $Cp^-$  is stabilized primarily by metal  $xz$  and  $yz$  and to a lesser extent (because of the larger energy gap) by metal  $x$  and  $y$ . Therefore, a total of the three Cp-metal bonding orbitals are occupied for any CpM fragment. There are also three metal-centered orbitals at moderate energy. The  $x^2-y^2$  and  $xy$  levels are stabilized to a small extent by the  $e_2$  set on  $Cp^-$ . The  $\delta$  overlap and large energy gap make this interaction relatively weak. Although the  $a_1 \pi$  level of  $Cp^-$  and  $z^2$  have the same symmetry, they overlap with each other to a minor extent. The  $a_1 \pi$  level lies approximately on the nodal plane of  $z^2$ . Consequently,  $z^2$  is left nonbonding. Contour plots of these three MOs are displayed in Figure 20.9. All three MOs are very localized on the metal. Metal  $xz$  and  $yz$  are significantly destabilized by the  $Cp^-$   $e_1$  set. However, metal  $x$  and  $y$  mix into the molecular orbital labeled  $e_1$  in Figure 20.8 bonding to the  $Cp^-$   $e_1$  set in second order. This is shown in 20.12. This second-order mixing keeps molecular  $e_1$  at moderate energy and hybridizes the metal-centered orbitals away from the  $Cp^-$  ligand. Inspection of Figure 20.8 shows another molecular orbital, labeled  $2a_1$ , at moderate energy. It is



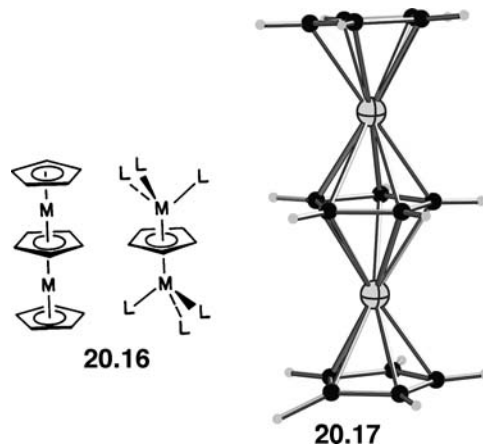
the middle member of the metal s, z, and Cp  $a_1$  union. It arises via a first-order orbital mixing between metal s and the Cp  $a_1$  orbital (antibonding) with a second-order mixing of metal z (bonding between metal and Cp) as in **20.13**. Molecular  $2a_1$  is again hybridized out, away from the Cp ligand. Not shown in Figure 20.8 are three levels primarily of metal x, y, and z character antibonding to Cp,  $e_1 + e_1$ , and the Cp-based  $e_2$  set which are destabilized by  $x^2 - y^2$  and  $xy$ . The important valence levels of a CpM fragment are then  $e_2 + la_1 + e_1 + 2a_1$  in Figure 20.8. A  $d^6$  CpM fragment (like CpMn) will have  $e_2 + la_1$  filled. The  $e_1 + 2a_1$  set of three levels are empty and because of their hybridization (see **20.12** and **20.13**) will form the strongest interactions with extra ligands.

The reader should carefully compare these valence orbitals in Figures 20.8 and 20.9 with those of a  $\text{ML}_3$  fragment in Figures 20.1 and 20.2. The  $\text{ML}_3$  fragment has the same three below, three above level pattern and almost identical atomic composition at the metal. In the CpM fragment it is clear that the  $e_2$  set is of  $\delta$  symmetry and  $e_1$  is of  $\pi$  symmetry. However,  $la_1$  in  $\text{ML}_3$  is primarily  $\delta$  with some  $\pi$  character and  $2e$  is mainly  $\pi$  with some  $\delta$  character. The  $e$  sets in  $\text{ML}_3$  are tilted off from the  $xz$  plane whereas the  $e$  sets in MCp are not. The tilting in  $\text{ML}_3$  comes about because of its octahedral parentage. The three  $\sigma$  donor orbitals of the L groups are highly localized and are situated at three corners of an octahedron. On the other hand, the three donor orbitals of  $\text{Cp}^-$  are delocalized, of course, over the entire Cp ring and have cylindrical symmetry. Therefore, metal  $\delta$  and  $\pi$  functions remain distinct. In most cases it makes no difference whether the  $e$  sets in  $\text{ML}_3$  and MCp are tilted or not. Thus for the same electron count, the fragments can be interchanged. This is a critical factor, however, in polyene- $\text{ML}_3$  and polyene-MCp rotational barriers [11]. When a polyene possesses a threefold localization of  $\pi$  donor orbitals, then the interaction with the  $2e$  acceptor set in  $\text{ML}_3$  will be maximized in one conformation. Examples of polyenes where this is found are given by hexa-alkylborazines, **20.14** (see Section 12.4) and the trimethylenemethane dianion, **20.15**. Therefore, a  $\text{Cr}(\text{CO})_3$

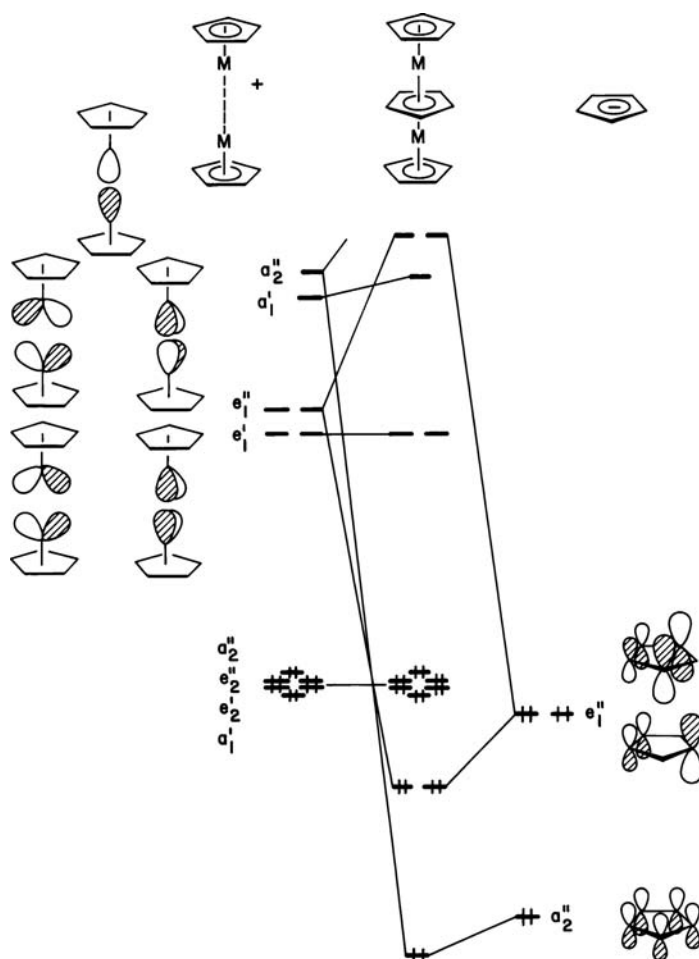


complex of **20.14** and  $\text{Fe}(\text{CO})_3^{2+}$  complex of **20.15** have substantial rotational barriers [11].

The advantage in knowing the form of the valence orbitals in  $\text{ML}_3$  and  $\text{MCp}$  fragments can be illustrated for triple-decker sandwiches, **20.16**. Based on our previous experience, we expect that a stable metal configuration will be one where

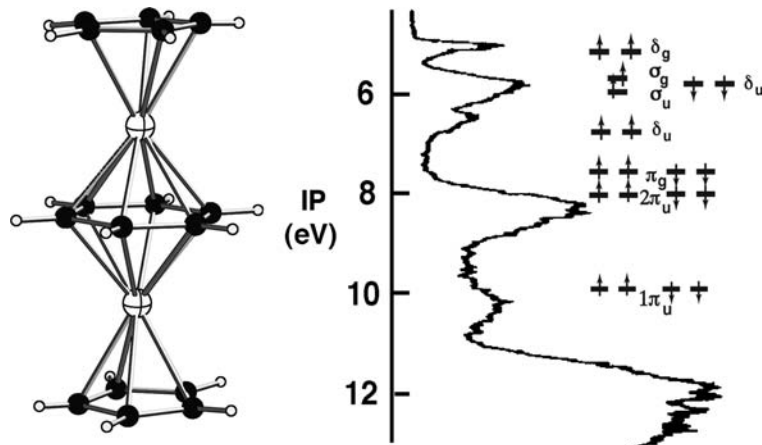


six electrons occupy the “ $t_{2g}$ -like” set. The ligands in **20.16** will present a total of 18 electrons to the metals, thus an electron count of 30 is anticipated to be a stable one. This is true, but complexes with up to four more electrons also exist. It is easy to see how this comes about [12]. An orbital interaction diagram for the  $\text{Cp}_3\text{M}_2$  example is given in Figure 20.10. In-phase and out-of-phase combinations of the valence orbitals for a  $\text{CpM}$  dimer are indicated on the left side of the figure. They are not split apart much in energy because of the large distance between the metal atoms. So there is a nest of six levels at low energy which correspond to the  $1a_1 + e_2$  set in  $\text{MCp}$ . At higher energy are the combinations derived from the  $2a_1 + e_1$  set. On the right side of this figure are shown the three donor orbitals of the middle  $\text{Cp}^-$  unit. They find good overlap matches with the  $a''_2$  and  $e''_1$  fragment orbitals that are drawn for the  $\text{CpM}$  dimer. The six metal-centered orbitals of the  $\text{Cp}_2\text{M}_2$  fragment,  $a'_1 + e'_2 + e''_2 + a''_2$ , are left nonbonding along with the in-phase combination of the  $\text{CpM}$   $e_1$  set which has  $e'_1$  symmetry. Figure 20.10 shows the occupancy for a 30-electron case (remember that there are six occupied levels not shown in this figure which are  $\text{Cp}-\text{M}$  bonding for the end  $\text{Cp}$  units). Notice that the  $\text{Cp}_2\text{M}_2$   $e'_1$  set lies at moderate energy and is well separated from the antibonding combination of  $\text{Cp}_2\text{M}_2$   $e''_1$  and the  $e''_1$  set from the central  $\text{Cp}^-$  ligand. Therefore, complexes with four more electrons are also stable;  $\text{Cp}_3\text{Ni}_2^+$ , **20.17**, is one such example [13]. One might naïvely think that since there are formally 17 electrons associated with each metal atom in the 34-electron systems, then there ought to be a direct metal–metal single bond. However, the distance between the nickel atoms in  $\text{Cp}_3\text{Ni}_2^+$  is 3.58 Å [14], which is far too long to permit any substantial metal–metal interaction. Likewise, in the 30-electron case, it is clear that there can be no metal–metal triple bond (see Figure 20.5). The middle  $\text{Cp}^-$  ligand effectively couples the electrons between the two  $\text{CpM}$  units. In other words, there is a strong through-bond rather than through-space interaction. The 18-electron rule obviously cannot be used for these situations. An MO-based, delocalized description like that presented in Figure 20.10 must be utilized. The middle “slice of bread” need not be a cyclopentadienyl ligand; benzene [15],  $\text{P}_3$  [16], and many carboranes [17] have been used. There are also

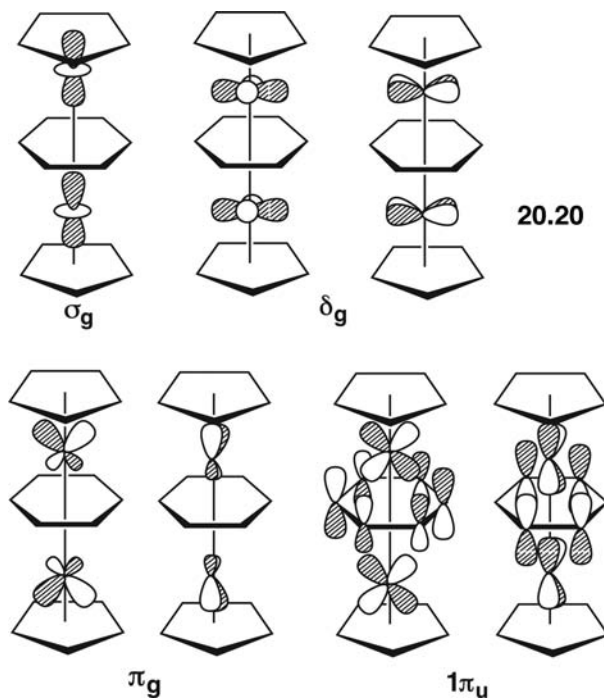
**FIGURE 20.10**

An orbital interaction diagram for a triple decker sandwich complex in  $D_{5h}$  symmetry.

many compounds with fewer than 30 electrons. Compounds with 24–28 electrons and middle rings of benzene,  $P_5$ ,  $P_6$  and even  $Pb_5$  have been synthesized [18,19]. We will examine one member of this set,  $Cp_2V_2(C_6H_6)$ , whose structure [20] is shown in **20.18**. The photoelectron spectrum for this compound and the related  $Cp_2V_2(1,3,5-C_6H_3Me_3)$  have been measured [21] and the former is plotted in **20.19**. There are

**20.18****20.19**

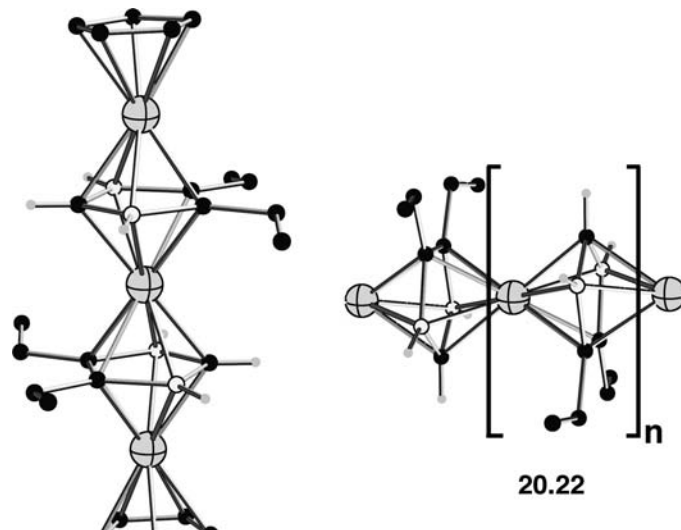
two V  $d^4$  metals and so we must be careful about the level ordering in the “ $t_{2g}$ -like” sets. In Figure 20.10,  $a'_1 + e'_2 + e''_2 + d''_2$  are just enumerated in no particular order. The eight electrons must be positioned so that four are unpaired. This has been determined experimentally [22], and DFT calculations at many levels have also given that the quintet state is more stable than the triplet which, in turn, is much more stable than the singlet state [23]. The photoelectron spectrum shows five low energy ionizations. The assignment of these bands has engendered some controversy. The nomenclature for these orbitals, which has been used by others, takes advantage of the near cylindrical symmetry of the cyclopentadienyl and benzene ligands. The molecule thus has effective  $D_{\infty h}$  symmetry. The two V  $z^2$  combinations are  $\sigma_g$  and  $\sigma_u$ . The in-phase combination,  $\sigma_g$  is shown in 20.20.  $\sigma_g$  and  $\sigma_u$  are not expected to be split much in energy. The V—V distance is very long (3.40 Å) and overlap with the



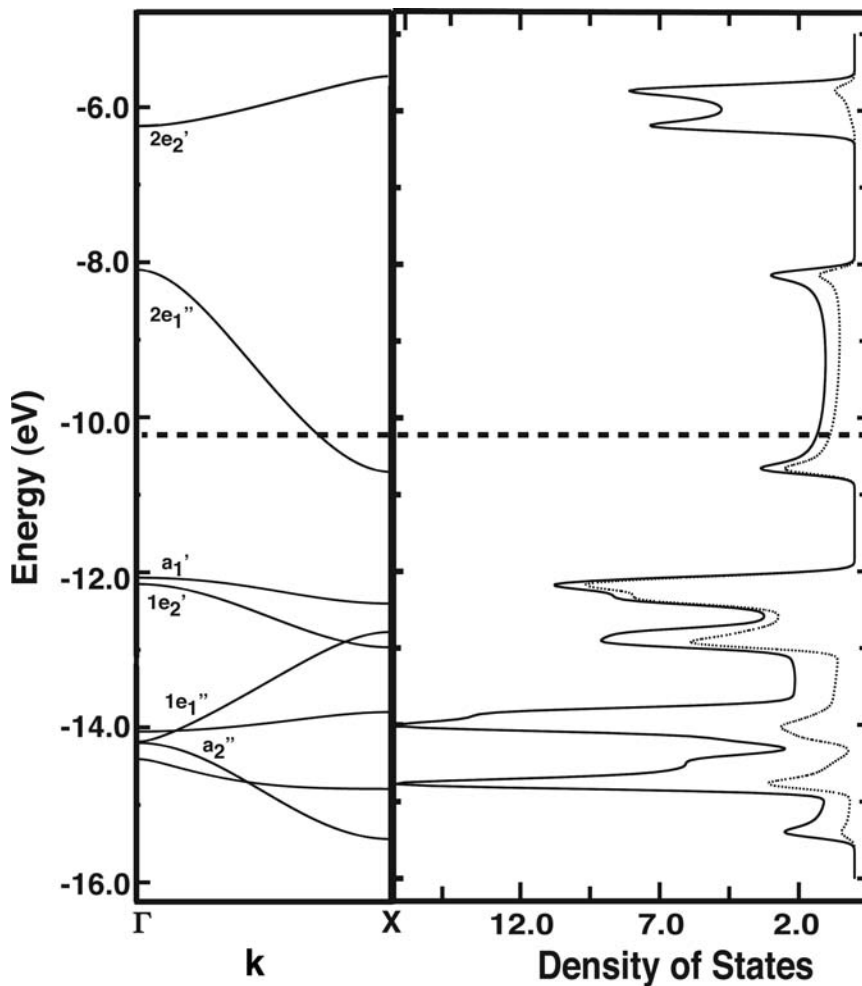
benzene  $\rho$  AOs is small; they lie in the nodal plane of the  $z^2$  functions. The same situation does not apply for the  $x^2 - y^2/xy$ ,  $\delta_g$ , and  $\delta_u$  combinations. The  $\delta_g$  set is shown in 20.20. It is essentially nonbonding with respect to the Cp and benzene ligands. The out-of phase combinations,  $\delta_u$  can and do overlap with and are stabilized by the  $e_{2u}$  set (see Figure 12.6) on benzene. Both  $\pi_g$  and  $2\pi_u$  are V hybrid  $xz/yz$  combinations that are strongly bonding to the Cp  $e''_1$  orbitals and, therefore, they are not split much in energy. Finally there is an orbital,  $1\pi_u$  in 20.20 which is concentrated on the benzene  $e_{1g}$  set and bonding to V  $xz/yz$ . The initial assignment of the lowest energy ionization was ascribed to the  $\sigma_g$  and  $\sigma_u$  MOs [21]. DFT calculations with several kinds of functionals and moderately-sized basis sets give the highest occupied molecular orbital (HOMO) to be the  $\delta_g$  MOs. A large triple zeta valence with  $d$  and  $f$  polarization functions on C and V, respectively, and the BP86 functional was used [24] to investigate the electronic structure of the molecule. The results are displayed on the right side of the PE spectrum in 20.19. Once again the highest orbitals are from the  $\delta_g$  set. The  $\sigma_g$  and  $\sigma_u$  MOs lie at lower energy and make up part of the second band in the PE spectrum. The four unpaired electrons are then associated with the  $\delta_g + \sigma_g + \sigma_u$  MOs. According to the calculations,  $\sigma_g$  and  $\sigma_u$  are split by 0.16 eV. What is most interesting is that the spin-up group of  $\delta_u$  lies at an

energy identical to that of  $\sigma_u$ . Recall from Sections 12.4 and 12.5 that the spin-up MOs may lie measurably higher than the spin-down analogs. This is the case here; the spin-down  $\delta_u$  set constitutes the third band in the PE spectrum. So the splitting between spin-up and spin-down for this case was computed to be 0.80 eV. For the remaining MOs, this difference was 0.16 eV or less and, thus, is no longer a factor in the interpretation of the PE spectrum. The fourth band is assigned to the  $\pi_g$  and  $2\pi_u$  combinations. The splitting between  $\pi_g$  and  $2\pi_u$  for either the spin-up or spin-down MOS was 0.06 eV. Therefore, the fourth band is associated with the ionization of all eight electrons. Finally, the fifth band is assigned to the  $1\pi_u$  set. Consistent with this assignment is the fact that this band lowers its ionization potential by 0.35 eV on going from benzene to 1,3,5-C<sub>6</sub>H<sub>3</sub>Me<sub>3</sub> while the other band positions stay roughly constant in terms of energy. So the assignment predicts a ratio of areas under the bands of 1:2:1:4:2 which is consistent with the experimental results. The predicted ionization potentials using Koopmanns' theorem are plotted using the energy scale in **20.19**. The  $\pi_g$  and  $2\pi_u$  ionizations are predicted to be 0.4 eV lower in energy than experiment. But the other four ionizations are within 0.2 eV of experiment. This represents an excellent fit to a difficult (and tricky) case.

For a tetradecker sandwich electron counts of 40–48 have been observed [25]. An example is provided by **20.21** [25b]. The outer two polyenes are cyclopenta-dienyls while the inner two are (4,5-diethyl)-1,3-diborole ligands and the metals are

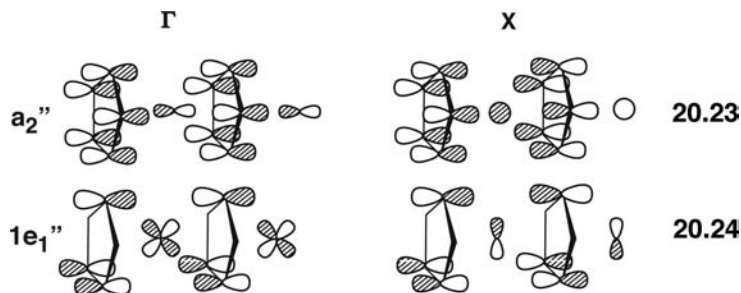


Ni. The electron count for this compound is 46 valence electrons. Larger sandwiches have been prepared and there is one report of a (4,5-diethyl)-1,3-diborole-Ni polymer [26]. It has been structurally categorized by EXAFS, and its conductivity characteristics are similar to heavily doped polyacetylene. Unfortunately, it is extremely air-sensitive. Two years prior to this study, in 1984, Michael Böhm predicted that a one-dimensional Cp-M polymer with 12 electrons in a unit cell would be stable and an insulator (or at best a semiconductor) [27]. Thus **22.22** with 13 electrons should be a conductor. Both the experimental and theoretical work has unfortunately been forgotten for the ensuing 30 years. Recently, there has been a flurry of theoretical effort (with no acknowledgement to previous work) on one-dimensional Cp-M [28], as well as, other metallocene polymers [29]. Let us use CpFe as an example. An  $e(k)$  versus  $k$  plot along with the density of states is presented in Figure 20.11. The construction of the bands is a relatively easy matter. The lowest

**FIGURE 20.11**

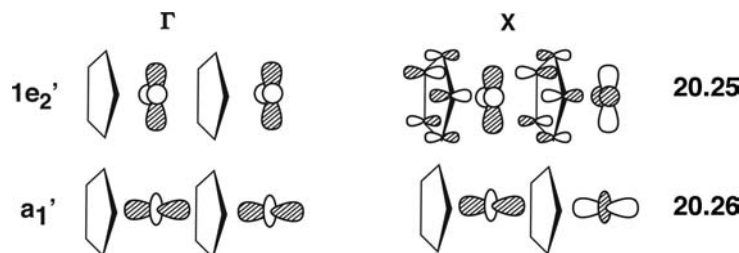
Band structure and density of states plots for a one-dimensional CpFe polymer. The horizontal dashed line indicates the Fermi level. The dotted line in the density of states plot shows the projection of Fe character.

Cp  $\pi$  orbital at the  $\Gamma$  point ( $k = 0$ ) interacts with the Fe  $z$  AO in a bonding fashion. This is shown for two unit cells in 20.23. At  $X$  ( $k = \pi/a$ ) the phase of Cp  $\pi$  inverts on going from one unit cell to the next and, therefore, Cp  $\pi$  now interacts with Fe  $s$ .

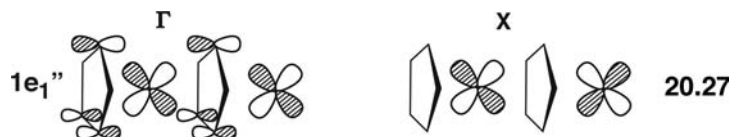


The interaction of Cp  $\pi$  with  $s$  is stronger than that with  $z$ . The  $\pi-s$  energy gap is, of course much smaller than  $\pi-z$  and actually the overlap between  $\pi$  and  $s$  is larger. Therefore, the band, labeled  $a_2''$  in Figure 20.11, is stabilized on going from  $\Gamma$  to  $X$ . The  $1e_1''$  band is predominately the Cp  $\pi$   $e_1$  set. At  $\Gamma$  the two crystal orbitals are stabilized by Fe  $xz$  and  $yz$ . The  $yz$  component is illustrated in 20.24. At  $X$  the stabilization of  $e_1$  now uses Fe  $x$  and  $y$ , which leads to much weaker interactions than

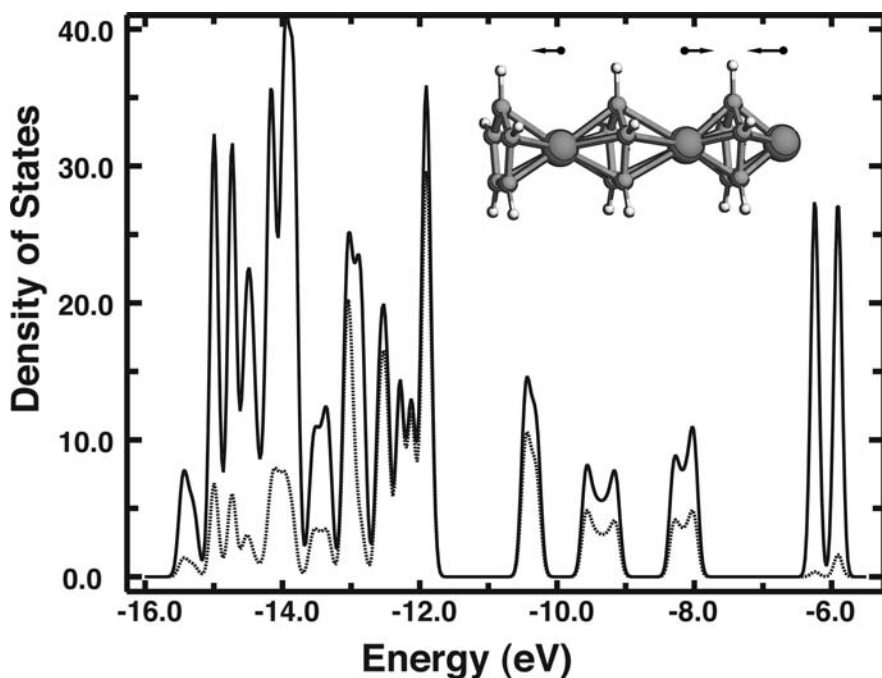
the Fe  $xz/yz$  does. Consequently, the band rises in energy on going from  $\Gamma$  to  $X$ . The fact that the  $1e_1''$  and  $a_2''$  bands meet at  $\Gamma$  is purely accidental. The other two bands in this energy region (both are  $e$  sets) are Cp  $\sigma$  combinations so there is little dispersion. In the density of states plot, the projection of Fe character is given by the dotted line. One can easily tell that the first four bands are heavily weighted on Cp. This is not the case for the  $a_1'$  and  $1e_1'$  bands which are primarily centered on Fe. The  $1e_1'$  set at  $\Gamma$ , one component of which is shown in **20.25**, is  $x^2-y^2$  and  $xy$  with a



small amount of Cp  $\sigma$  mixed in an antibonding fashion. At  $X$  there is some overlap with the Cp  $\pi$   $e_2$  set. This corresponds to the contour plot of  $e_2$  for CpMn in Figure 20.9. The result is that the  $1e_1''$  band goes down in energy from  $\Gamma$  to  $X$  without much dispersion. The two solutions to the Block equation for the  $a_1'$  ( $z^2$ ) band are presented in **20.26**. In actual fact, there is some antibonding to Cp  $\sigma$  at  $\Gamma$ . Recall that the overlap between  $z^2$  and Cp  $a_1 \pi$  is very small so there is little mixing between them at  $X$ . There are a total of six electrons from the Cp  $\pi$  manifold and six electrons that are metal-centered—the “ $t_{2g}$ ” set. This gives a saturated electron complex analogous to the electronic situation we saw for CpMn(CO)<sub>3</sub> in Figure 20.5 or the 30 electron Cp<sub>3</sub>M<sub>2</sub> example in Figure 20.10 (or ferrocene discussed in Section 20.3). The antibonding analog of **20.24**, one component is shown in **20.27**, lies at a

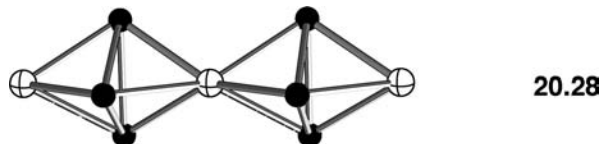


considerably higher energy and so a large band gap occurs between  $2e_1''$  and  $a_1'$ . From the drawing for the  $k = X$  solution in **20.27**, one might think that it should lie at about the same energy as the  $a_1'$  band. The reason for this again lies with the Cp  $\sigma$  levels. The lower of the two Cp  $\sigma$  bands in Figure 20.11 has the same symmetry and destabilizes  $2e_1''$  at the  $X$  point. The  $2e_1''$  band is partially filled for CpFe; the Fermi level is given by the horizontal dashed line in Figure 20.11. Recall that this is isoelectronic to the metallaborane polymer **20.22**. There are electron-spin issues that can arise with this electron count but certainly there is a possibility of a Peierls distortion, which provides energy lowering via geometrical distortion as we have seen throughout the past seven chapters. The  $2e_1''$  bands can be split in a number of ways. One interesting way to do this is to triple the unit cell and move the three metal atoms in the directions shown in the top middle section of Figure 20.12. This results in two Cp rings having short M—C distances and one with longer M—C distances. We will not present all of the electronic details associated with this distortion; however, note that the energy region from  $-15.6$  to  $\sim -13.2$  eV must correspond to the  $1a_2'' + 1e_1''$  and Cp  $\sigma$  bands in Figure 20.11. The region from  $-13.2$  to  $-11.8$  eV represents the  $1e_1' + 1a_1'$  bands. The feature around  $-6.0$  eV in Figure 20.11 and 20.12 corresponds to the Cp  $\pi^*$   $e_2$  set. Finally, the  $2e_1''$  bands are now split into three groups.

**FIGURE 20.12**

A density of states plot for a  $\text{Cp}_3\text{Fe}_3$  one-dimensional polymer. The dashed line corresponds to the projection of Fe AOs. The distortion used in this calculation involves shifting the Fe atoms 0.3 Å in the directions shown at the middle top of the figure.

With 36 valence electrons ( $\text{Cp}_3\text{Mn}_3$ ) the Fermi level lies in the large gap starting at  $-11.8$  eV just like that for the undistorted polymer. The addition of four electrons fills all states from  $-10.3$  eV. With 44 valence electrons ( $\text{Cp}_3\text{Ni}_2\text{Co}$ ), the second peak within the  $2e_g''$  group is completely filled. There are, of course, many other patterns that can be employed to fine-tune these “molecular wires.” The pattern displayed in Figure 20.11 is replicated for the entire  $\text{C}_n\text{H}_n\text{-M}$ , ( $n = 3\text{--}7$ ) series and should also hold for any more elaborate metallocene polymer. There will always be three polyene  $\pi$  bands bonding to the metal and three metal-centered nonbonding ones. At high energy will be the “ $e_g$ ” set of metal  $d$  orbitals antibonding to the polyene  $\pi$ . There are in fact at least two experimental examples of this structural motif.  $\text{Ba}_2\text{Si}_3\text{Ni}$  was prepared and structurally categorized in 2000 [30]. Its structure without the Ba cations is shown in 20.28. The Si—Si distances of 2.44 Å are consistent with the existence of a Si—Si  $\sigma$  bond. In a formalistic sense



then one could regard this as a  $\text{Si}_3^{6-}$  ligand, isoelectronic to  $\text{C}_3\text{H}_3^{6-}$  with all three  $\pi$  levels filled. This leaves  $\text{Ni}^{2+}$  isoelectronic to Fe and the electronic structure should (and does) bear a good deal of resemblance to the  $\text{CpFe}$  example in Figure 20.11. The compound is metallic and exhibits Pauli paramagnetism over a wide temperature range. The X-ray structure at room temperature shows no evidence for a Peierls distortion. Although the structure was not completely solved, the  $\text{Ba}_2\text{Ge}_3\text{Ni}$  congener has a very long unit cell and the Ge thermal parameters along the polymer

axis were very large, which is consistent with a geometrical distortion along the lines we have just described [30].

### 20.3 $Cp_2M$ AND METALLOCENES

We have previously discussed how a fac  $L_3$  set in an octahedrally based complex is equivalent to a  $Cp^-$  ligand. Thus the level splitting pattern for  $Cr(CO)_6^-$  (see Figure 15.1) is very similar to that in  $CpMn(CO)_3$  (see Figure 20.5). One can quibble about minor (although chemically important) differences, for example, the fac carbonyl set is a better  $\pi$  acceptor which stabilizes the metal  $t_{2g}$  levels more than the  $e_2$  acceptor set does in  $Cp^-$ . However, the basic three-below-two level pattern for the valence, metal-centered orbitals and their nodal structure occurs in both compounds. Replacing the three carbonyls in  $CpMn(CO)_3$  with  $Cp^-$  yields  $Cp_2Mn^-$  which is isoelectronic with  $Cp_2Fe$ , ferrocene. The six (localized) Cr—CO bonds in  $Cr(CO)_6^-$  are obvious. There should also be six Fe—C bonds in ferrocene. That is difficult to see in a localized sense. Figure 20.13 shows an orbital interaction diagram for ferrocene at a staggered (the Cp rings are staggered

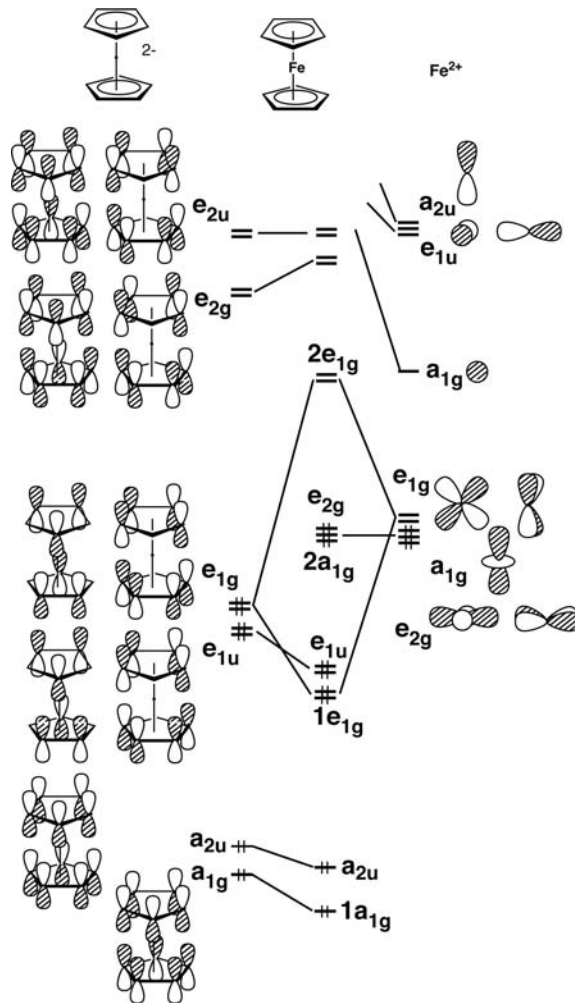


**FIGURE 20.13**

Construction of the molecular orbitals of ferrocene.

with respect to each other),  $D_{5d}$  geometry. The molecule has been partitioned into  $\text{Fe}^{2+}$  and  $\text{Cp}_2^{2-}$  units. The Cp levels of  $a_{1g}$  and  $a_{2u}$  symmetry are stabilized by metal s and z, respectively. Likewise the Cp  $\pi$  sets,  $e_{1u}$  and  $e_{1g}$  are stabilized by metal x, y, and xz, yz, respectively. Notice that as expected from perturbation theory considerations, the latter interaction is much stronger than the former. We have just described six occupied MOs which are bonding between Fe and the Cp rings. These are the six bonds that are analogous to the Cr—CO bonds in  $\text{Cr}(\text{CO})_6$  of  $1a_{1g}$ ,  $1t_{1u}$ , and  $1e_g$  symmetry (see Figure 15.1). At moderate energy are the molecular orbitals labeled  $e_{2g}$  and  $a_{1g}$ . They are basically the nonbonding  $x^2 - y^2$ , xy, and  $z^2$  set. Finally at higher energy is the molecular  $e_{1g}$  level. This is the antibonding combination of metal xz and yz with the  $e_{1g}$  set of  $\text{Cp}_2^{2-}$ . Notice that the octahedral splitting pattern of three-below-two has again been established. The photoelectron spectra of ferrocene and ruthenocene are displayed in Figure 20.14. The assignments for  $\text{Cp}_2\text{Fe}$  are derived from Penning ionization electron spectroscopy [31] and those for  $\text{Cp}_2\text{Ru}$  from a detailed study of substituent effects [32]. The basic electronic structure follows that given in Figure 20.13. The lowest ionization potentials originate from the  $e_g + 2a_{1g}$  MOs. These ionization potentials increase by about 0.5 eV on going from  $\text{Cp}_2\text{Fe}$  to  $\text{Cp}_2\text{Ru}$ . This is consistent with the larger electronegativity of Ru compared to Fe (Pauling electronegativity values are 2.2 and 1.8, respectively). The  $1e_{1g}$  ionization for  $\text{Cp}_2\text{Ru}$  is also 0.5 eV larger than that for  $\text{Cp}_2\text{Fe}$ . On the other hand, the ionization for the Cp  $\pi$  centered  $e_{1u}$  is 0.3 eV smaller in  $\text{Cp}_2\text{Ru}$ . This is possibly due to the fact that the 5p AOs of Ru are very diffuse and their overlap with the Cp  $\pi$  set is expected to be weaker than that in  $\text{Cp}_2\text{Fe}$ . It should be noted that in both instances, as well as in  $\text{Cp}_2\text{Os}$  [33] the  $e_u$  set lies at a higher energy than  $2a_{1g}$ . In other words, the stabilization afforded by

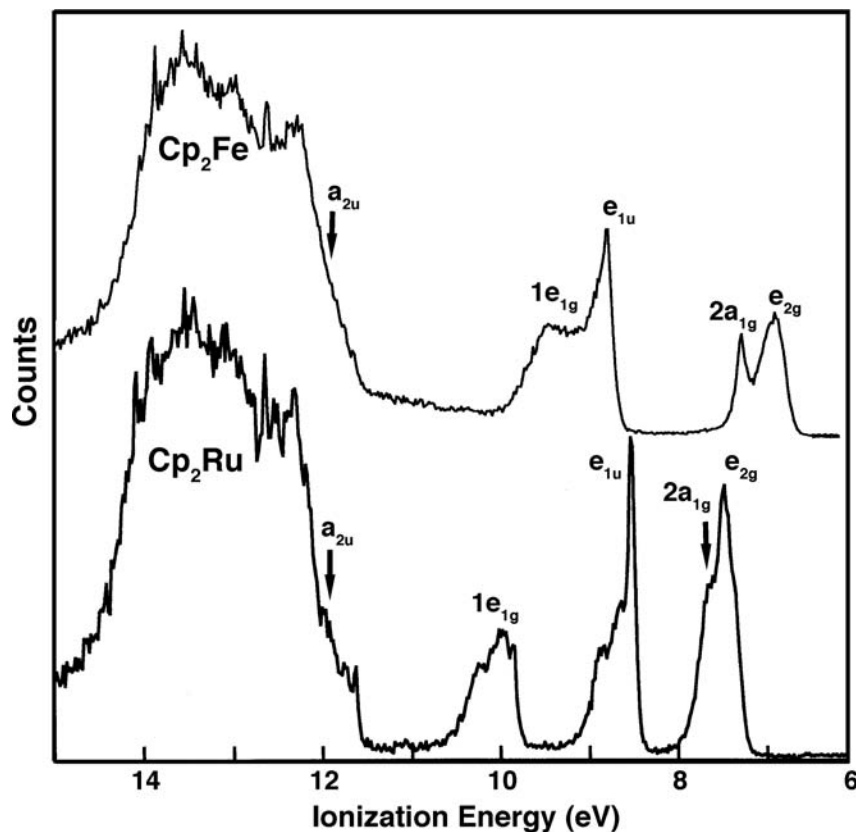
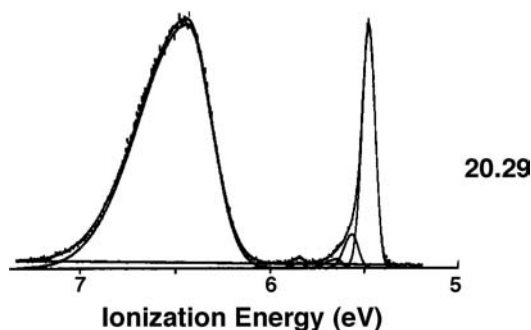


FIGURE 20.14

Photoelectron spectra of ferrocene and ruthenocene.

the  $\text{Cp} \pi^* e_{2g}$  set of orbitals (see Figure 20.13) must be quite small. The electronic structure for bisbenzene-Cr (**16.11**) is very similar to that in ferrocene. The main difference is that now the  $e_{2g}$  set has a larger ionization potential than  $a_{1g}$  [34]. The PE spectrum for this region is shown in **20.29**. Note that the  $a_{1g}$  band is very sharp, consistent with this being a nonbonding, metal-centered MO. The  $e_{2g}$  ionization is



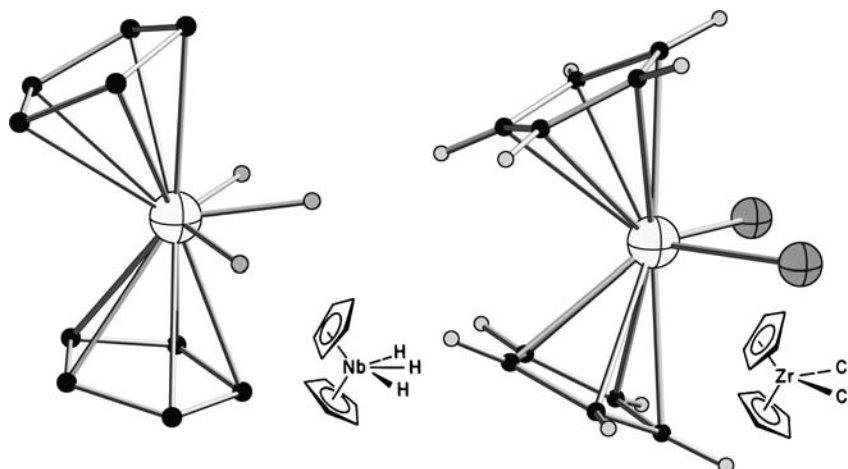
much broader and reflects unresolved vibrational splitting. An energy partitioning scheme has been used to investigate in a quantitative sense the metal–ligand bonding in  $\text{Cp}_2\text{Fe}$  and  $\text{Bz}_2\text{Cr}$  [35]. As expected, the major source of covalent bonding is derived from the  $e_{1g}$  orbitals (65%) with a much smaller contribution from  $e_{2g}$  (8%) and  $e_{1u}$  (11%). For  $\text{Bz}_2\text{Cr}$  there is a startling reversal:  $e_{1g}$  (15%),  $e_{2g}$  (73%), and  $e_{1u}$  (<1%). The provocative claim [35] is that while ferrocene has a traditional bonding composition with the  $\pi$  bonding from  $\text{Cp} \pi e_{2g}$  with  $\text{Fe} xz/yz$  far more important than  $\delta$  bonding between  $\text{Cp} \pi^* e_{1g}$  and  $\text{Fe} x^2-y^2/xy$ , chromocene is covalently held together by  $\delta$  bonding. Does this make sense from the experimental PE spectra results using Koopmans' theorem? Let us take the ionization potential of the  $a_{1g}$  orbital as the energy of a metal  $d$  AO in the electrostatic field provided by the molecule. For  $\text{Cp}_2\text{Fe}$  the  $e_{1g}$  MO is destabilized by 0.35 eV from  $a_{2g}$  which is certainly consistent with little  $\delta$  bonding. The destabilization is likely due to the overlap of  $\text{Fe} x^2-y^2/xy$  with  $\text{Cp} \sigma$  orbitals. To gauge the extent of  $\pi$  bonding, one needs the energy of the  $\text{Cp} \pi e_{2g}$  set. For the reasons mentioned previously, the  $e_{1u}$  ionization in  $\text{Cp}_2\text{Ru}$  would be a better standard for that and, therefore, the stabilization of  $\text{Cp} \pi e_{2g}$  with  $\text{Fe} xz/yz$  amounts to 0.90 eV. For chromocene, the ionization potential of the benzene  $\pi$  set will be close to 9.25 eV (this is the ionization potential for benzene  $\pi$ , see Figure 12.7. The  $e_{1u}$  combination in  $\text{Bz}_2\text{M}$ , M = Cr, Mo, and W, is at 9.56 eV. If this is taken as the ionization potential for the noninteracting benzene  $\pi$  set, then the stabilization of  $e_{2g}$  is only 0.24 eV. Thus the stabilization of benzene  $\pi e_{2g}$  is 0.65 eV. For the  $\delta$  combination, the  $e_{1g}$  MO is stabilized by 1.01 eV. Consequently, this analysis clearly supports the notion that  $\delta$  bonding is more important than  $\pi$  bonding in  $\text{Bz}_2\text{Cr}$ , whereas the opposite is true for  $\text{Cp}_2\text{Fe}$ . The  $\pi^*$  orbitals in benzene lie at a lower energy than those of  $\text{Cp}^-$  and the  $d$  AOs of Cr lie at a higher energy than those of  $\text{Fe}^{2+}$ . Therefore, the  $\delta$  interaction is much stronger in  $\text{Bz}_2\text{Cr}$  than it is in  $\text{Cp}_2\text{Fe}$ . On the other hand, the  $\text{Cp} \pi$  set lies at a higher energy than that in benzene so from an energy gap argument; the  $\pi$  bonding in  $\text{Cp}_2\text{Fe}$  is stronger than that in  $\text{Bz}_2\text{Cr}$ .

Ferrocene, an 18-electron complex, has the bottom nine MOs in Figure 20.13 filled through  $a_{1g}$ . There are thousands of derivatives and heterocyclic analogs that have been prepared including the all-inorganic  $(\text{P}_5)_2\text{Ti}^{2-}$  molecule [36]. This brings up another aspect of metallocene chemistry. A phosphorus atom is isoelectronic to CH; the CH  $\sigma$  bond is replaced by a lone-pair in P. So  $(\text{P}_5)_2\text{Ti}^{2-}$  is analogous to  $\text{Cp}_2\text{Ti}^{2-}$  or  $\text{Cp}_2\text{Cr}$  which have 16 electrons. Actually  $\text{Cp}_2\text{M}$  compounds from M = Ca to Ge exist. For  $\text{Cp}_2\text{V}$  with 15 electrons there are

three electrons in the  $a_{1g} + e_{2g}$  manifold. A  $^4A_{1g}$  ground state is obtained where there is one unpaired electron in each orbital [37]. For Cp<sub>2</sub>Cr there are two possible electron configurations. The singlet state with an  $(e_{2g})^4(a_{1g})^0$  configuration is 57 kcal/mol higher in energy than a triplet state with an  $(e_{2g})^2(a_{1g})^2$  configuration [38]. Distortion to a C<sub>2v</sub> or C<sub>2h</sub> geometry yields four triplet states all within 0.5 kcal/mol of each other and 5 kcal/mol lower than the D<sub>5d</sub> one. Contrast this with (P<sub>5</sub>)<sub>2</sub>Ti<sup>2+</sup> which has a  $^1A_{1g}$  ground state and the triplet states are computed to be 24 kcal/mol higher in energy [36]. The reason behind this is that, just as in chromocene, a very large  $\delta$  bonding interaction keeps e<sub>2g</sub> at a much lower energy than a<sub>1g</sub>. For Cp<sub>2</sub>Mn one might think that a doublet state with the configuration  $(a_{1g})^2(e_{2g})^3$  might be favored. In fact the  $^6A_{1g}$  state with a level ordering of  $(e_{2g})^2(a_{1g})^1(e_{1g})^2$  is essentially at the same energy. Cp<sub>2</sub>Co with 19 electrons has a  $^2E_{1g}$  state with a  $(e_{2g})^4(a_{1g})^2(e_{1g})^1$  configuration 2.5 kcal/mol higher in energy than Jahn—Teller distorted C<sub>2v</sub> or C<sub>2h</sub> geometries [37]. Cp<sub>2</sub>Ni with 20 electrons has also been prepared. Now there are two electrons in the molecular e<sub>1g</sub> levels and consequently a triplet state results. Therefore, the molecule has triplet ground state. The molecular e<sub>1g</sub> set (see Figure 20.6) is antibonding between the Cp rings and Fe. Therefore, occupation of e<sub>1g</sub> will cause the metal—carbon bond distance to increase; for example, the Fe—C distance in Cp<sub>2</sub>Fe is 2.064(3) Å while that in Cp<sub>2</sub>Co and Cp<sub>2</sub>Ni is 2.119(3) Å and 2.196(8) Å, respectively [39]. Likewise the Mn—C distance for low spin (MeC<sub>5</sub>H<sub>4</sub>)<sub>2</sub>Mn is 2.144(12) Å while that for the high-spin species increases to 2.380 (6) Å [39]. The photoelectron spectra [40] for a wide variety of metallocenes including the Cp<sub>2</sub>V–Cp<sub>2</sub>Ni series have been analyzed with some care.

## 20.4 Cp<sub>2</sub>ML<sub>n</sub> COMPLEXES

The last mononuclear transition metal fragment that we shall study in some depth is bent Cp<sub>2</sub>M. There exists a vast body of chemical information on Cp<sub>2</sub>ML<sub>n</sub> complexes where n = 1–3 and M is an early transition metal atom (e.g., Ti, V, Zr, Hf, Mo, etc.). There have been many theoretical treatments of these molecules [41]; the one we shall follow was given by Lauher and Hoffmann [42]. These Cp<sub>2</sub>ML<sub>n</sub> complexes are unique for several reasons; the L<sub>n</sub> groups are forced to lie in a common plane, see **20.30** for one example. There are obvious steric requirements; in **20.30** the

**20.30****20.31**

H–Nb–H angle is only  $61^\circ$  [43].  $\text{Cp}_2\text{ZrCl}_2$  [44], **20.31**, is illustrative of another common problem; it is a 16-electron complex and yet is even air stable. A 16-electron count at the metal is perhaps more common for these compounds than the 18-electron one. Finally, allowing for the fact that each  $\text{Cp}^-$  ligand forms three bonds to the metal, **20.30** and **20.31** are then 9 and 8 coordinate, respectively. These are high coordination numbers for a nonlanthanide metal; coordination numbers of 4–6 are far more common.

In **20.30** and **20.31** the Cp rings are bent back from the parallel geometry treated for metallocenes in Section 20.4. This is a pervasive feature for  $\text{Cp}_2\text{ML}_n$  complexes. It is easiest to derive the fragment orbitals of a bent  $\text{Cp}_2\text{M}$  unit from the parallel geometry. The important molecular orbitals of the metallocene that we shall study are the  $e_{2g}$  and  $a_{1g}$  orbitals of Figure 20.6. The other orbitals are either Cp centered or lie at too high an energy (for example the molecular  $2e_{1g}$  set in Figure 20.13). The three initial levels of a parallel  $\text{Cp}_2\text{M}$  system are shown on the left side of Figure 20.15. It does not matter whether the geometry of the Cp rings is staggered or eclipsed. For convenience, the orbitals are labeled in  $C_{2v}$  symmetry when the Cp rings are bent back as if we had utilized an eclipsed geometry. Bending back the Cp rings splits the  $e_{2g}$  set into orbitals of  $a_1$  and  $b_2$  symmetry. The  $b_2$  orbital rises in energy as the Cp rings are bent back. It loses some of the bonding to the Cp  $\pi^*$  orbitals and repulsive interactions with  $\text{Cp}\sigma$  levels are turned on. The same would happen to the other component of  $e_{2g}$  which is labeled  $1a_1$  in Figure 20.13. However, it mixes with what was  $2a_{1g}$ , now labeled  $2a_1$ . This mixing between  $1a_1$  and  $2a_1$  is shown on the right side of the figure and it serves to keep  $1a_1$  at constant energy. The  $2a_1$  orbital, however, rises rapidly in energy. This is partly due to the avoided crossing with  $1a_1$  and the fact that the  $a_{1g}$  combination of Cp  $\pi$  levels (see Figure 20.13) has a greater overlap with metal  $z^2$  at a bent geometry. Some metal s character and  $x^2-y^2$  from  $1a_1$  mix into  $2a_1$  so that the torus of  $z^2$  becomes hybridized away from the Cp ligands. As mentioned previously, the L groups in  $\text{Cp}_2\text{ML}_n$  complexes lie in the  $yz$  plane (for the coordinate system see Figure 20.15). A convenient view of these orbitals in the  $yz$  plane that we shall utilize for the remaining discussion is given in **20.32**. The contour plots are derived from B3LYP hybrid density functional

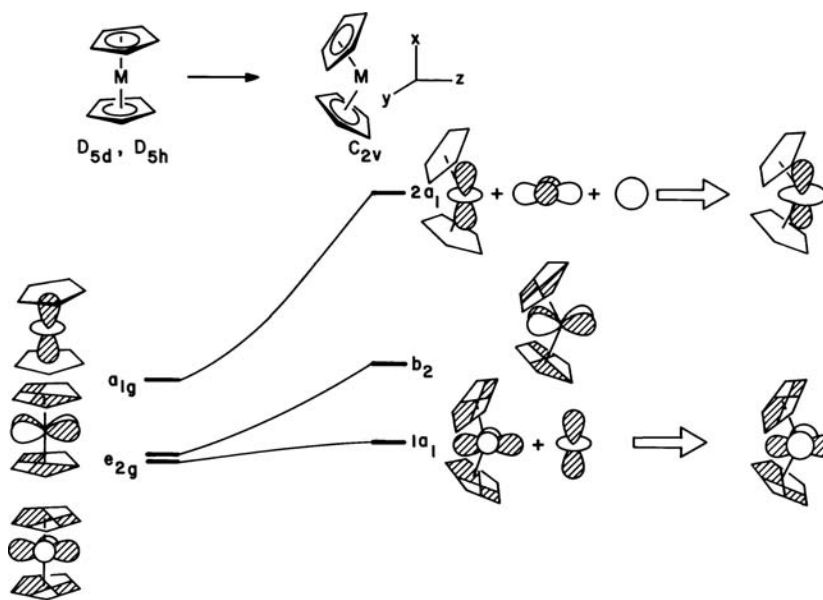
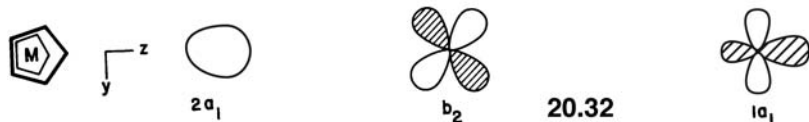
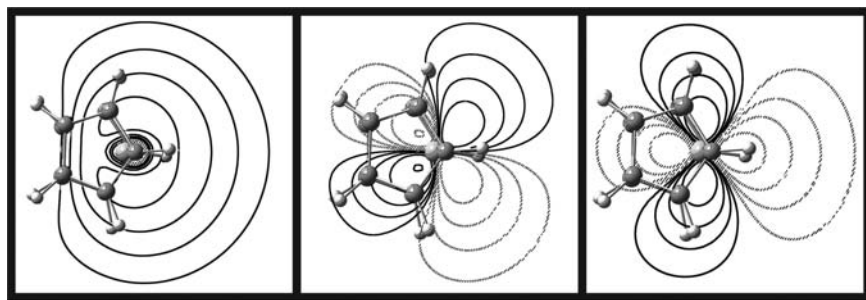


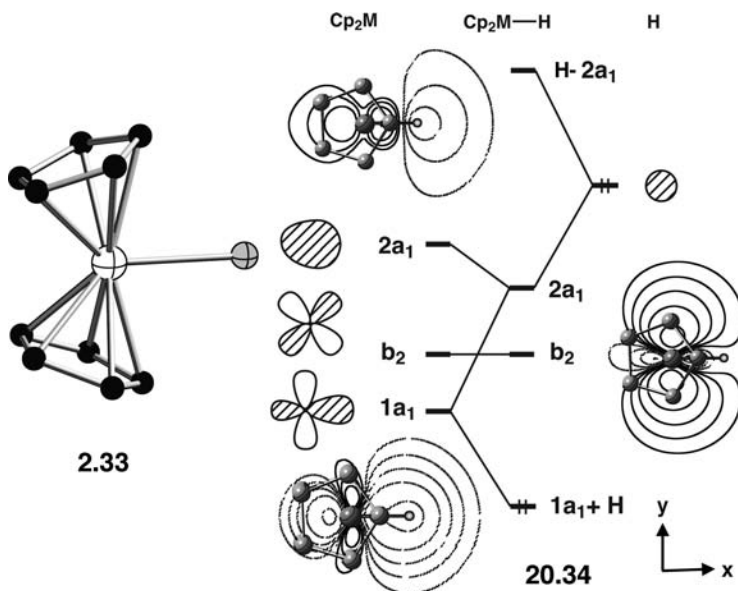
**FIGURE 20.15**

A Walsh diagram for bending back the Cp rings in the  $\text{Cp}_2\text{M}$  fragment. The shaded regions in the Cp rings for the  $e_{2g}$  set indicate the small bonding contribution from the Cp  $\pi^*$  orbitals.

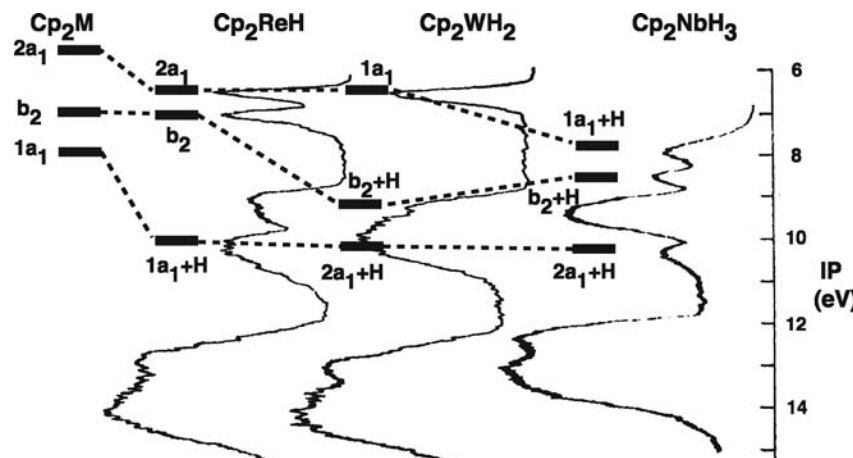


calculations on  $\text{Cp}_2\text{Zr}$  where the  $\text{Cp}—\text{Zr}—\text{Cp}$  angle was  $130^\circ$ . The reader should recall that the levels in **20.32** are derived from the  $t_{2g}$ -like set of a metallocene. They now have been split apart in energy and are somewhat hybridized in the direction of the  $L_n$  set.

An 18-electron  $\text{Cp}_2\text{M}-\text{H}$  complex will have a  $d^4$  count at the metal with the hydrogen ligand as a hydride. An example is  $\text{Cp}_2\text{ReH}$ . While this is a known compound, its structure has not been determined. **20.33** shows the geometry for the closely related  $\text{Cp}_2\text{Re}-\text{Cl}$  molecule [45]. Notice that the Cl ligand lies on the  $C_2$  axis. An interaction diagram for  $\text{Cp}_2\text{MH}$  with  $C_{2v}$  symmetry is given in **20.34**. The  $\text{Cp}_2\text{M}$   $b_2$  orbital is left nonbonding. The H s AO,  $1a_1$ , and  $2a_1$  orbitals have the same



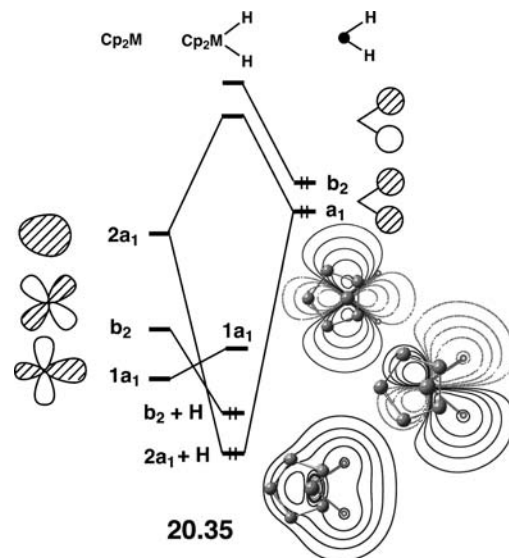
symmetry so a three-orbital interaction pattern is produced. The lowest MO, labeled  $1a_1+\text{H}$  in **20.34**, is the totally bonding combination. The highest MO,  $\text{H}-2a_1$ , is the antibonding analog. Contour plots of these MOs are also shown in **20.34**. The construction and shape of these orbitals is very similar to that presented for HF; see Figure 3.3 and in particular **3.12** and **3.14**. The middle, nonbonding MO has H s and  $2a_1$  mixed in a bonding fashion while  $1a_1$  mixes with the phase opposite to that in **20.34**. The net result of this mixing as illustrated by the contour plot is an orbital primarily localized on the metal and hybridized in the  $y$  direction, orthogonal to the

**FIGURE 20.16**

Correlation of the PE spectra for  $\text{Cp}_2\text{MH}_n$ .

$\text{M}-\text{H}$  bond. In essence, the  $x^2-y^2$  and  $z^2$  MOs at the metal mix to create a  $y^2$  orbital. With four electrons,  $\text{Cp}_2\text{ReH}$  has the  $b_2$  and  $2a_1$  MOs filled. The PE spectrum [46,47] of  $\text{Cp}_2\text{ReH}$  in Figure 20.16 shows the two lowest ionizations to be close in energy. This is consistent with the pattern in 20.34. With a  $d^2$ , 16-electron count there is now a small gap between the HOMO,  $b_2$ , and the LUMO,  $2a_1$ . Bending the hydrogen atom in the  $xy$  plane will allow  $2a_1$  to mix with and stabilize the  $b_2$  MO. Thus,  $\text{Cp}_2\text{TaH}$  is predicted to have  $C_s$  geometry. This molecule has been observed by IR and UV spectroscopy in low temperature Ar and  $\text{N}_2$  matrices [48].

The interaction diagram for a  $\text{Cp}_2\text{MH}_2$  molecule, 20.35, is straightforward. Within  $C_{2v}$  symmetry the two hydride s AOs generate fragment orbitals of  $a_1$  and  $b_2$



symmetry. The hydrogens lie close to the nodal surface of  $1a_1$  on  $\text{Cp}_2\text{M}$  so the primary interaction of  $a_1$  is with  $2a_1$ . There are, therefore, two  $\text{M}-\text{H}$  bonding MOs within the  $\text{Cp} \pi$  ionizations. Contour plots of them are shown on the right side of 20.35 for  $\text{Cp}_2\text{WH}_2$  at the B3LYP level. The  $1a_1$  orbital on  $\text{Cp}_2\text{M}$  is a nonbonding MO

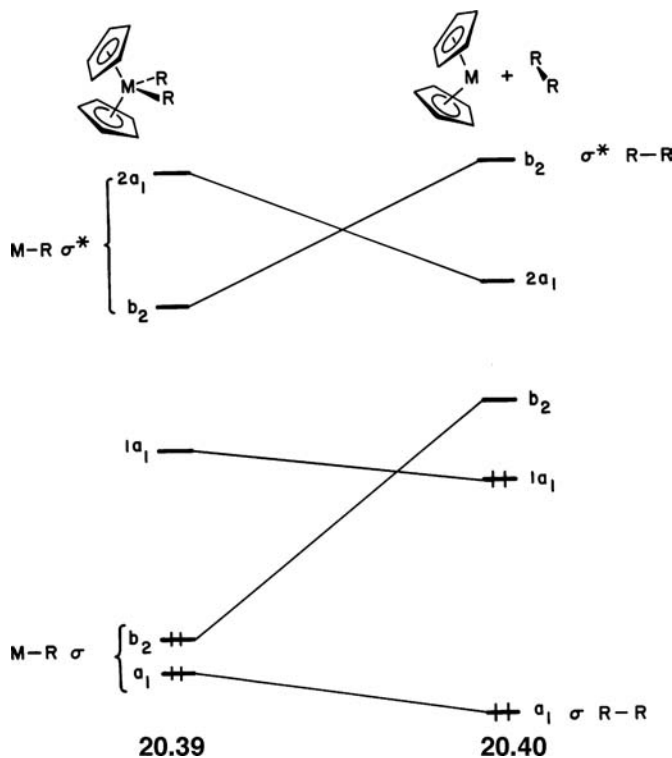
for the 18-electron,  $d^2 \text{Cp}_2\text{WH}_2$ ; the contour diagram for this orbital is also shown in **20.35**. Also as demonstrated by the PE spectrum, this is a metal lone-pair orbital, see Figure 20.16. For a 16 electron,  $d^0$  species, of course,  $1a_1$  is empty.

In  $\text{Cp}_2\text{NbH}_3$ , **20.30**, the metal is formally  $d^0$ . Therefore,  $1a_1$ ,  $b_2$ , and  $2a_1$  are empty. The three hydride ligands form symmetry-adapted combinations shown in **20.36–20.38**. They nicely match the nodal properties of **20.30**:  $1a_1$  with **20.38**,  $b_2$



with **20.37**, and  $2a_1$  with **20.36**. So all three donor functions are stabilized, see Figure 20.16, yielding a stable  $d^0$  complex with an 18-electron count.

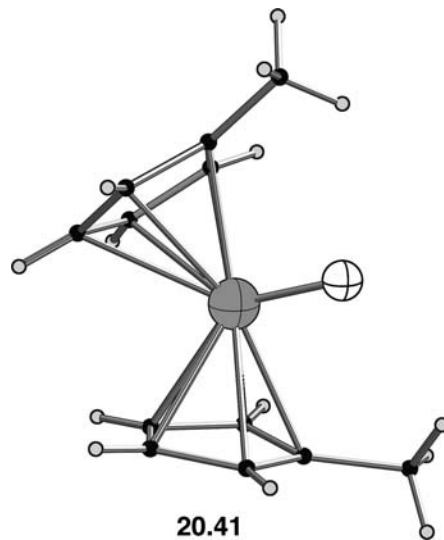
There are important reactivity differences between  $\text{Cp}_2\text{ML}_2$  systems, depending upon whether the  $1a_1$  orbital is filled or not. Consider reductive elimination in a dialkyl-substituted complex. In **20.39**, the orbitals of a  $d^0$   $\text{Cp}_2\text{MR}_2$  complex are listed. A correlation is drawn for reductive elimination to a  $d^2$   $\text{Cp}_2\text{M}$  complex along with the



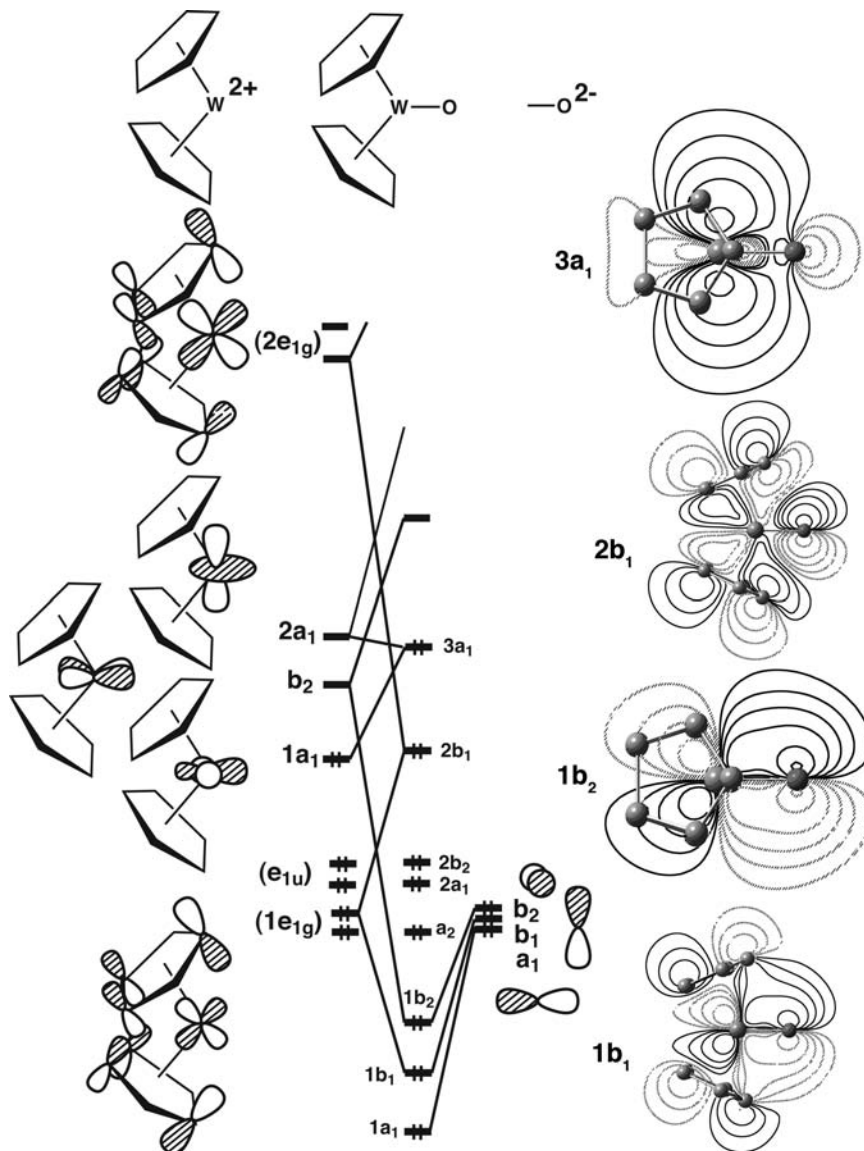
$\sigma$  and  $\sigma^*$  levels of an alkane in **20.40** where a least-motion pathway that conserves  $C_{2v}$  symmetry is followed. The reaction is symmetry-forbidden, a non-least-motion pathway must be followed, not unlike reductive elimination from an alkane to give a carbene and  $\text{H}_2$ , for example (see **19.74–19.78**). Furthermore,  $\text{Cp}_2\text{Ti}$  certainly has a triplet ground state; the singlet is estimated to lie from 8 to 19.3 kcal/mol above the triplet [39b,49] where the  $\text{Cp}$  rings are parallel so that  $1a_1$  and  $b_2$  form the  $e_{2g}$  set so there must also be an intersystem crossing that takes place. Experimentally [50], the

decomposition of  $d^0 \text{ Cp}_2\text{MR}_2$  has proven to be not a straightforward reductive elimination reaction. For example,  $\text{Cp}_2\text{M}(\text{CH}_3)_2$  ( $\text{M} = \text{Ti}, \text{Zr}, \text{Hf}$ ) decompose at moderate temperatures to yield  $\text{CH}_4$ , not  $\text{C}_2\text{H}_6$  [50]. The symmetry prohibition would be removed starting from an 18-electron,  $d^2 \text{ Cp}_2\text{MR}_2$  complex where  $1a_1$  is filled. However, notice that reductive elimination may still be energetically unfavorable since one M–R bonding orbital ( $b_2$ ) must rise to high energy ultimately becoming the  $b_2$  orbital of  $\text{Cp}_2\text{M}$ . There is a further complication, namely, that there is no reason for the  $\text{Cp}_2\text{M}$  product to remain bent. Most experimental [51] and theoretical [52] work have involved the  $\text{Cp}_2\text{WH}(\text{CH}_3)$  molecule. Thermolysis to form  $\text{CH}_4$  is an endothermic reaction and proceeds via a  $\text{Cp}_2\text{W}(\text{CH}_4)$  intermediate where there is a W–H agostic bond.  $\text{Cp}_2\text{W}$  is a ground-state triplet and, therefore, there is also a singlet to triplet interconversion along the reaction pathway.  $\text{Cp}_2\text{WH}_2$  and  $\text{Cp}_2\text{W}(\text{CH}_3)_2$  do not undergo reductive elimination reactions [51b]. Presumably the strength of the H–H bond makes the reaction from the former complex too endothermic and the need to reorient the methyl groups for the latter molecule renders an activation energy that is too high (compare **19.93** with **19.94**). The reader should refer back to Section 19.5 and compare the situation for reductive elimination there with the correlation in **20.39–20.40**. There are many differences because the ligand set has changed.

There are interesting  $\pi$ -bonding effects in  $\text{Cp}_2\text{ML}_n$  complexes.  $\text{Cp}_2\text{WO}$  is unusual for a number of reasons. The x-ray structure for the  $(\text{CH}_3\text{C}_5\text{H}_4)_2\text{WO}$  derivative is shown in **20.41** [53]. Counting the oxo group as  $\text{O}^{2-}$  yields a  $d^2$  count at the metal. Therefore, this would be a 16-electron complex considering only the  $\sigma$



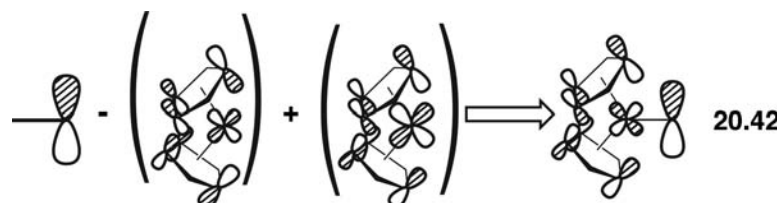
$\text{W}–\text{O}$  interaction. This is not a terribly unusual electron count for a  $\text{Cp}_2\text{ML}_n$  compound; however, the  $\text{W}–\text{O}$  distance of  $1.744(5)$  Å clearly indicates the presence of  $\text{W}–\text{O}$   $\pi$  bonding. If this was a triple bond, then the electron count at W becomes 20. The  $\text{W}–\text{C}$  distances are about  $0.07$  Å longer than other analogous  $\text{Cp}_2\text{M}$  complexes [53] which might be consistent with the 20 electron count, but the oxygen is very nucleophilic and reacts rapidly with a variety of electrophiles. For example, oxygen exchange with  $\text{H}_2\text{O}$  is very rapid. The mechanism is presumably one where water is deprotonated to form  $\text{Cp}_2\text{W}(\text{OH})^+$  which then forms a  $\text{Cp}_2\text{W}(\text{OH})_2$  intermediate. The orbitals of  $\text{Cp}_2\text{WO}$  are generated in Figure 20.17 from a  $\text{Cp}_2\text{W}$  fragment and, for convenience, only the  $p$  AOs of oxygen. The three important orbitals of the bent  $\text{Cp}_2\text{M}$  fragment (**20.32**) are illustrated on the middle left side of the Figure. The  $1a_1$  and  $2a_1$  fragment orbitals interact with the  $a_1 p$  AO of

**FIGURE 20.17**

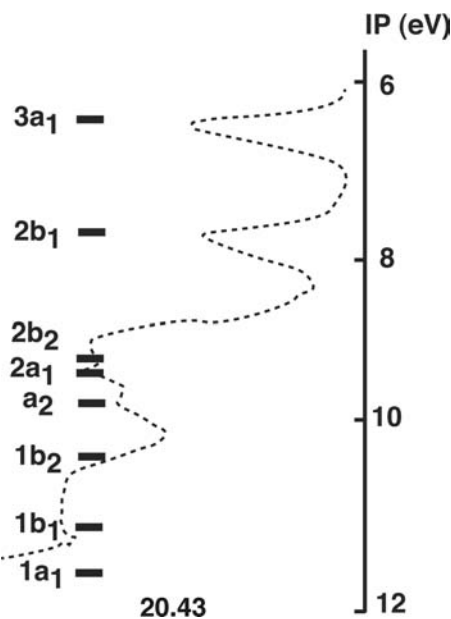
Construction of the MOs of  $\text{Cp}_2\text{WO}$ . Contour diagrams with the B3LYP hybrid functional of four MOs are shown on the right side of the figure.

oxygen to form a three orbital pattern just like that for  $\text{Cp}_2\text{Re-H}$  in 20.34. The fully bonding and nonbonding combinations,  $1a_1$  and  $3a_1$  respectively, are filled. The latter is computed to be the HOMO on the basis of B3LYP calculations [24] using a triple zeta plus polarization functions quality basis set. A contour diagram of the  $3a_1$  MO is shown on the upper right side of Figure 20.17. The  $\text{Cp}_2\text{W}$   $b_2$  fragment orbital has the correct symmetry and has a sizable  $\pi$ -type overlap with the  $b_2$  AO on oxygen. The bonding combination, labeled  $1b_2$ , is filled and a contour drawing of it is illustrated on the middle right side of the Figure. The antibonding combination is empty. This leaves us with the  $b_1$  O AO. Rather than being nonbonding, it does overlap with two fragment orbitals on  $\text{Cp}_2\text{W}$ . In the  $1e_{1g}$ ,  $2e_{1g}$ , and  $e_{1u}$  sets of  $\text{Cp}_2\text{M}$  (see Figure 20.13), there are two orbitals of  $b_1$  symmetry. The other four orbitals that do not interact much with the oxygen are left nonbonding. These are explicitly drawn on the left side of Figure 20.17. The placement of the oxygen  $p$  AOs relative to the  $1e_{1g}$  and  $e_{1u}$  sets is not certain. We have put them at approximately the same energy, but it has been shown that this does not matter much within a large range of energy values for O  $p$  [54].

The important point is that there is now another three orbital pattern setup in this molecule. Molecular  $1b_1$  is principally the  $1e_{1g}$  component with O  $p$  mixed into it in a bonding fashion and  $2e_{1g}$  mixed in second order with the phase shown in the Figure. A contour drawing of this MO on the right side highlights the fact that this is a good, delocalized W—O  $\pi$  bond. The middle  $b_1$  MO,  $2b_1$ , is constructed as shown by **20.42**. So  $1e_{1g}$  and  $2e_{1g}$  mix into O  $p$  in an antibonding and bonding fashion,



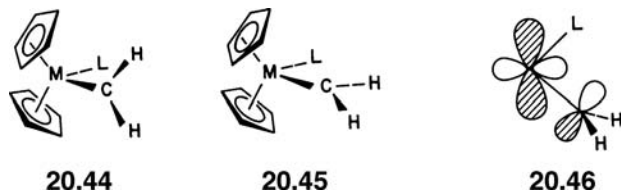
respectively. If the latter is more important, then there clearly are two W—O  $\pi$  bonds of  $b_2$  and  $b_1$  symmetry, along with the W—O  $\sigma$  bond. The W—O bond order is three. If, however, the former interaction is more important, then the W—O bond order will be less than three. What is shown in the contour diagram of  $2b_1$  in Figure 20.17 and the stylized construction of it in **20.42** is that the density on W decreases. The molecular orbital is concentrated on the Cp  $\pi$  and oxygen  $p$ AOs. It, therefore, should not be surprising that the oxo group is very nucleophilic. The fact that one component of  $2e_{1g}$  mixes into the  $2b_1$  MO should result in lengthening the W—C distances since this orbital is strongly W—C antibonding. Is this then a 20-electron complex? Perhaps, but the mixing of  $2e_{1g}$  keeps the energy of  $2b_1$  at moderate energy. The PE spectrum of  $(\text{CH}_3\text{C}_5\text{H}_4)_2\text{M-O}$ , M = Mo and W, has been measured [54]. There is some controversy about the assignments [53,54]. B3LYP calculations [24] with the triple zeta basis plus polarization functions on  $\text{Cp}_2\text{W-O}$  give the sequence shown in **20.43**. The dashed line is a tracing of the experimental PE spectrum. The agreement between experiment and theory is quite good. The  $2b_2$  is



predicted to have too large and  $1b_2$  too small of an ionization potential but the other four ionizations that can be measured with some accuracy are within 0.07 eV of their computed values. The calculations here are consistent with those

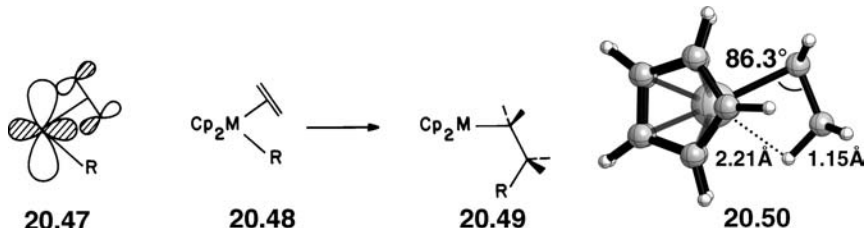
derived by Green et al. [54] with the exception of reversing the assignments for the  $2a_1$  and  $a_2$  MOs.

Consider a  $\text{Cp}_2\text{M}(\text{CH}_2)\text{L}$  complex. The carbene may be oriented as given by **20.44** or **20.45**. There are greater steric problems with **20.44**; the hydrogens on

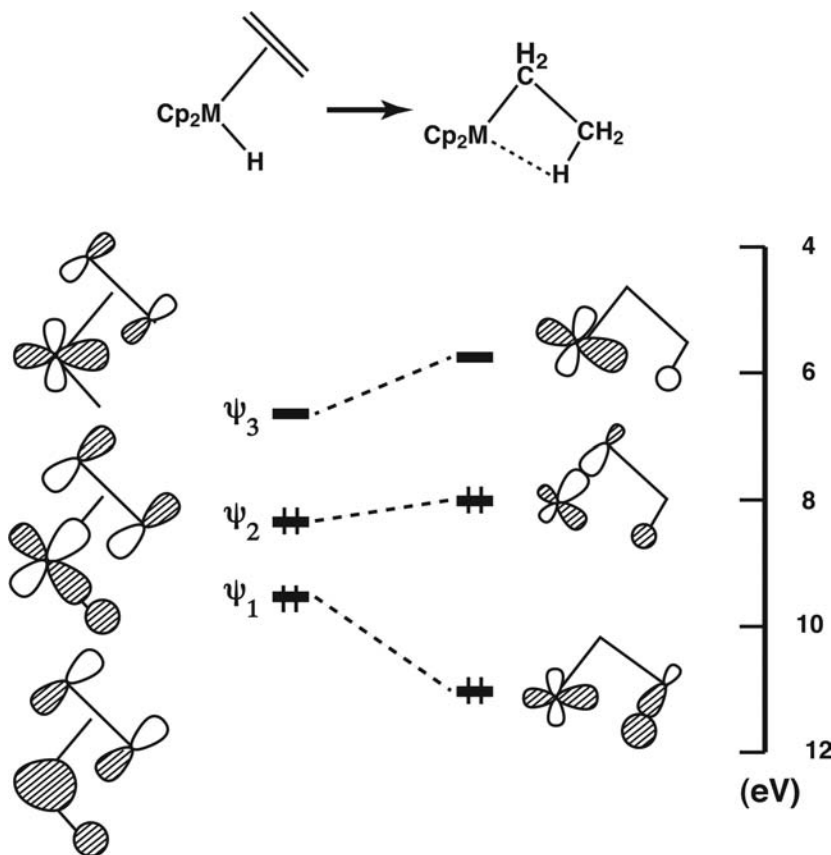


the carbenes are quite close to the  $\text{Cp}$  rings. Yet **20.44** is more stable than **20.45** and rotational barriers about the metal–carbene bond in the range of 15 to greater than 20 kcal/mol have been observed [55]. The electronic structure for the  $\sigma$  component in this molecule will correspond to that found for  $\text{Cp}_2\text{ML}_2$  in **20.35** but now one where  $1a_1$  is filled. In structure **20.44**, the carbene  $p$  orbital may also interact with  $1a_1$  as shown by **20.46** [56]. In **20.45** no such interaction exists with the valence orbitals. Consequently, a  $d^2$  complex where  $1a_1$  is filled (and the carbene  $p$  orbital is formally empty) will provide a maximum stabilizing interaction at the geometry given by **20.44**. For a  $d^0$  electron count, this orbital is not filled so conformation **20.45** is favored [57].

We saw in **15.31** and the discussion around it that the orbitals of  $\text{CH}_2$  were topologically like those in ethylene. Each has a donor orbital of  $a_1$  symmetry and a low-lying acceptor orbital. The electronic structure of an (alkyl)(olefin) $\text{MCp}_2$  complex is then similar to the  $\text{Cp}_2\text{M}$  (carbene) ones which we have just treated. **20.47** shows the  $1a_1-\pi^*$  interaction which is analogous to the  $\pi$  interaction in **20.46**.

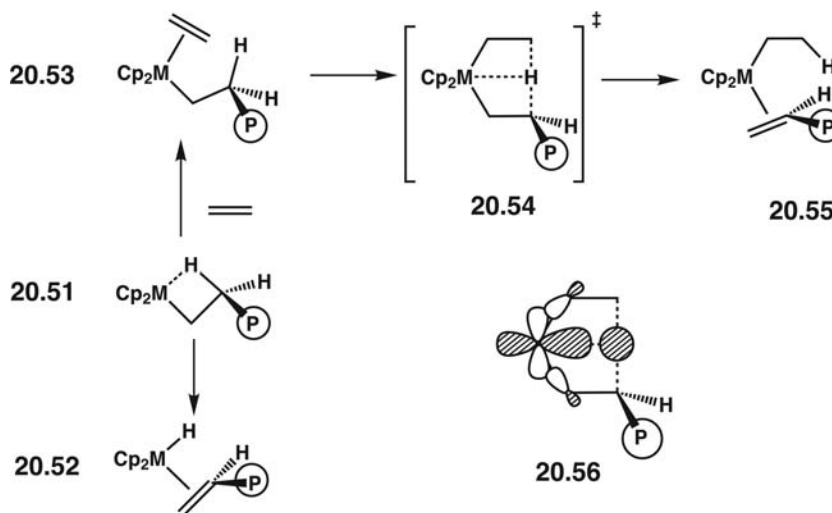


for the carbene case. These (alkyl)(olefin) $\text{MCp}_2$  species, **20.48**, are key intermediates for olefin polymerization using Ziegler–Natta catalysts. The alkyl group inserts into the metal olefin bond yielding **20.49** which picks up another olefin, and so on. There is one bit of complication here. The active Ziegler–Natta catalysts have a  $d^0$  electron configuration so **20.48** is a 16-electron complex and **20.49** is very electron deficient with only 14 electrons. Consequently, the metal forms an agostic bond with an alkyl hydrogen at the  $\beta$ ,  $\gamma$ , or  $\delta$  position. The resultant structure for  $\text{R} = \text{Et}$  and  $\text{M} = \text{Zr}^+$  is shown in **20.50**. Notice that the  $\text{C}-\text{H}$  distance is elongated compared to a normal value of 1.09 Å and the acute  $\text{Zr}-\text{C}-\text{C}$  angle of 86.3°. Theoretical work on this polymerization reaction is a mature field with techniques at nearly every theoretical level including the use of molecular dynamics simulations [58]. To summarize the salient electronic features, we shall look at the **20.48** to **20.49** transformation with  $\text{R} = \text{H}$  and a  $d^0$  transition metal for  $\text{M}$ . The olefin  $\pi$  and alkyl lone-pair orbitals present two donor functions to the metal. A pattern like that in **20.35** is again found except for the stabilization of  $1a_1$  by olefin  $\pi^*$  (**20.47**). These three MOs are depicted on the left side of Figure 20.18. On going from **20.48** to **20.49**, there is considerable intermixing between these orbitals along with their antibonding counterparts. The phases of  $\psi_1 - \psi_3$  have been adjusted so that  $\psi_2$  and

**FIGURE 20.18**

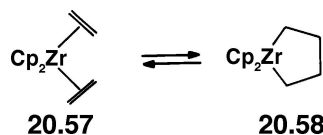
An orbital correlation diagram for the olefin insertion reaction. The orbital energies are experimental values taken from photoelectron spectra in Reference [59].

$\psi_3$  mix into  $\psi_1$  with the phases shown. The net result is the formation of a C—H  $\sigma$  bond that is stabilized somewhat by the agostic interaction shown in the figure.  $\psi_1$  and  $\psi_3$  mix into  $\psi_2$  with the opposite and same phase shown, respectively, to form the M—C  $\sigma$  orbital, which lies at a slightly higher energy. Finally,  $\psi_1$  and  $\psi_2$  mix into  $\psi_3$  with opposite phases from those shown, but the important feature is that as the reaction proceeds, the  $\text{Cp}_2\text{M}$   $1a_1$  fragment orbital loses the stabilizing overlap with olefin  $\pi^*$ . Therefore, this orbital is considerably destabilized. Consequently, an efficient catalyst will be one with  $1a_1$  empty—a  $d^0$ , 16-electron system. The orbital energies here do not come from molecular orbital calculations; they are experimentally determined values from photoelectron spectroscopy with  $\text{M} = \text{Nb}$  and  $\text{Ta}$  [59]. Notice the close relationship here to the olefin insertion reaction treated in Figure 18.9. In the latter example, the olefin  $\pi^*$  orbital acts merely to polarize the electron density in the C—H and M—C bonding regions. This also occurs in the present example; however,  $\pi^*$  sets an important role in stabilizing  $\text{Cp}_2\text{M}$   $1a_1$  on the  $\text{Cp}_2\text{M}(\text{olefin})(\text{hydride})$  side of the reaction. If this orbital is filled (as it is for a  $d^2$  complex), then the activation barrier for the **20.48** to **20.49** reaction is much higher in energy. Indeed the barrier for  $\text{M} = \text{Nb}$ ,  $\text{R} = \text{H}$  has been found to be 17.1 kcal/mol [60]. Calculations on the analogous reaction for  $\text{M} = \text{Zr}^+$ ,  $\text{R} = \text{H}$  did not find a minimum for **20.48**. Instead all attempts led to the formation of **20.50** with no activation barrier [24]. The polymerization cycle represented by the **20.48** to **20.49** reaction can undergo a termination reaction via a variety of steps. The two most common ones for the  $d^0$  system are  $\beta$ -elimination from **20.51** yielding **20.52** which is simply the reverse of the **20.48** to **20.49** reaction. The symbol P here represents

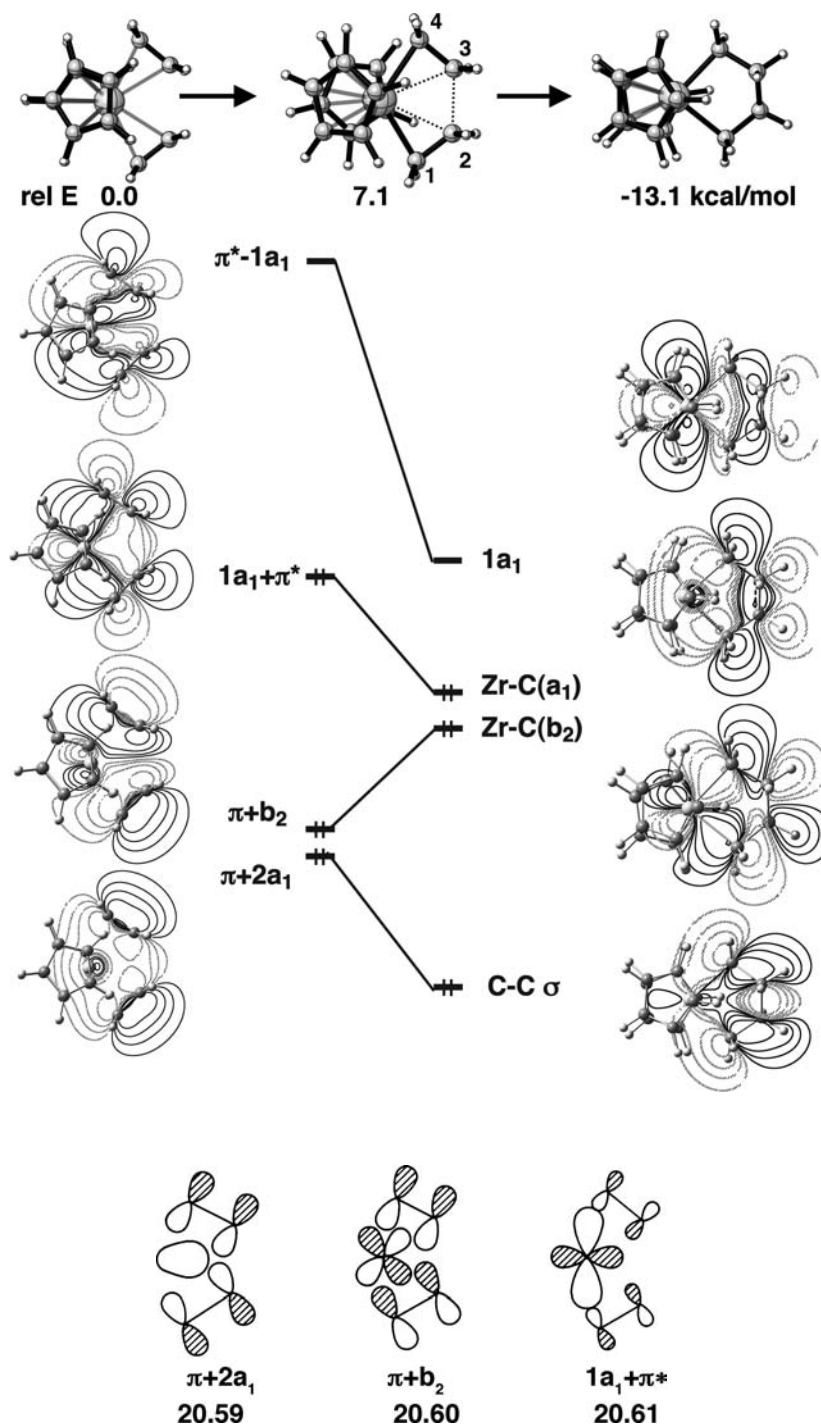


the long alkyl chain of the polymer. From **20.52**, the alkene can dissociate from the metal. An alternative is the  $\beta$ -hydride transfer. Here a  $\beta$  hydrogen from the polymer is transferred to the olefin monomer via a transition state resembling **20.54**. The resultant coordinated olefin in **20.55** can then undergo dissociation. Whether the  $\beta$ -elimination or the  $\beta$ -hydride transfer path is favored depends upon a number of factors [61]. Likewise, how much bonding there is between Zr and the bridging hydride is another concern. Dynamic simulations on  $\text{Cp}_2\text{Zr}(\text{ethyl})(\text{ethylene})^+$  reveal that the Zr—H distance varies from 1.95 to 2.05 Å at the transition state [62]. Notice that this is even shorter than the agostic bond in **20.50**. The  $d^0$   $\text{Cp}_2\text{M}$  unit is ideally set up to coordinate three ligands with its three important valence orbitals. Starting with two olefin  $\pi$  and  $\pi^*$  combinations along with the hydride s AO generates three filled donor combinations. The highest nicely overlaps with the  $1a_1$  fragment orbital on  $\text{Cp}_2\text{M}$  as shown in **20.56**. The lowest, fully symmetric combination matches the  $2a_1$   $\text{Cp}_2\text{M}$  orbital. Both exhibit significant bonding between the metal that the bridging hydride.

The oxidative coupling reaction, **20.57–20.58**, offers an interesting contrast to the  $(\text{olefin})_2\text{Fe}(\text{CO})_3$  rearrangement in Section 18.3. Both reactions involve



18-electron bis-olefin complexes rearranging to 16-electron metallacyclopentanes. The  $\text{Fe}(\text{CO})_3$  case was shown to be symmetry-forbidden. The orbitals of **20.58** are going to be very similar to those for  $\text{Cp}_2\text{ML}_2$  in **20.35**. Contour drawings of these MOs at the B3LYP level are displayed on the right side of Figure 20.19. This is a  $d^0$  complex, so  $1a_1$  is empty. The lowest MO is primarily localized between C(2) and C(3) and represents the C(2)-C(3)  $\sigma$  bond formed in the reaction. The orbitals of **20.57** are constructed as follows. In-phase and out-of-phase combinations of the ethylene  $\pi$  and  $\pi^*$  orbitals are of  $a_1$  and  $b_2$  symmetry. The  $a_1$  and  $b_2$  combinations of the ethylene  $\pi$  set are stabilized by the  $\text{Cp}_2\text{M}$   $2a_1$  and  $b_2$  fragment orbitals, respectively. The resultant molecular orbitals are shown in **20.59** and **20.60**. The  $1a_1$   $\text{Cp}_2\text{M}$  level is especially stabilized by the  $a_1$  combination of ethylene  $\pi^*$ ,

**FIGURE 20.19**

Orbital correlation diagram for the reaction of  $\text{Cp}_2\text{Zr}(\text{ethylene})_2$  to a zirconacyclopentane complex. The contour drawings and the molecular structure for the reactant, transition state, and product are derived from calculations at the B3LYP level.

as shown in **20.61**. Contour plots of these three MOs along with the antibonding counterpart of **20.61**,  $\pi^* - 1a_1$ , are shown on the left side of Figure 20.19. As the two olefins are coupled, a new C—C  $\sigma$  bond is formed. In other words, **20.59**, which is concentrated on the two olefins, is stabilized and will form the C—C  $\sigma$  bond in the zirconacyclopentane. A partial correlation for a least-motion pathway that conserves  $C_{2v}$  symmetry is shown in Figure 20.19. **20.60** smoothly correlates to the Zr—C  $\sigma$  orbital of  $b_2$  symmetry.  $1a_1 + \pi^*$  and  $\pi^* - 1a_1$  mix with each other to form the Zr—C  $\sigma$  orbital of  $a_1$  symmetry and the nonbonding  $1a_1$  MO which is the LUMO in the

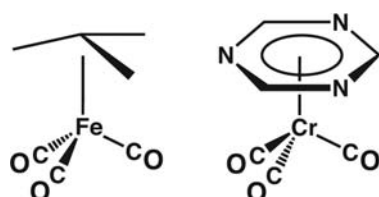
zirconacyclopentane. Therefore, the reaction is symmetry allowed. In actual fact, the zirconacyclopentane has a puckered, envelope conformation and this puckering is present in the computed [24] transition state for the reaction. The structure is shown at the top center of Figure 20.19. The C<sub>2</sub>–C<sub>3</sub> distance in the reactant decreases from 2.68 Å to 2.09 and 1.55 Å in the transition state and the product, respectively. The Zr–C<sub>2</sub> distance increases from 2.56 Å to 2.59 and 3.04 Å in the transition state and the product, respectively. Therefore, the transition state occurs early on the reaction path which maintains C<sub>s</sub> symmetry. Accordingly, the activation barrier is quite small, 7.1 kcal/mol and the reaction is exothermic by 13.1 kcal/mol. This reaction has been used synthetically [63], but the metallacycle is prone to undergo  $\alpha$  or  $\beta$  elimination reactions. A far more common synthetic sequence involves the coupling of Cp<sub>2</sub>Zr(acetylene)<sub>2</sub> [64] to form a zirconacyclopentadiene. Here the C<sub>2v</sub> path will be followed and the reader can easily verify that this will also be a symmetry-allowed reaction. For the same electron count in the reactant and product, we saw in Section 18.3 that a C<sub>2v</sub> Fe(CO)<sub>3</sub> complex gave a symmetry-forbidden reaction. The electronic details of a reaction are strongly influenced by the number and geometrical disposition of the auxiliary ligands. It is naïve to view the transition metal simply as an electronic black-box that supplies and accepts electrons from the organic portion of the molecule. Unfortunately, this attitude has been taken too many times in the past. One must not forget that the remaining ligands, be they multidentate like Cp or that of a  $\sigma$ -donor type like CO or phosphines, tailor the metal orbitals to specific shapes and energy patterns. Even with this provision, there are a tremendous number of analogies that can be used to simplify reactivity problems. A very important one that links organic, organometallic, inorganic, and main group chemistry is the subject of Chapter 21.

## PROBLEMS

- 20.1.** a. Develop the important valence orbitals of ( $\eta^6$ -benzene)M by interacting the  $\pi$  orbitals of benzene with the valence orbitals of M.  
 b. Interact the orbitals in (a) with the  $\sigma$ -donor orbitals of three carbonyls to get the orbitals of ( $\eta^6$ -benzene)Cr(CO)<sub>3</sub>.

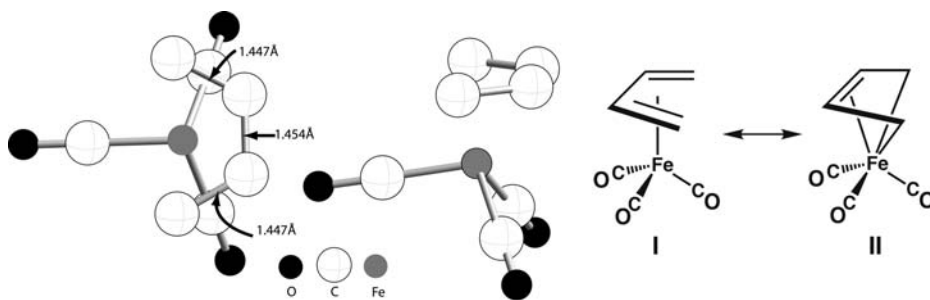


- 20.2.** a. The barrier to rotate around the Fe–C axis in trimethylenemethane–Fe(CO)<sub>3</sub> derivatives has been determined by NMR to be 18–24 kcal/mol. It is computed to be 22.4 kcal/mol at the B3LYP level. Determine the electronic origin of this barrier by interacting the  $\pi$  orbitals of trimethylenemethane (see 12.19) with Fe(CO)<sub>3</sub> at the staggered (shown below) and eclipsed geometries.



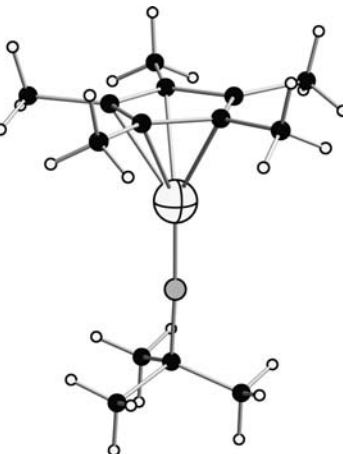
- b. The rotational barrier about the benzene-Cr axis in  $(\eta^6\text{-benzene})\text{Cr}(\text{CO})_3$  is tiny. It is estimated to be about 0.2 kcal/mol. On the other hand, the barrier in  $(\eta^6\text{-1,3,5-triazine})\text{Cr}(\text{CO})_3$ , above, was calculated to be 9.7 kcal/mol. Explain.

**20.3.** One of the first organometallic compounds to be prepared in a rational (or semi-rational) way was butadiene– $\text{Fe}(\text{CO})_3$  in 1958. Its x-ray structure was determined not long after that and is shown below from a top and side view. What is surprising about the structure, and is true for all of the other substituted butadiene– $\text{Fe}(\text{CO})_3$  complexes, as well as, isoelectronic analogs, is that instead of the butadiene ligand having short-long-short C–C bond lengths (as butadiene itself has), all three C–C bonds are about the same length. This structural feature has made some people think that besides structure I, another resonance structure like that in II can be drawn for butadiene– $\text{Fe}(\text{CO})_3$ .



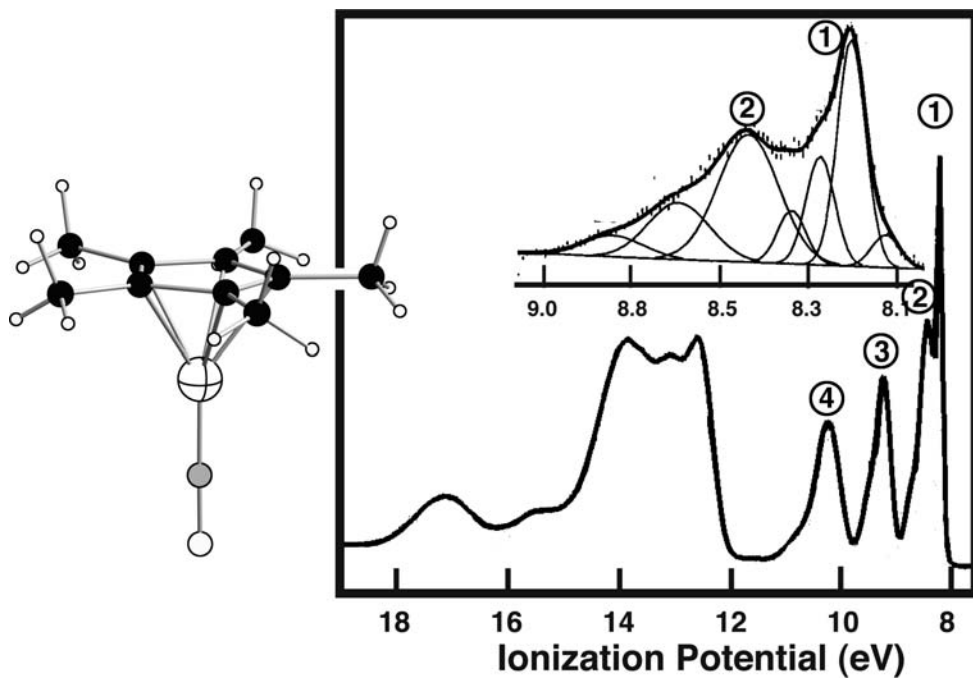
- a. Draw an orbital interaction diagram for interacting the  $\pi$  orbitals of butadiene with the important valence orbitals of  $\text{Fe}(\text{CO})_3$ . Put in the correct number of electrons.  
 b. Give an explanation based on your interaction diagram why the C–C bonds are all nearly the same length.

**20.4.** Bergmann et al. have prepared several  $\text{CpIr}(\text{imido})$  complexes. An example is  $(\text{Me}_5\text{C}_5)\text{Ir}(\text{N-}t\text{-Bu})$  reported in Reference [65]. Using  $\text{CpIr}$  and  $\text{NH}$  fragments develop the molecular orbitals for  $\text{CpIr}\equiv\text{NH}$ .

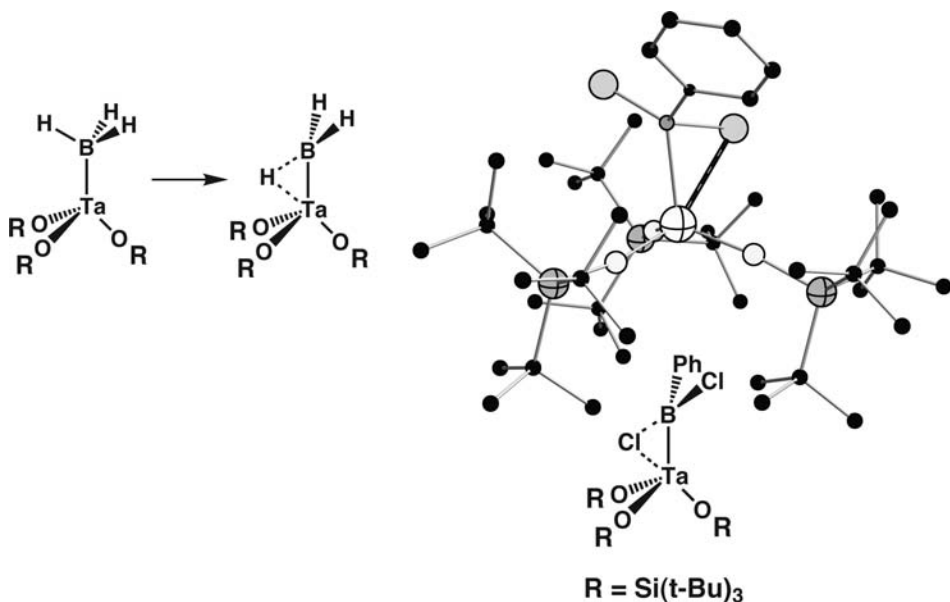


**20.5.** The assignment of the photoelectron spectrum of  $\text{CpNiNO}$  has engendered some controversy. The structure,  $(\text{Me}_5\text{C}_5)\text{NiNO}$  reported in Reference [66], is  $\text{C}_{5v}$ . The photoelectron spectrum taken from the data reported in Reference [67] is shown below. The inset of the low-energy region shows a band deconvolution of the first two peaks by the authors, and it suggests the presence of vibrational progressions from

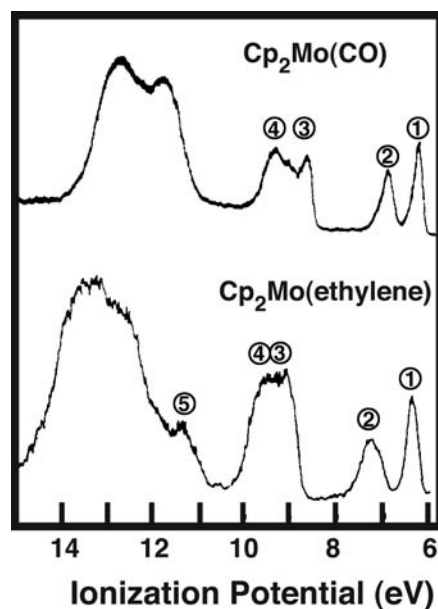
each band. Bancroft et al. suggest that the first four peaks correspond to ionizations from four molecular orbitals (three are degenerate  $e$  sets and one is  $a_1$  in terms of symmetry). An alternative assignment in Reference [68] puts the first two peaks as corresponding to one orbital set, peak 3 to two sets of orbitals. Draw an interaction diagram for  $\text{CpNiNO}$  using  $\text{CpNi}^-$  and  $\text{NO}^+$  fragments. Show how either assignment could account for the PE spectra.



- 20.6.** There is very good chemical evidence that  $(\text{RO})_3\text{Ta}(\text{BH}_3)$  does not have an ethane-like structure. Instead the  $\text{BH}_3$  group leans over so that there is a three-center two electron  $\text{Ta}-\text{H}-\text{B}$  bond established. An x-ray structure of a related  $\text{BCl}_2\text{Ph}$  complex along with computations has been reported in Reference [69]. Determine the important valence orbitals of  $(\text{HO})_3\text{Ta-BH}_3$  at a  $C_{3v}$  geometry and draw an Walsh diagram for the distortion to  $C_s$  symmetry as shown below.



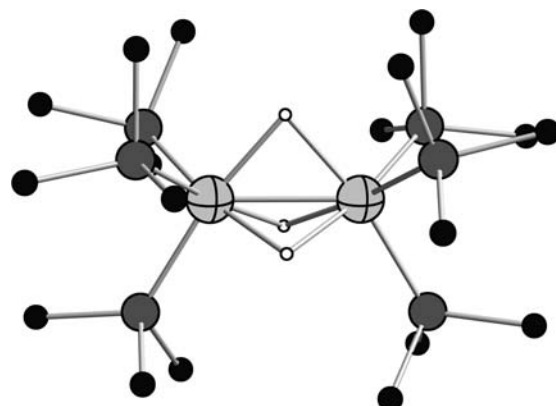
**20.7.** The photoelectron spectra of  $\text{Cp}_2\text{Mo}(\text{CO})$  and  $\text{Cp}_2\text{Mo}(\text{ethylene})$  from Reference [46] are shown below. Assign orbitals to the ionizations indicated below in the PE spectra. It should be noted that the  $3\sigma$  orbital of CO has an ionization potential of 14.01 eV and that for the  $\pi$  orbital in ethylene is 10.51 eV.



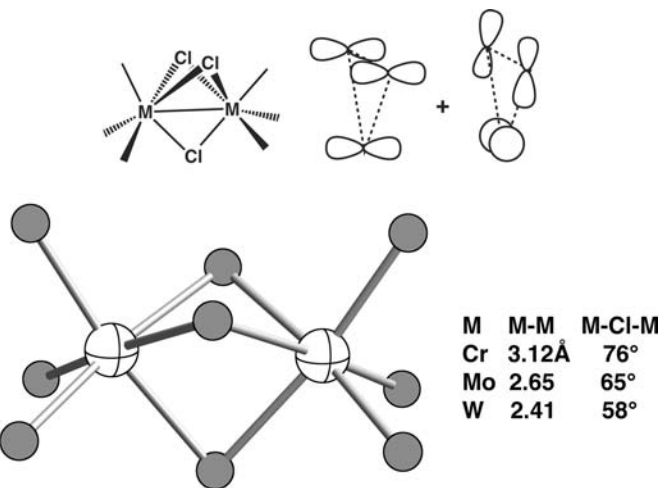
**20.8. a.** The structure of  $(\text{Me}_3\text{P})_6\text{Ru}_2\text{H}_3^+$  in Reference [70] is shown below. Form the orbitals of  $\text{Ru}_2\text{L}_6^{4+}$  with a fairly short Ru—Ru distance (it is  $2.540\text{\AA}$  in the Ru dimer). Then combine those fragment orbitals with the bridging  $\text{H}_3^{3-}$  unit.

b. On the basis of electron counting, what is the Ru—Ru bond order? How well does this correspond to the MO picture in a)?

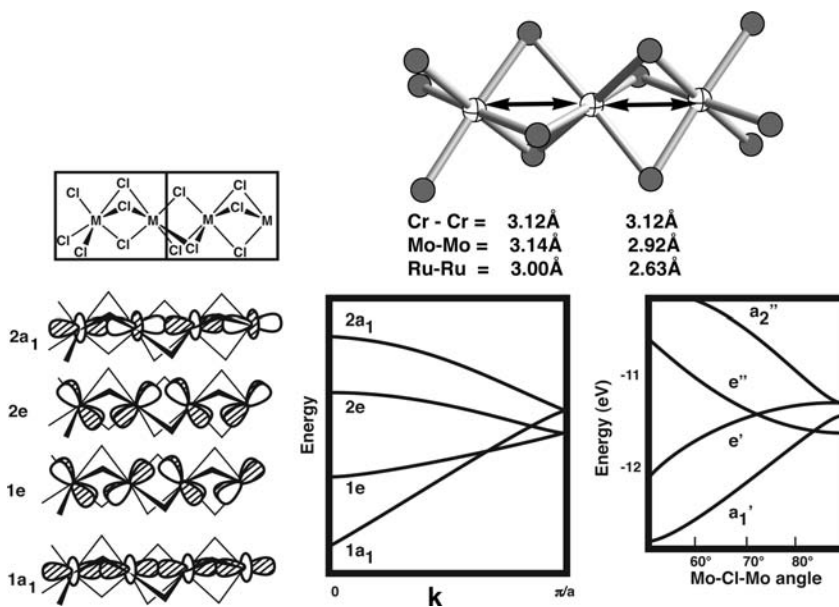
c. There is a compound with an essentially identical structure,  $(\text{triphos})_2\text{Rh}_2\text{H}_3^{2+}$ , where the Rh—Rh distance was found to be  $2.644\text{\AA}$ . Is this consistent with the MO picture? Should one expect further geometric deformations?



**20.9. a.** In this problem, we are going to discuss the related example of  $\text{M}_2\text{Cl}_9^{3-}$  dimers where  $\text{M} = \text{Cr}$ ,  $\text{Mo}$ , and  $\text{W}$ . Use just the  $1a_1 + 1e$  set to build the  $\text{M}_2\text{Cl}_6$  fragment. For the  $\text{Cl}_3^{3-}$  bridging fragment, just use the tangential  $p$  AO's parallel to the M—M bond as shown below. The other s and  $p$  Cl AO's form three combinations just like those in the previous problem and there are three lone-pairs pointed away from the M—M bond vector.



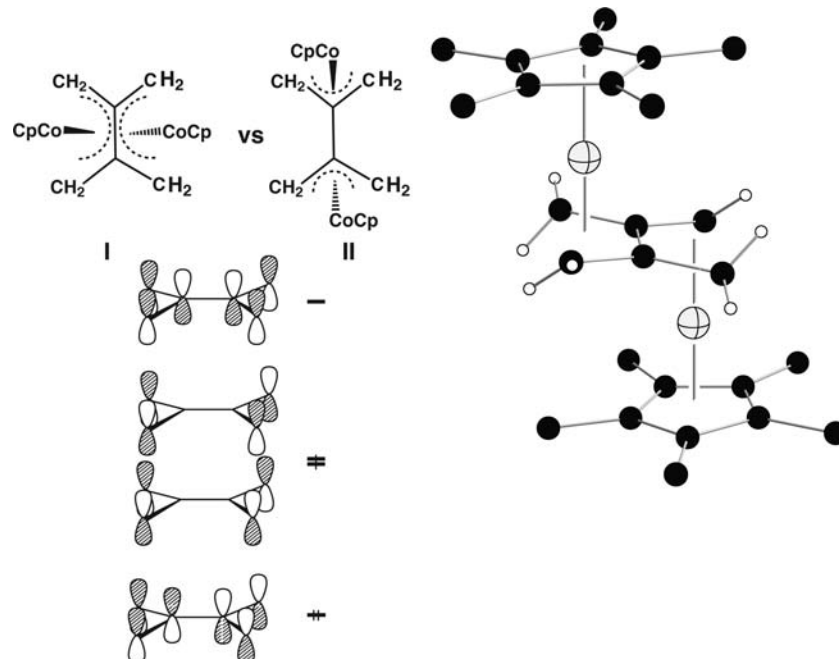
- b. Offer a rationale why the M—M bond lengths vary in the unusual way that they do. For reference, a Cl—M—Cl bond angle in an ideal octahedron is 70.5°.
- c. In the solid-state domain, there are a number of face-sharing octahedra that form a one-dimensional chain. They have the stoichiometry of  $\text{MX}_3$ . We briefly discussed the  $\text{TlI}_3$  example in Chapter 15 (see 15.58). Here our initial interest is in the  $d^3$  dimers.  $\text{CrCl}_3$  actually forms edge-shared octahedra with a layered structure. There is, however, the compound with one more electron,  $\text{CsCrCl}_3$ , which has a non-alternate Cr—Cr bond distance of 3.12 Å. Compounds isoelectronic to  $\text{CrCl}_3$  with the one-dimensional structure are  $\text{CsVCl}_3$  and  $\text{RbVCl}_3$ . Both have nonalternating V—V distances of 3.00 Å. The band structure of the “ $t_{2g}$ ” region is shown below. The unit cell is double the formula unit so there are six bands (two are degenerate  $e$  sets). Explain why the M—M distances do not alternate for  $\text{CrCl}_3$  and  $\text{CsVCl}_3$  using the band structure, but the Mo—Mo distances alternate. Also show what occurs for  $\text{RuCl}_3$  where again the Ru—Ru distances alternate for  $\text{MoCl}_3$ . In addition, the Ru—Cl distances also vary so that one set of fac distances are 2.32 Å while the adjacent fac set are 2.37 Å.



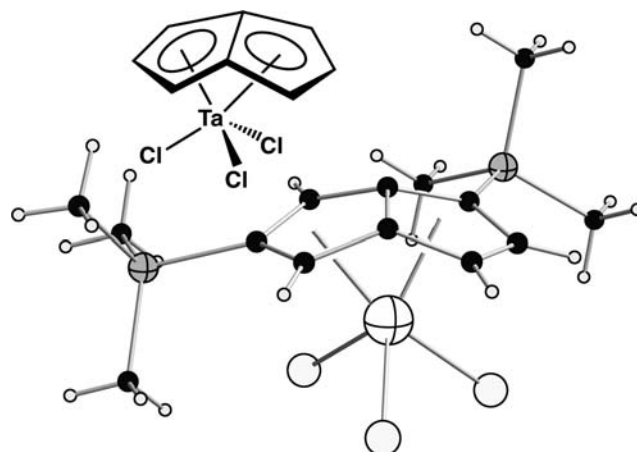
- d. The  $z^2$  bands vary in the expected manner: the bonding combination of the two  $z^2$  orbitals within the unit cell constitute the lower,  $1a_1$ , band while the antibonding

combination is in the upper band,  $2a_1$ . This is not the case for the  $e$  sets. One member of each  $e$  set is shown above. The M—M antibonding combination within the unit cell is now the lower band and the bonding combination is found in the upper band. Why is this the case? A hint is given in the Walsh diagram shown above for varying the Mo—Cl—Mo angle in  $Mo_2Cl_9^{3-}$ .

- 20.10.** The tetramethylene molecule (**12.22**) was briefly discussed in Chapter 12. A  $Cp_2Co_2$  transition metal complex of this very reactive ligand has been prepared. There are two possible geometries shown by **I** and **II**. The x-ray structure of this molecule in Reference [71] shows that geometry **I** is favored. Why is this? To simplify this problem, just use the  $e_1$  set on  $CpCo$  and the four tetramethylene MOs shown below. Use symmetry!



- 20.11.** Pentalene is another very reactive molecule that has been used as a ligand. An example is  $\eta^5, \eta^5$ -pentalene-TaCl<sub>3</sub> where both five-membered rings are coordinated to Ta. An example is given below in Reference [72]. Counting the ligand as pentalene<sup>2-</sup> gives a 16-electron complex. Take the occupied MOs of pentalene dianion; these are easily constructed by joining the C<sub>1</sub>—C<sub>5</sub> carbons in cyclo-octatetraene dianion in a way like that done in Figure 12.15. Interact these with TaCl<sub>3</sub><sup>2+</sup>.



---

**REFERENCES**

1. L. E. Orgel, *An Introduction to Transition-Metal Chemistry*, Wiley, New York (1960), p. 174.
2. M. Elian and R. Hoffmann, *Inorg. Chem.*, **14**, 1058 (1975); J. K. Burdett, *Inorg. Chem.*, **14**, 375 (1975); J. K. Burdett, *J. Chem. Soc., Faraday Trans. II*, **70**, 1599 (1974).
3. Y.-C. Tsai, C.-W. Hsu, J.-S. K. Yu, G.-H. Lee, Y. Wang, and T.-S. Kuo, *Angew. Chem. Int. Ed.*, **47**, 7250 (2008).
4. A. Dedieu, T. A. Albright, and R. Hoffmann, *J. Am. Chem. Soc.*, **101**, 3141 (1997).
5. S. Alvarez, *Coord. Chem. Rev.*, **193–195**, 13 (1999).
6. A. S. Kurlov and A. I. Gusev, *Phys. Rev. B*, **76**, 174115 (2007) and references therein; H. W. Hugosson, O. Eriksson, U. Jansson, and B. Johansson, *Phys. Rev. B*, **63**, 134108 (2001) for the closely related Mo<sub>2</sub>C.
7. (a) D. L. Lichtenberger and R. Fenske, *J. Am. Chem. Soc.*, **98**, 50 (1976); D. C. Calabro and D. L. Lichtenberger, *J. Am. Chem. Soc.*, **103**, 6846 (1981); D. C. Calabro, J. L. Hubbard, C. H. Blevins, III, A. C. Campbell, and D. L. Lichtenberger, *J. Am. Chem. Soc.*, **103**, 6839 (1981). (b) C. N. Field, J. C. Green, A. G. J. Moody, and M. R. F. Siggel, *Chem. Phys.*, **206**, 211 (1996). (c) C. I. Pongor, Z. Gengeliczki, L. Szepes, F. Axe, and B. Sztaray, *Organometallics*, **29**, 724 (2010).
8. M. Elian, M. M. L. Chen, D. M. P. Mingos, and R. Hoffmann, *Inorg. Chem.*, **15**, 1148 (1976).
9. J. F. Hartwig, *Organotransition Metal Chemistry: From Bonding to Catalysis*, University Science Books, Sausalito, CA (2009); R. Pettit, *J. Organomet. Chem.*, **100**, 205 (1975).
10. B. E. Bursten and R. F. Fenske, *Inorg. Chem.*, **18**, 1760 (1979).
11. T. A. Albright, P. Hofmann, and R. Hoffmann, *J. Am. Chem. Soc.*, **99**, 7546 (1977); T. A. Albright, *Acc. Chem. Res.*, **15**, 149 (1982).
12. J. W. Lauher, M. Elian, R. H. Summerville, and R. Hoffmann, *J. Am. Chem. Soc.*, **98**, 3219 (1976).
13. A. Salzer and H. Werner, *Angew. Chem.*, **84**, 949 (1972); W. Siebert, *Adv. Organomet. Chem.*, **18**, 301 (1980) for several other systems of the 30- and 34-electron type.
14. E. Dubler, M. Textor, H.-R. Oswald, and A. Salzer, *Angew. Chem.*, **86**, 125 (1974).
15. J. L. Priego, L. H. Doerrer, L. H. Rees, and M. L. H. Green, *Chem. Commun.*, 779 (2000).
16. C. Bianchini, M. Di Vaira, A. Meli, and L. Saconni, *J. Am. Chem. Soc.*, **103**, 1448 (1983).
17. W. Siebert, *Angew. Chem. Int. Ed.*, **24**, 943 (1985).
18. A. C. Reddy, E. D. Jemmis, O. J. Scherer, R. Winter, G. Heckmann, and G. Wömershäuser, *Organometallics*, **11**, 3894 (1992).
19. L. Yong, S. D. Hoffmann, T. F. Fässler, S. Riedel, and M. Kaupp, *Angew. Chem. Int. Ed.*, **44**, 2092 (2005).
20. A. D. Duff, K. Jonas, R. Goddard, H.-J. Kraus, and C. Krüger, *J. Am. Chem. Soc.*, **105**, 5479 (1983).
21. P. T. Chesky and M. B. Hall, *J. Am. Chem. Soc.*, **106**, 5186 (1984).
22. V. Beck, A. R. Cowley, and D. O'Hare, *Organometallics*, **23**, 4265 (2004).
23. B. Das and M. D. Raychaudhury, *J. Chem. Phys.*, **134**, 014709 (2011); H. Liu, Q. Li, Y. Xie, R. B. King, and H. F. Schaefer, III, *J. Phys. Chem. A*, **114**, 8156 (2010).
24. T. A. Albright, *unpublished calculations*.
25. (a) E. D. Jemmis and A. C. Reddy, *J. Am. Chem. Soc.*, **112**, 722 (1999). (b) W. Siebert, W. Herter, H. Schulz, S. Huck, H. Pritzkow, L. Zhu, and O. Eisenstein, *Chem. Ber.*, **126**, 1587 (1993).
26. T. Kuhlmann, S. Roth, J. Roziere, and W. Siebert, *Angew. Chem. Int. Ed.*, **25**, 105 (1986).
27. M. C. Böhm, *Z. Naturforsch.*, **39a**, 223 (1984); J. K. Burdett and E. Canadell, *Organometallics*, **4**, 805 (1985) where CpM as well as all of the examples in References [28] and [29] along with many more have been investigated.
28. Y. Li, G. Zhou, J. Li, J. Wu, B.-L. Gu, and W. Duan, *J. Phys. Chem. C*, **115**, 7292 (2011); H. Da, H. M. Jei, K. H. Lim, and S.-H. Yang, *J. Phys. Chem. C*, **114**, 21705 (2010); L. Wang, X. Gao, X. Yan, J. Zhou, Z. Gao, S. Nagase, S. Sanvito, Y. Maeda, T. Akasaka, W. N. Mei, and J. Lu, *J.*

- Phys. Chem. C*, **114**, 21893 (2010); L. Wang, Z. Cai, J. Wu, J. Lu, G. Luo, L. Lai, J. Zhou, R. Qin, Z. Gao, D. Yu, G. Li, W. N. Mei, and S. Sanvito, *Nano Lett.*, **8**, 3640 (2008).
29. L. Zhu and J. Wang, *J. Phys. Chem. C*, **113**, 8767 (2009); L. Wang, X. Gao, X. Yan, J. Zhou, Z. Gao, S. Nagase, S. Sanvito, Y. Maeda, T. Akasaka, W. N. Mei, and J. Lu, *J. Phys. Chem. C*, **114**, 21893 (2010); X. Wu and X. C. Zeng, *J. Am. Chem. Soc.*, **131**, 14246 (2009); Z. Zhang, X. Wu, W. Guo, and X. C. Zeng, *J. Phys. Chem. C*, **132**, 10215 (2010); A. Pramanik and H. S. Kang, *J. Phys. Chem. A*, **115**, 219 (2011); Y. Li, G. Zhou, J. Wu, and W. Duan, *J. Chem. Phys.*, **135**, 014702 (2011).
  30. J. Goodey, J. Mao, and A. M. Guloy, *J. Am. Chem. Soc.*, **122**, 10478 (2000); A. M. Guloy, *private communications*.
  31. N. Kishimoto and K. Ohno, *J. Phys. Chem. A*, **113**, 521 (2009).
  32. D. L. Lichtenberger, Y. Elkadi, N. E. Gruhn, R. P. Hughes, O. J. Curnow, and X. Zheng, *Organometallics*, **16**, 5209 (1997).
  33. D. L. Lichtenberger and A. S. Copenhaver, *J. Chem. Phys.*, **91**, 663 (1989).
  34. M. F. Ryan, D. E. Richardson, D. L. Lichtenberger, and N. E. Gruhn, *Organometallics*, **13**, 1190 (1994).
  35. V. M. Rayon and G. Frenking, *Organometallics*, **22**, 3304 (2003).
  36. E. Urnezius, W. W. Brennessel, C. J. Cramer, J. E. Ellis, and P. V. R. Schleyer, *Science*, **295**, 832 (2002).
  37. (a) Z.-F. Xu, Y. Xie, W.-L. Feng, and H. F. Schaefer, *J. Phys. Chem. A*, **107**, 2716 (2003). (b) M. Swart, *Inorg. Chim. Acta*, **360**, 179 (2007).
  38. R. Poli and I. Cacelli, *Eur. J. Inorg. Chem.*, 2324 (2005).
  39. A. Haaland, *Acc. Chem. Res.*, **12**, 415 (1975).
  40. J. C. Green, *Struct. Bonding*, **43**, 37 (1981).
  41. (a) J. L. Petersen, D. L. Lichtenberger, R. F. Fenske, and M. B. Hall, *J. Am. Chem. Soc.*, **97**, 6433 (1975); J. L. Petersen and L. F. Dahl, *J. Am. Chem. Soc.*, **96**, 2248 (1974); J. L. Petersen and L. F. Dahl, *J. Am. Chem. Soc.*, **97**, 6416 (1975); (b) H. H. Brintzinger, L. L. Lohr, Jr., and K. T. Wong, *J. Am. Chem. Soc.*, **97**, 5146 (1975); H. H. Brintzinger, *J. Organomet. Chem.*, **171**, 337 (1979). (c) N. W. Alcock, *J. Chem. Soc. A*, **2001** (1967). (d) For photoelectron spectroscopy studies on  $\text{Cp}_2\text{ML}_n$  complexes, see C. Cauletti, J. P. Clark, J. C. Green, S. E. Jackson, I. L. Fragala, E. Gilberto, and A. W. Coleman, *J. Electron Spectrosc.*, **18**, 61 (1980); H. van Dam, A. Terpstra, A. Oskam, and J. H. Teuben, *Z. Naturforsch.*, **36b**, 420 (1981). (e) J. C. Green, *Chem. Soc. Rev.*, **27**, 263 (1998).
  42. J. W. Lauher and R. Hoffmann, *J. Am. Chem. Soc.*, **98**, 1729 (1976).
  43. R. D. Wilson, T. F. Koetzle, D. W. Hart, A. Kvick, D. L. Tipton, and R. Bau, *J. Am. Chem. Soc.*, **99**, 1775 (1977); S. B. Jones and J. L. Petersen, *Inorg. Chem.*, **20**, 2889 (1981) for a more exotic example.
  44. T. Repo, M. Klinga, L. Mutikainen, Y. Su, M. Leskela, M. Polamo, *Acta Chem. Scand.*, **50**, 1116 (1996).
  45. C. Apostolidis, B. Kanellakopulos, R. Maier, J. Rebizant, and M. L. Ziegler, *J. Organomet. Chem.*, **409**, 243 (1991).
  46. J. C. Green, S. E. Jackson, and B. Higginson, *J. Chem. Soc., Dalton Trans.*, 403 (1975).
  47. D. L. Lichtenberger, G. P. Darsey, G. E. Kellogg, R. D. Sanner, V. G. Young, Jr. and J. R. Clark, *J. Am. Chem. Soc.*, **111**, 5019 (1989).
  48. R. F. G. Baynham, J. Chetwynd-Talbot, P. Grebenik, R. N. Perutz, and M. H. A. Powell, *J. Organomet. Chem.*, **284**, 229 (1985).
  49. M. A. Freitag and M. S. Gordon, *J. Phys. Chem. A*, **106**, 7921 (2002); M. Polasek and J. Kubista, *J. Organomet. Chem.*, **692**, 4083 (2007).
  50. V. P. Marin, L. I. Vyshinskaya, and G. A. Razuvaev, *Russ. Chem. Rev.*, **58**, 494 (1989) and references therein.
  51. (a) R. M. Bullock, C. E. L. Headford, K. M. Hennessy, S. E. Kegley, and J. R. Norton, *J. Am. Chem. Soc.*, **111**, 3897 (1989). (b) G. Parkin and J. E. Bercaw, *Organometallics*, **8**, 1172 (1989). (c) L. Labella, A. Chernega, and M. L. H. Green, *J. Chem. Soc., Dalton Trans.*, 395 (1995).

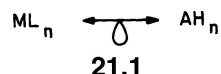
52. J. C. Green and C. N. Jardine, *J. Chem. Soc., Dalton Trans.*, 1057 (1998); M.-D. Su, and S.-Y. Chu, *J. Phys. Chem. A*, **105**, 3591 (2001); J. C. Green, J. N. Harvey, and R. Poli, *J. Chem. Soc., Dalton Trans.*, 1861 (2002); J. C. Green, *Polyhedron*, **24**, 1382 (2005); J.-L. Carreon-Macedo, J. N. Harvey, and R. Poli, *Eur. J. Inorg. Chem.*, 2999 (2005).
53. L. Luo, G. Lanza, I. L. Fragala, C. L. Stern, and T. J. Marks, *J. Am. Chem. Soc.*, **120**, 3111 (1998).
54. A. J. Bridgeman, L. Davis, S. J. Dixon, J. C. Green, and I. N. Wright, *J. Chem. Soc., Dalton Trans.*, 1023 (1995).
55. R. R. Schrock, *Science*, **219**, 13 (1983) and references therein.
56. The electronic structure of related metal–carbene complexes have also been studied by M. M. Franci, W. J. Pietro, R. F. Hout, Jr., and W. J. Hehre, *Organometallics*, **2**, 281 (1983); M. M. Franci and W. J. Hehre, *Organometallics*, **2**, 457 (1983).
57. M. Niehues, G. Erker, G. Kehr, P. Schwab, R. Fröhlich, O. Blacque, and H. Berke *Organometallics*, **21**, 2905 (2002) and references therein.
58. (a) For reviews see: L. Cavallo in *Computational Modeling of Homogeneous Catalysis*, F. Maseras and A. Lledos, editors, Kluwer Academic Press, New York (2002) p. 23–56. (b) A. Dedieu in *Organometallic Bonding and Reactivity*, J. M. Brown and P. Hofmann, editors, Springer, Berlin (1999) p. 69–108. (c) S. Niu and M. B. Hall, *Chem. Rev.*, **100**, 353 (2000).
59. D. L. Lichtenberger, G. P. Darsey, G. E. Kellogg, R. D. Sanner, V. G. Young, Jr. and J. R. Clark, *J. Am. Chem. Soc.*, **111**, 5019 (1989).
60. L. J. Ackerman, M. L. H. Green, J. C. Green, and J. E. Bercaw, *Organometallics*, **22**, 188 (2003).
61. G. Talarico and P. H. M. Budzelaar, *Organometallics*, **27**, 4098 (2008).
62. C. N. Rowley and T. K. Woo, *Organometallics*, **27**, 6405 (2008).
63. K. Fujita, H. Yorimitsu, H. Shinokubo, and K. Oshima, *J. Am. Chem. Soc.*, **126**, 6776 (2004).
64. A. D. Miller, J. L. McBee, and T. D. Tilley, *J. Am. Chem. Soc.*, **130**, 4992 (2008); Y. Liu, M. Liu, and Z. Song, *J. Am. Chem. Soc.*, **127**, 3662 (2005); For an early review see, S. Buchwald and R. B. Nielson, *Chem. Rev.*, **88**, 1047 (1988).
65. D. S. Glueck, F. J. Hollander, and R. G. Bergman, *J. Am. Chem. Soc.*, **111**, 2719 (1989).
66. D. V. Fomitchev, T. R. Furlani, and P. Coppens, *Inorg. Chem.*, **37**, 1519 (1998).
67. X. Li, J. S. Tse, G. M. Bancroft, R. J. Puddephatt, and K. H. Tan, *Inorg. Chem.*, **35**, 2515 (1996).
68. J. C. Green and P. Declava, *Coord. Chem. Rev.*, **249**, 209 (2005), and references therein.
69. J. B. Bonanno, T. P. Henry, P. T. Wolczanski, A. W. Pierpont, T. R. Cundari, *Inorg. Chem.*, **46**, 1222 (2007).
70. R. A. Jones, G. Wilkinson, I. J. Colquhoun, W. McFarlane, A. M. R. Galas, M. B. Hursthouse, *J. Chem. Soc., Dalton Trans.*, 2480 (1980)
71. P. Aguirre-Etcheverry, A. E. Ashley, G. S. Balazs, J. C. Green, A. R. Cowley, A. L. Thompson, and D. O'Hare, *Organometallics*, **29**, 5847 (2010).
72. Q. A. Abbasali, F. G. N. Cloke, P. B. Hitchcock, and S. C. P. Joseph, *Chem. Commun.*, 1541 (1997).

## 21.1 INTRODUCTION

In the preceding four chapters, we have developed a catalog of orbitals for various  $ML_n$  fragments. A recurring theme among what seems to be a myriad of fragment orbitals is the existence of relationships between them. These have paired the valence orbitals of a  $C_{4v}$   $ML_5$  fragment with those of  $C_{2v}$   $ML_3$ , the  $C_{2v}$   $ML_4$  orbitals with those of  $C_{2v}$   $ML_2$ , and the levels of  $C_{3v}$   $ML_3$  with those of  $MCp$ . The first two relationships come from the correspondence between the octahedral and square planar splitting patterns (Section 16.2). The third is a consequence of the fact that  $Cp^-$  presents three donor orbitals to the metal, which are topologically equivalent to a *fac*  $L_3$  donor set. There exist many more that we develop in a generalized way in this chapter. This relationship is called the isolobal analogy [1]. Two fragments (or molecules) are said to be isolobal if their frontier orbitals have

1. the same number,
2. the same symmetry properties,
3. the same occupation by electrons,
4. similar energy, and
5. similar radial extent.

The isolobal relationship is symbolized by a double-headed arrow with a teardrop, as shown in 21.1. Note that the first three criteria are absolute while the last two are qualitative comparisons. This isolobal analogy is a model designed to



see a forest rather than the trees it contains. Because the last two are more relaxed rules that meant to be followed in spirit, it may fail at times. What makes this

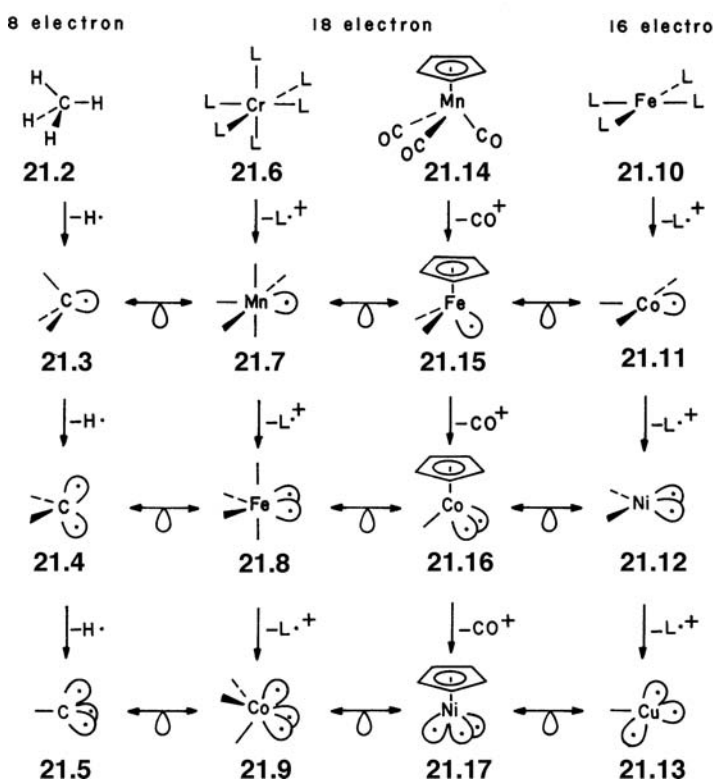
relationship so useful is that it relates the orbitals of inorganic/organometallic fragments to those in the organic/main group areas, namely the  $AH_n$  fragment orbitals that were developed in Chapters 7 and 9 to those of  $ML_n$ .

The utility of the isolobal analogy is that if a  $ML_n$  fragment is isolobal with a particular  $AH_n$  arrangement, then one should be able to replace the  $ML_n$  fragment in a molecule with a  $AH_n$  unit to produce a new compound (on paper at least). The two molecules should have a very similar electronic description and in a very qualitative sense have similar reactivity. The isolobal analogy is, therefore, a useful codifier of electronic, structural, and reactivity data, as well as a tool for predicting new compounds and reactions. The idea had its origins in Halpern's perceptive comments [2] about the similarities that exist between several organic and transition metal intermediates. The structural and stability patterns in boranes and transitional metal clusters developed by Wade [3] and Mingos [4] also played a role. But, it was Hoffmann [1] who showed the full utility of the isolobal analogy and extended it greatly.

## 21.2 GENERATION OF ISOLOBAL FRAGMENTS

The easiest way to see how particular fragments are isolobal is illustrated in Scheme 21.1. The archetypical molecule of organic chemistry is methane, 21.2. Breaking one C—H bond in a homolytic sense generates the methyl radical, 21.3. It

**SCHEME 21.1**



has one frontier orbital pointed in the direction of the missing hydrogen atom with one electron in it (Section 9.3). Removing another hydrogen atom creates methylene, 21.4. There are now two hybrid orbitals that in a localized sense point toward

the two missing hydrogens (Section 7.5). Removing still another hydrogen generates a methine fragment, **21.5**. It has three frontier orbitals (Section 9.2) with three electrons partitioned between them in some way. **21.3–21.5** are representative of the three fragments ( $\text{AH}_3$ ,  $\text{AH}_2$ ,  $\text{AH}$  where A is a main group element) that are the building blocks used throughout all of organic or main group chemistry with the exception of electron-rich, hypervalent molecules. Another starting point is  $\text{CrL}_6$ , **21.6**. The use of Cr here is totally arbitrary. What is important is that we have started with a  $d^6$  octahedral complex (consequently, it is a saturated 18-electron complex just as **21.2** is a saturated 8-electron compound). We now break one Cr—L bond in a *homolytic* fashion. One electron leaves with L, and the other remains at Cr. Therefore, a  $\text{L}_5\text{Cr}^-$  fragment is formed and  $\text{L}^+$  is lost (recall that L is a neutral two-electron donor). To make the number of charges manageable, let us move one element to the right in the Periodic Table; neutral  $\text{MnL}_5$  is isoelectronic to  $\text{CrL}_5^-$ . What is again important here is that **21.7** is a  $d^7$ ,  $\text{C}_{4v}\text{ML}_5$  fragment. It has one hybrid orbital directed toward the missing ligand (Section 17.2) with one electron in it. The hybrid orbital is composed of mainly metal *d* with some s and p character mixed into it and is of  $a_1$  symmetry. The frontier orbital of the methyl radical is also of  $a_1$  symmetry and is hybridized away from the remaining hydrogens. It is close to the traditional  $sp^3$  hybrid orbital. But what is important is that the single frontier orbital (with one electron in it) for both  $\text{MnL}_5$  and  $\text{CH}_3$  is directed out away from the remaining “ligands” and is of  $a_1$  symmetry. This means that  $\text{MnL}_5$  and  $\text{CH}_3$  are isolobal. So too is  $\text{Co}(\text{CN})_5^{3-}$ , another  $d^7$  system. We shall shortly explore the consequences of this, but for now we note that both  $\text{CH}_3$  and several  $d^7\text{ML}_5$  molecules have been studied by electronic spin resonance (ESR) spectroscopy and have been trapped in low-temperature matrices [5]. They display very similar chemistry, namely free radical abstraction reactions and dimerization [2]. Removing a second ligand from  $\text{MnL}_5$  and moving one element to the right in the periodic table generates the  $\text{C}_{2v}\text{FeL}_4$  fragment, **21.8**. It is isolobal to  $\text{CH}_2$ . Removing a third ligand generates the  $\text{C}_{3v}\text{CoL}_3$  fragment, which is isolobal to  $\text{CH}$ .

Our other starting point was the 16-electron square planar complex, **21.10**. The fragments that are generated by the removal of one to three  $\text{L}^+$  units are given by **21.11–21.13**. They will also find isolobal partners in the  $\text{CH}_3$  to  $\text{CH}$  series. There are many other starting points that could be utilized. For example,  $\text{CpMn}(\text{CO})_3$ , **21.14**, is an 18-electron complex with an octahedral splitting pattern (Section 20.1). Sequential removal of the three  $\text{CO}^+$  ligands generates **21.15–21.17**. The reader can easily verify that replacement of a *fac*  $\text{L}_3$  donor set by  $\text{Cp}^-$  in **21.7–21.9** generates the same fragments. One could just as easily have started from the 18 electron benzene- $\text{Cr}(\text{CO})_3$  or cyclobutadiene- $\text{Fe}(\text{CO})_3$  complexes. For now, any “octahedron”-based 18-electron or square planar 16-electron complex can be used as a starting point to derive fragments. One can also go down the column in the periodic table to generate alternative isolobal fragments. Thus,  $\text{CH}_2$  is isolobal to  $\text{C}_{2v}\text{Fe}(\text{CO})_4$ ,  $\text{Ru}(\text{CO})_4$ , and  $\text{Os}(\text{CO})_4$ . Likewise,  $(\text{CH}_3)_3\text{Sn}$  is isolobal to  $\text{Mn}(\text{CO})_5$ ,  $\text{Fe}(\text{CO})_5^+$ , or  $\text{Mo}(\text{CO})_5^-$ . Adjustments in the electron count of the frontier orbitals can also be made. For example,  $\text{CH}_3^+$  or  $\text{BH}_3$  will have one empty frontier orbital, so too will  $\text{Mn}(\text{CO})_5^+$ ,  $\text{Cr}(\text{CO})_5$ ,  $\text{CpMn}(\text{CO})_2^-$ ,  $(\text{Ph}_3\text{P})_3\text{Rh}^+$ , and  $\text{Mn}(\text{CO})_4\text{Cl}$ . Likewise,  $\text{CH}_3^-$ ,  $(\text{CH}_3)_3\text{Si}^-$ , and  $\text{NH}_3$  are isolobal to  $\text{Mn}(\text{CO})_5^-$ ,  $\text{Fe}(\text{CO})_5$ , and  $\text{Rh}(\text{CO})_5^+$  where all of the metal complexes are  $\text{C}_{4v}$  square pyramidal (not trigonal bipyramidal) fragments. Here, the one frontier orbital in each case has two electrons. It is important that when one considers the molecules in Scheme 21.1 as compounds in their own right, then there may well be some adjustments in the geometry. For example,  $\text{CH}_3^+$  by itself is trigonal while  $\text{CpMn}(\text{CO})_2$  is pyramidal and  $\text{CH}_3^-$  is pyramidal while  $\text{CpCo}(\text{CO})_2$  is trigonal. This was covered in some detail in Sections 9.3 and 19.5. The ground state for a  $d^{10}\text{ML}_2$  compound is linear [5] (see Section 16.3), not bent as shown in **21.12**. While a  $\text{C}_{4v}\text{Fe}(\text{CO})_5$  fragment is

isolobal to  $\text{CH}_3^-$ , its ground state is not the square pyramid but is certainly the  $D_{3h}$  trigonal bipyramidal geometry. But, given the geometries of the molecules shown by **21.4**, **21.8**, **12.12**, and **21.16**, all have singlet and triplet electronic states. The actual geometry of both states and the singlet-triplet energy difference in  $\text{CH}_2$  has been the subject of a tremendous amount of research (Section 8.8); much less is known about the other members of this series. Moreover, one can readily envision many other examples that are isolobal to  $\text{CH}_2$ . The isolobal analogy anticipates the behavior of those very reactive intermediates. However, our main concern is to use the isolobal analogy to generate alternative fragments in molecules. So, the geometry of the fragment in a molecule, not as an isolated species, is important.

The usefulness of the isolobal analogy is highlighted when a fragment is replaced with its isolobal analog in a molecule. Since  $\text{CH}_3$  is isolobal with  $\text{Mn}(\text{CO})_5$ ,  $\text{CpFe}(\text{CO})_2$ , or  $\text{Co}(\text{PR}_3)_3$ , one can replace one or both  $\text{CH}_3$  groups in ethane to give  $\text{CH}_3\text{Mn}(\text{CO})_5$ ,  $\text{Mn}_2(\text{CO})_{10}$ ,  $\text{CpFe}(\text{CO})_2(\text{CH}_3)$ , and so on. These are well-known molecules. The electronic description of the three is similar in that there is a  $\sigma$  bond present between C—C, C—Mn, Mn—Mn, or Fe—C. There are certainly other molecular orbitals present, particularly for the transition metal complexes where the  $t_{2g}$  set at the metals has been ignored. The  $\sigma$  bond strengths are certainly quite different. Figure 21.1 shows HF 3-21G contour plots of the frontier orbital in each example. The frontier orbitals for the transition metal fragments are quite diffuse. So, for example, the activation energy in a rearrangement reaction where a C—C bond is partially broken will be much higher than that for an isolobal example where say an Fe—C bond is broken by a similar amount.

Let us take a closer look at the composition of the frontier orbitals that are displayed in Scheme 21.1. Since  $\text{CH}_2$ ,  $\text{Fe}(\text{CO})_4$ ,  $\text{Ni}(\text{PPh}_3)_2$ , and  $\text{CpCo}(\text{CO})$  are isolobal, then each should have two orbitals with the same symmetry properties. The localized orbitals in Scheme 21.1 are not necessarily the proper symmetry-adapted orbitals that will be most useful for us. Linear combinations of the localized orbitals,

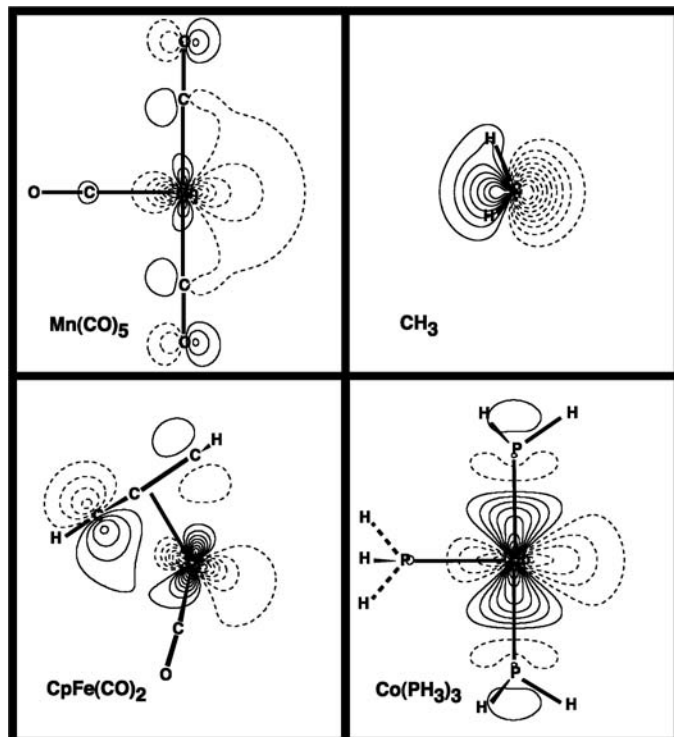
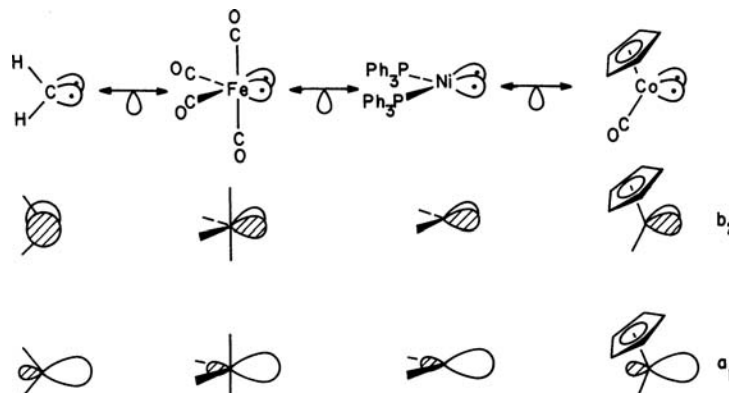


**FIGURE 21.1**

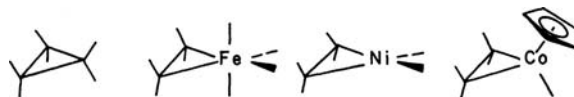
Contour plots of the frontier orbitals in four isolobal fragments at the HF 3-21G level.

however, can easily be generated. These are shown in **21.18**. Each fragment has one orbital of  $a_1$  and of  $b_2$  symmetry. For  $\text{Fe}(\text{CO})_4$  and  $\text{Ni}(\text{PPh}_3)_2$ , we saw that  $b_2$  was



21.18

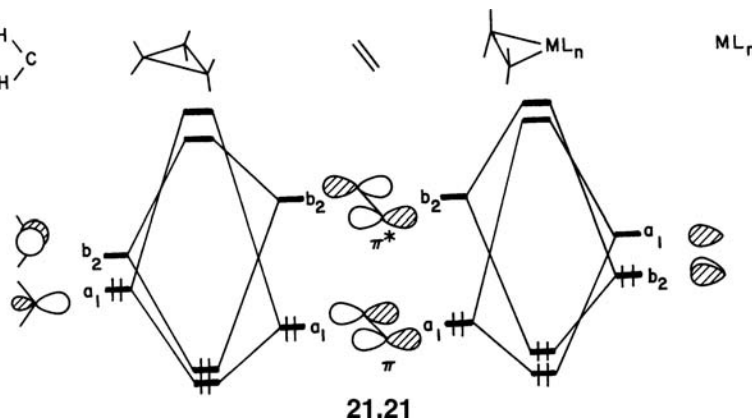
lower in energy than the  $a_1$  orbital (Sections 19.1, 19.3). This is a natural consequence of the fact that the  $b_2$  orbital consists primarily of metal  $d$  character and  $a_1$  is mainly metal  $s$  and  $p$ . In  $\text{CH}_2$ , it is  $a_1$  that lies lower than  $b_2$  (Section 7.3). So, for a  $\text{CH}_2$  fragment, we would assign the two electrons to the  $a_1$  orbital. For the three  $\text{ML}_n$  examples in **21.18**, the two electrons would go into the  $b_2$  level. That does not make much of a difference in a real molecule. The occupation of the fragment orbitals that make up a molecule is arbitrary. It is the electron distribution in the final molecule that is important, not the details in electron occupancy of these conceptual fragments. For example, consider cyclopropane, **21.19**, as being derived from the



21.19

21.20

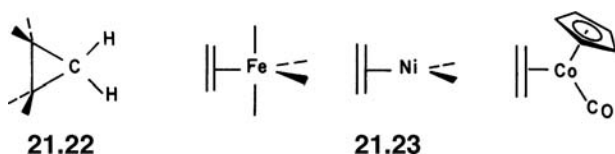
interaction of ethylene with a  $\text{CH}_2$  fragment. The overall bonding picture that we get should be comparable to that derived for any of the molecules in **21.20** where one  $\text{CH}_2$  fragment has been replaced by an isolobal partner from **21.18**. That this is true can be established from **21.21**. In each instance, the  $b_2$  orbital interacts with ethylene  $\pi^*$  and an  $a_1$  orbital with ethylene  $\pi$ . Two bonding and two antibonding molecular



orbitals are formed. Two electrons come from ethylene and two from the  $\text{CH}_2$  or  $\text{ML}_n$  fragment, which just fill the two bonding MOs. We recognize that the structures

in **21.20** are just metallacyclopropane formulations of metal–olefin complexes and **21.21** is the Dewar–Chatt–Duncanson model of bonding as described more fully in Sections 19.3 and 19.5. To draw cyclopropane as a carbene–ethylene complex will not be endearing to most organic chemists. On the other hand, one can then easily see why cyclopropane transmits electronic effects to the same extent as olefins without resorting to the Walsh model described in Section 11.2.1.

We cover several more complexes that can be traced back to cyclopropane in Section 21.3. For now, we note that the isolobal analogy nicely solves conformational issues. Let us rotate the ethylene unit in **21.19** and **21.20** by  $90^\circ$ . The ethylene  $\pi^*$  orbital is now of  $b_1$  symmetry and the  $b_2$  orbital in  $\text{CH}_2$  or  $\text{ML}_n$  is left occupied and nonbonding. Thus, **21.22** and **21.23** are high-energy structures. **21.22** contains one square planar

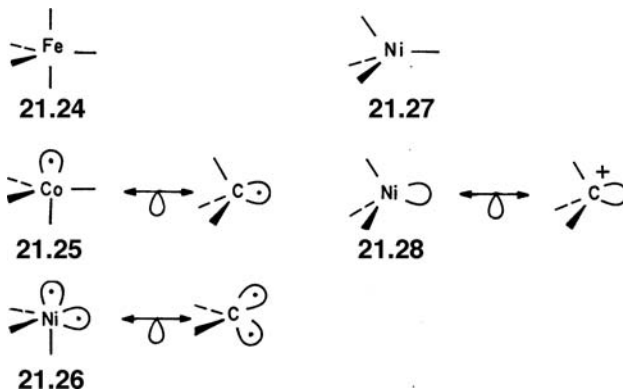


carbon and the nonbonding  $b_2$  orbital is readily identified with the nonbonding  $p$  orbital in square planar  $\text{CH}_4$  (Section 9.5). Of course the actual energy difference between **21.19** and **21.22** in cyclopropane will not be the same as the rotational barriers in the olefin complexes. The rotational barrier in each case depends on the strength of the  $b_2 + \pi^*$  interaction. As the interaction becomes stronger, the barrier becomes larger.

### 21.3 CAVEATS

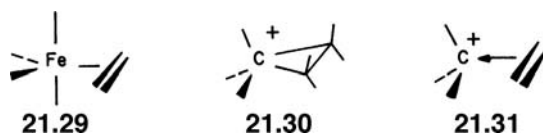
The strength of the interactions with frontier orbitals will depend on energy difference (electronegativity considerations) and overlap considerations. These will certainly vary from one isolobal fragment to another. Therefore, the isolobal analogy is to be used in a qualitative sense. Furthermore, kinetic stability is not something that can be assessed with this model and, therefore, the prediction of an isolable molecule is not assured.

There are two further important caveats that one must keep in mind when using the isolobal analogy. A normal operational order consists of replacing a fragment in a molecule with an isolobal one. We must be careful to establish the coordination mode (or number) at the transition metal because there is not an exact mapping of fragments in the isolobal analogy. If we use  $\text{Fe}(\text{CO})_5$ , **21.24**, as an 18-electron starting point, then one can



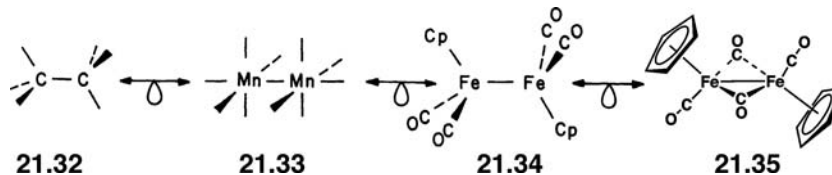
readily derive the sequence of fragments given by **21.25** and **21.26**.  $\text{Co}(\text{CO})_4$  and  $\text{Ni}(\text{CO})_3$  are isolobal with  $\text{CH}_3$  and  $\text{CH}_2$ , respectively. Suppose however, we started with  $\text{Ni}(\text{CO})_4$ , **21.27**, another 18-electron complex that is tetrahedral. Removal of

CO (in a heterolytic sense) generates  $\text{Ni}(\text{CO})_3$ , **21.28**, which is predicted to have one empty frontier orbital and is therefore isolobal to  $\text{CH}_3^+$ . Now, we have a problem—is  $\text{Ni}(\text{CO})_3$  isolobal to  $\text{CH}_2$  or  $\text{CH}_3^+$ ? In fact it is isolobal to both. If we use  $\text{Ni}(\text{CO})_3$  to reconstruct a trigonal bipyramidal, then it is isolobal to  $\text{CH}_2$ ; however, if it is used to form a tetrahedral complex then it is isolobal to  $\text{CH}_3^+$ . Suppose we remove an equatorial CO ligand from  $\text{Fe}(\text{CO})_5$  **21.24**. That creates a  $C_{2v}$   $\text{Fe}(\text{CO})_4$  ligand with one empty hybrid orbital, and the  $\text{Fe}(\text{CO})_4$  group is isolobal to  $\text{CH}_3^+$ . Ethylene- $\text{Fe}(\text{CO})_4$ , **21.29**, is then equivalent to protonated cyclopropane, **21.30**. But, we had said that ethylene- $\text{Fe}(\text{CO})_4$ , drawn in the metallacyclop propane form in



**21.20**, was equivalent to cyclopropane! The metallacyclop propane drawing emphasizes octahedral coordination at iron. The OC—Fe—CO angle in the equatorial plane should be  $\sim 90^\circ$ . In molecular orbital terms, this means that  $a_1 + \pi$  and  $b_2 + \pi^*$  interactions are both strong and of comparable magnitudes (i.e., there is substantial delocalization between the fragment orbitals in each bonding molecular orbital). Using the olefin-metal formulation in **21.29** emphasizes trigonal bipyramidal coordination at iron. The equatorial OC—Fe—CO angle then should be  $\sim 120^\circ$ . The important interaction here in molecular orbital terms is that between the empty  $a_1$  orbital on  $\text{Fe}(\text{CO})_4$  and the filled  $\pi$  orbital of ethylene. The  $b_2 + \pi^*$  interaction is neglected (or treated to be of minor importance). In this context, it is useful to rewrite protonated cyclopropane as in **21.31**, which emphasizes the principal mode of bonding, donation of electron density from the filled  $\pi$  orbital of ethylene to the empty hybrid orbital of  $\text{CH}_3$ . This is the essence of the bonding model we developed for the bridged geometry in the ethyl cation (Section 10.5), which came about in a totally different way! In actual fact, the OC—Fe—CO angles in olefin- $\text{Fe}(\text{CO})_4$  complexes [6] are normally  $\sim 110^\circ$  that is intermediate between two extremes that have been presented here. Cunden and Linck have shown [6b] that the OC—Fe—CO in fact decreases as the olefin becomes a better  $\pi$  acceptor, that is, the  $b_2 + \pi^*$  interaction becomes stronger. This is just what the isolobal analogy predicts. So, the inexact mapping of isolobal fragments, while it is complicating, nonetheless gives us different perspectives about the bonding in molecules that we may well have overlooked.

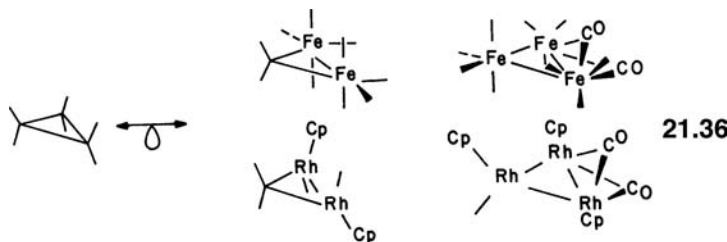
The most common ligand in transition metal chemistry is CO. It has a high lying, nicely directional donor orbital and a pair of low-lying acceptor levels. These are ideal components for a strong metal–carbon bond. CO also brings a real problem to the organometallic chemist, namely, it is one of the few ligands that can either bridge two or three metal centers or bond terminally to one transition metal. More importantly, pairwise bridging-terminal CO exchange is a very common feature in transition metal dimers and clusters, and there is often little energy difference between the two structural possibilities. This creates a second caveat when using the isolobal analogy. A pertinent example is offered by ethane. We have previously established that  $\text{CH}_3$  is isolobal to  $\text{Mn}(\text{CO})_5$  and, therefore, ethane, **21.32**, is equivalent to  $\text{Mn}_2(\text{CO})_{10}$ , **21.33**. But,  $\text{CpFe}(\text{CO})_2$  (**21.15** in Scheme 21.1) is also isolobal to  $\text{CH}_3$ . There should also be a  $\text{Cp}_2\text{Fe}_2(\text{CO})_4$  complex with a structure like **21.34**. Such a compound does exist, but it is not the ground-state structure. The bridged form, **21.35**, is more stable than **21.34**,



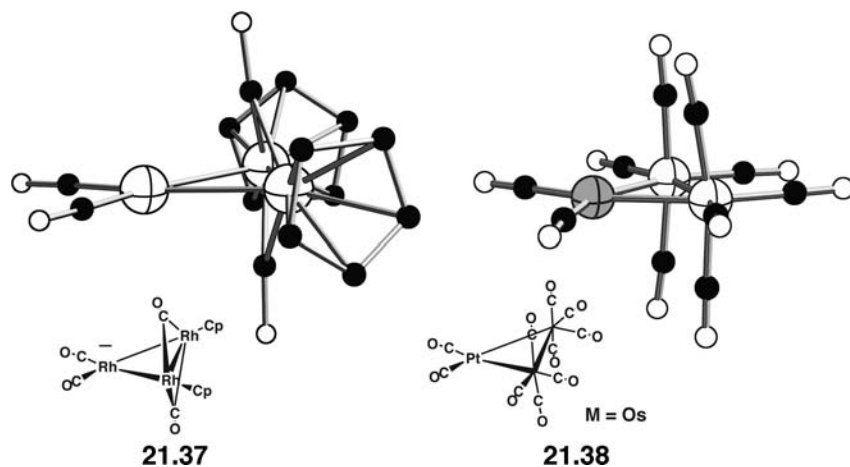
and there is a facile equilibrium between the two; see Figure 16.3 and the discussion around it. That certainly does not happen in ethane (Section 10.2). Bridging hydrogens and alkyl groups are found in carbonium ion and borane chemistry where the molecules are electron deficient, but not for saturated compounds. In a very qualitative sense, the valence orbital structure for **21.34** and **21.35** are similar. It is the metal  $t_{2g}$  and carbonyl  $\pi^*$  orbitals that are most perturbed as the carbonyls bridge. The organic/main group analogs, of course, do not have this set of “lone-pair” orbitals at the central atom. Remember that the metal  $t_{2g}$  set is neglected (for now) when using the isolobal analogy; therefore, **21.35** is regarded as being electronically equivalent to **21.34**. We shall shortly see here, but particularly in Chapter 22, many examples with a bridging hydrogens. It is most useful to remove these hydrogens as protons. Therefore, the electron count on the molecule remains the same. With these qualifications in mind, we turn to examples where the isolobal analogy can be used.

## 21.4 ILLUSTRATIONS OF THE ISOLOBAL ANALOGY

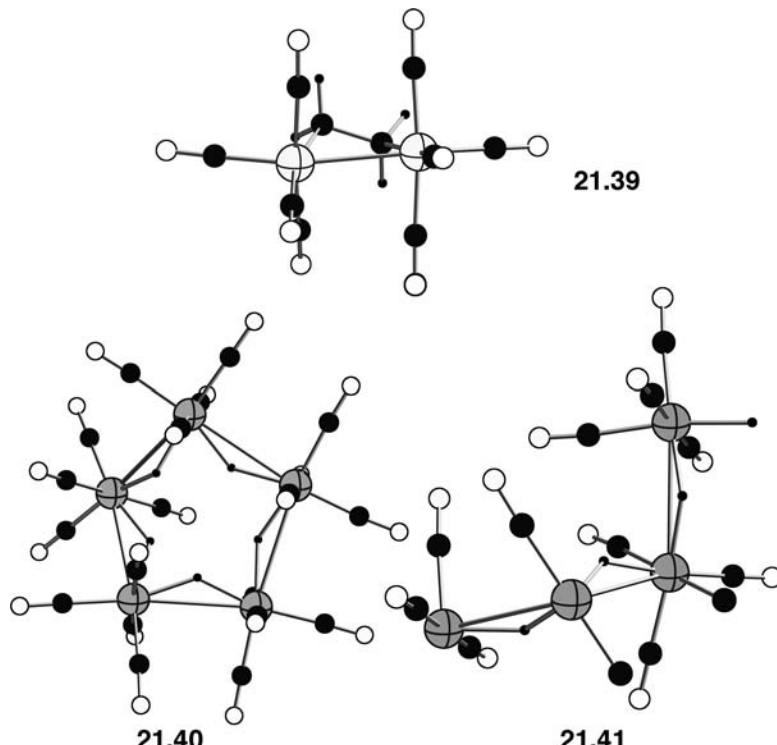
We replaced one  $\text{CH}_2$  in cyclopropane, **21.19**, with an isolobal  $\text{Fe}(\text{CO})_4$ ,  $\text{Ni}(\text{PPh}_3)_2$ , and  $\text{CpCo}(\text{CO})$  group to generate the metal–olefin complexes given by **21.20**. Replacing two or all three  $\text{CH}_2$  groups by the isolobal  $\text{Fe}(\text{CO})_4$  or  $\text{CpRh}(\text{CO})$  fragments generates the set of compounds shown in **21.36**, all of which are known. Notice that the structure of  $\text{Fe}_3(\text{CO})_{12}$  contains a pair of bridging carbonyls [7].



However, in the isoelectronic  $\text{Ru}_3(\text{CO})_{12}$  and  $\text{Os}_3(\text{CO})_{12}$ , all carbonyls are terminal [8]. Again, this implies a very small energy difference. The structure shown for  $\text{Cp}_3\text{Rh}_3(\text{CO})_3$  is one of several possibilities [9] that pass through an all-terminal CO structure. Mixed structures such as **21.37** [10] and **21.38** [11] also have been

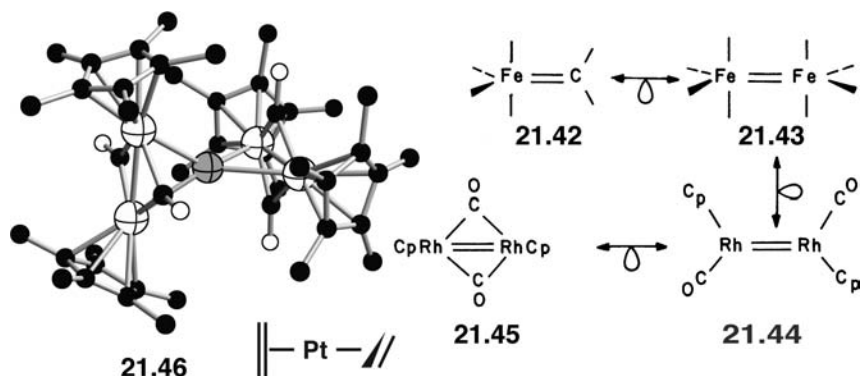


prepared. The bridging carbonyls in **21.37** actually lean toward the  $\text{Rh}(\text{CO})_2$  unit for reasons that are covered elsewhere [9], but the important point is that electronically the compounds bear a marked resemblance to cyclopropane. Furthermore, phosphine derivatives of **21.38** show an interesting rearrangement. NMR studies [12] have demonstrated that the  $\text{Os}_2$  unit rotates with respect to the Pt moiety like a metal–olefin complex passing from **21.20** to **21.23**. We need not stop with cyclopropane, for  $\text{Os}_2(\text{CO})_8(\text{CH}_2\text{CH}_2)$ , (**21.39**) has recently been prepared and structurally categorized [13].  $\text{Os}(\text{CO})_4$  is isolobal to  $\text{CH}_2$ , so **21.39** is immediately

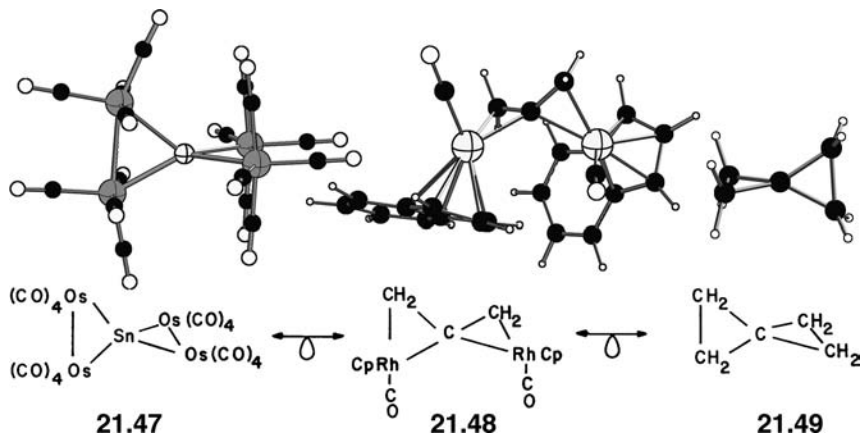


recognized as being equivalent to cyclobutane. Higher homologs have also been prepared. A particularly nice example is provided by the coupling of  $\text{Re}(\text{CO})_4\text{H}$  units together [14]. Counting the hydrogen as  $\text{H}^+$ , we then have  $\text{Re}(\text{CO})_4^-$  that is isoelectronic to  $\text{Os}(\text{CO})_4$ . **21.40** is then the transition metal analog of cyclopentane. There is also a cyclohexane analog. **21.41** is a polymer,  $[\text{Re}(\text{CO})_4\text{H}]_n$ , isolobal to polyethylene.

The simplest, stable organic compound containing the  $\text{CH}_2$  group is ethylene. It is reasonable to expect that the compounds given by **21.42**–**21.45** can be made.

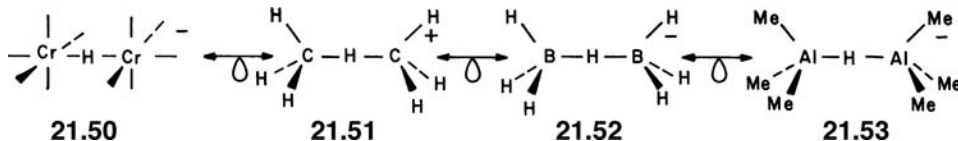


Derivatives of **21.42** have been prepared [15], and details concerning **21.43** in a low temperature matrix have been described in Section 19.3. **21.45** has been structurally categorized as the pentamethylcyclopentadienyl derivative (see **16.29**). Their kinetic stability is certainly limited. A high lying  $\pi$  orbital and low-lying  $\pi^*$  especially in **21.42–21.45** make these molecules extraordinarily reactive. One way to stabilize these species is to coordinate them to an  $ML_n$  fragment. It is easy to recognize that  $(CH_2)Fe_2(CO)_8$ , and the all-terminal form of  $Fe_3(CO)_{12}$  are just the  $Fe(CO)_4$  complexes of **21.42** and **21.43**, respectively (see **21.36**). **21.37** is a  $d^{10} ML_2$  complex of **21.45**. Two **21.45** fragments are coordinated to a single Pt atom in **21.46** [16]. This molecule is isolobal to  $(ethylene)_2Pt$ . The  $Os_2(CO)_8$  analog of **21.43** appears in **21.47** [17]. Replacing the  $Os(CO)_4$  groups with isolobal  $(indenyl)Rh(CO)$  and  $CH_2$  units, and the



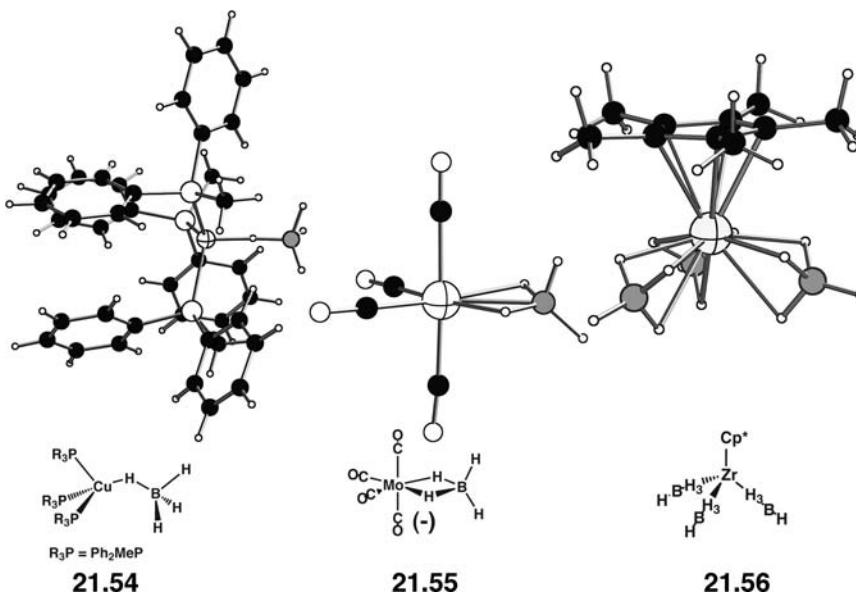
central Sn atom with an isoelectronic carbon generates **21.48** [18]. Both complexes are equivalent to spiropentane, **21.49**.

So far we have concentrated on isolobal analogs of  $CH_2$ . Let us now turn our attention to other fragments. In Section 17.4, we showed that for the hydrido bridged  $Cr(CO)_5$  dimer, **21.50**, a “closed” structure with a  $Cr—H—Cr$  angle of less than  $180^\circ$



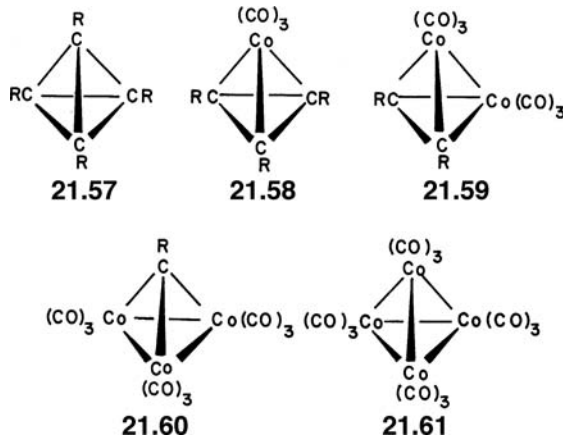
should be favored with a very low bending potential. All of the elements of an electron deficient, two-electron–three-center bonding pattern are present in **21.50**. Replacing each  $Cr(CO)_5$  group by the isolobal  $CH_3^+$  yields **21.51**. Cyclic derivatives of **21.51** have been prepared [19,20]. The actual structures are uncertain; however, it has been established that the hydrogen atom must be bridged symmetrically between the two carbons. Calculations on **21.51** [21] and alkyl analogs at various levels [22] have found that the most stable structure is highly bent, and it perhaps can be regarded as a protonated alkane. An isoelectronic compound, **21.52**, has been structurally categorized in the form of a  $(Ph_3P)_2N^+$  salt [23]. The  $B—H—B$  angle was found to be  $136^\circ$ . There must be a very low bending potential since **21.53** is linear [24]. We suspect that a variety of structures will be found for **21.52** by varying the counter cation that in turn can modify intermolecular packing forces. Notice that **21.50** or **21.51** can easily be traced back to an  $\eta^1$   $CH_4$  complex of  $Cr(CO)_5$ . Indeed, these  $\eta^1$  complexes of alkanes have been postulated as an intermediate on the way to the product of oxidative addition. Isoelectronic  $BH_4^-$  complexes are also known. An example is given by **21.54** [25]. Here,  $(R_3P)_3Cu^+$  is isoelectronic to  $Ni(CO)_3$ , which has one empty frontier orbital that coordinates to a two-electron  $B—H$   $\sigma$  bond. The

Cu—H—B bond angle was  $170.5^\circ$ . In other examples, this angle is considerably smaller, just like the situation for the isolobal **21.50**. A compound containing a  $C_{2v}$   $ML_4$  complex is shown in **21.55** [26]. A  $\text{Mo}(\text{CO})_4$  fragment has two frontier orbitals

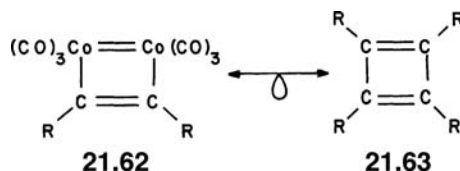


with no electrons, so it coordinates to two B—H  $\sigma$  bonds.  $\text{Mo}(\text{CO})_4$  is isolobal to  $\text{CH}_2^+$  or  $\text{BH}_2$ , so **21.55** is just an analog of diborane. It is tempting to speculate on the existence of an  $(\eta^2\text{-CH}_4)\text{Mo}(\text{CO})_4$  analog. **21.56** [27] contains three  $\eta^3\text{-BH}_4^-$  ligands ( $\text{Cp}^* = \text{Me}_5\text{C}_5$ ). If one considers that each two-electron B—H bond donates its electron density to  $\text{Zr}^{4+}$ , then **21.56** is a 24 electron complex! It turns out that a detailed study [28] of the electronic structure shows that there are three filled ligand-based MOs that do not find a bonding match with the Zr atomic orbitals. Thus, **21.56** is still an 18-electron complex. It is easy to take linear combinations of three B—H  $\sigma$  bonds. Within a local  $C_{3v}$  symmetry, they form combinations of  $a_1 + e$  symmetry; just like three fac carbonyl groups or the filled  $\pi$  orbitals of cyclopentadienyl anion. The  $\eta^3\text{-BH}_4^-$  ligand is, therefore, isolobal to  $\text{Cp}^-$ ! Indeed, replacing the  $\text{Cp}^*$  group in **21.56** gives  $(\eta^3\text{-BH}_4)_4\text{Zr}$ . This is a known compound with  $T_d$  symmetry [29]. Here, a ligand combination of  $t_2$  symmetry is rigorously nonbonding.

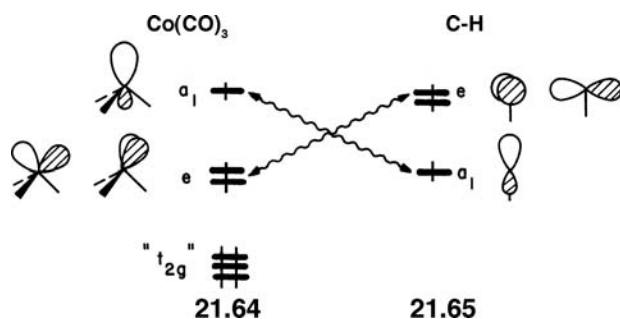
Scheme 21.1 shows that a CH fragment is isolobal to  $\text{Co}(\text{CO})_3$ ; both have three frontier orbitals with three electrons in them (**21.5** and **21.9**). The entire set of compounds given by **21.57–21.61** where CR groups have been sequentially replaced by



$\text{Co}(\text{CO})_3$  units has been prepared. Normally, **21.58** is written as a cyclopropenium complex, and **21.59** as an acetylene-bridged  $\text{Co}_2(\text{CO})_6$  dimer. It is a straightforward matter to take linear combinations of the Co—C  $\sigma$  bond orbitals to generate a set of orbitals that are equivalent to those derived from a cyclopropenium or acetylenemetal formulation. The structures of **21.61** and  $\text{Rh}_4(\text{CO})_{12}$  actually contain three bridging carbonyls [30], and both compounds show very facile CO scrambling.  $\text{Ir}_4(\text{CO})_{12}$  does indeed have the all-terminal structure [31] indicated in **21.61**. Notice that the acetylene ligand in **21.59** lies perpendicular to the Co—Co vector as it should for a metallatetrahedrane derivative. Rotation of the acetylene by  $90^\circ$  gives **21.62** that is now isolobal to cyclobutadiene **21.63**. The orbital structure of **21.62**

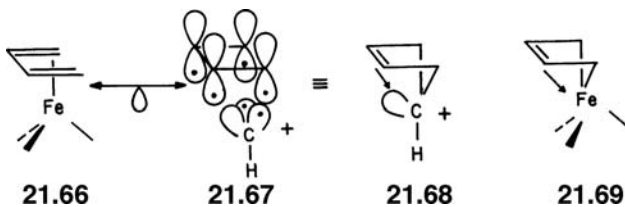


contains four levels of  $\pi$  symmetry; the two middle ones are nearly degenerate and constitute the highest occupied molecular orbital (HOMO) and lowest unoccupied molecular orbital (LUMO) for the molecule [32]. That is exactly the picture one gets for **21.63** (see Figure 12.5). Rotation of one “acetylene” unit by  $90^\circ$  in tetrahedrane to give cyclobutadiene is a symmetry-forbidden reaction. The same restriction applies to the **21.59** to **21.62** conversion [32]. The organometallic members of the tetrahedrane series have been known for many years. Tetrahedrane, **23.57**, itself is not known; compounds with large R groups (e.g., *t*-Bu) provide a hydrocarbon coating around the molecule to prevent attack from external reagents and also offer a “steric corset” minimizing steric interactions between the bulky groups compared with ring-opened intermediates [33]. The ring strain in tetrahedrane has been estimated to be 136 kcal/mol! [34]. It is doubtful that the ring strain in **23.59**–**23.61** is anything significant. A comparison of the  $\text{Co}(\text{CO})_3$  and CH fragments is given in **23.64** and **23.65**. The isolobal criteria outlined in the Introduction are

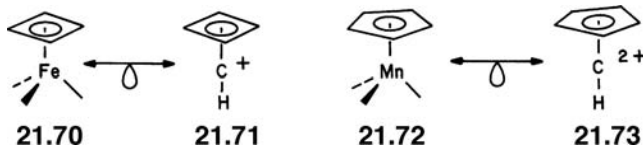


certainly fulfilled in this example, but there is a critical difference. The e set in  $\text{Co}(\text{CO})_3$  consists primarily of a Co d AO, so the lobes are oriented at angles of  $\sim 90^\circ$ , whereas in  $\text{C}-\text{H}$ , these are p AOs with angles of  $180^\circ$ . In the tetrahedrane series with bond angles of  $60^\circ$ , it is clear that the ring strain of a  $\text{Co}(\text{CO})_3$  group is much less than that associated with  $\text{C}-\text{H}$ . In other words, the isolobal analogy does not take ring strain into account.

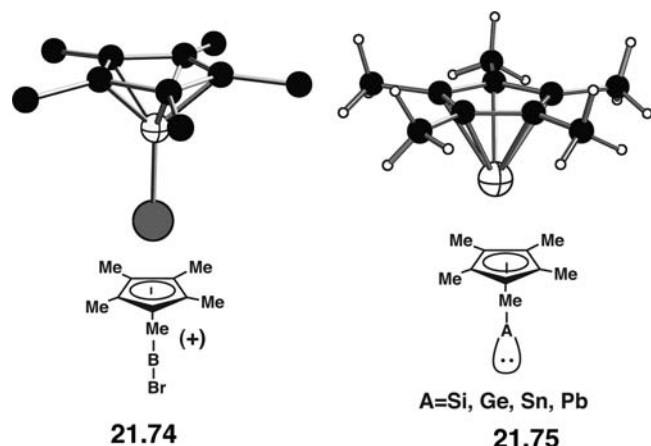
A fascinating series of organic compounds are produced when the  $\text{ML}_3$  unit is replaced in polyene– $\text{ML}_3$  complexes with an isolobal analog. Consider butadiene– $\text{Fe}(\text{CO})_3$ , **21.66**, as being constructed by the interaction of the four  $\pi$  electrons in the butadiene ligand with an  $\text{Fe}(\text{CO})_3$ , which is isolobal to  $\text{CH}^+$ . The  $\text{CH}^+$  fragment has three frontier orbitals with two electrons, shown in a localized manner by **21.67**.



Pairing the electrons to form two C—C  $\sigma$  bonds and one C—C  $\pi$  bond generates the nonclassical form of the 3-cyclopentenium cation, **21.68**. This sort of representation has actually been used for butadiene–Fe(CO)<sub>3</sub> complexes [35], see **21.69**. It might be anticipated from structure **21.66** that butadiene–Fe(CO)<sub>3</sub> complexes should have two short and one long (the middle bond) bonds. The x-ray structures of hundreds of derivatives have been obtained, and the results are that all three bonds have about the same length. One could argue about the structural consequences associated with donation from  $\pi_2$  and back-donation from  $\pi_3$ . However, this bond equalization can easily be established by invoking **21.69** as a resonance structure along with **21.66**. One can debate how much the donation from the  $\pi$  orbital in **21.68** to the empty hybrid orbital is worth. Let us start with a relative of **21.66**, namely, cyclobutadiene–Fe(CO)<sub>3</sub>, **21.70**. Its isolobal analog is the C<sub>5</sub>H<sub>5</sub><sup>+</sup> cation, **21.71**. A Mn(CO)<sub>3</sub> group is isolobal to CH<sup>2+</sup>, so **21.72** is isolobal to **21.73**, the



Hogeveen–Kwant dication [36a]. The electrons in both sets of complexes can be partitioned into a  $d^6$  ML<sub>3</sub> [i.e., Fe(CO)<sub>3</sub><sup>2+</sup> or Mn(CO)<sub>3</sub><sup>+</sup>] or CH<sup>3+</sup> units that interact with the cyclobutadiene<sup>2-</sup> or Cp<sup>-</sup> ligand. The polyene ligands then each have three filled  $\pi$  orbitals. Both fragments contain three empty frontier orbitals of  $a_1 + e$  symmetry (see **21.64** and **21.65**). They will just match the nodal properties of the three filled  $\pi$  levels of the two polyenes. The reader should carefully compare the orbital interaction diagrams in Figure 20.7 for **21.70** with that in Figure 11.5 for **21.71** and Figure 20.5 for **21.72** with Figure 11.6 for **21.73**. The basic ordering of the bonding molecular orbitals is indeed identical going from the organometallic to the all-organic complex. Species such as C<sub>5</sub>H<sub>5</sub><sup>+</sup> or C<sub>6</sub>H<sub>6</sub><sup>2+</sup> are certainly unusual and uncomfortable structures for organic chemists. Yet, all available experimental [36a] and theoretical [36b] evidence suggests that the apical carbon in each is symmetrically bonded to the four- and five-membered rings. The C<sub>6</sub>H<sub>6</sub><sup>2+</sup> potential energy surface has an interesting history. Benzene along with other polynuclear aromatic hydrocarbons has been identified in planetary nebulae [38]. Benzene is a highly efficient absorber of UV and soft x-ray radiation from the surrounding star and, therefore, is thought to contribute to the opacity of nebulae. There is good evidence that C<sub>6</sub>H<sub>6</sub><sup>2+</sup> is formed. The initial state is either a ground state triplet with D<sub>6h</sub> symmetry or a singlet that is strongly Jahn–Teller distorted [39,40] (recall from section 12.3 that the HOMO of benzene is the e<sub>1g</sub> set). There is a moderate activation barrier of 26.4 kcal/mol that leads to the global minimum, **21.73** which is 3.0 kcal/mol more stable than singlet benzene<sup>2+</sup> with the puckered structure [40]. So, it is tempting to speculate that **21.73** exists in the gas phase in nebulae along with low temperature superacid solutions. Several heterocyclic derivatives have been prepared, including **21.74** where boron has replaced the apical carbon atom [41]. There are several

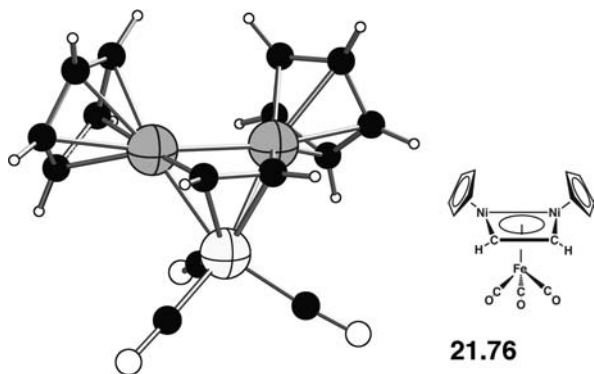


21.74

21.75

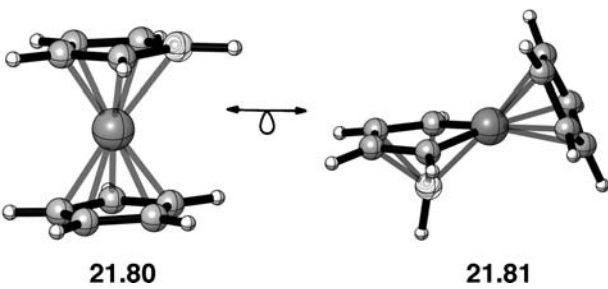
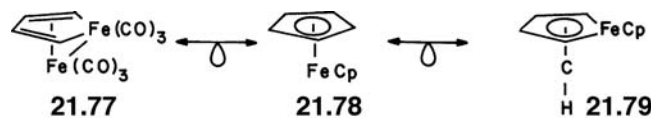
structures [42], 21.75, of a derivative of  $C_6H_6^{2+}$ . Deprotonating the apical carbon in 21.73 and replacing it with an isoelectronic group 14 atom gives 21.75. The group 14 atoms lie in the center of the pentamethyl-cyclopentadienyl ring, and the five central carbon atoms in the ring lie in a common plane in all of the structures. Heterocyclic analogs of 21.71 have also been isolated and structurally categorized [43].

One needs to be adaptable in viewing the structures of molecules. Normally, 21.76 is considered to be an acetylene coordinated to a trinuclear cluster [37]. There are some



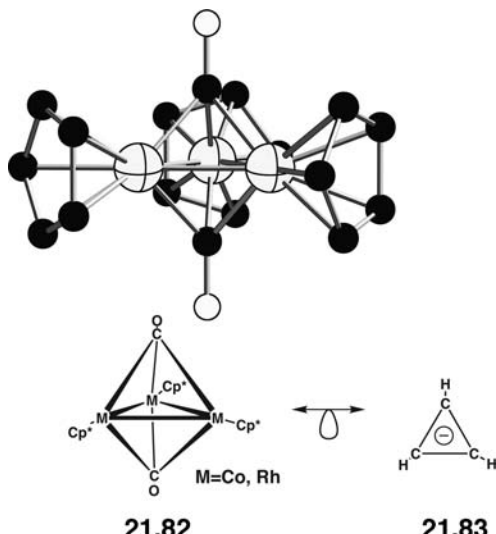
21.76

advantages in adopting this viewpoint, but we have drawn the structure in a different way. A CpNi fragment is isolobal to CH, so 21.76 is isolobal to cyclobutadiene–Fe( $CO$ )<sub>3</sub> or  $C_5H_5^+$ . Replacing the “basal” Fe( $CO$ )<sub>3</sub> group for CH<sup>+</sup> in the ferrole dimer, 21.77, yields CpFe( $CO$ )<sub>3</sub><sup>+</sup>, which in turn is isolobal to ferrocene, 21.78, when the



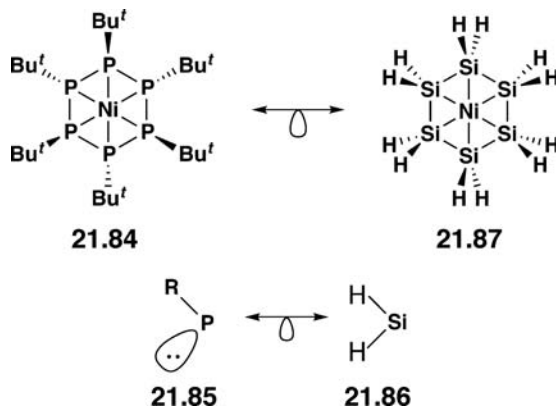
three carbonyl ligands are replaced by  $\text{Cp}^-$ . All of these complexes are stable and well known. But, suppose we substitute the “apical”  $\text{Fe}(\text{CO})_3$  fragment in **21.77** by  $\text{CH}^+$ ? Further substitution of a  $\text{Cp}^-$  ligand for the three carbonyls generates **21.79**, a nonclassical isomer of ferrocene! A search through the Cambridge Crystallography database in 2011 on  $\text{C}_{10}\text{H}_{10}\text{Fe}$  derivatives revealed that almost 9000 structures exist with the ferrocene structure. No complex like **21.79** has yet been prepared, but MO calculations [45] indicate a substantial HOMO–LUMO gap that implies some kinetic stability. The CH interactions with the ferrole ring are very similar in magnitude to those between the  $\text{FeCp}$  and  $\text{Cp}$  fragments in ferrocene. Since Fe is quite electropositive in comparison with C, there are two high lying Fe–C  $\sigma$  levels in the nonclassical isomer, **21.79**, which are not matched in ferrocene. Consequently, **21.79** is computed to be much less stable than the classical structure of ferrocene. Provided that there is a symmetry-allowed pathway from **21.79** to **21.78** (and there is one), there is probably not much chance of ever experimentally observing the nonclassical structure. However, given that there is nothing “wrong” with the basic orbital pattern in **21.79**, it might be possible to devise strategies that will overcome the thermodynamic problem and enable the synthesis of a derivative. One solution that comes quickly to mind is to replace the apical carbon atom with boron. B3LYP calculations [45] find two minima: the classical structure, **21.80**, where the BH group is incorporated in the five-membered ring, and the nonclassical species, **21.81**, where the BH is in the apical site. With a large triple zeta plus polarization basis, **21.81** is 37 kcal/mol higher in energy than **21.80**. Certainly, there are other paths to follow. The important point to recognize here is that the isolobal analogy has led us to consider a very unusual structure for a well-known compound. Several other examples where a  $\text{Fe}(\text{CO})_3$  group in transition metal complexes has been replaced by  $\text{CH}^+$  or BH can be cited [44], which lead to unusual structural possibilities. The isolobal analogy does not tell us whether or not these structures are stable ones, however. Rearrangement to a lower energy structure should always be considered. The isolobal analogy does give us compounds that have a similar electronic structure in terms of the number, symmetry type, and occupation of frontier molecular orbitals.

$\text{Cp}_3\text{Rh}_3(\text{CO})_3$ , **21.36**, and  $\text{Cp}_2\text{Rh}_3(\text{CO})_5^-$ , **21.37**, can be classified as being cyclopropane derivatives. It was proposed [9] that  $\text{Cp}_3\text{Rh}_3(\text{CO})_2$  would either have a triplet ground state or undergo a Jahn–Teller distortion. Using the isolobal analogy easily demonstrates that this should be the case. In **21.82**,  $\text{CpRh}$  is isolobal to  $\text{CH}^+$ . The two

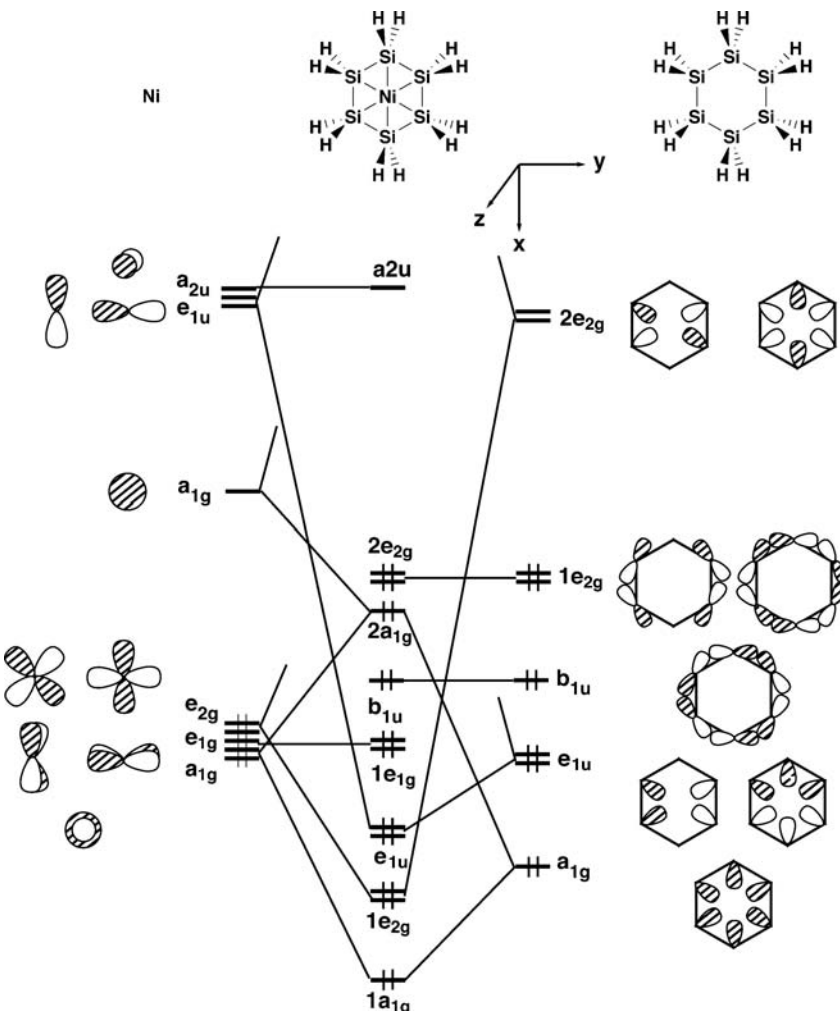


carbonyls are removed, each leaving their two electrons from the  $3\sigma$  MOs with the cluster. This generates the cyclopropenium anion, **21.83**, which has two electrons in the  $e''$  set (see Figure 12.5). A few years later, two compounds with the formula  $(Cp^*)_3M_3(CO)_2$  ( $M = Co, Rh$ ) were isolated, having the structure **21.82** [45]. The compound with  $M = Co$  was shown to exist in solution as a temperature-dependent equilibrium mixture of singlet and triplet spin states [46a]. On the other hand, the  $M = Rh$  compound [46b] was exclusively a singlet molecule and Jahn–Teller distorted, so that there were two short Rh–Rh distances and one long one. Furthermore, the two carbonyl ligands were shifted off-center, towards the longer Rh–Rh bond.

Fenske and coworkers [47] prepared and structurally categorized an unusual compound, **21.84**. The molecule has a  $NiP_6$  core that is planar. One would normally



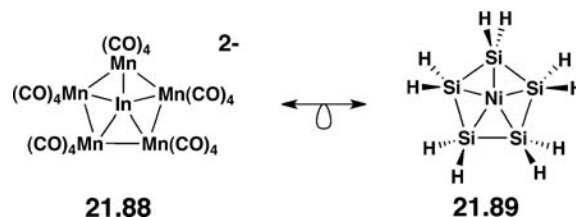
count the  $P(t\text{-}Bu)$  groups as two-electron  $\sigma$  donors. This would make **21.84** a 22-electron complex. That clearly cannot be right and, furthermore, the  $P$ – $P$  bond distances were found to be  $2.29\text{ \AA}$ , which are only  $0.08\text{ \AA}$  longer than that in  $P_6(t\text{-}Bu)_6$ . But, if they are two-electron  $P$ – $P$  bonds in **21.84**, then what holds the Ni inside the  $P_6(t\text{-}Bu)_6$  ring? Rather than working through the electronic details in **21.84**, we shall use the isolobal analogy to generate a more symmetrical compound. A  $P(t\text{-}Bu)$  group, **21.85**, is isolobal to  $SiH_2$ , **21.86**; replacement of the R group with H and protonation of the lone pair in **21.85** generates  $PH_2^+$ , which is isoelectronic to  $SiH_2$ . Therefore, **21.84** is isolobal with **21.87**, which is a flat silacyclohexane with a nickel atom stuck in the middle of it! An interaction diagram for this molecule is shown in Figure 21.2. In the left side are the AOs for the nickel atom. In the right side, we have used the radial and tangential orbitals of six  $SiH_2$  units to construct the MOs of silacyclohexane. Three radial and three tangential combinations make up the six  $Si$ – $Si$   $\sigma$  bonds. At high energy are two empty  $Si$ – $Si$  antibonding MOs that will figure into our analysis. The lowest radial combination,  $a_{1g}$ , overlaps with Ni s and  $z^2$  (the coordinate system is shown at the top right of Figure 21.2). A typical three-orbital pattern is formed with the bonding and nonbonding combinations filled. The filled Ni  $x^2-y^2$  and  $xy$  orbitals strongly overlap with the radial  $2e_{2g}$  set and are stabilized. Finally, Ni x and y stabilize the filled  $e_{1u}$  radial set on  $Si_6H_{12}$ . So, there are five stabilizing interactions between the two partners. Notice that the tangential  $b_{1u}$  MO is rigorously nonbonding. The  $1e_{2g}$  set has the correct symmetry to interact with Ni  $x^2-y^2$  and  $xy$ , but the overlap (particularly compared to  $2e_{2g}$ ) is very small. Thus, considerable  $Si$ – $Si$   $\sigma$  bonding remains in the complex. The electronic structure of **21.87** strongly resembles that in a 16-electron  $ML_3$  complex. The filled  $1e_{2g}$ ,  $1e_{1g}$ , and  $2a_{1g}$  MOs correspond to the  $e'$ ,  $e''$ , and  $a'_1$  orbitals, respectively, of  $D_{3h}$   $ML_3$  in Figure 18.3 and the discussion around it. The one exception is that  $1e_{2g}$  in the present case is greatly stabilized by

**FIGURE 21.2**

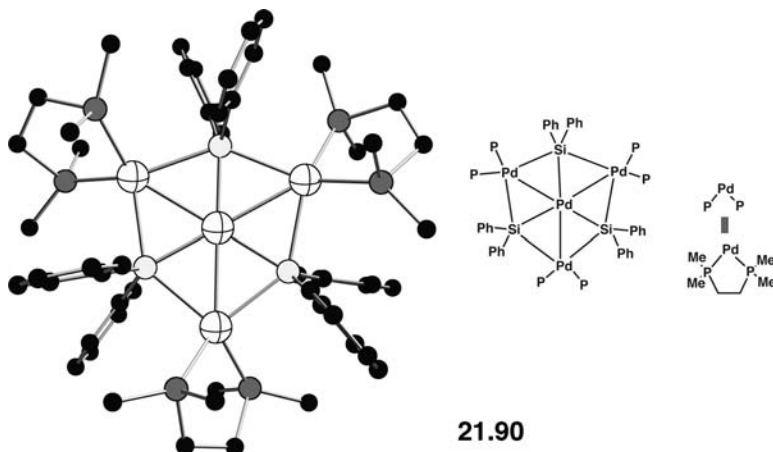
Orbital interaction diagram for  $\text{Ni}(\text{Si}_6\text{H}_{12})$  in  $D_{6h}$  symmetry.

the silicon radial set. **21.87** is computed [48] to be thermodynamically stable with respect to ground state Ni and silacyclohexane.

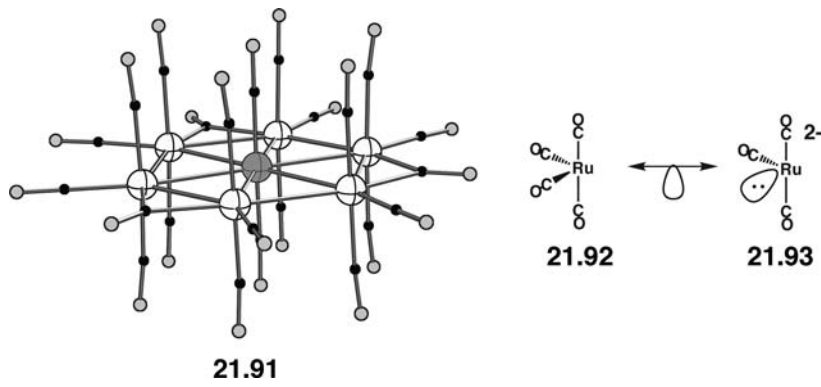
In **21.88** [102], the central atom is a main group element while the ring is composed of transition metal fragments. Counting the latter as  $\text{Mn}(\text{CO})_4^-$  groups



makes them isolobal to  $\text{SiH}_2$ ; therefore, the central atom is  $\text{In}^{3+}$ .  $\text{In}^{3+}$  has an empty s and p set of AOs and thus is isolobal in this case to  $\text{Ni}^0$ . **21.89** is also predicted [48] to be thermodynamically stable. Another example is given by **21.90** [49]. Here, the  $\text{PdL}_2$  group is isolobal to  $\text{SiR}_2$  and, therefore, **21.87** and **21.90** are isolobal. The



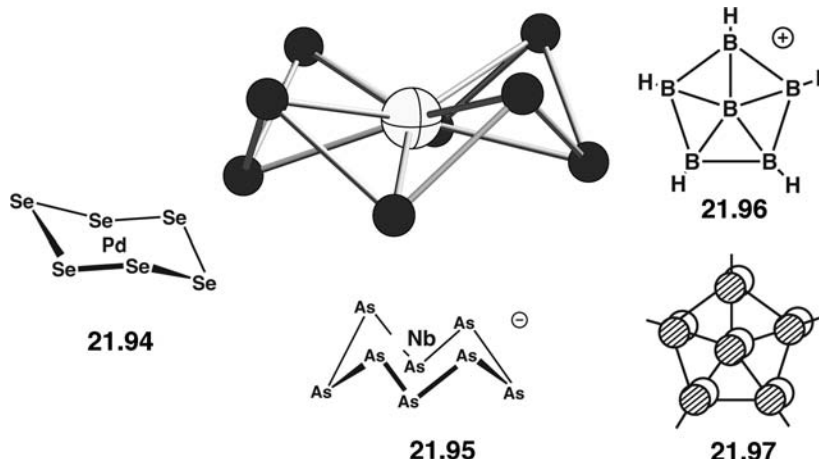
compound  $\text{H}_2\text{Pd}[\text{Re}(\text{CO})_4]_4[\text{SbPh}_2]_2$  has a similar structure [50] with a Pd atom in the middle of the  $\text{Re}_4\text{Sb}_2$  six-membered ring. Removing two protons and counting the two  $\text{SbPh}_2^+$  fragments makes them isolobal to  $\text{SiH}_2$ . This leaves four  $\text{Re}(\text{CO})_4^-$  units isolobal to  $\text{SiH}_2$ . Thus,  $\text{H}_2\text{Pd}[\text{Re}(\text{CO})_4]_4[\text{SbPh}_2]_2$  is isolobal to **21.87**. There are three criteria for designing stable alternative structures isolobal to **21.87** or **21.89**. The central atom must be a  $s^0p^0$  main group or  $d^{10}$  transition metal. The five or six-membered rings should have  $6$  electron  $\text{AH}_2$ ,  $\text{AH}$  or  $\text{A}$  groups and/or isolobal  $\text{ML}_n$  fragments. Finally, there is a size match between the size of the central atom and the “hole” in the ring. In other words, the central atom–ring atom distances and inter-ring distances need to be reasonable. In this regard, consider the  $\text{Ni}(\text{C}_6\text{H}_{12})$  analog of **21.87**. For an analogous  $D_{6h}$  geometry, the  $\text{Ni}–\text{C}$  distance should be around  $2.0\text{ \AA}$ , but then a  $\text{C}–\text{C}$  distance of  $2.0\text{ \AA}$  is much too long. Consequently, the  $D_{6h}$  geometry is not a minimum; it distorts to the  $D_{3h}$  trisethylene structure, **19.36** [48]. A number of extensions can be made to this pattern. For example,  $\text{IrRu}_6(\text{CO})_{23}^-$  is shown in **21.91** [51]. It has essentially  $D_{3h}$  symmetry. In this particular case, the central Ir atom is coordinated on both sides of the ring by carbonyl groups. Thus, Ir will use its  $z^2$  AO (the  $z$  axis lies along the  $\text{Ir}(\text{CO})_2$  axis). Furthermore, unlike the  $\text{AH}_2$  and  $\text{ML}_2$  examples that



we have treated, the ring Ru atoms have filled orbitals from their “ $t_{2g}$ ” sets that point directly toward the central Ir atom (see the  $1a_1$  MO in Figure 19.1 and 19.2). Consequently, the Ir  $x^2-y^2$  and  $xy$  AOs need to be empty. This means that the Ir atom should be in the +5 oxidation state with a  $d^4$  electron count. There are then six electrons that must be apportioned to the ring metal atoms. Making the normal assumption that the three bridging carbonyls are assigned as being terminal generates three  $\text{Ru}(\text{CO})_4$  groups, isolobal to  $\text{SiH}_2$ . The remaining three  $\text{Ru}(\text{CO})_3$  groups

then each accept a lone pair which, as shown in **21.92** and **21.93**, make them isolobal. This idea of using a lone pair in place of a hydrogen atom or carbonyl group will be used again in Chapter 22. So, the electronic structure of **21.91** can be traced all the way back to that in **21.84** by using the isolobal analogy.

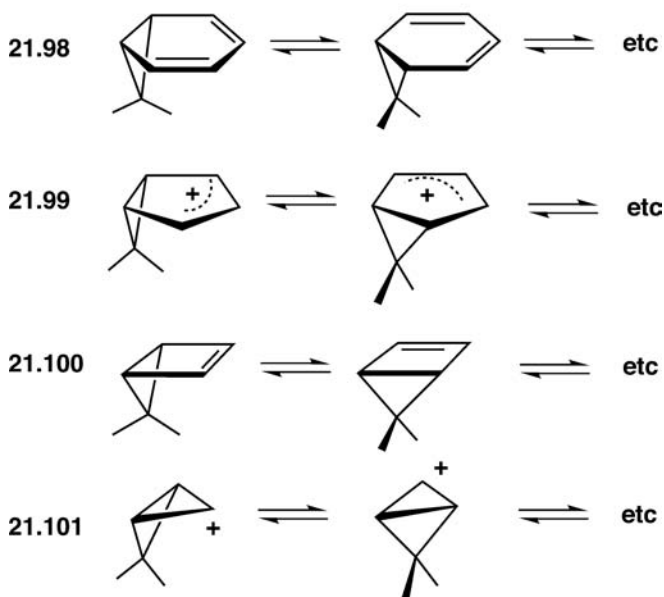
In **21.84**, the lone pair on the P(t-Bu) groups point away from the center of the ring in alternating directions. There is a theoretical prediction [51] that **21.94** should be stable in a  $D_{3d}$  geometry. A flat,  $D_{6h}$  structure is not favored because this



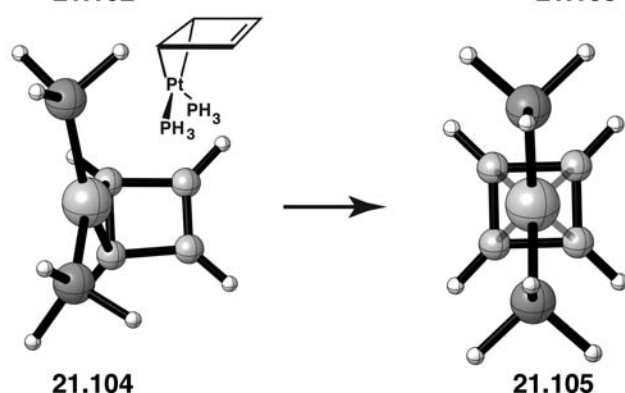
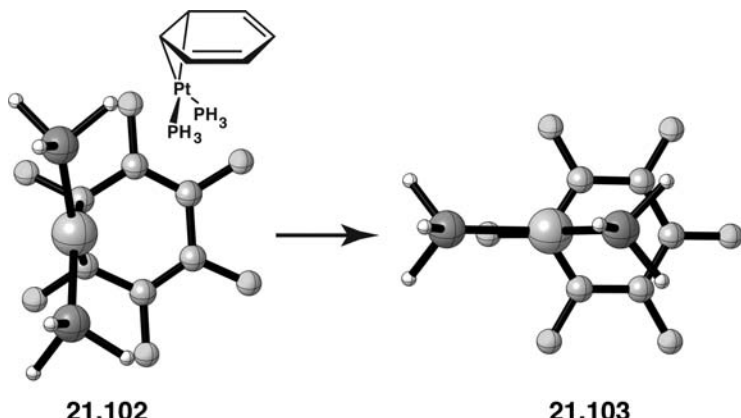
maximizes lone pair—lone pair repulsions on the Se atoms around the ring. For larger rings, for example, seven and eight-member rings, the radial combination analogous to  $2e_{2g}$  is filled so the metal should have a count of four less electrons that keep  $x^2 - y^2$  and  $xy$  empty [51]. To our knowledge, no  $d^6 A_7M$  or  $A_8M$  compound has been prepared. A somewhat different motif, however, is presented by a series of  $d^0 A_8M$  ( $A = \text{As, Sb}$ ) complexes [52]. An example is shown in **21.95**. The ring can be regarded as  $\text{As}_8^{8-}$ , and all of the metal  $d$  AO s are involved in bonding to the cycle [53]. There should also be examples of compounds with all main group atoms. So far, only theoretical models exist and these contain stabilized  $\pi$  conjugation around the ring. One example is given by **21.96** [54]. Here, counting the central boron atom as  $\text{B}^{3+}$  yields two-center–two-electron bonds around the ring and one  $\pi$  MO, **21.97**, filled. A number of other compounds with no hydrogens around the ring and outwardly pointing radial, lone-pair-type orbitals partially filled have also been reported, for example,  $\text{CB}_6^-$ , as well as compounds with boron atoms in the rings and transition metals in the center [55,56].

## 21.5 REACTIONS

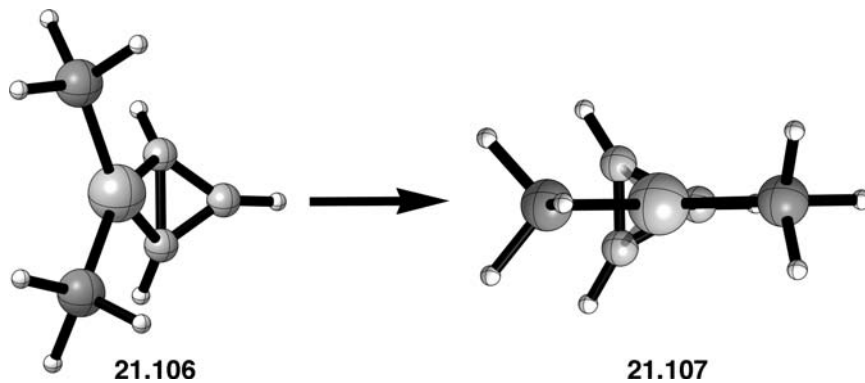
In the preceding discussion, we have used the isolobal analogy to generate new compounds and to provide conceptual links between classes of known molecules. It can also be used to provide clues about reaction mechanisms. Because the overlap and energy of isolobal fragment may widely vary, there often will be sizable differences in activation energies and, as we shall see, even differences in the reaction mechanism. Four problems are briefly outlined here. Circumambulation or the walk rearrangement is a reaction in organic chemistry wherein a  $\text{CH}_2$  (or  $\text{CR}_2$ ) group migrates around the periphery of a polyene ring by a sequence of sigmatropic rearrangements [57]. Four examples are shown in Scheme 21.2. The walk rearrangement in norcaradiene, **21.98**, has had a long history associated with it. The Woodward-Hoffmann orbital symmetry rules predict that the rearrangement should occur with retention of configuration at the migrating  $\text{CH}_2$  center. Experimentally [58],

**Scheme 21.2**

the reaction has been shown instead to proceed with inversion of configuration due to “subjacent orbital control” [59]. Theory’s most recent results have been ambivalent [60]. Transition states for both stereochemistries were located and found to be within 1 kcal/mol of each other. Circumambulation in bicyclo[2.1.0]pentene, **21.100**, has been shown to take place via the symmetry-allowed inversion of configuration by both experiment [61] and theory [62]. Let us replace the CH<sub>2</sub> groups in **21.98** and **21.100** with the isolobal Pt(PR<sub>3</sub>)<sub>2</sub> group. Several η<sup>2</sup>-benzene complexes, drawn in **21.102**, with a metallacyclopropane

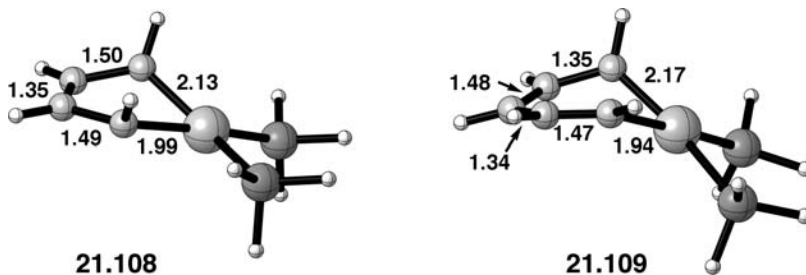


formulation have been prepared, and their analogous walk rearrangement is quite facile [63]. These reactions are called ring whizzing in organometallic chemistry. It is important to realize that the CH<sub>2</sub> and Pt(PR<sub>3</sub>)<sub>2</sub> groups need to have orientations perpendicular to each other. Notice in **21.18** that the b<sub>2</sub> MO is perpendicular to the CH<sub>2</sub> plane, but the analogous orbital for Pt(PR<sub>3</sub>)<sub>2</sub> lies in the PtP<sub>2</sub> plane. So, going from CH<sub>2</sub> in norcaradiene to the isolobal benzene-Pt(PR<sub>3</sub>)<sub>2</sub> analog requires a rotation by 90°. Interestingly, M06 hybrid density functional calculations [45] give **21.103** as the transition state for the rearrangement of C<sub>6</sub>F<sub>6</sub>Pt(PH<sub>3</sub>)<sub>2</sub>. This is the symmetry-allowed path, in other words, subjacent orbital control is not an important factor in setting the reaction mechanism for the organometallic compound. It is the fact that the b<sub>2</sub> orbital on Pt is so much more diffuse than the p AO on C that creates this difference. There are no d<sup>10</sup> Pt(PR<sub>3</sub>)<sub>2</sub> analogs of **21.100** that have been prepared. M06 calculations predict an η<sup>2</sup> ground state, **21.104**. The transition state for the rearrangement in **21.100** involves slippage and rotation, whereas the transition state for the organometallic analog, **21.105**, just involves slippage. Both reactions obey the Woodward–Hoffmann selection rules. Compared to the organometallic rearrangements, the organic compounds have widely different energies. **21.98** and **21.100** require about 47 and 28 kcal/mol, respectively. In **21.102** and **21.104**, the barriers are 3.6 and 9.9 kcal/mol, respectively. This is again a reflection of the different overlaps and relative energies for the isolobal fragments. The binding energies of C—C bonds are much stronger than the Pt—C bonds in these examples. Circumambulation in **21.99** requires about 15 kcal/mol and is a symmetry-allowed slippage plus rotation mechanism [64]. The Pt(PH<sub>3</sub>)<sub>2</sub> analog is predicted to require a minuscule 0.5 kcal/mol with direct slippage to an η<sup>5</sup> geometry [45]. The rearrangement of **21.106** to **21.107** actually has been observed experimentally [65] for a series of C<sub>3</sub>Ph<sub>3</sub>M(PPh<sub>3</sub>)<sub>2</sub><sup>+</sup> complexes where M is Pt, Pd, Ni. The x-ray structures [65] of four members in this class of compounds show a progression of geometries from the η<sup>2</sup> species, **21.106**, to the transition state, **21.107**, for the rearrangement. It is therefore possible to chart the reaction path experimentally via these structures. M06 calculations on C<sub>3</sub>H<sub>3</sub>Pt(PH<sub>3</sub>)<sub>2</sub><sup>+</sup> give an activation barrier of 2.8 kcal/mol for this process. The organic analog, **21.01**, undergoes this rearrangement with a barrier of about 20 kcal/mol [66].



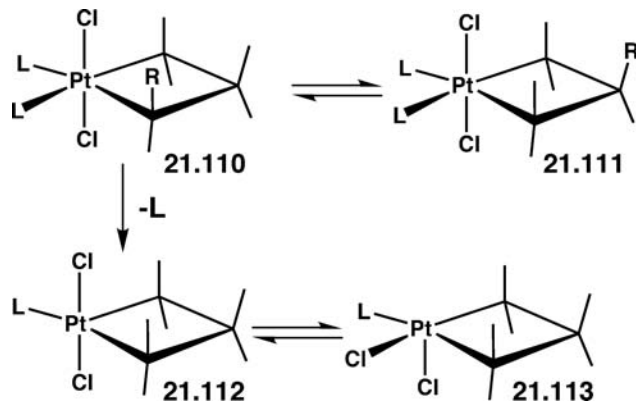
The walk rearrangement in **21.98** and **21.101** is experimentally complicated by an electrocyclic ring-opening reaction to give 1,3,5-cycloheptatriene and the cyclobutenyl cation, respectively. The barriers were found to be 11 and 8 kcal/mol for **21.98** [60] and **21.101** [67], respectively. The disrotatory ring-opening reactions are symmetry allowed in both cases. The isolobal analogs, **21.102** and **21.106**, also are predicted to have low barriers (29.3 and 4.6 kcal/mol, respectively) with symmetrical, symmetry-allowed transition states [45]. The most interesting case is presented by **21.100** and its isolobal partner, **21.104**. The disrotatory ring opening is symmetry

forbidden; in that, there is a HOMO–LUMO crossing if  $C_s$  symmetry is retained along the reaction path. The conrotatory path is geometrically impossible. Therefore, the experimental activation barrier for the ring opening of **21.100** to cyclopentadiene is 26.3 kcal/mol despite the fact that the reaction is exothermic by a gigantic 47.8 kcal/mol [68]. Similarly, the reaction of **21.104** to platinacyclopentadiene is computed to require 49.5 kcal/mol, and yet, the reaction is exothermic by 23.0 kcal/mol [45]. The structure of the transition state is displayed in **21.108**.



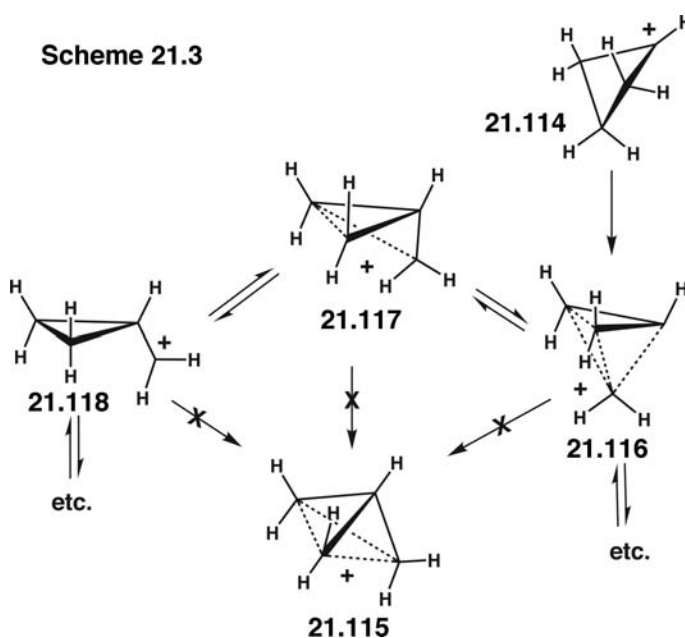
The HOMO–LUMO crossing is weakly avoided (see Section 4.7) by forcing the two Pt–C bond distances to be unequal. The ring-opening in  $\eta^3$ -cyclopentadienyl-Pt(PH<sub>3</sub>)<sub>2</sub><sup>+</sup> is also symmetry forbidden [45]. The activation barrier here is computed to be 54.7 kcal/mol. Here, the HOMO–LUMO crossing is avoided by undergoing a bond length distortion of the Kekulé-type shown in **21.109** [45,69].

The 1970s and 1980s witnessed the advent of mechanistic organometallic chemistry. The platinacyclobutanes shown in **21.110**, where L = pyridine, Cl<sup>−</sup>, THF, and so on, undergo a very interesting, facile rearrangement to **21.111**. It



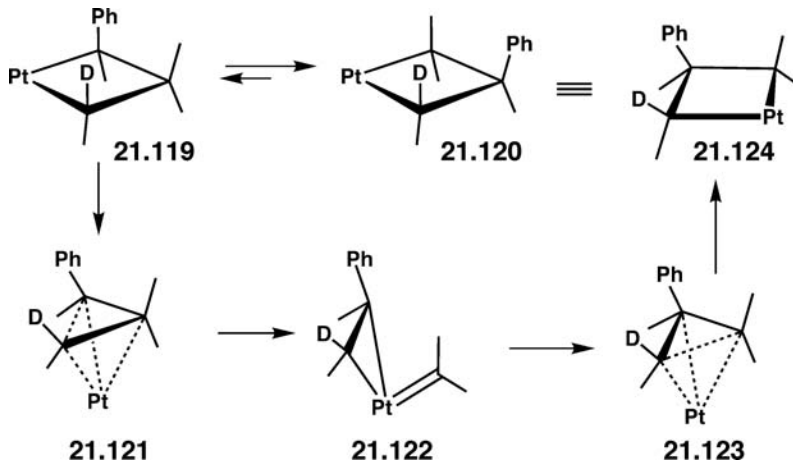
can be shown that the R group does not migrate from **21.110** to **21.111**. In fact, the  $\alpha$  carbon and its substituents change position with the  $\beta$  carbon. Another experimental detail is that ligand loss to give **21.112** and possible rearrangement to **21.113** precedes the rearrangement. **21.110** is a saturated 18 electron complex; thus, the PtL<sub>2</sub>Cl<sub>2</sub> fragment is isolobal to CH<sub>2</sub>. Losing a ligand (e.g., Cl<sup>−</sup>) from **21.110** to give **21.112** then generates a species isolobal to the cyclobutyl cation. Now, the structure and dynamics associated with the cyclobutyl cation, **21.114**, has a long history associated with it. Low temperature NMR has shown [70] that the three methylene groups are equivalent; however, the C<sub>3v</sub> structure, **21.115**, at the bottom of Scheme 21.3 cannot be the ground state for the C<sub>4</sub>H<sub>7</sub> cation. Each CH<sub>2</sub> group

Scheme 21.3



has a  $p$  AO associated with it. There is an e set at low energy with two electrons in it and a higher-lying  $a_2$  combination. Therefore, on the singlet manifold, 21.115, is Jahn–Teller unstable. Calculations [71] demonstrate that the cyclobutyl cation rearranges through three structures, 21.116–21.118, as illustrated in Scheme 21.3. The categorization of these stationary points as transition states or intermediates has proven to be difficult since they lie within 1–2 kcal/mol of each other depending upon the computational method. Thus,  $C_4H_7^+$  is like  $CH_5^+$  (see 14.57–14.59 and the discussion around it)—a molecule without a structure.

Returning to the platinacyclobutane problem, Casey and coworkers [72] provided two definitive stereochemical experiments that relate to the reaction mechanism. First, a crossover experiment showed that the reaction was intramolecular. Second, 21.119



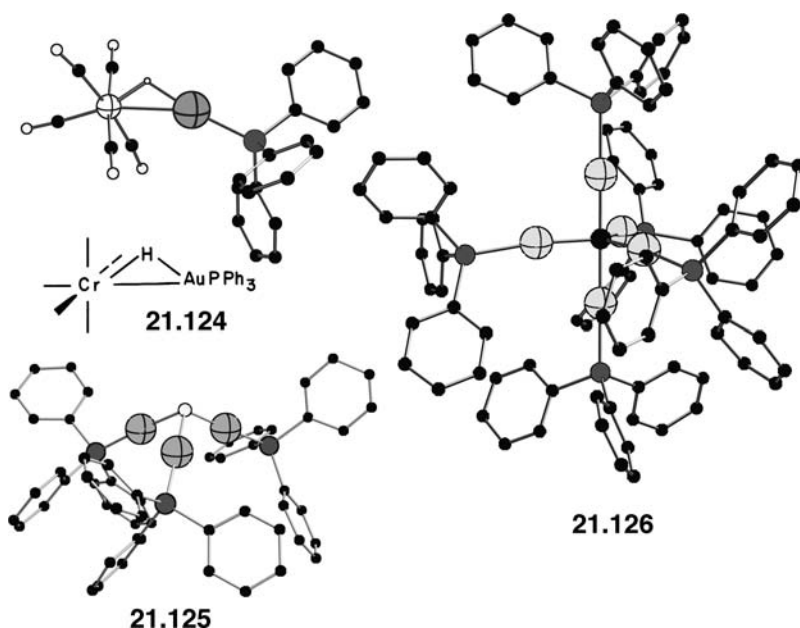
rearranged exclusively to 21.120. This stereochemical outcome puts severe limitations on the nature of the reaction mechanism. Using the isolobal analogy [73], the “open” cyclobutyl cation generated from 21.119 rearranges to structure 21.121 that is isolobal to the symmetrical ( $C_s$ ) bicyclobutyl cation, 21.116. Then, 21.121 rearranges to the isolobal analog of the cyclopropylcarbinyl cation (21.118), given by 21.122. Notice that this compound is a five-coordinate, 18-electron olefin carbene

complex. **21.122** can undergo the reverse reaction, this time leading to **21.123**, which then ring opens to **21.124**. Extended Hückel calculations [73] on  $C_3H_6PtCl_3^-$  yield a potential energy surface akin to the Mexican hat surface in Figure 7.7. Structures A–D correspond to the three “closed” geometries, **21.121** (and **21.123**) along with the three olefin–carbene complexes, **21.122**. The high point on the potential energy surface, E, is a tris–carbene complex. It is isolobal to the  $C_{3v}$   $C_3H_7^+$  geometry, **21.115** in Scheme 21.3. It is fair to say that the *a priori* construction of a reaction mechanism going from **21.119** to **21.124** would tax even the most feverish imagination. Recognizing the connection to the cyclobutyl cation and then using the isolobal analogy to predict intermediate structures is a much easier task.

We would be remiss to not offer another important caveat when using the isolobal analogy to predict reaction mechanisms. This involves reactions where spin crossing may or may not take place. An illustration is the insertion of  $CH_2$  into a C–H bond. The reaction pathway [74] for singlet  $CH_2$  involves a one step process with a three-center cyclic transition state. Retention of configuration is observed if the insertion occurs at a chiral carbon. On the other hand, triplet  $CH_2$  undergoes a radical type of abstraction mechanism [74]. We have seen before that  $CpML$  ( $M = Co, Rh$  and  $Ir$ ;  $L = CO, PR_3$ ) is isolobal to  $CH_2$ . In each case, the triplet state lies lower in energy than the singlet [75]. The potential energy surface for the triplet  $CpML$  interacting with  $CH_4$  is repulsive. It undergoes a crossing to the singlet state that ultimately forms the  $CpM(CH_3)(H)L$  insertion product. The energy, the effects of spin-orbit coupling, and the efficiency associated with this state crossing are complicated affairs and will not be discussed here [75].

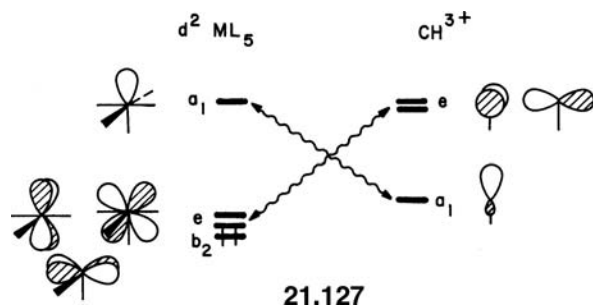
## 21.6 EXTENSIONS

The compounds that we have discussed in this chapter were either saturated or, at most, two electrons short of being saturated. Chapter 22 treats borane and transition metal clusters that are very electron deficient. A tool for comparing these compounds and predicting their structures will be described by employing these isolobal ideas. A  $(Ph_3P)Au^+$  fragment can be regarded as being derived from a linear, 14-electron,  $d^{10}$   $ML_2$  species. It is then isolobal to  $CH_3^+$  or  $Cr(CO)_5$ , so **21.124** can be related

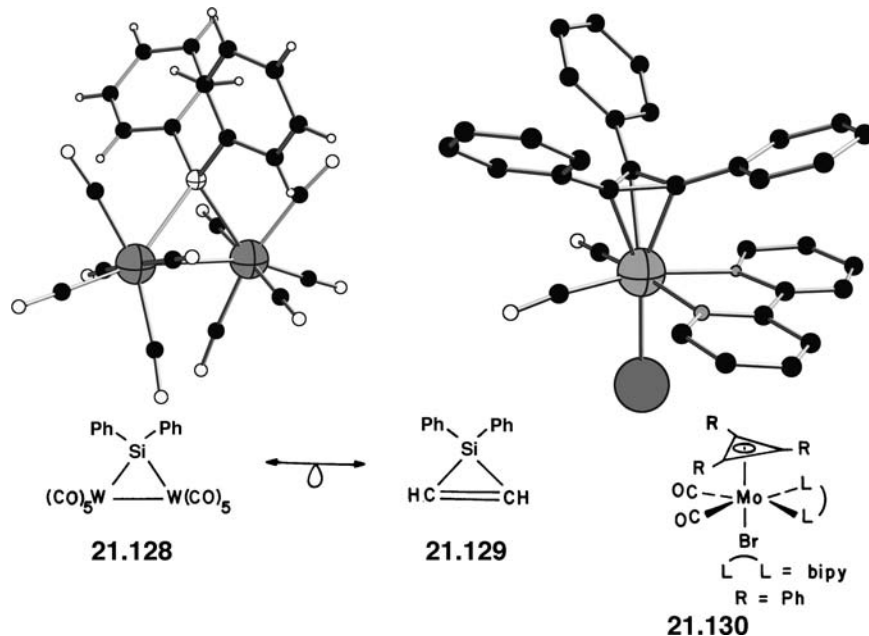


to **21.50–21.53**.  $\text{CH}_3^+$  and  $(\text{Ph}_3\text{P})\text{Au}^+$  each have one vacant frontier orbital that also makes them isolobal to  $\text{H}^+$ . Thus, **21.124** is isolobal to the dihydrogen complex,  $\text{H}_2\text{Cr}(\text{CO})_5$ , which was discussed in Section 15.3. The structure [76] of  $\text{O}(\text{AuPPh}_3)_3^+$  is shown in **21.125**. It is isolobal to the hydronium ion.  $\text{C}(\text{AuPPh}_3)_5^+$ , **21.126** [77], has a remarkable trigonal bipyramidal geometry at carbon. The structure of the isolobal  $\text{CH}_5^+$  was discussed in Section 14.3; the trigonal bipyramid is actually at high energy relative to several distorted structures. The structure of  $\text{HCo}(\text{CO})_4$  closely resembles that of  $(\text{Ph}_3\text{PAu})\text{Co}(\text{CO})_4$  [78]. In fact, there is a beautiful mapping between the structures of transition metal clusters containing the  $\text{Au}(\text{PR}_3)$  unit and those with an H atom [79,80].

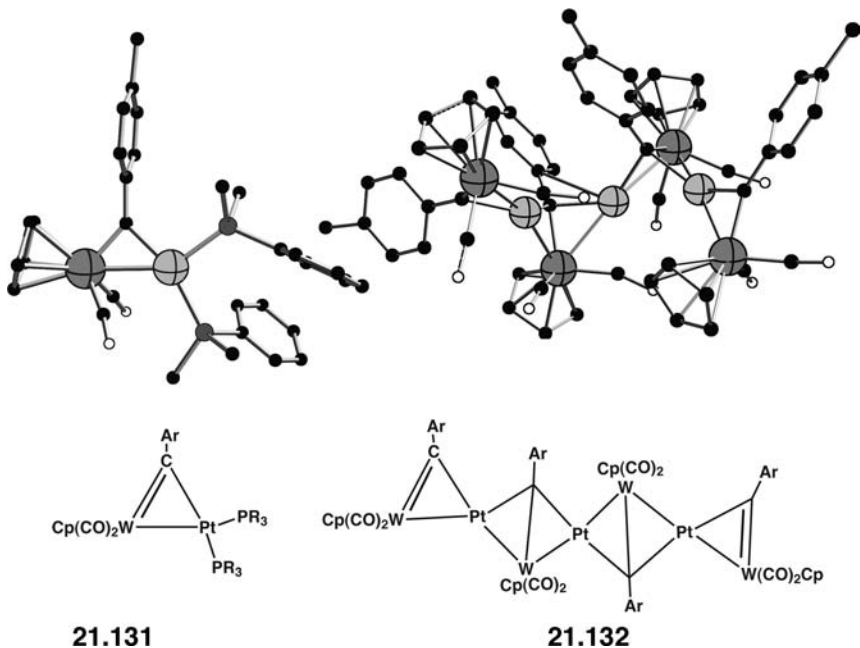
We have only used the isolobal analogy for transition metal complexes with coordination numbers up to six. For coordination numbers of 7–9, the members of the  $t_{2g}$  set must be utilized. Reference back to the generalized interaction diagram of Figure 16.2 shows that when  $n$  ligand donor levels interact with a transition metal,  $n$  M—L bonding and  $n$  M—L antibonding molecular orbitals are formed. Left behind are  $9-n$  nonbonding orbitals that are localized on the transition metal. Suppose  $n = 8$ , then a  $d^2$  complex is of the saturated, 18-electron type, and one member of what corresponded to the octahedral  $t_{2g}$  set is left nonbonding. The other two members of  $t_{2g}$  are used to form interactions with the surrounding ligands. Removal of three ligands from this eight-coordinate complex generates an  $\text{ML}_5$  fragment with three empty frontier orbitals. Therefore, a  $d^2$   $\text{ML}_5$  fragment is isolobal to  $\text{CH}^{3+}$ . This is shown in **21.127** where for convenience we have used an  $\text{ML}_5$  fragment of  $C_{4v}$  symmetry (Section 17.2). Compare the relationship in **21.127** with that in **21.64** and **21.65** with three less electrons. A  $d^6$   $\text{ML}_3$  fragment is



isolobal to  $d^2 \text{ML}_5$ ! Again, the isolobal mapping of fragments is not an exact one; many permutations are possible, and the coordination number at the metal in a compound must be established before making isolobal replacements. The reader may object to the fact that the metal  $t_{2g}$  set in **21.64** lies at much lower energy than  $a_1 + e$  for  $\text{CH}_3^+$ . In **21.127**, they are at comparable energies. We are making very qualitative arguments here, but this is not so bad of an approximation. A  $d^2$  metal will be one of the far left of the periodic table; therefore, it is more electropositive than the  $d^6$  metal in a  $\text{ML}_3$  fragment. In the context of **21.128** [81], the  $\text{W}(\text{CO})_5^+$  groups



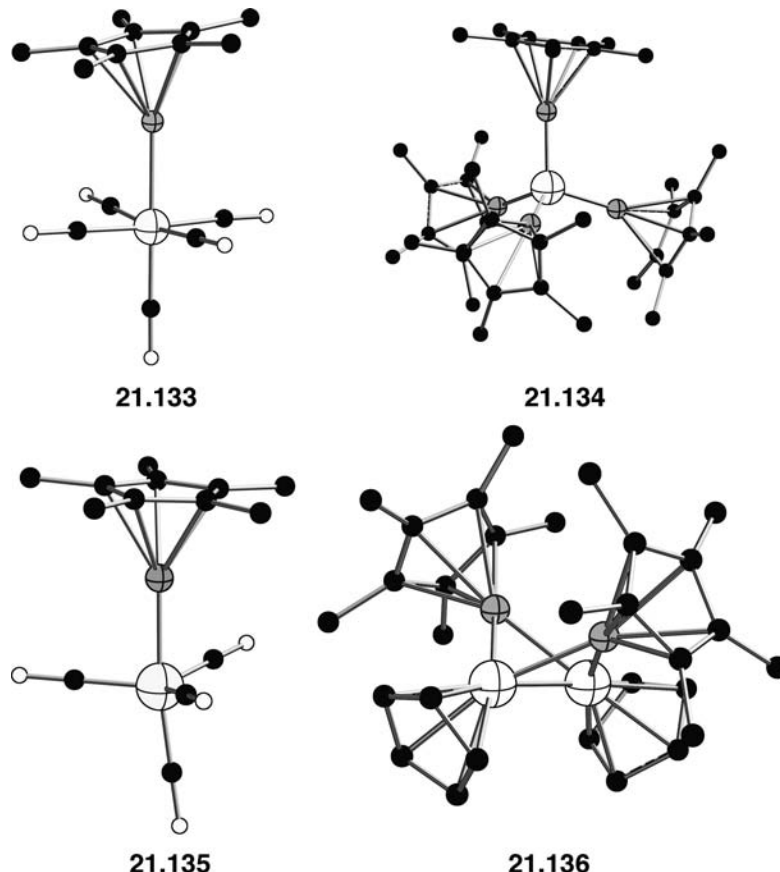
connected to  $\text{SiPh}_2^{2-}$  are  $d^5$  metals and thus isolobal to C—H. So, **21.128** is a silacyclopropene analog, **21.129**. The cyclopropenium complex **21.130** [82] is nothing more than another tetrahedrane, like **21.57–21.60**. Three carbonyls can be replaced by a  $\text{Cp}^-$  ligand, and so that  $\text{V}(\text{CO})_5$  where three electrons are distributed among the  $a_1 + e$  set in **21.127** is isolobal to  $\text{CpW}(\text{CO})_2$  and CH. **21.131** [83] can easily be related to an acetylene coordinated to  $\text{Pt}(\text{PR}_3)_2$  or to



cyclopropene by using this relationship. Stone and his group have used **21.131** as a building block to generate a series of organometallic ribbons. **21.132** [84] is an example of a 4-mer. **21.132** may look familiar. In Section 19.4, we studied the band structure of  $\text{K}_2\text{PdP}_2$  that is isolobal to a  $\text{Pd}(\text{C}_2\text{H}_2)$  or  $\text{Pt}[\text{CHCpW}(\text{CO})_2]$

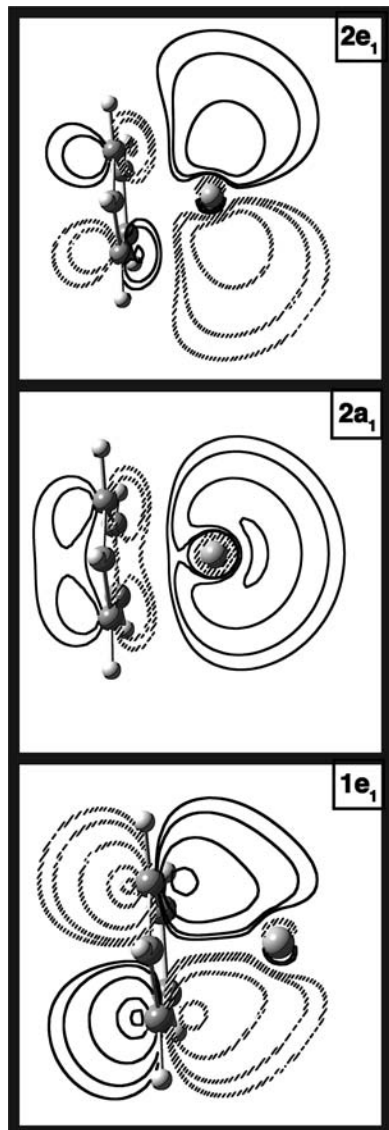
polymer! There are many more patterns that can be established when the restriction of octahedral and square planar coordination is removed [1b,85].

An interesting extension of isolobal analogs is given by a relatively new ligand,  $\text{Me}_5\text{C}_5\text{Al}$ . Structures **21.133–21.136** are some of the molecules that recently have been prepared [86]. **21.133** is  $(\text{Cp}^*\text{Al})\text{Cr}(\text{CO})_5$ ; **21.134** is  $(\text{Cp}^*\text{Al})_4\text{Ni}$  and **21.135**

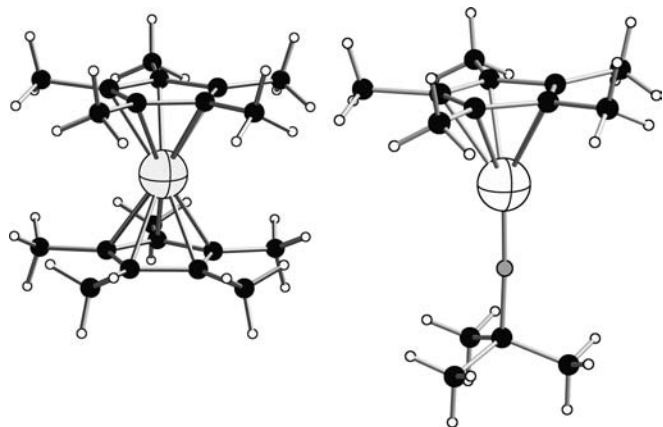


is  $(\text{Cp}^*\text{Al})\text{Fe}(\text{CO})_4$ . Their structural correspondence to  $\text{Cr}(\text{CO})_6$ ,  $\text{Ni}(\text{CO})_4$ , and  $\text{Fe}(\text{CO})_5$ , respectively, is clear. **21.136** is  $(\text{Cp}^*\text{Al})_2\text{Cp}_2\text{Ni}_2$  [87] that strongly resembles  $\text{Cp}_2\text{Ni}_2(\text{CO})_2$  in geometric terms. But, what about the electronic portion; is  $\text{Me}_5\text{C}_5\text{Al}$  an isolobal analog of CO? One can easily construct the orbitals of  $\text{CpAl}$  by interacting the  $s$  and  $p$  AOs of  $\text{Al}^+$  with the  $\pi$  orbitals of  $\text{Cp}^-$ . Contour drawings for one member of the  $1e$  and  $2e$  set along with the HOMO,  $2a_1$  are shown in Figure 21.3. These orbitals are derived from a B3LYP calculation on  $\text{CpAl}$ . The occupied  $1e_1$  set is concentrated on the  $\text{Cp}$  while the reverse is true for the empty  $2e_1$ . The HOMO in  $\text{CpAl}$  is concentrated on  $\text{Al}$  and hybridized away from the  $\text{Cp}$ . This is exactly analogous to the situation for CO (see Figure 6.8).  $\text{CpAl}$  perhaps is not as strong of a  $\pi$ -acceptor and a stronger  $\sigma$ -donor than CO [86c], but these are quantitative features that are unimportant in the isolobal analogy.

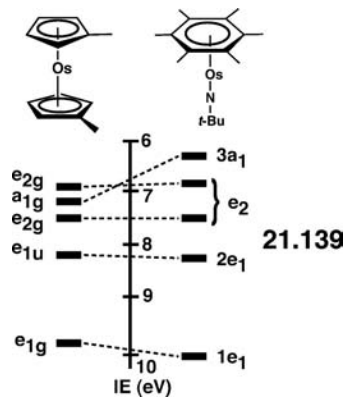
An interesting pairing exists between  $\text{Cp}^-$  and  $\text{R}-\text{N}^{2-}$  ligands.  $\text{Cp}^-$  has three occupied MOs that it uses for bonding, which have  $a''_2 + e''_1$  symmetry; see Figure 12.5.  $\text{R}-\text{N}^{2-}$  also has three filled MOs,  $2\sigma^+ + \pi$  in Figure 9.1. They have the same symmetry properties with respect to bonding with a transition metal. Thus, one can replace one  $\text{Cp}^-$  ligand in  $(\text{Cp}^*)_2\text{Os}$ , **21.137** [88], with  $(t\text{-Bu})\text{N}^{2-}$  to generate  $(\text{Cp}^*)(t\text{-BuN})\text{Os}^-$  or the isoelectronic  $(\text{Cp}^*)(t\text{-BuN})\text{Ir}$ , **21.138** [89]. The isolobal

**FIGURE 21.3**

Contour plots of the frontier orbitals for CpAl at the B3LYP level.

**21.137****21.138**

relationship between  $Cp^-$  and  $R-N^{2-}$  has been demonstrated quite clearly by comparing the PE spectra of  $(Cp^*)_2Os$  with  $(Me_6C_6)(t\text{-BuN})Os$  [90]. The assignment of the ionization potentials for  $(Cp^*)_2Os$  on the left side of 21.139 follows the development of the electronic structure in Section 20.3 (see Figures 20.13 and 20.14). The two ionizations associated with  $e_{2g}$  are due to spin-orbit coupling. On going to  $(Me_6C_6)(t\text{-BuN})Os$ , four out of the five ionizations stay at roughly the same energy. The ionization associated with  $a_{1g}$  is, however, decreased by 0.9 eV



on going to  $(Me_6C_6)(t\text{-BuN})Os$ . The  $a_{1g}$  orbital is primarily Os  $z^2$ . The overlap of  $z^2$  with the  $Cp\ a''_2$  MO is small. The nodal cone of  $z^2$  intersects with the carbon  $\pi$  MOs in the  $Cp$  ring. On the other hand, the  $2\sigma^+$  MO on R–N has maximal overlap with  $z^2$  and, therefore, will destabilize it. On going from 21.137 to 21.138, a  $Cp$  ligand has been replaced by  $(t\text{-Bu})N$ . Why not do this substitution twice for a  $Cp_2M$  fragment [91]? A  $Cp_2Hf$  or  $Cp_2Zr$  fragment then is isolobal to  $(RN)_2W$  or  $(RN)_2Mo$ . Contour plots for the three frontier orbitals in  $(t\text{-Bu})_2W$  at the B3LYP level are displayed in Figure 21.4. The reader should carefully compare these MOs with those for the  $Cp_2Zr$  fragment in 20.32. The similarity is striking. There are minor differences for the hybridization in  $1a_1$  and  $2a_1$  compared to  $Cp_2Zr$ , but this will not alter the basic chemistry. We discussed in Section 20.4 the  $d^0$   $Cp_2M$  catalysts for Ziegler–Natta polymerization. A number of olefin polymerization catalysts have been developed based on the replacement of  $Cp$  with R–N [92].

An extension can be made for the molecules that we study in Chapter 22, namely, boranes and transition metal clusters. Bridging hydrogen atoms are often found in both of these species. In general, it is not very helpful to rearrange them to a

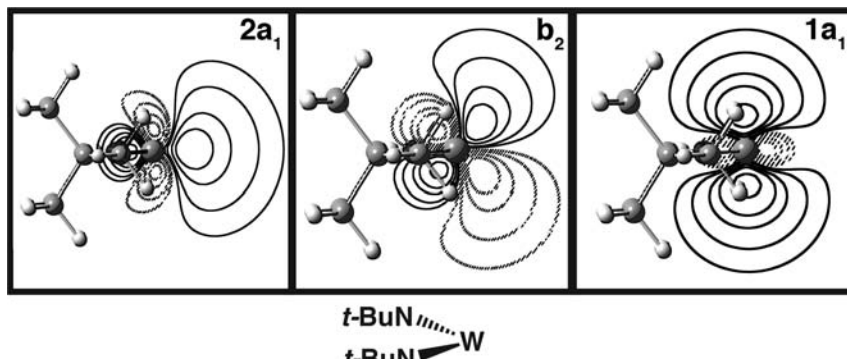
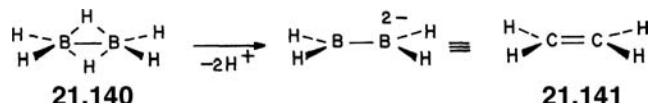


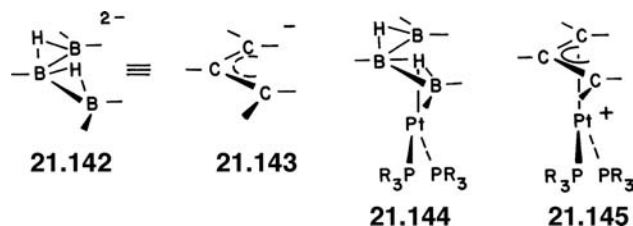
**FIGURE 21.4**

Contour plots of the three frontier orbitals in  $(t\text{-Bu})_2W$ .

terminal geometry, as we did for the bridging carbonyl groups. However, as we briefly mentioned before, it is useful to remove bridging hydrogens as protons. That may seem to be unreasonable, but actually bridging hydrogens does not change the underlying orbital structure in terms of symmetry. For example, the frontier molecular orbitals of diborane, **21.140**, were discussed in Section 10.2. Removal

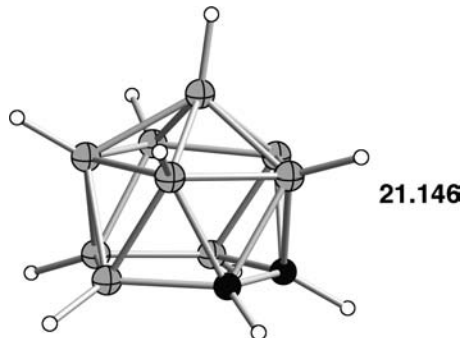


of two bridging protons gives  $\text{B}_2\text{H}_4^{2-}$ , which is isoelectronic to ethylene, **21.141**. The reader should compare the orbital structure of diborane in the right side of Figure 10.3 with ethylene in Figure 10.4 and their corresponding ionization potentials in Figure 10.6. Both have a LUMO of  $b_{2g}$  symmetry and occupied valence orbitals of  $b_{1g}$ ,  $a_g$ ,  $b_{1u}$ , and  $b_{2u}$  symmetry. To be sure, there is not an exact match in the level ordering of the occupied orbitals. For example, the  $b_{1u}$  ( $\pi$ ) orbital of ethylene is greatly stabilized by the bridging hydrogens in diborane (Figure 10.6), but we need not worry much about these quantitative details. The  $\pi$  orbitals of  $\text{B}_3\text{H}_2^{-2}$ , **21.142**,

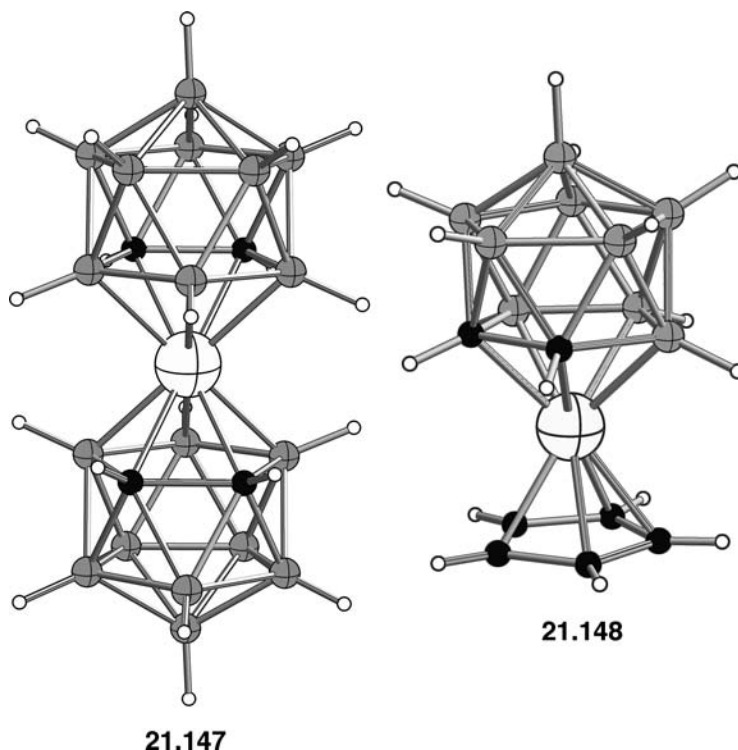


resemble those for the allyl anion, **21.143** [93]. Thus, the basic orbital interactions in **21.144** [94] are similar to those in **21.145**. A number of metallaborane analogs to sandwich compounds along these lines can be envisioned [95].

Still further connections can be made. Removing one cap from an icosahedral molecule gives a cage structure with a pentagonal open face, **21.146**. This is the structure for  $C_2B_9H_{11}^{2-}$ . Hawthorne [96] first suggested that the  $C_2B_9H_{11}^{2-}$  cage



was equivalent to  $Cp^-$ . In orbital terms, **21.146** has five frontier orbitals emanating from the open face, which have the same symmetry and occupation by electrons as the  $\pi$  orbitals of  $Cp^-$ . So, compounds like  $(C_2B_9H_{11})_2Fe^{2-}$ , **21.147** [97], and  $(C_2B_9H_{11})FeCp^-$ , **21.148** [98], have the basic ferrocene splitting pattern and orbital



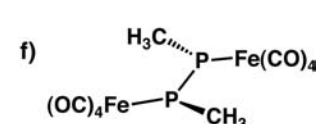
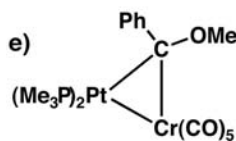
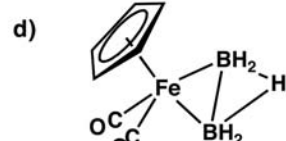
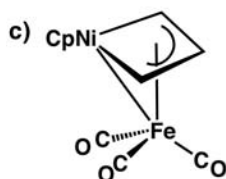
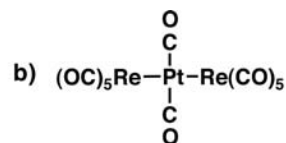
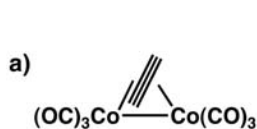
shapes [99]. How this comes about or, more precisely, the derivation of the orbital structures of large cluster compounds like **21.146** is the topic of Chapter 22.

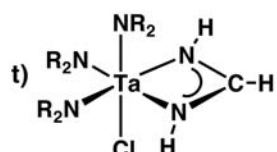
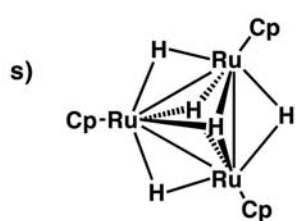
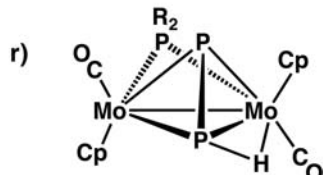
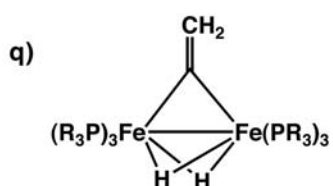
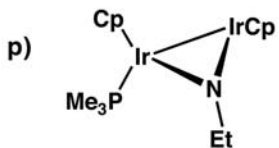
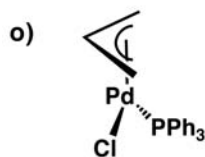
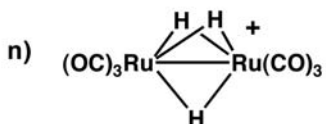
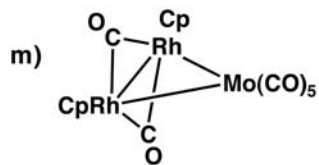
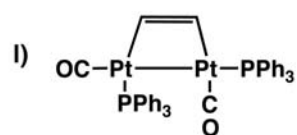
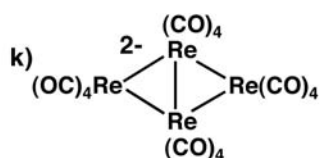
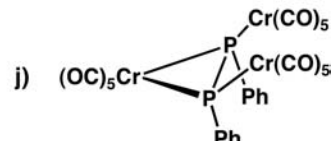
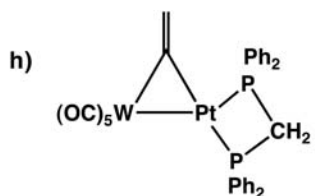
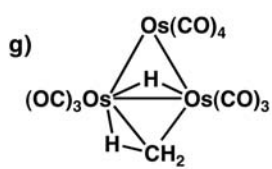
---

## PROBLEMS

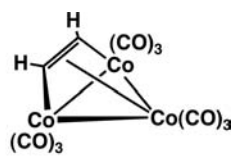
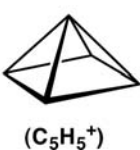
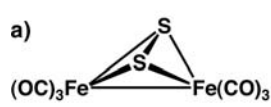
---

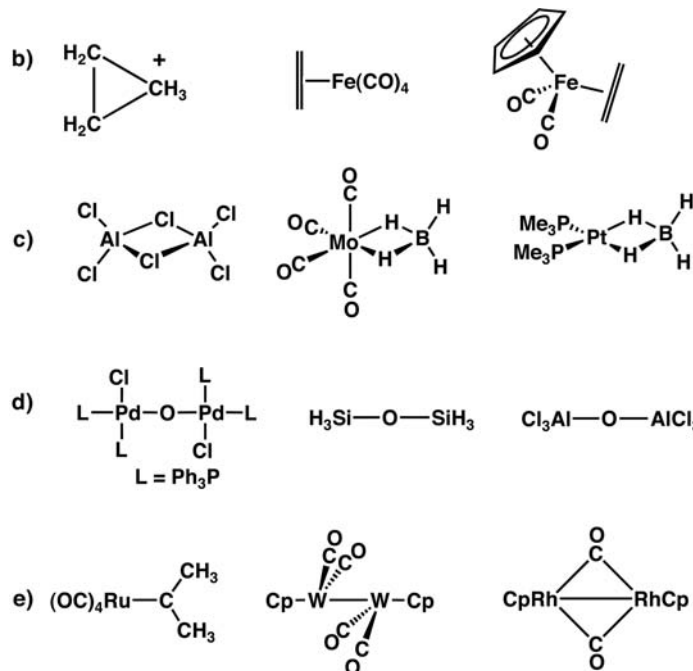
**21.1.** Draw the all-organic analog using the isolobal analogy.



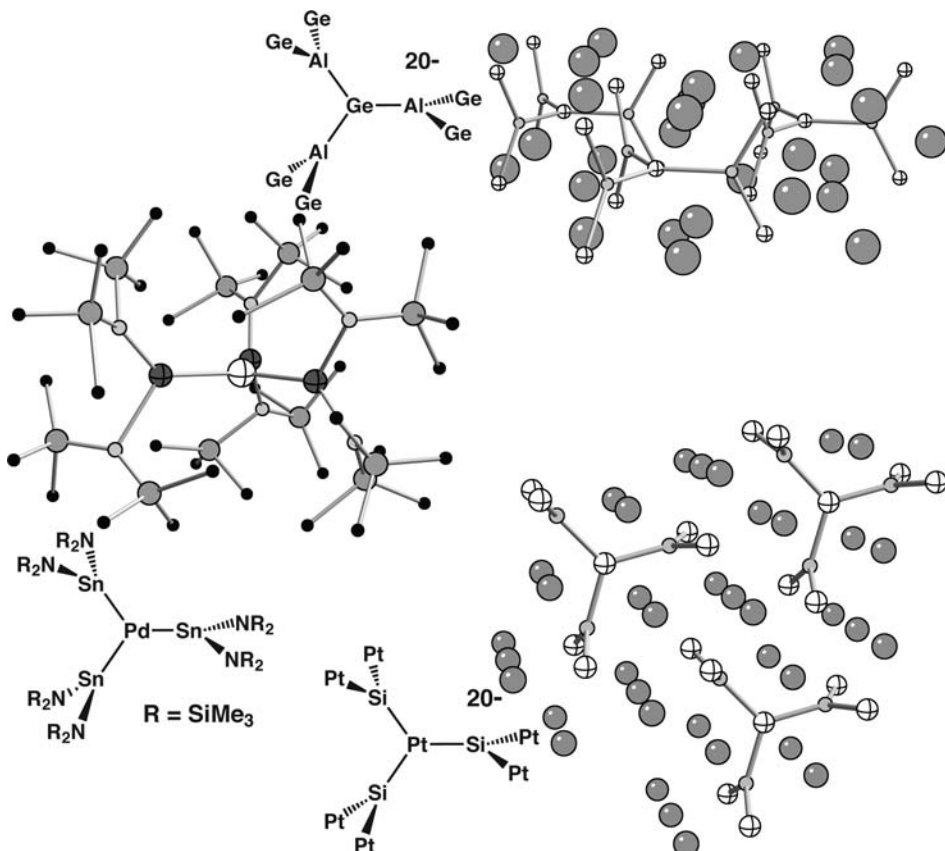


21.2. Which compound is not isolobal to the other two?





**21.3.** There are a number of compounds that have a basic  $AM_3B_6$  framework in common. The molecular compound by Al-Allaf et al. [100] on the left, below, contains a  $PdSn_3N_6$  core. There are two solid state compounds in the right side (see Reference [101])—which both have the same basic structure shown from a side view at the top, right for  $Ba_{10}Al_3Ge_7$  and from a top view for  $Ca_{10}Si_3Pt_7$  in the right bottom side.



The question is—are any of these compounds isolobal to each other? It would not (or should not) take too long to figure out that  $\text{Ba}_{10}\text{Al}_3\text{Ge}_7$  has an odd number of electrons while the other two have an even number. So, let the extra electron reside in the “sea” of Ba cations. Trying to backtrack fragments (e.g.,  $\text{SiPt}_2$ ) to something isolobal is not going to be helpful. The best approach is to figure out the bonding in each compound in a very qualitative fashion.

---

## REFERENCES

---

1. (a) M. Elian, M. M. L. Chen, D. M. P. Mingos, and R. Hoffmann, *Inorg. Chem.*, **15**, 1148 (1976); (b) R. Hoffmann, *Angew. Chem. Int. Ed.*, **21**, 711 (1982).
2. J. Halpern, *Advances in Chemistry; Homogeneous Catalysis*, No. 70, American Chemical Society, Washington, D.C. (1968) pp. 1–24.
3. K. Wade, *Chem. Commun.*, 792 (1971); K. Wade, *Inorg. Nucl. Chem. Lett.*, **8** (1972); p. 559, 563; K. Wade, *Adv. Inorg. Radiochem.*, **18** (1976).
4. D. M. P. Mingos, *Nature (London)*, *Phys. Sci.*, **236**, 99 (1972).
5. J. K. Burdett, *Coord. Chem. Rev.*, **27**, 1 (1978).
6. S. D. Ittel and J. A. Ibers, *Adv. Organomet. Chem.*, **14**, 33 (1976); L. S. Cunden and R. G. Linck, *Inorg. Chem.*, **50**, 4428 (2011).
7. F. A. Cotton and J. M. Troup, *J. Am. Chem. Soc.*, **96**, 4155 (1974).
8. M. R. Churchhill, F. J. Hollander, and J. P. Hutchinson, *Inorg. Chem.*, **16**, 2655 (1977); M. R. Churchill and B. G. DeBoer, *Inorg. Chem.*, **16**, 878 (1977).
9. A. R. Pinhas, T. A. Albright, P. Hofmann, and R. Hoffmann, *Helv. Chim. Acta*, **63**, 1 (1980) and references therein.
10. W. D. Jones, M. A. White, and R. G. Bergman, *J. Am. Chem. Soc.*, **100**, 6772 (1978).
11. R. D. Adams, G. Chen, J.-C. Lii and Wu, *Inorg. Chem.*, **30**, 1007 (1991).
12. J. Cooke, R. E. D. McClung, J. Takats, and R. D. Rodgers, *Organometallics*, **15**, 4459 (1996).
13. M. R. Burke, J. Takats, F.-W. Grevels, and J. G. A. Reuvers, *J. Am. Chem. Soc.*, **105**, 4092 (1983); K. M. Motyl, J. R. Norton, C. K. Schauer, and O. P. Anderson, *J. Am. Chem. Soc.*, **104**, 7325 (1982); B. R. Bender, R. Bertoncello, M. R. Burke, M. Casarin, G. Granozzi, J. R. Norton, and J. Takats, *Organometallics*, **8**, 1777 (1989).
14. M. Bergamo, T. Beringhelli, G. D’Alfonso, P. Mercandelli, M. Moret, and A. Sironi, *Angew. Chem. Int. Ed.*, **37**, 2128 (1998); N. Masciocchi, G. D’Alfonso, L. Garavaglia and A. Sironi, *Angew. Chem. Int. Ed.*, **39**, 4478 (2000); for a theoretical treatment of polymers isolobal to **21.41** see R. Hoffmann, C. Minot, and H. B. Gray, *J. Am. Chem. Soc.*, **106**, 2001 (1984).
15. E. O. Fischer, H.-J. Beck, C. G. Kreiter, J. Lynch, J. Muller, and E. Winkler, *Chem. Ber.*, **105**, 162 (1972); H. LeBozec, A. Gorgues, and P. H. Dixneuf, *J. Am. Chem. Soc.*, **100**, 3946 (1978).
16. M. Green, J. A. K. Howard, R. M. Mills, G. N. Pain, F. G. A. Stone, and P. Woodward, *Chem. Commun.* 869 (1981).
17. J. D. Cotton, S. A. R. Knox, I. Paul, and F. G. A. Stone, *J. Chem. Soc. A*, 264 (1967).
18. Y. N. Al-Obaidi, P. K. Baker, M. Green, N. D. White, and G. E. Taylor, *J. Chem. Soc., Dalton Trans.*, 2321 (1981).
19. R. P. Kirchen, K. Ranganayakulu, A. Rauk, B. P. Singh, and T. S. Sorensen, *J. Am. Chem. Soc.*, **103**, 588 (1981); R. P. Kirchen, N. Okazawa, K. Ranganayakulu, A. Rauk, and T. S. Sorensen, *J. Am. Chem. Soc.*, **103**, 597 (1981).
20. J. E. McMurry and T. Lecta, *J. Am. Chem. Soc.*, **115**, 10167 (1993); R. Ponec, G. Yuzhakov, and D. J. Tantillo, *J. Org. Chem.*, **69**, 2992 (2004).
21. R. M. Minyaev and V. I. Pavlov, *J. Mol. Struct. Theochem.*, **29**, 205 (1983); W. A. Lathan, W. J. Hehre, and J. A. Pople, *J. Am. Chem. Soc.*, **93**, 808 (1971); K. Raghavachari, R. A. Whiteside, J. A. Pople, and P. V. R. Schleyer, *J. Am. Chem. Soc.*, **103**, 5649 (1981).
22. Q. Li, K. C. Hunter, C. Seitz, and A. L. L. East, *J. Chem. Phys.*, **119**, 7148 (2003).
23. S. G. Shore, S. H. Lawrence, M. I. Watkins, and R. Bau, *J. Am. Chem. Soc.*, **104**, 7669 (1982).

24. J. L. Atwood, D. C. Hrncir, R. D. Rogers, and J. A. K. Howard, *J. Am. Chem. Soc.*, **103**, 6787 (1981); for calculations on this system see R. A. Chiles and C. E. Dykstra, *Chem. Phys. Lett.*, **92**, 471 (1982).
25. C. Katal, P. Grutsch, J. L. Atwood, and R. D. Rogers, *Inorg. Chem.*, **17**, 3558 (1978).
26. S. W. Kirtley, M. A. Andrews, R. Bau, G. W. Grynkewich, T. J. Marks, D. L. Tipton, and B. R. Whittlesey, *J. Am. Chem. Soc.*, **99**, 7154 (1977).
27. F.-C. Liu, C.-C. Yang, S.-C. Chen, G.-H. Lee, and S.-M. Peng, *J. Chem. Soc., Dalton Trans.*, 3599 (2008).
28. A. G. Csaszar, L. Hedberg, K. Hedberg, R. C. Burns, A. T. Wen, and M. J. McGlinchey, *Inorg. Chem.*, **30**, 1371 (1991); A. Nagy, L. Szepes, G. Vass, and L. Zanathy, *J. Organomet. Chem.*, **485**, 215 (1995).
29. J. C. Green, M. de Simone, M. Coreno, A. Jones, H. M. I. Pritchard, and G. S. McGrady, *Inorg. Chem.*, **44**, 7781 (2005); A. Haaland, D. J. Shorokhov, A. V. Tutukin, H. V. Volden, O. Swang, G. S. McGrady, N. Kaltsoyannis, A. J. Downs, C. Y. Tang, and J. F. C. Turner, *Inorg. Chem.*, **41**, 6646 (2002).
30. F. H. Carve, F. A. Cotton, and B. A. Frenz, *Inorg. Chem.*, **15**, 380 (1976); C. H. Wei, *Inorg. Chem.*, **8**, 2384 (1969).
31. M. R. Churchill and J. P. Hutchinson, *Inorg. Chem.*, **17**, 3528 (1978).
32. D. M. Hoffman, R. Hoffmann, and C. R. Fisel, *J. Am. Chem. Soc.*, **104**, 3858 (1982); D. M. Hoffman and R. Hoffmann, *J. Chem. Soc., Dalton Trans.*, 1471 (1982).
33. G. Maier, *Angew. Chem. Int. Ed.*, **27**, 309 (1988).
34. M. N. Glukhovtsev, S. Laiter, and A. Pross, *J. Phys. Chem.*, **99**, 6828 (1995).
35. See, for example, R. Mason and G. Wilkinson, *Experientia, Suppl.* **9**, 233 (1964).
36. (a) H. Hogeveen and P. W. Kwant, *Acc. Chem. Res.*, **8**, 413 (1975); H. Carnadi, C. Giordano, R. F. Heldeweg, H. Hogeveen, and E. M. G. A. van Kruchten, *Isr. J. Chem.*, **21**, 229 (1981) and references therein. (b) E. D. Jemmis, *J. Am. Chem. Soc.*, **104**, 7017 (1982); E. D. Jemmis and P. V. R. Schleyer, *J. Am. Chem. Soc.*, **104**, 4781 (1982); V. I. Minkin and R. M. Minyaev, *Russ. Chem. Rev.*, **51**, 332 (1982); H. Schwarz, *Angew. Chem. Int. Ed.*, **20**, 991 (1981); K. Krogh-Jespersen, *J. Am. Chem. Soc.*, **113**, 417 (1991).
37. G. Jaouen, A. Marinetti, B. Mentzen, R. Mutin, J.-Y. Saillard, B. G. Sayer, and M. J. McGlinchey, *Organometallics*, **1**, 753 (1982); A. Sironi, G. Gervasio, and E. Sappa, *J. Cluster Sci.*, **5**, 535 (1994).
38. H. M. Boechat-Roberty, R. Neves, S. Pilling, A. F. Lago, and G. G. B. de Souza, *Mon. Not. R. Astron. Soc.*, **394**, 810 (2009) and references therein.
39. J. H. D. Eland, *Chem. Phys.*, **345**, 82 (2008) and references therein.
40. M. Rosi, C. W. Bauschlicher, Jr., and E. L. O. Bakes, *Astrophys. J.*, **609**, 1192 (2004).
41. C. Dohmeier, R. Koppe, C. Robl, and H. Schnockel, *J. Organomet. Chem.*, **487**, 127 (1995).
42. P. Jutzi, F. Kohl, P. Hofmann, C. Kruger, and Y.-H. Ysay, *Chem. Ber.*, **113**, 757 (1980); P. Jutzi, A. Mix, B. Rummel, W. W. Schoeller, B. Neumann, H.-G. Stammmer, *Science*, **305**, 849 (2004); J. N. Jones, J. A. Moore, A. H. Cowley, C. L. B. Macdonald, *J. Chem. Soc., Dalton Trans.*, **3846** (2005) and references therein.
43. A. F. Richards, M. Brynda, M. M. Olmstead, and P. P. Power, *Organometallics*, **23**, 2841 (2004); C. Fish, M. Green, J. C. Jeffery, R. J. Kilby, J. M. Lynam, J. E. McGrady, D. A. Pantazis, C. A. Russell, and C. E. Willans, *Chem. Commun.*, 1375 (2006).
44. A. Sevin and A. Devaquet, *Nouv. J. Chim.*, **1**, 357 (1977); T. Clark and P. V. R. Schleyer, *Nouv. J. Chim.*, **2**, 665 (1978); K. Krogh-Jespersen, D. Cremer, D. Poppinger, J. A. Pople, P. v. R. Schleyer, and J. Chandrasekhar, *J. Am. Chem. Soc.*, **101**, 4843 (1979); J. Chandrasekhar, P. v. R. Schleyer, and H. B. Schlegel, *Tetrahedron Lett.*, 3393 (1978); J. A. Ulman, E. L. Andersen, and T. P. Fehlner, *J. Am. Chem. Soc.*, **100**, 456 (1978); R. L. DeKock and T. P. Fehlner, *Polyhedron*, **1**, 521 (1982); P. Brint, K. Pelin, and R. T. Spalding, *Inorg. Nucl. Chem. Lett.*, **16**, 391 (1980); P. Brint, K. Pelin, and R. T. Spalding, *J. Chem. Soc., Dalton Trans.*, **546**, 391 (1981).
45. T. A. Albright, unpublished calculations.

46. (a) W. L. Olson, A. M. Stacy, and L. F. Dahl, *J. Am. Chem. Soc.*, **108**, 7646 (1986). (b) A. C. Bray, M. Green, D. R. Hankey, J. A. K. Howard, O. Johnson, and F. G. A. Stone, *J. Organomet. Chem.*, **281** (1985).
47. R. Ahlrichs, D. Fenske, H. Oesen, and U. Schneider, *Angew. Chem. Int. Ed.*, **31**, 323 (1992).
48. H. Tang, D. M. Hoffman, T. A. Albright, H. Deng, and R. Hoffmann, *Angew. Chem. Int. Ed.*, **32**, 1616 (1993).
49. T. Yamada, A. Mawatari, M. Tanabe, K. Osakada, and T. Tanase, *Angew. Chem. Int. Ed.*, **48**, 568 (2009); M. Tanabe, N. Ishikawa, M. Chiba, T. Ide, K. Osakada, and T. Tanase, *J. Am. Chem. Soc.*, **133**, 18598 (2011).
50. R. D. Adams, W. C. Pearl, Jr., Y. O. Wong, Q. Zhang, M. B. Hall, and J. R. Walensky, *J. Am. Chem. Soc.*, **133**, 12994 (2011).
51. H. Tang, Ph.D. Dissertation, University of Houston (1995).
52. B. Kesani, J. Fettinger, B. Scott, and B. Eichhorn, *Inorg. Chem.*, **43**, 3840 (2004) and references therein.; See also H.G. von Schnering, J. Wok, D. Weber, R. Ramirez, and T. Meyer, *Angew. Chem. Int. Ed.*, **25**, 353 (1986).
53. D. M. P. Mingos, *New J. Chem.*, **17**, 531 (1993); see also J. Li and K. Wu, *Inorg. Chem.*, **39**, 1538 (2000).
54. H.-L. Yu, R.-L. Sang, and Y.-Y. Wu, *J. Phys. Chem. C*, **113**, 3382 (2009).
55. K. Exner and P. v. R. Schleyer, *Science*, **290**, 1937 (2000); R. M. Minyaev, and T. N. Gribanova, *Russ. Chem. Bull.*, **49**, 783 (2000).
56. K. Ito, Z. Pu, Q.-S. Li, and P. v. R. Schleyer, *Inorg. Chem.*, **47**, 1096 (2008); Z. Pu, K. Ito, P. v. R. Schleyer, and Q.-S. Li, *Inorg. Chem.*, **48**, 10679 (2009).
57. For a general review see V. I. Minkin, I. E. Mikhailov, G. A. Dushenko, and A. Zschunke, *Russ. Chem. Rev.* **72**, 867 (2003).
58. F.-G. Klärner and B. Brassel, *J. Am. Chem. Soc.*, **102**, 2469 (1980); F.-G. Klärner and F. Adamsky, *Chem. Ber.*, **116**, 299 (1983).
59. J. A. Berson and L. Salem, *J. Am. Chem. Soc.*, **94**, 8917 (1972).
60. A. A. Jarzecki, J. Gajewski, and E. R. Davidson, *J. Am. Chem. Soc.*, **121**, 6928 (1999).
61. F.-G. Klärner and F. Adamsky, *Angew. Chem. Int. Ed.*, **18**, 674 (1979).
62. J. Rodriguez-Otero, E. M. Cabaleiro-Lago, and A. Pena-Gallego, *Tetrahedron*, **63**, 2191 (2007).
63. J. Browning, M. Green, J. L. Spencer, and F. G. A. Stone, *J. Chem. Soc., Dalton Trans.*, **97** (1974); J. Browning and B. R. Penfold, *J. Cryst. Mol. Struct.*, **4**, 335 (1974); I. Bach, K.-R. Porschke, R. Goddard, C. Kopiske, C. Kruger, A. Rufinska, and K. Seevogel, *Organometallics*, **15**, 4959 (1996); C. N. Iverson, R. J. Lachicotte, C. Muller, W. D. Jones, *Organometallics*, **21**, 5320 (2002).
64. P. Vogel, M. Saunders, N. M. Hasty Jr., and J. A. Berson, *J. Am. Chem. Soc.*, **93**, 1551 (1971); W. J. Hehre, *J. Am. Chem. Soc.*, **96**, 5207 (1974).
65. C. Mealli, S. Midollini, S. Moneti, L. Sacconi, J. Silvestre, and T. A. Albright, *J. Am. Chem. Soc.*, **104**, 95 (1982).
66. W. J. Hehre and A. J. P. Devaquet, *J. Am. Chem. Soc.*, **98**, 4370 (1976); A. M. Genaev, G. E. Sal'nikov, and V. G. Shubin, *Russ. J. Org. Chem.*, **43**, 113 (2007).
67. G. A. Olah, J. S. Staral, R. J. Spear, and G. Liang, *J. Am. Chem. Soc.*, **97**, 5489 (1975).
68. L. M. Goldman, D. R. Glowacki, and B. K. Carpenter, *J. Am. Chem. Soc.*, **133**, 5312 (2011) and references therein.
69. M. A. Iron, A. C. B. Lucassen, H. Cohen, M. E. van der Boom, and J. M. L. Martin, *J. Am. Chem. Soc.*, **126**, 11699 (2004) have also reported calculations on this ring opening reaction.
70. M. Sanders and H.-U. Siehl, *J. Am. Chem. Soc.*, **102**, 6868 (1980) and references therein.
71. M. Saunders, K. E. Laidig, K. B. Wiberg, and P. v. R. Schleyer, *J. Am. Chem. Soc.*, **110**, 7652 (1988) and references therein; see also J. Casanova, D. R. KentIV, W. A. GoddardIII, and J. D. Roberts, *Proc. Natl. Acad. Sci. USA*, **100**, 15 (2003).
72. C. P. Casey, D. M. Scheck, and A. J. Shusterman, *J. Am. Chem. Soc.*, **101**, 4233 (1979).
73. C. N. Wilker and R. Hoffmann, *J. Am. Chem. Soc.*, **105**, 5285 (1983).
74. M. B. Smith and J. March, *March's Organic Chemistry*. 6th edition, Wiley-Interscience (2007) pp. 803–807.

75. J.-L. Carreon-Macedo and J. N. Harvey, *J. Am. Chem. Soc.*, **126**, 5789 (2004); A. Petit, P. Richard, I. Cacelli, and R. Poli, *Chem. Eur. J.*, **12**, 813 (2006).
76. L. G. Kuz'mina, A. A. Bagatur'yants, J. A. K. Howard, K. I. Grandberg, A. V. Karchava, E. S. Shubina, L. N. Saitkulova, and E. V. Bakhmutova, *J. Organomet. Chem.*, **575**, 39 (1999).
77. F. Scherbaum, A. Grohmann, G. Muller, and H. Schmidbaur, *Angew. Chem. Int. Ed.*, **28**, 463 (1989).
78. T. L. Blundell and H. M. Powell, *J. Chem. Soc. A*, 1685 (1971).
79. D. G. Evans and D. M. P. Mingos, *J. Organomet. Chem.*, **232**, 171 (1982).
80. J. W. Lauher and K. Wald, *J. Am. Chem. Soc.*, **103**, 7648 (1981); F. E. Simon and J. W. Lauher, *Inorg. Chem.*, **19**, 2338 (1980).
81. A. Gadek, A. Kochel, and T. Szymanska-Buzar, *Organometallics*, **22**, 4869 (2003).
82. M. G. B. Drew, B. J. Brisdon, and A. Day, *J. Chem. Soc., Dalton Trans.*, 1310 (1981).
83. T. V. Ashworth, J. A. K. Howard, and F. G. A. Stone, *J. Chem. Soc., Dalton Trans.*, 1609 (1980).
84. S. J. Davies, G. P. Elliott, J. A. K. Howard, C. M. Nunn, and F. G. A. Stone, *J. Chem. Soc., Dalton Trans.*, 2177 (1987).
85. F. G. A. Stone, *Angew. Chem. Int. Ed.*, **23**, 89 (1984).
86. (a) Q. Yu, A. Purath, A. Donchev, and H. Schnockel, *J. Organomet. Chem.*, **584**, 94 (1999).  
(b) B. Buchin, T. Steinke, C. Gemel, T. Cadenbach, and R. A. Fischer, *Z. Anorg. Allg. Chem.*, **631**, 2756 (2005). (c) J. Weiss, D. Stetzkamp, B. Nuber, R. A. Fischer, C. Boehme, and G. Frenking, *Angew. Chem. Int. Ed.*, **36**, 70 (1997).
87. C. Dohmeier, H. Krautscheid, and H. Schnockel, *Angew. Chem. Int. Ed.*, **33**, 2482 (1994).
88. I. I. Vorontsov, K. A. Potekhin, M. Yu. Antipin, and I. E. Zanin, *Kristallografiya (Russ. Crystallogr. Rep.)*, **45**, 266 (2000).
89. D. S. Glueck, F. J. Hollander, and R. G. Bergman, *J. Am. Chem. Soc.*, **111**, 2719 (1989).
90. D. S. Glueck, J. S. Green, R. I. Michelman, and I. N. Wright, *Organometallics*, **11**, 4221 (1992).
91. D. S. Williams, M. H. Schofield, and R. R. Schrock, *Organometallics*, **12**, 4560 (1993); J. Sundermeyer and D. Runge, *Angew. Chem. Int. Ed.*, **33**, 1255 (1994) and references therein.
92. See, for example, P. D. Bolton, N. Adams, E. Clot, A. R. Cowley, P. J. Wilson, M. Schröder, and P. Mountford, *Organometallics*, **25**, 5549 (2006); M. P. Coles, C. I. Dalby, V. C. Gibson, I. R. Little, E. L. Marshall, M. H. Ribeiro da Costa, and S. Mastroianni, *J. Organomet. Chem.*, **591**, 78 (1999).
93. C. E. Housecroft and T. P. Fehlner, *Inorg. Chem.*, **21**, 1739 (1982); R. L. DeKock, P. Deshmukh, T. P. Fehlner, C. E. Housecroft, J. S. Plotkin, and S. G. Shore, *J. Am. Chem. Soc.*, **105**, 815 (1983).
94. L. J. Guggenberger, A. R. Kane, and E. L. Muettterties, *J. Am. Chem. Soc.*, **94**, 5665 (1972).
95. T. N. Gribanova, A. G. Starikov, R. M. Minyaev, V. I. Minkin, M. R. Siebert, and D. J. Tantillo, *Chem. Eur. J.*, **16**, 2272 (2010).
96. M. F. Hawthorne and P. L. Pilling, *J. Am. Chem. Soc.*, **87**, 3987 (1965); M. F. Hawthorne, D. C. Young, T. D. Andrews, D. V. Howe, P. L. Pilling, A. D. Pitts, M. Reintjes, L. F. Warrent, Jr., and P. A. Wegner, *J. Am. Chem. Soc.*, **90**, 879 (1968).
97. X. Yang, W. A. King, M. Sabat, and T. J. Marks, *Organometallics*, **12**, 4254 (1993).
98. R. H. Herber, A. R. Kudinov, P. Zanello, I. Nowik, D. S. Perekalin, V. I. Meshcheryakov, K. A. Lyssenko, M. Corsini, and S. Fedi, *Eur. J. Inorg. Chem.*, 1786 (2006).
99. D. A. Brown, M. O. Fanning, and N. J. Fitzpatrick, *Inorg. Chem.*, **17**, 1620 (1978); D. A. Brown, M. O. Fanning, and N. J. Fitzpatrick, *Inorg. Chem.*, **19**, 1822 (1980).
100. T. A. K. Al-Allaf, C. Eaborn, P. B. Hitchcock, M. F. Lappert, and A. Pidcock, *Chem. Commun.*, **548** (1985).
101. I. Doverbratt, S. Ponou, S. Lidin, and D. C. Fredrickson, *Inorg. Chem.*, **51**, 11580 (2012).
102. M. Schollenberger, B. Nuber, and M. Ziegler, *Angew. Chem. Int. Ed.*, **31**, 350 (1992).

# Cluster Compounds

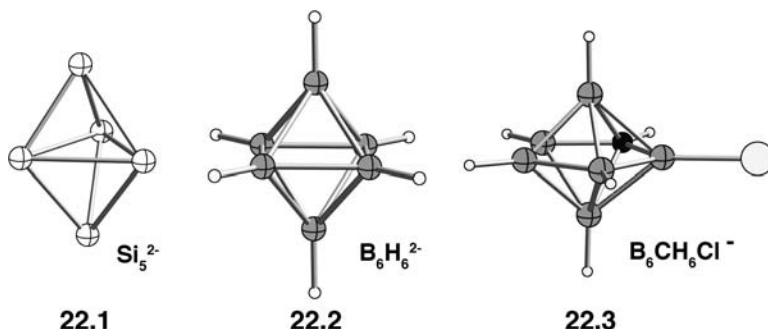
---

## 22.1 TYPES OF CLUSTER COMPOUNDS

---

An important class of compounds is one where the atoms are arranged at the vertices of a polyhedron to give a cage or cluster compound [1–8]. Most clusters are electron-precise, that is, they can be described solely in terms of two-electron two-center bonds and possibly one or more two-center four-electron bonds, and so on. But there are also many examples of clusters that are electron deficient. The most elementary example is, of course,  $\text{H}_3^+$  where there are two electrons but three H–H contacts. In previous chapters, we have mentioned several species of this type without drawing special attention to their cluster nature. The  $(\text{CH})_5^+$  and  $(\text{CH})_6^{2+}$  species of Section 11.4 are cluster compounds as are, for example, the molecules of 21.74–21.76. In this chapter, we describe in a simplistic way the skeletal orbitals of a large class of cage molecules, which are based on the deltahedra of Figure 22.1. As a result, we are able to derive a set of electron-counting rules that enable predictions to be made concerning the geometries of such species [5]. Notice that the simplest deltahedron, the tetrahedron, is not represented. It will be regarded as a derivative of the trigonal bipyramidal. This is by no means an inclusive list. There are larger examples, as well as ones wherein two or more deltahedra are fused together [3].

Such cluster compounds divide naturally into four major types: (a) Main group compounds that include the boranes, carboranes, and polyhedral compounds with other main group atoms. 22.1 [9], 22.2 [10], and 22.3 [11] are representative examples. In 22.1, it is reasonable to expect that each Si atom possesses a lone pair pointing away from the cluster. This means that there are  $5 \times 2 = 10$  electrons remaining for cluster bonding. There are, however, nine edges in the molecule. Thus, 22.1 is eight electrons short of making each edge a two-center two-electron bond. In 22.2, it is again reasonable to require that each B–H bond has two electrons. There are then a total of  $6(2) + 2 = 14$  electrons to be divided into 12 B–B bonds. The same situation applies for 22.3. There are  $6(2) + 3 + 1 = 16$  electrons for B–B and



B–C bonding with 15 edges. A recurring theme throughout this book has been that electron deficient compounds require a “closed” as opposed to an “open” geometry. Yet the origin of these electron counts remains a mystery, the fact that the clusters are based on deltahedra is understandable. (b) Transition metal cluster compounds (22.4 [12], 22.5 [13]). These invariably have cyclopentadienyl or carbonyl groups coordinated to the transition metal. In many of these compounds, the carbonyl groups are free to move about the surface of the metal cluster and the crystal structures of such species often show bridging CO groups. Similarly, there are often low-energy fluxional pathways associated with movement of hydrogen atoms in boranes and carboranes. In many of these transition metal containing examples, hydrogen atoms are often associated with the cluster. As we mentioned in the last

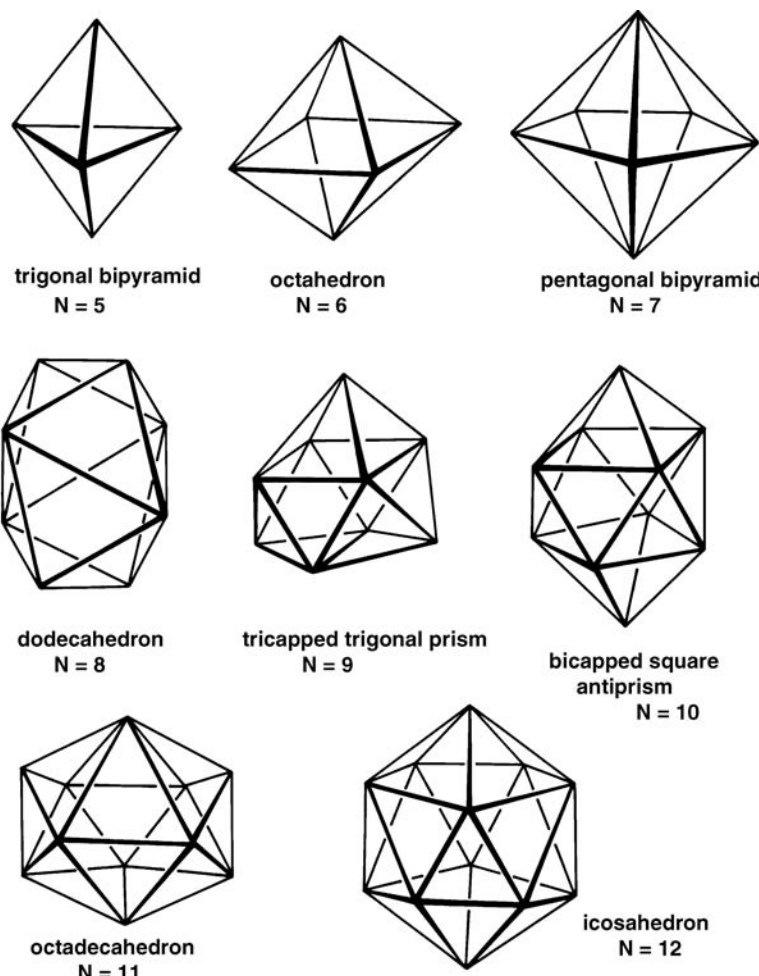
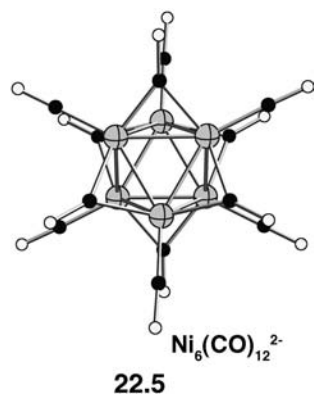
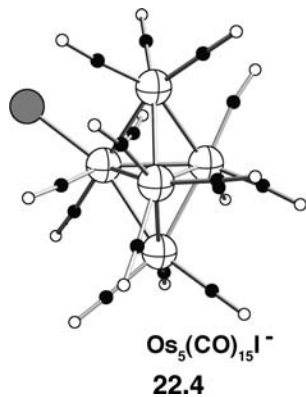
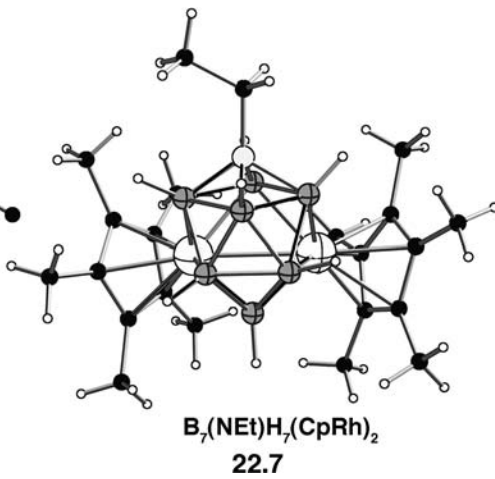
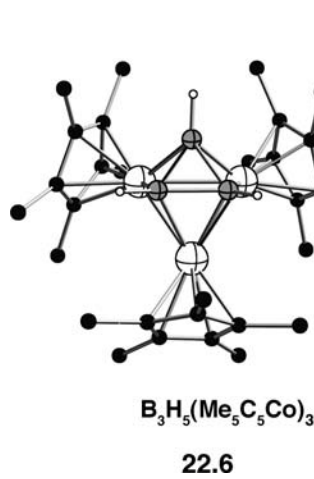


**FIGURE 22.1**

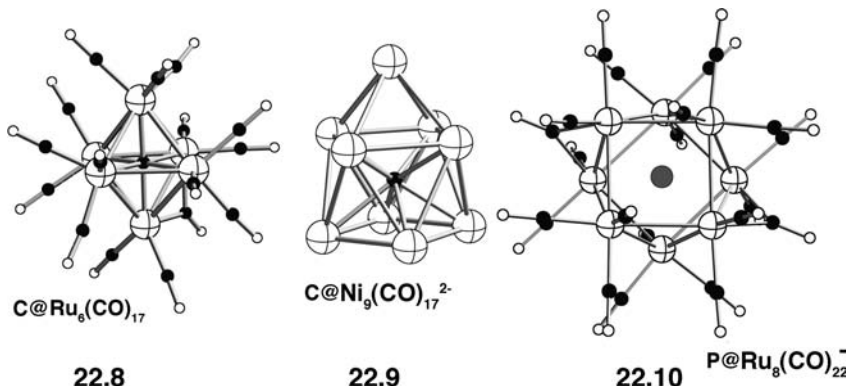
Deltahedra used by cage and cluster molecules.



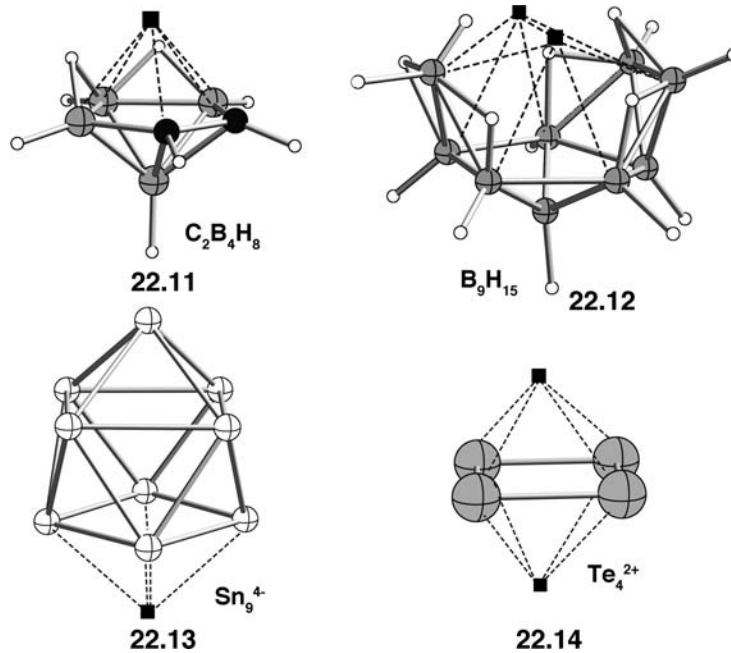
chapter, within the context of the isolobal analogy, bridging hydrogens can be removed as protons. This is also the case here. In previous chapters, we have had a relatively rigorous procedure in assigning oxidation states. In **22.4** and **22.5**, it is clear that this will lead to fractional charges and potential confusion. Therefore, we shall avoid this issue by assigning each ligand to be neutral and simply adding or subtracting electrons according to the overall charge on the molecule. Therefore, in **22.4**, the total number of electrons associated with the metals is  $[15(2) + 5(8) + 1 + 1] = 72$  electrons. For an 18 electron count at each metal one needs  $18(5) = 90$  electrons. Therefore, there need to be  $18/2 = 9$  Os–Os bonds. This is exactly the number of edges in **22.4**. In **22.5** there are  $[12(2) + 10(6) + 2] = 86$  electrons. For each nickel atom to be 18 electrons we need  $18(6) = 108$  electrons. The number of Ni–Ni bonds is then  $22/2 = 11$ . But there are 12 edges; therefore, the molecule must possess two delocalized three-center two-electron bonds in the molecule. (c) A few metallacarboranes are given by **22.6** [14] and **22.7** [15],



as well as, **21.148**. The counting schemes we developed for transition metals are different from those for the main group elements. We shall see a way around this using the isolobal analogy. The octahedral shape is evident for the  $\text{B}_3\text{Co}_3$  core in **22.6**. Note that two bridging hydrogens were not located in this structure. The bicapped square antiprism is represented in **22.7**. A nitrogen atom is part of the cluster. (d) Compounds that contain a small atom inside the polyhedron are illustrated in **22.8** [16], **22.9** [17] (the carbonyl groups for clarity have been left out of the drawing) and **22.10** [18]. Here, the @ sign refers to the atom(s), which are encapsulated by the cluster. Notice that the central carbon in **22.8** is equally bonded to six Ru atoms. If one counts the electrons associated with cluster metal atoms, there are  $[17(2) + 6(8) + 4] = 86$  electrons. This is precisely the same as **22.5**.



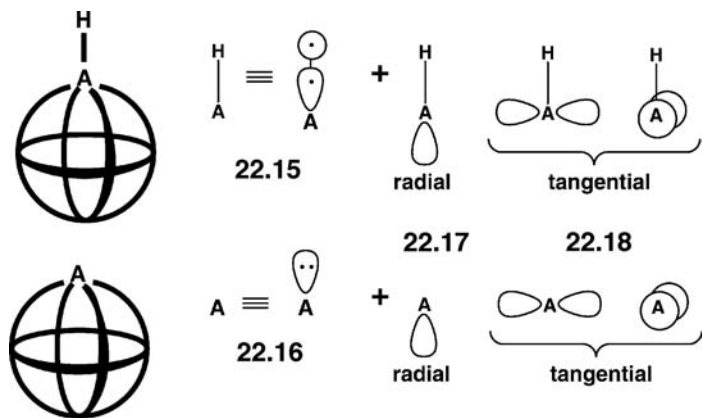
that also has an octahedral shape. Notice that all the four valence electrons on carbon are used in the count. The central atom is sometimes referred to as an encapsulated atom and this may be any atom, including a transition metal, from the periodic table. Furthermore, the cluster may be comprised main group atoms and a transition metal center. In **22.9**, the basic cluster shape is derived from the bicapped square antiprism; however, one of the caps is missing while in **22.10** both caps are absent. This brings up an important detail in our description and electron counting in these clusters. The deltahedron may be a complete one that has all of the vertices for the deltahedra in Figure 22.1 occupied. This is called a closo compound as in **22.1–22.8** or it may have one vertex missing (a nido species) as in **22.9, 22.11** [19], or **22.13** [20], two vertices missing (an arachno species) as in **22.10, 22.12** [21],



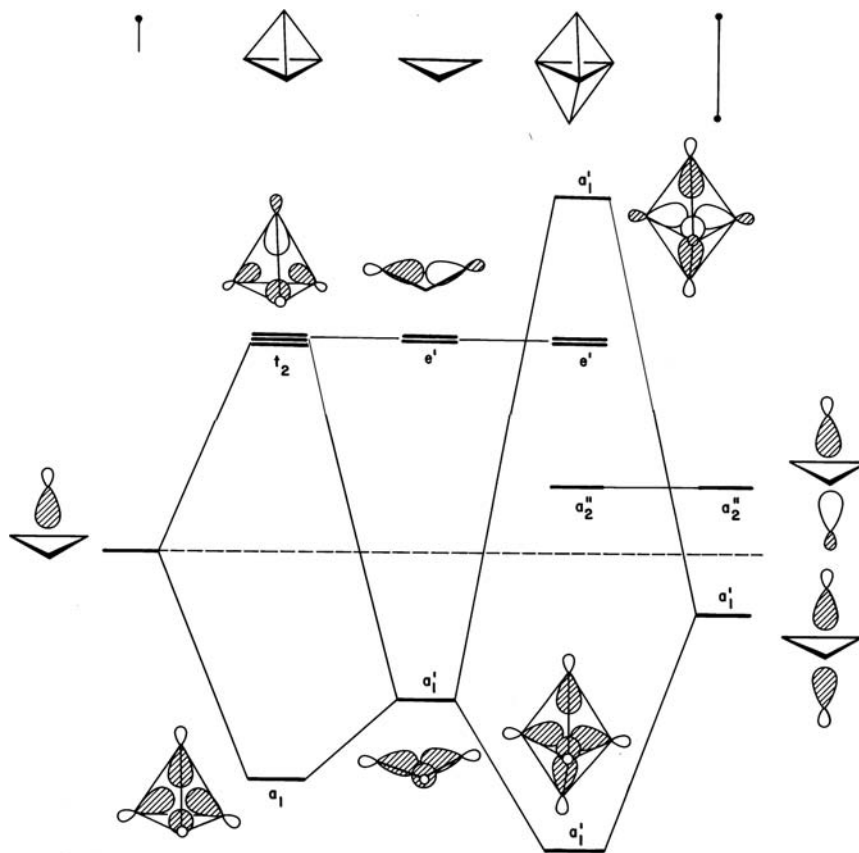
or **22.14** [22]. The black squares in these cases mark the vertex with the missing surface atom. Therefore,  $N=7$  for **22.11** (see Figure 22.1);  $N=11$  for **22.12**;  $N=10$  for **22.13**; and  $N=6$  for **22.14**. In many of these cases, the reader may be used to viewing these molecules, not as the remnants of a cage, but in a completely different way, perhaps. **22.14** might, for example, be regarded as being a delocalized square isolobal to cyclobutadiene dianion. In the previous chapter too, we have encouraged the reader to be imaginative when considering molecular geometry. We shall see that viewing these species as complete or fragmented deltahedra is a very profitable way to understand their structures.

## 22.2 CLUSTER ORBITALS

As mentioned earlier, one of the features of these molecules is that usually there are fewer electron pairs than close contacts (bonds) in the molecule. We derive a very general model for these systems by considering three types of orbital at each deltahedral vertex, assembled by considering the one  $s$  and three  $p$  orbitals at each center. Initially, then we focus on the main group examples 22.1–22.3 and 22.11–22.14. There is an orbital, 22.15, pointing away from each vertex of the



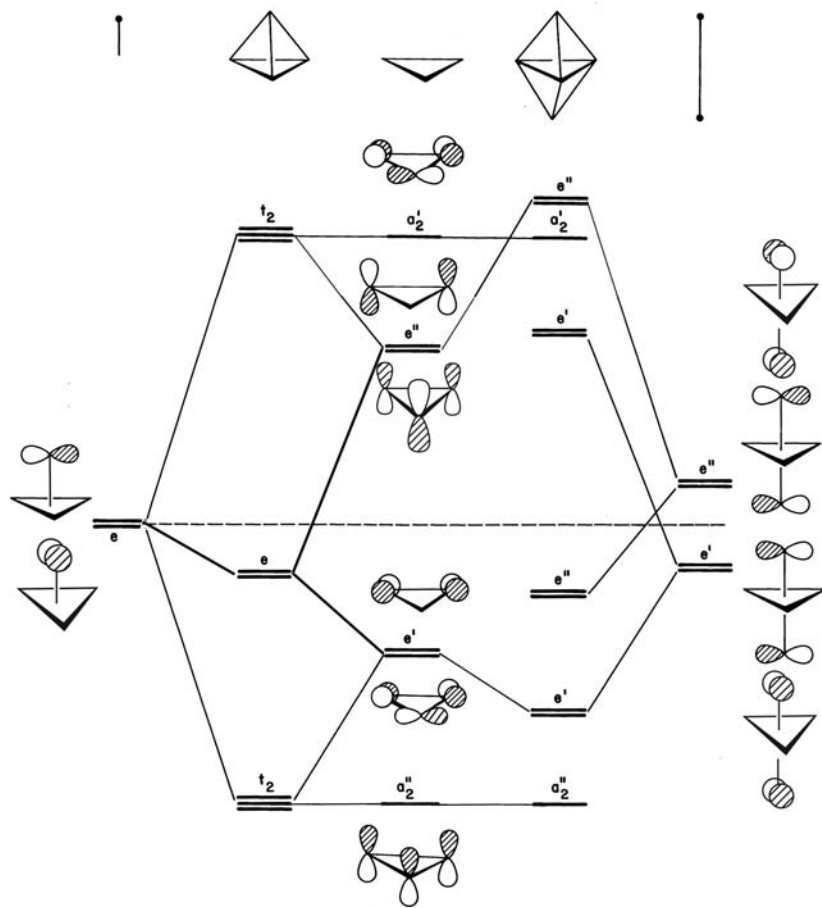
deltahedron which will be exclusively involved in extradeltahedral bonds, for example, the B–H bonds in 22.2 or outwardly pointing lone pairs in 22.1 as given by 22.16. This leaves three orbitals involved in skeletal bonding [5,9–12], a single radial orbital 22.17 that points toward the inside of the cage and two tangential orbitals 22.18. The orbital properties of the collection of inward pointing radial orbitals are easy to visualize. We assemble the nido trigonal bipyramidal (this is just the tetrahedron) and the trigonal bipyramidal itself by adding one or two capping orbitals to the triangular system. We readily recognize the orbital pattern of the triangular unit as being topologically analogous to the  $D_{3h}$ ,  $H_3^+$  system (Section 5.2). The resultant interaction diagram is shown in Figure 22.2. The horizontal dashed line indicates the energy of an isolated radial hybrid orbital. We have tilted the orbitals comprising the  $a_1$  combination in the triangle during the addition of an extra atom so that they point toward the centroid of the tetrahedron. The energy changes will then not be exactly as we have shown but the general picture is clear enough. The level pattern for the radial orbitals of the tetrahedron is identical to that shown for tetrahedral  $H_4$  in Figure 5.6. A strongly bonding combination of  $a_1$  symmetry is formed. The antibonding combination meets the two nonbonding orbitals located on the triangle to form a  $t_2$  set. When two extra atoms are added to the trigonal plane (to give the trigonal bipyramidal), the orbital combination antisymmetric with respect to this plane finds no symmetry match with the plane orbitals and so remains unchanged in energy. The symmetric combination ( $a_1'$ ) enters into bonding and antibonding combinations with the in-plane orbitals of the same symmetry. A similar construction can be carried out for the closo and nido octahedral on (square pyramid) starting with the square. The orbital picture is again a very simple one. The important result to note is that only one bonding orbital results from the combination of radial orbitals. All the others are antibonding. For larger polyhedra, the result is a little more involved. There is always one deep lying bonding orbital, the in-phase combination of the radial orbitals, but there may also be other bonding orbitals at higher energy.

**FIGURE 22.2**

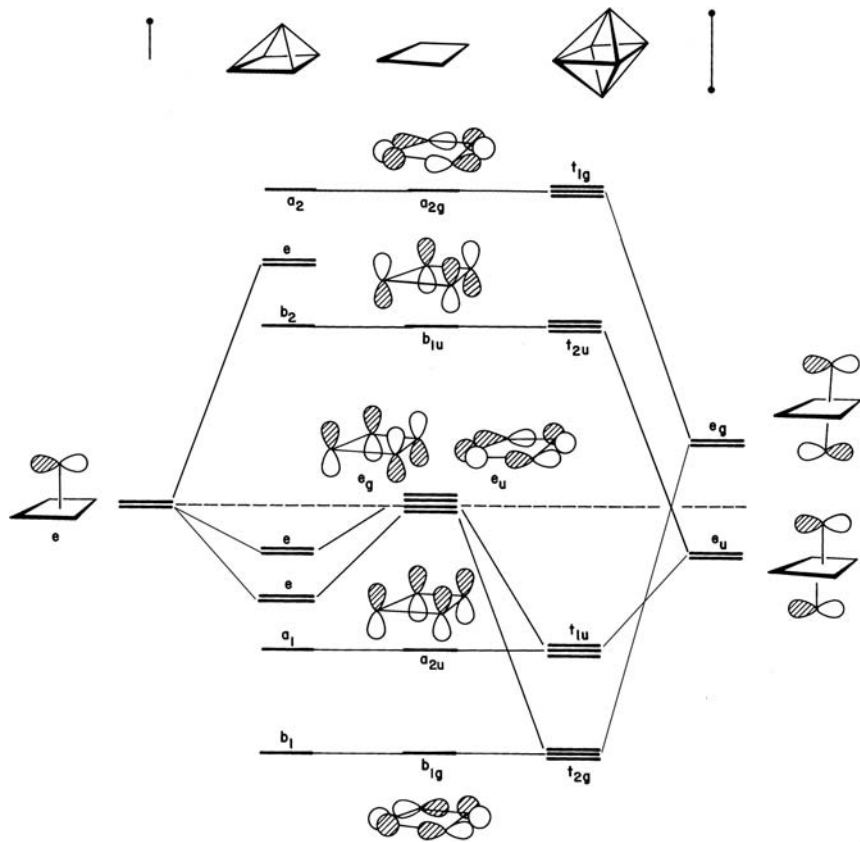
Derivation of orbital diagrams, built from the radial orbitals of the fragments, for the tetrahedron and the trigonal bipyramidal, by capping a trigonal planar unit with one or two new fragments, respectively. Notice that the tetrahedron is a nido trigonal bipyramidal.

The tangential orbitals are, in principle, no more complex to build up. In the middle of Figure 22.3, there are the  $p$  atomic orbitals (AOs) of the equilateral triangle. We have seen these several times before; they are the in-plane  $e'$  +  $a_2'$  set along with  $a_2''$  and  $e''$  orbitals that are perpendicular to the ring. The right side of Figure 22.3 shows what happens when the triangle is capped from above and below. The  $e'$  and  $e''$  orbital combinations on the capping atoms find symmetry matches with the orbitals of the triangle and lead to two pairs of bonding and two pairs of antibonding orbitals, one of each symmetry type. Five tangential molecular orbitals are bonding that along with the radial  $a_1'$  bonding combination (Figure 22.2) house a total of 12 electrons. In the tetrahedron, the capping orbitals of  $e$  symmetry (in  $C_{3v}$ ) mix with the two central atom  $e$  pairs to give a bonding, nonbonding, and antibonding trio. The top and bottom orbitals of the set are degenerate with the  $a_2'$  and  $a_2''$  orbitals of the trigonal plane and triply degenerate  $t_2$  orbitals result. The middle combination of the  $e$  sets is actually a little bonding. The overlap between the capping  $e$  set is larger with  $e''$  than it is with  $e'$ . So here again, there are a total of five low-energy (bonding or nonbonding) tangential orbitals along with the fully bonding radial combination implies that a molecule with 12 electrons should be stable.

Figure 22.4 shows the generation of the orbitals of the octahedron and the nido octahedron (square pyramid). The perpendicular orbitals of the central square are just the  $\pi$  orbitals of, say, cyclobutadiene. The in-plane  $\sigma$  orbitals were derived in **11.7**. The details of the origin of the new levels are a little difficult to follow because the “capping” orbitals may interact with both in-plane and perpendicular sets of orbitals of the square. In brief, the two pairs of capping orbitals at the right-hand side of Figure 22.4 interact with the two pairs of doubly degenerate plane orbitals to

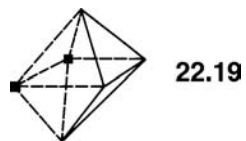
**FIGURE 22.3**

Assembly of the orbitals, derived from the tangential orbitals of the fragments, for the tetrahedron and trigonal bipyramidal, by capping a trigonal planar unit with one or two new fragments, respectively.

**FIGURE 22.4**

Assembly of the orbitals, derived from the tangential orbitals of the fragments, for the square pyramid and octahedron, by capping a square planar unit with one or two new fragments, respectively. Only one member of a degenerate orbital set is shown pictorially.

produce a set of four orbitals, two of which are bonding and two of which are antibonding. Each pair has the same energy as a nondegenerate orbital of the plane. The net result is a total of four triply degenerate sets. For the square pyramid, the three pairs of degenerate  $e$  orbitals (one from the capping atom, two from the square) lead to three new orbitals, two of which are bonding and one of which is antibonding. Figure 22.4 shows that when the square is “capped” from above and from below to give the square pyramid and then the octahedron, a total of six low-energy tangential orbitals are always present. Notice that a total of six low-energy orbitals of this type are found for the square too which constitute one arachno isomer of an octahedron. A similar result is obtained if the alternative arachno octahedral structure **22.19** is included, although this is a more difficult result to derive as a result of the lower symmetry of this species.

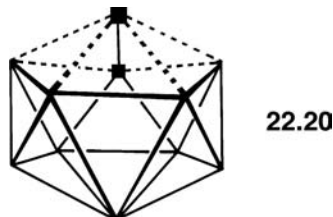


A general rule, which we may derive by extrapolation of these results, is that an  $n$ -vertex deltahedron has a total of  $n$  bonding tangential orbitals and one deep lying bonding radial orbital, giving  $n + 1$  low-energy orbitals in all [5,25,26]. This rule, very importantly, also applies to the nido and arachno cages where some of the  $n$  atoms are missing. The exception is the tetrahedron itself, which has a total of  $n + 2$  skeletal pairs. In addition to being a deltahedron (it is the simplest one), it is a nido trigonal bipyramidal and behaves electronically as such. Our earlier analysis has attempted to show in orbital terms how this comes about. It is not exact, since orbitals of the same symmetry, radial, and tangential can, and do mix with each other to change the picture a little. In particular, note for the octahedron that the combination of capping radial orbitals antisymmetric with respect to the square plane will mix with the tangential  $a_{2u}$  orbital (Figure 22.4). Likewise, there is some overlap, albeit small, between the tangential capping  $e_u$  pair and the radial  $e_u$  set. Similar situations exist for the other three clusters. In spite of such mixing, we are still left with a total of  $(n + 1)$  bonding orbitals for the  $n$ -vertex deltahedron. A more general group theoretical result, beyond the scope of this book, enables generation of this  $n + 1$  rule in a much more elegant and general fashion [25].

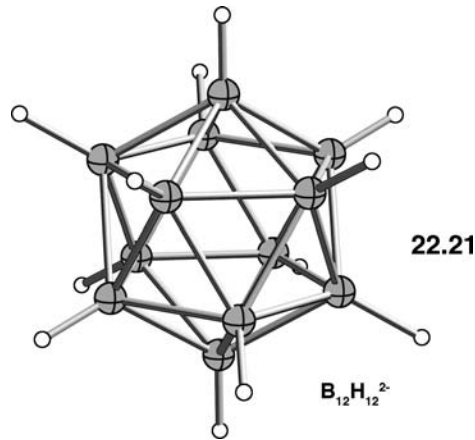
### 22.3 WADE'S RULES

The discussion above led to the conclusion that closo, nido, and arachno species based on an  $n$ -vertex polyhedron required  $(n + 1)$  skeletal electron pairs to fill all bonding orbitals and, by implication, lead to electronic stability. The application of this simple counting idea to cluster chemistry leads to a set of predictions known as Wade's rules [5]. The molecule **22.2** has a total of 26 electrons (13 pairs). Six pairs are used for the six external B–H bonds leaving seven pairs for skeletal bonding just the right number to fill all the bonding orbitals of the octahedron. For the molecule **22.3** count the Cl atom as H so then the formula is  $B_6CH_7^-$  there are a total of 30 valence electrons (= 15 pairs). Seven pairs are involved in external B–H and C–H bonds and therefore eight pairs remain for skeletal bonding, again just the right number to fill all seven tangential and one radial skeletal bonding orbitals of the

pentagonal bipyramid. If there are bridging hydrogen atoms in the molecule, it is sufficient to regard them theoretically as  $\text{H}^+$  ions coordinated to the heavy atom core. Thus, each bridging hydrogen atom contributes one electron to the skeletal electron count (SEP). For a carborane with the general formula  $[(\text{BH})_a(\text{CH})_b\text{H}_c]^{d-}$  containing  $c$  bridging hydrogen atoms the number of skeletal electron pairs is simply equal to  $1/2(2a + 3b + c + d)$ . Therefore, in **22.11**, there are  $1/2[2(4) + 3(2) + 2 + 0] = 8$  skeletal electron pairs. The geometry for **22.11** should be based on the  $N=7$  deltahedron, the pentagonal bipyramid. One can easily see in **22.11** that one cap has been removed; this is a nido structure. In **22.12**, we have  $1/2[2(9) + 6] = 12$  skeletal electron pairs. The structure is, therefore, based on the  $N=11$  octadecahedron. Nine of the vertices are filled; this is an arachno species. At first glace, it is not so easy to see that **22.12** is an arachno octadecahedron. Taking the structure from Figure 22.1 and rotating it by  $180^\circ$  yields **22.20**. The two missing



vertices are represented by black squares. There are, of course, many other ways to position the missing vertices. Wade's rules do not tell us which is favored. Nor do they tell us where to put the carbon atoms in structure **22.11**. We return to this subject shortly. An alternative method to determine the geometry puts each  $\text{BH}$  unit as contributing two electrons to the skeletal electron count and each  $\text{CH}$  unit as contributing three electrons, since an electron pair is absorbed by each  $\text{B}-\text{H}$  or  $\text{C}-\text{H}$  bond. For molecules containing skeletal atoms only, we must be careful to absorb two electrons per atom as lone pairs occupying the outward pointing orbital **22.16**. Yet the closo trigonal bipyramidal structure of  $\text{Si}_5^{2-}$ , **22.1**, each silicon atom contributes two electrons to a lone-pair orbital and the rest ( $5 \times 2 = 10$ ) to the skeletal bonding. When the negative charge is taken into account, there is just the right number of electrons, six pairs, to stabilize the trigonal bipyramidal. One interesting molecule in a historical context is the simple icosahedral species  $\text{B}_{12}\text{H}_{12}^{2-}$  (**22.21**). With the  $-2$  charge it has a total of  $1/2[(12 \times 2) + 2] = 13$



skeletal bonding electron pairs as befits the icosahedral geometry. Molecular orbital ideas using completely delocalized bonding as described here led [27] (in 1954!) to the prediction of a  $-2$  charge for this species, verified when the molecule was

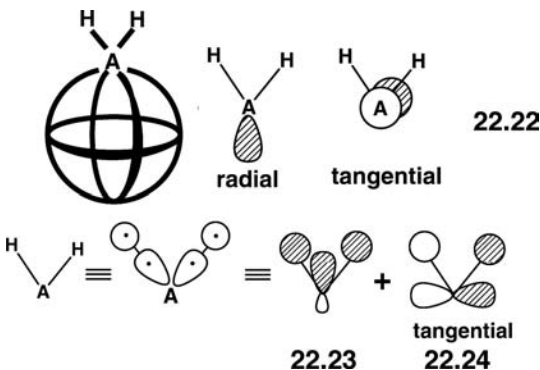
**TABLE 22.1** The Number of Skeletal Electrons Contributed by Main Group Cluster Units

A	A	A—H, A—X <sup>a</sup>	A—L <sup>b</sup>	AH <sub>2</sub>
Li, Na	-1	0	1	1
Be, Mg, Zn, Cd, Hg	0	1	2	2
B, Al, Ga, In, Tl	1	2	3	3
C, Si, Ge, Sn, Pb	2	3	4	4
N, P, As, Sb, Bi	3	4	5	5
O, S, Se, Te	4	5	6	6
F, Cl, Br, I	5	6		

<sup>a</sup>X = one-electron ligand, for example, halogen.

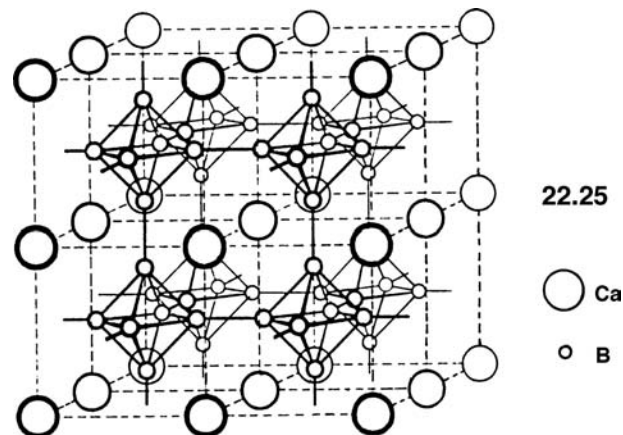
<sup>b</sup>L = two-electron ligand, for example, NH<sub>3</sub>, THF.

synthesized some years later. Table 22.1 lists the number of skeletal electrons contributed by each main group unit. It is easy to see how the number of skeletal electrons for the A, AH, AX, AL, and AH<sub>2</sub> cluster units is determined. If a vertex is occupied by a single atom A, two electrons must be placed in the extracyclic bond **22.16**. Each unit then uses the one radial and two tangential orbitals (**22.17** and **22.18**, respectively) for skeletal bonding. If a vertex is occupied by an AH or AX unit, the situation is similar except that only one electron needs to be placed in **22.16**. For AL (where L is a ligand carrying two electrons, such as PR<sub>3</sub>, N<sub>2</sub>, or NH<sub>3</sub>), no electrons need to be placed in this orbital. The AH<sub>2</sub> case is treated in exactly the same manner. The 2a<sub>1</sub> orbital (see Figure 7.2 and **7.8**) corresponds to the radial MO, **22.22**. The two tangential orbitals are b<sub>1</sub> and b<sub>2</sub>. The latter orbital is also involved in



A—H bonding. We formally assign that the A—H bonds are two-center two-electron ones. Symmetry-adapted combinations of them yield **22.23** and **22.24**. **22.24** is the second tangential orbital used for cluster bonding so the electrons in it also count as skeletal electrons. Thus, CH<sub>2</sub> contributes four electrons, rather than the two we may have initially thought.

In the solid state, there are many instances of infinite three-dimensional cage structures. **22.25** shows the structure of CaB<sub>6</sub> where boron octahedra are linked together via their vertices. Each B<sub>6</sub> octahedron needs a total of six electrons to form two-center two-electron bonds to the six adjacent octahedra and  $2(n+1) = 14$  electrons for skeletal bonding, a total of 20. The six boron atoms contain a total of  $6 \times 3 = 18$  valence electrons; the extra two come from the electropositive calcium atom [28]. A related structure is found [29] for Rb<sub>2</sub>Ga<sub>3</sub> (Rb<sub>4</sub>Ga<sub>6</sub>). This is composed of sheets of edge-linked Ga<sub>6</sub> octahedra, but in contrast to CaB<sub>6</sub> there are no linkages



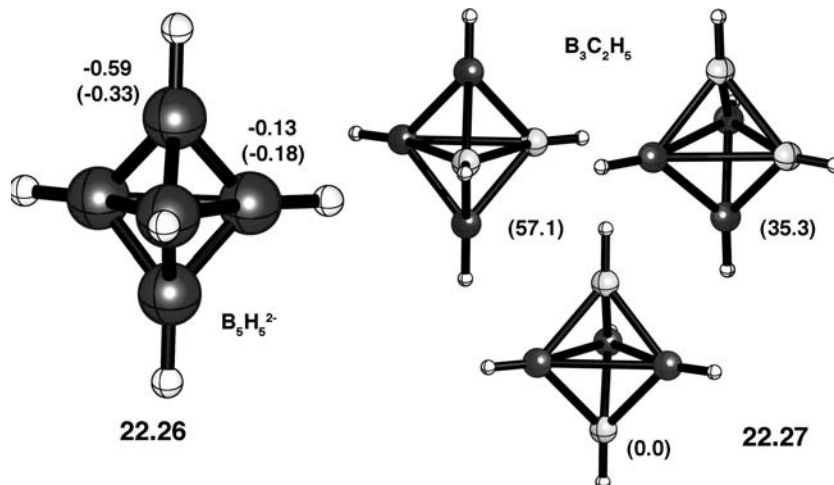
between the sheets. Electron counting here leads to a total of seven skeletal pairs per octahedron, a figure commensurate with its structure. There are many other structures of this type [30].  $\text{KGa}_3$  consists of vertex-linked  $\text{Ga}_8$  dodecahedra along with Ga atom spacers,  $\text{K}_3(\text{Ga}_8)(\text{Ga})$  and  $\text{Mg}_2\text{B}_{14}$  consists of icosahedra and isolated boron atoms,  $\text{Mg}_2(\text{B}_{12})(\text{B})_2$ .

Wade's rules predict the overall shape of the cluster. They do not energetically sort the isomers that are possible in, for example, a carborane or arachno cluster. One could, of course, do a series of calculations to address this issue, but this does not, by itself, tell us why or offer us some insight with which to make predictions. One of the earliest attempts to predict stability orderings was given by Williams [33]. There are two basic, empirical rules:

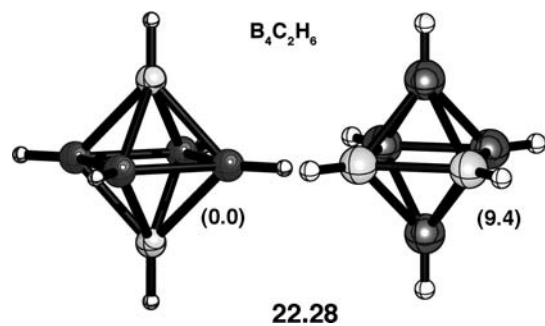
- (1) Electronegative atoms prefer to reside in positions of the lowest coordination number.
- (2) If the coordination numbers are identical, electronegative atoms prefer to be as far apart as possible in the cluster.

Rule (1) takes precedence over rule (2). One can understand the genesis of rule (1) by noting that more electropositive elements have diffuse AOs which can overlap more effectively in multicenter situations than the contacted AOs associated with a more electronegative atom. Rule (2) can be viewed as a manifestation of the fact that same charges repel each other. Another idea set forth by Jemmis [34] focused on the capping atoms for closo structures. A capping atom bonded to a five-membered ring will prefer to be a more electropositive atom, for example, boron, rather than carbon. The reason for this is again related to the diffuseness of the  $p$  AOs that will overlap better with the  $p$  AOs of a large ring. On the other hand, the overlap associated with capping a three- or four-membered ring will be optimal for a more contracted set of  $p$  AOs from, for example, carbon. Perhaps, the most general treatment of isomer stabilities was due to Gimarc and Ott [35] with their topological charge stabilization theory. The idea here is that the electronegative atom(s) will prefer positions of higher charge as derived by a calculation on a homolog. The theoretical underpinnings of this was presented in Section 12.7 and derived in equations 12.29–12.35.

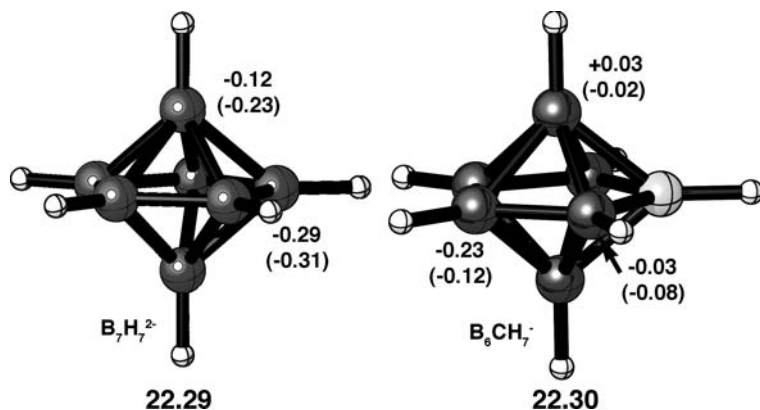
Let us take a couple of representative examples that illustrate these isomer stability rules. Starting with the  $N=5$  trigonal bipyramidal, there are two axial and three equatorial sites in the  $\text{B}_5\text{H}_5^{2-}$  structure, 22.26. The Williams and Jemmis rules clearly point to the fact that C—H groups should be substituted at the axial sites.



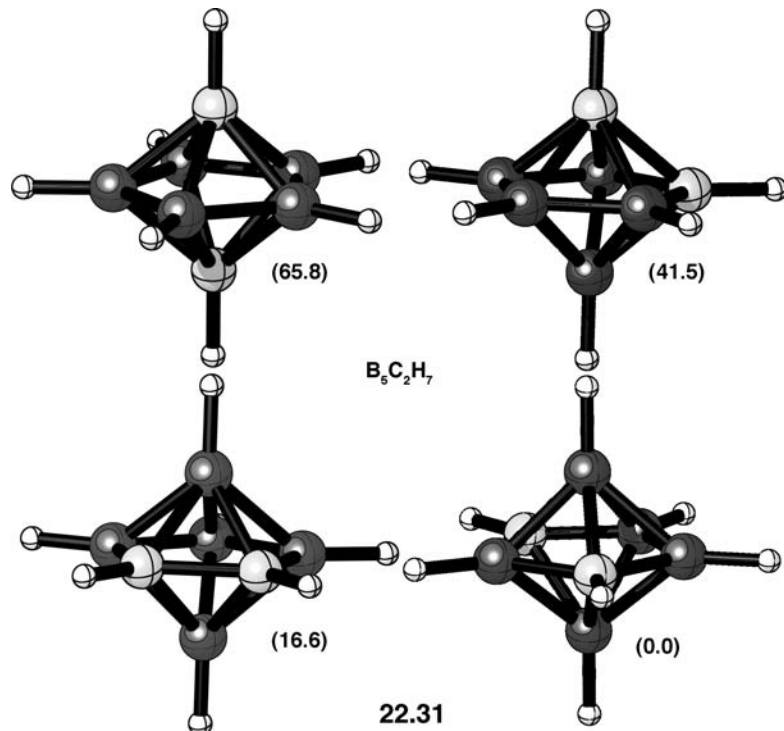
Topological charge stabilization also strongly supports this notion. B3LYP calculations [36] on  $\text{B}_5\text{H}_5^{2-}$  demonstrate a very severe basis set dependence of the computed charges using the Mullikan population scheme. However, a natural population analysis (NPA) using natural atomic orbitals [37a] or the Hirshfeld method [37b] are much less dependent on the basis set used. The NPA and Hirshfeld values (in parenthesis) for  $\text{B}_5\text{H}_5^{2-}$  are given in **22.26**. Both methods show the axial atoms to be much more negative than the equatorial ones. MP2 geometry optimizations with a large basis were carried out on  $\text{B}_4\text{CH}_5^-$  [38]. Carbon in the axial position was found to be 25.5 kcal/mol more stable than substitution of carbon in the equatorial plane. For  $\text{B}_3\text{C}_2\text{H}_5$  [38], the MP2 relative energies in kcal per mole are shown in **22.27**. The 1,5 isomer is, indeed, the most stable one by a wide margin. Experimentally, only the 1,5 isomer is known [39,40]. All the positions are equivalent in the octahedron. There are two isomers available for  $\text{B}_4\text{C}_2\text{H}_6$ . As shown in **22.28**, the 1,6 isomer is more stable than the 1,2 structure by 9.4 kcal/mol. This is in agreement with the fact that the



1,2 isomer rearranges quantitatively into the 1,6 isomer at  $250^\circ\text{C}$  [41]. The pentagonal bipyramidal ( $N=7$ ) offers an interesting contrast. Here, the capping, apical, atoms are six-coordinate, whereas the equatorial ones are five-coordinate. Williams and Jemmis' predictions then favor carbon to reside in an equatorial rather than an axial position. B3LYP calculations of the charges in  $\text{B}_7\text{H}_7^{2-}$  using the NPA and Hirshfeld (in parenthesis) methods are shown in **22.29**. Both techniques point to a larger negative charge on the equatorial positions compared to the axial ones. The MP2 calculations [38] find that the equatorial isomer of  $\text{B}_6\text{CH}_7^-$  is 30.5 kcal/mol

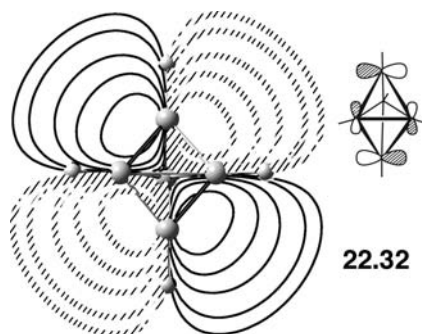


more stable than the axially substituted one. According to Williams rule (2), a second carbon atom should then be substituted at the fourth position, rather than the third position. Topological charge stabilization considerations also are in favor with this proposal. The charges for  $\text{B}_6\text{CH}_7^-$  are shown in 22.30. Notice that electron density is built up at the fourth position and diminished at the third position when a carbon atom is substituted at an equatorial site. The consensus is then that 2,4- $\text{B}_5\text{C}_2\text{H}_7$  should be the most stable isomer out of four possibilities. The results from MP2 calculations [38] are given in 22.31. The 2,4 isomer is by far the most stable one. The rearrangement between members of this group that has been studied [42], and all

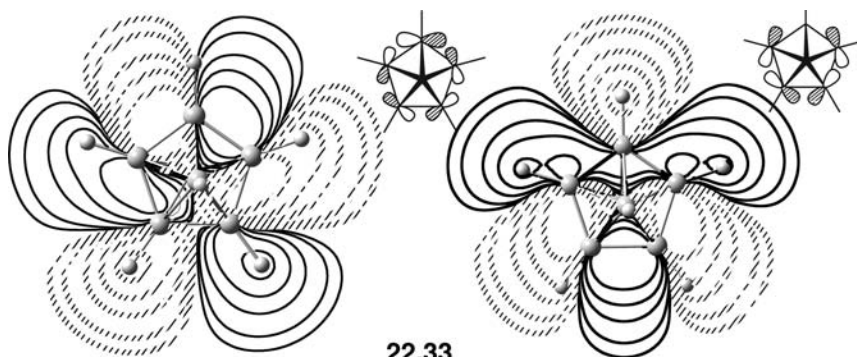


experimental data also point to the 2,4 isomer as being the most stable. The prediction of nido and arachno isomers is more difficult and is not discussed here [43].

The charge distribution for  $B_7H_7^{2-}$ , **22.29**, is exactly the opposite of the result found for  $B_5H_5^{2-}$ , **22.26**. The situation in  $B_5H_5^{2-}$  is reminiscent to that found for the  $PH_5$  trigonal bipyramidal (see Figure 14.16 and the discussion around it) where the  $2a_1'$  highest occupied molecular orbital (HOMO) is disproportionately larger at the axial positions. Here for  $B_5H_5^{2-}$ , the  $e''$  HOMO is concentrated on the axial positions. From Figure 22.3, one can see that the  $e''$  set on the apical boron atoms lie at lower energy than the  $e'' \pi^*$  set on equatorial  $B_3$ . This leads to larger coefficients at the axial sites. A contour plot of one member of the  $e''$  HOMO is shown in **22.32**. This was taken from a B3LYP calculation of  $B_5H_5^{2-}$ . The polarization toward the axial



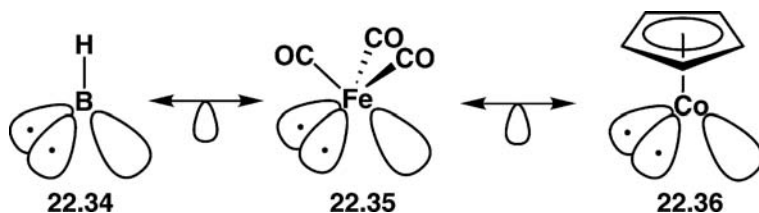
positions is quite evident. For  $B_7H_7^{2-}$ , the charge imbalance in **22.29** can be ascribed to the HOMO  $e'_2$  set. Contour drawings of the  $e'_2$  set are shown from a top view in **22.33**. There are no valence orbitals on the axial boron atoms that form  $e'_2$  symmetry-adapted combinations. On the other hand (discounting the B—H  $\sigma$ -based MOs), the other orbitals are delocalized over the entire molecule. Therefore, the electron density on the equatorial boron atoms is larger than that at the axial boron atoms.



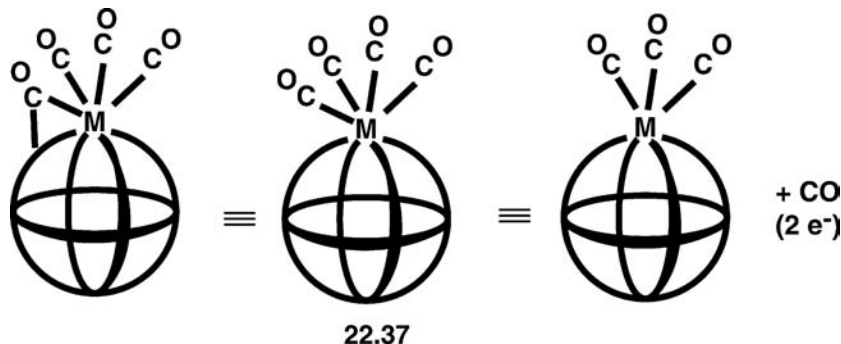
For transition metal containing systems, the generation of the number of skeletal electrons contributed by various building blocks is a little more complicated. In Chapter 16, we saw that in a single  $ML_n$  complex the metal valence orbitals split into a group of  $n\sigma^*$  orbitals and  $(9 - n)$  nonbonding orbitals. We assume in our treatment here that, out of this latter group, there are three [5,31,32] that are involved in skeletal bonding just like the three orbitals **22.17** and **22.18**. The other  $6 - n$  orbitals remain nonbonding orbitals and do not take part in skeletal interactions. It is a gross simplification but one which is justified in the sense that it works well in practice. It has strong links with the isolobal analogy in Chapter 21, as we discuss later. We need to know how many electrons lie in this group of three orbitals. For an  $M(CO)_n$  fragment, the total number of  $d$  electrons is simply equal to  $v$ , the number of valence electrons for the  $M(0)$  metal.  $2(6 - n)$  reside in the group of nonbonding orbitals, leaving  $v - 12 + 2n$  to participate in skeletal interactions.

In the case of a Cp unit, one electron is formally transferred to the  $\eta^5$  – Cp ring (effectively a triply coordinating ligand), hence each  $M(Cp)_m$  unit has a total of  $v - m$  valence electrons and  $6 - 3m$  nonbonding orbitals. This leaves  $(v - m) - 2(6 - 3m) = v - 12 + 5m$  electrons for skeletal bonding. Yet a  $[M_a(CO)_bCp_c]^{d-}$  cluster, the total number of skeletal electron pairs is simply  $1/2[SV - 12a + 2b + 5c + d]$ . Here, SV indicates the total number of valence ( $s + d$ ) electrons associated with the collection of a metal atoms, which need not all be the same. Just as with the case of a bridging H atom of a carborane it does not matter overall where the carbonyl groups are located. Whether they are terminal or bridging, their influence on the skeletal electron count is the same.

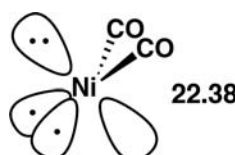
An alternative way to generate the number of skeletal electrons is via the isolobal analogy. We saw in the previous chapter that an A–H unit has three frontier orbitals and symmetry-adapted combinations of them (see 9.3 and 9.4) simply yield the radial and two tangential MOs of 22.17 and 22.18. So, a B–H fragment, 22.34, has three frontier orbitals with two electrons partitioned between



them. This is precisely the same as in  $Fe(CO)_3$ , 22.35, where the three orbitals are the  $2e + 2a_1$  set shown in Figure 20.1 or those in  $CpCo$ , 22.36, which correspond to  $2a_1 + e_1$  in 20.12 and 20.13. A  $M(CO)_4$  group or  $CpM(CO)$  is handled exactly analogous to  $AH_2$  in that the “extra”  $M-CO$  bond is counted as contributing to cluster bonding, 22.37. In the carborane field, all cluster atoms are treated as being



$A-R$  groups where  $A=H$ , a lone pair, and so on. In the transition metal world, the clusters are based on the octahedron. This brings up a related issue. A  $MI(CO)_2$  group is not treated in the same way as it is in the isolobal analogy. The  $ML_2$  case was derived from a 16-electron square planar or trigonal planar molecule as the starting point. Here,  $M(CO)_2$  is viewed as having three groups pointed away from the cluster, 22.38, with one of them as a metal-centered lone pair. Remember that



each metal also will have six “ $t_{2g}$ ” orbital localized at the metal. Therefore, a  $\text{Ni}(\text{CO})_2$  group is  $d^{10}$  and six electrons are in the “ $t_{2g}$ ”, two electrons are in the outer-pointing lone pair orbital; this leaves two electrons remaining as skeletal electrons for the cluster bonding. In the molecules of this chapter, square planar coordination is never observed at any deltahedral vertex. So in Scheme 21.1,  $\text{CH}_2$  and  $\text{FeL}_4$  are claimed to be isolobal species and accordingly they both contribute four electrons to skeletal bonding. Similarly,  $\text{CH}$ ,  $\text{Co}(\text{CO})_3$ , and  $\text{NiCp}$  are isolobal fragments according to Scheme 21.1 and indeed each contributes three electrons to skeletal bonding. Since a  $\text{CH}$  or  $\text{CR}$  group is isolobal and isoelectronic with a  $\text{Co}(\text{CO})_3$  or  $\text{Ir}(\text{CO})_3$  group the whole series of nido-trigonal bipyramidal structures (tetrahedra) are readily generated in 21.57–21.61. These all have a total of  $1/2(4 \times 3) = 6$  skeletal pairs. The  $\text{Co}_2(\text{CO})_6\text{C}_2\text{R}_2$  molecule is perhaps more often regarded as an acetylene complex but this series illustrates neatly the dominating electronic influence of the tetrahedral arrangement of heavy atoms. In fact, the one-to-one correspondence between the electron-counting ideas in this and the previous chapter is complete the exception of fragments derived from square or trigonal planar coordination. For example,  $\text{Ni}(\text{CO})_2$  contributes the same number of electrons to skeletal bonding as does  $\text{Cr}(\text{CO})_4$  (and not  $\text{Fe}(\text{CO})_4$ ). It is important to realize that the ligands around the metal need not be confined to carbonyl and cyclopentadienyl groups. Phosphines, halides, arenes, and so on, are found to be ligands and can be treated in the same manner. Hydrogen atoms are probably best removed as protons. A summary of the numbers of electrons contributed by some carbonyl- and cyclopentadienyl-bearing metal atom units is given in Table 22.2. The permutations of the building blocks of Tables 22.1 and 22.2 are almost endless.

So 22.5 can be written as  $[\text{Ni}(\text{CO})_2]_6^{2-}$  so there are  $1/2[6(2) + 2] = 7$  skeletal electron pairs which just fits  $N = 6$ , the octahedron. In 22.39 there are terminal, doubly bridging and even two triply bridging carbonyls. There is also a  $\text{Cl}^-$  ligand. We

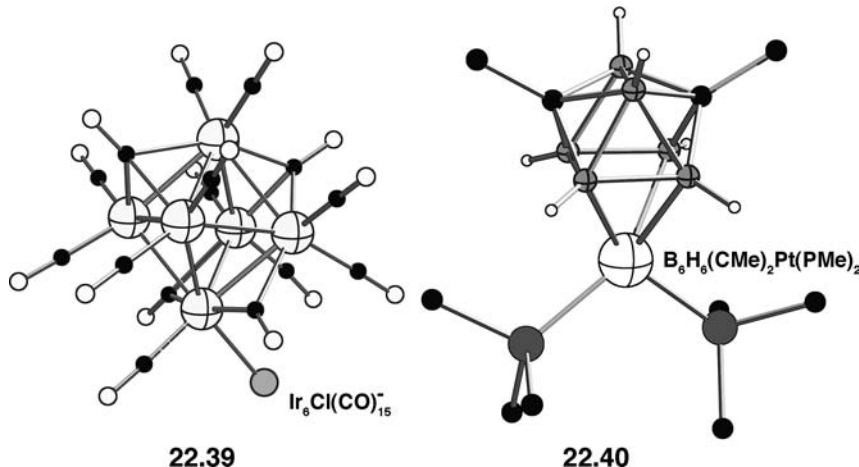
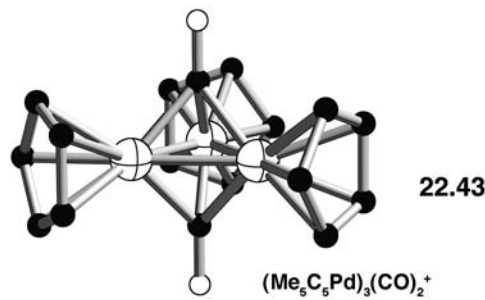
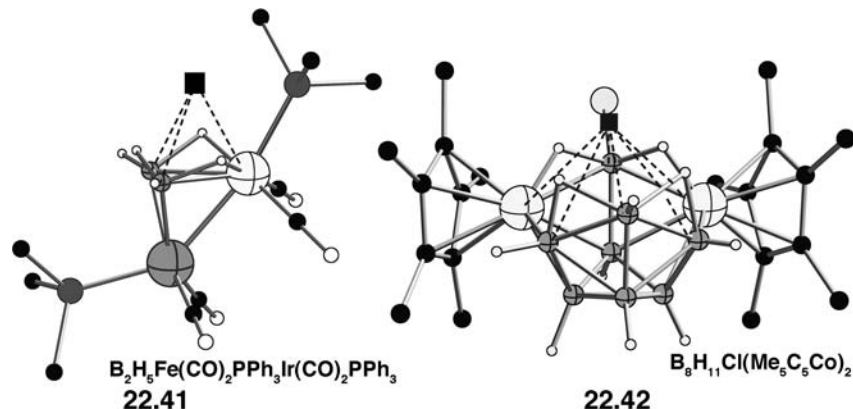


**TABLE 22.2** The Number of Skeletal Electrons Contributed by Transition Metal Cluster Units

M	MCp	$\text{M}(\text{CO})_3$	$\text{M}(\text{CO})_2$	$\text{M}(\text{CO})_4$
Cr, Mo, W		0		2
Mn, Tc, Re	0	1		3
Fe, Ru, Os	1	2	0	4
Co, Rh, Ir	2	3	1	5
Ni, Pd, Pt	3	4	2	6

could count this as  $[\text{Ir}(\text{CO})_3]_4[\text{Ir}(\text{CO})_2][\text{Ir}(\text{CO})\text{Cl}^-]$ . The  $[\text{Ir}(\text{CO})\text{Cl}^-]$  group could be regarded as a  $d^8 \text{IrL}_2$  fragment which then is isoelectronic to  $\text{OsL}_2$  plus one electron for the negative charge = 1 skeletal electron. The total skeletal electron count is then  $[4(3) + 1(1) + 1(1)] = 14$  skeletal electrons. Again this is just the right number for an octahedron. A related example is  $\text{Os}_5(\text{CO})_{15}\text{I}^-$ , 22.4. We could treat this as  $[\text{Os}(\text{CO})_3]_5 + \text{I}^-$ . Here the  $\text{I}^-$  ligand donates two electrons for skeletal bonding so the total electron count is  $[5(2) + 2] = 12$  which is the correct number for  $N = 5$ , the trigonal bipyramidal. In 22.6 remember that there are two bridging hydrogen atoms that were not located in the crystal structure, so the skeletal electron count is  $[3(2) + 3(2) + 2] = 14$ , just right for the octahedron. In 22.7, there is an N—Et group that (Table 22.1) contributes four skeletal electrons so the count becomes  $[7(2) + 2(2) + 4] = 22$  electrons which corresponds to  $N = 10$ , the bicapped square antiprism. The orientation of the crystal structure in 22.7 is such that the N—Et and one B—H group on the opposite side are the two caps. For 22.40, the count is  $[6(2) + 2(3) + 2] = 20$ . The structure is indeed based on the  $N = 9$ , tricapped trigonal prism where the  $(\text{BH})_6$  group forms the trigonal prism. Notice that the  $\text{Pt}(\text{PMe}_3)_2$  group is not canted as shown for  $\text{Ni}(\text{CO})_2$  in 22.38. This is normally the case for  $\text{ML}_2$  groups as part of a cluster compound. Electronically, there still is an extra lone pair that does not participate in cluster bonding.

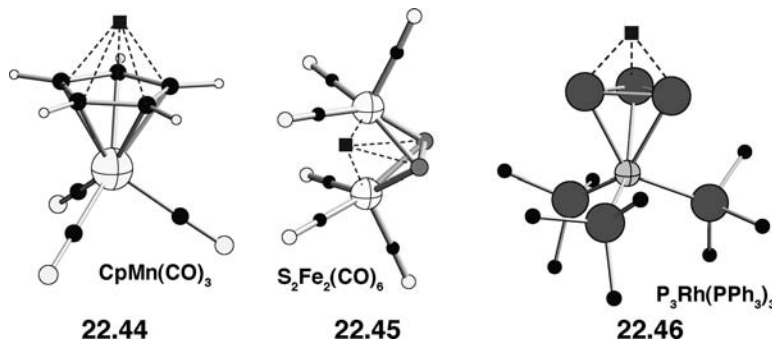
Nido and arachno metallacarboranes can easily be handled, but frequently some imagination is required to visualize the deltahedron. The structure shown in 22.41 [46] contains a number of groups—three bridging hydrogens, two



B—H groups, and  $\text{M}(\text{CO})_2\text{PPh}_3$  ( $\text{M}=\text{Fe, Ir}$ ) fragments. The electron count is  $[3 + 2(2) + 2 + 3] = 12$ . The structure then should be based on the  $N = 5$  trigonal bipyramidal. Four atoms define the cluster; it is a nido compound with the fifth vacant site indicated by the black square in 22.41. 22.42 [47] possesses seven B—H groups, one B—Cl and two  $\text{Me}_5\text{C}_5\text{Co}$  fragments along with four bridging hydrogen atoms. Therefore, the skeletal electron count is  $[7(2) + 1(2) + 2(2) + 4] = 24$ .

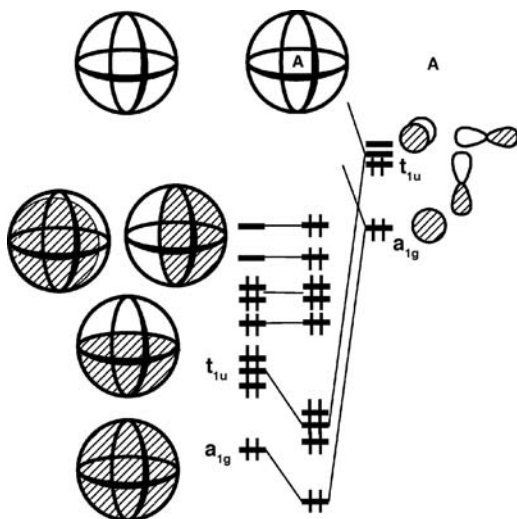
The cluster is based on the  $N=11$ , octadecahedron with one vacancy. **22.43** is an interesting example. One might count this as having three  $(\text{Me}_5\text{C}_5)\text{Pd}$  groups and two extra COs, thus, the skeletal electron count is  $[3(3) + 4 - 1] = 12$  electrons. The geometry here is based on the trigonal bipyramidal with the carbonyl groups lying in the vacant positions of the cluster framework. In actual fact compounds with two less electrons exist (see **21.82**), as well as examples with one or two more electrons than **22.43**. The structures over this four-electron range are all close to being the same.

Some examples include rather unusual species as well as traditional molecules viewed in a rather different light.  $\text{CpMn}(\text{CO})_3$  [48], **22.44** is isolobal with ferrocene and  $\text{C}_6\text{Me}_6^+$  with an apical  $\text{CMe}^{2+}$  unit along with **21.74** and **21.75**. All can be regarded simply as a nido pentagonal bipyramid (number of skeletal pairs =  $1/2[(6 \times 3) - 2] = 8$ ); ferrocene contains the isolobal  $\text{FeCp}$  unit in its place.



**22.45** [49] would normally be considered to have an Fe—Fe single bond. Whether there is a bond between the two sulfur atoms has engendered controversy. In terms of Wade's rules, we have  $1/2[2(2) + 2(4)] = 6$  skeletal electron pairs and so the structure should be represented as a  $N=5$ , nido trigonal bipyramid. There are also six electron pairs in **22.46** [50] making it a nido trigonal bipyramid. It is interesting to see that  $\text{C}_4\text{H}_4$  (also six pairs) is predicted to be a nido trigonal bipyramidal (i.e., a tetrahedron) rather than the (Jahn–Teller unstable) square, which is the predicted structure for  $\text{C}_4\text{H}_4^{2-}$  or  $\text{S}_4^{2+}$  (seven pairs). The tert-butyl derivative does have a tetrahedral geometry. There are many examples iso-electronic and isostructural to those in **22.46**. Other examples are  $\text{Co}(\text{CO})_3\text{As}_3$  and the tetrahedral structures found for elemental phosphorus ( $\text{P}_4$ ) and arsenic ( $\text{As}_4$ ) along with the series **21.58–21.61**.

The insertion of a small atom into the center of a cluster alters the counting rules, since there are extra orbitals to be included. A simplified picture is shown in Figure 22.5. Using octahedral symmetry, the  $t_{1u}$   $p$  orbitals and the  $a_{1g}$   $s$  orbital find partners in the bonding octahedral cluster orbitals. The  $p$  orbitals overlap with a symmetry-adapted combination of tangential orbitals and the  $s$  orbital with the bonding radial cluster orbital. The result is a new set of four orbitals that are both skeletal bonding and central atom–cluster bonding. The cluster plus central atom is stable, therefore, for the same total number of skeletal electrons as the cluster alone. Consider **22.8** as  $\text{C}@\text{[Ru}(\text{CO})_3\text{]_5}[\text{Ru}(\text{CO})_2]$ . There are then  $1/2[4 + 5(2) + 0] = 7$  skeletal electron pairs. This is just the right number for a closo octahedron. In **22.9**, there are several triply bridging carbonyls and the rest are terminal. One could count the  $2^-$  charge as representing a missing CO and, therefore, the count is  $1/2[4 + 9(2)] = 11$ . The  $N=10$ , bicapped square antiprism with one missing vertex (a nido structure) fits this structure. For **22.10** there are  $1/2[5 + 6(2) + 2(0) + 1] = 9$  skeletal electron pairs. Wade's rules clearly predict that it should be a  $N=8$  closo dodecahedron and clearly it is not. The shape is actually an arachno bicapped square

**FIGURE 22.5**

Generation of the lowest energy set of levels for an arbitrary deltahedron (the symmetry labels are appropriate for an octahedron) centered by a main group atom.

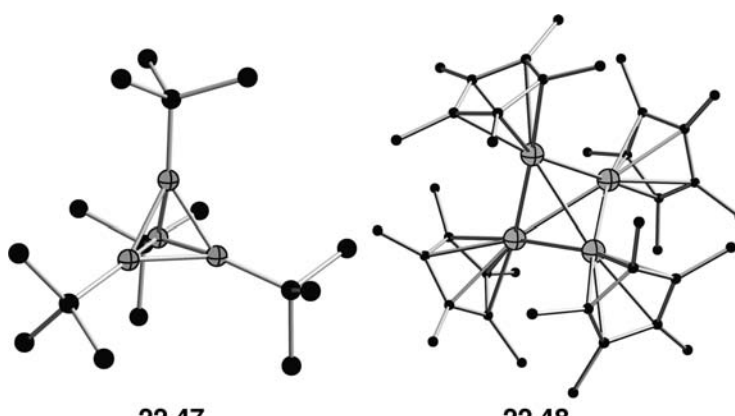
antiprism where both caps are missing. This means that there should be four more electrons or two COs that have been missed in the X-ray structure. This is hardly the case; Wade's rules have been violated and we see more examples in Section 22.4. There is a compound [51],  $\text{C}@\text{Ni}_8(\text{CO})_{16}^{2-}$ , has  $1/2[4 + 8(2) + 2] = 11$  skeletal electrons and does have the shape of an arachno bicapped square antiprism in accordance with Wade's rules.

## 22.4 VIOLATIONS

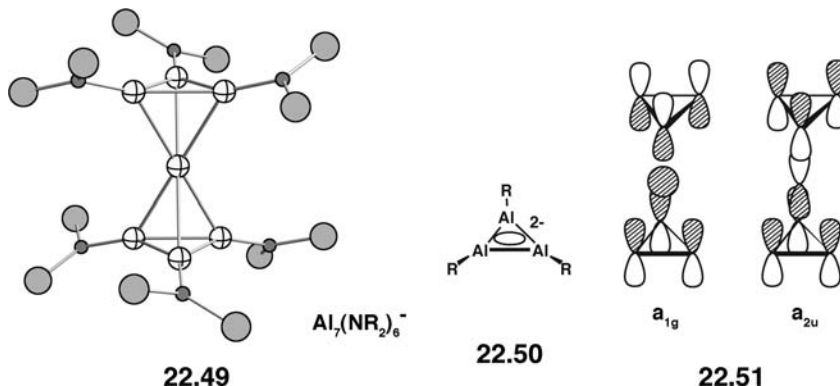
There are many!

The polyhedral skeletal electron-counting rules do have some theoretical underpinnings as outlined in Section 22.2. This is a simple and very useful model to rationalize molecular structures that cannot be framed within the standard two-electron two-center paradigm. Similar to the valence shell electron repulsion model and the isolobal analogy there are exceptions and these exceptions are quite interesting in and of themselves. We shall restrict our coverage here to the most common patterns where Wade's rules predict a different shape or instances where the molecules are not predicted to be stable.

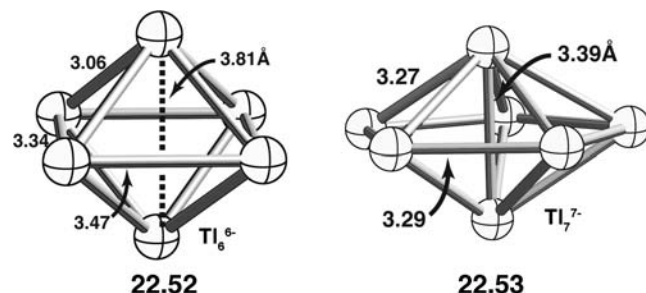
There are a number of tetrahedral clusters that have four skeletal pairs of electrons instead of the six expected for a nido trigonal bipyramidal. One example is given by 22.47 [52],  $\text{B}_4(\text{t-Bu})_4$ .  $\text{B}_4\text{Cl}_4$  also exists and has this same structure [53].



We mentioned before that the  $(\text{Me}_5\text{C}_5)\text{Al}$  fragment has a filled orbital HOMO,  $2a_1$  in Figure 21.3 and an empty  $2e_1$  set which are concentrated on Al. It too forms a tetrahedron with four skeletal electron pairs, **22.48** [54]. It is easy to see that this electron count should be stable. The fully symmetric,  $a_1$  combination of radial orbitals on the left side of Figure 22.2 and the bonding  $t_2$  set of tangential functions on the right side of Figure 22.3 are filled. The large gap then between filled  $t_2$  and the  $e$  set on the left side of Figure 22.3 implies that the tetrahedral structure should be stable with this electron count. An even more electron deficient cluster,  $\text{Al}_7(\text{NR}_2)_6^-$ , has been isolated [55], and its structure is shown in **22.49**. The Al—Al distance

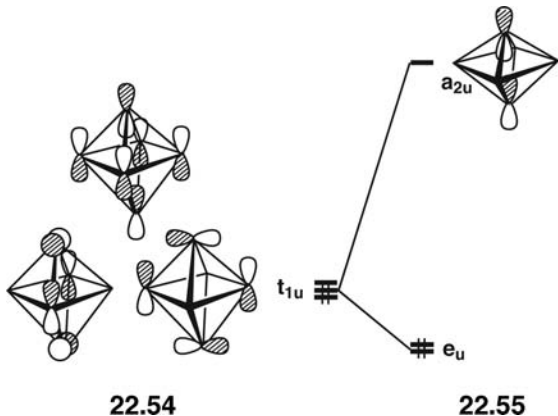


within each three-membered ring ( $2.53 \text{ \AA}$ ) is much shorter than that to the central Al ( $2.73 \text{ \AA}$ ). The best way to view the electronic structure in this compound is to let each three-membered ring be isoelectronic to the cyclopropenium cation, **22.50**. That is, there are three 2-center 2-electron  $\sigma$  bonds, and the fully symmetry  $\pi$  orbital is filled. Compounds akin to **22.50** have been isolated [56]. Symmetry-adapted combinations of the two  $\pi$  orbitals as demonstrated in **22.51** find a good overlap with the s and one  $p$  AO on the central Al atom. The molecule is held together by only four electrons [57]! There is another way that some clusters can deal with electron deficiency. In the solid-state KTI consists of  $\text{Ti}_6^{6-}$  clusters [58]. There are  $\frac{1}{2}[6(1) + 6] = 6$  skeletal electron pairs. But a closo octahedron requires seven pairs. What occurs is that the octahedron is compressed as shown in **22.52**.



There is a considerable span of  $\text{Ti}—\text{Ti}$  distances around the edges in **22.52**, but if one takes the average of them,  $3.18 \text{ \AA}$ , for a regular octahedron the two trans vertices would be  $4.50 \text{ \AA}$  apart. In  $\text{Ti}_6^{6-}$  they are  $3.81 \text{ \AA}$ . This certainly represents a

fairly weak Tl—Tl interaction but isolated  $\text{Ti}_7^{7-}$  clusters have also been found in the solid state [59], 22.53. The axial compression here is even greater. 22.53 is also electron deficient with seven (rather than eight) skeletal electrons. In both clusters, a “bond” is created between the two axial vertices. Perhaps, a more productive way to view this situation is that this represents a first-order Jahn–Teller distortion (see Section 7.4A). From the right side of Figure 22.4, one can see that an octahedral cluster molecule with six electron pairs will partially fill the  $t_{1u}$  set (remember that the fully symmetric radial set is also occupied). So at the octahedral geometry, 22.54 shows that a classic first-order Jahn–Teller is expected to occur. The  $e_g$  normal

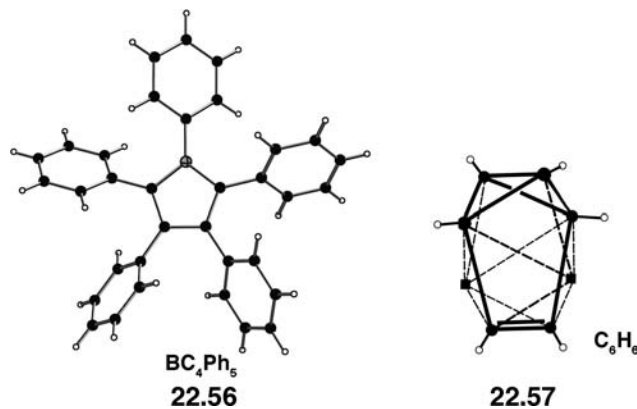


22.54

22.55

mode (see Appendix III) is one of the modes obtained from the cross-product of  $t_{1u}$ . This distortion in fact brings two trans atoms closer together and as shown in 22.55 this leads to splitting the  $t_{1u}$  set. A somewhat stabilized  $e_u$  set (in  $D_{4h}$  symmetry) is generated since overlap between the axial and equatorial  $p$  AOs is increased. Most importantly the third component of  $t_{1u}$  is greatly destabilized. Overlap between the axial and equatorial  $p$  AOs decreases and antibonding between the two axial atoms is turned on. One can view this MO as the  $\sigma^*$  MO between the axial cluster atoms. One should also note that the fully symmetric radial combination at low energy will also be stabilized since  $\sigma$  bonding between the two axial atoms is increased in this orbital. Precisely, the same thing happens in 22.53. We note that this is not the only possible structure for KTI. There are in fact seven alternative structures and which structure prevails is a complex and delicate matter [60].

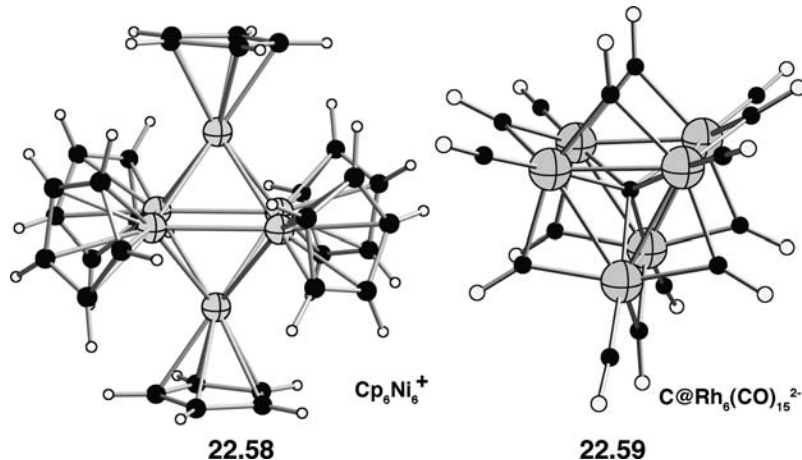
Although  $\text{C}_5\text{H}_5^+$  is predicted and observed to have a nido octahedral geometry (Figure 11.7 or 21.71), isoelectronic ( $\text{PhC}_4(\text{PhB})$ , 22.56 [61] is a planar ring rather than a square pyramid. The  $\text{C}_6\text{H}_6$  molecule with  $1/2(6 \times 3) = 8$  pairs should be an



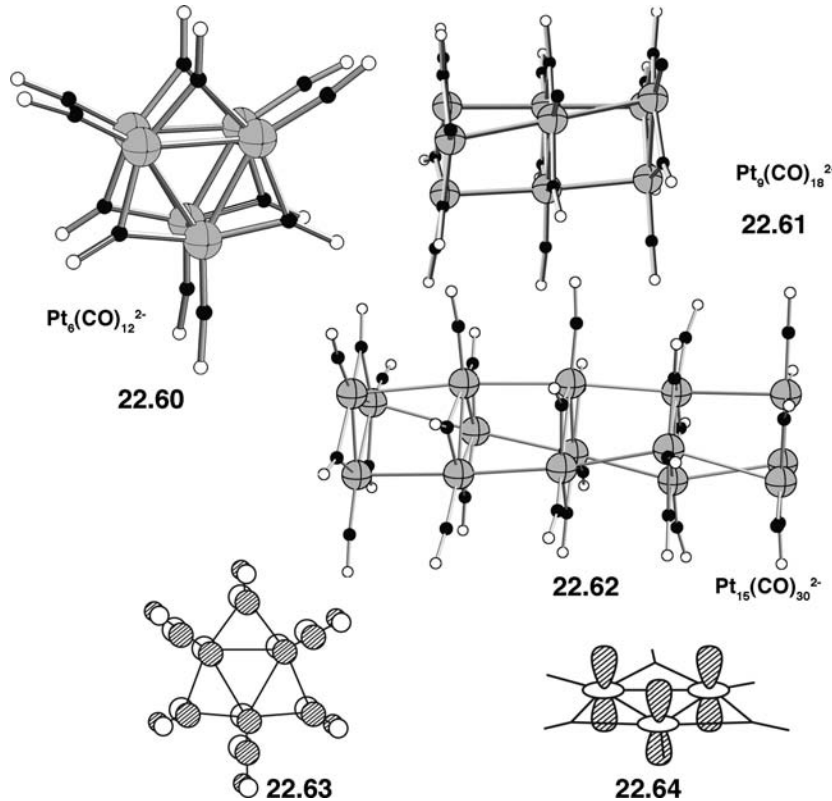
22.57

arachno  $D_{2d}$  dodecahedron. **22.57** shows the structure of benzvalene, a benzene isomer which is just this. The genesis of the problem here lies in the energetic competition between  $\pi$  bonding and multicenter  $\sigma$  bonding. A recurring theme in this book has been that  $\pi$  bonding in the first row of the periodic table is very strong in comparison to that in the later rows. Thus, benzene is much more stable than any other  $C_6H_6$  isomer. For example, the structure of  $Si_6H_6$  at the  $D_{6h}$  geometry is less stable than other cluster-like structures [62].

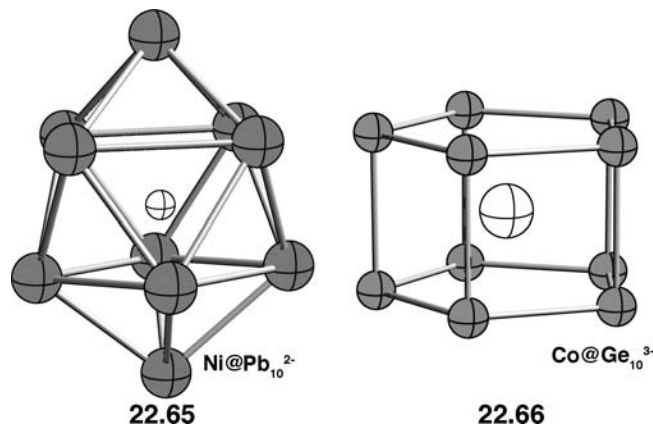
There are also a number of examples which, given their geometry, have too many electrons. The molecule  $Ni_6Cp_6^+$ , **22.58** [63], for example, has  $\frac{1}{2}[6(3) - 1] = 8.5$



skeletal electron pairs but has the octahedral skeleton expected for seven skeletal pairs. In **22.59** [64], there are  $\frac{1}{2}[3(3) + 3(1) + 4 + 2] = 9$  pairs of electrons. This is just right for forming nine 2-electron 2-center bonds in the trigonal prism. In fact this is a fairly common geometry with this electron count.  $Pt_3(CO)_{12}^{2-}$ , **22.60** [65] is

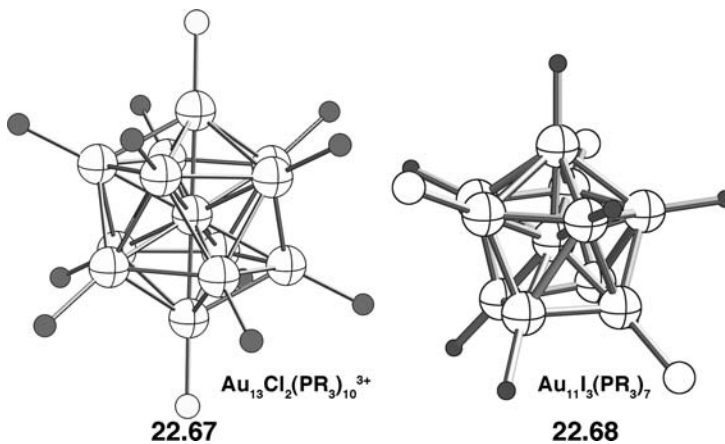


isoelectronic to  $\text{Ni}_3(\text{CO})_{12}^{2-}$ , **22.5**, but certainly not isostructural. **22.60** is clearly a trigonal prism with four skeletal electrons less than in **22.59**. In fact there are a series of polymers that have been prepared with the formula  $\text{Pt}_{3n}(\text{CO})_{6n}^{2-}$  where  $n=2, 3, 4, 5, 6$ , and 10. As shown for the trimer, **22.61** [65] and the pentamer, **22.62** [66], each Pt triangle is rotated with respect to the next one. This implies that there is not much energy difference between the trigonal prismatic and the octahedral geometry. In fact  $^{195}\text{Pt}$  NMR studies on the polymers have shown that the Pt triangles rotate freely about the  $C_3$  axis [67]. In **22.60** the Pt–Pt distance within the triangles averages  $2.65\text{\AA}$  while that between the triangles is  $3.03\text{\AA}$ . These distances are also representative of those found for **22.61** and **22.62**. The force holding the  $\text{Pt}_3(\text{CO})_6$  units together is small. The NMR studies show that there is also rapid exchange of  $\text{Pt}_3$  triangles between chains. We have not been entirely honest about the Ni analog, **22.5**. The Ni–Ni distance within triangles was found to be  $2.38\text{\AA}$  and that between triangles is  $2.74\text{\AA}$ . Therefore, the structure is not really an octahedron. For both  $\text{Pt}_3(\text{CO})_6^{2-}$  and the nickel analog, the HOMO is predicted [68] to be **22.63**. Thus, combining  $\text{Pt}_3(\text{CO})_6^{2-}$  with  $\text{Pt}_3(\text{CO})_6$  (where the LUMO is **22.63**) leads to a two-orbital two-electron stabilizing interaction. Each additional  $\text{Pt}_3(\text{CO})_6$  unit will interact in the same way and the totally bonding combination of **22.63** units will be filled. There are also repulsive interactions between the Pt triangles, most notably filled  $z^2$  combinations illustrated in **22.64**. Therefore, the net bonding between  $\text{Pt}_3(\text{CO})_6$  units is quite weak. Another electron rich cluster is given in **22.65** [69],  $\text{Ni}@\text{Pb}_{10}^{2-}$  which has 11 skeletal electron pairs in agreement with its bicapped

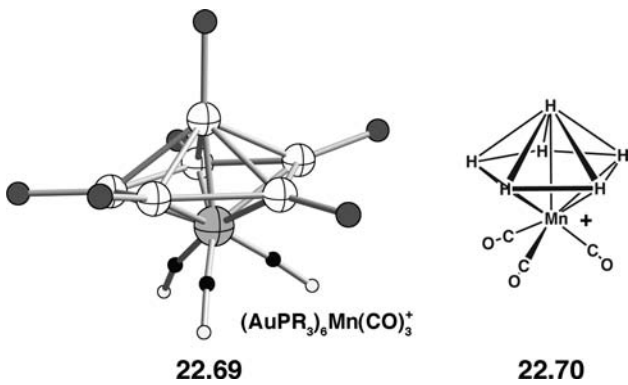


square antiprismatic structure. However, this counts Ni as a  $d^{10}$  metal which then donates no electrons to the cluster bonding.  $^{207}\text{Pb}$  NMR exhibits only one resonance for the two kinds of Pb atoms down to  $-45^\circ\text{C}$ , so there must be a low-energy dynamic process that renders the Pb atoms equivalent. An isoelectronic molecule is **22.66** [70],  $\text{Co}@\text{Ge}_{10}^{3-}$ . It has a pentagonal prismatic structure which one might think should be associated two-center two-electron bonds. If this is again a  $d^{10}$  metal then 11 pairs are far short of the 15 Ge–Ge edges. If one used the five electron pairs from Co, then there are too many electrons. Density functional theory (DFT) calculations [70] showed that the energy difference between the two structural types is actually quite small, however, at this time we are not aware of any model that can handle this, as well as, many other situations where there is an encapsulated metal atom [1].

Gold clusters pose an almost universal problem in terms of electron counting. **22.67** [71] and **22.68** [72] are typical examples. **22.67** is an icosahedron with an encapsulated gold atom. An Au—PR<sub>3</sub> group contains a sp hybrid pointed away from



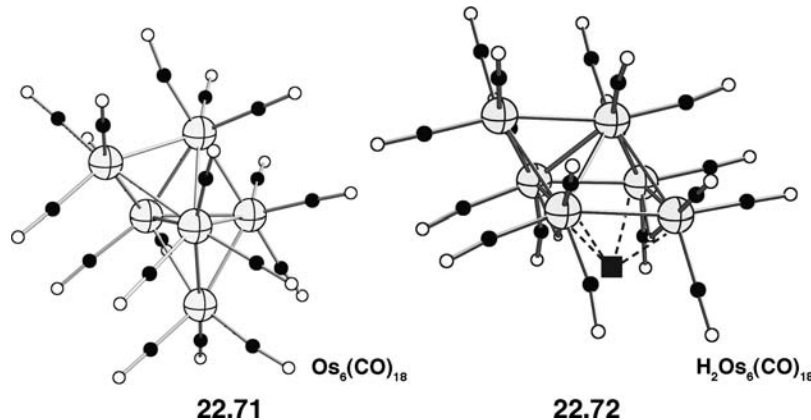
the phosphine which is occupied by one electron. The two tangential 6p AOs are empty. Therefore, one might consider each Au—PR<sub>3</sub> to contribute one, each Au—Cl to contribute zero and the encapsulated Au atom to contribute one skeletal electron. Therefore, **22.67** would have a grand total of only 4 skeletal electron pairs instead of the 13 predicted using Wade's rules. The 5d AOs of gold lie very low in energy and from almost all theoretical results can be regarded as core-like [73]. Nevertheless, if one chooses to use two d AOs as the tangential functions, **22.67** possesses 38 skeletal electrons! Clearly this is also unreasonable. **22.68** has similar problems associated with it. This structure is not derived from one of the deltahedra in Figure 22.1. Yet, its geometry is fairly common and there are even several examples where two or more Au<sub>11</sub> clusters are fused together. The bonding in these compounds has been studied at a number of levels [73,74]. As a final example, consider **22.69** [75]. Its shape, but not



the electronic structure, bears some resemblance to CpMn(CO)<sub>3</sub>, **22.44**. In Section 22.5, we pointed out the isolobal relationship between Au—PR<sub>3</sub> and a hydrogen atom. Therefore, **22.69** suggests that **22.70** or some derivative might be stable under some conditions [76]. Overall, however, the Wade scheme ties together a wide body of chemistry and is remarkably successful predicting the shapes of cluster compounds.

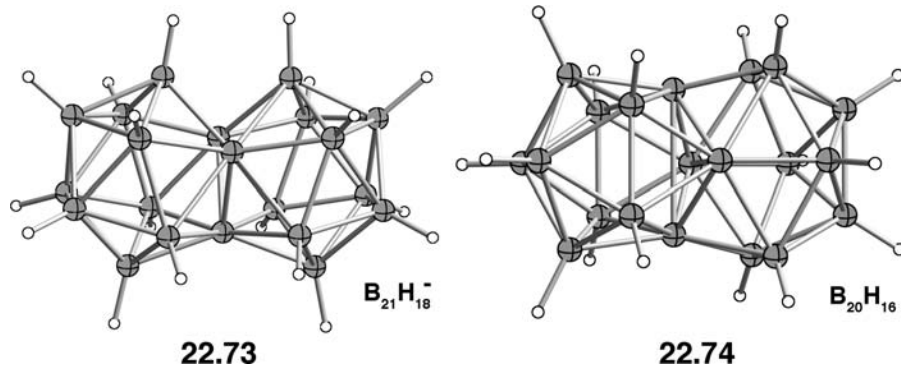
## 22.5 EXTENSIONS

An interesting variation of the deltahedra in Figure 22.1 are structures where the deltahedron is capped by an atom or group. The capping group simply utilizes the existing outward pointing orbitals presented by the face and no new orbital requirements are made on the deltahedron [77]. Such  $n$ -heavy atom species are then stable for a total of  $n$  skeletal electrons. Hence,  $\text{Os}_6(\text{CO})_{18}$ , 22.71 [78] has a total of six skeletal pairs and six metal atoms and exhibits the capped structure, but

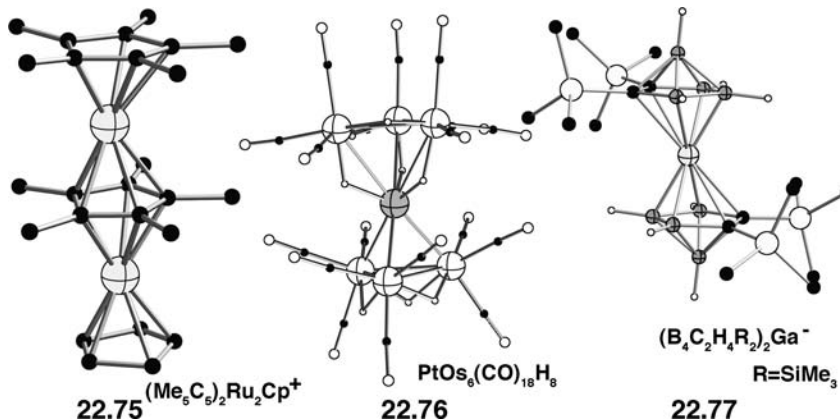


$\text{Co}_6(\text{CO})_{15}^{2-}$  with seven skeletal pairs and six metal atoms exhibits the closo octahedral structure. But this is not the only choice for a seven electron pair structure.  $\text{H}_2\text{Os}_6(\text{CO})_{18}$ , 22.72 [79], has seven electron pairs and is a capped nido octahedron. At the present time, there is no *a priori* way to predict whether the cluster will have a closo or a capped nido shape associated with it or, if there is a choice on which face the capping will occur.

Two or more clusters may be joined together by sharing a vertex, an edge or a face. There have been several models [2,80–82] used to count electrons in these compounds. Perhaps, the most successful has been the *mno* rule developed by Jemmis and coworkers [83]. Here the number of skeletal electron pairs,  $F(e)$ , is given by:  $F(e) = m + n + o + p - q$ , where  $m$  is the number of polyhedra that are joined together,  $n$  is the number of vertices,  $o$  is the number of vertices shared by a single atom,  $p$  is the number of missing vertices (nido = 1, arachno = 2, etc.) and  $q$  is the number of capping atoms. For the closo examples in the previous section,  $m = 1$ ,  $o = p = q = 0$ , so  $F(e) = n + 1$  which is just Wade's rule. Tables 22.1 and 22.2 can be used to construct the skeletal electron count for the compound with extra hydrogens, carbonyls, and so on, handled in the same way as in the previous sections. There is one further consideration. Main group atoms that are shared

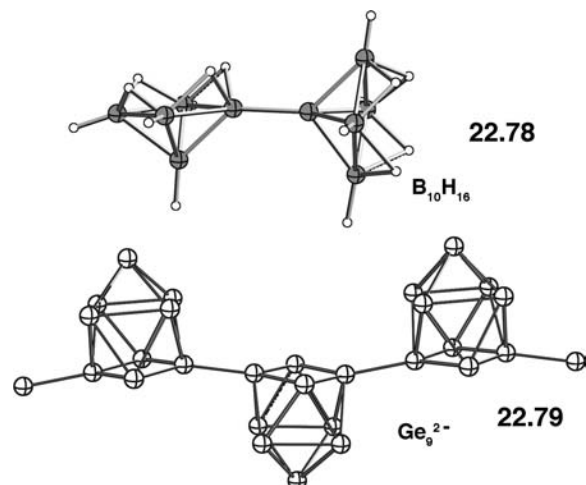


by two fused polyhedral will not have an outwardly pointing lone pair, thus, all valence electrons are counted as being skeletal electrons. For transition metals, it is important to note that there is always a filled “ $t_{2g}$ ” set localized on the metal. The remaining valence electrons will be used to contribute to skeletal electron bonding. In **22.71**  $F(e) = (1 + 6 + 0 + 0 - 1) = 6$  skeletal electron pairs, just as we counted before. Likewise for **22.72**  $F(e) = (1 + 6 + 0 + 1 - 1) = 7$  skeletal electron pairs. **22.73** [84] is a more complicated example of two fused icosahedra sharing one face.  $F(e) = (2 + 21 + 0 + 0 + 0) = 23$ . In terms of electron counting, we have  $1/2[18(2) + 3(3) + 1] = 23$  skeletal electron pairs which is in agreement with the *mno* rule. **22.74** [85] is a more complicated fusion where  $F(e) = (2 + 20 + 0 + 0 + 0) = 22$ . Notice that there are now four B atoms that the two polyhedral share so the electron count becomes  $1/2[16(2) + 4(3)] = 22$  electron pairs. The cyclopentadienyl anion conforms to Wade’s rules as an arachno pentagonal bipyramidal with eight skeletal electron pairs. We counted  $CpMn(CO)_3$ , **22.44**, as a nido pentagonal bipyramidal and, using the isolobal analogy, ferrocene (Section 20.3) could also be viewed in the same way. But one could also regard ferrocene as two  $Cp$  “clusters” that share an iron atom vertex. The *mno* rule then gives  $F(e) = (2 + 11 + 1 + 2 + 0) = 16$ . When counting the number of skeletal electron pairs, one must remember there is a “nonbonding”  $t_{2g}$  set on Fe so the count becomes  $1/2[10(3) + 2] = 16$  pairs. Triple-decker sandwich complexes can also be treated, for example, in **22.75** [86] there are  $1/2[15(3) + 2(2) - 1] = 24$  electron pairs and from the *mno* rule



$F(e) = (3 + 17 + 2 + 2) = 24$ . The structure of **22.76** [87] can also be viewed as a sandwich complex so that the two  $Os_3(CO)_9$  rings are nido clusters joined by the Pt atom. Removing the hydrogens as protons gives  $1/2[6(2) + 4 + 8] = 12$  pairs and this is in agreement with the *mno* rule;  $F(e) = (2 + 7 + 1 + 2)$ . Finally, **22.77** [88] is a rare example of an all-main group sandwich complexes with two pentagonal bipyramids and a bridging Ga atom. Here,  $F(e) = (2 + 13 + 1) = 16 = 1/2[8(2) + 4(3) + 3 + 1]$ .

If clusters are joined together by a bond, that bond is considered to be of the two-electron two-center type. A simple example is provided by **22.78** [89] where two nido pentagonal bipyramids are linked by one B—B bond.  $Ge_9^{2-}$  has a total of nine skeletal electron pairs which is just right for a closo tricapped trigonal prism. Indeed, this is the structure of this compound found many years ago [90]. But under different conditions the one-dimensional polymer shown in **22.79** is formed [91]. The  $Ge_9^{2-}$  clusters are now fashioned after a nido bicapped square antiprism. In accord with Wade’s rules, the  $Ge_9^{4-}$  cluster has this shape [90]. In a localized sense, one could view the formation of the two Ge—Ge  $\sigma$  bonds in **22.79** as taking one electron from each lone pair associated with the basal trans Ge atoms. The remaining two electrons are used to form the nido structure along with breaking the



Ge—Ge bond (not a two-center two electron one!) at the other two trans basal positions. From an MO perspective the transformation from discrete  $Ge_9^{2-}$  clusters to the 22.79 polymer can be constructed via the orbital correlation diagram in Figure 22.6. The highest occupied ( $e'$ ) and the lowest unoccupied ( $a''_2$ ) MOs of the  $Ge_9^{2-}$  cluster in  $D_{3h}$  symmetry are on the left side of the figure. On going to the nido,  $C_{4v}$  structure the primary geometrical change is lengthening the  $Ge(1)—Ge(3)$  bond and laterally displacing  $Ge(2)$  and  $Ge(4)$  slightly in the downward direction. Nothing much happens to the lower member of the  $e'$  set on the left of the figure. It smoothly correlates to an  $a_1$  MO on the  $C_{4v}$  side. The other member of  $e'$  strongly mixes with another MO of  $e'$  symmetry that lies lower in energy and is not shown in the figure. Consequently, it rises in energy and becomes one member of the  $e$  set at the  $C_{4v}$

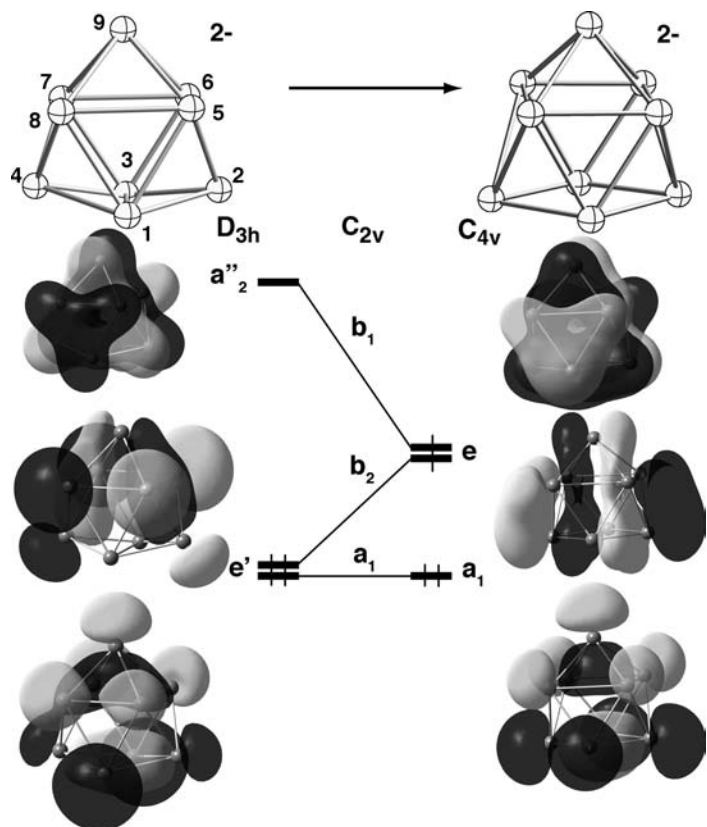
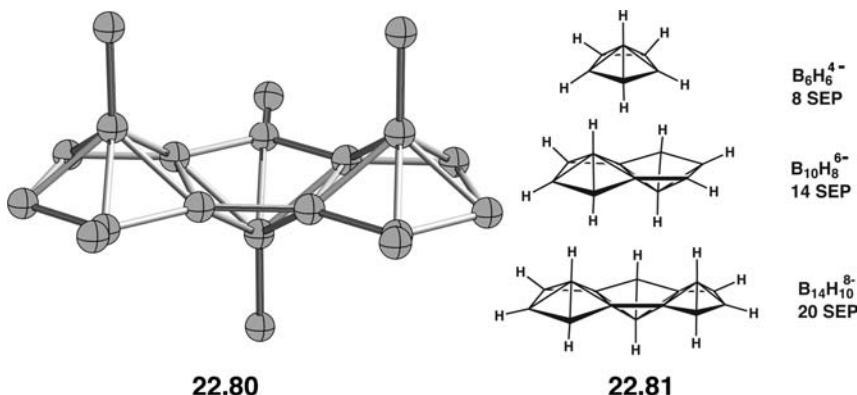


**FIGURE 22.6**

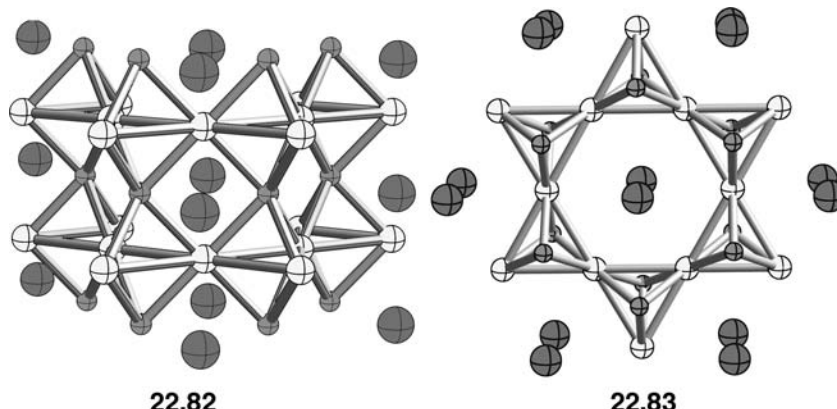
Construction of an orbital correlation diagram for the  $D_{3h}$  (a closo tricapped trigonal prism) to  $C_{4v}$  (a nido bicapped square antiprism) transformation in  $Ge_9^{2-}$ . The MOs are taken from a B3LYP calculation.

geometry. The  $a_2''$  MO is strongly Ge(1)—Ge(3) antibonding. So when this bond is broken, the orbital is stabilized and becomes the second member of the e set. From the relative energies of the MOs in Figure 22.6, it is easy to see why the  $D_{3h}$  structure is stable for  $\text{Ge}_9^{2-}$  and the addition of two electrons pushes the structure to the  $C_{4v}$  side. For  $\text{Ge}_9^{2-}$  the e set is half-filled at the  $C_{4v}$  geometry. The lower member of the e set in the figure has large coefficients on Ge(2) and Ge(4). Each center with one electron can then form a  $\sigma$  bond to the neighboring  $\text{Ge}_9^{2-}$  cluster giving the polymer shown in 22.79. There are many structures of  $\text{Ge}_9^{3-}$ . In all the cases, they have a  $C_{2v}$  geometry consistent with an orbital occupation of  $\dots (a_1)^2 (b_2)^2 (b_1)^1$  and a structure between that for  $D_{3h}$  and  $C_{2v}$ .

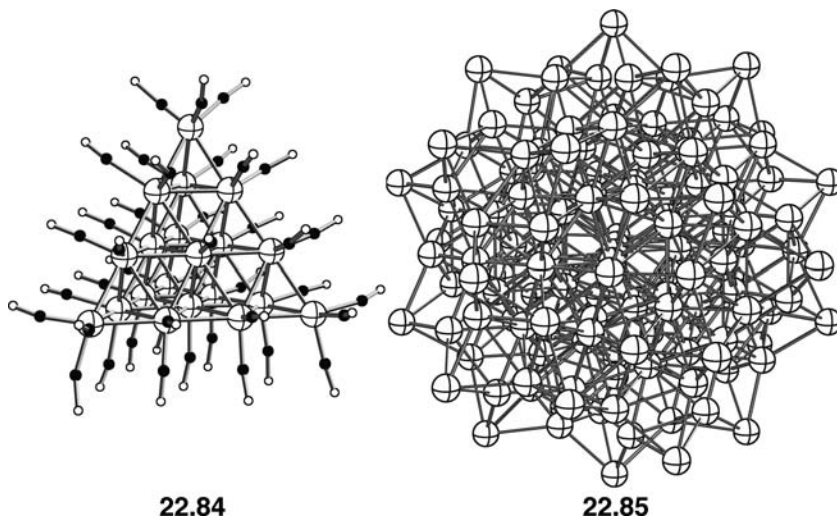
There are some three-dimensional clusters in the solid state with extended structures. A simple example was the  $\text{B}_6$  octahedra joined by exocyclic B—B bonds in  $\text{CaB}_6$ , 22.25.  $\text{MgB}_4$  forms edge-shared nido pentagonal bipyramids [92]. A portion of the structure is shown in 22.80. The electron counting here according to the mno rule can be established in the following way. Consider the nido pentagonal bipyramid series given in 22.81. The reader should verify the skeletal electron count for each structure and that each obeys the mno rule. Fusing a nido pentagonal bipyramidal unit to each compound via a shared edge increases the formula by  $\text{B}_4\text{H}_2^{2-}$ . Consider each



exocyclic B—B bond in  $\text{MgB}_4$  to be of the two-electron two-center type, similar to the B—H bonds in 22.81. Therefore,  $\text{MgB}_4$  regarded as  $\text{B}_4^{2-}$  contains two exocyclic B—B bonds and just the right electron count. The allotropes of boron consist of icosahedral clusters fused in various ways with bridging boron atoms. We will not discuss the examples of these and other Group 14 clusters here [82,93]. A number of cases in the solid-state world exist with extended structures where the mno rules are definitely not followed. There are a series of  $\text{A}_x\text{M}_3\text{B}_2$  compounds where A is an electro-positive element that donates its electrons to the  $\text{M}_3\text{B}_2$  trigonal bipyramidal units. A side view of the structure is shown in 22.82. A view from the top along the c-axis in 22.83



shows that this is a Kagome net structure. The compound in this series with the least number of electrons is LuOs<sub>3</sub>B<sub>2</sub> [94]. The Lu<sup>3+</sup> atoms are isolated and all of the other atoms share vertices so the skeletal electron count is  $3(2) + 2(3) + 3 = 13$  electrons, whereas a trigonal bipyramidal should have 12. The most electron rich member has the stoichiometry B<sub>2/3</sub>Pt<sub>3</sub>B<sub>2</sub> [95]. The same method of electron counting leads to  $3(4) + 2(3) + 4/3 = 19 \frac{1}{3}$  electrons. However, there is a structural distortion that occurs for these compounds where each triangle of Pt atoms shrinks and each neighboring triangle expands keeping the Pt—B distances constant. This leads to the alternation of pairs of B—B bonds within the trigonal bipyramids (like the Tl—Tl bonds in 22.52 and 22.53). Therefore one pair of electrons does not contribute to the count in the Pt<sub>3</sub>B<sub>2</sub> trigonal bipyramids and the electron count becomes  $17 \frac{1}{3}$ . It should not really come as a surprise that these compounds do not obey electron-counting rules; both are metallic and, in fact, both compounds are superconductors at low temperatures. The essence of radial and tangential bonding in these compounds, as well as, the electronic driving force for distortion can be coaxed from band structure and associated density of states calculations [96]. There are also a growing number of very large clusters, nanoparticles. A beautiful example is given by Os<sub>20</sub>(CO)<sub>40</sub><sup>2-</sup> which is shown in 22.84 [97]. The grand pyramid of osmium! There are ways to count skeletal electrons in



this complex [97], but a discrete molecule this size certainly challenges a detailed molecular orbital description. Consider 22.85 [98], Pd<sub>145</sub>(CO)<sub>60</sub>(PEt<sub>3</sub>)<sub>30</sub>, where only the Pd atoms are shown. This and other compounds like it can be viewed as a series of concentric shells. This is an emerging field of study [99].

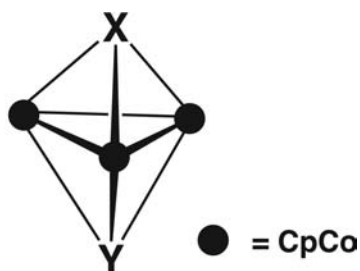
## PROBLEMS

**22.1.** Use Wade's rules to predict the approximate shape for the molecules listed below.

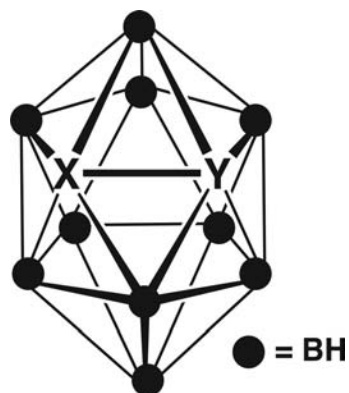
- a. B<sub>5</sub>H<sub>9</sub>
- b. C<sub>2</sub>B<sub>4</sub>H<sub>8</sub>
- c. C<sub>6</sub>H<sub>6</sub><sup>2+</sup>
- d. B<sub>4</sub>H<sub>8</sub>
- e. B<sub>9</sub>H<sub>15</sub>
- f. C<sub>5</sub>H<sub>5</sub><sup>-</sup>

- g.  $\text{Ni}_5(\text{CO})_{12}^{2+}$   
 h.  $\text{Co}_4\text{Ni}_2(\text{CO})_{14}^{2-}$   
 i.  $\text{Rh}_9\text{P}(\text{CO})_{21}^{2-}$  (the P atom is encapsulated)  
 j.  $\text{Cp}_2\text{Co}_2\text{C}_2\text{B}_6\text{H}_8$   
 k.  $\text{CCo}_8(\text{CO})_{18}^{2-}$  (the C atom is encapsulated)  
 l.  $\text{C}_2\text{H}_4\text{Pt}(\text{PPh}_3)_2$   
 m.  $\text{Os}_3(\text{CO})_{12}$   
 n.  $\text{Cp}_4\text{Co}_4(\text{PPh})\text{BH}_2$   
 o.  $\text{C}_2\text{B}_4\text{H}_6\text{Pt}(\text{PEt}_3)_2$

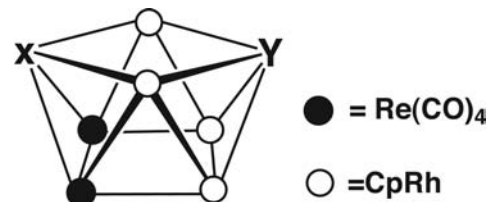
**22.2.** For the molecules shown below, choose among the X/Y combinations that obey Wade's rules.



	X	Y
i)	$\text{CpNi}$	$\text{CpNi}$
ii)	$\text{Fe}(\text{CO})_4$	$\text{CpCo}$
iii)	$\text{Ru}(\text{CO})_4$	$\text{NH}$
iv)	$\text{Fe}(\text{CO})_3$	$\text{Fe}(\text{CO})_3$
v)	$\text{CpCo}$	$\text{BH}$

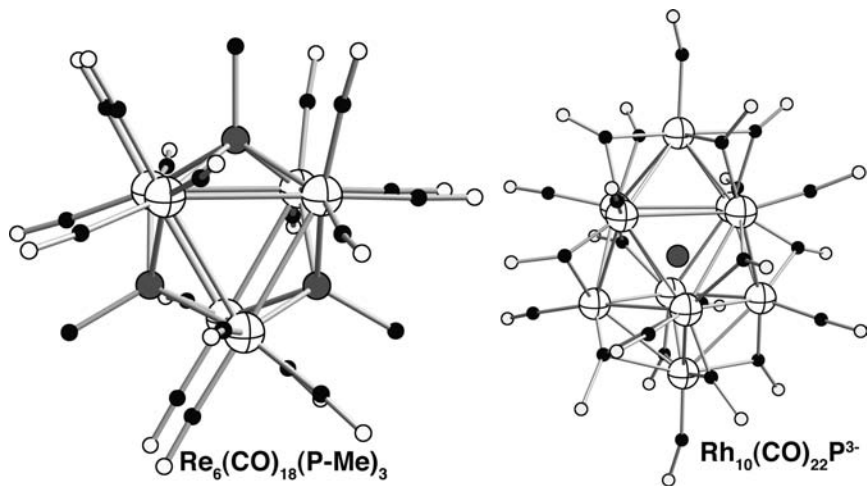
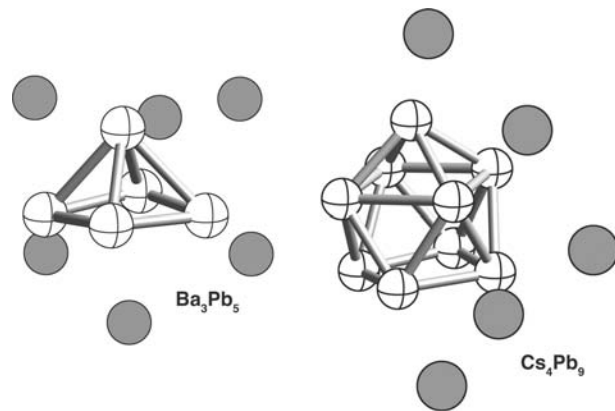


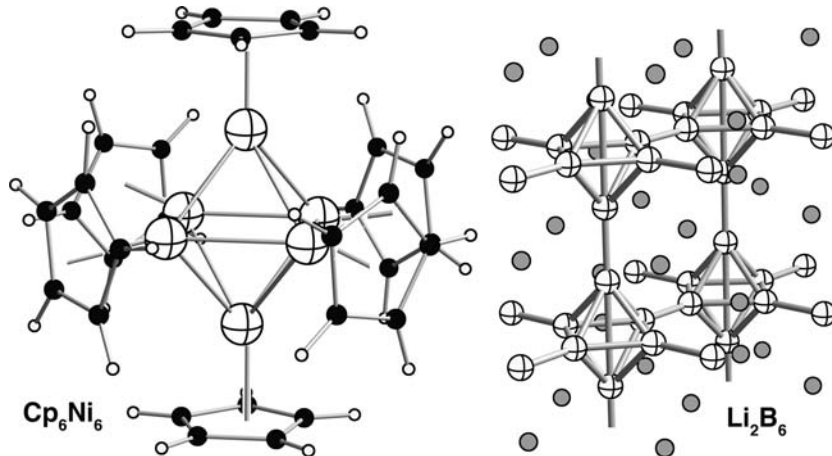
	X	Y
i)	$\text{Bi}$	$\text{S}$
ii)	$\text{S}$	$\text{S}$
iii)	$\text{P}$	$\text{CH}$
iv)	$\text{P}$	$\text{Bi}$
v)	$\text{BH}$	$\text{Bi}$



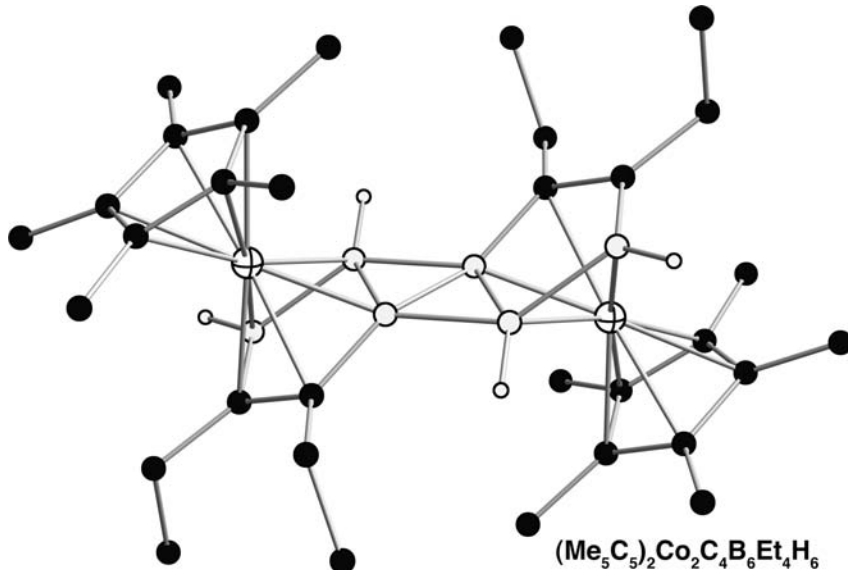
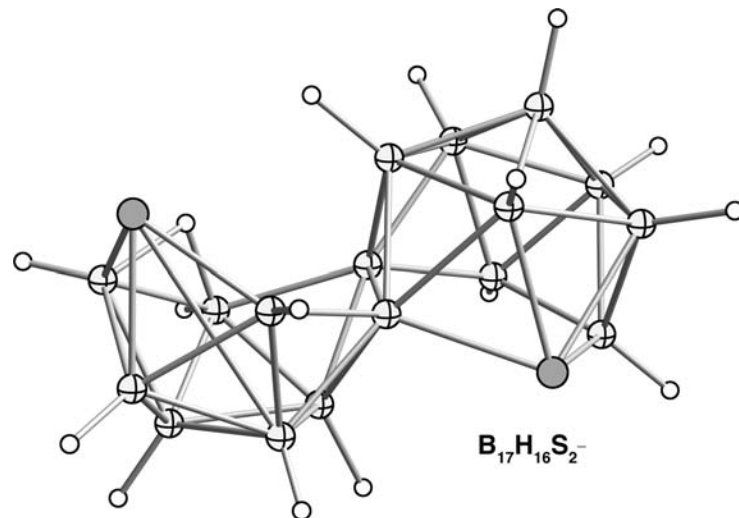
	X	Y
i)	$\text{Rh}(\text{CO})_3$	S
ii)	PMe	PMe
iii)	$\text{Rh}(\text{CO})_4$	CpPt
iv)	GeMe	GeMe
v)	In-OMe	Br

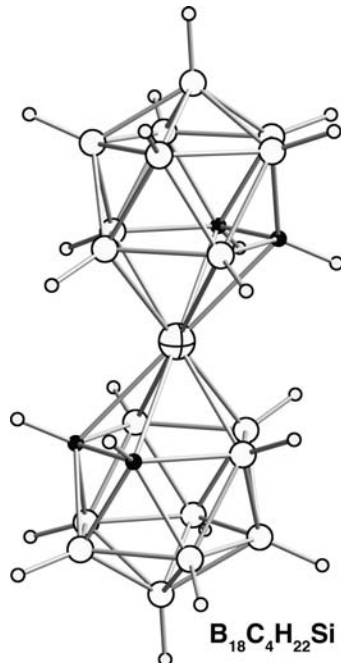
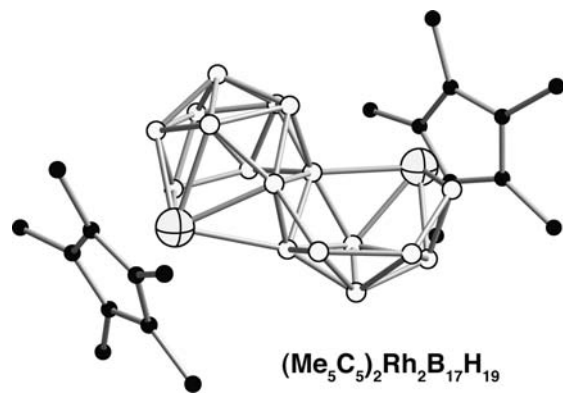
22.3. Do the compounds below conform to Wade's rules?



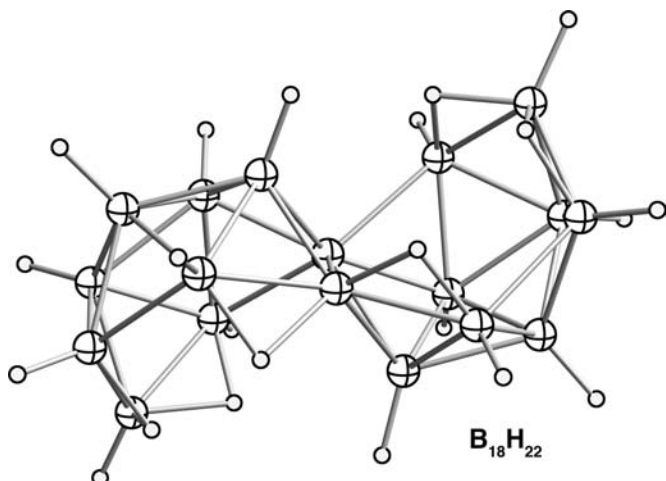


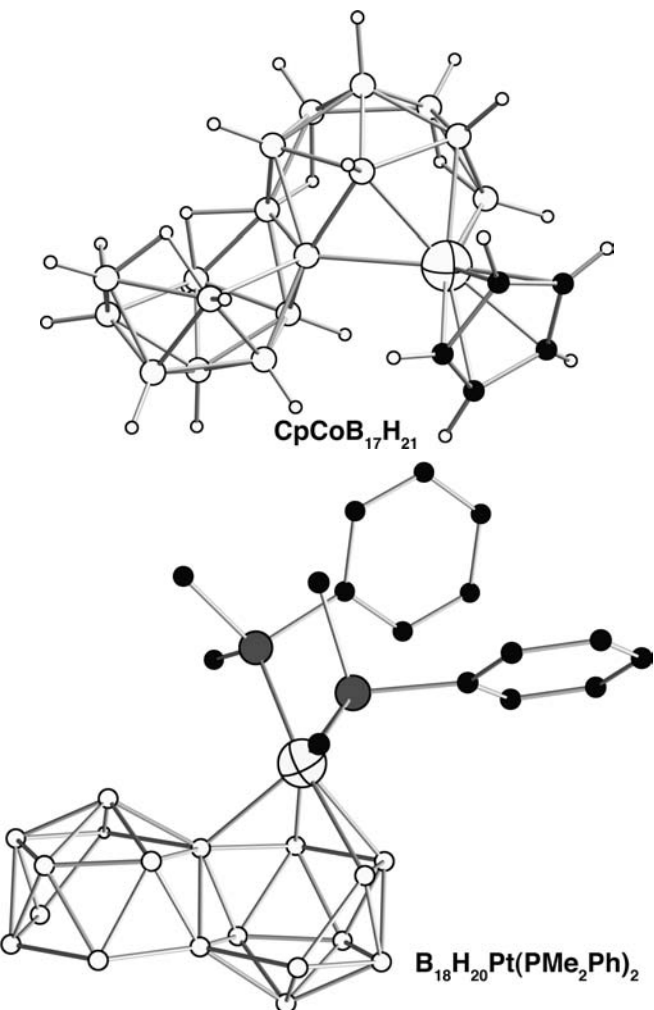
**22.4.** Use the *mno* rule (count the  $\text{Cp}$  ligands as part of the overall cluster) and determine whether or not the number of skeletal electrons corresponds to it for the following molecules:



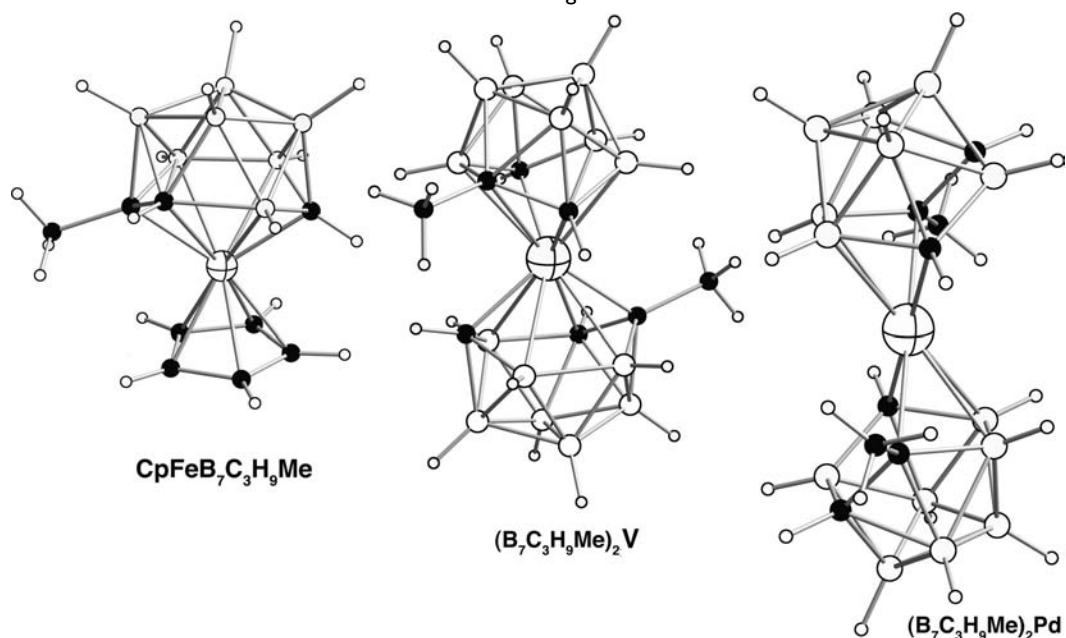


- 22.5. There are a number of borane families constructed by deprotonation of a borane and then reaction with electrophiles. One such family is presented by  $\text{B}_{18}\text{H}_{22}$ . For the following compounds count the number of skeletal electrons and determine if it follows the *mno* rule.

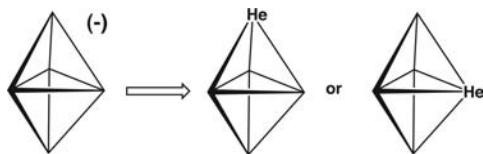




**22.6.** The  $\text{B}_7\text{C}_3\text{H}_9\text{Me}$  anion has been used as a  $\text{Cp}^-$  analog. Use the *mno* rule and count the skeletal electrons in the following structures:



- 22.7.** Consider a hypothetical  $\text{H}_5^-$  molecule that has a  $D_{3h}$  trigonal bipyramidal shape. If a He atom replaces one of the hydrogens, show using electronegativity perturbation theory whether it is better to put the He atom in the axial or the equatorial position.



## REFERENCES

1. T. P. Fehlner, J.-F. Halet, and J.-Y. Saillard, *Molecular Clusters*, Cambridge University Press, Cambridge (2007).
2. R. B. King, *Struct. Bond.*, **140**, 1 (2011).
3. S. Alvarez, *Dalton Trans.*, 2209 (2005).
4. E. L. Muetterties, editor, *Boron Hydride Chemistry*, Academic Press, New York (1975).
5. K. Wade, *Adv. Inorg. Chem. Radiochem.*, **18**, 1 (1976).
6. B. F. G. Johnson, editor, *Transition Metal Clusters*, Wiley, New York (1979).
7. R. N. Grimes, *Acct. Chem. Res.*, **11**, 420 (1978).
8. R. W. Rudolph, *Acc. Chem. Res.*, **9**, 446 (1976).
9. J. M. Goicoechea and S. C. Sevov, *J. Am. Chem. Soc.*, **126**, 6860 (2004).
10. M. Panda, K. Hofmann, M. H. Prosenc, and B. Albert, *Dalton Trans.*, 3956 (2008).
11. F. Schluter and E. Bernhardt, *Z. Anorg. Allg. Chem.*, **636**, 2462 (2010).
12. V. Rivera, G. M. Sheldrick, and M. B. Hursthouse, *Acta Crystallogr., Sect. B: Struct. Crystallogr. Cryst. Chem.*, **34**, 3376 (1978).
13. T. Eguchi, R. A. Harding, B. T. Heaton, G. Longoni, K. Miyagi, J. Nahring, N. Nakamura, H. N. Makayama, and A. K. Smith, *J. Chem. Soc., Dalton Trans.*, 479 (1997).
14. Y. Nishihara, K. J. Deck, M. Shang, T. P. Fehlner, B. S. Haggerty, and A. L. Rheingold, *Organometallics*, **13**, 4510 (1994).
15. U. Doerfler, J. D. Kennedy, L. Barton, C. M. Collins, and N. P. Rath, *J. Chem. Soc., Dalton Trans.*, 707 (1997).
16. D. Braga, F. Grepioni, P. J. Dyson, B. F. G. Johnson, P. Frediani, M. Bianchi, and F. Piacenti, *J. Chem. Soc., Dalton Trans.*, 2565 (1992).
17. A. Ceriotti, G. Longoni, M. Manassero, M. Perego, and M. Sansoni, *Inorg. Chem.*, **24**, 117 (1985).
18. M. D. Randles, A. C. Willis, M. P. Cifuentes, and M. G. Humphrey, *J. Organomet. Chem.*, **692**, 4467 (2007).
19. F. P. Boer, W. E. Streib, and W. N. Lipscomb, *Inorg. Chem.*, **3**, 1666 (1964).
20. J. D. Corbett and P. A. Edwards, *J. Am. Chem. Soc.*, **99**, 3313 (1977).
21. R. E. Dickerson, P. J. Wheatley, P. A. Howell, and W. N. Lipscomb, *J. Chem. Phys.*, **27**, 200 (1957).
22. J. Beck and M. Zink, *Z. Anorg. Allg. Chem.*, **635**, 692 (2009).
23. R. Hoffmann and W. N. Lipscomb, *J. Chem. Phys.*, **36**, 2179 (1962).
24. R. Hoffmann and M. Goutermann, *J. Chem. Phys.*, **36**, 2189 (1962).
25. A. J. Stone, *Inorg. Chem.*, **20**, 563 (1981); A. J. Stone and M. J. Alderton, *Inorg. Chem.*, **21**, 2297 (1982); D. J. Wales and A. J. Stone, *Inorg. Chem.*, **28**, 3120 (1989).
26. D. M. P. Mingos and D. J. Wales, *Introduction to Cluster Chemistry*, Prentice-Hall (1990).
27. H. C. Longuet-Higgins and M. de V. Roberts, *Proc. Roy. Soc.*, **224**, 336 (1954).
28. H. C. Longuet-Higgins and M. de V. Roberts, *Proc. Roy. Soc.*, **230**, 110 (1955).

29. S. C. Sevov and J. D. Corbett, *Z. Anorg. Allg. Chem.*, **619**, 128 (1993).
30. J. K. Burdett and E. Canadell, *J. Am. Chem. Soc.*, **112**, 7207 (1990).
31. D. M. P. Mingos, *Nature (Phys. Sci.)*, **236**, 99 (1972).
32. D. M. P. Mingos, *J. Chem. Soc. (Dalton)*, 133 (1974).
33. R. E. Williams and F. J. Gerhart, *J. Am. Chem. Soc.*, **87**, 3513 (1967); R. E. Williams, *Adv. Inorg. Radiochem.*, **18**, 67 (1976).
34. E. D. Jemmis, *J. Am. Chem. Soc.*, **104**, 7017 (1982).
35. J. J. Ott and B. M. Gimarc, *J. Am. Chem. Soc.*, **108**, 4303 (1986).
36. T. A. Albright, unpublished calculations.
37. (a) A. E. Reed, R. B. Weinstock, and F. Weinhold, *J. Chem. Phys.*, **83**, 735 (1985). (b) J. P. Richie and S. M. Bachrach, *J. Comp. Chem.*, **8**, 499 (1987).
38. P. v. R. Schleyer and K. Najafian, *Inorg. Chem.*, **37**, 3454 (1998); We note that large basis set computations at the B3LYP level have been reported. See, A. Salem, M. S. Deleuze, and J.-P. Francois, *Chem. Phys.*, **271**, 17 (2001). However, several relative energies are quite unphysical.
39. I. Shapiro, C. D. Good, and R. E. Williams, *J. Am. Chem. Soc.*, **84**, 3837 (1962).
40. M. Hofmann, M. A. Fox, R. Greatrex, P. von Ragué Schleyer, J. W. Bausch, and R. E. Williams, *Inorg. Chem.*, **35**, 6170 (1996).
41. T. Onak, R. P. Drake, and G. B. Dunks, *Inorg. Chem.*, **3**, 1686 (1964).
42. J. J. Ott, C. A. Brown, and B. M. Gimarc, *Inorg. Chem.*, **28**, 4269 (1989) and references therein.
43. M. Hofmann, M. A. Fox, R. Greatrex, P. von Ragué Schleyer, and R. E. Williams, *Inorg. Chem.*, **40**, 1790 (2001).
44. R. D. Pergola, L. Garlaschelli, S. Martinengo, F. Demartin, M. Manassero, N. Masciocchi, R. Bau, and D. Zhao, *J. Organomet. Chem.*, **396**, 385 (1990).
45. A. J. Welch, *J. Chem. Soc., Dalton Trans.*, 225 (1976).
46. J. Bould, N. P. Rath, and L. Barton, *Inorg. Chem.*, **35**, 35 (1996).
47. T. L. Venable, E. Sinn, and R. N. Grimes, *Inorg. Chem.*, **21**, 895 (1982).
48. N. M. Boag, D. Boucher, J. A. Davies, R. W. Miller, A. A. Pinkerton, and R. Syed, *Organometallics*, **7**, 791 (1988).
49. L. Eremenko, H. Berke, A. A. H. van der Zeijden, B. I. Kolobkov, and V. M. Novotortsev, *J. Organomet. Chem.*, **471**, 123 (1994).
50. B. M. Cossairt and C. C. Cummins, *Angew. Chem., Int. Ed.*, **49**, 1595 (2010).
51. A. Ceriotti, G. Longoni, M. Manassero, M. Perego, and M. Sansoni, *Inorg. Chem.*, **24**, 117 (1985).
52. T. Mennekes, P. Paetzold, R. Boese, and D. Blaser, *Angew. Chem., Int. Ed.*, **30**, 173 (1991).
53. P. T. Brain, A. J. Downs, M. Fanfarillo, M. J. Goode, A. G. Massey, D. W. H. Rankin, and H. E. Robertson, *J. Mol. Struct.*, **192**, 163 (1989); There are also Al, Ga and In examples, see W. Url, A. Jantschak, W. Saak, M. Kaupp, and R. Wartchow, *Organometallics*, **17**, 5009 (1998) and references therein.
54. Q. Yu, A. Purath, A. Donchev, and H. Schnöckel, *J. Organomet. Chem.*, **584**, 94 (1999).
55. A. Purath, R. Köppe, and H. Schnöckel, *Angew. Chem. Int. Ed.*, **38**, 2926 (1999).
56. R. J. Wright, M. Brynda, and P. P. Power, *Angew. Chem., Int. Ed.*, **45**, 5953 (2006); See also, G. H. Robinson, *Acc. Chem. Res.*, **32**, 773 (1999).
57. A molecule with one electron less has been reported in P. Yang, R. Köppe, T. Duan, J. Hartig, G. Hadiprono, B. Pilawa, I. Keilhauer, and H. Schnöckel, *Angew. Chem., Int. Ed.*, **46**, 3579 (2007). It decomposes when dissolved in organic solvents and it is apparently only stable in the solid state. Calculations on  $\text{Al}_7\text{H}_6$  and  $\text{Al}_7\text{H}_6^+$  in the gas phase were also reported. Here, one and two electrons are removed from the  $a_{2u}$  orbital in **22.51**. We have been unable to reproduce those calculations. In both cases, symmetry is broken and fragmented structures are produced.

58. Z. Dong and J. D. Corbett, *J. Am. Chem. Soc.*, **115**, 11299 (1993).
59. D. Huang, Z.C. Dong, and J. D. Corbett, *Inorg. Chem.*, **37**, 5881 (1998).
60. F. Wand and G. J. Miller, *Inorg. Chem.*, **50**, 7625 (2011).
61. H. Braunschweig, I. Fernandez, G. Frenking, and T. Kupfer, *Angew. Chem., Int. Ed.*, **47**, 1951 (2008).
62. K. Abersfelder, A. J. P. White, R. J. F. Berger, H. S. Rzepa, and D. Scheschkewitz, *Angew. Chem., Int. Ed.*, **50**, 7936 (2011).
63. M. S. Paquette and L. F. Dahl, *J. Am. Chem. Soc.*, **102**, 6621 (1980).
64. V. G. Albano, M. Sansoni, P. Chini, and S. Martinengo, *J. Chem. Soc., Dalton Trans.*, 651 (1973).
65. J. C. Calabrese, L. F. Dahl, P. Chini, G. Longoni, and S. Martinengo, *J. Am. Chem. Soc.*, **96**, 2614 (1974).
66. C. Femoni, F. Kaswalder, M. C. Iapalucci, G. Longoni, and S. Zacchini, *Eur. J. Inorg. Chem.*, 1483 (2007).
67. See, for example, C. Brown, B. T. Heaton, A. D. C. Towl, P. Chini, A. Fumagalli, G. Longoni, *J. Organomet. Chem.*, **233**, 181 (1979).
68. D. J. Underwood, R. Hoffmann, K. Tatsumi, A. Nakamura, and Y. Yamamoto, *J. Am. Chem. Soc.*, **107**, 5968 (1985).
69. E. N. Esenturk, J. Fettinger, and B. Eichhorn, *J. Am. Chem. Soc.*, **128**, 9178 (2006).
70. J.-Q. Wang, S. Stegmaier, and T. F. Fässler, *Angew. Chem., Int. Ed.*, **48**, 1998 (2009); M. M. Uta, D. Cioboc, and R. B. King, *Inorg. Chem.*, **51**, 3498 (2012).
71. C. E. Briant, B. R. C. Theobald, J. W. White, L. K. Bell, D. M. P. Mingos, and A. J. Welch, *Chem. Commun.*, 201 (1981).
72. J. M. M. Smits, P. T. Beurskens, J. W. A. van der Velden, and J. J. Bour, *J. Crystallogr. Spectrosc. Res.*, **13**, 373 (1983).
73. P. Pyykkö, *Angew. Chem. Int. Ed.*, **43**, 4412 (2004).
74. D. M. P. Mingos, *J. Chem. Soc., Dalton Trans.*, 1163 (1976).
75. J. Mielcke and J. Strahle, *Angew. Chem., Int. Ed.*, **31**, 464 (1992).
76. For other suggested complexes of hydrogen clusters see, J. K. Burdett and M. R. Pourian, *Organometallics*, **6**, 1684 (1987).
77. D. M. P. Mingos, *Nature (London) Phys. Sci.*, **236**, 99 (1972); D. M. P. Mingos and M. I. Forsyth, *J. Chem. Soc., Dalton Trans.*, 610 (1977).
78. A. J. Blake, B. F. G. Johnson, and J. G. M. Nairn, *Acta Crystallogr., Sect. C: Cryst. Struct. Commun.*, **50**, 1052 (1994).
79. R. Bau, S. A. Mason, L. Li, and W.-T. Wong, *J. Am. Chem. Soc.*, **119**, 11992 (1997).
80. D. M. P. Mingos, *Chem. Comm.*, 706 (1983).
81. B. K. Teo, *Inorg. Chem.*, **23**, 1251, 1257 (1984); B. K. Teo, *Inorg. Chem.*, **24**, 4209 (1985).
82. J. K. Burdett and E. Canadell, *Inorg. Chem.*, **30**, 1991 (1991).
83. E. D. Jemmis, M. M. Balakrishnarajan, and P. D. Pancharatna, *J. Am. Chem. Soc.*, **123**, 4313 (2001); E. D. Jemmis, M. M. Balakrishnarajan, and P. D. Pancharatna, *Chem. Rev.*, **102**, 93 (2002); E. D. Jemmis and E. G. Jayasree, *Acc. Chem. Res.*, **36**, 816 (2003).
84. E. Bernhardt, D. J. Brauer, M. Finze, and H. Willner, *Angew. Chem., Int. Ed.*, **46**, 2927 (2007).
85. R. D. Dobrott, L. B. Friedman, and W. N. Lipscomb, *J. Chem. Phys.*, **40**, 866 (1964).
86. A. R. Kudinov, M. I. Rybinskaya, Yu. T. Struchkov, A. I. Yanovsky and P.V. Petrovskii, *J. Organomet. Chem.*, **336**, 187 (1987).
87. R. D. Adams, M. P. Pompeo, and W. Wu, *Inorg. Chem.*, **30**, 2425 (1991).
88. N. S. Hosmane, K.-J. Lu, H. Zhang, and J. A. Maguire, *Organometallics*, **16**, 5163 (1997).
89. J. J. Bruguglio, P. J. Carroll, E. W. Corcoran Jr., and L. G. Sneddon, *Inorg. Chem.*, **25**, 4618 (1986).

90. C. H. E. Belin, J. D. Corbett, and A. Cisar, *J. Am. Chem. Soc.*, **99**, 7163 (1977).
91. C. Downie, Z. Tang, and A. M. Guloy, *Angew. Chem., Int. Ed.*, **39**, 338 (2000).
92. R. Naslin, A. Guette, and M. Barret, *J. Solid State Chem.*, **8**, 68 (1973).
93. J. K. Burdett and E. Canadell, *J. Am. Chem. Soc.*, **112**, 7207 (1990).
94. H. C. Ku, G. P. Meisner, F. Acker, and D. C. Johnston, *Solid State Commun.*, **35**, 91 (1980).
95. R. N. Shelton, *J. Less-Common Metals*, **62**, 191 (1978).
96. S. Seong, S. Y. Choi, and T. A. Albright, *Theor. Chem. Acc.*, **131**, 1091 (2012).
97. L. H. Gade, B. F. G. Johnson, J. Lewis, M. McPartlin, H. R. Powell, P. R. Raithby, and W.-T. Wong, *J. Chem. Soc., Dalton Trans.*, 521 (1994).
98. N. T. Tran, D. R. Powell, and L. F. Dahl, *Angew. Chem., Int. Ed.*, **39**, 4121 (2000).
99. V. A. Blatov, G. D. Ilyushin, and D.M. Proserpio, *Inorg. Chem.*, **50**, 5714 (2011).

# Chemistry on the Surface

---

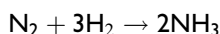
## 23.1 INTRODUCTION

---

In the previous chapters, we have been building molecular orbital constructions toward larger and larger systems. We have focused on intramolecular and intermolecular perturbation theory as techniques to uncover qualitative details about the electronic structure along with elementary electron counting rules and, most importantly, symmetry. In the solid state, these same ideas were applied within the unit cell, and the bands along with the density of states could be deduced from them. Frequently, the results of computations were presented in terms of geometric structures, energies, or pictures of orbitals. But these details, as well as those culled from experiments, were used to buttress the orbitally based arguments that preceded them. In surface science one is much more at the mercy of theoretical results. This does not mean, however, that one should forgo the critical analysis of the results and simply report the bottom-line numbers. We will use various techniques to try to understand where these computational results come from.

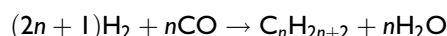
The chemistry at surfaces is unique. The three most important industrial processes that use heterogeneous catalysis are as follows:

1. The Haber–Bosch process:



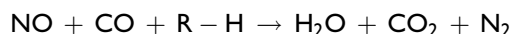
This reaction occurs on an iron surface with an alkali metal promoter. Over 100 million tons of ammonia is produced every year for use in fertilizers.

2. The Fischer–Tropsch process:



The reaction normally uses Fe or Co catalysts for the production of synthetic fuels.

3. The three-way catalyst:

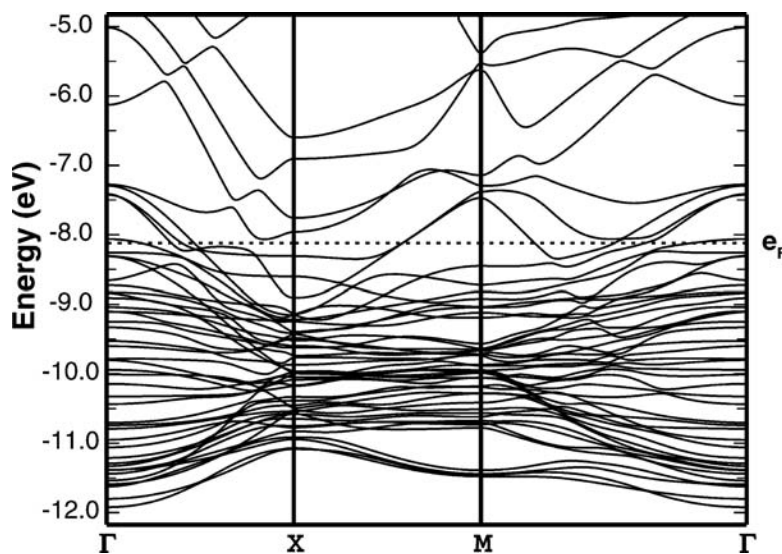


The catalyst is a Pt—Rh—Pb composite that is used in the catalytic converters for automobiles.

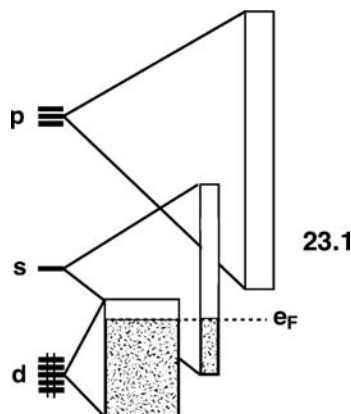
Each of these catalytic reactions is wildly impossible under homogeneous conditions (although the splitting of the N≡N bond has been accomplished). The number of available metals is, of course, small in number; however, there are a number of exposed surface shapes, alloys, added promoters, and inhibitors that greatly influence reactivity.

This is a difficult field to study. On the experimental side, the preparation of the surfaces and reactions must be studied using ultrahigh vacuum chambers to avoid contamination. The workhorse tools to determine structure and composition—X-ray and NMR spectroscopy—obviously cannot be used in a direct fashion. An arsenal of alternative methods has been developed, namely, low-energy electron diffraction (LEED), atomic force microscopy (AFM), and scanning tunneling microscopy (STM). The electronic structure of the surface–adsorbate interaction can be probed via ultraviolet photoelectron spectroscopy (UPS). This in general does not lead to much information. The chemisorbed species is strongly bonded to the substrate; therefore, strong vibrational coupling leads to very broad line widths. Multi-photon photoelectron (MPPE) spectroscopy can be polarization controlled so that, for example, ionizations from the  $\sigma$  manifold can be differentiated from the  $\pi$ . Furthermore, X-ray emission spectroscopy (XES) provides a method to locally study the electronic properties centered around one atomic site and angle-resolved measurements allow a separation of valence levels of different symmetries.

On the theoretical front there are also a number of problems. One could carry out “cluster” calculations where the surface atoms along with some number from the bulk are used in the calculation along with an adsorbate molecule. This naturally leads to the computation of very large clusters and concern about how to deal with edge effects on the cluster. Alternatively, one could do a two-dimensional calculation on a slab. The problem here is how many layers deep one needs to include for the representation of the bulk states. As we shall see, the bulk states matter. With three or four layers, the number of atoms in the unit cell becomes quite large and unwieldy. As an example, the bands for a four-layer model of an Ni (100) surface (we will define this in more detail shortly) are shown in Figure 23.1. This is a real spaghetti diagram! There are eight Ni atoms in the unit cell; it is an overwhelming burden to try to draw them out. The states from about  $-9$  to  $-12$  eV are primarily Ni  $d$ . Notice that many of the bands above this cut across the Fermi level, which is given by the dashed line. These are Ni  $s$  in character. Above  $-5$  eV is the Ni  $p$  bands. It is not at all clear which bands correspond mainly to surface Ni atoms or how much hybridization (mixing of  $d$  with  $s$ , etc.) occurs in any of them. A much simpler approach would be to take the valence orbitals of an Ni atom and expand them according to overlap considerations:  $s > p > d$ . This is given in 23.1. Notice that the Ni  $s$  block comes down below the  $d$  (consistent with the  $s$  bands crossing the Fermi level). Therefore, an Ni surface is not  $d^{10}$  but rather  $d^{10-x-y}s^x p^y$  where  $x > y$ .

**FIGURE 23.1**

The bands for a four layer Ni surface along the (100) plane. This is a calculation at the extended Hückel level.



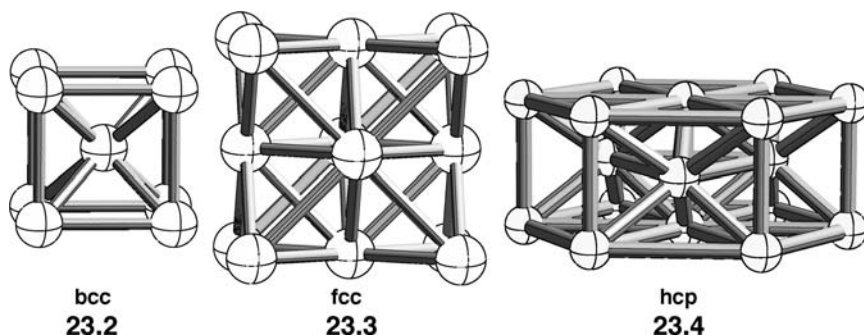
One could split each block further in terms of the overlap criteria  $\sigma > \pi > \delta$ , but this is really about as far as one can go and that is not too far! A theoretical analysis of the electronic structure will require us to use density of states (DOS) plots with the projected composition of atoms or orbital types along with COOP curves. Although computations at the Hartree–Fock or density functional levels are common, we shall exclusively use the extended Hückel method for the solid-state work.

---

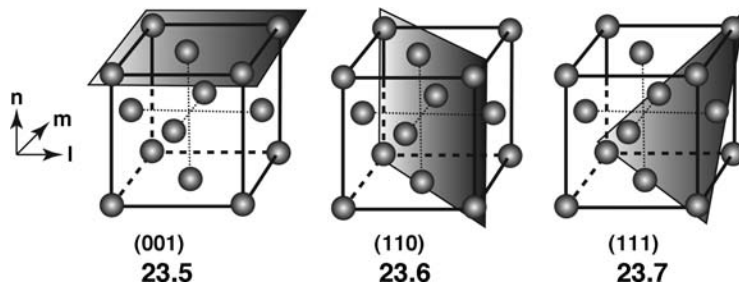
## 23.2 GENERAL STRUCTURAL CONSIDERATIONS

---

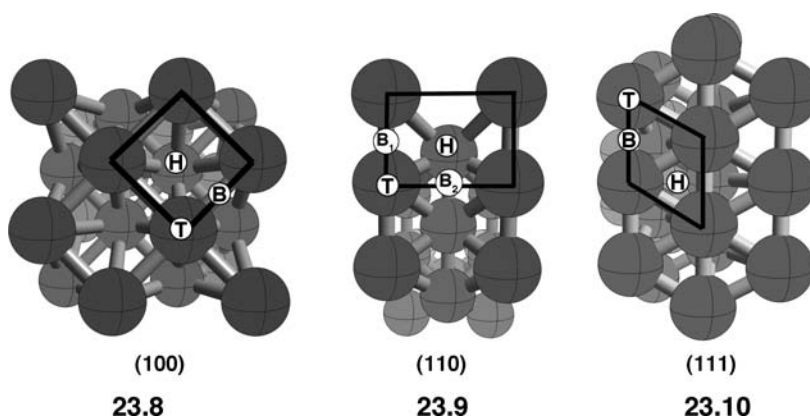
The structure (in the bulk region) of transition metals generally fall into three structural types: the body centered cubic (bcc), face centered cubic (fcc), and the much less common hexagonal close packed (hcp) structure, **23.2**, **23.3**, and **23.4**, respectively [1–4]. A crystal can be cleaved under ultrahigh vacuum and low temperatures at any angle to reveal a clean surface. The exposed surface can be categorized in the following way. An arbitrary coordinate system for a unit



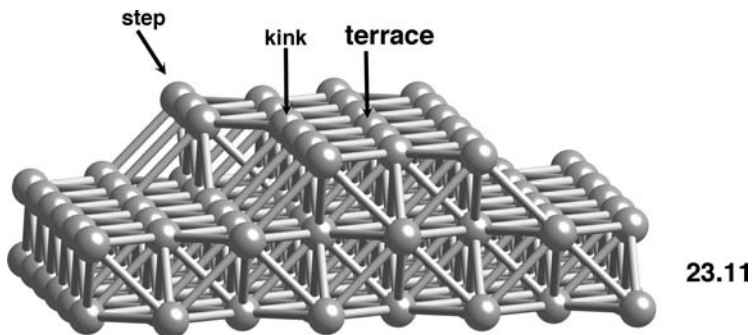
cell is given by a set of vectors  $l$ ,  $m$ , and  $n$ . For a cubic system, for example, **23.2** or **23.3**, this would be the  $x$ ,  $y$ , and  $z$  Cartesian coordinates. A direction in this lattice is given by what are called Miller indices. A vector then can be designated by  $[l, m, n]$ , where  $l$ ,  $m$ , and  $n$  are normally integers. The plane normal to this vector defines the relative positions of the atoms at the surface. Let us take the fcc lattice as an example. So a unit cell translation along the  $l$  axis generates the  $(001)$  plane as shown in **23.5**. Notice that for the fcc structure  $(001) \equiv (010) \equiv (100)$ . The  $(110)$  and  $(111)$  planes are generated in **23.6** and **23.7**, respectively. The exposed



surface for the  $(100)$  plane is easy to see. It is represented in **23.8** where the illusion of depth is provided by coloring the metal spheres with a lighter color. The H, B, and T labels will be discussed later. The  $(110)$  and  $(111)$  surfaces are shown in **23.9** and **23.10**, respectively. Different distances separate the surface atoms in each of these cases. Notice in the  $(110)$  cases that there are rows in the vertical position where the metal–metal distance is short. In the horizontal direction, rows

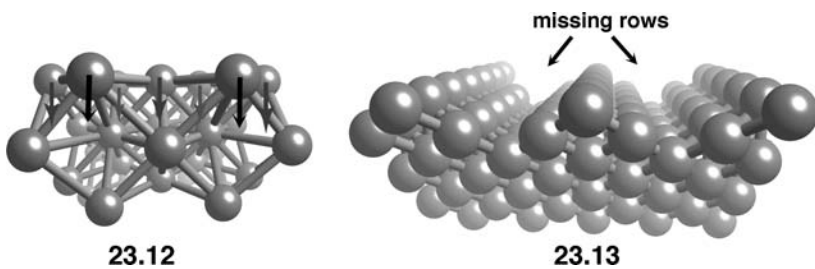


of surface atoms are separated by metal rows one layer into the slab so the metal–metal distance for surface atoms along the horizontal direction is large. The heavy black line illustrates the unit cell in each case. One can easily tell that the geometry and coordination number change for the bulk metal atoms in the bcc, fcc, and hcp structures. This is also true for the surface atoms in the fcc structures of **23.8–23.10**. The structures of the surfaces are, of course, idealized. In reality, there are several types of defects including single atom vacancies and the presence of adatoms. The most common defects are steps, kinks, and terraces as illustrated in **23.11**. The presence of steps and kinks can play a dramatic role in terms of reactivity.



We shall discuss this aspect, in general, shortly. Notice that for the flat (100) surface of an fcc lattice the coordination number is 8, whereas it is 7 for the (110) and 9 for the (111) surface. Careful inspection of **23.11** shows that the coordination number of a metal atom at a step or kink site can be as small as 6. As the coordination number becomes larger, one might expect that the net overlap becomes larger and so the bands become broader.

There are two further structural distortions that can occur on the flat surface. The top layer of a surface moves closer to the second layer (and to a much lesser extent the second layer moves closer to the third). This can be a contraction of more than 20% but more typical values are from 5–10% [5]. This distortion is shown in **23.12** by the arrows in a side view of the (100) surface for an fcc structure.

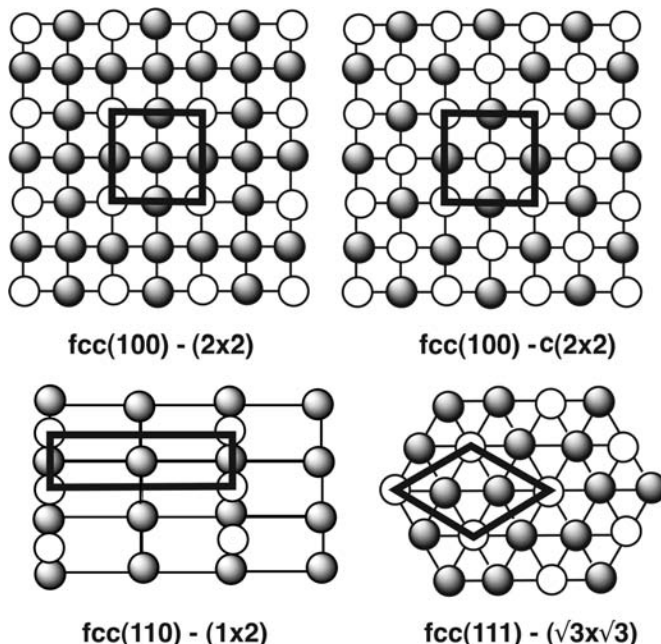


The driving force behind this is again based on coordination numbers. Metal atoms in the bulk are 12-coordinate, whereas they are 8 for the surface atoms in **23.12**. Thus, the surface atoms are coordinatively unsaturated and this electron deficiency can be partially ameliorated by forming stronger (shorter) bonds to metals in the second layer. A frequent occurrence in (110) surfaces is that every other row along the  $[1\bar{1}0]$  direction is missing. A side view of this surface reconstruction is given in **23.13**. There are also well-documented cases where adsorbates can drive the structure back to a flat surface. The electronic mechanism for these distortions is complicated and will not be repeated here [6]. Surface reconstructions in semiconductors are examined in Section 23.5.

### 23.3 GENERAL CONSIDERATIONS OF ADSORPTION ON SURFACES

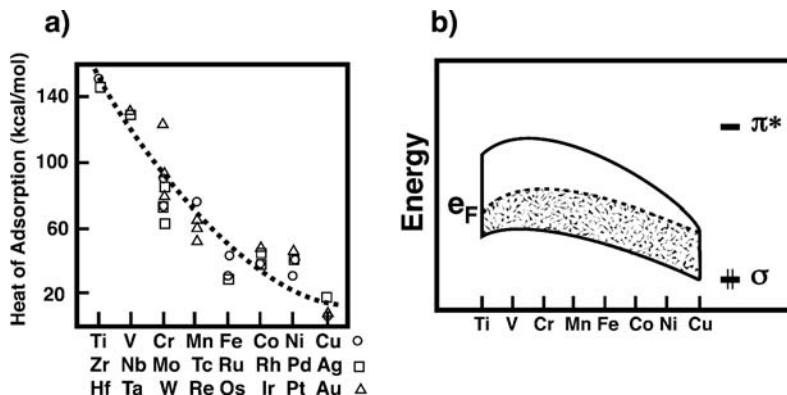
The binding of a molecule to a surface can occur in two fundamentally different ways [1,7]. Physisorption is the attraction of a molecule to the surface by dipolar attraction. This might be due to a dipole in the adsorbate or a simple van der Waals attraction. The interaction between the surface and the substrate is weak and typically is nondirectional or nearly so. That is, little energy difference is expected between the binding sites and diffusion across the surface should be rapid. Chemisorption involves the chemical binding of the substrate to the surface atoms. Consequently, there can be a significant orbital interaction between the two leading to strong binding energies. Now there can be site differences for interaction potentials. As illustrated in 23.8, there are three unique sites for binding on the fcc(100) face: the on-top position, labeled T, bridging between two metal, labeled B and fourfold coordination in a hole site, H. For the fcc(110) surface in 23.9, there are the analogous T and H positions. There are now two different bridging positions,  $B_1$  and  $B_2$ , because of the different metal–metal bond lengths. Finally, the fcc(111) surface, 23.10, presents the analogous T and B positions. There are two non-equivalent H positions within the unit cell that now feature coordination to three metal atoms. The unlabeled position contains a metal atom from the second layer directly below the threefold site, as shown, whereas the other hollow position, labeled H, does not have this feature. They are frequently called the hcp and fcc sites, respectively. In most cases, there is no differentiation between the two sites and so we neglect this aspect. The coverage of a substrate may change the unit cell. Some common examples are shown in Figure 23.2. All of the cases involve an fcc structure where the metal atoms at the surface are represented by shaded circles and the white circles are the adsorbate. The new unit cell is drawn by a heavy line. The two examples at the top of the figure are derived from the fcc(100) surface (see 23.8).

In both cases, the adsorbate occupies the T positions with half coverage and the unit cell is then doubled in the  $\mathbf{h}$  and  $\mathbf{k}$  directions so the Wood's notation for this



**FIGURE 23.2**

Four common examples of substrate coverage on an fcc structure. The surface metal atoms are represented by shaded circles and the adsorbate by white circles. The heavy line outlines the new unit cell for each example.

**FIGURE 23.3**

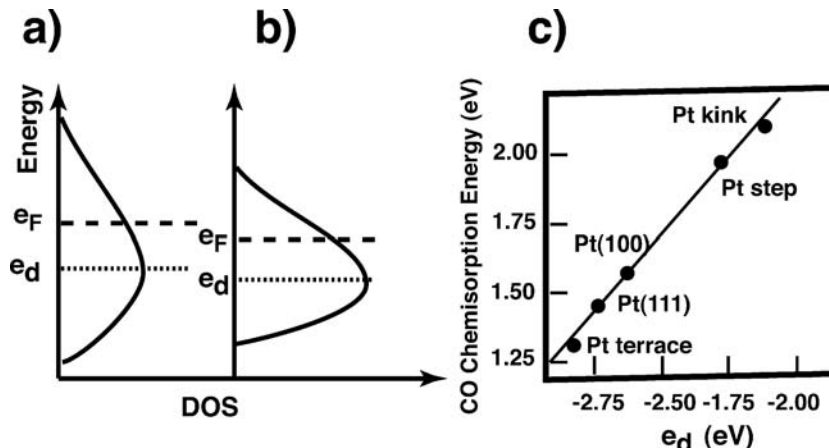
(a) Experimental binding energy of CO to metal surfaces for microcrystalline samples are plotted with respect to the atomic composition. (Adapted from Reference [7].) (b) A generalized plot of the energy and filling associated with the 3d bands in the first-row metals.

coverage is given by  $(2 \times 2)$ . The  $c(2 \times 2)$  notation for the top right example is for a centered geometry where a substrate is bound to the center surface metal in the new unit cell. In the lower left of Figure 23.2, the substrate is coordinated to the  $B_1$  positions (23.9). The unit cell is the same and doubled, respectively, in the vertical and horizontal directions so the Wood's notation is  $(1 \times 2)$ . Finally, the example on the lower right side of the figure expands the unit cell by  $\sqrt{3}$  in both directions. In the next section, one of the examples that we will explicitly cover is  $c(2 \times 2)$ -CO/Ni (100); this is represented by the structure on the top right side of Figure 23.2 where the white circles represent CO molecules bonded on-top to Ni atoms.

There are some general concerns about metal–adsorbate chemisorption that need to be addressed before we turn to specific cases. The adsorption energy is sensitive to a number of factors. The heat of adsorption will remain more or less constant at low-substrate coverage until substrate–substrate repulsion becomes significant which then reduces the heat of adsorption. For Ni, Pd, or Pt surfaces, this occurs at about one-half coverage. Experimental values for the heat of adsorption in microcrystalline samples of metals are shown in Figure 23.3a. The M–CO binding energy increases on going from right to left in the Periodic Table.

Since the metals are microcrystalline, there are various surfaces that are exposed to CO and, therefore, the binding energies should be regarded as an average. This trend in adsorption energies is a general phenomenon and is not unique for CO. There are several reasons why this happens. Figure 23.3b presents an idealized 3d bandwidth and filling for a metal surface along the first transition metal series [8]. On the right side is the orbital energy associated with a donor function on the adsorbate. This could be the  $3\sigma$  orbital of CO, the  $\pi$  orbital of ethylene or the  $sp^3$  hybrid in  $NH_3$ . Frequently, there is also a low-lying empty orbital on the adsorbate. This would be the  $2\pi$  orbital on CO or the  $\pi^*$  orbital on ethylene. Its relative energy is indicated by  $\pi^*$  in Figure 23.3b. The set of  $\sigma$  molecular orbitals will find more empty 3d orbitals to interact with on the left side of the periodic table. There will also be more repulsive four-electron–two-orbital repulsions on the right side (we will modify this picture somewhat in the next section). The filled 3d orbitals for the early transition metals lie higher in energy and, therefore, are closer to the energy of  $\pi^*$ . Finally notice that the bandwidths for the late transition metals are narrower than that on the left side of the periodic table. The  $d$  orbitals in the late transition metals are more contracted and, therefore, overlap with each other less. We shall show that a narrower bandwidth leads to smaller interaction energy.

The structure of the metal surface can also be an important factor in setting binding energies. The basic situation is outlined in Figure 23.4. Figure 23.4a and b shows an idealized energy versus density of states plot for the surface metal  $d$  region. The Fermi level is denoted as  $e_F$ . The most important interaction between CO and a

**FIGURE 23.4**

Schematic energy versus density of states plots for the  $d$  states of (a) the metal bulk and (b) the metal surface. The Fermi level and mean  $d$  orbital energy are given by  $e_F$  and  $e_d$ , respectively. (c) A plot of the computed CO binding energy to a Pt surface versus the calculated  $e_d$ . (Adapted from Reference [11].)

metal surface is via the  $2\pi$  ( $\pi^*$ ) MOs interacting with metal  $d$ . The dominant perturbation is then given by equation 23.1

$$\Delta E \approx \frac{(H_{d,\pi^*})^2}{e_d - e_{\pi^*}} \propto -\frac{(S_{d,\pi^*})^2}{e_d - e_{\pi^*}} \quad (23.1)$$

where  $e_d$  is the mean  $d$  orbital energy. This has proven to be a very useful approach for understanding the binding energies in a number of adsorbates besides CO [9,10]. The bandwidth has been made to become smaller on going from Figure 23.4a to b. The metal–metal bonding states rise in energy but not as much as the metal–metal antibonding ones are lowered in energy. The net result is then to lower the position of  $e_d$  and as a consequence the absolute magnitude of the binding energy ( $\Delta E$ ) is decreased. This is exactly what happens on going from the left to right side of the Periodic Table in Figure 23.3b. Density functional theory (DFT) calculations for CO binding on various Pt surfaces have been carried out and show the relationship between  $e_d$  and CO binding energy quite nicely [11]. This is shown in Figure 23.4c. Notice that the kinked and step sites are associated with much stronger binding. Recall that step and kinked sites are more coordinatively unsaturated than those on flat surfaces. The projected DOS for the metal  $d$  orbitals is also higher at these sites so there is more charge transfer particularly into CO  $\pi^*$  which will weaken the CO bond to the point of breaking it into C and O adatoms. This is considered to be the rate-determining step in the Fischer–Tropsch process. The adsorbed hydrogen atoms (from H<sub>2</sub>) then combine with carbon to form carbene ligands that then undergo oligomerization and reductive elimination reactions to ultimately form alkanes. It has been demonstrated via DFT calculations [12] that CO dissociation requires an activation barrier of 1.17 eV for the Rh(111) surface, but only 0.30 and 0.21 eV for the step and kinked sites, respectively. Dissociation reactions similar to this are said to be structure-sensitive. The transition states are very late so the relative binding energies of C and O to Rh is as strongly dependent on the coordination site as it is for CO itself (see Figure 23.4c). The reverse of this reaction, the recombination of coordinated C and O to form CO will then have an early transition state associated with it. The reaction will be very exothermic and, therefore, not nearly so susceptible to surface geometry or other factors.

Alkali metals and sulfur are common co-adsorbates. They act as chemical modifiers, speeding up or slowing down reactions. For example, there is no isotopic mixing using a mixture of <sup>12</sup>C<sup>18</sup>O and <sup>13</sup>C<sup>16</sup>O on Rh(111) [13]. However, the addition of 20% of a monolayer coverage of potassium causes roughly three CO molecules to dissociate per potassium atom. It creates a 17 kcal/mol increase in the

heat of adsorption of CO. This is not due to any direct interaction between the K and the coordinated CO. The primary effect is electrostatic [14]. Alkali metals pump electron density into the DOS thereby raising the energy of the Fermi level. As we shall see in the next section, this will increase electron density in the CO  $\pi^*$  orbitals weakening the C—O bond. Notice that the addition of alkali metals also raises  $e_d$ , therefore, the adsorption energy should become larger. In the Haber–Bosch process, the addition of potassium acts as a promoter; it facilitates N—N decomposition. But this is not the whole story. Since K is an electron donor, it actually weakens the NH<sub>3</sub>–metal bond. For example, addition of K decreases the heat of absorption of NH<sub>3</sub> to an Fe surface by 4 kcal/mol [1]. The addition of sulfur normally is used to inhibit reactivity. The principal reason for this behavior is that S forms strong bonds with many surface metal atoms [14,15]. Therefore, at low coverage S atoms occupy the most reactive sites, for example, kinks and steps. At higher coverage, the lone pair on S pointing out away from the surface is strongly repulsive to the incoming adsorbate.

## 23.4 DIATOMICS ON A SURFACE

There certainly are parallels that can be drawn between the way molecules react in the gas or liquid phases and at metal surfaces [16]. Our emphasis in this chapter is to compare and contrast the bonding on surfaces compared to the situation for discrete molecules in several illustrative examples. For example, how does the bonding between a CO and an Ni surface compare to that for a  $d^6$  ML<sub>5</sub> fragment? We shall see that there are many similarities; however, there are some important additional facets that surfaces bring to the table.

Probably, the most well-studied area in surface science has been the chemisorption of CO to a metal surface and we will start with this example. The photoelectron spectrum of CO on Ni(100) along with that for the bare Ni surface [17] is shown in Figure 23.5a and compared to the ionizations of free CO in the gas phase. The clean Ni(100) spectrum shows a large peak at an ionization potential of about 1 eV. It is primarily due to the  $d$  AOs. The origin of the peak at 6 eV is controversial [18]. The PE spectrum of CO on the Ni(100) surface is given by the solid line in Figure 23.5a. There are several items of note concerning this spectrum. First of all, there are three peaks that have been shown to be associated with the ionizations from chemisorbed CO. Notice that they are broad, featureless peaks that bear little resemblance to the ionizations from gaseous CO, which is displayed in

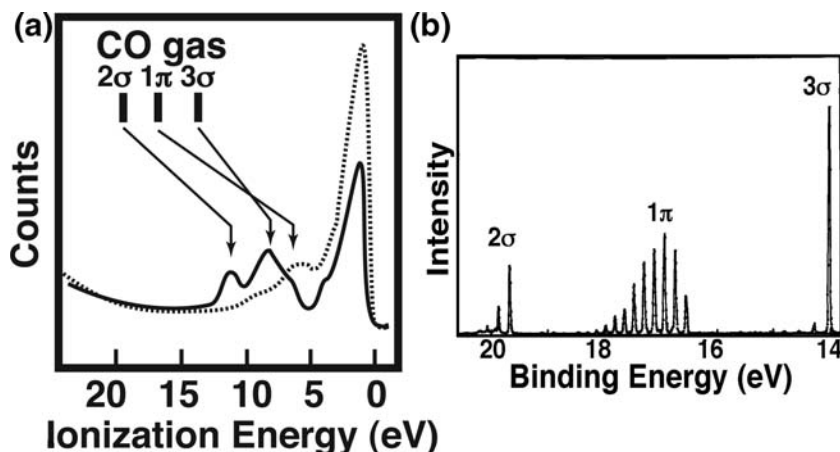
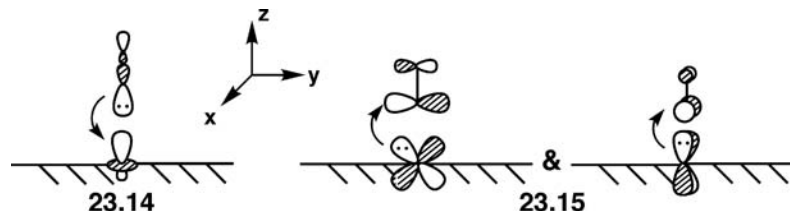


**FIGURE 23.5**

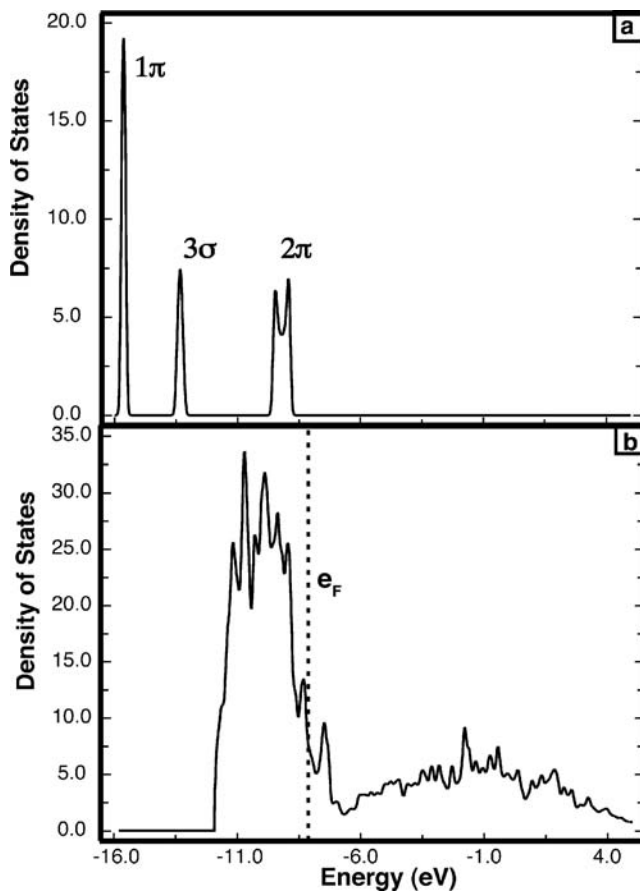
(a) Photoelectron spectrum of CO on Ni(100) shown by the solid line versus that for Ni(100) by itself (dotted line). The adiabatic ionization potentials for CO gas are plotted at the top. (b) He(I) PE spectrum of gaseous CO. (Adapted from Reference [18].)

Figure 23.5b. In other words, not only is all vibrational splitting lost, but the peaks associated with the ionizations are also considerably broadened. As mentioned in Section 23.1, this is a result of strong vibration coupling of CO to the Ni surface atoms. The three peaks in the PE spectrum are assigned to  $2\sigma$ ,  $1\pi$ , and  $3\sigma$ . The reader should refer Figures 6.7 and 6.8 along with the discussion around them for their shapes. What is most perplexing is that all the three ionizations are shifted to energies that are from 7.0 to 8.5 eV lower than in gaseous CO. One might think from the examples of metal–CO bonding in Section 15.3 that the  $2\sigma$ ,  $1\pi$ , and  $3\sigma$  orbitals would be stabilized by the Ni  $d$  AOs. Therefore, based on the Koopmans' theorem, they should lie at larger ionization energies. The problem here is that ionization potential is really the energy difference between the potential energy of the molecule,  $M$  and that of  $M^+$ , where one electron has been removed from a specific MO and the electron hole is confined to that MO. The strong coupling between the CO and the Ni surface creates a situation where the ionization of an electron from say, the  $1\pi$  CO centered orbitals creates a hole not on CO but rather at the top of the Fermi level. Thus, the ionization requires much less energy. There is an important difference in the magnitude of this relaxation effect. The ionization difference between the surface coordinated and the free gas CO is 8.4 and 8.5 eV for the  $1\pi$ - and  $2\sigma$ -based orbitals, respectively. On the other hand, this difference is noticeably smaller (approximately 7 eV) for the  $3\sigma$  ionization. This is consistent with the notion that the CO  $3\sigma$  orbital overlaps strongly with the Ni  $z^2$ ,  $s$  and  $z$  AOs. Therefore, the interaction between them is quite strong which then increases the ionization potential for the  $3\sigma$  ionization.

We shall start the theoretical exploration for a  $c(2 \times 2)$ CO coverage on Ni(100) in very qualitative terms using the Blyholder model [20]. The  $3\sigma$  highest occupied molecular orbitals (HOMO) of CO will form a bonding interaction with  $z^2/s/z$  hybrids on surface Ni atoms, **23.14**. The  $2\pi$  lowest unoccupied molecular orbitals (LUMOs) of CO form bonding combinations with  $xz/yz$  Ni surface orbitals, **23.15**.



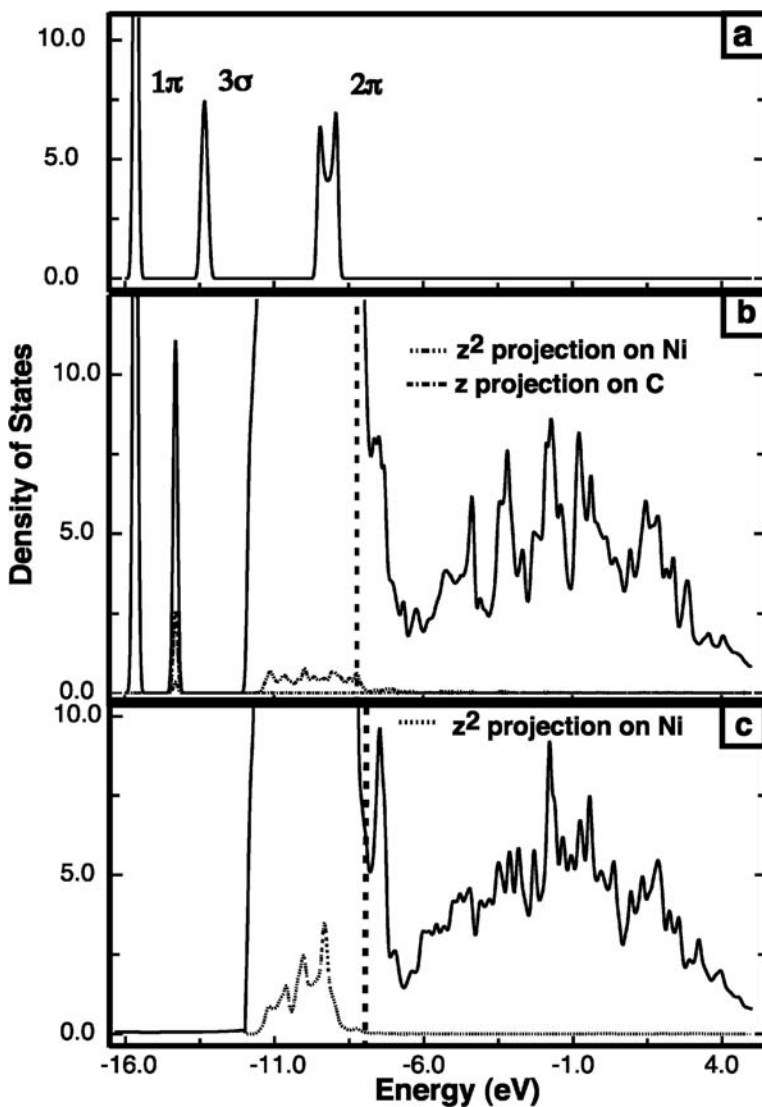
This is essentially analogous to the picture derived for the molecular cases in Chapter 15. The actual situation, as we shall shortly see, is a bit more complicated, but **23.14** and **23.15** do highlight the most important bonding features. A tight-binding exploration of the electronic features can be started by an examination of the DOS plot for the two interacting partners. Figure 23.6a shows the DOS for the free CO molecule. There is very little dispersion since the distance between CO molecules is 3.50 Å in the  $c(2 \times 2)$  structure on Ni(100). The  $2\sigma$  MO will figure into our later discussion is at much lower energy (~19.4 eV) and is not shown in the plot. The DOS of a four-layer Ni(100) slab is shown in Figure 23.6b. The states from just above the Fermi level ( $e_F$ ) to about -12 eV are principally Ni  $d$  in character. Those from 4 to -7 eV are predominately  $s$ , however, the  $s$  “band” also dips well into the  $d$  block. There are also states that contain Ni  $p$  character mixed into these energy regions so the actual electronic environment, as well as the band structure (Figure 23.1), is far too complicated to be meaningful at this level. The resultant combination of the orbitals for the  $\sigma$  system of bonding depicted in **23.14** is illustrated in

**FIGURE 23.6**

(a) Density of states plot for free CO with an intermolecular distance of 3.52 Å. (b) Density of states plot for an Ni(100) surface using a four metal atom slab. The Fermi level is marked as  $e_F$ . The DOS plots were obtained at the extended Hückel level.

Figure 23.7 as a rough interaction diagram. The starting orbitals of CO, Figure 23.7a, and Ni(100), Figure 23.7c, are plotted again with the projection of surface Ni  $z^2$  in the latter as given by the dotted line. The resultant, composite DOS plot is shown in Figure 23.7b. There is a technical detail that should be mentioned here. We are looking for those states represented by 23.14. Unfortunately, we cannot just pick out a combination of  $z^2$ , s, and  $p$  on Ni to give the  $dsp$  hybrid on the surface Ni atoms that point away from the surface. Nor can the s and z mixture on C and O be specified to show the contribution of the CO  $3\sigma$ . The compositions vary as a function of the energy. The best that we can do is to show just the  $z^2$  contributions on the surface Ni atoms and the z contributions on C with the realization that the number of states in the DOS plot will be underrepresented. They will, however, give a good idea of the energy dispersion of the states represented by 23.14. What is clear from the DOS plot in Figure 23.7b is that the CO  $3\sigma$  orbitals are stabilized (by about 2 eV) by interaction with the surface Ni atoms. Conversely, the  $z^2$  surface Ni orbitals are smeared out to higher energy as a result of this interaction. This is precisely what one would expect from the Blyholder model.

The  $\pi$  component of this interaction is developed in an analogous fashion in Figure 23.8. The  $1\pi$  orbitals barely move in energy. On the other hand, some of the  $2\pi$  orbitals, indicated by the dotted projections in Figure 23.8b, are stabilized and others are destabilized. Most of the surface Ni  $xz/yz$  orbitals appear to be at the same energy while some are stabilized and others destabilized. Notice that the  $2\pi$  orbitals in free CO are at the same energy as the surface Ni  $xz/yz$ . Thus, there is expected to be considerable mixing between them, in other words, both the bonding and the antibonding combinations will contain almost equal parts of  $2\pi$  and  $xz/yz$ . This

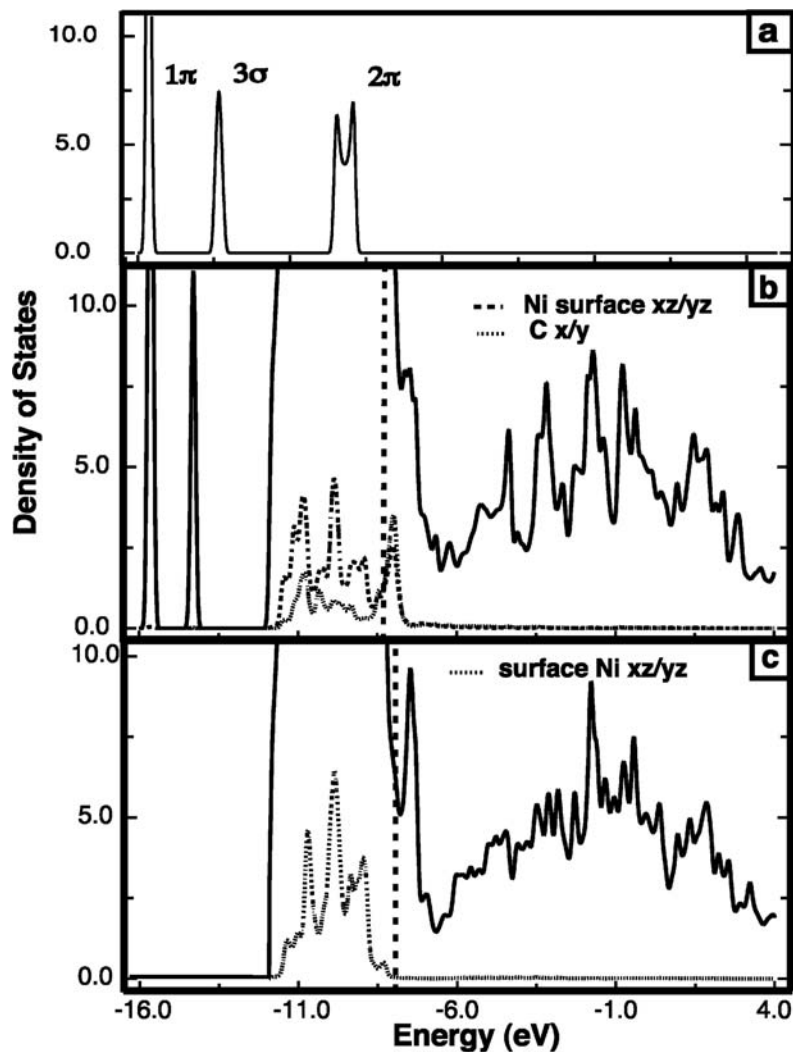


**FIGURE 23.7**

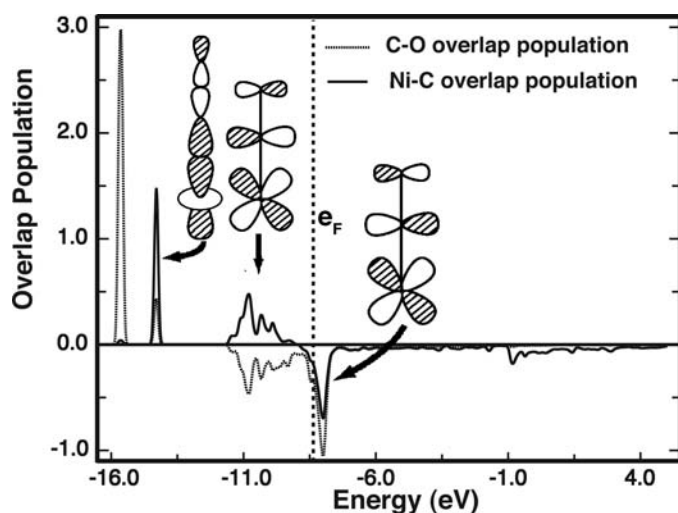
(a) DOS of free CO, and (c) DOS of the Ni(100) four Ni atom slab. The projection of  $z^2$  is given by the dotted line. (b) DOS of the  $c(2 \times 2)$ -CO/Ni(100) surface where the  $z^2$  projections are given by the dotted line and the  $z$  AO on C by the dot-dash line. The Fermi level in these plots is indicated by the dashed lines. All of the calculations are at the extended Hückel level.

explains the stabilization and destabilization of both projections in Figure 23.8b. It also is consistent with the Blyholder model sketched in 23.15.

There are other ways to search for these interactions. Here, we shall use the COOP curves (see Figure 13.5 and the discussion around it) where the overlap population between atoms or orbitals weighted by the DOS is plotted as a function of energy. An analogous energy-based analytical tool that uses the resonance integral has been employed by others [21,22]. Figure 23.9 gives the C—O (dotted line) and Ni—C (solid line) COOP curves for the  $c(2 \times 2)$ -CO/Ni(100) surface. The peak at  $-15.6$  eV in the DOS was assigned to the  $1\pi$  MO on CO and consistent with this is the large positive C—O overlap population at this energy in the COOP curve. Notice that there is also a small positive Ni—C overlap population at this energy which leads one to believe that there is a small amount of Ni  $xz/yz$  that mix into these states in a bonding manner. The peak at  $-13.4$  eV is strongly Ni—C bonding and also C—O bonding. This signals that Ni  $z^2$  mixes strongly into  $3\sigma$  in a bonding fashion as shown by the orbital picture in Figure 23.9. The region from around  $-11.4$  to  $-7.6$  eV is C—O antibonding. This is consistent with the existence of CO  $2\pi$  states

**FIGURE 23.8**

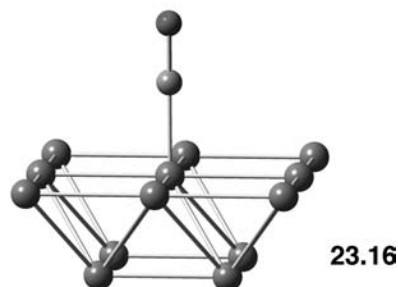
DOS of the  $c(2 \times 2)$ -CO/Ni(100) highlighting the  $\pi$  interactions. Details of these plots are the same as those given in Figure 23.7.

**FIGURE 23.9**

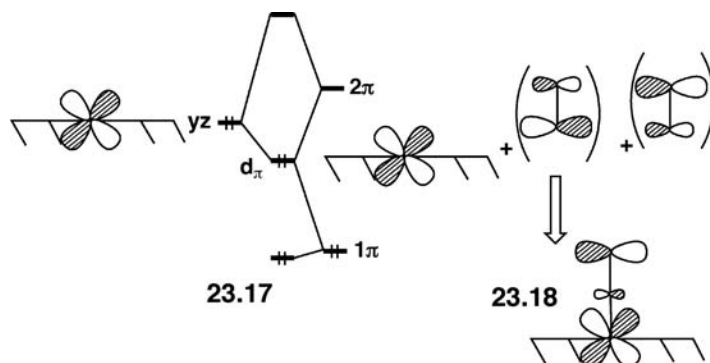
COOP curve for the  $c(2 \times 2)$ -CO/Ni(100) surface. The computational details are outlined in Figure 23.6.

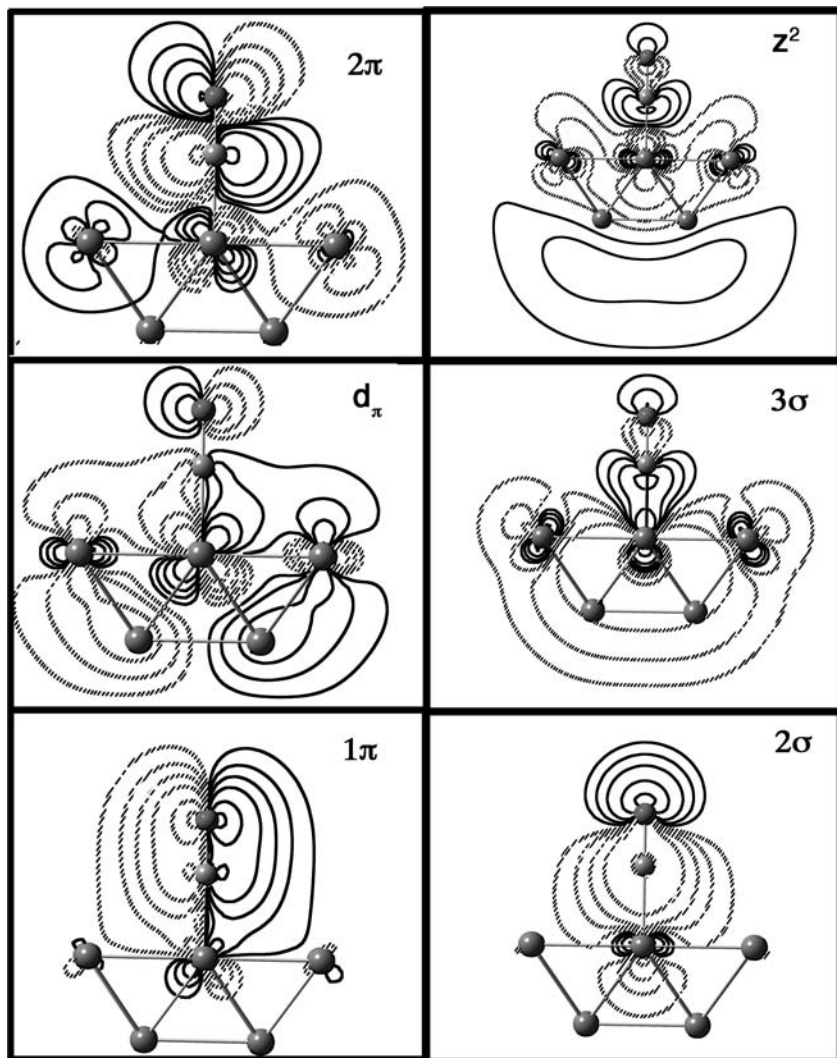
in this energy region. From  $-11.4\text{ eV}$  to just below the Fermi level, the Ni—C overlap population is positive. Therefore, these must represent the Ni  $xz/yz$  orbitals stabilized by  $2\pi$ . Careful inspection of Figure 23.9 shows that from the Fermi level to about  $1.5\text{ eV}$  below it the Ni—C and C—O overlap population approaches zero. This does not necessarily mean that there are no  $\pi$  states in this energy interval. Notice that the DOS projection of surface Ni  $xz/yz$  in the region is sizable in at least a portion of this energy interval. We shall return to this point shortly.

An alternative way to investigate the electronic structure is to carry out a so-called cluster calculation on a piece of the surface. **23.16** illustrates one approach



where a 13 Ni atom portion represents the Ni surface layer and bulk and there is one coordinated CO ligand on top of the central surface Ni atom. A B3LYP calculation was carried out [23] on this cluster to view the resulting wavefunctions. Figure 23.10 shows the relevant MOs. The left side shows three  $\pi$  orbitals that have the largest coefficients on the CO and/or the central Ni atom. The cluster has  $C_{4v}$  symmetry so each MO has a degenerate partner orthogonal to the plane shown in the figure. The lowest orbital on the left is clearly derived from CO  $1\pi$  while that at the top left is primarily CO  $2\pi$ . Note that the former has a small amount of Ni  $yz$  character mixed in a bonding fashion to  $1\pi$ . The latter MO has Ni  $yz$  mixed into  $2\pi$  in an antibonding fashion. The MO labeled  $d_\pi$  at the middle left of Figure 23.10 is Ni  $yz$  bonding to CO  $2\pi$ . This is in accord with the basic idea of the Blyholder model, but there is one aspect of this MO that might be puzzling to the reader. The amplitude of the wavefunction around carbon is quite small. This definitely should not be the case if its composition was solely derived from CO  $2\pi$ . What we have here is a typical three-orbital problem, no different from  $\text{H}_3$  in Section 3.2, allyl in Section 12.1, or, what is most germane, is the  $\text{L}_5\text{M}-\text{CO}$  example covered in Figure 15.3 and the discussion around it. The  $d_\pi$  MO is primarily Ni  $yz$  with  $2\pi$  and  $1\pi$  mixed into it, respectively, in a bonding fashion and antibonding fashion, as shown in **23.17**. A node develops at or close to the C atom; see **23.18**. The importance or extent to

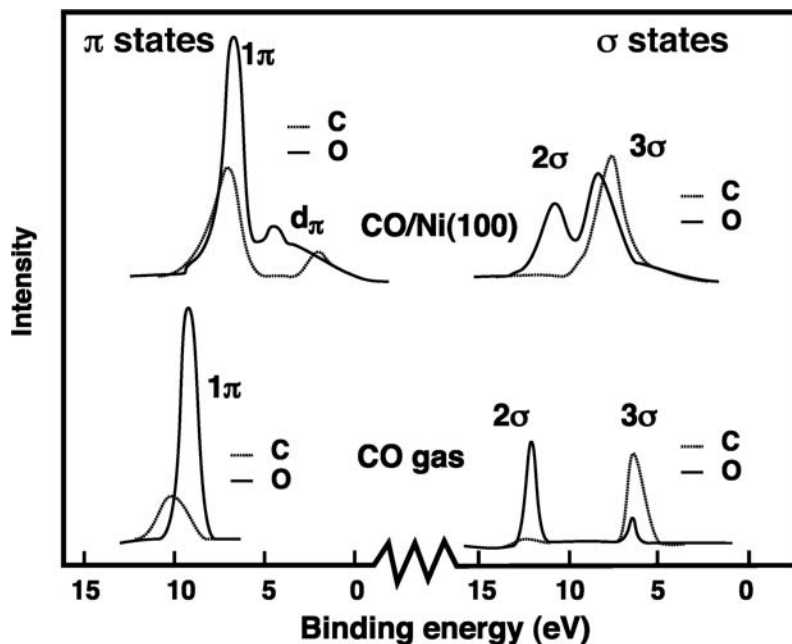


**FIGURE 23.10**

Contour diagrams in the  $yz$  plane for the three  $\pi$  (a) and  $\sigma$  (b) MOs that have the largest coefficients on the central Ni atom and/or CO. This is a B3LYP calculation on the 13 metal atom cluster shown in 23.16.

which  $1\pi$  mixes into the surface Ni  $yz/xz$  is controversial. The cluster model as well as the COOP curve just below the Fermi level having Ni—C and C—O overlap population close to zero despite the fact that there are plenty of Ni  $xz/yz$  states in this energy region all argue for the fact that the mixing of  $1\pi$  puts a node on the carbonyl carbon, just as it does for the molecular examples. An energy-based analysis [21] contends the opposite. What the COOP analysis does not really show, but the energy analysis and the cluster calculation does is that CO  $2\sigma$ ,  $3\sigma$ , and Ni  $z^2$  also mix together to yield a three-orbital pattern. The reader should work through the mixings, as well as the other two  $\pi$ -based MOs. Hence, a more critical analysis of the Blyholder model would add  $2\sigma$  and  $1\pi$  to the manifold of orbitals that involve a metal surface interacting with an on-top CO ligand.

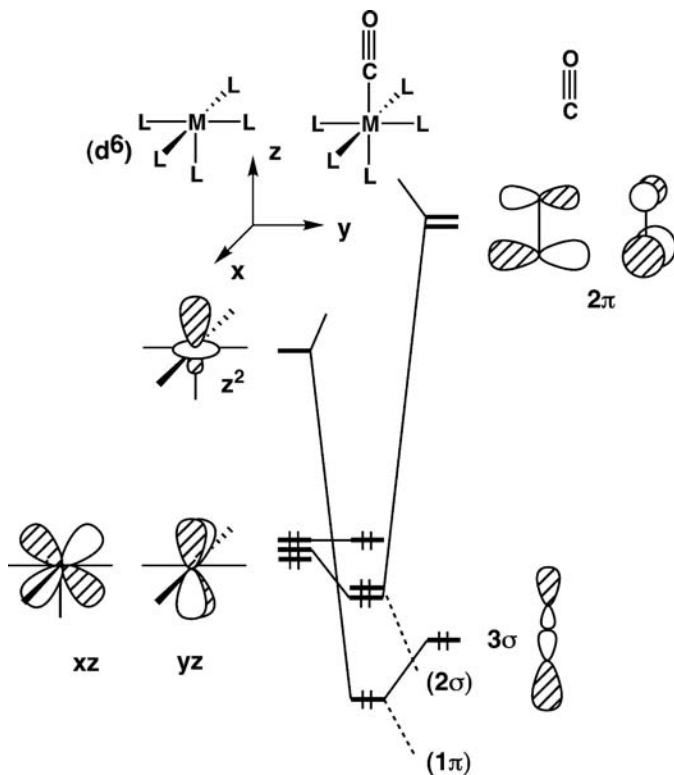
There is also a set of experimental results that have a bearing on this issue. In X-ray emission spectroscopy (XES), the core  $1s$  electron of C or O is ionized leaving a hole either on the O or the C atom. Due to atomic selection rules, only valence  $p$  electrons can decay into the  $1s$  core hole states which yields X-ray emission from either O or C atoms separately. Furthermore, the observations can be either perpendicular or parallel to the surface, which then leads to a separation of  $\sigma$  and  $\pi$  states. The spectrum [23b] for  $c(2 \times 2)$ -CO/Ni(100) is shown in Figure 23.11 along with gaseous CO as a comparison. The spectra are divided into those with  $\pi$  symmetry on the left side and  $\sigma$

**FIGURE 23.11**

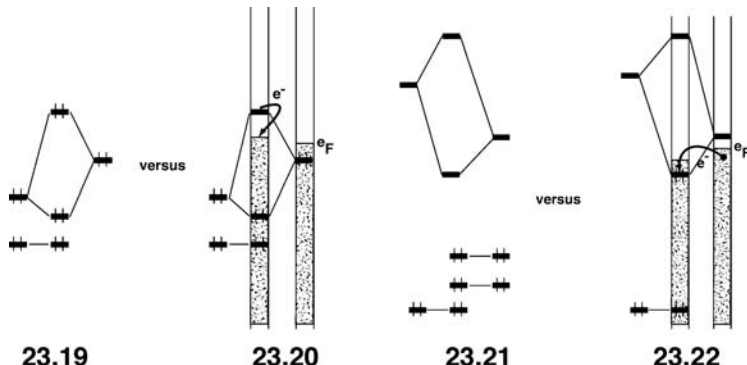
Experimental XE spectra for  $c(2 \times 2)$ -CO/Ni(100) along with free CO. The spectra have been adapted from Reference [23b]. The  $\sigma$  and  $\pi$  separation for gaseous CO does not exist so the spectra have been simplified to show only those portions that relate to the surface spectra.

symmetry on the right side. The dotted and solid lines give the  $p$  AO contributions from C and O, respectively. The  $1\pi$ ,  $2\sigma$ , and  $3\sigma$  peaks in CO gas are just what one would expect (notice that the very small C amplitude in  $2\sigma$  does not mean that the density on C is negligible; the XES experiment only probes the  $p$ , not the s states). On the Ni surface, these ionizations are at the positions given from the UPS experiment in Figure 23.5a. Interestingly, in the energy region labeled  $d_\pi$ , there is a peak associated with O at about 4.5 eV that has a long tail into the Fermi level. There is also a maximum for the C portion at 2 eV. This is the behavior that one would expect from the three-orbital model constructed in 23.17. The Ni  $d$  states around 4.5 eV contain O  $p$  character but little on C. As the energy of the states with surface  $xz/yz$  character increase, toward the Fermi level, the  $2\pi$  orbitals mix more and the  $1\pi$  less. Consequently, the intensity associated with C  $2p$  increases. This model also assumes that  $2\pi$  will mix into the  $1\pi$  MO in the second order (along with  $xz/yz$  in the first order). This puts more density on the middle atom, C. The XES result for CO gas shows  $1\pi$  to be highly polarized toward O. It is considerably less so on the Ni surface, which is in accord with  $2\pi$  mixing into these states. One can see something similar happening in the  $\sigma$  system. In the  $3\sigma$  MO, the  $2p$  character on C is much greater than that for O in CO gas. However,  $2p$  on O gains amplitude while that at C is diminished on the Ni surface. Here again  $3\sigma$  is the middle orbital in this three-orbital pattern.

So the Blyholder model can be modified to 2 three-orbital interactions rather than 2 two-orbital ones without any problem. There still is another conceptual problem that makes theory in surface science a little different than that in the molecular world. The Blyholder model uses a filled  $3\sigma$  orbital to interact with an empty Ni  $z^2$  or  $z^2$ -hybrid in 23.14. This is precisely analogous to what happens for CO bonding to a  $d^6$   $ML_5$  fragment repeated again in Figure 23.12. The filled  $xz/yz$  Ni surface orbitals interact with empty  $2\pi$  (23.15). Again there is a one-to-one correspondence in the molecular case. The problem with this picture on the Ni surface is that all, or nearly all of the surface Ni  $z^2$  states are filled, are not empty—see Figure 23.7a and c. In the molecular world, this would signal a strong two-orbital four-electron destabilization, as shown in 23.19. This is not necessarily the case on the surface. As demonstrated in 23.20, if the overlap is large enough, the antibonding combination may lie above the Fermi level and so the electrons in this

**FIGURE 23.12**

Orbital interaction diagram for interacting a  $d^6$   $ML_5$  fragment with CO.



antibonding orbital are deposited at the Fermi level (they become states in the bulk that formerly were not occupied. So what was a repulsive interaction is turned into an attractive one at the expense of the bulk).

In the molecular world, the interaction between two empty orbitals normally leads to two combinations with no electrons. This interaction, therefore, has no energetic consequence, 23.21. At the surface if the overlap is large enough, the bonding combination may lie below the Fermi level and become populated by electrons from the bulk, 23.22. Clearly, the situation in 23.20 must be applied to our  $c(2 \times 2)$ -CO/Ni(100) case in Figure 23.7. It is difficult to identify from Figure 23.8 whether 23.22 must be applied to the Ni  $xz/yz$ -CO  $2\pi$  interaction.

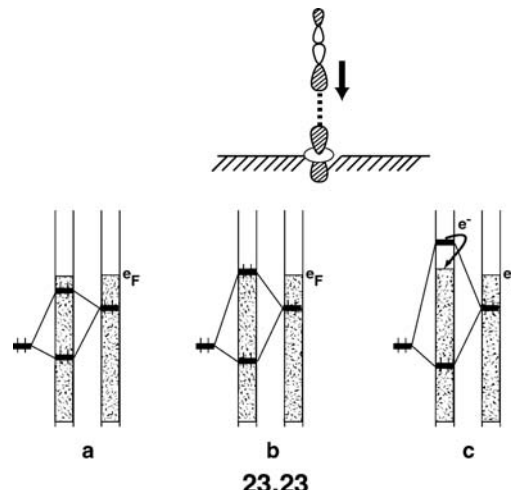
Table 23.1 reports the electron occupations for the various orbitals in question using the Mulliken population analysis at the extended Hückel level. For comparison, the molecular case chosen was  $H_5Ni^-$ -CO $^-$  where the hydrogen atoms mimic pure  $\sigma$  donor groups. Starting with  $H_5Ni^-$ -CO $^-$  the  $z^2$  and  $z$  AOs on  $H_5Ni^-$  gain 0.54 electrons (the population of Ni s is negligible). The  $3\sigma$  and  $2\sigma$  MOs on CO lose 0.53 electrons.  $NiH_5^-$  loses 0.48 electrons, whereas CO  $2\pi$  gains 0.51 electrons. The

**TABLE 23.1** Calculation of Electron Densities for  $\text{H}_5\text{Ni}-\text{CO}^-$  and  $\text{c}(2 \times 2)$ - $\text{CO}/\text{Ni}(100)$  at the Extended Hückel Level Using the Mulliken Population Scheme

Orbital	$\text{NiH}_5^-$	$\text{H}_5\text{Ni}-\text{CO}^-$	CO	$\text{Ni}(100)$	$\text{OC}-\text{Ni}(100)$	CO
$z^2$	0.00	0.34	—	1.93	1.43	—
$z$	0.00	0.20	—	0.01	0.17	—
$3\sigma$	—	1.59	2.00	—	1.62	2.00
$2\sigma$	—	1.88	2.00	—	1.88	2.00
$xz/yz$	4.00	3.52	—	3.81	3.31	—
$2\pi$	—	0.51	0.00	—	0.74	0.00

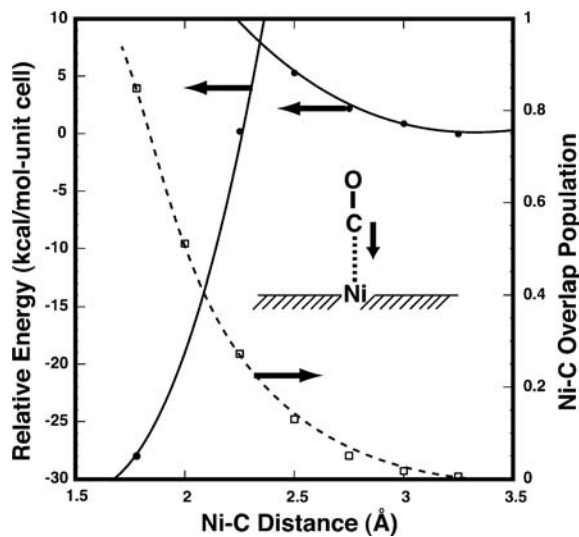
The electron densities for  $\text{Ni}(100)$  are those for the surface layer.

loss and gain of electrons cancel each other in each pair-wise interaction and this is certainly consistent with the picture in Figure 23.12. For the  $\text{c}(2 \times 2)$ - $\text{CO}/\text{Ni}(100)$  system, the picture is more complicated. The  $3\sigma$  and  $2\sigma$  MOs on CO lose 0.50 electrons; almost identical to that in the test molecule. However, the Ni surface  $z^2$  and  $z$  states do not gain electrons; they lose 0.67 electrons! This is only consistent with the interaction shown in 23.20 where both the CO and the Ni surface are depopulated by moving electrons from the antibonding combinations to the Ni bulk. In the  $\pi$  region, the surface  $xz/yz$  AOs (the Ni  $x/y$  AOs contribute very little to this interaction) lose 0.50 electrons; again remarkably similar to that in the molecule. However, CO  $2\pi$  gains 0.74 electrons—0.24 electrons more than  $xz/yz$  gave! This can only occur by the interaction diagramed in 23.22. Empty surface  $xz/yz$  states interact with empty  $2\pi$ , and the bonding combinations are filled with electrons from the bulk. The bulk acts as an electron reservoir, shuttling electrons to and from the surface-adsorbate regions. There are cases of activated chemisorption, where there is an activation energy associated with the adsorption. This is a natural consequence of 23.20. Consider the adsorption of CO on Ni(100). At long C—Ni distances, the overlap between Ni  $z^2$  and C  $z$  is small so the antibonding combination does not go above the Fermi level. The situation in 23.23a has an energy that is repulsive. It is not until 23.23b, where the  $\langle z^2 | z \rangle$  overlap increases because the Ni—C distance decreases, that this interaction becomes stabilizing. It is even more in 23.23c. Figure 23.13 shows the results from a set of extended Hückel calculations in  $\text{c}(2 \times 2)$ - $\text{CO}/\text{Ni}(100)$ . The relative energies per unit cell are plotted with respect to the Ni—C distance by the solid line. It would appear that there are two electronic states with a crossing at



23.23

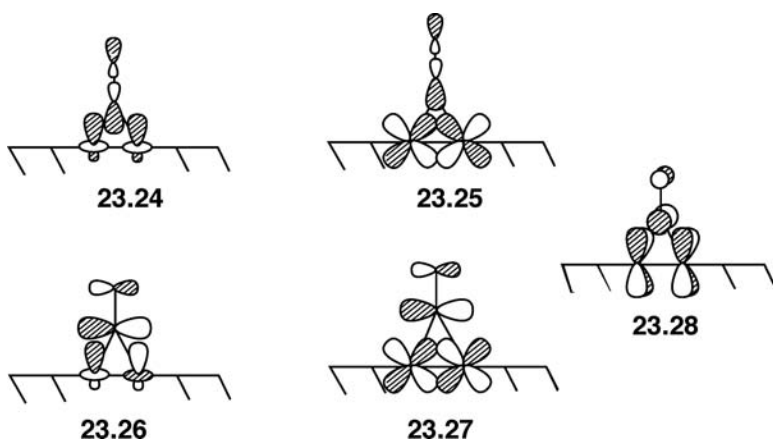
where the  $\langle z^2 | z \rangle$  overlap increases because the Ni—C distance decreases, that this interaction becomes stabilizing. It is even more in 23.23c. Figure 23.13 shows the results from a set of extended Hückel calculations in  $\text{c}(2 \times 2)$ - $\text{CO}/\text{Ni}(100)$ . The relative energies per unit cell are plotted with respect to the Ni—C distance by the solid line. It would appear that there are two electronic states with a crossing at

**FIGURE 23.13**

Extended Hückel computed relative energies per unit cell as a function of the Ni—C distance is plotted with the solid line for the  $c(2 \times 2)$ -CO/Ni(100). The dashed curve is the Ni—C overlap population.

about  $2.4\text{ \AA}$ . This is not really the case; it is where the Ni  $z^2$ —CO  $3\sigma$  interaction becomes attractive. The Ni—C overlap population rises in an almost exponential fashion since the overlap in both the  $\sigma$  and the  $\pi$  portions of the interaction are increasing with decreasing Ni—C distance. The reader should be aware that the extended Hückel method does not give reliable binding energies or bond lengths. We have chosen to use this method for its analytical features that can be applied and readily understood over this range of problems.

In the previous section, we reviewed the binding energy of CO to different transition metal surfaces. Recall that moving to the left side in the periodic table dramatically increases the CO binding energy (Figure 23.3). The principal reason behind this is the increased interaction of the metal  $d$  orbitals with CO  $2\pi$ . Therefore, the occupation of  $2\pi$  becomes larger for the early transition metals [24]. Since  $2\pi$  is strongly C—O antibonding, one might expect that the bond may become weak enough to break into C and O adatoms. This, in fact, does happen on going from Co to Fe, Ru to Mo, and Re to W [3]. Whether CO bonds to an on-top, bridge, or hollow position depends on the transition metal, the surface, and CO (and/or additional adsorbate) coverage. For example, at low-coverage CO coordinates to the bridge site first in Ni(111), however, on-top binding is preferred for Pt(111) and the hollow site is occupied first for Pd(111) [1]. Clearly, this is a difficult, complicated issue to address [25]. The two principal components for the on-top model, 23.14 and 23.15, use the same set of orbitals for a bridging geometry but now CO  $3\sigma$  interacts with the in-phase combination of  $z^2$  hybrids, 23.24, and the



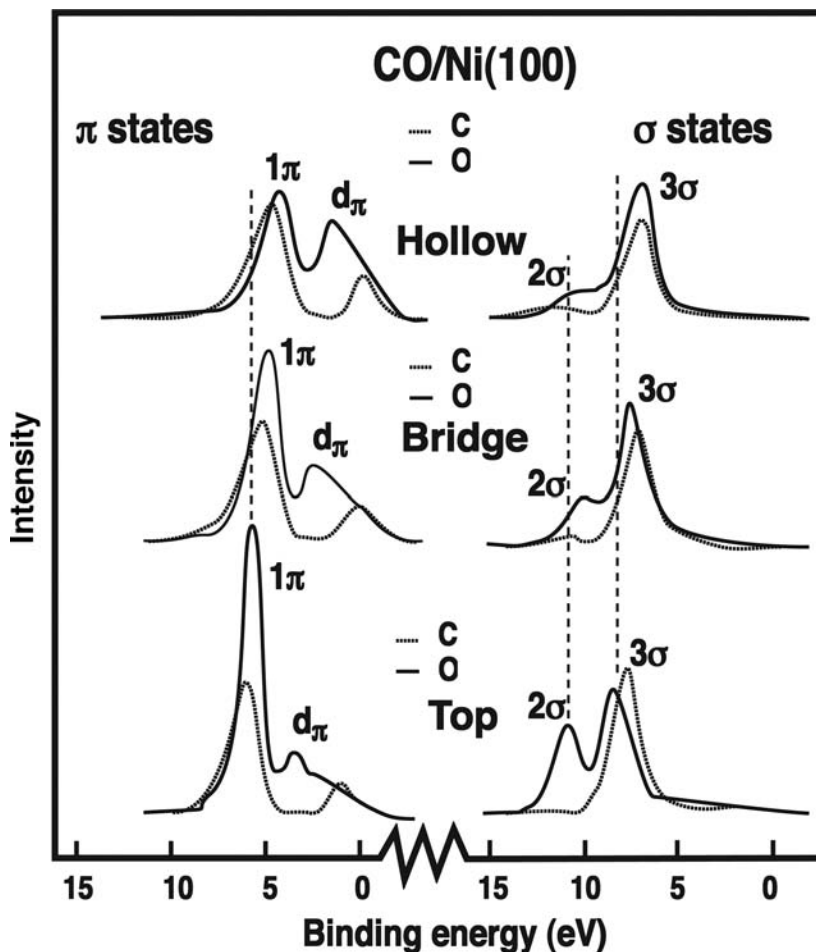


**FIGURE 23.14**

XE spectra for the three CO adsorption geometries on an Ni(100) surface. The dotted line corresponds to carbon 2p AOs, whereas the solid lines reference O 2p AO orbitals. (The plots are adapted from Reference [26].)

in-phase combination of two metal  $yz$  AOs, **23.25**. The out-of-phase combinations overlap with one member of CO  $2\pi$ , **23.26**, whereas the other member of  $2\pi$  interacts with metal  $xz$ , **23.27**. One can easily generate the appropriate symmetry adapted combinations of metal orbital to interact with  $3\sigma$  and  $2\pi$  for binding to the hollow. The question here is difficult because one must evaluate the net stabilization in **23.14** compared to **23.24** plus **23.25**. In general, one must be very cautious here, the  $\sigma$  interaction favors on-top while the  $\pi$  bonding is stronger at the bridge and hollow positions.

XES was used to study the different CO binding modes on an Ni(100) surface [26]. The spectra are reproduced in Figure 23.14. The on-top coordination mode is reproduced again at the bottom of the Figure as a comparison to the bridge and hollow binding geometries. The most striking differences lie in the  $\pi$  section of the spectra. The intensity of the  $d_{\pi}$  region increases greatly on going to the bridging and hollow geometries which is consistent with greater CO  $\pi$  bonding to Ni  $xz/yz$ . In particular, the maxima for the O 2p AO states increase greatly. The “middle” member of the three-orbital set becomes more localized on oxygen; see **23.18**. Notice also that the C 2p AO contribution increases relative to that for O 2p in the  $1\pi + xz/yz$  combination; the lowest level becomes more concentrated at the middle atom in the three-orbital pattern of **23.17**. These changes are consistent with the amount of  $\pi$  bonding in the Ni surface to CO being in the order: on-top < bridge < hollow. There are not nearly so great differences in the  $\sigma$

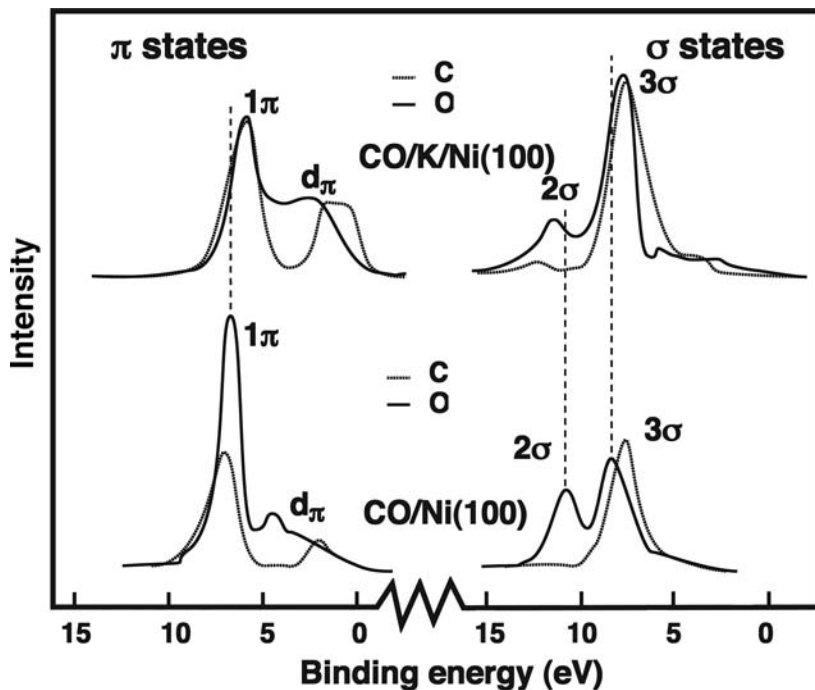


FIGURE 23.15

XE spectra of the CO/K/Ni(100) surface. The dotted and solid lines show the C and O 2p AO contributions, respectively. The CO/Ni(100) spectrum is shown at the bottom of the figure for reference. (The spectrum was adapted from Reference [27].)

portion of the spectra. The amount of O 2p character does increase in 3σ on going to the bridge and hollow sites. What is not clear is why the maxima in each of the peaks move by about 0.6 eV to lower binding energies on going from the on-top to bridging geometry and by about the same amount on going to the hollow structure. The on-top structure is favored for the Ni(100) surface. A bridged geometry can be stabilized by low hydrogen coverage. A larger hydrogen concentration produces the hollow geometry. Perhaps, hydrogen adsorption has something to do with the shifts to lower binding potentials in the XE spectra or this might be a referencing problem.

We mentioned previously that potassium is a promoter for the adsorption of CO. Figure 23.15 shows the XE spectra [27] for the K/CO/Ni(100) surface where CO is coordinated in the hollow position. The spectrum for the on-top CO/Ni(100) parent is again shown for reference. The K atoms are thought not to be directly coordinated to the Ni surface, but to rather lie at approximately the height of the oxygen atoms by analogy to the K/CO/Ni(111) structure [28]. Therefore, the most likely scenario is one where the K atoms have donated their electron to the states at the Fermi level, which is predominately Ni xz/yz bonding to CO 2π. The oxygen atoms will then become more negatively charged and an ionic interaction is established between K<sup>+</sup> and O<sup>-</sup>. Since the Fermi level is raised, there will be a greater interaction with CO 2π. Consistent with this is the very large amplitude that develops on the C 2p region for d<sub>π</sub> near the Fermi level. One might think that the Ni—C bond should be made stronger by the addition of K atoms. Taking electrons from the CO 3σ orbital by interaction with the Ni z<sup>2</sup> hybrid does not weaken the CO bond. As discussed in Section 6.5, the 3σ MO is actually slightly C—O antibonding so removal of electrons from it will actually slightly strengthen the C—O bonds. However, the filling of CO 2π has important structural consequences. The 2π MO is strongly C—O antibonding and, therefore, increased occupation of CO 2π will greatly weaken the C—O bond and eventually break it.

Molecular nitrogen also is chemisorbed on metal surfaces. The structures obtained for these surfaces all show N<sub>2</sub> coordinated perpendicular to the surface

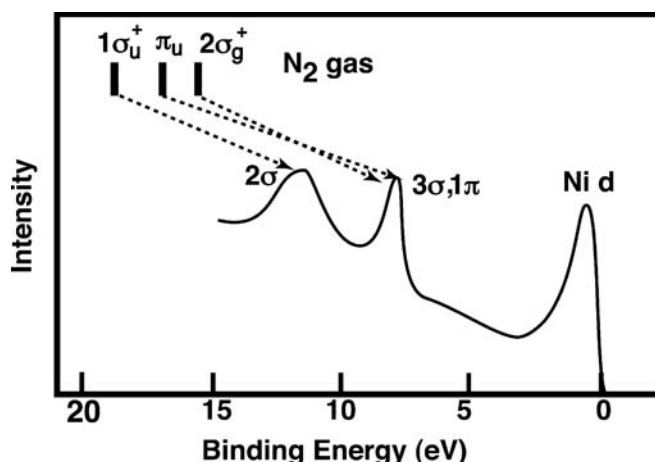
**TABLE 23.2 Energies of the Frontier Orbitals (eV) in Some Related Diatomics from B3LYP Calculations with a 6-311+G\* Basis Set**

Molecule	Nonbonding	$\pi$	$\pi^*$
CO	-14.2	-17.6	-2.0
N <sub>2</sub>	-16.0	-17.2	-2.0
NO	-18.1	-18.9	-8.6
O <sub>2</sub>	-20.4	-20.8	-12.0

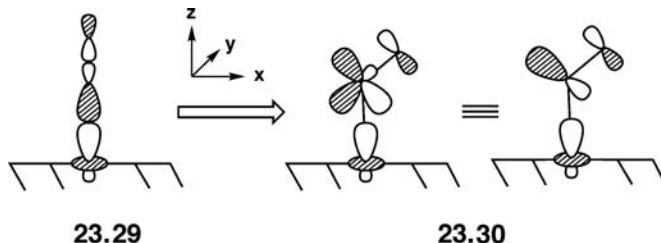
just like CO. The chemisorption energy is in general less than that for the isoelectronic CO. Table 23.2 lists scaled eigenvalues for the nonbonding  $\sigma$ ,  $\pi$ , and  $\pi^*$  MOs for some diatomic molecules. The orbital energies here were obtained from B3LYP calculations using a 6-311+G\* basis set which has been shown to accurately reproduce experimental ionization potentials and electron affinities [29]. Notice that the  $\pi$  and  $\pi^*$  energies for CO and N<sub>2</sub> are very close to each other. Therefore, one might expect that the  $\pi$  bonding to the surface  $xz/yz$  metal orbitals would be similar. However, the nonbonding  $\sigma$  orbital for N<sub>2</sub> ( $2\sigma_g^+$ ) lies nearly 1.5 eV lower in energy than that in CO ( $3\sigma$ ). The metal–N<sub>2</sub>  $\sigma$ -bonding should then be weaker than that for metal–CO. The XE spectra are in agreement with these predictions [30]. Figure 23.16 displays the UPS results for N<sub>2</sub> adsorbed on-top of Ni(110). The ionizations for N<sub>2</sub> gas are at the top of the spectrum. Just as for the CO/Ni(100) case in Figure 23.5a, the ionization energies decrease upon coordination to the surface. In CO/Ni(100), the  $3\sigma$  ionization, however, was not shifted as much as the  $2\sigma$  and  $1\pi$  ones, which was attributed to the strong bonding of  $3\sigma$  to the Ni  $z^2$  hybrid on the surface. This does not occur for  $2\sigma_g^+$  in Figure 23.16; that is consistent with the weaker  $\sigma$  donation in N<sub>2</sub>. On going to NO one electron is added to the  $2\pi$  set. Furthermore,  $2\pi$  lies at much lower energy because of the increased electronegativity of O compared to N; see Table 23.2. The geometry of NO on metal surfaces can again be on-top, bridged, or hollow and is a function of coverage, metal and surface, much similar to the situation for CO and N<sub>2</sub>. In all the cases, the N end is coordinated to the metal surface. The polarization of  $3\sigma$  and  $2\pi$  enhance the bonding to the surface at this geometry. There is one additional factor to consider, namely, bending the NO group away from being perpendicular to the surface. In Section 17.5, we analyzed this bending of molecules as a function of electron count, and we encourage the readers to review this section. Filling the molecular orbital, which is a metal

**FIGURE 23.16**

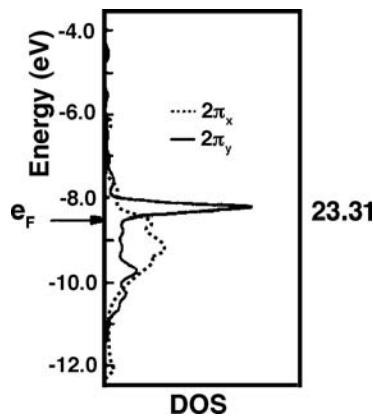
Photoelectron spectrum of N<sub>2</sub> adsorbed on an Ni(110) surface. The bars at the top indicate the ionizations for N<sub>2</sub> gas. (Adapted from Reference [31].)



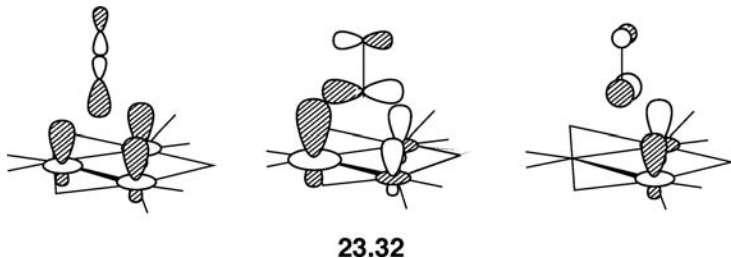
$z^2$ -hybrid antibonding to  $3\sigma$  favors a bent M—N—O geometry. This surface analog for an on-top coordination is shown in 28.29. Metal—N antibonding is



relieved. If the M—N—O bending is in the  $xz$  plane, NO  $2\pi_x$  will mix into the orbital as shown in 23.30. M—N bonding is strengthened at the expense of weakening the N—O bond by increased occupation of  $2\pi_x$ . As shown in 23.30, this M—N  $\sigma$  antibonding interaction is turned into a lone pair-type orbital concentrated on N. An extended Hückel calculation for NO/Ni(111) nicely shows this [32]. The DOS projections for the  $2\pi_x$  (dotted line) and  $2\pi_y$  (solid line) states are shown in 23.31. At a linear geometry the DOS for  $2\pi_x$  looks similar to that shown



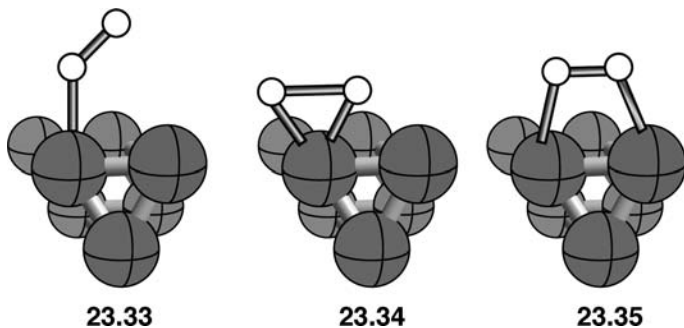
in 23.31 for  $2\pi_y$ . Bending by  $60^\circ$  in the  $xz$  plane causes the  $2\pi_x$  contribution to smear out and move to lower energies. The  $2\pi_y$  occupation stays relatively constant; from 0.91 electrons at the linear geometry to 0.93 electrons at the  $60^\circ$  structure. On the other hand, the occupation of  $2\pi_x$  increases greatly, from 0.91 to 1.52 electrons. At the hollow, threefold geometry  $2\sigma$  and the  $2\pi$  set are actively involved in  $\sigma$  bonding to the metal  $z^2$  hybrids, 23.32. Of course, surface



metal  $xz$  and  $yz$  also mix into these combinations. Therefore, the  $2\pi$  set is already being strongly utilized and we find no compelling reason why NO should bend. The very low energy of NO  $2\pi$  makes bridging and hollow sites favorable. The on-top sites should have bent NO geometries for late transition metals and linear

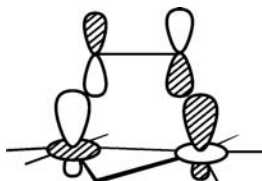
geometries are more favorable for earlier transition metals. However, just like CO, early transition metals will favor dissociation to N and O adatoms. The available literature appears to be mostly consistent with this. On the Ru(001) surface NO binds at the on-top and hollow position. In both cases the NO is linear, perpendicular to the surface [33]. XES shows features that are very similar to the CO on Ni(100) cases in Figure 23.14 with the exception that the  $d_{\pi}$  region is more intense compared to CO (the species coordinated to the hollow site is, as expected, more intense than that for the on-top) [33]. On an Ni(100) surface at low coverage, NO coordinates to the fourfold site (see 23.8) and is perpendicular to the surface [34]. Oxygen atoms bond preferentially at the hollow sites, so the on-top geometry is favored for subsequent NO coverage. The NO ligand is bent from linearity by  $40^\circ \pm 10^\circ$  [35]. On Ni(111), NO prefers the hollow sites and is essentially linear with a bending angle of  $7^\circ \pm 5^\circ$  [36]. On a Pt(111) surface both the hollow and the on-top sites are occupied with the former linear and the latter at a bending angle of  $52^\circ$  [37].

The dynamics associated with the exposure of a diatomic molecule to a metal surface can be quite complex. Considering chemisorption (rather than physisorption), the diatomic can approach either end-on (perpendicular to the surface), parallel to the surface or at some intermediate angle(s). The attack might be favored for the on-top, bridge, or hollow positions. Furthermore, there may be a barrier for absorption (an activated event) or it can be barrier-less. The adsorbed dimer may be intact with some residual bonding between the two atoms or it can decay directly into dissociated adatoms. Finally, the adsorbed dimer can be in a precursor state, which then dissociates via a transition state with an activation barrier. The reaction of  $O_2$  with metal surfaces has been extensively investigated and nearly all of the adsorption scenarios have been proposed. As mentioned in Table 23.2, notice that the  $\sigma$  level ( $2\sigma_g^+$ ) lies at a very low energy. Bonding to the surface via  $\sigma$  is expected to be of minimal importance; hence, parallel approaches to the surface are expected to be favored. The  $\pi^*$  MO ( $\pi_g$ ) is now half-full and, of course, the ground state is a triplet at long O–metal distances. At some point, there will be a crossing to the singlet state and O=O will have the  $\pi$  and  $\pi^*$  orbitals parallel to the surface filled. The perpendicular  $\pi$  and  $\pi^*$  orbitals are then, respectively, filled and empty and will be the dominant source of  $O_2$ –surface bonding. Singlet O=O is isoelectronic to ethylene. We shall pursue this analogy shortly. The most studied surface has been Pd(111). Experimental evidence from the O–O stretching frequencies has indicated the existence of three species which have been assigned to have the geometries shown in 23.33–23.35 [38]. 23.33 and 23.34 correspond to on-top



geometries with the former akin to the bent NO on-top structure and the latter similar to a metal–olefin complex. 23.35 is analogous to a metallacycle and is normally given the nomenclature T–B–T. At low coverage and at low temperatures, 23.34 is formed first. This is slowly transformed into 23.35 which then undergoes dissociation into O atoms at higher temperatures. It is easy to see why

O—O dissociation occurs in this structure. Empty  $\pi^*$  will interact with filled metal  $z^2$  hybrids, **23.36**. Thus, electron density flows from the filled metal surface to  $\pi^*$ ,



23.36

which is strongly O—O antibonding. In formal terms there is still an intact O—O  $\sigma$  bond, however, similar to  $F_2$  this is expected to be quite weak. A DOS and COOP plot of this structure is shown in Figure 23.17. The dotted line in Figure 23.17a represents the total density of states at the extended Hückel level for a three metal atom model with one-half  $O_2$  coverage [39]. The solid line is the oxygen character magnified by three times. The heavy bars on the right side of Figure 23.17a are the calculated orbital energies for free  $O_2$ . Upon coordination the two  $\pi_u$  and two  $\pi_g$  orbitals are no longer degenerate pairs. Those parallel to the surface are labeled  $\pi_x$  and  $\pi_x^*$ . As seen in the figure, these two MOs on  $O_2$  interact only very weakly with the surface. On the other hand, as anticipated by **23.36**, the two  $\pi$  MOs perpendicular to the Pd surface (designated  $\pi_z$  and  $\pi_z^*$ ) interact very strongly. Both  $\pi_z$  and  $\pi_z^*$  are stabilized by bonding interactions with Pd surface AOs. Notice from the COOP in Figure 23.17b that the peak at  $-15.5$  eV is both Pd—O and

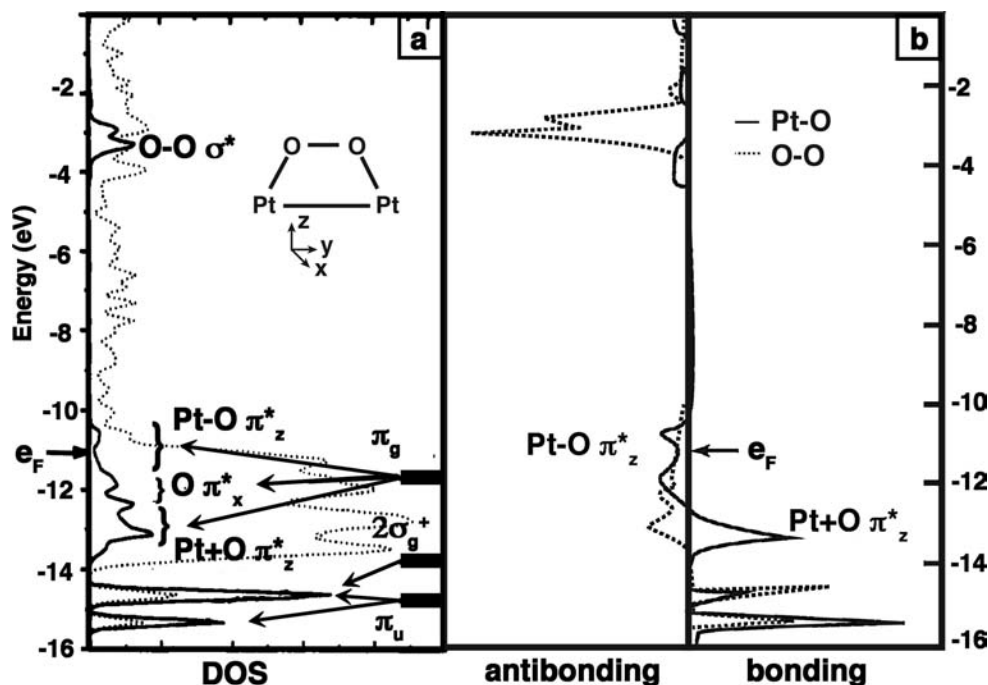
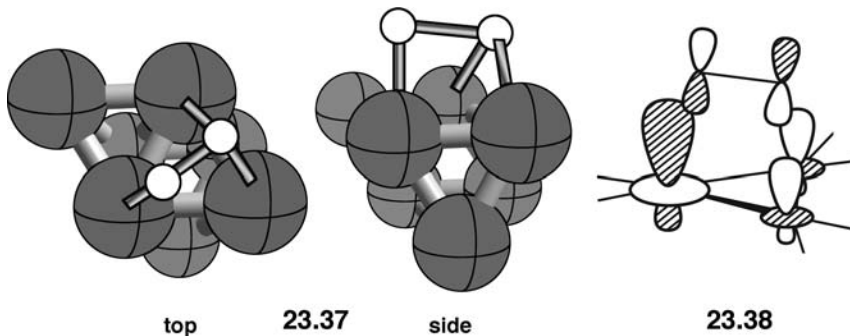


FIGURE 23.17

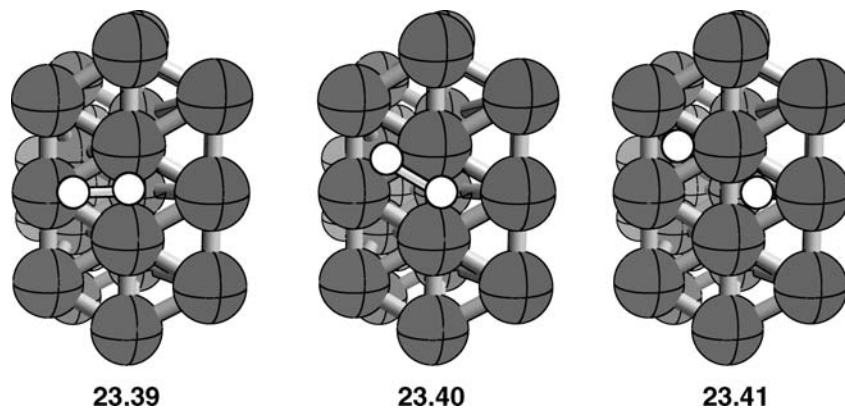
(a) DOS plot for the T—B—T geometry (**23.35**). The total DOS is given by the dotted line and the projection of O character (magnified by three times) is represented by the solid line. (b) COOP plots for **23.35** where the Pt—O and O—O overlap population is given, respectively, by the solid line and dotted lines. The Fermi level is designated by  $e_F$ . (Adapted from Reference [39].)

O—O bonding, which is consistent with  $\pi_z$  bonding to Pd. Whereas, the peak at  $-13.3\text{ eV}$  is Pd—O bonding but O—O antibonding; they are the  $\pi_z^*$  states bonding to Pd. The corresponding antibonding orbitals are spread out from about  $-11.5$  to  $-10.2\text{ eV}$ . The O—O  $\sigma^*$  orbital ( $2\sigma_u^+$  for the free  $\text{O}_2$  molecule) is at very high energy, about  $-3\text{ eV}$ . As the O—O bond is stretched, these states will rapidly fall in energy and become populated thereby breaking the O—O bond. The proposed structure from experiment, **23.33**, is formed only at high coverage [38].

Density functional calculations [40,41] have been carried out to investigate these structures. Structure **23.35** was located, however, **23.34**, rearranges to a T—H—B structure shown from two views in **23.37**. Just as in the T—B—T geometry there is much better overlap between  $\text{O}_2 \pi_z^*$  and the Pd  $z^2$  hybrids,



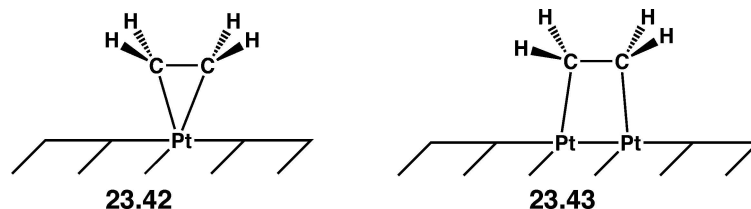
as shown in **23.38**. These structures were also found for the Pt(111) surface. No structure analogous to the  $\eta^2$   $\text{O}_2$  complex **23.34** was located. The  $\pi_z^*$  overlap in **23.36** and **23.38** with Pd/Pt is much larger than that for an  $\eta^2$  complex. Molecular dynamics calculations [42] gave the dissociation barrier for  $\text{O}_2$  on the Pt(111) surface to be 13–24 kcal/mol depending on the coverage. A top view of this process starts with the T—H—B structure, **23.39** which then rotates the left oxygen atom in a



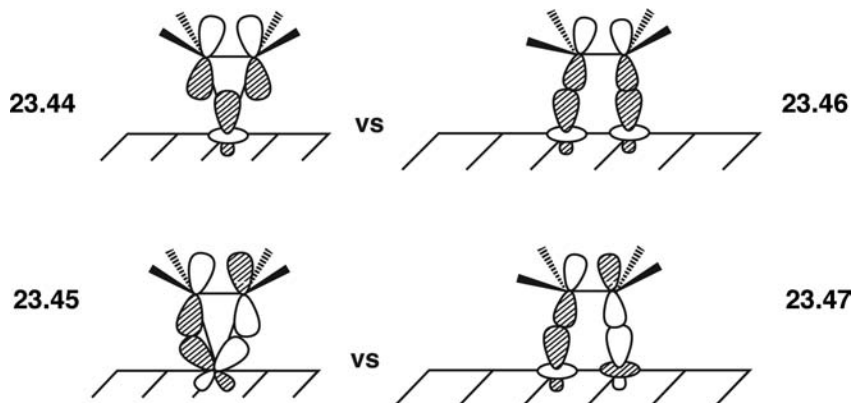
clockwise direction and stretches the O—O bond to a transition state, **23.40**. Stretching the O—O bond more leads to the product state **23.41** where each oxygen atom lies in a hollow. The bonding here is indeed very easy to see. A  $sp$  hybrid on oxygen bonds to the symmetric combination of  $z^2$  hybrids analogous to that shown for CO at the H geometry on the left side of **23.32**. The other  $sp$  hybrid is directed out away from the surface and represents the lone pair orbital on O. The two remaining  $p$  AOs on oxygen overlap with the  $e$  set of  $z^2$  hybrids just as CO  $2\pi$  does on the middle and right side of **23.32**. Much less is known about  $\text{O}_2$  on the Ni(111) surface. At most temperatures  $\text{O}_2$  dissociates directly to O adatoms. At low temperatures, there is a

claim that one  $O_2$  precursor state exists with  $O_2$  perpendicular to the surface and coordinated to an H position. However, DFT calculations indicate that only the T—H—B geometry exists akin to 23.37. The T—B—T structure is actually a saddle point and there is a very small, 5 kcal/mol barrier for dissociation [41].

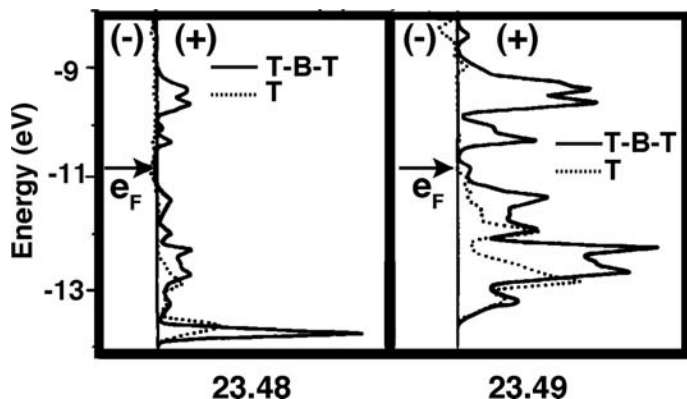
Ethylene adsorbed on early transition metals undergoes fragmentation reactions to yield  $CH_x$  fragments. On a Pt(111) or Pd(111) surface ethylene initially is chemisorbed in an intact geometry. At higher temperatures, it rearranges by a series of reactions that lead to a tricoordinated ethylidyne ( $C—CH_3$ ) and ultimately to polymers. The mechanisms for these reactions have been studied extensively by experimental and theoretical means. They are complicated [1,16,43–47] and will not be reviewed here. Our concerns will be confined to the geometry of the coordinated ethylene ligand. Most of the experimental work has pointed to an  $\eta^2$ , on-top geometry, 23.42, that forms at low temperatures and is followed by a



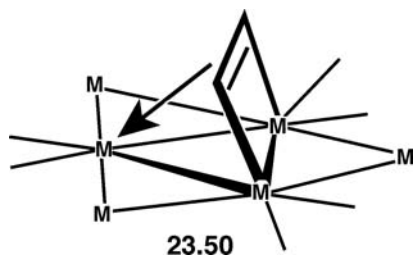
T—B—T (di- $\eta^1$ ) structure, 23.43, at higher temperatures. Theoretical work using several density functionals have consistently found that 23.43 is more stable than 23.42. For Pt(111), this difference ranged from 16.4 kcal/mol in one study [46] to 8.8–10.8 kcal/mol depending on coverage in another [44b]. Yet another DFT study gave a 9.9 kcal/mol difference and a small 2.9 kcal/mol activation barrier for the rearrangement of  $\eta^2$  to the T—B—T state [47] while a 35 metal atom cluster B3LYP calculation gave 15.9 kcal/mol difference but the T structure collapsed without activation to the T—B—T one [48]. An STM study at 50 K has indicated that the two coordination modes coexist [49]! For the Pd(111) surface the difference is computed to be smaller, 2.1 kcal/mol [45] to 2.9–4.6 kcal/mol [44]. However, a LEED study [50] at 80 K has indicated that the T—B—T structure is the only one present on a clean Pd(111) surface. On the other hand, subsurface hydrogen (from the adsorption of  $H_2$ ) makes the  $\eta^2$  geometry to be favored and it is this type of structure that undergoes hydrogenation of olefins to yield alkanes. That the di- $\eta^1$  structure is more stable than  $\eta^2$  is in-line with the results of  $O_2$  coordination that we have just covered. But throughout Chapters 15–21, we have covered the bonding in metal–olefin complexes with various electron counts and  $ML_n$  structures. What favors 23.43 over 23.42? Taking the Pt(111) surface as an example, it is easy to predict that the two most important interactions in 23.43 are derived from the forward donation of ethylene  $\pi$  to the  $z^2$  hybrid on Pt, 23.44.



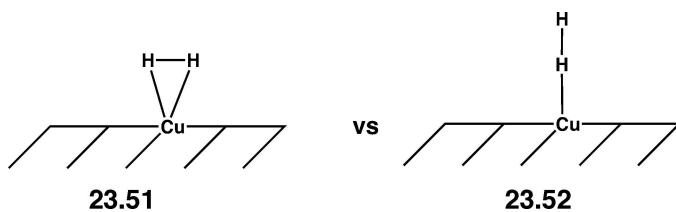
Back-donation occurs from Pt  $xz$  to ethylene  $\pi^*$ , **23.45**. For the di- $\eta^1$  geometry ethylene  $\pi$  and  $\pi^*$  both interact with Pt  $z^2$  hybrids (Pt  $xz$  combinations can also mix into these combinations but the overlap is much smaller) [51]. They are explicitly drawn in **23.46** and **23.47**. The question then boils down to which of the interactions offers greater Pt—C bonding neglecting coverage and entry issues. A COOP curve of the Pt—C overlap populations most easily highlights the differences. In **23.48**, the total Pt—C overlap population at the



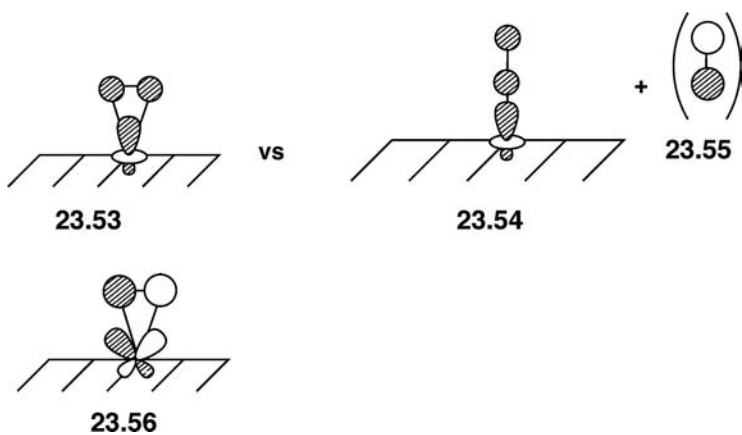
extended Hückel level is plotted for the on-top (dotted line) and T—B—T (solid line) geometries [51]. The sharp peaks at  $-13.8\text{ eV}$  correspond to ethylene  $\pi$  states, and it would appear that the T—B—T offers greater Pt—C bonding. However, this is not clear-cut. At  $-14.9\text{ eV}$  the C—C  $\sigma$  orbital mixes with the Pt  $z^2$  hybrid(s) and this is much more important for the on-top structure. Ultimately, the  $\sigma + \pi$  contribution for the Pt—C overlap population was found to be 0.173 for T—B—T versus 0.183 for the on-top geometry [51]. In other words, there is a very slight preference for **23.42**. The COOP curve in **23.49** dissects the Pt—C overlap population into just that for ethylene  $\pi^* - \text{Pt}$ . One can readily see that below the Fermi level there is much larger bonding for the di- $\eta^1$  compared to the  $\eta^2$  geometry. The  $\pi^*$  contributions to the Pt—C overlap population were 0.215 versus 0.113, respectively [51]. The overlap in **23.47** is greater than that in **23.45**. But the lowest energy structure for the O<sub>2</sub>/Pt(111) and Pd(111) cases was the T—H—B coordination mode, **23.37**. A detailed diffuse LEED experiment on Pt(111) at 200 K in fact points to this structure where the C—C vector of the coordinated ethylene lies at an angle of about 22° with respect to the surface [52]. Theory has not been kind to this proposal. DFT calculations find the structure to lie 12.5 kcal/mol [46], 12.6 kcal/mol [47], or 15.5 kcal/mol [53] higher in energy than the T—B—T ground state. On the other hand, acetylene on Pt(111) or Pd(111) does lie over a hollow point on the basis of LEED [54], STM [55], and theory [48,56]. It is not quite analogous to the T—H—B structure in **23.37**, but rather one rotated about the C—C midpoint by 90° perpendicular to the surface. It uses one  $\pi$  bond in the acetylene to form two  $\eta^1\sigma$ -bonds which leaves the second to  $\pi$  bond in an  $\eta^2$  manner as shown in **23.50**. An analysis of this as well as several other structural possibilities has been given elsewhere [57]. The discussion here underscores the experimental and theoretical difficulty in pinpointing structural and energetic details for even the most elementary species.



In most cases that we have treated it is pretty obvious whether the favored approach of the molecule is parallel to or perpendicular to the surface. The  $3\sigma$  and  $2\pi$  orbitals of CO clearly favor a perpendicular path. The  $\pi$  and  $\pi^*$  orbitals of ethylene favor a parallel approach. So what is the favored path for a dihydrogen molecule? Is it the parallel approach, **23.51**, or a perpendicular path, **23.52**?

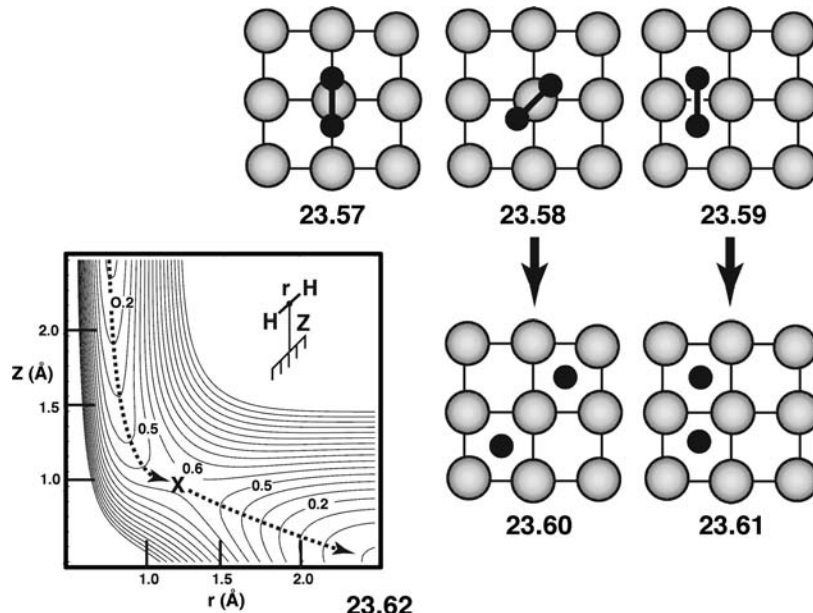


The interactions are easy to evaluate.  $H_2$  has a filled  $\sigma_g^+$  level and an empty  $\sigma_u^+$  one. We should note here that the model we have chosen is the Cu(100) surface. For earlier transition metal surfaces  $H_2$  adds and dissociates with no activation barrier. For Cu(100) the dissociation is activated, that is, an activation barrier lies between free  $H_2$  gas and the dissociated product. The energetics and reaction paths for the Cu(111) surface are very similar.  $H_2 \sigma_g^+$  will interact with the  $z^2$  hybrid in both geometries. This is illustrated in **23.53** and **23.54**. Clearly there is greater overlap

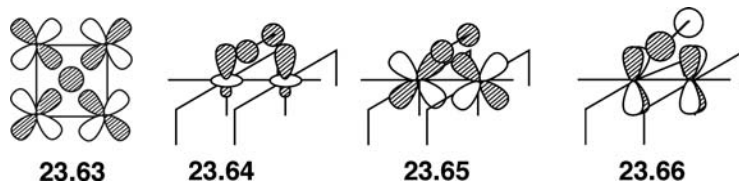


associated with **23.53**. One should remember that for copper these hybrids may well contain as much or even more Cu s and z than  $z^2$  character. However, at long distances both bonding and antibonding combinations of  $z^2$  hybrids and  $H_2 \sigma_g^+$  are expected to be filled and it is this feature that sets up the activation barrier. Notice that this is precisely analogous to the Ni  $z^2$ -CO  $3\sigma$  situation in Figure 23.13. For the perpendicular approach,  $H_2 \sigma_u^+$ , **23.55**, can mix into both bonding and antibonding states. This aspect will favor the perpendicular path over a parallel

approach. However, empty  $H_2 \sigma_u^+$  states mix into filled Cu  $xz/yz$  hybrids when oriented in the parallel geometry and this is the decisive factor for determining the optimal path. In fact all the DFT calculations [58–61] have shown that the energy associated with the perpendicular path is repulsive. The full six-dimensional surface of  $H_2$  on Cu(100) has been constructed [60,61] by taking two-dimensional cuts from several starting points and varying  $r$ , the distance between the two hydrogens and  $Z$ , the distance of the  $H_2$  unit from the surface. Three starting points are shown in 23.57–23.59. The paths over the B–T–B, 23.57 and



H–T–H, 23.58, positions correspond nicely to the model presented by 23.53 and 23.56. The activation barrier for the former was found to be 16.1 kcal/mol with  $r = 1.43 \text{ \AA}$  and  $Z = 1.39 \text{ \AA}$ . In other words, the H–H bond is essentially broken but the distance to the surface is quite long. The 2D slice with the lowest activation energy (11.1 kcal/mol [58] or 13.1 kcal/mol [59]) is actually the H–B–H one, 23.59. An elbow plot of the surface adapted from Reference [59] is shown in 23.62. The “transition state” here is marked by an “X”. Here  $r = 1.23 \text{ \AA}$  [58] or  $1.22 \text{ \AA}$  [59] and  $Z = 1.05 \text{ \AA}$  [58] or  $0.98 \text{ \AA}$  [59]. The H–H bond is again nearly broken but the  $H_2$ -surface distance is much shorter. In other words, this crossing point comes at a later point, close to the structure of the product. Note that 23.59 smoothly passes into 23.61 by lengthening  $r$  and decreasing  $Z$ . The final product is one where the hydrogen atoms sit in a fourfold hollow, 23.60 or 23.61. Here, the hydrogen atom lies only  $0.53 \text{ \AA}$  from the top of the surface. So the H s AO now does not overlap well with Cu  $z$  or  $z^2$  instead it will primarily overlap with Cu  $s$  and  $xy$ ; 23.63 illustrates the latter. The principal interactions for the

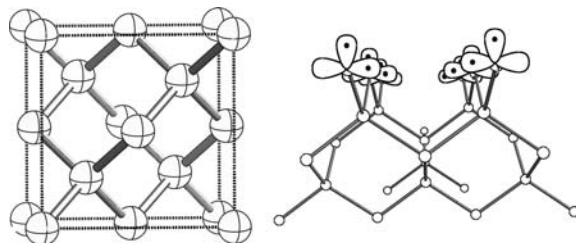


H–B–H geometry on the reactant side do not change much from that 23.53 and 23.56. 23.64 and 23.65 corresponding, respectively, to 23.53 and 23.66, match the

nodal properties of **23.56**. Our suspicion is that at long Z distances the overlap on-top is stronger with  $H_2 \sigma_g^+$  and especially  $\sigma_u^+$ . Therefore, initially the reaction path occurs via the approach shown in **23.57** and the coordinated  $H_2$  unit slides with a lateral motion to the  $H-B-H$  structure and finally to the dissociated product, **23.61**. This reaction path has been proposed for the dissociative absorption of  $H_2$  on a Rh(100) surface [62]. An equally attractive route would be the direct conversion of **23.58** to **23.60**. There are very specific procedures and criteria for locating transition states and following reaction paths in the molecular domain. In the solid state these techniques are by and large lacking at the present time.

## 23.5 THE SURFACE OF SEMICONDUCTORS

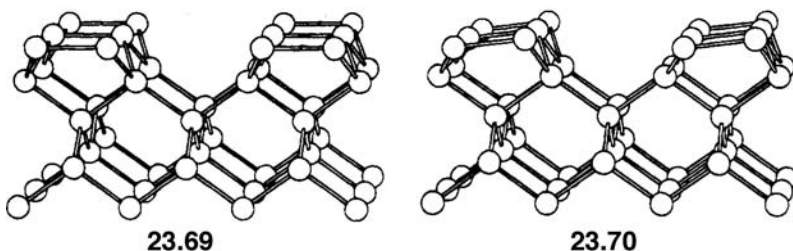
In this section, we will only consider semiconductors based on the diamond structure, **23.67**, where all atoms are  $sp^3$  hybridized. Any cleaved surface leaves dangling bonds on the outermost surface atoms. A side view of the silicon (100) surface is shown in **23.68**. The Si atoms at the surface are two-coordinate;



23.67

23.68

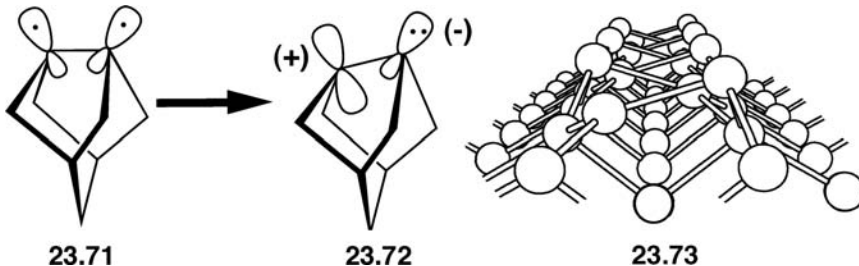
therefore, they have two orbitals with two electrons in them. We have taken a carbene perspective and put one electron in an  $sp^2$  hybridized orbital perpendicular to the surface and the other electron in an orthogonal  $p$  AO. While partially filled, dangling bonds pose no problems for metals, main group elements favor structural distortion to pair electrons forming bonds. Therefore, reconstruction of the surface atoms and atoms below is the norm for semiconductors [63]. We shall limit our coverage to the Si (100) surface which has received most of the attention. It is easy to see from **23.68** that lateral motions of the uppermost Si atoms create Si—Si  $\sigma$  bonds from the  $p$  AOs parallel to the surface. What is left then are Si orbitals perpendicular to the surface with one electron in each one. They can overlap in a  $\pi$  type fashion to create  $\pi$  bonds. There are two distinct ways to accomplish this, **23.69** and **23.70**. Structure **23.69** is often called the symmetric dimer model.



23.69

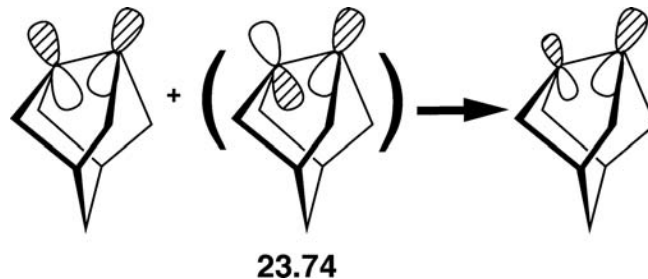
23.70

One might think that an Si–Si double bond has formed but notice that the four “substituents” around the Si–Si double bond are in a highly pyramidal, “cisoid” arrangement. We saw this same feature, not for Si but for the higher group 14 elements in Section 10.3.C. What this means is that the  $\pi$  and  $\pi^*$  levels are not split by much energy; they have diradicaloid character, **23.71**. We saw in Section 10.3.I

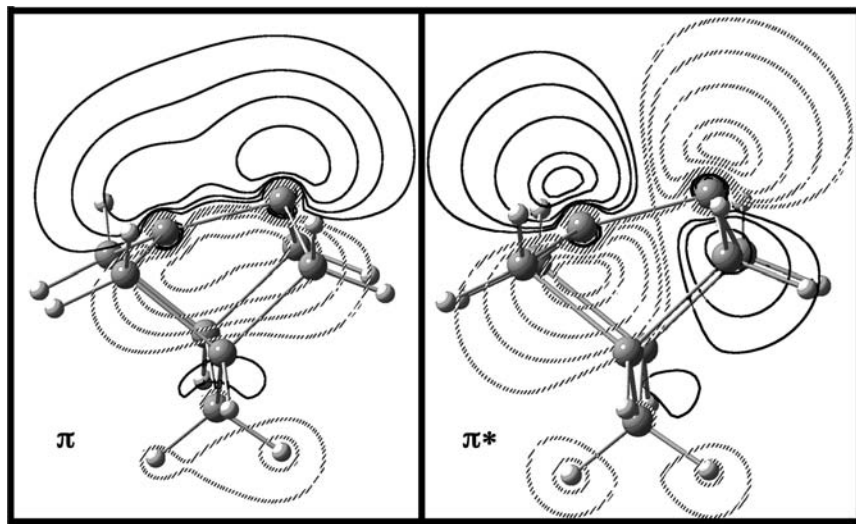


that twisting about a C=C bond not only generated a diradicaloid state, but also with pyramidalization at one end a zwiterionic state can be formed. Here, as shown by **23.72**, a lateral motion of one bridging Si atom can flatten that center while the second remains pyramidal. The  $\pi$  and  $\pi^*$  orbitals mix with each other so that electron density at the pyramidal silicon atom increases while that at the planar one decreases. Thus, a zwiterionic state is generated. We do not mean to imply that the bridging Si atom on the left has an empty  $p$  AO and the one on the right a filled s and  $p$  hybrid, but rather, as we shall shortly see, the  $\pi$  and  $\pi^*$  orbitals are polarized in that direction and a dipole moment across the Si=Si bond is created. The full asymmetric dimer model is displayed in **23.70**. A variant that doubles the unit cell size is drawn in **23.73**. Structural data have pinpointed either **23.70** or **23.73** as the most likely structure for the Si(100) surface with the latter being favored [63,64].

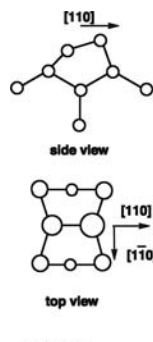
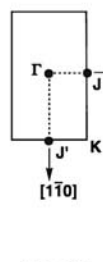
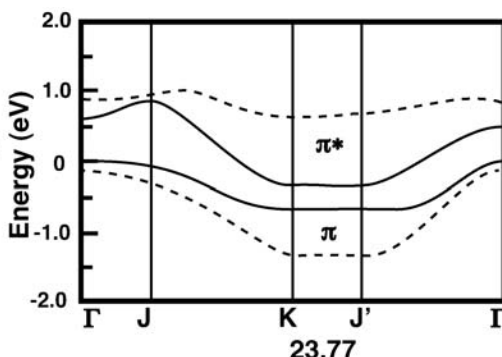
Buckling the Si dimers causes the  $\pi$  and  $\pi^*$  orbitals to mix with each other. This is demonstrated in **23.74** for the mixing of  $\pi^*$  into  $\pi$ . Recall from Section 9.3 and



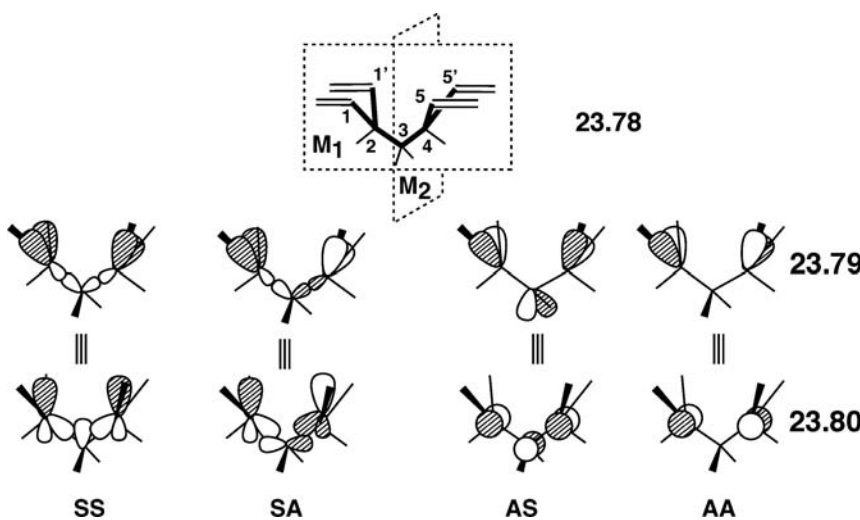
especially Figure 9.7 that a six electron, SiH<sub>3</sub> molecule prefers to be planar, whereas a seven or eight electron SiH<sub>3</sub> molecule is pyramidal. Thus, the geometric distortion of the dimer is the driving force for the orbital mixing. Contour plots of the  $\pi$  and  $\pi^*$  MOs in an Si<sub>9</sub>H<sub>12</sub> cluster model of the asymmetric dimer are displayed in Figure 23.18. These are B3LYP hybrid density functional calculations using a 6-311G(d) basis set. As anticipated by **23.74**, the  $\pi$  orbital has more electron density on the pyramidal Si atom while  $\pi^*$  is more localized on the planar Si. However, the  $\pi$  and  $\pi^*$  character in these two MOs is clearly obvious. Let us turn now to the band structure of these  $\pi$  and  $\pi^*$  states. The directions of interest are shown in side and top views of the top three Si rows from a side and top view in **23.75**. The Brillouin zone for the symmetric (**23.69**) and asymmetric (**23.70**) dimer models is given in **23.76**. The tight binding band structure for the Si(100) surface is shown in **23.77** [65].

**FIGURE 23.18**

Contour plots of the  $\pi$  and  $\pi^*$  orbitals in an  $\text{Si}_9\text{H}_{12}$  cluster model of the asymmetric dimer. These calculations were performed at the B3LYP level.

**23.75****23.76**

The solid line shows the evolution of the  $\pi$  and  $\pi^*$  bands for the symmetric model. At the  $\Gamma$  point,  $\pi$  and  $\pi^*$  retain the same phase going along the  $[110]$  and  $[1\bar{1}0]$  directions. At the  $J$  point, the phase of the two orbitals alternates along  $[110]$  but stays the same along  $[1\bar{1}0]$ . At the  $K$  point, both orbitals change phase in both directions. Finally, at  $J'$ , the phase along  $[110]$  stays the same but alternates along the  $[1\bar{1}0]$  direction. The dispersion is modest, about 0.6 eV, but why is there any dispersion at all? This distance between dimers is 5.37 and 3.83 Å in the  $[110]$  and  $[1\bar{1}0]$  directions, respectively. This is far too long for any meaningful  $\pi$ -type overlap. The dispersion for the  $\pi$  and  $\pi^*$  bands is due to through-bond conjugation. The reader should refer back to Section 11.3 to review the details associated with this mode of communication. The Si—Si  $\sigma$  bonds of greatest importance will be those closest to the  $\pi$  and  $\pi^*$  orbitals of the dimer. The basic Si—Si  $\sigma$  coupling unit is shown at the top of **23.78**. In this analysis, we have used the Si(1)—Si(2), along with Si(1')—Si(2), Si(2)—Si(3), Si(3)—Si(4) and Si(4)—Si(5), along with Si(4)—Si(5') bonds, are used in this analysis. In this case, it is the most antibonding combination of the filled Si—Si  $\sigma$  bonds. These are shown from a bond orbital perspective in **23.79**. Each combination is then simplified in **23.80** and classified as being symmetric (S) or antisymmetric (A) with respect to the two mirror planes of symmetry,  $M_1$  and  $M_2$ . To see how the conjugation will take place, it is perhaps best to compare **23.69** with **23.78**. The Si—Si  $\pi$  and  $\pi^*$  levels are, of course, on the first silicon layer, Si(1), Si(1'), Si(5), and Si(5'). Consider them to be roughly pointed perpendicular to the surface.



The second- and third-row silicon atoms that run in a zigzag pattern along the  $[1\bar{1}0]$  direction are used to construct the through-bond network. SS and SA in **23.80** can interact with the  $\pi$  band at the  $\Gamma$  and  $J$  points. See the top two illustrations in Figure 23.19. Since these two are filled, they will overlap with Si—Si  $\pi$  in an antibonding manner and destabilize the  $\pi$  band at both the  $\Gamma$  and  $J$  points. At the  $J'$  and  $K$  points, the SA and AA combinations, respectively, interact with the  $\pi$  in an antibonding manner. The result is shown by the bottom two structures in Figure 23.19. One can see that the overlap between the  $\pi$  orbitals of the dimers and the orbitals in the Si—Si  $\sigma$  coupling unit are larger at  $\Gamma$  and  $J$  than they are at the  $J'$  and  $K$  points. Consequently, the band at the  $\Gamma$  and  $J$  points lie higher in energy than at  $J'$  and  $K$ . This is precisely what occurs in **23.77**. The reader can verify that exactly the same pattern unfolds for the  $\pi^*$  band. The picture presented here is somewhat simplified because the  $\sigma$  coupling for  $\Gamma$

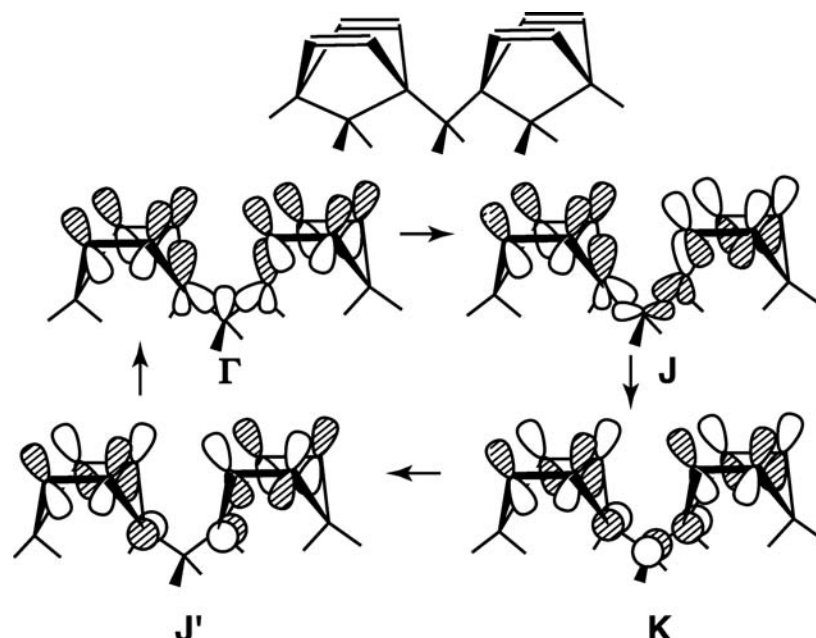
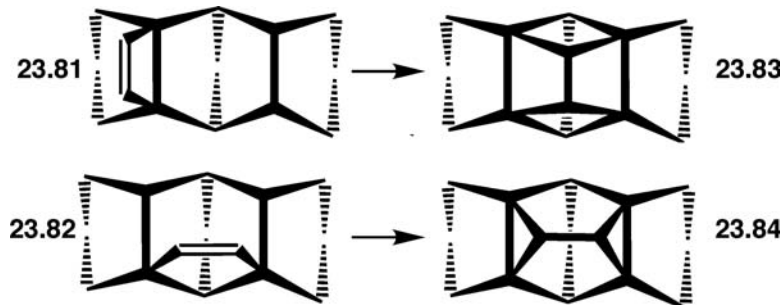


**FIGURE 23.19**

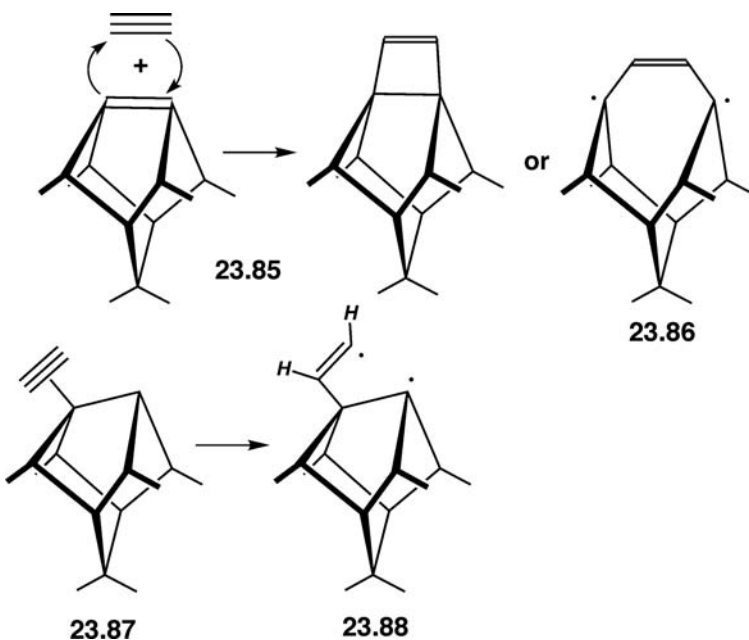
The crystal orbitals associated with the  $\pi$  band at several high symmetry points corresponding to the energy versus  $k$  plot in **23.77**.

and  $\mathbf{J}$  actually runs the whole length of the second and third row of Si atoms along the  $[1\bar{1}0]$  direction. The AS and AA coupling units in the  $[1\bar{1}0]$  direction actually will contain coefficients at Si (1), ( $1'$ ), (5), and ( $5'$ ); however, these AOs are orthogonal to the  $p$  AOs that make up the  $\pi$  and  $\pi^*$  orbitals. This model also explains why there is little or no dispersion along the  $\Gamma$  to  $\mathbf{J}$  and the  $\mathbf{K}$  to  $\mathbf{J}'$  lines for the  $\pi$  and  $\pi^*$  bands. The dashed line in 23.77 shows what occurs when the dimers are buckled as in 23.70. Now  $\pi$  and  $\pi^*$  mix with each other, as shown in 23.74. The  $\pi^*$  upper band mixes in and stabilizes the lower band, whereas  $\pi$  mixes in and destabilizes the upper band. This creates a band gap that is an important electronic feature for the Si(100) surface. The symmetrical dimer model predicts a metallic state. Angle-resolved photoemission spectroscopy has been used to study the band structure associated with the Si(100) surface states [66]. A comparison has been made to calculated excitation energies using a Green's function approach with a screened Coulomb interaction at the DFT level [67]. The level of agreement using the geometry shown in 23.73 is remarkable.

The Si—Si dimerization energy going from the unreconstructed geometry, 23.68, to the symmetrical structure, 23.69, is substantial—over 30 kcal/mol for each dimer formed. On the other hand, the distortion from the symmetrical to the buckled model, 23.70, lowers the energy by around 3–4 kcal/mol per dimer and alternating the buckling motion to 23.73 gives another 1–2 kcal/mol per dimer [68]. It is the diradicaloid character of the Si—Si double bonds that makes the Si(100) surface so active for a large number of cycloadditions [69]. Olefins, dienes, acetylene, furans, and even benzene add to the surface to form two Si—C  $\sigma$  bonds. Let us examine the addition of acetylene. Most of the recent experimental and theoretical work [70–73] has pointed to the most stable product being one where the acetylene has undergone a formal  $[2+2]$  cycloaddition across the Si—Si double bond of one dimer. The product of the reaction is shown from a top view in 23.81. There is also a minority product where the acetylene

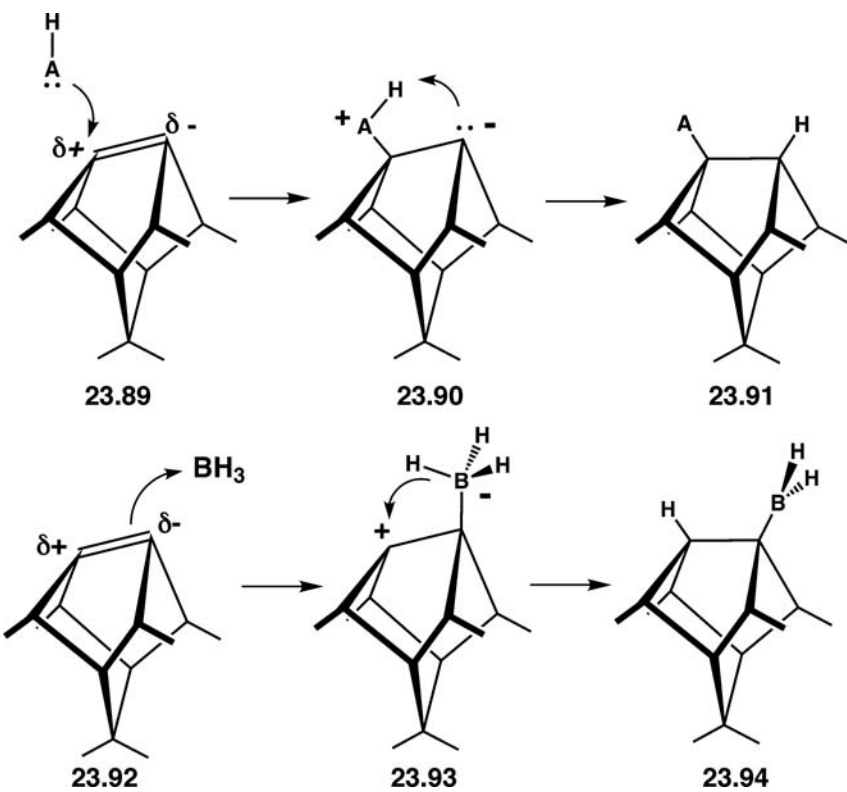


adds across two rows, 23.82. DFT calculations [70] have indicated that slipping across rows, from one dimer to the next via 23.83 is very difficult and requires about 46 kcal/mol. However, the end-bridged adduct, 23.82 can migrate from one end to another in a facile manner via 23.84 that requires only 16 kcal/mol. There is no conversion between 23.81 and 23.82 since this requires approximately 63 kcal/mol [70]. The pathway for the addition of acetylene is not entirely clear. A concerted addition, 23.85, is symmetry forbidden [74,75]. It is precisely analogous to the  $[2+2]$  dimerization of ethylene, which was discussed in Section 11.2.2. Furthermore, the so-called broken dimer, 23.86, lies about 27 kcal/mol above the disilacyclobutene structure. DFT calculations on a cluster model [74] located a  $\pi$  complex, 23.87. Notice that the acetylene is coordinated, as expected, to the Si atom that is electron deficient. The  $\pi$  complex then

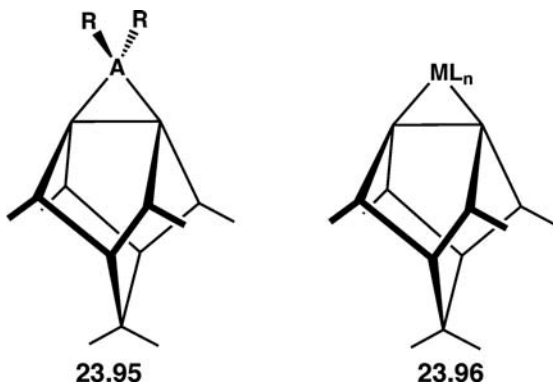


rearranges to a diradical intermediate, **23.88** and this intermediate in turn collapses to the dimer. DFT calculations using an extended slab [70] located the  $\pi$  complex; however, a diradical intermediate analogous to **23.88** was not found. Finally, the most recent theoretical effort [73] did not find either minimum; rather, the approach of acetylene to yield the **23.81** dimer proceeded without activation. On the other hand, the path to the end-bridged adduct, **23.82**, did proceed by a weakly bound  $\pi$  complex (where the acetylene has been rotated by 90°, out of the plane of the paper) and a diradical transition state. For the reaction of ethylene on Si(100), HREELS spectra [78] at 48 K have been interpreted as being derived from a  $\pi$  complex that then collapses to the disilacyclobutane structure analogous to **23.81** above 70 K. The regiochemistry associated with the reaction of propene and 2-methylpropene is also consistent with the formation of a  $\pi$  complex at the electron deficient Si atom [79]. The most reliable calculations, to date, of the reaction mechanism are due to Gordon and coworkers [80], who used multireference wavefunctions on a large cluster to unambiguously locate minima, transition states, and follow reaction paths. Two reaction channels were found. In the first channel, a  $\pi$  complex is generated and this passes through a transition state that is markedly asynchronous (the two Si—C bonds have very different bond lengths). In the second channel, a diradical intermediate is formed which then undergoes ring closure. The two reaction channels are very close in energy and the branching ratio between them should be very dependent on experimental conditions. The diradical intermediate can undergo rotation around the Si—C bond to form an end-bridged species akin to **23.82** and there is experimental evidence [81] for this coordination mode as a minor product.

The polarization in **23.72** of the asymmetric Si—Si dimer nicely explains the addition of A—H (A—H = H<sub>2</sub>O, NH<sub>3</sub>, and H<sub>2</sub>) to the Si(100) surface [82,83]. The initial step is the nucleophilic addition of A—H to the lower Si surface atom, **23.89**. This intermediate, **23.90**, transfers a hydrogen atom to the adjacent Si, **23.91**. Electrophiles, BF<sub>3</sub> [82] and BH<sub>3</sub> [84] add to the upper Si atom, **23.92**, to give intermediate **23.93**. The hydride then migrates to the adjacent Si position to give **23.94**. As



illustrated in Figure 23.18, the Si—Si dimer, whether buckled or not, has  $\pi$  and  $\pi^*$  orbitals. The reactions should also parallel those in alkenes and silenes. The addition of carbenes, nitrenes, silylenes, and so on has been predicted to add across the Si=Si bond to form stable multifunctional surfaces, **23.95** [85]. The isolobal analogy also



suggests that  $\text{ML}_n$  units should bind to the Si dimers [86], **23.96**, which leads to a wide range of possibilities that can be examined. The Si surface is, of course, just one of many semiconductor surfaces. Creating hybrid materials with specifically engineered properties really only comes about when the structure and electronic details of the surface are mastered. There is great technological potential in this area.

---

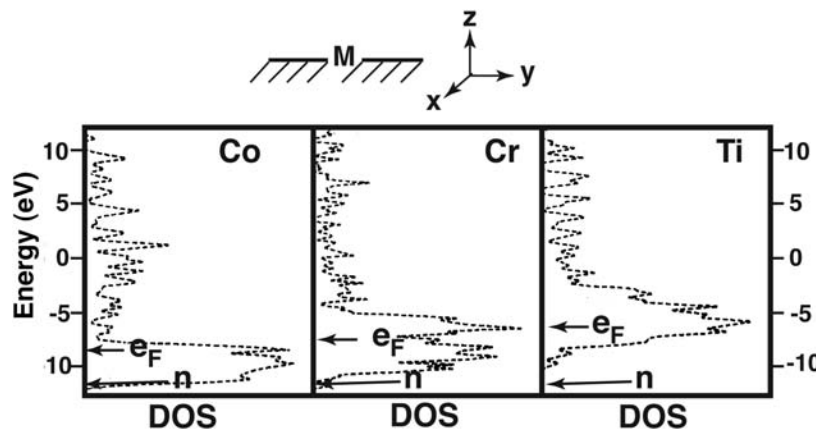
## PROBLEMS

---

**23.1.** The Fischer–Tropsch process was discovered nearly 90 years ago. It converts H<sub>2</sub> and CO into hydrocarbons by means of a heterogeneous catalyst, normally cobalt based. This is a commercially important process with several plants in South Africa and Malaysia and many more starting up around the world. The exact mechanism for this transformation is most certainly quite complex, but ultimately organic radicals on the surface must undergo a reductive elimination reaction. In the next couple of problems we shall examine some of the mechanistic issues that arise. Consider the (111) surface of an fcc metal (see 23.10).

- Make a judgment as to what adsorption site will be the most stable one for a CH<sub>3</sub>, CH<sub>2</sub>, and CH radical for simplicity using only the d AOs at the metal surface.
- There are two possible geometries for CH<sub>2</sub> on a bridge site, that is, where the plane of the CH<sub>2</sub> lies parallel or perpendicular to the M–M bond. Determine which orientation is the most stable one.

**23.2.** We will use three surfaces from an in-depth theoretical study by Zheng et al. [88]: Ti (0001), Cr (110), and Co (0001). Using the coordinate system below, a tabulation of the number of electrons associated with the surface atoms and a total DOS plot for the three metals is also given below. The position of the Fermi level and the energy for the nonbonding orbital of a methyl group is shown as e<sub>F</sub> and n, respectively.

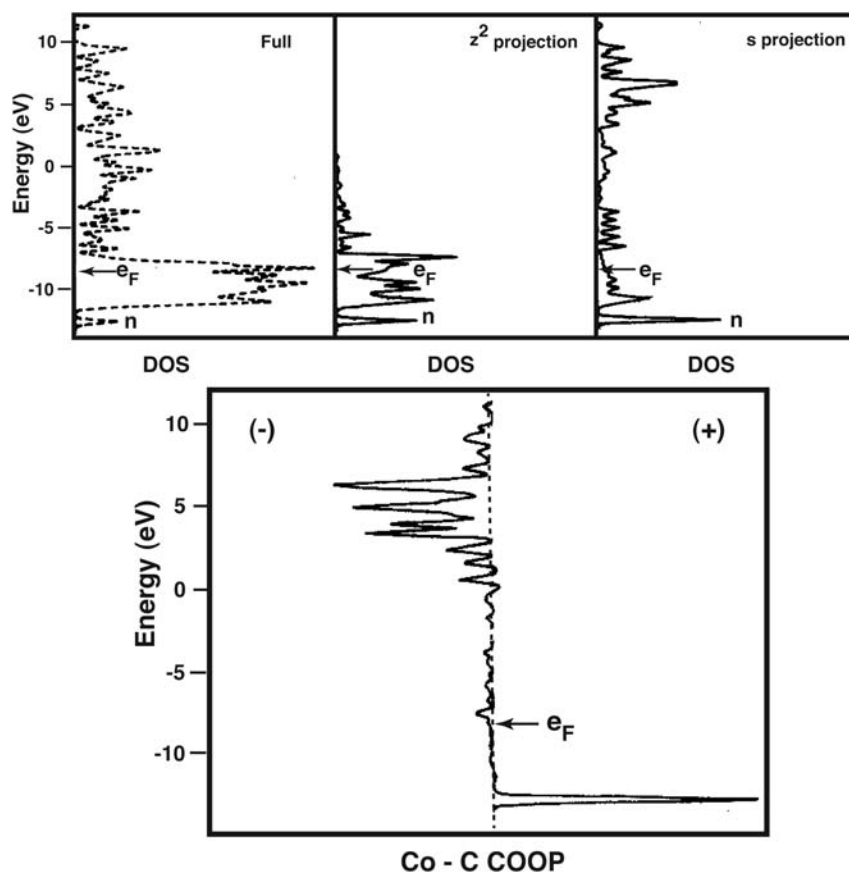



---

	Electron Populations		
	Co(0001)	Cr(110)	Ti(0001)
(x <sup>2</sup> – y <sup>2</sup> ) + (xy)	3.1	2.1	1.3
z <sup>2</sup>	1.7	1.0	0.6
xz + yz	3.5	2.1	1.2
s	0.7	0.8	0.8
p	0.3	0.3	0.2
Total	9.3	6.3	4.1

---

The DOS, selected projections of the DOS, and the Co–C COOP curve for a methyl group coordinated on top of the metal for the Co(0001) surface is shown below. Describe the Co–CH<sub>3</sub> interactions in three regions: (a) from –13 to –12 eV, (b) from –12 to –3 eV, and (c) from 1 to 10 eV.



- 23.3.** The relative binding energies for a methyl group at the three coordination sites is given below for the three surfaces under consideration, as well as Pt(111) studied at the EHT and two DFT levels (the B3LYP calculations are for a Pt<sub>28</sub> cluster while all of the others are derived from a tight-binding three-layer slab).

**Relative Energies for a Methyl Group Binding to Metal Surfaces in kcal/mol**

Metal	Top	Bridge	Cap	Method
Ti(0001)	0	12	2	EHT <sup>a</sup>
Cr(110)	0	21	21	EHT <sup>a</sup>
Co(0001)	0	25	32	EHT <sup>a</sup>
Pt(111)	0	18	23	EHT <sup>b</sup>
Pt(111)	0	16	18	PW91 <sup>b</sup>
Pt(111)	0	27	31	B3LYP <sup>c</sup>

<sup>a</sup> From Reference [88].

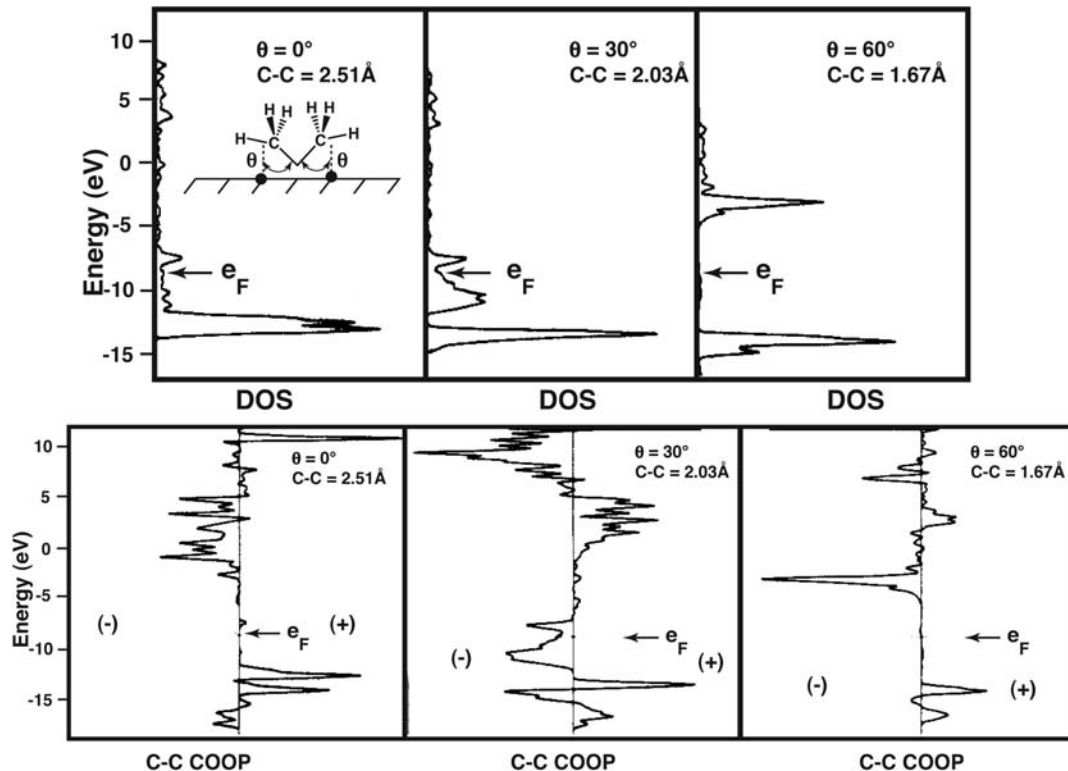
<sup>b</sup> From Reference [89].

<sup>c</sup> From Reference [90].

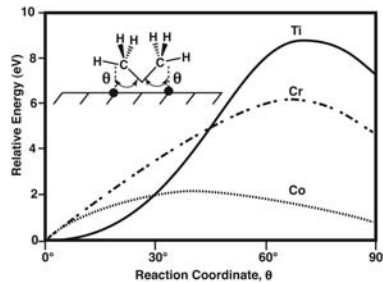
- Describe the migration path for moving a methyl group from one on-top position to an adjacent one.
- While there are a variety of surfaces and methods reported in the table above, the results are quite clear: early transition metals will have a much lower barrier for migration than the later ones. Offer a rationale for this behavior.

**23.4.** The final step in the Fisher–Tropsch synthesis is the coupling of organic radicals on the surface. For this reaction, we have chosen from Zheng et al. [88] the coupling of methyl radicals on the Co(0001) surface from on-top positions.

- a. The  $\text{CH}_3$   $n$  group projection of the DOS for three steps along an idealized reaction coordinate is shown below along with the C–C COOP curves at these three points. Describe what is occurring in the DOS plots as  $\theta$  increases.

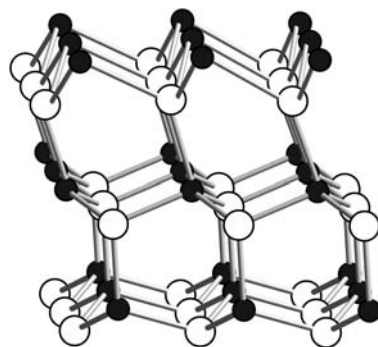


- b. These are extended Hückel calculations that are not likely to provide reliable estimates of the reaction barriers; however, qualitative features should be reliable. Shown below is the energetic evolution along this very idealized reaction path for the Ti(0001), Cr(110), and Co(0001) surfaces. Offer a hypothesis as to why the activation energy decreases going from Ti to Co.



- c. Given the information gleaned from the past problems and this one, where in the Periodic Table should one expect to find the best Fischer–Tropsch catalyst? Why?

**23.5.** The wurtzite structure is found for ZnS, CdS, CdSe, and so on. It is a derivative of the diamond or silicon structure in that every atom is tetrahedral. The surface of CdS and the other members undergo reconstruction to give something closely resembling that in Si and shown in 23.73. A representative cross-section is shown below.



- a. For CdSe which elements correspond to the black and the white circles? Why?
- b. Where does  $\text{NH}_3$  attack? Where does  $\text{BH}_3$  attack?
- 23.6.** If one cleaves a crystal of silicon, for example, exposing the (100) plane under high-vacuum conditions, that surface is extraordinarily reactive. One can pacify the surface by exposure to  $\text{H}_2$  or more commonly HF. Show a mechanism for each reaction starting from the reconstructed surface (use **23.72**).
- 23.7.** Singlet  $\text{CH}_2$  also reacts with the Si (100) surface. Using the symmetric dimer model (**23.71**), show the product and a reaction mechanism leading to it.

## REFERENCES

1. G. A. Somorjai, *Introduction to Surface Chemistry and Catalysis*, Wiley, New York (1994).
2. K. Binder, M. Bowker, J. E. Inglesfield, and P. J. Rous, *Cohesion and Structure of Surfaces*, Elsevier, Amsterdam (1995).
3. K. W. Kolasinski, *Surface Science*, 2nd edition, Wiley, New York (2008).
4. D. P. Woodruff, in *Chemical Bonding at Surfaces and Interfaces*, A. Nilsson, L. G. M. Pettersson, and J. K. Nørskov, editors, Elsevier, Amsterdam (2008), pp. 1–56.
5. G. A. Somorjai, *Introduction to Surface Chemistry and Catalysis*, Wiley, New York (1994), pp. 89–91.
6. J. K. Burdett, P. T. Czech, and T. F. Fässler, *Inorg. Chem.*, **31**, 129 (1992).
7. G. A. Somorjai, *Introduction to Surface Chemistry and Catalysis*, Wiley, New York (1994), p. 320.
8. R. Hoffmann, *Rev. Mod. Phys.*, **60**, 601 (1988).
9. T. Bligaard and J. K. Nørskov, in *Chemical Bonding at Surfaces and Interfaces*, A. Nilsson, L. G. M. Pettersson, and J. K. Nørskov, editors, Elsevier, Amsterdam (2008), pp. 255–321.
10. A. Gross, *Theoretical Surface Science*, Springer-Verlag, Hiedelberg (2009), pp. 130–135.
11. B. Hammer, O.H. Nielsen, and J. K. Nørskov, *Cat. Lett.*, **46**, 31 (1997).
12. Z.-P. Liu and P. Hu, *J. Am. Chem. Soc.*, **125**, 1958 (2003).
13. J. E. Crowell, W. T. Tysoe, and G. A. Somorjai, *J. Phys. Chem.*, **89**, 1598 (1985).
14. J. J. Mortensen, B. Hammer, and J. K. Nørskov, *Surf. Sci.*, **414**, 315 (1998).
15. A. Gross, *Theoretical Surface Science*, Springer-Verlag, Hiedelberg (2009), pp. 143–146.
16. See, for example, F. Zaera, *Chem. Rev.*, **95**, 2651 (1995); F. Zaera, *Prog. Surf. Sci.*, **69**, 1 (2001).
17. P. R. Norton, R. L. Tapping, and J. W. Goodale, *Chem. Phys. Lett.*, **41**, 247 (1976).
18. J. Kanski, P. O. Nilsson, and C. G. Larsson, *Solid State Commun.*, **35**, 397 (1980).
19. B. Wannberg, D. Nordfors, K. L. Tan, L. Karlsson, and L. Mattison, *J. Elec. Spectr. Rel. Phenom.*, **47**, 147 (1988).
20. G. J. Blyholder, *J. Phys. Chem.*, **68**, 2772 (1964).
21. W. V. Glassey, G. A. Papoian, and R. Hoffmann, *J. Chem. Phys.*, **111**, 893 (1999).

22. R. Dronskowski and P. E. Blöchl, *J. Phys. Chem.*, **97**, 8617 (1993).
23. (a) T. A. Albright, *unpublished calculations*. The results were in-line with those using a different DFT functional and basis in (b) M. Föhlisch, M. Nyberg, P. Bennich, L. Triguero, J. Hasselström, O. Karis, L. G. M. Pettersson, and A. Nilsson, *J. Chem. Phys.*, **112**, 1946 (2000).
24. S.-S. Sung and R. Hoffmann, *J. Am. Chem. Soc.*, **107**, 578 (1985).
25. Y.-T. Wong and R. Hoffmann, *J. Phys. Chem.*, **95**, 859 (1991); W. V. Glassey and R. Hoffmann, *J. Chem. Phys. B*, **105**, 3245 (2001).
26. A. Föhlisch, M. Nyberg, J. Hasselström, O. Karis, L. G. M. Pettersson, and A. Nilsson, *Phys. Rev. Lett.*, **85**, 3309 (2000).
27. T. Bligaard and J. K. Nørskov, in *Chemical Bonding at Surfaces and Interfaces*, A. Nilsson, L. G. M. Pettersson, and J. K. Nørskov, editors, Elsevier, Amsterdam (2008), pp. 101–103.
28. R. Davis, D. P. Woodruff, O. Schaff, V. Fernandez, K. M. Schindler, P. Hofmann, K. U. Weiss, R. Dippel, V. Fritzche, and A. M. Bradshaw, *Phys. Rev. Lett.*, **74**, 1621 (1995).
29. C.-G. Zhan, J. A. Nichols, and D. A. Dixon, *J. Phys. Chem. A*, **107**, 4184 (2003).
30. P. Bennich, T. Wiell, O. Karis, M. Weinelt, N. Wassdahl, A. Nilsson, M. Nyberg, L. G. M. Pettersson, J. Stöhr, and M. Samant, *Phys. Rev. B*, **57**, 9274 (1998).
31. K. Horn, J. Dinardo, W. Eberhardt, and H. J. Freund, *Surf. Sci.*, **118**, 465 (1982).
32. S.-S. Sung, R. Hoffmann, and P. A. Thiel, *J. Phys. Chem.*, **90**, 1380 (1986).
33. M. Stichler, C. Keller, C. Heske, M. Staufer, U. Birkenheuer, N. Rösch, W. Wurth, and D. Menzel, *Surf. Sci.*, **448**, 164 (2000); M. Staufer, U. Birkenheuer, T. Belling, F. Nörtemann, N. Rösch, M. Stichler, C. Keller, W. Wurth, D. Menzel, L.G.M. Pettersson, A. Föhlisch, and A. Nilsson, *J. Chem. Phys.*, **111**, 4704 (1999), and references therein.
34. G. Odorfer, R. Jaeger, G. Illing, H. Kuhlenbeck, and H.-J. Freund, *Surf. Sci.*, **233**, 44 (1990); H. Geisler, G. Odorfer, G. Illing, R. Jaeger, and H.-J. Freund, *Surf. Sci.*, **234**, 237 (1990).
35. C. Westphal, F. Fegel, J. Bansmann, M. Getzlaff, G. Schönhense, J. A. Stephens, and V. McKoy, *Phys. Rev. B*, **50**, 17534 (1994).
36. L. D. Mapledoram, A. Wander, and D. A. King, *Chem. Phys. Lett.*, **208**, 409 (1993).
37. H. Aizawa, Y. Morikawa, S. Tsuneyuki, K. Fukutani, and T. Ohno, *J. Surf. Sci. Nanotech.*, **5**, 122 (2007).
38. K. W. Kolasinski, F. Cemic, and E. Hasselbrink, *Chem. Phys. Lett.*, **219**, 113 (1994); K. W. Kolasinski, *Surface Science*, 2nd edition, Wiley, New York (2008), p. 141.
39. A. W. E. Chan, R. Hoffmann, and W. Ho, *Langmuir*, **8**, 1111 (1992).
40. K. Honkala and K. Laasonen, *J. Chem. Phys.*, **115**, 2297 (2001).
41. A. Eichler, F. Mittendorfer, and J. Hafner, *Phys. Rev. B*, **62**, 4744 (2000).
42. P. Valentini, T. E. Schwartzentruber, and I. Cozmuta, *Surf. Sci.*, **605**, 1941 (2011).
43. C. M. Kim, H. S. Jeong, and E. H. Kim, *Surf. Sci.*, **459**, L457 (2000).
44. (a) Z.-X. Chen, H. A. Aleksandrov, D. Basaran, and N. Rösch, *J. Phys. Chem. C*, **114**, 17683 (2010). (b) Z.-J. Zhao, L. V. Moskaleva, H. A. Aleksandrov, D. Basaran, and N. Rösch, *J. Phys. Chem. C*, **114**, 12190 (2010), and references therein.
45. J. Andersin, N. Lopez, and K. Honka, *J. Phys. Chem. C*, **113**, 8278 (2009).
46. Q. Ge and D. A. King, *J. Chem. Phys.*, **110**, 4699 (1999).
47. G. W. Watson, R. P. K. Wells, D. J. Wilcock, and G. J. Hutchings, *J. Phys. Chem. B*, **104**, 6439 (2000).
48. T. Jacob and W. A. GoddardIII, *J. Phys. Chem. B*, **109**, 297 (2005).
49. T. Okada, Y. Kim, Y. Sainoo, T. Komeda, M. Trenary, and M. Kawai, *J. Phys. Chem. Lett.*, **2**, 2263 (2011).
50. T. Zheng, D. Stacchiola, H. C. Poon, D. K. Saldin, and W. T. Tysoe, *Surf. Sci.*, **564**, 71 (2004).
51. Y.-T. Wong and R. Hoffmann, *J. Chem. Soc., Faraday Trans.*, **86**, 4083 (1990).
52. R. Döll, C. A. Gerken, M. A. Van Hove, and G. A. Somorjai, *Surf. Sci.*, **374**, 151 (1997).

53. R. M. Watwe, R. D. Cortright, J. K. Nørskov, and J. A. Dumesic, *J. Phys. Chem. B*, **104**, 2299 (2000).
54. L. L. Kesmodel, L. H. Dubois, and G. A. Somorjai, *J. Chem. Phys.*, **70**, 2180 (1979).
55. O. Nakagoe, N. Takagi, and Y. Matsumoto, *Surf. Sci.*, **514**, 414 (2002); C. Matsumoto, Y. Kim, T. Okawa, Y. Sainoo, and M. Kawai, *Surf. Sci.*, **587**, 19 (2005).
56. P. A. Sheth, M. Neurock, and C. M. Smith, *J. Phys. Chem. B*, **107**, 2009 (2003).
57. J. Silvestre and R. Hoffmann, *Langmuir*, **1**, 621 (1985).
58. G. Wiesenecker, G.-J. Kroes, and E.-J. Baerends, *J. Chem. Phys.*, **104**, 7344 (1996).
59. S. Sakung and A. Groß, *Surf. Sci.*, **525**, 107 (2003).
60. G.-J. Kroes, A. Groß, E.-J. Baerends, M. Scheffler, and D. A. McCormack, *Accts. Chem. Res.*, **35**, 193 (2002), and references therein.
61. G.-J. Kroes, *Prog. Surf. Sci.*, **60**, 1 (1999), and references therein.
62. A. Eichler, G. Kresse, and J. Hafner, *Phys. Rev. Lett.*, **77**, 1119 (1996).
63. C. B. Duke, *Chem. Rev.*, **96**, 1237 (1996).
64. G. A. Somorjai, *Introduction to Surface Chemistry and Catalysis*, Wiley, New York (1994), p. 99; K. Binder, M. Bowker, J. E. Inglesfield, and P. J. Rous, *Cohesion and Structure of Surfaces*, Elsevier, Amsterdam (1995), pp. 39–42.
65. D. J. Chadi, *Phys. Rev. Lett.*, **43**, 43 (1979). The results here are very close to those at the extended Hückel and DFT-GW levels, see D. Kienle, K. H. Bevan, G.-C. Liang, L. Siddiqui, J. I. Cerdá, and A. W. Ghosh, *J. App. Phys.*, **100**, 043715 (2006).
66. L. S. O. Johansson, R. I. G. Uhrber, P. Måtensson, and G. V. Hanson, *Phys. Rev. B*, **42**, 1305 (1990).
67. J. E. Northrup, *Phys. Rev. B*, **47**, 10032 (1993).
68. W. M. Lampart, D. P. Schofield, R. A. Christie, and K. D. Jordan, *Mol. Phys.*, **106**, 1697 (2008) and references therein.
69. R. G. Hamers, S. K. Coulter, M. D. Ellison, J. S. Hovis, D. F. Padowitz, M. P. Schwartz, C. M. Greenlieff, and J. N. RussellJr., *Acc. Chem. Res.*, **33**, 617 (2000).
70. D. C. Sorescu, and K. D. Jordan, *J. Phys. Chem. B*, **104**, 8259 (2000).
71. P. T. Czeka, H. Lin, W. A. Hofer, and A. Gulans, *Surf. Sci.*, **605**, 1341 (2011) and references therein.
72. T. Mineva, R. Nathaniel, K. L. Kostov, and W. Widdra, *J. Chem. Phys.*, **125**, 194712 (2006).
73. N. Takeuchi, *Surf. Sci.*, **601**, 3361 (2007).
74. Q. Liu and R. Hoffmann, *J. Am. Chem. Soc.*, **117**, 4082 (1995).
75. We strongly suspect that extended slab calculations [76] for the addition of ethylene to the Si(100) surface which show a very low energy concerted [2 + 2] path in fact miss the transition state. An example [77] is provided by the dimerization of P<sub>2</sub> along D<sub>2d</sub> symmetry where the sharp cusp in the potential energy surface at the crossing point was missed despite the fact that reasonably small steps were taken. Slab calculations, to date, do not search for and categorize stationary points nor, of course, follow minimum energy reaction paths. This has created some confusion in the literature, besides the technical differences regarding the method or treatment of the slab. Arguments have been made that some of the crystal orbitals at selected k points have the correct symmetry in the asymmetric dimer model to render the concerted reaction of ethylene on Si(100) symmetry allowed [78]. While this is most certainly true, it, as pointed out sometime ago [74], is unreasonable to expect that a monolayer of acetylene or ethylene ligands concertedly approach the Si surface. Furthermore, there are many occupied states that do show the expected repulsion associated with a symmetry forbidden reaction. Do these molecules then bounce off the surface? We think not. Reactions on a surface are random, isolated events. We suspect that extended slab calculations using a very low coverage will be more reliable in terms of mechanistic details than those carried out at saturation. Cluster models are better in this regard since they do represent localized events on the surface. Furthermore, analytical or numerical gradients are available. The problem here is that cluster size effects can become critical and need to be evaluated on a case-by-case basis.

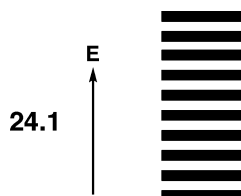
76. X. L. Fan, Y. F. Zhang, W. M. Lau, and Z. F. Liu, *Phys. Rev. B*, **72**, 165305 (2005) and references therein.
77. R. Osman, P. Coffey, and J. R. Van Wazer, *Inorg. Chem.*, **15**, 287 (1976).
78. P. M. Ryan, L. C. Teague, and J. J. Boland, *J. Am. Chem. Soc.*, **131**, 6768 (2009).
79. M. Nagao, H. Umeyama, K. Mukai, Y. Yamashita, J. Yoshinobu, K. Akagi, and S. Tsuneyuk, *J. Am. Chem. Soc.*, **126**, 9922 (2004).
80. K. Oguchi, M. Nagao, H. Umeyama, T. Katayama, Y. Yamashita, K. Mukai, J. Yoshinobu, K. Akagi, and S. Tsuneyuk, *J. Am. Chem. Soc.*, **129**, 1242 (2007).
81. H. S. Lee, C. H. Choi, and M. S. Gordon, *J. Chem. Phys. B*, **109**, 5067 (2005).
82. K. L. Kostov, R. Nathaniel, T. Mineva, and W. Widdra, *J. Chem. Phys.*, **133**, 054705 (2010).
83. J. Yoshinobu, *Prog. Sur. Sci.*, **77**, 37 (2004).
84. A. Gross, *Theoretical Surface Science*, Springer-Verlag, Hiedelberg (2009), pp. 224–228.
85. R. Konecny and D. J. Doren, *J. Phys. Chem. B*, **101**, 10983 (1997).
86. B.-Z. Sun, W.-K. Chen, and Y.-J. Xu, *J. Chem. Phys. C*, **114**, 6543 (2010).
87. R. Konecny and R. Hoffmann, *J. Am. Chem. Soc.*, **121**, 7918 (1999).
88. C. Zheng, Y. Apelog, and R. Hoffmann, *J. Amer. Chem. Soc.*, **110**, 749 (1988).
89. G. Papoian, J. K. Norskov, and R. Hoffmann, *J. Amer. Chem. Soc.*, **122**, 4129 (2000).
90. T. Jacob, R. P. Muller, and W. A. GoddardIII, *J. Phys. Chem., B*, **107**, 9465 (2003).

# Magnetic Properties

## 24.1 INTRODUCTION

In this chapter, we briefly review important concepts and phenomena that one encounters in reading the current literature on magnetic solids containing magnetic ions typically of transition-metal elements (for recent reviews, see [1]). We mentioned the influence of spin on orbital energies in Section 16.5. A more complete discussion is given in this chapter. This chapter is intended for those who possess minimal knowledge of the terminologies and mathematical treatments employed in describing magnetic properties. Thus our discussion will be on a qualitative level from the perspective of electronic structure.

Compared with strong orbital interactions leading to chemical bonding, the interactions between magnetic ions responsible for magnetic properties are extremely weak. Consequently, the magnetic states are closely packed in energy, as in **24.1**, which makes it impossible to understand the magnetic properties of a



system by focusing on a few individual magnetic energy levels. This is in sharp contrast to the case of strong orbital interactions in which the structure and reactivity of a compound can be reasonably well accounted for in terms of its frontier orbitals. What one needs in understanding the magnetic properties of a system is its magnetic excitation energy spectrum, which is described by using a spin Hamiltonian defined in terms of a few spin exchange parameters. The geometrical pattern of the spin exchange paths (or magnetic bonds) is known as the spin lattice. The utility of such a model Hamiltonian is to capture the essence of the underlying

physics and chemistry behind the observed magnetic properties by using a spin lattice defined with a minimal set of magnetic bonds. Nevertheless, the orbital interaction picture familiar to chemists plays a decisive role in understanding the spin lattice that specifies the spin Hamiltonian for a given magnetic system.

An important difference between strong and weak orbital interactions should be emphasized. In the *d*-block levels of a system, each transition-metal ion M has its *nd* orbitals combined out-of-phase with the *np* orbitals of their surrounding ligand atoms L. In discussing the strong orbital interactions leading to chemical bonding and structure, our focus is on the “head” parts (i.e., the *nd* orbital parts) of all the occupied *d*-block levels. However, in discussing the weak orbital interactions leading to magnetic bonds, we focus on the “tail” parts (i.e., the *np* orbitals on the ligands) of the magnetic *d*-block levels (i.e., the singly-occupied *d*-block levels) [1].

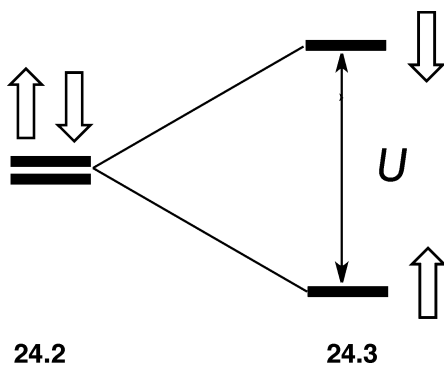
In the following discussion, we will use the orbital and spin angular momenta as classical vectors (**L** and **S**, respectively) as well as quantum mechanical operators ( $\hat{L}$  and  $\hat{S}$ , respectively). Given the orbital and spin angular quantum numbers *L* and *S*, respectively, the magnitudes of the associated momenta **L** and **S** in units of  $\hbar$  are given by *L* and *S*, respectively. The  $2L+1$  substates associated with *L* are defined by its  $L_z$  components ( $L_z = -L, -L+1, \dots, L-1$ , and  $L$ ), and the  $2S+1$  substates associated with *S* by its  $S_z$  components ( $S_z = -S, -S+1, \dots, S-1$ , and  $S$ ). In the absence of spin-orbit coupling (SOC), the orbital and spin angular momentum states are specified by using two quantum numbers, namely, by  $|L, L_z\rangle$  and  $|S, S_z\rangle$ , respectively. A few quantum mechanical results we need in this review are concerned with how these states behave when the operators associated with  $\hat{L}$  and  $\hat{S}$  act on them.

In this chapter, diverse topics and concepts are discussed in each section. To delineate different subjects, each section is subdivided. This chapter is organized as follows: We examine several issues concerning magnetic insulating states in Section 24.2, and discuss various magnetic properties arising from magnetic moments in Section 24.3. Section 24.4 describes how to quantitatively determine spin exchange constants and how to think about them in terms of orbital interactions, and Section 24.5 various aspects of magnetic structures such as collinear versus noncollinear, long-range versus short-range, and antiferromagnetic versus ferromagnetic spin arrangements. We discuss an energy gap in magnetic energy spectrum and its consequences in Section 24.6, and describe several important consequence of SOC in Section 24.7. In Section 24.8 we examine the spin lattices of several representative magnetic systems, in order to demonstrate the need to interpret magnetic properties on the basis of considering their electronic structures. How to describe magnetic properties beyond the level of spin exchange interactions is discussed in Section 24.9. Finally, the essential points of this chapter are briefly summarized in Section 24.10.

## 24.2 THE MAGNETIC INSULATING STATE

### 24.2.1 Electronic Structures

The magnetic properties of a system containing magnetic ions are essentially related to how its electronic energy is affected by external magnetic field (Section 24.3.1). Since molecules and crystalline solids with magnetic ions are characterized by open-shell electronic structures, it is important to know how such electronic structures are generated. Currently, the electronic structures of molecules and crystalline solids are described largely on the basis of density functional theory (DFT) [2]. In the non-spin-polarized DFT, each energy level of a system accommodates two electrons because the up-spin and down-spin levels are treated as degenerate (24.2). Thus an energy band of a given solid is described by the up-spin and down-spin subbands



which are degenerate in energy. Any solid then with partially filled bands has no energy gap between the highest-occupied and the lowest-unoccupied band levels (Figure 24.1a), and is therefore predicted to be a nonmagnetic metal. Obviously, this prediction is contrary to the experimental observation that a solid with partially filled bands can be a magnetic insulator [3,4], in which the up-spin and down-spin subbands differ in energy such that an energy gap (i.e., a band gap) occurs between the highest-occupied and the lowest-unoccupied subbands (Figure 24.1b).

The failure of the non-spin-polarized DFT in describing magnetic insulators is remedied in part by using spin-polarized DFT, which allows up-spin and down-spin subbands to differ in their spatial orbitals and, hence, they differ in energy. For most magnetic insulators, this splitting of the up-spin and down-spin subbands given by the spin-polarized DFT is not large enough to produce a band gap (Figure 24.1c). This deficiency of the spin-polarized DFT (i.e., the band gap is underestimated) is empirically corrected by using the spin-polarized DFT +  $U$  method [5], in which the effective on-site repulsion  $U^{\text{eff}} = U - J$ , where  $U$  is the on-site repulsion and  $J$  ( $\approx 1 \text{ eV}$ ) is the exchange-correction, is added on the magnetic ions (mostly transition-metal ions) so as to enhance the spin polarization of their  $nd$  orbitals (24.3). There are two slightly different ways of doing DFT +  $U$  calculations; In the DFT +  $U$  method of Dudarev et al. [5a] the energy formula includes only the difference  $U - J$ , while in the DFT +  $U$  method of Liechtenstein et al. [5b], the energy formula includes  $U$  and  $J$  separately, hence allowing greater flexibility in SCF calculations. At the current stage of DFT, it is unfortunately impossible to predict whether a solid with partially filled bands will be a metal or a magnetic insulator. Once such a solid is experimentally known to be a metal or a magnetic insulator, one can carry out spin-polarized DFT +  $U$  calculations to determine the range of the  $U^{\text{eff}}$  values that gives rise to metallic or magnetic insulating states. In describing a magnetic insulator by the DFT +  $U$  method, therefore, it is essential to first establish the range

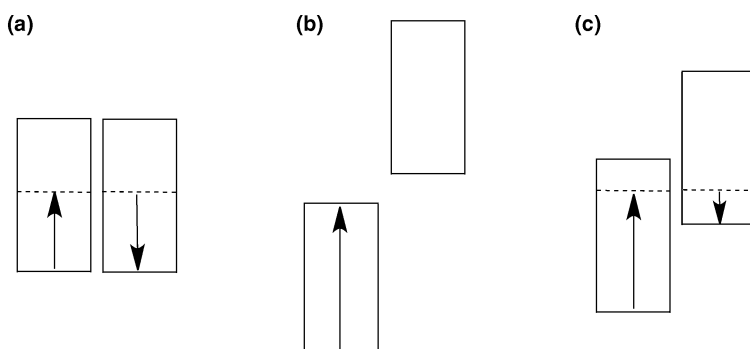


**FIGURE 24.1**

Filling the up-spin and down-spin bands with two electrons leading to (a) a nonmagnetic metallic, (b) a magnetic insulating and (c) a magnetic metallic state.

of the  $U^{\text{eff}}$  values producing a band gap and then explore its chemistry and physics on the basis of consistent trends resulting from such  $U^{\text{eff}}$  parameters.

An alternative way of correcting the DFT deficiency of band gap underestimation is the hybrid functional method [6–8]. Here the exchange-correlation functional needed for calculations is obtained by mixing some amount of the Hartree–Fock (HF) exchange potential, which overestimates band gap, into the DFT functional. The B3LYP hybrid is quite popular in the molecular area. In essence, the hybrid functional method is equivalent to the DFT +  $U$  method. It is also empirical because the amount of HF exchange potential to mix is empirically adjusted (e.g., the B3LYP hybrid functional has 20% of HF exchange potential mixed in).

#### 24.2.2 Factors Affecting the Effective On-Site Repulsion

The effective on-site repulsion  $U^{\text{eff}}$  is related to the extent of electron correlation, which is large for dense electron density distribution. Thus the value of  $U^{\text{eff}}$  necessary for DFT +  $U$  calculations for  $nd$  transition-metal elements should increase as the  $nd$  orbital becomes more contracted. The degree of the  $nd$  orbital contraction increases in the order  $5d < 4d \ll 3d$ . Recall that the  $3d$  atomic orbitals (AOs) have no suborbital counterparts for screening. This explains why magnetic insulators are much more abundant among compounds of  $3d$  elements than from those of  $4d$  or  $5d$  elements. Nevertheless, magnetic insulators are found from compounds of  $4d$  and  $5d$  elements when they are present in high oxidation states, because their  $4d$  and  $5d$  orbitals become significantly contracted in such a case.

The typical problem one faces in analyzing the properties of magnetic compounds in terms of DFT +  $U$  calculations can be illustrated by considering the oxides of the  $5d$  element osmium,  $\text{Na}_2\text{OsO}_4$  [9],  $\text{NaOsO}_3$  [10],  $\text{Ca}_3\text{LiOsO}_6$  [11,12],  $\text{Sr}_2\text{CuOsO}_6$  [13,14],  $\text{Sr}_2\text{NiOsO}_6$  [14,15] and  $\text{Ba}_2\text{NaOsO}_6$  [16–18]. The Os oxidation states in these compounds are rather high ranging from +5 to +7, and these oxides are all magnetic insulators except for  $\text{Na}_2\text{OsO}_4$ . The  $U^{\text{eff}}$  values of Os needed to reproduce the experimental observations of these oxides by DFT +  $U$  calculations vary from one compound to another, but there is an important trend to observe. The Os oxidation states and the Os—O bond lengths found in  $\text{Na}_2\text{OsO}_4$ ,  $\text{NaOsO}_3$ ,  $\text{Ca}_3\text{LiOsO}_6$ ,  $\text{Sr}_2\text{CuOsO}_6$ ,  $\text{Sr}_2\text{NiOsO}_6$ , and  $\text{Ba}_2\text{NaOsO}_6$  are listed in Table 24.1. For  $\text{NaOsO}_3$  [10b] and  $\text{Ca}_3\text{LiOsO}_6$  containing  $\text{Os}^{5+}$  ( $d^3$ ) ions,  $U^{\text{eff}} \approx 2.0\text{--}2.5\text{ eV}$  is needed to reproduce their experimental Curie–Weiss temperatures (see Section 24.3.4)  $\theta = -1949$  and  $-260\text{ K}$ , respectively, by using the spin exchange parameters determined from DFT +  $U$  calculations [12]. For  $\text{Sr}_2\text{CuOsO}_6$  and  $\text{Sr}_2\text{NiOsO}_6$  containing  $\text{Os}^{6+}$  ( $d^2$ ) ions,  $U^{\text{eff}} \approx 4.0\text{ eV}$  is needed to predict their magnetic insulating states in terms of

**TABLE 24.1** The Os—O Bond Lengths of the  $\text{OsO}_6$  Octahedra as well as the BVS and the Oxidation State of the  $\text{Os}^{n+}$  Ions Found in the Osmium Oxides<sup>a</sup>

	Os—O Bond Lengths of $\text{OsO}_6$	BVS	Oxidation	$U^{\text{eff}}$
$\text{Na}_2\text{OsO}_4$	1.772 ( $\times 2$ ), 2.004 ( $\times 2$ ), 2.050 ( $\times 2$ )	5.69 (2.85) <sup>b</sup>	+6	0
$\text{NaOsO}_3$	1.945 ( $\times 2$ ), 1.939 ( $\times 2$ ), 1.940 ( $\times 2$ )	5.38	+5	2.0
$\text{Ca}_3\text{LiOsO}_6$	1.956 ( $\times 6$ )	5.18	+5	2.5
$\text{Sr}_2\text{CuOsO}_6$	1.928 ( $\times 2$ ), 1.888 ( $\times 2$ )	6.00	+6	4.0
$\text{Sr}_2\text{NiOsO}_6$	1.923 ( $\times 2$ ), 1.911 ( $\times 4$ )	5.78	+6	4.0
$\text{Ba}_2\text{NaOsO}_6$	1.869 ( $\times 6$ )	6.54	+7	>4.0

<sup>a</sup>The  $U^{\text{eff}}$  values appropriate for describing them by DFT+ $U$  calculations are also listed.

<sup>b</sup>The number in the parenthesis was obtained by using only the four Os—O<sub>eq</sub> bonds.

DFT +  $U$  calculations predict [14]. These above observations reflect that the Os<sup>6+</sup> ions have more contracted 5d orbitals than do the Os<sup>5+</sup> ions, and hence require a larger  $U^{\text{eff}}$  value.

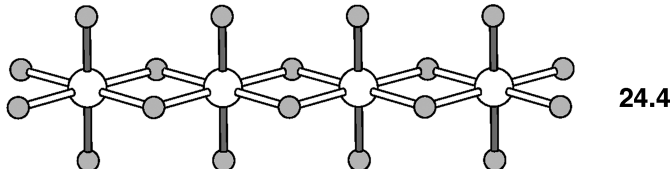
An apparently surprising observation is that  $U^{\text{eff}} \approx 0$  for NaOsO<sub>3</sub> although it has Os<sup>6+</sup> ions. In general, the oxidation state of an atom A in a molecule or in a solid can be estimated by calculating the bond valence  $v_i$  [19,20] for each A—B bond  $i$  the atom A makes with its surrounding atoms B,

$$v_i = \exp\left(\frac{r_0 - r_i}{0.37}\right) \quad (24.1a)$$

where  $r_0$  is the reference bond length (in Å) for bonds A—B while  $r_i$  is the length of a particular A—B bond  $i$  (in Å). Thus the bond valence  $v_i$  is 1 if  $r_i = r_0$  and it increases exponentially if  $r_i < r_0$ , or decreases exponentially if  $r_i > r_0$ . The bond valence  $v_i$  has the meaning of the amount of electrons the atom A loses as a consequence of forming the A—B bond  $i$ . Therefore, the bond valence sum (BVS) for the atom A

$$\text{BVS} = \sum_i v_i \quad (24.1b)$$

is the total amount of electrons the atom A lost (to form the bonds), that is, the oxidation state of A. For the Os—O bonds, the constant  $r_0 = 1.901$  Å gives BVS = 6.00 for the Os<sup>6+</sup> ion of Sr<sub>2</sub>CuOsO<sub>6</sub>. The BVS values and the Os—O bond lengths found for the osmium oxides are listed in Table 24.1. As expected, the BVS values for NaOsO<sub>3</sub> and Ca<sub>3</sub>LiOsO<sub>6</sub> containing Os<sup>5+</sup> ions are close to +5, those for Sr<sub>2</sub>CuOsO<sub>6</sub> and Sr<sub>2</sub>NiOsO<sub>6</sub> containing Os<sup>6+</sup> ions close to +6, and those for Na<sub>2</sub>OsO<sub>4</sub> containing Os<sup>7+</sup> ions close to +7. The BVS of Na<sub>2</sub>OsO<sub>4</sub> with Os<sup>6+</sup> ion is close to +6, suggesting apparently that it has contracted 5d orbitals. This oxide consists of OsO<sub>4</sub> chains made up of edge-sharing OsO<sub>6</sub> octahedra (24.4) [9], in which the OsO<sub>6</sub> octahedra are axially compressed with the short axial Os—O



bonds (1.772 Å) perpendicular to the chain axis and with the equatorial Os—O bonds longer than 2.0 Å. If the local z-axis is taken along the short axial Os—O bonds, the d-orbital splitting pattern of each OsO<sub>6</sub> octahedron is given by  $xy < xz, yz \ll x^2 - y^2 < z^2$ . This also indicates that the  $xy$  orbital is more diffuse than the  $xz, yz$  orbitals, and the  $x^2 - y^2$  orbital than the  $z^2$  orbital. Then, the Os<sup>6+</sup> ( $d^2$ ) ion in this axially compressed OsO<sub>6</sub> octahedron, which adopts the  $(xy)^2$  electron configuration, has no strong electron correlation and hence requires  $U^{\text{eff}} \approx 0$ . If we use only the equatorial Os—O bonds lying in the plane of the  $xy$  orbital, which directly affects the two electrons occupying the  $xy$  orbital, the BVS becomes close to +3. In other words, the Os<sup>6+</sup> ions of Na<sub>2</sub>OsO<sub>4</sub> have diffuse 5d orbitals as far as the  $d^2$  electrons occupying the  $xy$  orbital are concerned.

Ba<sub>2</sub>NaOsO<sub>6</sub> has a negative Curie–Weiss temperature ( $\theta \approx -10$  K). As will be discussed later (Section 24.3.4), the dominant spin exchange is antiferromagnetic (AFM) if  $\theta < 0$ , but is ferromagnetic (FM) if  $\theta > 0$ . Thus the dominant spin exchange between the Os<sup>7+</sup> ions is AFM, but it undergoes a FM ordering below  $T_C = 6.8$  K with low magnetic moment ( $\sim 0.2 \mu_B$ ) [16,17]. This observation arises because the Os<sup>7+</sup> ( $d^1$ ) ions with electron configuration  $(t_{2g})^1$  undergo a weak orbital ordering

(Section 24.5.4). DFT +  $U$  calculations [10b,18] for  $\text{Ba}_2\text{NaOsO}_6$  with  $U^{\text{eff}}$  up to 4 eV show that the FM state has no band gap because the  $t_{2g}^{\uparrow}$  and  $t_{2g}^{\downarrow}$  bands overlap. However, the AFM state in which the  $\text{Os}_4$  tetrahedron of a unit cell repeat with two up-spins and two down-spins begins to have a band gap when  $U^{\text{eff}} \geq 3.5$  eV. The triply-degenerate  $t_{2g}$  level of an  $\text{OsO}_6$  octahedron is split into three separate sublevels if the effect of SOC of the  $\text{Os}^{7+}$  ions is taken into consideration [18], so DFT + SOC calculations for the FM state show a band gap when  $U^{\text{eff}}$  is as low as 2.7 eV. So far, however, DFT +  $U$  calculations for  $\text{Ba}_2\text{NaOsO}_6$  with  $U^{\text{eff}} > 4$  eV and analyses of its spin exchange interactions have not been successful [10b], which prevented the determination of the  $U^{\text{eff}}$  value reproducing the Curie–Weiss temperature ( $\theta \approx -10$  K).

### 24.2.3 Effect of Spin Arrangement on the Band Gap

In the spin-polarized DFT +  $U$  method, the up-spin and down-spin  $nd$  levels of each spin site are split by  $U$  (24.3). We discussed this before in Section 16.5; see 16.55 and 16.56. As an example, consider a spin dimer made up of two spin sites 1 and 2 with one orbital and one unpaired spin per site. For the FM arrangement of the two spins (Figure 24.2a), both spin sites have the up-spin level lower in energy by  $U$  than the down-spin level (by convention). For the AFM arrangement of the two spins (Figure 24.2b), the up-spin site has the up-spin level lower in energy by  $U$  than the down-spin level, while the opposite is true for the down-spin site. Between the two spin sites, only the levels of the same spin can have orbital interaction so that the interaction between the two spin sites is a degenerate orbital interaction for the FM arrangement, but a nondegenerate orbital interaction for the AFM arrangement. Provided that the electrons at sites 1 and 2 are described by orbitals  $\phi_1$  and  $\phi_2$ , respectively, the hopping (resonance) integral  $t$  is given by  $t = \langle \phi_1 | \hat{H}^{\text{eff}} | \phi_2 \rangle$ , where  $\hat{H}^{\text{eff}}$  is the effective Hamiltonian describing the spin dimer. Then the strength of the orbital interaction between the two spin sites is proportional to the hopping integral  $t$  for the FM arrangement, but to  $t^2/U$  for the AFM arrangement. In general,  $t$  is considerably greater in magnitude than  $t^2/U$ .

The observation stated earlier has an important implication. Consider a one-dimensional chain, a two-dimensional square lattice, and a three-dimensional cubic lattice made up of equivalent spin sites with one orbital and one electron per site and with the effective hopping integral  $t$  between nearest neighbor (NN) sites. In the FM arrangement of the spins, each spin site has the up-spin level lower in energy by

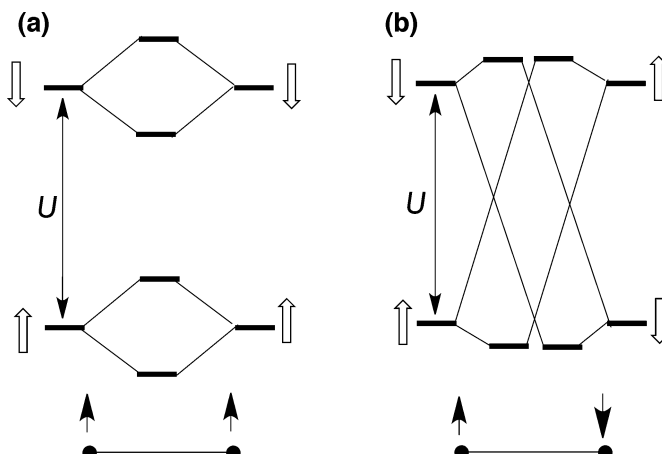
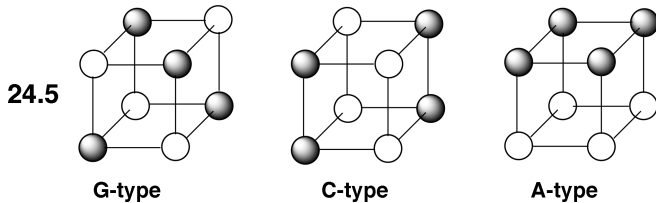


**FIGURE 24.2**

Dependence of the orbital interactions between two spin sites in a spin dimer on the (a) FM and (b) AFM spin arrangements. Each spin site is assumed to have one electron and one orbital.

$U$  than the down-spin level. Thus the up-spin and down-spin bands of this FM state, separated by  $U$ , will each have the width  $W = 2zt$ , where  $z$  is the number of NN sites connected by  $t$  (i.e.,  $z = 2, 4, 6$  for the 1D chain, 2D square, and 3D cubic systems, respectively). Therefore, if  $U > W$ , the up-spin and down-spin bands are separated with a band gap  $U - W$  so that the system will be a magnetic insulator (Figure 24.1b). If  $U < W$ , however, the up-spin and down-spin bands overlap so that the system becomes a magnetic metal (Figure 24.1c). Suppose now that the spins of the one-dimensional, two-dimensional, and three-dimensional systems have an AFM arrangement between nearest neighbors sites. Then the widths of the up-spin and down-spin bands are each given by  $W = 2zt^2/U$ . Since  $t^2/U$  is smaller than  $t$  in magnitude, so the bandwidth is smaller for the AFM state than for the FM state. Consequently, a system with partially filled band is more likely to have a band gap in the AFM state than in the FM state.

A 3D cubic lattice of spin sites may adopt several different AFM states, for example, the G-, C- and A-types, as depicted in 24.5 where the gray and white spheres indicate up- and down-spin sites. The G-type structure has AFM interactions in three different directions, the C-type in two different directions, and the A-type in



one direction. As a consequence, if all these three AFM states were to have band gaps, their band gaps should decrease in the order, G-type > C-type > A-type. Therefore, for an ideal simple cubic 3D magnetic system, it is possible that while the G- and C-type AFM states have a band gap, the A-type AFM state does not, and also that while the G-type AFM state has a band gap, but the C- and A-type AFM states do not. Such a dependence of band gap on the type of AFM interactions explains why, as the temperature is lowered, the band gaps of certain antiferromagnets such as  $\text{NaOsO}_3$  [10] and  $\text{Cd}_2\text{Os}_2\text{O}_7$  [21] increase continuously without changing their geometries. This kind of metal-insulator transition driven by AFM interactions is known as the Slater transition [22].

## 24.3 PROPERTIES ASSOCIATED WITH THE MAGNETIC MOMENT

### 24.3.1 The Magnetic Moment

The magnetic properties of a compound containing magnetic ions are largely determined by the magnetic moments,  $\vec{\mu}$ , of the ions. In general, the magnetic moment  $\vec{\mu}$  of a system refers to the change of its energy  $E$  with respect to the applied magnetic field  $\mathbf{H}$ ,

$$\vec{\mu} = - \frac{\partial E}{\partial \vec{H}} \quad (24.2)$$

A magnetic system is isotropic if its magnetic moment is nonzero in all directions, but is uniaxial if its magnetic moment is nonzero in only one direction. Magnetic ions are

characterized by their orbital and spin angular momenta ( $\mathbf{L}$  and  $\mathbf{S}$ , respectively) and hence by the associated magnetic moment  $\mu$ ,

$$\mu = -(\mathbf{L} + g\mathbf{S})\mu_B \quad (24.3)$$

where  $\mu_B$  is the Bohr magneton, and the electron g-factor,  $g$ , is 2.0023 (hereafter,  $g = 2$  for simplicity). For magnetic ions in molecules and solids, the orbital momentum is typically quenched ( $\mathbf{L} \approx 0$ ) due to the low symmetry of their environments so that the magnetic moments are well approximated by the spin-only moments,  $\mu \approx -2S\mu_B$ .

To illustrate how the orbital moment quenching comes about, we consider a system of one electron, for which the total energy is simply the energy of the occupied orbital [23]. Application of a magnetic field  $\mathbf{H}$  gives rise to the Zeeman interaction  $\hat{H}_Z$ . Without loss of generality, we may assume that the field of strength  $H$  is applied along the  $z$ -direction. Then  $\hat{H}_Z$  is written as

$$\hat{H}_Z = \mu_B \hat{\mathbf{L}} \cdot \vec{H} = \mu_B H \hat{L}_z \quad (24.4)$$

As a specific example, consider that one electron is present in one of the three  $p$  orbitals  $p_i$  ( $i = x, y, z$ ), for which the effective one-electron Hamiltonian  $\hat{H}^{\text{eff}}$  satisfies

$$\hat{H}^{\text{eff}} p_i = \varepsilon_i p_i \quad (i = x, y, z) \quad (24.5)$$

where  $\varepsilon_x$ ,  $\varepsilon_y$ , and  $\varepsilon_z$  are the energies of the orbitals  $p_x$ ,  $p_y$ , and  $p_z$ , respectively. This system under a magnetic field is described by the Hamiltonian  $\hat{H} = \hat{H}^{\text{eff}} + \hat{H}_Z$ . Then, by using the nonzero integrals,  $\langle p_z | \hat{L}_x | p_y \rangle = \langle p_x | \hat{L}_y | p_z \rangle = \langle p_y | \hat{L}_z | p_x \rangle = i$ , the matrix representation of  $\hat{H}$  in terms of the three orbitals  $p_x$ ,  $p_y$ , and  $p_z$ , that is,  $\langle p_i | \hat{H} | p_j \rangle$  ( $i, j = x, y, z$ ), is obtained as

$$\begin{pmatrix} \varepsilon_x & -i\mu_B H & 0 \\ i\mu_B H & \varepsilon_y & 0 \\ 0 & 0 & \varepsilon_z \end{pmatrix}. \quad (24.6)$$

The diagonalization of this matrix leads to three energies

$$\begin{aligned} E_1 &= \frac{1}{2} \left[ (\varepsilon_x + \varepsilon_y) - \sqrt{(\varepsilon_x - \varepsilon_y)^2 + 4\mu_B^2 H^2} \right] \\ E_2 &= \frac{1}{2} \left[ (\varepsilon_x + \varepsilon_y) + \sqrt{(\varepsilon_x - \varepsilon_y)^2 + 4\mu_B^2 H^2} \right], \\ E_3 &= \varepsilon_z \end{aligned} \quad (24.7)$$

Suppose that the ground state is given by  $E_1$ . Then the orbital angular momentum  $L$  of the single electron is given by

$$L \equiv \frac{\partial E_1}{\mu_B \partial H} = \frac{-2\mu_B H}{\sqrt{(\varepsilon_x - \varepsilon_y)^2 + 4\mu_B^2 H^2}} \quad (24.8)$$

If the  $p_x$  and  $p_y$  levels are degenerate (i.e., if  $\varepsilon_x = \varepsilon_y$ ), the  $L$  value becomes  $-1$  in units of  $\hbar$ . When the symmetry of the system is lowered, the degeneracy of the  $p_x$  and  $p_y$

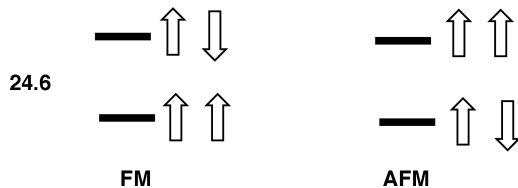
levels is lifted. In such a case, the energy difference  $|\varepsilon_x - \varepsilon_y|$  is generally much greater than  $\mu_B H$ , because the latter term is very small. For example, at the magnetic field of 1 Tesla ( $H = 1\text{ T}$ ),  $\mu_B H = 5.8 \times 10^{-2}\text{ meV} = 0.67\text{ K}$  in  $k_B$  units. (Other useful energy scales are 1 meV = 11.6 K = 8.06 cm<sup>-1</sup>, and 1 cm<sup>-1</sup> = 1.44 K.) As a result,

$$L = -\frac{2\mu_B H}{|\varepsilon_x - \varepsilon_y|}, \quad (24.9)$$

which is much smaller than  $-1$  in magnitude. In other words, the orbital moment is quenched when  $\varepsilon_x \neq \varepsilon_y$ . If  $E_3 < E_1$ , the ground state is given by  $E_3$ . In this case, the orbital moment of the system is zero, because its energy does not depend on the applied field  $H$ .

### 24.3.2 Magnetization

For a magnetic compound, an experimental quantity of interest at a given temperature is the magnetization **M**, namely, the average moment per unit volume. In general, the magnetization of a magnetic compound depends on temperature and external magnetic field **H** applied to the compound, because the moments of adjacent magnetic ions tend to have a FM or AFM arrangement due to their spin exchange interactions. For simplicity, consider the energy states of a spin dimer (i.e., a system with two spin sites), although our discussion is also valid for a magnetic system with more than two spin sites. Then the spin exchange interaction generates two states, “magnetic bonding” and “magnetic antibonding” states, as depicted in 24.6. Any spin exchange path leading to such an interaction may be regarded as a

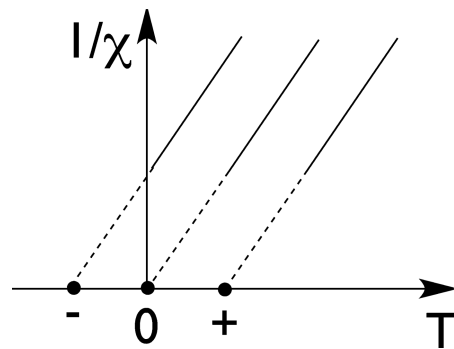


magnetic bond to distinguish from a chemical bond. When the spin exchange interaction is FM, the magnetic bonding and antibonding states have FM and AFM spin arrangements, respectively, but the opposite is the case if the spin exchange interaction is AFM. It is important to recall the very small energy scale involved in magnetic systems. At a given temperature, the tendency for the moments to adopt a FM or an AFM arrangement is counterbalanced by the available thermal energy  $k_B T$ , because both the magnetic bonding and antibonding states will be populated according to the Boltzmann distribution. At high temperature, both states are almost equally populated, so that the magnetization **M** is zero although the magnetic system has nonzero moments locally, thereby leading to the paramagnetic state. As the temperature is lowered, the bonding magnetic state is more preferentially populated than the antibonding magnetic state, hence reducing the paramagnetic behavior.

### 24.3.3 Magnetic Susceptibility

At a given temperature  $T$ , the magnetization **M** of a magnetic compound is proportional to the applied magnetic field **H** when the field is weak.

$$\mathbf{M} = \chi \mathbf{H}, \quad (24.10)$$

**FIGURE 24.3**

Plots of  $1/\chi$  versus  $T$  showing three different Curie-Weiss temperature: (a)  $\theta < 0$ , (b)  $\theta = 0$ , and (c)  $\theta > 0$ . The solid lines indicate that the plots follow the Curie-Weiss law, and the dashed lines that this law is not obeyed in the low temperature region.

where the proportionality constant is the magnetic susceptibility. At a given magnetic field, the temperature-dependence of the magnetic susceptibility follows the Curie-Weiss law in the high temperature region where the compound is paramagnetic,

$$\chi = \frac{C}{T - \theta} \quad \text{or} \quad \frac{1}{\chi} = \frac{1}{C}T - \frac{\theta}{C} \quad (24.11)$$

here  $C$  is the Curie constant (Figure 24.3). The  $1/\chi$  versus  $T$  plot is linear in the high-temperature region where the compound is paramagnetic (solid lines). With decreasing  $T$ , the  $1/\chi$  versus  $T$  plot usually deviates from linearity. We note that interesting magnetic systems are those whose magnetic susceptibilities deviate strongly from the Curie-Weiss law below a certain temperature because they are likely to exhibit interesting properties due to their strong spin exchange interactions. The two important quantities one can extract from the temperature-dependent magnetic susceptibility by fitting it with the Curie-Weiss law are the effective moment  $\mu_{\text{eff}}$  and the Curie-Weiss temperature,  $\theta$ . When we use the molar magnetic susceptibility  $\chi_m$  for a system with spin  $S$  magnetic ions, the effective moment  $\mu_{\text{eff}}$  (in units of  $\mu_B$ ) is related to  $\chi_m$  and  $S$  as follows,

$$\mu_{\text{eff}} = 2.828\sqrt{\chi_m T} = 2\sqrt{S(S+1)} \quad (24.12)$$

which provides information about the spin  $S$  in the paramagnetic region, and hence about how many unpaired spins the magnetic ion has. On the other hand, the Curie-Weiss temperature  $\theta$  has information about the nature of the dominant spin exchange interaction.  $\theta = 0$ , if the spin exchange interactions between magnetic ions are weak so that the magnetic compound is paramagnetic at all temperatures.  $\theta < 0$ , when the dominant spin exchange interaction is AFM.  $\theta > 0$ , when the dominant spin exchange interaction is FM. A magnetic compound consisting of spin  $S$  ions can have various spin exchange paths (magnetic bonds)  $i$  ( $= 1, 2, \dots$ ) and, therefore, have the associated spin exchange constants  $J_i$ . In the mean field approximation [24], the Curie-Weiss temperature  $\theta$  is related to  $J_i$  as,

$$\theta = \frac{S(S+1)}{3k_B} \sum_i z_i J_i, \quad (24.13)$$

where the summation runs over all adjacent neighbors of a given spin site,  $z_i$  is the number of adjacent neighbors connected by  $J_i$ .

### 24.3.4 Experimental Investigation of Magnetic Energy Levels

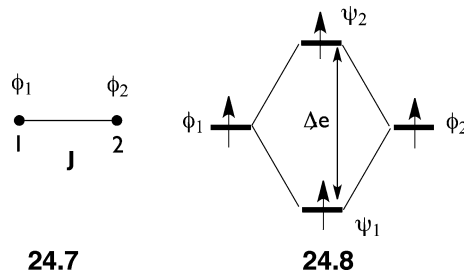
Magnetic systems possess low-lying magnetic excited states (24.1) that can be thermally populated according to the Boltzmann distribution. These states are closely packed in energy so that the physical properties of a magnetic system at a given  $T$  does not represent the property of a single state but a weighted average of the properties of many magnetic states weighted by their Boltzmann factors. It is the temperature-dependence of this Boltzmann averaging that governs the magnetic susceptibility ( $\chi$ ) at a given magnetic field  $\mathbf{H}$  or the magnetic specific heat ( $C_{p,\text{mag}}$ ) as a function of temperature. Alternatively, the population changes in the magnetic energy levels can be probed by measuring the magnetization  $\mathbf{M}$  at a very low temperature as a function of magnetic field  $\mathbf{H}$  because the energy  $\mu_B H$  supplied to the system changes the populations of its magnetic energy levels.

As discussed earlier, the magnetic susceptibility, specific heat, and magnetization ( $\chi$ ,  $C_{p,\text{mag}}$ , and  $\mathbf{M}$ ) measurements probe the magnetic excited states indirectly because they represent the properties resulting from various excited states populated according to the Boltzmann distribution. One can probe the individual low-lying magnetic excited states by performing inelastic neutron scattering measurements at a very low temperature where the populations of the magnetic and vibrational excited states are practically zero. In these experiments, a magnetic system is bombarded with a beam of cold (i.e., low-energy) neutrons at certain energy so that its magnetic excited levels become populated by absorbing energy from the bombarding neutrons. The magnetic excitation energies are deduced by measuring the energy loss of the neutrons scattered away from the compound. The spin-wave dispersion relation (i.e., the dependence of the absorption energy on momentum transfer  $Q$ ) resulting from these measurements [25] can be analyzed by using various spin Hamiltonians to determine the spin lattice appropriate for the system under investigation.

## 24.4 SYMMETRIC SPIN EXCHANGE

### 24.4.1 Mapping Analysis for a Spin Dimer

To gain insight into the meaning of the symmetric (or Heisenberg) spin exchange interaction, we consider a spin dimer consisting of two equivalent spin-1/2 spin sites, 1 and 2, with one electron at each spin site (24.7) [1,26]. The energy of the spin



dimer arising from the spin exchange interaction between the spins  $\mathbf{S}_1$  and  $\mathbf{S}_2$  is given by the Heisenberg spin Hamiltonian

$$\hat{H}_{\text{spin}} = -J \hat{\mathbf{S}}_1 \cdot \hat{\mathbf{S}}_2, \quad (24.14)$$

where  $J$  is the spin exchange parameter (or constant). This Hamiltonian describes an isotropic magnetic system because the energy has three Cartesian components due

to  $\mathbf{S}_1 \cdot \mathbf{S}_2 = S_{1x}S_{2x} + S_{1y}S_{2y} + S_{1z}S_{2z}$ . Given the dot product between  $\mathbf{S}_1$  and  $\mathbf{S}_2$ , the lowest energy for  $J > 0$  occurs when the spins are FM, but that for  $J < 0$  when the spins are AFM. In either case, the Heisenberg spin Hamiltonian leads to a collinear spin arrangement.

In principle, the spin at site  $i$  ( $= 1, 2$ ) of the spin dimer can have either up-spin  $\alpha$  or down-spin  $\beta$  state. For a single spin  $S = 1/2$  and  $S_z = \pm 1/2$  so that, in terms of the  $|S, S_z\rangle$  notations, these states are given by

$$\alpha = \left| \frac{1}{2}, \frac{1}{2} \right\rangle, \text{ and } \beta = \left| \frac{1}{2}, -\frac{1}{2} \right\rangle \quad (24.15)$$

which obey the following relationships:

$$\begin{aligned} \hat{S}_z |S, S_z\rangle &= S_z |S, S_z\rangle \\ \hat{S}_+ |S, S_z\rangle &= \sqrt{S(S+1) - S_z(S_z+1)} |S, S_z+1\rangle \\ \hat{S}_- |S, S_z\rangle &= \sqrt{S(S+1) - S_z(S_z-1)} |S, S_z-1\rangle \end{aligned} \quad (24.16)$$

where  $\hat{S}_+ = \hat{S}_x + i\hat{S}_y$  and  $\hat{S}_- = \hat{S}_x - i\hat{S}_y$  are the ladder operators.  $|S, S_z\rangle$  is an eigenstate of  $\hat{S}_z$ , but is not an eigenstate of  $\hat{S}_+$  and  $\hat{S}_-$ . Since  $\hat{S}(i) = \hat{i}\hat{S}_x(i) + \hat{j}\hat{S}_y(i) + \hat{k}\hat{S}_z(i)$  ( $i = 1, 2$ ), equation 24.14 is rewritten as

$$\begin{aligned} \hat{H}_{\text{spin}} &= -J[\hat{S}_x(1)\hat{S}_x(2) + \hat{S}_y(1)\hat{S}_y(2) + \hat{S}_z(1)\hat{S}_z(2)] \\ &= -J\hat{S}_z(1)\hat{S}_z(2) - (J/2)[\hat{S}_+(1)\hat{S}_-(2) + \hat{S}_-(1)\hat{S}_+(2)] \end{aligned} \quad (24.17)$$

The eigenstates of  $\hat{H}_{\text{spin}}$  allowed for the spin dimer are the singlet state  $|S\rangle$  and triplet state  $|T\rangle$ ,

$$\begin{aligned} |T\rangle &= \alpha(1)\alpha(2), \beta(1)\beta(2), \text{ or } [\alpha(1)\beta(2) + \beta(1)\alpha(2)]/\sqrt{2} \\ |S\rangle &= [\alpha(1)\beta(2) - \beta(1)\alpha(2)]/\sqrt{2} \end{aligned} \quad (24.18)$$

Note that the broken-symmetry (or Néel) states,  $\alpha(1)\beta(2)$  and  $\beta(1)\alpha(2)$ , interact through  $\hat{H}_{\text{spin}}$  (see equation 24.17) to give the symmetry-adapted states  $|S\rangle$  and  $|T\rangle$ .

We evaluate the energies of  $|T\rangle$  and  $|S\rangle$ ,  $E_{\text{spin}}(T)$  and  $E_{\text{spin}}(S)$ , respectively, by using equation 24.17 to find  $E_{\text{spin}}(T) = -J/4$  and  $E_{\text{spin}}(S) = 3J/4$ . Thus the energy difference between the two states is given by

$$\Delta E_{\text{spin}} = E_{\text{spin}}(S) - E_{\text{spin}}(T) = J \quad (24.19)$$

so the spin exchange constant  $J$  represents the energy difference between the singlet and triplet spin states of the spin dimer. The singlet state is lower in energy than the triplet state if the spin exchange  $J$  is AFM (i.e.,  $J < 0$ ), and the opposite is the case if the spin exchange  $J$  is FM (i.e.,  $J > 0$ ).

We now examine how the triplet and singlet states of the spin dimer are described in terms of electronic structure calculations. This closely follows the material in Sections 8.5 and 8.8. The electronic Hamiltonian  $\hat{H}_{\text{elec}}$  for this two-electron system can be written as

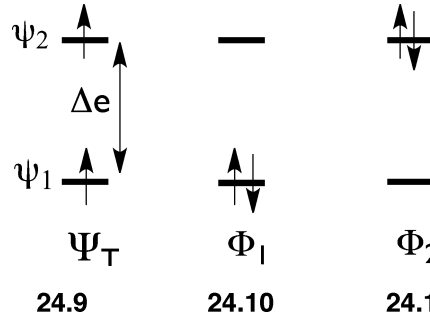
$$\hat{H}_{\text{elec}} = \hat{h}(1) + \hat{h}(2) + 1/r_{12} \quad (24.20)$$

where  $\hat{h}(i)$  is the one-electron energy (i.e., the kinetic and the electron–nuclear attraction energies) of the electron  $i$  ( $= 1, 2$ ), and  $r_{12}$  is the distance between

electrons 1 and 2. Assume that the unpaired electrons at sites 1 and 2 are accommodated in the orbitals  $\phi_1$  and  $\phi_2$ , respectively, in the absence of interaction between them. Such singly occupied orbitals are referred to as magnetic orbitals. The weak interaction between  $\phi_1$  and  $\phi_2$  leads to the two levels  $\psi_1$  and  $\psi_2$  of the dimer separated by a small energy gap  $\Delta e$  (24.8), which are approximated by

$$\begin{aligned}\psi_1 &\approx (\phi_1 + \phi_2)/\sqrt{2} \\ \psi_2 &\approx (\phi_1 - \phi_2)/\sqrt{2}\end{aligned}\quad (24.21)$$

As depicted in 24.12, one of the three triplet-state wave functions is represented by the electron configuration  $\Psi_T$ . When  $\Delta e$  is very small (compared with that



24.9

24.10

24.11

expected for chemical bonding), the singlet-state electron configurations  $\Phi_1$  (24.10) and  $\Phi_2$  (24.11) are very close in energy, and interact strongly under  $\hat{H}_{\text{elec}}$  to give  $\langle \Phi_1 | \hat{H}_{\text{elec}} | \Phi_2 \rangle = K_{12}$ , where  $K_{12}$  is the exchange repulsion between  $\phi_1$  and  $\phi_2$  (see below). Thus the true singlet state  $\psi_S$  is described by the lower energy state of the configuration-interaction wave functions  $\Psi_i$  ( $i = 1, 2$ ),

$$\Psi_i = C_{1i}\Phi_1 + C_{2i}\Phi_2 \quad (i = 1, 2) \quad (24.22)$$

namely,  $\Psi_S = \Psi_1$ . The energies of  $\Psi_S$  and  $\Psi_T$ ,  $E_{\text{CI}}(S)$  and  $E_{\text{CI}}(T)$ , respectively, can be evaluated in terms of  $\hat{H}_{\text{elec}}$  by using the dimer orbitals  $\Psi_1$  and  $\Psi_2$  determined from the calculations for the triplet state  $\Psi_T$ . Then, after some manipulations, the electronic energy difference between the singlet and triplet state is written as [26]

$$\Delta E_{\text{CI}} = E_{\text{CI}}(S) - E_{\text{CI}}(T) = 2K_{12} - \frac{(\Delta e)^2}{U^{\text{eff}}} \quad (24.23)$$

where  $K_{12}$  is the exchange repulsion between  $\phi_1$  and  $\phi_2$ ,

$$K_{12} = \langle \phi_1(1)\phi_2(2) | 1/r_{12} | \phi_2(1)\phi_1(2) \rangle$$

The effective on-site repulsion  $U^{\text{eff}}$  is given by  $U^{\text{eff}} = J_{11} - J_{12}$ , where  $J_{11}$  and  $J_{12}$  are the Coulomb repulsion integrals,

$$\begin{aligned}J_{11} &= \langle \phi_1(1)\phi_1(2) | 1/r_{12} | \phi_1(1)\phi_1(2) \rangle \\ J_{12} &= \langle \phi_1(1)\phi_2(2) | 1/r_{12} | \phi_1(1)\phi_2(2) \rangle\end{aligned}$$

Therefore, by mapping the energy spectrum of  $\hat{H}_{\text{spin}}$  onto that of  $\hat{H}_{\text{elec}}$ , namely,  $\Delta E_{\text{spin}} = \Delta E_{\text{CI}}$ , we obtain

$$J = \Delta E_{\text{CI}} = 2K_{12} - \frac{(\Delta e)^2}{U^{\text{eff}}} \quad (24.24)$$

It is important to note the qualitative aspect of the spin exchange  $J$  on the basis of the equation 24.24. Since the repulsion terms  $K_{12}$  and  $U^{\text{eff}}$  are always positive, the spin exchange  $J$  is divided into the FM and AFM components  $J_F (> 0)$  and  $J_{\text{AF}} (< 0)$ , respectively. That is,

$$J = J_F + J_{\text{AF}} \quad (24.25)$$

where

$$J_F = 2K_{12} \quad (24.26)$$

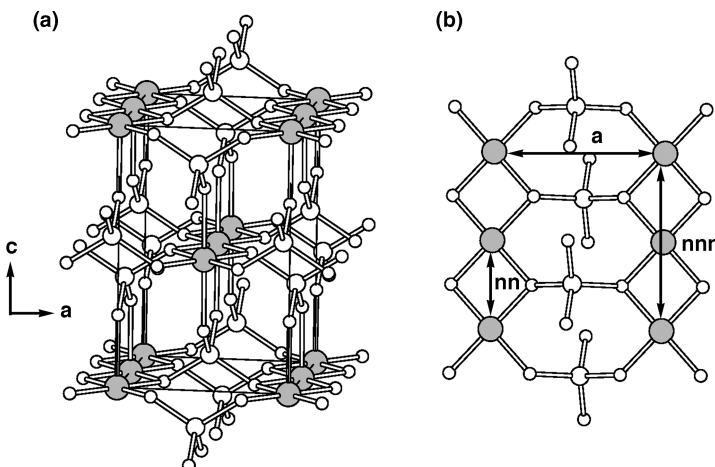
$$J_{\text{AF}} = -\frac{(\Delta e)^2}{U^{\text{eff}}} \quad (24.27)$$

The FM term  $J_F$  term becomes stronger with increasing the exchange integral  $K_{12}$ , which in turn increases with increasing the overlap density,  $\phi_1\phi_2$ . The AFM term  $J_{\text{AF}}$  becomes stronger with increasing  $\Delta e$ , which in turn becomes larger with increasing the overlap integral,  $\langle\phi_1|\phi_2\rangle$ . In addition, the  $J_{\text{AF}}$  term becomes weaker with increasing the on-site repulsion,  $U^{\text{eff}}$ .

#### 24.4.2 Through-Space and Through-Bond Orbital Interactions Leading to Spin Exchange

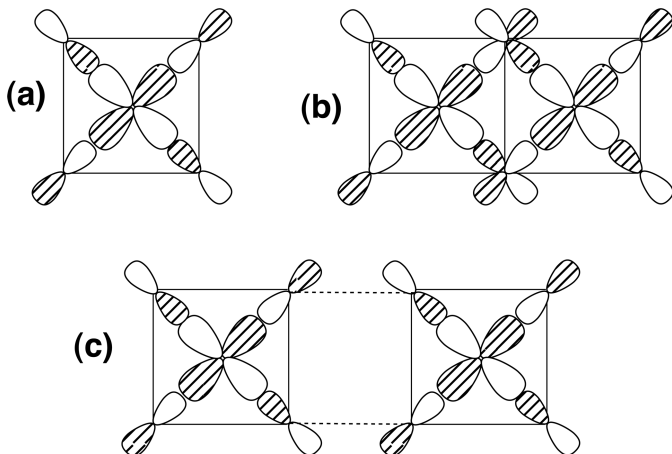
As a representative example, capturing the essence of spin exchange interactions, let us examine those of  $\text{LiCuVO}_4$  [27,28] in which the  $\text{CuO}_2$  ribbon chains, made up of edge-sharing  $\text{CuO}_4$  square planes running along the  $b$ -direction are interconnected along the  $a$ -direction by sharing corners with  $\text{VO}_4$  tetrahedra. This is shown in Figure 24.4a. In  $\text{LiCuVO}_4$  the  $\text{Cu}^{2+}(S=1/2, d^9)$  ions are magnetic, but the  $\text{V}^{5+}(d^0)$  ions are nonmagnetic. As for the spin exchange paths of  $\text{LiCuVO}_4$ , we consider the NN and next-nearest-neighbor (NNN) intrachain spin exchanges,  $J_{nn}$  and  $J_{nnn}$ , respectively, in each  $\text{CuO}_2$  ribbon chain as well as the interchain spin exchange  $J_a$  along the  $a$ -direction (Figure 24.4b).

The magnetic orbital of the  $\text{Cu}^{2+}(S=1/2, d^9)$  ion is given by the  $x^2-y^2$   $\sigma^*$ -antibonding orbital contained in the  $\text{CuO}_4$  square plane (Figure 24.5a), in which the Cu 3d  $x^2-y^2$  orbital is combined out-of-phase with the 2p orbitals of the four



**FIGURE 24.4**

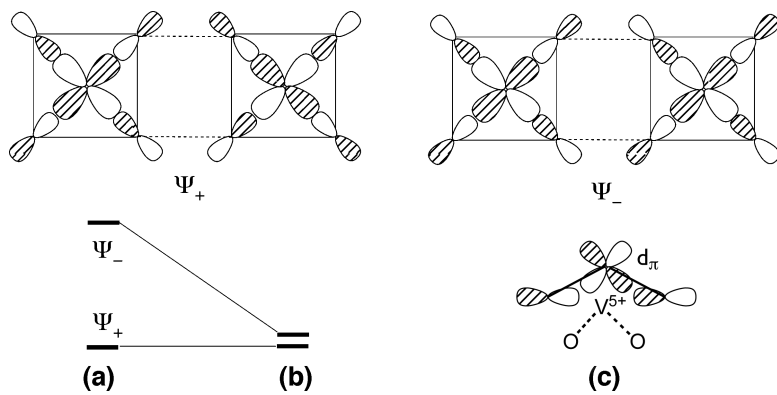
(a) Perspective view of the crystal structure of  $\text{LiCuVO}_4$  showing the  $\text{CuO}_2$  ribbon chains interconnected by  $\text{VO}_4$  tetrahedra. The Cu atoms are indicated by large shaded circles, the V atoms by medium unshaded circles, and the O atoms by small unshaded circles. (b) The intrachain spin exchange paths  $J_{nn}$  and  $J_{nnn}$  as well as the interchain spin exchange path  $J_a$  of  $\text{LiCuVO}_4$ .

**FIGURE 24.5**

(a) The  $x^2 - y^2$  magnetic orbital of a  $\text{CuO}_4$  square plane. (b) The Cu–O–Cu spin exchange interaction between nearest-neighbor  $\text{CuO}_4$  square planes in a  $\text{CuO}_2$  ribbon chain. (c) The Cu–O...O–Cu spin exchange interaction between next-nearest neighbor  $\text{CuO}_4$  square planes in a  $\text{CuO}_2$  ribbon chain.

surrounding O ligands. As already emphasized [1], it is not the “head” part (the Cu 3d  $x^2 - y^2$  orbital) but the “tail” part (the O 2p orbitals) of the magnetic orbital that controls the magnitudes and signs of these spin exchange interactions. (Here, we employ a localized approach in contrast to the delocalized treatment we have used in previous chapters. Thus the magnetic orbital of a transition-metal magnetic ion in a magnetic solid is a singly filled d-block orbital of the cluster made up of the magnetic ion and its first-coordinate ligand atoms.) Let us first consider the Cu–O–Cu superexchange (SE)  $J_{nn}$ . When the  $x^2 - y^2$  magnetic orbitals  $\phi_1$  and  $\phi_2$  of the two spin sites are brought together to form the Cu–O–Cu bridges, the O 2p orbital tails at the bridging O atoms make a nearly orthogonal arrangement (Figure 24.5b). Thus the overlap integral  $\langle \phi_1 | \phi_2 \rangle$  between the two magnetic orbitals is almost zero, which leads to  $J_{AF} \approx 0$ . In contrast, the overlap density  $\phi_1 \phi_2$  of the magnetic orbitals is substantial, which leads to nonzero  $J_F$ . As a consequence, the  $J_{nn}$  exchange becomes FM [27b,28].

For the intrachain Cu–O...O–Cu super-superexchange (SSE)  $J_{nnn}$  (Figure 24.5c), the O 2p orbital tails of the magnetic orbitals  $\phi_1$  and  $\phi_2$  at the terminal O atoms are well separated by the O...O contacts. Thus the overlap density  $\phi_1 \phi_2$  of the magnetic orbitals is negligible leading to  $J_F \approx 0$ . However, the overlap integral  $\langle \phi_1 | \phi_2 \rangle$  is nonzero because the O 2p tails of  $\phi_1$  and  $\phi_2$  overlap through the O...O contacts. This through-space interaction between  $\phi_1$  and  $\phi_2$  produces a large energy split  $\Delta e$  between  $\Psi_+$  and  $\Psi_-$ , which are in-phase and out-of-phase combinations of  $\phi_1$  and  $\phi_2$ , respectively (Figure 24.6a), thereby leading to nonzero  $J_{AF}$ . Consequently, the  $J_{nnn}$  exchange becomes AFM [27b,28].

**FIGURE 24.6**

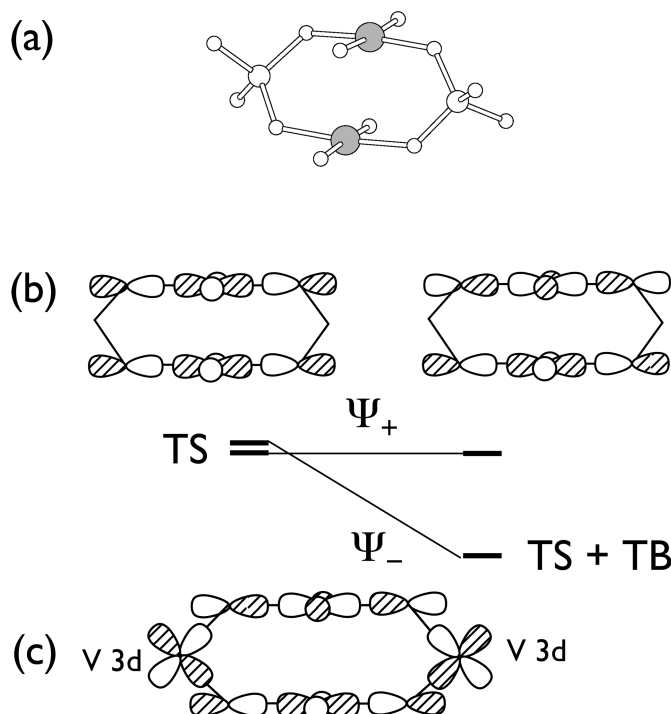
The through-space and through-bond interactions between the two  $x^2 - y^2$  magnetic orbitals in the Cu–O...V<sup>5+</sup>...O–Cu interchain spin exchange  $J_a$  in  $\text{LiCuVO}_4$ : (a) The energy split between  $\Psi_+$  and  $\Psi_-$  due to the through-space interaction. (b) The energy split between  $\Psi_+$  and  $\Psi_-$  due to the through-space and through-bond interactions. (c) The bonding interaction of the V d orbital with the O 2p tails of  $\Psi_-$  in the O...V<sup>5+</sup>...O bridge.

In the interchain spin exchange path  $J_a$ , the two  $\text{CuO}_4$  square planes are corner-shared with  $\text{VO}_4$  tetrahedra. Notice from Figure 15.2 that from the averaged state ionization potentials vanadium 3d orbitals lie over 3.5 eV higher in energy than Cu 3d set. The  $\text{Cu } x^2 - y^2$  magnetic orbital, though  $\sigma$  antibonding to the oxygen p AOs, still lies at a lower energy than the V 3d set. Thus in the  $\text{Cu}-\text{O}\cdots\text{V}^{5+}\cdots\text{O}-\text{Cu}$  SSE paths, the empty V 3d orbitals should interact in a bonding manner with the  $\text{Cu } x^2 - y^2$  orbitals. In the absence of the V 3d orbitals, the energy split  $\Delta e$  between  $\Psi_+$  and  $\Psi_-$  arising from the through-space interaction between  $\phi_1$  and  $\phi_2$  would be substantial, as expected from the intrachain exchange  $J_{\text{nnn}}$ , so that one might expect a strong AFM exchange for  $J_{\text{inter}}$ . However, in the  $\text{Cu}-\text{O}\cdots\text{V}^{5+}\cdots\text{O}-\text{Cu}$  exchange paths, the bridging  $\text{VO}_4$  units provides a through-bond interaction between the empty V 3d $_{\pi}$  orbitals and the O 2p tails of the magnetic orbitals on the O $\cdots$ O contacts. By symmetry, this through-bond interaction is possible only with  $\Psi_-$  (Figure 24.6b,c). The V 3d $_{\pi}$  orbital being empty, the O 2p tails of  $\Psi_-$  on the O $\cdots$ O contacts interact in-phase with the empty V 3d orbital hence lowering the  $\Psi_-$  level, whereas  $\Psi_+$  is unaffected by the V 3d $_{\pi}$  orbital, thereby reducing the energy split  $\Delta e$  between  $\Psi_+$  and  $\Psi_-$  of the  $\text{Cu}-\text{O}\cdots\text{V}^{5+}\cdots\text{O}-\text{Cu}$  exchange paths and consequently weakening the interchain spin exchange  $J_{\text{inter}}$  [27b,28]. As a consequence, the magnetic properties are dominated by the one-dimensional character of the  $\text{CuO}_2$  ribbon chain via  $J_{\text{NN}}$ .

As another example of showing the interplay between the through-space and through-bond spin exchange interaction, we consider the spin gap system  $\text{BaCu}_2\text{V}_2\text{O}_8$  [29–31] in which two  $\text{CuO}_4$  square planes, stacked on top of each other, are bridged by two  $\text{VO}_4$  tetrahedra as illustrated in Figure 24.7a. Since the two  $\text{CuO}_4$  units are nearly parallel to each other, the overlap between  $\phi_1$  and  $\phi_2$  is of  $\delta$ -type so that the through-space interaction between  $\phi_1$  and  $\phi_2$  leads to a negligibly small energy split  $\Delta e$  between  $\Psi_+$  and  $\Psi_-$  (Figure 24.7b). In the  $\text{Cu}-\text{O}\cdots\text{V}^{5+}\cdots\text{O}-\text{Cu}$  exchange paths, the bridging  $\text{VO}_4$  units provides a through-bond interaction between the empty V 3d orbitals and the O 2p tails on the O $\cdots$ O contacts. This

**FIGURE 24.7**

The through-space (TS) and through-bond (TB) interactions between the two  $x^2 - y^2$  magnetic orbitals in the  $\text{Cu}-\text{O}\cdots\text{V}^{5+}\cdots\text{O}-\text{Cu}$  spin exchange found in  $\text{BaCu}_2\text{V}_2\text{O}_8$ : (a) The spin dimer in which two  $\text{CuO}_4$  square planes stacked on top of each other are bridged by two  $\text{VO}_4$  tetrahedra. The Cu atoms are indicated by large shaded circles. (b) The energy split between  $\Psi_+$  and  $\Psi_-$  due to the TS interaction, and that due to the TS and TB interactions. (c) The bonding interactions of the V 3d orbitals with the O 2p tails of  $\Psi_-$  in the O $\cdots\text{V}^{5+}\cdots\text{O}$  bridges.



through-bond interaction is possible only with  $\Psi_-$  (Figure 24.7c) in which the O 2p tails of the O $\cdots$ O contacts are out-of-phase. These O 2p tails interact in-phase with the empty V 3d orbital hence lowering the  $\Psi_-$  level below  $\Psi_+$ , while  $\Psi_+$  is unaffected by the V 3d $_{\pi}$  orbital. This enhances the energy split  $\Delta e$  between  $\Psi_+$  and  $\Psi_-$  of the Cu–O $\cdots$ V $^{5+}$  $\cdots$ O–Cu exchange paths and hence leads to a strong AFM spin exchange (Figure 24.7b) [31], which is responsible for the observed spin gap behavior of BaCu<sub>2</sub>V<sub>2</sub>O<sub>8</sub> [29] and also for the observation from the <sup>51</sup>V NMR study [30] that the V sites have nonzero spin densities. The latter reflects the fact that the V 3d orbitals mix into the magnetic orbital  $\Psi_-$ .

In general, the transition-metal cations, M $^{x+}$  ( $x$  = oxidation state) of a magnetic system form ML<sub>n</sub> polyhedra with surrounding main-group elements L (typically,  $n = 4–6$ ). For the magnetic M $^{x+}$  cation, some d-block levels of ML<sub>n</sub> polyhedron are singly occupied thereby becoming magnetic orbitals, in which the M nd-orbitals are combined out-of-phase with the L np-orbitals. When these ML<sub>n</sub> polyhedra are condensed together by sharing a corner, an edge or a face, they give rise to M–L–M SEs described by the Goodenough–Kanamori rules [32]. When these polyhedra are not condensed by sharing corners, they give rise to M–L $\cdots$ L–M SSEs [1]. It is the L np tails of the magnetic orbitals that control the magnitudes and signs of such spin exchange interactions. Concerning the M–L $\cdots$ L–M spin exchanges, there are several important consequences of this observation [1]:

- (a) The strength of a given M–L $\cdots$ L–M spin exchange is not determined by the shortness of the M $\cdots$ M distance, but rather by that of the L $\cdots$ L distance; it is strong when the L $\cdots$ L distance is in the vicinity of the Van der Waals radii sum or shorter.
- (b) In a given magnetic system consisting of both M–L–M and M–L $\cdots$ L–M spin exchanges, the M–L $\cdots$ L–M spin exchanges are very often stronger than the M–L–M spin exchanges.
- (c) The strength of an M–L $\cdots$ L–M spin exchange determined by through-space interaction between the L np tails on the L $\cdots$ L contact can be significantly modified when the L $\cdots$ L contact has a through-bond interaction with the intervening d<sup>0</sup> [27,31] metal cation A $^{y+}$  ( $y$  = oxidation state) or even the p<sup>0</sup> metal cation (e.g., Cs<sup>+</sup> as found for Cs<sub>2</sub>CuCl<sub>4</sub> [33]). Such an M–L $\cdots$ A $^{y+}$  $\cdots$ L–M spin exchange becomes strong if the corresponding M–L $\cdots$ L–M through-space exchange is weak, but becomes weaker if the corresponding M–L $\cdots$ L–M through-space exchange is strong. This is so because the empty d $_{\pi}$  orbital of A $^{y+}$  interacts only with the  $\Psi_-$  orbital of the M–L $\cdots$ L–M exchange. In general, the empty d $_{\pi}$  orbital has a much stronger through-bond effect than does the empty p $_{\pi}$  orbital.

#### 24.4.3 Mapping Analysis Based on Broken-Symmetry States

With DFT calculations, the energy-mapping between the energy spectra of  $\hat{H}_{\text{elec}}$  and  $\hat{H}_{\text{spin}}$  is carried out by using high-spin and broken-symmetry states ( $|HS\rangle$  and  $|BS\rangle$ , respectively) [1,34–37]. For example, let us reconsider the spin dimer shown in 24.10, for which the pure-spin  $|HS\rangle$  and  $|BS\rangle$  states are given by

$$\begin{aligned} |HS\rangle &= \alpha(1)\alpha(2) \text{ or } \beta(1)\beta(2) \\ |BS\rangle &= \alpha(1)\beta(2) \text{ or } \beta(1)\alpha(2) \end{aligned} \quad (24.28)$$

Here the  $|HS\rangle$  state is an eigenstate of the spin Hamiltonian  $\hat{H}_{\text{spin}}$  in equation 24.14, but the  $|BS\rangle$  state is not. In terms of this Hamiltonian, the energies of the

collinear-spin states  $|HS\rangle$  and  $|BS\rangle$ ,  $E_{\text{spin}}(HS) = \langle HS|\hat{H}_{\text{spin}}|HS\rangle$  and  $E_{\text{spin}}(BS) = \langle BS|\hat{H}_{\text{spin}}|BS\rangle$ , respectively, are given by  $E_{\text{spin}}(HS) = -J/4$  and  $E_{\text{spin}}(BS) = +J/4$ . Thus

$$\Delta E_{\text{spin}} = E_{\text{spin}}(BS) - E_{\text{spin}}(HS) = J/2 \quad (24.29)$$

In terms of DFT, the electronic structures of the  $|HS\rangle$  and  $|BS\rangle$  states are readily calculated to determine their energies,  $E_{\text{DFT}}(HS)$  and  $E_{\text{DFT}}(BS)$ , respectively, and hence obtain the energy difference

$$\Delta E_{\text{DFT}} = E_{\text{DFT}}(BS) - E_{\text{DFT}}(HS) \quad (24.30)$$

Consequently, by mapping  $\Delta E_{\text{spin}}$  onto  $\Delta E_{\text{DFT}}$ , we obtain

$$J/2 = \Delta E_{\text{DFT}} \quad (24.31)$$

The energy-mapping analysis based on DFT calculations employs the broken-symmetry state that is not an eigenstate of the spin Hamiltonian (equation 24.14). For a general spin Hamiltonian defined in terms of several spin exchange parameters, it is impossible to determine its eigenstates analytically and is also difficult to determine them numerically. For any realistic magnetic system requiring a spin Hamiltonian defined in terms of various spin exchange parameters, the energy-mapping analysis based on DFT greatly facilitates the quantitative evaluation of the spin exchange parameters because it does not rely on the eigenstates but on the broken-symmetry states of the spin Hamiltonian. For broken-symmetry states, the energy expressions of the spin Hamiltonian can be readily written down (see below) and the corresponding electronic energies can be readily determined by DFT calculations.

In general, the magnetic energy levels of a magnetic system are described by employing a Heisenberg spin Hamiltonian  $\hat{H}_{\text{spin}}$  defined in terms of several different spin exchange parameters,

$$\hat{H}_{\text{spin}} = -\sum_{i>j} J_{ij} \hat{S}_i \cdot \hat{S}_j \quad (24.32)$$

where  $\hat{S}_i$  and  $\hat{S}_j$  are the spins at the spin sites  $i$  and  $j$ , respectively, and  $J_{ij}$  is the spin exchange parameters describing the sign and strength of the interaction between the spin sites  $i$  and  $j$ . This model Hamiltonian generates a set of magnetic energy levels as the sum of pair-wise interactions  $J_{ij} \hat{S}_i \cdot \hat{S}_j$ . As already mentioned, there is no analytical solution for the eigenstates of such a general spin Hamiltonian. In evaluating the spin exchange interactions and hence the magnetic structure of a given magnetic system by employing the energy-mapping method based on DFT calculations, one needs to follow the four steps:

- (a) Select a set of  $N$  spin exchange paths  $J_{ij}$  ( $= J_1, J_2, \dots, J_N$ ) for a given magnetic system on the basis of inspecting the geometrical arrangement of its magnetic ions and also considering the nature of its M–L–M and M–L $\cdots$ –L–M interaction paths.
- (b) Construct  $N+1$  ordered spin states (i.e., broken-symmetry states)  $i = 1, 2, \dots, N+1$ , in which all spins are collinear so that any given pair of spins has either FM or AFM arrangement. For a general spin dimer whose spin sites  $i$  and  $j$  possess  $N_i$  and  $N_j$  unpaired spins (hence, spins  $S_i = N_i/2$  and  $S_j = N_j/2$ ), respectively, the spin exchange energies of the FM and AFM arrangements ( $E_{\text{FM}}$  and  $E_{\text{AFM}}$ , respectively) are given by [36,37]

$$\begin{aligned} E_{\text{FM}} &= -N_i N_j J_{ij}/4 = -S_i S_j J_{ij} \\ E_{\text{AFM}} &= +N_i N_j J_{ij}/4 = +S_i S_j J_{ij} \end{aligned} \quad (24.33)$$

where  $J_{ij}$  ( $= J_1, J_2, \dots, J_N$ ) is the spin exchange parameter for the spin exchange path  $ij = 1, 2, \dots, N$ . Thus the total spin exchange energy of an ordered spin arrangement is readily obtained by summing up all pair-wise interactions to find the energy expression  $E_{\text{spin}}(i)$  ( $i = 1, 2, \dots, N + 1$ ) in terms of the parameters to be determined and hence the  $N$  relative energies

$$\Delta E_{\text{spin}}(i - 1) = E_{\text{spin}}(i) - E_{\text{spin}}(1) \quad (i = 2, 3, \dots; N + 1) \quad (24.34a)$$

- (c) Determine the electronic energies  $E_{\text{DFT}}(i)$  of  $N + 1$  ordered spin states  $i = 1, 2, \dots, N + 1$  by DFT calculations to obtain the  $N$  relative energies

$$\Delta E_{\text{DFT}}(i - 1) = E_{\text{DFT}}(i) - E_{\text{DFT}}(1) \quad (j = 2, 3, \dots; N + 1) \quad (24.34b)$$

As already mentioned, DFT calculations for a magnetic insulator tend to give a metallic electronic structure because the electron correlation of a magnetic ion leading to spin polarization is not well described. Since we deal with the energy spectrum of a magnetic insulator, it is necessary that the electronic structure of each ordered spin state obtained from DFT calculations be magnetic insulating. To ensure this aspect, it is necessary to perform DFT +  $U$  calculations [5] by adding on-site repulsion  $U$  on magnetic ions. Furthermore, as can be seen from equation 24.27, the AFM component of a spin exchange decreases with increasing  $U$  so that the magnitude and sign of a spin exchange constant may be affected by  $U$ . It is therefore necessary to carry out DFT +  $U$  calculations with several different  $U$  values.

- (d) Finally, determine the values of  $J_1, J_2, \dots, J_N$  by mapping the  $N$  relative energies  $\Delta E_{\text{DFT}}$  onto the  $N$  relative energies  $\Delta E_{\text{spin}}$ ,

$$\Delta E_{\text{DFT}}(i - 1) = \Delta E_{\text{spin}}(i - 1) \quad (i = 2 - N + 1) \quad (24.35)$$

In determining  $N$  spin exchanges  $J_1, J_2, \dots, J_N$ , one may employ more than  $N + 1$  ordered spin states, hence obtaining more than  $N$  relative energies  $\Delta E_{\text{DFT}}$  and  $\Delta E_{\text{spin}}$  for the mapping. In this case, the  $N$  parameters  $J_1, J_2, \dots, J_N$  can be determined by performing least-squares fitting analysis. Given DFT +  $U$  calculations with several different  $U$  values, one obtains several sets of the  $J_1, J_2, \dots, J_N$  values. It is important to find trends common to these sets. To determine which set is most appropriate, one might evaluate the Curie–Weiss temperature  $\theta$  in terms of the calculated  $J_1, J_2, \dots, J_N$  values by using equation 24.14. There is no guarantee, of course, that the set that gives  $\theta$  close to the experimental value represents the only solution. As already pointed out, the purpose of using a spin Hamiltonian is to quantitatively describe the observed experimental data (namely, the temperature dependence of  $\chi$ ,  $C_{\text{p,mag}}$  and  $\bar{M}$  as well as the excitation spectrum measured from neutron scattering measurements) with a minimal set of  $J_{ij}$  values hence capturing the essence of the chemistry and physics involved. Experimentally, such a set of  $J_{ij}$  values for a given magnetic system is deduced first by choosing a few spin exchange paths  $J_{ij}$  that one considers as important for the system and then by evaluating their signs and magnitudes such that the energy spectrum of the resulting spin Hamiltonian best simulates the observed experimental data. The numerical values of  $J_{ij}$  deduced from this fitting analysis depends on what spin lattice model one employs for the fitting, and hence more than one spin lattice may fit the experimental data equally well.

This nonuniqueness of the fitting analysis has been the source of controversies in the literature over the years. From the viewpoint of doing physics (namely, providing a quantitative mathematical analysis using a model Hamiltonian with minimum

adjustable parameters) for a given magnetic system, it is appealing to select a spin lattice model that can generate interesting and novel physics. If the chosen spin lattice model is not the true spin lattice for the system, then the physics generated is irrelevant for the system and becomes “a solution in search of a problem”. The latter situation occurs not infrequently in the field of magnetic studies. Ultimately, the spin lattice of a magnetic system deduced from experimental fitting analysis should be consistent with the one determined from the energy-mapping analysis based on DFT calculations, because the observed magnetic properties are a consequence of the electronic structure of the magnetic system.

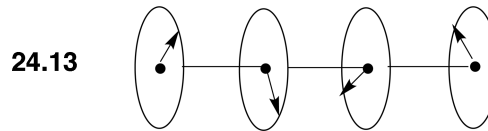
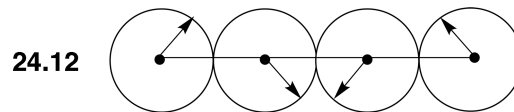
## 24.5 MAGNETIC STRUCTURE

### 24.5.1 Spin Frustration and Noncollinear Spin Arrangement

In each CuO<sub>2</sub> ribbon chain of LiCuVO<sub>4</sub> discussed in Section 24.4.2, a FM arrangement of all spins would be energetically favorable if only the FM exchange  $J_{nn}$  is considered. However, this arrangement is energetically unfavorable according to the AFM exchange  $J_{nnn}$  because it forces an AFM arrangement for every NNN spin pairs. Consequently, the spin exchanges  $J_{nn}$  and  $J_{nnn}$  in each CuO<sub>2</sub> ribbon chain give rise to spin frustration. [38,39] To reduce the extent of this spin frustration, which arises from a collinear spin arrangement, and hence lower the energy, each CuO<sub>2</sub> ribbon chain adopts a spiral spin arrangement [26] in which the NN spin pairs are nearly orthogonal to each other while the NNN spin pairs have an AFM arrangement. In reciprocal units, the periodicity  $q$  of the spiral spin arrangement is related to the  $J_{nn}/J_{nnn}$  ratio as [27b,40]

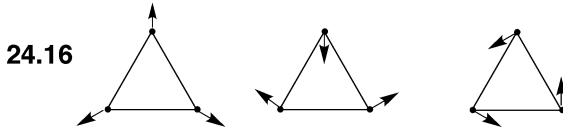
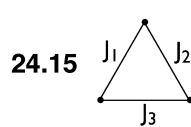
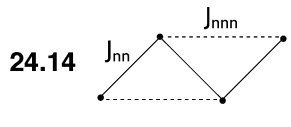
$$q = \frac{1}{2\pi} \arctan \left( -\frac{J_{nn}}{4J_{nnn}} \right) \quad (24.36)$$

For example, when  $J_{nn}=0$  and  $J_{nnn}<0$ ,  $q=0.25$  so that the magnetic unit cell quadruples along the chain direction. In principle, such a spiral-spin arrangement can be cycloidal (24.12) in which the plane of the spin rotation contains the chain-propagation direction, or helical (24.13) in which the plane of the spin rotation is perpendicular to the chain-propagation direction. It is very important to note that Heisenberg spin exchange interactions determine the relative spin arrangement of a magnetic system, but do not control the absolute spin orientation in space. It is SOC

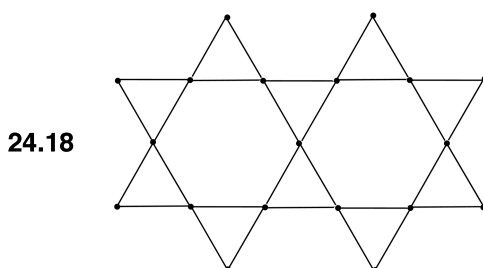
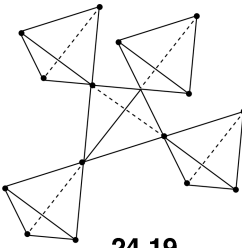
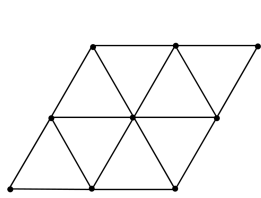


[23] and magnetic dipole–dipole (MDD) interactions [41] that provide the preferred spin orientation in space (see Sections 24.5.2 and 24.7.1).

The spin frustration in the linear CuO<sub>2</sub> ribbon chain arising from  $J_{nn}$  and  $J_{nnn}$  is topologically equivalent to that in a zigzag chain with  $J_{nn}$  and  $J_{nnn}$  (24.14), which consists of ( $J_{nn}, J_{nn}, J_{nnn}$ ) triangles. In general, any spin exchange triangle ( $J_1, J_2, J_3$ ) made up of three magnetic bonds (24.15) is spin-frustrated if all magnetic bonds are AFM



or if two magnetic bonds are FM and the remaining one is AFM. A spin-frustrated equilateral triangle made up of an AFM exchange  $J$  ( $J_1 = J_2 = J_3 = J < 0$ ) adopts the  $120^\circ$  spin arrangements (i.e., noncollinear spin arrangements) (24.16). Representative examples of extended solids showing spin frustration are the triangular (24.17), Kagome (24.18) and pyrochlore (24.19) spin lattices with NN AFM spin exchange.



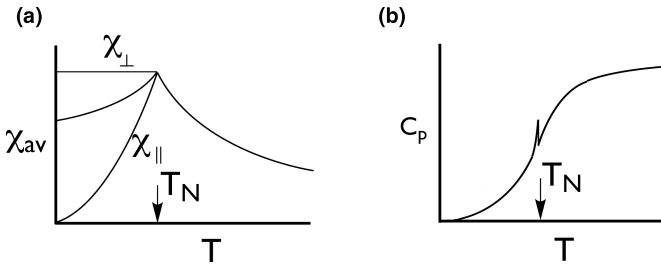
From the viewpoint of energy, the presence of spin frustration means that the magnetic ground state is highly degenerate, namely, many different spin arrangements have the same energy. How this degeneracy can be broken by weak perturbation is a fascinating research topic in condensed matter physics. Experimentally, a magnetic system with dominant AFM interaction (i.e., with negative Curie–Weiss temperature  $\theta$ ) is considered to be significantly spin-frustrated if the frustration index [38]

$$f = |\theta|/T_N \quad (24.37)$$

is greater than 6, where  $T_N$  is the Néel temperature, namely, the temperature below which the system undergoes a three-dimensional AFM ordering.

### 24.5.2 Long-Range Antiferromagnetic Order

A magnetic system described by a Heisenberg spin Hamiltonian undergoes a three-dimensional long-range magnetic order if interactions between spin sites occur in all three directions so that its magnetic properties are three-dimensional in nature [42]. Here, the interactions leading to a long-range magnetic order can be spin exchange interactions and/or MDD interactions (see below). In terms of magnetic susceptibility, a three-dimensional AFM order is signaled by a sharp change in the  $\chi$  versus  $T$

**FIGURE 24.8**

The temperature dependence of (a) the magnetic susceptibility and (b) the specific heat of a magnetic solid undergoing a three-dimensional AFM ordering below  $T_N$ . For a single crystal sample with spin oriented along certain direction below  $T_N$ , the magnetic susceptibilities measured with magnetic field applied parallel and perpendicular to the spin direction are denoted by  $\chi_{\parallel}$  and  $\chi_{\perp}$ , respectively. The magnetic susceptibility measured for powder samples is denoted by  $\chi_{\text{av}}$ .

plot below  $T_N$  (Figure 24.8a). For the susceptibility measurement of an oriented single crystal, the  $\chi$  versus  $T$  plot depends on the direction of the probing magnetic field; for the field  $H_{\parallel}$  applied parallel to the easy axis (i.e., along the direction of the ordered spin moment), the susceptibility  $\chi_{\parallel}(T)$  approaches zero as  $T$  approaches zero. For the field  $H_{\perp}$  applied perpendicular to the easy axis, the susceptibility  $\chi_{\perp}(T)$  remains constant at the value at  $T_N$ ,  $\chi(T_N)$  as  $T$  approaches zero. For a powder sample, the powder-averaged susceptibility  $\chi_{\text{av}}(T)$  approaches the value  $\chi_{\text{av}}(0)$  as  $T$  approaches zero (Figure 24.8a).

$$\chi_{\text{av}}(0) = \left[ 2\chi_{\perp}(0) + \chi_{\parallel}(0) \right] / 3 = \frac{2}{3} \chi_{\perp}(T_N) \quad (24.38)$$

The occurrence of such a three dimensional AFM order is signaled by a  $\lambda$ -anomaly in the temperature dependence of the specific heat  $C_{p,\text{tot}}$  (Figure 24.8b), which has contributions from the populated vibrational and magnetic energy levels. Thus magnetic specific heat  $C_{p,\text{mag}}$  is obtained from the measured  $C_{p,\text{tot}}$  by subtracting the vibrational (phonon) specific heat  $C_{p,\text{vib}}$ , that is,  $C_{p,\text{mag}} = C_{p,\text{tot}} - C_{p,\text{vib}}$ , but the determination of  $C_{p,\text{vib}}$  is a nontrivial task. For a magnetic solid made up of spin  $S$  magnetic ions, the magnetic entropy change  $\Delta S$  associated with a three dimensional magnetic ordering is related to the loss of the spin degrees of freedom,  $2S + 1$ , as

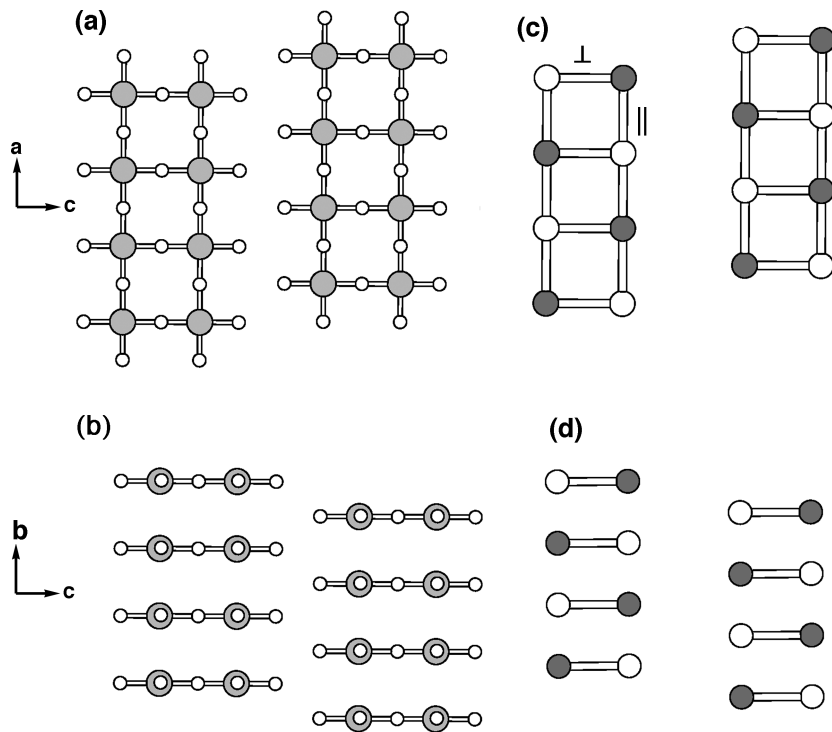
$$\Delta S = R \ln(2S + 1) \quad (24.39)$$

Experimentally,  $\Delta S$  is determined from the measured  $C_{p,\text{mag}}$  versus  $T$  data as

$$\Delta S = \int \frac{C_{p,\text{mag}}}{T} dT \quad (24.40)$$

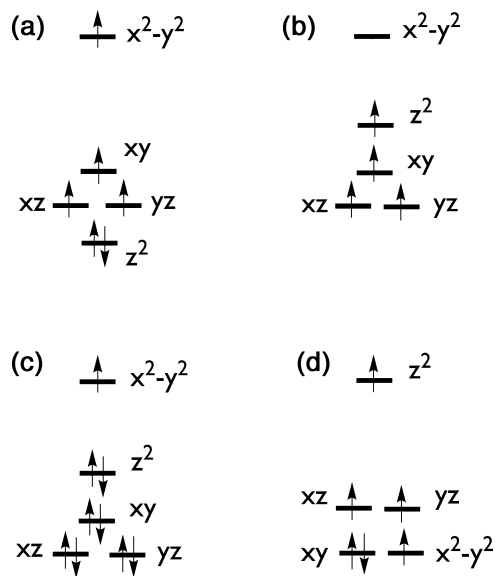
It should be pointed out that the  $\Delta S$  value expected from equation 24.39 assumes that there is no short-range order before the three dimensional long-range order takes place (see Section 24.5.3 for further discussion).

In most cases of magnetic solids undergoing a three-dimensional AFM order, spin exchange interactions occur in three directions. However, a two-dimensional AFM system can undergo a three-dimensional AFM order at high  $T_N$  with the help of MDD interactions, as found for the two-leg spin ladder compound  $\text{Sr}_3\text{Fe}_2\text{O}_5$  [41,43,44]. In this compound,  $\text{FeO}_4$  square planes containing high-spin  $\text{Fe}^{2+}$  ( $S = 2$ ,  $d^6$ ) ions share corners to form  $\text{Fe}_2\text{O}_5$  two-leg spin ladders along the  $b$ -direction, which are stacked along the  $a$ -direction to form  $\text{Fe}_2\text{O}_5$  slabs parallel to the  $ab$ -plane (Figure 24.9a,b). These slabs repeat along the  $c$ -direction such that adjacent  $\text{Fe}_2\text{O}_5$

**FIGURE 24.9**

Schematic projection views showing the  $\text{Fe}_2\text{O}_5$  ladders of  $\text{Sr}_3\text{Fe}_2\text{O}_5$  (a) along the  $a$ -direction and (b) along the  $b$ -direction. The AFM ordering in the  $\text{Fe}_2\text{O}_5$  ladders of  $\text{Sr}_3\text{Fe}_2\text{O}_5$  viewed (c) along the  $a$ -direction and (d) along the  $b$ -direction. In (a) and (b) the Fe atoms are indicated by large shaded circles. In (c) and (d) the shaded and unshaded circles represent up-spin and down-spin  $\text{Fe}^{2+}$  sites, respectively.

slabs differ in their  $a$ -axis height by  $a/2$  and in their  $b$ -axis height by  $b/2$ . The high-spin  $\text{Fe}^{2+}$  ( $d^6$ ) ion of a  $\text{FeO}_4$  square plane has the  $d$ -state split pattern,  $z^2 < (\text{xz}, \text{yz}) < \text{xy} < x^2 - y^2$  (Figure 24.10a) [41], and hence the electron configuration,  $(z^2)^2(\text{xz}, \text{yz})^1(\text{xy})^1(x^2 - y^2)^1$  leading to four magnetic orbitals. Within each two-leg spin ladder, the spin exchanges  $J_{||}$  along the legs and  $J_{\perp}$  along the rungs are both strongly AFM due to their linear  $\text{Fe}-\text{O}-\text{Fe}$  exchange paths and the  $x^2 - y^2$  magnetic orbitals involved (Figure 24.9b). The spin exchange  $J_a$  along the stacking direction of the spin ladders is also strongly AFM (Figure 24.9d) because the magnetic orbitals  $\text{xz}$  and  $\text{yz}$  overlap directly through space across the  $\text{Fe} \dots \text{Fe}$  contact (3.503 Å) [41]. The latter situation is the same as that found for the three dimensional antiferromagnet  $\text{SrFeO}_2$  [45,46], in which the  $\text{FeO}_2$  sheets made up

**FIGURE 24.10**

The  $d$ -level splitting patterns of (a) a high-spin  $\text{Fe}^{2+}$  ( $d^6$ ) ion in a  $\text{FeO}_4$  square plane, (b) a high-spin  $\text{Mn}^{3+}$  ( $d^4$ ) ion in an axially elongated  $\text{MnO}_6$  octahedron, (c) a  $\text{Cu}^{2+}$  ( $d^9$ ) ion in an axially elongated  $\text{CuO}_6$  octahedron, (d) a high-spin  $\text{Fe}^{2+}$  ( $d^6$ ) ion located at a linear coordinate site ( $D_{3d}$  local symmetry) of  $(\text{Me}_3\text{Si})_3\text{C}-\text{Fe}-\text{C}(\text{SiMe}_3)_3$ . The local  $z$ -axis is perpendicular to the  $\text{FeO}_4$  square plane in (a), and along the elongated  $\text{Mn}-\text{O}$  and  $\text{Cu}-\text{O}$  bonds in (b) and (c), respectively, and along the  $\text{C}-\text{Fe}-\text{C}$  axis in (d).

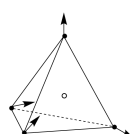
of corner-sharing  $\text{FeO}_4$  square planes stacked along the  $c$ -direction with  $\text{Sr}^{2+}$  ions in between adjacent  $\text{FeO}_2$  sheets. Thus in each two-dimensional  $\text{Fe}_2\text{O}_5$  slab, adjacent spin sites have a strong AFM coupling that doubles the cell along the  $a$ - and  $b$ -directions (Figure 24.9b,d). The exchange interactions between adjacent  $\text{Fe}_2\text{O}_5$  slabs vanish, since any given spin site of one slab is located above the center of an AFM rectangle ( $J_{\perp}, J_a, J_{\perp}, J_a$ ) of its adjacent slab. Consequently, as far as the spin exchange interactions are concerned,  $\text{Sr}_3\text{Fe}_2\text{O}_5$  is a two-dimensional AFM system and hence cannot undergo a three-dimensional AFM order [42]. Experimentally, however, it undergoes a three-dimensional AFM order at  $T_N = 296$  K leading to a (2 $a$ , 2 $b$ ,  $c$ ) magnetic supercell [44].

The additional interaction along the  $c$ -direction that  $\text{Sr}_3\text{Fe}_2\text{O}_5$  needs to undergo a three-dimensional AFM order is provided by the MDD interaction, which is a long-range interaction. The MDD interaction is weak, being of the order of 0.1 meV for two spin-1/2 ions separated by 2 Å. Given that two spins located at sites  $i$  and  $j$  are described by the distance  $r_{ij}$  with the unit vector  $\mathbf{e}_{ij}$  along the distance, the MDD interaction is described by [41]

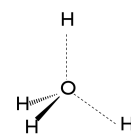
$$\left(\frac{g^2 \mu_B^2}{a_0^3}\right) \left(\frac{a_0}{r_{ij}}\right)^3 \left[ -3(\vec{S}_i \cdot \vec{e}_{ij})(\vec{S}_j \cdot \vec{e}_{ij}) + (\vec{S}_i \cdot \vec{S}_j) \right] \quad (24.41)$$

where  $a_0$  is the Bohr radius (0.529177 Å), and  $(g\mu_B)^2/(a_0)^3 = 0.725$  meV. The MDD effect on the preferred spin orientation of a given magnetic solid can be examined by comparing the MDD interaction energies calculated for a number of ordered spin arrangements. In summing the MDD interactions between various pairs of spin sites, it is necessary to employ the Ewald summation method [47]. Calculations of the MDD interaction energies of  $\text{Sr}_3\text{Fe}_2\text{O}_5$  with the spin orientations fixed along the  $a$ ,  $b$ - and  $c$ -directions (|| $a$ , || $b$  and || $c$ , respectively) show that the relative stabilities of the spin orientations decrease in the order, || $c$ >|| $b$ >|| $a$ , namely, the spins of  $\text{Sr}_3\text{Fe}_2\text{O}_5$  prefer the || $c$  direction (i.e., the rung direction of the two-leg ladder). The same conclusion is reached in terms of the magnetic anisotropy energies determined from DFT +  $U$  calculations with SOC effects included (see Section 24.7.1) [41].

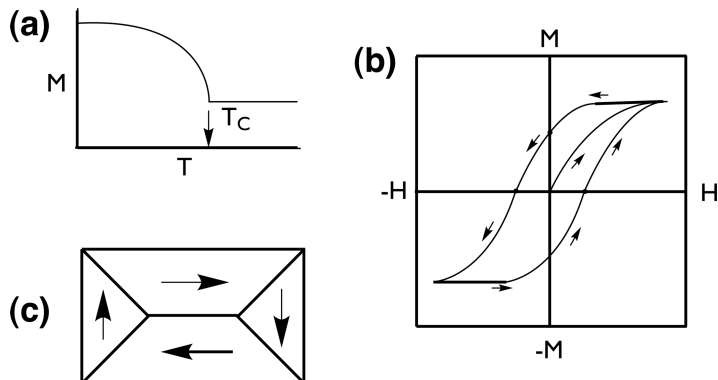
In discussing the three-dimensional magnetic order and the spin orientation of a magnetic solid, the MDD interaction is often neglected. However, this interaction can become nonnegligible especially when the spin  $S$  of a magnetic ion is large, because the MDD interaction is proportional to  $S^2$ . For example, in the magnetic compounds  $\text{Dy}_2\text{Ti}_2\text{O}_7$  and  $\text{Ho}_2\text{Ti}_2\text{O}_7$ , the rare-earth ions  $\text{Ho}^{3+}$  ( $f^{10}$ ) and  $\text{Dy}^{3+}$  ( $f^9$ ) form a pyrochlore spin lattice (24.20). The spin exchange between these ions should be negligible because their magnetic orbitals are given by their 4f orbitals. Given the pyrochlore spin lattice, the weak interactions between these ions are highly spin-frustrated. Nevertheless, at a very low temperature,  $\text{Dy}_2\text{Ti}_2\text{O}_7$  and  $\text{Ho}_2\text{Ti}_2\text{O}_7$  undergo a three-dimensional long-range magnetic order because of the MDD interaction [48]. In the ordered magnetic structure, the spins in each tetrahedron of spin sites have a “two-in-two-out” orientation (24.20), which resembles the arrangement of the two O—H bonds and two O...H hydrogen bonds around a  $\text{H}_2\text{O}$  molecule in ice (24.21). Thus  $\text{Dy}_2\text{Ti}_2\text{O}_7$  and  $\text{Ho}_2\text{Ti}_2\text{O}_7$  are known as spin ice systems.



24.20



24.21

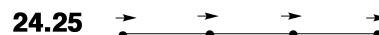
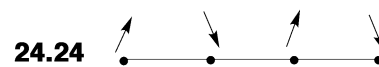
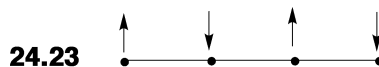
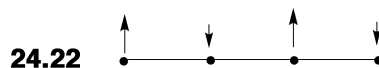
**FIGURE 24.11**

Representative properties of a magnetic system undergoing a ferromagnetic transition below  $T_c$ . (a) Magnetization versus temperature. (b) Magnetization versus magnetic field measured at a low temperature below  $T_c$ . (c) Ferromagnetic domains of a sample with different spin directions.

### 24.5.3 Ferromagnetic and Ferromagnetic-Like Transitions

For a magnetic system undergoing a FM phase transition below a critical temperature  $T_c$ , the magnetization  $\mathbf{M}$  as a function of temperature  $T$  shows a sharp increase below  $T_c$  and gradually approaches the saturation limit, as depicted in Figure 24.11a. At a low temperature below  $T_c$  the magnetization  $\mathbf{M}$  as a function of magnetic field  $\mathbf{H}$  exhibits a hysteresis loop as shown in Figure 24.11b. In the absence of magnetic field, a FM system does not have a single FM domain but possesses a large number of smaller FM domains such that the spin arrangement within each domain is FM, but that between adjacent domains is not (Figure 24.11c) [49]. The MDD interaction, which is a long-range interaction, is energetically unfavorable for a single FM domain. To avoid this unfavorable long-range MDD interaction, the system develops a large number of smaller FM domains with different spin orientations [49]. The non-FM spin arrangements in the regions between the domain boundaries are energetically unfavorable in terms of spin exchange interactions, but the removal of a single-domain FM order is energetically favorable in terms of the MDD interaction. In FM materials, the MDD interaction overcomes the unfavorable effect of the non-FM spin arrangements along the boundaries between adjacent FM domains.

A ferrimagnetic system, which contains two types of magnetic ions with different moments, undergoes an AFM ordering between the two types of ions (24.22) and as



a result generates a net nonzero moment. An AFM system (24.23) can generate a small net moment when its moments undergo spin canting (24.24), because it generates small net magnetic moments at the spin sites (24.25). The spin canting arises from the Dzyaloshinskii–Moriya (DM) interaction (see Section 24.7.4) [50]. The occurrence of spin canting in an AFM system is signaled by a sharp increase in the magnetic susceptibility at a low temperature. Below a certain low temperature, the magnetic susceptibility of a compound may depend on whether or not a magnetic

field is applied to its powder sample while it is being cooled. In such a case, a field-cooled (FC) sample generally exhibits a higher susceptibility than does a zero-field-cooled (ZFC) sample (24.31), which can occur when the sample undergoes a weak spin canting below a certain temperature hence acquiring a weak FM character.

#### 24.5.4 Typical Cases Leading to Ferromagnetic Interaction

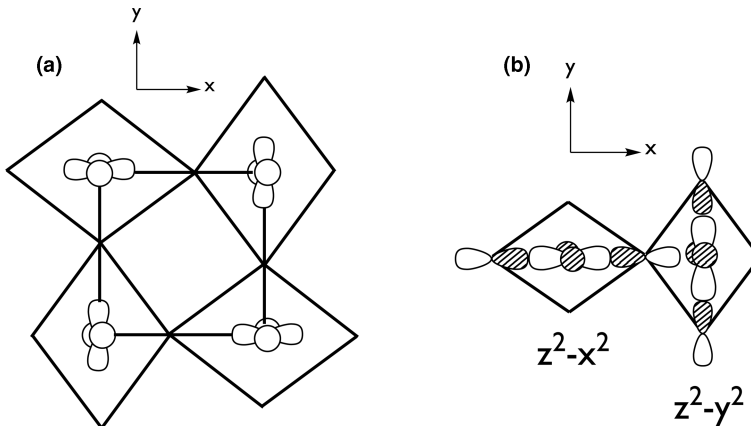
It is of interest to examine the typical situations leading to FM spin exchanges. Our discussion in Section 24.4.1 shows that, to have a FM spin exchange  $J$ , its  $J_F$  component should be stronger than its AFM component  $J_{AF}$ , namely, the overlap density between the magnetic orbitals involved should be large but the overlap integral between them should be small. An orbital ordering (equivalently, a cooperative Jahn–Teller distortion) leading to a FM exchange is related to the previously stated observation. In the perovskite fluoride  $\text{KCuF}_3$  made up of corner-sharing  $\text{CuF}_6$  octahedra [51], each  $\text{CuF}_6$  octahedron containing a  $\text{Cu}^{2+}$  ion undergoes a Jahn–Teller distortion to have short, medium, and long Cu–F distances (hereafter,  $\text{Cu}–\text{F}_s$ ,  $\text{Cu}–\text{F}_m$ , and  $\text{Cu}–\text{F}_l$ , respectively). Each  $\text{CuF}_6$  octahedron has the linear  $\text{F}_m–\text{Cu}–\text{F}_m$  unit along the  $c$ -direction, sharing the  $\text{F}_m$  atoms between adjacent  $\text{CuF}_6$  octahedra. In the  $ab$ -plane, each  $\text{CuF}_6$  octahedron has the linear  $\text{F}_s–\text{Cu}–\text{F}_s$  and  $\text{F}_l–\text{Cu}–\text{F}_l$  units perpendicular to each other, and the  $\text{Cu}–\text{F}_s$  bonds of one  $\text{CuF}_6$  octahedron are corner-shared with the  $\text{Cu}–\text{F}_l$  bonds of its adjacent  $\text{CuF}_6$  octahedra (Figure 24.12a). Let us consider this cooperative Jahn–Teller distortion (or orbital order) [52] from the viewpoint of an ideal  $\text{CuF}_6$  octahedron for which, by considering only the electrons at the  $e_g$  level, the electron configuration is given by  $(x^2 – y^2, z^2)^3$ . Since the  $x^2 – y^2$  and  $z^2$  (i.e.,  $3z^2 – r^2$ , to be precise) orbitals are degenerate, one can generate an alternative representation from their linear combinations

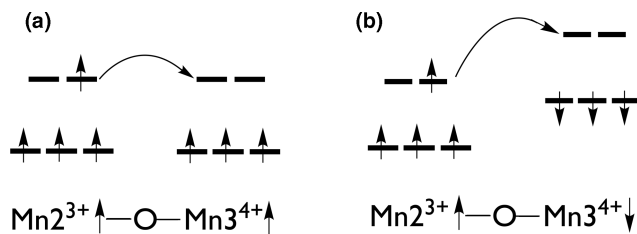
$$(3z^2 – r^2) \pm (x^2 – y^2) \rightarrow (z^2 – x^2, z^2 – y^2) \quad (24.42)$$

In the structure with the cooperative Jahn–Teller distortion (Figure 24.12a), the degeneracy of the  $z^2 – x^2$  and  $z^2 – y^2$  levels at each  $\text{CuF}_6$  octahedron is lifted. For each  $\text{CuF}_6$  octahedron with the  $\text{Cu}–\text{F}_l$  bonds along the  $x$ -direction, the  $z^2 – x^2$  is lower in energy than the  $z^2 – y^2$  level so that the  $z^2 – x^2$  is doubly occupied, and the  $z^2 – y^2$  level is singly occupied to become the magnetic orbital. The opposite happens for each  $\text{CuF}_6$  octahedron with the  $\text{Cu}–\text{F}_s$  bonds along the  $x$ -direction. Consequently, the magnetic orbitals are orthogonally ordered as depicted in Figure 24.12a. In this orbital ordered state, the spin exchange between neighboring sites is FM. It should be recalled that the  $z^2 – x^2$  and  $z^2 – y^2$  magnetic orbitals have the F 2p orbital tails as indicated in Figure 24.12b. Therefore, given the  $z^2 – x^2$  and  $z^2 – y^2$  magnetic orbitals

**FIGURE 24.12**

(a) The arrangement of the  $z^2 – x^2$  and  $z^2 – y^2$  orbitals of the  $\text{Cu}^{2+}$  ions in the  $\text{CuF}_4$  layer (parallel to the  $ab$ -plane) of  $\text{KCuF}_3$  in the orbital-ordered state. (b) The arrangement of the  $z^2 – x^2$  and  $z^2 – y^2$  orbitals of two adjacent  $\text{Cu}^{2+}$  sites in the  $\text{CuF}_4$  layer in the orbital-ordered state, showing the presence of strong overlap density between them hence leading to a FM spin exchange.



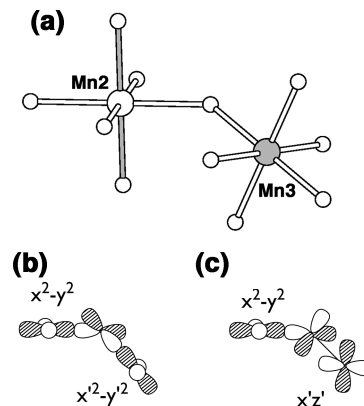
**FIGURE 24.13**

Interaction between two  $\text{Mn}^{3+}$  and  $\text{Mn}^{4+}$  sites (in octahedral environments) linked by a  $\text{Mn}-\text{O}-\text{Mn}$  bridge in the (a) FM and (b) AFM arrangements of their spins. Here it is assumed that  $\text{Mn}^{3+}\text{O}_6$  and  $\text{Mn}^{4+}\text{O}_6$  octahedra have the same structure.

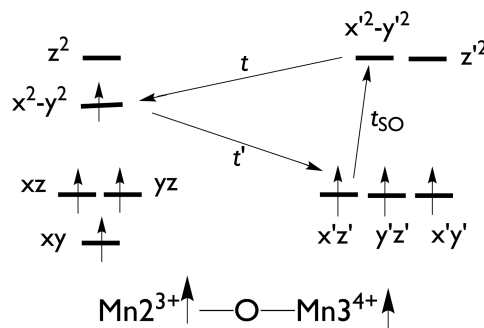
on adjacent  $\text{Cu}^{2+}$  sites, the overlap integral between them is zero by symmetry while the overlap density between them, which involves the  $\text{F} 2p$  tail of one magnetic orbital and the  $\text{Cu} 3d$  head of the other magnetic orbital (Figure 24.12b), is substantial because of the short  $\text{Cu}-\text{F}_s$  distance involved.

For magnetic oxides with mixed-valent magnetic ions  $\text{M}$  and  $\text{M}'$ , the  $\text{M}-\text{O}-\text{M}'$  spin exchange is commonly referred to as the double exchange [53], which can be either FM or AFM. We distinguish two different cases of double exchange. Let us first consider the case when the local structures of the spin sites are identical so that, as depicted in Figure 24.13a for high-spin  $\text{Mn}^{3+}$  ( $d^4$ ) and  $\text{Mn}^{4+}$  ( $d^3$ ) ions in octahedral environments, their  $d$ -block levels can be treated as identical. The strength of the hopping integral  $t$  between the spin sites is determined largely by the interaction between their  $e_g$  magnetic orbitals because the latter arise from  $\sigma^*$ -antibonding between the  $\text{Mn} 3d$  and  $\text{O} 2p$  orbitals. If the two adjacent  $\text{Mn}^{3+}$  and  $\text{Mn}^{4+}$  spins have a FM arrangement (Figure 24.13a), the filled  $e_g\uparrow$  level of the  $\text{Mn}^{3+}$  site and the empty  $e_g\uparrow$  level of the  $\text{Mn}^{4+}$  site are identical in energy so that the electron hopping from the  $\text{Mn}^{3+}$  to the  $\text{Mn}^{4+}$  site involves a degenerate orbital interaction. If the two adjacent  $\text{Mn}^{3+}$  and  $\text{Mn}^{4+}$  spins were to have an AFM arrangement (Figure 24.13b), the filled  $e_g\uparrow$  level of the  $\text{Mn}^{3+}$  site would be well separated from the empty  $e_g\uparrow$  level of the  $\text{Mn}^{4+}$  site (see Figure 24.2). Thus the electron hopping from the  $\text{Mn}^{3+}$  to the  $\text{Mn}^{4+}$  site involves a nondegenerate orbital interaction. Consequently, between adjacent  $\text{Mn}^{3+}$  to the  $\text{Mn}^{4+}$  ions, the FM arrangement is energetically more favorable than the AFM arrangement. This hopping gives rise to mobile electrons, and hence to a metallic conductivity.

As discussed in Section 17.4, a high spin  $d^3/d^4$  transition metal dimer is expected to be mixed valent, that is, the geometries are the two metal octahedra will be different. We now examine the case when mixed-valent spin sites possess different local structures by considering one specific  $\text{Mn}-\text{O}-\text{Mn}$  spin exchange interaction of  $\text{CaMn}_7\text{O}_{12}$ , which has three nonequivalent Mn atoms, that is, Mn1, Mn2, and Mn3. The spin exchange between the high-spin  $\text{Mn}^{2+}$  ( $d^4$ ) and  $\text{Mn}^{3+}$  ( $d^3$ ) ions has the  $\text{Mn}^{2+}-\text{O}-\text{Mn}^{3+}$  angle of  $137.6^\circ$  (Figure 24.14a) [54,55], in which the  $\text{Mn}^{2+}$  ( $d^4$ ) ion forms an axially compressed  $\text{MnO}_6$  octahedron, and the  $\text{Mn}^{3+}$  ( $d^3$ ) ion a nearly ideal  $\text{MnO}_6$  octahedron. The local coordinates around the  $\text{Mn}^{2+}\text{O}_6$  and  $\text{Mn}^{3+}\text{O}_6$  octahedra are described by  $(x, y, z)$  and  $(x', y', z')$ , respectively. If the two adjacent  $\text{Mn}^{2+}$  and  $\text{Mn}^{3+}$  spins have a FM arrangement, there is a small energy gap in the filled  $x^2 - y^2$  level of the  $\text{Mn}^{2+}$  site and the empty  $x'^2 - y'^2$  level of the  $\text{Mn}^{3+}$  site has a small energy gap (Figure 24.15) [55]. This energy gap would be greater if the two adjacent  $\text{Mn}^{2+}$  and  $\text{Mn}^{3+}$  spins were to have an AFM arrangement (see Figure 24.2). In terms of this energy gap consideration, the FM arrangement is favored over the AFM arrangement. However, the  $\text{Mn}^{2+}-\text{O}-\text{Mn}^{3+}$  angle of this exchange path is rather large ( $137.6^\circ$ ), so that the overlap integral as well as the overlap density between the  $\text{O} 2p$  tails of the two  $x^2 - y^2$  magnetic orbitals at the shared O atom are both strong (Figure 24.14b), leading to the competition of the  $J_F$  and  $J_{AF}$

**FIGURE 24.14**

The spin exchange between the high-spin  $\text{Mn}^{2+}$  ( $d^4$ ) and  $\text{Mn}^{3+}$  ( $d^3$ ) ions: (a) A perspective view of the exchange path. The short  $\text{Mn}2\text{-O}$  bonds of the axially-compressed  $\text{Mn}_2\text{O}_6$  octahedron are shaded. (b) The arrangement of the  $\text{O } 2p$  tails of the  $x^2 - y^2$  magnetic orbital of  $\text{Mn}^{2+}$  and the  $x'^2 - y'^2$  magnetic orbital of  $\text{Mn}^{3+}$  at the  $\text{O}$  atom of the  $\text{Mn}^{2+}\text{-O-}\text{Mn}^{3+}$  bridge. (c) The arrangement of the  $\text{O } 2p$  tails of the  $x^2 - y^2$  magnetic orbital of  $\text{Mn}^{2+}$  and the  $x'z'$  magnetic orbital of  $\text{Mn}^{3+}$  at the shared  $\text{O}$  atom of the  $\text{Mn}^{2+}\text{-O-}\text{Mn}^{3+}$  bridge.

**FIGURE 24.15**

The  $d$ -block levels of the axially compressed  $\text{Mn}_2\text{O}_6$  octahedron and the nearly ideal  $\text{Mn}_3\text{O}_6$  octahedra forming the  $\text{Mn}^{2+}\text{-O-}\text{Mn}^{3+}$  exchange path with  $\text{Mn}^{2+}\text{-O-}\text{Mn}^{3+} = 137.6^\circ$  in  $\text{CaMn}_7\text{O}_{12}$ . The energy levels are given assuming that the  $\text{Mn}^{2+}$  and  $\text{Mn}^{3+}$  spins have a FM arrangement. The  $x^2 - y^2$  magnetic orbital of  $\text{Mn}^{2+}$  interacts strongly with the  $x'^2 - y'^2$  magnetic orbital of  $\text{Mn}^{3+}$  and also with the  $x'z'$  magnetic orbital of  $\text{Mn}^{3+}$ . At the  $\text{Mn}^{3+}$  site the  $x^2 - y^2$  magnetic orbital interacts with the  $x'z'$  magnetic orbital by SOC.

contributions. Indeed, DFT +  $U$  calculations for  $\text{CaMn}_7\text{O}_{12}$  with  $U^{\text{eff}}$  on Mn show that this exchange is FM when  $U^{\text{eff}}$  is greater than a certain value (i.e.,  $\sim 3$  eV), but is AFM otherwise [55]. This is understandable because the  $J_{\text{AF}}$  term is diminished with increasing  $U^{\text{eff}}$  (equation 24.27).

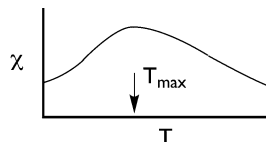
For the spin exchange between  $\text{Mn}^{2+}$  ( $d^4$ ) and  $\text{Mn}^{3+}$  ( $d^3$ ) ions in  $\text{CaMn}_7\text{O}_{12}$  discussed earlier, we note that the  $\text{O } 2p$  tail of the  $x^2 - y^2$  magnetic orbital of the  $\text{Mn}^{3+}$  ion also overlaps well with that of the  $x'z'$  magnetic orbital of the  $\text{Mn}^{3+}$  ion (Figure 24.14c). As will be discussed later, this gives to a very strong DM interaction between the  $\text{Mn}^{2+}$  and  $\text{Mn}^{3+}$  sites (see Section 24.7.4) [55].

### 24.5.5 Short-Range Order

Two dimensional, one-dimensional, and zero-dimensional magnetic systems described by a Heisenberg spin Hamiltonian cannot have a long-range magnetic order. Due to the absence of a long-range magnetic order, these systems exhibit no  $\lambda$ -type anomaly in the temperature-dependence of  $C_{p,\text{mag}}$ . Nevertheless, they can exhibit short-range order, namely, patches with AFM order are made and broken dynamically with no communication between different ordered patches. The occurrence of such a short-range order in a uniform Heisenberg AFM chain described by the NN AFM exchange  $J$  (24.26) is manifested by the presence of an extended broad maximum in the  $\chi$  versus  $T$  plot (24.27). For a Heisenberg AFM uniform chain made



24.26



24.27

up of spin  $S$  ions with NN spin exchange  $J$ , suppose that the magnetic susceptibility maximum  $\chi_{\max}$  occurs at temperature  $T_{\max}$ . Then the spin exchange  $J$  is related to the  $T_{\max}$  as [56]

$$\frac{k_B T_{\max}}{|J|} = C \quad (24.43)$$

where the constant  $C = 0.641$  for  $S = 1/2$ ,  $1.35$  for  $S = 1$ ,  $2.38$  for  $S = 3/2$ ,  $3.55$  for  $S = 2$ , and  $5.30$  for  $S = 5/2$ .

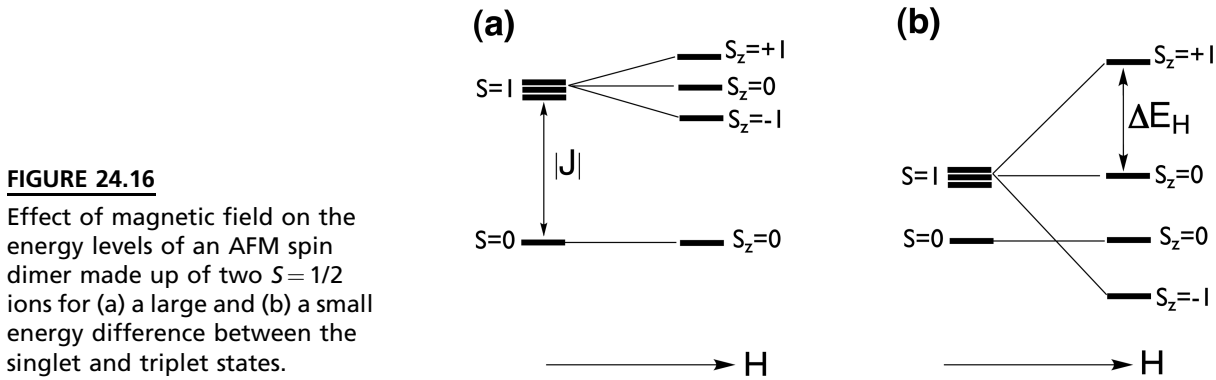
A magnetic system that is primarily a one-dimensional AF chain may possess weak interchain interactions in the remaining two directions. In such a case, the system will exhibit a short-range-order behavior, which is then followed by a three-dimensional long-range order. The entropy change  $\Delta S$  determined from the associated  $C_{p,\text{mag}}$  versus  $T$  curve is smaller than  $R \ln(2S + 1)$ , because the system has lost some entropy due to the short-range order. That is, the three-dimensional order in such a case is an order of the short-range-ordered segments.

## 24.6 THE ENERGY GAP IN THE MAGNETIC ENERGY SPECTRUM

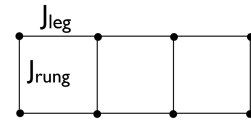
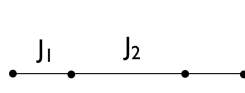
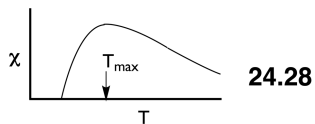
### 24.6.1 Spin Gap and Field-Induced Magnetic Order

The  $\chi$  versus  $T$  plot of a uniform Heisenberg AFM chain shows that the susceptibility at  $T = 0$  is nonzero (24.27), which is due to the fact that there is no energy gap between the magnetic ground and excited states. This is true for a one-dimensional Heisenberg uniform AFM chain made up of half-integer-spin ions. However, this is not the case for the chains made up of integer-spin ions according to the Haldane conjecture [57], which predicts that there is an energy gap between the magnetic ground and excited states. Indeed, experimentally, the quasi one-dimensional Heisenberg antiferromagnet  $\text{Ni}(\text{C}_2\text{H}_8\text{N}_2)_2\text{NO}_2(\text{ClO}_4)$ , containing uniform chains of  $S = 1$   $\text{Ni}^{2+}$  ions, are found to have a spin gap [58].

Certain AFM systems made up of half-integer-spin ions have a substantial energy gap between the magnetic ground and excited states. For example, consider a spin dimer with AFM spin exchange  $J$ . If the magnitude of the exchange  $J$  is large and the applied magnetic field is weak, the lowest Zeeman split level (i.e.,  $S_z = -1$  level) of the

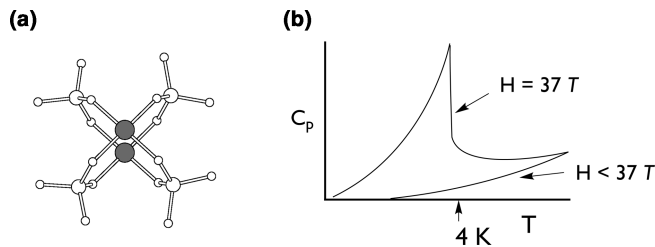


triplet state is still well above the singlet state so that, below a certain temperature, the available thermal energy  $k_B T$  is not large enough to thermally populate the  $S_z = -1$  level (Figure 24.16a). Consequently, the magnetic susceptibility becomes zero below a certain temperature (24.28). Namely, an AFM spin dimer is a spin-gapped system. Other representative spin-gap systems include a Heisenberg alternating chain (24.29) with two different spin exchanges (AFM  $J_1$  and AFM  $J_2$ , or AFM  $J_1$



and FM  $J_2$ , see Section 24.8.2) and a two-leg spin ladder with AFM rung and leg spin exchanges ( $J_{\text{rung}}$  and  $J_{\text{leg}}$ , respectively) (24.30).

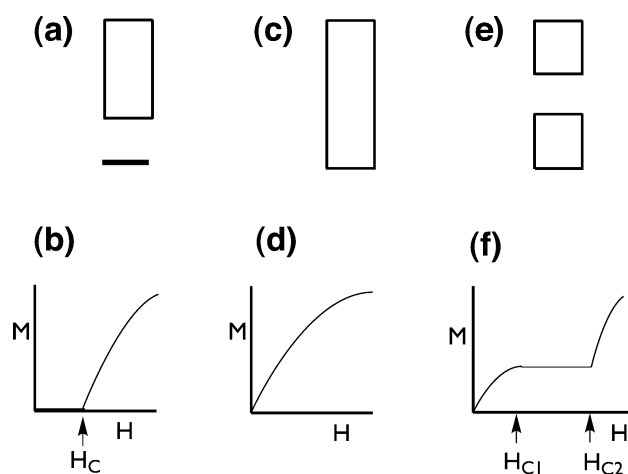
A magnetic system consisting of AFM spin dimers, being a zero-dimensional magnetic system, cannot undergo a three-dimensional long-range order [42]. An interesting situation occurs for an AFM spin dimer with small  $|J|$  when a large magnetic field is applied. In such a case, the  $S_z = -1$  level of the triplet state becomes lower in energy than the  $S_z = 0$  level of the singlet state (Figure 24.16b). As a result, the spin dimer behaves as an integer-spin (i.e., Bose-Einstein) system. This means that all spin dimers can have the same lowest-energy state, namely, the magnetic system now has a three-dimensional long range order although there is no interaction between the spin dimers. Such a field-induced three-dimensional ordering occurs in  $\text{BaCuSi}_2\text{O}_6$ , [59,60] in which each spin dimer is made up of two  $\text{CuO}_4$  square planes stacked on top of each other and corner-shared with four  $\text{SiO}_4$  tetrahedra (Figure 24.17a). The  $\text{Cu}-\text{O}\dots\text{Si}^{4+}\dots\text{O}-\text{Cu}$  spin exchange is weak, so that the spin exchange  $J$  for this spin dimer is weak. The specific heat measurements on  $\text{BaCuSi}_2\text{O}_6$  show a  $\lambda$ -like anomaly when the applied magnetic field greater than 34 T, thereby showing a field-induced three-dimensional ordering in  $\text{BaCuSi}_2\text{O}_6$  (Figure 24.17b) [60].

**FIGURE 24.17**

(a) A spin dimer unit of  $\text{BaCuSi}_2\text{O}_6$ , in which two  $\text{CuO}_4$  square planes are stacked on top of each other and are corner-shared with four  $\text{SiO}_4$  tetrahedra. (b) The specific heat of  $\text{BaCuSi}_2\text{O}_6$  measured in the absence and presence of strong magnetic field. It shows a  $\lambda$ -like anomaly when the applied magnetic field greater than 34 T, thereby showing a field-induced three-dimensional ordering in  $\text{BaCuSi}_2\text{O}_6$ .

### 24.6.2 Magnetization Plateaus

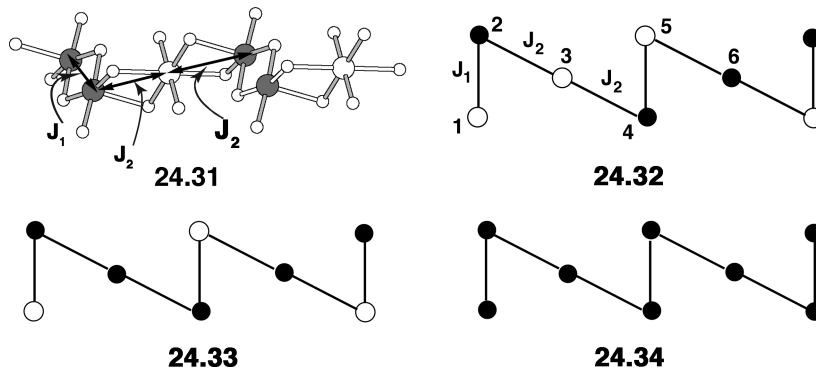
Let us examine the energy spectrum of a magnetic system from the viewpoint of its allowed energies under a magnetic field by considering an AFM spin dimer. As depicted in Figure 24.16, the singlet state is unaffected by the magnetic field but the triplet state is split into three levels by the field. The energy difference  $\Delta E_H$  between the adjacent Zeeman split levels increases continuously from zero at  $H=0$  with increasing  $H$ . Therefore, the allowed energy spectrum of the spin dimer under magnetic field can be depicted as in Figure 24.18a, where it is assumed that the field is not strong enough for the  $S_z = -1$  level of the triplet state to reach the  $S_z = 0$  level of the singlet ground state. The energy band associated with the triplet state indicates the region of energy that can be reached continuously by increasing the field  $H$ ; the allowed energies of the triplet are given by the midpoint of the band at  $H=0$ , and sweep toward the band bottom and the band top with increasing  $H$  from zero. The magnetization  $M$  of the above spin dimer as a function of  $H$  at a very low temperature behaves as shown in Figure 24.18b, which shows  $M=0$  until  $H$  reaches a critical value  $H_c$  because, at field  $H$  smaller than  $H_c$ , the system cannot reach the bottom of the triplet band so that  $M=0$ . Once  $H > H_c$ ,  $M$  increases gradually with increasing  $H$ . The flat region of the  $M$  versus  $H$  plot is known as the magnetization plateau. Since this plateau occurs at  $M=0$ , it is a zero magnetization plateau. All spin-gap systems should show a zero magnetization plateau. If the energy spectrum of a magnetic system under magnetic field has no energy gap (Figure 24.18c), the  $M$  increases

**FIGURE 24.18**

Schematic diagrams showing how the magnetization plateau is related to an energy gap of the energy spectrum that a magnetic system can have under magnetic field. A spin gap in the energy spectrum, (a), leads to the zero magnetization plateau, (b). A magnetic system with no energy gap, (c), shows no magnetization plateau, (d). An energy gap in the middle of the energy spectrum, (e), leads to a finite magnetization plateau, (f).

gradually with increasing  $H$  with no magnetization plateau until the magnetization reaches its saturation value (Figure 24.18d).

It should be noted that the energy bands of a magnetic system under magnetic field may possess an energy gap in the middle of the energy spectrum (Figure 24.18e). In such a case the magnetization plateau of the  $M$  versus  $H$  plot occurs at a nonzero  $M$  value (i.e., finite magnetization plateau) between two critical magnetic fields  $H_{c1}$  and  $H_{c2}$  (Figure 24.18f). Such a finite magnetization plateau is found for a low-dimensional AFM system such as  $\text{Cu}_3(\text{P}_2\text{O}_6\text{OH})_2$  [61–63] and  $\text{Cu}_3(\text{CO}_3)_2(\text{OH})_2$  [64,65], which exhibit a 1/3 magnetization plateau. The oxide  $\text{Cu}_3(\text{P}_2\text{O}_6\text{OH})_2$  consists of zigzag AFM chains of  $\text{Cu}^{2+}$  ions depicted in 24.31, and these chains interact to give rise to two-dimensional magnetic character [63]. Nevertheless, the



1/3 magnetization plateaus can be readily rationalized by considering this one-dimensional AFM chain defined by two spin exchanges  $J_1$  and  $J_2$ . The repeat unit of this AFM chain has six spin-1/2  $\text{Cu}^{2+}$  ions with the magnetic bond sequence of  $J_1\text{-}J_2\text{-}J_2\text{-}J_1\text{-}J_2\text{-}J_2$ . The AFM arrangement (24.32) has zero net moment so the average moment  $m$  per spin site is zero.  $J_2$  is considerably weaker than  $J_1$  (i.e.,  $J_2/J_1 \approx 0.01$ ) [63], so the spin moments at the sites making only  $J_2$  magnetic bonds will be broken first to eventually line up with the field  $H$  as the latter increases from zero. This leads to the initial increase in  $M$  with increasing  $H$ . The magnetic structure corresponding to the 1/3 magnetization plateau is depicted in 24.33, in which the spin at site 3 is flipped so that  $m = 1/3$ . The spin flips at sites 1 and 5 will lead to the saturation magnetization ( $m = 1$ ) (24.34). However, the  $J_1$  magnetic bond is strong so that this does not happen unless the field is stronger than a critical value  $H_{c2}$ . This explains why a 1/3 magnetization plateau occurs between  $H_{c1}$  and  $H_{c2}$ . For an AFM chain made up of spin  $S$  magnetic ions with  $n$  sites per magnetic unit cell, the average magnetization per site  $m$  is predicted to occur if

$$n(S - m) = \text{integer} \quad (24.44)$$

The magnetic structure of  $\text{Cu}_3(\text{OH})_2(\text{CO}_3)_2$  will be discussed in Section 24.8.3.

## 24.7 SPIN-ORBIT COUPLING

### 24.7.1 Spin Orientation

Experimentally, the spin orientations of a magnetic solid are determined by neutron diffraction measurements. From the viewpoint of theory, the spin orientation in

coordinate space is set by SOC, which for an atom with many unpaired electrons and total spin  $S$  is expressed as

$$\hat{H}_{SO} = \lambda \hat{S} \cdot \hat{L} \quad (24.45)$$

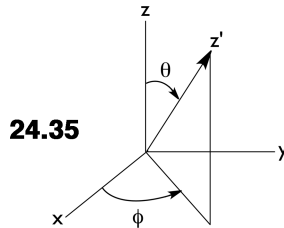
where the SOC constant  $\lambda$  is positive if the electron shell containing unpaired electrons is less than half-filled [e.g.,  $V^{4+}$  ( $d^1$ )], but is negative if the shell is more than half-filled [e.g.,  $Cu^{2+}$  ( $d^9$ )]. The lowest energy spin-orbit coupled state for  $\lambda > 0$  is obtained when  $\mathbf{L}$  and  $\mathbf{S}$  are antiparallel leading to  $\mathbf{J} = \mathbf{L} - \mathbf{S}$ , but that for  $\lambda < 0$  when  $\mathbf{L}$  and  $\mathbf{S}$  are parallel leading to  $\mathbf{J} = \mathbf{L} + \mathbf{S}$ . In a magnetic solid the magnetic moment of each spin site results from the spin moment interacting with the unquenched orbital moment under  $H_{SO}$ . In general, the magnitude of  $\lambda$  increases on going from the  $3d$  to  $4d$  to  $5d$  in a given family of transition-metal atoms, and also with increasing the oxidation state for a given  $nd$  element [23,66].

An important consequence of SOC is that the spin gets a preferred orientation in space with respect to the crystal lattice. Before we examine how this comes about, it is necessary to recall that the orbital angular momentum states  $|L, L_z\rangle$  follow the relationships

$$\begin{aligned}\hat{L}_z |L, L_z\rangle &= L_z |L, L_z\rangle \\ \hat{L}_+ |L, L_z\rangle &= \sqrt{L(L+1) - L_z(L_z+1)} |L, L_z+1\rangle \\ \hat{L}_- |L, L_z\rangle &= \sqrt{L(L+1) - L_z(L_z-1)} |L, L_z-1\rangle\end{aligned} \quad (24.46)$$

where the ladder operators are given by  $\hat{L}_+ = \hat{L}_x + i\hat{L}_y$  and  $\hat{L}_- = \hat{L}_x - i\hat{L}_y$ . That is,  $|L, L_z\rangle$  is an eigenstate of  $\hat{L}_z$ , but is not an eigenstate of  $\hat{L}_+$  and  $\hat{L}_-$ . The spin states  $|S, S_z\rangle$  follow the analogous relationships as discussed earlier (equation 24.16). These relationships play an important role in our discussion of SOC and spin orientation in space which are described in the forthcoming text.

To gain insight into how the  $\hat{S} \cdot \hat{L}$  term governs the spin orientation in space, it is necessary to employ two independent coordinate systems, that is,  $(x, y, z)$  for  $\hat{L}$  and  $(x', y', z')$  for  $\hat{S}$ . Then, the preferred spin direction  $z'$  is described by the two angles  $(\theta, \phi)$ , where  $\theta$  and  $\phi$  as the azimuthal and polar angles of the preferred spin direction with



respect to the  $(x, y, z)$  coordinate system (24.35). As a consequence, the  $\hat{H}_{SO} = \lambda \hat{S} \cdot \hat{L}$  term is written as [23,67]

$$\begin{aligned}\hat{H}_{SO} &= \lambda \hat{S}_{z'} \left( \hat{L}_z \cos \theta + \frac{1}{2} \hat{L}_+ e^{-i\varphi} \sin \theta + \frac{1}{2} \hat{L}_- e^{i\varphi} \sin \theta \right) \\ &\quad + \frac{\lambda}{2} \hat{S}_{+'} \left( -\hat{L}_z \sin \theta - \hat{L}_+ e^{-i\varphi} \sin^2 \frac{\theta}{2} + \hat{L}_- e^{i\varphi} \cos^2 \frac{\theta}{2} \right) \\ &\quad + \frac{\lambda}{2} \hat{S}_{-'} \left( -\hat{L}_z \sin \theta + \hat{L}_+ e^{-i\varphi} \cos^2 \frac{\theta}{2} - \hat{L}_- e^{i\varphi} \sin^2 \frac{\theta}{2} \right)\end{aligned} \quad (24.47)$$

This expression shows how the SOC energy depends on the spin orientation ( $\theta, \phi$ ). To determine the energetically favorable spin orientation of a magnetic solid, one can determine its total energy on the basis of DFT +  $U$  + SOC calculations as a function of the spin orientation [68]. Then, the preferred spin orientation is the direction that provides the lowest total energy. Experimentally, neutron diffraction refinements at a very low temperature provide information about the magnitudes and orientations of the moments at the spin sites of a magnetic solid. In the following discussion of the preferred spin orientation, it is convenient to express the d-levels  $x^2 - y^2$ ,  $xy$ ,  $yz$ ,  $xz$ , and  $z^2$  in terms of the spherical harmonics  $Y_2^m$  ( $m = -2, -1, 0, 1, 2$ ) as shown in equation 24.48 (note that the  $l$  and  $m$  values of the spherical harmonics  $Y_l^m$  correspond to  $L$  and  $L_z$  values, respectively).

$$\begin{aligned} x^2 - y^2 &\propto (Y_2^2 + Y_2^{-2})/\sqrt{2} \\ xy &\propto -i(Y_2^2 - Y_2^{-2})/\sqrt{2} \\ yz &\propto i(Y_2^1 + Y_2^{-1})/\sqrt{2} \\ xz &\propto -(Y_2^1 - Y_2^{-1})/\sqrt{2} \\ z^2 &\propto Y_2^0 \end{aligned} \quad (24.48)$$

On the basis of the  $m$  values, the d-states can be classified in terms of  $d_m$  ( $m = \pm 2, \pm 1, 0$ ) so that we have the following equivalences:

$$\begin{aligned} (x^2 - y^2, xy) &\leftrightarrow (d_2, d_{-2}) \\ (xz, yz) &\leftrightarrow (d_1, d_{-1}) \\ z^2 &\leftrightarrow d_0 \end{aligned} \quad (24.49)$$

For a qualitative discussion of spin orientation, it is convenient to rewrite the SOC Hamiltonian  $\hat{H}_{\text{SO}}$  as

$$\hat{H}_{\text{SO}} = \hat{H}_{\text{SO}}^0 + \hat{H}'_{\text{SO}} \quad (24.50)$$

where  $\hat{H}_{\text{SO}}^0$  is the “spin-conserving” term (i.e., the first line of equation 24.47).

$$\hat{H}_{\text{SO}}^0 = \lambda \hat{S}_z' \left( \hat{L}_z \cos \theta + \frac{1}{2} \hat{L}_+ e^{-i\varphi} \sin \theta + \frac{1}{2} \hat{L}_- e^{i\varphi} \sin \theta \right) \quad (24.51)$$

and  $\hat{H}'_{\text{SO}}$  is the “spin-nonconserving” term (i.e., the second and third lines of equation 24.47)

$$\begin{aligned} \hat{H}'_{\text{SO}} = & \frac{\lambda}{2} \hat{S}_{+'} \left( -\hat{L}_z \sin \theta - \hat{L}_+ e^{-i\varphi} \sin^2 \frac{\theta}{2} + \hat{L}_- e^{i\varphi} \cos^2 \frac{\theta}{2} \right) \\ & + \frac{\lambda}{2} \hat{S}_{-'} \left( -\hat{L}_z \sin \theta + \hat{L}_+ e^{-i\varphi} \cos^2 \frac{\theta}{2} - \hat{L}_- e^{i\varphi} \sin^2 \frac{\theta}{2} \right) \end{aligned} \quad (24.52)$$

The preferred spin orientation can be understood on the basis of perturbation theory by treating these SOC Hamiltonians as perturbation with the split d-block levels of a magnetic ion as unperturbed states. When an occupied d-level  $i = \Psi_o \uparrow$  (or  $\Psi_o \downarrow$ ) with energy  $e_i$  interacts with an unoccupied d-level  $j = \Psi_u \uparrow$  (or  $\Psi_u \downarrow$ ) with energy  $e_j$  via the matrix element  $\langle i | \hat{H}_{\text{SO}}^0 | j \rangle$ , the associated energy lowering is given by

$$\Delta E_{\text{SO}} = - \frac{|\langle i | \hat{H}_{\text{SO}}^0 | j \rangle|^2}{|e_i - e_j|} \quad (24.53a)$$

(Here  $\left| \langle i | \hat{H}_{SO}^0 | j \rangle \right|^2$  represents  $\langle i | \hat{H}_{SO}^0 | j \rangle \langle j | \hat{H}_{SO}^0 | i \rangle$ .) When an occupied d-level  $i = \Psi_o \uparrow$  with energy  $e_i$  interacts with an unoccupied d-level  $j = \Psi_u \downarrow$  with energy  $e_j$  via the matrix element  $\langle i | \hat{H}'_{SO} | j \rangle$ , the associated energy lowering is given by

$$\Delta E_{SO} = -\frac{\left| \langle i | \hat{H}'_{SO} | j \rangle \right|^2}{|e_i - e_j|} \quad (24.53b)$$

In determining the preferred spin orientation, the most important interaction between occupied and unoccupied spin levels is the one with the smallest energy gap  $\Delta e = (e_i - e_j)$ . The d-levels of same  $|m|$  values (e.g., between  $xz$  and  $yz$ , and between  $xy$  and  $x^2 - y^2$ ) interact through the operator  $\hat{L}_z$  to give nonzero  $\langle i | \hat{H}_{SO}^0 | j \rangle$  and  $\langle i | \hat{H}'_{SO} | j \rangle$ . The d-levels of different  $m$  values with  $\Delta m = 1$  (e.g., between  $xz/yz$  and  $xy/(x^2 - y^2)$ , and between  $z^2$  and  $xz/yz$ ) interact through the ladder operators  $\hat{L}_+$  and  $\hat{L}_-$  to give nonzero  $\langle i | \hat{H}_{SO}^0 | j \rangle$  and  $\langle i | \hat{H}'_{SO} | j \rangle$ . The  $z^2$  orbital cannot interact with the  $xy$  ( $x^2 - y^2$ ) orbitals under SOC because their  $m$  values differ by  $\Delta m = 2$ .

To illustrate the use of equation 24.51, we consider two examples. The high-spin  $\text{Fe}^{2+}$  ( $d^6$ ) ions of the  $\text{FeO}_4$  square planes in  $\text{Sr}_3\text{Fe}_2\text{O}_5$  [41,43,44] and  $\text{SrFeO}_2$  [45,46] exhibit easy-plane anisotropy (i.e., the  $\theta = 90^\circ$  spin orientation), while the high-spin  $\text{Mn}^{3+}$  ( $d^4$ ) ions of axially elongated  $\text{MnO}_6$  octahedra in  $\text{TbMnO}_3$  [69,70] and  $\text{Ag}_2\text{MnO}_2$  [71] show easy-axis anisotropy (i.e., the  $\theta = 0^\circ$  spin orientation). The high-spin  $\text{Fe}^{2+}$  ( $d^6$ ) ion of a  $\text{FeO}_4$  square plane has the d-state splitting pattern  $(z^2)^2 < (xz, yz)^2 < (xy)^1 < (x^2 - y^2)^1$  (Figure 24.10a). In the spin-polarized description associated with DFT +  $U$  calculations [41,44], this splitting pattern is equivalent to

$$(z^2 \uparrow)^1 < (xz \uparrow, yz \uparrow)^1 < (xy \uparrow)^1 < (x^2 - y^2 \uparrow)^1 \\ < (z^2 \downarrow)^1 < (xz \downarrow, yz \downarrow)^0 < (xy \downarrow)^0 < (x^2 - y^2 \downarrow)^0$$

Namely, for the high-spin  $\text{Fe}^{2+}$  ( $d^6$ ) ion, the lowest energy gap between the occupied and unoccupied levels occurs between the  $z^2 \downarrow$  and the  $xz \downarrow/yz \downarrow$  levels. Since these levels differ in their  $m$  values by  $\pm 1$ , their interaction leads to a maximum energy gain when the spin is perpendicular to the orbital z-axis (i.e.,  $\theta = 90^\circ$ ). Namely, the preferred spin orientation of the  $\text{Fe}^{2+}$  ion is perpendicular to the z-axis (i.e., easy-plane anisotropy). For the high-spin  $\text{Mn}^{3+}$  ( $d^4$ ) ion of an axially elongated  $\text{MnO}_6$  octahedron (with the z-axis taken along the elongated Mn–O bond) (Figure 24.10b), the  $\text{Mn}^{3+}$  ion has the d-state splitting pattern [70,71]

$$(xz \uparrow, yz \uparrow)^1 < (xy \uparrow)^1 < (z^2 \uparrow)^1 < (x^2 - y^2 \uparrow)^0$$

so that the lowest energy gap between occupied and unoccupied levels occurs between the  $z^2 \uparrow$  and  $(x^2 - y^2) \uparrow$  levels. However, these two cannot interact under  $\hat{H}_{SO}^0$  because their  $m$  values differ by  $\Delta m = 2$ . The next lowest energy gap occurs for the  $xy \uparrow$  and the  $x^2 - y^2 \uparrow$  levels, for which  $\Delta m = 0$ , and their interaction leads to a maximum energy gain if  $\theta = 0^\circ$ . Namely, the preferred spin direction is parallel to the orbital z-axis (i.e., easy-axis anisotropy).

To illustrate the use of equation 24.52, we consider the  $\text{Cu}^{2+}$  ( $d^9, S = 1/2$ ) ion of a  $\text{CuO}_4$  square plane (or an axially elongated  $\text{CuO}_6$  octahedron) with the d-electron configuration  $(xz, yz)^4 < (xy)^2 < (z^2)^2 < (x^2 - y^2)^1$  (Figure 24.10c). In the spin-polarized description associated with DFT +  $U$  calculations, this splitting pattern means the sequence  $(xz \uparrow, yz \uparrow)^2 < (xy \uparrow)^1 < (z^2 \uparrow)^1 < (x^2 - y^2 \uparrow)^1$  for the up-spin d-states, and the sequence  $(xz \downarrow, yz \downarrow)^2 < (xy \downarrow)^1 < (z^2 \downarrow)^1 < (x^2 - y^2 \downarrow)^0$  for the down-spin d-states. According to the spin-polarized DFT +  $U$  calculations for compounds consisting of  $\text{CuL}_4$  ( $L = \text{O}, \text{Cl}, \text{Br}$ ) square planes [e.g.,  $\text{LiCuVO}_4$  [27,28],  $\text{Bi}_2\text{CuO}_4$  [73],  $\text{CuCl}_2$  [74],

and CuBr<sub>2</sub> [75]; the up-spin and down-spin d-states overlap in energy substantially such that the energy gap between  $(x^2 - y^2\uparrow)^1$  and  $(x^2 - y^2\downarrow)^0$  is considerably smaller than the gap the  $(x^2 - y^2\downarrow)^0$  level makes with any other down-spin d-levels [72]. Therefore, one might consider [1b] that the spin orientation will be governed by  $\hat{H}'_{SO}$  rather than by  $\hat{H}_{SO}^0$ , and the energy-lowering associated with  $\hat{H}'_{SO}$  is maximum when  $\theta = 90^\circ$  (equation 24.52) so that the Cu<sup>2+</sup> spin of a CuL<sub>4</sub> square plane would have easy-plane anisotropy. Indeed, direct DFT + U + SOC calculations for LiCuVO<sub>4</sub>, Bi<sub>2</sub>CuO<sub>4</sub>, CuCl<sub>2</sub>, and CuBr<sub>2</sub> show that their Cu<sup>2+</sup> ions have easy-plane anisotropy, but the above reasoning is incorrect because the  $\langle x^2 - y^2 | \hat{L}_z | x^2 - y^2 \rangle$  term is zero [23]. The empty  $(x^2 - y^2\downarrow)$  interacts with filled levels under SOC to generate nonzero matrix elements  $\langle xy | \hat{L}_z | x^2 - y^2 \rangle$ ,  $\langle xz | \hat{L}_\pm | x^2 - y^2 \rangle$ , and  $\langle yz | \hat{L}_\pm | x^2 - y^2 \rangle$  [23]. The DFT + U calculations for LiCuVO<sub>4</sub>, Bi<sub>2</sub>CuO<sub>4</sub>, CuCl<sub>2</sub>, and CuBr<sub>2</sub> [72] show that the top of the filled xz<sub>↓</sub> and yz<sub>↓</sub> bands, being dispersive, is much closer to the empty  $(x^2 - y^2\downarrow)$  band than is the filled xy<sub>↓</sub> band, and hence the interaction of the xz<sub>↓</sub> and yz<sub>↓</sub> bands with the  $(x^2 - y^2\downarrow)$  band through the spin-conserving SOC Hamiltonian  $\hat{H}_{SO}^0$  leads to the easy-plane anisotropy. See the next section for further discussion.

#### 24.7.2 Single-Ion Anisotropy

The preferred spin orientation of a magnetic ion leads to its single-ion magnetic anisotropy (or magnetocrystalline anisotropy). The simplest way of describing this magnetic anisotropy in terms of a spin Hamiltonian is to introduce the term  $A_i \hat{S}_{iz}^2$  for each magnetic ion *i* into a spin Hamiltonian. Here the spin  $\hat{S}_{iz}$  is defined by the local z-axis of the ion *i*, and the constant  $A_i$  is related to the energy difference between the ||z and  $\perp z$  spin orientations [ $E_i(\parallel z)$  and  $E_i(\perp z)$ , respectively] obtained from DFT + U + SOC calculations. That is,

$$A_i \hat{S}_{iz}^2 = E_i(\parallel z) - E_i(\perp z) \quad (24.54)$$

so that the  $A_i < 0$  for easy-axis anisotropy, and  $A_i > 0$  for easy-plane anisotropy.

In the effective spin approximation, one circumvents the need to explicitly describe the unquenched orbital moments of a magnetic system by treating the system as a spin-only system. The effect of unquenched orbital moments is treated indirectly by introducing anisotropic g-factors. As a consequence, for a magnetic ion with nondegenerate magnetic orbital (e.g., Cu<sup>2+</sup>), the SOC Hamiltonian  $\hat{H}_{SO}$  is replaced with the zero-field spin Hamiltonian  $\hat{H}_{zf}$

$$\begin{aligned} \hat{H}_{zf} &= D \hat{S}_z^2 + E (\hat{S}_x^2 - \hat{S}_y^2) - D \hat{S}^2 / 3 \\ &= D \hat{S}_z^2 + E (\hat{S}_+ \hat{S}_+ + \hat{S}_- \hat{S}_-) / 2 - D \hat{S}^2 / 3 \end{aligned} \quad (24.55)$$

where  $D \propto \lambda^2(\delta L_{||} - \delta L_{\perp})$ , where  $\delta L_{||}$  and  $\delta L_{\perp}$  are the unquenched orbital angular momenta along the ||z and  $\perp z$  directions, respectively, and  $E \propto \lambda^2(\delta L_x - \delta L_y)$ , where  $\delta L_x$  and  $\delta L_y$  are the unquenched orbital angular momenta along the x- and y-directions, respectively. The effective spin approximation leads to an interesting conclusion that a  $S = 1/2$  ion has no single-ion magnetic anisotropy [23]. This comes from the observation that the up-spin and down-spin states,  $\alpha = |\frac{1}{2}, \frac{1}{2}\rangle$  and  $\beta = |\frac{1}{2}, -\frac{1}{2}\rangle$ , do not interact under  $\hat{H}_{zf}$ , namely,  $\langle \alpha | \hat{H}_{zf} | \beta \rangle = 0$ . The latter means that the up-spin and down-spin states remain degenerate under SOC, so the  $S = 1/2$  ion has no preferred spin orientation. However, the neutron diffraction measurements for LiCuVO<sub>4</sub>, [27a] CuCl<sub>2</sub> [74], and CuBr<sub>2</sub>, [75] which consist of CuL<sub>2</sub> ribbon chains made up of edge-sharing CuL<sub>4</sub> square planes ( $L = O, Cl, Br$ ), show that the Cu<sup>2+</sup> ( $S = 1/2, d^9$ ) spins possess easy-plane anisotropy, that is, the spins prefer to lie in the plane of the  $x^2 - y^2$  magnetic orbital in these compounds. Experimentally, it

has been controversial whether the Cu<sup>2+</sup> ion of Bi<sub>2</sub>CuO<sub>4</sub> has easy-plane [73b] or easy-axis [73a] magnetic anisotropy. As mentioned in Section 7.2, DFT + U + SOC calculations for LiCuVO<sub>4</sub>, Bi<sub>2</sub>CuO<sub>4</sub>, CuCl<sub>2</sub>, and CuBr<sub>2</sub> predict the in-plane anisotropy for the Cu<sup>2+</sup> ion, and our analysis shows why this should be the case. Thus “no magnetic anisotropy for a S = 1/2 magnetic ion” predicted from the effective spin approximation is inconsistent with experiment and DFT + U + SOC calculations.

### 24.7.3 Uniaxial Magnetism versus Jahn–Teller Instability

When a transition-metal magnetic ion is located at a coordination site with threefold or higher rotational symmetry, its d-states have doubly-degenerate levels, namely, (xz, yz) and (xy, x<sup>2</sup> – y<sup>2</sup>), if the z-axis is taken along the rotational axis. When such an ion has a more than half-filled d-shell, its d-electron configuration may lead to an unevenly filled degenerate level, which leads to first-order Jahn–Teller instability (Section 7.4). A representative example is found for the high-spin Fe<sup>2+</sup> (S = 2, d<sup>6</sup>) ion at the D<sub>3d</sub> symmetry site in (Me<sub>3</sub>Si)<sub>3</sub>C–Fe–C(SiMe<sub>3</sub>)<sub>3</sub>, in which the Fe<sup>2+</sup> ion in the linear C–Fe–C coordination has the electron configuration (xy, x<sup>2</sup>–y<sup>2</sup>)<sup>3</sup>(xz, yz)<sup>2</sup>(z<sup>2</sup>)<sup>1</sup> (Figure 24.10d) [77,78]. The latter has an unquenched orbital angular momentum of magnitude L = 2 (in units of  $\hbar$ ). Since the Fe<sup>2+</sup> (S = 2, L = 2) ion has its d-shell more than half-filled, its SOC constant  $\lambda$  is negative so that, in its spin-orbit coupled states, the lowest-energy state arises from J = S + L = 4 and consists of the doublet described by J<sub>z</sub> = ±4 [78]. For convenience, the functions  $\Phi_4$  and  $\Phi_{-4}$  may be used to represent this doublet.

To examine the magnetic moment associated with the doublet  $\Phi_4$  and  $\Phi_{-4}$ , we consider if the doublet is split in energy under magnetic field  $\mathbf{H}$  (see equation 24.2) [78]. The Zeeman interaction under magnetic field is given by

$$\hat{H}_Z = \mu_B(\hat{L} + 2\hat{S}) \cdot \vec{H} \quad (24.56)$$

If we take the z-axis along the linear C–Fe–C direction, the Zeeman interaction for the field along the z-direction,  $H_{||}$ , is written as

$$\hat{H}_{Z||} = \mu_B(\hat{L}_z + 2\hat{S}_z)H_{||} \quad (24.57a)$$

This Hamiltonian gives rise to nonzero matrix element between two states with identical  $J_z$  value. The Zeeman interaction for the field perpendicular to the z-direction,  $H_{\perp}$ , is written as

$$\hat{H}_{Z\perp} = \mu_B[(\hat{L}_+ + \hat{L}_-)/2 + (\hat{S}_+ + \hat{S}_-)]H_{\perp} \quad (24.57b)$$

which leads to a nonzero matrix element between two states only if their  $J_z$  value difference  $-J_z$  is equal to one. For the field along the z-direction,

$$\langle \Phi_4 | \hat{H}_{Z||} | \Phi_4 \rangle = -\langle \Phi_{-4} | \hat{H}_{Z||} | \Phi_{-4} \rangle \neq 0, \quad \text{and} \quad \langle \Phi_4 | \hat{H}_{Z||} | \Phi_{-4} \rangle = 0$$

Thus, for  $H_{||}$ , the doublets are split in energy by

$$\Delta E_{||} = 2\langle \Phi_4 | \hat{H}_{Z||} | \Phi_4 \rangle \quad (24.58a)$$

so that there is a nonzero magnetic moment parallel to the z-direction. For the field perpendicular to the z-direction,

$$\langle \Phi_4 | \hat{H}_{Z\perp} | \Phi_4 \rangle = \langle \Phi_{-4} | \hat{H}_{Z\perp} | \Phi_{-4} \rangle = 0, \quad \text{and} \quad \langle \Phi_4 | \hat{H}_{Z\perp} | \Phi_{-4} \rangle = 0$$

Thus, for  $H_{\perp}$ , the doublets  $\Phi_4$  and  $\Phi_{-4}$  do not split so that the split energy  $\Delta E_{||}$  is zero,

$$\Delta E_{||} = 0 \quad (24.58b)$$

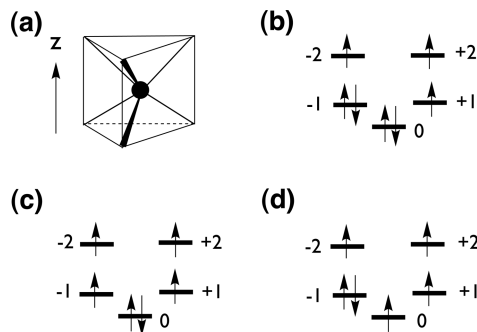


FIGURE 24.19

(a) A  $\text{CoO}_6$  trigonal prism found in  $\text{Ca}_3\text{CoMO}_6$  ( $M = \text{Co, Rh, Ir}$ ). (b) The  $d$ -electron configuration of a high-spin  $\text{Co}^{2+}$  ( $S = 3/2$ ,  $d^7$ ) ion at a  $\text{CoO}_6$  trigonal prism. (c) The  $d$ -electron configuration of a  $\text{Co}^{3+}$  ( $S = 2$ ,  $d^6$ ) ion at an isolated  $\text{CoO}_6$  trigonal prism. (d) The  $d$ -electron configuration of a  $\text{Co}^{3+}$  ( $S = 2$ ,  $d^6$ ) ion at the  $\text{CoO}_6$  trigonal prism of  $\text{Ca}_3\text{Co}_2\text{O}_6$ .

Consequently, the magnetic moment is zero along all directions perpendicular to the  $z$ -axis and hence the linear C–Fe–C system with high-spin  $\text{Fe}^{2+}$  ion is uniaxial. The  $g$ -factors for the parallel and perpendicular directions are then given by

$$g_{||} = \frac{\Delta E_{||}}{\mu_B H_{||}} = \frac{2\langle \Phi_4 | \hat{L}_z + 2\hat{S}_z | \Phi_4 \rangle}{\mu_B H_{||}} = 12 \quad (24.59\text{a})$$

$$g_{\perp} = \frac{\Delta E_{\perp}}{\mu_B H_{\perp}} = 0 \quad (24.59\text{b})$$

A similar situation occurs for a high-spin  $\text{Co}^{2+}$  ( $S = 3/2$ ,  $d^7$ ) or  $\text{Co}^{3+}$  ( $S = 2$ ,  $d^6$ ) ion in a  $\text{CoO}_6$  trigonal prism (Figure 24.19a) [78–80]. A  $\text{Co}^{2+}$  ( $S = 3/2$ ,  $d^7$ ) ion at a trigonal prism site in  $\text{Ca}_3\text{CoRhO}_6$  and  $\text{Ca}_3\text{ColrO}_6$  [79,80] has the electron configuration  $(z^2)^2(xy, x^2 - y^2)^3(xz, yz)^2$  (Figure 24.19b; see also Figure 15.10) so that  $L = 2$  and hence  $J = 7/2$ . Therefore, in the lowest-energy doublet state,  $\Delta J_z = 7$  so that the high-spin  $\text{Co}^{2+}$  ion of a  $\text{CoO}_6$  trigonal prism is uniaxial [79]. An interesting situation is presented by a high-spin  $\text{Co}^{3+}$  ( $S = 2$ ,  $d^6$ ) in a  $\text{CoO}_6$  trigonal prism in  $\text{Ca}_3\text{Co}_2\text{O}_6$  [78–80]. An isolated  $\text{CoO}_6$  trigonal prism is expected to have the configuration  $(z^2)^2(xy, x^2 - y^2)^2(xz, yz)^2$  with  $L = 0$  (Figure 24.19c), so it should not have uniaxial magnetism. Nevertheless, uniaxial magnetism is found for the high-spin  $\text{Co}^{3+}$  ( $S = 2$ ,  $d^6$ ) ions of the  $\text{CoO}_6$  trigonal prisms in  $\text{Ca}_3\text{Co}_2\text{O}_6$  as if its configuration is  $(z^2)^1(xy, x^2 - y^2)^3(xz, yz)^2$  with  $L = 2$  (Figure 24.19d) [23,78,79]. In understanding why this happens, one needs to consider the three different factors affecting the relative energies of the  $\text{Co}$   $3d$  states, as discussed in the following text.

$\text{Ca}_3\text{Co}_2\text{O}_6$  consists of  $\text{Co}_2\text{O}_6$  chains in which  $\text{CoO}_6$  trigonal prisms alternate with  $\text{CoO}_6$  octahedra by sharing their faces (Figure 24.20a). For simplicity, trigonal prism and octahedral  $\text{CoO}_6$  will be referred to as TP and OCT  $\text{CoO}_6$ , respectively. Due to the face-sharing, the NN  $\text{Co}\dots\text{Co}$  distance in the  $\text{Co}_2\text{O}_6$  chain is very short (2.595 Å).  $\text{Ca}_3\text{Co}_2\text{O}_6$  shows that the TP  $\text{Co}^{3+}$  ion has the  $L = 2$  configuration  $(d_0)^1(d_2, d_{-2})^3(d_1, d_{-1})^2$  in the DFT +  $U$  + SOC calculations but the  $L = 0$  configuration  $(d_0)^2(d_2, d_{-2})^2(d_1, d_{-1})^2$  in the DFT +  $U$  calculations [79,81]. To understand the switching of the  $L = 0$  configuration to the  $L = 2$  configuration by the action of SOC, one needs to consider three effects, that is, the spin arrangement between adjacent TP and OCT  $\text{Co}^{3+}$  ions, the direct metal–metal interaction between them, and the SOC on the TP  $\text{Co}^{3+}$  ion. It is convenient to discuss these factors by considering an isolated dimer made up of adjacent TP  $\text{CoO}_6$  and OCT  $\text{CoO}_6$ . We first consider the interaction between the  $z^2$  orbitals of adjacent  $\text{Co}^{3+}$  ions. In a one-electron tight-

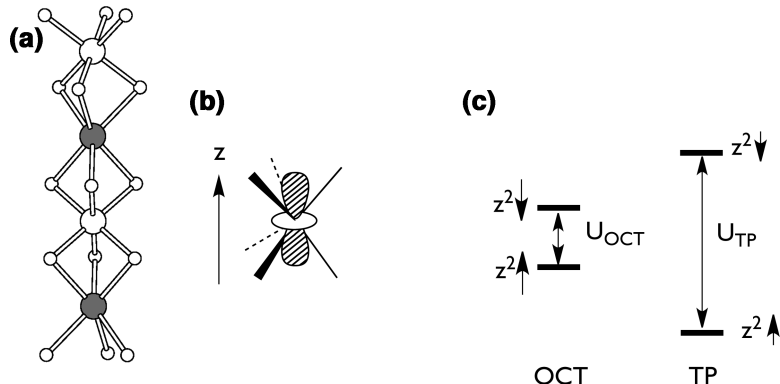
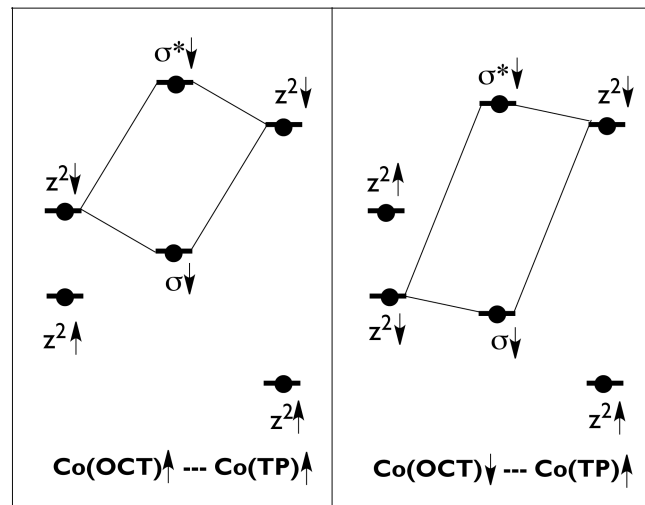


FIGURE 24.20

(a) The  $\text{CoMO}_6$  ( $M=\text{Co, Rh, Ir}$ ) chain, made up of face sharing  $\text{CoO}_6$  trigonal prisms and  $\text{MO}_6$  octahedra, found in  $\text{Ca}_3\text{CoMO}_6$ . The Co atoms of the  $\text{CoO}_6$  trigonal prisms are indicated by shaded circles. (b) The  $z^2$  orbital of an  $\text{MO}_6$  octahedron. (c) The up-spin and down-spin  $z^2$  orbitals at the octahedral and trigonal prism sites of a  $\text{CoMO}_6$  ( $M=\text{Co, Rh, Ir}$ ) chain.

binding description, the high-spin  $\text{Co}^{3+}$  ( $d^6$ ) ion of an isolated TP  $\text{CoO}_6$  has the  $(d_0)^2(d_2, d_{-2})^2(d_1, d_{-1})^2$  configuration while the low-spin  $\text{Co}^{3+}$  ( $d^6$ ) ion of an isolated OCT  $\text{CoO}_6$  has the  $(t_{2g})^6$  configuration. The OCT  $\text{CoO}_6$  in  $\text{Ca}_3\text{Co}_2\text{O}_6$  has  $C_3$  symmetry, so the  $t_{2g}$  level is split into the  $1a$  and  $1e$  set. The  $z^2$  orbital of the TP  $\text{Co}^{3+}$  ion can overlap strongly in a sigma fashion, and hence interact strongly with the  $1a$  orbital, that is, the  $z^2$  orbital (Figure 24.20b), of the OCT  $\text{Co}^{3+}$  ion through the shared triangular face. In describing such an interaction at the spin-polarized DFT +  $U$  level, it should be noted that one-electron energy levels given by tight-binding calculations are split into the up-spin and down-spin levels by the spin-polarization/on-site repulsion as depicted in Figure 24.20c [23,79]. The  $z^2\uparrow$  and  $z^2\downarrow$  levels of the OCT  $\text{Co}^{3+}$  ion are split less than those of the TP  $\text{Co}^{3+}$  ion because, to a first approximation, the OCT site has a low-spin  $\text{Co}^{3+}$  ion whereas the TP site has a high-spin  $\text{Co}^{3+}$  ion. Since both TP and OCT sites have  $\text{Co}^{3+}$  ions, the midpoint between their  $z^2\uparrow$  and  $z^2\downarrow$  levels should be nearly the same. According to equation 24.53, the  $L=0$  configuration of the TP  $\text{Co}^{3+}$  ion can be written as  $(d_0)^2(d_2, d_{-2})^2(d_1, d_{-1})^2$  in one-electron picture, which means in terms of spin polarized DFT +  $U$  calculations  $(d_0\uparrow)^1 < (d_2\uparrow, d_{-2}\uparrow)^2 < (d_1\uparrow, d_{-1}\uparrow)^2 < (d_0\downarrow)^1 < (d_2\downarrow, d_{-2}\downarrow)^0 < (d_1\downarrow, d_{-1}\downarrow)^0$  so the HOMO and LUMO of the TP  $\text{CoO}_6$  are given by the  $d_0\downarrow$  and  $(d_2\downarrow, d_{-2}\downarrow)$  levels, respectively. Therefore, if one of the four electrons present in the two  $z^2$  orbitals of adjacent TP and OCT  $\text{Co}^{3+}$  ions is transferred to the  $(d_2\downarrow, d_{-2}\downarrow)$  level of the TP  $\text{Co}^{3+}$  ion, the resulting electron configuration of the TP  $\text{Co}^{3+}$  ion would be close to  $(d_0)^1(d_2, d_{-2})^3(d_1, d_{-1})^2$ .

Consider that the spins of the TP and OCT  $\text{Co}^{3+}$  ions have the FM arrangement as indicated in 24.36, as found experimentally. Here the closed circles refer to an

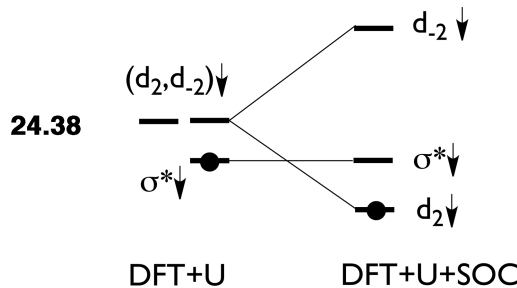


24.36

24.37

occupied orbital. The highest occupied level resulting from the  $z^2$  orbitals of the two  $\text{Co}^{3+}$  ions is the sigma antibonding level  $\sigma^*\downarrow$ , in which the weight of the trigonal-prism  $z^2\downarrow$  orbital is larger than that of the octahedral  $z^2\downarrow$  orbital because the former lies higher in energy than the latter. In the DFT +  $U$  level of description, the occupied  $\sigma^*\downarrow$  level lies below the empty  $(d_2, d_{-2})\downarrow$  level of the TP  $\text{Co}^{3+}$  ion. If the TP and OCT  $\text{Co}^{3+}$  ions were to have the AFM arrangement as indicated in 24.37, the resulting occupied  $\sigma^*\downarrow$  level would be lower lying compared with that resulting from the FM arrangement.

The effect of the SOC interaction at the TP  $\text{Co}^{3+}$  ion site is depicted in 24.38,



where the SOC splits the unoccupied degenerate level  $(d_2\downarrow, d_{-2}\downarrow)$  into the  $d_2\downarrow$  below  $d_{-2}\downarrow$  pattern since  $\lambda < 0$  for  $\text{Co}^{3+}$  ( $d^6$ ). When the unoccupied  $d_2\downarrow$  level is lowered below the occupied  $\sigma^*\downarrow$  level, an electron transfer occurs from the  $\sigma^*\downarrow$  level to the  $d_2\downarrow$  level. Since the  $\sigma^*\downarrow$  level has a greater weight on the trigonal-prism  $z^2\downarrow$  orbital, this charge transfer effectively amounts to the configuration switch of the TP  $\text{Co}^{3+}$  from the  $L=0$  configuration  $(d_0)^2(d_2, d_{-2})^2(d_1, d_{-1})^2$  to the  $L=2$  configuration  $(d_0)^1(d_2, d_{-2})^3(d_1, d_{-1})^2$ . This is why the TP  $\text{Co}^{3+}$  ion has the  $(d_0)^2(d_2, d_{-2})^2(d_1, d_{-1})^2$  configuration at the DFT +  $U$  level, but has the  $(d_0)^1(d_2, d_{-2})^3(d_1, d_{-1})^2$  configuration at the DFT +  $U$  + SOC level.

Note from Figure 24.19 that the  $L=2$  electron configurations responsible for uniaxial magnetism induce a first-order Jahn–Teller distortion (see Section 7.4) [79], which removes the threefold rotational symmetry and hence lifts the degeneracies of  $(d_2, d_{-2})$  and  $(d_1, d_{-1})$ . As a result, the orbital moment is strongly quenched. DFT +  $U$  + SOC calculations for  $\text{Ca}_3\text{CoMO}_6$  ( $\text{M} = \text{Co}, \text{Rh}, \text{Ir}$ ) show that the orbital moments  $\mu_L$  of the TP  $\text{Co}^{3+}$  ion in  $\text{Ca}_3\text{Co}_2\text{O}_6$  and the TP  $\text{Co}^{2+}$  ions of  $\text{Ca}_3\text{CoRhO}_6$ ,  $\text{Ca}_3\text{CoIrO}_6$  are approximately  $1.5\mu_B$  in the absence of Jahn–Teller distortion, but are considerably reduced to approximately  $0.5\mu_B$  when a Jahn–Teller distortion is allowed to take place [79]. That is, the loss of the threefold rotational symmetry significantly quenches the orbital moment.

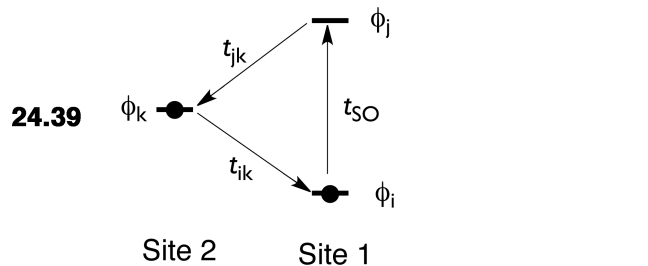
#### 24.7.4 The Dzyaloshinskii–Moriya Interaction

We now examine the SOC in a spin dimer made up of two spin sites 1 and 2, for which the SOC Hamiltonian is given by [23]

$$\hat{H}_{\text{SO}} = \lambda \hat{\vec{L}} \cdot \hat{\vec{S}} = \lambda (\hat{L}_1 + \hat{L}_2) \cdot (\hat{S}_1 + \hat{S}_2) \approx \lambda (\hat{L}_1 \cdot \hat{S}_1 + \hat{L}_2 \cdot \hat{S}_2) \quad (24.60)$$

where the last equality follows from the fact that the SOC is a local interaction. Despite the local nature of SOC, the two spin sites can interact indirectly hence influencing their relative spin orientations. As illustrated in 24.39, we suppose that

an occupied orbital  $\phi_i$  interacts with an unoccupied orbital  $\phi_j$  at spin site 1 via SOC, and that the  $\phi_i$  and  $\phi_k$  of site 1 interact with an occupied orbital  $\phi_k$  of site 2 via orbital



interaction. The orbital mixing between  $\phi_i$  and  $\phi_k$  introduces the spin character of site 2 into  $\phi_i$  of site 1 while that between  $\phi_j$  and  $\phi_k$  introduces the spin character of site 2 into  $\phi_j$  of site 1. Namely,

$$\begin{aligned}\phi_i &\rightarrow \phi'_i \approx (1 - \gamma^2)\phi_i + \gamma\phi_k \\ \phi_j &\rightarrow \phi'_j \approx (1 - \gamma^2)\phi_j + \gamma\phi_k\end{aligned}$$

where  $\gamma$  refers to a small mixing coefficient. Then, the SOC between such modified  $\phi'_i$  and  $\phi'_j$  at site 1 indirectly introduces the interaction between the spins at sites 1 and 2. For a spin dimer, there can be a number of interactions like the one depicted in **24.39** at both spin sites, so summing up all such contributions gives rise to the DM interaction energy  $E_{DM}$  between spin sites 1 and 2.

Suppose that  $\delta\mathbf{L}_1$  and  $\delta\mathbf{L}_2$  are the unquenched orbital angular momenta at sites 1 and 2, respectively. Then, use of the  $\hat{H}_{SO}$  (equation 24.60) as perturbation leads to the DM interaction energy  $E_{DM}$ , [23,50]

$$E_{DM} = [\lambda J_{12}(\delta\mathbf{L}_1 - \delta\mathbf{L}_2)] \cdot (\mathbf{S}_1 \times \mathbf{S}_2) \equiv \mathbf{D}_{12} \cdot (\mathbf{S}_1 \times \mathbf{S}_2) \quad (24.61)$$

In equation 24.61, the DM vector  $\mathbf{D}_{12}$  is related to the difference in the unquenched orbital angular momenta on the two magnetic sites 1 and 2, namely,

$$\mathbf{D}_{12} = \lambda J_{12}(\delta\mathbf{L}_1 - \delta\mathbf{L}_2) \quad (24.62)$$

For a spin dimer with Heisenberg exchange  $J_{12}$ , the strength of its DM exchange  $\mathbf{D}_{12}$  is discussed by considering the ratio  $|D_{12}/J_{12}|$ , which is often approximated by  $|D_{12}/J_{12}| \approx \Delta g/g$ , where  $\Delta g$  is the contribution of the orbital moment to the g-factor  $g$  in the effective spin approximation. In general, the  $\Delta g/g$  value is at most 0.1. An implicit assumption behind this reasoning is that the spin sites 1 and 2 have an identical chemical environment. This estimate is not valid when the two spin sites have different chemical environments. As depicted in **24.39**, the magnitude of a DM vector  $\mathbf{D}_{12}$  is determined by the three matrix elements,  $t_{SO} = \langle \phi_i | \hat{H}_{SO} | \phi_j \rangle$ ,  $t_{ik} = \langle \phi_i | \hat{H}^{eff} | \phi_k \rangle$ , and  $t_{jk} = \langle \phi_j | \hat{H}^{eff} | \phi_k \rangle$ . When  $t_{SO}$ ,  $t_{ik}$  and  $t_{jk}$  are all strong, the resulting DM vector  $\mathbf{D}_{12}$  can be unusually large. For example, it was found that  $|D_{12}/J_{12}| \approx 0.54$  for one Mn<sub>2</sub>-O-Mn<sub>3</sub> exchange path of CaMn<sub>7</sub>O<sub>12</sub> (Figure 24.15) [55].

So far, a spin dimer made up of spin sites 1 and 2 has been described by the spin Hamiltonian

$$\hat{H}_{\text{spin}} = -J_{12}\hat{S}_1 \cdot \hat{S}_2 \quad (24.14a)$$

composed of only the Heisenberg spin exchange (Section 24.4.I). This Hamiltonian leads to a collinear spin arrangement (either FM or AFM) for a spin dimer. To allow for a canting of the spins  $\mathbf{S}_1$  and  $\mathbf{S}_2$  from the collinear arrangement (typically from the AFM arrangement), it is necessary to include the DM exchange  $\vec{D}_{12} \cdot (\hat{\mathbf{S}}_1 \times \hat{\mathbf{S}}_2)$ , which is a consequence of SOC [23,50], into the spin Hamiltonian. That is,

$$\hat{H}_{\text{spin}} = -J_{12}\hat{\mathbf{S}}_1 \cdot \hat{\mathbf{S}}_2 + \vec{D}_{12} \cdot (\hat{\mathbf{S}}_1 \times \hat{\mathbf{S}}_2) \quad (24.63)$$

The  $\hat{\mathbf{S}}_1 \times \hat{\mathbf{S}}_2$  term, being proportional to  $\sin \theta$  where  $\theta$  is the angle between  $\mathbf{S}_1$  and  $\mathbf{S}_2$ , is nonzero only if the two spins are not collinear. Thus the DM interaction  $\vec{D}_{12} \cdot (\hat{\mathbf{S}}_1 \times \hat{\mathbf{S}}_2)$  induces spin canting. (Of course, even if a model Hamiltonian consists of only Heisenberg spin exchanges, a magnetic system with many spin sites can have a noncollinear spin arrangement if there exists spin frustration as discussed in Section 24.5.I.)

As discussed in Section 24.4.A, the Heisenberg exchange  $J_{12}$  of equation 24.63 can be evaluated on the basis of energy-mapping analysis by considering two collinear spin states  $|HS\rangle$  and  $|BS\rangle$  (i.e., FM and AFM spin arrangements, respectively) because the DM exchange  $\vec{D}_{12} \cdot (\hat{\mathbf{S}}_1 \times \hat{\mathbf{S}}_2)$  is zero for such collinear spin states. To evaluate the DM vector  $\vec{D}_{12}$ , we carry out energy-mapping analysis on the basis of DFT +  $U + \text{SOC}$  calculations [82]. In terms of its Cartesian components,  $\vec{D}_{12}$  is expressed as  $\vec{D}_{12} = \hat{i}D_x + \hat{j}D_y + \hat{k}D_z$ . Therefore, the DM interaction energy  $\vec{D}_{12} \cdot (\hat{\mathbf{S}}_1 \times \hat{\mathbf{S}}_2)$  is rewritten as

$$\begin{aligned} \vec{D}_{12} \cdot (\hat{\mathbf{S}}_1 \times \hat{\mathbf{S}}_2) &= (\hat{i}D_x + \hat{j}D_y + \hat{k}D_z) \cdot \begin{pmatrix} \hat{i} & \hat{j} & \hat{k} \\ \hat{S}_{1x} & \hat{S}_{1y} & \hat{S}_{1z} \\ \hat{S}_{2x} & \hat{S}_{2y} & \hat{S}_{2z} \end{pmatrix} \\ &= D_x(\hat{S}_{1y}\hat{S}_{2z} - \hat{S}_{1z}\hat{S}_{2y}) + D_y(\hat{S}_{1z}\hat{S}_{2x} - \hat{S}_{1x}\hat{S}_{2z}) + D_z(\hat{S}_{1x}\hat{S}_{2y} - \hat{S}_{1y}\hat{S}_{2x}) \end{aligned} \quad (24.64)$$

To determine the  $D_z$  component, we consider the following two orthogonally ordered spin states,

$$\text{State 1: } \mathbf{S}_1 = (S, 0, 0) \quad \text{and} \quad \mathbf{S}_2 = (0, S, 0)$$

$$\text{State 2: } \mathbf{S}_1 = (S, 0, 0) \quad \text{and} \quad \mathbf{S}_2 = (0, -S, 0)$$

where  $S$  is the length of the spin. In state 1, the spins at sites 1 and 2 are along the positive  $x$  and the positive  $y$  directions, respectively. In state 2, the spins at sites 1 and 2 are along the positive  $x$  and the negative  $y$  directions, respectively. For these states,  $\mathbf{S}_1 \cdot \mathbf{S}_2 = 0$  and  $|\mathbf{S}_1 \times \mathbf{S}_2| = S^2$  so that, according to equation 24.63, the energies of the two states are given by  $E_1 = S^2 D_z$ , and  $E_2 = -S^2 D_z$ . Consequently,

$$D_z = \frac{1}{2}(E_1 - E_2)/S^2 \quad (24.65a)$$

Thus, the  $D_z$  is determined by evaluating the energies  $E_1$  and  $E_2$  on the basis of DFT +  $U + \text{SOC}$  calculations.

The  $D_y$  and  $D_x$  components are determined in a similar manner. Using the following two orthogonal spin states,

$$\text{State 3: } \mathbf{S}_1 = (S, 0, 0) \quad \text{and} \quad \mathbf{S}_2 = (0, 0, -S)$$

$$\text{State 4: } \mathbf{S}_1 = (S, 0, 0) \quad \text{and} \quad \mathbf{S}_2 = (0, 0, S)$$

the  $D_y$  component is obtained as

$$D_y = \frac{1}{2}(E_3 - E_4)/S^2 \quad (24.65b)$$

In terms of the following two orthogonal spin states,

$$\text{State 5: } \mathbf{S}_1 = (0, S, 0) \quad \text{and} \quad \mathbf{S}_2 = (0, 0, S)$$

$$\text{State 6: } \mathbf{S}_1 = (0, S, 0) \quad \text{and} \quad \mathbf{S}_2 = (0, 0, -S)$$

the  $D_x$  term is given by

$$D_x = \frac{1}{2}(E_5 - E_6)/S^2 \quad (24.65c)$$

#### 24.7.5 Singlet-Triplet Mixing Under Spin-Orbit Coupling

In Section 8.5, we discussed the singlet and triplet excited states,  $\Phi_S$  and  $\Phi_T$ , respectively, resulting from a singlet ground state  $\Phi_G$ . In the absence of SOC, the excited states  $\Phi_S$  and  $\Phi_T$  do not interact. The spin parts of the singlet and triplet states are given by

$$\begin{aligned} |S\rangle &= |s = 0, s_z = 0\rangle \\ |T\rangle &= |s = 1, s_z = -1\rangle, |s = 1, s_z = 0\rangle, \text{ or } |s = 1, s_z = 1\rangle \end{aligned} \quad (24.66)$$

Under SOC, these two states interact because the interaction term  $\langle T|\hat{H}_{SO}|S\rangle$  is nonzero. Namely, according to equation 24.52,

$$\langle T|\hat{H}_{SO}|S\rangle = \langle T|\hat{H}'_{SO}|S\rangle = \langle T|\hat{S}_{+'}|S\rangle \left( -\frac{\lambda}{2}\hat{L}_z \sin \theta \right) \quad (24.67a)$$

Since the  $\langle T|\hat{S}_{+'}|S\rangle$  term is nonzero,  $\langle \Phi_T|\hat{H}_{SO}|\Phi_S\rangle$  is nonzero,

$$\langle \Phi_T|\hat{H}_{SO}|\Phi_S\rangle = \langle \Phi_T|\hat{H}'_{SO}|\Phi_S\rangle \equiv \gamma \quad (24.67b)$$

where  $\gamma$  represents a very small nonzero number. This means that under SOC, the states  $\Phi_S$  and  $\Phi_T$  interact to generate mixed states,

$$\begin{aligned} \Phi'_S &\approx (1 - \gamma^2)\Phi_S + \gamma\Phi_T \\ \Phi'_T &\approx \gamma\Phi_S + (1 - \gamma^2)\Phi_T \end{aligned} \quad (24.68)$$

so that there exist no pure singlet and no pure triplet states. Consequently, the transition dipole moment  $\langle \Phi_G|e\vec{r}|\Phi'_T\rangle$  between the ground singlet state  $\Phi_G$  and the “triplet” excited state  $\Phi'_T$  is nonzero, because

$$\langle \Phi_G|e\vec{r}|\Phi'_T\rangle = \gamma\langle \Phi_G|e\vec{r}|\Phi_S\rangle \neq 0 \quad (24.69)$$

This explains why the transition from the “triplet” excited state  $\Phi'_T$  to the singlet ground state  $\Phi_G$  (i.e., phosphorescence) takes place, though very weakly. The forbiddenness of this transition is true only when the effect of SOC is neglected.

## 24.8 WHAT APPEARS VERSUS WHAT IS

For a number of magnetic systems, the energy-mapping analysis based on DFT +  $U$  calculations has been essential in correctly explaining their magnetic structures. In this section, we discuss a few representative examples of such magnetic systems to emphasize the importance of finding relevant spin lattices on the basis of proper electronic structure calculations.

### 24.8.1 Idle Spin in $\text{Cu}_3(\text{OH})_4\text{SO}_4$

Idle-spin magnets constitute an interesting class of magnetic solids that undergo a long-range magnetic ordering without an ordered moment on certain spin sites. In general, such idle-spin sites engage in frustrated spin exchanges with neighboring spin sites. In the magnetic oxide  $\text{Cu}_3(\text{OH})_4\text{SO}_4$ , which has been regarded to exhibit idle-spin behavior [83], two nonequivalent Cu atoms, Cu(1) and Cu(2), form Cu(2)–Cu(1)–Cu(2) triple chains (Figure 24.21). The  $\text{CuO}_4$  square planes containing the  $x^2 - y^2$  magnetic orbitals of the Cu(1) and Cu(2) atoms form an edge-sharing Cu(1)  $\text{O}_2$  ribbon chain (hereafter Cu(1) chain) and a corner-sharing  $\text{Cu}(2)\text{O}_3$  chain (hereafter Cu(2) chain) along the  $b$ -direction (Figure 24.21a). Each Cu(2)–Cu(1)–Cu(2) triple chain results from condensing one Cu(1) chain with two Cu(2) chains by corner-sharing. The magnetic susceptibility and the specific heat data reveal that  $\text{Cu}_3(\text{OH})_4\text{SO}_4$  undergoes long-range magnetic ordering below  $T_N = 5.3$  K. However, there has been no evidence for low-dimensional short range AFM ordering, and the magnetic entropy associated with the long-range ordering anomaly near  $T_N$  is very close to  $3R \ln 2$  as expected for the ordering of three  $S = 1/2$  entities, indicating the absence of extended short-range AFM ordering (see Section 24.5.2). Neutron diffraction measurements at 1.4 K point to a FM coupling between the spins in each Cu(2) chain, with their spin moments oriented along the  $c$ -axis, and an AFM coupling between the two Cu(2) chains in each Cu(2)–Cu(1)–Cu(2) triple chain.  $\text{Cu}_3(\text{OH})_4\text{SO}_4$  was proposed to be an idle-spin magnet because no long-range magnetic order was detected in the Cu(1) chains from the neutron diffraction data [83]. However, this conclusion was questioned in the magnetization study [84] based on single crystal samples of  $\text{Cu}_3(\text{OH})_4\text{SO}_4$ .

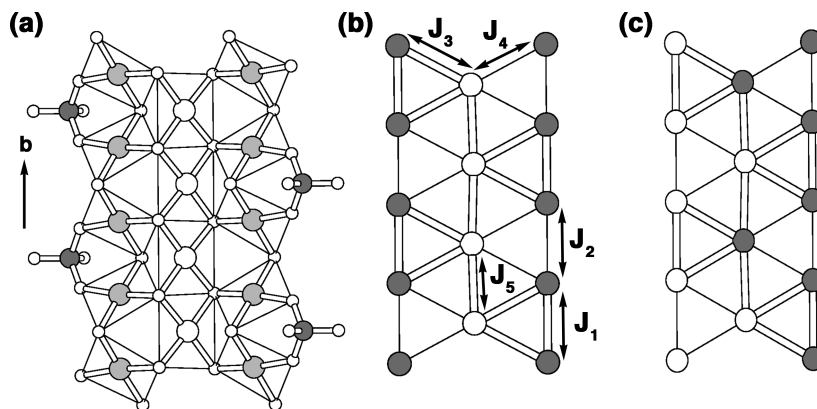


**FIGURE 24.21**

(a) A perspective view of the Cu(2)–Cu(1)–Cu(2) triple chain found in  $\text{Cu}_3(\text{OH})_4\text{SO}_4$ , where Cu(1) = large empty circle, Cu(2) = large shaded circle, O = small white circle, and S = medium shaded circle. (b) The spin exchange paths  $J_1$ – $J_5$  of the Cu(2)–Cu(1)–Cu(2) triple chain. (c) The ground-state magnetic structure of the Cu(2)–Cu(1)–Cu(2) triple chain, where the shaded and unshaded circles represent the up-spin and down-spin  $\text{Cu}^{2+}$  sites, respectively.

Due to the presence of the  $\text{SO}_4$  tetrahedra corner-sharing with the Cu(2) chains (Figure 24.21a), there occurs two kinds of NN spin exchanges ( $J_1$  and  $J_2$ ) along each Cu(2) chain, and two kinds of NN spin exchanges ( $J_3$  and  $J_4$ ) between adjacent Cu(1) and Cu(2) chains (Figure 24.21b). DFT +  $U$  calculations show [85] that the spin exchanges of  $\text{Cu}_3(\text{OH})_4\text{SO}_4$  are dominated by  $J_1$ ,  $J_3$ , and  $J_5$ , that the NN exchange  $J_5$  of the Cu(1) chain is the strongest of all exchange constants and that  $J_5$  and  $J_3$  are both AFM while  $J_1$  is FM. Thus the spins in each Cu(1) chain should have an AFM coupling according to  $J_5$  (Figure 24.21c). In each Cu(2)–Cu(1)–Cu(2) triple chain, this AFM Cu(1) chain interacts with the outside Cu(2) chains through the AFM exchanges  $J_3$  and  $J_4$ . The AFM exchange  $J_3$ , being stronger than  $J_4$  by a factor of approximately 3, forces a FM arrangement of the spins in each Cu(2) chain and an AFM arrangement between the two outside Cu(2) chains (Figure 24.21c). The resulting FM spin arrangement of each Cu(2) chain is reinforced by the FM exchanges  $J_1$  and  $J_2$ .

The chemical repeat unit of each Cu(1) chain contains two Cu atoms, and so does the magnetic unit cell of the antiferromagnetically coupled Cu(1) chain. Therefore, the AFM ordering of the Cu(1) chains does not generate extra magnetic Bragg peaks in neutron diffraction measurements. This possibility of an AFM ordering of the Cu(1) spins was not considered in the neutron diffraction study [83] concluding that the Cu(1) spins are idle spins.

#### 24.8.2 The FM–AFM versus AFM–AFM Chain

The spin gap systems  $\text{Na}_3\text{Cu}_2\text{SbO}_6$  [86] and  $\text{Na}_2\text{Cu}_2\text{TeO}_6$  [87] consist of the  $\text{Cu}_2\text{MO}_6$  ( $M = \text{Sb, Te}$ ) layers made up of edge-sharing  $\text{MO}_6$  and  $\text{CuO}_6$  octahedra (Figure 24.22). Each  $\text{CuO}_6$  octahedron is axially elongated due to its  $\text{Cu}^{2+}$  ion, and the  $\text{CuO}_6$  octahedra are present in the form of edge-sharing  $\text{Cu}_2\text{O}_{10}$  dimers. In the  $\text{Cu}_2\text{MO}_6$  ( $M = \text{Sb, Te}$ ) layers, the  $\text{Cu}^{2+}$  ions form a honeycomb pattern with the  $M^{n+}$  (i.e.,  $\text{Sb}^{5+}$ ,  $\text{Te}^{6+}$ ) ions occupying the centers of the  $\text{Cu}^{2+}$ -ion hexagons. Since the  $\text{Cu}_2\text{MO}_6$  ( $M = \text{Sb, Te}$ ) layers are well separated by Na atoms, the magnetic properties of  $\text{Na}_3\text{Cu}_2\text{SbO}_6$  and  $\text{Na}_2\text{Cu}_2\text{TeO}_6$  are described in terms of the spin lattice associated with their  $\text{Cu}_2\text{MO}_6$  ( $M = \text{Sb, Te}$ ) layers. As indicated in Figure 24.22, there are three spin exchange paths ( $J_1$ ,  $J_2$ , and  $J_3$ ) to consider between the adjacent  $\text{Cu}^{2+}$  ions of a given  $\text{Cu}_2\text{MO}_6$  ( $M = \text{Sb, Te}$ ) layer.

The magnetic susceptibilities of  $\text{Na}_3\text{Cu}_2\text{SbO}_6$  and  $\text{Na}_2\text{Cu}_2\text{TeO}_6$  is almost equally well described by an alternating chain model with AFM–AFM spin exchanges and by that with AFM–FM spin exchanges [86,88]. It is difficult to determine which model is correct by the fitting analyses involving the Boltzmann averaging (i.e., the analyses of

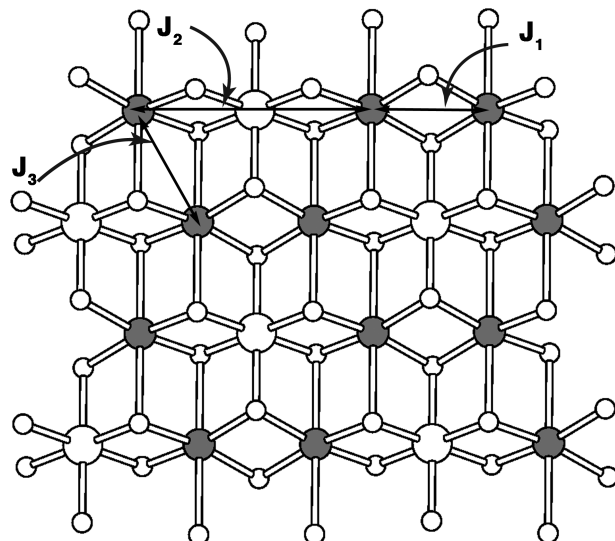


**FIGURE 24.22**

The  $\text{Cu}_2\text{MO}_6$  ( $M = \text{Sb, Te}$ ) layer found in  $\text{Na}_3\text{Cu}_2\text{SbO}_6$  and  $\text{Na}_2\text{Cu}_2\text{TeO}_6$ , where the Cu atoms are indicated by shaded circles, and the Sb/Te atoms by large unshaded circles. In this layer, the  $\text{Cu}^{2+}$  ions form a honeycomb pattern.

the magnetic susceptibility and specific heat data). However, DFT +  $U$  calculations show that  $J_3$  is negligible compared with  $J_1$  and  $J_2$ , and that the AFM–FM model is correct with FM  $J_1$  and AFM  $J_2$  [89]. Experimentally, the difference between the AFM–AFM and AFM–FM chain models can be distinguished by neutron scattering measurements, because the two models are different in the wave-vector dependence of the spin-wave dispersion relations. Indeed, neutron scattering experiments on single crystal samples of  $\text{Na}_3\text{Cu}_2\text{SbO}_6$  showed that the AFM–FM chain model is the correct one [90], in agreement with the theoretical prediction based on the energy-mapping analysis.

#### 24.8.3 Diamond Chains

The structure of the quaternary magnetic oxide  $\text{Bi}_4\text{Cu}_3\text{V}_2\text{O}_{14}$  can be described in terms of  $\text{Cu}_3\text{V}_2\text{O}_{12}$  chains running along the  $a$ -direction (Figure 24.23a), in which corner-sharing  $\text{CuO}_4$  square planes form a  $\text{Cu}_3\text{O}_8$  triple-chain consisting of three nearly coplanar  $\text{CuO}_4$  chains and the outer two  $\text{CuO}_4$  chains are capped by  $\text{VO}_4$  tetrahedra via corner-sharing [91]. Therefore, if the  $\text{CuO}_4$  units of the  $\text{Cu}_3\text{O}_8$  triple-chain are regarded as ideal square planes, the  $\text{Cu}^{2+}$  ions form a diamond chain (Figure 24.23b) with identical Cu–O–Cu SE interactions and identical Cu–O...O–Cu SSE interactions. The magnetic susceptibility of  $\text{Bi}_4\text{Cu}_3\text{V}_2\text{O}_{14}$  shows the characteristic feature of a low-dimensional antiferromagnet (i.e., a broad maximum around 20.5 K), and the susceptibility between 100–320 K is well reproduced by the Curie–Weiss law with  $\theta = -48.1 \text{ K}$  [92]. The specific heat measurement shows a  $\lambda$ -type peak at  $T_N = 6 \text{ K}$ , and the  $^{49}\text{V}$  NMR measurements at 4.2 K indicate an AFM ground state. If we neglect the SSE interactions and assume that the SE interactions are identical, the spin lattice of the  $\text{Cu}_3\text{O}_8$  triple-chain becomes a diamond chain, and the ground state of such a chain is ferrimagnetic provided that the SE interactions are AFM. However,  $\text{Bi}_4\text{Cu}_3\text{V}_2\text{O}_{14}$  does not exhibit ferrimagnetic behavior in the magnetic susceptibility above  $T_N$  and in the magnetization curve below  $T_N$ .

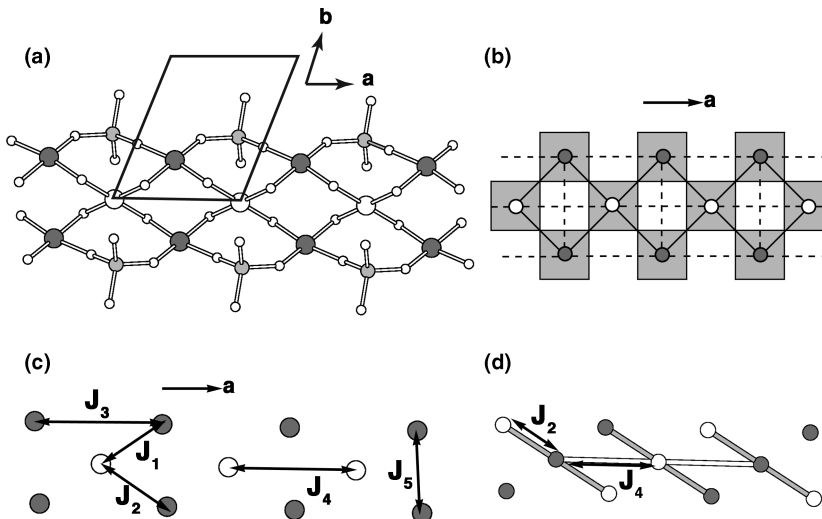


**FIGURE 24.23**

(a) A perspective view of the  $\text{Cu}_3\text{V}_2\text{O}_{12}$  triple chain found in  $\text{Bi}_4\text{Cu}_3\text{V}_2\text{O}_{14}$ , where the Cu1 and Cu2 atoms are indicated by large shaded and large unshaded circles, respectively. (b) An idealized view of the  $\text{Cu}^{2+}$  ion arrangement in the  $\text{Cu}_3\text{V}_2\text{O}_{12}$  triple chain as a diamond chain. (c) The spin exchange paths of the  $\text{Cu}_3\text{V}_2\text{O}_{12}$  triple chain. (d) The spin lattice of the  $\text{Cu}_3\text{V}_2\text{O}_{12}$  triple chain defined by the two strongest spin exchanges  $J_2$  and  $J_4$ , in which the linear AFM trimers defined by  $J_2$  are antiferromagnetically coupled by  $J_4$  through their middle  $\text{Cu}^{2+}$  ions to form an AFM chain along the  $a$ -direction.

**TABLE 24.2** The Values of  $J_1$ – $J_5$  and the Geometrical Parameters Associated with the Spin Exchange Paths of  $\text{Bi}_4\text{Cu}_3\text{V}_2\text{O}_{14}$

	Value (meV)	$\angle \text{Cu}–\text{O}–\text{Cu}$ ( $^\circ$ )	$\text{O}…\text{O}$ ( $\text{\AA}$ )
$J_1$	–1.9	103.4	
$J_2$	–15.7	114.5	
$J_3$	0.9		2.729
$J_4$	–18.7		2.646
$J_5$	–3.6		2.906

The magnetic properties of  $\text{Bi}_4\text{Cu}_3\text{V}_2\text{O}_{14}$  are puzzling only when the structure of the  $\text{Cu}_3\text{O}_8$  triple-chain is assumed to be as symmetrical as idealized in Figure 24.23b.  $\text{Bi}_4\text{Cu}_3\text{V}_2\text{O}_{14}$  has two nonequivalent Cu atoms, Cu1 and Cu2, which form  $\text{CuO}_4$  square planes containing their magnetic orbitals. Each  $\text{Cu}_2\text{O}_4$  square plane is corner-shared with four neighboring  $\text{Cu}_1\text{O}_4$  square planes, while each  $\text{Cu}_1\text{O}_4$  is corner-shared with two neighboring  $\text{Cu}_2\text{O}_4$  square planes and two neighboring  $\text{VO}_4$  tetrahedra (Figure 24.23a). The oxygen atoms of the  $\text{Cu}_3\text{V}_2\text{O}_{12}$  chain are not equivalent, so the SE paths  $J_1$  and  $J_2$  are nonequivalent, and so are the SSE paths  $J_3$ ,  $J_4$ , and  $J_5$  (Figure 24.23c). The values of  $J_1$ – $J_5$  obtained from DFT +  $U$  calculations [93] and their associated geometrical parameters are summarized in Table 24.2.  $J_2$  is much stronger than  $J_1$  because the  $\text{Cu}–\text{O}–\text{Cu}$  angle for  $J_2$  is greater than that for  $J_1$ , while  $J_4$  is the strongest one of  $J_3$ ,  $J_4$ , and  $J_5$  because the two  $\text{O}…\text{O}$  contact distances associated with  $J_4$  are symmetrical and are substantially shorter compared with the corresponding  $\text{O}…\text{O}$  distances associated with  $J_3$  and  $J_5$  (Table 24.2). As depicted in Figure 24.23d, the two strongest spin exchanges  $J_2$  and  $J_4$  lead to the spin lattice in which the linear AFM trimers defined by  $J_2$  are antiferromagnetically coupled by  $J_4$  through their middle  $\text{Cu}^{2+}$  ions to form an AFM chain along the  $a$ -direction. In essence, the spin lattice of the  $\text{Cu}_3\text{V}_2\text{O}_{12}$  chain is not a diamond chain but an AFM chain of made up of linear AFM trimers.

Another system actively probed in connection with the diamond-chain model is the mineral Azurite,  $\text{Cu}_3(\text{CO}_3)_2(\text{OH})_2$ , in which  $\text{Cu}_2\text{O}_6$  dimer units made up of edge-sharing  $\text{CuO}_4$  square planes are corner-shared with  $\text{CuO}_4$  square planar monomers to form “diamond” chains (Figure 24.24a), and  $\text{CO}_3$  units connect adjacent diamond chains from the  $\text{CuO}_4$  monomers of one diamond chain to the  $\text{Cu}_2\text{O}_6$  dimers of its adjacent diamond chains. The magnetic susceptibility  $\chi(T)$  of Azurite shows two broad peaks at  $\sim 22$  K and  $\sim 4.4$  K. Initially, Kikuchi et al. interpreted the high-temperature part of the susceptibility in terms of the diamond-chain model with spin frustration (i.e., AFM spin exchange  $J_2$ ,  $J_1$ , and  $J_3$  in Figure 24.24b) [94]. In explaining the low-temperature part of the susceptibility, namely, the double-peak feature of  $\chi(T)$ , it was found necessary to employ the diamond chain model with no spin

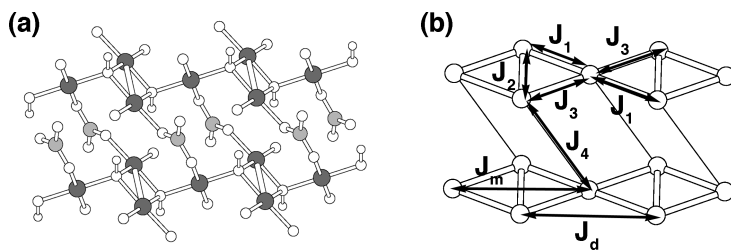


**FIGURE 24.24**

(a) A perspective view of the “diamond” chains made up of corner-sharing  $\text{Cu}_2\text{O}_6$  dimers and  $\text{CuO}_4$  square-planar monomers in Azurite,  $\text{Cu}_3(\text{CO}_3)_2(\text{OH})_2$ . The  $\text{CO}_3$  units connect adjacent diamond chains from the  $\text{CuO}_4$  monomers of one diamond chain to the  $\text{Cu}_2\text{O}_6$  dimers of its adjacent diamond chains. (b) The intrachain and interchain spin exchange paths in Azurite.

**TABLE 24.3 Geometrical Parameters Associated with the Spin Exchange Paths of Azurite  $\text{Cu}_3(\text{CO}_3)_2(\text{OH})_2$**

Value (K) Calculated	Value (K) <sup>a</sup>	$\text{Cu} \dots \text{Cu}$ (Å)	$\angle \text{Cu}-\text{O}-\text{Cu}$ (°)	$\text{O} \dots \text{O}$ (Å)
$J_1$	-89.4	-1	3.275	113.7
$J_2$	-363.3	-55	2.983	97.9
$J_3$	-86.1	+20	3.290	113.4
$J_4$	-46.3		4.872	2.219
$J_m$	-0.1	-10.1	5.849	2.597
$J_d$	6.7	-1.8	5.849	3.893

<sup>a</sup>Reference [96].

frustration (i.e., AFM  $J_2$  and  $J_1$ , and FM  $J_3$ ) [95]. More recently, Rule et al. [96] analyzed their specific heat and inelastic neutron scattering data in terms of the diamond-chain model without spin frustration by introducing two additional spin exchange parameters  $J_m$  and  $J_d$  (Figure 24.24b). Their fitting analysis of the spin-wave dispersion data led to the exchange parameters listed in Table 24.3.

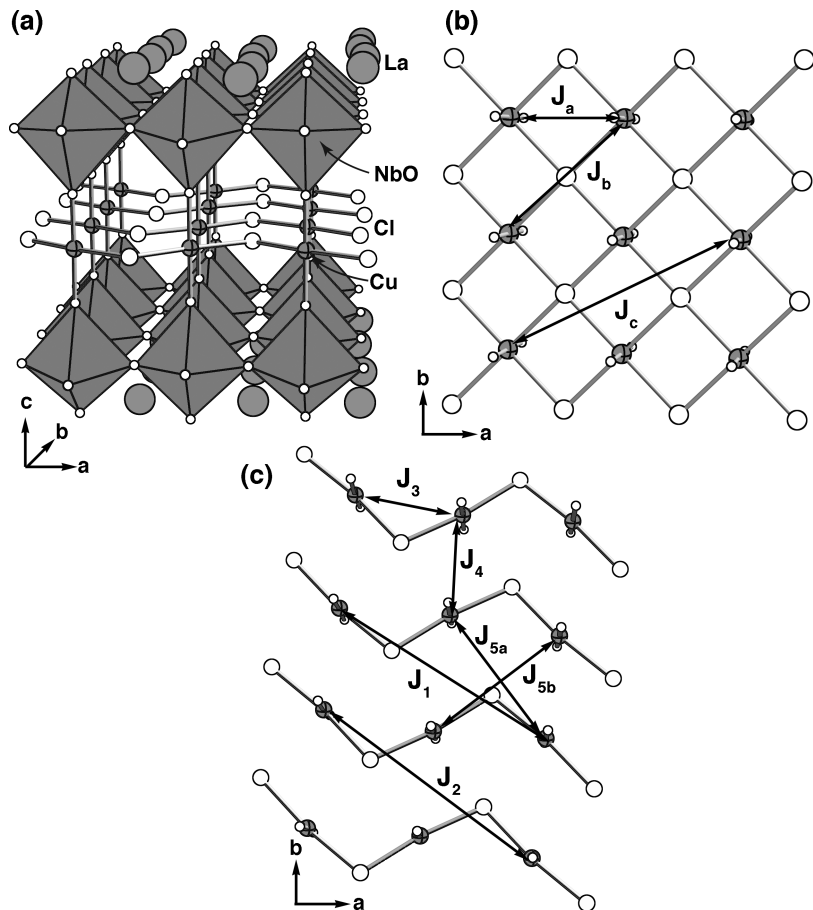
Given the structural parameters associated with these spin exchange paths (Table 24.3) and the well-known structure–property relationships established for spin exchange interactions [1,32], the exchange parameters deduced by Rule et al. [96] raise the following questions:

- (a) The Cu–O–Cu SE paths  $J_1$  and  $J_3$  are very similar. Thus it is unlikely that  $J_1$  and  $J_3$  can differ markedly in sign and magnitude.
- (b) The Cu–O–Cu angle for  $J_3$  (113.4°) is much greater than 90°. Therefore, it is unlikely that the Cu–O–Cu SE  $J_3$  can be strongly FM rather than being AFM. In fact, both  $J_1$  and  $J_3$  should be almost equally AFM.
- (c) Adjacent  $\text{CuO}_4$  monomers within each diamond chain have an arrangement leading to a negligible overlap between their magnetic orbitals. Thus it is unlikely that the SSE  $J_m$  can be strongly AFM.
- (d) The diamond-chain model proposed to analyze the magnetic properties of Azurite neglects the SSE  $J_d$  between adjacent diamond chains in the *ab*-plane (Figure 24.24b). Because of the short O...O contact distance (2.219 Å) through a  $\text{CO}_3$  bridge, this interchain interaction linking the monomers of one chain to the dimers of its adjacent chains can be substantially AFM, thereby suggesting a 2D character for Azurite. Thus it is unlikely that a one-dimensional diamond-chain model is appropriate for Azurite.

Indeed, all these concerns were verified by the spin exchanges of  $\text{Cu}_3(\text{CO}_3)_2(\text{OH})_2$  determined from the energy-mapping analysis based on DFT +  $U$  calculations (Table 24.3) [65].

#### 24.8.4 Spin Gap Behavior of a Two-Dimensional Square Net

In the crystal structure of  $(\text{CuCl})\text{LaNb}_2\text{O}_7$ , the  $\text{CuCl}$  sheets alternate with the  $\text{Nb}_2\text{O}_7$  double-perovskite slabs (containing  $\text{La}^{3+}$  ions located at the eight-coordinate sites) along the *c*-direction as shown in Figure 24.25a. Each Cu atom is capped on top and bottom with an O atom from the  $\text{Nb}_2\text{O}_7$  slabs so every  $\text{CuCl}$  sheet becomes a  $\text{CuClO}_2$  layer. According to an early X-ray powder diffraction study [97] the  $\text{Cu}^{2+}$  ions of the  $\text{CuClO}_2$  layers, the sole magnetic ions in  $(\text{CuCl})\text{LaNb}_2\text{O}_7$ , form a square lattice such that each  $\text{CuCl}_4\text{O}_2$  octahedron has  $D_{4h}$  symmetry with  $\text{Cu}-\text{Cl} = 2.746$  Å and  $\text{Cu}-\text{O} = 1.841$  Å. This is shown in Figure 24.25b. This structure is unreasonable for several reasons. First, the Cu–Cl bond is somewhat long compared with the

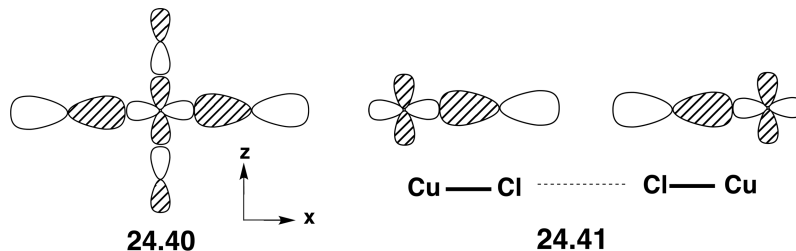
**FIGURE 24.25**

(a) The orthorhombic structure of  $(\text{CuCl})\text{LaNb}_2\text{O}_7$ . (b) The CuClO<sub>2</sub> layer of the previously proposed tetragonal  $(\text{CuCl})\text{LaNb}_2\text{O}_7$  in which each CuCl<sub>4</sub>O<sub>2</sub> octahedron has  $D_{4h}$  symmetry. (c) The CuClO<sub>2</sub> layer of orthorhombic  $(\text{CuCl})\text{LaNb}_2\text{O}_7$ , in which each CuCl<sub>2</sub>O<sub>2</sub> square plane consists of two Cu–O and two short Cu–Cl bonds.

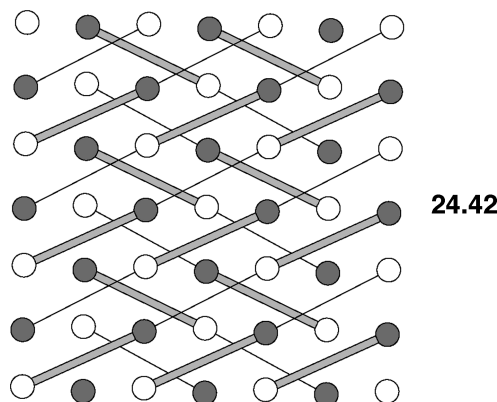
value expected from the ionic radii sum (i.e.,  $2.54 \text{ \AA}$ ). Second, the coordinate environment of a Cu<sup>2+</sup> ion (i.e., four long and two short bonds) is unreasonable. We have shown in Section 15.4 (Figure 15.8) that a tetragonal compressed structure for Cu<sup>2+</sup> is less stable than the tetragonally elongated one. Third, with this structure of the CuClO<sub>2</sub> layer, the magnetic properties of  $(\text{CuCl})\text{LaNb}_2\text{O}_7$  are difficult to explain. In the CuClO<sub>2</sub> layer of Figure 24.25b, the spin exchange  $J_b$  with a linear Cu–Cl–Cu linkage is expected to be AFM, thereby forming two two-dimensional AFM square lattices. These two AFM lattices interact through the exchanges  $J_a$  with  $\angle \text{Cu}–\text{Cl}–\text{Cu} = 90^\circ$ , which is most likely FM. Thus some spin frustration might be expected between the two two-dimensional AFM square lattices. In any event, the magnetic susceptibility of a two-dimensional AFM square lattice has a broad maximum with nonzero value at  $T = 0$  [98]. The magnetic susceptibility of  $(\text{CuCl})\text{LaNb}_2\text{O}_7$  shows a broad maximum at 16.5 K but decreases sharply to zero below 16.5 K hence leading to a spin gap [99]. The general features of this magnetic susceptibility are reasonably well described by an isolated spin dimer model. Furthermore, when an isolated spin dimer model is used to analyze the observed  $Q$ -dependence of the neutron scattering intensity profile, the Cu...Cu distance of the dimer corresponds to that expected from the spin exchange  $J_c$  (Figure 24.25b) [99].

The correct crystal structure (Figure 24.25a) of  $(\text{CuCl})\text{LaNb}_2\text{O}_7$  [100], which is orthorhombic, differs markedly from the tetragonal structure previously reported. In the CuClO<sub>2</sub> layer depicted in Figure 24.25c, each copper ion is coordinated octahedrally by two oxygen ligands with a distance of  $1.865 \text{ \AA}$  as well as four chlorine ligands with two shorter bonds ( $2.386 \text{ \AA}$ ,  $2.389 \text{ \AA}$ ) and two very long “bonds” ( $3.136 \text{ \AA}$ ,  $3.188 \text{ \AA}$ ). We encountered this same situation in Section 16.4 for the Lifschitz

salts. It is probably just as accurate to classify central layer of  $\text{Cu}^{2+}$  ions as being  $\text{CuO}_2\text{Cl}_2$  square planes. The shorter Cu—Cl bonds then form the Cu—Cl—Cu—Cl zigzag chains along the  $a$ -direction, and these chains are interconnected by the long Cu—Cl bonds. When the local  $z$ - and  $x$ -axes for each  $\text{Cu}^{2+}$  ion are taken along the Cu—O and the short Cu—Cl bonds, respectively, the overall symmetry of the magnetic orbital including the ligand  $p$ -orbitals has the  $z^2 - x^2$  character (24.40). Notice that the orbitals here are heavily weighted on the Cl ligands. This is a result of the fact that the  $d$  AOs of  $\text{Cu}^{2+}$  lie at a low energy in comparison to the Cl  $p$  AOs. The orbital still has the symmetry of  $z^2 - x^2$ , and as a result the spin exchange interactions



in the  $\text{CuClO}_2$  layer become highly anisotropic. For the spin exchange paths  $J_1 - J_5$  of this layer shown in Figure 24.25c, their geometrical parameters are summarized in Table 24.4, and so are the values of  $J_1 - J_5$  determined from DFT+ $U$  calculations. The strongest AFM exchange  $J_1$  is of the Cu—Cl...Cl—Cu SSE type as shown in 24.41, and  $J_2$  is the weaker AFM exchange of the same type. Other exchanges are all FM and are of the Cu—Cl—Cu SE type. Thus as depicted in 24.42, where  $J_1$  and  $J_2$  paths are shown as cylinders and thin lines, respectively, the magnetic properties of  $(\text{CuCl})\text{LaNb}_2\text{O}_7$



can be described by the AFM—AFM (i.e.,  $J_1 - J_2$ ) alternating AFM chain, which has a spin gap. Since  $J_2$  is considerably weaker than  $J_1$ , they can also be described by an isolated AFM (i.e.,  $J_1$ ) dimer.

**TABLE 24.4** Geometrical Parameters Associated With the Spin Exchange Paths of  $(\text{CuCl})\text{LaNb}_2\text{O}_7$

$J_s$	$J_s/J_1$ <sup>a</sup>	Cu...Cu ( $\text{\AA}$ )	Cl...Cl ( $\text{\AA}$ )	$\angle \text{Cu}-\text{Cl} \dots \text{Cl}$ ( $^\circ$ )	$\angle \text{Cu}-\text{Cl}-\text{Cu}$ ( $^\circ$ )
$J_1$	1.00	8.5325	3.8347	164.9	
$J_2$	0.18	8.8184	4.2314	156.0	
$J_3$	-0.39	3.8859			109.0
$J_4$	-0.04	3.6244			80.8
$J_{5a}$	-0.38	5.4604			156.7
$J_{5b}$	-0.14	5.5043			170.2

<sup>a</sup> $J_1 = -87.5 \text{ K}$ .

---

## 24.9 MODEL HAMILTONIANS BEYOND THE LEVEL OF SPIN EXCHANGE

---

There are cases when a model Hamiltonian including only spin exchange interactions is not adequate in describing magnetic systems. In such cases, a model Hamiltonian is improved by adding other energy terms, as can be seen from equations 24.14a and (24.63). The spin Hamiltonian of equation 24.63 depends only on the relative

$$\hat{H}_{\text{spin}} = -J_{12}\hat{S}_1 \cdot \hat{S}_2 \quad (24.14a)$$

$$\hat{H}_{\text{spin}} = -J_{12}\hat{S}_1 \cdot \hat{S}_2 + \vec{D}_{12} \cdot (\hat{S}_1 \times \hat{S}_2) \quad (24.63)$$

orientations of the two spins. To describe the effect of absolute spin orientations on magnetic properties, one may introduce the single-ion anisotropy energy term  $A\hat{S}_z^2$  for each magnetic ion into the spin Hamiltonian as described in Section 24.7.2. Then, the model Hamiltonian can be rewritten as

$$\hat{H}_{\text{spin}} = -J_{12}\hat{S}_1 \cdot \hat{S}_2 + \vec{D}_{12} \cdot (\hat{S}_1 \times \hat{S}_2) + A_1\hat{S}_{1z}^2 + A_2\hat{S}_{2z}^2 \quad (24.70)$$

Finally, we mention another term known as a biquadratic (BQ) spin exchange, which is written as  $K_{12}(\hat{S}_1 \cdot \hat{S}_2)^2$  [101]. If the constant  $K_{12}$  is negative, this term favors a collinear spin arrangement regardless of whether it is FM or AFM. Consideration of a BQ spin exchange was found necessary in discussing the magnetic interactions of transition-metal ions with rare-earth ions [102]. If the BQ exchange were to be added in the model Hamiltonian, we have

$$\hat{H}_{\text{spin}} = -J_{12}\hat{S}_1 \cdot \hat{S}_2 + K_{12}(\hat{S}_1 \cdot \hat{S}_2)^2 + \vec{D}_{12} \cdot (\hat{S}_1 \times \hat{S}_2) + A_1\hat{S}_{1z}^2 + A_2\hat{S}_{2z}^2 \quad (24.71)$$

As can be seen from the equation 24.71, one can make the model Hamiltonian quite complex. In general, use of an elaborate model Hamiltonian is undesirable and is not warranted because the objective of using a model Hamiltonian is to describe the essence of the chemistry/physics involved with a minimal number of parameters. Nevertheless, it is important to understand what each term of the model Hamiltonian stands for.

---

## 24.10 SUMMARY REMARKS

---

We surveyed various concepts and phenomena concerning magnetic properties from the perspective of electronic structure. Interactions between magnetic ions are weak so that the energy levels of a magnetic system are closely packed. Thus a succinct description of the associated magnetic properties requires the use of a model Hamiltonian defined in terms of several energy terms, which include Heisenberg exchange, DM exchange, BQ exchange, and single-ion magnetic anisotropy. The signs and values of the constants specifying these terms can be determined on the basis of energy mapping analysis [1b], in which the energy spectrum of a magnetic system determined from electronic structure calculations for a set of broken-symmetry states is mapped onto that determined by a model Hamiltonian defined in terms of parameters.

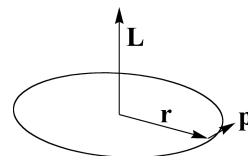
The literature on magnetic studies shows many examples in which the magnetic properties of a system were interpreted with a spin lattice irrelevant for the system largely because the selection of spin lattice relies on the geometrical pattern of

magnetic ion arrangement and is motivated by the desire to do novel physics. This unfortunately embarrassing situation can be avoided by determining a spin lattice on the basis of electronic structure calculations and considerations [1].

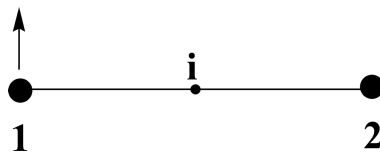
SOC plays an important role in determining magnetic properties [23]. It is interesting that the spin orientation of a transition-metal magnetic ion can be readily explained in terms of perturbation theory by considering its split *d*-block levels as unperturbed states with the SOC Hamiltonian  $\hat{H}_{\text{SO}}$  as perturbation. Given  $J$  as the Heisenberg exchange of a spin exchange path, the strength of the associated DM exchange  $D$  is frequently estimated by  $|D/J| \approx \Delta g/g \approx 0.1$  or less. This estimate is valid only when the two spin sites have an identical chemical environment. When the two spin sites are not chemically equivalent, the  $|D/J|$  ratio can become very large because all three hopping processes leading to DM interaction can become large [55].

## PROBLEMS

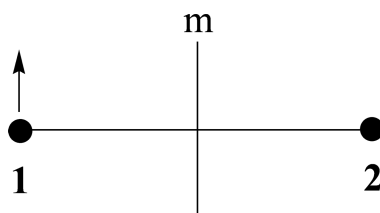
- 24.1.** The following problems are concerned with how the spin orientation of an electron in space is affected by symmetry operations. In answering these questions, recall that the angular momentum  $\mathbf{L}$  of an electron circling around an axis at a distance  $r$  from the axis of rotation with tangential linear momentum  $\mathbf{p}$  is given by  $\mathbf{L} = \mathbf{r} \times \mathbf{p}$ , where  $\mathbf{r}$  is the distance vector (see below), and that the spin angular momentum  $\mathbf{S}$  of an electron is similar in symmetry properties to the orbital angular momentum  $\mathbf{L}$ .



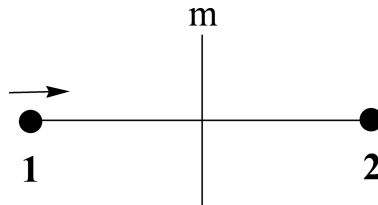
- a. The spin sites **1** and **2** below are related to each other by inversion symmetry *i*. If the spin of site **1** has the orientation depicted, what should be the orientation of the spin at site **2**?



- b. The spin sites **1** and **2** are now related to each other by mirror plane of symmetry *m*. If the spin of site **1** has the orientation parallel to the mirror plane as depicted, what should be the orientation of the spin at site **2**?



- c. The spin sites **1** and **2** are related to each other by mirror plane of symmetry  $m$ . If the spin of site **1** has the orientation perpendicular to the mirror plane as depicted, what should be the orientation of the spin at site **2**?



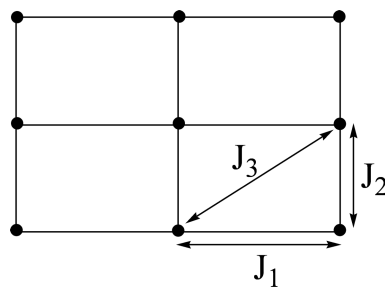
- 24.2.** What happens to the orientation of a spin under time-reversal symmetry (i.e., under the symmetry operation of reversing the time ( $t \rightarrow -t$ )?
- 24.3.** According to Kramers degeneracy theorem, the energy levels of a system with an odd total number of electrons remain at least doubly-degenerate in the presence of purely electric fields (i.e., no magnetic fields), which is a consequence of the time reversal invariance of electric fields. Why is this degeneracy lifted by magnetic field  $\mathbf{H}$ ?
- 24.4.** The  $S=1$  state is triply degenerate and is described by three functions  $|S, S_z\rangle = |1, 1\rangle, |1, 0\rangle$ , and  $|1, -1\rangle$ . Under the effect of spin-orbit coupling, this degeneracy is split even in the absence of magnetic field, which is known as zero-field splitting (ZFS). Show how the degeneracy is split by using the ZFS Hamiltonian  $\hat{H}_{\text{zf}}$  given by

$$\hat{H}_{\text{zf}} = D\hat{S}_z^2 + E(\hat{S}_+ \hat{S}_+ + \hat{S}_- \hat{S}_-) / 2 - D\hat{S}^2 / 3.$$

- 24.5.** The  $S=1/2$  state is doubly-degenerate and is described by two functions  $|S, S_z\rangle = |1/2, 1/2\rangle$  and  $|1/2, -1/2\rangle$ . These two states are not split by the ZFS Hamiltonian  $\hat{H}_{\text{zf}}$ , and obeys Kramer's degenerate theorem. Show this.
- 24.6.** The rectangular spin lattice shown below consists of identical magnetic ions spin  $S$ , and is described by three spin exchange parameters  $J_1, J_2$ , and  $J_3$ . To determine the values of  $J_1, J_2$ , and  $J_3$  in terms of energy mapping analysis based on DFT calculations, it is necessary to consider four different ordered spin states, and evaluate their energies in terms of the spin Hamiltonian

$$\hat{H}_{\text{spin}} = - \sum_{i < j} J_{ij} \hat{S}_i \cdot \hat{S}_j$$

which is defined in terms of the three parameters, that is,  $J_{ij} = J_1, J_2$ , or  $J_3$ . Suggest four ordered spin states and write down their total spin exchange energies.



- 24.7.** An antiferromagnetic (AFM) spin dimer made up of two spin-1/2 ions is described by the spin Hamiltonian

$$\hat{H}_{\text{spin}} = -J\hat{S}_1 \cdot \hat{S}_2,$$

where  $J < 0$ . For this system, the ground state is described by the singlet state  $\Phi_S$ , and the triplet state by  $\Phi_{T1}, \Phi_{T2}$  and  $\Phi_{T3}$ .

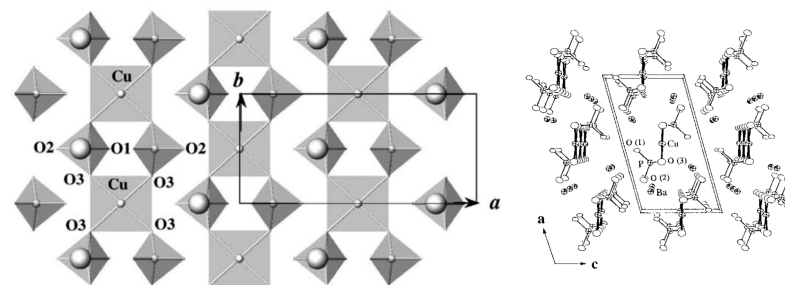
$$\begin{aligned}\Phi_S &\equiv |0, 0\rangle = \frac{1}{\sqrt{2}}[\alpha(1)\beta(2) - \beta(1)\alpha(2)] \\ &= \frac{1}{\sqrt{2}}\left(\left|\frac{1}{2}, \frac{1}{2}\right\rangle_1 \left|\frac{1}{2}, -\frac{1}{2}\right\rangle_2 - \left|\frac{1}{2}, -\frac{1}{2}\right\rangle_1 \left|\frac{1}{2}, \frac{1}{2}\right\rangle_2\right) \\ \Phi_{T1} &\equiv |1, 0\rangle = \frac{1}{\sqrt{2}}[\alpha(1)\beta(2) + \beta(1)\alpha(2)] \\ &= \frac{1}{\sqrt{2}}\left(\left|\frac{1}{2}, \frac{1}{2}\right\rangle_1 \left|\frac{1}{2}, -\frac{1}{2}\right\rangle_2 + \left|\frac{1}{2}, -\frac{1}{2}\right\rangle_1 \left|\frac{1}{2}, \frac{1}{2}\right\rangle_2\right) \\ \Phi_{T2} &\equiv |1, 1\rangle = \alpha(1)\alpha(2) = \left|\frac{1}{2}, \frac{1}{2}\right\rangle_1 \left|\frac{1}{2}, \frac{1}{2}\right\rangle_2 \\ \Phi_{T3} &\equiv |1, -1\rangle = \beta(1)\beta(2) = \left|\frac{1}{2}, -\frac{1}{2}\right\rangle_1 \left|\frac{1}{2}, -\frac{1}{2}\right\rangle_2\end{aligned}$$

When the midpoint between the spin sites 1 and 2 is not a center of inversion, the DM vector  $\vec{D}$  is nonzero. In such a case, the spin dimer can be described by the spin Hamiltonian

$$\hat{H}_{\text{spin}} = -J\hat{S}_1 \cdot \hat{S}_2 + \vec{D} \cdot (\hat{S}_1 \times \hat{S}_2).$$

Considering that the DM interaction  $\vec{D} \cdot (\hat{S}_1 \times \hat{S}_2)$  as perturbation, examine how the ground state energy and wave functions of the spin dimer are described under the effect of the DM interaction.

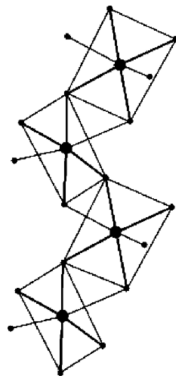
- 24.8.** In the magnetic solids  $A_2Cu(PO_4)_2$  ( $A = Ba, Sr$ ) consisting of  $Cu^{2+}$  ions, the  $Cu(O)_4$  square planes are isolated from one another, as depicted below.



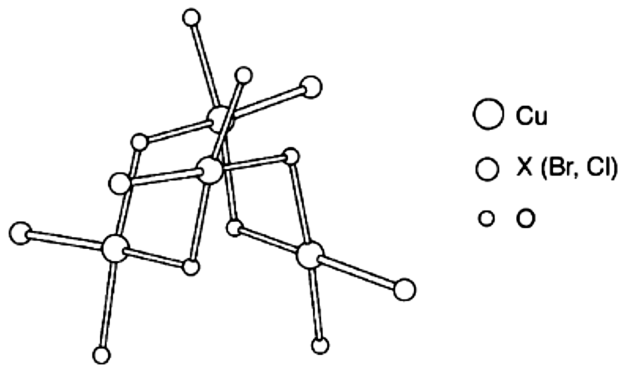
However, the magnetic properties of  $A_2Cu(PO_4)_2$  ( $A = Ba, Sr$ ) are described by a uniform AFM chain model. Explain why this should be the case.

- 24.9.** The magnetic oxide  $CaCuGe_2O_6$  consists of  $CuO_4$  chains made up of edge-sharing  $CuO_6$  octahedra, which are axially elongated. Thus if one considers the  $Cu(O_{eq})_4$

square planes made up of four short Cu–O<sub>eq</sub> bonds, each CuO<sub>4</sub> chain can be viewed as a Cu(O<sub>eq</sub>)<sub>3</sub> chain made up of corner-sharing Cu(O<sub>eq</sub>)<sub>4</sub> square planes, shown below. Thus one might have expected that the magnetic susceptibility of CaCuGe<sub>2</sub>O<sub>6</sub> is described by a uniform AFM chain model. However, it is described by an isolated Heisenberg dimer model. Explain why this is the case.



- 24.10.** The magnetic orbital of a Cu<sup>2+</sup> ion in Cu<sub>2</sub>Te<sub>2</sub>O<sub>5</sub>X<sub>2</sub> (X = Cl, Br) is contained in the CuO<sub>3</sub>X square plane. Every four CuO<sub>3</sub>X units share their oxygen corners to form a tetrahedron of four Cu<sup>2+</sup> ions (below), and such Cu<sub>4</sub> tetrahedral units are isolated from one another. Consequently, one might consider using an isolated AFM tetrahedron model for Cu<sub>2</sub>Te<sub>2</sub>O<sub>5</sub>X<sub>2</sub> (X = Cl, Br), thereby expecting spin frustration. However, the magnetic susceptibility of Cu<sub>2</sub>Te<sub>2</sub>O<sub>5</sub>X<sub>2</sub> (X = Cl, Br) shows a spin-gapped behavior with no spin frustration. Explain why this is the case.



## REFERENCES

- (a) M.-H. Whangbo, H.-J. Koo, and D. Dai, *J. Solid State Chem.*, **176**, 417 (2003). (b) H.-J. Xiang, C. Lee, H.-J. Koo, X. G. Gong, and M.-H. Whangbo, *Dalton Trans.*, **42**, 823 (2013)
- R. G. Parr and W. Yang, *Density-Functional Theory of Atoms and Molecules*, Oxford University Press, (1989); K. Capelle, arXiv:cond-mat/0211443v5 [cond-mat.mtrl-sci] 18 Nov 2006.
- N. F. Mott, *Metal-Insulator Transitions*, Taylor & Francis, Ltd., (1974).
- M.-H. Whangbo, *J. Chem. Phys.*, **70**, 4963 (1979).
- (a) S. L. Dudarev, G. A. Botton, S. Y. Savrasov, C. J. Humphreys, and A. P. Sutton, *Phys. Rev. B*, **57**, 1505 (1998). (b) A. I. Liechtenstein, V. I. Anisimov, and J. Zaanen, *Phys. Rev. B*, **52**, 5467 (1995).
- A. D. Becke, *J. Chem. Phys.*, **98**, 1372 (1993).

7. C. T. Lee, W. Yang, and R. G. Parr, *Phys. Rev. B*, **37**, 785 (1988).
8. J. Heyd, G. E. Scuseria, and M. Ernzerhof, *J. Chem. Phys.*, **118**, 8207 (2003).
9. Y. G. Shi, Y. F. Guo, S. Yu, M. Arai, A. A. Belik, A. Sato, K. Yamaura, E. Takayama-Muromachi, T. Varga, and J. F. Mitchell, *J. Solid State Chem.*, **183**, 402 (2010).
10. (a) Y. G. Shi, Y. F. Guo, S. Yu, M. Arai, A. A. Belik, A. Sato, K. Yamaura, E. Takayama-Muromachi, H. F. Tian, H. X. Yang, J. Q. Li, T. Varga, J. F. Mitchell, and S. Okamoto, *Phys. Rev. B*, **80**, 161104 (2009). (b) J. Kang, C. Lee, and M.-H. Whangbo, *unpublished results*.
11. Y. Shi, Y. Guo, S. Yu, M. Arai, A. Sato, A. A. Belik, K. Yamaura, and E. Takayama-Muromachi, *J. Am. Chem. Soc.*, **132**, 8474 (2010).
12. E. J. Kan, F. Wu, C. Lee, J. Kang, and M.-H. Whangbo, *Inorg. Chem.*, **50**, 4182 (2011).
13. M. W. Lufaso, W. R. Gemmill, S. J. Mugavero, III, S.-J. Kim, Y. Lee, T. Vogt, and H.-C. zur Loya, *J. Solid State Chem.*, **181**, 623 (2008).
14. C. Tian, A. C. Wibowo, H.-C. zur Loya, and M.-H. Whangbo, *Inorg. Chem.*, **50**, 4142 (2011).
15. R. Macquart, S.-J. Kim, W. R. Gemmill, J. K. Stalick, Y. Lee, T. Vogt, and H.-C. zur Loya, *Inorg. Chem.*, **44**, 9676 (2005).
16. A. S. Erickson, S. Misra, G. J. Miller, R. R. Gupta, Z. Schlesinger, W. A. Harrison, J. M. Kim, and I. R. Fisher, *Phys. Rev. Lett.*, **99**, 016404 (2007).
17. K. E. Stitzer, M. D. Smith, and H.-C. zur Loya, *Solid State Sci.*, **4**, 311 (2002).
18. H. J. Xiang and M.-H. Whangbo, *Phys. Rev. B*, **75**, 052407 (2007).
19. I. D. Brown and D. Altermatt, *Acta Cryst. B*, **41**, 244 (1985).
20. N. E. Brese and M. O'Keeffe, *Acta Cryst. B*, **47**, 192 (1991).
21. (a) W. J. Padilla, D. Mandrus, and D. N. Basov, *Phys. Rev. B*, **66**, 035120 (2002). (b) W.-J. Son and M.-H. Whangbo, *unpublished results*.
22. J. C. Slater, *Phys. Rev.*, **82**, 538 (1951).
23. D. Dai, H. J. Xiang, and M.-H. Whangbo, *J. Comput. Chem.*, **29**, 2187 (2008).
24. J. S. Smart, *Effective Field Theory of Magnetism*, Saunders, Philadelphia, (1966).
25. G. L. Squires, *Introduction to the Theory of Thermal Neutron Scattering*, Cambridge University Press, (1978).
26. P. J. Hay, J. C. Thibeault, and R. Hoffmann, *J. Am. Chem. Soc.*, **97**, 4884 (1975).
27. (a) B. J. Gibson, R. K. Kremer, A. V. Prokofiev, W. Assmus, and G. J. McIntyre, *Physica B*, **350**, e253 (2004). (b) D. Dai, H.-J. Koo, and M.-H. Whangbo, *Inorg. Chem.*, **43**, 4026 (2004).
28. H.-J. Koo, C. Lee, M.-H. Whangbo, G. J. McIntyre, and R. K. Kremer, *Inorg. Chem.*, **50**, 3582 (2011).
29. Z. He, T. Kyômen, and M. Itoh, *Phys. Rev. B*, **69**, 220407 (2004).
30. K. Ghoshray, B. Pahari, B. Bandyopadhyay, R. Sarkar, and A. Ghoshray, *Phys. Rev. B*, **71**, 214401 (2005).
31. H.-J. Koo and M.-H. Whangbo, *Inorg. Chem.*, **45**, 4440 (2006).
32. J. B. Goodenough, *Magnetism and the Chemical Bond*, Wiley-Interscience, New York, (1963).
33. C. Lee, J. Kang, K. H. Lee, and M.-H. Whangbo, *Inorg. Chem.*, **48**, 4185 (2009).
34. L. Noodleman, *J. Chem. Phys.*, **74**, 5737 (1981).
35. L. Noodleman and E. R. Davidson, *Chem. Phys.*, **109**, 131 (1986).
36. D. Dai and M.-H. Whangbo, *J. Chem. Phys.*, **114**, 2887 (2001).
37. D. Dai and M.-H. Whangbo, *J. Chem. Phys.*, **118**, 29 (2003).
38. J. E. Greidan, *J. Mater. Chem.*, **11**, 37 (2001) and the references cited therein.
39. D. Dai and M.-H. Whangbo, *J. Chem. Phys.*, **121**, 672 (2004).
40. C. K. Majumdar and D. Ghosh, *J. Math. Phys.*, **10**, 1388 (1969).
41. H.-J. Koo, H. J. Xiang, C. Lee, and M.-H. Whangbo, *Inorg. Chem.*, **48**, 9051 (2009).
42. N. D. Mermin and H. Wagner, *Phys. Rev. Lett.*, **17**, 1133 (1966).
43. H. Kageyama, T. Watanabe, Y. Tsujimoto, A. Kitada, Y. Sumida, K. Kanamori, K. Yoshimura, N. Hayashi, S. Muranaka, M. Takano, M. Ceretti, W. Paulus, C. Ritter, and G. André, *Angew. Chem. Int. Ed.*, **47**, 5740 (2008).

44. N. Hayashi, H. Kageyama, Y. Tsujimoto, T. Watanabe, S. Muranaka, T. Ono, S. Nasu, Y. Ajiro, K. Yoshimura, and M. Takano, *J. Phys. Soc. Jpn.*, **79**, 123709 (2010).
45. Y. Tsujimoto, C. Tassel, N. Hayashi, T. Watanabe, H. Kageyama, K. Yoshimura, M. Takano, M. Ceretti, C. Ritter, and W. Paulus, *Nature* **450**, 1062 (2007).
46. H. J. Xiang, S.-H. Wei, and M.-H. Whangbo, *Phys. Rev. Lett.*, **100**, 167207 (2008).
47. P. P. Ewald, *Ann. Phys.*, **64**, 253 (1921); T. Darden, D. York, and L. Pedersen, *J. Chem. Phys.*, **98**, 10089 (1993); H. Wang, F. Dommert, and C. Holm, *J. Chem. Phys.*, **133**, 034117 (2010).
48. S. T. Bramwell and M. J. P. Gingras, *Science*, **294**, 1495 (2001) and the references cited therein.
49. N. W. Ashcroft and N. D. Mermin, *Solid State Physics*, Saunders College, Philadelphia (1976), pp. 718–722.
50. T. Moriya, *Phys. Rev. Lett.*, **4**, 228 (1960).
51. R. H. Buttner, E. N. Maslen, and N. Spadaccini, *Acta Cryst. B*, **46**, 131 (1990).
52. K. I. Kugel and D. I. Khomskii, *Sov. Phys. Usp.* **25**, 231 (1982).
53. C. Zerner, *Phys. Rev.*, **82**, 403 (1951).
54. R. D. Johnson, L. C. Chapon, D. D. Khalyavin, P. Manuel, P. G. Radaelli, and C. Martin, *Phys. Rev. Lett.*, **108**, 067201 (2012).
55. X. Z. Lu, M.-H. Whangbo, S. A. Dong, X. G. Gong, and H. J. Xiang, *Phys. Rev. Lett.*, **108**, 187204 (2012).
56. G. Ananthakrishna, L. F. Weiss, D. C. Foyt, and D. J. Klein, *Physica*, **81B**, 275 (1976).
57. F. Haldane, *Phys. Lett. A*, **93**, 464 (1983); F. Haldane, *Phys. Rev. Lett.*, **50**, 1153 (1983); I. Affleck and E. H. Lieb, *Lett. Math. Phys.*, **12**, 57 (1986).
58. J. P. Renard, M. Verdaguer, L. P. Regnault, W. A. C. Erkelens, J. Rossat-Mignod, and W. G. Stirling, *Europhys. Lett.*, **3**, 945 (1987).
59. L.W. Finger, R. M. Hazen, and R. J. Hemley, *Am. Mineral.*, **74**, 952 (1989).
60. M. Jaime, V. F. Correa, N. Harrison, C. D. Batista, N. Kawashima, Y. Kazuma, G. A. Jorge, R. Stern, I. Heinmaa, S. A. Zvyagin, Y. Sasago, and K. Uchinokura, *Phys. Rev. Lett.*, **93**, 087203 (2004).
61. M. Hase, M. Kohno, H. Kitazawa, N. Tsujii, O. Suzuki, K. Ozawa, G. Kido, M. Imai, and X. Hu, *Phys. Rev. B*, **73**, 104419 (2006).
62. M. Hase, M. Matsuda, K. Kakurai, K. Ozawa, H. Kitazawa, N. Tsujii, A. Dönni, M. Kohno, and X. Hu, *Phys. Rev. B*, **76**, 064431 (2007).
63. H.-J. Koo and M.-H. Whangbo, *Inorg. Chem.*, **49**, 9253 (2010).
64. H. Ohta, S. Okubo, T. Kamikawa, T. Kunimoto, Y. Inagaki, H. Kikuchi, T. Saito, M. Azuma, and M. Takano, *J. Phys. Soc. Jpn.*, **72**, 2464 (2003).
65. J. Kang, C. Lee, R. K. Kremer, and M.-H. Whangbo, *J. Phys.: Condens. Matter*, **21**, 392201 (2009).
66. F. E. Mapp and D. J. Machin, *Magnetism and Transition Metal Complexes*, Long Chapman and Hall, London (1973).
67. X. Wang, R. Wu, D.-S. Wang, and A. J. Freeman, *Phys. Rev. B*, **54**, 61 (1996).
68. J. Kuneš, P. Novák, R. Schmid, P. Blaha, and K. Schwarz, *Phys. Rev. B*, **64**, 153102 (2001).
69. M. Kenzelmann, A. B. Harris, S. Jonas, C. Broholm, J. Schefer, S. B. Kim, C. L. Zhang, S.-W. Cheong, O. P. Vajk, and J. W. Lynn, *Phys. Rev. Lett.*, **95**, 087206 (2005).
70. H. J. Xiang, S.-H. Wei, M.-H. Whangbo, and J. L. F. Da Silva, *Phys. Rev. Lett.*, **101**, 037209 (2008).
71. S. Ji, E. J. Kan, M.-H. Whangbo, J.-H. Kim, Y. Qiu, M. Matsuda, H. Yoshida, Z. Hiroi, M. A. Green, T. Ziman, and S.-H. Lee, *Phys. Rev. B*, **81**, 094421 (2010).
72. J. Liu, H.-J. Koo, H. J. Xiang, R. K. Kremer and M.-H. Whangbo, *unpublished results*.
73. (a) J. P. Attfield, *J. Phys.: Condens. Matter*, **1**, 7045 (1989). (b) M. Herak, M. Miljak, G. Dhalenne, and A. Revcolevschi, *J. Phys.: Condens. Matter*, **22**, 026006 (2010) and the references cited therein.

74. M. G. Banks, R. K. Kremer, C. Hoch, A. Simon, B. Ouladdiaf, J.-M. Broto, H. Rakoto, C. Lee, and M.-H. Whangbo, *Phys. Rev. B*, **80**, 024404 (2009).
75. C. Lee, H.-J. Koo, M.-H. Whangbo, R. K. Kremer, and A. Simon, *Phys. Rev. B*, **86**, 060407 (2012).
76. B. D. White, W. M. Pätzold, and J. J. Neumeier, *Phys. Rev. B*, **82**, 094439 (2010) and the references cited therein.
77. W. M. Reiff, A. M. LaPointe, and E. H. Witten, *J. Am. Chem. Soc.*, **126**, 10206 (2004).
78. D. Dai and M.-H. Whangbo, *Inorg. Chem.*, **44**, 4407 (2005).
79. Y. Zhang, E. J. Kan, H. J. Xiang, A. Villesuzanne, and M.-H. Whangbo, *Inorg. Chem.*, **50**, 1758 (2011).
80. K. Takubo, T. Mizokawa, S. Hirata, J.-Y. Son, A. Fujimori, D. Topwal, D. D. Sarma, S. Rayaprol, and E.-V. Sampathkumaran, *Phys. Rev. B*, **71**, 073406 (2005).
81. H. Wu, M. W. Haverkort, Z. Hu, D. I. Khomskii, and L. H. Tjeng, *Phys. Rev. Lett.* **95**, 186401 (2005).
82. H. J. Xiang, E. J. Kan, S.-H. Wei, M.-H. Whangbo, and X. G. Gong, *Phys. Rev. B*, **84**, 224429 (2011).
83. S. Vilminot, M. Richard-Plouet, G. André, D. Swierczynski, M. Guillot, F. Bourée-Vigneron, M. Drillon, *J. Solid State Chem.*, **170**, 255 (2003).
84. S. Hara, H. Kondo, H. Sato, *J. Phys. Soc. Jpn.*, **80**, 43701 (2011).
85. H.-J. Koo, R. K. Kremer, and M.-H. Whangbo, *J. Phys. Soc. Jpn.*, **81**, 063704 (2012).
86. Y. Miura, R. Hirai, Y. Kobayashi, and M. Sato, *J. Phys. Soc. Jpn.*, **75**, 84707 (2006).
87. J. Xu, A. Assoud, N. Soheilnia, S. Derakhshan, H. L. Cuthbert, J. E. Greedan, JM.-H. Whangbo, and H. Kleinke, *Inorg. Chem.*, **44**, 5042 (2005).
88. S. Derakhshan, H. L. Cuthbert, J. E. Greedan, B. Rahman, and T. Saha-Dasgupta, *Phys. Rev. B*, **76**, 104403 (2007).
89. H.-J. Koo and M.-H. Whangbo, *Inorg. Chem.*, **47**, 128 (2008).
90. Y. Miura, Y. Yasui, T. Moyoshi, M. Sato, and K. Kakurai, *J. Phys. Soc. Jpn.*, **77**, 104709 (2008).
91. G. B. Deacon, B. M. Gatehouse, and G. N. Ward, *Acta Crystallogr., Sect. C: Cryst. Struct. Commun.*, **50**, 1178 (1994).
92. H. Sakurai, K. Yoshimura, K. Kosuge, N. Tsujii, H. Abe, H. Kitazawa, G. Kido, H. Michor, and G. Hilscher, *J. Phys. Soc. Jpn.*, **71**, 1161 (2002).
93. H.-J. Koo and M.-H. Whangbo, *Inorg. Chem.*, **47**, 4779 (2008).
94. H. Kikuchi, Y. Fujii, M. Chiba, S. Mitsudo, T. Idehara, T. Tonegawa, K. Okamoto, T. Sakai, T. Kuwai, and H. Ohta, *Phys. Rev. Lett.*, **94**, 227201 (2005).
95. G. Bo and G. Su, *Phys. Rev. Lett.*, **97**, 089701 (2006).
96. K. C. Rule, A. U. B. Wolter, S. Süllow, D. A. Tennant, A. Brühl, S. Köhler, B. Wolf, M. Lang, and J. Schreuer, *Phys. Rev. Lett.*, **100**, 117202 (2008).
97. T. A. Kodenkandath, J. N. Lalena, W. L. Zhou, E. E. Carpenter, C. Sangregorio, A. U. Falster, W. B. Simmons, Jr., C. J. O'Connor, and J. B. Wiley, *J. Am. Chem. Soc.*, **121**, 10743 (1999).
98. M. Takahashi, *Phys. Rev. B*, **40**, 2494 (1989).
99. H. Kageyama, T. Kitano, N. Oba, M. Nishi, S. Nagai, K. Hirota, L. Viciu, J. B. Wiley, J. Yasuda, Y. Baba, Y. Ajiro, and K. Yoshimura, *J. Phys. Soc. Jpn.*, **74**, 1702 (2005).
100. C. Tassel, J. Kang, C. Lee, O. Hernandez, Y. Qiu, W. Paulus, B. Lake, T. Guidi, M.-H. Whangbo, H. Kageyama, and S.-H. Lee, *Phys. Rev. Lett.*, **105**, 167205 (2010).
101. J. Sólyom, *Phys. Rev. B*, **36**, 8642 (1987); P. Novák, I. Chaplygin, G. Seifert, S. Gemming, and R. Laskowski, *Comput. Mater. Sci.*, **79**, 44 (2008); A. Furrer, F. Juranyi, K. W. Krämer, and Th. Strässle, *Phys. Rev. B*, **77**, 174410 (2008).
102. C. Lee, E. J. Kan, H. J. Xiang, R. K. Kremer, S.-H. Lee, Z. Hiroi, and M.-H. Whangbo, *Inorg. Chem.*, **51**, 6890 (2012).

**APPENDIX I**

# Perturbational Molecular Orbital Theory

---

## I.1 MATRIX REPRESENTATION

---

To simplify the discussion of perturbational molecular orbital (MO) theory, it is necessary to consider matrix representations of MO theory [1,2]. To construct the MOs  $\psi_i$  as a linear combinations of the atomic orbitals (AOs),  $\chi_1, \chi_2, \dots, \chi_m$ ,

$$\psi_i = \sum_{\mu} C_{\mu i} \chi_{\mu} \quad (i = 1, 2, \dots, m) \quad (1)$$

we first calculate the matrix elements  $H_{\mu\nu}$  and  $S_{\mu\nu}$  over the AO basis

$$H_{\mu\nu} = \langle \chi_{\mu} | H^{\text{eff}} | \chi_{\nu} \rangle \quad (\mu, \nu = 1, 2, \dots, m) \quad (2a)$$

$$S_{\mu\nu} = \langle \chi_{\mu} | \chi_{\nu} \rangle \quad (\mu, \nu = 1, 2, \dots, m) \quad (2b)$$

which lead to the  $m \times m$  matrices **H** and **S**

$$\mathbf{H} = \begin{pmatrix} H_{11} & H_{12} & \cdots & H_{1m} \\ H_{21} & H_{22} & \cdots & H_{2m} \\ \vdots & \vdots & \ddots & \vdots \\ H_{m1} & H_{m2} & \cdots & H_{mm} \end{pmatrix} \quad (3a)$$

$$\mathbf{S} = \begin{pmatrix} S_{11} & S_{12} & \cdots & S_{1m} \\ S_{21} & S_{22} & \cdots & S_{2m} \\ \vdots & \vdots & \ddots & \vdots \\ S_{m1} & S_{m2} & \cdots & S_{mm} \end{pmatrix} \quad (3b)$$

To express Eq. I in matrix notation, we define the row vector  $\chi$  of the AOs and the column vector of the AO coefficients  $\mathbf{C}_i$

$$\chi = (\chi_1 \quad \chi_2 \quad \cdots \quad \chi_m) \quad (4a)$$

$$\mathbf{C}_i = \begin{pmatrix} C_{1i} \\ C_{2i} \\ \vdots \\ C_{mi} \end{pmatrix} \quad (4b)$$

Then,  $\psi_i$  is rewritten as

$$\psi_i = (\chi_1 \quad \chi_2 \quad \cdots \quad \chi_m) \begin{pmatrix} C_{1i} \\ C_{2i} \\ \vdots \\ C_{mi} \end{pmatrix} = \chi \mathbf{C}_i \quad (4c)$$

The MO coefficients  $C_{\mu i}$  ( $\mu, i = 1, 2, \dots, m$ ) form the  $m \times m$  matrix  $\mathbf{C}$ ,

$$\mathbf{C} = \begin{pmatrix} C_{11} & C_{12} & \cdots & C_{1m} \\ C_{21} & C_{22} & \cdots & C_{2m} \\ \vdots & \vdots & \vdots & \vdots \\ C_{m1} & C_{m2} & \cdots & C_{mm} \end{pmatrix} \quad (5)$$

where the  $i$ th column represents the column vector  $\mathbf{C}_i$ . If the diagonal matrix  $\mathbf{e}$  of the MO energies  $e_i$  ( $i = 1, 2, \dots, m$ ) is defined as

$$\mathbf{e} = \begin{pmatrix} e_1 & 0 & \cdots & 0 \\ 0 & e_2 & \cdots & 0 \\ \vdots & \vdots & \vdots & \vdots \\ 0 & 0 & \cdots & e_m \end{pmatrix} \quad (6)$$

then the  $\mathbf{H}$ ,  $\mathbf{S}$ ,  $\mathbf{C}$ , and  $\mathbf{e}$  matrices are related as follows

$$\mathbf{HC} = \mathbf{SCe} \quad (7a)$$

Thus, once the  $\mathbf{H}$  and  $\mathbf{S}$  matrices are evaluated for a given set of AOs  $\{\chi_1, \chi_2, \dots, \chi_m\}$ , then the MOs  $\psi_i$  and their orbital energies  $e_i$  are obtained by solving the pseudo-eigenvalue problem, Eq. 7a. For an MO  $\psi_p$ , Eq. 7a becomes

$$(\mathbf{H} - e_p \mathbf{S}) \mathbf{C}_i = 0 \quad (7b)$$

Consider a composite molecule AB consisting of fragments A and B. For convenience, consider that the set of AOs  $\{\chi_1, \chi_2, \dots, \chi_n, \chi_{n+1}, \chi_{n+2}, \dots, \chi_m\}$  describing the molecule AB are arranged such that

$$\chi_1, \chi_2, \dots, \chi_n \in A \quad (8a)$$

$$\chi_{n+1}, \chi_{n+2}, \dots, \chi_m \in B \quad (8b)$$

Then the **H** and **S** matrices are partitioned as follows:

$$\mathbf{H} = \begin{pmatrix} \mathbf{H}_A & \mathbf{H}_{AB} \\ \mathbf{H}_{BA} & \mathbf{H}_B \end{pmatrix} \quad (9a)$$

$$\mathbf{S} = \begin{pmatrix} \mathbf{S}_A & \mathbf{S}_{AB} \\ \mathbf{S}_{BA} & \mathbf{S}_B \end{pmatrix} \quad (9b)$$

where  $\mathbf{H}_{BA}$  and  $\mathbf{S}_{BA}$  are transposes of  $\mathbf{H}_{AB}$  and  $\mathbf{S}_{AB}$ , respectively, that is,  $\mathbf{H}_{BA} = (\mathbf{H}_{AB})^\dagger$  and  $\mathbf{S}_{BA} = (\mathbf{S}_{AB})^\dagger$ . The elements of the submatrices are defined as

$$(\mathbf{H}_A)_{\mu\nu} = \langle \chi_\mu | H^{\text{eff}} | \chi_\nu \rangle \quad \chi_\mu, \chi_\nu \in A \quad (10a)$$

$$(\mathbf{H}_B)_{\mu\nu} = \langle \chi_\mu | H^{\text{eff}} | \chi_\nu \rangle \quad \chi_\mu, \chi_\nu \in B \quad (10b)$$

$$(\mathbf{H}_{AB})_{\mu\nu} \langle \chi_\mu | H^{\text{eff}} | \chi_\nu \rangle \quad \chi_\mu \in A, \chi_\nu \in B \quad (10c)$$

$$(\mathbf{S}_A)_{\mu\nu} = \langle \chi_\mu | \chi_\nu \rangle \quad \chi_\mu, \chi_\nu \in A \quad (10d)$$

$$(\mathbf{S}_B)_{\mu\nu} = \langle \chi_\mu | \chi_\nu \rangle \quad \chi_\mu, \chi_\nu \in B \quad (10e)$$

$$(\mathbf{S}_{AB})_{\mu\nu} \langle \chi_\mu | \chi_\nu \rangle \quad \chi_\mu \in A, \chi_\nu \in B \quad (10f)$$

Suppose that the fragments A and B are molecules, and they are described by the AO basis sets  $\{\chi_1, \chi_2, \dots, \chi_n\}$  and  $\{\chi_{n+1}, \chi_{n+2}, \dots, \chi_m\}$ , respectively. Then the pseudo-eigenvalue equations describing A and B can be written as

$$\mathbf{H}_A^\circ \mathbf{C}_A^\circ = \mathbf{S}_A^\circ \mathbf{C}_A^\circ \mathbf{e}_A^\circ \quad (11a)$$

$$\mathbf{H}_B^\circ \mathbf{C}_B^\circ = \mathbf{S}_B^\circ \mathbf{C}_B^\circ \mathbf{e}_B^\circ \quad (11b)$$

where the superscript  $\circ$  was added to remind us that the molecules A and B may differ slightly from the corresponding fragments of the composite molecule AB in geometry and potential. It is convenient to express the MOs of A and B in terms of the AO basis set of AB. For this purpose, we introduce the following matrices:

$$\mathbf{H}^\circ = \begin{pmatrix} \mathbf{H}_A^\circ & \mathbf{0} \\ \mathbf{0} & \mathbf{H}_B^\circ \end{pmatrix} \quad (12a)$$

$$\mathbf{S}^\circ = \begin{pmatrix} \mathbf{S}_A^\circ & \mathbf{0} \\ \mathbf{0} & \mathbf{S}_B^\circ \end{pmatrix} \quad (12b)$$

$$\mathbf{C}^\circ = \begin{pmatrix} \mathbf{C}_A^\circ & \mathbf{0} \\ \mathbf{0} & \mathbf{C}_B^\circ \end{pmatrix} \quad (12c)$$

$$\mathbf{e}^\circ = \begin{pmatrix} \mathbf{e}_A^\circ & \mathbf{0} \\ \mathbf{0} & \mathbf{e}_B^\circ \end{pmatrix} \quad (12d)$$

These matrices satisfy the pseudo-eigenvalue equation

$$\mathbf{H}^\circ \mathbf{C}^\circ = \mathbf{S}^\circ \mathbf{C}^\circ \mathbf{e}^\circ \quad (13a)$$

which is equivalent to Eq. 11. The MO  $\psi_i^\circ$  belongs to fragment A if  $1 \leq i \leq n$ , and to fragment B if  $n+1 \leq i \leq m$ . Equation 13.a expresses the MOs  $\psi_i^\circ$  of the fragments A and B in terms of the AO basis set used for the composite system AB

$$\psi_i^\circ = (\chi_1 \quad \chi_2 \quad \cdots \quad \chi_m) \begin{pmatrix} C_{1i}^\circ \\ C_{2i}^\circ \\ \vdots \\ C_{mi}^\circ \end{pmatrix} = \chi \mathbf{C}_i^\circ \quad (13b)$$

For an MO  $\psi_i^\circ$ , Eq. 13.a is rewritten as

$$(\mathbf{H}^\circ - e_i^\circ \mathbf{S}^\circ) \mathbf{C}_i^\circ = 0 \quad (13c)$$

## I.2 CORRELATION BETWEEN THE MOs OF PERTURBED AND UNPERTURBED SYSTEMS: EXACT RELATIONSHIPS

Let us consider that Eqs 7 and 13 describe perturbed and unperturbed systems, respectively, and examine the relationship between the MOs  $\psi_i$  and  $\psi_i^\circ$ . For a composite molecule discussed above, the perturbation is an intermolecular perturbation. In general, however, Eqs 7 and 13 are also valid for the discussion of geometry and electronegativity perturbations. For example, for a geometry perturbation, Eqs 7 and 13 describe the MOs for two slightly different geometries of the same molecule with the geometry of the higher symmetry typically assumed to be the unperturbed system.

The MOs  $\psi_i$  can be expressed in terms of the AOs as in Eq. 1 or in terms of the MOs  $\psi_j^\circ$  as in Eq. 14

$$\psi_i = \sum_{\mu} T_{ji} \psi_j^\circ \quad (14)$$

where  $T_{ji}$  is the coefficient of the MO  $\psi_j^\circ$  in the MO  $\psi_i$ . Equation 14 implicitly assumes that the AOs describing  $\psi_i$  have the same positions in space as do the AOs describing  $\psi_j^\circ$ . (In the case of a geometry perturbation, this assumption breaks down. Nevertheless, the results derived from the assumption are still applicable to the case of a geometry perturbation. As will be shown below, the perturbational molecular orbital theory aims at finding the relationship between the AO coefficients  $C_{\mu i}$  of the MOs  $\psi_i$  and the AO coefficients  $C_{\mu i}^\circ$  of the MOs  $\psi_j^\circ$ .) By defining the column vector  $\mathbf{T}_i$  of the coefficients  $T_{ji}$  as

$$\mathbf{T}_i = \begin{pmatrix} T_{1i} \\ T_{2i} \\ \vdots \\ T_{mi} \end{pmatrix} \quad (15)$$

it is found that the coefficients  $C_{\mu i}$  and  $T_{ji}$  are related by

$$\mathbf{C}_i = \mathbf{C}^\circ \mathbf{T}_i \quad (16)$$

and the  $T_{ji}$  element is given by

$$T_{ji} = (\mathbf{C}_j^\circ)^T \mathbf{S}^\circ \mathbf{C}_i \quad (17)$$

where  $(\mathbf{C}_j^\circ)^T$  is the transpose of the column vector  $\mathbf{C}_j^\circ$ , that is, the row vector of the coefficients  $C_{\mu j}^\circ$

$$(\mathbf{C}_j^\circ)^T = (C_{1j}^\circ \ C_{2j}^\circ \ \cdots \ C_{mj}^\circ) \quad (18)$$

### I.3 CORRELATION BETWEEN THE MOs OF PERTURBED AND UNPERTURBED SYSTEMS: APPROXIMATE RELATIONSHIPS

We now consider the relationship between the MOs  $\psi_i$  and  $\psi_j^\circ$  from the viewpoint of perturbation theory. For this purpose, we rewrite the  $\mathbf{H}$  and  $\mathbf{S}$  matrices as

$$\mathbf{H} = \mathbf{H}^\circ + \delta\mathbf{H}^\circ \quad (19a)$$

$$\mathbf{S} = \mathbf{S}^\circ + \delta\mathbf{S}^\circ \quad (19b)$$

where  $\delta\mathbf{H}^\circ$  and  $\delta\mathbf{S}^\circ$  are given by

$$\delta\mathbf{H}^\circ = \begin{pmatrix} \mathbf{H}_A - \mathbf{H}_A^\circ & \mathbf{H}_{AB} \\ \mathbf{H}_{BA} & \mathbf{H}_B - \mathbf{H}_B^\circ \end{pmatrix} \quad (20a)$$

$$\delta\mathbf{S}^\circ = \begin{pmatrix} \mathbf{S}_A - \mathbf{S}_A^\circ & \mathbf{S}_{AB} \\ \mathbf{S}_{BA} & \mathbf{S}_B - \mathbf{S}_B^\circ \end{pmatrix} \quad (20b)$$

The overlap integrals  $\tilde{S}_{ij}$  and the interaction energies  $\tilde{H}_{ij}$  between the MOs  $\psi_i^\circ$  and  $\psi_j^\circ$  are given by

$$\tilde{H}_{ij} = (\mathbf{C}_i^\circ)^T \delta\mathbf{H} \mathbf{C}_j^\circ \quad (21a)$$

$$\tilde{S}_{ij} = (\mathbf{C}_i^\circ)^T \delta\mathbf{S}^\circ \mathbf{C}_j^\circ \quad (21b)$$

These matrix elements lead to the  $m \times m$  matrices  $\tilde{\mathbf{H}}$  and  $\tilde{\mathbf{S}}$ . In terms of  $\tilde{\mathbf{H}}$  and  $\tilde{\mathbf{S}}$ , Eq. I.3 is rewritten as

$$\{(\mathbf{e}^\circ + \tilde{\mathbf{H}}) - e_i(\mathbf{1} + \tilde{\mathbf{S}})\} \mathbf{T}_i = 0 \quad (22a)$$

which can be recast in the following form

$$(\mathbf{h} - e_i \mathbf{s}) \mathbf{T}_i = 0 \quad (22b)$$

Let us now consider the following perturbation expansions:

$$e_i = e_i^{(0)} + \lambda e_i^{(1)} + \lambda^2 e_i^{(2)} + \dots \quad (23a)$$

$$\mathbf{T}_i = \mathbf{T}_i^{(0)} + \lambda \mathbf{T}_i^{(1)} + \lambda^2 \mathbf{T}_i^{(2)} + \dots \quad (23b)$$

$$\mathbf{h} = \mathbf{h}^{(0)} + \lambda \mathbf{h}^{(1)} \quad (23c)$$

$$\mathbf{s} = \mathbf{s}^{(0)} + \lambda \mathbf{s}^{(1)} \quad (23d)$$

and the following choices

$$\mathbf{h}^{(0)} = \mathbf{e}^\circ = \begin{pmatrix} e_1^\circ & 0 & \cdots & 0 \\ 0 & e_2^\circ & \cdots & 0 \\ \vdots & \vdots & \ddots & \vdots \\ 0 & 0 & \cdots & e_m^\circ \end{pmatrix} \quad (24a)$$

$$\mathbf{h}^{(1)} = \tilde{\mathbf{H}} = \begin{pmatrix} \tilde{H}_{11} & \tilde{H}_{12} & \cdots & \tilde{H}_{1m} \\ \tilde{H}_{21} & \tilde{H}_{22} & \cdots & \tilde{H}_{2m} \\ \vdots & \vdots & \ddots & \vdots \\ \tilde{H}_{m1} & \tilde{H}_{m2} & \cdots & \tilde{H}_{mm} \end{pmatrix} \quad (24b)$$

$$\mathbf{s}^{(0)} = \mathbf{I} = \begin{pmatrix} 1 & 0 & 0 & \cdots & 0 \\ 0 & 1 & 0 & \cdots & 0 \\ 0 & 0 & 1 & \cdots & 0 \\ \vdots & \vdots & \vdots & \ddots & \vdots \\ 0 & 0 & 0 & \cdots & 1 \end{pmatrix} \quad (24c)$$

$$\mathbf{s}^{(1)} = \tilde{\mathbf{S}} = \begin{pmatrix} \tilde{S}_{11} & \tilde{S}_{12} & \tilde{S}_{13} & \cdots & \tilde{S}_{1m} \\ \tilde{S}_{21} & \tilde{S}_{22} & \tilde{S}_{23} & \cdots & \tilde{S}_{2m} \\ \tilde{S}_{31} & \tilde{S}_{32} & \tilde{S}_{33} & \cdots & \tilde{S}_{3m} \\ \vdots & \vdots & \vdots & \ddots & \vdots \\ \tilde{S}_{m1} & \tilde{S}_{m2} & \tilde{S}_{m3} & \cdots & \tilde{S}_{mm} \end{pmatrix} \quad (24d)$$

where  $\lambda$  is the order parameter. Then by inserting Eqs 23 and 24 into Eq. 22b and rearranging the terms according to the powers of  $\lambda$ , we obtain the following results:

**Zero-order in  $\lambda$ :**

$$(\mathbf{e}^\circ - e_i^{(0)})\mathbf{T}_i^{(0)} = 0 \quad (25a)$$

**First-order in  $\lambda$ :**

$$(\tilde{\mathbf{H}} - e_i^{(0)}\tilde{\mathbf{S}} - e_i^{(1)}\mathbf{1})\mathbf{T}_i^{(0)} + (\mathbf{e}^\circ - e_i^{(0)}\mathbf{1})\mathbf{T}_i^{(1)} = 0 \quad (25b)$$

**Second-order in  $\lambda$ :**

$$-(e_i^{(1)}\tilde{\mathbf{S}} + e_i^{(2)}\mathbf{1})\mathbf{T}_i^{(0)} + (\tilde{\mathbf{H}} - e_i^{(0)}\tilde{\mathbf{S}} - e_i^{(1)}\mathbf{1})\mathbf{T}_i^{(1)} + (\mathbf{e}^\circ - e_i^{(0)}\mathbf{1})\mathbf{T}_i^{(2)} = 0 \quad (25c)$$

The  $T_{ji}$  elements of the zero-order solution  $\mathbf{T}_i^{(0)}$  are given by

$$T_{ji} = \delta_{ji} \quad (26)$$

where  $\delta_{ji}$  is the Kronecker delta. Thus, the following relationships hold:

$$(\mathbf{T}_j^{(0)})^T \mathbf{1} \mathbf{T}_i^{(0)} = \delta_{ji} \quad (27a)$$

$$(\mathbf{T}_j^{(0)})^T \tilde{\mathbf{S}} \mathbf{T}_i^{(0)} = \tilde{S}_{ji} = \tilde{S}_{ij} \quad (27b)$$

$$(\mathbf{T}_j^{(0)})^T \mathbf{e}^\circ \mathbf{T}_i^{(0)} = e_i^\circ \delta_{ji} \quad (27c)$$

$$(\mathbf{T}_j^{(0)})^T \tilde{\mathbf{H}} \mathbf{T}_i^{(0)} = \tilde{H}_{ji} = \tilde{H}_{ij} \quad (27d)$$

where  $(\mathbf{T}_j^{(0)})^T$  is the transpose of  $\mathbf{T}_{j(0)}^{(0)}$ . Thus, by left-multiplying Eq. 25a with  $(\mathbf{T}_i^{(0)})^T$ , we obtain the zero-order energy  $e_i^\circ$

$$e_i^{(0)} = e_i^\circ \quad (28)$$

To solve the first-order expression, Eq. 25b, we expand the first-order correction  $\mathbf{T}_i^{(1)}$  as a linear combination of the zero-order vectors  $\mathbf{T}_k^{(0)}$

$$\mathbf{T}_i^{(1)} = \sum_k a_{ki}^{(1)} \mathbf{T}_k^{(0)} \quad (29)$$

so that Eq. 25b is rewritten as

$$(\tilde{\mathbf{H}} - e_i^{(0)} \tilde{\mathbf{S}} - e_i^{(1)} \mathbf{1}) \mathbf{T}_i^{(0)} + \sum_k a_{ki}^{(1)} (\mathbf{e}^\circ - e_i^{(0)} \mathbf{1}) \mathbf{T}_k^{(0)} = 0 \quad (30)$$

By left-multiplying Eq. 30 with  $(\mathbf{T}_i^{(0)})^T$ , we obtain the first-order energy  $e_i^{(1)}$

$$e_i^{(1)} = \tilde{H}_{ii} - e_i^\circ \tilde{S}_{ii} \quad (31)$$

By left-multiplying Eq. 30 with  $(\mathbf{T}_j^{(0)})^T (j \neq i)$ , we obtain the first-order expansion coefficients

$$a_{ji}^{(1)} = \frac{\tilde{H}_{ij} - e_i^\circ \tilde{S}_{ij}}{e_i^\circ - e_j^\circ} \quad (j = i) \quad (32)$$

To solve the second-order expression, Eq. 25c, we expand the  $\mathbf{T}_i^{(0)}$  term as a linear combination of the zero-order vectors  $\mathbf{T}_k^{(0)}$

$$\mathbf{T}_i^{(2)} = \sum_k b_{ki}^{(2)} \mathbf{T}_k^{(0)} \quad (33)$$

Thus Eq. 25c is rewritten as

$$-(e_i^{(1)} \tilde{\mathbf{S}} + e_i^{(2)} \mathbf{1}) \mathbf{T}_i^{(0)} + \sum_k a_{ki} (\tilde{\mathbf{H}} - e_i^{(0)} \tilde{\mathbf{S}} - e_i^{(1)} \mathbf{1}) \mathbf{T}_k^{(0)} + \sum_k b_{ki}^{(2)} (e^\circ - e_i^{(0)} \mathbf{1}) \mathbf{T}_k^{(0)} = 0 \quad (34)$$

Thus left-multiplying Eq. 34 with  $(\mathbf{T}_i^{(0)})^T$ , we obtain the second-order energy

$$e_i^{(2)} = -(\tilde{H}_{ii} - e_i^\circ \tilde{S}_{ii}) \tilde{S}_{ii} + \sum_j \frac{(\tilde{H}_{ij} - e_i^\circ \tilde{S}_{ij})^2}{e_i^\circ - e_j^\circ} \quad (j = i) \quad (35)$$

By left-multiplying Eq. 34 with  $(\mathbf{T}_j^{(0)})^T$  ( $j \neq i$ ), we obtain the second-order coefficients

$$b_{ji}^{(2)} = \frac{-(\tilde{H}_{ii} - e_i^\circ \tilde{S}_{ii}) \tilde{S}_{ij}}{e_i^\circ - e_j^\circ} + \sum_{k \neq i} \frac{(\tilde{H}_{ik} - e_i^\circ \tilde{S}_{ik})(\tilde{H}_{kj} - e_i^\circ \tilde{S}_{kj})}{(e_i^\circ - e_j^\circ)(e_i^\circ - e_k^\circ)} \quad (j = i) \quad (36)$$

In the matrix notation, the normalization of MO  $\psi_i$  is written as

$$0 = \langle \psi_i | \psi_i \rangle - 1 = (\mathbf{C}_j)^T \mathbf{S} \mathbf{C}_i - 1 = (\mathbf{T}_i)^T (\mathbf{1} + \tilde{\mathbf{S}}) \mathbf{T}_i - 1 \quad (37)$$

From Eqs 23b, 23d, 24c, 24d, and 37, the following results are obtained:

**Zero-order in  $\lambda$ :**

$$(\mathbf{T}_i^{(0)})^T \mathbf{1} \mathbf{T}_i^{(0)} - 1 = 0 \quad (38a)$$

**First-order in  $\lambda$ :**

$$(\mathbf{T}_i^{(1)})^T \mathbf{1} \mathbf{T}_i^{(0)} + (\mathbf{T}_i^{(0)})^T \tilde{\mathbf{S}} \mathbf{T}_i^{(0)} + (\mathbf{T}_i^{(0)})^T \mathbf{1} \mathbf{T}_i^{(1)} = 0 \quad (38b)$$

**Second-order in  $\lambda$ :**

$$(\mathbf{T}_i^{(2)})^T \mathbf{1} \mathbf{T}_i^{(0)} + (\mathbf{T}_i^{(1)})^T \tilde{\mathbf{S}} \mathbf{T}_i^{(0)} + (\mathbf{T}_i^{(0)})^T \tilde{\mathbf{S}} \mathbf{T}_i^{(1)} + (\mathbf{T}_i^{(1)})^T \mathbf{1} \mathbf{T}_i^{(1)} + (\mathbf{T}_i^{(0)})^T \mathbf{1} \mathbf{T}_i^{(2)} = 0 \quad (38c)$$

Equation 38a leads to the zero-order result,

$$\mathbf{T}_{ii}^{(0)} = 1 \quad (39a)$$

Equation 38b to the first-order correction,

$$T_{ii}^{(1)} = -\frac{1}{2} \tilde{S}_{ii} \quad (39b)$$

and Eq. 38c to the second-order correction

$$T_{ii}^{(2)} = -\sum_{j \neq i} \frac{(\tilde{H}_{ij} - e_i^\circ \tilde{S}_{ij}) \tilde{S}_{ij}}{e_i^\circ - e_j^\circ} - \frac{1}{2} \sum_{j \neq i} \left( \frac{\tilde{H}_{ij} - e_i^\circ \tilde{S}_{ij}}{e_i^\circ - e_j^\circ} \right)^2 \quad (39c)$$

Consequently, the MO energies and coefficients correct to second order are given as follows:

$$e_i = e_i^\circ + (\tilde{H}_{ii} - e_i^\circ \tilde{S}_{ii}) + \sum_{j \neq i} \frac{(\tilde{H}_{ij} - e_i^\circ \tilde{S}_{ij})^2}{e_i^\circ - e_j^\circ} \quad (40a)$$

$$T_{ii} = 1 - \frac{1}{2} \tilde{S}_{ii} - \sum_{j \neq i} \frac{(\tilde{H}_{ij} - e_i^\circ \tilde{S}_{ij}) \tilde{S}_{ij}}{e_i^\circ - e_j^\circ} - \frac{1}{2} \sum_{j \neq i} \left( \frac{\tilde{H}_{ij} - e_i^\circ \tilde{S}_{ij}}{e_i^\circ - e_j^\circ} \right)^2 \quad (40b)$$

$$T_{ji} = \frac{(\tilde{H}_{ij} - e_i^\circ \tilde{S}_{ij})}{e_i^\circ - e_j^\circ} - \frac{(\tilde{H}_{ii} - e_i^\circ \tilde{S}_{ii}) \tilde{S}_{ij}}{e_i^\circ - e_j^\circ} + \sum_{k \neq i} \frac{(\tilde{H}_{ik} - e_i^\circ \tilde{S}_{ik})(\tilde{H}_{kj} - e_i^\circ \tilde{S}_{kj})}{(e_i^\circ - e_j^\circ)(e_i^\circ - e_k^\circ)} \quad (j = i) \quad (40c)$$

(40c)

---

## I.4 THE SPECIAL CASE OF AN INTERMOLECULAR PERTURBATION

---

In the case of an intermolecular perturbation between fragments A and B in a composite molecule AB, it is possible that

$$\mathbf{H}_A = \mathbf{H}_A^\circ \quad (41a)$$

$$\mathbf{S}_A = \mathbf{S}_A^\circ \quad (41b)$$

This situation arises when the geometries of the molecules A and B are identical with the corresponding fragments of the composite molecule AB, if MO calculations are carried out by a non-self-consistent-field method such as the extended Hückel method. In such a case, the diagonal blocks of the matrices  $\delta\mathbf{H}^\circ$  and  $\delta\mathbf{S}^\circ$  are zero (Eq. 20). Consequently,

$$\tilde{H}_{ii} = 0 \quad (42a)$$

$$\tilde{H}_{ij} = \tilde{S}_{ij} = 0, \text{ if } \psi_i^\circ, \psi_j^\circ \in \text{the same fragment} \quad (42b)$$

so that Eq 40a–c are simplified as

$$e_i = e_i^\circ + \sum_{j \neq i} \frac{(\tilde{H}_{ij} - e_i^\circ \tilde{S}_{ij})^2}{e_i^\circ - e_j^\circ} \quad (j = i) \quad (43a)$$

$$T_{ii} = 1 - \sum_{j \neq i} \frac{(\tilde{H}_{ij} - e_i^\circ \tilde{S}_{ij}) \tilde{S}_{ij}}{e_i^\circ - e_j^\circ} - \frac{1}{2} \sum_{j \neq i} \left( \frac{\tilde{H}_{ij} - e_i^\circ \tilde{S}_{ij}}{e_i^\circ - e_j^\circ} \right)^2 \quad (j = i) \quad (43b)$$

$$T_{ji} = \frac{(\tilde{H}_{ij} - e_i^\circ \tilde{S}_{ij})}{e_i^\circ - e_j^\circ} + \sum_{k \neq i} \frac{(\tilde{H}_{ik} - e_i^\circ \tilde{S}_{ik})(\tilde{H}_{kj} - e_i^\circ \tilde{S}_{kj})}{(e_i^\circ - e_j^\circ)(e_i^\circ - e_k^\circ)} \quad (j = i) \quad (43c)$$

---

## I.5 DEGENERATE PERTURBATIONS

---

In the discussion earlier, it was assumed that there is no degeneracy in the MOs  $\psi_i^\circ$ . When there is a degeneracy, it is necessary to solve an appropriate secular determinant. For example, consider that the MOs  $\psi_i^\circ$  and  $\psi_j^\circ$  are degenerate (i.e.,  $e_i^\circ = e_j^\circ$ ), and these MOs interact via the matrix elements  $\tilde{H}_{ij}$  and  $\tilde{S}_{ij}$ . The  $2 \times 2$  secular determinant appropriate for this situation is

$$\begin{vmatrix} e_i^\circ - e_i & \tilde{H}_{ij} - e_i \tilde{S}_{ij} \\ \tilde{H}_{ij} - e_i \tilde{S}_{ij} & e_i^\circ - e_i \end{vmatrix} = 0 \quad (44)$$

When  $\tilde{H}_{ij}$  is negative, solution of Eq. 44 provides two new energy levels

$$e_i = \frac{e_i^\circ + \tilde{H}_{ij}}{1 + \tilde{S}_{ij}} \quad (45)$$

$$e_j = \frac{e_j^\circ - \tilde{H}_{ij}}{1 - \tilde{S}_{ij}} \quad (46)$$

The corresponding MOs are given by

$$\psi_i = \frac{\psi_i^\circ + \psi_j^\circ}{\sqrt{2 + 2\tilde{S}_{ij}}} \quad (47a)$$

$$\psi_j = \frac{\psi_i^\circ - \psi_j^\circ}{\sqrt{2 - 2\tilde{S}_{ij}}} \quad (47b)$$

As mentioned in Chapter 3, these MOs  $\psi_i$  and  $\psi_j$  can undergo further orbital interactions with other MOs  $\psi_k^\circ$  via nondegenerate perturbations.

---

## REFERENCES

---

1. M.-H. Whangbo, H. B. Schlegel, and S. Wolfe, *J. Am. Chem. Soc.*, **99**, 1296 (1977).
2. M.-H. Whangbo, *Computational Theoretical Organic Chemistry*, R. Daudel, I. G. Csizmadia, editors, Reidel, Boston, 233 (1981).

## APPENDIX II

## Some Common Group Tables

$C_s$	$E$	$\sigma$
$A'$		
$A''$		-

$C_2$	$E$	$C_2$
$A$		
$B$		-

$$\varepsilon = \exp(2\pi i/3)$$

$C_3$	$E$	$C_3$	$C_3^2$
$A$			
$E$	{     }	$\varepsilon$ $\varepsilon^*$	$\varepsilon^*$ $\varepsilon$

$C_4$	$E$	$C_4$	$C_2$	$C_4^3$
$A$				
$B$		-		-
$E$	{     }	$i$ $-i$	-  -	$-i$ $i$

$C_{2v}$	$E$	$C_2$	$\sigma_v(xz)$	$\sigma_v(yz)$
$A_1$				
$A_2$			-	-
$B_1$		-		-
$B_2$		-	-	

$C_{3v}$	$E$	$2C_3$	$3\sigma_v$
$A_1$			
$A_2$			-
$E$	2	-	0

$C_{4v}$	$E$	$2C_4$	$C_2$	$2\sigma_v$	$2\sigma_d$
$A_1$					
$A_2$				-	-
$B_1$		-			-
$B_2$		-		-	
$E$	2	0	-2	0	0

$C_{5v}$	$E$	$2C_5$	$2C_5^2$	$5\sigma_v$
$A_1$				
$A_2$				-
$E_1$	2	$2 \cos 72^\circ$	$2 \cos 144^\circ$	0
$E_2$	2	$2 \cos 144^\circ$	$2 \cos 72^\circ$	0

$C_{6v}$	$E$	$2C_6$	$2C_3$	$C_2$	$3\sigma_v$	$3\sigma_d$
$A_1$						
$A_2$					-	-
$B_1$		-		-		-
$B_2$		-		-	-	
$E_1$	2		-	-2	0	0
$E_2$	2	-	-	2	0	0

$C_{2h}$	$E$	$C_2$	$i$	$\sigma_h$
$A_g$				
$B_g$		-		-
$A_u$			-	-
$B_u$		-	-	

$D_{2h}$	$E$	$C_2(z)$	$C_2(y)$	$C_2(x)$	$i$	$\sigma(xy)$	$\sigma(xz)$	$\sigma(yz)$
$A_g$								
$B_{1g}$			-	-			-	-
$B_{2g}$		-		-		-		-
$B_{3g}$		-	-			-	-	
$A_u$					-	-	-	-
$B_{1u}$			-	-	-	-		
$B_{2u}$		-		-	-		-	
$B_{3u}$		-	-		-			-

$D_{3h}$	$E$	$2C_3$	$3C_2$	$\sigma_h$	$2S_3$	$3\sigma_v$
$A'_1$						
$A'_2$			-			-
$E'$	2	-	0	2	-	0
$A''_1$				-	-	-
$A''_2$			-	-	-	
$E''$	2	-	0	-2		0

$D_{4h}$	$E$	$2C_4$	$C_2$	$2C'_2$	$2C''_2$	$i$	$2S_4$	$\sigma_h$	$2\sigma_v$	$2\sigma_d$
$A_{1g}$										
$A_{2g}$				-	-				-	-
$B_{1g}$		-			-		-			-
$B_{2g}$		-		-			-		-	
$E_g$	2	0	-2	0	0	2	0	-2	0	0
$A_{1u}$						-	-	-	-	-
$A_{2u}$				-	-	-	-	-		
$B_{1u}$		-			-	-		-	-	
$B_{2u}$		-		-		-		-		-
$E_u$	2	0	-2	0	0	-2	0	2	0	0

$D_{5h}$	$E$	$2C_5$	$2C_5^2$	$5C_2$	$\sigma_h$	$2S_5$	$2S_5^3$	$5\sigma_v$
$A'_1$								
$A'_2$				-				-
$E'_1$	2	$2 \cos 72^\circ$	$2 \cos 144^\circ$	0	2	$2 \cos 72^\circ$	$2 \cos 144^\circ$	0
$E'_2$	2	$2 \cos 144^\circ$	$2 \cos 72^\circ$	0	2	$2 \cos 144^\circ$	$2 \cos 72^\circ$	0
$A''_1$					-	-	-	-
$A''_2$				-	-	-	-	
$E''_1$	2	$2 \cos 72^\circ$	$2 \cos 144^\circ$	0	-2	$-2 \cos 72^\circ$	$-2 \cos 144^\circ$	0
$E''_2$	2	$2 \cos 144^\circ$	$2 \cos 72^\circ$	0	-2	$-2 \cos 144^\circ$	$-2 \cos 72^\circ$	0

$D_{6h}$	$E$	$2C_6$	$2C_3$	$C_2$	$3C'_2$	$3C''_2$	$i$	$2S_3$	$2S_6$	$\sigma_h$	$3\sigma_d$	$3\sigma_v$
$A_{1g}$												
$A_{2g}$					-	-				-	-	-
$B_{1g}$		-		-		-		-		-		-
$B_{2g}$		-		-	-			-		-	-	
$E_{1g}$	2		-	-2	0	0	2		-	-2	0	0
$E_{2g}$	2	-	-	2	0	0	2	-	-	2	0	0
$A_{1u}$							-	-	-	-	-	-
$A_{2u}$					-	-	-	-	-	-		
$B_{1u}$		-		-		-	-		-		-	
$B_{2u}$		-		-	-		-		-			-
$E_{1u}$	2		-	-2	0	0	-2	-		2	0	0
$E_{2u}$	2	-	-	2	0	0	-2			-2	0	0

$D_{2d}$	$E$	$2S_4$	$C_2$	$2C'_2$	$2\sigma_d$
$A_1$					
$A_2$				-	-
$B_1$		-			-
$B_2$		-		-	
$E$	2	0	-2	0	0

$D_{3d}$	$E$	$2C_3$	$3C_2$	$i$	$2S_6$	$3\sigma_d$
$A_{1g}$						
$A_{2g}$			-			-
$E_g$	2	-	0	2	-	0
$A_{1u}$				-	-	-
$A_{2u}$			-	-	-	
$E_u$	2	-	0	-2		0

$D_{4d}$	$E$	$2S_8$	$2C_4$	$2S_8^3$	$C_2$	$4C'_2$	$4\sigma_d$
$A_1$							
$A_2$						-	-
$B_1$		-		-			-
$B_2$		-		-		-	
$E_1$	2	$\sqrt{2}$	0	$-\sqrt{2}$	-2	0	0
$E_2$	2	0	-2	0	2	0	0
$E_3$	2	-2	0	$\sqrt{2}$	-2	0	0

$D_{5d}$	$E$	$2C_5$	$2C_5^2$	$5C_2$	$i$	$2S_{10}^3$	$2S_{10}$	$2\sigma_d$
$A_{1g}$								
$A_{2g}$				-				-
$E_{1g}$	2	$2 \cos 72^\circ$	$2 \cos 144^\circ$	0	2	$2 \cos 72^\circ$	$2 \cos 144^\circ$	0
$E_{2g}$	2	$2 \cos 144^\circ$	$2 \cos 72^\circ$	0	2	$2 \cos 144^\circ$	$2 \cos 72^\circ$	0
$A_{1u}$					-	-	-	-
$A_{2u}$				-	-	-	-	
$E_{1u}$	2	$2 \cos 72^\circ$	$2 \cos 144^\circ$	0	-2	$-2 \cos 72^\circ$	$-2 \cos 144^\circ$	0
$E_{2u}$	2	$2 \cos 144^\circ$	$2 \cos 72^\circ$	0	-2	$-2 \cos 144^\circ$	$-2 \cos 72^\circ$	0

$D_{6d}$	$E$	$2S_{12}$	$2C_6$	$2S_4$	$2C_3$	$2S_{12}^5$	$C_2$	$6C'_2$	$6\sigma_d$
$A_1$									
$A_2$								-	-
$B_1$		-		-		-			-
$B_2$		-		-		-		-	
$E_1$	2	$\sqrt{3}$		0	-	$-\sqrt{3}$	-2	0	0
$E_2$	2		-	-2	-		2	0	0
$E_3$	2	0	-2	0	2	0	-2	0	0
$E_4$	2	-	-	2	-	-	-2	0	0
$E_5$	2	$\sqrt{3}$		0	-	$\sqrt{3}$	-2	0	0

$T_d$	$E$	$8C_3$	$3C_2$	$6S_4$	$6\sigma_d$
$A_1$					
$A_2$					-
$E$	2	-	2	-0	0
$T_1$	3	0	-		-
$T_2$	3	0	-	-	

$O_h$	$E$	$8C_3$	$6C_2$	$6C_4$	$3C_2$	$i$	$6S_4$	$8S_6$	$3\sigma_h$	$6\sigma_d$
$A_{1g}$										
$A_{2g}$			-	-			-			-
$E_g$	2	-	0	0	2	2	0	-	2	0
$T_{1g}$	3	0	-		-	3		0	-	-
$T_{2g}$	3	0		-	-	3	-	0	-	
$A_{1u}$						-	-	-	-	-
$A_{2u}$				-	-		-		-	
$E_u$	2	-	0	0	2	-2	0		-2	0
$T_{1u}$	3	0	-		-	-3	-	0		
$T_{2u}$	3	0		-	-	-3		0		-

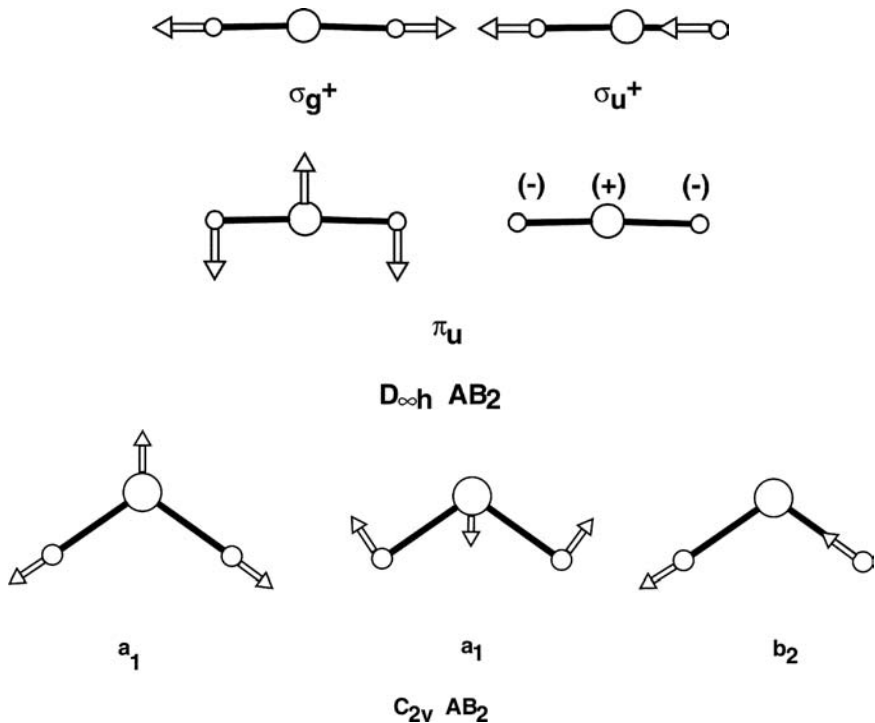
$C_{\infty v}$	$E$	$2C_{\infty}\phi$	$2C_{\infty}2\phi$	...	${}^{\infty}\sigma v$
$\Sigma^+ (= A_1)$				...	
$\Sigma^- (= A_2)$				...	-
$\Pi (= E_1)$	2	$2\cos\phi$	$2\cos 2\phi$	...	0
$\Delta (= E_2)$	2	$2\cos 2\phi$	$2\cos 4\phi$	...	0

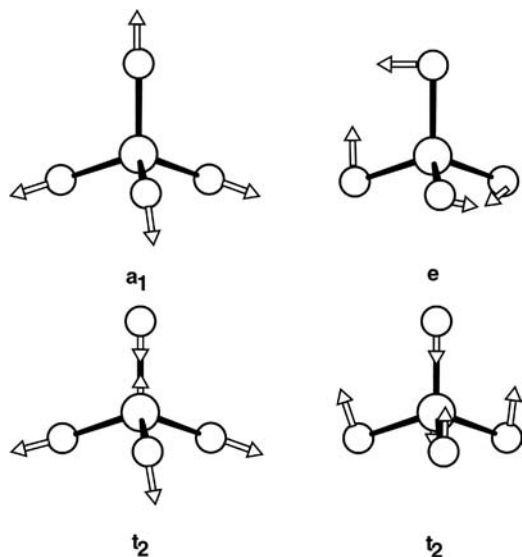
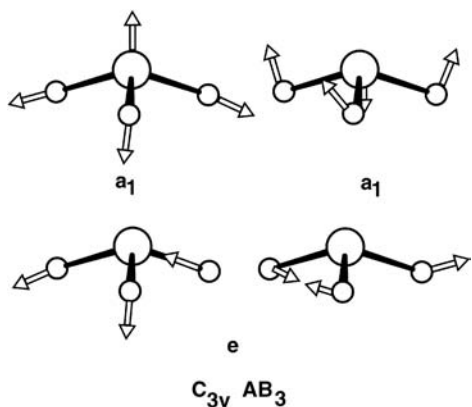
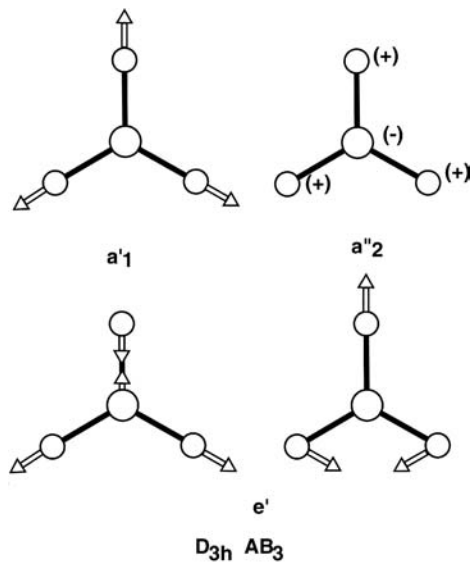
$D_{\infty h}$	$E$	$2C_{\infty}\phi$	...	${}^{\infty}\sigma v$	$i$	$2S_{\infty}\phi$	...	${}^{\infty}\sigma v$
$\Sigma_g^+$			...				...	
$\Sigma_g^-$			...	-			...	-
$\Pi_g$	2	$2\cos\phi$	...	0	2	$-2\cos\phi$	...	0
$\Delta_g$	2	$2\cos 2\phi$	...	0	2	$2\cos\phi$	...	0
$\Sigma_u^+$			...		-	-	...	-
$\Sigma_u^-$			...	-	-	-	...	
$\Pi_u$	2	$2\cos\phi$	...	0	-2	$2\cos\phi$	...	0
$\Delta_u$	2	$2\cos 2\phi$	...	0	-2	$-2\cos\phi$	...	0

## APPENDIX III

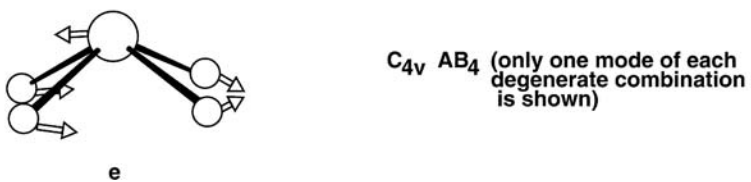
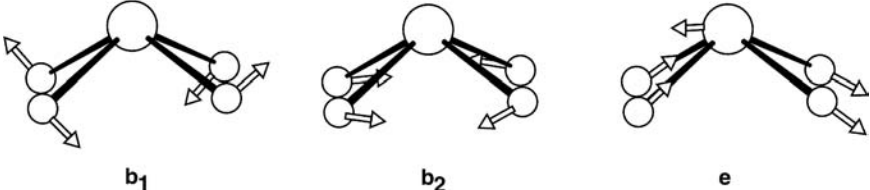
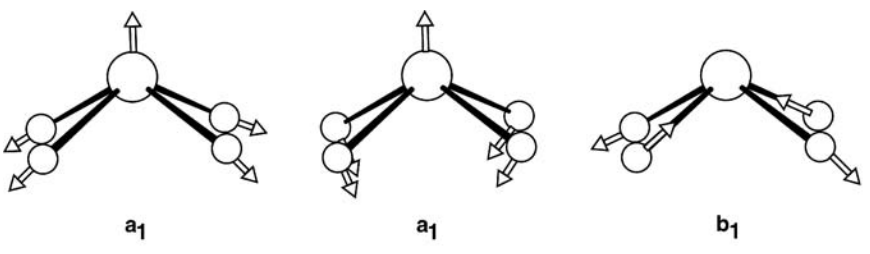
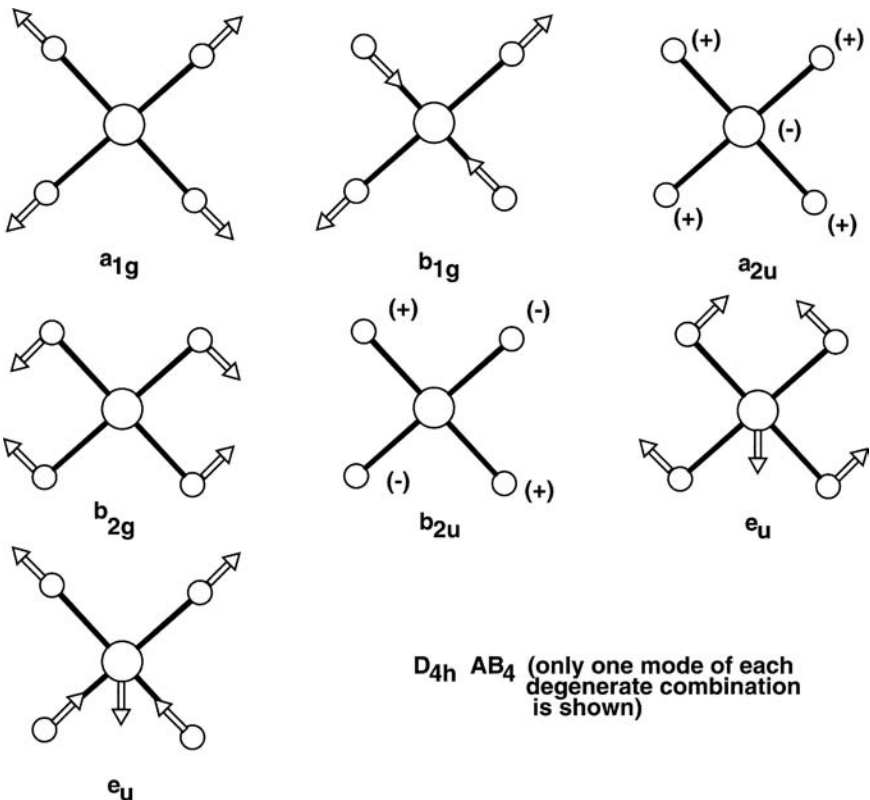
## Normal Modes for Some Common Structural Types

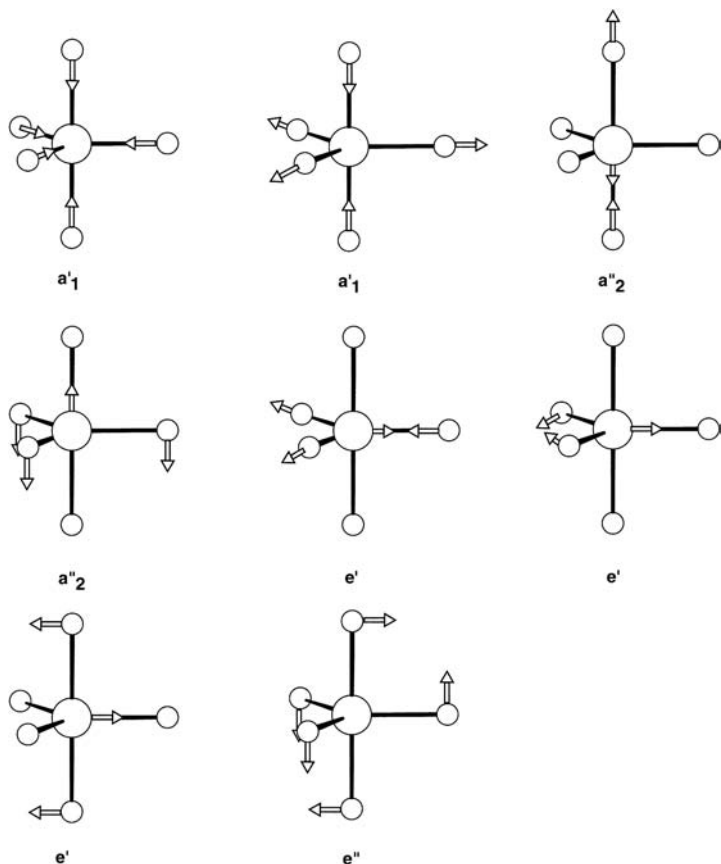
For the molecules in this appendix, the symbols (+) and (−) are used for displacement vectors above and behind the plane of the paper, respectively. The length of the displacement vectors has been drawn in an arbitrary manner and will depend on the relative masses of the A and B atoms.



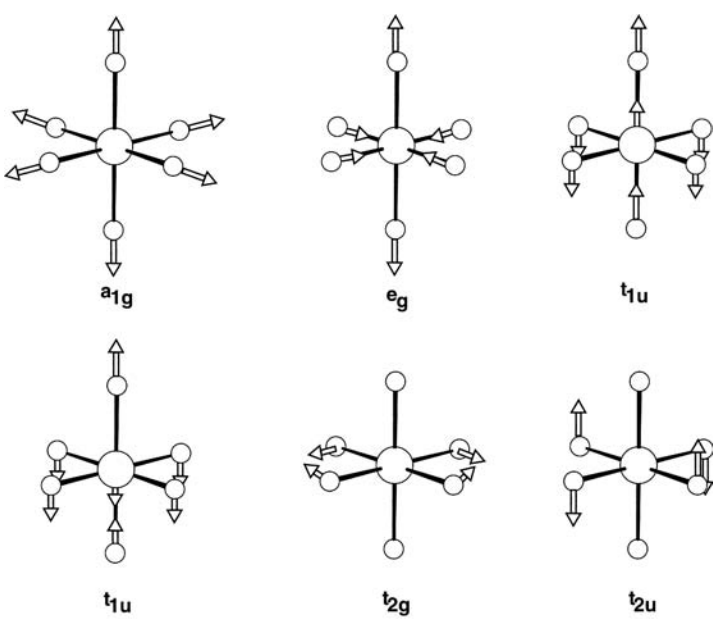


$T_d$   $AB_4$  (only one mode of each degenerate combination is shown)

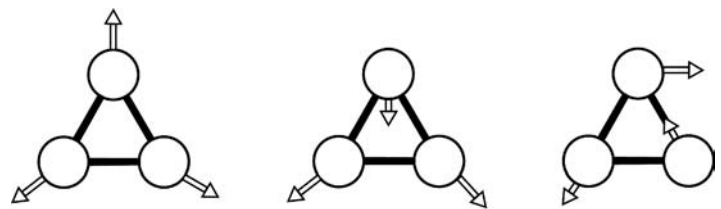
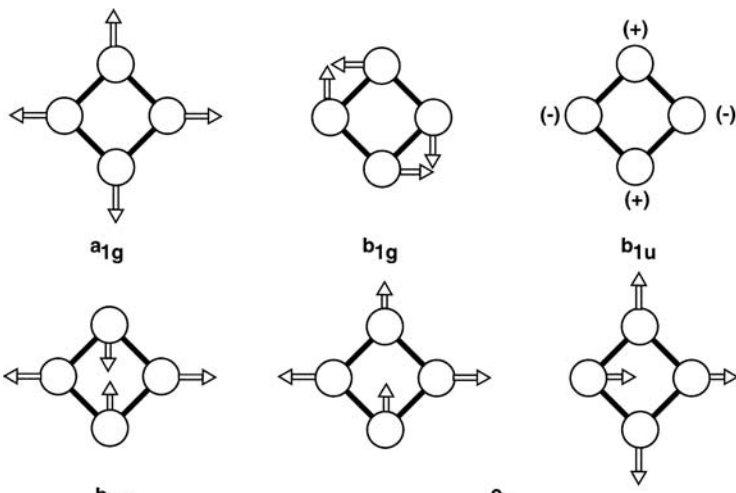
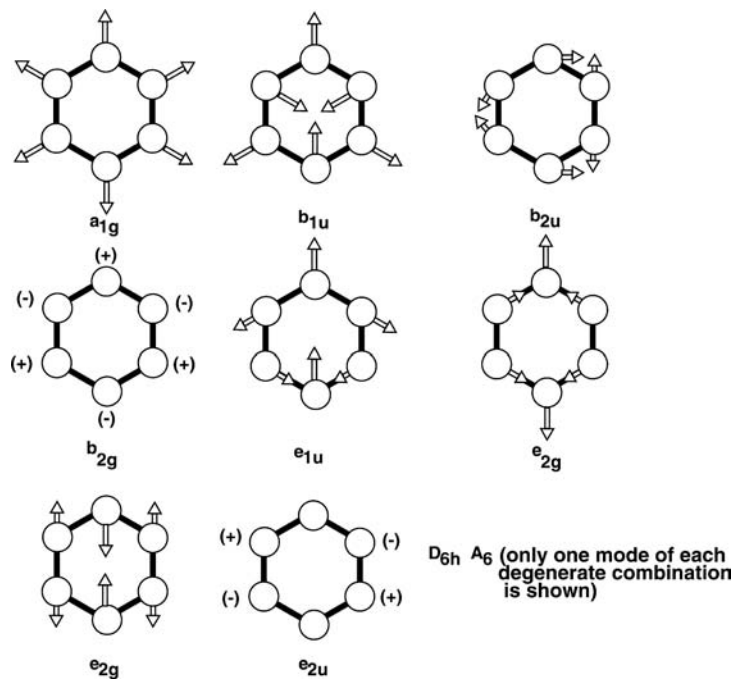




$D_{3h}$   $AB_5$  (only one mode of each degenerate combination is shown)



$O_h$   $AB_6$  (only one mode of each degenerate combination is shown)

 $a'_1$  $D_{3h} A_3$  $e'$  $b_{2g}$  $e_u$  $D_{4h} A_4$  $e_{2g}$  $e_{2u}$

# Index

- acetylene on metal surfaces 718, 719  
adamantyl cation 224  
adsorption on surfaces general 694, 696–699  
AFM-AFM chain 779  
A-frame complexes 524, 525  
 $\text{Ag}_2\text{MnO}_2$  769  
 $\text{AH}$  179  
 $\text{AH}_2$  123–125, 127  
 $\text{AH}_2\text{AH}_2$  221  
 $\text{AH}_2\text{BH}_2$  220  
 $\text{AH}_3$  70, 71, 80, 182–184, 201  
     $\text{C}_{2v}$  370, 383, 384  
 $\text{AH}_3\text{BH}$  232  
 $\text{AH}_3\text{BH}_2$  223  
 $\text{AH}_4$  72  
     $\text{C}_{2v}$  372  
     $\text{D}_{4h}$  363  
 $\text{AH}_5$ ,  $\text{C}_{4v}$  367–369  
     $\text{D}_{3h}$  387, 388  
 $\text{AH}_6$ , octahedral 360  
 $\text{AH}_n$  198  
 $\text{A}_2$ , homonuclear diatomic 99  
 $\text{A}_2\text{H}_4$  208  
 $\text{A}_2\text{H}_6$  204, 210  
 $\text{AlH}_2$  133  
 $\text{AMO}_3$  429, 430  
 $\text{Al}_2$  102, 104  
 $\text{Al}_4^{2-}$  266  
allyl 273  
angular node 4  
10-annulene 294  
anomeric effect 233  
Antiferromagnetic ordering 459, 460  
 $\text{Ar}$  199, 200  
aromatic systems 281  
    cyclobutadiene<sup>2-</sup> 281  
    cyclopentadienyl<sup>-</sup> 281  
    benzene 281  
    cycloheptatriene<sup>+</sup> 281  
 $\text{Ar}_2$  102  
 $\text{As}(\text{CH}_3)_3$  188  
 $\text{AsF}_3$  188  
 $\text{AsH}_3$  188, 189  
 $\text{As}_2$  104, 117  
 $\text{As}_4\text{S}_4$  301, 302  
 $\text{As}_4\text{Se}_4$  301  
 $\text{Au}(\text{PR}_3)$  639, 640  
 $(\text{Au-PR}_3)_4^{2+}$  85  
azulene 161  
    ionization potential 162  
    electron affinity 162  
    excitation energy 162  
Azurite 781, 782  
 $\text{BaBiO}_3$  373–375  
 $\text{Ba}_2\text{Bi}_2\text{Sb}$  379  
 $\text{BaCrS}_2$  496, 497  
 $\text{Ba}_2\text{Cu}(\text{PO}_4)_2$  788  
 $\text{BaCuSi}_2\text{O}_6$  764, 765  
 $\text{BaCu}_2\text{V}_2\text{O}_8$  750, 751  
 $\text{BaGe}_2$  378  
 $\text{Ba}_2\text{Ge}_4$  355  
 $\text{Ba}_2\text{GeP}_2$  356  
 $\text{BaHgO}_4$  355  
 $\text{Ba}_{1-x}\text{K}_x\text{BiO}_3$  superconductivity in 375  
 $\text{BaLiSi}_2$  338  
 $\text{BaMg}_{0.1}\text{Li}_{0.9}\text{Si}_2$  337  
 $\text{Ba}_2\text{NaOsO}_6$  738, 739, 740  
band dispersion 318  
    band folding 326  
    effect of overlap 323  
    sulfur chain 335, 336  
band gap 315  
band gap, effect of spin arrangement on 740  
band orbital 321  
 $\text{BaNiS}_2$  496, 497  
 $\text{BaPdAs}_2$  497, 498  
 $\text{Ba}_2\text{Si}_3\text{Ni}$  591  
barrelene 305  
 $\text{BaSi}$  351  
 $\text{Ba}_3\text{Si}_4$  351  
 $\text{BaTiO}_3$  426–428  
BCS theory 349  
 $\text{Be}_2$  102, 103  
 $\text{BeH}_2$  133  
 $\text{BeH}_3^+$  385  
benzene 109, 110, 278–280  
     $\text{D}_{6h}$  versus  $\text{D}_{3h}$  284  
inorganic 295, 296  
Second-order Jahn-Teller distortion 285  
 $\text{benzene-Cr}(\text{CO})_3$  607  
 $(\text{benzene})_2\text{Ge}^+$  397  
 $\text{BH}_2$  133, 145  
 $\text{BH}_3$  185, 187, 189  
 $\text{BH}_4^{2+}$  149, 197  
 $\text{B}_2$  102, 104, 120  
 $\text{B}_2\text{C}$  235  
 $\text{B}_2\text{H}_6$  187, 206, 208  
bicapped pentagonal antiprism 75  
bicapped tetrahedron distortions 418–420, 433  
 $\text{Bi}(\text{CH}_3)_3$  188  
 $\text{Bi}_2\text{CuO}_4$  769, 770, 771  
 $\text{Bi}_4\text{Cu}_3\text{V}_2\text{O}_{14}$  780, 781  
bicyclobutane 261  
bicyclo[1.1.0]butane 214  
bicyclo[3.1.0]hexane 214  
bicyclodienes 257, 258  
bicyclo[2.1.1]hexene 251  
bicyclo[3.1.0]hexyl tosylate 245  
bicyclo[2.2.0]cyclohexane 266  
 $\text{BiF}_3$  188  
 $\text{Bi}_2\text{Se}_3$  349  
bismethylenecyclobutane 269  
 $\text{Bi}_2\text{Te}_3$  349  
biquadratic spin exchange 785  
Blyholder model 700  
Bloch function 318, 321  
 $\text{BN}$  355  
 $\text{B}_2\text{N}$  111  
 $\text{B}_3\text{N}_3\text{H}_3$  295, 296  
 $\text{B}_4\text{N}_5\text{H}_6$  302  
 $\text{B}_2\text{N}_2\text{R}_4$  300, 307  
 $\text{B}(\text{OH})_3$  75  
 $\text{B}_2\text{O}$  111  
Bohlman band 226  
Boltzmann distribution 745  
bond order 103  
bond stretch isomerization 260  
bond valence 738, 739  
borazine 295, 296  
Bose-Einstein system 764

- boundary surface 2  
 $\text{BrF}_5$  75  
 bridging carbonyls 446, 447  
 Brillouin's theorem 166  
 Brillouin zone 339, 340  
 bromonium ion 265, 266  
 1,3-butadiene 177, 213  
 butadiene-Fe(CO)<sub>3</sub> 608  
 $\text{BrF}_3$  370, 371  
 $\text{BrF}_5$  369  
 $\text{C}_2$  102, 104, 118  
 $\text{C}_2^{2-}$  106, 107  
 $\text{C}_{60}$  282  
 $\text{C}_{78}$  282  
 $\text{CaBe}_2\text{Ge}_2$  378  
 $\text{Ca}_3\text{Co}_2\text{O}_6$  772, 773, 774  
 $\text{Ca}_3\text{ColrO}_6$  772  
 $\text{Ca}_3\text{CoRhO}_6$  772  
 $\text{CaCuGe}_2\text{O}_6$  788  
 $\text{Ca}_3\text{LiOsO}_6$  738, 739  
 $\text{Ca}_3\text{Mn}_7\text{O}_{12}$  761, 762, 766–767  
 strong Dzyaloshinskii-Moriya interaction 762  
 carbene complexes 410, 411, 413–415  
 carbon nanotube 282  
 $\text{CaSi}_2$  351  
 $\text{Ca}_2\text{Si}$  350  
 $\text{Cd}_2$  104  
 $\text{Cd}_2\text{Os}_2\text{O}_7$  741  
 $\text{CH}$  46  
 $\text{CH}_2$  133, 138, 145, 163, 170  
 $\text{CH}_2$ , dimerization of 218  
 $\text{CH}_2^{2+}$  198  
 $\text{CH}_3^-$  201  
 $\text{CH}_3^+$  185, 186  
 $\text{CH}_4$  49, 193, 199, 200  
 $\text{CH}_4^{2+}$  149, 197, 198, 201  
 $\text{CH}_5^+$  390, 391  
 $\text{C}_2\text{H}_2$  209, 210  
 $\text{C}_2\text{H}_4$  75, 209, 210, 219, 228  
 $\text{C}_2\text{H}_5^+$  223, 225  
 $\text{C}_2\text{H}_5^-$  225–227  
 $\text{C}_2\text{H}_6$  204–207  
 $\text{C}_2\text{H}_6^+$  207  
 $\text{C}_3\text{H}_4$  149  
 $\text{C}_3\text{H}_4\text{D}_2$  75  
 $\text{C}_5\text{H}_5^+$  261, 262, 263  
 $\text{C}_6\text{H}_6^{2+}$  isolobal analogs 628, 629  
 $\text{C}_6\text{H}_6^{2+}$  265  
 $\text{C}_6\text{H}_6^{2+}$  265  
 $\text{C}_7\text{H}_7^+$  75  
 $\text{C}_{18}\text{H}_{18}$  284  
 charge density wave 344  
 charge polarization 216  
 open versus closed bond-stretch isomer 262, 263  
 $\text{CH}_2\text{CH}=\text{O}$  192  
 $(\text{CH}_2)_2\text{ML}_4$  564  
 $\text{CH}_2\text{ML}_5$  498  
 $\text{CH}_2\text{NO}_2$  192  
 $\text{CH}_2=\text{O}$  227, 228  
 $\text{CH}_3\text{Mn}(\text{CO})_5$  519  
 $\text{CH}_3\text{OH}$  232  
 $\text{CH}_3\text{PtCl}_3^{2-}$  519  
 $(\text{C}_2\text{H}_4)\text{Ag}^+$  542, 543  
 $(\text{C}_2\text{H}_4)\text{M}_2\text{L}_{2n}$  545–547  
 $(\text{C}_2\text{H}_4)\text{Os}(\text{CO})_4$  542, 543  
 $(\text{C}_2\text{H}_4)_3\text{Ni}$  540, 541  
 $(\text{C}_2\text{H}_4)\text{Pt}(\text{PH}_3)_2$  542, 543  
 $\text{C}_5\text{H}_5\text{X}$  heterocycles 298, 299  
 $(\text{C}_2\text{R}_4)\text{Pt}(\text{PH}_3)_2$  543, 544  
 $\text{ClF}_3$  370, 371  
 $\text{Cl}_2$  102, 104  
 $\text{CIH}$  199, 200  
 closed-shell 153–158  
 Fock operator 154, 155  
 Coulomb operator 155  
 exchange operator 155  
 total electron-electron repulsion 156  
 total energy 156  
 SCF iteration 157  
 effective potential, occupied 158  
 unoccupied 158  
 singlet state 158  
 cluster electrons for inorganic fragments 666–669  
 cluster orbitals 657  
 $\text{Cl}_3\text{WC}_3\text{H}_3$  515–518  
 $(\text{C}_5\text{Me}_5)\text{B}-\text{Br}^+$  264  
 $\text{C}_5\text{Me}_5\text{-M}$  264  
 $\text{C}_5\text{Me}_5\text{Si}^+$  269  
 $\text{C}_6\text{Me}_6^{2+}$  264  
 $\text{CN}_2$  235  
 $\text{C}_4(\text{NR}_2)_2(\text{CO}_2\text{R})_2$  300  
 $\text{CO}$  46, 106, 107, 109  
 $\text{CO}_2$  235  
 $\text{Co}_2(\eta^5\text{-C}_5\text{Me}_5)_2(\mu\text{-CO})_2$  164  
 conduction band 315  
 configuration interaction 165  
 symmetry-forbidden reaction 167  
 $\text{CH}_2$  168, 169  
 conjugation in three dimensions 303  
 conrotatory electrocyclization 177  
 $\text{CO}$  on Ni(100), cluster model 704, 705  
 X-ray emission spectroscopy 710, 711  
 $\text{c}(2 \times 2)$  CO on Ni(100), DOS 700–704  
 X-ray emission spectroscopy 705, 706  
 COOP curve 324  
 Cooper pair 350  
 cooperative Jahn-Teller distortion 760  
 $\text{Co}(\text{PMe}_3)_4^+$  532  
 copper oxide superconductors 454  
 Coulomb repulsion 154, 155  
 $\text{CpAl}$  642, 643  
 $\text{CpCo}(\text{CO})_2$  549–552  
 $\text{Cp}_2\text{Co}_2(\text{tetramethylene})$  612  
 CpFe chains 588–591  
 $\text{CpFe}(\text{CO})_2^+$  551, 552  
 $\text{CpIr}(\text{NH})$  608  
 $\text{CpM}$  581–584  
 $\text{CpMn}(\text{CO})_2$  551, 552  
 $\text{CpMn}(\text{CO})_3$  578–580  
 $\text{Cp}_2\text{M}(\text{ethylene})_2$  coupling 605–607  
 $\text{Cp}_2\text{ML}_n$  595–597  
 $\text{Cp}_2\text{Mo}(\text{CO})$  610  
 $\text{Cp}_2\text{Mo}(\text{ethylene})$  610  
 $\text{Cp}_2\text{MR}_2$  reductive elimination 599, 600  
 $\text{CpMn}(\text{CO})_3$  579, 580  
 $\text{Cp}_3\text{NbH}_3$  598, 599  
 $\text{CpNi}(\text{NO})$  608, 609  
 $\text{Cp}_2\text{ReH}$  597, 598  
 $\text{Cp}_2\text{V}_2(\text{C}_6\text{H}_6)$  586–588  
 $\text{CpV}(\text{CO})_4$  561  
 $\text{Cp}_2\text{WH}_2$  598  
 $\text{Cp}_2\text{WO}$  600–603  
 $\text{Cr}(\text{CH}_3)_4$  451  
 $\text{Cr}(\text{CO})_5$  170, 468, 475–477  
 $\text{Cr}(\text{CO})_6$  164  
 $\text{Cr}(\text{CO})_6$  PE spectrum 408, 409  
 $\text{CrH}_6$  421, 422  
 cross-conjugated polyene 291  
 crystal orbital overlap population 324  
 $\text{Cs}_2\text{CuCl}_4$  751  
 $\text{Cs}_2\text{O}$  196  
 cubic lattice 345  
 $\text{CuBr}_2$  417, 770, 771  
 $\text{CuCl}_2$  769, 770, 771  
 $(\text{CuCl})\text{LaNb}_2\text{O}_7$  782–784  
 $\text{Cu}_3(\text{CO}_2)_2(\text{OH})_2$  766, 781, 782  
 $\text{CuO}_2^{2-}$  455, 456  
 $\text{CuO}_2$  ribbon chain 748, 754  
 $\text{Cu}_3(\text{OH})_4\text{SO}_4$  778, 779  
 $\text{Cu}_3(\text{P}_2\text{O}_6\text{OH})_2$  766  
 $\text{Cu}_2\text{Te}_2\text{O}_5\text{Br}_2$  789  
 $\text{Cu}_2\text{Te}_2\text{O}_5\text{Cl}_2$  789  
 cyclic polyenes 277, 278  
 cycloalkane isolobal analogs 623, 624  
 cyclobutane 77  
 in-plane  $\sigma$  orbitals 246–248  
 in caged structure 250  
 cyclobutadiene 92, 94  
 singlet versus triplet 285  
 cyclobutadiene-Fe(CO)<sub>3</sub> 580, 581  
 cyclobutene 177  
 cycloheptatriene 75  
 cyclohexane, monosubstituted 233  
 cyclohexane, 1,3,5-trimethyl 75  
 cyclooctatetraene 75  
 cyclopropane 241  
 in-plane  $\sigma$  orbitals of 242, 243  
 protonation of 245  
 cyclopropenium 93  
 cyclopropenium radical 266  
 cyclopropenyl 92

- cyclopentadienyl anion 120, 121  
 cyclotriplumbane 242
- 1,4-dehydrobenzene 307  
 deltahedra 654  
 density functional method 174  
 density of states 320  
 DFT+U method 737  
 diamond 347  
 diamond chain 780  
 diazabicyclooctane 253  
 diazanaphthalene 269  
 diazene-Cr(CO)<sub>5</sub> 523  
 1,1-dicarboxycyclopropane 245  
 2,3-dichloro-1,4-dioxane 233  
 Diels-Alder reaction 250  
 dimethylcyclopropyl carbocation 244  
 Dirac cones 349  
 Dirac point 349  
 direct product 65  
 disjoint degenerate orbital 290  
 disrotatory electrocyclization 177  
 double exchange 761  
 double zeta basis set 6  
 DOS plot 320  
 dynamic spin polarization 290, 291  
 Dzyaloshinskii-Moriya interaction 774–energy-mapping analysis 775
- effective nuclear charge 6  
 effective potential 8  
 electron correlation 165  
 main group atoms 27  
 electron affinity 160  
 ethylene 276  
 1,3-butadiene 276  
 1,3,5-hexatrene 276  
 electronegativity perturbation 97  
 electronegativity, scale 26  
 electron correlation 738  
 electron counting,  
   in hypervalent solid state compounds 376–380  
   in transition metal complexes 438–440  
 electron transmission spectroscopy 217  
 electron transfer, inner sphere 487, 488  
 elemental As 352  
 elemental black phosphorus 347  
 encapsulated atoms 670, 671  
 energy band 313  
 energy scale, magnetic field 743  
 ethylene, addition of singlet carbone on 246  
 ethylene, concerted dimerization of 249  
 ethylene-Fe(CO)<sub>4</sub> 533–535  
 (ethylene)<sub>2</sub>Fe(CO)<sub>3</sub>, C–C coupling reaction 511–515
- ethylene, isolobal analogs 624, 625  
 ethylene-ML<sub>2</sub> 539, 540  
 ethylene on metal surfaces 717, 718  
 (ethylene)PtCl<sub>3</sub><sup>−</sup> 520, 521  
 ethylene, trans-1,2-difluoro 75  
 exchange repulsion 154, 155  
   overlap density 161  
 excited state, singlet 159  
   triplet 159
- F<sub>2</sub> 101, 102, 104  
 F<sub>3</sub><sup>−</sup> 235  
 FCH<sub>2</sub>CH<sub>2</sub><sup>−</sup> 230  
 Fe(CO)<sub>4</sub> 170  
 Fe(CH<sub>3</sub>)<sub>4</sub> 451  
 Fe(CO)<sub>5</sub> 473, 474  
 Fe(CO)<sub>4</sub> 529–531  
 Fe<sub>2</sub>(CO)<sub>8</sub> 536, 537  
 Fe[C(SiMe<sub>3</sub>)<sub>3</sub>]<sub>2</sub> 771  
 Fermi surface 343, 344  
 Fermi surface nesting 344, 345  
 Fermi vector 319  
 ferrimagnetic-like transition 759  
   spin canting 759  
   Dzyaloshinskii-Moriya interaction 759  
 ferrocene 592–594  
 ferrocene isolobal analogs 629, 630  
 ferromagnetic ordering 459, 460  
 ferromagnetic transition 759  
   ferromagnetic domain 759  
   typical cases 760–  
 FH 199, 200  
 FH<sub>2</sub><sup>+</sup> 138, 139  
 field-induced three-dimensional ordering 764  
 first-order mixing 37, 39  
 Fischer-Tropisch process 728–730  
 fitting analysis, nonuniqueness of 753  
 FM-AFM chain 779  
 4n π electron system  
   cyclooctatetraene 282, 283  
   cyclobutadiene 283, 284  
   Jahn-Teller distortion 283  
   C<sub>4</sub>H<sub>4</sub><sup>2−</sup> 284  
 4n+2 π electron rule 281  
 fragment orbital 204  
 F<sub>4</sub>SCH<sub>2</sub> 393  
 F<sub>5</sub>SCH<sup>2−</sup> 393
- Ga<sub>2</sub> 104  
 GaIn<sub>2</sub> 355  
 GaS 352  
 Gaussian type orbital 5–7  
 Ge<sub>2</sub> 104  
 GeH<sub>2</sub> 138, 170  
 GeH<sub>3</sub> 189  
 Ge<sub>2</sub>H<sub>4</sub> 219  
 GdSi 350
- gold clusters 676  
 graphite 347, 348, 352  
 group theory 47
- H<sub>2</sub> 21, 22, 33, 38, 79, 171  
   solid 96  
   photoelectron spectrum 115  
 H<sub>3</sub>, linear 13, 38, 43, 69, 81, 109, 135  
   equilateral 79, 81, 135, 139, 140  
   isosceles 80, 135, 139, 140  
 H<sub>3</sub><sup>+</sup> 81, 82, 111, 225  
 H<sub>3</sub><sup>−</sup> 81, 82, 111, 227  
 H<sub>4</sub>, rectangular 82, 83  
   square planar 44, 82, 83, 85  
   tetrahedral 73, 84, 85  
   linear 85  
   D<sub>3h</sub> 121  
 H<sub>4</sub><sup>2+</sup> 85  
 H<sub>4</sub><sup>−</sup> 85  
 H<sub>5</sub>, pentagonal 88, 90  
   square pyramid 94  
   trigonalbipyramidal 95  
 H<sub>5</sub><sup>+</sup> 95  
 H<sub>6</sub>, hexagonal 88, 89, 95  
   octahedral 95, 121, 122  
 H<sub>n</sub>, cyclic 92  
   Hückel 93  
   Möbius 93  
 H<sub>4</sub>A<sub>3</sub> 148  
 Hartree-Fock method 165, 174  
 HC 181, 182  
 HClI<sub>3</sub> 196  
 (H<sub>3</sub>C)<sub>3</sub>P 236  
 H<sub>3</sub>C-S-CH<sub>3</sub> 236  
 HCr<sub>2</sub>(CO)<sub>10</sub><sup>−</sup> 482, 483  
 He<sub>2</sub> 24  
 HF 38, 42, 43, 181, 182  
 Hg<sub>2</sub> 104  
 H-He<sup>+</sup> 33, 34  
 high-spin versus low-spin 353  
 H<sub>2</sub>N-BH<sub>2</sub> 214  
 H<sub>2</sub>NCHO 91, 196  
 H<sub>2</sub>N-OH 201, 202  
 HO<sup>−</sup> 165  
 H<sub>2</sub>O 48, 70, 127, 128, 133, 137–139, 141–144  
 H<sub>2</sub>O<sub>2</sub> 75  
 H<sub>3</sub>P<sup>+</sup>-CH<sub>2</sub><sup>−</sup> 231  
 H<sub>2</sub>PCH=O 191, 196  
 H<sub>2</sub>S 131  
 H<sub>2</sub>Se 137, 138, 144  
 H<sub>3</sub>Si-O-SiH<sub>3</sub> 231  
 H<sub>3</sub>Si-S-SiH<sub>3</sub> 236  
 (H<sub>3</sub>Si)<sub>3</sub>P 236  
 H<sub>2</sub>SiSiH<sub>2</sub> 234, 235  
 H<sub>2</sub>Te 137, 138, 144  
 Hückel theory 274, 275, 276  
   valence ionization potential 146  
 Hund's rule 18

- $\text{H}_2\text{Fe}(\text{CO})_4$  559–561  
 $\text{H}_2\text{ML}_5$  499  
 $\text{H}_2$  on Cu surfaces 719–721  
 $\text{H}_2\text{S}^+ \text{CH}_2^-$  222  
hopping integral 11  
*cis,trans*-1,3,5-hexatriene 214  
hybrid functional method 738
- $\text{I}_2$  104  
idle spin 778, 779  
 $\text{In}_2$  104  
inelastic neutron scattering 745  
insulator 315  
ionization potentials  
     $\text{C}_5\text{H}_5\text{X}$  heterocycles 298, 299  
    donor substituted arenes 297  
    ethylene 276  
    1,3-butadiene 276  
    1,3,5-hexatrene 276  
     $\text{H}_3\text{Si}(\text{SiH}_2)_n\text{SiH}_3$  276  
ionization potential 160  
ionization potential, vertical 114  
    adiabatic 114  
isolobal caveats 621–623  
isolobal definition of 616  
isolobal fragments generation of 617, 618  
isolobal reactions 634–639  
7-isopropylidenenorbonadiene 304, 305
- Jahn-Teller distortion  
    first order 134, 135  
    pseudo Jahn-Teller 136  
        square  $\text{H}_4$  136  
        cyclobutadiene 136  
    second-order 136, 137, 238
- $\text{K}_2$  104  
 $\text{KCuF}_3$  760  
 $\text{K}_3\text{In}_2\text{As}_3$  356  
Koopmans' theorem 113, 114, 161  
 $\text{K}_4\text{P}_2\text{Be}$  355  
 $\text{K}_2\text{PdP}_2$  547–549  
Kramers degeneracy theorem 787  
 $\text{KrF}_6$  362  
 $\text{K}_4\text{Si}_4$  351  
 $\text{K}_5\text{TiO}_4$  355
- $\text{La}_2\text{CdGe}_2$  380–383  
 $\text{LaCuO}_4$  453  
ladder operators, spin 746  
    orbital 767  
 $\text{LaGaBi}_2$  379  
laticyclic 306  
 $\text{Li}_2$  102, 103, 104  
 $\text{LiCuVO}_4$  748, 754, 769–771  
Lifshitz salts 453  
 $\text{LiH}$  31  
 $\text{LiH}_3$  201
- linear chain polyene 273  
 $\text{Li}_2\text{O}$  196  
 $\text{Li}_2\text{Sb}$  377  
 $\text{LiSn}$  380  
 $\text{Li}_3\text{Al}_2$  356  
 $\text{Li}_9\text{Ge}_4$  356  
longicyclic 304  
long-range antiferromagnetic ordering 755, 756  
    magnetic entropy 756  
    magnetic susceptibility 756  
low versus high spin state 162
- magnetic bonds 735  
magnetic d-block levels 736  
magnetic dipole-dipole interaction 754, 758  
    Ewald summation method 758  
ferromagnetic domains 759  
 $\text{Dy}_2\text{Ti}_2\text{O}_7$  758  
 $\text{Ho}_2\text{Ti}_2\text{O}_7$  758  
    spin ice 758  
     $\text{Sr}_3\text{Fe}_2\text{O}_5$  758  
magnetic insulating 736, 737  
magnetic metallic 737  
magnetic moment, isotropic 741  
    uniaxial 741  
magnetization, magnetic bonding 743  
    magnetic antibonding 743  
magnetization plateau 765  
    energy gap 765  
    finite magnetization plateau 765  
    zero magnetization plateau 765  
magnetic specific heat 745  
magnetic susceptibility 743, 744  
    Curie-Weiss temperature 744  
    effective moment 744  
    mean-field approximation 744  
mapping analysis 745–748  
    based on broken-symmetry states 751–754  
 $\text{MCl}_3$  chains 611, 612  
 $\text{M}_2\text{Cl}_9^{3-}$  610, 611  
 $\text{M}(\text{CO})_6$  bonding in 409, 410  
MCSCF 172  
metal 315  
metallabenzenes 432  
metallacyclobutadiene 432, 515–518  
metallacyclopropanes versus metal-olefins 541–544, 620–621  
metallocenes 592–595  
metal-metal bonds electron counting in 445, 446  
 $\text{Mg}_2$  102, 103  
 $\text{MgB}_2$  350  
 $\text{MgH}_2$  133  
 $\text{M}(\text{H}_2\text{O})_6^{2+}$  431  
Miller indices 694  
 $\text{ML}_2 \text{C}_{2v}$  537–539
- $\text{ML}_3 \text{C}_{2v}$  503  
 $\text{C}_{3v}$  570–574  
 $\text{ML}_4 \text{C}_{2v}$  527–529  
 $\text{D}_{4h}$  436–438  
    square planar to tetrahedral 448–452  
 $\text{ML}_4\text{X}$  chains 423, 424  
 $\text{ML}_5 \text{C}_{4v}$  466–468  
 $\text{ML}_5\text{L-M-L}$  bending 469–471  
 $\text{ML}_5\text{C}_{4v}$  to  $\text{D}_{3h}$  471–473  
 $\text{ML}_5$ , alternate geometries 474, 475  
 $\text{ML}_5$ ,  $\pi$  effects 478–480  
 $\text{ML}_7 \text{D}_{5h}$  500  
 $\text{M}_2\text{L}_{10}\text{X}$  distortions 484–489  
 $\text{ML}_n$ , generalized interaction diagram 439  
 $\text{ML}_6$ , octahedral 403, 404  
mno rule 677, 678  
 $\text{Mo}(\text{CO})_6$  PE spectra 408, 409  
 $\text{Mn}(\text{CO})_6^+$  164  
Möller-Plesset perturbation theory 172, 173  
molecular Hamiltonian 152  
molecular vibration 73  
    of  $\text{H}_2\text{O}$  74, 75  
multiconfiguration wavefunction 165
- $\text{N}_2$  102, 103, 109, 112, 113, 117  
    photoelectron spectrum 116  
 $\text{Na}_2$  102, 104  
 $\text{Na}_3\text{Cu}_2\text{SbO}_6$  779  
 $\text{Na}_3\text{Cu}_2\text{TeO}_6$  779  
 $\text{Na}_2\text{Fe}(\text{CO})_4$  531  
 $\text{NaMnP}$  457, 458  
 $\text{NaOsO}_3$  738, 739, 741  
 $\text{Na}_2\text{OsO}_4$  738, 739  
naphthalene 161, 294  
    ionization potential 162  
    electronaffinity 162  
    excitation energy 162
- $\text{Nb}_2$  119  
 $\text{NbCl}_4$  chains 424, 425  
 $\text{NbCl}_5\text{O}^{2-}$  431  
 $\text{NbO}$  197, 462, 463  
 $\text{N}(\text{CH}_3)_3$  188, 190  
 $\text{Ne}$  199  
 $\text{Ne}_2$  24, 102  
 $\text{NF}_3$  188, 190  
 $\text{NH}_2$  133, 145  
 $\text{NH}_2^-$  138, 139  
 $\text{NH}_2\text{NH}_2$  222  
 $\text{NH}_3$  48, 184, 188, 190, 199, 200, 201  
 $\text{NH}_3^+$  189  
 $\text{NH}_4^+$  193  
 $\text{Ni}(100)$ , surface band structure 692, 693  
 $\text{Ni}(\text{CO})_4$  450  
 $\text{NiF}_4^{2-}$  452  
 $\text{NiH}_3^-$  bending 505, 506

- Ni(PF<sub>3</sub>)<sub>4</sub>** 450  
**Ni(PPPh<sub>3</sub>)<sub>3</sub>** 506  
**Ni(PPPh<sub>3</sub>)<sub>3</sub><sup>+</sup>** 506  
nitrosyl bending in ML<sub>5</sub> complexes 489–492  
N-R fragments 642–644  
N<sub>2</sub> on Ni(110) 712  
NO on Ni(111) 713, 714  
N<sub>2</sub>O 111  
norbornadiene 305  
nodal plane 3, 5  
noncrossing rule 67, 68  
reaction coordinate 68  
avoided crossing 68  
HOMO-LUMO crossing 68  
symmetry-forbidden 68  
noncollinear spin arrangement 754  
non-magnetic metallic 737  
nondisjoint orbital 292  
N(SiMe<sub>3</sub>)<sub>3</sub> 231  
N(SiH<sub>3</sub>)<sub>3</sub> 192  
nucleophilic attack on metal-olefins 544, 545  
O<sub>2</sub> 101, 102, 104  
octahedron orbitals 658–660  
octahedron -  $\pi$  effects 406–412  
OF<sub>2</sub> 61, 235  
OH<sub>2</sub> 199, 200  
OH<sub>3</sub><sup>+</sup> 201  
Os(CO)<sub>4</sub> 531  
Os(N-Ar)<sub>3</sub> 511  
olefin insertion 521–523, 603–605  
olefin-ML<sub>4</sub> 533–535  
on-site repulsion 738  
O<sub>2</sub>ML<sub>5</sub> M-O-O bending 499, 500  
O<sub>2</sub> on metal surfaces 714–717  
operator, projection 63  
orbital correlation diagram 81  
orbital hybridization 97, 98  
orbital moment quenching 742  
orbital ordering 760  
orbital interaction, 16–24  
degenerate 16, 21  
high-spin 18  
low-spin 18  
nondegenerate 18, 22, 23  
two-orbital four-electron 17, 18, 20, 24  
two-orbital two-electron 17, 18, 20, 24  
overlap integral 8–11  
angular dependence 10, 11  
molecular basis 35  
type 9  
overlap density 287  
exchange integral 287  
oxidative addition 552–560  
oxyallyl 307  
P<sub>2</sub> 102, 103, 104, 117  
P<sub>4</sub> 75  
P<sub>6</sub><sup>4-</sup> 297  
Pauli exclusion principle 153  
Pauli repulsion 6  
PbO 395, 396  
PbTiO<sub>3</sub> 428, 429  
P(CH<sub>3</sub>)<sub>3</sub> 188  
Pd<sub>3</sub>Cl<sub>9</sub><sup>3-</sup> 525  
pentalene, inorganic 302  
pentalene-TaCl<sub>3</sub> 612  
perovskites 429  
perturbation  
degenerate 43, 44  
electronegativity 32, 34  
geometry 32, 34, 129  
intermolecular 32, 34, 35, 43  
nondegenerate 44  
PF<sub>3</sub> 188  
PF<sub>5</sub> 75, 388–390  
PH<sub>2</sub> 133  
PH<sub>3</sub> 186, 188, 189, 199  
(Ph<sub>3</sub>P)<sub>3</sub>RhCl 532  
PH<sub>5</sub> 392  
PH<sub>2</sub>NH<sub>2</sub> 223  
photoelectron spectroscopy 113, 114  
photoelectron spectrum  
acrylonitrile 215  
allene 237  
barralene 305  
benzene 281, 308  
B<sub>2</sub>H<sub>6</sub> 211  
bicyclo[2.2.0]octane 305  
bicyclo[2.2.0]octadiene 305  
1,3-butadiene 306  
1,3-butadiyne 306  
C<sub>60</sub> 281  
C<sub>2</sub>H<sub>2</sub> 210  
C<sub>2</sub>H<sub>4</sub> 210, 211  
C<sub>2</sub>H<sub>6</sub> 210  
CO on Ni(100) 699, 700  
CO<sub>2</sub> 235  
CpMn(CO)<sub>3</sub> 579, 580  
CpCo(CO)<sub>2</sub> 551  
Cp<sub>2</sub>V<sub>2</sub>(C<sub>6</sub>H<sub>6</sub>) 586–588  
cyclopropene 268  
cyclopropane 268  
diazabicyclooctane 254  
ethylene 308  
Fe(CO)<sub>5</sub> 473, 474  
H<sub>2</sub>C=NH 235  
H<sub>2</sub>C=PH 235  
7-isopropylidenenorbonadiene 305  
methylenecyclopropane 268  
methylenecyclopentene 268  
N<sub>2</sub>O 235  
hexafluorobenzene 308  
N<sub>2</sub> on Ni(110) 712  
naphthalene 309  
Ni(CO)<sub>4</sub> 450  
Ni(PF<sub>3</sub>)<sub>4</sub> 450  
octafluoronaphthalene 309  
pentafluoropyridine 309  
poly-ynes 310  
pyridine 309  
Re<sub>2</sub>Cl<sub>8</sub><sup>2-</sup> 535, 536  
Re<sub>2</sub>(CO)<sub>10</sub> 481, 482  
phosphorescence 777  
PH<sub>2</sub>PH<sub>2</sub> 222  
 $\pi$ -bonding effect 190, 191  
pointgroup 51  
Abelian 53, 57  
conjugacy class 52  
linear 58  
order 51  
product 58  
Schoenflies symbol 52  
polarization function 6  
polyacene 356  
polyacetylene 329  
electronegativity perturbation 332  
Peierls distortion 330  
soliton 332  
polydiazacene 357  
polyene 78  
polyorganonitrile 333  
population, 29–31  
gross 29  
Mulliken 29  
net 28  
overlap 28  
two-orbital two electron 30  
two-orbital four electron 30  
preferred spin orientation 767  
DFT+U+SOC calculations 768  
SOC Hamiltonian as  
perturbation 768–769  
propellane 259  
PtCl<sub>3</sub><sup>-</sup> 504, 505  
PtCl<sub>4</sub><sup>2-</sup> 75  
PtCl<sub>6</sub><sup>2-</sup> 75  
Pt<sub>3</sub>(CNR)<sub>6</sub> 563, 564  
PtH<sub>4</sub><sup>2-</sup> 48, 51  
PtF<sub>4</sub><sup>2-</sup> 452  
Pt(PPh<sub>3</sub>)<sub>3</sub> 506  
Pt<sup>2+</sup>/Pt<sup>4+</sup> mixed valence chains 488, 489  
pyridine 109, 110, 308  
pyrrole 120, 121  
radial function 2, 5  
radial node 3, 4, 6  
Rb<sub>2</sub> 104  
Rb<sub>4</sub>P<sub>6</sub> 297  
Re<sub>2</sub>Cl<sub>8</sub><sup>2-</sup> 535, 536  
Re<sub>3</sub>Cl<sub>9</sub> 564–566

- $\text{Re}_2\text{Cl}_{10}^{4-}$  480–482  
 $\text{Re}_2(\text{CO})_{10}$  480–482  
 $\text{Re}_2(\text{CO})_{10}$  481, 482  
 reductive elimination 552–560  
 $\text{ReO}_3$  433  
 representation 53  
 basis of 54, 55  
 character of 55  
 character table 57, 62  
 dimension 56, 58  
 irreducible 56, 59  
 order of 57  
 reducible 56, 59  
 totally symmetric 57, 66  
 resonance integral 11  
 molecular basis 35  
 Wolfsberg–Helmholtz formula 11, 34, 105  
 retinal 214  
 $\text{Rh}(\text{PMe}_3)_4^+$  532  
 $\text{Rh}(\text{PPh}_3)_3^+$  507  
 ring whizzing 634–636  
 $(\text{RO})_3\text{Ta}(\text{BH}_3)$  609  
 $\text{R}_3\text{P}-\text{Au}$  201  
 $(\text{R}_3\text{P})_6\text{Ru}_2\text{H}_3^{2+}$  610  
 $\text{Ru}(\text{C}_6\text{F}_5\text{S})_2(\text{PPh}_3)_2$  532  
 $\text{Ru}(\text{CO})_4$  531  
 $\text{Ru}_3(\text{CO})_{12}$  562  
 Rundle–Pimentel bonding scheme 361  
 Ruddlesden–Popper phases 425, 426  
 $\text{Ru}(\text{NMe}_2)_2(\text{CO})_4$  432
- $\text{S}_2$  102, 103, 104  
 $\text{Sb}_2$  104  
 $\text{Sb}(\text{CH}_3)_3$  188  
 $\text{SbF}_3$  188  
 $\text{SbH}_3$  188, 189  
 $\text{Sb}_2\text{Te}_3$  349  
 $\text{S}(\text{t-Bu})_2$  147  
 $\text{S}(\text{CH}_3)_2$  147  
 Schlenk's hydrocarbon 293  
 Schmidt orthogonalization 64  
 $\text{Se}_2$  104  
 $\text{Se}_3\text{Br}_8^{2-}$  75  
 $\text{Se}_4\text{Br}_{14}^{2-}$  394  
 second-order energy correction 38  
 second-order mixing 37, 38, 39  
 secular equation 12, 13  
 secular determinant 13  
 self-consistent-field 36  
 semibullvalene 251  
 $\text{SF}_4$  62, 373, 386, 387  
 $\text{SF}_6$  d orbitals in 361, 362  
 $\text{SH}_2$  133, 137, 138, 141, 144, 170  
 photoelectron spectrum 145, 147  
 valence ionization potential 146  
 $\text{SH}_2$  199, 200  
 $\text{SH}_4$  148
- $\text{SH}_6$  360  
 short-range order 763  
 susceptibility maximum 763  
 $\text{Si}_2$  102, 104  
 $\text{Si}_4^{6-}$  chain 338  
 $\text{SiH}_3$  189  
 $\text{SiH}_4$  199, 200  
 $\text{Si}_2\text{H}_4$  219  
 $\text{Si}$  (100) surface reaction with acetylene 725, 726  
 $\text{Si}$  (100) surface reaction with  $\text{H}_2\text{O}$ ,  $\text{H}_3\text{N}$  and  $\text{H}_2$  726, 727  
 $\text{Si}$  (100) surface symmetric dimer model 721, 723–725  
 $\text{Si}$  (100) surface unsymmetric dimer model 721–723  
 sigmatropic rearrangements 634–636  
 single-ion anisotropy 770  
 zero-field spin Hamiltonian 770  
 effective spin approximation 770  
 easy-axis anisotropy 769  
 easy-plane anisotropy 771  
 Slater determinant 153  
 Slater transition 741  
 Slater type orbitals 5–7  
 $\text{Sn}_2$  104  
 $\text{SnH}_3$  189  
 $\text{Sn}_2\text{H}_4$  219  
 $\text{S}_2\text{N}_2$  295, 297, 300  
 $\text{S}_3\text{N}_3^-$  296, 297  
 $\text{S}_4\text{N}_4$  300, 301  
 $\text{S}_4\text{N}_4^{2+}$  301  
 $(\text{SN})_x$  333  
 $\text{SO}_2$  PE spectrum 393  
 spin exchange parameter 290  
 spin dimer 745  
 spin exchange,  
 symmetric 745  
 Heisenberg 745  
 through-space interaction 748–749, 751  
 through-bond interaction 748–751  
 spin frustration 754  
 equilateral triangle 755  
 frustration index 755  
 Kagome lattice 755  
 pyrochlore lattice 755  
 triangular lattice 755  
 spin gap 763  
 magnetic field-induced magnetic order 763  
 Haldane conjecture 763  
 $\text{Ni}(\text{C}_2\text{H}_8\text{N}_2)_2\text{NO}_2(\text{ClO}_4)$  763  
 spin dimer 764  
 alternating chain 764  
 two-leg ladder 764  
 spin Hamiltonian 735, 736  
 spin lattice 735
- spin-orbit coupling 736, 766  
 spin-conserving term 768  
 spin-nonconserving term 768  
 singlet-triplet mixing 777  
 spin polarization  
 in a  $\pi$  radical 285, 286  
 allyl radical 288  
 spin-wave dispersion 745  
 spiral spin arrangement 754  
 cycloidal 754  
 helical 754  
 spiro-antiaromatic 303  
 spiro-aromatic 303  
 spiro-nonatetraene 304  
 spiro-octatrienylcation 304  
 square cyclobutadiene  
 singlet versus triplet state 289  
 square hydrogen net 340, 341–343  
 square lattice 340  
 $\text{SrCa}_2\text{In}_2\text{Ge}$  351, 354  
 $\text{Sr}_2\text{CuOsO}_6$  738, 739  
 $\text{SrFeO}_2$  460, 757, 769  
 $\text{Sr}_3\text{Fe}_2\text{O}_5$  756–758, 769  
 $\text{Sr}_3\text{In}_5$  398  
 $\text{Sr}_2\text{NiOsO}_6$  738, 739  
 state averaged ionization potential,  
 charging effect 26  
 relativistic effect 26  
 screening 25  
 s-p energy gap 25, 26  
 substituent effect 214  
 methyl substituted olefin 217  
 substituted olefin 216  
 sudden polarization 211, 213  
 superconductivity 349  
 superexchange 749  
 Goodenough–Kanamori rule 751  
 super-superexchange 749  
 surface reconstructions transition metals 695  
 symmetry operations 48  
 rotation 48  
 improper rotation 48  
 horizontal mirror plane 48  
 vertical mirror plane 48  
 inverse 50  
 symmetry of spin  
 inversion 786  
 mirror plane of symmetry 786, 787  
 time reversal 787
- $\text{Te}_4^{2+}$  397  
 tetracyanoethylene 217  
 tetragonal distortions 416, 417  
 tetrahedrane isolobal analogs 626, 627  
 tetramethyleneethane 293  
 tetrasilabicyclobutane,  $\text{Si}_4\text{H}_6$  260  
 tetrathiafulvalene 217

- TCNQ 337  
 $\text{Te}_2$  104  
three-center bonding 139  
  two-electron 140  
  four-electron 139, 140, 141  
three-orbital problem 38  
through-bond coupling units 256  
through-bond conjugation 112, 113, 116  
through-bond interaction 241, 253  
through-space conjugation 304  
through-space interaction 241  
 $\text{TiCl}_4$  451  
 $\text{TiO}$  197  
 $\text{TiO}_2$  430, 431  
TMTSF 337  
TMTTF 337  
topological charge stabilization 302  
topological insulator 349  
transition metals kink 695  
transition metals step 695  
transition metals structure 693, 694  
transition metals terrace 695  
tricyclooctadiene 251  
  ethylene and cyclobutane units of 251  
  butadiene and cyclobutane units of 252  
tricyclo-3,7-octadiene 255  
trigonal pyramid orbitals 658–660  
2,4,6-trimethyl-1,3-dioxane 233  
trimethylenemethane 291, 307  
trimethylenemethane- $\text{Fe}(\text{CO})_3$  607  
triple-decker sandwiches 585–588  
tris(acetylene) $\text{W}(\text{PMe}_3)_3$  444  
TTF 337  
uniaxial magnetism 771  
  versus Jahn-Teller instability 771, 774  
  g-factor 772  
valence band 315  
valence shell electron pair repulsion model 141, 365, 366  
van Hove singularity 320  
variational theorem 5, 12, 13  
 $\text{V}_2\text{O}_5$  492–494  
 $\text{V}(\text{CO})_6^-$  164  
Wade's rules 660–663  
Wade's rules violations 671–676  
Walsh diagram 131, 135  
wavevector 317  
William's rules 663–666  
Wolsberg-Helmholz approximation 131  
Wood's notation 696, 697  
Wurtzite surface 730, 731  
 $\text{WC}_3$  575–577  
 $\text{W}_2(\text{carboxylate})_4$  PE spectrum 536  
 $\text{W}_2\text{Cl}_6$  75, 574  
 $\text{W}(\text{CH}_3)_6$  421  
 $\text{W}(\text{CO})_6$  PE spectra 408, 409  
 $\text{WF}_6$  421  
 $\text{WH}_6$  421  
 $\text{WS}_2$  433  
 $\text{XCH}_2\text{CH}_2^-$  229  
 $\text{XCH}_2\text{OH}$  232, 233  
 $\text{XeF}_3^-$  385  
 $\text{XeF}_3^+$  385  
 $\text{XeF}_5^-$  366, 367  
 $\text{XeF}_6$  364  
 $\text{YBa}_2\text{Cu}_3\text{O}_7$  494–496  
Zeeman interaction 742  
zero-field splitting Hamiltonian 787  
Ziegler-Natta polymerization 603–605  
Zintl-Klemm concept 350  
 $\zeta$  value, electronegativity 5  
 $\zeta$  value, energy optimized 5  
 $\text{Zn}_2$  104  
 $\text{ZnS}$  352  
 $\text{ZrS}_2$  433  
zwitterionic 212, 213